

# Mathematical Modeling and Optimization of Industrial Problems

Guest Editors: M. Montaz Ali, Aderemi O. Adewumi, Nachamada Blamah,  
and Olabisi Falowo





---

# **Mathematical Modeling and Optimization of Industrial Problems**

Journal of Applied Mathematics

---

## **Mathematical Modeling and Optimization of Industrial Problems**

Guest Editors: M. Montaz Ali, Aderemi O. Adewumi,  
Nachamada Blamah, and Olabisi Falowo



---

Copyright © 2015 Hindawi Publishing Corporation. All rights reserved.

This is a special issue published in "Journal of Applied Mathematics." All articles are open access articles distributed under the Creative Commons Attribution License, which permits unrestricted use, distribution, and reproduction in any medium, provided the original work is properly cited.

## Editorial Board

- Saeid Abbasbandy, Iran  
Mina B. Abd-El-Malek, Egypt  
Mohamed A. Abdou, Egypt  
Subhas Abel, India  
Mostafa Adimy, France  
Carlos J. S. Alves, Portugal  
Mohamad Alwash, USA  
Igor Andrianov, Germany  
Sabri Arik, Turkey  
Francis T.K. Au, Hong Kong  
Olivier Bahn, Canada  
Roberto Barrio, Spain  
Alfredo Bellen, Italy  
Jafar Biazar, Iran  
Hester Bijl, The Netherlands  
Anjan Biswas, Saudi Arabia  
Stephane P.A. Bordas, USA  
James Robert Buchanan, USA  
Alberto Cabada, Spain  
Xiao Chuan Cai, USA  
Jinde Cao, China  
Alexandre Carvalho, Brazil  
Song Cen, China  
Qianshun S. Chang, China  
Tai-Ping Chang, Taiwan  
Shih-sen Chang, China  
Rushan Chen, China  
Xinfu Chen, USA  
Ke Chen, UK  
Eric Cheng, Hong Kong  
Francisco Chiclana, UK  
Jen-Tzung Chien, Taiwan  
C. S. Chien, Taiwan  
Han H. Choi, Republic of Korea  
Tin-Tai Chow, China  
M. S. H. Chowdhury, Malaysia  
Carlos Conca, Chile  
Vitor Costa, Portugal  
Livija Cveticanin, Serbia  
Eric de Sturler, USA  
Orazio Descalzi, Chile  
Kai Diethelm, Germany  
Vit Dolejsi, Czech Republic  
Bo-Qing Dong, China  
Magdy A. Ezzat, Egypt
- Meng Fan, China  
Ya Ping Fang, China  
Antonio J. M. Ferreira, Portugal  
Michel Fliess, France  
M. A. Fontelos, Spain  
Huijun Gao, China  
Bernard J. Geurts, The Netherlands  
Jamshid Ghaboussi, USA  
Pablo González-Vera, Spain  
Laurent Gosse, Italy  
K. S. Govinder, South Africa  
Jose L. Gracia, Spain  
Yuantong Gu, Australia  
Zhihong GUAN, China  
Nicola Guglielmi, Italy  
Frederico G. Guimarães, Brazil  
Vijay Gupta, India  
Bo Han, China  
Maoan Han, China  
Pierre Hansen, Canada  
Ferenc Hartung, Hungary  
Xiaoqiao He, Hong Kong  
Luis Javier Herrera, Spain  
J. Hoenderkamp, The Netherlands  
Ying Hu, France  
Ning Hu, Japan  
Zhilong L. Huang, China  
Kazufumi Ito, USA  
Takeshi Iwamoto, Japan  
George Jaiani, Georgia  
Zhongxiao Jia, China  
Tarun Kant, India  
Ido Kanter, Israel  
Abdul Hamid Kara, South Africa  
Hamid Reza Karimi, Norway  
Jae-Wook Kim, UK  
Jong Hae Kim, Republic of Korea  
Kazutake Komori, Japan  
Fanrong Kong, USA  
Vadim . Krysko, Russia  
Jin L. Kuang, Singapore  
Mirosław Lachowicz, Poland  
Hak-Keung Lam, UK  
Tak-Wah Lam, Hong Kong  
PGL Leach, Cyprus
- Yongkun Li, China  
Wan-Tong Li, China  
J. Liang, China  
Ching-Jong Liao, Taiwan  
Chong Lin, China  
Mingzhu Liu, China  
Chein-Shan Liu, Taiwan  
Kang Liu, USA  
Yansheng Liu, China  
Fawang Liu, Australia  
Shutian Liu, China  
Zhijun Liu, China  
Julián López-Gómez, Spain  
Shiping Lu, China  
Gert Lube, Germany  
Nazim Idrisoglu Mahmudov, Turkey  
Oluwole Daniel Makinde, South Africa  
Francisco J. Marcellán, Spain  
Guiomar Martín-Herrán, Spain  
Nicola Mastronardi, Italy  
Michael McAleer, The Netherlands  
Stephane Metens, France  
Michael Meylan, Australia  
Alain Miranville, France  
Ram N. Mohapatra, USA  
Jaime E. Munoz Rivera, Brazil  
Javier Murillo, Spain  
Roberto Natalini, Italy  
Srinivasan Natesan, India  
Jiri Nedoma, Czech Republic  
Jianlei Niu, Hong Kong  
Roger Ohayon, France  
Javier Oliver, Spain  
Donal O'Regan, Ireland  
Martin Ostoja-Starzewski, USA  
Turgut Öziş, Turkey  
Claudio Padra, Argentina  
Reinaldo Martinez Palhares, Brazil  
Francesco Pellicano, Italy  
Juan Manuel Peña, Spain  
Ricardo Perera, Spain  
Malgorzata Peszynska, USA  
James F. Peters, Canada  
Mark A. Petersen, South Africa  
Miodrag Petkovic, Serbia

Vu Ngoc Phat, Vietnam  
Andrew Pickering, Spain  
Hector Pomares, Spain  
Maurizio Porfiri, USA  
Mario Primicerio, Italy  
Morteza Rafei, The Netherlands  
Roberto Renò, Italy  
Jacek Rokicki, Poland  
Dirk Roose, Belgium  
Carla Roque, Portugal  
Debasish Roy, India  
Samir H. Saker, Egypt  
Marcelo A. Savi, Brazil  
Wolfgang Schmidt, Germany  
Eckart Schnack, Germany  
Mehmet Sezer, Turkey  
Naseer Shahzad, Saudi Arabia  
Fatemeh Shakeri, Iran  
Jian Hua Shen, China  
Hui-Shen Shen, China  
Fernando Simões, Portugal  
Theodore E. Simos, Greece

Abdel-Maksoud A. Soliman, Egypt  
Xinyu Song, China  
Qiankun Song, China  
Yuri N. Sotskov, Belarus  
Peter J. C. Spreij, The Netherlands  
Niclas Strömberg, Sweden  
Ray KL Su, Hong Kong  
Jitao Sun, China  
Wenyu Sun, China  
XianHua Tang, China  
Alexander Timokha, Norway  
Mariano Torrisi, Italy  
Jung-Fa Tsai, Taiwan  
Ch Tsitouras, Greece  
Kuppalapalle Vajravelu, USA  
Alvaro Valencia, Chile  
Erik Van Vleck, USA  
Ezio Venturino, Italy  
Jesus Vigo-Aguiar, Spain  
Michael N. Vrahatis, Greece  
Baolin Wang, China  
Mingxin Wang, China

Qing-Wen Wang, China  
Guangchen Wang, China  
Junjie Wei, China  
Li Weili, China  
Martin Weiser, Germany  
Frank Werner, Germany  
Shanhe Wu, China  
Dongmei Xiao, China  
Gongnan Xie, China  
Yuesheng Xu, USA  
Suh-Yuh Yang, Taiwan  
Bo Yu, China  
Jinyun Yuan, Brazil  
Alejandro Zarzo, Spain  
Guisheng Zhai, Japan  
Jianming Zhan, China  
Zhihua Zhang, China  
Jingxin Zhang, Australia  
Shan Zhao, USA  
Chongbin Zhao, Australia  
Renat Zhdanov, USA  
Hongping Zhu, China

# Contents

**Mathematical Modeling and Optimization of Industrial Problems**, M. Montaz Ali, Aderemi O. Adewumi, Nachamada Blamah, and Olabisi Falowo  
Volume 2015, Article ID 438471, 3 pages

**Improved Crosstalk Reduction on Multiview 3D Display by Using BILS Algorithm**, Xiaoyan Wang and Chunping Hou  
Volume 2014, Article ID 428602, 13 pages

**An Efficient Biobjective Heuristic for Scheduling Workflows on Heterogeneous DVS-Enabled Processors**, Pengji Zhou and Wei Zheng  
Volume 2014, Article ID 370917, 15 pages

**Intelligent Inventory Control via Ruminative Reinforcement Learning**, Tatpong Katanyukul and Edwin K. P. Chong  
Volume 2014, Article ID 238357, 8 pages

**An Analytical Solution by HAM for Nonlinear Simulation of Deepwater SCR Installation**, Yi Wang, Ji-jun Gu, Chen An, Meng-lan Duan, and Ning He  
Volume 2014, Article ID 801781, 9 pages

**A Scheduling Problem in the Baking Industry**, Felipe Augusto Moreira da Silva, Antonio Carlos Moretti, and Anibal Tavares de Azevedo  
Volume 2014, Article ID 964120, 14 pages

**TLCD Parametric Optimization for the Vibration Control of Building Structures Based on Linear Matrix Inequality**, Linsheng Huo, Chunxu Qu, and Hongnan Li  
Volume 2014, Article ID 527530, 10 pages

**Modeling and Model Predictive Power and Rate Control of Wireless Communication Networks**, Cunwu Han, Dehui Sun, Song Bi, Lei Liu, and Zhengxi Li  
Volume 2014, Article ID 642673, 10 pages

**Determine the Inflow Performance Relationship of Water Producing Gas Well Using Multiobjective Optimization Method**, Xiao-Hua Tan, Jian-Yi Liu, Jia-Hui Zhao, Xiao-Ping Li, Guang-Dong Zhang, Chuan Tang, and Li Li  
Volume 2014, Article ID 105636, 7 pages

**Multiobjective Fuzzy Mixed Assembly Line Sequencing Optimization Model**, Farzad Tahriri, Siti Zawiah Md Dawal, and Zahari Taha  
Volume 2014, Article ID 179085, 19 pages

**A Dynamic Model of the Tragedy of the Commons in Marketing-Intensive Industries**, Dohoon Kim  
Volume 2014, Article ID 952046, 11 pages

**A Novel Classification Approach through Integration of Rough Sets and Back-Propagation Neural Network**, Lei Si, Xin-hua Liu, Chao Tan, and Zhong-bin Wang  
Volume 2014, Article ID 797432, 11 pages

**Robot Calibration for Cooperative Process under Typical Installation**, Yahui Gan, Xianzhong Dai, and Donghui Dong  
Volume 2014, Article ID 576420, 12 pages

**Modelling Laser Milling of Microcavities for the Manufacturing of DES with Ensembles**, Pedro Santos, Daniel Teixidor, Jesus Maudes, and Joaquim Ciurana  
Volume 2014, Article ID 439091, 15 pages

**Lightweight Design of an Outer Tie Rod for an Electrical Vehicle**, Young-Chul Park, Seung-Kul Baek, Bu-Kyo Seo, Jong-Kyu Kim, and Kwon-Hee Lee  
Volume 2014, Article ID 942645, 6 pages

**Metaheuristic Algorithm for Solving Biobjective Possibility Planning Model of Location-Allocation in Disaster Relief Logistics**, Farnaz Barzinpour, Mohsen Saffarian, Ahmad Makoui, and Ebrahim Teimoury  
Volume 2014, Article ID 239868, 17 pages

**Modeling and Optimization of Beam Pumping System Based on Intelligent Computing for Energy Saving**, Xiaohua Gu, Taifu Li, Zhiqiang Liao, Liping Yang, and Ling Nie  
Volume 2014, Article ID 317130, 7 pages

**Hierarchical Agent-Based Integrated Modelling Approach for Microgrids with Adoption of EVs and HRES**, Peng Han, Jinkuan Wang, Yan Li, and Yinghua Han  
Volume 2014, Article ID 808549, 10 pages

**Solving Dynamic Traveling Salesman Problem Using Dynamic Gaussian Process Regression**, Stephen M. Akandwanaho, Aderemi O. Adewumi, and Ayodele A. Adebisi  
Volume 2014, Article ID 818529, 10 pages

**Classification of Phishing Email Using Random Forest Machine Learning Technique**, Andronicus A. Akinyelu and Aderemi O. Adewumi  
Volume 2014, Article ID 425731, 6 pages

**Numerical Investigation of Gas Mixture Length of Nitrogen Replacement in Large-Diameter Natural Gas Pipeline without Isolator**, Hongjun Zhu and Qinghua Han  
Volume 2014, Article ID 542343, 11 pages

**Track-to-Track Association Based on Structural Similarity in the Presence of Sensor Biases**, Hongyan Zhu and Suying Han  
Volume 2014, Article ID 294657, 8 pages

**Partitioned Quasi-Newton Approximation for Direct Collocation Methods and Its Application to the Fuel-Optimal Control of a Diesel Engine**, Jonas Asprion, Oscar Chinellato, and Lino Guzzella  
Volume 2014, Article ID 341716, 6 pages

**Finite Queueing Modeling and Optimization: A Selected Review**, F. R. B. Cruz and T. van Woensel  
Volume 2014, Article ID 374962, 11 pages

**Quality Prediction and Control of Reducing Pipe Based on EOS-ELM-RPLS Mathematics Modeling Method**, Dong Xiao, Jichun Wang, and Huixin Tian  
Volume 2014, Article ID 298218, 13 pages

**Airline Overbooking Problem with Uncertain No-Shows**, Chunxiao Zhang, Congrong Guo, and Shenghui Yi  
Volume 2014, Article ID 304217, 7 pages

**An Inventory Model under Trapezoidal Type Demand, Weibull-Distributed Deterioration, and Partial Backlogging**, Lianxia Zhao  
Volume 2014, Article ID 747419, 10 pages

**Predictive Models of Current, Voltage, and Power Losses on Electric Transmission Lines**, O. M. Bamigbola, M. M. Ali, and K. O. Awodele  
Volume 2014, Article ID 146937, 5 pages

**Centralized Resource Allocation for Connecting Radial and Nonradial Models**, A. Mirsalehy, M. R. Abu Bakar, G. R. Jahanshahloo, F. Hosseinzadeh Lotfi, and L. S. Lee  
Volume 2014, Article ID 974075, 12 pages

**Flow Merging and Hub Route Optimization in Collaborative Transportation**, Kerui Weng and Zi-hao Xu  
Volume 2014, Article ID 621487, 8 pages

**Weighted Multimodel Predictive Function Control for Automatic Train Operation System**, Shuhuan Wen, Jingwei Yang, Ahmad B. Rad, Shengyong Chen, and Pengcheng Hao  
Volume 2014, Article ID 520627, 8 pages

**Mathematical Model of Pipeline Abandonment and Recovery in Deepwater**, Xia-Guang Zeng, Meng-Lan Duan, and Chen An  
Volume 2014, Article ID 298281, 7 pages

**A New Decision Model for Reducing Trim Loss and Inventory in the Paper Industry**, Fu-Kwun Wang and Feng-Tai Liu  
Volume 2014, Article ID 987054, 10 pages

**New Product Development in an Emerging Economy: Analysing the Role of Supplier Involvement Practices by Using Bayesian Markov Chain Monte Carlo Technique**, Kanagi Kanapathy, Kok Wei Khong, and Rob Dekkers  
Volume 2014, Article ID 542606, 12 pages

**Three-Dimensional Temperature Distribution Produced by a Moving Laser Beam**, R. Uyhan  
Volume 2013, Article ID 649590, 6 pages

## Editorial

# Mathematical Modeling and Optimization of Industrial Problems

**M. Montaz Ali,<sup>1</sup> Aderemi O. Adewumi,<sup>2</sup> Nachamada Blamah,<sup>2,3</sup> and Olabisi Falowo<sup>4</sup>**

<sup>1</sup>Centre for Systems and Engineering, Faculty of Engineering, University of the Witwatersrand, Johannesburg, South Africa

<sup>2</sup>School of Mathematics, Statistics & Computer Science, University of KwaZulu-Natal, Durban, South Africa

<sup>3</sup>Department of Computer Science, University of Jos, Jos, Nigeria

<sup>4</sup>Department of Electrical and Electronic Engineering, University of Cape Town, Cape Town, South Africa

Correspondence should be addressed to M. Montaz Ali; [montaz.ali@wits.ac.za](mailto:montaz.ali@wits.ac.za)

Received 11 December 2014; Accepted 11 December 2014

Copyright © 2015 M. Montaz Ali et al. This is an open access article distributed under the Creative Commons Attribution License, which permits unrestricted use, distribution, and reproduction in any medium, provided the original work is properly cited.

Optimization plays an ever-increasing role in mathematics, economics, engineering, health sciences, management, life sciences, and almost all other fields of study. Many optimization problems exist in the real world including space planning, networking, logistic management, financial planning, and risk management. These problems are NP-hard in nature; hence, finding an optimal solution is often difficult, demanding highly efficient techniques. Many exact and heuristic algorithms have been proposed out of these challenging and practically relevant optimization problems including those that draw inspiration from nature.

The aim of this special issue is to showcase how heuristics, operations research, computational intelligence, and other optimization techniques have been successfully applied to solve real-world industrial optimization problems. Researchers were invited to contribute original research and review articles that explore, model, and solve real life optimization problems in various fields. The special issue attracted many high quality papers of which few were selected based on set quality criteria after rigorous peer-review, revision, and editorial processes. The published high quality papers cover various applications of optimization to varying problems especially in the industries including engineering, inventory, logistics, and marketing, scheduling, resource, and transportation planning, computing and ICT, water and gas resource management, and data mining. Most papers dwell on modeling of real-world industrial problems, innovative optimization technique for solving real-world problems including heuristics, finite methods, operation

research techniques, intelligent algorithms, and agent-based methods. Many of the papers propose innovative techniques for solving specified problem while others present improved methods compared with existing ones. Here, we present a summary of the published papers categorized according to the problem domain addressed.

*Engineering.* Papers in the engineering domain cover interests in electrical, mechanical, and building engineering. L. Huo et al. present an optimal design methodology for tuned liquid column dampers (TLCDs) based on the  $H_\infty$  control theory using the Dalian Xinghai Financial Business Building as case study in their paper titled “TLCD Parametric Optimization for the Vibration Control of Building Structures Based on Linear Matrix Inequality.”

Y.-C. Park et al. present a “Lightweight Design of an Outer Tie Rod for an Electrical Vehicle” which was achieved through efficient material selection using finite element analysis and metamodel-based optimization technique in order to minimize the weight while satisfying critical design requirements. Furthermore, the paper “Hierarchical Agent-Based Integrated Modelling Approach for Microgrids with Adoption of EVs and HRES” by P. Han et al. addresses the challenge to microgrid, brought about by the recent adoption of electric vehicles and hybrid renewable energy systems, by proposing a hierarchical agent-based method which is useful for energy management, electricity consumption prediction, the EV scheduling control, and HRES deployment optimization. Finally in electrical, “Predictive Models of Current,

Voltage, and Power Losses on Electric Transmission Lines” O. M. Bamigbola et al. formulated mathematical physics expressions that depict the evolution of current and voltage on a typical transmission line and derived models to predict available current and voltage at any point on the transmission line.

In the paper “Partitioned Quasi-Newton Approximation for Direct Collocation Methods and Its Application to the Fuel-Optimal Control of a Diesel Engine,” J. Asprión et al. presented an efficient technique to resolve memory limitations, preserve the correct sparsity pattern, and generate more accurate curvature information as it applies to engineering problems with special focus on fuel-optimal and emission-constrained control of a turbocharged diesel engine. “Finite Queueing Modeling and Optimization: A Selected Review” by F. R. B. Cruz and T. van Woensel is a comprehensive review of queueing modeling issues and related performance evaluation and optimization approaches for joint manufacturing and product engineering.

D. Xiao et al. in their paper “Quality Prediction and Control of Reducing Pipe Based on EOS-ELM-RPLS Mathematics Modeling Method” present an algorithm to predict the quality of reducing pipe during the inspection of inhomogeneous transverse and longitudinal wall thicknesses during the production of seamless steel. In “Three-Dimensional Temperature Distribution Produced by a Moving Laser Beam” R. Uyhan used a simplified theoretical model to study the three-dimensional unsteady temperature field produced by moving laser beam in an axisymmetric laser beam.

*The Computing and ICT.* The Computing and ICT groups of papers dwell on computer graphics, multiprocessor computing, wireless communication, electronic fraud prevention, and robotics. X. Wang and C. Hou in the paper “Improved Crosstalk Reduction on Multiview 3D Display by Using BILS Algorithm” present a system-introduced crosstalk measurement and derive an improved crosstalk reduction method to address the problem of crosstalk that degrades the quality of the 3D image. Their improved method seeks an optimal solution to this box-constrained integer least squares (BILS) problem that substantially decreases the Euclidean distance between a solution and its target. The paper “An Efficient Biobjective Heuristic for Scheduling Workflows on Heterogeneous DVS-Enabled Processors” by P. Zhou and W. Zheng addressed the problem of energy consumption, expressed in terms of execution time of application, in multiprocessing computing. The authors proposed a heuristic that finds a schedule for a workflow, on a bounded number of heterogeneous (dynamic voltage scaling) DVS-enabled processors, so as to minimize both makespan (overall execution time of the application) and energy consumption.

Furthermore, C. Han et al. in their paper, “Modeling and Model Predictive Power and Rate Control of Wireless Communication Networks,” present a novel power and rate control system model for wireless communication networks and proposed a delay-dependent model predictive power and rate control method. The derived optimization model is solved using linear matrix inequality (LMI) technique. Finally, A. A. Akinyelu and A. O. Adewumi in “Classification

of Phishing Email Using Random Forest Machine Learning Technique” propose an efficient random forest technique for phishing email detection.

The paper “Robot Calibration for Cooperative Process under Typical Installation” by Y. Gan et al. introduces simple but efficient operation procedure and calibration condition to solve the base frame calibration problem for cooperative robots which was validated on two practical industrial robots. In “Track-to-Track Association Based on Structural Similarity in the Presence of Sensor Biases,” H. Zhu and S. Han address the problem of track-to-track association in the presence of sensor biases by introducing the structural feature for each local track, which describes the spatial relationship with its neighbouring targets.

*Inventory, Logistics, and Marketing.* There are five papers in the inventory control, logistics, and marketing applications. The paper titled “Intelligent Inventory Control via Ruminative Reinforcement Learning” by T. Katanyukul and E. K. P. Chong proposed a new ruminative reinforcement learning (RRL) method for inventory management with promising results. Similarly, the challenge of trim loss and inventory in paper industry was addressed by F.-K. Wang and F.-T. Liu in their paper. In a bid to optimize order allocation and cutting trim loss, the authors present a new decision model based on the adjustment of scheduling and limitation of inventory quantity to differentiate trim loss and inventory distribution data. Furthermore, “An Inventory Model under Trapezoidal Type Demand, Weibull-Distributed Deterioration, and Partial Backlogging” by L. Zhao proposed an inventory model and policy for Weibull-distributed deterioration items with trapezoidal type demand rate, in which shortages are allowed and partial backlogging depends on the waiting time for the next replenishment.

D. Kim in the paper “A Dynamic Model of the Tragedy of the Commons in Marketing-Intensive Industries” provides the analysis of the processes of a dynamic model introduced to prevent business ecosystem from being plunged into Tragedy of the Commons (ToC) thereby enhancing sustainable growth and competitiveness of the business ecosystem.

Finally, in “Metaheuristic Algorithm for Solving Biobjective Possibility Planning Model of Location-Allocation in Disaster Relief Logistics” by F. Barzinpour et al., a multiobjective model for periodic location and allocation of distribution centres to damaged areas during natural disaster in order to distribute relief commodities is presented and solved using GA.

*Water and Gas Resource Management.* There are also five papers dealing with water, oil, and gas resource management. Y. Wang et al. in their paper “An Analytical Solution by HAM for Nonlinear Simulation of Deepwater SCR Installation” seek to optimize the time taken during installation path calculation by numerical simulation software in steel catenary riser (SCR) by establishing a mechanical model that makes use of homotopy analysis method to simplify its analytical solution while dimensional analysis was considered in making initial guess solution. X.-H. Tan et al. establish a new mathematical model of gas-water two-phase

flow to “Determine the Inflow Performance Relationship of Water Producing Gas Well Using Multiobjective Optimization Method” thus overcoming the limitation of well testing on site. Also, in “Numerical Investigation of Gas Mixture Length of Nitrogen Replacement in Large-Diameter Natural Gas Pipeline without Isolator” by H. Zhu and Q. Han, a computational fluid dynamic model coupled to a species-transportation model was used to investigate the gas mixture length of nitrogen replacement in large-diameter pipeline without isolator.

In “Modeling and Optimization of Beam Pumping System Based on Intelligent Computing for Energy Saving,” X. Gu et al. present a novel intelligent technique for optimizing beam pumping system for petroleum enterprises in China in order to save energy. In “Mathematical Model of Pipeline Abandonment and Recovery in Deepwater,” X.-G. Zeng et al. deal with the challenge of pipeline abandonment and recovery in offshore oil and gas engineering by introducing a third-order differential equation which is solved using a novel technique.

*Scheduling, Resource, and Transportation Planning.* A few papers consider scheduling, resources, and transport planning within different domain area. The paper “A Scheduling Problem in the Baking Industry” by F. A. M. da Silva et al. presents greedy and genetic algorithm (GA) to handle a real-world scheduling problem in the baking industry arising from increasing production rates, growing demand, and resource constraints. The main objective is to optimize both delivery time and profit maximization. The paper “Multiobjective Fuzzy Mixed Assembly Line Sequencing Optimization Model” by F. Tahriri et al. addresses the research gap in the assembly line sequencing optimization model for mixed-model production lines by presenting an integrated model of job shop and assembly production lines for factories with modular layouts that seeks to minimize the makespan, setup time, and cost simultaneously in the mixed-model assembly lines. GA was employed to solve the derived model.

S. M. Akandwanaho et al. in “Solving Dynamic Traveling Salesman Problem Using Dynamic Gaussian Process Regression” present a hybridization of dynamic Gaussian process regression with nearest neighbor and iterated local search to the track dynamic optima for the dynamic traveling salesman problem. In “Airline Overbooking Problem with Uncertain No-Shows,” C. Zhang et al. present an idea that seeks to minimize the effect of no-shows and any other uncertain human behaviour or unexpected events in an airline overbooking problem of a new single-leg flight with discount fare. “Centralized Resource Allocation for Connecting Radial and Nonradial Models” by A. Mirsalehy et al. examines an alternative approach to the centralized resource allocation model that indicates that all units are under the control of an entity of the centralized decision maker.

“Flow Merging and Hub Route Optimization in Collaborative Transportation” by K. Weng and Z. Xu studies the optimal hub routing problem of merged tasks in collaborative transportation being applicable in logistics, postal services, airline, and other transportation systems and presents two heuristics to solve the derived mixed integer programming

model. S. Wen et al. in “Weighted Multimodel Predictive Function Control for Automatic Train Operation System” design a speed controller for train operation based on the input and output data of the train in order to obtain a predictive model about the system based on weighted indicators.

In “New Product Development in an Emerging Economy: Analysing the Role of Supplier Involvement Practices by Using Bayesian Markov Chain Monte Carlo Technique,” K. Kanapathy et al. use structural equation modelling and Bayesian Markov Chain Monte Carlo algorithm in a case of 146 companies in China to determine whether the positive relationship found between supplier involvement practices and new product development performances in developed economies also holds in emerging economies.

*Data Mining.* L. Si et al. present “A Novel Classification Approach through Integration of Rough Sets and Back-Propagation Neural Network” which essentially hybridizes the underlying techniques for application in data mining. P. Santos et al. in their paper “Modelling Laser Milling of Microcavities for the Manufacturing of DES with Ensembles” study the laser-milling process of microcavities in the manufacture of drug-eluting stents (DES). A set of designed experiments using different regression methods (ensemble, support vector, ANN, and linear and nearest neighbour) were conducted with ensemble regression as the most efficient technique.

In conclusion, this special issue has contributed to the field of optimization and modelling of real-world problem as well as development of innovative optimization techniques for handling such problem. We hope that ideas generated in this issue will provoke further research and thoughts in the field of mathematical modelling, optimization, and optimization techniques.

## Acknowledgment

We would like to express our profound gratitude to all the reviewers whose professional expertise contributed immensely to the outcome of this special issue.

M. Montaz Ali  
Aderemi O. Adewumi  
Nachamada Blamah  
Olabisi Falowo

## Research Article

# Improved Crosstalk Reduction on Multiview 3D Display by Using BILS Algorithm

**Xiaoyan Wang and Chunping Hou**

*School of Electronic and Information Engineering, Tianjin University, Tianjin 300072, China*

Correspondence should be addressed to Xiaoyan Wang; wangxytju@163.com

Received 4 December 2013; Accepted 10 July 2014; Published 24 July 2014

Academic Editor: Nachamada Blamah

Copyright © 2014 X. Wang and C. Hou. This is an open access article distributed under the Creative Commons Attribution License, which permits unrestricted use, distribution, and reproduction in any medium, provided the original work is properly cited.

In multiview three-dimensional (3D) displays, crosstalk is one of the most annoying artefacts degrading the quality of the 3D image. In this paper, we present a system-introduced crosstalk measurement method and derive an improved crosstalk reduction method. The proposed measurement method is applied to measure the exact crosstalk among subpixels corresponding to different view images and the obtained results are very effective for crosstalk reduction method. Furthermore, an improved crosstalk reduction method is proposed to alleviate crosstalk by searching for the optimal integral intensity values of subpixels on the synthetic image. The derived algorithm based on modified Schnorr-Euchner strategy is implemented to seek the optimal solution to this box-constrained integer least squares (BILS) problem, such that the Euclidean distance between solution and its target decreases substantially. The method we develop is applicable to both multiview 3D parallax barrier displays and multiview 3D lenticular displays. Both simulation and experimental results indicate that the derived method is capable of improving 3D image quality more effectively than the existing method on multiview 3D displays.

## 1. Introduction

Crosstalk is a critical factor affecting the image quality in multiview three-dimensional (3D) displays [1], which is caused by the incomplete isolation of different image channels. In order to mitigate the Moiré fringe [2] and balance the horizontal versus vertical resolution [3] of 3D displays, the slanted parallax barrier or lenticular lens array is used [4]. However, the shape of subpixels on the display screen is rectangular or triangle and so on, and the shape of visible image observed through a slanted slit cannot exactly coincide with boundary of subpixels. This causes the viewers to observe not only the intended view image but also the other unintended view images and leads to the crosstalk observed at the optimal viewing positions on multiview 3D displays.

As introduced in [5], the available mathematical definitions of crosstalk are diverse and sometimes contradictory. In 2009, Huang et al. defined two terms [6]: system crosstalk that is independent of the content (determined only by the display) and viewer crosstalk that varies depending on the content. Most of literatures concerning the methodology

[7, 8] for measuring system-introduced crosstalk on multiview 3D displays provided the methods based on the illumination measurement. However, it is often difficult to measure the amount of crosstalk exactly, due to the complexity of the system, lack of measurements, reluctance of manufacturers to release data, and difficulty of making the measurement [5].

A number of methods [9, 10] for crosstalk reduction on multiview 3D displays have been proposed in the literatures to date. For instance, lowering aperture ratio and fixing a special 3D barriers are both effective for crosstalk cancellation. But these methods are at the cost of the intensity or extra devices. Recently, Li et al. [11] have suggested a method to eliminate the crosstalk by correcting the subpixels values on synthetic image. Despite the fact that this method to some extent reduced the crosstalk, the crosstalk coefficients matrix was obtained by the illumination measurement. The experiment error of crosstalk measurement influenced the results of crosstalk reduction. Moreover, how to obtain the solutions to the equations of crosstalk elimination was not mentioned.

Few research efforts have been devoted to reducing crosstalk effectively on multiview 3D displays by taking it

as a box-constrained integer least squares (BILS) problem. Lattice reduction [12] is a powerful mathematical tool for solving diverse problems involving point lattices. In [13], the enumeration strategies by Schnorr-Euchner, Pohst, and Kannan were introduced. It was found that the Schnorr-Euchner strategy is substantially faster than the other two [14]. An efficient search method based on the Schnorr-Euchner enumeration strategy (see [15]) for solving integer least squares (ILS) problem was implemented in [16]. The method was then modified in [17] to solve the BILS problem by taking the box constraint into account.

In this paper, we extend the definition of system-introduced crosstalk to the multiview 3D displays and present a mathematical method for exactly measuring the system-introduced crosstalk observed at the optimal viewing position. Crosstalk between the neighboring view images is not always equal to the exact crosstalk between subpixels corresponding to different view images. Our method is applied to obtain the crosstalk coefficient matrix  $\mathbf{A}$ , in which precise crosstalk between the subpixels is presented. The obtained results are more effective for crosstalk reduction method than for the one via the typical experiment. Moreover, we adopt the variable  $a$  to simulate the slight movement of viewable image, while the viewer is moving parallel to the display screen in the viewing zone such that the more exact crosstalk at the optimal viewing position is obtained. One of major contributions in this paper is the proposal of reasonable measurement method of system-introduced crosstalk between the neighbouring subpixels above and below corresponding to the different view images.

In actual display devices, the subpixel values are constrained to the integer set  $\mathbb{Z}$ . Without regard to it, the crosstalk elimination result still remains the biggest accumulated quantization error, which has the negative impact on image quality. That means the crosstalk elimination [11] on multiview 3D displays is not as complete as expected. Hence, it is effective by taking reduction process as a BILS problem. In this paper, we concentrate our efforts on developing a crosstalk reduction method, which gives a few modifications of Schnorr-Euchner strategy based algorithms given in [17], to correct for the synthetic image with the minimum quantization error. The experiments demonstrate that the proposed method reduces crosstalk effectively and greatly improves the 3D image quality. Moreover, based on the fact that the proposed method is based on the geometrical relationship of parallax barrier and subpixels, it is applied to eliminate crosstalk between the neighbouring subpixels above and below, rather than the neighbouring view images. If the distribution mode of view images changes on the synthetic images [18], that is, the neighbouring subpixels above and below do not correspond to the neighbouring view images, the method [11] becomes invalid. In contrast, the improved method still remains effective.

The following notation is used in the paper.  $\mathbb{R}^{m \times n}$  and  $\mathbb{R}^n$  denote the set of all real  $m \times n$  matrices and the set of all real  $n$ -vectors, respectively.  $\mathbb{Z}^{m \times n}$  and  $\mathbb{Z}^n$  denote the set of all integer  $m \times n$  matrices and the set of all integer  $n$ -vectors, respectively.  $\mathbf{I}_{m \times n} \in \mathbb{Z}^{m \times n}$  denotes  $m \times n$  matrix with all entries equal to 1. For a real scalar  $z$ ,  $\lfloor z \rfloor$  stands for its nearest

integer,  $\lfloor z \rfloor$  stands for the largest integer less than or equal to  $z$ , and  $\lceil z \rceil$  stands for the smallest integer greater than or equal to  $z$ . The operation  $\text{sign}(z)$  returns  $-1$  if  $z \leq 0$  and  $1$  if  $z > 0$ . For a matrix  $\mathbf{A}$ ,  $\mathbf{a}_j$  denotes the  $j$ th column of  $\mathbf{A}$ ,  $a_{kj}$  denotes the  $k$ th entry of vector  $\mathbf{a}_j$ , and  $\mathbf{A}^T$  denotes the transposed matrix of  $\mathbf{A}$ . Bold upper case letters and bold lower case letters denote matrices and vectors, respectively.

## 2. Crosstalk Measurement and Crosstalk Reduction Method

*2.1. Crosstalk Measurement Method.* Multiview 3D displays provide 3D perception without requiring any form of special glasses or other user-mounted devices. Among them, parallax barrier displays and lenticular displays are prevalent in actual devices, as indicated in Figure 1. The synthetic image prepared for the 8-view 3D display is synthesized by 8 different view images, as can be seen in Figure 2. The rectangles represent the subpixels, and the numbers marked in them indicate view image numbers. The subpixels illuminated with color in Figure 2(a) are prepared for the observer at the first optimal viewing position. At the same time, the visible image observed through the slits is illustrated in Figure 2(b). They do not overlap perfectly; that is the main cause of crosstalk observed at optimal viewing position.

We extend the definition of system-introduced crosstalk [6] from stereoscopic display to the multiview 3D display and precisely define the system-introduced crosstalk observed at the  $n$ th optimal viewing position on the  $N$ -view 3D display as follows:

$$\chi_n = \frac{\sum_{l=1, l \neq n}^N Y_l - Y_B}{Y_n - Y_B}, \quad (1)$$

where  $Y_l$  ( $l = 1 \cdots N$ ) denotes the luminance measured at the  $n$ th optimal viewing position with white in the  $l$ th view image and black in all of other view images on the synthetic image and  $Y_B$  denotes the environmental light intensity. This definition is black-white crosstalk, since it uses full-black and full-white images in the testing scheme. Full-white and full-black are used because maximum leakage usually occurs when the pixels in the desired view image are full-black and the pixels in the other view images are full-white. The crosstalk between the neighboring view images on  $N$ -view 3D display was considered in formula (1), rather than the crosstalk between the left eye image and the right eye image given in [6].

For the  $N$ -view 3D display,  $\sum_{l=1, l \neq n}^N Y_l - Y_B$  in formula (1) is replaced with  $s_1$ , which is the viewable area of unintended view images observed at the  $n$ th optimum viewing position.  $Y_n - Y_B$  is replaced with  $s_2$ , which is the viewable area of intended view image observed at the  $n$ th optimum viewing position. Thus, we define the system-introduced crosstalk as follows:

$$\chi_n = \frac{s_1}{s_2} = \frac{\sum_{m=1}^v \sum_{i=2}^h s_4(i-1, m) + \sum_{m=1}^v \sum_{i=1}^{h-1} s_5(i+1, m)}{\sum_{m=1}^v \sum_{i=1}^h s_3(i, m)}, \quad (2)$$

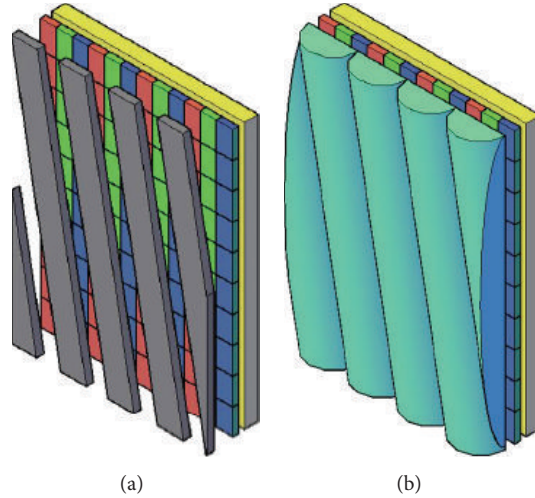


FIGURE 1: Structures of two kinds of multiview 3D displays. (a) A parallax barrier display. (b) A lenticular display.

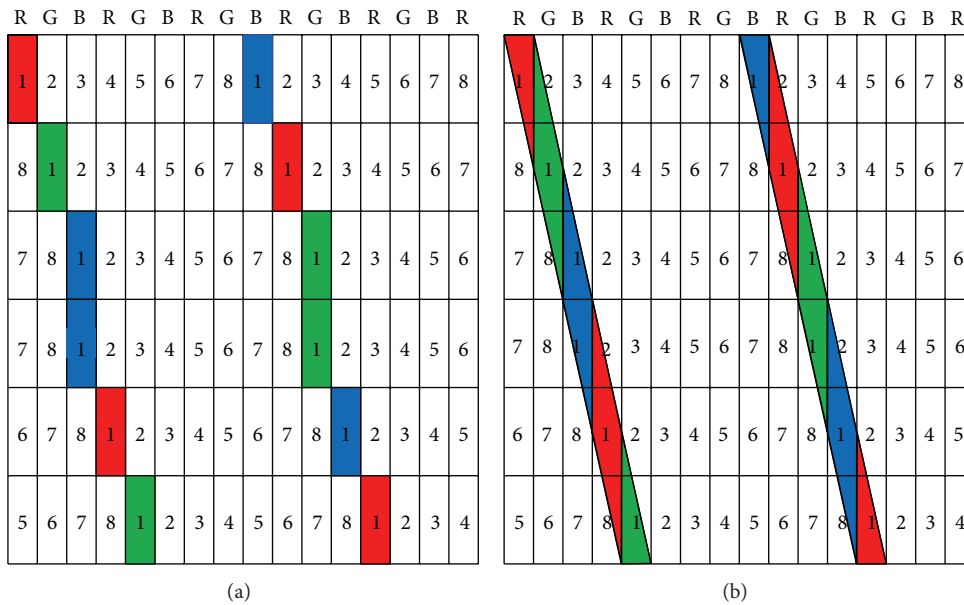


FIGURE 2: Distribution mode of 8 different view images' subpixels on the synthetic image. (a) View image prepared for the first viewing position. (b) Visible image observed through the slits at the first viewing position.

where  $(i, m)$  denotes the subpixel that is in the  $i$ th row on synthetic image observed through the  $m$ th slit at the  $n$ th optimal viewing position,  $\nu$  denotes the number of slits, and  $h$  denotes the vertical resolution of the synthetic image.  $s_3$  denotes the viewable area of subpixel belonging to the intended view image and  $s_4$  and  $s_5$  denote the viewable areas of neighboring unintended subpixel above and below respectively. The distributions of  $s_3$ ,  $s_4$ , and  $s_5$  are illustrated in Figure 3. The dotted lines present the edges of slits. The rectangles present the subpixels on the display screen.

Based on the image composition theory, the subpixels showing the intended view image are determined in all subpixels observed at the  $n$ th optimal viewing position. Calculate

$s_3$ ,  $s_4$ , and  $s_5$  and substitute the results into expression (2) to obtain the system-introduced crosstalk.

Let the visible area's width observed through a slit on the synthetic image be  $t$  (this equals the width of one subpixel). As a result,  $s_3$ ,  $s_4$ , and  $s_5$  remain constant when  $m$  varies over the range of  $[1, \nu]$ . When we substitute  $s_3(i) = s_3(i, 1)$ ,  $s_4(i-1) = s_4(i-1, 1)$ ,  $s_5(i+1) = s_5(i+1, 1)$  for  $s_3(i, m)$ ,  $s_4(i-1, m)$ ,  $s_5(i+1, m)$  respectively, formula (2) is still valid.  $m = 1$  means that subpixels are observed through the first integral slit. Therefore, the system-introduced crosstalk on the multiview 3D display at the  $n$ th viewing position is derived as

$$\chi_n = \frac{s_1}{s_2} = \frac{\sum_{i=2}^h s_4(i-1) + \sum_{i=1}^{h-1} s_5(i+1)}{\sum_{i=1}^h s_3(i)} \quad (3)$$

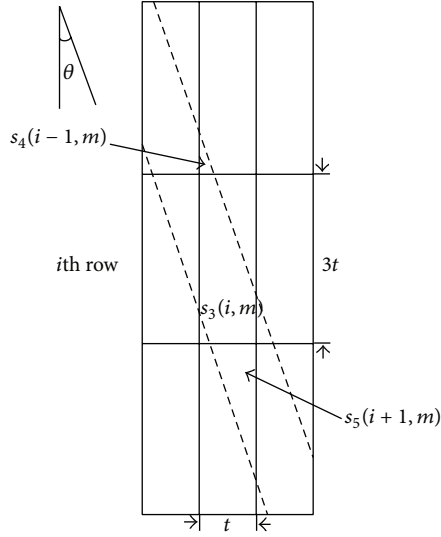


FIGURE 3: Illustration of system-introduced crosstalk measurement method.

Depending on the slant angle of parallax barrier  $\theta$ , the system-introduced crosstalk measurement is proposed as follows.

(1) Crosstalk measurement when  $\theta \leq \arctan(1/3)$ : when the subpixel is divided equally by the left side of the slit, the intercept length on the bottom edge of the subpixel is  $t - \Delta_0 = t - |(3t \cdot \tan \theta - t)/2| = (t + 3t \tan \theta)/2$ . Let the intercept of subpixel on the lower limb by the left edge of the first integral slit be  $\Delta_1(i) = 3it \cdot \tan \theta - \lfloor 3it \cdot \tan \theta \rfloor$ .

When  $\Delta_1(i) \geq t - \Delta_0$ , the subpixel in the  $i$ th row  $\lfloor 3i \cdot \tan \theta \rfloor + 2$ th column on the synthetic image shows the color belonging to intended view image. Consider

$$\begin{aligned} s_3(i) &= \frac{3}{2}t^2 + |\Delta_1(i) + \Delta_0 - t| \times 3t, \\ s_4(i-1) &= \frac{(2\Delta_0 + \Delta_1(i) - t)^2}{2 \tan \theta}, \\ s_5(i+1) &= 0. \end{aligned} \quad (4)$$

When  $\Delta_1(i) < t - \Delta_0$ , the subpixel in the  $i$ th row  $\lfloor 3i \cdot \tan \theta \rfloor + 1$ th column on the synthetic image shows the color belonging to intended view image.

If  $\Delta_0 \geq t - \Delta_0 - \Delta_1(i)$ ,

$$\begin{aligned} s_3(i) &= \frac{3}{2}t^2 + |\Delta_1(i) + \Delta_0 - t| \times 3t, \\ s_4(i-1) &= 0, \\ s_5(i+1) &= \frac{(t - \Delta_1(i))^2}{2 \tan \theta}. \end{aligned} \quad (5)$$

If  $\Delta_0 < t - \Delta_0 - \Delta_1(i)$ ,

$$\begin{aligned} s_3(i) &= 3t^2 - \frac{\Delta_1^2(i)}{2 \tan \theta} - \frac{(t - 2\Delta_0 - \Delta_1(i))^2}{2 \tan \theta}, \\ s_4(i-1) &= 0, \\ s_5(i+1) &= \frac{(t - \Delta_1(i))^2}{2 \tan \theta}. \end{aligned} \quad (6)$$

(2) Crosstalk measurement when  $\theta > \arctan(1/3)$ : when the subpixel is evenly divided by the left side of the slit, the intercept length on the bottom edge of this subpixel is  $\Delta_0 = |(3t \cdot \tan \theta - t)/2|$ . When the subpixel in the  $i$ th row is intercepted by the left edge of the first integral slit,  $\Delta_1(i) = 3it \cdot \tan \theta - \lfloor 3it \cdot \tan \theta \rfloor$ .

When  $\Delta_1(i) > \Delta_0$ , the subpixel in the  $i$ th row  $\lfloor 3i \cdot \tan \theta \rfloor + 1$ th column on the synthetic image shows the color belonging to intended view image.

If  $\Delta_1(i) - \Delta_0 \leq \Delta_0$ ,

$$\begin{aligned} s_3(i) &= \frac{(2\Delta_1(i) + t)t}{2 \tan \theta} - \frac{\Delta_1^2(i)}{2 \tan \theta}, \\ s_4(i-1) &= 0, \\ s_5(i+1) &= \frac{(t - \Delta_1(i))^2}{2 \tan \theta}. \end{aligned} \quad (7)$$

If  $\Delta_1(i) - \Delta_0 > \Delta_0$ ,

$$\begin{aligned} s_3(i) &= 3t^2 - \frac{\Delta_1^2(i)}{2 \tan \theta} - \frac{(t + 2\Delta_0 - \Delta_1(i))^2}{2 \tan \theta}, \\ s_4(i-1) &= \frac{(\Delta_1(i) - 2\Delta_0)^2}{2 \tan \theta}, \\ s_5(i+1) &= \frac{(t - \Delta_1(i))^2}{2 \tan \theta}. \end{aligned} \quad (8)$$

When  $\Delta_1(i) \leq \Delta_0$ , the subpixel in the  $i$ th row  $\lfloor 3i \cdot \tan \theta \rfloor$ th column on the synthetic image shows color belonging to intended view image.

If  $\Delta_0 - \Delta_1(i) \leq t - \Delta_0$ ,

$$\begin{aligned} s_3(i) &= 3t^2 - \frac{(2\Delta_0 - \Delta_1(i))^2}{2 \tan \theta} - \frac{(2\Delta_1(i) + t)t}{2 \tan \theta}, \\ s_4(i-1) &= \frac{(t + \Delta_1(i) - 2\Delta_0)^2}{2 \tan \theta}, \\ s_5(i+1) &= 0. \end{aligned} \quad (9)$$

If  $\Delta_0 - \Delta_1(i) > t - \Delta_0$ ,

$$\begin{aligned} s_3(i) &= 3t^2 - \frac{[2(2\Delta_0 - \Delta_1(i) - t) + t]t}{2 \tan \theta} - \frac{(2\Delta_1(i) + t)t}{2 \tan \theta}, \\ s_4(i-1) &= 0, \\ s_5(i+1) &= 0. \end{aligned} \quad (10)$$

Substituting these results into expression (3) obtains the system-introduced crosstalk for arbitrary multiview 3D display.

In the method given above, the top left corner of the visible image observed through the first integral slit and the top left corner of synthetic image coincide. Variable  $a$  is used to denote the distance from the top left corner of the visible image observed through the first integral slit to the top left corner of synthetic image. Let  $a$  be within the range of  $[0, t]$ . Then,  $\Delta_1(i) = 3it \cdot \tan \theta + a - [3it \cdot \tan \theta + a]$ . The following calculation procedure is the same as that given above.

Varying  $a$  from 0 to  $t$  simulates the slight movement of visible image on the synthetic image, while the viewing position is moving parallel to the display screen in the viewing zone. The crosstalk varies with the variable  $a$ . Thus, we define the system-introduced crosstalk as  $\chi_n = \min_{a \in [0, t]} \chi_n(a)$  that is the system-introduced crosstalk observed at the optimal viewing point.

**2.2. Improved Crosstalk Reduction Method.** For crosstalk reduction, the neighboring subpixels in the same column should be considered because the subpixels in same column on synthetic image show the same color, which is the main leakage among different view images. What we want to do is to correct the subpixel value on the synthetic image from  $b(i, j)$  to  $x(i, j)$  such that the leakage from the neighboring subpixels in same column will become useful for the image quality of multiview 3D displays; that is,

$$b(i, j) = \begin{cases} \frac{s_3(i)x(i, j) + s_5(i+1)x(i+1, j)}{s_3(i) + s_5(i+1)} & i = 1 \\ \frac{s_4(i-1)x(i-1, j) + s_3(i)x(i, j) + s_5(i+1)x(i+1, j)}{s_4(i-1) + s_3(i) + s_5(i+1)} & 2 \leq i \leq h-1 \\ \frac{s_4(i-1)x(i-1, j) + s_3(i)x(i, j)}{s_4(i-1) + s_3(i)} & i = h, \end{cases} \quad (11)$$

where  $b(i, j)$  and  $x(i, j)$  denote the subpixel values in the  $i$ th row  $j$  column on the synthetic image before and after correction, respectively. That means that the intensity obtained at the  $n$ th optimal viewing position is equal to the intensity of the  $n$ th intended view image, after correction. To solve this problem, it can be written as follows:

$$\mathbf{AX} = \mathbf{B}, \quad (12)$$

where  $\mathbf{B} \in \mathbb{Z}^{w \times h}$  and  $\mathbf{X} \in \mathbb{Z}^{w \times h}$  are the synthetic images before and after correction, respectively.  $\mathbf{A} \in \mathbb{R}^{h \times h}$  is the crosstalk coefficient matrix. The entry of  $\mathbf{A}$ ,  $a(p, q)$  denotes the leakage degree from the subpixel in the  $q$ th row  $j$ th column to the one in the  $p$ th row  $j$ th column on the synthetic image.  $p$  and  $q$  are both the numbers from 1 to  $h$ . We obtain  $a(p, q)$  by the proposed method, which exactly reflects the

crosstalk among the subpixels corresponding to different view images on the synthetic image, rather than among the whole neighboring view images.

In the actual display devices,  $x(i, j)$  is set to be 0, if  $x(i, j) < 0$ ;  $x(i, j)$  is set to be 255, if  $x(i, j) > 255$ ; and  $x(i, j)$  is set to be  $\lfloor x(i, j) \rfloor$ , if  $x(i, j) \notin \mathbb{Z}$ . This operation causes the fact that the unique solution to problem (12),  $\mathbf{X} = \mathbf{A}^{-1}\mathbf{B}$ , may not be the optimal solution, which means crosstalk elimination does not perform completely.

If the rank of  $\mathbf{A}$  is  $h$ , which means  $\mathbf{A}$  is full rank, the equation set has the unique solution  $\mathbf{X} = \mathbf{A}^{-1}\mathbf{B}$ . However,  $\mathbf{B}$  is constrained to the box  $\mathcal{B}_B = \{\mathbf{B} \in \mathbb{Z}^{w \times h} : \mathbf{L} \leq \mathbf{B} \leq \mathbf{U}\}$ , where  $\mathbf{L} = 0 \times \mathbf{I}_{w \times h}$  and  $\mathbf{U} = 255 \times \mathbf{I}_{w \times h}$ . Hence  $\mathbf{X}$  may be in following two boxes:

- (1)  $\mathcal{B}_1 = \{\mathbf{X} \in \mathbb{Z}^{w \times h} : \mathbf{X} < \mathbf{L} \text{ or } \mathbf{X} > \mathbf{U}\}$ ;
- (2)  $\mathcal{B}_2 = \{\mathbf{X} \notin \mathbb{Z}^{w \times h} : \mathbf{L} \leq \mathbf{X} \leq \mathbf{U}\}$ .

We propose an alternative method to obtain the optimum solution to equations set (12). For the given  $\mathbf{B}$ ,  $\mathbf{X}$  is the solution to a BILS problem:

$$\min_{\mathbf{X} \in \mathcal{B}_X} \|\mathbf{B} - \mathbf{AX}\|_2^2 \quad (13)$$

$$\mathcal{B}_X = \{\mathbf{X} \in \mathbb{Z}^{w \times h} : \mathbf{L} \leq \mathbf{X} \leq \mathbf{U}\},$$

where  $\|\cdot\|_2$  denotes the Euclidean norm.

Given a real  $h$ -vector  $\mathbf{b}_j$  and a real  $h \times h$  matrix  $\mathbf{A}$  with full column rank, lattice reduction is applied to solve the problem:

$$\min_{\mathbf{x}_j \in \mathcal{B}_x} \|\mathbf{b}_j - \mathbf{Ax}_j\|_2^2, \quad (14)$$

$$\mathcal{B}_x = \{\mathbf{x}_j \in \mathbb{Z}^h : \mathbf{l}_j \leq \mathbf{x}_j \leq \mathbf{u}_j\}$$

for  $j = 1, 2, \dots, w$ . The optimal solution to problem (14) is also the solution to (13). In lattice theory,  $\mathbf{A}$  is called the generator matrix of the lattice  $\mathcal{L}(\mathbf{A}) = \{\mathbf{Ax}_j : \mathbf{x}_j \in \mathbb{Z}^h\}$ ,  $\mathbf{b}_j$  is called the input vector, and (14) is referred to as a closest-point problem, since it is the problem to find a point in the lattice which is closest to the given input point  $\mathbf{b}_j$ .

At first, we transform the matrix  $\mathbf{A}$  to an upper triangular matrix, which has good properties to make the search algorithm more efficient. Here, this can be performed by the **QR** decomposition of  $\mathbf{A}$ :

$$\mathbf{AP} = \mathbf{QR}, \quad (15)$$

where  $\mathbf{P} \in \mathbb{Z}^{h \times h}$  is a permutation matrix,  $\mathbf{Q} \in \mathbb{R}^{h \times h}$  is orthogonal, and  $\mathbf{R} \in \mathbb{R}^{h \times h}$  is nonsingular upper triangular. With the **QR** decomposition, we have

$$\|\mathbf{b}_j - \mathbf{Ax}_j\|_2^2 = \|\mathbf{Q}^T \mathbf{b}_j - \mathbf{RP}^T \mathbf{x}_j\|_2^2. \quad (16)$$

Define

$$\bar{\mathbf{b}}_j = \mathbf{Q}^T \mathbf{b}_j, \quad \mathbf{z}_j = \mathbf{P}^T \mathbf{x}_j, \quad \bar{\mathbf{l}}_j = \mathbf{P}^T \mathbf{l}_j, \quad \bar{\mathbf{u}}_j = \mathbf{P}^T \mathbf{u}_j, \quad (17)$$

where  $\mathbf{l}_j$  is the lower bound of  $\mathbf{x}_j$  and  $\mathbf{u}_j$  is the upper bound of  $\mathbf{x}_j$ .  $\bar{\mathbf{l}}_j$  is the lower bound of  $\mathbf{z}_j$ ;  $\bar{\mathbf{u}}_j$  is the upper bound of  $\mathbf{z}_j$ . Here,  $l_{1j} = l_{2j} = \dots = l_{hj} = 0$ ;  $u_{1j} = u_{2j} = \dots = u_{hj} = 255$ .

When  $\mathbf{P}$  is an identity matrix, BILS problem (14) is equivalent to the following one:

$$\min_{\mathbf{z}_j \in \mathcal{B}_z} \|\bar{\mathbf{b}}_j - \mathbf{R}\mathbf{z}_j\|_2^2 \quad (18)$$

$$\mathcal{B}_z = \{\mathbf{z}_j \in \mathbb{Z}^h : \bar{\mathbf{l}}_j \leq \mathbf{z}_j \leq \bar{\mathbf{u}}_j\},$$

for  $j = 1, 2, \dots, w$ .

Then the proposed algorithm tries to solve (18). Note that, if  $\hat{\mathbf{z}}_j$  is the solution to (18), then  $\hat{\mathbf{x}}_j = \mathbf{P}\hat{\mathbf{z}}_j = \hat{\mathbf{z}}_j$  is the solution to (14) and  $\hat{\mathbf{X}}$  is the solution to (13).

We provide a search algorithm which avoids some drawbacks of algorithm BGBF (Algorithm 1) [17]. Our algorithm is applied to obtain the correction result of synthetic image one column by one column. When we input  $\mathbf{b} = \bar{\mathbf{b}}_j$  ( $j$  is the number from 1 to  $w$ ), the correction result of this column  $\hat{\mathbf{z}} = \hat{\mathbf{z}}_j$  is obtained. After  $w$  times operations, synthetic image is processed to the correction result  $\hat{\mathbf{Z}}$ . Thus, we obtain the final correction result  $\hat{\mathbf{X}} = \hat{\mathbf{Z}}$ .

In Step 1 or Step 3, the last value of  $z_k$  may be the lower bound  $l_k$  or the upper bound  $u_k$ . To avoid enumerating some integers outside the interval  $[l_k, u_k]$  in Step 5, we set  $\Delta_k = -\text{sign}(\rho_k)$ . For instance, when  $\lfloor s_k \rfloor > u_k$  in Step 1 or Step 3,  $z_k = \lfloor s_k \rfloor > u_k$ ,  $z_k = \min(z_k, u_k) = u_k$ , and the offset variable  $\Delta_k = -1$  (since  $\rho_k = (s_k - z_k)r_{kk} = (s_k - u_k)r_{kk} > 0$ ), which means the next value is  $z_k := z_k - 1 = u_k - 1$ . This process mostly avoids enumerating integer beyond the box constraint. However, when  $u_k - 0.5 \leq s_k < u_k$ ,  $\lfloor s_k \rfloor = u_k$ ,  $\rho_k = (s_k - z_k)r_{kk} = (s_k - u_k)r_{kk} < 0$ , and  $\Delta_k = -\text{sign}(\rho_k) = 1$ ,  $z_k = z_k + \Delta_k$  will be outside the interval  $[l_k, u_k]$ . To avoid this happening, we set  $\Delta_k := -1$  and compute  $z_k := z_k + \Delta_k$  if  $z_k + \Delta_k > u_k$  in Step 5; we set  $\Delta_k := 1$  and compute  $z_k := z_k + \Delta_k$  if  $z_k + \Delta_k < l_k$ ; otherwise, we compute  $z_k := z_k + \Delta_k$  and  $\Delta_k := -\Delta_k - \text{sign}(\Delta_k)$ . Therefore, our algorithm always enumerates the integers within the box constraint at each level.

In algorithm BGBF, if  $T > \beta$  and  $k \neq h$  in Step 4, that means no any other integer will satisfy inequality  $\sum_{l=k}^h r_{ll}^2 (s_l - z_l)^2 < \beta$  in level  $k$ . If  $\rho_l = 0$  ( $l = k + 1, k + 2 \dots h$ ) at that time, there is still not any other integer satisfying the inequality and we should exit loop directly and return the optimal solution  $\hat{\mathbf{z}}$ . Therefore, if  $T > \beta$ ,  $k < h$ , and  $\rho_l = 0$  ( $l = k + 1, k + 2 \dots h$ ), our algorithm exits the loop and returns the optimal solution  $\hat{\mathbf{z}} = \hat{\mathbf{z}}_j$ ; otherwise go back to level  $k + 1$ .

### 3. Results and Discussion

In this section, we aim to validate the improved crosstalk reduction method on multiview 3D displays, both qualitatively and quantitatively. We first give a specific example to demonstrate that the improved method alleviates the crosstalk on multiview 3D lenticular display effectively. Then computer simulation is carried out to compare the crosstalk correction results with typical method on two test

sequences. Numerical results are presented to validate the performance of the improved method in terms of the mean square error (MSE) and peak signal-to-noise ratio (PSNR). Finally, a photometer is used for measurement to compare the crosstalk reduction results by the improved method and typical method. The experiment results indicate that the improved method eliminates the crosstalk more effectively and improves the quality of the 3D images further.

At first, we compare the crosstalk values obtained via the proposed method and measured through the experimental method. To verify the effectiveness of the proposed crosstalk measurement method, a photometer (FS-5500TSL) is used to measure the crosstalk at the optimal viewing position. At first, 8 black-and-white test images are obtained in which each view image is white (that means that the subpixel values corresponding to the certain view image are equal to 255) and, in turn, presented on the display screen. In the black-and-white test image, only subpixel values corresponding to the certain view image are equal to 255, and all of the other subpixel values are equal to 0. We perform the experiment, using a multiview 3D parallax barrier display screen (42HD, provided by Tianjin 3-D Imaging Technique Co. Ltd.) is used to display synthetic images. Then, measure environmental light intensity and each test images intensity, respectively, along the horizontal direction at the optimal viewing distance. The photometer is used for luminance measurements. The luminances  $Y_I$  and  $Y_B$  are obtained; then crosstalk  $\chi_n = 0.38$  is got through formula (1). Through the proposed crosstalk measurement method, we get the crosstalk  $\chi_n = 0.38$  when  $\alpha = \arctan(2/9)$  on the multiview 3D display. The result well matches the actual measured crosstalk value. The close agreement between the proposed method and measured crosstalk results demonstrates that the proposed crosstalk measurement method can be used to measure the crosstalk on the multiview 3D display.

In our implementation,  $\hat{a} = \arg \min_a \chi_n(a)$  and the crosstalk coefficient matrices  $\mathbf{A} \in \mathbb{R}^{h \times h}$  are obtained by the proposed system-introduced crosstalk measurement method. The improved crosstalk reduction method is applied to calculate the correction values of subpixels one column by one column. However, when dimension  $h$  is large, the search time becomes significant. So  $A$  is rewritten as

$$A = \begin{pmatrix} \bar{A}_1 & 0 & \dots & 0 \\ 0 & \bar{A}_2 & \dots & 0 \\ \vdots & \vdots & \ddots & \vdots \\ 0 & 0 & \dots & \bar{A}_{\lceil h/r \rceil} \end{pmatrix}, \quad (19)$$

where  $\bar{A}_l \in \mathbb{R}^{r \times r}$ . To determine  $r$ , we analyze the relationship of neighboring subpixels in the same column. For example, when parallax barrier is slanted at the angle of  $\arctan(2/9)$ , we get the distribution mode of different view images' subpixels on the synthetic image, illustrated in Figure 2. Taking the first column on the left as an example, the third and fourth subpixels belong to the seventh view image and are observed at the seventh optimal viewing position. That means the third and fourth subpixels do not interact and are not related to each other. Consequently, we consider that every 3 subpixel

**Input:** The upper triangular matrix  $\mathbf{R} \in \mathbb{R}^{h \times h}$  with positive diagonal entries, the vector  $\mathbf{b} = \bar{\mathbf{b}}_j \in \mathbb{Z}^h$ , the lower bound vector  $\mathbf{l} = \bar{\mathbf{l}}_j \in \mathbb{Z}^h$ , the upper bound vector  $\mathbf{u} = \bar{\mathbf{u}}_j \in \mathbb{Z}^h$ , the initial hyper-ellipsoid bound  $\beta$ .

**Output:** The solution  $\hat{\mathbf{z}} \in \mathbb{Z}^h$  to the BILS Problem (18).

**Step 1. (Initialization)** Set  $k := h, T_k := 0$ ,  
 Compute  $s_k := b_k / r_{kk}, z_k := \lfloor s_k \rfloor$ ,  
 $z_k := \max(z_k, l_k), z_k := \min(z_k, u_k)$ ,  
 $\rho_k := (s_k - z_k)r_{kk}, \Delta_k := -\text{sign}(\rho_k)$ .

**Step 2.** Compute  $T := T_k + \rho_k^2$ ,  
**if**  $T < \beta$  and  $k \neq 1$ , **then**  
 Go to Step 3  
**else**  
 Go to Step 4  
**end if**

**Step 3.** Set  $T_{k-1} := T, k := k - 1$   
 Compute  $s_k := (b_k - \sum_{m=k+1}^h r_{km}z_m) / r_{kk}$ ,  
 $z_k := \lfloor s_k \rfloor, z_k := \max(z_k, l_k), z_k := \min(z_k, u_k)$ ,  
 $\rho_k := (s_k - z_k)r_{kk}, \Delta_k := -\text{sign}(\rho_k)$ .  
 Go to Step 2

**Step 4. If**  $T < \beta$ , **then**  
 Set  $\beta := T, \hat{\mathbf{z}} := \mathbf{z}, k := k + 1$ ,  
**else if**  $k = h$ , **then**  
 Terminate  
**else**  
 $k := k + 1$   
**if**  $\rho_k = 0$ , **then**  
 $K := k$   
**repeat**  
**if**  $k = h$ , **then**  
 Terminate  
**end if**  
 $k := k + 1$   
**until**  $\rho_k \neq 0$   
**if**  $k \neq h$ , **then**  
 $k := K$   
**end if**  
**end if**  
**end if**

**Step 5. If**  $z_k + \Delta_k > u_k$ , **then**  
 Set  $\Delta_k := -1$   
 Compute  $z_k := z_k + \Delta_k$   
**else if**  $z_k + \Delta_k < l_k$ , **then**  
 Set  $\Delta_k := 1$   
 Compute  $z_k := z_k + \Delta_k$   
**else**  
 Compute  $z_k := z_k + \Delta_k, \Delta_k := -\Delta_k - \text{sign}(\Delta_k)$   
**end if**  
 Compute  $\rho_k := (s_k - z_k)r_{kk}$   
 Go to Step 2.

ALGORITHM 1: Crosstalk reduction algorithm.

values are correlative in one column; that is,  $r = 3$  when  $\theta = \arctan(2/9)$ . Obviously, when  $\theta < \arctan(1/3)$ ,  $r$  can be determined easily in the same way. When  $\theta \geq \arctan(1/3)$ , we can determine  $r$ , according to the need.

We input the vector  $\mathbf{b} = \mathbf{Q}_l^T \mathbf{b}_j^l$  and upper triangle matrix  $\mathbf{R}_l \in \mathbb{R}^{r \times r}$ , where  $\mathbf{R}_l$  and  $\mathbf{Q}_l \in \mathbb{R}^{r \times r}$  are the results of QR composition of  $\bar{\mathbf{A}}_l, \mathbf{b}_j^l = (b_{l,j}, b_{l+1,j}, \dots, b_{l+r-1,j})^T$

( $l$  is the number from 1 to  $\lceil h/r \rceil$ ;  $j$  is the number from 1 to  $w$ ). After one operation, output  $\hat{\mathbf{z}} = (\hat{z}_{l,j}, \hat{z}_{l+1,j}, \dots, \hat{z}_{l+r-1,j})^T$ . After  $\lceil h/r \rceil \times w$  times operations, the correction result  $\hat{\mathbf{X}}$  is obtained.

First, we give a specific example to demonstrate the effectiveness of the proposed method for a group of images of a scene "Euro." A multiview 3D lenticular display screen

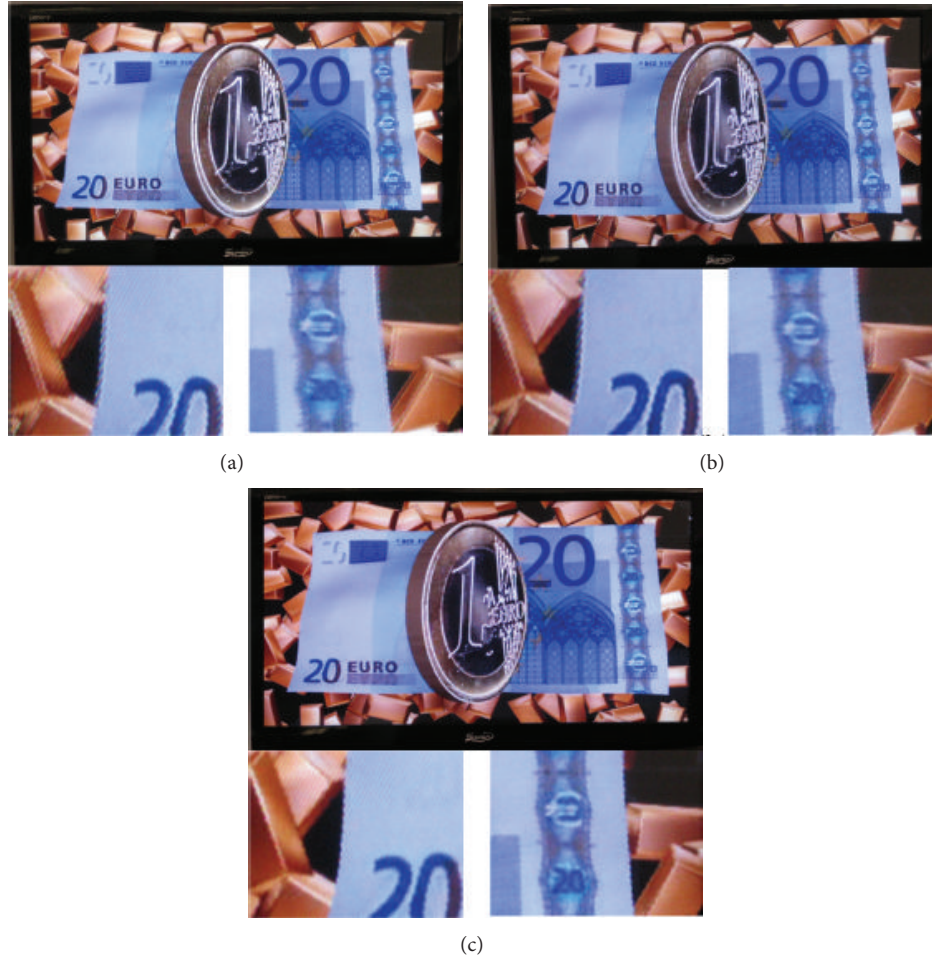


FIGURE 4: Photos of a scene “Euro” taken at the fourth optimal viewing position. (a) Result before correction. (b) Result by method given in [11]. (c) Result by our method.

(46HD, provided by SuperD Co. Ltd.) is used to display synthetic images. The result before correction and the result by the method in [11] and our method are presented on the display screen, respectively. Figure 4 shows the photos taken at the fourth optimal viewing position. As can be seen the edges of “Euro” are blurring in the result before correction and it is still not good enough in the result by the method in [11]. Compared with Figures 4(a) and 4(b), the photo in Figure 4(c) is the clearest, especially at the boundaries of “golden bricks.” Furthermore, it can be observed from Figure 4 that objects’ jagged edges (such as Euro edges and the golden stick’ edges) are still obvious in the result by the method in [11]. In contrast, our method well solves this problem; the phenomenon of contour jaggies largely disappears in the result by our method. It can be discovered from the experiment results that the proposed method reduces the crosstalk more effectively on the multiview 3D lenticular display.

Then, we compare the correction results obtained by the proposed method and the method in [11] for two test sequences in terms of MSE and PSNR. Two test sequences are used in our implementation, namely, “Fireman” and “Lotus.”

They are obtained from Tianjin 3D Imaging Technique Co. Ltd., Tianjin, China, which are 3D test sequences with proper parallax between adjacent views. The resolution of “Fireman” is  $1024 \times 600$ , while the resolution of “Lotus” is  $1920 \times 1024$ . To be fair, the commonly used metric MSE is used to evaluate the residual crosstalk, which is defined as  $MSE = (1/(h \times w))\|\mathbf{A}\mathbf{X} - \mathbf{B}\|_2^2$ . Note that the MSE is converted to the PSNR based upon the relationship  $PSNR = 10 \log_{10}(255^2/MSE)$ . Figure 5 plots the PSNR values versus both the frame and the view numbers in two sequences. For a close-up look, as an example, Figure 6 compares our correction results with the results by the method in [11]. The PSNR values versus the frame number for each view of “Fireman” are shown in the figure. Furthermore, the MSE curves for each view of “Lotus” are plotted in Figure 7, showing the frame-level residual crosstalk (MSE) of each view versus the frame number. It can be concluded that the improved method performs better than the typical method for both sequences in terms of MSE and PSNR.

The MSE per frame in results by the method in [11] and our method for two test sequences is compared. Figure 8 plots the MSE versus the frames for the sequences “Fireman” and

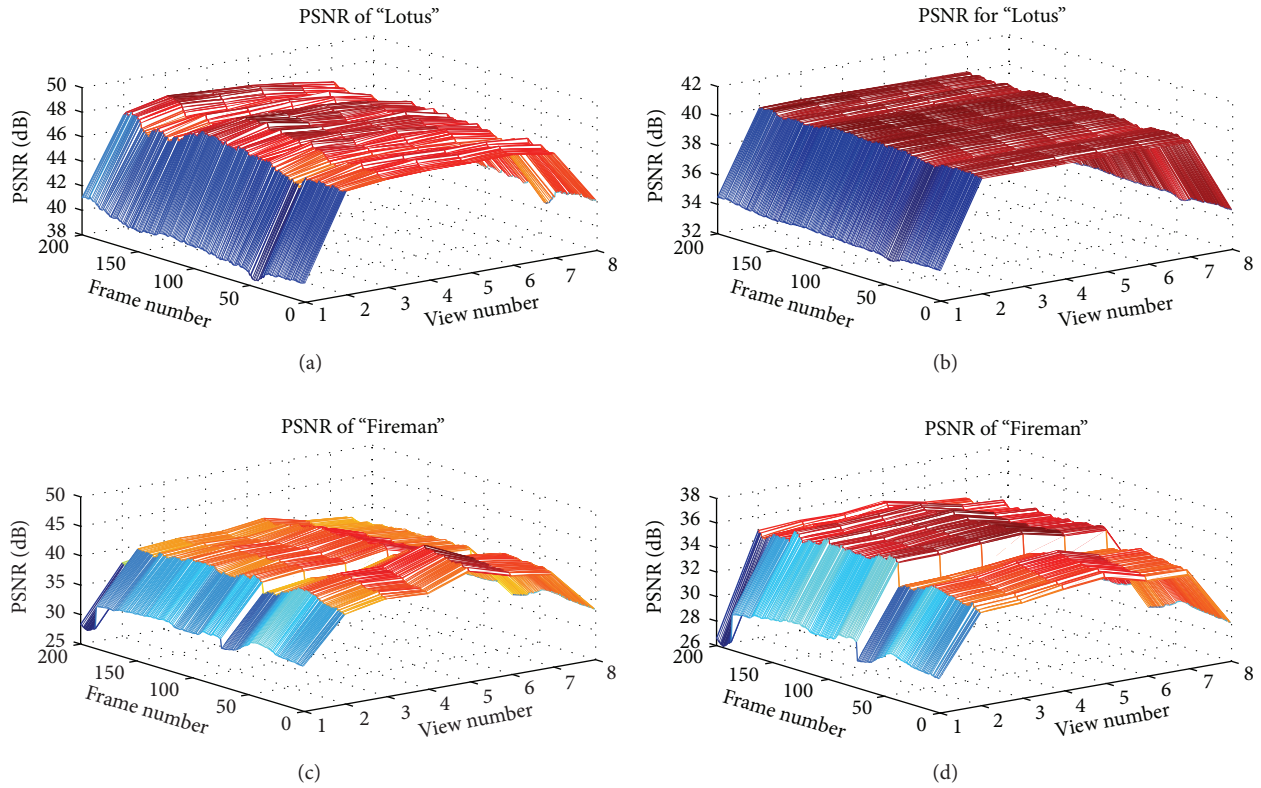


FIGURE 5: PSNR versus both the frame and the view numbers in corrected sequences. (a) PSNR of corrected “Lotus” by our method. (b) PSNR of corrected “Lotus” by the method in [11]. (c) PSNR of corrected “Fireman” by our method. (d) PSNR of corrected “Fireman” by the method in [11].

“Lotus.” As can be seen, the intensity observed at the optimal viewing position in the correction result by our method is very near to the intensity of intended view image; that is, the residual crosstalk reduces greatly in the results by our method.

We then estimate the average PSNR per view for the two test sequences. Table 1 lists the average residual crosstalk (PSNR) of each view of the two test sequences in results by the method in [11] and our method. These comparative results clearly demonstrate that the crosstalk reduction is better performed in our results.

To further verify the effectiveness of the proposed method, a photometer is used to measure the luminance at the optimal viewing position in our experiment. The screen we use for the measurements is the same 8-view 3D lenticular display as mentioned above. The screen is placed in a dark room and test images (before and after correction) and various reference images are displayed on it alternatively. The typical experiment measures crosstalk based on maximum pixel value. However, the pixel value is a random variable from 0 to 255 in the practical application, which is rarely 0 or 255. Furthermore, while the intended view image is observed, the other view images are all observed at the same time, rather than being observed alternatively. In typical experiment,

TABLE 1: Crosstalk reduction results (PSNR) comparison in two sequences.

Sequences	PSNR (dB)		
	Before correction	Method in [11]	Our method
“Fireman”			
View 1	26.0711	29.0970	32.5948
View 2	31.3607	34.7981	40.8481
View 3	31.5242	34.9284	41.7979
View 4	32.1086	35.2510	41.5759
View 5	32.0063	35.5148	43.1056
View 6	31.3716	34.7109	41.0957
View 7	31.3093	34.5597	40.3676
View 8	26.1231	29.2921	33.0626
“Lotus”			
View 1	30.1898	34.1157	39.7694
View 2	36.0433	39.9944	46.7904
View 3	36.0373	40.0222	47.4171
View 4	36.0175	39.9877	47.2790
View 5	36.0111	39.9765	47.2212
View 6	35.9936	39.9391	47.0899
View 7	35.9739	39.8958	46.5392
View 8	30.1766	34.6226	42.0747

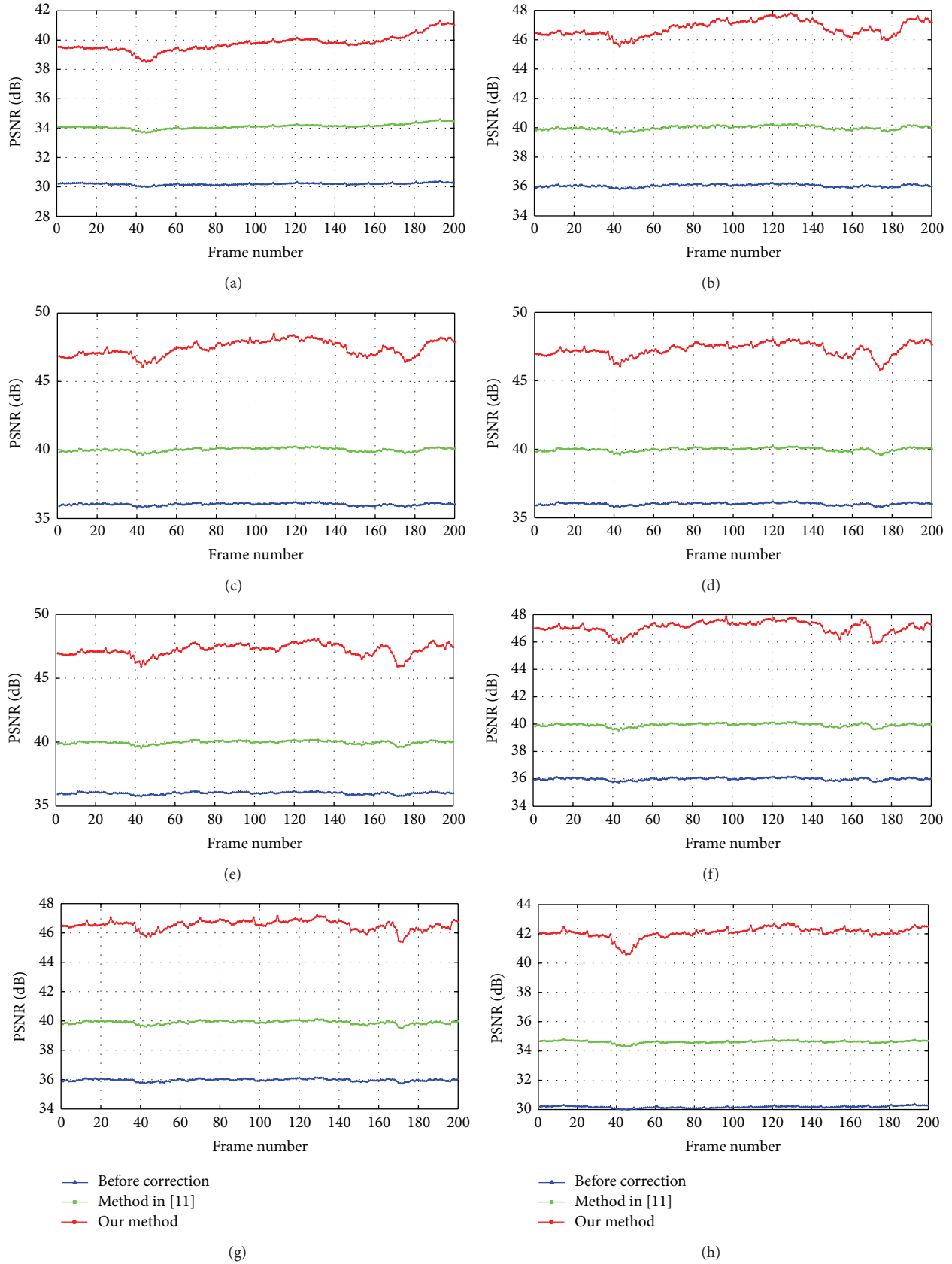


FIGURE 6: PSNR versus frames for each view in “Lotus.” (a) PSNR of view 1 in “Lotus.” (b) PSNR of view 2 in “Lotus.” (c) PSNR of view 3 in “Lotus.” (d) PSNR of view 4 in “Lotus.” (e) PSNR of view 5 in “Lotus.” (f) PSNR of view 6 in “Lotus.” (g) PSNR of view 7 in “Lotus.” (h) PSNR of view 8 in “Lotus.”

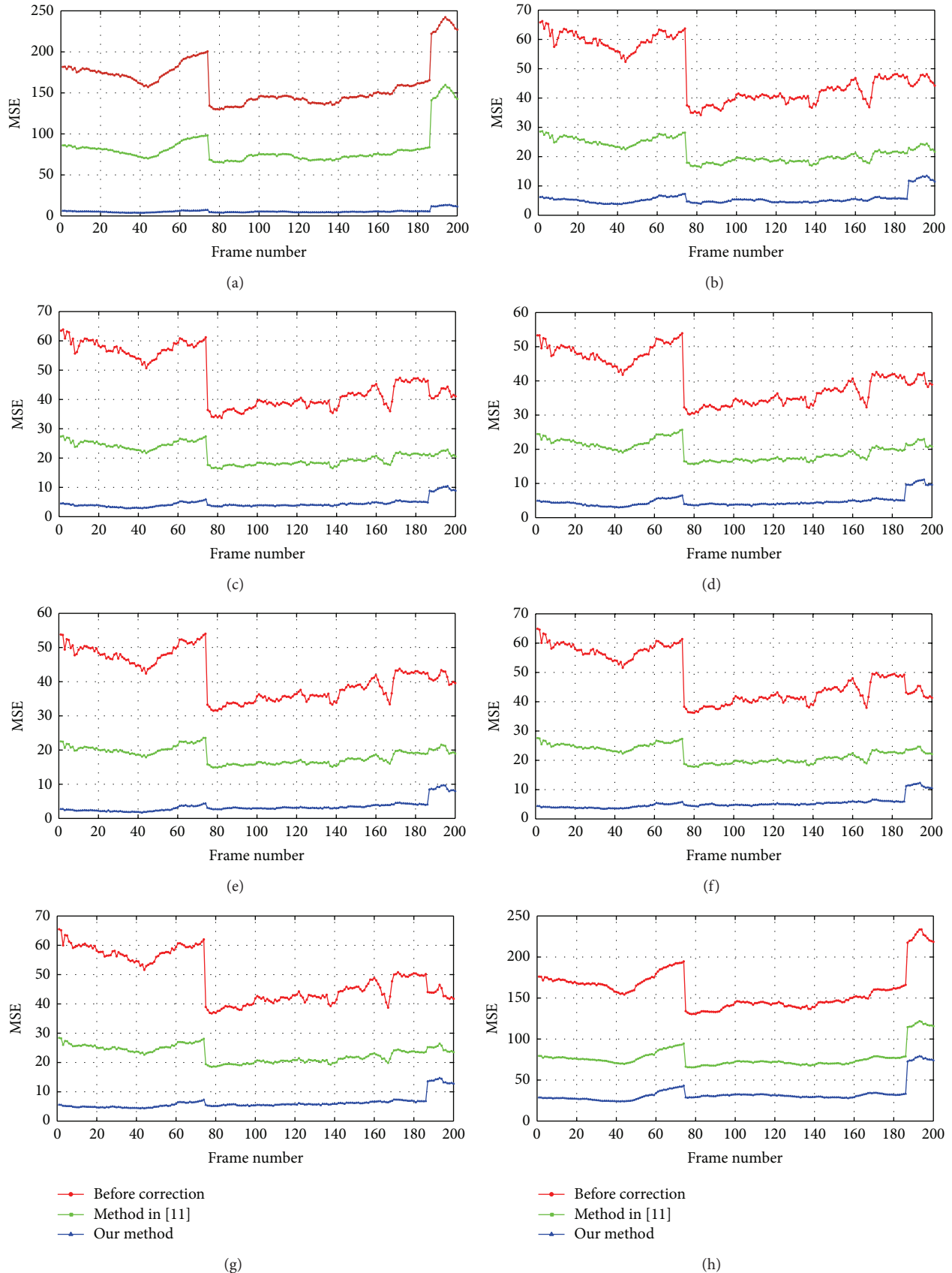


FIGURE 7: MSE versus frames for each view in "Fireman." (a) MSE of view 1 in "Fireman." (b) MSE of view 2 in "Fireman." (c) MSE of view 3 in "Fireman." (d) MSE of view 4 in "Fireman." (e) MSE of view 5 in "Fireman." (f) MSE of view 6 in "Fireman." (g) MSE of view 7 in "Fireman." (h) MSE of view 8 in "Fireman."

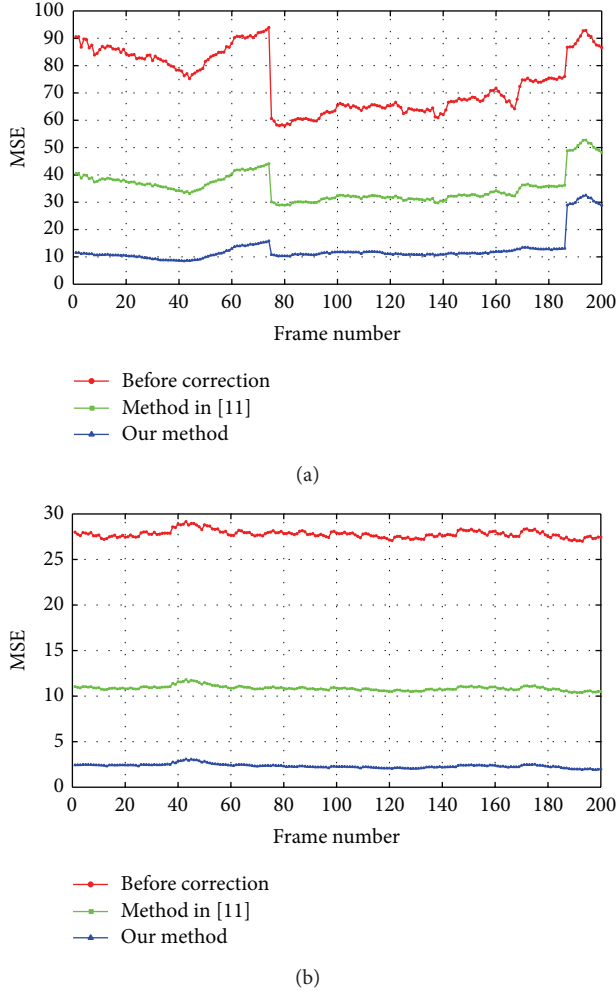


FIGURE 8: MSE versus frames in “Fireman” and “Lotus.”

when the luminance measured at the  $n$ th optimal viewing position is near to the intended luminance in the  $n$ th test image, the influence on the other viewing position is not evaluated. To be fair, we decide to use only one test image and 8 reference images for comparison. The test image is composed of 8 view images,  $V_1 = V_2 = 20$ ,  $V_3 = V_4 = 220$ ,  $V_5 = V_6 = 40$ , and  $V_7 = V_8 = 200$ , where  $V_n$  denotes pixel value of the  $n$ th view image. The luminance  $I_n$  is measured at the  $n$ th optimal viewing position by the photometer when the test image is presented on the screen. The intended view image’s luminance  $I_{ref_n}$  for the  $n$ th viewing position is obtained at the  $n$ th viewing position when the  $n$ th reference image is presented on the screen.  $V_1 = V_2 = \dots = V_8 = V_n$  in the  $n$ th reference image; that is, there is no crosstalk for  $n$ th view image. Absolute deviation is used to evaluate the performance, which is defined as  $|I_n - I_{ref_n}|$ . The corrected test images by the method in [11] and our method are presented on the display screen, respectively. Table 2 lists the deviation values of the correction results for each view by our method and the method in [11]. These comparative results clearly demonstrate that luminance measured in our result is very close to the intended view image’s luminance,

TABLE 2: Crosstalk reduction results (absolute deviation) comparison.

View number	Absolute deviation ( $\text{Cd/m}^2$ )	
	Method in [11]	Our method
1	6.609	5.968
2	8.532	7.919
3	18.503	2.000
4	16.945	0.855
5	3.040	2.584
6	11.063	10.624
7	21.049	2.042
8	21.173	1.741

which means the viewer crosstalk is eliminated largely by the proposed method.

## 4. Conclusions

Despite the fact that many researchers have been devoted to evaluating and eliminating the crosstalk in the stereoscopic display, there is still a lack of work on crosstalk reduction on multiview 3D displays. Typical methods for crosstalk measurement are based on the experiments, which cannot measure the precise crosstalk. In this paper, a system-introduced crosstalk measurement method is proposed to obtain crosstalk when slant angle of parallax barrier is an independent variable. Through this method, the crosstalk coefficient matrix  $\mathbf{A}$  is obtained. Moreover, we improve the lattice search algorithm to reduce the crosstalk on multiview 3D displays, which overcomes some shortcomings of algorithm BGBF. Both simulations and experimental results are presented to demonstrate that proposed method is capable of effectively reducing crosstalk on multiview 3D displays.

In practical applications, our system-introduced crosstalk measurement method can be employed to study the performance of multiview 3D techniques and our crosstalk reduction technology can improve the multiview 3D viewing quality. We hope the reader can implement our algorithms without difficulty.

## Conflict of Interests

The authors declare that there is no conflict of interests regarding the publication of this paper.

## Acknowledgments

This work was supported by National 863 Programm (no. 2012AA03A301) and by Ph.D. Programs Foundation of Ministry of Education of China (no. 20110032110029).

## References

- [1] L. Xing, J. You, T. Ebrahimi, and A. Perkis, “Assessment of stereoscopic crosstalk perception,” *IEEE Transactions on Multimedia*, vol. 14, no. 2, pp. 326–337, 2012.

- [2] V. V. Saveljev, "Characteristics of Moiré spectra in autostereoscopic three-dimensional displays," *Journal of Display Technology*, vol. 7, no. 5, pp. 259–266, 2011.
- [3] C. van Berkel, "Image preparation for 3d lcd," in *Stereoscopic Displays and Virtual Reality Systems VI*, vol. 3639 of *Proceedings of SPIE*, pp. 84–91, 1999.
- [4] H. Urey, K. V. Chellappan, E. Erden, and P. Surman, "State of the art in stereoscopic and autostereoscopic displays," *Proceedings of the IEEE*, vol. 99, no. 4, pp. 540–555, 2011.
- [5] A. J. Woods, "How are crosstalk and ghosting defined in the stereoscopic literature?" in *Stereoscopic Displays and Applications*, vol. 7863 of *Proceedings of SPIE*, pp. 1–12, 2011.
- [6] K. Huang, K. Lee, and H. Lin, "Crosstalk issue in stereo/autostereoscopic display," in *Proceedings of the International Display Manufacturing Conference*, pp. 2–18, 2009.
- [7] A. Boev, A. Gotchev, and K. Egiazarian, "Crosstalk measurement methodology for auto-stereoscopic screens," in *Proceedings of the 1st International Conference on 3DTV*, pp. 1–4, May 2007.
- [8] K. Vermeirsch, G. van Hoey, M. van Beurden, and P. Surman, "Measurement and evaluation of head tracked autostereoscopic displays," in *Proceedings of the 5th 3DTV Conference: The True Vision - Capture, Transmission and Display of 3D Video (3DTV-CON '11)*, pp. 1–4, May 2011.
- [9] C. Lee, G. Seo, J. Lee, T. H. Han, and J. G. Park, "Autostereoscopic 3D displays with reduced crosstalk," *Optics Express*, vol. 19, no. 24, pp. 24762–24774, 2011.
- [10] W. Zhao, Q. Wang, A. Wang, and D. Li, "Autostereoscopic display based on two-layer lenticular lenses," *Optics Letters*, vol. 35, no. 24, pp. 4127–4129, 2010.
- [11] X. Li, Q. Wang, D. Li, and A. Wang, "Image processing to eliminate crosstalk between neighboring view images in three-dimensional lenticular display," *IEEE/OSA Journal of Display Technology*, vol. 7, no. 8, pp. 443–447, 2011.
- [12] D. Wubben, D. Seethaler, J. Jalden, and G. Matz, "Lattice reduction," *IEEE Signal Processing Magazine*, vol. 28, no. 3, pp. 70–91, 2011.
- [13] M. O. Damen, H. El Gamal, and G. Caire, "On maximum-likelihood detection and the search for the closest lattice point," *IEEE Transactions on Information Theory*, vol. 49, no. 10, pp. 2389–2402, 2003.
- [14] X. Chang and Q. Han, "Solving box-constrained integer least squares problems," *IEEE Transactions on Wireless Communications*, vol. 7, no. 1, pp. 277–287, 2008.
- [15] C. Schnorr and M. Euchner, "Lattice basis reduction: improved practical algorithms and solving subset sum problems," *Mathematical Programming*, vol. 66, no. 2, pp. 181–199, 1994.
- [16] E. Agrell, T. Eriksson, and A. A. Vardy, "Closest point search in lattices," *IEEE Transactions on Information Theory*, vol. 48, no. 8, pp. 2201–2214, 2002.
- [17] J. Boutros, N. Gresset, L. Brunel, and M. Fossorier, "Soft-input soft-output lattice sphere decoder for linear channels," in *Proceeding of the IEEE Global Telecommunications Conference (GLOBECOM '03)*, vol. 3, pp. 1583–1587, December 2003.
- [18] H. Lim, S. H. Kim, Y. G. Lee, and H. Park, "A simultaneous view interpolation and multiplexing method using stereo image pairs for lenticular display," in *Proceedings of the 14th IEEE International Conference on Image Processing (ICIP '07)*, pp. V205–V208, San Antonio, Tex, USA, September 2007.

## Research Article

# An Efficient Biobjective Heuristic for Scheduling Workflows on Heterogeneous DVS-Enabled Processors

**Pengji Zhou and Wei Zheng**

*School of Information Science and Technology, Xiamen University, Xiamen 361005, China*

Correspondence should be addressed to Wei Zheng; [zhengw@xmu.edu.cn](mailto:zhengw@xmu.edu.cn)

Received 5 December 2013; Accepted 12 June 2014; Published 8 July 2014

Academic Editor: Aderemi Oluyinka Adewumi

Copyright © 2014 P. Zhou and W. Zheng. This is an open access article distributed under the Creative Commons Attribution License, which permits unrestricted use, distribution, and reproduction in any medium, provided the original work is properly cited.

Energy consumption has recently become a major concern to multiprocessor computing systems, of which the primary performance goal has traditionally been reducing execution time of applications. In the context of scheduling, there have been increasing research interests on algorithms using dynamic voltage scaling (DVS), which allows processors to operate at lower voltage supply levels at the expense of sacrificing processing speed, to acquire a satisfactory trade-off between quality of schedule and energy consumption. The problem considered in this paper is to find a schedule for a workflow, which is normally a precedence constrained application, on a bounded number of heterogeneous DVS-enabled processors, so as to minimize both makespan (overall execution time of the application) and energy consumption. A fast and efficient heuristic is proposed and evaluated using simulation with two real-world applications as well as randomly generated ones.

## 1. Introduction

During the last few decades, explosions in the volume of computation and/or data have stimulated a variety of researches on multiprocessor platforms (such as grids and clouds) to host complicated applications such as workflows [1, 2], which are widely used in the engineering, business, and science fields. It is not difficult to imagine that these powerful platforms, with a large (and still increasing) group of computing, storage, and connection equipment, must consume an enormous amount of energy. It has been estimated that the annual data center energy consumption in 2011 in the United States is over 100 billion kWh and at a cost of \$7.4 billion [3]. According to [4], in the United States, energy consumed by the information and communication technology equipment is roughly 8% of the total and will increase 50% within a decade. This, undoubtedly, will further deteriorate the environment with increasing CO<sub>2</sub> emission.

The increasingly challenging energy problem urges growing need in developing energy-efficient solutions for multiprocessor platforms. However, most of the current researches on resource management of these platforms (e.g., Condor [5], Pegasus [6], etc.) mainly focus on achieving performance

goals like high performance, high throughput, high reliability, and/or high availability to cater to users' requirements. As a result, most existing multiprocessor platforms generally lack capability on energy saving. This renders energy consumption problem an urgent and crucial issue to address.

Recent advancement in hardware technologies [7] (including dynamic voltage and frequency scaling, resource hibernation, memory optimization, solid state drives, energy-efficient computer monitors, etc.) have dealt with the energy consumption issues to some extent. However, it still remains a serious concern for software techniques such as scheduling algorithms (especially in a multiprocessor platform) to achieve substantial energy saving.

In this paper we consider workflow scheduling based on DVS, as it has demonstrated to be a promising technique in an abundance of literatures [8–12]. DVS enables processors to dynamically adjust voltage supply levels (VSLs) and CPU frequencies aiming to reduce power consumption, while an acceptable amount of performance sacrifice is paid as the expense.

With the aim at simultaneously minimizing makespan and energy consumption, the general form of the problem we considered here boils down to biobjective DAG scheduling,

as we assume every workflow application is represented by a directed acyclic graph (DAG). In particular, we focus on DAG scheduling for admission control of service- and market-oriented computing environments such as clouds, where a user and a service provider need to reach an agreement before the execution of the user application, and users are free to choose among different service providers. In such a scenario, a service provider needs the DAG scheduling return a competitive makespan (to attract customers) and a low energy consumption (for energy saving). Moreover, the scheduling should be performed in *short time* as users normally require a real-time response. There have been a few biobjective DAG scheduling heuristics in the literature. Some of these heuristics may provide quick response, but their performance leaves a considerable space to improve. Other heuristics may exhibit satisfactory performance but the scheduling cost is extremely high, and therefore not particularly suitable for the scenario discussed above. The need for fast and efficient DAG scheduling heuristics, suitable for real admission control of clouds, motivates the work presented in this paper.

This paper presents a new biobjective heuristic with the objective to simultaneously provide effective DVS-based DAG scheduling and fast scheduling time. Our heuristic is an enhancement of energy conscious scheduling heuristic (ECS) [11], which could make a quick scheduling decision, whereas the scheduling performance is often limited due to local optimum. With deliberation, we refine the core of ECS, namely, propose a novel objective function used by the RS (relative superiority) and a new criteria used by the MCER (makespan-conservative energy reduction technique) phases of ECS, to derive a new heuristic. The comparison results obtained from our extensive evaluation show that our approach can make significant improvement on both makespan optimization and energy reduction while still meeting real-time response requirement. This indicates that our approach can be easily applied to admission control of service- and market-oriented computing systems.

The remainder of the paper is organized as follows. Section 2 describes the background and related work. Section 3 describes the models used in our study and specifies the problem to be addressed. The proposed scheduling approach is presented in Section 4 with an illustrative example. The results of our comparative evaluation are shown in Section 5. Finally, the paper is concluded in Section 6.

## 2. Related Work

Dozens of static DAG scheduling heuristics aiming at minimizing makespan for heterogeneous multiprocessor systems have been presented in the literature. These heuristics are designed following different design principles. We hereby roughly classify these heuristics into list-scheduling algorithms [13–16], duplication-based algorithms [17–19], clustering algorithms [20, 21], and guided random search methods [22, 23]. Apparently, all these heuristics are different with our study in that their scheduling does not take energy consumption into account.

As DVS is a promising energy saving technique that can be incorporated into scheduling, a large number of scheduling algorithms based on DVS have been proposed for diverse applications and computing platforms. The majority of these DVS-based scheduling heuristics are conducted on homogeneous computing systems [9, 10, 24, 25], or single-processor systems [3, 26, 27], or focused on independent tasks [28–30]. These heuristics cannot address issues like task dependency and processor heterogeneity, which are addressed in our study.

There are also DVS-based scheduling heuristics focusing on DAG applications as well as heterogeneous systems. Huang et al. [12] proposed an enhanced energy-efficient scheduling algorithm to reduce energy consumption while meeting performance-based service level agreement (e.g., deadline constraint). This algorithm exploited the slack room between initially scheduled tasks and reallocated them in a global manner to achieve power saving. Unlike this work, applications considered in our study are not deadline-constrained, and the evaluation of the quality of schedules should be measured on both makespan and energy consumption.

Evolutionary techniques (i.e., genetic algorithm) have been widely applied to various problems (i.e., energy supply [31], space allocation [32], and multiobjective scheduling [33], etc.). Mezmaiz et al. [34] proposed a hybrid genetic algorithm using DVS to simultaneously minimize makespan and energy consumption. Algorithms based on evolutionary techniques normally perform well on optimization. However, these algorithms usually require significantly high scheduling costs, even though modification may be applied to improve their efficiency [35]. As a result, these algorithms are naturally too time-consuming for admission control of clouds where a real-time response is required.

Energy-conscious scheduling heuristic (ECS) [11] is a list-scheduling algorithm aiming at simultaneously minimizing makespan and energy consumption with a low complexity. The heuristic consists of two phases. In the first phase, the heuristic applies bottom-level ranking to prioritize tasks, and then, in turn, selects the processor and the VSL for the current task so that the devised objective function, which is defined as relative superiority (RS), can be maximized. After the first phase, a temporary schedule is generated. In the second phase, a new criterion is used, which is defined as makespan-conservative energy reduction technique (MCER). That is, for each prioritized task in the current schedule, all of other combinations of task, processor, and VSL are checked to see whether any of these combinations reduces the energy consumption of the task without increasing the current makespan. If so, such a combination is applied to obtain a new schedule. After the second phase, the newest schedule is returned as the scheduling result. Evaluation results demonstrate that ECS significantly outperforms energy unconscious heuristics on energy consumption. However, the RS and MCER used by ECS, which are the cores of the algorithm, consider only local optimality. As a result, the scheduling decisions made by ECS tend to be confined to a local optimum. This motivates our work to propose novel objective function and criteria and devise a new heuristic.

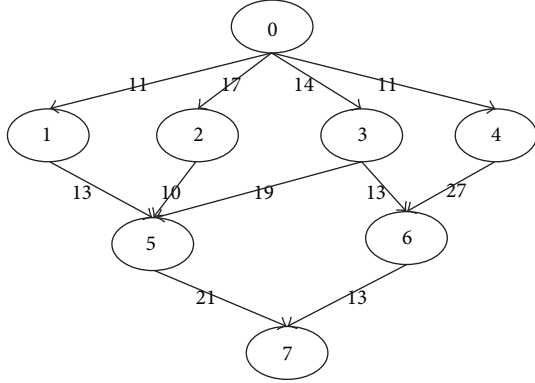


FIGURE 1: A simple DAG G.

The experimental results presented in Section 5 clearly show that our approach obtains schedules which are better than those found by ECS on both makespan optimization and energy reduction.

### 3. Problem Description

In this section, we describe the application model, the system model, and the energy model that used in our work and then specify the problem we are going to address.

**3.1. Application Model.** We use a directed acyclic graph (DAG) to represent an application to be scheduled (shown in Figure 1 with its details in Table 3). In a DAG, nodes denote tasks and edges that represent data transmission between tasks. In our work, we use  $G = (N, E)$  to represent a DAG, which consists of a set of nodes  $N$  and a set of edges  $E$ . A node  $i \in N$  represents the corresponded task and an edge  $(i, j) \in E$  represents the intercommunication and precedence constraint between node  $i$  and  $j$ . For an edge  $(i, j)$ ,  $i$  is called a parent node of  $j$ , and  $j$  is called a child node of  $i$ . A child node cannot start execution until all of its parents have finished and all the required data transmission has arrived. Parentless nodes are called *source nodes*; childless node are called *sink node*. Apparently, an entry node of  $G$  must be a source node and an exit node a sink node. For standardization, we specify in this paper that a DAG has only a single entry node and a single exit node. One can easily see that all DAGs with multiple entry or exit nodes can be equivalently transformed to this standardization [36]. For illustration, a simple example DAG is shown in Figure 1, where the weight attached to each edge denotes the amount of data to be transmitted.

In order to meet precedence constraint, the start time and the finish time of task  $j$  on processor  $q \in N$  are computed by

$$\begin{aligned} ST(j, q) &= \max \left\{ FT(l^*, q), \max_{k \in \text{Par}_j} \{ FT(k, p_k) \right. \\ &\quad \left. + TC((k, p_k), (j, q)) \} \right\}, \\ FT(j, q) &= ST(j, q) + EC(j, q), \end{aligned} \quad (1)$$

where  $EC(j, q)$  represents the execution time of task  $j$  on processor  $q$ ;  $FT(l^*, q)$  denotes the finish time of task  $l^*$  which is the currently last task on processor  $q$ ;  $\text{Par}_j$  represents the set of all parent tasks of task  $j$ ;  $p_k$  denotes the processor which task  $k$  is assigned to, and if there is no task assigned to processor  $q$ ,  $FT(l^*, q)$  is equal to zero. In the case of the entry task, we have

$$ST(\text{entrynode}, p_{\text{entrynode}}) = 0. \quad (2)$$

After the scheduling is completed, the *makespan* of the schedule, is defined as

$$\text{makespan} = \max_{k \in N} FT(k, p_k). \quad (3)$$

**3.2. System Model.** We consider a set of DVS-enabled heterogeneous processors which are fully interconnected and equally capable of running any applications. All the processors can run at different voltage and frequency levels. While the processor is in idle, it stays at its lowest voltage and lowest frequency level for the maximal energy saving [37]. Hereby we assume a set of DVS-enabled processors (denoted by  $P$ ) that are fully connected. It is assumed that the time needed to transmit per unit of data from one processor to another, named *transmission rate*, is constant and preknown (as illustrated in Table 2). Therefore, the time needed to transmit data from one processor to another, named *transmission latency*, is computed by

$$TC((i, p), (j, q)) = TD(i, j) \times TR(p, q), \quad (4)$$

where  $TD(i, j)$  denotes the amount of transmitted data from task  $i$  to  $j$  and  $TR(p, q)$  if task  $i$  and  $j$  are allocated to the same processor, the transmission latency is zero. It is also assumed that one processor can only run one task at a time and no preemption is considered.

Each processor can operate in a set of voltage supply levels (VSL, denoted by  $V$ ), each of which is corresponded to a specific relative speed (as illustrated in Table 1). For task  $n_i$ , we assume its execution time on a processor  $p$ , which operates on VSL 0 (denoted by  $EC(i, p, v_{p,0})$ ), is preknown; thereby, the execution time of  $n_i$  on a different VSL  $j$  (denoted by  $EC(i, p, v_{p,j})$ ) can be obtained by the ratio of  $EC(i, p, v_{p,0})$  and the relative speed of VSL  $j$ .

**3.3. Energy Consumption Model.** We adopt the energy model used in [11], which is derived from the power consumption model in complementary metal-oxide semiconductor (CMOS) logic circuits. Since we assume the processors consume a certain amount of energy while idling, the total energy consumption of the execution for a DAG is comprised of direct and indirect energy consumption. The direct energy consumption is defined as

$$E_d = \sum_{i=1}^n \alpha V_i^2 \Delta t_i, \quad (5)$$

where  $n$  is the number of tasks,  $\alpha$  is a device related constant,  $V_i$  is the voltage on which the processor operates

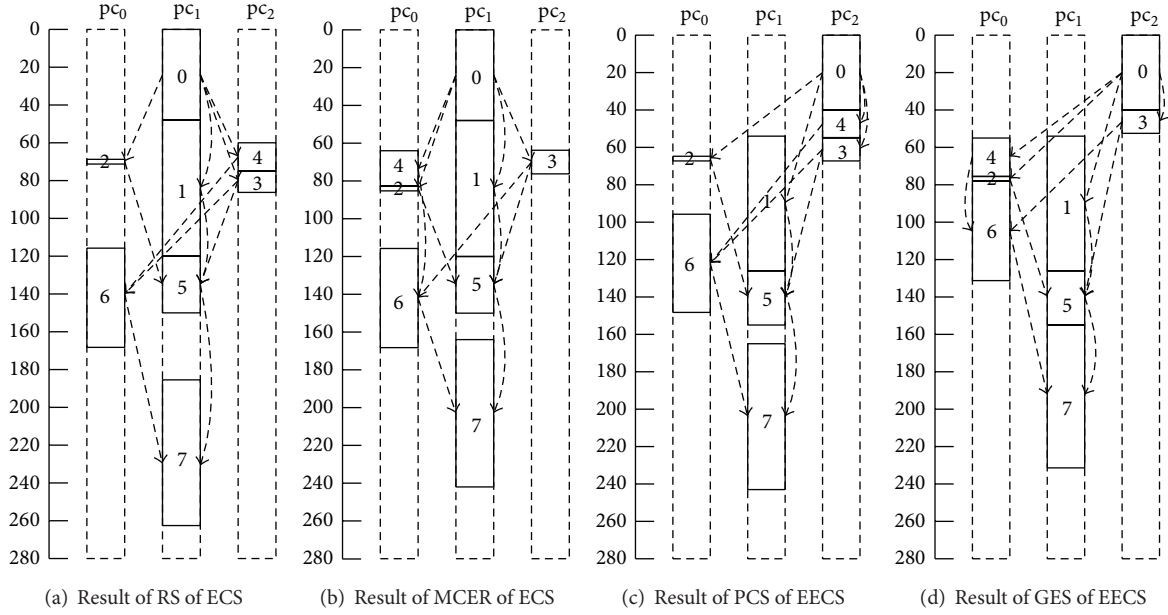
FIGURE 2: Schedules of  $G$  with EECS and ECS algorithms.

TABLE 1: Voltage relative speed pairs.

Level	$pc_0$		$pc_1$		$pc_2$	
	Voltage ( $v_k$ )	Speed (%)	Voltage ( $v_k$ )	Speed (%)	Voltage ( $v_k$ )	Speed (%)
0	1.60	100	1.20	100	2.00	100
1	1.40	85	1.10	90	1.70	80
2	1.20	70	1.00	80	1.40	60
3	1.00	55	0.90	70	1.10	40
4	0.80	40	0.80	60		
5			0.70	50		

TABLE 2: Transmission rate between different processors.

Connected processors	Transmission rate
$pc_0$ and $pc_1$	1.27
$pc_0$ and $pc_2$	1.53
$pc_1$ and $pc_2$	1.10

TABLE 3: Computation cost with VSL 0.

Task	$pc_0$	$pc_1$	$pc_2$	Task	$pc_0$	$pc_1$	$pc_2$
0	36	24	16	4	8	35	6
1	27	36	41	5	25	15	36
2	1	33	48	6	21	21	33
3	30	6	5	7	34	39	31

when executing task  $i$ , and  $\Delta t_i$  is the amount of time taken for  $n_i$ 's execution. On the other hand, the indirect energy consumption is defined as

$$E_i = \sum_{j=1}^p \sum_{d_{j,k} \in D_j} \alpha V_{j,\text{low}}^2 \Delta w_{j,k}, \quad (6)$$

where  $p$  is the number of processors,  $D_j$  is the set of idling slots (between time 0 and the makespan) on processor  $p_j$ ,  $V_{j,\text{low}}$  is the lowest supply voltage on  $p_j$ , and  $\Delta w_{j,k}$  is the amount of idling time for  $d_{j,k}$ . Then, the total energy consumption is defined as

$$E_{\text{total}} = E_d + E_i. \quad (7)$$

**3.4. Scheduling Problem.** The scheduling problem in this study is allocating  $n$  tasks in a DAG to  $p$  DVS-enabled heterogeneous processors, to simultaneously minimize makespan and energy consumption while still meeting precedence constraints between tasks. We assume all DAGs start execution at time 0 and the makespan is defined as the latest finish time of  $n$  tasks after the scheduling is completed.

## 4. Methodology

In this section, we present the proposed new heuristic enhanced energy conscious scheduling heuristic (EECS), as well as a simple example for illustration purpose.

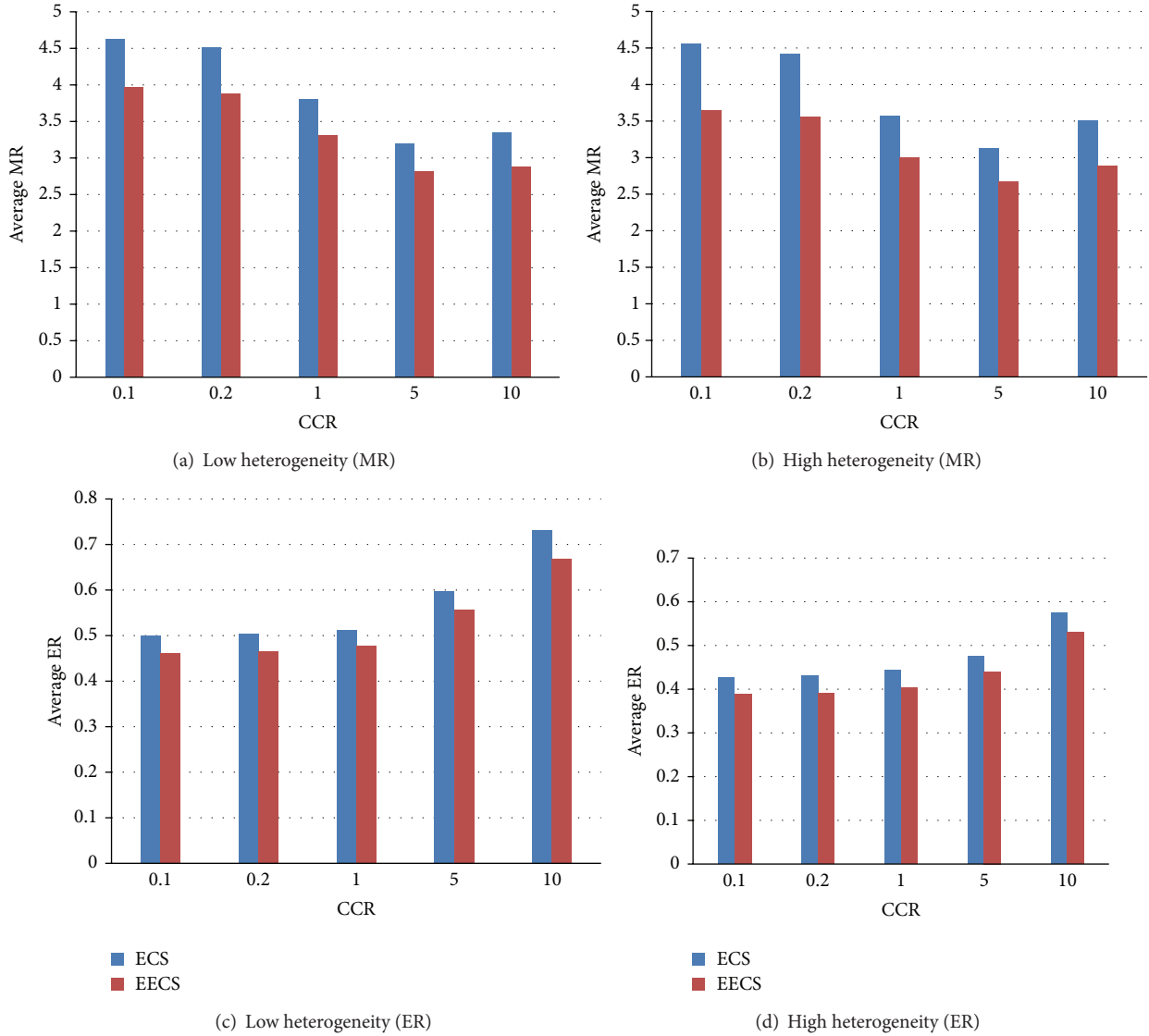


FIGURE 3: Laplace, 49 nodes (different heterogeneities of processors).

TABLE 4: Task priorities of G.

$n_i$	0	1	2	3	4	5	6	7
$b$ -level	178.50	138.87	127.63	125.67	128.00	87.30	76.57	34.67

TABLE 5: The schedule results of EECS and ECS for G.

	Result of RS of ECS	Result of MCER of ECS	Result of PCS of EECS	Result of GES of EECS
Makespan	264.42	242.8	243.32	232.1
Energy	25946.87	23915.8	23967.02	22861.85

TABLE 6: Experimental parameters.

Parameter	Value
The number of tasks	$U(20, 200)$
CCR	{0.1, 0.2, 1, 5, 10}
The number of processors	{3, 5, 8}
Processors heterogeneity	{low, high}

4.1. *Proposed Heuristic.* As presented in Algorithm 1, our heuristic first prioritizes tasks based on bottom-level ranking (denoted by  $b$ -level), which is computed by adding the average computation and communication costs along the

longest path of the exit node in the DAG. Next, Algorithm 2 is applied to the prioritized tasks to generate an initial schedule. However, scheduling decisions made in Algorithm 2 are

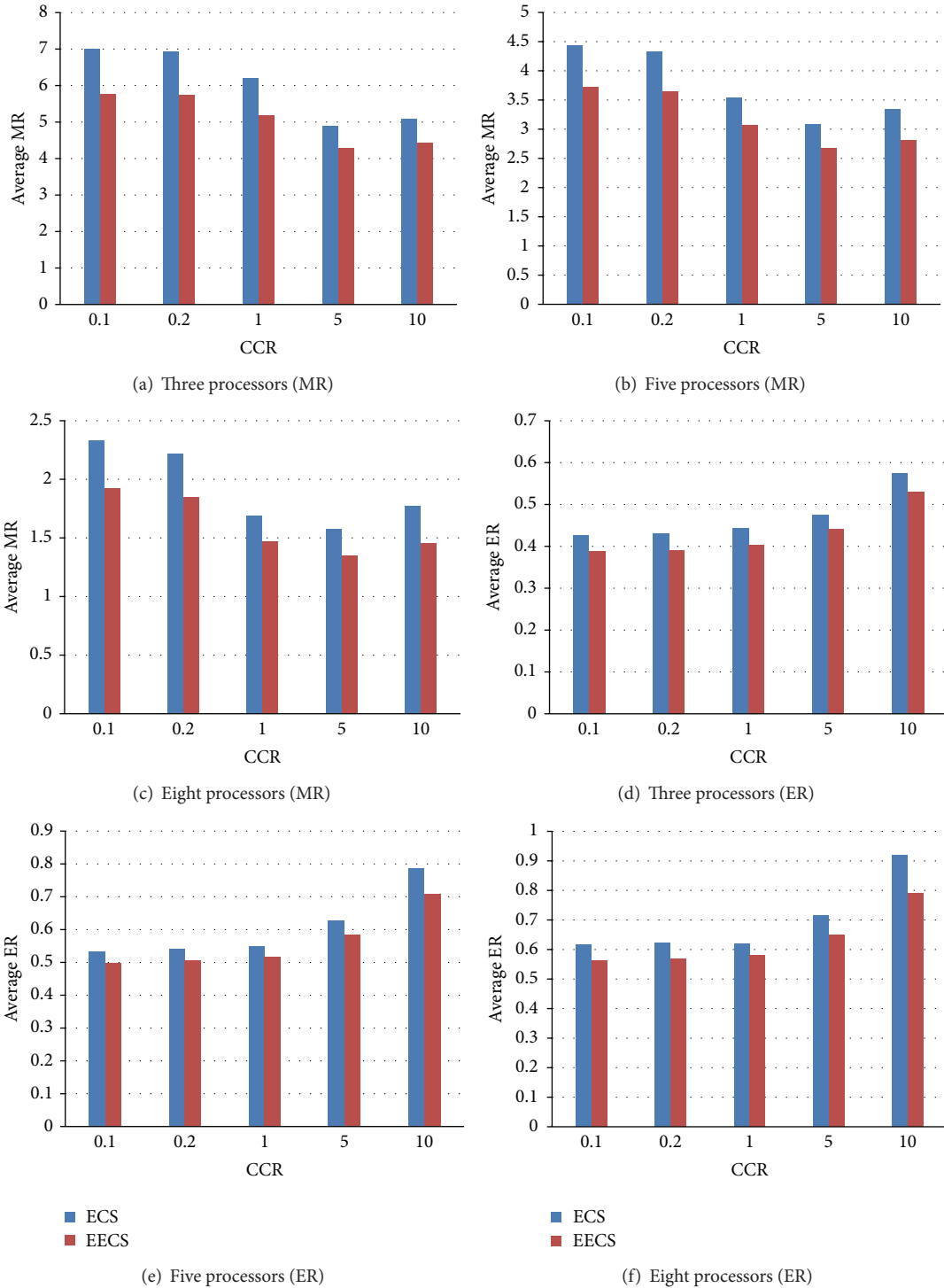


FIGURE 4: Laplace, 49 nodes (different sizes of processors).

inevitably limited by local greed. Therefore, the generated schedule is adjusted by Algorithm 3 for further optimization.

Algorithm 2 explains how the scheduling decision is made for each task in the initial schedule. We make scheduling decisions for tasks in turn. In each turn, one task is assigned a specific processor with a specific VSL, which

is picked up from all possible combinations of processor and VSL, for optimum. Note that our scheduling aims at minimization on two objectives (i.e., makespan and energy consumption), which normally conflict with each other. This indicates the evaluation of a processor-VSL combination is not straightforward. In order to make a comparison between

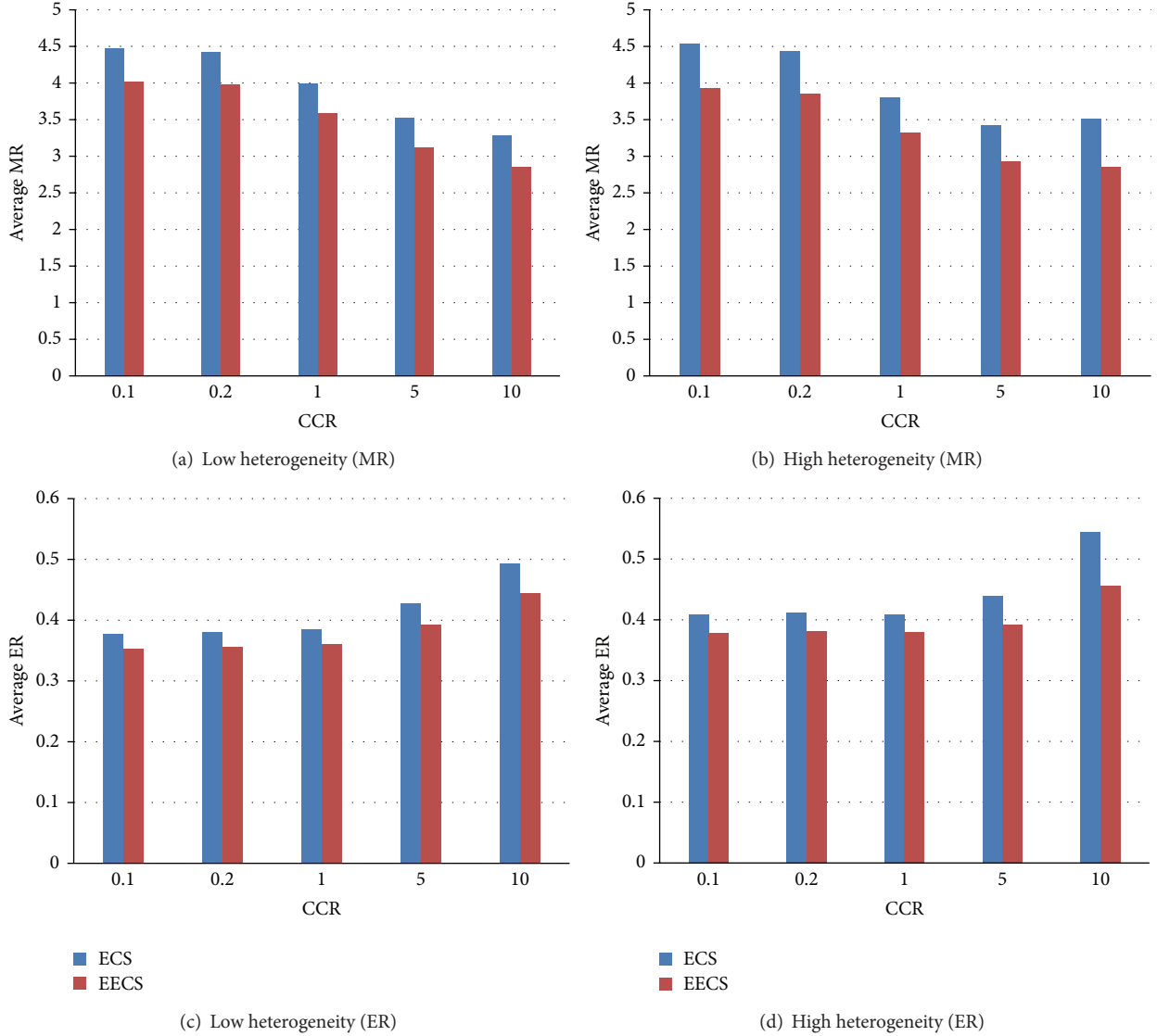


FIGURE 5: LIGO, 77 nodes (different heterogeneities of processors).

TABLE 7: Comparative results of different sizes of processors.

	Improvement by EECS over ECS					
	3		5		8	
	Makespan	Energy	Makespan	Energy	Makespan	Energy
Random	10.2%	6.1%	11.01%	7.52%	15.12%	11.81%
LIGO	10.54%	7.25%	12.18%	8.01%	14.28%	9.67%
Laplace	15.73%	8.34%	14.98%	7.49%	16.26%	9.88%
Average	12.16%	7.23%	12.73%	7.67%	15.22%	10.45%

two combinations, we devise substitution score (SUBS). For task  $n_i$ ,  $SUBS(n_i, p', v', p, v)$  quantifies the score gained if a processor-VSL combination  $(p, v)$  is replaced by  $(p', v')$ . SUBS deliberately takes into account the trade-off between makespan minimization and energy reduction. As defined in (8), SUBS is a sum of three factors. The first factor is local energy factor, which is the difference of energy caused by

the substitution with normalization by the energy consumption of current task. The second factor is local execution time factor, which is the difference of task execution time caused by the substitution with normalization by the execution time of current task. The third factor is makespan factor, which is the difference of task finish time caused by the substitution with normalization by the execution time of current task.

**Input:** A DAG  $G(N, E)$  and a set  $P$  of DVS-enabled processors.  
**Output:** A schedule  $S$  of  $G$  onto  $P$ .

- (1) Compute the weights of nodes and edges averaged over different processors.
- (2) Compute the bottom-level ranking for each node.
- (3) Sort all tasks in the non-ascending order of bottom-level and put them into list  $L$ .
- (4) Generate an initial schedule with consideration on makespan-energy tradeoff (by Algorithm 2).
- (5) Adjust the schedule for global energy saving. (by Algorithm 3).

ALGORITHM 1: EECS heuristic outline.

- (1) **for** each sorted task  $n_i$  in  $L$  **do**
- (2)   let  $p_{\text{opt}}$  be  $p_0$ .
- (3)   let  $v_{\text{opt}}$  be  $v_{p_0,0}$ .
- (4)   **for** each processor  $p_j$  in  $P$  **do**
- (5)     **for** each voltage  $v_{p_j,k}$  in  $V$  **do**
- (6)       Compute  $S_{\text{stay}} = \text{SUBS}(n_i, p_{\text{opt}}, v_{\text{opt}}, p_j, v_{p_j,k})$  as defined in (8).
- (7)       Compute  $S_{\text{change}} = \text{SUBS}(n_i, p_j, v_{p_j,k}, p_{\text{opt}}, v_{\text{opt}})$  as defined in (8).
- (8)       **if**  $S_{\text{stay}}$  is greater than  $S_{\text{change}}$  **then**
- (9)         Assign  $p_j$  and  $v_{p_j,k}$  to  $p_{\text{opt}}$  and  $v_{\text{opt}}$ , respectively.
- (10)      **end if**
- (11)    **end for**
- (12)   **end for**
- (13)   Allocate task  $n_i$  on  $p_{\text{opt}}$  with  $v_{\text{opt}}$ .
- (14) **end for**

ALGORITHM 2: Pairwise comparison and selection.

As defined in (8), in the case of  $p = p'$ , the makespan factor is ignored, as the sign of makespan factor is always in accordance with the sign of local execution time factor:

$$\text{SUBS}(n_i, p', v', p, v) = \begin{cases} \frac{E_d(n_i, p', v') - E_d(n_i, p, v)}{E_d(n_i, p, v)} + \frac{\text{EC}(n_i, p', v') - \text{EC}(n_i, p, v)}{\text{EC}(n_i, p, v)} + \frac{\text{FT}(n_i, p', v') - \text{FT}(n_i, p, v)}{\text{EC}(n_i, p, v)} & \text{if } p \neq p' \\ \frac{E_d(n_i, p', v') - E_d(n_i, p, v)}{E_d(n_i, p, v)} + \frac{\text{EC}(n_i, p', v') - \text{EC}(n_i, p, v)}{\text{EC}(n_i, p, v)} & \text{otherwise,} \end{cases} \quad (8)$$

where, for task  $n_i$  on processor  $p$  with VSL  $v$ ,  $E_d(n_i, p, v)$  denotes the directed energy consumption of  $n_i$ ,  $\text{EC}(n_i, p, v)$  the execution time of  $n_i$ , and  $\text{FT}(n_i, p, v)$  the finish time of  $n_i$ .

In Algorithm 3, for each scheduled task, we check whether there exists another processor-VSL combination, which, by replacing the currently scheduled combination, can reduce the total energy consumption (different with the MCER technique used in ECS, which consider only the energy consumption of the current task) without increasing the makespan. If so, the replacement will be enforced.

TABLE 8: Comparative results of different heterogeneities of processors.

	Improvement by EECS over ECS			
	Low		High	
	Makespan	Energy	Makespan	Energy
Random	11.0%	7.25%	14.14%	9.49%
LIGO	10.83%	7.66%	14.42%	10.1%
Laplace	13.51%	7.52%	17.84%	9.75%
Average	11.78%	7.48%	15.47%	9.78%

Based on the above description, it is not difficult to compute that the complexity of our heuristic is  $O(n \log n + 2((e + n)pv))$ , where  $n$  is the number of DAG nodes,  $e$  the number of DAG edges,  $p$  the number of processors, and  $v$  the number of VSLs.

**4.2. An Example.** A simple DAG with 8 nodes is used here for illustration purpose. Figure 1 shows the DAG structure and the size of data to transmit between two interdependent tasks. Three processors (as depicted in Table 1) are assumed to run the DAG, and the execution time of each task on each processor is provided in Table 3. Additionally, Table 2 provides the data transmission rates among these processors.

Table 4 provides the *b-level* results computed for each node of the DAG example. According to these results, the tasks are sorted as follows:  $\{0, 1, 4, 2, 3, 5, 6, 7\}$ .

```

(1) for each task  $n_i$  sorted in  $L$  do
(2)   let  $p_{\text{opt}}$  be the processor on which  $n_i$  is currently scheduled.
(3)   let  $v_{\text{opt}}$  be the VSL to which  $n_i$  is currently assigned.
(4)   for each processor  $p_j$  in  $P$  do
(5)     for each voltage  $v_{p_j,k}$  in  $V$  do
(6)       Tentatively reallocate  $n_i$  onto  $p_j$  with  $v_{p_j}$ .
(7)       Recompute the makespan.
(8)       Recompute the total energy consumption  $E_{\text{total}}$  as defined in (7).
(9)       if no increase in makespan and the total energy consumption is reduced then
(10)        Assign  $p_j, v_{p_j,k}$  to  $p_{\text{opt}}, v_{\text{opt}}$ , respectively.
(11)        Update the makespan and the total energy consumption.
(12)       end if
(13)     end for
(14)   end for
(15)   Allocate  $n_i$  on  $p_{\text{opt}}$  with  $v_{\text{opt}}$ .
(16) end for

```

ALGORITHM 3: Global energy saving.

TABLE 9: Comparative results of Figure 5: LIGO, 77 nodes (different heterogeneities of processors).

	ECS				EECS			
	Low heterogeneity		High heterogeneity		Low heterogeneity		High heterogeneity	
	MR (%)	ER (%)	MR (%)	ER (%)	MR (%)	ER (%)	MR (%)	ER (%)
0.1	4.47	0.37	4.53	0.41	4.02	0.35	3.93	0.38
0.2	4.42	0.38	4.44	0.41	3.98	0.36	3.85	0.38
1	4.0	0.39	3.81	0.40	3.59	0.36	3.32	0.38
5	3.53	0.43	3.43	0.44	3.12	0.39	2.93	0.39
10	3.28	0.49	3.52	0.54	2.85	0.44	2.85	0.46

Figure 2(a) depicts the schedule generated by the first phase (i.e., RS) of ECS, and Figure 2(b) is the schedule finally obtained by ECS after applying MCER. Figures 2(c) and 2(d) show the schedules generated by the PCS phase and the GES phases of EECS, respectively. The corresponding makespan and energy consumption for each schedule is provided in Table 5.

In this specific example, the PCS phase of EECS generates a better schedule (with shorter makespan and less energy consumption) than the one obtained by the RS phase of ECS. By comparing Figures 2(c) and 2(d), we clearly see the effectiveness of GES on energy reduction without increasing the makespan. Although for ECS, MCER can also improve the schedule quality obtained by RS. However, the final schedule of ECS is still 4.41% down on makespan minimization and 4.60% down on energy reduction, in comparison with the result obtained by EECS. This implies that EECS can outperform ECS on both minimizing makespan and reducing energy. We verify this implication in the next section.

## 5. Performance Evaluation

In this section, we compare our algorithm (EECS) with ECS. We consider DAGs derived from real-world workflow applications and a simulated heterogeneous system, which consists of processors with DVS parameter setting derived

from real CPU models. Simulation results demonstrate the significant improvement our algorithm makes both on makespan optimization and energy saving.

*5.1. Experimental Setting.* In our evaluation, we considered randomly generated DAGs and two real-world applications, which are LIGO [38] with 77 nodes and Laplace equation solver [39] with 49 nodes. When generating random DAGs, we followed the method presented in [40]. Figure 1 illustrates how a random DAG looks like. Note that the node number of LIGO and Laplace is fixed, while the node number of a random DAG randomly selected from the range of [20, 200].

We also considered different numbers of resources: 3, 5, and 8. All processors are DVS-enabled and the VSL parameter is randomly selected from Table 1. In order to model task execution times, we adopted the method presented in [41]. In this method, in brief, two values are selected from a uniform distribution in a certain interval. The product of the two selected values is computed and adopted as a generation of one task execution time. We classified the task execution times generated from the interval [10, 50] into low heterogeneity, those from [10, 1000] into high heterogeneity.

The computation and communication ratio (CCR) is a measure that indicates whether the DAG is communication intensive, computation intensive, or moderate. The definition

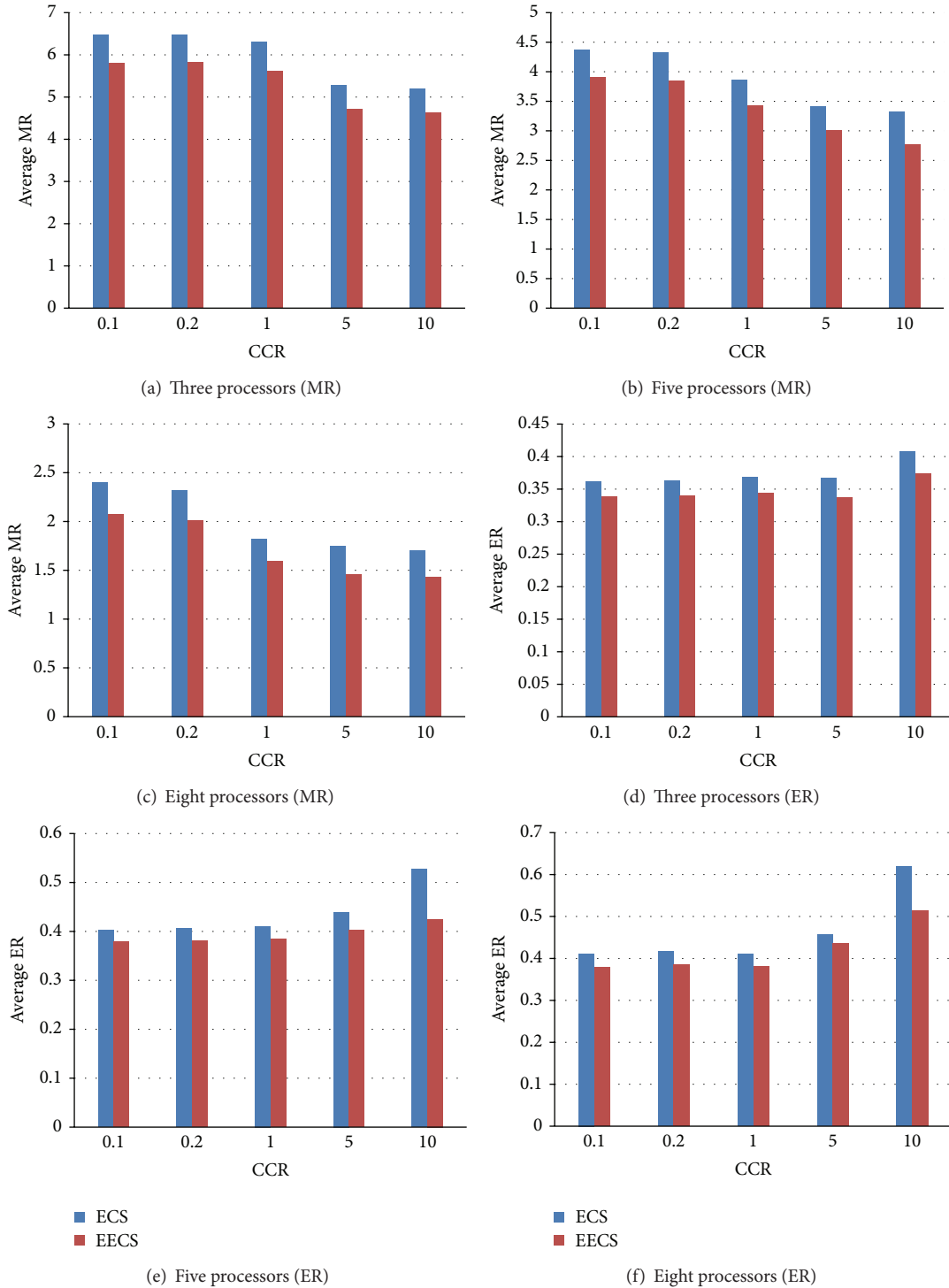


FIGURE 6: LIGO, 77 nodes (different sizes of processors).

of CCR is the ratio between the average communication cost and the average computation cost on the target system. We considered five specific CCR values: 0.1, 0.2, 1.0, 5, and 10. With a set of generated task execution times, the communication costs of the tasks were randomly generated to keep consistency with the given CCR.

For every competing heuristic (ECS and EECS), the number of experiments conducted is 45000. Table 6 summarized the parameters used in our experiments. Specifically, for each type of DAG, the base DAG set consists of 500 random samples. This figure is combined with 5 different CCRs, 3 different numbers of processors, 2 different types

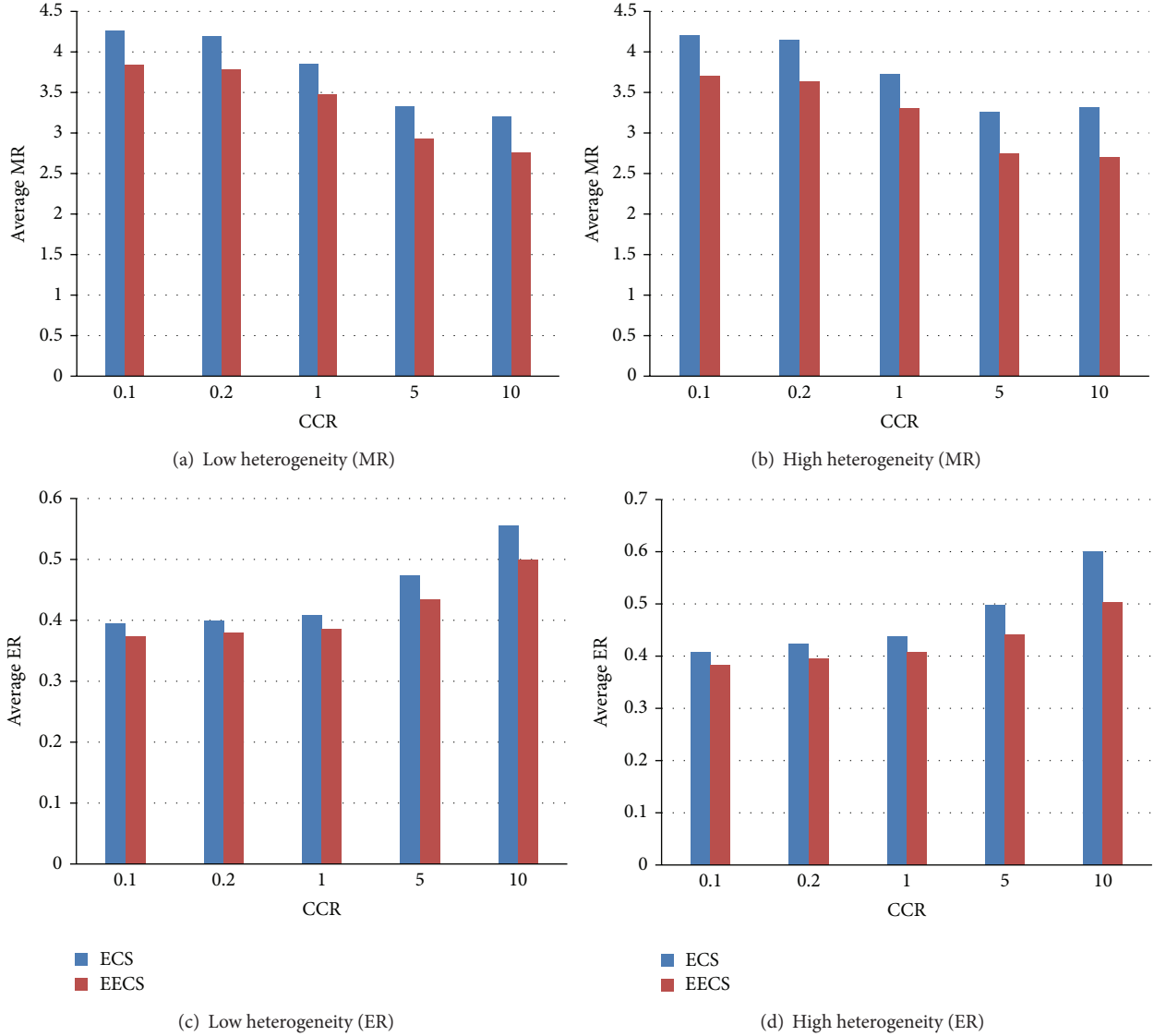


FIGURE 7: Random DAGs (different heterogeneities of processors).

of heterogeneity, and 3 different DAG types, which leads to the result of 45000. In each experiment, every algorithm is used to generate a schedule with makespan and energy consumption. Hence, the total number of experiments in our evaluation is 90000 (two algorithms were evaluated).

Finally, all the experiments were implemented by Java and run on a PC with AMD A6 CPU running at 2.20 GHz with 4 GB memory.

**5.2. Comparison Metrics.** In our evaluation, we consider makespan and energy consumption are equally performance metrics. For a given schedule, its makespan is normalized to a lower bound, which is the sum of the execution and communication costs of tasks along the critical path (denoted by  $M_{cp}$ ), while its energy consumption is normalized to an upper bound, which is the total energy consumption of the schedule in which every task is scheduled so that the energy consumption is maximized (denoted by  $E_{max}$ ).

Specifically, for each experiment, the performance of each heuristic (ECS and EECS) is normalized to MR (makespan ratio) and ER (energy ratio) defined as follows:

$$MR = \frac{M}{M_{cp}}, \quad ER = \frac{E}{E_{max}}, \quad (9)$$

where  $M$  is the makespan of the schedule and  $E$  the energy consumption of the schedule.

**5.3. Experimental Results.** The results for each of the two different scheduling heuristics on the three different types of DAGs (note that for each DAG, results impacted by number of processors and results impacted by heterogeneity are both considered; this results in 6 pairs) are shown in Figures 3, 4, 5, 6, 7, and 8. Particularly, the actual comparative results of Figures 5 and 6 are shown in Tables 9 and 10, respectively. The results are normalized to MR and ER, respectively, as

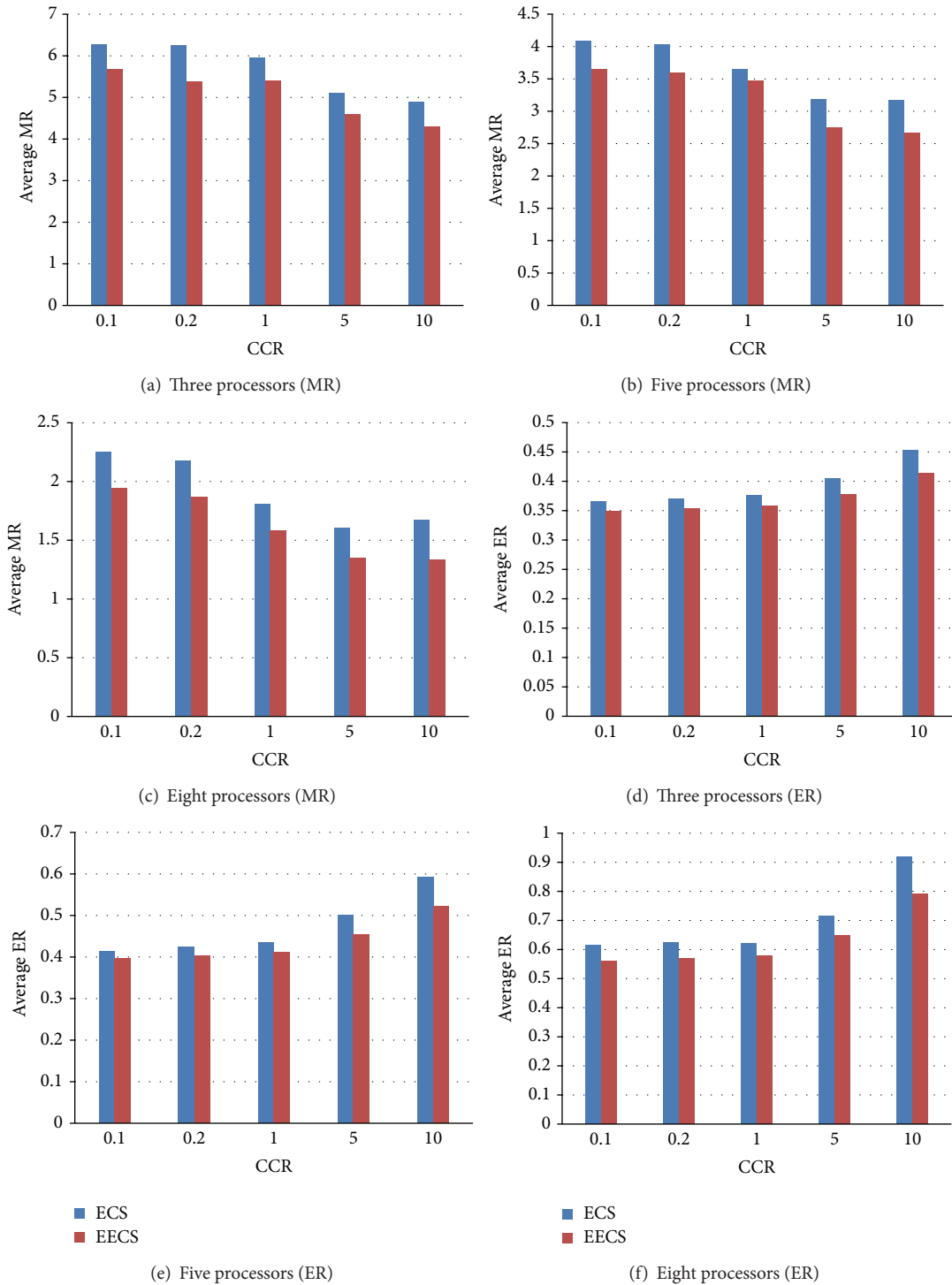


FIGURE 8: Random DAGs (different sizes of processors).

presented in Section 5.2. Recall that for each heuristic, all results are averaged over 500 runs.

In all cases depicted in the result figures, it is clear that EECS always obtained a MR and a ER less than their counterpart that ECS achieved. This indicates that EECS outperforms ECS in all cases on both makespan optimization and energy reduction.

It is interesting to see that the makespan improvement of EECS over ECS is somehow correlated with CCR. When Laplace is used, for both low and high heterogeneities, the MR difference between EECS and ECS is decreased, as CCR increases from 0.1 to 5. Then, this difference significantly increases, as CCR changes from 5 to 10. Such a variation of MR difference can also be observed when LIGO and random

TABLE 10: Comparative results of Figure 6: LIGO, 77 nodes (different sizes of processors).

	ECS						EECS					
	3		5		8		3		5		8	
	MR (%)	ER (%)										
0.1	6.48	0.36	4.38	0.40	2.40	0.41	5.81	0.34	3.90	0.38	2.08	0.38
0.2	6.47	0.36	4.33	0.41	2.32	0.42	5.82	0.34	3.84	0.38	2.01	0.38
1	6.30	0.37	3.86	0.41	1.82	0.41	5.62	0.35	3.43	0.39	1.59	0.38
5	5.27	0.38	3.42	0.44	1.75	0.46	4.72	0.33	3.02	0.40	1.45	0.44
10	5.20	0.41	3.32	0.53	1.70	0.62	4.64	0.37	2.78	0.43	1.43	0.51

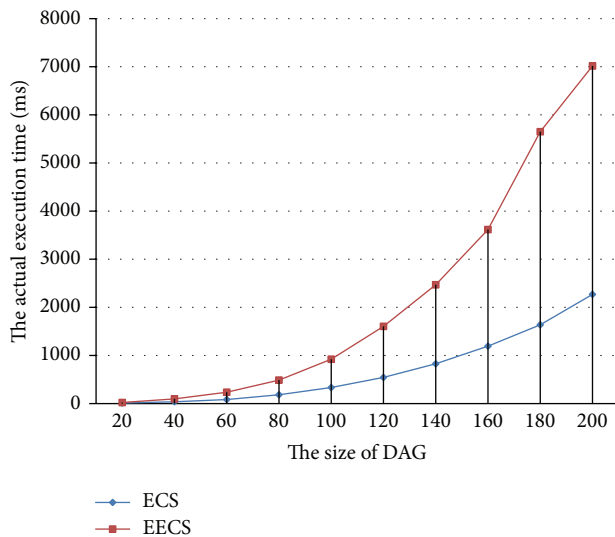


FIGURE 9: The actual execution time of compared heuristics.

is used with high heterogeneity. The ER difference between EECS and ECS varies little when CCR is not more than 5.0. However, a significant increase of ER difference can be seen when CCR changes from 5 to 10. These observations imply EECS may perform particularly better than ECS in the scenario where CCR is high.

Table 7 summarized the comparative results between ECS and EECS in terms of the change of number of processors. As the size of LIGO and Laplace is fixed, different settings of processor number may correspond to a specific scenario. Here, using 3 processors indicate a “resource-hungry” situation, 8 processors indicate a “resource-rich” situation, and 5 processors indicate a medium. When LIGO is used, the improvement of EECS over ECS, on both makespan and energy, increases as the number of processors grows. In the case of Laplace, such an improvement hits the lowest when 5 processors are used, while reaching the highest when 8 processors are used. So, it seems that EECS may obtain a greater improvement over ECS in a “resource-rich” scenario.

The comparative results between ECS and EECS in terms of different processor heterogeneities are summarized in Table 8. It is clearly suggested that the advantage of EECS over ECS may be magnified as the heterogeneity of processor turns from low to high.

From Tables 7 and 8, we can see that ECS may obtain a makespan up to 17.84% and energy consumption 10.1% more than EECS. Averagely, EECS significantly outperforms ECS by 12% on makespan minimization and 8% on energy reduction.

Aside from the comparison of scheduling performance, we assessed the running times of ECS and EECS for DAGs with different sizes. The results are shown in Figure 9. Although EECS and ECS are both based on list-scheduling, EECS needs a bit more running time than ECS as the computation involved in EECS is more complicated. However, as can be seen in the graph, when scheduling a DAG with 200 nodes, EECS only needs around 7 seconds on average. This suggests that EECS can still cope well with the real-time requirement of workflow scheduling for admission control of market-oriented systems.

## 6. Conclusion

This paper proposed EECS, a novel efficient biobjective DAG scheduling heuristic based on the enhancement to the energy conscious scheduling heuristic ECS. The proposed heuristic aims at simultaneously minimizing makespan and energy consumption with a low complexity. The experimental results suggest that EECS can significantly outperform the existing approach (i.e., ECS) on both makespan optimization and energy reduction. It also appears that EECS has a low execution time cost and thus is able to produce a schedule as a real-time response to users in market-oriented systems.

Based on the work in this paper, further work could try to examine the performance of EECS in an uncertain environment. Further study could investigate how EECS can cope with significant overestimation or underestimation of task execution time and assess its robustness against such uncertainties.

## Conflict of Interests

The authors declare that there is no conflict of interests regarding the publication of this paper.

## Acknowledgment

The work is supported by National Natural Science Foundation of China (NSFC, Grant no. 61202361).

## References

- [1] E. Deelman, D. Gannon, M. S. Shields, and I. Taylor, "Workflows and e-Science: an overview of workflow system features and capabilities," *Future Generation Computer Systems*, vol. 25, no. 5, pp. 528–540, 2009.
- [2] G. Juve, E. Deelman, G. B. Berriman, B. P. Berman, and P. Maechling, "An evaluation of the cost and performance of scientific workflows on Amazon EC2," *Journal of Grid Computing*, vol. 10, no. 1, pp. 5–21, 2012.
- [3] R. Bianchini and R. Rajamony, "Power and energy management for server systems," *Computer*, vol. 37, no. 11, pp. 68–76, 2004.
- [4] R. Brown, *Report to Congress on Server and Data Center Energy Efficiency: Public Law 109-431*, Lawrence Berkeley National Laboratory, 2008.
- [5] J. Frey, T. Tannenbaum, M. Livny, I. Foster, and S. Tuecke, "Condor-G: a computation management agent for multi-institutional grids," *Cluster Computing*, vol. 5, no. 3, pp. 237–246, 2002.
- [6] K. Lee, N. W. Paton, R. Sakellariou, E. Deelman, A. A. A. Fernandes, and G. Mehta, "Adaptive workflow processing and execution in pegasus," *Concurrency Computation Practice and Experience*, vol. 21, no. 16, pp. 1965–1981, 2009.
- [7] V. Venkatachalam and M. Franz, "Power reduction techniques for microprocessor systems," *ACM Computing Surveys*, vol. 37, no. 3, pp. 195–237, 2005.
- [8] K. Q. Li, "Energy efficient scheduling of parallel tasks on multiprocessor computers," *The Journal of Supercomputing*, vol. 60, no. 2, pp. 223–247, 2012.
- [9] K. H. Kim, R. Buyya, and J. Kim, "Power aware scheduling of bag-of-tasks applications with deadline constraints on DVS-enabled clusters," in *Proceedings of the 7th IEEE International Symposium on Cluster Computing and the Grid (CCGrid '07)*, pp. 541–548, May 2007.
- [10] L. Wang, G. von Laszewski, J. Dayal, and F. Wang, "Towards energy aware scheduling for precedence constrained parallel tasks in a cluster with DVFS," in *Proceedings of the 10th IEEE/ACM International Symposium on Cluster, Cloud, and Grid Computing (CCGrid '10)*, pp. 368–377, May 2010.
- [11] Y. C. Lee and A. Y. Zomaya, "Energy conscious scheduling for distributed computing systems under different operating conditions," *IEEE Transactions on Parallel and Distributed Systems*, vol. 22, no. 8, pp. 1374–1381, 2011.
- [12] Q. Huang, S. Su, J. Li, P. Xu, K. Shuang, and X. Huang, "Enhanced energy-efficient scheduling for parallel applications in cloud," in *Proceedings of the 12th IEEE/ACM International Symposium on Cluster, Cloud and Grid Computing (CCGrid '12)*, pp. 781–786, Ottawa, Canada, May 2012.
- [13] Y. Kwok and I. Ahmad, "Dynamic critical-path scheduling: an effective technique for allocating task graphs to multiprocessors," *IEEE Transactions on Parallel and Distributed Systems*, vol. 7, no. 5, pp. 506–521, 1996.
- [14] R. Sakellariou and H. Zhao, "A hybrid heuristic for DAG scheduling on heterogeneous systems," in *Proceedings of the 18th International Parallel and Distributed Processing Symposium (IPDPS '04)*, pp. 111–124, Santa Fe, NM, USA, April 2004.
- [15] G. C. Sih and E. A. Lee, "Compile-time scheduling heuristic for interconnection-constrained heterogeneous processor architectures," *IEEE Transactions on Parallel and Distributed Systems*, vol. 4, no. 2, pp. 175–187, 1993.
- [16] H. Topcuoglu, S. Hariri, and M. Wu, "Performance-effective and low-complexity task scheduling for heterogeneous computing," *IEEE Transactions on Parallel and Distributed Systems*, vol. 13, no. 3, pp. 260–274, 2002.
- [17] D. Bozdag, U. Catalyurek, and F. Ozguner, "A task duplication based bottom-up scheduling algorithm for heterogeneous environments," in *Proceedings of the 20th International Parallel and Distributed Processing Symposium (IPDPS '06)*, 2006.
- [18] S. Ranaweera and D. P. Agrawal, "A scalable task duplication based scheduling algorithm for heterogeneous systems," in *Proceedings of the 14th International Parallel and Distributed Processing Symposium*, pp. 383–390, 2000.
- [19] S. Ranaweera and D. P. Agrawal, "A task duplication based scheduling algorithm for heterogeneous systems," in *Proceedings of the 14th International Parallel and Distributed Processing Symposium*, pp. 445–450, 2000.
- [20] B. Cirou and E. Jeannot, "Triplet: a clustering scheduling algorithm for heterogeneous systems," in *Proceedings of the International Conference on Parallel Processing Workshops*, pp. 231–236, 2001.
- [21] J. C. Liou and M. A. Palis, "An efficient task clustering heuristic for scheduling DAGs on multiprocessors," in *Proceedings of the Workshop on Scheduling and Resource Management for Parallel and Distributed Processing*, pp. 152–156, 1996.
- [22] T. D. Braun, H. J. Siegel, N. Beck et al., "A Comparison study of static mapping heuristics for a class of meta-tasks on heterogeneous computing systems," in *Proceedings of the 8th Heterogeneous Computing Workshop (HCW '99)*, pp. 15–29, April 1999.
- [23] M. Coli and P. Palazzari, "Real time pipelined system design through simulated annealing," *Journal of Systems Architecture*, vol. 42, no. 6–7, pp. 465–475, 1996.
- [24] R. Ge, X. Feng, and K. W. Cameron, "Performance-constrained distributed DVS scheduling for scientific applications on power-aware clusters," in *Proceedings of the ACM/IEEE conference on Supercomputing*, p. 34, November 2005.
- [25] D. Zhu, R. Melhem, and B. R. Childers, "Scheduling with dynamic voltage/speed adjustment using slack reclamation in multiprocessor real-time systems," *IEEE Transactions on Parallel and Distributed Systems*, vol. 14, no. 7, pp. 686–700, 2003.
- [26] S. S. Zhang and A. Chatha, "Approximation algorithm for the temperature-aware scheduling problem," in *Proceedings of the IEEE/ACM International Conference on Computer-Aided Design (ICCAD '07)*, pp. 281–288, November 2007.
- [27] X. L. Zhong and C. Z. Xu, "Energy-aware modeling and scheduling for dynamic voltage scaling with statistical real-time guarantee," *IEEE Transactions on Computers*, vol. 56, no. 3, pp. 358–372, 2007.
- [28] Y. Yu and V. K. Prasanna, "Power-aware resource allocation for independent tasks in heterogeneous real-time system," in *Proceedings of the 9th International Conference on Parallel and Distributed Systems*, pp. 341–348, 2002.
- [29] X. Zhu and P. Lu, "A two-phase scheduling strategy for real-time applications with security requirements on heterogeneous clusters," *Computers and Electrical Engineering*, vol. 35, no. 6, pp. 980–993, 2009.
- [30] X. Zhu, C. He, K. Li, and X. Qin, "Adaptive energy-efficient scheduling for real-time tasks on DVS-enabled heterogeneous clusters," *Journal of Parallel and Distributed Computing*, vol. 72, no. 6, pp. 751–763, 2012.
- [31] W. F. Sacco, C. A. M. N. A. Pereira, P. P. M. Soares, and R. Schirru, "Genetic algorithms applied to turbine extraction optimization of a pressurized-water reactor," *Applied Energy*, vol. 73, no. 3–4, pp. 217–222, 2002.

- [32] A. O. Adewumi and M. M. Ali, "A multi-level genetic algorithm for a multi-stage space allocation problem," *Mathematical and Computer Modelling*, vol. 51, no. 1-2, pp. 109–126, 2010.
- [33] A. K. M. K. A. Talukder, M. Kirley, and R. Buyya, "Multiobjective differential evolution for scheduling workflow applications on global Grids," *Concurrency and Computation: Practice and Experience*, vol. 21, no. 13, pp. 1742–1756, 2009.
- [34] M. Mezmaiz, N. Melab, Y. Kessaci et al., "A parallel bi-objective hybrid metaheuristic for energy-aware scheduling for cloud computing systems," *Journal of Parallel and Distributed Computing*, vol. 71, no. 11, pp. 1497–1508, 2011.
- [35] M. M. Ali and A. Törn, "Population set-based global optimization algorithms: some modifications and numerical studies," *Computers and Operations Research*, vol. 31, no. 10, pp. 1703–1725, 2004.
- [36] W. Zheng and R. Sakellariou, "Stochastic DAG scheduling using a Monte Carlo approach," *Journal of Parallel and Distributed Computing*, vol. 73, no. 12, pp. 1673–1689, 2013.
- [37] R. Min, T. Furrer, and A. Chandrakasan, "Dynamic voltage scaling techniques for distributed microsensor networks," in *Proceedings of the IEEE Computer Society Workshop on Very Large Scale Integration*, pp. 92–99, 2000.
- [38] D. Brown, P. Brady, A. Dietz, J. Cao, B. Johnson, and J. McNabb, "A case study on the use of workflow technologies for scientific analysis: gravitational wave data analysis," in *Workflows for e-Science: Science Workflows for Grids*, pp. 39–59, 2006.
- [39] M. Wu and D. D. Gajski, "Hypertool: a programming aid for message-passing systems," *IEEE Transactions on Parallel and Distributed Systems*, vol. 1, no. 3, pp. 330–343, 1990.
- [40] W. Zheng, *Explorations in grid workflow scheduling [Ph.D. thesis]*, The University of Manchester, 2010.
- [41] S. Ali, H. J. Siegel, M. Maheswaran, and D. Hensgen, "Task execution time modeling for heterogeneous computing systems," in *Proceedings of the 9th Heterogeneous Computing Workshop*, pp. 185–199, 2000.

## Research Article

# Intelligent Inventory Control via Ruminative Reinforcement Learning

Tatpong Katanyukul<sup>1</sup> and Edwin K. P. Chong<sup>2</sup>

<sup>1</sup> Faculty of Engineering, Khon Kaen University, Computer Engineering Building,  
123 Moo 16, Mitraparb Road, Muang, Khon Kaen 40002, Thailand

<sup>2</sup> Department of Electrical and Computer Engineering, Colorado State University,  
1373 Campus Delivery, Fort Collins, CO 80523-1373, USA

Correspondence should be addressed to Tatpong Katanyukul; [tatpong@gmail.com](mailto:tatpong@gmail.com)

Received 30 December 2013; Accepted 29 May 2014; Published 7 July 2014

Academic Editor: Aderemi Oluyinka Adewumi

Copyright © 2014 T. Katanyukul and E. K. P. Chong. This is an open access article distributed under the Creative Commons Attribution License, which permits unrestricted use, distribution, and reproduction in any medium, provided the original work is properly cited.

Inventory management is a sequential decision problem that can be solved with reinforcement learning (RL). Although RL in its conventional form does not require domain knowledge, exploiting such knowledge of problem structure, usually available in inventory management, can be beneficial to improving the learning quality and speed of RL. Ruminative reinforcement learning (RRL) has been introduced recently based on this approach. RRL is motivated by how humans contemplate the consequences of their actions in trying to learn how to make a better decision. This study further investigates the issues of RRL and proposes new RRL methods applied to inventory management. Our investigation provides insight into different RRL characteristics, and our experimental results show the viability of the new methods.

## 1. Introduction

Inventory management is a crucial business activity and can be modeled as a sequential decision problem. Bertsimas and Thiele [1], among others, addressed the need for an efficient and flexible inventory solution that is also simple to implement in practice. This may be among the reasons for extensive studies of reinforcement learning (RL) application to inventory management.

RL [2, 3] is an approach to solve sequential decision problems based on learning the underlying state value or state-action value. Relying on learning mechanism, RL in its typical form does not require knowledge of a structure of the problem. Therefore, RL has been studied in wide range of sequential decision problems, for example, virtual machine configuration [4], robotics [5], helicopter control [6], ventilation, heating and air conditioning control [7], electricity trade [8], financial management [9], water resource management [10], and inventory management [11]. Acceptance of RL is credited to RL's effectiveness, potential possibilities [12], link

to mammal learning processes [13, 14], and its model-free property [15].

Despite fascination with RL's model-free property, most inventory management problems can naturally be formulated into a well-structured part interacting with another part that is less understood. That is, replenishment cost, holding cost, and penalty cost can be determined precisely in advance. On the other hand, customer demand or, in some cases, delivery time or availability of supplies is usually less predictable. However, once a value of a less predictable variable is known, the period cost can be determined precisely. Specifically, a warehouse would know its period inventory cost after its replenishment has arrived and all demand orders in the period have been observed. Calculation of a period cost is a well-defined formula, while another part, for example, demand, is less predictable. Knowledge about the well-structured part can be exploited, while a learning mechanism can be used to handle the less understood part.

Utilizing this knowledge, Kim et al. [16] proposed *asynchronous action-reward learning*, which used simulation to

evaluate consequences of actions not taken in order to accelerate the learning process in a stateless system. Extending the idea to state-based system, Katanyukul [17] developed ruminative reinforcement learning (RRL) methods, that is, ruminative SARSA (RSarsa) and policy-weighted RSarsa (PRS). The RRL approach is motivated by how humans contemplate consequences of their actions to improve their learning hoping to make a better decision. His study of RRL reveals good potential of the approach. However, existing individual methods show strengths in different scenarios: RSarsa is shown to have fast learning but leads to inferior learning quality in a long-term run. PRS is shown to lead to superior learning quality in a long-term run, but with slower rate.

Our proposed method here is developed to exploit the fast learning characteristic of RSarsa and good learning quality in a long-term run of PRS. Our experimental results show effectiveness of the proposed method and support our assumption underlying development of RRL.

## 2. Background

An objective of a sequential inventory management is to minimize a long-term cost,  $C_0(s_0) = \min_{a_0, \dots, a_T} \sum_{t=0}^T \gamma^t E[c_t | s_0, a_0, \dots, a_T]$ , subject to  $a_t \in A_{s_t}$  for  $t = 0, \dots, T$ , where  $E[c_t | s_0, a_0, \dots, a_T]$  is the expected period cost of period  $t$  given an initial state  $s_0$  and actions  $a_0, \dots, a_T$  over periods 0 to  $T$ , respectively;  $\gamma$  is a discount factor; and  $A_{s_t}$  is a feasible action set at state  $s_t$ . Under certain assumptions, the problem can be posed as a Markov decision problem (MDP) (see [15] for details). In this case, what we seek is an *optimal policy*, which maps each state to an optimal action. Given an arbitrary policy  $\pi$ , the long-term state cost for that policy can be written as

$$C^\pi(s) = r^\pi(s) + \gamma \sum_{s'} p^\pi(s' | s) C^\pi(s'), \quad (1)$$

where  $r^\pi(s)$  is an expected period state cost,  $p^\pi(s' | s)$  is a transition probability—the probability of the next state being  $s'$  when the current state is  $s$ . The superscript  $\pi$  notation indicates dependence on the policy  $\pi$ . In practice, exact solution to (1) is difficult to find. Reinforcement learning (RL) [2] provides a framework to find an approximate solution. An approximate long-term cost of state  $s$  is obtained by summation of the period cost and a long-term cost of the next state  $Q(s) = r(s) + \gamma Q(s')$ .

The RL approach is based on temporal difference (TD) learning, which uses temporal difference error  $\psi$  (2) to estimate the long-term cost (3):

$$\psi = r + \gamma Q(s', a') - Q(s, a) \quad (2)$$

$$Q^{(\text{new})}(s, a) = Q^{(\text{old})}(s, a) + \alpha \cdot \psi, \quad (3)$$

where  $r$  is the period cost, which corresponds to taking action  $a$  in state  $s$ ,  $\alpha$  is a learning rate, and  $s'$  and  $a'$  are the state and action taken in the next period, respectively.

Once the values of  $Q(s, a)$  are thoroughly learned, they are good approximations of long-term costs. We often refer to  $Q(s, a)$  as the “Q-value.” Most RL methods determine the

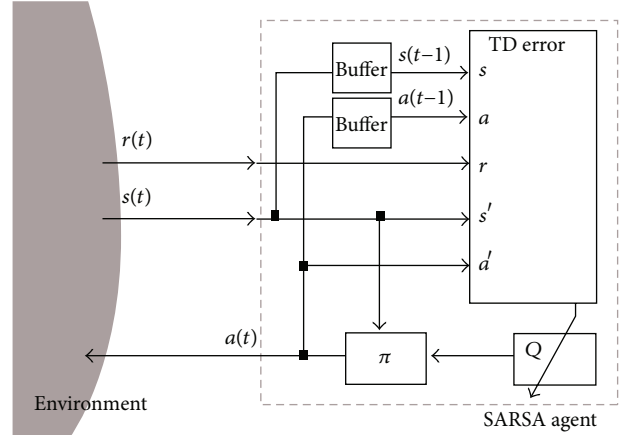


FIGURE 1: SARSA agent and interacting variables (this figure is adapted from Figure 6.15 of Sutton and Barto [2]).

actions to take based on Q-values. These methods include SARSA [2], a widely used RL algorithm. We use SARSA as a benchmark, representing a conventional RL method, to compare with other methods under investigation. In each period, given observed state  $s$ , action taken  $a$ , observed period cost  $r$ , observed next state  $s'$ , and anticipating next action taken  $a'$ , the SARSA algorithm updates the Q-value based on TD learning (2) and (3).

Based on the Q-value, we can define a policy  $\pi$  to determine an action to take at each state. The policy is usually stochastic, defined by a probability  $p(a | s)$  to take an action  $a$  given a state  $s$ . The policy has to balance between taking the best action based on the currently learned Q-value and trying another alternative. Trying another alternative gives the learning agent a chance to explore thoroughly the consequences of its state-action space. This helps to create a constructive cycle of improving the quality of learned Q-values, which in turn will help the agent to choose better actions and reduce the chance to get stuck in a local optimum. This is an issue of balancing between *exploitation* and *exploration*, as discussed in Sutton and Barto [2]. (Since the RL algorithm is autonomous and interacts with its environment, we sometimes use the term “learning agent.”)

An  $\epsilon$ -greedy policy is a general RL policy, which also is easy to implement. With probability  $\epsilon$ , the policy chooses an action randomly from  $a \in A(s)$ , where  $A(s)$  is a set of allowable actions given state  $s$ . Otherwise, it takes an action corresponding to the minimal current Q-value,  $a^* = \arg \min_a Q(s, a)$ .

## 3. Ruminative Reinforcement Learning

The conventional RL approach, SARSA, assumes that the agent knows only the current state  $s$ , the action  $a$  it takes, the period cost  $r$ , the next state  $s'$ , and the action  $a'$  it will take in the next state. Each period, the SARSA agent updates the Q-value based on the TD error calculated with these five variables. Figure 1 illustrates the SARSA agent, the five variables it needs to update the Q-value, and its interaction with its environment.

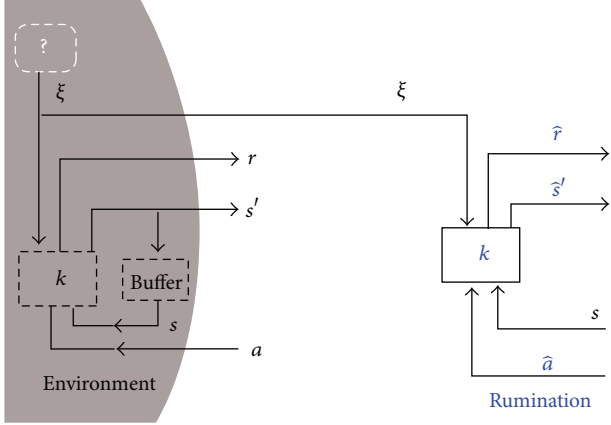


FIGURE 2: Environment, knowledge of its structure, and rumination.

However, in inventory management problems, we usually have extra knowledge about the environment. That is, the problem structure can naturally be formulated such that the period cost  $r$  and next state  $s'$  are determined by a function  $k : s, a, \xi \mapsto r, s'$ , where  $\xi$  is an extra information variable. This variable  $\xi$  captures the stochastic aspect of the problem. The process generating  $\xi$  may be unknown, but the value of  $\xi$  is fully observable after the period is over. Given a value of  $\xi$ , along with  $s$  and  $a$ , the deterministic function  $k$  can precisely determine  $r$  and  $s'$ .

Without this extra knowledge, each period, the SARSA agent updates only one value of  $Q(s, a)$  corresponding to current state  $s$  and action taken  $a$ . However, with the function  $k$  and an observed value of  $\xi$ , we can do “rumination”: evaluating the consequences of other actions  $\hat{a}$ , even those that were not taken. Figure 2 illustrates rumination and its associated variables. Given the rumination mechanism, we can provide information required by SARSA’s TD calculation for any underlying action. Katanyukul [17] introduced this rumination idea and incorporated it into the SARSA algorithm, resulting in the *ruminative SARSA (RSarsa)* algorithm. Algorithm 1 shows the RSarsa algorithm. It should be noted that RSarsa is similar to SARSA, but with inclusion of rumination from line 8 to line 13.

The experiments in [17] showed that RSarsa had performed significantly better than SARSA in early periods (indicating faster learning), but its performance was inferior to SARSA in later periods (indicating poor convergence to the appropriate long-term state cost approximation). Katanyukul [17] attributed RSarsa’s poor long-term learning quality to its lack of natural action visitation frequency.

TD learning (2) and (3) update the  $Q$ -value as an approximation of the long-term state cost. The transition probability  $p^\pi(s' | s)$  in (1) does not appear explicitly in the TD learning calculation. Conventional RL relies on sampling trajectories to reflect the natural frequency of visits to state-action pairs corresponding to the transition probability. It updates only the state-action pairs as they are actually visited; therefore, it does not require explicit calculation of the transition probability and still eventually converges to a good approximation.

However, because RSarsa does rumination for all actions ignoring their sampling frequency, this is equivalent to

```

(L00) Initialize  $Q(s, a)$ .
(L01) Observe  $s$ .
(L02) Determine  $a$  by policy  $\pi$ .
(L03) For each period,
(L04)   observe  $r, s'$ , and  $\xi$ ;
(L05)   determine  $a'$  by policy  $\pi$ ;
(L06)   calculate  $\psi = r + \gamma Q(s', a') - Q(s, a)$ ;
(L07)   update  $Q(s, a) \leftarrow Q(s, a) + \alpha \cdot \psi$ ;
(L08)   for each  $\hat{a} \in \hat{A}(s)$ ,
(L09)     calculate  $\hat{r}, \hat{s}'$  with  $k(s, \hat{a}, \xi)$ ,
(L10)     determine  $\hat{a}'$ ,
(L11)     calculate  $\psi = \hat{r} + \gamma Q(\hat{s}', \hat{a}') - Q(s, \hat{a})$ ,
(L12)     update  $Q(s, \hat{a}) \leftarrow Q(s, \hat{a}) + \alpha \cdot \psi$ 
(L13)   until ruminated all  $\hat{a} \in \hat{A}$ ;
(L14)   set  $s \leftarrow s'$  and  $a \leftarrow a'$ 
(L15) until termination.

```

ALGORITHM 1: RSarsa algorithm.

disregarding the transition probability, which leads to RSarsa’s poor long-term learning quality.

To address this issue, Katanyukul [17] proposed *policy-weighted RSarsa (PRS)*. PRS explicitly calculates probabilities of actions to be ruminated and adjusts the weights of their updates. PRS is similar to RSarsa, but the rumination update (line 12 in Algorithm 1) is replaced by

$$Q(s, \hat{a}) \leftarrow Q(s, \hat{a}) + \beta \cdot \psi, \quad (4)$$

where  $\beta = \alpha \cdot p(\hat{a})$  and  $p(\hat{a})$  is the probability of taking action  $\hat{a}$  in state  $s$  with policy  $\pi$ . Given an  $\epsilon$ -greedy policy, we have  $p(\hat{a}) = \epsilon/|\hat{A}(s)|$  for  $\hat{a} \neq a^*$  and  $p(\hat{a}) = \epsilon/|\hat{A}(s)| + (1 - \epsilon)$  otherwise, where  $|\hat{A}(s)|$  is a number of allowable actions. PRS has been shown to perform well in early and later periods, compared to SARSA. However, RSarsa is reported to significantly outperform PRS in early periods.

## 4. New Methods

According to the results of [17], although RSarsa may converge to a wrong approximation, RSarsa was shown to perform impressively in the very early periods. This suggests that if we jump-start the learning agent with RSarsa and then later switch to PRS, before the  $Q$ -values settle into bad spots, we may be able to achieve both faster learning and good approximation for a long-term run.

*PRS.Beta.* We first introduce a straightforward idea, called PRS.Beta, where we will use a varying ruminative learning rate as a mechanism to shift from full rumination (RSarsa) to policy-weighted rumination (PRS). Similar to PRS, the rumination update is determined by (4). However, the value of the rumination learning rate  $\beta$  is determined by

$$\beta = \alpha \cdot \{1 - (1 - p(\hat{a})) \cdot f\}, \quad (5)$$

where  $f$  is a function having a value between 0 and 1. When  $f \rightarrow 0$ ,  $\beta \rightarrow \alpha$  and the algorithm will behave like RSarsa.

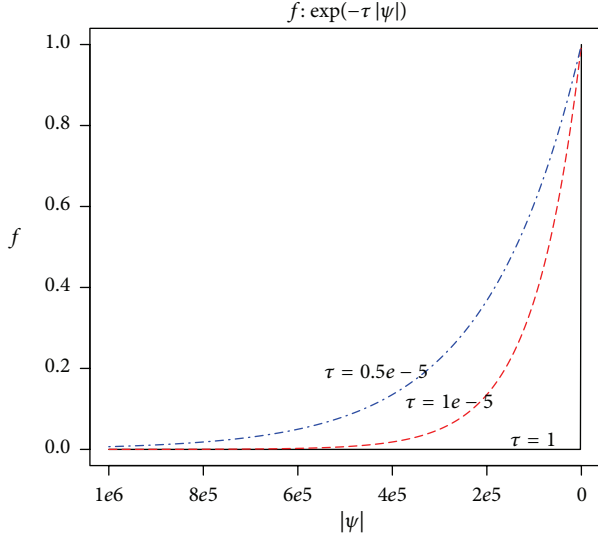


FIGURE 3: Function  $\exp(-\tau|\psi|)$  and effects of different  $\tau$  values.

When  $f \rightarrow 1$ ,  $\beta \rightarrow \alpha \cdot p(\hat{a})$  and the algorithm will behave like PRS. We want  $f$  to start out close to 0 and grow to 1 at a proper rate. By examining our preliminary experiments, the TD error will get smaller as the learning converges. This is actually a property of TD learning. Given this property, we can use the magnitude of the TD error  $|\psi|$  to control the shifting, such that

$$f(\psi) = \exp(-\tau \cdot |\psi|), \quad (6)$$

where  $\tau$  is a scaling factor. Figure 3 illustrates the effects of different values of  $\tau$ . Since the magnitude of  $\tau$  should be relative to  $|\psi|$ , we set  $\tau = |2/(r + Q(s, a))|$ , so that the magnitude of  $\tau$  will be in a proper scale relative to  $|\psi|$  and automatically adjusted.

*RSarsa.TD.* Building on the PRS.Beta method above, we next propose another method, called RSarsa.TD. The underlying idea is that since SARSA performs well in a long-term run (see [2] for theoretical discussion of SARSA's optimality and convergence properties), then after we speed up the early learning process with rumination, we can just switch back to SARSA. This approach is to utilize the fast learning characteristic of full rumination in early periods and to avoid its poor long-term performance. In addition, as a computational cost of rumination is proportional to the size of the ruminative action space  $|\widehat{A}(s)|$ , this also helps to reduce the computational cost incurred by rumination. It is also intuitively appealing in the sense that we do rumination only when we need it.

The intuition to selectively do rumination was introduced in [17] in an attempt to reduce the extra computational cost from rumination. There, the probability to do rumination was a function of the magnitude of the TD error:

$$p(\text{rumination}) = 1 - \exp\left(-\left|\frac{2\psi}{r + Q(s, a)}\right|\right). \quad (7)$$

However, Katanyukul [17] investigated this selective rumination only with the policy-weighted method and called it PRS.TD. Although PRS.TD was able to improve the computational cost of the rumination approach, the inventory management performance of PRS.TD was reported to have mixed results, implying that incorporation of selective rumination may deteriorate performance of PRS.

This performance deterioration may be due to using  $p(\text{rumination})$  with policy weighted correction. Both schemes use  $|\psi|$  to control their effect of rumination; therefore, they might have an effect equivalent to overcorrecting the state-transition probability. Unlike PRS, RSarsa does not correct the state-transition probability. Incorporating selective rumination (7) will be the only scheme controlling rumination with  $|\psi|$ . Therefore, we expect that this approach may allow the advantage of RSarsa's fast learning, while maintaining the long-term learning quality of SARSA.

## 5. Experiments and Results

Our study uses computer simulations to conduct numerical experiments on three inventory management problem settings (P1, P2, and P3). All problems are periodic review single-echelon with nonzero setup cost. P1 and P2 have one-period lead time. P3 has two-period lead time. The same Markov model is used to govern all problem environments, but with different settings. For P1 and P2, the problem state space is  $\mathbb{I} \times \{0, \mathbb{I}^+\}$ , for on-hand and in-transit inventories:  $x$  and  $b^{(1)}$ , respectively. P3's state space is  $\mathbb{I} \times \{0, \mathbb{I}^+\} \times \{0, \mathbb{I}^+\}$ , for  $x$  and in-transit inventories  $b^{(1)}$  and  $b^{(2)}$ . The action space is  $\{0, \mathbb{I}^+\}$ , for replenishment order  $a$ .

The state transition is specified by

$$\begin{aligned} x_{t+1} &= x_t + b_t^{(1)} - d_t, \\ b_{t+1}^{(i)} &= b_t^{(i+1)}, \quad \text{for } i = 1, \dots, L-1, \\ b_{t+1}^{(L)} &= a_t, \end{aligned} \quad (8)$$

where  $L$  is a number of lead time periods.

The inventory period cost is calculated from the equation

$$\begin{aligned} r_t &= K \cdot \delta(a_t) + G \cdot a_t + H \cdot x_{t+1} \cdot \delta(x_{t+1}) \\ &\quad - B \cdot x_{t+1} \cdot \delta(-x_{t+1}), \end{aligned} \quad (9)$$

where  $K$ ,  $G$ ,  $H$ , and  $B$  are setup, unit, holding, and penalty costs, respectively, and  $\delta(\cdot)$  is a step function. Five RL agents are studied: SARSA, RSarsa, PRS, RSarsa.TD, and PRS.Beta.

Each experiment is repeated 10 times. In each repetition, an agent is initialized with all zero Q-values. Then, the experiment is run consecutively for  $N_E$  episodes. Each episode starts with initial state and action as follows: for all problems,  $b_1^{(1)}$  and  $a_1$  are initialized with values randomly drawn between 0 and 100. In P1,  $x_1$  is initialized to 50; in P2,  $x_1$  is initialized from randomly drawn values between  $-50$  and 400; in P3,  $x_1$  is initialized to 100 and randomly drawn values of  $b^{(2)}$  between 0 and 100. Each episode ends when  $N_p$  periods are reached or an agent has visited a termination

TABLE I: Experimental results.

Line			Methods			
	SARSA	RSarsa	PRS	RSarsa.TD	PRS.Beta	
Relative computation time/epoch						
1	P1	1	30	26	5	30
2	P2	1	20	21	3	19
3	P3	1	31	29	6	31
Average cost of early periods						
4	P1	8,421	7,619 (W)	8,379 (p0.43)	7,597 (W)	7,450 (W)
5	P2	4,935	4,606 (W)	4,792 (p0.06)	4,685 (W)	4,411 (W)
6	P3	10,502	8,694 (W)	9,958 (p0.20)	9,390 (p0.07)	8,472 (W)
Average cost of later periods						
7	P1	7,214	7,355 (p0.68)	7,051 (W)	7,110 (p0.11)	7,010 (W)
8	P2	4,308	4,388 (p0.90)	4,248 (p0.14)	4,375 (p0.84)	4,194 (W)
9	P3	8,613	8,139 (p0.29)	8,312 (p0.37)	8,486 (p0.43)	7,664 (p0.18)

state, which is a state lying outside a valid range of  $Q$ -value implementation. The maximum number of periods in each episode,  $N_p$ , defines the length of the problem horizon, while the number of episodes  $N_E$  specifies a variety of problem scenarios, that is, different initial states and actions.

Three problem settings are used in our experiments. Problem 1 (P1) has  $N_E = 100$ ,  $N_p = 60$ ,  $K = 200$ ,  $G = 100$ ,  $B = 200$ , and  $H = 20$ . Demand  $d_t$  is normally distributed, with mean 50 and standard deviation 10, denoted as  $d_t \sim \mathcal{N}(50, 10^2)$ . The environment state  $[x, b^{(1)}]$  is set as the RL agent state  $s = [x, b^{(1)}]$ . Problem 2 (P2) has  $N_E = 500$ ,  $N_p = 60$ ,  $K = 200$ ,  $G = 50$ ,  $B = 200$ , and  $H = 20$ , with demand  $d_t \sim \mathcal{N}(50, 10^2)$ . The RL agent state is set as the inventory level  $s = x + b^{(1)}$ . Therefore, the RL agent state is one-dimensional. Problem 3 (P3) has  $N_E = 500$ ,  $N_p = 60$ ,  $K = 200$ ,  $G = 50$ ,  $B = 200$ , and  $H = 20$ . The demand  $d_t$  is ARI/GARCH(1,1):  $d_t = a_0 + a_1 \cdot d_{t-1} + \epsilon_t$ ;  $\epsilon_t = e_t \cdot \sigma_t$  and  $\sigma_t^2 = \nu_0 + \nu_1 \cdot \epsilon_{t-1}^2 + \nu_2 \cdot \sigma_{t-1}^2$ , where  $a_0$  and  $a_1$  are ARI model parameters;  $\nu_0$ ,  $\nu_1$ , and  $\nu_2$  are GARCH(1,1) parameters; and  $e_t$  is white noise distributed according to  $\mathcal{N}(0, 1)$ . The values of ARI/GARCH(1,1) in our experiments are  $a_0 = 2$ ,  $a_1 = 0.8$ ,  $\nu_0 = 100$ ,  $\nu_1 = 0.1$ , and  $\nu_2 = 0.8$ , with initial values  $d_1 = 50$ ,  $\sigma_1^2 = 100$ , and  $\epsilon_1 = 2$ . The RL agent state in P3 is three-dimensional  $s = [x, b^{(1)}, b^{(2)}]$ . In all three problem settings, the RL agent period cost and action are the inventory period cost and replenishment order, respectively. For RSarsa, PRS, RSarsa.TD, and PRS.Beta, the extra information required by rumination is the inventory demand variable  $\xi = d_t$ .

The  $Q$ -value is implemented using grid tile coding [2] without hashing. Tile coding is a function approximation method based on a linear combination of weights of activated features, called “tiles.” The approximation function with argument  $\mathbf{z}$  is given by

$$f(\mathbf{z}) = w_1 \phi_1(\mathbf{z}) + w_2 \phi_2(\mathbf{z}) + \dots + w_M \phi_M(\mathbf{z}), \quad (10)$$

where  $w_1, w_2, \dots, w_M$  are tile weights and  $\phi_1(\mathbf{z}), \phi_2(\mathbf{z}), \dots, \phi_M(\mathbf{z})$  are tile activation functions  $\phi_i(\mathbf{z}) = 1$  only when  $\mathbf{z}$  lies inside the hypercube of the  $i$ th tile.

The tile configuration, that is,  $\phi_1(\mathbf{z}), \dots, \phi_M(\mathbf{z})$ , is predefined. Each  $Q$ -value is stored using tile coding through the weights. Given a value  $Q$  to store at any entry of  $\mathbf{z}$ , the weights are updated according to

$$w_i = w_i^{(\text{old})} + \frac{(Q - Q^{(\text{old})})}{N}, \quad (11)$$

where  $w_i^{(\text{old})}$  and  $Q^{(\text{old})}$  are the weight (of the  $i$ th tile) and approximation before the new update. Variable  $N$  is for a number of tiling layers.

For P1, we use a tile coding with 10 tiling layers. Each layer has  $8 \times 3 \times 4$  three-dimensional tiles, covering multidimensional state-action space of  $[-300, 500] \times [0, 150] \times [0, 150]$  corresponding to  $s = [x, b^{(1)}]$  and  $a$ . This means that this tile coding allows only a state lying in  $[-300, 500] \times [0, 150]$  and a value of action between 0 and 150. The dimensions, along  $x$ ,  $b^{(1)}$ , and  $a$ , are partitioned into 8, 3, and 4 partitions, creating 96 three-dimensional hypercubes for each tiling layer. All layers are overlapping to constitute an entire tile coding set. Layer overlapping is arranged randomly. For P2, we use a tile coding with 5 tiling layers. Each tiling has  $11 \times 5$  two-dimensional tiles, covering the space of  $[-300, 650] \times [0, 150]$  corresponding to  $s = (x + b^{(1)})$  and  $a$ . For P3, we use a tile coding with 10 tiling layers. Each tiling has  $8 \times 3 \times 3 \times 4$  four-dimensional tiles, covering the space of  $[-400, 1200] \times [0, 150] \times [0, 150] \times [0, 150]$  corresponding to  $s = [x, b^{(1)}, b^{(2)}]$  and  $a$ .

All RL agents use the  $\epsilon$ -greedy policy with  $\epsilon = 0.2$ . The learning update uses the learning rate  $\alpha = 0.7$  and discount factor  $\gamma = 0.8$ .

Figures 4, 5, and 6 show moving averages (of degree 1000) of period costs, in P1, P2, and P3, obtained with different learning agents, as indicated in the legends (“R.TD” is short for RSarsa.TD). Figures 7 and 8 show box plots of average costs obtained with the different methods in early and later periods, respectively.

The results are summarized in Table 1. The computation costs of the methods are measured by relative average computation time per epoch, shown in lines 1–3. Average

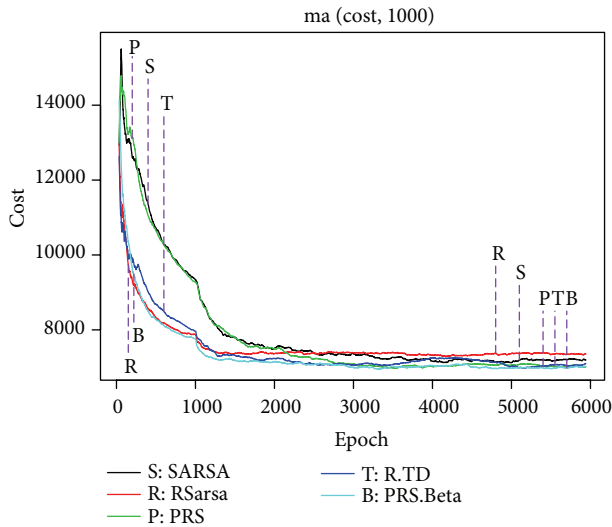


FIGURE 4: Moving average of period costs, P1.

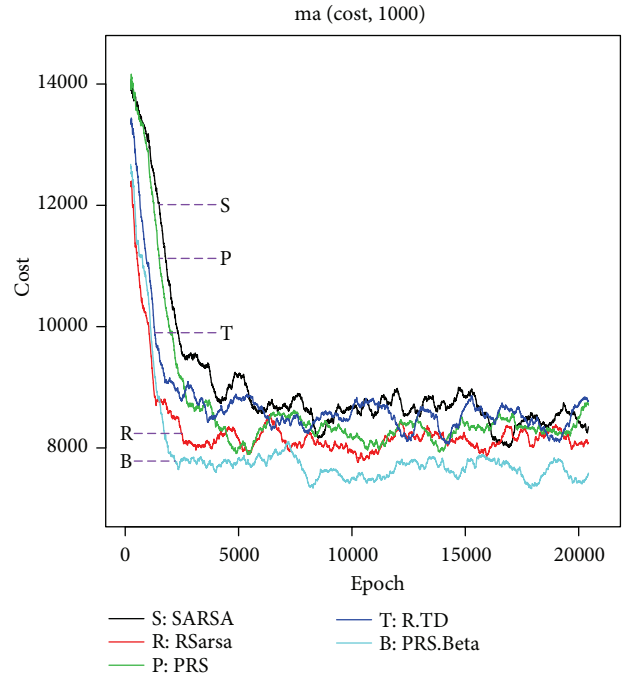


FIGURE 6: Moving average of period costs, P3.

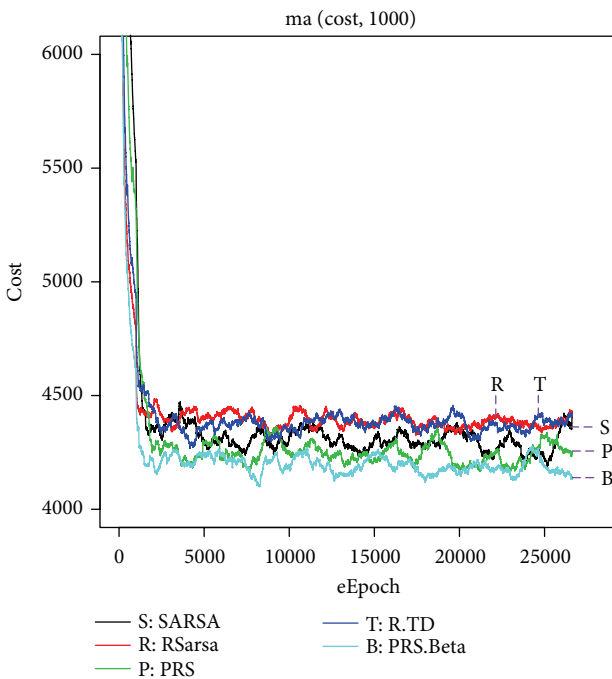


FIGURE 5: Moving average of period costs, P2.

costs are used as the inventory management performance and they are shown in lines 4–6 for early periods (periods 1–2000 in P1 and P2 and periods 1–4000 in P3) and lines 7–9 for later periods (periods after early periods). The numbers in each entry indicate average costs obtained from the corresponding methods. Parentheses reveal results from one-side Wilcoxon’s rank sum tests: “W” indicates that the average cost is significantly lower than an average cost obtained from SARSA ( $P < 0.05$ ); otherwise, the  $P$  value is shown instead.

The computation costs of RSarsa, PRS, and PRS.Beta (full rumination) are about 20–30 times of SARSA (RL without

rumination). RSarsa.TD (selective rumination) dramatically reduces the computation cost of rumination at scales of 5–7 times. An evaluation of the effectiveness of each method (compared to SARSA) shows that RSarsa and PRS.Beta significantly outperform SARSA in early periods for all 3 problems. Average costs obtained from RSarsa.TD are lower than ones from SARSA, but significance tests can confirm only results in P1 and P2. It should be noted that PRS results do not show significant improvement over SARSA. This agrees with results in a previous study [17]. With respect to performance in later periods, average costs of PRS and PRS.Beta are lower than SARSA’s in all 3 problems. However, significance tests can confirm only few results (P1 for PRS and P1 and P2 for PRS.Beta).

Table 2 shows a summary of results from significance tests comparing the previous study’s RRL methods (RSarsa and PRS) to our proposed methods (RSarsa.TD and PRS.Beta). The entries with “W” indicate that our proposed method on the corresponding column significantly outperforms a previous method on the corresponding row ( $P < 0.05$ ). Otherwise, the  $P$  value is indicated.

## 6. Conclusions and Discussion

Our results have shown that PRS.Beta achieves our goal, which is to address the slow learning rate of PRS, as it significantly outperforms PRS in early periods in all 3 problems, and to address the long-term learning quality of RSarsa, as it significantly outperforms RSarsa in later periods in P1 and P2 and its average cost is lower than RSarsa’s in P3. It should be noted that although the performance of RSarsa.TD may not seem impressive when compared to PRS.Beta’s, RSarsa.TD

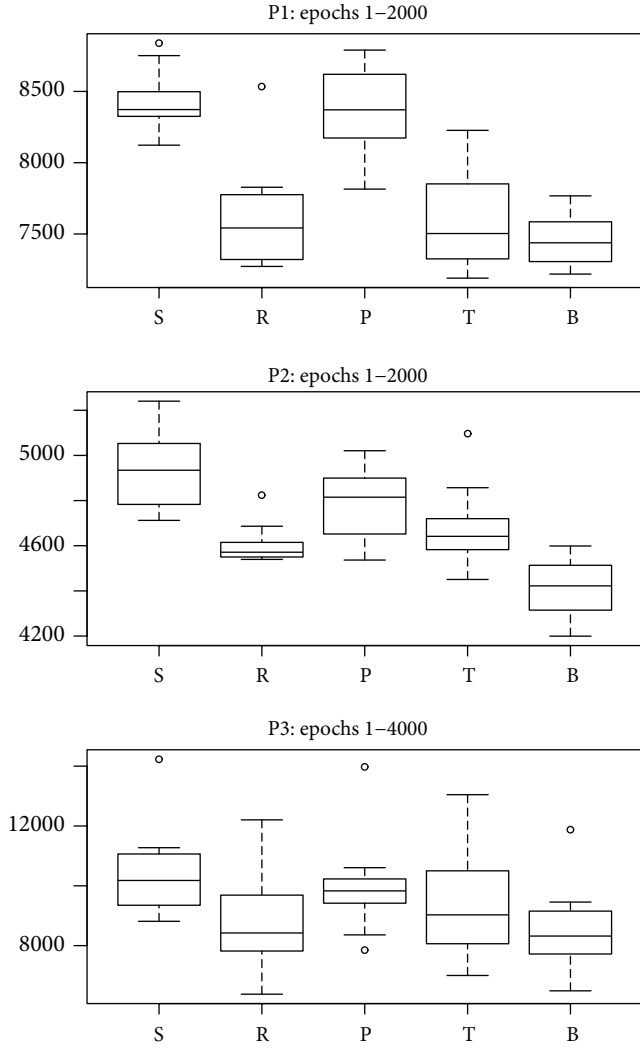


FIGURE 7: Average costs in early periods.

requires less computational cost. Therefore, as RSarsa.TD shows some improvement over SARSA, this reveals that selective rumination is still worth further study.

It should be noted that PRS.Beta employs TD error to control its behavior (6). The notion to extend TD error to determine learning factors is not limited only to rumination. It may be beneficial to use the TD error signal to determine other learning factors, such as the learning rate, for an adaptive-learning-rate agent. A high TD error indicates that the agent has a lot to learn, that what it has learned is wrong, or that things are changing. For each of these cases, the goal is to make the agent learn more quickly. So, a high TD error should be a clue to increase the learning rate, increase the degree of rumination, or increase the chance to do more exploration.

To address issues in RL worth investigation, more efficient Q-value representations should be among the priorities. Regardless of the action policy, every RL policy relies on Q-values to determine the action to take. Function approximations suitable to represent Q-values should facilitate efficient

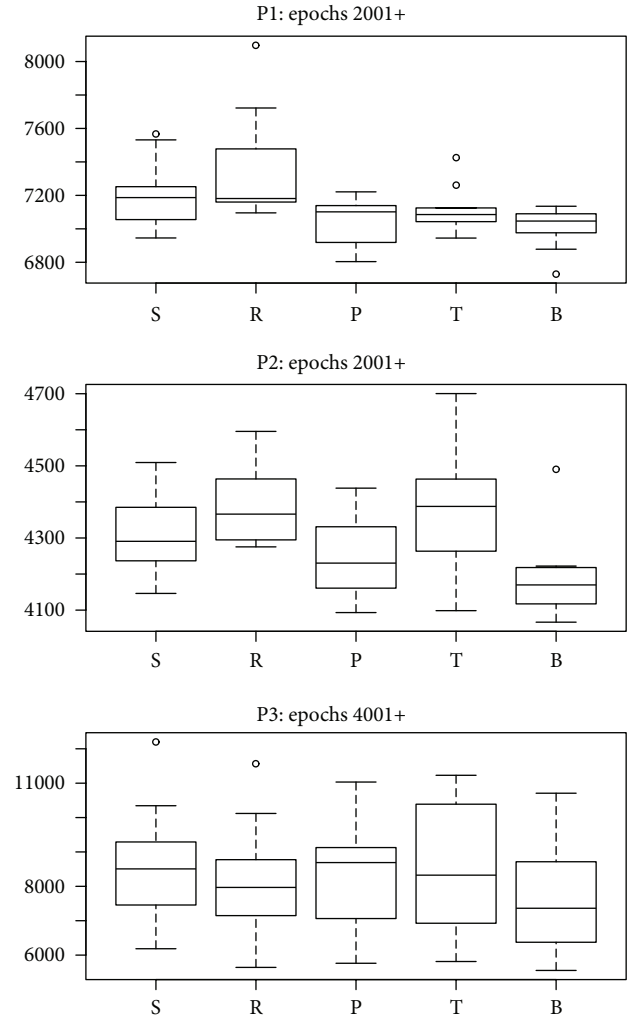


FIGURE 8: Average costs in late periods.

TABLE 2: Experimental results.

Line			RSarsa.TD	PRS.Beta
Early periods				
1	P1	RSarsa	0.49	0.16
2		PRS	W	W
3	P2	RSarsa	0.95	W
4		PRS	0.10	W
5	P3	RSarsa	0.80	0.37
6		PRS	0.26	W
Later periods				
7	P1	RSarsa	W	W
8		PRS	0.63	0.14
9	P2	RSarsa	0.46	W
10		PRS	0.97	0.12
11	P3	RSarsa	0.66	0.26
12		PRS	0.60	0.18

realization of an action policy. For example,  $\epsilon$ -greedy policy has to search for an optimal action. A Q-value representation

suitable for an  $\epsilon$ -greedy policy should allow efficient search for an optimal action given a state. Another general RL action policy is the *softmax* policy [2]. Given a state, the softmax policy has to evaluate the probabilities of candidate actions based on their associated Q-values. A representation that facilitates efficient mapping from Q-values to the probabilities would have great practical importance in this case. Due to the interaction between the Q-value representation and the action policy, there are considerable efforts to combine these two concepts. This is an active research direction under the rubric of *policy gradient RL* [18].

There are many issues in RL needed to be explored, theoretically and for application. Our findings reported in this paper provide another step in understanding and applying RL to practical inventory management problems. Even though we only investigated inventory management problems here, our methods can be applied beyond this specific domain. This early step in the study of using TD error to control learning factors, along with investigation of other issues in RL, would yield a more robust learning agent that is useful in a wide range of practical applications.

### Conflict of Interests

The authors declare that there is no conflict of interests regarding the publication of this paper.

### Acknowledgment

The authors would like to thank the Colorado State University Libraries Open Access Research and Scholarship Fund for supporting the publication of this paper.

### References

- [1] D. Bertsimas and A. Thiele, "A robust optimization approach to inventory theory," *Operations Research*, vol. 54, no. 1, pp. 150–168, 2006.
- [2] R. S. Sutton and A. G. Barto, *Reinforcement Learning*, MIT Press, Boston, Mass, USA, 1998.
- [3] W. B. Powell, *Approximate Dynamic Programming: Solving the Curses of Dimensionality*, Wiley Series in Probability and Statistics, Wiley-Interscience, Hoboken, NJ, USA, 2007.
- [4] J. Rao, X. Bu, C. Z. Xu, L. Wang, and G. Yin, "VCONF: a reinforcement learning approach to virtual machines auto-configuration," in *Proceedings of the 6th International Conference on Autonomic Computing (ICAC '09)*, pp. 137–146, ACM, Barcelona, Spain, June 2009.
- [5] S. G. Khan, G. Herrmann, F. L. Lewis, T. Pipe, and C. Melhuish, "Reinforcement learning and optimal adaptive control: an overview and implementation examples," *Annual Reviews in Control*, vol. 36, no. 1, pp. 42–59, 2012.
- [6] A. Coates, P. Abbeel, and A. Y. Ng, "Apprenticeship learning for helicopter control," *Communications of the ACM*, vol. 52, no. 7, pp. 97–105, 2009.
- [7] C. W. Anderson, D. Hittle, M. Kretchmar, and P. Young, "Robust reinforcement learning for heating, ventilation, and air conditioning control of buildings," in *Handbook of Learning and Approximate Dynamic Programming*, J. Si, A. Barto, W. Powell, and D. Wunsch, Eds., pp. 517–534, John Wiley & Sons, New York, NY, USA, 2004.
- [8] R. Lincoln, S. Galloway, B. Stephen, and G. Burt, "Comparing policy gradient and value function based reinforcement learning methods in simulated electrical power trade," *IEEE Transactions on Power Systems*, vol. 27, no. 1, pp. 373–380, 2012.
- [9] Z. Tan, C. Quek, and P. Y. K. Cheng, "Stock trading with cycles: a financial application of ANFIS and reinforcement learning," *Expert Systems with Applications*, vol. 38, no. 5, pp. 4741–4755, 2011.
- [10] A. Castelletti, F. Pianosi, and M. Restelli, "A multiobjective reinforcement learning approach to water resources systems operation: pareto frontier approximation in a single run," *Water Resources Research*, vol. 49, no. 6, pp. 3476–3486, 2013.
- [11] T. Katanyukul, E. K. P. Chong, and W. S. Duff, "Intelligent inventory control: is bootstrapping worth implementing?" in *Intelligent Information Processing VI*, vol. 385 of *IFIP Advances in Information and Communication Technology*, pp. 58–67, Springer, New York, NY, USA, 2012.
- [12] T. Akiyama, H. Hachiyama, and M. Sugiyama, "Efficient exploration through active learning for value function approximation in reinforcement learning," *Neural Networks*, vol. 23, no. 5, pp. 639–648, 2010.
- [13] K. Doya, "Metalearning and neuromodulation," *Neural Networks*, vol. 15, no. 4–6, pp. 495–506, 2002.
- [14] P. Dayan and N. D. Daw, "Decision theory, reinforcement learning, and the brain," *Cognitive, Affective and Behavioral Neuroscience*, vol. 8, no. 4, pp. 429–453, 2008.
- [15] T. Katanyukul, W. S. Duff, and E. K. P. Chong, "Approximate dynamic programming for an inventory problem: empirical comparison," *Computers and Industrial Engineering*, vol. 60, no. 4, pp. 719–743, 2011.
- [16] C. O. Kim, I. H. Kwon, and J. G. Baek, "Asynchronous action-reward learning for nonstationary serial supply chain inventory control," *Applied Intelligence*, vol. 28, no. 1, pp. 1–16, 2008.
- [17] T. Katanyukul, "Ruminative reinforcement learning: improve intelligent inventory control by ruminating on the past," in *Proceedings of the 5th International Conference on Computer Science and Information Technology (ICCSIT '13)*, Academic Publisher, Paris, France, 2013.
- [18] N. A. Vien, H. Yu, and T. Chung, "Hessian matrix distribution for Bayesian policy gradient reinforcement learning," *Information Sciences*, vol. 181, no. 9, pp. 1671–1685, 2011.

## Research Article

# An Analytical Solution by HAM for Nonlinear Simulation of Deepwater SCR Installation

Yi Wang,<sup>1</sup> Ji-jun Gu,<sup>1</sup> Chen An,<sup>1</sup> Meng-lan Duan,<sup>1</sup> and Ning He<sup>2</sup>

<sup>1</sup> Offshore Oil/Gas Research Center, China University of Petroleum, Beijing 102249, China

<sup>2</sup> Offshore Oil Engineering Co., Ltd., Tianjin 300452, China

Correspondence should be addressed to Yi Wang; wangyizyn@sina.com

Received 10 December 2013; Revised 29 May 2014; Accepted 5 June 2014; Published 2 July 2014

Academic Editor: Aderemi Oluyinka Adewumi

Copyright © 2014 Yi Wang et al. This is an open access article distributed under the Creative Commons Attribution License, which permits unrestricted use, distribution, and reproduction in any medium, provided the original work is properly cited.

Steel catenary riser (SCR) is a cost-effective riser system that is widely used in deepwater offshore oilfields development. During SCR J-lay installation, the movement of pull-head must be carefully controlled to ensure riser safety. Since the SCR installation path calculation through numerical simulation software is usually time-consuming, this paper has established a mechanical model for SCR installation by making use of homotopy analysis method (HAM) to simplify its analytical solution, and dimensional analysis was considered in making initial guess solution. Based on this analytical solution, a program within the framework of MATLAB was developed to predict the two-dimensional riser behavior during installation, and a sensitivity analysis for different values of the control variables was carried out. Engineers may efficiently optimize the installation path by the application of this technique.

## 1. Introduction

In response to increasing global demand of energy from fossil fuels and the replacement of depleting oil and gas reserves in most matured fields in the world, operating companies in the oil industry are expanding their exploration and production operations into deepwater. In deepwater exploration, SCRs are widely used as a cost-effective riser system which is connecting offshore platforms and subsea production systems. During SCR installation as shown in Figure 1, the pull-head is transferred from installation vessel to platform by Abandon & Recovery (A&R) wire from installation vessel and pull-in wire from the platform. The transfer process is usually carried out by J-lay vessel, since the S-lay vessel cannot install SCR independently [1, 2]. The transfer process is divided into prelay and postlay, depending on whether the offshore platform is on site [3].

The shape of SCR will be affected by the route of pull-head during installation controlled by both the A&R and the pull-in wire, and the maximum stresses to be encountered during the transfer process must be obtained before installation [4]. A large number of papers have been published on this issue. The catenary theory is a simple model for evaluating the

tension and curvature of SCR [5], but it cannot simulate the rapid change of the inclination angle because it ignores the bending stiffness [6]. The nonlinear large deformation beam theory is more appropriate for simulating the riser near touchdown point (TDP) considering the large-angle deformation [7, 8]. Dixon and Rultledge [9] applied Plunkett's expansions in analyzing J-lay method. Guarracino and Mallardo [10] developed the expansions to analyze the S-lay method. Dai et al. [11] used line integration technique to analyze the tensions of A&R wire while considering the movement of installation vessel. Xing et al. [12] established a nonlinear mechanical model to analyze the pipeline lifting process and applied a shooting method in solving the moving boundary problem. Lenci and Callegari [13] investigated some analytical models to analyze the J-lay method, but the solution is not easy to obtain because the equations are highly nonlinear. García-Palacios et al. [14] used two-dimensional Navier-Bernoulli beam to analyze pipeline laying process, and an updated Lagrangian formulation for the nonlinear analysis was obtained. Nowadays, finite element software such as OrcaFlex is commonly used to solve optimal installation path problem. But it might be time-consuming depending on the performance of computer. Therefore, a simple and

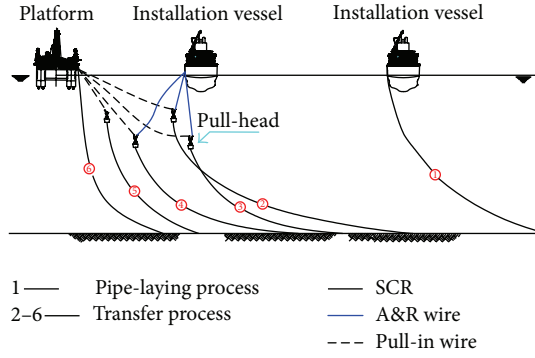


FIGURE 1: SCR installation procedure.

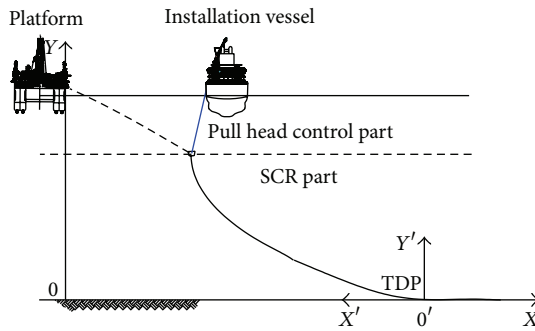


FIGURE 2: Mechanical model for transfer process of SCR installation.

effective SCR installation model is still important for engineers to understand the nature and relevance of the complex phenomena during installation. Thus, an analytical solution for SCR installation can substantially reduce design time and provide a quick evaluation of actual installation setting.

The structural model presented in this paper is a simple and practical method to obtain the static configuration and the mechanical load parameters for SCR transfer process. The bending stiffness and large deformation of the part suspended in water are taken into consideration. The governing equation system is derived and the analytical approximate solution is obtained by means of HAM. Compared with the available commercial software such as OrcaFlex, the calculation of the present model has the advantage of high stability and being time-saving. A series of parameters such as initial installation angle, maximum lower depth of pull-head, water depth, and distance between installation vessel and offshore platform are considered during the stress analysis of SCR installation.

## 2. Nonlinear Model of SCR Installation

The mechanical model used to simulate the behavior of transfer process during SCR installation is composed of two parts, as presented in Figure 2. In pull-head control part, the catenary theory is used to simulate the A&R wire and pull-in wire [15]. In SCR part, the nonlinear large deformation beam theory is used to simulate the suspended segment [16]. The hypotheses considered in the model are summarized as follows.

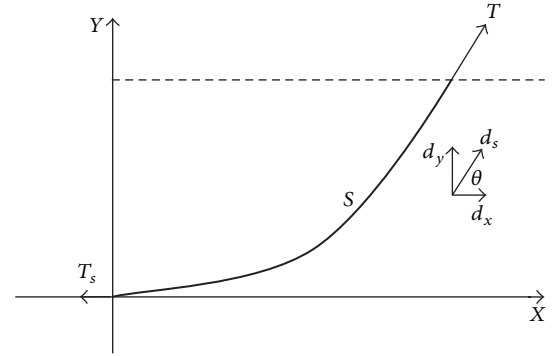


FIGURE 3: Catenary axis and forces.

- (1) The dynamic movement of the installation vessel and platform are not considered.
- (2) The gravitational and hydrostatic forces are the only loads upon the riser during installation operations.
- (3) The SCR material is linear elastic, and the behavior of SCR is modeled as a two-dimensional beam subjected to axial and bending deformations. Torsional and shear deformation are not considered.
- (4) The seabed is rigid. Two parts of the model are solved in the local coordinate system  $X'O'Y'$ , respectively and transformed to the global coordinate system  $XOY$ , finally. The TDP of SCR is the origin of local coordinate system  $X'O'Y'$ .

**2.1. Pull-Head Control Part.** The location of pull-head is important for SCR shape control. It is controlled by the length of A&R wire from installation vessel and pull-in wire from platform. Based on catenary theory as shown in Figure 3, the following equations can be obtained:

$$S = \sqrt{y^2 + 2\frac{T_s}{w}y} \quad (1)$$

$$x = \frac{T_s}{w} \ln \left[ \frac{w}{T_s}y + 1 + \sqrt{\left(\frac{w}{T_s}y + 1\right)^2 - 1} \right], \quad (2)$$

where  $T$  is axial tension at pull-head,  $T_s$  is axial tension at TDP,  $w$  is the submerged weight per unit length of the riser, and  $S$  is the length of SCR.

The transfer process is typically carried out by two steps. The first step is to lower the pull-head by increasing the length of A&R wire from installation vessel, and the second step is to pull-in the pull-head by decreasing the length of pull-in wire from platform.

The geometrical relationship in lowering step is shown in Figure 4. Assuming the initial position of pull-head before transfer process is at  $(x_0, y_0)$ , the increasing length of A&R wire  $\Delta L$  will change the pull-head position to  $(x_1, y_1)$ ,  $S_0$  is the suspended segment length of the SCR at the initial position,  $S_1$  is the suspended segment length of the SCR after lowering,  $\Delta x$  is the horizontal position's change of TDP,  $\Delta x_1$

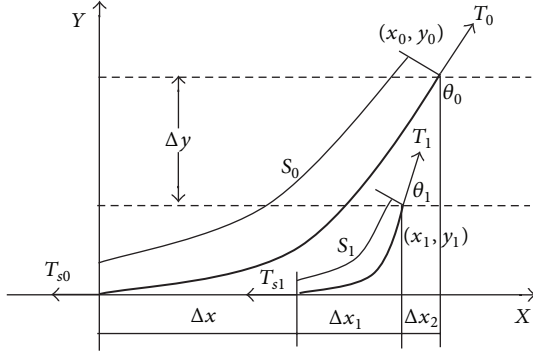


FIGURE 4: Geometrical relationship for lowering step.

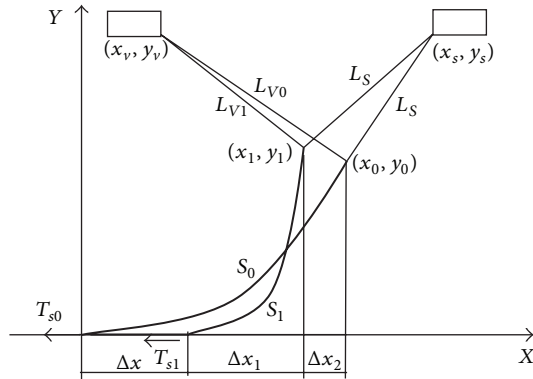


FIGURE 5: Geometrical relationship for pull-in step.

is the horizontal length of  $S_1$ ,  $\Delta x_2$  is the horizontal position change of pull-head, and  $\Delta y$  is the vertical position change of pull-head. The following relations can be obtained:

$$x_0 = \Delta x + \Delta x_1 + \Delta x_2 \quad (3)$$

$$s_0 = \Delta x + s_1. \quad (4)$$

Based on (1)–(4), the pull-head control model for the lowering step can be obtained:

$$x_1 = y_0 \sqrt{1 + 2A} - y_1 \sqrt{1 + 2B} + y_1 B \ln \left[ \frac{1}{B} + 1 + \sqrt{\left(\frac{1}{B} + 1\right)^2 - 1} \right] + \Delta L \cos \theta_1, \quad (5)$$

where  $A = \cos \theta_0 / (1 - \cos \theta_0)$ ,  $B = (1 - \cos \theta_1) / \cos \theta_1$ .

The geometrical relationship in pull-in step is shown in Figure 5. Assuming the initial position of the installation vessel is at  $(x_s, y_s)$ , with the initial position of platform being at  $(x_v, y_v)$ , while the initial position of pull-head is at  $(x_0, y_0)$ , the increasing length of pull-in wire  $\Delta L$  will change the pull-head position to  $(x_1, y_1)$ .  $S_0$  is the suspended segment length of the SCR at initial position, and  $S_1$  is the suspended segment length of the SCR after pull-in, whereas  $\Delta x$  is the horizontal position's change of TDP,  $\Delta x_1$  is horizontal length of  $S_1$ , and

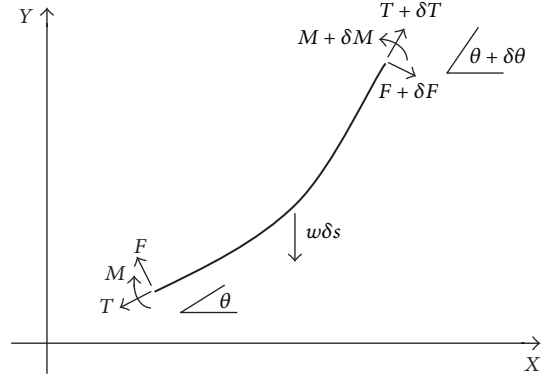


FIGURE 6: Forces on a large deformation beam segment  $\delta s$ .

$\Delta x_2$  is horizontal position's change of pull-head. Therefore, the following equations can be obtained:

$$L_s = \sqrt{(x_s - x_0)^2 + (y_s - y_0)^2} \quad (6)$$

$$= \sqrt{(x_s - x_1)^2 + (y_s - y_1)^2}$$

$$\Delta L = \sqrt{(x_v - x_0)^2 + (y_v - y_0)^2} \quad (7)$$

$$- \sqrt{(x_v - x_1)^2 + (y_v - y_1)^2}$$

$$x_0 = \Delta x + \Delta x_1 + \Delta x_2. \quad (8)$$

By combining (1), (2), and (6) in (8), the pull-head control model for the pull-in step can be obtained:

$$x_1 = y_0 \sqrt{1 + 2A} - y_1 \sqrt{1 + 2B} + y_1 B \ln \left[ \frac{1}{B} + 1 + \sqrt{\left(\frac{1}{B} + 1\right)^2 - 1} \right]. \quad (9)$$

**2.2. SCR Part.** An infinitesimal element with length  $ds$  based on the nonlinear large deformation beam theory is presented in Figure 6. The force equilibrium equation normal to the segment's axial direction is established by (10), and the force equilibrium equation in the segment's axial direction is established by (11). Consider

$$\delta F - T \delta \theta + w \delta s \cos \theta = 0 \quad (10)$$

$$\delta T = w \delta s \sin \theta, \quad (11)$$

where  $F$  is shear force ( $F = dM/ds$ ),  $T$  is axial tension, and  $M$  is bending moment. Then, (10) can be written as follows:

$$\frac{d^2 M}{ds^2} - T \frac{d\theta}{ds} + w \cos \theta = 0. \quad (12)$$

According to large deformation beam theory, the curvature  $1/R = M/EI = d\theta/ds$ , where  $EI$  is the flexural rigidity. Therefore, (12) can be written in the following form:

$$\frac{d^2}{ds^2} \left( EI \frac{d\theta}{ds} \right) - T \frac{d\theta}{ds} + w \cos \theta = 0. \quad (13)$$

By simplifying (11) and (13), the mechanical model for large deformation beam can be obtained as follows:

$$EI \frac{d^3 \theta}{ds^3} - T \frac{d\theta}{ds} + w \cos \theta = 0 \quad (14)$$

$$\frac{dT}{ds} = w \sin \theta. \quad (15)$$

The boundary condition at top point of riser is  $d\theta_T/d\varepsilon = 0$ , and the boundary conditions at TDP are  $\theta_D = \theta^*$ ,  $d\theta_D/d\varepsilon = \sin \theta^*$ , and  $T(\varepsilon) = F_T \cos \omega_T \cos \theta^*$ , where  $F_T$  is the lifting load at the top of riser,  $\omega_T$  is the angel between lifting load and the  $x$ -axis,  $\theta^*$  is the angel between riser and the  $x$ -axis at TDP.

Equation (14) is a third-order nonlinear differential equation with an unknown variable  $\theta$ . It can be solved using numerical method such as the finite element method [17] or the finite difference method [18]. However, we provide the analytical solution by HAM in this paper.

### 3. HAM Solution for SCR Installation Model

*3.1. Basic Idea of HAM.* Perturbation technique has been widely used for nonlinear problem [19] which is dependent on small physical parameters. Liao [20] proposed a general analytical method known as HAM for nonlinear problems by using the basic ideas of the homotopy in topology. HAM provides us with great freedom to select proper base functions for approximate solutions of nonlinear problems and a simple way to get enough accurate analytical approximations.

For the nonlinear differential equations with general form:

$$A[u(x)] = 0 \quad x \in R^n. \quad (16)$$

$A$  is the nonlinear operator for all equations,  $u(x)$  is an unknown solution for all equations, and  $x$  is the independent variables. Based on the basic concept of HAM, the embedded parameter  $p \in [0, 1]$  and the initial guess of the exact solution  $u_0(x)$  are introduced. The homotopy which is the so-called zero-order deformation equation can be constructed as follows:

$$(1-p)L[\phi(x;p) - u_0(x)] = p\hbar H(x)A[\phi(x;p)] \quad p \in [0, 1], \quad (17)$$

where  $\hbar$  is a nonzero auxiliary parameter,  $H(x)$  is a nonzero auxiliary function,  $L$  is an auxiliary linear operator that satisfies the property  $L[0] = 0$ , and  $\phi(x;p)$  is an unknown function. It is obvious that, when  $p = 0$  and  $p = 1$ , the following relations hold, respectively:

$$\phi(x;0) = u_0(x), \quad \phi(x;1) = u(x). \quad (18)$$

Thus, as  $p$  increases from 0 to 1, the solution  $\phi(x;p)$  varies from the initial guess  $u_0(x)$  to the accurate solution  $u(x)$ . Expand  $\phi(x;p)$  by Taylor's theorem in a power series of  $p$ :

$$\phi(x;p) = u_0(x) + \sum_{k=1}^{+\infty} u_k(x) p^k, \quad (19)$$

where  $u_k(x) = (1/k!)(\partial^k \phi(x;p)/\partial p^k)|_{p=0}$ .

Assuming that  $L$ ,  $u_0(x)$ ,  $\hbar$ , and  $H(x)$  are properly chosen; the power series (19) converges at  $p = 1$ , and the solution series can be obtained as follows:

$$u(x) = u_0(x) + \sum_{k=1}^{+\infty} u_k(x). \quad (20)$$

Differentiating the zero-order deformation equation (17)  $m$  times with respect to  $p$ , dividing by  $m!$ , and setting  $p = 0$ ,  $m$ th-order deformation equation can be obtained:

$$L[u_k(x) - \chi_k u_{k-1}(x)] = \hbar H(x) R_k(x), \quad (21)$$

where

$$\chi_k = \begin{cases} 0, & k \leq 1 \\ 1, & k > 1, \end{cases} \quad (22)$$

$$R_k(x) = \frac{1}{(k-1)!} \left. \frac{\partial^{k-1} A[\phi(x;p)]}{\partial p^{k-1}} \right|_{p=0}.$$

*3.2. Solution of the Mechanical Model for SCR Part by HAM.* A dimensionless parameter  $\varepsilon = s/l$  is introduced to (14) and (15), and HAM is used to obtain the analytical approximation of this mechanical model.

Assuming that  $\varphi^\theta(\varepsilon, q)$  is the homotopy which is connected to the original equation, solution  $\theta(\varepsilon)$ , and the initial guess solution  $\theta_0(\varepsilon)$ ,  $\varphi^T(\varepsilon, q)$  is the homotopy which is connected to the original equation solution  $T(\varepsilon)$  and the initial guess solution  $T_0(\varepsilon)$ . The embedded parameter  $q \in [0, 1]$ , the nonzero auxiliary parameters  $\hbar_\theta$  and  $\hbar_T$ , the auxiliary linear operators  $L_\theta$  and  $L_T$ , and the nonzero auxiliary functions  $H_\theta(\varepsilon)$  and  $H_T(\varepsilon)$  are introduced. The nonlinear operators for (14) and (15) are

$$\begin{aligned} N_\theta[\varphi^\theta(\varepsilon, q), \varphi^T(\varepsilon, q)] &= \frac{\partial^3 \varphi^\theta(\varepsilon, q)}{\partial \varepsilon^3} - \frac{l^2}{EI} \varphi^T(\varepsilon, q) \frac{\partial \varphi^\theta(\varepsilon, q)}{\partial \varepsilon} \\ &+ \frac{wl^3}{EI} \cos[\varphi^\theta(\varepsilon, q)] \end{aligned} \quad (23)$$

$$\begin{aligned} N_T[\varphi^\theta(\varepsilon, q), \varphi^T(\varepsilon, q)] &= \frac{\partial \varphi^T(\varepsilon, q)}{\partial \varepsilon} - lw \sin[\varphi^\theta(\varepsilon, q)]. \end{aligned}$$

Thus, zero-order deformation equations can be obtained as follows:

$$\begin{aligned} (1-q)L_\theta[\varphi^\theta(\varepsilon, q) - \theta_0(\varepsilon)] &= \hbar_\theta H_\theta(\varepsilon) q N_\theta[\varphi^\theta(\varepsilon, q), \varphi^T(\varepsilon, q)] \\ (1-q)L_T[\varphi^T(\varepsilon, q) - T_0(\varepsilon)] &= \hbar_T H_T(\varepsilon) q N_T[\varphi^\theta(\varepsilon, q), \varphi^T(\varepsilon, q)] \end{aligned} \quad (24)$$

which satisfies the initial conditions  $\varphi^\theta(\varepsilon, 0) = \theta_0(\varepsilon)$  and  $\varphi^T(\varepsilon, 0) = T_0(\varepsilon)$ .

Applying (20) to this case, we can write

$$\begin{aligned} \theta(\varepsilon) &= \varphi^\theta(\varepsilon, 1) = \varphi^\theta(\varepsilon, 0) + \sum_{m=1}^{+\infty} \frac{1}{m!} \frac{\partial^m}{\partial q^m} \varphi^\theta(\varepsilon, q) \Big|_{q=0} \\ &= \theta_0(\varepsilon) + \sum_{m=1}^{+\infty} \theta_m(\varepsilon) \end{aligned} \tag{25}$$

$$\begin{aligned} T(\varepsilon) &= \varphi^T(\varepsilon, 1) = \varphi^T(\varepsilon, 0) + \sum_{m=1}^{+\infty} \frac{1}{m!} \frac{\partial^m}{\partial q^m} \varphi^T(\varepsilon, q) \Big|_{q=0} \\ &= T_0(\varepsilon) + \sum_{m=1}^{+\infty} T_m(\varepsilon), \end{aligned}$$

where  $\theta_m(\varepsilon) = (1/m!)(\partial^m/\partial q^m)\varphi^\theta(\varepsilon, q)|_{q=0}$  and  $T_m(\varepsilon) = (1/m!)(\partial^m/\partial q^m)\varphi^T(\varepsilon, q)|_{q=0}$ .

The  $m$ th-order deformation equations (21) for this particular case are

$$\begin{aligned} L_\theta [\theta_m(\varepsilon) - \chi_m \theta_{m-1}(\varepsilon)] &= \hbar_\theta H_\theta(\varepsilon) R_m^\theta [\theta_{m-1}(\varepsilon), T_{m-1}(\varepsilon)] \\ L_T [T_m(\varepsilon) - \chi_m T_{m-1}(\varepsilon)] &= \hbar_T H_T(\varepsilon) R_m^T [\theta_{m-1}(\varepsilon), T_{m-1}(\varepsilon)], \end{aligned} \tag{26}$$

where

$$\chi_k = \begin{cases} 0, & k \leq 1 \\ 1, & k > 1, \end{cases}$$

$$\begin{aligned} R_m^\theta [\theta_{m-1}(\varepsilon), T_{m-1}(\varepsilon)] &= \theta_{m-1}'''(\varepsilon) - \frac{l^2}{EI} \sum_{k=0}^{m-1} T_k(\varepsilon) \theta'_{m-1-k}(\varepsilon) \\ &+ \frac{wl^3}{EI(m-1)!} \frac{\partial^{m-1}}{\partial q^{m-1}} \cos [\varphi^\theta(\varepsilon, q)] \Big|_{q=0}, \end{aligned} \tag{27}$$

$$\begin{aligned} R_m^T [\theta_{m-1}(\varepsilon), T_{m-1}(\varepsilon)] &= T_{m-1}'(\varepsilon) - \frac{lw}{(m-1)!} \frac{\partial^{m-1}}{\partial q^{m-1}} \sin [\varphi^\theta(\varepsilon, q)] \Big|_{q=0}. \end{aligned}$$

We select the nonzero auxiliary function as

$$H_\theta(\varepsilon) = \frac{s^2}{EIT}, \quad H_T(\varepsilon) = \frac{1}{EIT}. \tag{28}$$

Referring to the catenary equation, we select the initial guess solution  $\theta_0(\varepsilon)$  and  $T_0(\varepsilon)$  as

$$\theta_0(\varepsilon) = \arctan\left(\frac{awl\varepsilon^k}{G}\right), \quad T_0(\varepsilon) = \sqrt{(lw\varepsilon)^2 + G^2}, \tag{29}$$

where  $G = F_0 \cos \omega_0$  and  $a$  and  $k$  are adjustment parameters which is related to the length of riser  $l$ . Through dimensional analysis, the following relationship can be obtained:

$$\frac{l}{l_0} = \left(\frac{EIw_0}{EI_0w}\right)^{1/3}. \tag{30}$$

If we select the length of riser  $l_0$  under the condition  $EI_0 = 50$  and  $w_0 = 350.59$ , the adjustment parameters  $a$  and  $k$  can be expressed with respect to  $l_0$ :

$$a = \begin{cases} 1.02755 - 1.84502e^{-l_0/1.43616} & l_0 \leq 6 \\ 0.947 + 0.009l_0 & l_0 \leq 10 \\ 1.035 & l_0 \leq 14 \\ 1.08931 - 0.00385l_0 & l_0 \leq 23 \\ 0.98683 + 688.37803e^{-l_0/2.11687} & l_0 \leq 26 \\ 0.96059 + 0.00113l_0 & l_0 \leq 40 \\ 1 & l_0 > 40 \end{cases}$$

$$k = \begin{cases} 0.00541e^{l_0/0.48212} + 1.35738 & l_0 \leq 2 \\ 1.28217e^{-l_0/2.36014} - 0.00781l_0 + 1.19157 & l_0 \leq 25 \\ 1 & l_0 > 25. \end{cases} \tag{31}$$

Considering the boundary conditions at TDP ( $\varepsilon = 0$ ) and top point of riser ( $\varepsilon = 1$ ) in mechanical model for part I, the following boundary conditions can be obtained:

$$\begin{aligned} \varepsilon = 0: \theta(\varepsilon) = 0, \quad \frac{d\theta(\varepsilon)}{d\varepsilon} = 0, \quad T(\varepsilon) = F_0 \cos \omega_0 \\ \varepsilon = 1: \frac{d\theta(\varepsilon)}{d\varepsilon} = 0. \end{aligned} \tag{32}$$

When the nonzero auxiliary parameters are selected as  $\hbar_\theta = 0.1$  and  $\hbar_T = 1$ , the analytical approximate solution of  $\theta(\varepsilon)$  and  $T(\varepsilon)$  can be written as

$$\begin{aligned} \theta(\varepsilon) &= \arctan\left(\frac{awl_0\varepsilon^k}{G}\right) + \frac{\hbar_\theta\varepsilon^2}{EI_0T} \\ &\times \left\{ \frac{C}{D} - \frac{3C}{kD} - \frac{8a^2\varepsilon^{2k}l_0^2w_0^2C}{G^2D^2} + \frac{2C}{k^2D} \right. \\ &+ \frac{6a^2s^{3k}l_0^2w_0^2C}{\varepsilon^k k G^2 D^2} + \frac{8a^4s^{5k}l_0^4w_0^4C}{\varepsilon^k G^4 D^3} \\ &\left. + \frac{l_0^3[(l_0w_0s)^2 + G^2]^{0.5}\varepsilon^2C}{EI_0k^2l_0D} + \frac{l_0^3w_0}{EI_0D^{0.5}} \right\} \\ T(\varepsilon) &= \sqrt{(lw\varepsilon)^2 + G^2} + \frac{\hbar_T}{EIT} \\ &\times \left\{ \frac{l^2w^2\varepsilon}{[(lw\varepsilon)^2 + G^2]^{0.5}} - lw \sin \left[ \arctan\left(\frac{wl\varepsilon}{G}\right) \right] \right\}, \end{aligned} \tag{33}$$

where  $C = a\varepsilon^k k^3 l_0 w_0 / \varepsilon^3 G$ ,  $D = 1 + (a^2 \varepsilon^{2k} l_0^2 w_0^2 / G^2)$ .

TABLE 1: Parameters of SCR.

Parameter	Value
Outer diameter (m)	0.3048
Inner diameter (m)	0.2743
Flexural rigidity (N·m <sup>2</sup> )	3.1340E07
Weight submerged (N/m)	350.59
Density (kg/m <sup>3</sup> )	7850

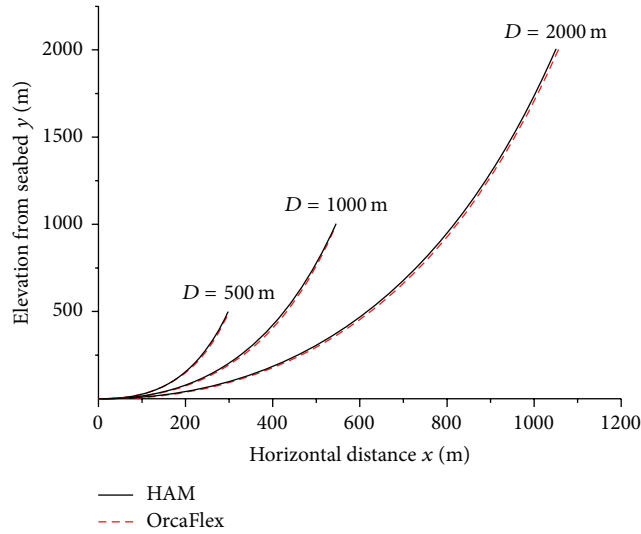


FIGURE 7: Configuration results comparison between HAM and OrcaFlex in different water depth.

#### 4. Results and Discussion

In order to implement the SCR installation model as described above, a computer program has been developed within the framework of MATLAB language program. The efficiency and accuracy of this model is verified by comparison with the numerical results of OrcaFlex. The parameters of SCR used for verification and analysis are detailed in Table 1.

The overall configuration and axial tension calculated by the proposed method and OrcaFlex are compared as shown in Figures 7 and 8, respectively. In different water depth conditions, the results are well coincided, which prove that the analytical method is accurate and can be used to analyze SCR installation problem. Some critical parameters are summarized in Table 2, where  $X$  is horizontal distance from TDP to the top point of riser,  $Y_{top}$  is vertical distance from seabed, and  $T_{max}$  is maximum axial tension at the top point of riser.

Postlay method is selected for SCR installation parameters analysis. In this method, the offshore platform is on site. When SCR is laid near to the offshore platform by installation vessel, SCR pull-head is firstly connected to the A&R wire and the cable from offshore platform, which is lifted only by the A&R wire. Increase the length of A&R wire to lower pull-head to the maximum depth and then decrease the length of cable from offshore platform until pull-head is finally lifted to the hang-off position. Note that the dynamic positioning (DP) system always maintains the installation vessel and

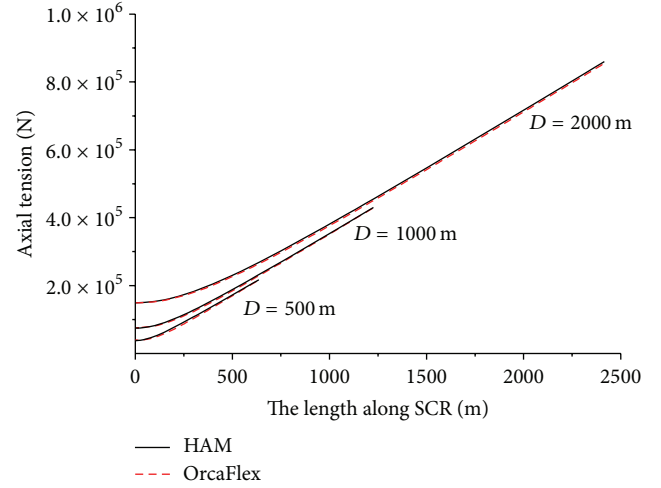


FIGURE 8: Axial tension results comparison between HAM and OrcaFlex in different water depth.

offshore platform position in the original place during SCR installation.

The safety of SCR during installation is affected by many factors. The most important one is that the variation of SCR maximum stress caused by the change of installation shape should be within the allowable stress. In order to investigate the influence of the initial installation angle, the maximum lower depth of pull-head, water depth, and the distance between installation vessel and offshore platform, the parameters shown in Table 1 are used for SCR, with following hypotheses.

- (1) Assume that the initial installation angle is  $\theta_I$ , the maximum lower depth of pull-head is  $D_L$ , water depth is  $D$ , and the distance between installation vessel and offshore platform is  $D_V$ .
- (2) Assume that the horizontal position of pull-head is  $X_{ph}$ , which has zero value at the position of the installation vessel and has maximum value at the position of the offshore platform.
- (3) Assume that the vertical position of pull-head is  $Y_{ph}$ , which has zero value at sea level and has maximum value at  $D_L$ .

The maximum stress results under different conditions are summarized in Table 3.

**4.1. Influence of  $\theta_I$ .** Usually, deepwater SCR is installed by J-lay vessel, and the installation angle (the angle between the J-lay tower and the vertical direction) will affect the SCR installation shape. Under the conditions that  $D_L$  is 30 m,  $D_V$  is 35 m,  $D$  is 1000 m, and  $\theta_I$  is 8°, 10° and 12°, respectively, the maximum stresses of SCR during installation are shown in Figure 9. It clearly shows that, with the small rise of  $\theta_I$ , the maximum stresses on SCR increase rapidly. It can be observed that the J-lay method is more suitable for deepwater SCR installation than S-lay method, since it can control the  $\theta_I$  nearly to zero.

TABLE 2: Critical results.

Item	$D = 500 \text{ m}$			$D = 1000 \text{ m}$			$D = 2000 \text{ m}$		
	$X \text{ (m)}$	$Y_{\text{top}} \text{ (m)}$	$T_{\text{max}} \text{ (N)}$	$X \text{ (m)}$	$Y_{\text{top}} \text{ (m)}$	$T_{\text{max}} \text{ (N)}$	$X \text{ (m)}$	$Y_{\text{top}} \text{ (m)}$	$T_{\text{max}} \text{ (N)}$
HAM	297.97	499.41	217071	545.43	1004.09	429937	1050.67	2006.54	859997
OrcaFlex	299.89	499.91	214430	546.57	1002.77	428228	1056.20	2003.68	853240
Difference	0.64%	-0.1%	-1.23%	0.21%	-0.13%	-0.4%	0.53%	-0.14%	-0.79%

TABLE 3: Maximum stress results.

$\theta_I \text{ (}^\circ\text{)}$	$D_L \text{ (m)}$	$D \text{ (m)}$	$D_V \text{ (m)}$	$\sigma_{\text{max}} \text{ (MPa)}$
8	30	1000	35	169.37
10	30	1000	35	215.15
12	30	1000	35	273.91
10	33	1000	35	218.09
10	36	1000	35	221.10
10	35	1000	35	219.98
10	35	1500	35	135.79
10	35	2000	35	100.23
10	35	1000	30	217.84
10	35	1000	40	222.21

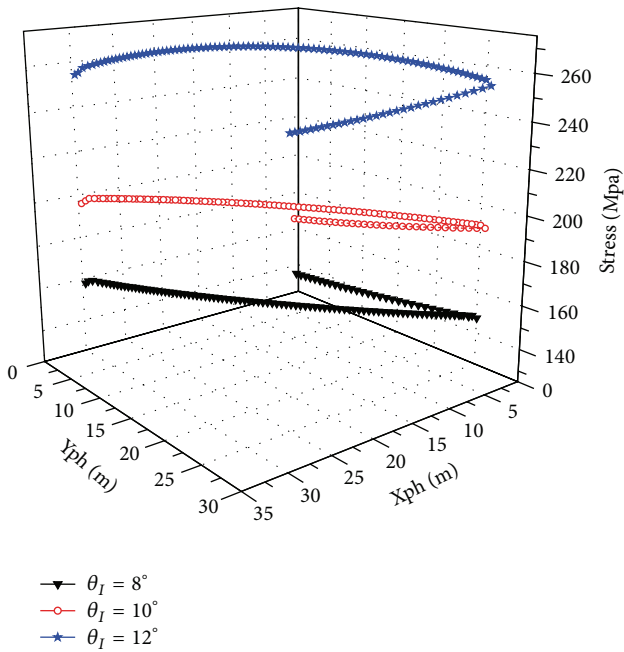


FIGURE 9: Maximum stresses in different  $\theta_I$ .

4.2. Influence of  $D_L$ . Under the condition that  $\theta_I$  is  $10^\circ$ ,  $D_V$  is 35 m,  $D$  is 1000 m, and  $D_L$  is 30 m, 33 m, and 36 m, respectively, the maximum stresses of SCR during installation are shown in Figure 10. The calculated results show that, with the rise of  $D_L$ , the maximum stresses on SCR increase accordingly. It is necessary to control  $D_L$  at its minimum value in order to avoid the interference of auxiliary installation equipment to keep SCR under safe condition.

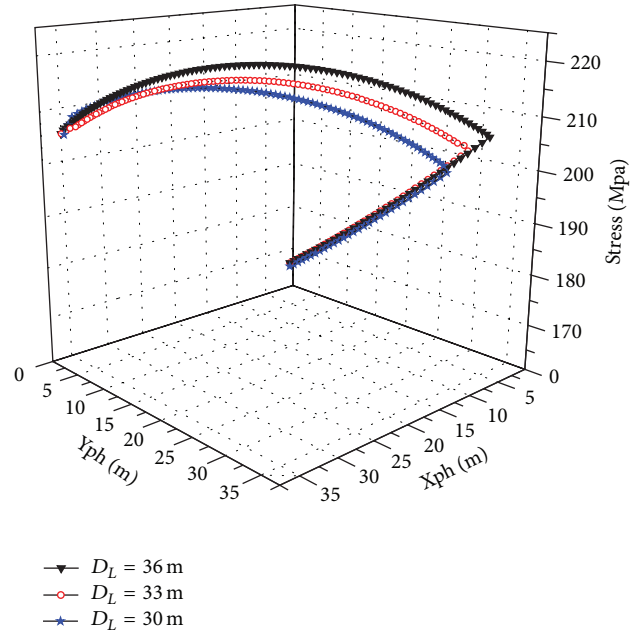


FIGURE 10: Maximum stresses in different  $D_L$ .

4.3. Influence of  $D$ . Under the condition that  $\theta_I$  is  $10^\circ$ ,  $D_V$  is 35 m,  $D_L$  is 35 m, and  $D$  is 1000 m, 1500 m, and 2000 m, respectively, the maximum stresses on SCR during installation are shown in Figure 11. The calculated results show that, with the decrease of  $D$ , the maximum stresses on SCR increase rapidly. It is necessary to pay more attention to the control of installation path in shallow water. This is because the SCR length increases as water depth increases, and the relative change in installation shape is greater in shallow water than in deep water.

4.4. Influence of  $D_V$ . Under the condition that  $\theta_I$  is  $10^\circ$ ,  $D$  is 1000 m,  $D_L$  is 35 m, and  $D_V$  is 30 m, 35 m, and 40 m, respectively, the maximum stresses on SCR during installation are shown in Figure 12. The calculated results show that, with the rise of  $D_V$ , the maximum stresses on SCR increase accordingly. It can be inferred that, for the safety of installation vessel and offshore platform, smaller values of  $D_V$  are preferred for SCR installation.

## 5. Conclusion

A simple model for analyzing the static behavior of the deep-water SCR during installation is proposed, while the non-linear large deformation beam theory is applied and HAM

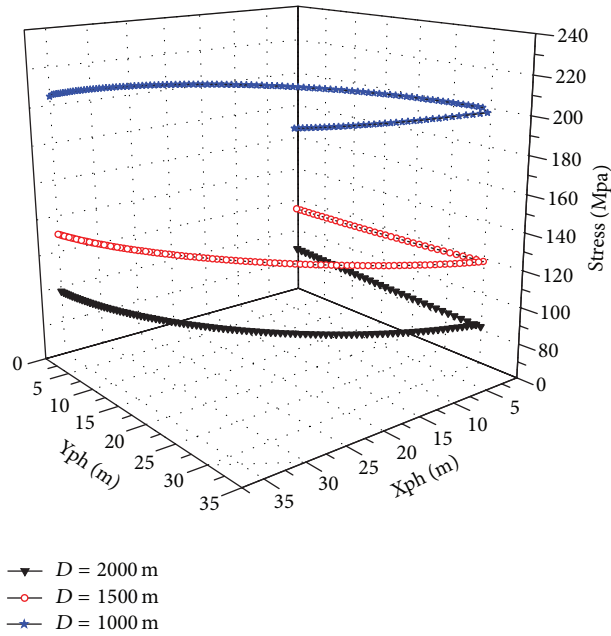


FIGURE 11: Maximum stresses in different  $D$ .

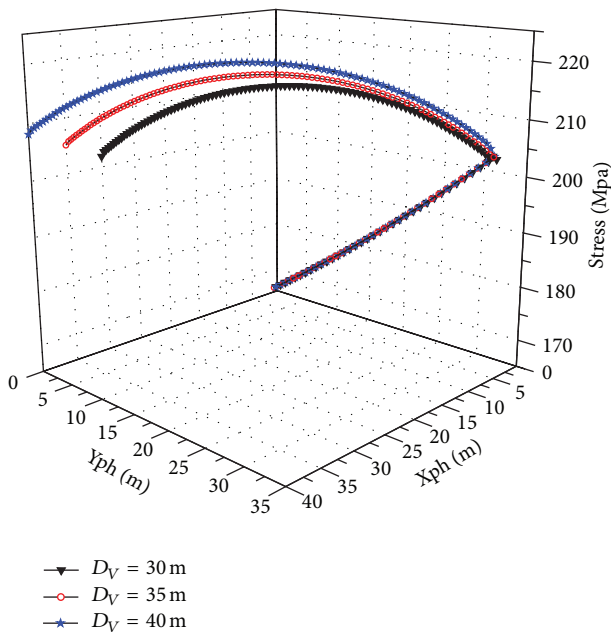


FIGURE 12: Maximum stresses in different  $D_v$ .

is used to obtain an analytical approximate solution for this model. This model has the main advantage of time-saving and its practicality. In comparison with the results calculated using the software OrcaFlex, a positive agreement is obtained, which demonstrates that the analytical approximate solution is reliable.

The presented model is applied to analyze the influence of different parameters. Some valuable conclusions can be drawn as follows.

- (1) Larger initial installation angle causes higher maximum stress during SCR installation, and the J-lay tower is preferred to be placed in an almost vertical position during SCR installation in order to reduce the initial installation angle.
- (2) The maximum stress during SCR installation increases with the lower depth of pull-head. The pull-head should be controlled at the minimum lower depth to keep the safety of SCR during installation.
- (3) As water becomes deeper, the maximum stress during SCR installation becomes smaller, which is beneficial to the safety of SCR. However, the increasing axial tension induced by its self-weight brings higher requirements on the capacity of the installation vessel.
- (4) A longer distance between the installation vessel and the offshore platform can cause a little increase in the maximum stress during SCR installation. To avoid the interference between the installation vessel and the offshore platform, a smaller distance between them is preferred for SCR installation.

This paper reports reasonable approach to the deepwater SCR installation analysis. However, as some assumptions are made for simplifying the investigation, further work needs to be carried out to integrate these assumptions, such as the effect of pipe-soil interaction.

### Conflict of Interests

The authors declare that there is no conflict of interests regarding the publication of this paper.

### Acknowledgments

This paper is financially supported by the National Natural Science Foundation of China (Grant no. 51349002), the China National Science and Technology Major Projects on Pipe Laying and Lifting Vessel (Grant no. 2011ZX05027-002), and the Higher Education Specialized Research Fund for the Doctoral Program (Grant no. 20130007120009). Sincerely, the authors' thanks also go to colleagues in the COOEC Ltd. and Offshore Oil/Gas Research Centre of CUP, who are involved in this wide range of researches. The authors also highly appreciate the reviewers and the editors' careful checking and valuable comments on this paper.

### References

- [1] F. Kopp and D. W. Barry, "Design and installation of auger pipelines," in *Proceedings of the 1994 Offshore Technology Conference*, Houston, Tex, USA, 1994.
- [2] G. Chaudhury, J. Kennefick, and J. R. McDermott, "Design, testing, and installation of steel catenary risers," in *Proceedings of the 31st Annual Offshore Technology Conference (OCT '99)*, Houston, Tex, USA, May 2000.
- [3] J. van der Graaf, D. Wolbers, and P. Boerkamp, "Field experience with the construction of large diameter steel catenary risers in deep water," in *Proceedings of the Offshore Technology Conference*, Houston, Tex, USA, May 2005.

- [4] X. Wang and X. Zhou, "Installation method evaluation of export SCRs," in *Proceedings of the 2001 Offshore Technology Conference*, Houston, Tex, USA, May 2001.
- [5] Y. Bai and Q. Bai, *Subsea Pipelines and Risers*, Elsevier, Amsterdam, The Netherlands, 2005.
- [6] Y. Nishi, "Static analysis of axially moving cables applied for mining nodules on the deep sea floor," *Applied Ocean Research*, vol. 34, pp. 45–51, 2012.
- [7] P. S. Charles, *Fundamentals of Marine Riser Mechanical: Basic Principles and Simplified Analyses*, PennWell, Tulsa, Okla, USA, 2007.
- [8] X. G. Zeng, M. L. Duan, and J. H. Chen, "Resarch on several mathematical models of offshore pipe lifting or lowering by one point," *The Ocean Engineering*, vol. 31, no. 1, pp. 32–37, 2013.
- [9] D. A. Dixon and D. R. Rultledge, "Stiffened catenary calculation in pipeline laying problem," *Journal of Engineering for Industry*, vol. 90, no. 1, pp. 153–160, 1968.
- [10] F. Guarracino and V. Mallardo, "A refined analytical analysis of submerged pipelines in seabed laying," *Applied Ocean Research*, vol. 21, no. 6, pp. 281–293, 1999.
- [11] Y. J. Dai, J. Z. Song, and G. Feng, "A study on abandonment and recovery operation of submarine pipelines," *Ocean Engineering*, vol. 18, no. 3, pp. 75–78, 2000 (Chinese).
- [12] Z. J. Xing, T. C. Liu, and X. H. Zeng, "Nonlinear analysis of submarine pipelines during single point lifting," *Ocean Engineering*, vol. 20, no. 3, pp. 29–33, 2002 (Chinese).
- [13] S. Lenci and M. Callegari, "Simple analytical models for the J-lay problem," *Acta Mechanica*, vol. 178, no. 1-2, pp. 23–39, 2005.
- [14] J. García-Palacios, A. Samartin, and V. Negro, "A nonlinear analysis of laying a floating pipeline on the seabed," *Engineering Structures*, vol. 31, no. 5, pp. 1120–1131, 2009.
- [15] T. K. Datta, "Abandonment and recovery solution of submarine pipelines," *Applied Ocean Research*, vol. 4, no. 4, pp. 247–252, 1982.
- [16] C. P. Sparks, *Fundamentals of Marine Riser Mechanics: Basic Principles and Simplified Analyses*, Penn Well Corporation, Tulsa, Okla, USA, 2007.
- [17] I. K. Chatjigeorgiou, "A finite differences formulation for the linear and nonlinear dynamics of 2D catenary risers," *Ocean Engineering*, vol. 35, no. 7, pp. 616–636, 2008.
- [18] H. Park and D. Jung, "A finite element method for dynamic analysis of long slender marine structures under combined parametric and forcing excitations," *Ocean Engineering*, vol. 29, no. 11, pp. 1313–1325, 2002.
- [19] A. H. Nayfeh, *Perturbation Methods*, Cambridge University Press, London, UK, 1973.
- [20] J. S. Liao, *The proposed homotopy analysis technique for the solution of nonlinear problems [Ph.D. thesis]*, Shanghai Jiao Tong University, 1992.

## Research Article

# A Scheduling Problem in the Baking Industry

Felipe Augusto Moreira da Silva,<sup>1</sup> Antonio Carlos Moretti,<sup>2</sup> and Anibal Tavares de Azevedo<sup>2</sup>

<sup>1</sup> Department of Applied Mathematics, Institute of Mathematics, Statistics and Scientific Computing,  
State University of Campinas, Campinas, SP, Brazil

<sup>2</sup> School of Applied Sciences, State University of Campinas, Limeira, SP, Brazil

Correspondence should be addressed to Felipe Augusto Moreira da Silva; [felipe\\_amsilva@yahoo.com.br](mailto:felipe_amsilva@yahoo.com.br)

Received 5 December 2013; Revised 29 April 2014; Accepted 29 April 2014; Published 19 June 2014

Academic Editor: Nachamada Blamah

Copyright © 2014 Felipe Augusto Moreira da Silva et al. This is an open access article distributed under the Creative Commons Attribution License, which permits unrestricted use, distribution, and reproduction in any medium, provided the original work is properly cited.

This paper addresses a scheduling problem in an actual industrial environment of a baking industry where production rates have been growing every year and the need for optimized planning becomes increasingly important in order to address all the features presented by the problem. This problem contains relevant aspects of production, such as parallel production, setup time, batch production, and delivery date. We will also consider several aspects pertaining to transportation, such as the transportation capacity with different vehicles and sales production with several customers. This approach studies an atypical problem compared to those that have already been studied in literature. In order to solve the problem, we suggest two approaches: using the greedy heuristic and the genetic algorithm, which will be compared to small problems with the optimal solution solved as an integer linear programming problem, and we will present results for a real example compared with its upper bounds. The work provides us with a new mathematical formulation of scheduling problem that is not based on traveling salesman problem. It considers delivery date and the profit maximization and not the makespan minimization. And it also provides an analysis of the algorithms runtime.

## 1. Introduction

Production planning problems have been studied extensively since the early twentieth century, and they can be found throughout literature. One of the pioneers in the work on these problems was Henry Gantt in his book “Work, Wages and Profit” [1] in which he demonstrates the need for a job schedule in order to increase production efficiency.

Currently many industries are seeking solutions for the job sequencing problem in order to increase productivity, reduce costs and, consequently, increase profit. Due to the burgeoning consumption of foodstuffs worldwide, optimized planning is necessary. For decades in the industry, planning rules were used in order to prioritize products by taking into account only a few production stages, but, given the increase of complexity and modernization of production, planning as a whole has to be optimized; that is, the entire production chain, from production and stock to shipping and sales, must be taken into account.

The purpose of this paper is to study planning problems applied to baking industry, where, in the current scenario, companies have high product turnover; that is, the goods are highly perishable and companies cannot meet all the demands for their products made by customers; and these decisions are highly correlated to production planning and transportation.

The difficulty of the problem in question is to define a production sequence in each line considering setup and production times, together with jobs that have set dates to be executed, in such a way as to maximize company profit. Thus, the problem has particular production characteristics, such as batch production and a scenario with several parallel production lines. Another relevant point to be considered in this study is that the solution should be found in a timely computational manner for planning purposes, as it is to be executed for the next 24 hours and cannot run for longer than minutes, allowing the implementation of planning in hours following the decision.

There are many variations of scheduling problems, many of them widely studied in literature, but the problem studied here is not found in literature with all of the features proposed herein; we can only find methods to solve part of the problem.

Because of the diversity of production planning problems, the problems can be divided into classes. The ratings found for the more general problem of sequencing are flow-shop and job-shop. For flow-shop each process is identified in one job and job-shop is the problem where the order of each process may not be the same in one job. This problem presented here is a flow-shop problem.

In studies of flow-shop problems, the first theoretical results were presented to minimize the makespan, that is, total production time, with Johnson [2] and Bellman [3] determining the optimal sequence for the cases with two machines and special cases with three machines. More general cases for sequencing with three machines came from Lomnicki [4] and Ignall, and Schrage [5] by applying branch and bound methods introduced by Little [6]. For the problem of flow-shop with more than two machines Garey et al. [7] proved that it is NP-hard; thus we can only solve small problems accurately with algorithms such as branch-bound. Therefore, heuristic methods are proposed for the problem.

In order to study the flow-shop problem with a family setup, Sridhar and Rajendran [8] propose a heuristic to minimize the total time with an algorithm based on simulated annealing. Ziegler [9] proposes a method to minimize the total time weighted by weights in the process. Schaller [10] presents a new approach to the problem of flow-shop setup with families to minimize the makespan. Schaller [11] proposes a new lower bound for the problem and implements a two-stage heuristic algorithm based on branch and bound.

França et al. [12] works on the same problem, but with the Schaller genetic algorithm with local search, "memetic algorithms" (MA), and [13] achieves superior results by using hybrid methods with tabu search and the genetic algorithm.

The problems with delivery dates were studied by Croce et al. [14], who showed a genetic algorithm in which each chromosome consists of  $m$  subchromosomes, one for each machine, which identifies each transaction made by the machine. According to the authors, the results were better than those found by Adams et al. [15], but at greater computational cost. Sittisathanchai and Dagli [16] also present a genetic algorithm where the chromosome represents the operational sequence.

Flexible scheduling involves problems where we have the option of executing operations on different machines. This kind of problem is more comprehensive than the problem of traditional scheduling and production in parallel, which ensures that a transaction is made only by a single machine. Arthanari and Ramaswamy [17] were pioneers with exact two-stage methods, using two identical parallel machines in the first stage and one machine in the second stage. Later, Brah and Hunsucker [18] worked on the development of more general branch and bound algorithms, but for problems with more than 8 jobs, 5 stages and 2 or 3 machines, processing time becomes impractical.

For multistage jobs, Sawik [19] proposed a constructive heuristic in which the route of a job is determined at

each iteration. Kittichartphayak and Ding [20] developed a heuristic similar to Sawik [19], but for larger orders of tasks and stages, which was extended by Guinet and Solomon [21]. Smutnicki and Nowicki [22] propose the use of tabu search in the work with satisfactory results.

The studied problem is a flow-shop problem with parallel production, setup times, batch production, due date, and transportation capacity, which in large scale justify the use of metaheuristic to solve it.

## 2. Materials and Methods

*2.1. Mathematical Modeling.* The scheduling problem can be modeled as a mixed integer linear programming problem.

The problem requires a short-term study in great detail; that is, the study will be forecast to take place over two to seven days from the current day. Given the high level of time detail, it is necessary to deal with accuracies in minutes, as the setup time and production time may occur within minutes. Therefore, a discretization of time can result in inaccuracies because a large number of periods can cause a problem with a large number of variables, thus making it unenforceable, and a small number of time periods may not address the problem with the required accuracy.

Traditional approaches of the scheduling problem are based on the traveling salesman problem, where a variable represents the precedence order of task. But in this case it is necessary to know what time each product will be ready for shipment. Accordingly, a new model is proposed to represent the job sequencing where each variable represents which jobs are executed in each time period (Figure 1).

This problem is defined in a set of period  $E$ , where  $E = \{0, \dots, e_{\max}\}$  and  $e_{\max}$  is the last period. Production is defined in two stages: in the first one, a preproduct known as mass is produced, and, in the second stage, a mass is transformed into a final product. The set of mass will be represented by  $M$  and the set of products determined by the set  $P$ . Each product  $p \in P$  will be produced by a single mass that can produce more than one product defined by  $\text{Prod}(m) \subset P$ . Each mass has its production cost defined by  $\text{cost}_1(m)$ , which defines the cost of producing each product. The production time of each mass is represented by  $t(m)$ , and the setup time to prepare the mass of two products 1 and 2 is  $s(m_1, m_2)$ .

Production occurs through two processes. The first process works in a mixer, which mixes all the ingredients of a mass, and the cost of ingredients will determine the profits from the products made with this mass. After the mixer, there is a second process, where the mass will be roasted, sliced, and packaged. In this second case the mass will be transformed into the final product. Products can be grouped into classes due to of the production characteristics, such as cooking time, types of cuts, and packaging. Therefore, within a production line different products with those that have the same production characteristics can be produced.

The production lines will be represented according to the set  $L$ , and mass produced on each line will be determined by set  $\text{Lin}$  where for each  $l$  we have  $\text{Lin}(l) \subset M$ , where

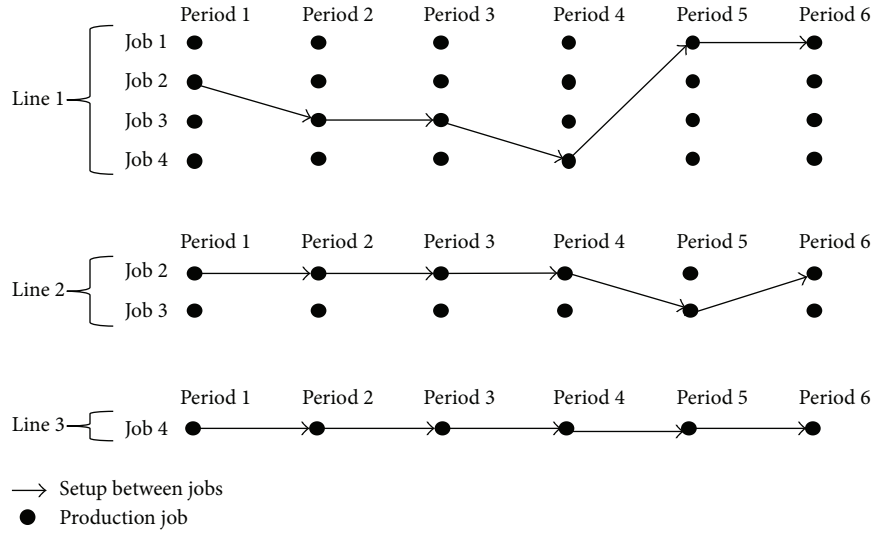


FIGURE 1: Job sequencing representation.

an input can be present in more than one production line. We emphasize that the production of masses will occur in production batches, and each mass has a certain number of units produced per batch represented by  $\text{batch}(m)$ .

One of the objectives of the problem is to fulfill the demand. Demand is divided by markets such that each market requests a daily mix of products. These requests can be fully addressed, or partially addressed, or not addressed at all. If the market is not attained there is no penalty, only the profit made by that market will not be obtained.

The amount of products to be manufactured is a function of demand for each market. The customers will be represented by the set  $C$ , the demand in each customer for a product in a period will be  $d(c, p, e)$ , and the profit for each sale will be  $\text{profit}(p, c)$ .

In order to transport products to markets, there are options of trucks with different capacities that can be used; all types of trucks will be represented by  $T$ , with the cost of each truck given by  $\text{cost}_2(c, t)$  and capacity by  $\text{cap}(t)$ . The service to the customer should take place at a specific time because the trucks have schedules for loading in factories and unloading at customers' premises; accordingly, the demands of each market should be seen at a predefined period.

A summary of model features and variables is given in Figure 2.

To describe the model, consider the following model parameters.

### 2.1.1. Sets

- $E$ : set of periods.
- $M$ : set of mass.
- $P$ : set of products.
- $\text{Prod}(m)$ : set of products produced by mass  $m$ .
- $L$ : set of production line.
- $\text{Lin}(l)$ : set of mass produced in production line  $l$ .

$C$ : set of customer.

$T$ : set of trucks.

### 2.1.2. Data

$\text{cost}_1(m)$ : production cost of mass  $m$ .

$t(m)$ : production time of mass  $m$ .

$s(m_1, m_2)$ : setup time from mass  $m_1$  to mass  $m_2$ .

$\text{batch}(m)$ : production batch of mass  $m$ .

$d(c, p, e)$ : demand of customer  $c$ , product  $p$  in period  $e$ .

$\text{profit}(c, p)$ : sales profit of product  $p$  in customer  $c$ .

$\text{cost}_2(c, t)$ : transportation cost by truck  $t$  to customer  $c$ .

$\text{cap}(t)$ : transportation capacity of truck  $t$ .

Define the following set of variables.

### 2.1.3. Variables

$z(l, m, e) = \{1, \text{if mass } m \text{ is produced by production line } l \text{ in period } e; 0, \text{ otherwise}\}.$

$y(c, t, e)$ : integer amount of truck  $t$  sender off to customer  $c$  in period  $e$ .

$\text{stk}(p, e)$ : stock quantity of product  $p$  in period  $e$ .

$x(l, p, e)$ : quantity of product  $p$  produced in production line  $l$  and period  $e$ .

$v(c, p, e)$ : quantity of product  $p$  sold at customer  $c$  and period  $e$ .

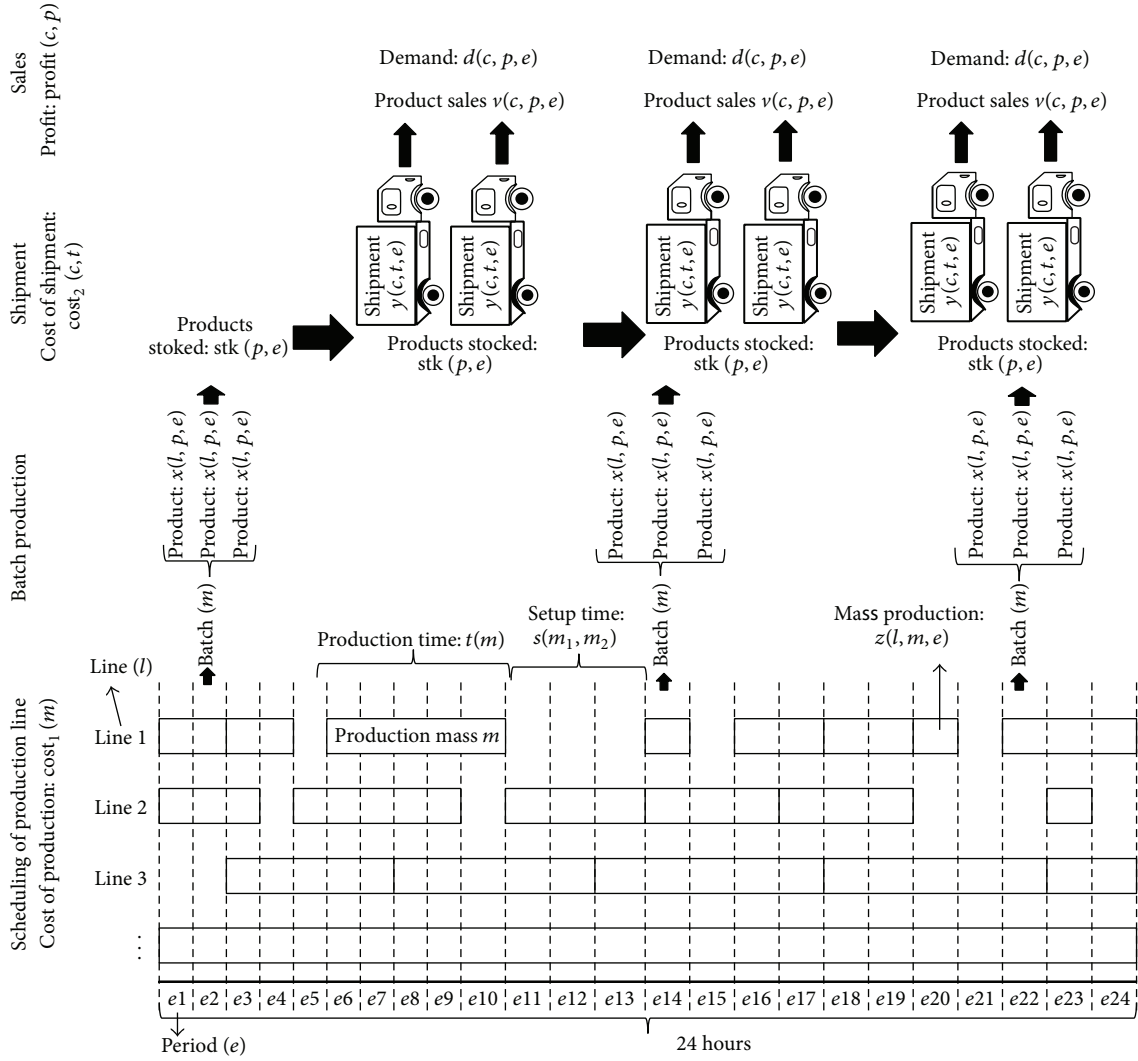


FIGURE 2: Map of production, shipment, and sales.

### 2.1.4. Constraints

- (1) Unique constraint on the use of the line at each period: in each line, only one product can be produced per period because it is not possible for a machine to run two products simultaneously

$$\forall e, l \quad \sum_{m \in M} z(l, m, e) \leq 1, \quad (1)$$

where  $z(l, m, e)$  is a binary variable that represents the production of mass  $m$  in period  $e$  and line  $l$ .

- (2) Constraints of stock training: at each period, the stock is formed by the stock from the previous period plus the sum of what was produced, minus the sale for a given product

$$\begin{aligned} \forall e, p \quad \text{stk}(p, e) &= \text{stk}(p, e-1) \\ &+ \sum_{l \in L} x(l, p, e-t(m)) - \sum_{c \in C} v(c, p, e), \end{aligned} \quad (2)$$

where  $\text{stk}(p, e)$  is the stock of product  $p$  in the period  $e$ ,  $t(m)$  is time of production for mass  $m$  that produces  $p$ ,  $x(l, p, e)$  is the amount of production of product  $p$  in the period  $e$  and line  $l$ , and  $v(c, p, e)$  is the sales of product  $p$  in the customer  $c$  and the period  $e$ .

- (3) Demand constraints: at each customer, the sale of a product cannot exceed the requested demand

$$\forall c, p, e \quad v(c, p, e) \leq d(c, p, e). \quad (3)$$

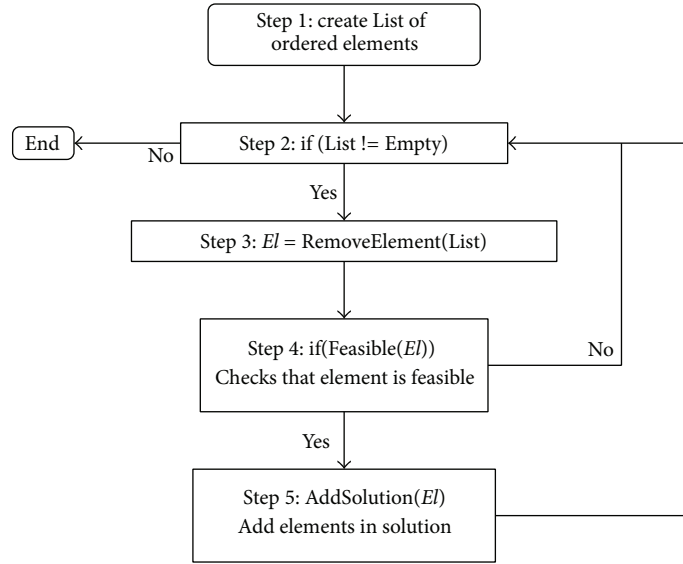


FIGURE 3: Representation of the greedy heuristic.

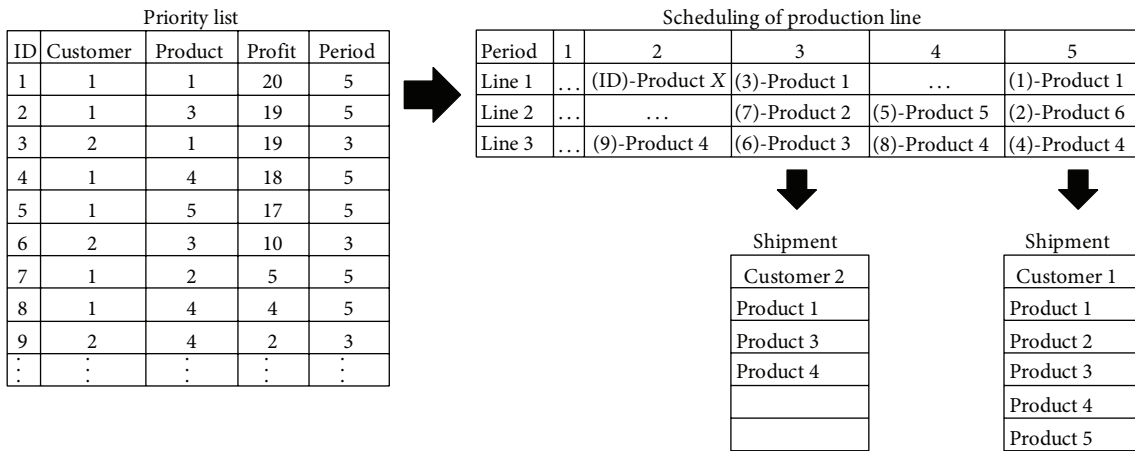


FIGURE 4: Matrix representation of solution to the greedy heuristic.

(4) Constraints of setup time (cleaning and change of mass in the production line): at each exchange of mass the machine should be stopped by a number of periods defined by  $s(m, m_1)$ . Therefore, if the machine is used for a mass  $m$ , the other mass  $m_1$  cannot use the machine for the next  $s(m, m_1)$  periods

$$\forall e, l, m \quad P * (1 - z(l, m, e)) \geq \sum_{m_1 \in \text{Lin}(l)} \sum_{i=1}^{s(m, m_1)} z(l, m_1, e + i), \quad (4)$$

where  $P$  is a large enough number compared to the variables and problem constants.

(5) Production batch constraints: each mass production creates several units of products; then if a mass is

produced, the amount of batch( $m$ ) units of products is produced

$$\forall l, m, e \quad \sum_{i \in \text{Prod}(m)} x(l, i, e) = \text{batch}(m) * z(l, m, e). \quad (5)$$

(6) Constraints of transport capacity: there is a limit to the amount of goods that each truck can transport; therefore, if a truck is used, a maximum of  $\text{cap}(t)$  units of products will be sent by truck  $t$ , where the truck is filled with baskets of the equal dimensions

$$\forall c, e \quad \sum_{p \in P} v(c, p, e) \leq \sum_{t \in T} \text{cap}(t) * y(c, t, e), \quad (6)$$

where  $y(c, t, e)$  is the amount of trucks used for customer  $c$  over period  $e$  and type of trucks  $t$ .

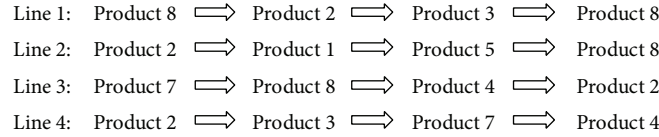


FIGURE 5: Production scheduling.

8	2	3	8
2	1	5	8
7	9	4	2
2	3	7	4

FIGURE 6: Matrix representation of solution to the genetic algorithm.

2.1.5. *Objective Function.* The objective of the problem is to maximize profit, that is, maximize the difference between the sale price of each product in each market and production costs of each product combined with transportation costs. The problem presented is characterized as a mixed integer linear programming problem

$$\begin{aligned}
 f(v, y) = & \sum_{c \in C} \sum_{p \in P} \sum_{e \in E} \text{profit}(c, p) * v(c, p, e) \\
 & - \sum_{c \in C} \sum_{t \in T} \sum_{e \in E} \text{cost}_2(c, t) * y(c, t, e) \\
 & - \sum_{l \in L} \sum_{m \in M} \sum_{e \in E} \text{cost}_1(m) * z(l, m, e).
 \end{aligned}
 \tag{7}$$

The mixed integer linear programming problem consists of

$$\begin{aligned}
 \text{Max} \quad & f(v, y) \\
 \text{s.t.} \quad & (1), (2), (3), (4), (5), (6) \\
 & \text{where } x, v, \text{stk} \in R_+, \\
 & z, y \in Z_+.
 \end{aligned}
 \tag{8}$$

2.2. *Solution Methods and Implementation Details.* Several methods are proposed to solve the problem. This problem can be solved by an exact method for solving integer linear programming problems, such as branch-bound. The solution will be presented through the Xpress solver using the interior point method and branch-bound in the default solver configuration. Other solution methods presented will be a method based on a greedy heuristic (Figure 4) and also metaheuristics of the genetic algorithm type to solve the problem.

2.2.1. *Greedy Heuristic.* The greedy algorithm can be found in Introduction to Algorithms by Cormen et al. [23] or Bendall

and Margot [24]. In the context of scheduling delivery date problems, the problem is solved exactly for one machine in ([25], page 207).

The greedy heuristic can be divided into two phases:

- (1) start-up and creation of the priority list ordered,
- (2) production sequencing.

A list of priorities should be created to be used in the algorithm; accordingly, the following criteria will be used:

$$\begin{aligned}
 \text{Priority}(c, p) &= ((\text{Sales Price}(c, p) - \text{Production Cost}(m) \\
 &\quad - \text{Average Cost of Shipping}(p))) \\
 &\quad \times ((\text{Production Time}(m) - \text{Average Setup}(m)))^{-1},
 \end{aligned}
 \tag{9}$$

where each product is  $p$ ,  $m$  is mass that produces the product  $p$ ,  $c$  is a customer, and

$$\begin{aligned}
 \text{Average Cost of Shipping}(p) &= \frac{\sum_{c \in C | d(c, e, p) \neq 0} \sum_{t \in T} \text{cost}_2(c, t)}{\sum_{t \in T} \text{cap}(t)}, \\
 \text{Average Setup}(m) &= \frac{\sum_{m_1 \in M | s(m, m_1) \neq 0} s(m, m_1)}{|\{m_1 \in M | s(m, m_1) \neq 0\}|}.
 \end{aligned}
 \tag{10}$$

For each product in each market we can prioritize the one with the biggest impact in the objective function and it will have the highest execution priority.

In the production sequencing for each element of the list *Priority*, we checked whether it would be possible to run it on a production line so that the solution does not become infeasible; that is, for each element determined by a product, market, and delivery time, we have to run it before the delivery time. Thus, if space is available (idle line space before the delivery time longer than production and setup time of the product in question) in a line that produces this element, this product will run within this space. If space is not available, the element is discarded. We note that the task should be executed as late as possible, in order to ensure that products with earlier delivery times and lower priorities can occupy earlier positions in the sequence.

At the production adjustment stage, the algorithm will only place idle time between the execution of two tasks at the end of the stage, because idle time between two tasks is

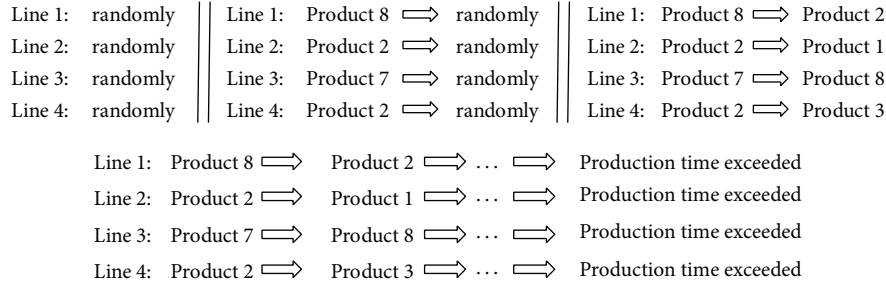


FIGURE 7: Creation of initial population to genetic algorithm.

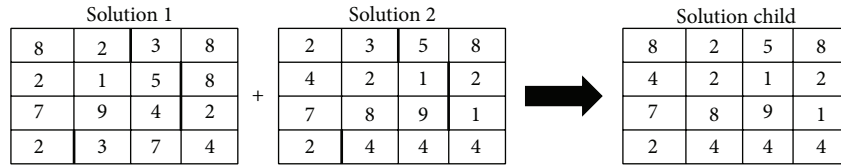


FIGURE 8: Crossover to genetic algorithm.

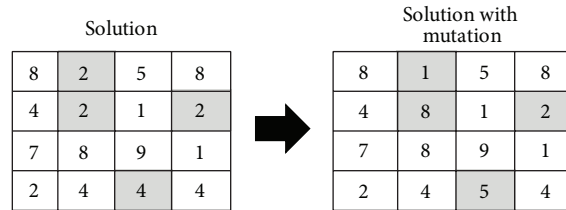


FIGURE 9: Mutation to genetic algorithm.

impractical; therefore it can be adjusted without any loss in objective function.

We can represent the heuristic by means of Figure 3.

$El$  is one element of *priority* list that represents a sale of product  $p$  in customer  $c$ .

**2.2.2. Genetic Algorithm.** The application of methods for using genetic algorithm in scheduling problems can be found at Allahverdi et al. [26], which shows several authors working with genetic algorithms in different scheduling problems.

The genetic algorithm is based on building an initial population where each individual represents a possible solution, and, through this population, building new populations through an evolutionary process to find better solutions.

We can divide the algorithm into a few steps: initial population, crossover, mutation, and selection.

To represent an element of the population on the genetic algorithm will be used one matrix; this representation is unusual to the genetic algorithm in implementations already known. Each row represents a production line and each column a product that has been produced. This matrix has dimension  $\mathbb{Z}^{n \times m}$ , with  $n$  being quantity of lines and  $m$  maximum quantity of products produced.

For each production line we will have a set of genes where each gene represents the product to be produced. Therefore, the solution is represented by a set of schedules of lines, which

are sets of chromosomes, where each chromosome is a set of genes as shown in Figure 5, which represents in each line what will be produced by the genetic algorithm represented in Figure 6.

(1) *Creation of Initial Population.* The initial population is created randomly by respecting the feasibility of the solution. For each element of the population vectors are created, and each vector represents a production line and each matrix element represents the product that will be produced according to Figure 7, in order that the sum of production time and setup of a line does not exceed the maximum time that the line can operate. Thus, we can create all the elements of the population.

(2) *Crossover.* The crossover phase will start the process of building the next population. At this stage, two elements are chosen at a time, and these two elements exchange components from their solutions with each other. This exchange of components is known as crossover; it is executed by choosing two random points of each parent chromosome, and these components are inherited to the new solution that will be created. After a certain number of children are formed, the crossover phase is over (Figure 8).

(3) *Mutation.* In this phase, each child element created in the crossover phase is mutated, in numbers determined by

```

begin
  /* Upper Bound/;
  at = 0;
  v = 0;
  foreach p ∈ P do
    foreach i ∈ {n, ..., 1} | ei ∈ E do
      Qtprov(p, ej) = Qt(p, ej);
      foreach j ∈ Dp,i do
        v(p, cj) = min(d(p, cj) - at(p, c)j, Qtprov(p, ej));
        Qtprov(p, ej) = Qtprov(p, ej) - v(p, cj);
        L = L + v(p, cj) * l(p, cj);
        at(p, cj) = at(p, cj) + v(p, cj);
      end
    end
  end
end

```

ALGORITHM 1: Upper bound to genetic algorithm.

the mutation rate of their genes. This is done by randomly choosing a gene and replacing it with another element so that the solution remains feasible. This new element is also chosen randomly (Figure 9).

(4) *Selection*. Selection can be executed in various manners. Here, this will be done in two different ways: tournament and selection of the best individual. After creating the child elements of the population in the previous steps, a new population will be formed to run a new iteration. With the option of choice of both parent and child components for the next generation, the tournament will randomly select a predetermined number of elements and among them the ones with the best objective function; this process is repeated until a new generation is built. Through the method of selecting the best individual, the best individuals comprise the new population.

Algorithm 1 is proposed to calculate the upper bound of the elements of genetic algorithm. In this algorithm we introduce  $L$  as the desired upper bound;  $Qt(p, e_j)$  is the amount of product  $p$  produced between the steps  $e_{j-1}$  and  $e_j$ ,  $at(p, c_j)$  is the amount of the product  $p$  met in customer  $c_j$ , and  $D_{(p,i)}$  is the vector of customer indices, sorted by the profit of product  $p$  from the period  $e_i$  to period  $e_n$ .

We can represent the metaheuristics with Figure 10.

2.2.3. *Efficiency*. To evaluate the efficiency of greedy and genetic algorithm, a new ILP model is presented. It is necessary because greedy algorithm is calculated through priority list defined in (9) and genetic algorithm through of upper bound calculation defined in Algorithm 1. This model is easy to resolve due to little quantity of integer variables. To all tests the runtime was less than 10 seconds.

For the model to follow, each method will supply a resulting scheduling to the model that evaluates the efficiency, which will obtain the value of a function of an ILP problem as efficiency of the method.

The index  $P$ ,  $E$ ,  $C$ , and  $T$  and the parameters  $d(c, p)$ ,  $l(p, c)$ ,  $cost_2(c, t)$ , and  $cap(t)$  were defined in Section 2 and given  $Qt(p, e)$  as the amount of product  $p$  available for shipment during period  $e$  calculated by scheduling informed as a parameter. And we obtain the real variable  $v(c, p)$  being the amount of product  $p$  sold at the customer  $c$  and the integer variables  $env(c, t, p, e)$  are the quantity of product  $p$  shipped to customer  $c$  by truck  $t$  over period  $e$  and  $z(c, t, e)$  is the truck release  $t$  to customer  $t$  in the period  $e$ .

#### Constraints

- (1) Demand: inequality defined in (3).
- (2) Total sales of each product to the market

$$\forall p, c \quad v(c, p) = \sum_{t \in T} \sum_{e \in E} env(c, t, p, e). \quad (11)$$

- (3) Shipment of products according to the period

$$\forall p, e \quad \sum_{(e' \in E | e' \leq e)} \sum_{t \in T} \sum_{c \in C} env(c, t, p, e') \leq Qt(p, e). \quad (12)$$

- (4) Truck capacity

$$\forall c, t, e \quad \sum_{p \in P} env(c, t, p, e) \leq Cap(t) * z(c, t, e). \quad (13)$$

The objective function is defined by (7).

Thus, we have the integer linear programming problem that will give us the result of each method for the presented problem

$$\begin{aligned}
 & \text{Max} \quad (7) \\
 & \text{s.t.} \quad (3), (11), (12), (13) \\
 & \quad \text{where } v \in R_+, \\
 & \quad \text{env}, z \in Z_+.
 \end{aligned} \quad (14)$$

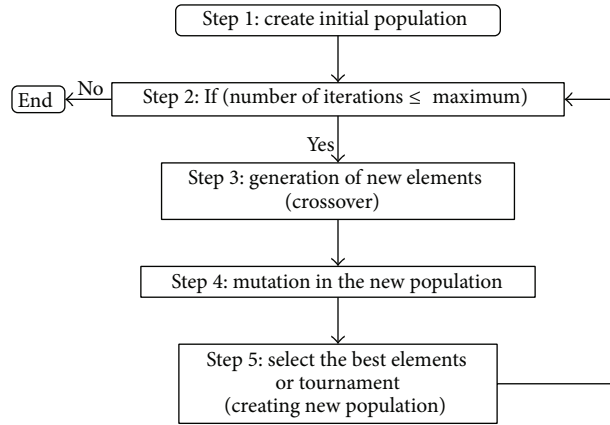


FIGURE 10: Representation of the genetic algorithm.

### 3. Results and Discussion

The following are the results of a presentation by a real example of baking industry and the analysis of the complexity of each method. The tests were carried out on a computer equipped with Intel Core i7, 2.93 GHz, 6 GB of memory, and the 64-bit Windows 7 operating system. The resolution of integer linear programming models was calculated by the solver XPress 7.1. The greedy heuristic and genetic algorithm methods were implemented in C-language.

**3.1. Algorithm Performance.** In order to analyze the performance of the greedy heuristic, we will calculate the processing time of the algorithm due to the growth of its dimensions. First we will examine the additional time as a function of the growing number of products and markets. Accordingly, we fix the number of production lines at 40 and the number of vehicles at 5.

*Greedy Heuristic.* The analysis will be executed with randomly generated data, calculating the average run time of the greedy heuristic as shown in Figure 11.

The plotted points suggest the adjustment of a linear curve, where we can calculate the parameters of the curve by the method of least squares and get the value of  $R^2 = 0.9966$ , where  $R^2 = \sum (\text{error}_i)^2 / (n - 1)$  and error is the difference between the value of the curve and points and  $n$  the total points used, which shows a linear correlation between the data; therefore the complexity depending on the products and markets is approximately (no. product) \* (no. markets) that is,  $O(p * c)$ .

Now if we fix the number of products and markets we can analyze the variation in the runtime depending on the number of lines and production options for each product. We will set this for 80 products, 20 destinations, and 5 vehicles.

Figure 12 presents the result of complexity in terms of lines and options for each product line.

We can see by Figure 12 that the curve is a 2-degree polynomial and, by applying least squares, we get  $R^2 = 0.9746$

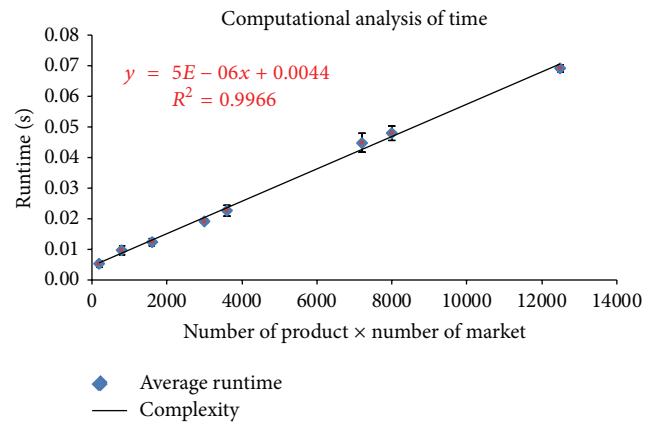


FIGURE 11: Complexity analysis of the greedy heuristic to quantity of product × market.

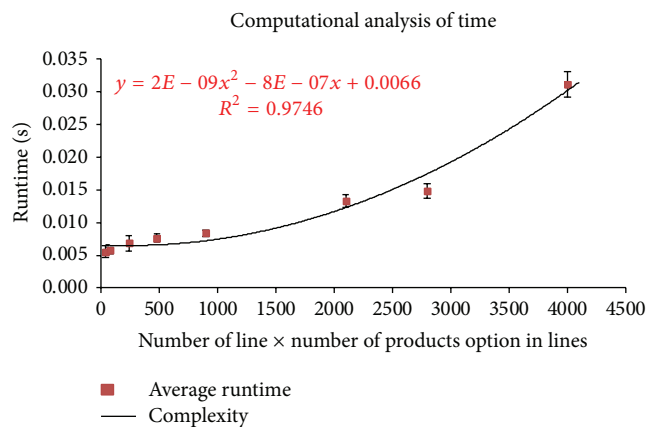


FIGURE 12: Complexity analysis of the greedy heuristic to number of lines × products option in lines.

showing a correlation between the variables, and it can be said that complexity in terms of production lines is  $O(l^2)$ .

*Genetic Algorithm.* We can repeat the analysis for the genetic algorithm.

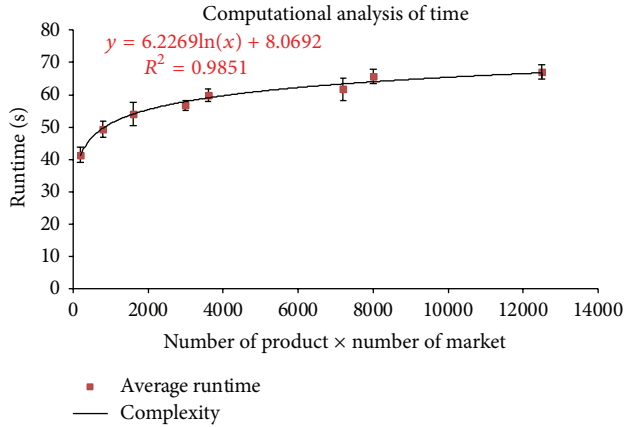


FIGURE 13: Complexity analysis of the genetic algorithm to quantity product  $\times$  market.

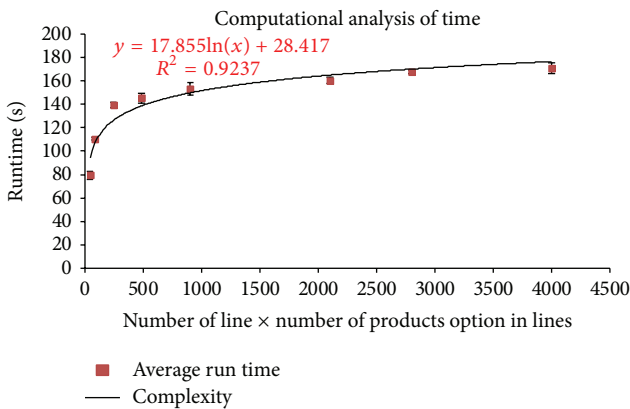


FIGURE 14: Complexity analysis of the genetic algorithm to number of lines  $\times$  products option in lines.

The set of points (product  $\times$  destination, time) in Figure 13 suggests a logarithmic function as a setting curve. By finding the parameters by the method of least squares, we obtain the function shown in Figure 13 and we find  $R^2$  with the value of 0.9851; then we can say that the complexity of the algorithm regarding products and destinations is  $O(\log(p * m))$ .

The set of points (line option  $\times$  product-line, time) in Figure 14 suggests a setting curve logarithmic function. After finding the parameters by least squares we can say that the complexity is  $O(\log(l))$ .

**3.2. Convergence of Genetic Algorithm.** The parameters used to genetic algorithm are in Table 1, and the best settings towards accuracy (approximation of optimal solution) and runtime were AG6, AG16, and AG17, which presented the convergence in 15.

Several parameters were used for genetic algorithm as shown in Table 1; the choice of the best parameters was done by results of run time and accuracy. The genetic algorithm proved little sensitiveness in relation to the variation of

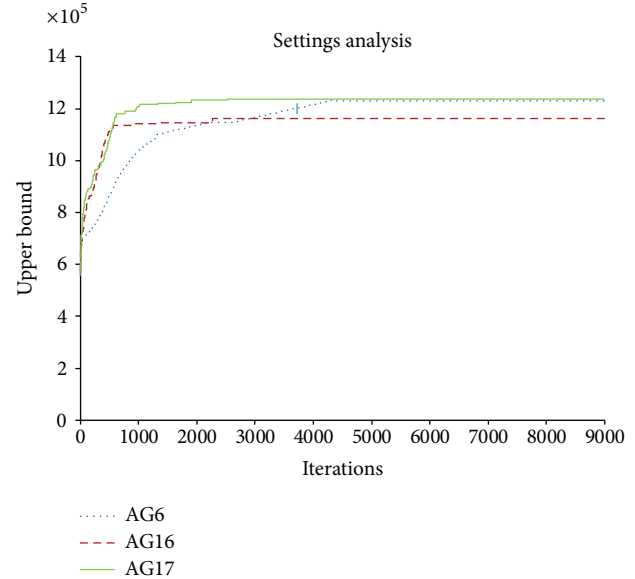


FIGURE 15: Convergence of genetic algorithm to the best parameters.

mutation rate, but high sensitiveness in relation to the selection mode and population size.

Regarding selection mode, the best selection mode found quicker and better solutions if compared to the tournament mode. The convergence of best selection is quicker than the tournament one because it prioritizes the best solutions to continue the methods while tournament tries to select the best participants in a random subset of a given population. This is done in an attempt to find better solutions in other feasible regions.

Therefore, we conclude that the best solutions can be found around a best solution elected by the mode; this is noticed when greedy heuristic and genetic algorithm (when using best select mode with high mutation rate (0.10) and large population size (100 elements)) get good solutions; that is, genetic algorithm gets the best solutions in finding good points and exploring this region around the elected location, and this is why we use the AG17 set.

Analyzing the set of parameters that use the best selection mode, in Figure 15 we can observe the convergence of the sets. AG17 presented the greatest benefit in general: runtime, accuracy, and convergence, while AG16 set had a faster convergence but it converged to a worse solution than AG17 and AG6. The AG6 set got the solution next to AG17, but its convergence was slower if compared to AG17 because it did not explore other feasible regions due to its small population size, taking a bigger runtime.

**3.3. Result of Solutions.** In Table 3 the efficiency of algorithms that represent the quality of solutions obtained and the instances tested in Table 2 is presented. The data from the tests executed can be found in [27].

In comparing greedy heuristic with genetic algorithm results the first one had a quicker runtime but a worse accuracy. The runtime difference can be explained due to

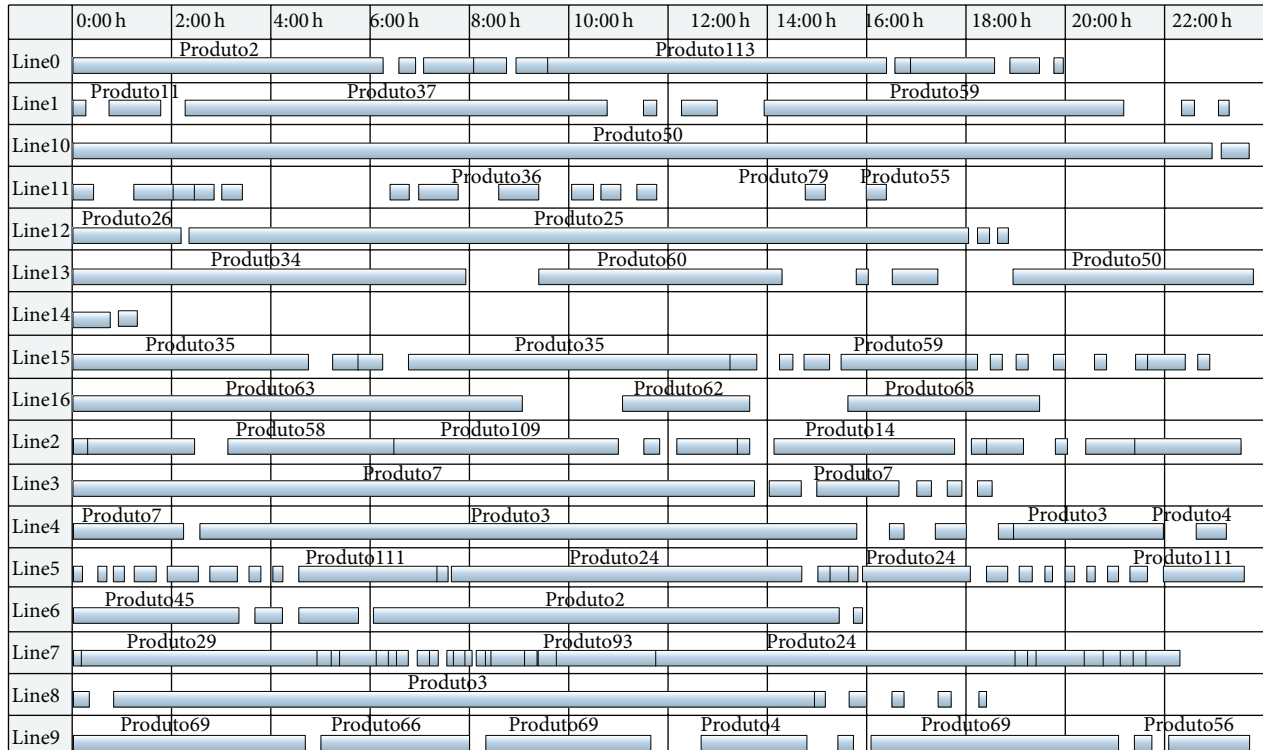


FIGURE 16: Best production planning (genetic algorithm), Gantt Chart.

TABLE 1: Genetic algorithm—settings.

Settings	Mutation	Select	Population size
AG1	0.01	Tournament	25
AG2	0.05	Tournament	25
AG3	0.10	Tournament	25
AG4	0.01	Best select	25
AG5	0.05	Best select	25
AG6	0.10	Best select	25
AG7	0.01	Tournament	50
AG8	0.05	Tournament	50
AG9	0.10	Tournament	50
AG10	0.01	Best select	50
AG11	0.05	Best select	50
AG12	0.10	Best select	50
AG13	0.01	Tournament	100
AG14	0.05	Tournament	100
AG15	0.10	Tournament	100
AG16	0.01	Best select	100
AG17	0.05	Best select	100
AG18	0.10	Best select	100

TABLE 2: Instances to evaluate efficiency.

Problem	Product	Market	Line	Trucks
AE1	11	11	1	5
AE2	25	10	5	5
AE3	50	10	10	5
AE4	60	13	10	5
AE5	70	14	10	5
AE6	80	16	17	5
AE7	90	18	17	5
AE8	115	21	17	5

greedy heuristic which executed less and simpler iterations than genetic algorithm. In the other hand it explores a smaller space to find good solutions.

Genetic algorithm got better accuracy than greedy heuristic which can be seen in Table 3, which is expected because metaheuristics does a search for best solution in a bigger

region inside feasible region than greedy heuristic. Although genetic algorithm had worse runtime, it is acceptable because it is within expectation in practical (for the biggest instance was 1.5 minutes) and the accuracy was very satisfactory (for small instances less than 10% of upper bound obtained for ILP).

The objective of the problem is to maximize the profit through the best operation including production sequencing and shipments. Figure 16 and Table 4 demonstrate the best solution according to genetic algorithm to real data (AE8), with the sequencing of each production line over a period of 24 hours.

We can ascertain that the genetic algorithm in its AG17 parameterization had the best performance; for instance AE1 approached the upper bound of the ILP and obtained most of the best solutions. The greedy heuristic presented satisfactory solutions for some instances, but for others it was well below

TABLE 3: Comparison of results.

Problem	Greedy heuristic		AG06		AG16		AG17		ILP		
	FO	Time (s)	FO	Time (s)	FO	Time (s)	FO	Time (s)	FO	Best bound	Time (s)
AE1	12,733	<0.001	19,259	1.22	19,227	2.76	<b>20,354</b>	10.25	6,904	22,750	723.8
AE2	56,077	<0.001	54,127	9.49	54,778	20.59	<b>59,823</b>	20.57	54,324	60,567	1134.5
AE3	<b>120,162</b>	0.004	115,224	9.59	108,431	46.94	117,770	41.50	—	—	—
AE4	234,464	0.005	379,281	10.93	376,080	51.07	<b>394,101</b>	55.73	—	—	—
AE5	417,773	0.005	<b>494,619</b>	11.32	491,676	51.31	22,750	57.56	—	—	—
AE6	1,044,610	0.006	1,042,940	14.85	1,151,700	55.98	<b>1,151,920</b>	59.75	—	—	—
AE7	1,141,410	0.006	<b>1,237,610</b>	18.45	1,177,440	58.86	1,235,990	62.41	—	—	—
AE8	1,174,730	0.007	1,247,800	18.74	1,180,000	67.64	<b>1,250,010</b>	92.64	—	—	—

TABLE 4: Best production planning (genetic algorithm)—real data.

Line00	Product2\22 Product2\2	Product47\2 Product45\1	Product45\6	Product113\4	Product47\4	Product113\41	Product47\2	Product113\10
Line01	Product70\1 Product10\2	Product11\4	Product37\34	Product71\1	Product48\3	Product59\29	Product15\1	Product48\1
Line02	Product32\1 Product32\1	Product109\9 Product109\3	Product58\12 Product58\1	Product109\19 Product14\3	Product14\1 Product109\9	Product32\4	Product109\1	Product14\11
Line03	Product7\49	Product44\2	Product7\6	Product44\1	Product7\1	Product44\1		
Line04	Product7\8	Product3\44	Product4\1	Product32\2	Product3\1	Product3\10	Product4\2	
Line05	Product42\1 Product111\14 Product88\1	Product51\1 Product110\1 Product75\1	Product52\1 Product24\39 Product89\1	Product87\2 Product111\1 Product72\1	Product90\2 Product91\2 Product87\1	Product12\3 Product104\1 Product54\2	Product88\1 Product24\12 Product111\8	Product24\1 Product111\2 Product74\1
Line06	Product45\20	Product2\2	Product45\7	Product2\33	Product47\1			
Line07	Product56\1 Product29\1 Product92\1 Product13\2	Product29\19 Product41\1 Product40\1 Product92\1	Product36\8 Product12\1 Product93\8 Product36\8	Product98\1 Product101\1 Product24\40 Product56\4	Product24\4 Product55\1 Product38\1	Product27\1 Product13\1 Product56\1	Product13\1 Product36\3 Product30\4	Product92\1 Product24\4 Product40\1
Line08	Product46\2	Product3\47	Product109\1	Product46\2	Product58\1	Product4\1	Product46\1	
Line09	Product69\14 Product66\6	Product66\9	Product69\10	Product68\1	Product4\7	Product32\1	Product69\15	Product67\1
Line10	Product50\77	Product20\2						
Line11	Product85\1 Product83\1	Product86\2 Product84\1	Product112\2 Product81\1	Product85\1 Product79\1	Product82\1 Product86\1	Product78\1	Product85\2	Product86\2
Line12	Product26\9	Product25\65	Product26\1	Product25\1				
Line13	Product34\34	Product60\28	Product21\1	Product23\4	Product60\28			
Line14	Product31\2	Product76\1						
Line15	Product35\19 Product114\1	Product11\2 Product80\1	Product114\2 Product48\1	Product35\26 Product35\1	Product114\2 Product39\1	Product39\1 Product10\1	Product80\2 Product114\3	Product59\10 Product80\1
Line16	Product63\7	Product62\2	Product63\3					

Legend: product XX \N batches.

the best solution; however, the run time was low, unlike the genetic algorithm, which has a greater runtime and ILP, which has a nonviable runtime for executing a plan that needs to be put in place within hours.

Among the parameterizations of the genetic algorithm, AG17 was efficient and stable; although in two instances AG6 was more efficient, in others it was well below the objective function value of AG17, showing some instability with changes in the dimensions of the problem. AG16 failed the best objective function values compared to the others.

The genetic algorithm was efficient for solutions with data from actual dimensions with an acceptable runtime and better objective function value compared to the greedy heuristic, showing whether it is applicable to the problem and stable on the variation of the dimensions of the problem.

In the evaluation of all methods with all the parameterizations presented, the one that performed best was the AG17 parameterization of the genetic algorithm, as it had the best approach for small problems and the best objective function value compared to other possibilities presented. AG17 also

had low run-time, losing to the instances of the greedy heuristic and for some tests below AG16 parameterization, but the quality of the solution of the greedy heuristic is well below the genetic algorithm and the AG16 instance in terms of execution time was very close to the AG17 instance.

#### 4. Conclusions

The aim of this study was to represent a widely regarded scheduling problem in the baking industry, which has conflicting variables, and to propose a mathematical solution to solve it through methods such as genetic algorithm and greedy heuristic.

In this study it was possible to formalize the problem with a mathematical representation so that it can be solved as an ILP problem, because in literature we cannot find a representation of the problem as a whole, only part of the problem.

One of the contributions of this paper is a new model to scheduling problem that is not based in traveling salesman problem (TSP). Due to complexity of due date and the maximization of profit and not minimization of makespan this problem cannot be modeled as TSP.

It was demonstrated that the real scheduling problem is able to be modeling as mixed integer linear program problem different the classical models. And it is possible to resolve this problem utilizing metaheuristics to find good solutions.

The solutions from greedy heuristic presented a very low runtime and the value of objective functions was the next best solution obtained. And the algorithm was shown to have polynomial order of complexity in practical, which shows that even if the problem grows over time it is still acceptable.

However, the genetic algorithm showed strong adaptation to the problem, so the solution was easily represented to be used by the genetic algorithm, making the algorithm easy to implement. The results showed themselves to be very efficient, obtaining good quality solutions for some instances which came close to the upper bound obtained in solving the ILP. The algorithm also proved to be efficient for larger instances, obtaining good solutions in an acceptable runtime, that is, within the limits to enable a viable plan. In the complexity analysis, the algorithm proved itself to be efficient in having logarithmic complexity, which shows that even with the growth of the problem the running time should not vary greatly, thus enabling the execution of the algorithm for larger problems.

#### Conflict of Interests

The authors declare that there is no conflict of interests regarding the publication of this paper.

#### References

- [1] H. L. Gantt, *Work, Wages, and Profits*, Engineering Magazine, New York, NY, USA, 1916.
- [2] S. M. Johnson, "Optimal two- and three-stage production schedules with setup times included," *Naval Research Logistics Quarterly*, vol. 1, no. 1, pp. 61–68, 1954.
- [3] R. Bellman, "The theory of dynamic programming," *Bulletin of the American Mathematical Society*, vol. 60, no. 6, pp. 503–515, 1954.
- [4] Z. A. Lomnicki, "A branch-and-bound algorithm for the exact solution of the three-machine scheduling problem," *Operational Research Quarterly*, vol. 16, pp. 89–100, 1965.
- [5] E. Ignall and L. Schrage, "Application of the branch -and-bound technique to some flowshop scheduling problems," *Operations Research*, vol. 13, no. 3, pp. 400–412, 1965.
- [6] J. D. C. Little, K. G. Murty, D. W. Sweeney, and C. Karel, "An algorithm for the traveling salesman problem," *Operations Research*, vol. 11, no. 6, pp. 972–989, 1963.
- [7] M. R. Garey, D. S. Johnson, and R. Sethi, "The complexity of flowshop and jobshop scheduling," *Mathematics of Operations Research*, vol. 1, no. 2, pp. 117–129, 1976.
- [8] J. Sridhar and C. Rajendran, "Scheduling in a cellular manufacturing system: a simulated annealing approach," *International Journal of Production Research*, vol. 31, no. 12, pp. 2927–2945, 1993.
- [9] C. Rajendran and H. Ziegler, "Heuristics for scheduling in flowshops and owline-based manufacturing cells to minimize the sum of weighted owtime and weighted tardiness of jobs," *Computers & Industrial Engineering*, vol. 37, no. 4, pp. 671–690, 1999.
- [10] J. E. Schaller, J. N. D. Gupta, and A. J. Vakharia, "Scheduling a flowline manufacturing cell with sequence dependent family setup times," *European Journal of Operational Research*, vol. 125, no. 2, pp. 324–339, 2000.
- [11] J. Schaller, "A new lower bound for the flow shop group scheduling problem," *Computers & Industrial Engineering*, vol. 41, no. 2, pp. 151–161, 2001.
- [12] P. M. França, J. N. D. Gupta, A. S. Mendes, P. Moscato, and K. J. Veltink, "Evolutionary algorithms for scheduling a flowshop manufacturing cell with sequence dependent family setups," *Computers & Industrial Engineering*, vol. 48, no. 3, pp. 491–506, 2005.
- [13] S. H. Hendizadeh, H. Faramarzi, S. A. Mansouri, J. N. D. Gupta, and T. Y. ElMekkawy, "Meta-heuristics for scheduling a flowline manufacturing cell with sequence dependent family setup times," *International Journal of Production Economics*, vol. 111, no. 2, pp. 593–605, 2008.
- [14] F. D. Croce, R. Tadei, and G. Volta, "A genetic algorithm for the job shop problem," *Computers & Operations Research*, vol. 22, no. 1, pp. 15–24, 1995.
- [15] J. Adams, E. Balas, and D. Zawack, "The shifting bottleneck procedure for job shop scheduling," *Management Science*, vol. 34, no. 3, pp. 391–401, 1988.
- [16] C. H. Dagli and S. Sittisathanchai, "Genetic neuro-scheduler: a new approach for job shop scheduling," *International Journal of Production Economics*, vol. 41, no. 1–3, pp. 135–145, 1995.
- [17] T. S. Arthanari and K. G. Ramaswamy, "An extension of two machine sequencing problem," *Operation Research*, vol. 8, pp. 10–22, 1971.
- [18] S. A. Brah and J. L. Hunsucker, "Branch and bound algorithm for the flowshop with multiple processors," *European Journal of Operational Research*, vol. 51, no. 1, pp. 88–99, 1991.
- [19] T. J. Sawik, "A scheduling algorithm for flexible flow lines with limited intermediate buffers," *Applied Stochastic Models and Data Analysis*, vol. 9, no. 2, pp. 127–138, 1993.
- [20] F.-Y. Ding and D. Kittichartphayak, "Heuristics for scheduling flexible flow lines, computers," *Industrial Engineering*, vol. 26, no. 1, pp. 27–34, 1994.

- [21] A. Guinet, M. M. Solomon, P. K. Kedia, and A. Dussauchoy, "A computational study of heuristics for two-stage flexible flow-shops," *International Journal of Production Research*, vol. 34, no. 5, pp. 1399–1415, 1996.
- [22] E. Nowicki and C. Smutnicki, "The flow shop with parallel machines: a tabu search approach," *European Journal of Operational Research*, vol. 106, no. 2-3, pp. 226–253, 1998.
- [23] T. H. Cormen, C. E. Leiserson, R. L. Rivest, and C. Stein, "Greedy algorithms," in *Introduction to Algorithms*, pp. 379–399, MIT Press, Cambridge, Mass, USA, 2001.
- [24] G. Bendall and F. Margot, "Greedy type resistance of combinatorial problems," *Discrete Optimization*, vol. 3, no. 4, pp. 288–298, 2006.
- [25] D. L. Applegate, R. E. Bixby, V. Chvatal, and W. J. Cook, *The Travelling Salesman Problem: A Computational Study*, Princeton University Press, Princeton, NJ, USA, 2006.
- [26] A. Allahverdi, C. T. Ng, T. C. E. Cheng, and M. Y. Kovalyov, "A survey of scheduling problems with setup times or costs," *European Journal of Operational Research*, vol. 187, no. 3, pp. 985–1032, 2008.
- [27] F. A. M. da Silva, *The application of scheduling in the industry [M.S. dissertation]*, University of Campinas, São Paulo, Brazil, 2011.

## Research Article

# TLCD Parametric Optimization for the Vibration Control of Building Structures Based on Linear Matrix Inequality

Linsheng Huo, Chunxu Qu, and Hongnan Li

Faculty of Infrastructure Engineering, Dalian University of Technology, Dalian 116024, China

Correspondence should be addressed to Linsheng Huo; [lshuo@dlut.edu.cn](mailto:lshuo@dlut.edu.cn)

Received 12 December 2013; Revised 26 May 2014; Accepted 29 May 2014; Published 18 June 2014

Academic Editor: Aderemi Oluyinka Adewumi

Copyright © 2014 Linsheng Huo et al. This is an open access article distributed under the Creative Commons Attribution License, which permits unrestricted use, distribution, and reproduction in any medium, provided the original work is properly cited.

Passive liquid dampers have been used to effectively reduce the dynamic response of civil infrastructures subjected to earthquakes or strong winds. The design of liquid dampers for structural vibration control involves the determination of the optimal parameters. This paper presents an optimal design methodology for tuned liquid column dampers (TLCDs) based on the  $H_\infty$  control theory. A practical structure, Dalian Xinghai Financial Business Building, is used to illustrate the feasibility of the optimal procedure. The model of structure is built by the finite element method and simplified to the lumped mass model. To facilitate the design of TLCDs, the TLCD parametric optimization problem is transferred to the feedback controller design problem. Through the bounded real lemma, an optimization problem with bilinear matrix inequality (BMI) constraints is constructed to design a static output feedback  $H_\infty$  controller. Iterative linear matrix inequality method is employed and it added some value range constraints to solve the BMI problem. After the TLCD parameters are optimized, the responses of displacement and acceleration in frequency domain and time domain are compared for the structure with and without TLCD. It is validated that the TLCD with the optimized parameters can make the structure satisfy the need for safety and comfort.

## 1. Introduction

Civil structural buildings can be damaged under heavy excitation, such as earthquake. The obvious vibration induced by some slight excitations, such as slight earthquakes and strong winds, can make the people in the building feel uncomfortable. Passive control is an effective strategy to suppress the vibration [1–4]. However, a lot of passive control devices are needed to be instrumented additionally. If there is already some device as a part of the building, it will not cost so much to deal with the vibration control. Tuned liquid column damper (TLCD) is first proposed by Sakai et al. [5], which can change its dynamics by tuning the mass, stiffness, and damping. So TLCD can be designed to make its dynamics be suitable for the vibration control of a building. In the tall building, the liquid tank filled with fresh water has to be instrumented for the fire protection or daily supply. TLCD can be set in the building as a liquid tank and also used for vibration control.

Considering Building 1 in Dalian Xinghai Financial Business Building, this paper presents a building vibration

control example with TLCD. The finite element model is built and compared with the lumped mass model. It is found that these two models are pretty close. The TLCD dynamics is introduced, and the building dynamics with TLCD is discussed. Motivated by the method proposed by Moreno and Thomson [6], the formulation is derived to transfer the parametric optimization problem of TLCD to design a feedback controller problem.

For the feedback controller problem, this paper focuses on how to design a static output feedback  $H_\infty$  controller. According to the bounded real lemma [7], designing the static  $H_\infty$  controller is an optimization problem with bilinear matrix inequality (BMI) constraints. However, BMI is not a convex problem and cannot be solved with the general off-the-shelf packages as linear matrix inequality (LMI). To solve the static output feedback  $H_\infty$  controller, Rubió-Massegú et al. [8] produced a simple expression of the controller, in which the corresponding symmetric variable matrix in the bounded real lemma is congruent with a block diagonal matrix. However, this variable matrix cannot represent all its possible results because there may exist some matrix



FIGURE 1: The buildings in Dalian Xinghai Bay Financial Business District.

that is not congruent with the block diagonal matrix. So the controller is conservative, and the desired controller may not be obtained. Zečević and Šiljak [9] present another method to design the static output feedback controller by making some transformations between the output matrix and controller matrix. Unfortunately, this method also supposed some relationship between output matrix and controller. So, the controller is also conservative. This paper employs the iterative linear matrix inequality (ILMI) method proposed by Cao et al. [10] and adds some value range restrictions into ILMI method. ILMI is solving a generalized eigenvalue minimization problem and does the iteration till satisfying the predetermined tolerance.

After the desired controller is obtained, the optimal parameters of TLCD are determined. The responses of the displacement and acceleration in frequency domain and time domain are compared to illustrate the performance of the optimized TLCD.

## 2. Practical Model

This paper considers the vibration control of a building subjected to the earthquake excitation, which has 46 stories and is 149.95 meters high, as shown in Figure 1.

The building has a frame-shear-wall structure and can be modeled by the finite element software ETABS. The finite element model contains 5472 joints, 13691 frame elements, and 4472 cell elements as shown in Figure 2.

Figure 2 displays the structural three-dimensional diagram as Figure 2(a) and structural top floor plan diagram as Figure 2(b). The first two vibration periods of the finite element model are 3.346829 s and 2.69537 s. The corresponding vibration modes are shown in Figures 3(a) and 3(b).

However, the computation for the responses of the finite element model will cost a lot of time. Therefore, the lumped mass can be used to simplify the finite element model, which has 46 degrees of freedom (DOF) as shown in Figure 3(c). The structural masses are concentrated on each floor, and the interstory damping and stiffness between two lumped masses can be calculated from the finite element model.

TABLE 1: Comparison with difference of the period between two models.

	First vibration period	Second vibration period
Finite element model	3.3468	2.6954
Lumped mass model	3.1312	2.6123
Difference	6.44%	3.08%

To describe the difference between the finite element model and the lumped mass model, the vibration periods have been compared in Table 1.

The difference in the 3rd row of Table 1 shows how different the two types of models are and can be calculated as the following expression:

$$\frac{|T_f - T_l|}{T_f} \times 100\%, \quad (1)$$

where  $T_f$  and  $T_l$  are the vibration periods of the finite element model and lumped mass model, respectively. The above comparison illustrates that there is little difference between the finite element model and lumped mass model. So, the lumped mass model can be used to approximate the practical structure building. In Table 1, the first and second vibration periods are the first mode along Y direction and the first mode along X direction, respectively. It means that the structural stiffness along X direction is larger than the one along Y direction; that is to say, the structure along Y direction is weaker than that along X direction. So, the lumped mass model can be built only considering the stiffness and damping along Y direction. The structure is subjected to an earthquake, whose dynamics can be formulated as follows:

$$\mathbf{M}\ddot{\mathbf{x}} + \mathbf{C}\dot{\mathbf{x}} + \mathbf{K}\mathbf{x} = -\mathbf{M}\ddot{x}_g, \quad (2)$$

where

$$\mathbf{M} = \begin{bmatrix} m_1 & 0 & 0 \\ 0 & \ddots & 0 \\ 0 & 0 & m_n \end{bmatrix},$$

$$\mathbf{C} = \begin{bmatrix} c_1 + c_2 & -c_2 & 0 \\ -c_2 & \ddots & -c_n \\ 0 & -c_n & c_n \end{bmatrix}, \quad (3)$$

$$\mathbf{K} = \begin{bmatrix} k_1 + k_2 & -k_2 & 0 \\ -k_2 & \ddots & -k_n \\ 0 & -k_n & k_n \end{bmatrix},$$

where the elements  $m_i$ ,  $c_i$ , and  $k_i$  in matrices  $\mathbf{M}$ ,  $\mathbf{C}$ , and  $\mathbf{K}$  are the mass, damping, and stiffness of the  $i$ th floor ( $i = 1, \dots, n$ ,  $n = 46$ ). It should be noted that matrices  $\mathbf{C}$  and  $\mathbf{K}$  are calculated along Y direction.  $\ddot{x}_g$  is the unidirectional earthquake acceleration. The relative displacement vector  $\mathbf{x} \in \mathcal{R}^{n \times 1}$  is defined as

$$\mathbf{x} = [x_1 \ x_2 \ \cdots \ x_n]^T. \quad (4)$$

For the tall building, the structural design proposed does not only make the building satisfy safety requirement during

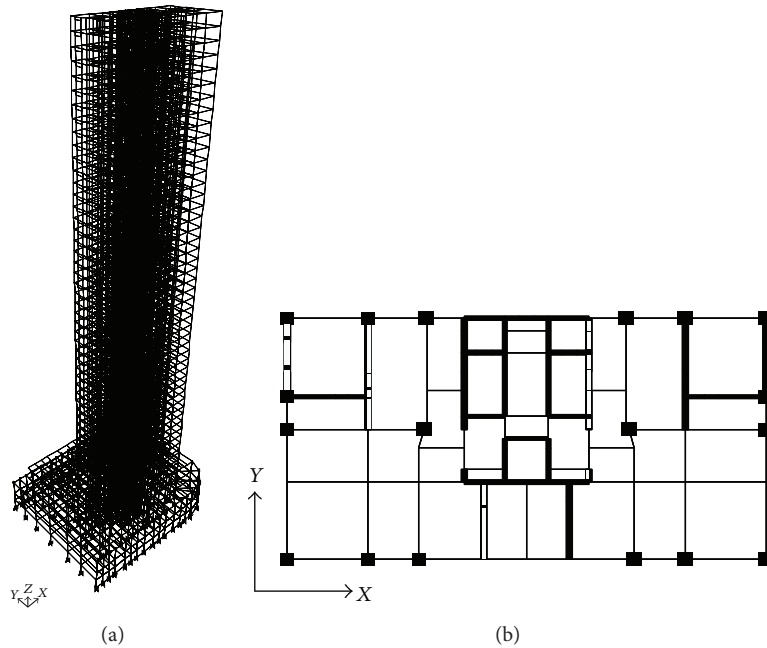


FIGURE 2: Structural diagram: (a) structural three-dimensional diagram; (b) structural top floor plan diagram.

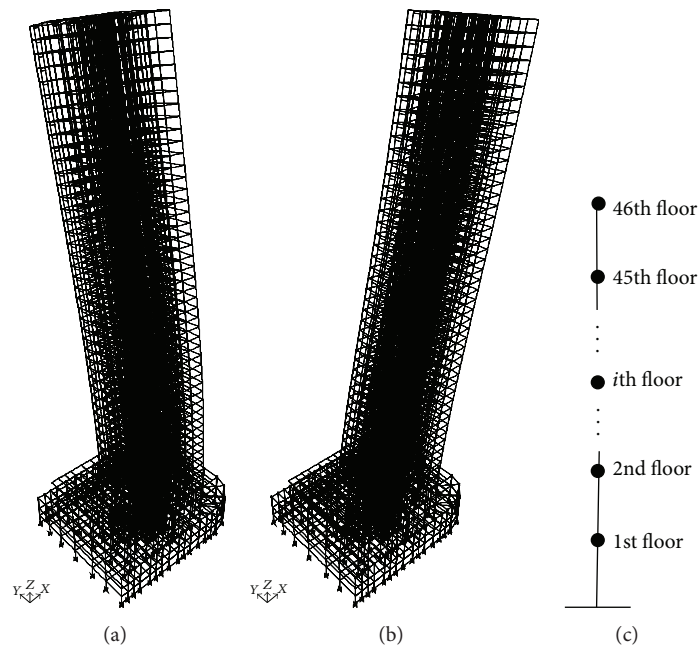


FIGURE 3: Structural diagram: (a) the first vibration mode; (b) the second vibration mode; (c) the lumped mass model.

the earthquake excitation but also make the people in the building feel comfortable during the slight external excitation, such as wind excitation. The safe requirements mean that the interstory drifts of the vibrating building should be smaller. The comfortable requirement needs the acceleration of the building to be smaller.

A liquid tank with fresh water has to be set in a tall building, which would be used for the fire protection or daily supply. So, the structural vibration can be suppressed by

the liquid tank with appropriate dynamics. The dynamics of the liquid tank can be designed by the tank shapes. This paper employs the tank with the shape of two columns that is called the tuned liquid column damper (TLCD).

### 3. TLCD Design

3.1. *The Dynamics of the Structure with TLCD.* The structure of the tuned liquid column damper (TLCD) is shown as

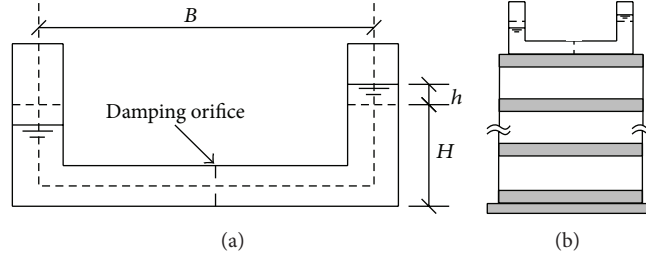


FIGURE 4: Tuned liquid column damper system: (a) tuned liquid column damper; (b) the building with tuned liquid column damper.

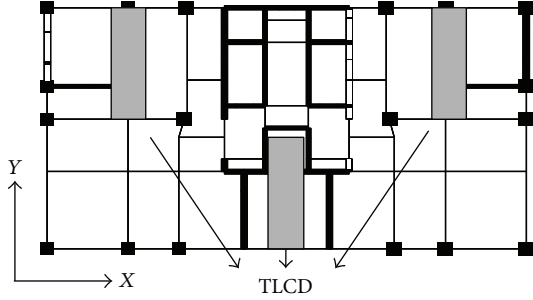


FIGURE 5: Deployment of three TLCDs on the top floor.

Figure 4(a). When it is located on the top floor of the building as shown in Figure 4(b), the TLCD dynamics can be described as the following equation, which is derived by Lagrange's method:

$$\rho A (2H + B) \ddot{h} + \frac{1}{2} \rho A \xi |\dot{h}| \dot{h} + 2\rho A g h = -\rho A B (\ddot{x}_{46} + \ddot{x}_g), \quad (5)$$

where  $\rho$  is the liquid density,  $h$  is the displacement of the liquid in the damper,  $H$  is the vertical length of the liquid column when the liquid is quiescent,  $A$  is the cross-sectional area of the tube,  $B$  is the horizontal length of the column, and  $\xi$  is the head-loss coefficient.  $\ddot{x}_g$  is the unidirectional earthquake acceleration.  $\ddot{x}_{46}$  is the relative acceleration (with respect to the ground) for the top floor of the building. Equation (5) can be simplified as

$$m_T \ddot{h} + c_T \dot{h} + k_T h = -\alpha m_T (\ddot{x}_{46} + \ddot{x}_g), \quad (6)$$

where  $m_T = \rho A L$  means the mass of liquid in the tube,  $c_T = 2m_T \omega_T \zeta_T$  is the equivalent damping of the liquid damper,  $\omega_T$  is the first resonant frequency of TLCD,  $\zeta_T$  is the damping ratio of the liquid damper,  $k_T = 2\rho A g$  expresses the stiffness of the liquid column,  $g$  is the gravitational constant, and  $\alpha = B/L$  denotes the length ratio. According to (4) and (6), the dynamics of the structure instrumented with TLCD on the top floor can be formulated as

$$\mathbf{M}_s \ddot{\mathbf{q}} + \mathbf{C}_s \dot{\mathbf{q}} + \mathbf{K}_s \mathbf{q} = \mathbf{T}_w \ddot{x}_g, \quad (7)$$

where

$$\begin{aligned} \mathbf{M}_s &= \begin{bmatrix} m_1 & 0 & 0 & 0 \\ 0 & \ddots & 0 & 0 \\ 0 & 0 & m_n + m_T & \alpha m_T \\ 0 & 0 & \alpha m_T & m_T \end{bmatrix}, \\ \mathbf{C}_s &= \begin{bmatrix} c_1 + c_2 & -c_2 & 0 & 0 \\ -c_2 & \ddots & -c_n & 0 \\ 0 & -c_n & c_n & 0 \\ 0 & 0 & 0 & c_T \end{bmatrix}, \\ \mathbf{K}_s &= \begin{bmatrix} k_1 + k_2 & -k_2 & 0 & 0 \\ -k_2 & \ddots & -k_n & 0 \\ 0 & -k_n & k_n & 0 \\ 0 & 0 & 0 & k_T \end{bmatrix}, \\ \mathbf{T}_w &= - \begin{bmatrix} m_1 & 0 & 0 & 0 \\ 0 & \ddots & 0 & 0 \\ 0 & 0 & m_n + m_T & 0 \\ 0 & 0 & 0 & \alpha m_T \end{bmatrix}, \end{aligned} \quad (8)$$

$$\mathbf{q} = [q_1 \ \cdots \ q_n \ q_{n+1}]^T = [x_1 \ \cdots \ x_n \ h]^T \in \mathfrak{R}^{(n+1) \times 1}.$$

From (7), it is found that the dynamics of the structure instrumented with TLCD can be influenced by the TLCD parameters, such as  $m_T$ ,  $c_T$ , and  $k_T$ . When a TLCD is needed to be designed for a building structure, the value ranges for the mass ratio, frequency tuning ratio, and damping ratio are always given first, which can be determined uniquely by  $m_T$ ,  $c_T$ , and  $k_T$ . In practical engineering, mass ratio is usually predetermined to satisfy the architectural requirements. Therefore, only frequency tuning ratio and damping ratio should be optimized during the TLCD designing. There are the following relationships with  $m_T$ ,  $c_T$ , and  $k_T$ :

$$\tau = \frac{\omega_T}{\omega_s} = \frac{\sqrt{k_T}}{\omega_s \sqrt{m_T}}, \quad (9)$$

$$\zeta_T = \frac{c_T}{2m_T \omega_T} = \frac{c_T}{2\sqrt{m_T k_T}},$$

where  $\tau$  is the frequency tuning ratio,  $\omega_s$  is the first resonant frequency of the building, and  $\zeta_T$  is the TLCD damping ratio as defined above. The TLCD designing objective is to optimize the parameters  $\tau$  and  $\zeta_T$  such that the structural vibration is reduced and satisfies the need for safety and comfort. From (9),  $c_T$  and  $k_T$  can replace the parameters  $\tau$  and  $\zeta_T$  to be optimized.

3.2. *Transfer Parametric Optimization to Controller Design.* In order to optimize the parameters  $c_T$  and  $k_T$  in (8), they are separated from the matrices  $\mathbf{C}_s$  and  $\mathbf{K}_s$ . Equation (7) is equal to the following expression:

$$\mathbf{M}_s \ddot{\mathbf{q}} + \overline{\mathbf{C}} \dot{\mathbf{q}} + \overline{\mathbf{K}} \mathbf{q} = \mathbf{T}_w \ddot{\mathbf{x}}_g + \mathbf{T}_u p(t), \quad (10)$$

where

$$\begin{aligned} \overline{\mathbf{C}} &= \begin{bmatrix} c_1 + c_2 & -c_2 & 0 & 0 \\ -c_2 & \ddots & -c_n & 0 \\ 0 & -c_n & c_n & 0 \\ 0 & 0 & 0 & 0 \end{bmatrix}, \\ \overline{\mathbf{K}} &= \begin{bmatrix} k_1 + k_2 & -k_2 & 0 & 0 \\ -k_2 & \ddots & -k_n & 0 \\ 0 & -k_n & k_n & 0 \\ 0 & 0 & 0 & 0 \end{bmatrix}, \\ \mathbf{T}_u &= [\mathbf{0}_{1 \times n} \quad -1]^T, \\ p(t) &= [k_T \quad c_T] \begin{bmatrix} h \\ \dot{h} \end{bmatrix}. \end{aligned} \quad (11)$$

Equation (10) can be recognized as the structure with the mass matrix  $\mathbf{M}_s$ , damping matrix  $\overline{\mathbf{C}}$ , and stiffness matrix  $\overline{\mathbf{K}}$  subjected to the earthquake excitation  $\ddot{\mathbf{x}}_g$  and the control force  $p(t)$ . An appropriate control force  $p(t)$  can suppress the structural vibration. From (12), the value of the control force can be decided by the matrix  $[k_T \quad c_T]$  and would vary with the TLCD state  $[h \quad \dot{h}]^T$ . Equation (10) can be represented by the augmented system in state-space as

$$\begin{aligned} \dot{\mathbf{z}} &= \mathbf{A} \mathbf{z} + \mathbf{B}_1 \ddot{\mathbf{x}}_g + \mathbf{B}_2 p(t), \\ \mathbf{y}_z &= \mathbf{C}_1 \mathbf{z} + \mathbf{D}_{11} \ddot{\mathbf{x}}_g + \mathbf{D}_{12} p(t), \\ \mathbf{y}_m &= \mathbf{C}_2 \mathbf{z} + \mathbf{D}_{21} \ddot{\mathbf{x}}_g + \mathbf{D}_{22} p(t), \end{aligned} \quad (13)$$

where

$$\mathbf{z} = [\mathbf{q} \quad \dot{\mathbf{q}}]^T; \quad \mathbf{y}_m = [h \quad \dot{h}]^T. \quad (14)$$

Matrices  $\mathbf{C}_1$ ,  $\mathbf{D}_{11}$ , and  $\mathbf{D}_{12}$  can be determined according to objective output  $\mathbf{y}_z$ , which is always the combination of the

structural interstory drifts and the weighted control force. Other matrices in (13) are denoted as

$$\begin{aligned} & \left[ \begin{array}{c|c|c} \mathbf{A} & \mathbf{B}_1 & \mathbf{B}_2 \\ \hline \mathbf{C}_2 & \mathbf{D}_{21} & \mathbf{D}_{22} \end{array} \right] \\ & = \left[ \begin{array}{c|c|c|c} \mathbf{0}_{(n+1) \times (n+1)} & \mathbf{I}_{(n+1) \times (n+1)} & \mathbf{0} & \mathbf{0} \\ \hline -\mathbf{M}_s^{-1} \overline{\mathbf{K}} & -\mathbf{M}_s^{-1} \overline{\mathbf{C}} & \mathbf{M}_s^{-1} \mathbf{T}_w & \mathbf{M}_s^{-1} \mathbf{T}_u \\ \hline \mathbf{0}_{1 \times n} & 1 & \mathbf{0}_{1 \times n} & 0 \\ \hline \mathbf{0}_{1 \times n} & 0 & \mathbf{0}_{1 \times n} & 1 \end{array} \right]. \end{aligned} \quad (15)$$

The control force  $p(t)$  in (12) can be rewritten as

$$p(t) = \mathbf{G} \mathbf{y}_m = [k_T \quad c_T] \begin{bmatrix} h \\ \dot{h} \end{bmatrix}. \quad (16)$$

So, the TLCD parametric optimization problem is transferred to the controller design problem, that is, to design a controller  $\mathbf{G}$  to suppress the structural vibration efficiently.

3.3.  *$H_\infty$  Static Output Feedback Controller Design.* Taking (16) into (13) to complete the feedback loop, the closed-loop system can be represented as

$$\begin{aligned} \dot{\mathbf{z}} &= \mathbf{A}_{\text{CL}} \mathbf{z} + \mathbf{B}_{\text{CL}} \ddot{\mathbf{x}}_g, \\ \mathbf{y}_z &= \mathbf{C}_{\text{CL}} \mathbf{z} + \mathbf{D}_{\text{CL}} \ddot{\mathbf{x}}_g, \end{aligned} \quad (17)$$

where

$$\begin{aligned} \mathbf{A}_{\text{CL}} &= \mathbf{A} + \mathbf{B}_2 \mathbf{G} \mathbf{C}_2 \\ \mathbf{B}_{\text{CL}} &= \mathbf{B}_1 + \mathbf{B}_2 \mathbf{G} \mathbf{D}_{21} \\ \mathbf{C}_{\text{CL}} &= \mathbf{C}_1 + \mathbf{D}_{12} \mathbf{G} \mathbf{C}_2 \\ \mathbf{D}_{\text{CL}} &= \mathbf{D}_{11} + \mathbf{D}_{12} \mathbf{G} \mathbf{D}_{21}. \end{aligned} \quad (18)$$

This paper focuses on how to design a static output feedback  $H_\infty$  controller  $\mathbf{G}$  in (16). Some concepts about  $H_\infty$  can refer to [11]. According to the bounded real lemma [7], an  $H_\infty$  controller can be designed to stabilize the closed-loop system in (17) and make the transfer function norm of the closed-loop system smaller than a given scalar  $\gamma$ , if and only if there exists a symmetric positive definite matrix  $\mathbf{X}_{\text{CL}} > 0$  to satisfy the following matrix inequality:

$$\begin{bmatrix} \mathbf{A}_{\text{CL}}^T \mathbf{X}_{\text{CL}} + \mathbf{X}_{\text{CL}} \mathbf{A}_{\text{CL}} & \mathbf{X}_{\text{CL}} \mathbf{B}_{\text{CL}} & \mathbf{C}_{\text{CL}}^T \\ \mathbf{B}_{\text{CL}}^T \mathbf{X}_{\text{CL}} & -\gamma \mathbf{I} & \mathbf{D}_{\text{CL}}^T \\ \mathbf{C}_{\text{CL}} & \mathbf{D}_{\text{CL}} & -\gamma \mathbf{I} \end{bmatrix} < \mathbf{0}. \quad (19)$$

Substitute (18) into (19):

$$\begin{bmatrix} (\mathbf{A} + \mathbf{B}_2 \mathbf{G} \mathbf{C}_2)^T \mathbf{X}_{\text{CL}} + \mathbf{X}_{\text{CL}} (\mathbf{A} + \mathbf{B}_2 \mathbf{G} \mathbf{C}_2) & \mathbf{X}_{\text{CL}} (\mathbf{B}_1 + \mathbf{B}_2 \mathbf{G} \mathbf{D}_{21}) & (\mathbf{C}_1 + \mathbf{D}_{12} \mathbf{G} \mathbf{C}_2)^T \\ (\mathbf{B}_1 + \mathbf{B}_2 \mathbf{G} \mathbf{D}_{21})^T \mathbf{X}_{\text{CL}} & -\gamma \mathbf{I} & (\mathbf{D}_{11} + \mathbf{D}_{12} \mathbf{G} \mathbf{D}_{21})^T \\ \mathbf{C}_1 + \mathbf{D}_{12} \mathbf{G} \mathbf{C}_2 & \mathbf{D}_{11} + \mathbf{D}_{12} \mathbf{G} \mathbf{D}_{21} & -\gamma \mathbf{I} \end{bmatrix} < \mathbf{0}. \quad (20)$$

In practical engineering, there are always some value ranges for the frequency tuning ratio  $\tau$  and damping ratio  $\zeta_T$ . So, the value ranges for  $k_T$  and  $c_T$  in  $\mathbf{G}$  can be calculated from (9) and formulated as

$$\begin{aligned} c_T &= \mathbf{L}_c \mathbf{G} \mathbf{R}_c, & c_T^l &\leq \mathbf{L}_c \mathbf{G} \mathbf{R}_c \leq c_T^u, \\ k_T &= \mathbf{L}_k \mathbf{G} \mathbf{R}_k, & k_T^l &\leq \mathbf{L}_k \mathbf{G} \mathbf{R}_k \leq k_T^u, \end{aligned} \quad (21)$$

where

$$\begin{aligned} \mathbf{L}_c &= [1], & \mathbf{R}_c &= [0 \ 1]^T, \\ \mathbf{L}_k &= [1], & \mathbf{R}_k &= [1 \ 0]^T. \end{aligned} \quad (22)$$

In (21),  $c_T^u$  and  $c_T^l$  are denoted as the upper and lower boundary for  $c_T$  and  $k_T^u$  and  $k_T^l$  are the upper and lower boundary for  $k_T$ , respectively. So, the controller  $\mathbf{G}$  should be searched with the constraints (20) and (21). However, it is a bilinear matrix inequality problem, which is nonconvex. Rubió-Massegú et al. [8] and Zečević and Šiljak [9] proposed new approaches to deal with the static output feedback problem, respectively. But the controllers obtained by these two methods are both conservative due to the predefined restrictions. This paper employs the iterative linear matrix inequality (ILMI) method proposed by Cao et al. [10] and adds the constraints (21) into this method to numerically calculate the static output feedback controller  $\mathbf{G}$ . In order to use ILMI method, (20) should be rewritten into another form:

$$(\bar{\mathbf{A}} + \bar{\mathbf{B}}\bar{\mathbf{G}}\bar{\mathbf{C}})^T \mathbf{P} + \mathbf{P} (\bar{\mathbf{A}} + \bar{\mathbf{B}}\bar{\mathbf{G}}\bar{\mathbf{C}}) < \mathbf{0}, \quad (23)$$

$$\begin{aligned} &\text{Minimize} && \alpha_i \\ &\text{s.t.} && \begin{pmatrix} \bar{\mathbf{A}}^T \mathbf{P}_i + \mathbf{P}_i \bar{\mathbf{A}} - \mathbf{X}_i \bar{\mathbf{B}} \bar{\mathbf{B}}^T \mathbf{P}_i - \mathbf{P}_i \bar{\mathbf{B}} \bar{\mathbf{B}}^T \mathbf{X}_i + \mathbf{X}_i \bar{\mathbf{B}} \bar{\mathbf{B}}^T \mathbf{X}_i - \alpha_i \mathbf{P}_i & (\bar{\mathbf{B}}^T \mathbf{P}_i + \bar{\mathbf{G}}\bar{\mathbf{C}})^T \\ & \bar{\mathbf{B}}^T \mathbf{P}_i + \bar{\mathbf{G}}\bar{\mathbf{C}} & -\mathbf{I} \end{pmatrix} < \mathbf{0} \\ &&& \mathbf{P}_i = \mathbf{P}_i^T > \mathbf{0} \\ &&& c_T^l \leq \mathbf{L}_c \mathbf{G} \mathbf{R}_c \leq c_T^u, \quad k_T^l \leq \mathbf{L}_k \mathbf{G} \mathbf{R}_k \leq k_T^u. \end{aligned} \quad (26)$$

Set  $\alpha_i^*$  = the minimized  $\alpha_i$ .

*Step 3.* If  $\alpha_i^* \leq 0$ ,  $\mathbf{G}$  is the desired static output feedback gain in (16). Iteration can be stopped.

*Step 4.* Solve the variable matrices  $\mathbf{P}_i$  and  $\mathbf{G}$  by minimizing trace ( $\mathbf{P}_i$ ) with the constraints in (26), where  $\alpha_i = \alpha_i^*$ . Set  $\mathbf{P}_i^*$  = the solution  $\mathbf{P}_i$ .

*Step 5.* Compare  $\mathbf{X}_i$  and  $\mathbf{P}_i^*$ . If  $\|\mathbf{X}_i - \mathbf{P}_i^*\|$  is smaller than a given tolerance, go to Step 6; else set  $i = i + 1$  and  $\mathbf{X}_i = \mathbf{P}_i^*$ , and then go to Step 2.

*Step 6.* The system may not be stabilized through the output feedback gain in (20) with the constraints (21). Stop the iteration.

where

$$\begin{aligned} \mathbf{P} &= \begin{pmatrix} \mathbf{X}_{\text{CL}} & \mathbf{0} & \mathbf{0} \\ \mathbf{0} & \mathbf{I} & \mathbf{0} \\ \mathbf{0} & \mathbf{0} & \mathbf{I} \end{pmatrix}, & \bar{\mathbf{A}} &= \begin{pmatrix} \mathbf{A} & \mathbf{B}_1 & \mathbf{0} \\ \mathbf{0} & -\gamma \mathbf{I}/2 & \mathbf{0} \\ \mathbf{C}_1 & \mathbf{D}_{11} & -\gamma \mathbf{I}/2 \end{pmatrix}, \\ && \bar{\mathbf{B}} &= \begin{pmatrix} \mathbf{B}_2 \\ \mathbf{0} \\ \mathbf{D}_{12} \end{pmatrix}, & \bar{\mathbf{C}} &= (\mathbf{C}_2 \ \mathbf{D}_{21} \ \mathbf{0}). \end{aligned} \quad (24)$$

Equation (23) is a Lyapunov inequality, which means that there is a static output feedback to stabilize the system  $(\bar{\mathbf{A}}, \bar{\mathbf{B}}, \bar{\mathbf{C}})$ . So, the ILMI method can be used for the system  $(\bar{\mathbf{A}}, \bar{\mathbf{B}}, \bar{\mathbf{C}})$  and summarized as follows.

*Step 1.* According to the value range of the parameters  $\tau$  and  $\zeta_T$ , set the lower boundaries  $c_T^l$  and  $k_T^l$  and upper boundaries  $c_T^u$  and  $k_T^u$  for  $c_T$  and  $k_T$ , respectively. Select  $\mathbf{Q} > \mathbf{0}$  and solve  $\mathbf{P}$  from the following algebraic Riccati equation:

$$\bar{\mathbf{A}}^T \mathbf{P} + \mathbf{P} \bar{\mathbf{A}} - \bar{\mathbf{P}} \bar{\mathbf{B}} \bar{\mathbf{B}}^T \mathbf{P} + \mathbf{Q} = \mathbf{0}. \quad (25)$$

Set  $i = 1$  and  $\mathbf{X}_1 = \mathbf{P}$ .

*Step 2.* Solve the following convex problem for  $\mathbf{P}_i$ ,  $\mathbf{G}$ , and  $\alpha_i$ :

It should be noted that the matrix  $\mathbf{Q}$  in (25) of Step 1 can influence the convergence of the ILMI method. If the iteration cannot be converged, another  $\mathbf{Q}$  should be chosen.  $\mathbf{Q}$  is always set to the identity matrix such that the iteration may obtain a good convergence. Another notice is that the convex problem in Step 2 is a generalized eigenvalue minimization problem. It can be solved through the PEMBMI solver in Yalmip [12].

## 4. Calculation Results

For the building modeled in the first section, the TLCDs can be instrumented on the top floor and used for fire protection or daily supply, whose deployment is shown in Figure 5.

For the three TLCDs, they are first assumed to be one TLCD for the purpose of simplicity during optimization.

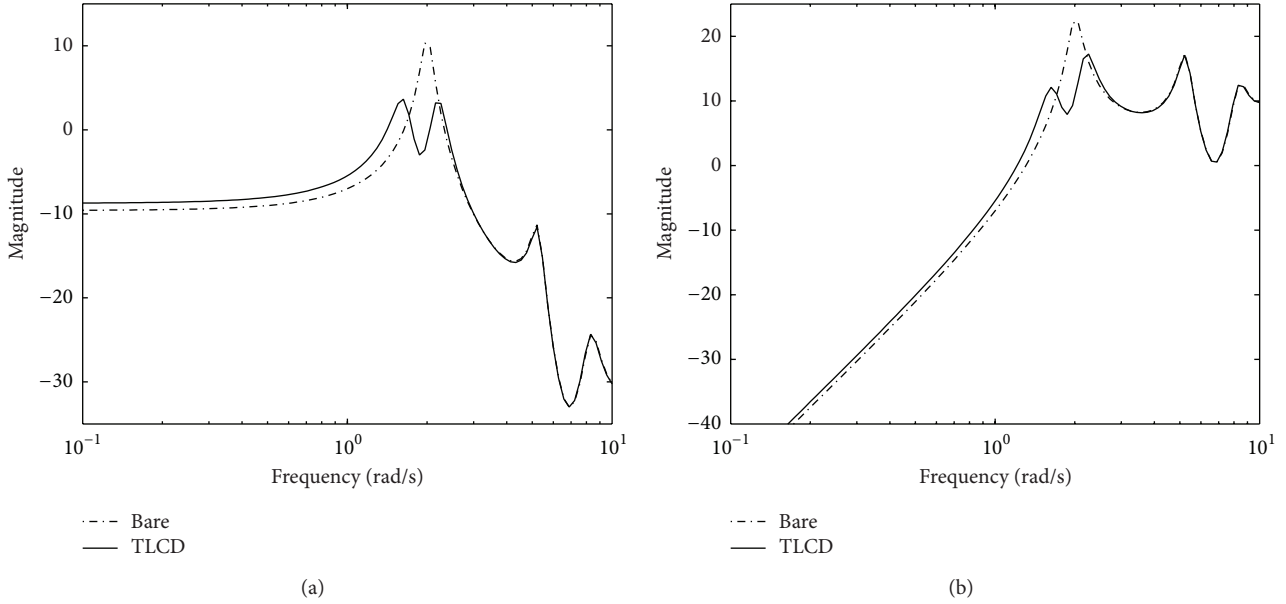


FIGURE 6: Frequency response curve comparisons: (a) frequency response for displacement; (b) frequency response for acceleration.

After the assumed TLCD is optimized, it would be divided into three same TLCDs, whose total mass ratio, frequency tuning ratio, and damping ratio are, respectively, equal to the optimized parameters. To design the TLCD, its mass ratio is pregiven to be 0.015, which means that  $m_T$  is 1.5% of the structural total mass. And the value ranges for its frequency tuning ratio  $\tau$  and damping ratio  $\zeta_T$  are set to be 0~2.0 and 0~0.1. So, the ranges for  $k_T$  and  $c_T$  can be derived as  $0 = c_T^l < c_T < c_T^u = 1.3373 \times 10^6$  and  $0 = k_T^l < k_T < k_T^u = 4.1923 \times 10^7$  according to (9). The length ratio  $\alpha$  in (6) is set to be 0.8. The parametric optimizing process described in the last section is used. After the iteration of the ILMI method, the static output feedback controller  $\mathbf{G}$  in (16) is obtained:

$$\mathbf{G} = [k_T \quad c_T] = [7.83 \times 10^6 \quad 5.78 \times 10^5]. \quad (27)$$

Then, the parameters  $\tau$  and  $\zeta_T$  are determined as

$$\tau = 0.86452; \quad \zeta_T = 0.09988. \quad (28)$$

To study the TLCD performance, the frequency response comparisons between the lumped model without TLCD and that with the optimized TLCD are shown in Figure 6.

Figure 6(a) is the frequency response for the top floor displacement. The dashed line named Bare denotes the frequency response of the structural top floor displacement without TLCD, while the solid line named TLCD is for the response with TLCD. It is found that the frequency response peak is reduced by TLCD, which can reduce the vibration response in time domain indirectly. It means that the building instrumented with TLCD may satisfy the safety need more easily than that without TLCD. Figure 6(b) is the frequency response for the top floor acceleration. The dashed line and solid line have similar definition with that in Figure 6(a). It illustrates that the TLCD can reduce the vibration acceleration and make the building satisfy the

comfortable requirement. The comparison in the frequency domain can reflect the inherent property of the structure with TLCD.

In practical engineering analysis, it is necessary to make some comparisons in the time domain. Some earthquake waves should be chosen to verify that the structural vibration can be reduced, subjected to any earthquake excitation. There are four earthquake waves to be chosen, which are Kobe wave, El Centro wave, North wave, and Hach wave. Their peak accelerations are scaled to  $0.8337 \text{ m/s}^2$ ,  $0.3495 \text{ m/s}^2$ ,  $0.8428 \text{ m/s}^2$ , and  $0.2294 \text{ m/s}^2$ , respectively. Due to the space limitation, only the top floor responses are compared as shown in Figures 7 and 8.

In Figure 7, the dashed line named Bare means the structure without TLCD and the solid line named TLCD is the one with TLCD control. From this figure, all the solid line can reduce the corresponding dashed line a lot. In order to describe the reduction precisely, the reduction ratios for the top floor displacement under the different earthquake waves are calculated according to the following equation:

$$\begin{aligned} & \text{reduction ratio} \\ &= \frac{(\text{Bare structural response}) - (\text{TLCD structural response})}{\text{Bare structural response}} \\ & \quad \times 100\%. \end{aligned} \quad (29)$$

The reduction ratios are 3.13%, 31.31%, 16.13, and 28.55% under the Kobe wave, El Centro wave, North wave, and Hach wave, respectively. It means that the TLCD can suppress the structural displacement vibration efficiently, which can decrease the component damage and make the structure safe. The acceleration comparisons are also made as shown in Figure 8.

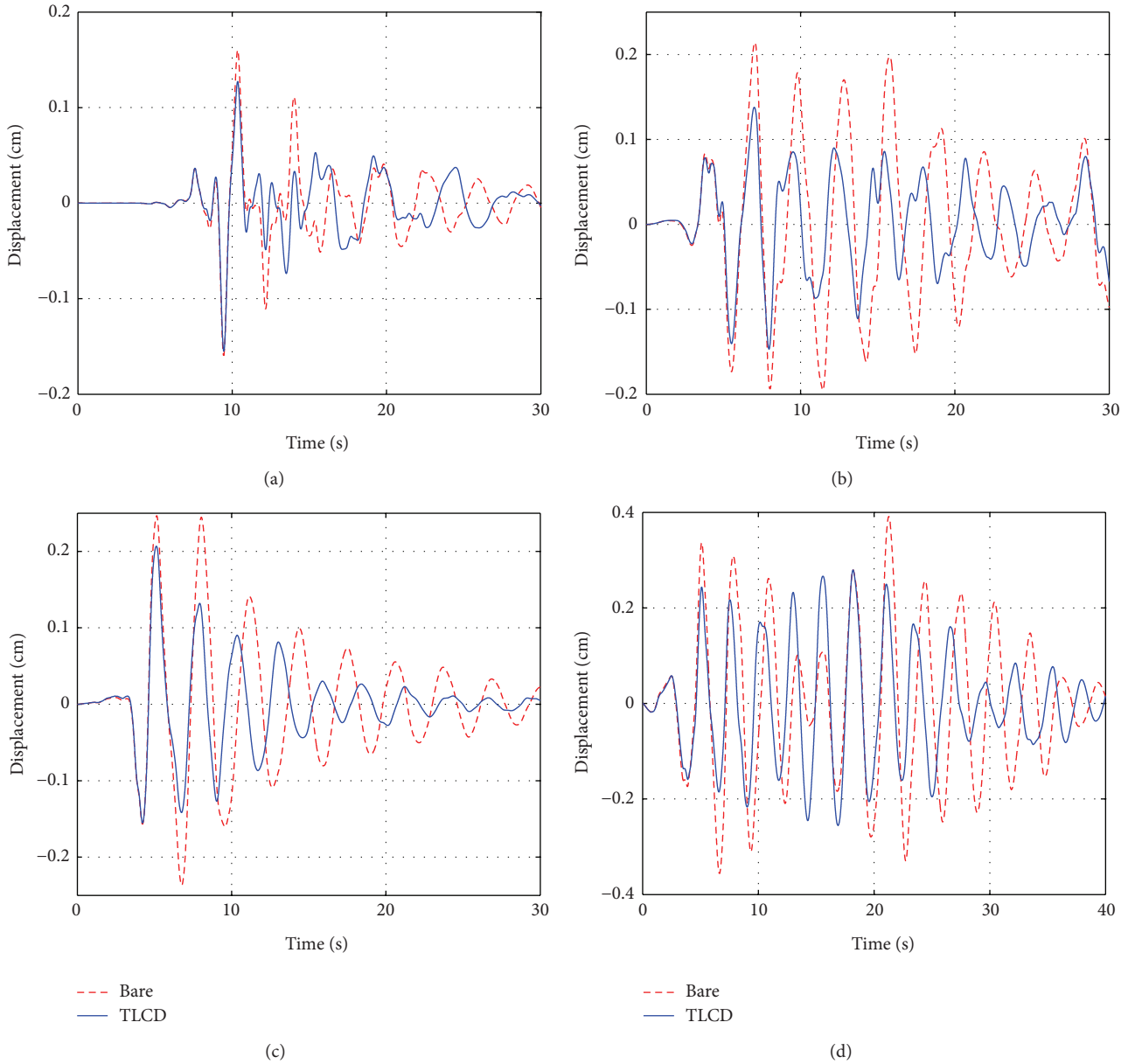


FIGURE 7: Time history comparison for the top floor displacement: (a) under Kobe wave; (b) under El Centro wave; (c) under North wave; (d) under Hach wave.

In Figure 8, the dashed line and solid line have the same definition as that in Figure 7. In the four figures, all the solid line can reduce the peak value of the corresponding dashed line. The reduction ratios for the top floor acceleration under the four earthquake waves are also calculated as (29), which are 3.54%, 4.05%, 5.09%, and 8.84%, respectively. It means that TLCD can make the structure satisfy the requirement for comfort.

## 5. Conclusion

This paper optimizes the parameters of TLCD for Building 1 in Dalian Xinghai Financial Business Building with

the consideration of the earthquake excitation. The building is built to the finite element model and the lumped mass model, respectively. After the comparison of these two models, they are pretty close. The lumped model is adopted due to the simple calculation process for optimization.

TLCD is used to suppress the structural vibration subjected to the earthquake excitation. The TLCD parameters are considered to be optimized. Through the equation derivation, the parametric optimization problem is transferred to the feedback controller design problem. The controller is the static output feedback controller with some value range constraints. This paper designs a static  $H_\infty$  controller. According to bounded real lemma, a bilinear matrix inequality (BMI) is constructed. To solve the BMI problem, the iterative linear

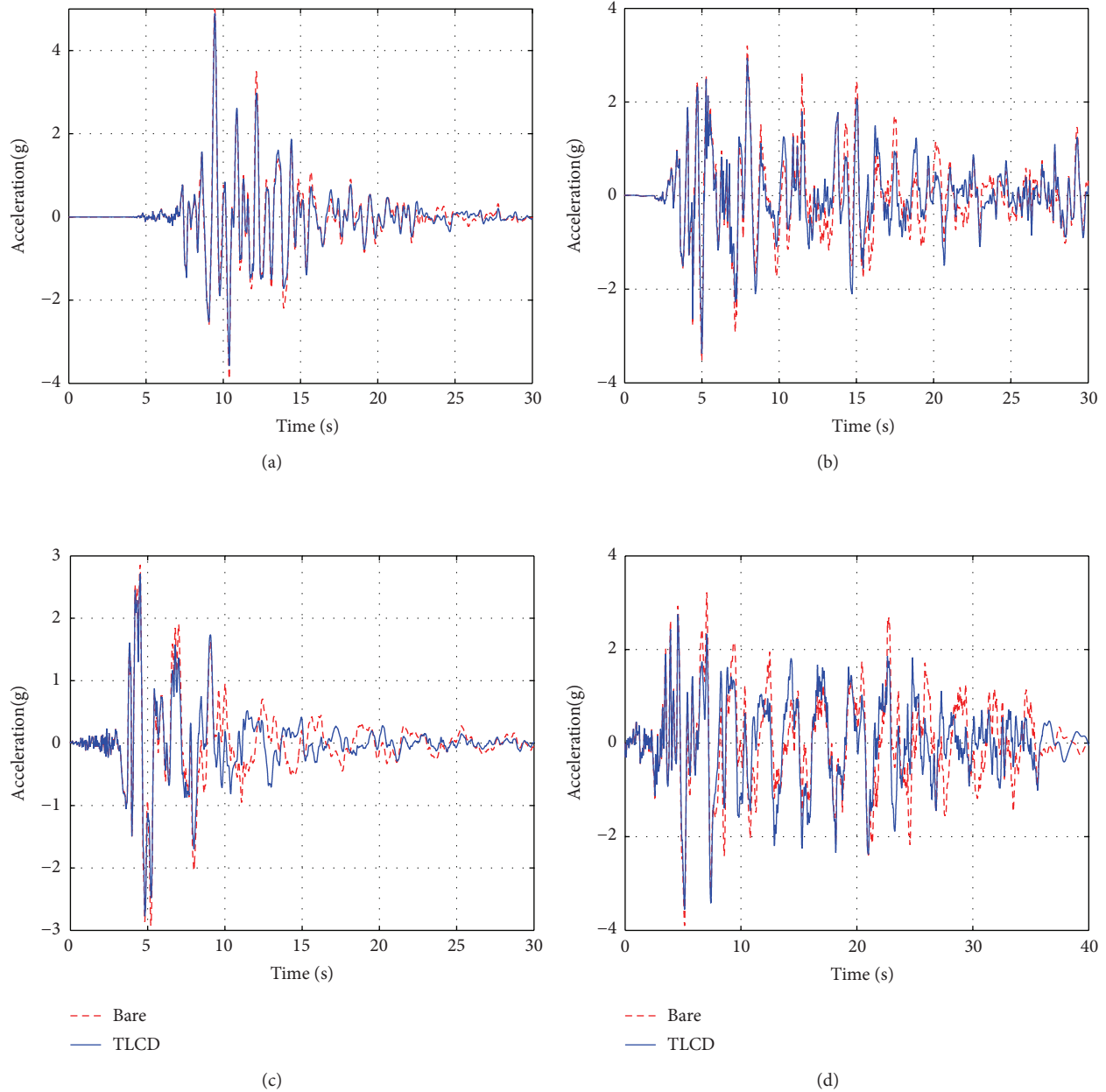


FIGURE 8: Time history comparison for the top floor acceleration: (a) under Kobe wave; (b) under El Centro wave; (c) under North wave; (d) under Hach wave.

matrix inequality (ILMI) is employed and added by the value range constraints. After the iteration, the feedback controller is calculated. Then the frequency tuning ratio and damping ratio of TLCD are determined. To illustrate the TLCD performance, the frequency responses of the top floor displacement and acceleration for the building without and with TLCD in frequency domain are compared. In time domain, the displacement and acceleration responses are compared, subjected to the four earthquake waves. It is found that TLCD can reduce both the displacements and accelerations of the building. It means that the TLCD can make the structure satisfy the need for safety and comfort.

### Conflict of Interests

The authors declare that there is no conflict of interests regarding the publication of this paper.

### Acknowledgments

The authors would like to thank the support of the National Natural Science Foundation of China (Grant nos. 51121005 and 51261120375).

## References

- [1] G. W. Housner, L. A. Bergman, T. K. Caughey et al., “Structural control: past, present, and future,” *Journal of Engineering Mechanics*, vol. 123, no. 9, pp. 897–971, 1997.
- [2] C.-C. Lin, C.-L. Chen, and J.-F. Wang, “Vibration control of structures with initially accelerated passive tuned mass dampers under near-fault earthquake excitation,” *Computer-Aided Civil and Infrastructure Engineering*, vol. 25, no. 1, pp. 69–75, 2010.
- [3] A. S. Pall and C. Marsh, “Response of friction damped braced frames,” *Journal of the Structural Division*, vol. 108, no. 6, pp. 1313–1323, 1982.
- [4] J. T. P. Yao, “Concept of structural control,” *Journal of Structural Division*, vol. 98, no. 7, pp. 1567–1574, 1972.
- [5] F. Sakai, S. Takaeda, and T. Tamaki, “Tuned liquid column damper-new type device for suppression of building vibrations,” in *Proceedings of the International Conference on Highrise Buildings*, Nanjing, China, 1989.
- [6] C. P. Moreno and P. Thomson, “Design of an optimal tuned mass damper for a system with parametric uncertainty,” *Annals of Operations Research*, vol. 181, pp. 783–793, 2010.
- [7] U. Mackenroth, *Robust Control Systems: Theory and Case Studies*, Springer, Berlin, Germany, 2004.
- [8] J. Rubió-Massegú, F. Palacios-Quiñonero, and J. M. Rossell, “Decentralized static output-feedback  $H_\infty$  controller design for buildings under seismic excitation,” *Earthquake Engineering and Structural Dynamics*, vol. 41, no. 7, pp. 1199–1205, 2012.
- [9] A. I. Zečević and D. D. Šiljak, “Design of robust static output feedback for large-scale systems,” *IEEE Transactions on Automatic Control*, vol. 49, no. 11, pp. 2040–2044, 2004.
- [10] Y.-Y. Cao, Y.-X. Sun, and W.-J. Mao, “Output feedback decentralized stabilization: ILMI approach,” *Systems & Control Letters*, vol. 35, no. 3, pp. 183–194, 1998.
- [11] Y. Wang, “Time-delayed dynamic output feedback  $H_\infty$  controller design for civil structures: a decentralized approach through homotopic transformation,” *Structural Control and Health Monitoring*, vol. 18, no. 2, pp. 121–139, 2011.
- [12] M. Kočvara and M. Stingl, “Pennon: a code for convex nonlinear and semidefinite programming,” *Optimization Methods & Software*, vol. 18, no. 3, pp. 317–333, 2003.

## Research Article

# Modeling and Model Predictive Power and Rate Control of Wireless Communication Networks

**Cunwu Han, Dehui Sun, Song Bi, Lei Liu, and Zhengxi Li**

*Beijing Key Laboratory of Fieldbus Technology and Automation, North China University of Technology, Beijing 100144, China*

Correspondence should be addressed to Cunwu Han; [cwhan@ncut.edu.cn](mailto:cwhan@ncut.edu.cn)

Received 6 December 2013; Accepted 29 May 2014; Published 17 June 2014

Academic Editor: Aderemi Oluyinka Adewumi

Copyright © 2014 Cunwu Han et al. This is an open access article distributed under the Creative Commons Attribution License, which permits unrestricted use, distribution, and reproduction in any medium, provided the original work is properly cited.

A novel power and rate control system model for wireless communication networks is presented, which includes uncertainties, input constraints, and time-varying delays in both state and control input. A robust delay-dependent model predictive power and rate control method is proposed, and the state feedback control law is obtained by solving an optimization problem that is derived by using linear matrix inequality (LMI) techniques. Simulation results are given to illustrate the effectiveness of the proposed method.

## 1. Introduction

Power and rate control for wireless communication networks has attracted a great deal of interest during recent decades. The objective of power and rate control is to guarantee the quality of service (QoS) with the lowest transmit power and the maximum transmission data rate in order to maximize the capacity and throughput of the network. However, low power may lead to the degradation of communication quality or even unreliable connection, while high data rates may cause data bursts in the network. Therefore, transmit power and transmission rate must be effectively controlled for wireless communication networks.

There have been a lot of effective power and rate control methods reported in the literature. Generally speaking, the methods can be broadly classified into three categories: (i) resource allocation under perfect power control [1–4]; that is, the received power is well controlled at the target level, and then the transmission rate and power are optimised by maximizing the throughput, (ii) a snap-shot evaluation of the power and rate allocations pertaining to a given realisation of channel gains for each of the users [5, 6], and (iii) power control based on resource allocation [7–14]; that is, the optimal transmission rate can be obtained according to the resource allocation, and the optimal target signal-to-interference ratio (SIR) can be relatively determined, and then

the power control is used to determine an optimal transmit power for each user to drive its actual SIR towards the optimal target SIR. The third method will be used in this paper.

System modeling is an important requirement for power and rate control of wireless communication networks. A simplified linear system model was presented in [7], which considered round-trip delay and treated the effects of channel fading and interference as an additive disturbance. A frame/slot structure was presented in [8], which was used to implement practically a power and rate control system. A high order model as a cascade system was presented in [9, 10], which was used to cancel the effect of time delay. However, parameter uncertainties were not considered in these models. State space models with and without uncertain dynamics were presented in [11], but the time delay was not considered. An extended version of state space model in [11] with state delay was presented in [12], but it only considered the time delay in state and in rate control, while the time delay in input and in power control was not considered. In addition, all the models did not consider the time-varying delays and input constraints. Therefore, a new system model is needed for power and rate control to increase the QoS, which should include uncertainties, input constraints, and time-varying state and input delays in both rate control and power control. This motivates the work of this paper.

A challenge issue in power and rate control is to maintain robustness to time delay [9, 10, 12]. To compensate for the effect of time delay, power and rate control algorithms have been presented by using a multiple-mode Smith prediction filter in [7] and by using a high order model in [9, 10]. From a system-theoretic perspective, a power and rate control algorithm for wireless networks with state delay was presented in [12], which minimized the bound on the error variance between the desired and actual SIR. However, almost all existing power and rate control methods are limited to consider known and constant time delay. Unfortunately, the time delay is often unknown and even time-varying in real network environments.

In the previous work, we presented power and rate control algorithms for wireless networks with time-varying state delay via adaptive control technique [13] and via robust  $H_\infty$  control approach [14]. However, as in [12], the time delay only in rate control was considered, while the time delay in power control was not considered. In fact, the power control is more sensitive to time delay than the rate control. Additionally, only the state time delay was considered in [12–14], but the input delay was not considered. To the best knowledge of the authors, research on power and rate control for wireless communication networks with time-varying delays in both state and control input has not been investigated, which is another motivation of this paper.

Another challenge issue in power and rate control is to maintain robustness to uncertainties and input constraints. It is well known that robust control with linear matrix inequality (LMI) is a powerful technique to cope with uncertainties, and model predictive control (MPC) has strong ability to handle input constraints [15, 16]. Therefore, a robust MPC with LMI can be extended to power and rate control for wireless communication networks with uncertainties and input constraints, which is the third motivation of this paper.

The main contributions of this paper are as follows. (1) In the control theoretic framework, a novel power and rate control system model is presented, which includes uncertainties, input constraints, and time-varying state and input delays in both rate control and power control. (2) A robust model predictive power and rate control method is presented for wireless communication networks with uncertainties, input constraints, and time-varying state and input delays. The state feedback control law is obtained by solving an optimization problem that is derived by using LMI.

The rest of this paper is organized as follows. The power and rate control system model and problem formulation are presented in Section 2. A robust model predictive power and rate control algorithm is presented in Section 3. Simulation results are given in Section 4. And Section 5 concludes the paper.

*Notation.* In this paper,  $\mathbf{A}^T$  and  $\mathbf{A}^{-1}$  denote the transpose and the inverse of a matrix  $\mathbf{A}$ , respectively;  $R^{n \times m}$  denotes the set of all  $n \times m$  real matrices;  $\mathbf{A} > 0$  ( $\mathbf{A} < 0$ ) means that  $\mathbf{A}$  is symmetric positive definite (negative definite);  $\mathbf{I}$  is an appropriately dimensioned identity matrix;  $\text{diag}\{\dots\}$  denotes a block-diagonal matrix;  $\|\mathbf{x}\|^2 = \mathbf{x}^T \mathbf{x}$ ,  $\|\mathbf{x}\|_p^2 = \mathbf{x}^T \mathbf{P} \mathbf{x}$ ;

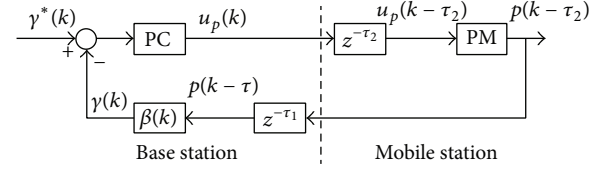


FIGURE 1: Time delays in power control.

the symmetric terms in a symmetric matrix are denoted by \*; for example,

$$\begin{bmatrix} \mathbf{X} & \mathbf{Y}^T \\ \mathbf{Y} & \mathbf{Z} \end{bmatrix} = \begin{bmatrix} \mathbf{X} & * \\ \mathbf{Y} & \mathbf{Z} \end{bmatrix}. \quad (1)$$

## 2. System Model and Problem Formulation

In this section, we briefly describe the time delay effects, power control, and rate control in Sections 2.1, 2.2, and 2.3, respectively, and then, in the control theoretic framework, derive the power and rate control system model for uncertain wireless communication networks with input constraints and time-varying delays in both state and control input in Section 2.4 and finally give the problem formulation in Section 2.5.

*2.1. Effects of Time Delays.* In wireless communication networks, time delays are mainly due to the signal processing and signal transmission [9, 15]. For convenience of analysis, as depicted in Figure 1 for the power control loop, let  $\tau_1$  denote the time delay in uplink channel (including the signal processing delay at base station (BS) and the signal transmission delay from mobile station (MS) to BS), and let  $\tau_2$  denote the time delay in downlink channel (including the signal processing delay at MS and the signal transmission delay from BS to MS). The total round-trip delay in the network is  $\tau = \tau_1 + \tau_2$ . Practical value of the round-trip delay is between 2 and 4 at the sampling rate of 800 Hz [10, 17]. To illustrate the effects of time delays in power control design, let us examine how a power control command  $u_p(k + 1)$  is produced. The effect of time delay in rate control design can be straightforward.

In the uplink power controller, with respect to the operation at MS, there are three main components related to the power control [18]: a quantization reconstructor, a power multiplier (PM), and a power limiter. At time instant  $k$ , the quantization reconstructor is employed to recover the power control update command  $u_p(k)$  sent from BS, which is then fed into the power multiplier, resulting in the transmit power  $p(k)$ , which will be limited to the interval  $[P_{\min}, P_{\max}]$  due to the physical limitation of power amplifier. Because of the downlink time delay  $\tau_2$ , the transmit power at MS should be  $p(k - \tau_2)$ . It is then transmitted to BS through the uplink channel with the uplink time delay  $\tau_1$ . That is, the transmitted power at MS is  $p(k - \tau_2)$ , and the received power at BS is  $p(k - \tau_2 - \tau_1) = p(k - \tau)$ .

At BS, there are four major components related to the power control [17, 18]: an SIR measurement circuit, an SIR

comparator, a power control circuit (PC), and a quantizer. The received SIR  $\gamma(k)$ , which is related to  $p(k - \tau)$ , is measured by the SIR measurement circuit. The tracking error can be obtained by comparison between the received SIR  $\gamma(k)$  and the target SIR  $\gamma^*(k)$  (which can be obtained by the rate controller as shown later). The error is fed into the power controller. The power controller generates a power control update command  $u'_p(k+1)$  according to an appropriate power control algorithm to make the received SIR  $\gamma(k)$  track the target SIR  $\gamma^*(k)$  efficiently. The quantizer transfers the update signal from analog  $u'_p(k+1)$  to digital bits  $u_p(k+1)$  based on a quantization scalar.  $u_p(k+1)$  is then transmitted to MS through the downlink channel.

**2.2. Power Control.** According to the analysis in Section 2.1, the received SIR at BS for MS  $i$  at time  $k$  can be expressed as

$$\gamma_i(k) = \frac{g_{ii}(k) p_i(k - \tau_i)}{\sum_{j=1, j \neq i}^n g_{ij}(k) p_j(k - \tau_j) + \sigma_i^2}, \quad (2)$$

where  $\gamma_i(k)$  is a measurement of the actual SIR,  $g_{ij}(k)$  represents the channel gain from the  $j$ th MS to the intended BS of the  $i$ th cell,  $p_j(k)$  is the transmit power from the  $j$ th MS,  $n$  is the number of MSs using the same channel including the intracell and intercell users,  $\sigma_i^2$  is the power of the white Gaussian noise at the receiver of BS, and  $\tau_j$  is the round-trip delay. Now let

$$\beta_i(k) = \frac{g_{ii}(k)}{\sum_{j=1, j \neq i}^n g_{ij}(k) p_j(k - \tau_j) + \sigma_i^2} \quad (3)$$

denote the scaling factor that determines how  $p_i(k - \tau_i)$  affects the achieved  $\gamma_i(k)$  in (2); that is,

$$\gamma_i(k) = \beta_i(k) p_i(k - \tau_i). \quad (4)$$

By introducing logarithmic variables, with  $\bar{\gamma}_i(k) = \ln[\gamma_i(k)]$ ,  $\bar{\beta}_i(k) = \ln \beta_i(k)$ , and  $\bar{p}_i(k) = \ln p_i(k)$ , we can rewrite (4) as, in dB scale,

$$\bar{\gamma}_i(k) = \bar{\beta}_i(k) + \bar{p}_i(k - \tau_i), \quad (5)$$

where  $\bar{\beta}_i(k)$  is referred to as the effective channel gain.

Introduce random walk model for  $\bar{\beta}_i(k)$  defined by [10]

$$\bar{\beta}_i(k+1) = \bar{\beta}_i(k) + n_i(k), \quad (6)$$

where  $n_i(k)$  is a zero mean disturbance of variance  $\sigma_n^2$  and is independent of  $\bar{p}_i(k)$ . This model is based on the assumption that MSs in the network do not jointly optimize their power levels in any centralized manner and only do so independently in a distributed sense.

The distributed power control (DPC) algorithm (in dB scale) for each MS is given by

$$\bar{p}_i(k+1) = \bar{p}_i(k) + \alpha_i [\bar{\gamma}_i^*(k) - \bar{\gamma}_i(k)], \quad (7)$$

where  $\alpha_i$  is a step-size parameter that is allowed to vary from one MS to another,  $\gamma_i^*(k)$  is a desired value of SIR, and  $\bar{\gamma}_i^*(k) = \ln \gamma_i^*(k)$ .

In order to make the actual SIR  $\gamma_i(k)$  track the desired SIR  $\gamma_i^*(k)$ , as in [12], we employ a power control sequence  $u_{ip}(k)$  in (7) as follows:

$$\bar{p}_i(k+1) = \bar{p}_i(k) + \alpha_i [\bar{\gamma}_i^*(k) - \bar{\gamma}_i(k)] + b_{ip} u_{ip}(k), \quad (8)$$

for a given factor  $b_{ip}$  and control sequence  $u_{ip}(k)$  to be determined.

Then from (5), (6), and (8), we find that the achieved  $\bar{\gamma}_i(k)$  varies according to the following rule:

$$\begin{aligned} \bar{\gamma}_i(k+1) &= \bar{\beta}_i(k+1) + \bar{p}_i(k+1 - \tau_i) \\ &= [\bar{\beta}_i(k) + n_i(k)] \\ &\quad + \{\bar{p}_i(k - \tau_i) + \alpha_i [\bar{\gamma}_i^*(k - \tau_i) - \bar{\gamma}_i(k - \tau_i)] \\ &\quad + b_{ip} u(k - \tau_i)\} \\ &= [\bar{\beta}_i(k) + n_i(k)] + [\bar{\gamma}_i(k) - \bar{\beta}_i(k)] + \alpha_i \bar{\gamma}_i^*(k - \tau_i) \\ &\quad - \alpha_i \bar{\gamma}_i(k - \tau_i) + b_{ip} u(k - \tau_i) \\ &= \bar{\gamma}_i(k) - \alpha_i \bar{\gamma}_i(k - \tau_i) + \alpha_i \bar{\gamma}_i^*(k - \tau_i) \\ &\quad + b_{ip} u(k - \tau_i) + n_i(k). \end{aligned} \quad (9)$$

*Remark 1.* Almost all existing power and rate control methods did not consider the time delay from the transmitted power to the received SIR, that is, assuming  $\tau_i = 0$  in (2). From the analysis of the dynamics as mentioned in Section 2.1, the effect of this time delay must be considered. This paper considers such a time delay which is mainly different from the existing power and rate control methods.

**2.3. Rate Control.** Let  $f_i(k)$  denote the flow rate at MS  $i$  at time  $k$ ; for any MS in the network, the following flow-rate control algorithm is given by [12]

$$\begin{aligned} f_i(k+1) &= f_i(k) + \mu [d(k) - c_1(k) f_i(k) - c_2(k) f_i(k - \tau_i)], \end{aligned} \quad (10)$$

where  $\mu > 0$  is a step-size parameter and  $c_1(k)$  and  $c_2(k)$  are measures of the amount of congestion in the network at time  $k$ .  $d(k)$  controls the amount of rate increase per iteration, which is a zero mean random variable with variance  $\sigma_d^2$ .  $\tau_i$  is nonzero for any controller that incorporates round-trip delay time. Equation (10) is a typical rate control strategy incorporated in wireless communication networks and in computer networks.

According to Shannon's capacity formula, there is a plausible choice for SIR level in order to achieve a rate value  $f_i(k)$ ; namely, the SIR level should be at least at a value  $\gamma_i^*(k)$ , that is, related to  $f_i(k)$  given by

$$f_i(k) = \frac{1}{2} \log_2 [1 + \gamma_i^*(k)]. \quad (11)$$

Usually, during normal network operation,  $\gamma_i^*(k) \gg 1$ . Thus,  $f_i(k)$  is proportional to  $\log_2 \gamma_i^*(k)$ . Using the fact and (10), the desired SIR varies, in dB scale, according to the following rule:

$$\begin{aligned} \bar{\gamma}_i^*(k+1) &= [1 - \mu c_1(k)] \bar{\gamma}_i^*(k) \\ &\quad - \mu c_2(k) \bar{\gamma}_i^*(k - \tau_i) + \bar{\mu} d(k), \end{aligned} \quad (12)$$

where  $\bar{\mu} = 20 \mu / \log_2(10)$ .

Like that mentioned in Section 2.2, as in [12], and considering the round trip time delay, we add a rate control sequence  $u_{if}(k)$  in (12) as follows:

$$\begin{aligned} \bar{\gamma}_i^*(k+1) &= [1 - \mu c_1(k)] \bar{\gamma}_i^*(k) - \mu c_2(k) \bar{\gamma}_i^*(k - \tau_i) \\ &\quad + b_{if} u_{if}(k - \tau_i) + \bar{\mu} d(k). \end{aligned} \quad (13)$$

*Remark 2.* The power and rate control algorithms, presented in [10–12], just considered the time delay in rate control, while the time delay in power control was not considered, that is, in the case  $\tau_i = 0$  in (2). In fact, the power control is more sensitive to time delay than the rate control. So the time delay in power control must be considered. Furthermore, the time delay in control input was not considered in those algorithms, that is, in the case  $\tau_i = 0$  in  $u_{ip}(k - \tau_i)$  in (9) and in  $u_{if}(k - \tau_i)$  in (13).

*2.4. Joint Power and Rate Control.* For simplicity of notation, in the following, the MS index  $i$  is dropped. And we introduce the two-dimensional state vector:

$$\mathbf{x}(k) = \begin{bmatrix} \bar{\gamma}(k) \\ \bar{\gamma}^*(k) \end{bmatrix}. \quad (14)$$

Then from (9) and (13), we can obtain

$$\begin{aligned} \mathbf{x}(k+1) &= \begin{bmatrix} 1 & 0 \\ 0 & 1 - \mu c_1(k) \end{bmatrix} \mathbf{x}(k) + \begin{bmatrix} -\alpha & \alpha \\ 0 & -\mu c_2(k) \end{bmatrix} \mathbf{x}(k - \tau) \\ &\quad + \begin{bmatrix} b_p & 0 \\ 0 & b_f \end{bmatrix} \mathbf{u}(k - \tau) + \begin{bmatrix} n(k) \\ \bar{\mu} d(k) \end{bmatrix}, \end{aligned} \quad (15)$$

or, more compactly,

$$\begin{aligned} \mathbf{x}(k+1) &= \mathbf{A}(k) \mathbf{x}(k) + \mathbf{A}_d(k) \mathbf{x}(k - \tau) \\ &\quad + \mathbf{B} \mathbf{u}(k - \tau) + \boldsymbol{\omega}(k), \end{aligned} \quad (16)$$

where

$$\begin{aligned} \mathbf{A}(k) &= \begin{bmatrix} 1 & 0 \\ 0 & 1 - \mu c_1(k) \end{bmatrix}, & \mathbf{A}_d(k) &= \begin{bmatrix} -\alpha & \alpha \\ 0 & -\mu c_2(k) \end{bmatrix}, \\ \mathbf{B} &= \begin{bmatrix} b_p & 0 \\ 0 & b_f \end{bmatrix}, & \boldsymbol{\omega}(k) &= \begin{bmatrix} n(k) \\ \bar{\mu} d(k) \end{bmatrix}, \end{aligned} \quad (17)$$

where  $\tau$  is a nonzero integer that incorporates round-trip time delay and  $\boldsymbol{\omega}(k)$  is a zero mean random vector with covariance matrix:

$$E \{ \boldsymbol{\omega}(k) \boldsymbol{\omega}^T(k) \} = \begin{bmatrix} \sigma_n^2 & 0 \\ 0 & \bar{\mu}^2 \sigma_d^2 \end{bmatrix}. \quad (18)$$

We now consider uncertainties that arise due to the lack of perfect knowledge about the network dynamics. For example, the congestion control parameters  $c_1(k)$  and  $c_2(k)$  are usually not known exactly and have to be estimated; the estimation process introduces errors in the assumed state-space model. The uncertainty in  $c_1(k)$  can be modelled as [12]

$$c_1(k) = c_1 + DF(k) \bar{d}, \quad (19)$$

where  $F(k)$  is a zero mean random noise with variance  $\sigma_F^2$ ,  $D$  and  $\bar{d}$  are known scalars, and  $c_1$  is unknown but bounded as

$$c_{1,l} \leq c_1 \leq c_{1,u} \quad (20)$$

for some known positive scalars  $\{c_{1,l}, c_{1,u}\}$ . In other words, we allow for both deterministic and stochastic uncertainties in  $c_1(k)$ . In this way, the matrix  $\mathbf{A}(k)$  in (16) is not known exactly, but it can be modelled as  $\mathbf{A}(k) = \mathbf{A} + \Delta \mathbf{A}(k)$ , where

$$\mathbf{A} = \begin{bmatrix} 1 & 0 \\ 0 & 1 - \mu c_1 \end{bmatrix}, \quad (21)$$

$$\Delta \mathbf{A}(k) = DF(k) \mathbf{E}_a,$$

where

$$\mathbf{E}_a = \begin{bmatrix} 0 & 0 \\ 0 & -\bar{\mu} \bar{d} \end{bmatrix}. \quad (22)$$

Likewise, let  $c_2$  be bounded as  $c_{2,l} \leq c_2 \leq c_{2,u}$ . In this way, the matrix  $\mathbf{A}_d(k)$  in (16) is also not known exactly but can be now modelled as  $\mathbf{A}_d(k) = \mathbf{A}_d + \Delta \mathbf{A}_d(k)$ , where

$$\mathbf{A}_d = \begin{bmatrix} -\alpha & \alpha \\ 0 & -\mu c_2 \end{bmatrix}, \quad (23)$$

$$\Delta \mathbf{A}_d(k) = DF(k) \mathbf{E}_d,$$

where

$$\mathbf{E}_d = \begin{bmatrix} 0 & 0 \\ 0 & -\bar{\mu} \bar{d}_d \end{bmatrix}. \quad (24)$$

Then the power and rate control system with time-varying state and input delays and uncertainties can be written as

$$\begin{aligned} \mathbf{x}(k+1) &= \mathbf{A}(k) \mathbf{x}(k) + \mathbf{A}_d(k) \mathbf{x}(k - \tau_k) \\ &\quad + \mathbf{B} \mathbf{u}(k - \tau_k) + \boldsymbol{\omega}(k), \end{aligned} \quad (25)$$

$$\mathbf{x}(k) = 0, \quad k \in [-\tau_M, 0],$$

where  $\Delta \mathbf{A}(k)$  and  $\Delta \mathbf{A}_d(k)$  are time-varying uncertain matrices of the form

$$[\Delta \mathbf{A}(k), \Delta \mathbf{A}_d(k)] = DF(k) [\mathbf{E}_a, \mathbf{E}_d], \quad (26)$$

with  $\mathbf{F}(k)^T \mathbf{F}(k) \leq \mathbf{I}$ . Such parameter uncertainties  $\Delta \mathbf{A}(k)$  and  $\Delta \mathbf{A}_d(k)$  are said to be admissible. And it is assumed that, for the set of uncertainties  $\Omega$ ,  $[\mathbf{A}(k) \mid \mathbf{A}_d(k)] \in \Omega$ .  $\tau_k$  is a round-trip time-varying delay and satisfies

$$0 \leq \tau_m \leq \tau_k \leq \tau_M, \quad (27)$$

where  $\tau_m$  and  $\tau_M$  are known lower and upper delay bounds. The control input is constrained by

$$-\bar{\mathbf{u}} \leq \mathbf{u}(k+i) \leq \bar{\mathbf{u}}, \quad i \geq 0. \quad (28)$$

**2.5. Problem Formulation.** Define the following robust performance index at each time  $k$ :

$$\min_{\mathbf{u}(k+j|k), j \geq 0} \max_{[\mathbf{A}(k+j) \mid \mathbf{A}_d(k+j)] \in \Omega} J(k), \quad (29)$$

subject to

$$J(k) = \sum_{j=0}^{\infty} \left\{ \|\mathbf{x}(k+j|k)\|_{\mathbf{Q}_1}^2 + \|\mathbf{u}(k+j|k)\|_{\mathbf{R}}^2 \right\},$$

$$\begin{aligned} & \mathbf{x}(k+j+1|k) \\ &= \mathbf{A}(k+j) \mathbf{x}(k+j|k) + \mathbf{A}_d(k+j) \\ & \quad \times \mathbf{x}(k+j-\tau_k|k) + \mathbf{B} \mathbf{u}(k+j|k) + \boldsymbol{\omega}(k+j), \\ & -\bar{\mathbf{u}} \leq \mathbf{u}(k+j) (= \mathbf{K} \mathbf{x}(k+j|k)) \leq \bar{\mathbf{u}}, \quad j \in [0, \infty), \end{aligned} \quad (30)$$

where  $J(k)$  is the performance index function with respect to  $\mathbf{x}(k)$ ,  $\mathbf{Q}_1 > 0$  and  $\mathbf{R} > 0$  are weighting matrices,  $\phi(\mathbf{x}, \mathbf{u}, j) = \|\mathbf{x}(k+j|k)\|_{\mathbf{Q}_1}^2 + \|\mathbf{u}(k+j|k)\|_{\mathbf{R}}^2$  is the stage cost,  $\mathbf{x}(k+j|k)$  is the value of vector  $\mathbf{x}$  at future time  $k+j$  ( $j > 0$ ) predicted at time  $k$ ,  $\mathbf{x}(k|k) = \mathbf{x}(k)$ , and  $\mathbf{x}(k-i|k) = \mathbf{x}(k-i)$  for  $i > 1$ .

Equations (29)-(30) are a constrained min-max optimization problem corresponding to a worst-case infinite-horizon MPC with a quadratic objective.

The goal of this paper is to find a state feedback control law  $\mathbf{u}(k) = \mathbf{K} \mathbf{x}(k)$  for system (25) via the MPC strategy by solving the optimization problem (29)-(30).

Before ending this section, we introduce the following lemma, which is useful to prove our results.

**Lemma 3** (see [19]). *Let  $\mathbf{D}$ ,  $\mathbf{E}$ , and  $\mathbf{F}$  be real matrices of appropriate dimensions, with  $\mathbf{F}^T \mathbf{F} \leq \mathbf{I}$ , and then there exists a scalar  $\varepsilon \geq 0$ , such that the following inequality holds:*

$$\mathbf{D} \mathbf{F} \mathbf{E} + \mathbf{E}^T \mathbf{F}^T \mathbf{D}^T \leq \varepsilon \mathbf{D} \mathbf{D}^T + \varepsilon^{-1} \mathbf{E}^T \mathbf{E}. \quad (31)$$

### 3. Model Predictive Power and Rate Control

In this section, we will design the robust state feedback controller for system (25) via the MPC strategy by solving the optimization problem (29)-(30). However, the exact solution to the min-max optimization problem (29)-(30) in general

is not tractable. To obtain a practical optimization problem, following a similar approach as in [15], we will relax the min-max problem into another optimization problem which minimizes an upper bound on the worst value of the original cost function  $J(k)$ .

Consider a Lyapunov-Krasovskii functional at time  $k$

$$V(\mathbf{x}(k)) = V_1(\mathbf{x}(k)) + V_2(\mathbf{x}(k)) + V_3(\mathbf{x}(k)), \quad (32)$$

where

$$V_1(\mathbf{x}(k)) = \mathbf{x}^T(k) \mathbf{P} \mathbf{x}(k), \quad (33)$$

$$V_2(\mathbf{x}(k)) = \sum_{i=k-\tau_k}^{k-1} \mathbf{x}^T(i) \mathbf{P}_d \mathbf{x}(i), \quad (34)$$

$$V_3(\mathbf{x}(k)) = \sum_{j=-\tau_M+1}^{-\tau_m} \sum_{i=k+j}^{k-1} \mathbf{x}^T(i) \mathbf{P}_d \mathbf{x}(i), \quad (35)$$

where  $\mathbf{P} = \mathbf{P}^T > 0$ ,  $\mathbf{P}_d = \mathbf{P}_d^T > 0$ .

An upper bound on the worst value of the cost function  $J(k)$  is obtained whenever the following inequality is satisfied for any  $[\mathbf{A}(k+j|k) \mid \mathbf{A}_d(k+j|k)] \in \Omega$ ,  $j \geq 0$ :

$$V(\mathbf{x}(k+j+1|k)) - V(\mathbf{x}(k+j|k)) \leq -\phi(\mathbf{x}, \mathbf{u}, k). \quad (36)$$

For  $J(k)$  to be finite, we must have  $\mathbf{x}(\infty|k) = 0$ , and hence  $V(\mathbf{x}(\infty|k)) = 0$ . Hence summing both sides of (36) from  $j = 0$  to  $j = \infty$  yields  $-V(\mathbf{x}(k|k)) \leq -J(k)$ , and it follows that

$$J(k) \leq V(\mathbf{x}(k|k)) \leq v(k), \quad (37)$$

where  $v(k) > 0$  is defined to be the upper bound of the cost function  $J(k)$ . This implies

$$\max_{[\mathbf{A}(k+j) \mid \mathbf{A}_d(k+j)] \in \Omega, j \geq 0} J(k) \leq v(k). \quad (38)$$

Then, from (38), the original min-max optimization problem (29)-(30) is turned into the following optimization problem that minimizes this upper bound  $v(k)$ :

$$\min_{v(k), \mathbf{K}, \mathbf{P}, \mathbf{P}_d} v(k), \quad (39)$$

subject to (30) and (38).

**Theorem 4.** *Consider the power and rate control system (25) subject to (26)-(28). If there exist matrices  $\mathbf{Q} = \mathbf{Q}^T > 0$ ,  $\mathbf{Q}_d = \mathbf{Q}_d^T > 0$ , and  $\mathbf{Y}, \mathbf{Z} > 0$  with appropriate dimension, and scalars  $\varepsilon > 0$  and  $v(k) > 0$ , such that the following optimization problem is solvable:*

$$\min_{v(k), \mathbf{Q}, \mathbf{Q}_d, \mathbf{Y}, \mathbf{Z}, \varepsilon} v(k), \quad (40)$$

subject to

$$\begin{bmatrix} -\mathbf{Q} & * & * & * & * & * & * & * \\ (\tau_s + 1)^{1/2} \mathbf{Q} & -\mathbf{Q}_d & * & * & * & * & * & * \\ \mathbf{Q}_1^{1/2} \mathbf{Q} & \mathbf{0} & -v(k) \mathbf{I} & * & * & * & * & * \\ \mathbf{R}^{1/2} & \mathbf{0} & \mathbf{0} & -v(k) \mathbf{I} & * & * & * & * \\ \mathbf{0} & \mathbf{0} & \mathbf{0} & \mathbf{0} & -\mathbf{Q}_d & * & * & * \\ \mathbf{0} & \mathbf{0} & \mathbf{0} & \mathbf{0} & 0 & -v(k) \mathbf{I} & * & * \\ \mathbf{A}\mathbf{Q} & \mathbf{0} & \mathbf{0} & \mathbf{0} & \mathbf{A}_d \mathbf{Q}_d + \mathbf{B}\mathbf{Y} & \mathbf{I} & \varepsilon \mathbf{D}^T \mathbf{D} - \mathbf{Q} & * \\ \mathbf{E}_a \mathbf{Q} & \mathbf{0} & \mathbf{0} & \mathbf{0} & \mathbf{E}_d \mathbf{Q}_d & \mathbf{0} & \mathbf{0} & -\varepsilon \mathbf{I} \end{bmatrix} \leq 0, \quad (41)$$

$$\begin{bmatrix} 1 & * \\ \xi_3(k) & \Lambda \end{bmatrix} \geq 0, \quad (42)$$

$$\begin{bmatrix} \mathbf{Z} & * \\ \mathbf{Y}^T & \mathbf{Q} \end{bmatrix} \geq 0, \quad \mathbf{Z}_{jj} \leq \bar{u}_j^2, \quad j = 1, \dots, m, \quad (43)$$

where  $\tau_s = \tau_M - \tau_m$ , and

$$\begin{aligned} \mathbf{Q} &= v\mathbf{P}^{-1}, & \mathbf{Q}_d &= v\mathbf{P}_d^{-1}, & \mathbf{Y} &= \mathbf{K}\mathbf{Q}_d, \\ \xi_3(k) &= [\mathbf{x}^T(k), \mathbf{x}^T(k-1), \dots, \mathbf{x}^T(k-\tau_m), \\ & \quad \mathbf{x}^T(k-\tau_m-1), \dots, \mathbf{x}^T(k-\tau_M)]^T, \\ \Lambda &= \text{diag} \left( \mathbf{Q}, \frac{\mathbf{Q}_d}{\tau_s+1}, \dots, \frac{\mathbf{Q}_d}{\tau_s+1}, \frac{\mathbf{Q}_d}{\tau_s}, \dots, \mathbf{Q}_d \right), \end{aligned} \quad (44)$$

then the state feedback controller  $\mathbf{u}(k) = \mathbf{K}\mathbf{x}(k)$  minimizes the upper bound of the cost function, where the feedback matrix  $\mathbf{K}$  is obtained from the solution of (40)–(43) given by

$$\mathbf{K} = \mathbf{Y}\mathbf{Q}_d^{-1}. \quad (45)$$

The proof of Theorem 4 is presented in the Appendix.

Theorem 4 has given a sufficient condition for the existence of the robust MPC controller at time  $k$ . In order to prove the stability of the closed loop, a lemma is given as follows.

**Lemma 5** (see [15]). *If the optimization problem in Theorem 4 is feasible at time  $k$ , then it is feasible for all times  $k+j$ ,  $j > 0$ .*

Next, we can give the following theorem to stabilize the closed-loop system.

**Theorem 6.** *If the optimization problem (40)–(43) is feasible at time  $k$ , then the state feedback controller  $\mathbf{u}(k) = \mathbf{K}\mathbf{x}(k)$  from Theorem 4 robustly asymptotically stabilizes the closed-loop system.*

*Proof.* It is known that the optimization problem (40)–(43) is feasible from Lemma 5. So we assume that  $\mathbf{P}^*(k)$ ,  $\mathbf{P}_d^*(k)$

and  $\mathbf{P}^*(k+1)$ ,  $\mathbf{P}_d^*(k+1)$  denote the optimal values of problem (40)–(43) at times  $k$  and  $k+1$ , respectively, and  $\mathbf{x}^*(k|k)$  and  $\mathbf{x}^*(k+1|k+1)$  are optimal state correspondingly.

Since  $\mathbf{P}^*(k+1)$  and  $\mathbf{P}_d^*(k+1)$  are optimal, whereas  $\mathbf{P}^*(k)$ ,  $\mathbf{P}_d^*(k)$  are feasible at time  $k+1$ , we have

$$\begin{aligned} & \mathbf{x}^{*T}(k+1|k+1) \mathbf{P}^*(k+1) \mathbf{x}^*(k+1|k+1) \\ & \leq \mathbf{x}^{*T}(k+1|k+1) \mathbf{P}^*(k) \mathbf{x}^*(k+1|k+1), \\ & \mathbf{x}^T(k+1-i|k+1) \mathbf{P}_d^*(k+1) \mathbf{x}(k+1-i|k+1) \\ & \leq \mathbf{x}^T(k+1-i|k+1) \mathbf{P}_d^*(k) \mathbf{x}(k+1-i|k+1). \end{aligned} \quad (46)$$

From Theorem 4, we have an invariant set  $\Gamma$  for the predicted states of system (25),

$$\begin{aligned} \Gamma &= \{ \mathbf{x}(k+i|k) \in R^n \mid \xi_3^T(k+i|k) \Lambda_3 \xi_3(k+i|k) \leq v \} \\ &= \{ \mathbf{x}(k+i|k) \in R^n \mid \xi_3^T(k+i|k) \Lambda \xi_3(k+i|k) \leq 1 \}, \\ & \quad i \geq 0 \end{aligned} \quad (47)$$

and  $\mathbf{u}(k+j|k) = \mathbf{K}\mathbf{x}(k+j|k)$ ,  $j \geq 0$ . Then for any  $[\mathbf{A}(k) \mid \mathbf{A}_d(k)] \in \Omega$ , we have

$$\begin{aligned} & \mathbf{x}^T(k+1|k) \mathbf{P}(k) \mathbf{x}(k+1|k) \\ & < \mathbf{x}^T(k|k) \mathbf{P}(k) \mathbf{x}(k|k), \quad \mathbf{x}(k|k) \neq 0. \end{aligned} \quad (48)$$

Noting  $\mathbf{x}(k+1-i | k+1) < \mathbf{x}(k+1-i | k)$ ,  $i = 1, 2, \dots, \tau_k$ , that implies

$$\begin{aligned} & \mathbf{x}^T(k+1-i | k+1) \mathbf{P}_d^* \mathbf{x}(k+1-i | k+1) \\ & \leq \mathbf{x}^T(k+1-i | k) \mathbf{P}_d^* \mathbf{x}(k+1-i | k), \quad (49) \\ & \quad i = 1, 2, \dots, \tau_k. \end{aligned}$$

Since the measured state

$$\begin{aligned} \mathbf{x}(k+1 | k+1) &= \mathbf{x}(k+1) \\ &= \mathbf{A}(k) \mathbf{x}(k | k) + (\mathbf{A}_d(k) + \mathbf{BK}) \\ & \quad \times \mathbf{x}(k - \tau_k | k) + \boldsymbol{\omega}(k) \end{aligned} \quad (50)$$

for some  $[\mathbf{A}(k) | \mathbf{A}_d(k)] \in \boldsymbol{\Omega}$ , it must also satisfy the inequality (48). Combining this with (46) and (49) and according to (32)–(35), we can obtain that

$$V(\mathbf{x}^*(k+1 | k+1)) \leq V(\mathbf{x}^*(k | k)). \quad (51)$$

Therefore,  $V(\mathbf{x}(k))$  is a monotonically nonincreasing and bounded Lyapunov function. Hence, the closed-loop system is robustly asymptotically stable. This completes the proof.  $\square$

#### 4. Simulation Results

To illustrate the performance of the proposed algorithm, we simulate a network using the model proposed in [12] for the channel gain from the  $i$ th MS to its BS. In this model, the channel gain is given by

$$G_{ii}(k) = S_0 d_{ii}^{-\delta_i}(k) \cdot 10^{0.1\zeta_i(k)}, \quad (52)$$

where  $S_0$  is a function of the carrier frequency and  $d_{ii}^{-\delta_i}(k)$  is the exponential path loss, which depends on the distance  $d_{ii}(k)$  from the MS  $i$  to its BS and the path-loss exponent,  $\delta_i \in \mathbb{R}$ , which typically takes values between 2 and 6 (we take 4 in the simulation). The term  $10^{0.1\zeta_i(k)}$  corresponds to the effect of shadowing (from building, terrain, or foliage), where  $\zeta_i(k) \in \mathbb{R}$  is a zero mean Gaussian random variable with variance  $\sigma_{\zeta_i}^2$ , which usually ranges between 6 and 12. The values  $c_1(k)$  and  $c_2(k)$  are chosen as random variables between 0 and 0.5.  $n(k)$  and  $d(k)$  are zero mean with variance 0.01. Moreover, take  $\bar{\mu} = 0.8$ ,  $\alpha = 0.2$ .

As indicated in [9, 17], the practical value of the round-trip delay is between 2 and 4 at the sampling rate of 800 Hz and is indicated in [18], and the typical value of the round-trip time delay (sum of the downlink and uplink delay) is between 0 and 4 for IS-95 wireless networks and is 2 for wideband code-division multiple access (WCDMA) wireless networks. In the simulations, we assume the time delay to be changed from 0 to 4, that is,  $0 = \tau_m \leq \tau_k \leq \tau_M = 4$ .

The target SIR is set to be 10 dB, and the input constraints are  $0 < \mathbf{u}(k+i) \leq 1$ ,  $i \geq 0$ . The parameters of MPC controller are set as follows: the prediction horizon is  $N = 5$  and the control horizon is  $N_u = 2$ .

Figure 2 shows the tracking error between the actual SIR and the target SIR by using the proposed model predictive power and rate control method. It is confirmed that the proposed method has good tracking performance for the wireless communication network with time-varying delays, uncertainties, and input constraints. As comparison, the traditional robust power and rate control method presented in [12] is also used for the network with the same parameters; however, only the time delay in state and in rate control is considered, that is, in the case  $\tau_i = 0$  in (9) and in  $u_{if}(k - \tau_i)$  of (13), and the constant time delay  $\tau = 3$  is used in the design procedure. The tracking error is also shown in Figure 2. It is shown that the proposed method has less tracking error than the traditional robust power and rate control method.

#### 5. Conclusion

Most existing power and rate control methods are limited to consider known and constant time delay, especially some methods only considering the time delay in state and in power control. This paper has presented a novel power and rate control system model, which includes uncertainties, input constraints, and time-varying delays in both state and input, not only in the rate control but also in the power control. A robust model predictive power and rate control method is proposed, and the state feedback control law is obtained by solving an optimization problem that is derived by using linear matrix inequality (LMI). Simulation result shows that the proposed method has better performance than the traditional power and rate control methods.

#### Appendix

*Proof of Theorem 4.* Under the state feedback control  $\mathbf{u}(k) = \mathbf{K}\mathbf{x}(k)$ , the closed-loop system can be written as

$$\mathbf{x}(k+1) = \bar{\mathbf{A}}(k) \mathbf{x}(k) + \bar{\mathbf{A}}_d \mathbf{x}(k - \tau_k) + \boldsymbol{\omega}(k), \quad (A.1)$$

where

$$\begin{aligned} \bar{\mathbf{A}}(k) &= \mathbf{A} + \mathbf{DF}(k) \mathbf{E}_a, \\ \bar{\mathbf{A}}_d(k) &= \mathbf{A}_d + \mathbf{BK} + \mathbf{DF}(k) \mathbf{E}_d. \end{aligned} \quad (A.2)$$

Define  $\Delta V(\mathbf{x}(k)) = V(\mathbf{x}(k+1 | k)) - V(\mathbf{x}(k | k))$ ; then along the solution of (25), we have

$$\Delta V(\mathbf{x}(k)) = \Delta V_1(\mathbf{x}(k)) + \Delta V_2(\mathbf{x}(k)) + \Delta V_3(\mathbf{x}(k)), \quad (A.3)$$

$$\begin{aligned} \Delta V_1(\mathbf{x}(k)) &= \mathbf{x}^T(k+1 | k) \mathbf{P} \mathbf{x}(k+1 | k) - \mathbf{x}^T(k) \mathbf{P} \mathbf{x}(k) \\ &= \boldsymbol{\xi}^T(k) \boldsymbol{\Pi}_1^T \mathbf{P} \boldsymbol{\Pi}_1 \boldsymbol{\xi}(k) - \mathbf{x}^T(k) \mathbf{P} \mathbf{x}(k), \end{aligned} \quad (A.4)$$

where

$$\xi(k) = [\mathbf{x}^T(k), \mathbf{x}^T(k - \tau_k), \omega(k)^T]^T, \quad \Pi_1 = [\bar{\mathbf{A}}, \bar{\mathbf{A}}_d, \mathbf{I}], \quad (\text{A.5})$$

$$\begin{aligned} \Delta V_2(\mathbf{x}(k)) &= \sum_{i=k+1-\tau_{k+1}}^k \mathbf{x}^T(i) \mathbf{P}_d \mathbf{x}(i) - \sum_{i=k-\tau_k}^{k-1} \mathbf{x}^T(i) \mathbf{P}_d \mathbf{x}(i) \\ &= \mathbf{x}^T(k) \mathbf{P}_d \mathbf{x}(k) - \mathbf{x}^T(k - \tau_k) \mathbf{P}_d \mathbf{x}(k - \tau_k) \\ &\quad + \sum_{i=k+1-\tau_{k+1}}^{k-1} \mathbf{x}^T(i) \mathbf{P}_d \mathbf{x}(i) - \sum_{i=k-\tau_k}^{k-1} \mathbf{x}^T(i) \mathbf{P}_d \mathbf{x}(i) \\ &\leq \mathbf{x}^T(k) \mathbf{P}_d \mathbf{x}(k) - \mathbf{x}^T(k - \tau_k) \mathbf{P}_d \mathbf{x}(k - \tau_k) \\ &\quad + \sum_{i=k+1-\tau_M}^{k-1} \mathbf{x}^T(i) \mathbf{P}_d \mathbf{x}(i) - \sum_{i=k-\tau_m+1}^{k-1} \mathbf{x}^T(i) \mathbf{P}_d \mathbf{x}(i) \\ &= \mathbf{x}^T(k) \mathbf{P}_d \mathbf{x}(k) - \mathbf{x}^T(k - \tau_k) \mathbf{P}_d \mathbf{x}(k - \tau_k) \\ &\quad + \sum_{i=k+1-\tau_M}^{k-\tau_m} \mathbf{x}^T(i) \mathbf{P}_d \mathbf{x}(i), \end{aligned}$$

$$\begin{aligned} \Delta V_3(\mathbf{x}(k)) &= \sum_{j=-\tau_M+1}^{-\tau_m} \left[ \sum_{i=k+j+1}^k \mathbf{x}^T(i) \mathbf{P}_d \mathbf{x}(i) - \sum_{i=k+j}^{k-1} \mathbf{x}^T(i) \mathbf{P}_d \mathbf{x}(i) \right] \\ &= \sum_{j=-\tau_M+1}^{-\tau_m} [\mathbf{x}^T(k) \mathbf{P}_d \mathbf{x}(k) - \mathbf{x}^T(k+j) \mathbf{P}_d \mathbf{x}(k+j)] \\ &= \tau_s \mathbf{x}^T(k) \mathbf{P}_d \mathbf{x}(k) - \sum_{i=k+1-\tau_M}^{k-\tau_m} \mathbf{x}^T(i) \mathbf{P}_d \mathbf{x}(i). \end{aligned} \quad (\text{A.6})$$

Combining (A.4) and (A.6), we have

$$\Delta V(\mathbf{x}(k)) \leq \xi^T(k) (\Theta_1 + \Pi_1^T \mathbf{P} \Pi_1) \xi(k), \quad (\text{A.7})$$

where  $\Theta_1 = \text{diag}((\tau_s + 1)\mathbf{P}_d - \mathbf{P}, -\mathbf{P}_d, \mathbf{0})$ .

Considering (36) with  $\mathbf{u}(k) = \mathbf{K}\mathbf{x}(k)$ , we obtain

$$\Delta V(\mathbf{x}(k)) + \phi(\mathbf{x}, \mathbf{u}, k) = \xi^T(k) (\Theta_2 + \Pi_1^T \mathbf{P} \Pi_1) \xi(k) \leq 0, \quad (\text{A.8})$$

where  $\Theta_2 = \text{diag}((\tau_s + 1)\mathbf{P}_d - \mathbf{P} + \mathbf{Q}_1 + \mathbf{K}^T \mathbf{R} \mathbf{K}, -\mathbf{P}_d, \mathbf{0})$ . Then

$$\Theta_2 + \Pi_1^T \mathbf{P} \Pi_1 \leq 0. \quad (\text{A.9})$$

In the following, we will prove that (A.9) is equivalent to (41).

Substituting  $\mathbf{Q} = v(k)\mathbf{P}^{-1}$  and  $\mathbf{Q}_d = v(k)\mathbf{P}_d^{-1}$  into (A.9), noting  $\bar{\mathbf{A}}$  and  $\bar{\mathbf{A}}_d$  in (A.1), and using Schur complement yield

$$\Xi + \Psi_D \mathbf{F} \Psi_E + \Psi_E^T \mathbf{F}^T \Psi_D^T \leq 0, \quad (\text{A.10})$$

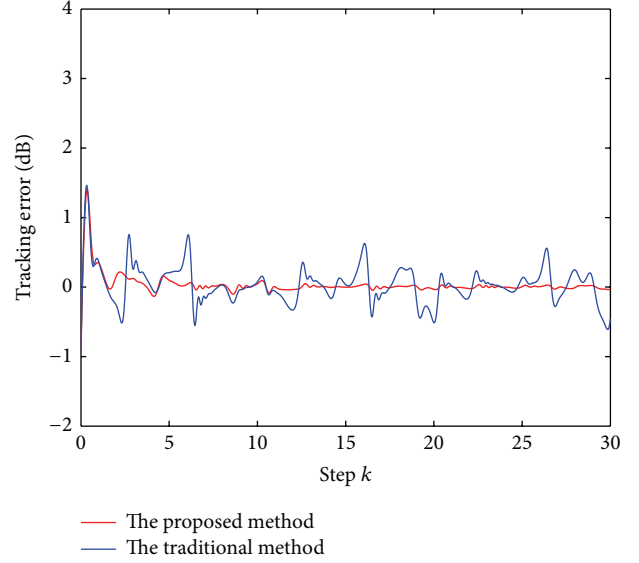


FIGURE 2: Tracking error between the actual SIR and the target SIR.

where

$$\Xi = \begin{bmatrix} \Phi_{11} & * & * \\ \mathbf{0} & \bar{\mathbf{A}}_d + \mathbf{B} \mathbf{K} & \mathbf{Q} \\ \bar{\mathbf{A}} & \bar{\mathbf{A}}_d + \mathbf{B} \mathbf{K} & \mathbf{Q} \end{bmatrix} \leq 0,$$

$$\Phi_{11} = (\tau_s + 1) \mathbf{Q}_d^{-1} - \mathbf{Q}^{-1} + v^{-1}(k) (\mathbf{Q}_1 + \mathbf{K}^T \mathbf{R} \mathbf{K}), \quad (\text{A.11})$$

$$\Phi_{22} = -\mathbf{Q}_d^{-1}, \quad \Psi_D = [\mathbf{0} \ \mathbf{0} \ \mathbf{D}^T]^T,$$

$$\Psi_E = [\mathbf{E}_a \ \mathbf{E}_d \ \mathbf{D}^T]^T.$$

According to Lemma 3, there exists a scalar  $\varepsilon > 0$ , such that the following inequality holds:

$$\Psi_D \mathbf{F} \Psi_E + \Psi_E^T \mathbf{F}^T \Psi_D^T \leq \varepsilon \Psi_D \Psi_D^T + \varepsilon^{-1} \Psi_E^T \Psi_E. \quad (\text{A.12})$$

Using Schur complement, it follows that

$$\begin{bmatrix} \Phi_{11} & * & * & * \\ \mathbf{0} & -\mathbf{Q}_d^{-1} & * & * \\ \bar{\mathbf{A}} & \bar{\mathbf{A}}_d + \mathbf{B} \mathbf{K} & \varepsilon \mathbf{D}^T \mathbf{D} - \mathbf{Q} & * \\ \mathbf{E}_a & \mathbf{E}_d & \mathbf{0} & -\varepsilon \mathbf{I} \end{bmatrix} \leq 0. \quad (\text{A.13})$$

In order to design the controller and obtain the state feedback gain  $\mathbf{K}$ , pre- and postmultiplying (A.13) by  $\text{diag}(\mathbf{Q}, \mathbf{Q}_d, \mathbf{I}, \mathbf{I})$ , and considering  $\mathbf{Y} = \mathbf{K} \mathbf{Q}_d$ , we have

$$\begin{bmatrix} \bar{\Phi}_{11} & * & * & * \\ \mathbf{0} & -\mathbf{Q}_d & * & * \\ \bar{\mathbf{A}} \mathbf{Q} & \bar{\mathbf{A}}_d \mathbf{Q}_d + \mathbf{B} \mathbf{Y} & \varepsilon \mathbf{D}^T \mathbf{D} - \mathbf{Q} & * \\ \mathbf{E}_a \mathbf{Q} & \mathbf{E}_d \mathbf{Q}_d & \mathbf{0} & -\varepsilon \mathbf{I} \end{bmatrix} \leq 0, \quad (\text{A.14})$$

where

$$\bar{\Phi}_{11} = (\tau_s + 1) \mathbf{Q} \mathbf{Q}_d^T \mathbf{Q} - \mathbf{Q} + v^{-1}(k) \mathbf{Q} \mathbf{Q}_1 \mathbf{Q} + v^{-1}(k) \mathbf{Y}^T \mathbf{R} \mathbf{Y}. \quad (\text{A.15})$$

Then using Schur complement again, (41) is obtained. Furthermore, the feedback matrix  $\mathbf{K}$  is given by  $\mathbf{K} = \mathbf{Y}\mathbf{Q}_d^{-1}$ .

The next step of the proof involves the LMI (42). Equations (34) and (35) can be rewritten as

$$\begin{aligned} V_2(\mathbf{x}(k)) &= \sum_{i=k-\tau_k}^{k-1} \mathbf{x}^T(i) \mathbf{P}_d \mathbf{x}(i) \\ &\leq \sum_{i=k-\tau_M}^{k-1} \mathbf{x}^T(i) \mathbf{P}_d \mathbf{x}(i) \\ &= \xi_1^T(k-1) \Lambda_1 \xi_1(k-1), \end{aligned} \quad (\text{A.16})$$

where

$$\begin{aligned} \xi_1(k-1) &= [\mathbf{x}^T(k-1), \dots, \mathbf{x}^T(k-\tau_M)]^T, \\ \Lambda_1 &= \mathbf{diag}(\mathbf{P}_d, \dots, \mathbf{P}_d), \end{aligned} \quad (\text{A.17})$$

$$\begin{aligned} V_3(\mathbf{x}(k)) &= \sum_{j=-\tau_M+1}^{-\tau_m} \sum_{i=k+j}^{k-1} \mathbf{x}^T(i) \mathbf{P}_d \mathbf{x}(i) \\ &= \xi_2^T(k-1) \Lambda_2 \xi_2(k-1), \end{aligned} \quad (\text{A.18})$$

where

$$\begin{aligned} \xi_2(k-1) &= [\mathbf{x}^T(k-1), \mathbf{x}^T(k-2), \dots, \mathbf{x}^T(k-\tau_m), \\ &\quad \mathbf{x}^T(k-\tau_m-1), \dots, \mathbf{x}^T(k-\tau_M+1)]^T, \\ \Lambda_2 &= \mathbf{diag}(\tau_s \mathbf{P}_d, \dots, \tau_s \mathbf{P}_d, (\tau_s-1) \mathbf{P}_d, \dots, \mathbf{P}_d). \end{aligned} \quad (\text{A.19})$$

Summing (33), (A.16), and (A.18), we can conclude that

$$V(\mathbf{x}(k)) = \xi_3^T(k) \Lambda_3 \xi_3(k), \quad (\text{A.20})$$

where

$$\begin{aligned} \xi_3(k) &= [\mathbf{x}^T(k), \mathbf{x}^T(k-1), \dots, \mathbf{x}^T(k-\tau_m), \\ &\quad \mathbf{x}^T(k-\tau_m-1), \dots, \mathbf{x}^T(k-\tau_M)]^T, \\ \Lambda_3 &= \mathbf{diag}(\mathbf{P}, (\tau_s+1) \mathbf{P}_d, \dots, (\tau_s+1) \mathbf{P}_d, \tau_s \mathbf{P}_d, \dots, \mathbf{P}_d). \end{aligned} \quad (\text{A.21})$$

Combining (36) with (A.20), noting  $\mathbf{Q} = v(k)\mathbf{P}^{-1}$  and  $\mathbf{Q}_d = v(k)\mathbf{P}_d^{-1}$ , and then using Schur complement, the LMIs (42) can be obtained.

Following [15], the input constraint (28) is equivalent to (43). This completes the proof.  $\square$

## Conflict of Interests

The authors declare that there is no conflict of interests regarding the publication of this paper.

## Acknowledgments

This work is supported by the National Natural Science Foundation of China (61174116), the Beijing Natural Science Foundation (4142014), and the Scientific Research Foundation of North China University of Technology (20130017). The authors would like to thank the reviewers for their helpful suggestions and comments.

## References

- [1] M. Chiang, "Balancing transport and physical layers in wireless multihop networks: jointly optimal congestion control and power control," *IEEE Journal on Selected Areas in Communications*, vol. 23, no. 1, pp. 104–116, 2005.
- [2] A. T. Hoang, Y.-C. Liang, and M. H. Islam, "Power control and channel allocation in cognitive radio networks with primary users' cooperation," *IEEE Transactions on Mobile Computing*, vol. 9, no. 3, pp. 348–360, 2010.
- [3] N. H. Tran and C. S. Hong, "Joint rate and power control in wireless network: a novel successive approximations method," *IEEE Communications Letters*, vol. 14, no. 9, pp. 872–874, 2010.
- [4] M. R. Musku, A. T. Chronopoulos, D. C. Popescu, and A. Ștefănescu, "A game-theoretic approach to joint rate and power control for uplink CDMA communications," *IEEE Transactions on Communications*, vol. 58, no. 3, pp. 923–932, 2010.
- [5] F. Berggren and S.-L. Kim, "Energy-efficient control of rate and power in DS-CDMA systems," *IEEE Transactions on Wireless Communications*, vol. 3, no. 3, pp. 725–733, 2004.
- [6] C. C. Chai, T. T. Tjhung, and L. C. Leck, "Combined power and rate adaptation for wireless cellular systems," *IEEE Transactions on Wireless Communications*, vol. 4, no. 1, pp. 6–13, 2005.
- [7] B.-S. Chen, C.-Y. Yang, and S.-Y. Li, "Adaptive two-loop power tracking control in CDMA systems with the utility optimization," *IEEE Transactions on Wireless Communications*, vol. 7, no. 4, pp. 1358–1368, 2008.
- [8] L. Zhao and J. W. Mark, "Joint rate and power adaptation for radio resource management in uplink wideband code division multiple access systems," *IET Communications*, vol. 2, no. 4, pp. 562–572, 2008.
- [9] A. Möller, U. T. Jönsson, M. Blomgren, and F. Gunnarsson, "Congestion-based rate and power control in wireless cellular networks," in *Proceedings of the IEEE Global Communications Conference (GLOBECOM '11)*, Houston, Tex, USA, December 2011.
- [10] A. Moller, U. T. Jönsson, M. Blomgren, and F. Gunnarsson, "Stability of rate and power control algorithms in wireless cellular networks," in *Proceedings of the Joint 50th IEEE Conference on Decision and Control and European Control Conference (CDC-ECC '11)*, pp. 4535–4541, Orlando, Fla, USA, December 2011.
- [11] A. Subramanian and A. H. Sayed, "Joint rate and power control algorithms for wireless networks," *IEEE Transactions on Signal Processing*, vol. 53, no. 11, pp. 4204–4214, 2005.
- [12] A. Subramanian and A. H. Sayed, "A robust power and rate control method for state-delayed wireless networks," *Automatica*, vol. 41, no. 11, pp. 1917–1924, 2005.
- [13] C. Han, D. Sun, Y. Shi, and S. Bi, "Adaptive power and rate control for wireless networks with time-varying delay," in *Proceedings of the IASTED International Conference on Control and Applications (CA '13)*, pp. 60–66, Honolulu, Hawaii, USA, August 2013.

- [14] C. Han, D. Sun, and L. Liu, "Performance analysis of power and rate control for wireless networks with time-varying delay," in *Proceedings of the IEEE International Conference on Computer Science and Automation Engineering (CSAE '13)*, pp. 1309–1313, Guangzhou, China, November 2013.
- [15] M. V. Kothare, V. Balakrishnan, and M. Morari, "Robust constrained model predictive control using linear matrix inequalities," *Automatica*, vol. 32, no. 10, pp. 1361–1379, 1996.
- [16] D. Q. Mayne, J. B. Rawlings, C. V. Rao, and P. O. M. Scokaert, "Constrained model predictive control: stability and optimality," *Automatica*, vol. 36, no. 6, pp. 789–814, 2000.
- [17] H. Zhang and P. N. Pathirana, "Uplink power control via adaptive hidden-markov-model-based pathloss estimation," *IEEE Transactions on Mobile Computing*, vol. 12, no. 4, pp. 657–665, 2013.
- [18] C.-Y. Yang and B.-S. Chen, "Robust power control of CDMA cellular radio systems with time-varying delays," *Signal Processing*, vol. 90, no. 1, pp. 363–372, 2010.
- [19] L. Xie, "Output feedback  $H_\infty$  control of systems with parameter uncertainty," *International Journal of Control*, vol. 63, no. 4, pp. 741–750, 1996.

## Research Article

# Determine the Inflow Performance Relationship of Water Producing Gas Well Using Multiobjective Optimization Method

Xiao-Hua Tan,<sup>1</sup> Jian-Yi Liu,<sup>1</sup> Jia-Hui Zhao,<sup>1</sup> Xiao-Ping Li,<sup>1</sup> Guang-Dong Zhang,<sup>1</sup> Chuan Tang,<sup>2</sup> and Li Li<sup>3</sup>

<sup>1</sup> State Key Laboratory of Oil and Gas Reservoir Geology and Exploitation, Southwest Petroleum University, Xindu Road 8, Chengdu 610500, China

<sup>2</sup> Shell China Exploration & Production Co. Ltd., 8F Yanlord Landmark Office Building, No. 1, Section 2, Renmin South Road, Chengdu 610500, China

<sup>3</sup> Oil & Gas Technology Research Institute, PetroChina Changqing Oilfield Company, Xi'an 710018, China

Correspondence should be addressed to Xiao-Hua Tan; xiaohua-tan@163.com

Received 12 December 2013; Accepted 26 May 2014; Published 16 June 2014

Academic Editor: Nachamada Blamah

Copyright © 2014 Xiao-Hua Tan et al. This is an open access article distributed under the Creative Commons Attribution License, which permits unrestricted use, distribution, and reproduction in any medium, provided the original work is properly cited.

During the development of water drive gas reservoirs, the phenomena of gas escaping from water and water separating out from gas will change the seepage characteristics of formation fluid. Therefore, the traditional gas-water two-phase inflow performance relationship (IPR) models are not suitable for calculating the water producing gas well inflow performance relationship in water drive gas reservoirs. Based on the basic theory of fluid mechanics in porous medium, using the principle of mass conservation, and considering the process of dissolution and volatilization of gas and water formation, this paper establishes a new mathematical model of gas-water two-phase flow. Multiobjective optimization method is used to automatically match the sample well production data in water drive gas reservoirs and then we can achieve the sample well's productivity equation, relative permeability curve, water influx intensity, and single well controlled reserves. In addition, the influence of different production gas water ratios (GWR) and gas-soluble water coefficients on absolute open flow rate ( $q_{AOF}$ ) is discussed. This method remedied the limitation of well testing on site and was considered to be a new way to analyze the production behaviors in water producing gas well.

## 1. Introduction

Well productivity is one of primary concerns in field development and provides the basis for field development strategy [1]. Xiaoping and Birong [2] put forward a method to deduce the binomial productivity equation which could calculate the inflow performance relationship (IPR) curve of water producing gas well and presented the application of the IPR curve in determining gas and water production rate from water producing gas well. Zhu et al. [3] proposed three new formation evaluation parameters for low permeability gas reservoir, On the basis of the rate controlled mercury injection, nuclear magnetic resonance and physical simulation technologies. Wang et al. [4] analyzed gas and water phase relative permeability through cores with three different permeability leaves by the establishment of physical

simulation experiment system and experimental process of water-gas mutual flooding.

Park et al. [5] proposed a fuzzy nonlinear programming approach to design production systems of gas fields. The synthetic optimization method could find a globally compromise solution and offer a new alternative with significant improvement over the existing conventional techniques. Cardoso [6] found that reduced-order model is well suited for reservoir simulation. Han et al. [7] presented a multi-objective evolutionary algorithm applied to history matching of water flooding projects, that is to search a feasible set of geological properties showing the reliable future performance. Cancelliere et al. [8] discussed benefits, limitations and drawbacks of assisted history matching, based on multi objective optimization and heuristic strategies. Attention was focused on the possibility offered by these methodologies of

obtaining a number of calibrated reservoir models. Shelkov et al. [9] described a comparison of single and multi-objective history matching of a medium-sized field in Western Siberia with nearly 100 wells and over 10 years of history. And they compared the performance of both single and multi objective versions of particle swarm optimization. Tan et al. studied the transient flow and two-phase flow behaviors in porous media [10–12]. Some of their research results can be used to solve the problem of inflow performance relationship of water producing gas well.

## 2. Gas-Water Two Phase IPR Equation

We assume the reservoir is homogeneous with uniform thickness, total compressibility of rock and fluid is low and constant. The water phase flow is isothermal and Darcy flow, and the gas phase flow is isothermal and non-Darcy flow at high velocity, ignoring the impact of gravity and capillary forces. No chemical reaction exists between gas and water phase. Fundamental filtration equations for the gas and water phase are defined as [13]

$$\begin{aligned} \frac{dp}{dr} &= \frac{\mu_g}{kk_{rg}} v_g + \beta_g \rho_g v_g^2, \\ \frac{dp}{dr} &= \frac{\mu_w}{kk_{rw}} v_w, \end{aligned} \quad (1)$$

where,  $p$  is pressure,  $r$  is radial distance,  $\mu_g$ ,  $\mu_w$  is gas and water viscosity, respectively,  $k$  is absolute permeability,  $k_{rg}$ ,  $k_{rw}$  is gas and water phase relative permeability respectively,  $v_g$ ,  $v_w$  is gas and water phase flow velocity,  $\beta_g$  is turbulence velocity coefficient,  $\rho_g$  is gas density.

Under the boundary condition of steady radial state flow, the integral of (1) can be written as follows [14]

$$\begin{aligned} \int_{p_{wf}}^{p_R} \frac{kk_{rg}}{B_g \mu_g} dp &= \int_{r_w}^{r_e} \frac{q_g}{2\pi r h} dr + \frac{q_g^2}{4\pi^2 h^2} \int_{r_w}^{r_e} \frac{\beta_g \rho_g k k_{rg} B_g}{\mu_g r^2} dr, \\ \int_{p_{wf}}^{p_R} \frac{kk_{rw}}{B_w \mu_w} dp &= \int_{r_w}^{r_e} \frac{q_w}{2\pi r h} dr, \end{aligned} \quad (2)$$

where  $p_R$  is reservoir pressure,  $p_{wf}$  is bottom hole flowing pressure,  $r_e$ ,  $r_w$  is external boundary and wellbore radius respectively,  $B_g B_w$  is gas and water volume factor, respectively,  $q_g q_w$  is gas and water production rate, respectively,  $h$  is reservoir thickness.

Fevang and Whitson [15] defined the gas and water phase pseudo pressure in two phase filtration. The equations are as follows

$$\begin{aligned} \Delta m(p)_g &= \int_{p_{wf}}^{p_R} \left( \frac{k_{rw}}{B_w \mu_w} R_{sgw} + \frac{k_{rg}}{B_g \mu_g} \right) dp, \\ \Delta m(p)_w &= \int_{p_{wf}}^{p_R} \left( \frac{k_{rw}}{B_w \mu_w} + \frac{k_{rg}}{B_g \mu_g} R_{swg} \right) dp, \end{aligned} \quad (3)$$

where,  $R_{sgw}$  is solution gas water ratio and  $R_{swg}$  is solution water gas ratio.

By combing (2) and (3), the gas and water phase pseudo pressure can be expressed

$$\begin{aligned} \Delta m(p)_g &= q_g \left( \frac{1}{R_{pgw}} \int_{r_w}^{r_e} \frac{R_{sgw}}{2\pi r h k} dr + \int_{r_w}^{r_e} \frac{1}{2\pi r h k} dr \right) \\ &\quad + \frac{q_g^2}{4\pi^2 h^2} \int_{r_w}^{r_e} \frac{\beta_g \rho_g k k_{rg} B_g}{\mu_g r^2} dr, \\ \Delta m(p)_w &= q_w \left( \int_{r_w}^{r_e} \frac{1}{2\pi r h k} dr + R_{pgw} \int_{r_w}^{r_e} \frac{R_{sgw}}{2\pi r h k} dr \right) \\ &\quad + \frac{q_w^2 R_{pgw}^2}{4\pi^2 h^2} \int_{r_w}^{r_e} \frac{\beta_g \rho_g k k_{rg} B_g}{\mu_g r^2} dr, \end{aligned} \quad (4)$$

where  $R_{pgw}$  is production gas water ratio.

In order to simplify the expressions of gas and water phase pseudo pressure, we define four parameters

$$\begin{aligned} A &= \int_{r_w}^{r_e} \frac{1}{2\pi r h k} dr, \\ B &= \frac{1}{4\pi^2 h^2} \int_{r_w}^{r_e} \frac{\beta_g \rho_g k k_{rg} B_g}{\mu_g r^2} dr, \\ C_g &= \int_{r_w}^{r_e} \frac{R_{sgw}}{2\pi r h k} dr, \\ C_w &= \int_{r_w}^{r_e} \frac{R_{swg}}{2\pi r h k} dr. \end{aligned} \quad (5)$$

By combing (4), we obtain the gas-water two phase IPR equation (6).

$$\begin{aligned} q_g &= \left( - \left( A + \left( \frac{1}{R_{pgw}} \right) C_g \right) \right. \\ &\quad \left. + \sqrt{\left( A + \left( \frac{1}{R_{pgw}} \right) C_g \right)^2 + 4B \cdot \Delta m(p)_g} \right) (2B)^{-1}, \\ q_w &= \left( - \left( A + R_{pgw} C_w \right) \right. \\ &\quad \left. + \sqrt{\left( A + R_{pgw} C_w \right)^2 + 4BR_{pgw}^2 \cdot \Delta m(p)_w} \right) \\ &\quad \times \left( 2BR_{pgw}^2 \right)^{-1}, \\ \Delta m(p)_g &= \int_{p_{wf}}^{p_R} \left( \frac{k_{rw}}{B_w \mu_w} R_{sgw} + \frac{k_{rg}}{B_g \mu_g} \right) dp, \\ \Delta m(p)_w &= \int_{p_{wf}}^{p_R} \left( \frac{k_{rw}}{B_w \mu_w} + \frac{k_{rg}}{B_g \mu_g} R_{swg} \right) dp. \end{aligned} \quad (6)$$

This equation is determined by the four parameters  $A, B, C_g, C_w$ , where  $A$  is laminar coefficient,  $B$  is turbulence coefficient,  $C_g$  is gas soluble coefficient, representing dissolved gas within gas well control range,  $C_w$  is water soluble coefficient, representing dissolved formation water in gas within the well control range.

### 3. Gas-Water Two Phase Comprehensive Model and the Solution

3.1. Gas and Water Relative Permeability. Gas and water phase relative permeability  $k_{rg}, k_{rw}$  are needed in order to calculate the gas-water two phase IPR equation.  $k_{rg}, k_{rw}$  is a function of water saturation  $S_w$ , the empirical equations are represented as follows [15]

$$k_{rg} = (1 - (S_w - S_{wi}))^2 \left(1 - (S_w - S_{wi})^{(5-D)/(3-D)}\right), \quad (7)$$

$$k_{rw} = (S_w - S_{wi})^{(11-3D)/(3-D)},$$

where,  $S_w$  is water saturation in reservoir,  $S_{wi}$  is initial water saturation,  $D$  is relative permeability index.

From (7), we obtain

$$\frac{k_{rg}}{k_{rw}} = \frac{(1 - (S_w - S_{wi}))^2 \left(1 - (S_w - S_{wi})^{(5-D)/(3-D)}\right)}{(S_w - S_{wi})^{(11-3D)/(3-D)}}. \quad (8)$$

Using the ratio of gas and water production, a method aimed to obtain the ration of gas and water phase relative permeability is proposed by Jokhio and Tiab [16].

$$\frac{k_{rg}}{k_{rw}} = \left(\frac{B_g \mu_g}{B_w \mu_w}\right) \frac{(R_{pgw} - R_{sgw})}{(1 - R_{pgw} R_{swg})}. \quad (9)$$

The parameters  $\mu_g, \mu_w, B_g, B_w, R_{swg}, R_{sgw}$  in (9) are functions of pressure  $p$ . Therefore, the ratio of gas and water phase relative permeability  $k_{rg}/k_{rw}$  can be obtained by means of  $p$  and  $R_{pgw}$ . Then  $S_w$  can be calculated. At last,  $k_{rg}, k_{rw}$  can be obtained.

By Combining (8) and (9), we obtain:

$$\frac{(1 - (S_w - S_{wi}))^2 \left(1 - (S_w - S_{wi})^{(5-D)/(3-D)}\right)}{(S_w - S_{wi})^{(11-3D)/(3-D)}} = \left(\frac{B_g \mu_g}{B_w \mu_w}\right) \frac{(R_{pgw} - R_{sgw})}{(1 - R_{pgw} R_{swg})}. \quad (10)$$

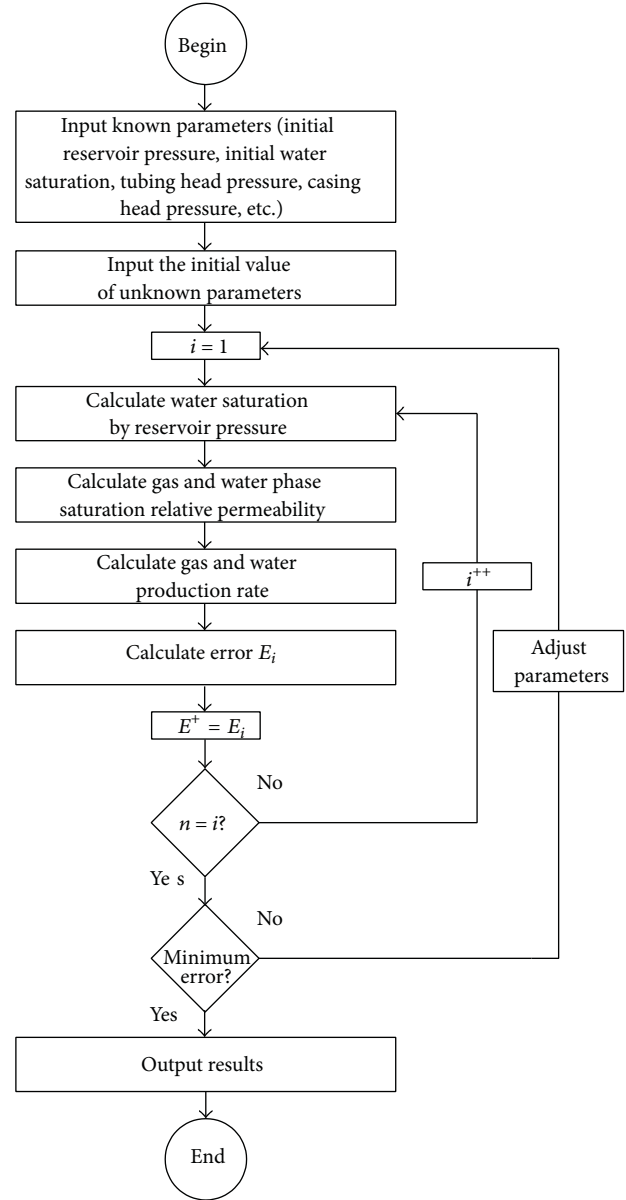


FIGURE 1

From (7) and (10), the equations for calculating  $k_{rg}, k_{rw}$  are defined as follows

$$k_{rg} = (1 - (S_w - S_{wi}))^2 \left(1 - (S_w - S_{wi})^{(5-D)/(3-D)}\right),$$

$$k_{rw} = (S_w - S_{wi})^{(11-3D)/(3-D)},$$

$$\frac{(1 - (S_w - S_{wi}))^2 \left(1 - (S_w - S_{wi})^{(5-D)/(3-D)}\right)}{(S_w - S_{wi})^{(11-3D)/(3-D)}} = \left(\frac{B_g \mu_g}{B_w \mu_w}\right) \frac{(R_{pgw} - R_{sgw})}{(1 - R_{pgw} R_{swg})}. \quad (11)$$

Based on the material balance equation in the water drive gas reservoir, the relationships between average formation

pressure and geologic reserve, cumulative gas production and water invasion intensity can be obtained in (12) [17]

$$\frac{p}{z} = \frac{p_i}{z_i} \left( \frac{1 - (G_p/G)}{1 - (G_p/G)^R} \right), \quad (12)$$

where,  $p$ ,  $p_i$  is current and initial reservoir pressure, respectively,  $z$ ,  $z_i$  is gas deviation factor under current and initial reservoir pressure, respectively,  $G_p$ ,  $G$  is cumulative gas production and dynamic reserves, respectively,  $R$  is water invasion coefficient.

**3.2. Gas-Water Two Phase Comprehensive Model.** By Combining (6), (10) and (12), the gas-water two phase comprehensive model can be expressed

$$\begin{aligned} q_g &= \left( - \left( A + \frac{1}{R_{pgw}} C_g \right) \right. \\ &\quad \left. + \sqrt{\left( A + \frac{1}{R_{pgw}} C_g \right)^2 + 4B \cdot \Delta m(p)_g} \right) (2B)^{-1}, \\ q_w &= \left( - (A + R_{pgw} C_w) \right. \\ &\quad \left. + \sqrt{(A + R_{pgw} C_w)^2 + 4BR_{pgw}^2 \cdot \Delta m(p)_w} \right) \\ &\quad \times (2BR_{pgw}^2)^{-1}, \\ \Delta m(p)_g &= \int_{p_{wf}}^{p_r} \left( \frac{k_{rw}}{B_w \mu_w} R_{sgw} + \frac{k_{rg}}{B_g \mu_g} \right) dp, \\ \Delta m(p)_w &= \int_{p_{wf}}^{p_r} \left( \frac{k_{rw}}{B_w \mu_w} + \frac{k_{rg}}{B_g \mu_g} R_{swg} \right) dp, \\ k_{rg} &= (1 - (S_w - S_{wi}))^2 \left( 1 - (S_w - S_{wi})^{(5-D)/(3-D)} \right), \\ k_{rw} &= (S_w - S_{wi})^{(11-3D)/(3-D)}, \\ &= \frac{(1 - (S_w - S_{wi}))^2 \left( 1 - (S_w - S_{wi})^{(5-D)/(3-D)} \right)}{(S_w - S_{wi})^{(11-3D)/(3-D)}} \\ &= \left( \frac{B_g \mu_g}{B_w \mu_w} \right) \left( \frac{R_{pgw} - R_{sgw}}{1 - R_{pgw} R_{swg}} \right), \\ \frac{P}{Z} &= \frac{P_i}{Z_i} \left( \frac{1 - (G_p/G)}{1 - (G_p/G)^R} \right). \end{aligned} \quad (13)$$

**3.3. The Solution of Gas-Water Two Phase Comprehensive Model.** As (13) shows above, Laminar coefficient  $A$ , turbulence coefficient  $B$ , gas soluble coefficient  $C_g$ , water soluble

TABLE 1: The basic parameters of an actual well.

Well depth (m)	The relative density of gas	The relative density of water	Formation pressure (MPa)	Formation temperature (°C)	Initial water saturation
2994	0.78	1.02	30.08	78	0.35

TABLE 2: The target parameter in an actual well.

$A$	$B$	$C_g$	$C_w$	$D$	$R$	$G$ ( $10^8 \text{ m}^3$ )
$1.41 \times 10^{-5}$	$5.23 \times 10^{-10}$	0.12	$4.21 \times 10^{-6}$	-1.97	5.37	3.59

coefficient  $C_w$ , relative permeability index  $D$ , water invasion coefficient  $R$  and single well controlled reserves  $G$  are needed to solve. An automatic fitting multi-objective optimization method is given in this paper to solve the problem in the complicated percolation model mentioned above. The essence of this method is seeking the best fitting between theoretical value and measured value. The solution is defined as follows

$$\begin{aligned} E &= \sum_{i=1}^n (q_g(A, B, C_g, C_w, D, R, G) - q_g)^2 \\ &\quad + \sum_{i=1}^n (q_w(A, B, C_g, C_w, D, R, G) - q_w)^2, \end{aligned} \quad (14)$$

where,  $q_g(A, B, C_g, C_w, D, R, G)$  and  $q_w(A, B, C_g, C_w, D, R, G)$  is theoretical gas and water production rate, respectively,  $q_g$  and  $q_w$  are actual gas and water production rate, respectively,  $E$  is expressed as the target function to be fitted. The proper parameters can be obtained to minimum the target function by means of the automatic fitting method. The flow chart for plotting type curves is shown in Figure 1.

## 4. Case Analysis

**4.1. Calculating of the Target Parameter.** During the process of acquiring the parameters like laminar coefficient  $A$ , turbulence coefficient  $B$ , gas soluble coefficient  $C_g$ , water soluble coefficient  $C_w$ , relative permeability index  $D$ , water invasion intensity  $R$  and single well controlled reserve  $G$ , the theoretical gas and water production can be obtained based on (13). By fitting the practical gas and water production on the basis of the automatically fitting method in (14), the result shown in Figure 2 can be acquired. It is clearly that the theoretical results verified with the practical ones which indicates the reliability of the results. The basic parameters of an actual well are shown in Table 1.

The parameters like laminar coefficient  $A$ , turbulence coefficient  $B$ , gas soluble coefficient  $C_g$ , water soluble coefficient  $C_w$ , relative permeability index  $D$ , water invasion intensity  $R$  and single well controlled reserve  $G$  are shown in Table 2.

The value of water soluble coefficient in this table is very small which suggests that the content of the formation water dissolving into the natural gas is little. And the energy of the

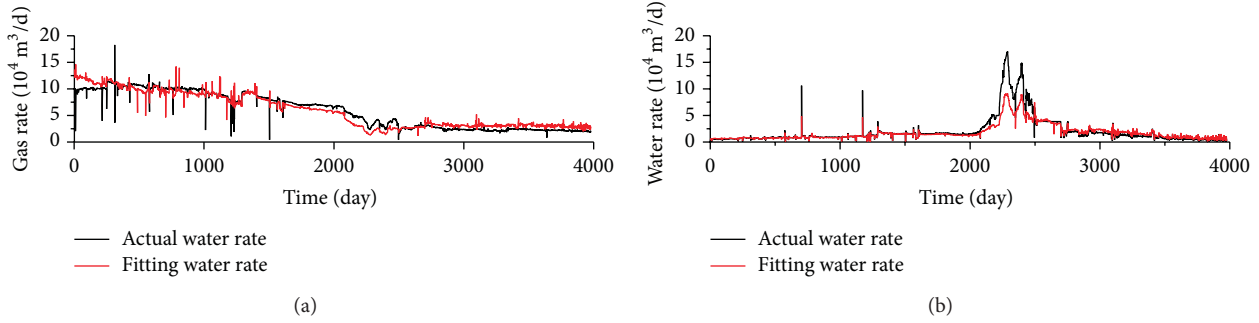


FIGURE 2

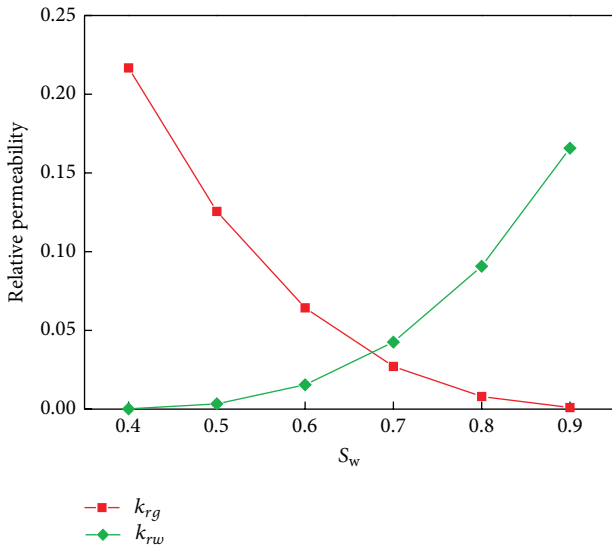


FIGURE 3

TABLE 3: The absolute open flow rates in different production gas water ratios.

GWR ( $10^4 \text{ m}^3/\text{m}^3$ )	$q_{AOF}$ ( $10^4 \text{ m}^3/\text{d}$ )
1	32.76
0.5	31.71
0.2	28.79
0.1	24.61

formation water in the well controlled range is weak when the water invasion intensity is greater than 4. The gas and water phase relative permeability curve in different water saturations is obtained. The results are shown in Figure 3.

4.2. *The IPR Curves of Water Producing Gas Well.* The IPR curves in different production gas water ratios (GWR) are expressed in Figure 4. It is noted that the IPR curves expressed with a left offset when production gas water ratio decreases. Because when the GWR decreases, the water saturation in formation increases, and the flow resistance increases too. It becomes harder to flow in formation when the GWR decreases. The absolute open flow rates ( $q_{AOF}$ ) of

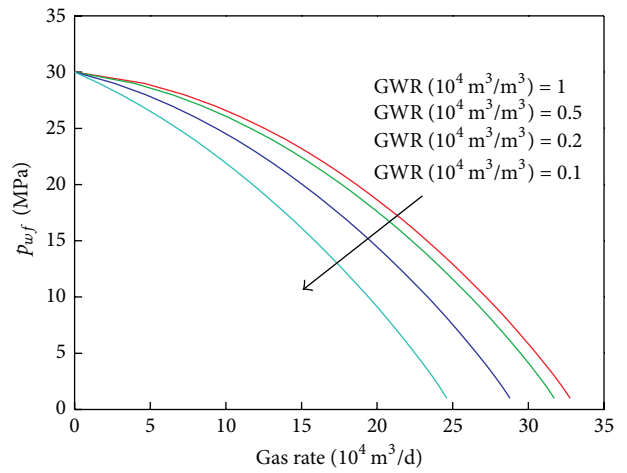


FIGURE 4

water producing gas well in different production gas water ratios can be shown in Table 3. From the curves, when the production gas water ratios is 1, 0.5, 0.2 and 0.1, respectively, the absolute open flow rates reduced 32.76, 31.71, 28.79, and  $24.61 \times 10^4 \text{ m}^3/\text{d}$  accordingly. The absolute open flow rates is reducing by 3.21%, 12.12% and 24.88% when compared to the one whose production gas water ratio is 0.1. It is shown that water invasion will greatly reduce the gas production capacity of water producing gas well.

The IPR curves in different gas soluble coefficient are shown in Figure 5. It can be concluded that the IPR curves expressed with a left offset when the gas soluble coefficient increases. Gas soluble coefficient represents the solubility of gas in water, which lead to a bigger flow resistance. The absolute open flow rates ( $q_{AOF}$ ) of water producing gas well in different gas soluble coefficient can be shown in Table 4. From the curves, it is clearly that when gas soluble coefficient is 0.1, 0.5, 1 and 2, respectively, absolute open flow rates is 32.94, 29.57, 25.91 and  $20.22 \times 10^4 \text{ m}^3/\text{d}$ , respectively. The absolute open flow rates are reduced by 10.23%, 21.34% and 38.62% when compared to the one whose gas soluble coefficient is 0.1. It is shown that the more gas dissolved in the formation water, the more liquid phase will exist in the formation fluid. It will increase the gas flowing resistance and result in the greater productivity impairment.

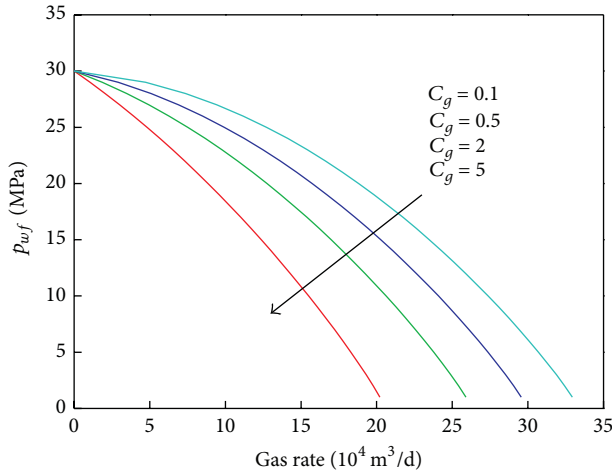


FIGURE 5

TABLE 4: The absolute open flow rate in different gas-soluble coefficients.

$C_g$	$q_{AOF}$ ( $10^4$ m <sup>3</sup> /d)
0.1	32.94
0.5	29.57
2	25.91
5	20.22

## 5. Conclusions

Based on the basic theory of fluid mechanics in porous medium, taking the solution and volatilization of gas and water into consideration, a gas-water two phase IPR equation was established. Combining with gas-water two phase IPR equation, relative permeability equation and material balance equation in the water drive gas reservoir, we deduced the gas-water two phase comprehensive model, which is influenced by laminar coefficient, turbulence coefficient, gas soluble coefficient, water soluble coefficient, relative permeability index, water invasion intensity and single well controlled reserve. The influences of different production gas water ratios and gas soluble coefficients on the absolute open flow rate were discussed. The method proposed in this paper provided a new theoretical method for single well analysis of productivity and inflow performance, and got rid of the limitation that the well productivity can be only determined according to field well test.

## Conflict of Interests

The authors declare that there is no conflict of interests regarding the publication of this paper.

## Acknowledgment

The authors are grateful for financial support from the National Science Fund for Distinguished Young Scholars of China (Grant No. 51125019).

## References

- [1] M. Kelkar, *Natural Gas Engineering*, PennWell Books, 2008.
- [2] L. Xiaoping and Z. Birong, "A new IPR curve of gas-water well in gas reservoirs undergoing simultaneous water production," in *Proceedings of the Technical Meeting/Petroleum Conference of The South Saskatchewan Section*, Petroleum Society of Canada, Regina, Canada, 1999.
- [3] G. Zhu, X. Liu, S. Miao, and S. Gao, "New formation evaluation parameters of low permeability water bearing gas reservoirs and its application," in *Proceedings of the International Oil and Gas Conference and Exhibition in China*, pp. 2683–2690, Society of Petroleum Engineers, Beijing, China, June 2010.
- [4] J. Wang, C. Sun, L. Tang, C. Li, and H. Xu, "Study on fluids flow characteristics of water-gas mutual flooding in sandstone underground gas storage with edge water," in *Proceedings of the 6th International Petroleum Technology Conference*, pp. 5004–5010, Beijing, China, March 2013.
- [5] H. J. Park, J. S. Lim, J. Roh, J. M. Kang, and B. H. Min, "Production system optimization of gas fields using hybrid fuzzy-genetic approach," in *Proceedings of the SPE Europec/EAGE Annual Conference and Exhibition*, pp. 813–820, Society of Petroleum Engineers, Vienna, Austria, June 2006.
- [6] M. A. Cardoso, "Reduced-order models for reservoir simulation," in *Proceedings of the SPE Annual Technical Conference and Exhibition*, Society of Petroleum Engineers, New Orleans, La, USA, 2009.
- [7] Y. M. Han, C. Park, and J. M. Kang, "Estimation of future production performance based on multi-objective history matching in a water-flooding project," in *Proceedings of the SPE EUROPEC/EAGE Annual Conference and Exhibition*, pp. 1222–1233, Society of Petroleum Engineers, Barcelona, Spain, June 2010.
- [8] M. Cancelliere, F. Verga, and D. Viberti, "Benefits and limitations of assisted history matching," in *Proceedings of the Offshore Europe Oil and Gas Conference and Exhibition*, pp. 935–943, Aberdeen, UK, September 2011.
- [9] V. Shelkov, M. Christie, D. Eydinov, D. Arnold, V. Demyanov, and J. Talbot, "Use of multi-objective algorithms in history matching of a real field," in *Proceedings of the SPE Reservoir Simulation Symposium*, pp. 57–67, The Woodlands, Tex, USA, February 2013.
- [10] X. H. Tan, X. P. Li, J. Y. Liu, C. Tang, and J. M. Li, "Pressure transient analysis of dual fractal reservoir," *Journal of Applied Mathematics*, vol. 2013, Article ID 137518, 9 pages, 2013.
- [11] X. H. Tan, X. P. Li, J. Y. Liu, G. D. Zhang, and L. H. Zhang, "Analysis of permeability for transient two-phase flow in fractal porous media," *Journal of Applied Physics*, vol. 115, no. 11, Article ID 113502, 2014.
- [12] X. H. Tan, J. Y. Liu, J. H. Zhao, X. P. Li, G. D. Zhang, and C. Tang, "A pressure transient model for power-law fluids in porous media embedded with a tree-shaped fractal network," *Mathematical Problems in Engineering*, vol. 2014, Article ID 405640, 8 pages, 2014.
- [13] E. Sánchez-Palencia, "Fluid flow in porous media," in *Non-Homogeneous Media and Vibration Theory*, pp. 129–157, 1980.
- [14] J. Bear, *Dynamics of Fluids in Porous Media*, American Elsevier Publishing Company, 1972.
- [15] Ø. Fevang and C. H. Whitson, "Modeling gas-condensate well deliverability," *SPE Reservoir Engineering*, vol. 11, no. 4, pp. 221–230, 1996.

- [16] S. A. Jokhio and D. Tiab, "Establishing Inflow Performance Relationship (IPR) for gas condensate wells," in *Proceedings of the SPE Gas Technology Symposium*, pp. 33–52, Society of Petroleum Engineers, Alberta, Canada, May 2002.
- [17] B. C. Craft, M. F. Hawkins, and R. E. Terry, *Applied Petroleum Reservoir Engineering*, Prentice Hall, New York, NY, USA, 2nd edition, 1991.

## Research Article

# Multiobjective Fuzzy Mixed Assembly Line Sequencing Optimization Model

Farzad Tahriri,<sup>1</sup> Siti Zawiah Md Dawal,<sup>1</sup> and Zahari Taha<sup>2</sup>

<sup>1</sup> Department of Mechanical Engineering, Centre for Product Design and Manufacturing, Faculty of Engineering, University of Malaya, 50603 Kuala Lumpur, Malaysia

<sup>2</sup> Faculty of Mechanical Engineering, Universiti Malaysia Pahang, 26600 Pekan, Pahang Darul Makmur, Malaysia

Correspondence should be addressed to Farzad Tahriri; farzad\_tahriri@hotmail.com

Received 8 November 2013; Revised 20 February 2014; Accepted 11 March 2014; Published 8 May 2014

Academic Editor: Olabisi Falowo

Copyright © 2014 Farzad Tahriri et al. This is an open access article distributed under the Creative Commons Attribution License, which permits unrestricted use, distribution, and reproduction in any medium, provided the original work is properly cited.

It can be deduced from previous studies that there exists a research gap in assembly line sequencing optimization model for mixed-model production lines. In particular, there is a lack of studies which focus on the integration between job shop and assembly lines using fuzzy techniques. Hence, this paper is aimed at addressing the multiobjective mixed-model assembly line sequencing problem by integrating job shop and assembly production lines for factories with modular layouts. The primary goal is to minimize the make-span, setup time, and cost simultaneously in mixed-model assembly lines. Such conflicting goals arise when switching between different products. A genetic algorithm (GA) approach is used to solve this problem, in which trapezoidal fuzzy numbers are implemented for variables such as operation and travelling time in order to generate results with higher accuracy and representative of real-case data.

## 1. Introduction

It is known that an efficient and effective production line sequencing and scheduling are required for manufacturing industries due to the fluctuations in market demand and increasing competition on the global scale. Hence, manufacturers are gearing towards optimizing the design of manufacturing systems in the shortest time possible in order to enhance competitiveness. The production lines of a multistage process can be generally classified as job-shop (JS) and flow-shop (FS) line processing, in which each type complies with a set of sequential operations. Production sequential operation is established in the factories in which the materials undergo a refining process in order to produce a product that is suitable for onward consumption and the components are assembled to make finished articles. Raw materials require a sequence of treatments to render them useful. Development of optimization methods for solving JS and FS problems effectively is of utmost importance to the apparel industry and other manufacturing industries which require similar assembly operations at large. JS and FS involve the assignment of a set of tasks to workstations

(machines) in a predefined sequence while optimizing one or more objectives without violating the restrictions imposed by the production line [1]. Most of the problems involving line balancing and sequencing problem in JS and FS fall within the NP-hard class of combinatorial optimization problems, which results in a critical need to develop efficient algorithms to attain optimum solutions [1–6]. It can be extremely time-consuming for optimum-seeking methods to obtain optimum solutions within a vast search space [2].

Efficient and effective JS and FS sequencing and scheduling is required for recent manufacturing processes in order to achieve higher customer satisfaction and shorter production lead times and enhance competitiveness in the escalating volatile market demand. This emphasizes the significance of just-in-time (JIT) and agile manufacturing in the modern era. To cope with such circumstances, JS and FS assembly lines are shifting towards mixed-model assembly lines, in which multiple models are produced on a constant basis. Therefore, sequencing with multiobjective goals is a critical operation scheduling that directly affects the efficiency of mixed-model production assembly lines for factories with modular layouts. It will be noted that modular layouts are

layouts which integrate JS and FS. Owing to the importance of this issue, this study is aimed at developing a multiobjective mixed-production line sequencing model by implementing genetic algorithms (GAs) and fuzzy logic.

## 2. Mixed-Model Assembly Line Sequencing

Mixed-model assembly lines (MMAL) have been widely used by manufacturers and they play a key role in producing a variety of products. Products with similar characteristics are assembled with different processing times on the same assembly line at very low cost [7–9]. This, in turn, requires the implementation of cost-efficient and flexible production systems. MMAL reduce setup operations to an extent that various models from a common base product can be manufactured in intermixed sequences. However, the observed diversity of MMAL makes thorough sequence planning essential in order to exploit the benefits of assembly line production. These benefits include diversified small lot production and prompt response to sudden changes in demand for models without large inventories [10]. Mixed-model sequencing (MMS) aims at avoiding or minimizing sequence-dependent work overload based on detailed scheduling which explicitly accounts for operation time, worker movement, station borders, and other operational characteristics of the line [10].

Solving the MMS problem involves determining a production sequence for multiple products along a modular layout. In order to reach this goal, manufacturers aim to achieve optimum scheduling times with minimum cost. Furthermore, it is impractical for manufacturers to constantly alter their machine layouts when producing a new product. For companies with fixed factory machine layouts, optimization of production lines is solely based on altering the sequence of production lines. However, this approach poses the following challenges that need to be addressed:

- (1) production of various products using existing facilities such as the number and location of machines, travelling time between the machines, and limited number of workers for different products;
- (2) assignment of parts from different products to the machines, in which the optimum sequence needs to be considered in order to minimize scheduling time. Problems also arise when changing the setup number of the machines;
- (3) assignment of parts to other parts during product assembly, in which the parts that are ready for assembly need to be considered in order to minimize the scheduling time required to assemble the product;
- (4) identification of the best minimum setup number and setup cost sequencing, in which the above mentioned issues need to be considered simultaneously.

It can be seen that identifying the best scheduling and sequencing production line is a challenging task, particularly for the production of a mixed-model from a large number of providers with multiple objectives. MMS is a NP-hard

problem which requires an effective model. A unique and stable model is needed to facilitate MMS in the production of mixed products in a manufacturing environment with multiple parts, machines, products, and assemblies in order to minimize scheduling time, idle time of the machines, setup number, and setup cost as well as to maximize the number of products and assembly of various products. An effective model provides companies with a means to reschedule their production lines based on the changing demands of a flexible market. The effective utilization of MMAL requires solving two problems in a sequential manner, as follows.

- (1) Levelling workloads for stations on the line: this is known as line design and balancing.
- (2) Maintaining a constant rate of usage for each part used on the production line: this involves determining the production sequence for various models.

The first goal involves sequencing the mixed-models in order to achieve a balanced workload at each assembly station, whereas the second goal involves sequencing the mixed-models in order to minimize variations in the usage of various parts and components over time [8, 9, 11]. A number of MMS studies attempted at solving mixed-model sequencing problems using sequencing procedures that will optimize various system measures such as throughput, scheduling time, number of stations, idle time, flow time, line length, work-in-process, and raw material demand deviations [12–16].

Zhu et al. [17] studied the complexity of product variety of MMAL defined by the operators such as selection of parts, tools, and fixtures as well as assembly procedures in sequence planning. The aim was to reduce manufacturing complexity in a multiproduct, multistage, manual assembly line environment. The methodology was developed to determine optimum assembly sequences which will minimize system complexity. Rekiek et al. [18] and De Lit et al. [19] developed an approach which integrates product family design (including assembly sequences) with the assembly system so that multiple products can be assembled on the same line. A new alternative for mixed-model assembly for low-volume manufacturing environments was investigated by Heike et al. [7]. The efficient utilization of labour and/or machinery presents significant challenges. The models developed focus on evaluating and understanding different alternatives for mixed-model assembly in the aerospace industry. These models include one linear and two nonlinear programs which are formulated to evaluate constant and variable scheduling time policies. The models were successfully implemented on an airplane assembly process characterized by low-volume manufacturing. Bukchin et al. [20] proposed a mathematical formulation for MMAL designs based on the make-to-order production policy. Hence, the arrival sequence is randomly distributed according to demand proportions, rendering the balancing procedure an important aspect of the design process. An integrated machine tool selection and sequencing model was proposed by Moona et al. [21]. The model determines machine visiting sequences for all part types, such that the total production time for

the production order is minimized and the workloads between machine tools are balanced. Numerical experiments were carried out using problems of various sizes in order to demonstrate the efficiency of the proposed GA on the integrated machine tool selection and sequencing problem.

Khan and Day [22] introduced a knowledge-based design methodology (KBDM) for automated and manual assembly lines, which can be applied equally well to single, multi-, and mixed-product assembly lines with either deterministic or stochastic operation times. Mendes et al. [23] developed simulation models for varying the levels of demand and line configurations and utilized a mixed-model PC camera assembly line. The simulation models were used to compare flow time and resource utilization, which provide operational support and help fine-tune line configurations. Joly and Frein [24] investigated a set of vehicles within an industrial environment in order to minimize manufacturing costs by considering assembly and paint shop objectives. The approach was implemented to solve a problem with a monoobjective function. One heuristic (a progressive, construction-sequence algorithm) and three metaheuristics (simulated annealing, variable neighbourhood search, and an evolutionary algorithm) were described and compared.

The use of GA for mixed-model sequencing line problems is discussed as follows. Ghosh and Gagnon [25] introduced a mathematical programming model and an iterative GA-based procedure for MALBP with parallel work stations, in which the goal was to maximize the production rate of the line for a predetermined number of operators. An intelligence-based GA was developed by Norozi et al. [26] in order to tackle the complexity of sequencing in parallel MMAL. A spreading and cutting sequencing (SCS) model using GA was implemented by Wong et al. [27] to solve the sequencing problem of a computerized fabric cutting system used in the garment industry. The job sequence of spreading and cutting operation can be optimized by reducing the completion time for daily operation of fabric spreading and cutting as well as improving the utilization of machines. Ponnambalam et al. [28] studied the performance of GAs for a multilevel MMAL sequencing problem. Both single objective and multiple objectives were considered. The main objective of the multiobjective GA was to minimize the total utility work levelling, parts usage, and total setup cost. Development of optimization methods for solving JS and FS that are involving assembly line balancing/sequencing in mixed-model problems falls under the NP-hard class problem. Optimization involves exploiting the capabilities of mathematical programming in order to minimize the overall make-span and setup objectives for sets of single lines [26]. Evolutionary computing is a research area within computer science for solving combinatorial optimization and complex problems based on the principles of generic population-based heuristic techniques. In the advent of metaheuristic algorithms in recent years, numerous complex scheduling problems have been studied and solved using metaheuristic search techniques such as ant colony optimization (ACO), tabu search (TS), genetic algorithm (GA), and simulated annealing (SA). Metaheuristic algorithms are used

to overcome the complexity of sequencing in assembly lines [26].

GA was introduced by David Goldberg based on the procedure of natural mechanism and natural genetics. The population is composed of a collection of chromosomes in which each string is encoded and the problem is solved as a finite length of genes [26]. Good gene characteristics produce new generations. After several evolutions, the genes become highly adaptive to a given environment [29]. GAs have been proven to be highly effective for achieving optimum or near-optimum solutions in complex real-world optimization problems. However, GAs are limited by the fact that their performance is very sensitive to parameter settings [29]. GA design consists of two key steps, namely, genetic operations and parameter settings [29]. The genetic operations involve choosing a suitable selection method. The typical methods for selection are roulette, tournament, stochastic uniform, remainder, and uniform selection. Selection is the only operation of evolution and thus choosing a suitable selection method is important. Parameter settings involve setting the required parameters and variables for controlling the algorithms such as population size, number of generations, the number of selected candidates, crossover rate, and mutation rate [30].

### 2.1. Multiobjective Mixed-Production Line Optimization.

Multiobjective formulations are realistic models of numerous complex engineering optimization problems. In most real-life problems, the objectives often contradict one another and optimizing a particular solution with respect to a single objective may give undesirable results for other objectives. Being a population-based approach, GA is well suited to solve multiobjective optimization problems [31]. A generic single-objective GA can be modified to search for a set of multiple nondominated solutions in a single run. The ability of GAs to simultaneously search different regions of a solution space makes it possible to search a diverse set of solutions for difficult problems with nonconvex, discontinuous, and multimodal solution spaces. Multiobjective optimization problems can be found in various fields, such as product and process design, finance, aircraft design, oil and gas industry, automobile design, or wherever optimum decisions are needed, by considering the trade-offs between multiple conflicting objectives. If more than one criterion is to be treated simultaneously, then it is a multiobjective optimization problem. Maximizing the profit and minimizing the cost of a product, maximizing the performance and minimizing fuel consumption of a vehicle, and minimizing the weight while maximizing the strength of a particular component are all examples of multiobjective optimization problems. If the multiobjective problem is well formed, there will not be a single solution that simultaneously minimizes each objective to its fullest. In each case, the aim is to search for a solution in which each objective has been optimized to an extent that if the objectives are optimized further, other objectives will suffer as a result. The search for an optimum solution and quantifying the extent to which this solution is superior compared to other such solutions

(note that there will generally be many solutions) are the goal when setting up and solving a multiobjective optimization problem. Most of the real-world decision problems involve multiple conflicting objectives that need to be tackled while adhering to the various constraints. In multiobjective problems, there may not exist a solution which is the best with respect to all objectives. It will be highlighted that there will be a set of solutions which are superior to other solutions in the search space when all objectives are considered but are inferior to the solutions for one or more objectives. These solutions are called nondominated solutions [32].

The job-shop scheduling problem with sequence-dependent setup times (SDST-JSP) is a generalization of the classical JSS, in which the setup operation of a machine is required when the machine switches between two jobs. The common goal of SDST-JSP is to minimize the completion time of the last job (make-span). SDST-JSP has been investigated by a number of researchers. A new multiobjective GA (MOGA) was introduced by Zacharia and Nearchou [33] for solving fuzzy assembly line balancing of SALBP-2 comprising multiple objectives, that is, minimizing the fuzzy scheduling time, balancing the fuzzy delay time, and smoothing the fuzzy index of the line. McMullen [34] proposed a technique to generate production sequences, whereby the number of setups and scheduling flexibility are considered. These objectives are inversely correlated, which poses a challenge for optimizing both objectives simultaneously. An efficient frontier approach was exploited for problems where simultaneous maximization of flexibility and minimization of setups are desired. McMullen [35] presented a relatively new approach using ACO to address a two-objective production-sequencing problem by stimulating the artificial intelligence agents of virtual ants to obtain desirable solutions for manufacturing logistics. The first objective involves minimizing the number of setups, while the second objective involves optimizing the stability of material usage rates. McMullen [36] developed a technique which addresses a JIT production-scheduling problem consisting of two objectives, namely, minimization of setups between product variants and optimization of schedule flexibility. These objectives are inversely correlated, which poses a challenge in attaining desirable results for both objectives. An efficient frontier approach was employed to address the problem, which yields desirable sequences for both objectives. The artificial neural network approach using Kohonen self-organizing map (SOM) was implemented to determine sequences which are desirable in terms of the number of setups and flexibility. McMullen and Tarasewich [37] introduced an efficient frontier approach to support sequencing decisions. A beam-search heuristic approach was used to effectively generate efficient frontiers. Rahimi-Vahed et al. [8] addressed a multiobjective sequencing problem using a mathematical formulation which considers three objectives simultaneously. These objectives are minimizing the total utility work, minimizing variations in the total production rate, and minimizing the total setup cost. The scatter search methodology was used to generate a set of solutions that approximates the nondominated frontiers where simultaneous minimization

of the above mentioned objectives is desired. Javadi et al. [9] proposed a fuzzy goal programming approach to solve a multiobjective mixed-model assembly line sequencing problem for a JIT production system. Three objectives are solved simultaneously as mentioned in [8]. These objectives comprise minimization of the total utility work and variations in the total production rate and total setup cost. The fuzzy goal programming based approach was proposed to solve the problem because of the conflicting objectives. Bard et al. [38] investigated the sequencing of MMAL, which was perceived as a multiobjective problem. They developed a method to minimize the overall line length and maintain a constant rate for part usage. The problem was solved using the weighted sum and tabu search methods. McMullen [39] focused on minimizing the number of setups and maintaining a constant rate for part usage, in which the multiobjective problem was solved using the TS method. McMullen and Frazier [40] developed an SA method for the model used by McMullen [39] as well as TS method. Ponnambalam et al. [28] compared the performance of selection mechanisms (i.e., Pareto stratum-niche cubicle and selection based on scalar fitness function values). The objectives of their study were to minimize variations in part usage, total utility work, and setup cost. The results indicated that the GA which incorporates Pareto stratum-niche cubicle exhibits superior performance compared to GAs with other selection mechanisms. Giard and Jeunet [41] presented an integer programming formulation for sequencing in mixed-model assembly lines, whereby the number of temporarily hired utility workers and the numbers of sequence-dependent setups are optimized simultaneously via a cost function. The objective function is a cost function involving two elements, namely, the cost associated with additional utility workers and setup cost.

## 2.2. Application of Fuzzy Numbers in Assembly Line Models.

Fuzzy set theory accounts for the ambiguities involved when assigning processing and scheduling times as well as the uncertainty contained within such time variables [42]. The data of real-world problems are imprecise, vague, or uncertain, in which the input data can only be estimated within this uncertainty. The uncertainty may be represented by a fuzzy number. The membership function of fuzzy data represents the grade of satisfaction of the decision-maker. The concept of fuzzy numbers was introduced to treat imprecise data such as the processing and travelling time of each job [43, 44]. The time variables were represented by triangular fuzzy numbers, which allow practitioners to account for ambiguities when assigning processing and scheduling times, while maintaining the variability of the stochastic environment [42].

Gen et al. [43] and Tsujimura et al. [44] proposed a new method for treating the data of real-world problems by introducing a fuzzy assembly line balancing based on GA. Fuzzy variables were implemented by Fonseca et al. [42] in order to solve assembly line balancing. Fuzzy set theory is a viable alternative method for modelling and solving stochastic assembly line balancing problems. The variability and uncertainty in assembly line balancing problems have

been traditionally modelled by statistical distribution. A novel fuzzy extension of the simple assembly line balancing problem (SALBP) was proposed by Zacharia and Nearchou [33]. The fuzzy job processing times reflect the uncertainty, variability, and imprecision with which real-world production systems are afflicted. The job processing times are formulated by triangular fuzzy membership functions. A new MOGA was introduced for solving the fuzzy SALBP in order to minimize the fuzzy scheduling time, fuzzy balance delay time, and fuzzy smoothness index of the line.

*2.3. Summary of Previous Studies and Findings.* It can be observed from the literature review that the majority of works are focused on an assembly line balancing and only a few papers address mixed-assembly line sequencing. Hence, mixed-assembly line sequencing needs to be investigated in detail. Most papers focused on the number and order of mixed-models, neglecting the assignment of a product's sub-parts to their respective machines (job sequence). In addition, most papers overlook the designation and adaptation of parts with other parts as well as their final assembly. It is found that the production of mixed-models is influenced by a number of criteria, which limits the applicability of the research results in real production line conditions. It will be highlighted that only one criterion was considered in previous works such as operation line, and therefore other factors such as the travelling time of the conveyor were neglected. Deterministic time has also been of interest in most studies. It will be highlighted that only assembly line balancing was carried out in previous works in order to minimize the prediction time for input data, which include the travelling and processing times for each available job. Although the results from mixed-assembly line sequencing studies are applicable in real manufacturing environments, little is known about fuzzy mixed-model assembly line sequencing. Hence, it is evident that there is a lack of studies which implements the concept of fuzzy time in order to minimize the prediction time of input data.

In general, the research papers can be classified into two groups, whereby the first group focuses solely on objective criteria, while the second group focuses on multiobjective investigations. A critical evaluation of previous works clarifies that addressing these objectives involves the development of various methods, in which MMAL sequencing is the ideal method for a single objective. Comparison of various GA methods reveals that multiobjective studies have not been investigated extensively, unlike single-objective studies. Much effort has been made to intensify and accelerate the running of GA methods to achieve optimum results. Although mixed-model assembly line sequencing is of prime importance, there is a lack of studies which focus on this topic. In this paper, a hybrid method is proposed, in which mixed-model assembly line sequencing is integrated with the operating and travelling time in the form of fuzzy numbers of a multiobjective optimization problem. The hybrid method will provide manufacturers with an ideal and feasible alternative since mixed-model assembly line sequencing is integrated into a software application. This has been ignored

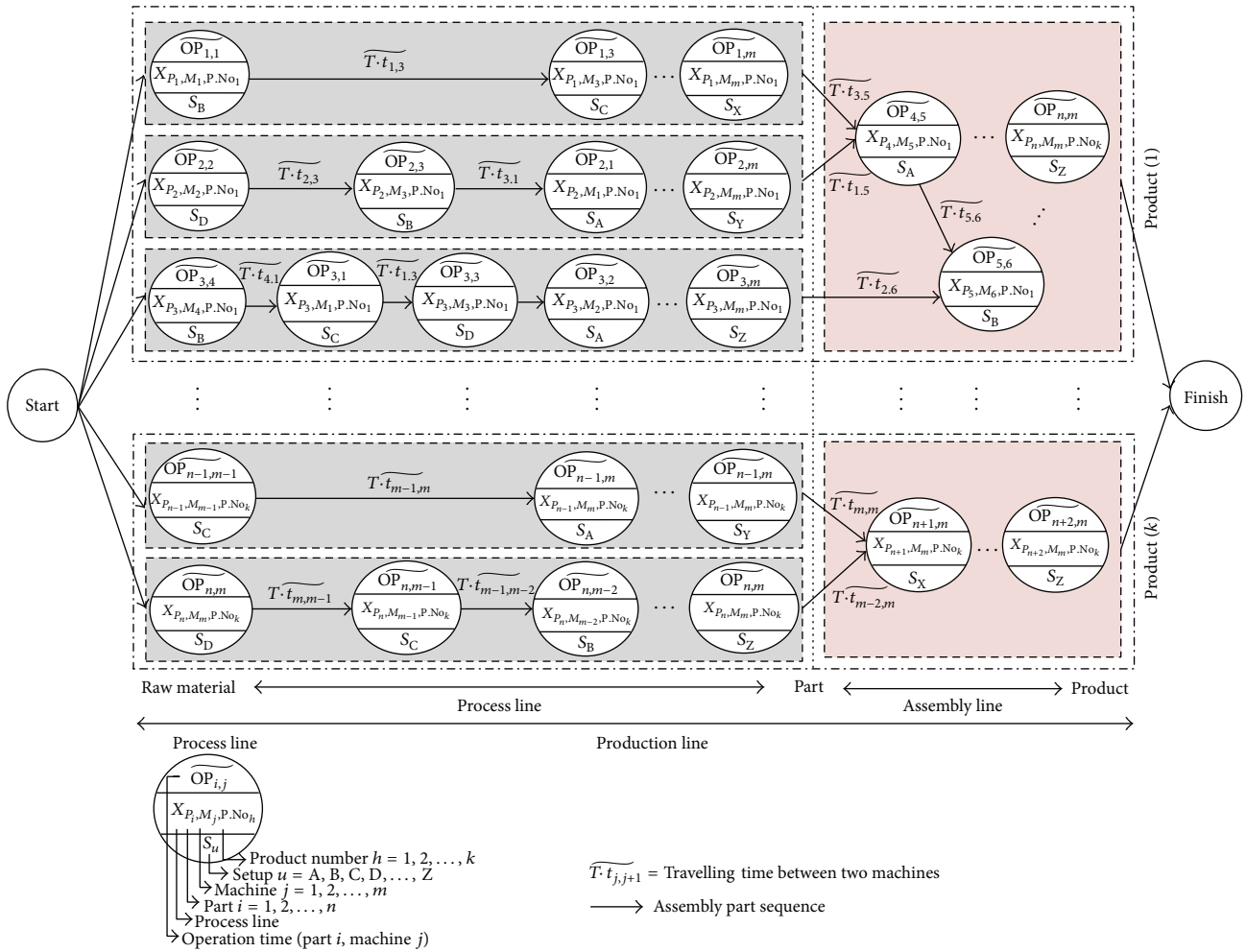
in previous works and much effort is needed to address the above issue.

### 3. Problem Definition and Assumptions

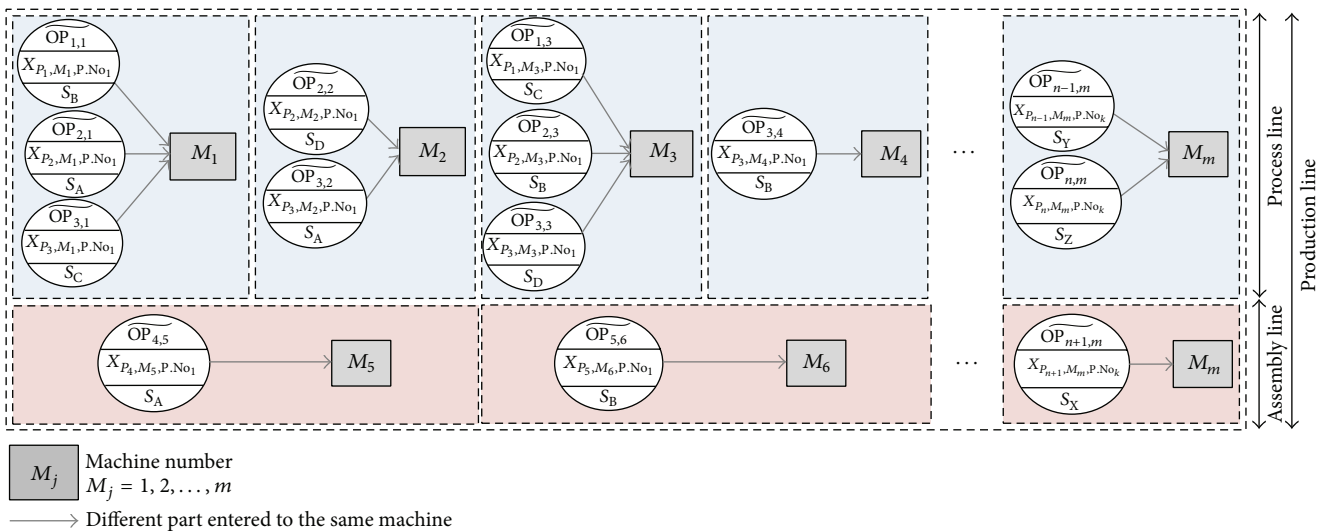
In a highly competitive market, companies try to produce various kinds of products to meet market demand. One manufacturing problem that is often associated with scheduling practices is mixed-model production line sequencing as shown in Figure 1. Solving this problem involves determining the optimal sequence for jobs ( $J_q$ ) which includes the assigned part ( $P_i$ ) to machine ( $M_j$ ), considering each of the jobs with the availability of the machines ( $M_j$ ) in job-shop. Moreover, with the need to solve the problem of determining the jobs ( $J_q$ ) which includes assembly of the parts ( $P_i$ ) in the assembly line for multiple products along a modular layout. The main solid arrows in Figure 1(a) represent the sequence to produce the parts, followed by a discrete part manufacturing assembly, leading to the final product. Likewise, the elapsed traveling time between machines for manufacturing a part is given by  $(\overline{T \cdot t_{i,j}})$ . To satisfy the no-wait restriction, the completion time of the operation ( $\overline{OP_{i,j}}$ ) must be equal to the earliest time to start the operation. There must not be any waiting time in the processing of any consecutive operations of each of the jobs. Figure 1(b) represented by gray lines provides insight into problems involving the determining of the optimal number of setup tool changes sequencing ( $S_u$ ) of jobs ( $J_q$ ) assigned to "m" machines, throughout the job-shop and assembly production line.

The following assumptions are taken in the multiobjective evaluation: (i) all jobs are available at zero time; (ii) the conveyor (operator movement) moves at a constant speed. If job overlapping occurs, the remaining work will be accomplished by temporary operators; (iii) the job operation begins when the part enters the machine. Once the job is completed, the operator will move the part to the next machine; (iv) at a given time, only one job can be processed on one machine; (v) the operator is assigned to each selected part that is assigned to each machine; (vi) the position of the machines on the assembly line varies from one another depending on the user input, which is based on the travelling time; (vii) once operation has started on a machine, it cannot be interrupted before completion, either on or between the machines; (viii) the assembly line can process jobs for a product family, which is described by a joint priority matrix; (ix) the processing time varies for different jobs and these jobs are allocated to the same machine, no matter what the optimum processing time for each job might be; (x) the demand for all products as well as the sequence of the products entering the assembly line is predetermined; (xi) the completion time for all jobs is represented by a fuzzy number.

The goal is to minimize the make-span or total completion time and minimize the number of change tools setups for each machine in mixed-model production line sequencing of all the jobs without waiting between successive operations of a job by using the fuzzy operation and travelling time which makes the solution more realistic.



(a) The precedence problem in parts of the raw material process for producing a product



(b) The precedence problem of parts assigned to each machine based on changing the machine setup

FIGURE 1: The precedence of a multiobjective mixed-model production line sequencing problem.

#### 4. Model Derivation

The objectives of the function value, for multiobjective mixed-production assembly line sequencing, are categorized into two main objectives: (1) minimizing the total make-span and (2) minimizing the total setup number as discussed in the following.

*4.1. Minimizing the Total Make-Span.* The step involves evaluating each chromosome based on the make-span by considering the product number and assembly sequence for a gene code ( $X_q$ ). The  $Y_1, Y_2, Y_3$ , and  $\widetilde{S \cdot t}(X_q)$  are computed in which ( $X_q$ ) are calculated as follows.  $Y_1$  is determined by checking the start time ( $\widetilde{S \cdot t}$ ) of the parts ( $P_i$ ) entering the machines ( $M_j$ ), based on the sequence assigned to the machines. This is expressed by

$$Y_1 = \begin{cases} 0, & P(X_q) \neq P(X_{q'}) \\ \widetilde{S \cdot t}(X_{q'}) + \widetilde{OP}(X_{q'}) + \widetilde{T \cdot t}(X_{q'}), & P(X_q) = P(X_{q'}) \end{cases} \quad (1)$$

$$q' = q - 1, q - 2, \dots, q - (q - 1), \quad q = 1, \dots, e.$$

$Y_2$  is determined by checking the start time ( $\widetilde{S \cdot t}$ ) machine's availability ( $M_j$ ) assigned to produce the parts ( $P_i$ ), as given by

$$Y_2 = \begin{cases} 0, & M(X_q) \neq M(X_{q'}) \\ \widetilde{S \cdot t}(X_{q'}) + \widetilde{OP}(X_{q'}), & M(X_q) = M(X_{q'}) \end{cases} \quad (2)$$

$$q' = q - 1, q - 2, \dots, q - (q - 1), \quad q = 1, \dots, e.$$

$Y_3$  is then determined by checking the start time ( $\widetilde{S \cdot t}$ ) of the parts ( $P_i$ ) entering the machines ( $M_j$ ) based on the sequence of the part's assembly (A.S.<sub>p</sub>) for each product (P.No.<sub>h</sub>) as given by (5) and (6). For each  $X_q$ , where  $q = 1, 2, \dots, e$ , note that the product number (P.No( $X_q$ )) and assembly sequence (A.S( $X_q$ )) are important. Equations (3) through (6) are given below.

(i) Consider

$$\text{If } A.S(X_q) = 0 \implies Y_3 = 0, \quad q = 1, 2, \dots, e \quad (3)$$

$$\text{If } A.S(X_q) \neq 0 \implies \text{compares} = P.No(X_q), \quad (4)$$

$$P.No(X_{q-1}).$$

(ii) If  $P.No(X_q) = P.No(X_{q-1})$ , then

$$Y_3 = \begin{cases} \widetilde{S \cdot t}(X_{q-1}) & A.S(X_q) = A.S(X_{q-1}) \\ \widetilde{S \cdot t}(X_{q-1}) + \widetilde{OP}(X_{q-1}) \\ \quad + \widetilde{T \cdot t}(X_{q-1}), & A.S(X_q) \neq A.S(X_{q-1}) \end{cases} \quad (5)$$

$$q = 1, 2, 3, \dots, e.$$

(iii) If  $P.No(X_q) \neq P.No(X_{q-1})$  when searching gene code  $X_{q'}$ , where  $q' = q - 1, q - 2, \dots, q - (q - 1)$ , go backwards one by one until  $P.No(X_q) = P.No(X_{q'})$  is met as follows:

$$Y_3 = \begin{cases} \widetilde{S \cdot t}(X_{q'}) & A.S(X_q) = A.S(X_{q'}) \\ \widetilde{S \cdot t}(X_{q'}) + \widetilde{OP}(X_{q'}) \\ \quad + \widetilde{T \cdot t}(X_{q'}), & A.S(X_q) \neq A.S(X_{q'}) \end{cases} \quad (6)$$

$$q' = q - 1, q - 2, \dots, q - (q - 1), \quad q = 1, 2, 3, \dots, e.$$

The start time is obtained using (7), in which  $Y_1, Y_2, Y_3$  are determined from the previous steps. Consider

$$\widetilde{S \cdot t}(X_q) = \text{Max}(Y_1, Y_2, Y_3); \quad X_q, q = 1, 2, \dots, e. \quad (7)$$

*Note.* In the first run, if  $Y_1 = Y_2 = Y_3 = 0$ , then  $\widetilde{S \cdot t} = \text{Max}(Y_1, Y_2, Y_3) + \widetilde{T \cdot t}$ .

The make-span fitness function is then calculated for all chromosomes using

$$T.C.T = \text{Max} \widetilde{S \cdot t}(X_q) + \widetilde{OP}(X_q); \quad q = 1, 2, \dots, e. \quad (8)$$

*4.2. Minimizing the Setup Number.* In many industries, sequence-dependent setups are considered as an important item in assembly operations. The model considering sequence-dependent setups is considered in this paper. The machine number  $M(X_q)$  and the setup number  $S(X_q)$  are defined for the element ( $X_q$ ) in the chromosome, where  $q = 1, 2, \dots, e$ ; the total setup number at the beginning is T.S.N = 0. All the genes  $X_q$ , where  $q = 1, 2, \dots, e$ , in the chromosomes one by one will be checked and total setup number (T.S.N) based on the  $M(X_q)$  and  $S(X_q)$  has been determined for all  $X_q$  as shown in

(i)

$$\text{If } M(X_q) \neq M(X_{q'}), \quad \text{where } q = 1, 2, 3, \dots, e,$$

$$\text{and } q' = q - 1, q - 2, \dots, q - (q - 1) \quad (9)$$

then T.S.N = T.S.N + 1;

(ii)

$$\text{If } M(X_q) = M(X_{q'}), \quad \text{where } q = 1, 2, 3, \dots, e,$$

and  $q' = q - 1, q - 2, \dots, q - (q - 1)$  then

$$T.S.N = \begin{cases} T.S.N + 1 & S(M(X_q)) = S(M(X_{q'})) \\ T.S.N + 0 & S(M(X_q)) \neq S(M(X_{q'})) \end{cases} \quad (10)$$

$$q = 1, 2, 3, \dots, e, \quad q' = q - 1, q - 2, \dots, q - (q - 1).$$

#### 5. Fuzzification of the Mixed-Model Line Sequencing

In order to develop a fuzzy version of the mixed-model line sequencing, operation and travelling time had to represent a fuzzy number, which is applied for the processing

and scheduling time of each robot and machine. The fuzzy sets that are most appropriate to represent these values are triangular fuzzy numbers (TFN) due to the nature of the processing and scheduling times. Rather than assigning a specific value for each time variable as in the case of deterministic time methods, TFN establish extreme points to represent the most and least likely values of the individual variables. The use of TFN in-time modelling enables users to account for variability and ambiguity, similar to statistical distributions. However, TFN differ from statistical distributions such that they do not require prior knowledge or historical data when establishing their values. This is a major advantage of using TFN compared to statistics. TFN are achieved by defining the existing deterministic time as the most likely values for the new TFN. This implies that the deterministic value represents the fuzzy element in the set, with a membership value of 1. A value of 1 is added or subtracted from the most likely values in order to get the least likely values for the new TFN, with a membership value of 0. This same procedure is applied to adapt the deterministic scheduling times in the fuzzy domain [42]. No major changes are required when adapting these heuristics to handle fuzzy processing and scheduling times.

## 6. Solution Algorithm

In this study, a multiobjective optimization model is developed for a mixed-model process, comprising the manufacture of parts, assignment of parts to their respective machines, and assembly of parts to form the final products. The multi objective mixed model involves minimizing the make-span and setup cost. The operation time and travelling time are represented by fuzzy numbers. It will be highlighted that the steps for GA modelling include model, constraints, fitness function, and satisfying multiple objectives within the domain of model restrictions, fitness function, and multiobjective cases. These steps are carried out for various types of applications and include input data, fuzzy variables, and initialization of parameters, evaluation, crossover rate, mutation rate, and termination. The input data are coded by considering the sequence of part production stages, sequence of product assembly, and sequence of part allocation to each machine during the initialization of parameters. The proposed model consists of input data and fuzzy variables. Care is taken to ensure that the setup and operation time for each machine as well as the travelling time of the parts between various machines are accounted for. The evaluation stage involves developing the multiobjective fitness functions. Nine rules are used to control the crossover rate during the crossover stage, whereas eight rules were used to control the mutation rate during the mutation stage. Two rules are designed for the termination stage in order to control termination and gain optimum results. Sorting, selection of tournament candidates, elitism, and new population size were performed based on the existing conditions.

The model is developed based on the works of [1, 5, 8, 28, 34, 45, 46]. A contribution of this paper is the development of a multiobjective fuzzy mixed production line sequencing optimization model using the genetic algorithm approach

by integrating job-shop and assembly production lines for factories with modular layouts. The significance of this model is for those factories who want to produce the various kinds of products with fixed machine just by changing the sequencing of the products. The model helps the manager to sequence and schedule the production line easily and accurately by taking the market demand into consideration. The line sequencing is optimized based on the make-span and also the setup number of the production line. The flow chart of the proposed multiobjective fuzzy mixed-production assembly line sequencing model is shown in Figure 2.

## 7. Development of Multiobjective Genetic Algorithm

The procedure used in the development of the model is described in detail as follows.

*Step 1* (input data). The first step involves identifying the machine number ( $M_j$ ) such as CNC, NC, and robot, as well as assigning the parts ( $P_i$ ) to their respective machines and robots based on the production and assembly line sequence. Also, it needs to identify the fuzzy completion time of the operation ( $(\overline{OP})_{i,j}$ ) and fuzzy traveling time between machines in order to manufacture a part by  $((\overline{T \cdot t})_{i,j})$ .

*Step 2* (initialization of parameters). Initialization involves setting the parameters of the GA, creating the scores for the simulation, and creating the first generation of chromosomes based on the Notations section. The results of the model will depend on the difficulties encountered during production planning and sequencing. The general schematic for reading data in mixed-production assembly line problems is presented in Figure 3. Figure 3 shows the number of finished products, the number of tasks involved in the total production line ( $J_q$ ), the order of parts in the assembly ( $A.S._p$ ), and the setup of each machine ( $S_u$ ). Figure 3 also shows the number of parts ( $P_i$ ) and the order for manufacturing each part. For example, the user proceeds to the next item (part) once the order of the manufacturing process is completed for each part.  $M_j$  represents the number of machines used for manufacturing parts and various products. The dashed arrows illustrate the coherence between these machines ( $M_j$ ) during various phases of the production line. The fuzzy operation time ( $\overline{OP}_{i,j}$ ) and fuzzy traveling time ( $\overline{T \cdot t}_{i,j}$ ) are presented in Figure 3. The first column of Figure 3 (i.e., gene code ( $X_q$ )) shows the coding of each row, which will be discussed later.

From the data shown in Figure 3, the number of existing gene codes in the first column represents empty chromosomes ( $X_i$ ), which are formed based on the job numbers. Once the chromosomes have been formed, the chromosomes will be filled with numbers via stochastic repeating. The numbers vary between 0 and the maximum number of genes in the chromosomes. The gene codes are filled up by random numbers, neglecting the encoding sequence of the produced chromosomes. Once the chromosomes have

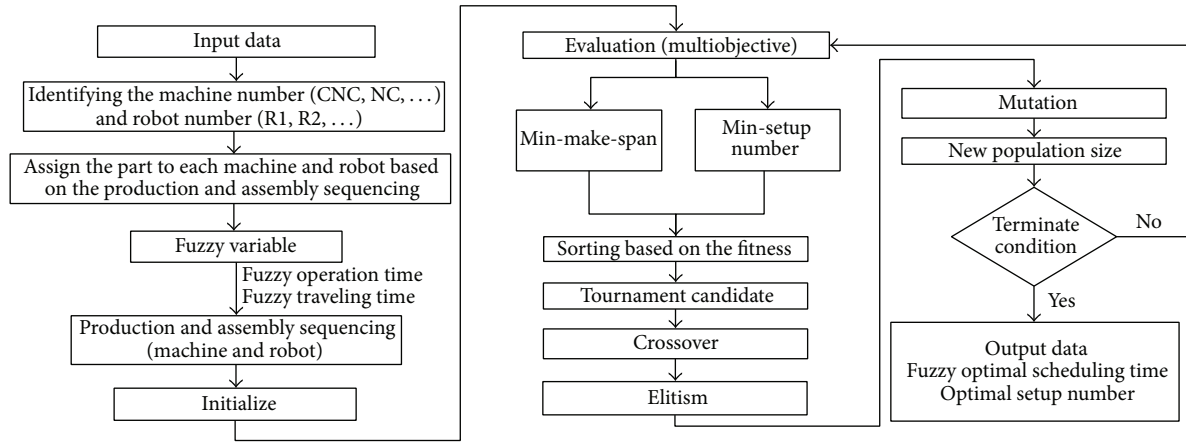


FIGURE 2: Flow chart of the proposed multiobjective fuzzy mixed-production assembly line sequencing model.

Gene code ( $X_q$ )	Jobs ( $J_q$ )	Product number ( $P.No._h$ )	Assembly sequence ( $A.S._p$ )	Setup ( $S_u$ )	Part ( $P_i$ )	Machine ( $M_j$ )	Fuzzy operation time ( $\overline{OP}$ )	Fuzzy travelling time ( $\overline{T \cdot t}$ )
1	$J_1$	$P.No_1$	$A.S._0$	$S_A$	$P_1$	$M_1$	$\overline{OP}(a_0, b_0, c_0)$	$\overline{T \cdot t}(a_0, b_0, c_0)$
2	$J_2$	$P.No_1$	$A.S._0$	$S_A$	$P_1$	$M_3$	$\overline{OP}(a_1, b_1, c_1)$	$\overline{T \cdot t}(a_1, b_1, c_1)$
⋮	⋮	⋮	⋮	⋮	⋮	⋮	⋮	⋮
⋮	⋮	$P.No_1$	$A.S._0$	$S_A$	$P_1$	$M_m$	⋮	⋮
⋮	⋮	$P.No_1$	$A.S._0$	$S_A$	$P_2$	$M_2$	⋮	⋮
⋮	⋮	$P.No_1$	$A.S._0$	$S_B$	$P_2$	$M_3$	⋮	⋮
⋮	⋮	$P.No_1$	$A.S._0$	$S_A$	$P_2$	$M_1$	⋮	⋮
⋮	⋮	⋮	⋮	⋮	⋮	⋮	⋮	⋮
⋮	⋮	$P.No_1$	$A.S._0$	$S_B$	$P_2$	$M_m$	⋮	⋮
⋮	⋮	$P.No_1$	$A.S._0$	$S_C$	$P_3$	$M_4$	⋮	⋮
⋮	⋮	$P.No_1$	$A.S._0$	$S_A$	$P_3$	$M_1$	⋮	⋮
⋮	⋮	$P.No_1$	$A.S._0$	$S_A$	$P_3$	$M_3$	⋮	⋮
⋮	⋮	$P.No_1$	$A.S._0$	$S_B$	$P_3$	$M_7$	⋮	⋮
⋮	⋮	⋮	⋮	⋮	⋮	⋮	⋮	⋮
⋮	⋮	$P.No_1$	$A.S._0$	$S_A$	$P_3$	$M_m$	⋮	⋮
⋮	⋮	$P.No_1$	$A.S._1$	$S_B$	$P_4$	$M_6$	⋮	⋮
⋮	⋮	$P.No_1$	$A.S._2$	$S_C$	$P_5$	$M_7$	⋮	⋮
⋮	⋮	⋮	⋮	⋮	⋮	⋮	⋮	⋮
⋮	⋮	$P.No_1$	$A.S._v$	$S_A$	$P_n$	$M_m$	⋮	⋮
⋮	⋮	$P.No_2$	$A.S._0$	$S_B$	$P_4$	$M_5$	⋮	⋮
⋮	⋮	$P.No_2$	$A.S._0$	$S_A$	$P_4$	$M_2$	⋮	⋮
⋮	⋮	$P.No_2$	$A.S._0$	$S_A$	$P_4$	$M_4$	⋮	⋮
⋮	⋮	⋮	⋮	⋮	⋮	⋮	⋮	⋮
⋮	⋮	$P.No_2$	$A.S._0$	$S_A$	$P_4$	$M_m$	⋮	⋮
⋮	⋮	$P.No_2$	$A.S._0$	$S_B$	$P_5$	$M_4$	⋮	⋮
⋮	⋮	$P.No_2$	$A.S._0$	$S_A$	$P_5$	$M_5$	⋮	⋮
⋮	⋮	$P.No_2$	$A.S._0$	$S_A$	$P_5$	$M_6$	⋮	⋮
⋮	⋮	⋮	⋮	⋮	⋮	⋮	⋮	⋮
⋮	⋮	$P.No_2$	$A.S._0$	$S_C$	$P_5$	$M_m$	⋮	⋮
⋮	⋮	$P.No_2$	$A.S._1$	$S_B$	$P_6$	$M_5$	⋮	⋮
⋮	⋮	⋮	⋮	⋮	⋮	⋮	⋮	⋮
⋮	⋮	$P.No_2$	$A.S._v$	$S_A$	$P_n$	$M_m$	⋮	⋮
⋮	⋮	⋮	⋮	⋮	⋮	⋮	⋮	⋮
$X_e$	$J_e$	$P.No_k$	$A.S._v$	$S_z$	$P_n$	$M_m$	$\overline{OP}(a_n, b_n, c_n)$	$\overline{T \cdot t}(a_n, b_n, c_n)$

FIGURE 3: General schematic of reading data for the mixed-model assembly line problem.

been filled with random numbers, the classified gene code numbers are ranked as a possible sequence which can be used by the GA. The steps are described briefly as follows.

*Identification of the First of Each Part Type's Gene Code.* The first of each part type's gene code is identified using (11), whereby each part has a sequence of gene codes with  $f$ -elements, where  $W_z$ ,  $z = 1, 2, \dots, f$ , have the same part number. Consider

$$X_q - W_1 \leq (f - 1). \quad (11)$$

*Classification Based on the Product's Part Sequence.* Each gene code number in the chromosome line is compared to the previous one. Three conditions are used when comparing the gene code numbers and are described below.

- (1) The first or existing gene code number fills up the new chromosome without any changes in the gene code number.
- (2) If the gene code number is the same as other gene code numbers in the chromosome, the chromosome is filled up with the addition of one number out of the existing gene code numbers.
- (3) If the gene code number is different from other gene code numbers within the chromosome, the existing gene code number fills up the chromosome without any changes in the gene code number.

*Classification Based on the Assembly Sequence.* Once the product's part sequence has been classified, the chromosome is filled up using the assembly sequence number relating to a gene code ( $X_q$ ) of the specific chromosome. Finally, the final gene code numbers are ranked by two sequence filters, which accounts for the assembly sequence code and product's part sequence.

*Step 3 (multiobjective evaluation).* After initializing the population size, each chromosome must be evaluated during each generation of the selection process. The fitness function value involves evaluating each chromosome by minimizing the make-span and considering the product number and assembly sequence for a gene code ( $X_q$ ) which are defined as (1) through (8). Moreover, the evaluation of each chromosome for the second objective function to minimize the setup number in mixed-model line sequencing is defined as (9) through (10). Finally the total fitness values of the efficient frontiers are calculated based on these two objectives [35]. This is accomplished by looking up the score of each gene in the chromosome, by means of adding and averaging the scores for the chromosome. This step is repeated for each possible chromosome ( $X_q$ ) in the population size. The elite chromosome of the generation is determined as part of the evaluation process.

*Step 4 (sorting).* The total fitness value is calculated for the population size based on Step 3. Calculations are carried out

in ascending order from "Min" to "Max" for the total fitness values of all chromosomes.

*Step 5 (tournament candidate selection).* The chromosomes are selected for the next generation using the tournament selection scheme, which is a proportionate random selection method. Two parent chromosomes are selected from a population according to their fitness function values.

The main characteristics of tournament selection are summarized as follows.

- (i) Tournament selection is quite useful in certain situations, such as multiobjective optimization.
- (ii) Tournament selection uses only local information.
- (iii) Tournament selection is easily implemented with low time complexity.
- (iv) Tournament selection can be easily implemented in a parallel environment.

However, tournament selection also suffers from selection bias, which means that the best one will not be selected if it is very unlucky.

*Step 6 (crossover selection).* Crossover probability crosses over parents to form new offspring (children). In the crossover phase, all chromosomes (except for the elite chromosome) are paired up and crossed over with a probability crossover rate. Crossover is accomplished by choosing a site randomly along the length of the chromosome and exchanging the genes of two chromosomes (parents) for each gene past this crossover site. The steps for crossover are as follows.

- (1) Identify the number of different requirements for manufactured products ( $P.No._h$ ).
- (2) Create the one random number between product type numbers ( $P.No._h$ ) as follows:

$$\begin{aligned} &\text{for (int } h = 1; i < P.No._h; h++) \\ &\{ \\ &\quad \text{Product Random} = \text{rand}() \% \text{Product}; \\ &\}. \end{aligned} \quad (12)$$

- (3) Identify the gene code number ( $X_q$ ) for the selected product obtained from the previous step.
- (4) Search and identify the gene code from parent A based on random product selection and transfer these gene codes to child B, which is exactly at the same gene location.
- (5) Search and identify the gene code from parent B based on random product selection and transfer the gene code to child A, which is exactly at the same gene location.
- (6) Transfer the remaining gene code from parent A to the gene blank of child A.

- (7) Transfer the remaining gene code from parent B to the gene blank of child B.
- (8) Calculate the number of crossovers based on the crossover rate ( $CR(t)$ ) from Step 9 and population size (PS) using

$$\text{Number of crossovers} = \frac{CR(t) \times PS}{2}. \quad (13)$$

- (9) Once new offspring have been created, the new offspring will have previous chromosomes in the current generation.

*Step 7 (elitism).* In crossover operation, the worst or weakest chromosomes will fade away, whereas the characteristics of the chromosomes will change continuously during mutation operation. The elite chromosome will not be subjected to mutation in the next generation. Consequently, GA does not lead to annihilation since several chromosomes (one, two, or three) from each generation are transferred directly to the next generation. Mutation is not applied on chromosomes which are immune. It is possible to maintain a fixed fitness value in some generations, but they will never deteriorate. The first three best chromosomes are selected in the elitism step.

*Step 8 (mutation).* Following the crossover operation, the genes will mutate to any of the codes with a mutation rate for each gene in the chromosomes, with the exception of the elite chromosome. When the crossover and mutation operations are complete, the chromosomes will be evaluated for another round of selection and reproduction. Considering elitism and after identifying the parts in which mutation will be applied, the number of mutations in each generation is calculated using (14) based on the mutation rate ( $Pm(t)$ ), population size (PS), and maximum gene code ( $Max .X_q$ ) as follows:

$$\text{Number of mutations} \cong [(PS \times Max .X_i) \times Pm]. \quad (14)$$

After identifying the number of gene mutations, a set of rules needs to be devised for the mutation of genes from point A to point B and vice versa, while focusing on the stability of the chromosome sequence. It is important that the sequence of the chromosomes is not displaced. There are eight sets of rules for this step which are classified into two groups as follows.

- (1) Four rules are used to check the mutation based on the part sequence (Rules 1 and 2) and product assembly (Rules 3 and 4) of genes from A to B.
- (2) Four rules are used to check the mutation based on the part sequence (Rules 5 and 6) and product assembly (Rules 7 and 8) of genes from B to A.

The first group of gene mutation from A to B is illustrated in Figure 4. Likewise, the second group of gene mutation from B to A is illustrated in Figure 5.

*Note.*

- (i) Care should be taken to ensure that the position of A is before B.



FIGURE 4: General overview of the first group of gene mutation.



FIGURE 5: General overview of the second group of gene mutation.

- (ii) The above eight mutation rules should be checked thoroughly to ensure their ideal applications. In the adverse case, the above eight rules ought to be done over.

*Step 9 (new population size).* Having performed crossover, elitism, and mutation operations, the most ideal chromosomes of the current generation are compared and evaluated to identify its total value, after checking its termination in the following step.

*Step 10 (termination).* The loop of chromosome generations is terminated when certain conditions are met. The elite chromosome is returned as the best solution once the termination criteria are met. The termination criteria are listed below.

- (1) If the number of generations reaches its maximum, the loop of chromosome generations is terminated.
- (2) If there are no changes in the elite solution (i.e., no changes in fitness function value), the loop of chromosome generations is terminated using

$$\text{Fitness Value}(X_q) - \text{Fitness Value}(X_{q+1}) \leq 0.0001. \quad (15)$$

## 8. Computational Results

The results of the multiobjective fuzzy mixed-model assembly line model are presented in this section. Each metaheuristic model is verified, validated, and tested using a test-bed. It seems natural that one of the crucial elements for comparing heuristics is the test-bed onto which the heuristics are tested. Hence, test-beds are essential when comparing two metaheuristics. Silberholz and Golden [47] studied how to create and classify instances in a new test-bed and how to ensure that other researchers have access to the problems for future metaheuristic comparisons. Silberholz and Golden [47] proposed that two types of test-beds may be used for comparing metaheuristics, namely, (1) existing test-beds and (2) new test-beds. Existing test-beds are used when comparing a new metaheuristic to an existing one. It is advantageous to test problem instances that have been tested in previous studies. The results will be compared on a by-instance basis, allowing relative gap calculations between the two heuristics. New test-beds are developed when an existing test-bed is insufficient. For instance, there are no test-beds available for

TABLE 1: Input data for numerical example.

Number of jobs ( $J_q$ )	Number of products (P.No. $_h$ )	Number of parts ( $P_i$ )	Number of lathe machines, CNC, and robots ( $M_j$ )	Number of machine setup tools ( $S_u$ )
50	4	20	5	5

cases where metaheuristics are written specifically for a new problem and thus a new test-bed needs to be developed for this purpose. A new test-bed also needs to be developed if the existing test-beds are insufficient, which are often due to the fact that the test-beds are too small to effectively test a heuristic. There are two points which need to be addressed when developing new test-beds, that is, the purpose of developing the test-beds and the accessibility of new test instances [47]. The purpose of a problem suite is to emulate real-world problem instances with a variety of test cases and difficulty levels. When creating a new test-bed, the focus is to provide others with accessibility to problem instances. This enables other researchers to make comparisons easily, while ensuring that the problem instances are widely used. One way to ensure this is to create a simple generating function for the problem instances. Capturing the real aspects of a problem is particularly significant when developing a new test-bed. In this section, the results are presented based on the development of new test-beds due to the fact that the existing test-beds are inadequate. This is followed by a discussion on the identification of the optimum scheduling time for a fuzzy mixed-model assembly line sequencing problem.

**8.1. Input Data.** A hypothetical numerical example is designed to test the fuzzy mixed-model assembly line sequencing problem. The input data of the hypothetical numerical example is given in Table 1, consisting of 50 jobs and 20 parts in order to produce four products. There are five machine tools (one lathe, two CNC, and two robots) assigned to assemble four products.

**8.2. Initialization of Parameters and Fuzzy Variables.** The initialization of parameters for the mixed-model assembly line sequencing example is shown in Table 3. It can be seen that 50 jobs ( $J_q$ ;  $q = 1, 2, \dots, 50$ ) are required to produce 20 parts ( $P_i$ ;  $i = 0, 1, \dots, 19$ ) and these parts are assembled to produce four types of product (P.No. $_h$ ;  $h = 1, 2, 3, 4$ ). The number of tool changes is 5 ( $S_u$ ;  $u = A, B, C, D, \text{ and } E$ ) and these tools are assigned to five machines ( $M(X_q)$ ;  $q = 0, 1, 2, 3, 4$ ). The job sequence is dependent upon the part and product assembly and is described as follows. First, the job number is assigned to produce the first product, ranging from 1 to 10 (P.No. $_1$ ,  $h = 1$ ;  $J_q$ ,  $q = 1, 2, \dots, 10$ ). It will be highlighted that there are 10 jobs in this case and they are sequenced to produce three parts according to the following order. Job numbers 1, 2, and 3 are assigned to produce Part (0) ( $(P_i)$ ,  $i = 0 \rightarrow J_1, J_2, J_3$ ), while job numbers 4 and 5 are assigned to produce Part (1) ( $(P_i)$ ,  $i = 1 \rightarrow J_4, J_5$ ). Job numbers 6 and 7 are assigned to produce Part (2) ( $(P_i)$ ,  $i = 2 \rightarrow J_6, J_7$ ), whereas job numbers 8, 9, and 10 are assigned to produce Part (3), which is a subpart of the

product assembly ( $(P_i)$ ,  $i = 3 \rightarrow J_8, J_9, J_{10}$ ). Production of the second, third, and fourth products is based on the sequence described for Product (1), as shown in Table 2. The fuzzy processing time of each job ( $J_q$ ,  $q = 1, 2, \dots, 10$ ) is defined as a triplet  $(a_1, a_2, a_3)$ . The total operating time is based on the fuzzy triangular time and is required to complete the jobs sequentially when producing each part, in which each part is assigned to a machine ( $M_j$ ,  $j = 0, 1, 2, 3, 4$ ). The total operating time is defined as  $(\widetilde{OP}_{i,j} = (a_1, a_2, a_3); i = 0, 1, 2, \dots, 19; j = 0, 1, \dots, 5; a = \text{time})$ . The total travelling time based on the above information is defined as  $(\widetilde{T} \cdot t_{i,j} = (a_1, a_2, a_3); i = 0, 1, 2, \dots, 19; j = 0, 1, \dots, 5; a = \text{time})$ . The operation and travelling time are fuzzy numbers, which are indicated by “ $a_1$ ,” “ $a_2$ ,” and “ $a_3$ .” The parameters “ $a_1$ ,” “ $a_2$ ,” and “ $a_3$ ” represent the optimistic time, normal time, and pessimistic time, respectively.

**8.3. Model Development.** A numerical example for mixed-model assembly line sequencing is presented in Figure 6, based on the parameters listed in Table 2. The solid arrows represent the order of the product line (sequence of part production), discrete part manufacturing, and assembly, leading to the finished products, as indicated by the job numbers. Suppose that the production process involves manufacturing four products using the same assembly line. In other words, four different products are manufactured simultaneously on the assembly line, and hence the problem is a mixed-model assembly line problem. In this example, 20 parts need to be manufactured using five machines. From Figure 6, the order of the production of parts is represented by the dashed rectangles and is termed as the process line. The assembly lines are represented by the dotted rectangles. The assignment of parts to their respective machines based on job number is illustrated in Figure 7.

**8.4. Multiobjective Evaluation.** The optimized optimistic, medium, and pessimistic starting times ( $\widetilde{S} \cdot t$ ) are shown in the sixth column of Table 3, based on the GA encoding chromosome sequence ( $X_q$ ) and job sequence ( $J_q$ ). The final optimized optimistic start time is 59.5, whereas the final medium and pessimistic start times are 69 and 85.5, respectively.

The scheduling of existing optimistic time for mixed-model assembly line sequencing (machine versus optimistic time) is shown in Figure 8(a), whereas the scheduling for optimized optimistic scheduling time is shown in Figure 8(b). This chart is created to demonstrate the allocated time and setup number based on the part assembly sequence for each mixed-model. The existing optimistic total scheduling time is obtained to be 166 min, whereas the optimized optimistic total scheduled time is 62.5 min, which indicates significant

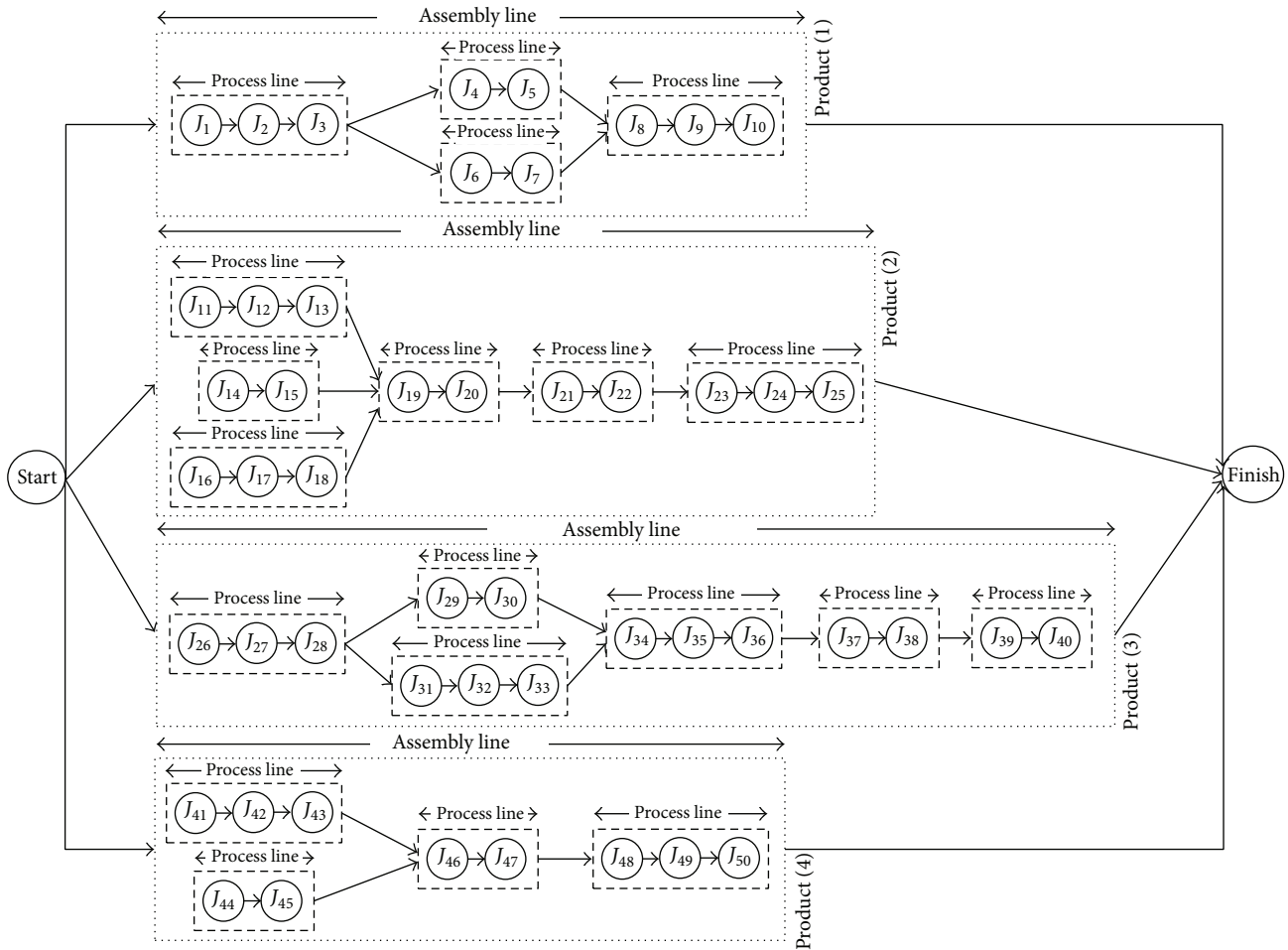


FIGURE 6: Example of mixed-model assembly line sequencing (50 jobs, 20 parts, 4 products).

time-savings. Moreover, the total fuzzy setup numbers for the existing and optimized optimistic data are 44 and 36, respectively.

The percentage of the existing and optimized fuzzy numbers which represent the efficiency and idle time of the machines is presented in Table 4. The efficiency and idle time are categorized as optimistic, medium, and pessimistic. The lowest efficiency is obtained for Machine (4), in which the optimistic, medium, and pessimistic times which are 3.3%, 6.4%, and 3.9% increase to 8.7%, 21.9%, and 11.7%. The highest idle time is also obtained for Machine (4), whereby the optimistic, medium, and pessimistic times which are 96.7%, 93.6%, and 96.1% decrease to 91.35%, 78.1%, and 88.3%.

The final results based on the existing and optimized data are shown in Table 5. The overall results show that the existing fuzzy data is improved by optimization. The total fuzzy existing scheduling time is optimized from 166, 250, and 266 to 62.5, 73, and 88.5. The total fuzzy setup numbers for the existing and optimized data are 44, 44, and 44 and 36, 36, and 39, respectively. The total fuzzy existing efficient frontier is 105, 147, and 155, while the optimized ones are 49.25, 54.5, and 63.75. The total fuzzy existing cycle and

setup time are optimized from 254, 338, and 354 to 135, 145, and 168. The total fuzzy operation setup times for the existing and optimized data are 88, 88, and 88 and 72, 72, and 78, respectively. The total fuzzy existing changing setup cost is optimized from \$ 3520, \$ 3520, and \$ 3520 to \$ 2880, \$ 2880, and \$ 3120. The total fuzzy units produced per day for the existing and optimized data are approximately 1.80, 1.92, and 2.89 and 5.33, 6.58, and 7.62, respectively. The total existing fuzzy percentage efficiency is optimized from 10.32%, 10.90%, and 11.45% to 30.16%, 32.22%, and 35.34%.

## 9. Conclusion

It is known that mixed-model assembly line sequencing is a problem which involves job-shop and assembly line with multiple conflicting objectives, namely, minimizing the setup time and make-span. These objectives have been achieved successfully and tested using a hypothetical numerical example. An optimization model is developed using GA for the mixed-model assembly line sequencing problem in order to address conflicting objectives which involve minimizing

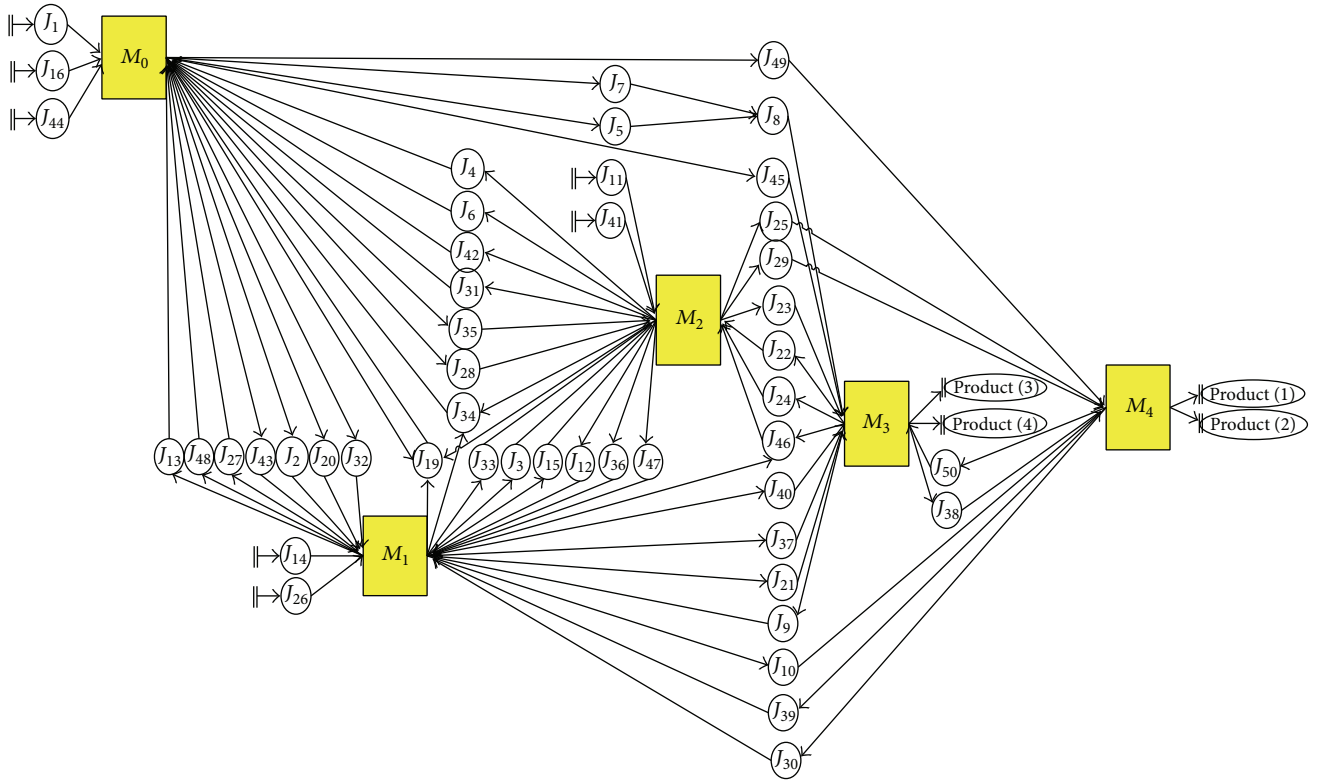
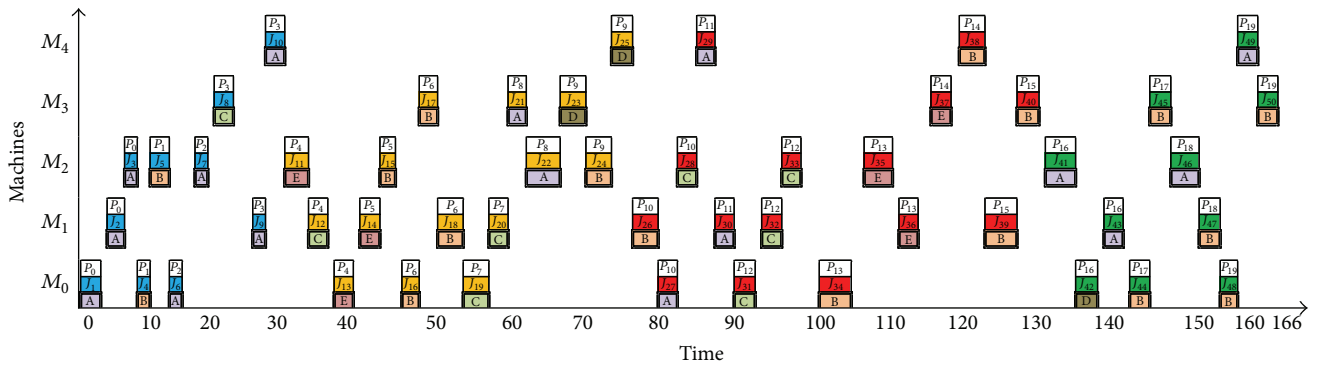
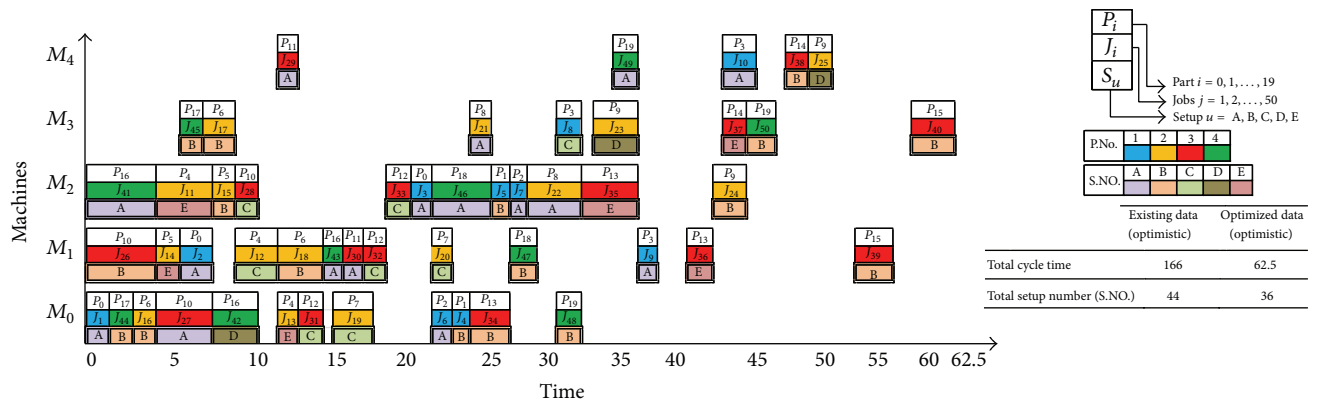


FIGURE 7: Assignment of parts to their respective machines based on the example for mixed-model assembly line sequencing.



(a) Existing optimistic time scheduling



(b) Optimized optimistic time scheduling

FIGURE 8: Optimistic time scheduling for mixed-model assembly line sequencing.

TABLE 2: Fuzzy variables and initialization of parameters.

$X_q$	$J_q$	P.No. <sub><i>h</i></sub>	A.S. <sub><i>p</i></sub>	$S_u$	$P_i$	$M_j$	$\overline{OP}_{i,j}$			$\overline{T} \cdot \overline{t}_{i,j}$		
1	$J_1$	P.No. <sub>1</sub>	A.S. <sub>0</sub>	$S_A$	$P_0$	$M_0$	1.50	2	2.50	0.50	1	1.5
2	$J_2$	P.No. <sub>1</sub>	A.S. <sub>0</sub>	$S_A$	$P_0$	$M_1$	2.50	3	3.50	4.50	5	5.5
3	$J_3$	P.No. <sub>1</sub>	A.S. <sub>0</sub>	$S_A$	$P_0$	$M_2$	0.50	1	1.50	0.50	1	1.5
4	$J_4$	P.No. <sub>1</sub>	A.S. <sub>1</sub>	$S_B$	$P_1$	$M_0$	0.50	1	1.50	1.50	2	2.5
5	$J_5$	P.No. <sub>1</sub>	A.S. <sub>1</sub>	$S_B$	$P_1$	$M_2$	1.50	2	2.50	2.50	3	3.5
6	$J_6$	P.No. <sub>1</sub>	A.S. <sub>1</sub>	$S_A$	$P_2$	$M_0$	1.50	2	2.50	2.50	3	3.5
7	$J_7$	P.No. <sub>1</sub>	A.S. <sub>1</sub>	$S_A$	$P_2$	$M_2$	0.50	1	1.50	2.50	3	3.5
8	$J_8$	P.No. <sub>1</sub>	A.S. <sub>2</sub>	$S_C$	$P_3$	$M_3$	1.50	2	2.50	3.50	4	4.5
9	$J_9$	P.No. <sub>1</sub>	A.S. <sub>2</sub>	$S_A$	$P_3$	$M_1$	2.50	3	3.50	4.50	5	5.5
10	$J_{10}$	P.No. <sub>1</sub>	A.S. <sub>2</sub>	$S_A$	$P_3$	$M_4$	1.50	2	2.50	0.50	1	1.5
11	$J_{11}$	P.No. <sub>2</sub>	A.S. <sub>0</sub>	$S_E$	$P_4$	$M_2$	3.50	4	4.50	1.50	2	2.5
12	$J_{12}$	P.No. <sub>2</sub>	A.S. <sub>0</sub>	$S_C$	$P_4$	$M_1$	2.50	3	3.50	0.50	1	1.5
13	$J_{13}$	P.No. <sub>2</sub>	A.S. <sub>0</sub>	$S_E$	$P_4$	$M_0$	1.50	2	2.50	2.50	3	3.5
14	$J_{14}$	P.No. <sub>2</sub>	A.S. <sub>0</sub>	$S_E$	$P_5$	$M_1$	0.50	1	1.50	1.50	2	2.5
15	$J_{15}$	P.No. <sub>2</sub>	A.S. <sub>0</sub>	$S_B$	$P_5$	$M_2$	0.50	1	1.50	0.50	1	1.5
16	$J_{16}$	P.No. <sub>2</sub>	A.S. <sub>0</sub>	$S_B$	$P_6$	$M_0$	1.50	2	2.50	3.50	4	4.5
17	$J_{17}$	P.No. <sub>2</sub>	A.S. <sub>0</sub>	$S_B$	$P_6$	$M_3$	1.50	2	2.50	0.50	1	1.5
18	$J_{18}$	P.No. <sub>2</sub>	A.S. <sub>0</sub>	$S_B$	$P_6$	$M_1$	2.50	3	3.50	1.50	2	2.5
19	$J_{19}$	P.No. <sub>2</sub>	A.S. <sub>1</sub>	$S_C$	$P_7$	$M_0$	2.50	3	3.50	2.50	3	3.5
20	$J_{20}$	P.No. <sub>2</sub>	A.S. <sub>1</sub>	$S_C$	$P_7$	$M_1$	0.50	1	1.50	1.50	2	2.5
21	$J_{21}$	P.No. <sub>2</sub>	A.S. <sub>2</sub>	$S_A$	$P_8$	$M_3$	0.50	1	1.50	0.50	1	1.5
22	$J_{22}$	P.No. <sub>2</sub>	A.S. <sub>2</sub>	$S_A$	$P_8$	$M_2$	4.50	5	5.50	1.50	2	2.5
23	$J_{23}$	P.No. <sub>2</sub>	A.S. <sub>3</sub>	$S_D$	$P_9$	$M_3$	2.50	3	3.50	2.50	3	3.5
24	$J_{24}$	P.No. <sub>2</sub>	A.S. <sub>3</sub>	$S_B$	$P_9$	$M_2$	1.50	2	2.50	1.50	2	2.5
25	$J_{25}$	P.No. <sub>2</sub>	A.S. <sub>3</sub>	$S_D$	$P_9$	$M_4$	0.50	1	1.50	4.50	5	5.5
26	$J_{26}$	P.No. <sub>3</sub>	A.S. <sub>0</sub>	$S_B$	$P_{10}$	$M_1$	3.50	4	4.50	0.50	1	1.5
27	$J_{27}$	P.No. <sub>3</sub>	A.S. <sub>0</sub>	$S_A$	$P_{10}$	$M_0$	2.50	3	3.50	0.50	1	1.5
28	$J_{28}$	P.No. <sub>3</sub>	A.S. <sub>0</sub>	$S_C$	$P_{10}$	$M_2$	1.50	2	2.50	2.50	3	3.5
29	$J_{29}$	P.No. <sub>3</sub>	A.S. <sub>1</sub>	$S_A$	$P_{11}$	$M_4$	0.50	1	1.50	1.50	2	2.5
30	$J_{30}$	P.No. <sub>3</sub>	A.S. <sub>1</sub>	$S_A$	$P_{11}$	$M_1$	1.50	2	2.50	1.50	2	2.5
31	$J_{31}$	P.No. <sub>3</sub>	A.S. <sub>1</sub>	$S_C$	$P_{12}$	$M_0$	0.50	1	1.50	1.50	2	2.5
32	$J_{32}$	P.No. <sub>3</sub>	A.S. <sub>1</sub>	$S_C$	$P_{12}$	$M_1$	1.50	2	2.50	0.50	1	1.5
33	$J_{33}$	P.No. <sub>3</sub>	A.S. <sub>1</sub>	$S_C$	$P_{12}$	$M_2$	2.50	3	3.50	2.50	3	3.5
34	$J_{34}$	P.No. <sub>3</sub>	A.S. <sub>2</sub>	$S_B$	$P_{13}$	$M_0$	3.50	4	4.50	3.50	4	4.5
35	$J_{35}$	P.No. <sub>3</sub>	A.S. <sub>2</sub>	$S_E$	$P_{13}$	$M_2$	4.50	5	5.50	4.50	5	5.5
36	$J_{36}$	P.No. <sub>3</sub>	A.S. <sub>2</sub>	$S_E$	$P_{13}$	$M_1$	1.50	2	2.50	0.50	1	1.5
37	$J_{37}$	P.No. <sub>3</sub>	A.S. <sub>3</sub>	$S_E$	$P_{14}$	$M_3$	0.50	1	1.50	4.50	5	5.5
38	$J_{38}$	P.No. <sub>3</sub>	A.S. <sub>3</sub>	$S_B$	$P_{14}$	$M_4$	2.50	3	3.50	2.50	3	3.5
39	$J_{39}$	P.No. <sub>3</sub>	A.S. <sub>4</sub>	$S_B$	$P_{15}$	$M_1$	4.50	5	5.50	1.50	2	2.5
40	$J_{40}$	P.No. <sub>3</sub>	A.S. <sub>4</sub>	$S_B$	$P_{15}$	$M_3$	3.50	4	4.50	0.50	1	1.5
41	$J_{41}$	P.No. <sub>4</sub>	A.S. <sub>0</sub>	$S_A$	$P_{16}$	$M_2$	3.50	4	4.50	0.50	1	1.5
42	$J_{42}$	P.No. <sub>4</sub>	A.S. <sub>0</sub>	$S_D$	$P_{16}$	$M_0$	2.50	3	3.50	2.50	3	3.5
43	$J_{43}$	P.No. <sub>4</sub>	A.S. <sub>0</sub>	$S_A$	$P_{16}$	$M_1$	1.50	2	2.50	1.50	2	2.5
44	$J_{44}$	P.No. <sub>4</sub>	A.S. <sub>0</sub>	$S_B$	$P_{17}$	$M_0$	0.50	1	1.50	3.50	4	4.5
45	$J_{45}$	P.No. <sub>4</sub>	A.S. <sub>0</sub>	$S_B$	$P_{17}$	$M_3$	0.50	1	1.50	0.50	1	1.5
46	$J_{46}$	P.No. <sub>4</sub>	A.S. <sub>1</sub>	$S_A$	$P_{18}$	$M_2$	3.50	4	4.50	1.50	2	2.5
47	$J_{47}$	P.No. <sub>4</sub>	A.S. <sub>1</sub>	$S_B$	$P_{18}$	$M_1$	2.50	3	3.50	1.50	2	2.5
48	$J_{48}$	P.No. <sub>4</sub>	A.S. <sub>2</sub>	$S_B$	$P_{19}$	$M_0$	1.50	2	2.50	2.50	3	3.5
49	$J_{49}$	P.No. <sub>4</sub>	A.S. <sub>2</sub>	$S_A$	$P_{19}$	$M_4$	0.50	1	1.50	1.50	2	2.5
50	$J_{50}$	P.No. <sub>4</sub>	A.S. <sub>2</sub>	$S_B$	$P_{19}$	$M_3$	3.50	4	4.50	2.50	3	3.5

TABLE 3: Optimized scheduling time based on optimistic, medium, and pessimistic data.

Optimize optimistic results							Optimize medium results							Optimize pessimistic results						
$X_q$	$J_q$	P.No. <sub>h</sub>	$S_u$	$P_i$	$M_j$	S.T	$X_q$	$J_q$	P.No. <sub>h</sub>	$S_u$	$P_i$	$M_j$	S.T	$X_q$	$J_q$	P.No. <sub>h</sub>	$S_u$	$P_i$	$M_j$	S.T
41	$J_{41}$	P.No. <sub>4</sub>	$S_A$	$P_{16}$	$M_2$	0.5	41	$J_{41}$	P.No. <sub>4</sub>	$S_A$	$P_{16}$	$M_2$	1	26	$J_{26}$	P.No. <sub>3</sub>	$S_B$	$P_{10}$	$M_1$	1.5
1	$J_1$	P.No. <sub>1</sub>	$S_A$	$P_0$	$M_0$	0.5	1	$J_1$	P.No. <sub>1</sub>	$S_A$	$P_0$	$M_0$	1	11	$J_{11}$	P.No. <sub>2</sub>	$S_E$	$P_4$	$M_2$	2.5
26	$J_{26}$	P.No. <sub>3</sub>	$S_B$	$P_{10}$	$M_1$	0.5	16	$J_{16}$	P.No. <sub>2</sub>	$S_B$	$P_6$	$M_0$	3	1	$J_1$	P.No. <sub>1</sub>	$S_A$	$P_0$	$M_0$	1.5
44	$J_{44}$	P.No. <sub>4</sub>	$S_B$	$P_{17}$	$M_0$	2	26	$J_{26}$	P.No. <sub>3</sub>	$S_B$	$P_{10}$	$M_1$	1	12	$J_{12}$	P.No. <sub>2</sub>	$S_C$	$P_4$	$M_1$	9.5
16	$J_{16}$	P.No. <sub>2</sub>	$S_B$	$P_6$	$M_0$	2.5	44	$J_{44}$	P.No. <sub>4</sub>	$S_B$	$P_{17}$	$M_0$	5	41	$J_{41}$	P.No. <sub>4</sub>	$S_A$	$P_{16}$	$M_2$	7
14	$J_{14}$	P.No. <sub>2</sub>	$S_B$	$P_5$	$M_1$	4	2	$J_2$	P.No. <sub>1</sub>	$S_A$	$P_0$	$M_1$	5	14	$J_{14}$	P.No. <sub>2</sub>	$S_E$	$P_5$	$M_1$	13
11	$J_{11}$	P.No. <sub>2</sub>	$S_E$	$P_4$	$M_2$	4	11	$J_{11}$	P.No. <sub>2</sub>	$S_E$	$P_4$	$M_2$	5	27	$J_{27}$	P.No. <sub>3</sub>	$S_A$	$P_{10}$	$M_0$	7.5
45	$J_{45}$	P.No. <sub>4</sub>	$S_B$	$P_{17}$	$M_3$	6	42	$J_{42}$	P.No. <sub>4</sub>	$S_D$	$P_{16}$	$M_0$	6	2	$J_2$	P.No. <sub>1</sub>	$S_A$	$P_0$	$M_1$	14.5
2	$J_2$	P.No. <sub>1</sub>	$S_A$	$P_0$	$M_1$	4.5	45	$J_{45}$	P.No. <sub>4</sub>	$S_B$	$P_{17}$	$M_3$	10	16	$J_{16}$	P.No. <sub>2</sub>	$S_B$	$P_6$	$M_0$	11
17	$J_{17}$	P.No. <sub>2</sub>	$S_B$	$P_6$	$M_3$	7.5	17	$J_{17}$	P.No. <sub>2</sub>	$S_B$	$P_6$	$M_3$	12	28	$J_{28}$	P.No. <sub>3</sub>	$S_C$	$P_{10}$	$M_2$	12.5
12	$J_{12}$	P.No. <sub>2</sub>	$S_C$	$P_4$	$M_1$	9	14	$J_{14}$	P.No. <sub>2</sub>	$S_E$	$P_5$	$M_1$	8	42	$J_{42}$	P.No. <sub>4</sub>	$S_D$	$P_{16}$	$M_0$	13.5
27	$J_{27}$	P.No. <sub>3</sub>	$S_A$	$P_{10}$	$M_0$	4.5	27	$J_{27}$	P.No. <sub>3</sub>	$S_A$	$P_{10}$	$M_0$	9	15	$J_{15}$	P.No. <sub>2</sub>	$S_B$	$P_5$	$M_2$	17
15	$J_{15}$	P.No. <sub>2</sub>	$S_B$	$P_5$	$M_2$	7.5	12	$J_{12}$	P.No. <sub>2</sub>	$S_C$	$P_4$	$M_1$	11	44	$J_{44}$	P.No. <sub>4</sub>	$S_B$	$P_{17}$	$M_0$	17
42	$J_{42}$	P.No. <sub>4</sub>	$S_D$	$P_{16}$	$M_0$	7	15	$J_{15}$	P.No. <sub>2</sub>	$S_B$	$P_5$	$M_2$	11	43	$J_{43}$	P.No. <sub>4</sub>	$S_A$	$P_{16}$	$M_1$	20.5
13	$J_{13}$	P.No. <sub>2</sub>	$S_E$	$P_4$	$M_0$	12	46	$J_{46}$	P.No. <sub>4</sub>	$S_A$	$P_{18}$	$M_2$	13	17	$J_{17}$	P.No. <sub>2</sub>	$S_B$	$P_6$	$M_3$	18
18	$J_{18}$	P.No. <sub>2</sub>	$S_B$	$P_6$	$M_1$	11.5	43	$J_{43}$	P.No. <sub>4</sub>	$S_A$	$P_{16}$	$M_1$	14	13	$J_{13}$	P.No. <sub>2</sub>	$S_E$	$P_4$	$M_0$	18.5
28	$J_{28}$	P.No. <sub>3</sub>	$S_C$	$P_{10}$	$M_2$	8	13	$J_{13}$	P.No. <sub>2</sub>	$S_E$	$P_4$	$M_0$	15	18	$J_{18}$	P.No. <sub>2</sub>	$S_B$	$P_6$	$M_1$	23
43	$J_{43}$	P.No. <sub>4</sub>	$S_A$	$P_{16}$	$M_1$	14	3	$J_3$	P.No. <sub>1</sub>	$S_A$	$P_0$	$M_2$	17	29	$J_{29}$	P.No. <sub>3</sub>	$S_A$	$P_{11}$	$M_4$	18.5
29	$J_{29}$	P.No. <sub>3</sub>	$S_A$	$P_{11}$	$M_4$	12	18	$J_{18}$	P.No. <sub>2</sub>	$S_B$	$P_6$	$M_1$	16	45	$J_{45}$	P.No. <sub>4</sub>	$S_B$	$P_{17}$	$M_3$	23
31	$J_{31}$	P.No. <sub>3</sub>	$S_C$	$P_{12}$	$M_0$	13.5	31	$J_{31}$	P.No. <sub>3</sub>	$S_C$	$P_{12}$	$M_0$	17	3	$J_3$	P.No. <sub>1</sub>	$S_A$	$P_0$	$M_2$	23.5
30	$J_{30}$	P.No. <sub>3</sub>	$S_A$	$P_{11}$	$M_1$	15.5	32	$J_{32}$	P.No. <sub>3</sub>	$S_C$	$P_{12}$	$M_1$	20	31	$J_{31}$	P.No. <sub>3</sub>	$S_C$	$P_{12}$	$M_0$	21
32	$J_{32}$	P.No. <sub>3</sub>	$S_C$	$P_{12}$	$M_1$	17	28	$J_{28}$	P.No. <sub>3</sub>	$S_C$	$P_{10}$	$M_2$	18	32	$J_{32}$	P.No. <sub>3</sub>	$S_C$	$P_{12}$	$M_1$	26.5
33	$J_{33}$	P.No. <sub>3</sub>	$S_C$	$P_{12}$	$M_2$	19	19	$J_{19}$	P.No. <sub>2</sub>	$S_C$	$P_7$	$M_0$	21	46	$J_{46}$	P.No. <sub>4</sub>	$S_A$	$P_{18}$	$M_2$	26
19	$J_{19}$	P.No. <sub>2</sub>	$S_C$	$P_7$	$M_0$	16	29	$J_{29}$	P.No. <sub>3</sub>	$S_A$	$P_{11}$	$M_4$	23	30	$J_{30}$	P.No. <sub>3</sub>	$S_A$	$P_{11}$	$M_1$	29
3	$J_3$	P.No. <sub>1</sub>	$S_A$	$P_0$	$M_2$	21.5	6	$J_6$	P.No. <sub>1</sub>	$S_A$	$P_2$	$M_0$	24	19	$J_{19}$	P.No. <sub>2</sub>	$S_C$	$P_7$	$M_0$	29
6	$J_6$	P.No. <sub>1</sub>	$S_A$	$P_2$	$M_0$	22.5	20	$J_{20}$	P.No. <sub>2</sub>	$S_C$	$P_7$	$M_1$	27	6	$J_6$	P.No. <sub>1</sub>	$S_A$	$P_2$	$M_0$	32.5
4	$J_4$	P.No. <sub>1</sub>	$S_B$	$P_1$	$M_0$	24	33	$J_{33}$	P.No. <sub>3</sub>	$S_C$	$P_{12}$	$M_2$	23	33	$J_{33}$	P.No. <sub>3</sub>	$S_C$	$P_{12}$	$M_2$	30.5
20	$J_{20}$	P.No. <sub>2</sub>	$S_C$	$P_7$	$M_1$	22.5	4	$J_4$	P.No. <sub>1</sub>	$S_B$	$P_1$	$M_0$	26	7	$J_7$	P.No. <sub>1</sub>	$S_A$	$P_2$	$M_2$	38.5
46	$J_{46}$	P.No. <sub>4</sub>	$S_A$	$P_{18}$	$M_2$	22.5	5	$J_5$	P.No. <sub>1</sub>	$S_B$	$P_1$	$M_2$	29	47	$J_{47}$	P.No. <sub>4</sub>	$S_B$	$P_{18}$	$M_1$	33
5	$J_5$	P.No. <sub>1</sub>	$S_B$	$P_1$	$M_2$	26	34	$J_{34}$	P.No. <sub>3</sub>	$S_B$	$P_{13}$	$M_0$	29	4	$J_4$	P.No. <sub>1</sub>	$S_B$	$P_1$	$M_0$	35
21	$J_{21}$	P.No. <sub>2</sub>	$S_A$	$P_8$	$M_3$	24.5	47	$J_{47}$	P.No. <sub>4</sub>	$S_B$	$P_{18}$	$M_1$	29	5	$J_5$	P.No. <sub>1</sub>	$S_B$	$P_1$	$M_2$	40
7	$J_7$	P.No. <sub>1</sub>	$S_A$	$P_2$	$M_2$	27.5	21	$J_{21}$	P.No. <sub>2</sub>	$S_A$	$P_8$	$M_3$	30	20	$J_{20}$	P.No. <sub>2</sub>	$S_C$	$P_7$	$M_1$	36.5
47	$J_{47}$	P.No. <sub>4</sub>	$S_B$	$P_{18}$	$M_1$	27.5	7	$J_7$	P.No. <sub>1</sub>	$S_A$	$P_2$	$M_2$	31	34	$J_{34}$	P.No. <sub>3</sub>	$S_B$	$P_{13}$	$M_0$	37.5
22	$J_{22}$	P.No. <sub>2</sub>	$S_A$	$P_8$	$M_2$	28	30	$J_{30}$	P.No. <sub>3</sub>	$S_A$	$P_{11}$	$M_1$	32	21	$J_{21}$	P.No. <sub>2</sub>	$S_A$	$P_8$	$M_3$	40.5
34	$J_{34}$	P.No. <sub>3</sub>	$S_B$	$P_{13}$	$M_0$	24.5	22	$J_{22}$	P.No. <sub>2</sub>	$S_A$	$P_8$	$M_2$	32	35	$J_{35}$	P.No. <sub>3</sub>	$S_E$	$P_{13}$	$M_2$	46.5
48	$J_{48}$	P.No. <sub>4</sub>	$S_B$	$P_{19}$	$M_0$	31.5	48	$J_{48}$	P.No. <sub>4</sub>	$S_B$	$P_{19}$	$M_0$	34	48	$J_{38}$	P.No. <sub>4</sub>	$S_B$	$P_{19}$	$M_0$	42
49	$J_{49}$	P.No. <sub>4</sub>	$S_A$	$P_{19}$	$M_4$	35.5	35	$J_{35}$	P.No. <sub>3</sub>	$S_E$	$P_{13}$	$M_2$	37	49	$J_{49}$	P.No. <sub>4</sub>	$S_A$	$P_{19}$	$M_4$	48
8	$J_8$	P.No. <sub>1</sub>	$S_C$	$P_3$	$M_3$	31.5	8	$J_8$	P.No. <sub>1</sub>	$S_C$	$P_3$	$M_3$	36	8	$J_8$	P.No. <sub>1</sub>	$S_C$	$P_3$	$M_3$	46
35	$J_{35}$	P.No. <sub>3</sub>	$S_E$	$P_{13}$	$M_2$	32.5	49	$J_{49}$	P.No. <sub>4</sub>	$S_A$	$P_{19}$	$M_4$	39	9	$J_9$	P.No. <sub>1</sub>	$S_A$	$P_3$	$M_1$	53
9	$J_9$	P.No. <sub>1</sub>	$S_A$	$P_3$	$M_1$	36.5	9	$J_9$	P.No. <sub>1</sub>	$S_A$	$P_3$	$M_1$	42	22	$J_{22}$	P.No. <sub>2</sub>	$S_A$	$P_8$	$M_2$	52
10	$J_{10}$	P.No. <sub>1</sub>	$S_A$	$P_3$	$M_4$	43.5	23	$J_{23}$	P.No. <sub>2</sub>	$S_D$	$P_9$	$M_3$	39	36	$J_{36}$	P.No. <sub>3</sub>	$S_E$	$P_{13}$	$M_1$	57.5
23	$J_{23}$	P.No. <sub>2</sub>	$S_D$	$P_9$	$M_3$	34	36	$J_{36}$	P.No. <sub>3</sub>	$S_E$	$P_{13}$	$M_1$	47	10	$J_{10}$	P.No. <sub>1</sub>	$S_A$	$P_3$	$M_4$	62
36	$J_{36}$	P.No. <sub>3</sub>	$S_E$	$P_{13}$	$M_1$	41.5	10	$J_{10}$	P.No. <sub>1</sub>	$S_A$	$P_3$	$M_4$	50	23	$J_{23}$	P.No. <sub>2</sub>	$S_D$	$P_9$	$M_3$	60
37	$J_{37}$	P.No. <sub>3</sub>	$S_E$	$P_{14}$	$M_3$	43.5	37	$J_{37}$	P.No. <sub>3</sub>	$S_E$	$P_{14}$	$M_3$	50	37	$J_{37}$	P.No. <sub>3</sub>	$S_E$	$P_{14}$	$M_3$	63.5
50	$J_{50}$	P.No. <sub>4</sub>	$S_B$	$P_{19}$	$M_3$	44	50	$J_{50}$	P.No. <sub>4</sub>	$S_B$	$P_{19}$	$M_3$	51	50	$J_{50}$	P.No. <sub>4</sub>	$S_B$	$P_{19}$	$M_3$	65
24	$J_{24}$	P.No. <sub>2</sub>	$S_B$	$P_9$	$M_2$	43.5	24	$J_{24}$	P.No. <sub>2</sub>	$S_B$	$P_9$	$M_2$	50	24	$J_{24}$	P.No. <sub>2</sub>	$S_B$	$P_9$	$M_2$	67
38	$J_{38}$	P.No. <sub>3</sub>	$S_B$	$P_{14}$	$M_4$	48.5	25	$J_{25}$	P.No. <sub>2</sub>	$S_D$	$P_9$	$M_4$	54	38	$J_{38}$	P.No. <sub>3</sub>	$S_B$	$P_{14}$	$M_4$	70.5
25	$J_{25}$	P.No. <sub>2</sub>	$S_D$	$P_9$	$M_4$	51	38	$J_{38}$	P.No. <sub>3</sub>	$S_B$	$P_{14}$	$M_4$	56	39	$J_{39}$	P.No. <sub>3</sub>	$S_B$	$P_{15}$	$M_1$	77.5
39	$J_{39}$	P.No. <sub>3</sub>	$S_B$	$P_{15}$	$M_1$	53.5	39	$J_{39}$	P.No. <sub>3</sub>	$S_B$	$P_{15}$	$M_1$	62	25	$J_{25}$	P.No. <sub>2</sub>	$S_D$	$P_9$	$M_4$	77.5
40	$J_{40}$	P.No. <sub>3</sub>	$S_B$	$P_{15}$	$M_3$	59.5	40	$J_{40}$	P.No. <sub>3</sub>	$S_B$	$P_{15}$	$M_3$	69	40	$J_{40}$	P.No. <sub>3</sub>	$S_B$	$P_{15}$	$M_3$	85.5

TABLE 4: Percentage of existing and optimized fuzzy numbers representing the efficiency and idle time of machines.

	Existing data		Optimized data	
	Efficiency	Idle time	Efficiency	Idle time
	(Opt, Med, Pes)	(Opt, Med, Pes)	(Opt, Med, Pes)	(Opt, Med, Pes)
Machine (0)	(12%, 10.4%, 12%)	(88%, 89.6%, 88%)	(31.7%, 35.6%, 35.6%)	(68.3%, 64.4%, 64.4%)
Machine (1)	(16.6%, 13.6%, 15.2%)	(83.4%, 86.4%, 84.8%)	(43.7%, 46.6%, 45%)	(56.3%, 53.4%, 55%)
Machine (2)	(16.9%, 13.6%, 15%)	(83.1%, 86.4%, 85%)	(44.4%, 46.6%, 44.4%)	(55.6%, 53.4%, 55.6%)
Machine (3)	(8.4%, 7.6%, 8.3%)	(91.6%, 92.4%, 91.7%)	(22.2%, 26.0%, 24.4%)	(77.8%, 74%, 75.6%)
Machine (4)	(3.3%, 6.4%, 3.9%)	(96.7%, 93.6%, 96.1%)	(8.7%, 21.9%, 11.7%)	(91.35, 78.1%, 88.3%)

TABLE 5: Summary of the final results based on existing and optimized data.

	Existing data (Opt, Med, Pes)	Optimized data (Opt, Med, Pes)
Total scheduling time	(166, 250, 266)	(62.5, 73, 88.5)
Total setup number (No.)	(44, 44, 44)	(36, 36, 39)
Total efficient frontier	(105, 147, 155)	(49.25, 54.5, 63.75)
Total scheduling time with setup time	(254, 338, 354)	(135, 145, 168)
Total operation setup time	(88, 88, 88)	(72, 72, 78)
Total changing setup cost (\$)	(3520, 3520, 3520)	(2880, 2880, 3120)
Total units produced per day	(2.89, 1.92, 1.80)	(7.62, 6.58, 5.33)
Total efficiency (%)	(11.45%, 10.32%, 10.90%)	(30.16%, 35.34%, 32.22%)
Total idle time (%)	(88.55%, 89.68%, 89.10%)	(69.84%, 64.66%, 67.78%)

the make-span (i.e., minimizing scheduling time, travelling time, and machine idle time and maximizing production) and minimizing the setup time (i.e., minimizing the number of machine setup tool changes and minimizing the machine setup cost) simultaneously that occur when switching between different products. The triangular fuzzy numbers are applied for variables such as operation and travelling time. The hypothetical numerical example comprises 50 jobs to produce 20 parts using five machines in order to assemble four products. The fuzzy numbers are categorized as optimistic, medium, and pessimistic fuzzy total scheduling time. The results show that the fuzzy total scheduling time which is 166, 250, and 266 decreases to 62.5, 73, and 88.5 after optimization. Comparison is made between the existing and optimized results representing the efficiency and idle time of each machine. The existing and optimized results of the total scheduling time, total setup number, total efficient frontier, total scheduling time with setup time, total operation setup time, total changing setup cost (\$), and total units produced per day are also compared.

**Notations**

- $i$ : An index used for parts;  $i = 1, 2, \dots, n$
- $j$ : An index used for machines;  
 $j = 1, 2, \dots, m$
- $n$ : Number of total parts
- $m$ : Number of total machines

- $u$ : An index used for a setup change for the machine;  $u = A, B, \dots, Z$
- $p$ : An index used for an assembly sequence;  
 $p = 1, 2, \dots, v$
- $v$ : Maximum number of assembly sequence orders in each product
- $h$ : An index used for a product number;  
 $h = 1, 2, \dots, k$
- $k$ : Total product
- $q$ : An index used for gene code number in each chromosome;  $q = 1, 2, \dots, e$
- $e$ : Total gene on each chromosome
- $z$ : An index used for a same part's gene code
- $f$ : Number of same part's gene code
- $a$ : An index used for showing an optimistic time
- $b$ : An index used for showing an average time
- $c$ : An index used for showing a pessimistic time
- $X_q$ : The gene code number in the chromosome;  
 $q = 1, 2, \dots, e$
- $X_{q'}$ : The alleviated gene code number in the chromosome;  $q' = q - 1, q - 2, \dots, q - (q - 1)$
- $J_q$ : The number of tasks involved in the total production line;  $q = 1, 2, \dots, e$
- $P_i$ : Number of parts;  $i = 1, 2, \dots, n$
- $M_j$ : Machine use for manufacturing parts and various products;  $j = 1, 2, \dots, m$
- $S_u$ : Setup number based on the jobs, assigned to each machine;  $u = A, B, \dots, Z$

P.No.<sub>*h*</sub>: Product number;  $h = 1, 2, \dots, k$   
 A.S.<sub>*p*</sub>: The order of parts in the assembly;  
 $p = 1, 2, \dots, v$   
 $\widetilde{OP}_{i,j}$ : Fuzzy operation time of parts  $P_i$ ,  
 $i = 1, 2, \dots, n$ , in machine  $M_j$ ,  $i = 1, 2, \dots, m$ ,  
 defined as a triplet  $(a, b, c)$   
 $\widetilde{T \cdot t}_{i,j}$ : Fuzzy traveling time of parts  $P_i$ ,  
 $i = 1, 2, \dots, n$ , travel between each machine  
 $M_j$ ,  $j = 1, 2, \dots, m$ , defined as a triplet  
 $(a, b, c)$   
 $W_z$ : A sequence of the same part's gene code with  
 $f$ -elements,  $W_z, z = 1, 2, \dots, f$   
 $\widetilde{S \cdot t}$ : Fuzzy start time  
 $Y_1$ : Checking the start time ( $\widetilde{S \cdot t}$ ), based on the  
 part's sequencing ( $P_i$ ) assigned to the  
 machine ( $M_j$ )  
 $Y_2$ : Checking the start time ( $\widetilde{S \cdot t}$ ) of machine's  
 availability ( $M_j$ ) assigned to produce the  
 parts ( $P_i$ )  
 $Y_3$ : Checking the start time ( $\widetilde{S \cdot t}$ ) of the parts  
 entering the machines based on the sequence  
 of the part's assembly ( $A.S._p$ ) for each  
 product ( $P.No._h$ )  
 T.S.N: Total setup number  
 T.C.T: Total completion time  
 PS: Population size  
 CR( $t$ ): Crossover rate  
 Pm( $t$ ): Mutation rate  
 Max . $X_q$ : Maximum gene code.

## Conflict of Interests

The authors declare that there is no conflict of interests regarding the publication of this paper.

## Acknowledgment

The authors would like to acknowledge the Ministry of Higher Education for the financial support under High Impact research Grant UM.C/HIR/MOHE/ENG/35 (D000035-16001).

## References

- [1] Z. X. Guo, W. K. Wong, S. Y. S. Leung, J. T. Fan, and S. F. Chan, "Mathematical model and genetic optimization for the job shop scheduling problem in a mixed- and multi-product assembly environment: a case study based on the apparel industry," *Computers & Industrial Engineering*, vol. 50, no. 3, pp. 202–219, 2006.
- [2] S. O. Tasan and S. Tunali, "A review of the current applications of genetic algorithms in assembly line balancing," *Journal of Intelligent Manufacturing*, vol. 19, no. 1, pp. 49–69, 2008.
- [3] N. Kriengkarakot and N. Pianthong, "The assembly line balancing problem: review articles," *KKU Engineering Journal*, vol. 34, no. 2, pp. 133–140, 2012.
- [4] I. Baybars, "A survey of exact algorithms for the simple assembly line balancing problem," *Management Science*, vol. 32, no. 8, pp. 909–932, 1986.
- [5] Z. Taha, F. Tahriri, and A. Zuhdi, "Job sequencing and layout optimization in virtual production line," *Journal of Quality*, vol. 18, no. 4, pp. 351–374, 2011.
- [6] P. Brucker and T. Kampmeyer, "Cyclic job shop scheduling problems with blocking," *Annals of Operations Research*, vol. 159, no. 1, pp. 161–181, 2008.
- [7] G. Heike, M. Ramulu, E. Sorenson, P. Shanahan, and K. Moinzadeh, "Mixed model assembly alternatives for low-volume manufacturing: the case of the aerospace industry," *International Journal of Production Economics*, vol. 72, no. 2, pp. 103–120, 2001.
- [8] A. R. Rahimi-Vahed, M. Rabbani, R. Tavakkoli-Moghaddam, S. A. Torabi, and F. Jolai, "A multi-objective scatter search for a mixed-model assembly line sequencing problem," *Advanced Engineering Informatics*, vol. 21, no. 1, pp. 85–99, 2007.
- [9] B. Javadi, A. Rahimi-Vahed, M. Rabbani, and M. Dangchi, "Solving a multi-objective mixed-model assembly line sequencing problem by a fuzzy goal programming approach," *International Journal of Advanced Manufacturing Technology*, vol. 39, no. 9-10, pp. 975–982, 2008.
- [10] N. Boysen, M. Flidner, and A. Scholl, "Sequencing mixed-model assembly lines: survey, classification and model critique," *European Journal of Operational Research*, vol. 192, no. 2, pp. 349–373, 2009.
- [11] Y. Monden, *Toyota Production System: Practical Approach to Production Management*, Industrial Engineering and Management Press, Institute of Industrial Engineers, Norcross, Ga, USA, 1997.
- [12] J. F. Bard, E. Dar-El, and A. Shtub, "Analytic framework for sequencing mixed model assembly lines," *The International Journal of Production Research*, vol. 30, no. 1, pp. 35–48, 1992.
- [13] E. M. Dar-El, "Mixed-model assembly line sequencing problems," *Omega*, vol. 6, no. 4, pp. 313–323, 1978.
- [14] E. M. Dar-El and R. F. Cothier, "Assembly line sequencing for model mix," *The International Journal of Production Research*, vol. 13, no. 5, pp. 463–477, 1975.
- [15] E. M. Dar-El and A. Nadivi, "A mixed-model sequencing application," *The International Journal of Production Research*, vol. 19, no. 1, pp. 69–84, 1981.
- [16] C. Merengo, F. Nava, and A. Pozzetti, "Balancing and sequencing manual mixed-model assembly lines," *The International Journal of Production Research*, vol. 37, no. 12, pp. 2835–2860, 1999.
- [17] X. Zhu, S. J. Hu, Y. Koren, S. P. Marin, and N. Huang, "Sequence planning to minimize complexity in mixed-model assembly lines," in *Proceedings of the IEEE International Symposium on Assembly and Manufacturing (ISAM '07)*, pp. 251–258, July 2007.
- [18] B. Rekiek, P. De Lit, and A. Delchambre, "Designing mixed-product assembly lines," *IEEE Transactions on Robotics and Automation*, vol. 16, no. 3, pp. 268–280, 2000.
- [19] P. De Lit, A. Delchambre, and J.-M. Henrioud, "An integrated approach for product family and assembly system design," *IEEE Transactions on Robotics and Automation*, vol. 19, no. 2, pp. 324–334, 2003.
- [20] J. Bukchin, E. M. Dar-El, and J. Rubinovitz, "Mixed model assembly line design in a make-to-order environment," *Computers & Industrial Engineering*, vol. 41, no. 4, pp. 405–421, 2001.
- [21] C. Moon, M. Lee, Y. Seo, and Y. H. Lee, "Integrated machine tool selection and operation sequencing with capacity and precedence constraints using genetic algorithm," *Computers & Industrial Engineering*, vol. 43, no. 3, pp. 605–621, 2002.

- [22] A. Khan and A. J. Day, "A knowledge based design methodology for manufacturing assembly lines," *Computers & Industrial Engineering*, vol. 41, no. 4, pp. 441–467, 2001.
- [23] A. R. Mendes, A. L. Ramos, A. S. Simaria, and P. M. Vilarinho, "Combining heuristic procedures and simulation models for balancing a PC camera assembly line," *Computers & Industrial Engineering*, vol. 49, no. 3, pp. 413–431, 2005.
- [24] A. Joly and Y. Frein, "Heuristics for an industrial car sequencing problem considering paint and assembly shop objectives," *Computers & Industrial Engineering*, vol. 55, no. 2, pp. 295–310, 2008.
- [25] S. Ghosh and R. J. Gagnon, "Comprehensive literature review and analysis of the design, balancing and scheduling of assembly systems," *The International Journal of Production Research*, vol. 27, no. 4, pp. 637–670, 1989.
- [26] A. Norozi, M. K. Ariffin, and N. Ismail, "Application of intelligence based genetic algorithm for job sequencing problem on parallel mixed-model assembly line," *American Journal of Engineering and Applied Sciences*, vol. 3, no. 1, pp. 831–840, 2010.
- [27] W. K. Wong, C. K. Chan, and W. H. Ip, "Optimization of spreading and cutting sequencing model in garment manufacturing," *Computers in Industry*, vol. 43, no. 1, pp. 1–10, 2000.
- [28] S. G. Ponnambalam, P. Aravindan, and M. Subba Rao, "Genetic algorithms for sequencing problems in mixed model assembly lines," *Computers & Industrial Engineering*, vol. 45, no. 4, pp. 669–690, 2003.
- [29] S.-M. Im and J.-J. Lee, "Adaptive crossover, mutation and selection using fuzzy system for genetic algorithms," *Artificial Life and Robotics*, vol. 13, no. 1, pp. 129–133, 2008.
- [30] R. Subbu, A. C. Sanderson, and P. P. Bonissone, "Fuzzy logic controlled genetic algorithms versus tuned genetic algorithms: an agile manufacturing application," in *Proceedings of the IEEE International Symposium on Intelligent Control (ISIC '98)*, pp. 434–440, September 1998.
- [31] M. Gen, R. Chen, and L. Lin, *Network Models and Optimization: Multiobjective Genetic Algorithm Approach*, Springer, New York, NY, USA, 2008.
- [32] B. S. P. Reddy and C. S. P. Rao, "A hybrid multi-objective GA for simultaneous scheduling of machines and AGVs in FMS," *International Journal of Advanced Manufacturing Technology*, vol. 31, no. 5-6, pp. 602–613, 2006.
- [33] P. T. Zacharia and A. C. Nearchou, "Multi-objective fuzzy assembly line balancing using genetic algorithms," *Journal of Intelligent Manufacturing*, vol. 23, no. 3, pp. 615–627, 2012.
- [34] P. R. McMullen, "An efficient frontier approach to addressing JIT sequencing problems with setups via search heuristics," *Computers & Industrial Engineering*, vol. 41, no. 3, pp. 335–353, 2001.
- [35] P. R. McMullen, "An ant colony optimization approach to addressing a JIT sequencing problem with multiple objectives," *Artificial Intelligence in Engineering*, vol. 15, no. 3, pp. 309–317, 2001.
- [36] P. R. McMullen, "A Kohonen self-organizing map approach to addressing a multiple objective, mixed-model JIT sequencing problem," *International Journal of Production Economics*, vol. 72, no. 1, pp. 59–71, 2001.
- [37] P. R. McMullen and P. Tarasewich, "A beam search heuristic method for mixed-model scheduling with setups," *International Journal of Production Economics*, vol. 96, no. 2, pp. 273–283, 2005.
- [38] J. F. Bard, A. Shtub, and S. B. Joshi, "Sequencing mixed-model assembly lines to level parts usage and minimize line length," *The International Journal of Production Research*, vol. 32, no. 10, pp. 2431–2454, 1994.
- [39] P. R. McMullen, "JIT sequencing for mixed-model assembly lines with setups using Tabu Search," *Production Planning & Control*, vol. 9, no. 5, pp. 504–510, 1998.
- [40] P. R. McMullen and G. V. Frazier, "A simulated annealing approach to mixed-model sequencing with multiple objectives on a just-in-time line," *IIE Transactions*, vol. 32, no. 8, pp. 679–686, 2000.
- [41] V. Giard and J. Jeunet, "Optimal sequencing of mixed models with sequence-dependent setups and utility workers on an assembly line," *International Journal of Production Economics*, vol. 123, no. 2, pp. 290–300, 2010.
- [42] D. J. Fonseca, C. L. Guest, M. Elam, and C. L. Karr, "A fuzzy logic approach to assembly line balancing," *Mathware & Soft Computing*, vol. 12, no. 1, pp. 57–74, 2005.
- [43] M. Gen, Y. Tsujimura, and Y. Li, "Fuzzy assembly line balancing using genetic algorithms," *Computers & Industrial Engineering*, vol. 31, no. 3-4, pp. 631–634, 1996.
- [44] Y. Tsujimura, M. Gen, and E. Kubota, "Solving fuzzy assembly-line balancing problem with genetic algorithms," *Computers & Industrial Engineering*, vol. 29, no. 1-4, pp. 543–547, 1995.
- [45] W. Cheung and H. Zhou, "Using genetic algorithms and heuristics for job shop scheduling with sequence-dependent setup times," *Annals of Operations Research*, vol. 107, no. 1–4, pp. 65–81, 2001.
- [46] G. Mosheiov, A. Sarig, and J. Sidney, "The Browne-Yechiali single-machine sequence is optimal for flow-shops," *Computers and Operations Research*, vol. 37, no. 11, pp. 1965–1967, 2010.
- [47] J. Silberholz and B. Golden, "Comparison of metaheuristics," in *Handbook of Metaheuristics*, Springer, New York, NY, USA, 2010.

## Research Article

# A Dynamic Model of the Tragedy of the Commons in Marketing-Intensive Industries

**Dohoon Kim**

*School of Management, Kyung Hee University, 26, Kyungheedaero, Dongdaemun-gu, Seoul 130-701, Republic of Korea*

Correspondence should be addressed to Dohoon Kim; [dyohaankhu@khu.ac.kr](mailto:dyohaankhu@khu.ac.kr)

Received 18 January 2014; Revised 17 March 2014; Accepted 18 March 2014; Published 27 April 2014

Academic Editor: Nachamada Blamah

Copyright © 2014 Dohoon Kim. This is an open access article distributed under the Creative Commons Attribution License, which permits unrestricted use, distribution, and reproduction in any medium, provided the original work is properly cited.

This study provides a dynamic model and analyzes its process that may plunge the business ecosystem into ToC (the Tragedy of the Commons). When developing the model, we have in mind some industries where the marketing competition to secure a large installed base is intense. The social commerce industry is a representative example of this type of industries, but the scope of this study is not limited to the industry. We first introduce a previous study focusing on the static Nash equilibrium, and then present an extended version of the basic model in a dynamic perspective. According to our analyses on the dynamic equilibria together with their stability, there may be a unique interior equilibrium, but it is highly likely unstable. In addition, possible (near) boundary equilibria are also unstable for a wide range of parameter values. We also conduct some numerical experiments and discover cycles as solutions to some particular instances. Since those cycles contain the ToC traps, a policy measure or regulation may need to be employed. Our approach and results will help to figure out a clue to escape from the ToC trap, thereby shedding new light on the sustainable growth of the business ecosystem, which is prone to excessive marketing competition.

## 1. Introduction

As the mobile services and SNS (social network service) are becoming the most common and popular media to access and use the Internet, they are rapidly replacing PCs and other types of information devices dedicated to serve a specific purpose. Information flows through social media keep increasing and will change the way of organizing and leading businesses and industries. For example, marketing practice has entered a new horizon, where mobile social media plays a central role in firms' marketing campaign and reduces the entry barrier by expanding the spheres of activities and lowering the access costs. One can find representative cases in the social commerce industry which utilizes social media as a commercial platform. It is not surprising to discover a strong incentive to construct a business model with Facebook and Twitter, each of which retains more than 1 billion and 5,000 million users over the globe, respectively.

Despite their tremendous success in creating new service markets and expanding the business areas, SNS platforms and other e-commerce providers based on social media face many challenges in practice. In particular, the social commerce

providers have experienced rise and fall over a short period of time right after their beginning (MacMillan [1–3], Reibstein [4], Webster [5], and Wheeler [6]). Indeed, the number of providers is decreasing in many countries. Groupon, the first global social commerce company, went through hardship in its IPO (initial public offering) and suffered sharp drops of its stock price right after the IPO.

These problems and challenges are not found only in the social commerce area. In effect, when innovators and pioneers plan to monetize eyeballs, they are likely to be exposed to the risk that arises from those problems. In that sense, the issue may be generally embedded or innate property of many business areas, which directly or indirectly depend on the installed base (Kumar and Rajan [7] and Patel [8]). Even for Facebook and Twitter, for example, the dream of advertising revenue has yet to be substantially realized, and many potential investors are still stuck at the thinking that if these providers could secure a large number of users, they would be able to sell new products and services to their users in the future (Cusumano [9], Kruschwitz [10], and Leber [11]).

If this is the case, the entire industry is highly likely to plunge into a marketing competition, where each player competes to expand its prospective installed base by reinforcing marketing activities in a broad sense. SNS, social commerce, online/mobile games, telecom services, and many ICT business areas experience and suffer from marketing wars fighting for customers and users.

One of the major backgrounds of the marketing competition comes from the cost structure of the corresponding industry. For example, a low entry barrier as in the case of social commerce (Anderson et al. [12], Reibstein [4], Wheeler [6], and Urstadt [13]) makes it possible for a great number of potential players to enter the industry once they observe a positive gain above the normal profits. Seeking the first mover's advantage may be another driver of the marketing war. In such a case, relatively few competing providers spend lots of cash on advertising activities. Telecom operators and pharmaceutical companies are the best example of this case. We will call this type of industries the "marketing-intensive industry."

However, it is not easy to find analytical studies about the marketing competition of this kind. One major reason for the meager literature on this inherent weakness of the marketing-intensive industries can be found in a tradition of economic studies. That is, firms and providers are typically assumed to seek for the profit, not for the market share. But, recent changes occurring across the broad range of industries defy this tradition. One of them is fusion or convergence across multiple industries, which conceals the exact financial gain of a company participating in a business ecosystem built upon multiple industries. Another big change is referred to as "servicification," which emphasizes the trend that services are increasingly essential as both inputs and outputs in many industries including even traditional manufacturing areas such as automobile and consumer electronics (Lodefalk [14], Schmitt and Hatfield [15], and Stephen and Toubia [16]). The ICT industries, particularly social media services, experience both trends, thereby exposing themselves to fierce competition for market share.

This study suggests a modeling framework for and conducts analysis of the marketing-intensive industries vulnerable to the risk of collapse due to excessive competition to expand the installed base. Such industries are prone to getting mired in marketing wars due to inherent properties in the business model itself (Though we started this section with mentioning the social media industry as one of representative instances that fit our model assumptions, the application scope of our approach will not be confined to social media and other ICT industries). We first develop a stylized business model that captures the essential features of the competition process. Our approach focuses on the relationship between key decision issues such as marketing inputs and market value. As more providers join the industry thanks to the low entry barrier, they are inevitably faced with fierce competition. This may lead to sharp increase in the expenditure related to marketing and advertising activities in a broad sense. This type of competition may lead the industry away from its optimal development path and, at worst, toward a

collapse of the entire business ecosystem as described in some ICT business cases above.

Having such a case, the situation that we will deal with in this study resembles ToC (the tragedy of the commons; Alroy [17], Hardin [18], Greco and Floridi [19], and Knowledge at Wharton [20]), where the user market (the commons in our metaphor) is vulnerable to exploitation by providers' aggressive marketing to enhance their installed base. Thus, another goal of this study should be to examine the possibilities and conditions that ToC may occur in such a business ecosystem. In fact, oscillations and/or emergence of ToC are not a special case but rather common in dynamic formulations. They have been observed in many different circumstances. In particular, with a structured population (Perc and Szolnoki [21], Perc et al. [22], Santos et al. [23], Szolnoki and Perc [24], Szolnoki and Perc [25], and Szolnoki and Perc [26]). However, such a dynamic nature not unusual in natural phenomenon may also prevail over stable equilibria, particularly in the business areas characterized by severe marketing competition on the basis of a perfectly mixed population. If it is true, we should examine the possibility of unintended consequences of an excessive competition as it is likely to impinge upon market maturity. For that purpose, we will analyze the process that plunges the business ecosystem into ToC and conduct some experiments in order to investigate the effects of the parameters in our model. Our approach and expected results will help to discover some clues to escape from this kind of traps, thereby shedding new light on the sustainable growth of the marketing-intensive industries such as the social media businesses. We will also present some policy implications that could be attained in the course of implementation of our suggestions to alleviate the risk of ToC.

In one of the previous researches on this subject, Kim [27] presents static game models that deal with homogeneous as well as heterogeneous providers in the social commerce industry. In this study, we will also build game models with heterogeneous providers and derive explicit equilibria in a dynamic setting. This study primarily takes the social media industries into account but is not confined within a specific industry as in Kim's study [27]. In particular, the dynamics adopted in our model will show sharp contrasts between static and dynamic approaches in terms of the equilibria, stability, and their resulting insights.

This paper is organized as follows. The next section introduces the basic model and static analysis. Section 3 provides our dynamic model and analysis and compares the results with ones from the static case. In the next section, we present some experiment outcomes together with their lessons and policy implications. Our final section concludes this study and suggests some future works.

## 2. Basic Model and Analysis

*2.1. Basic Model.* Let us suppose a player set composed of  $N$  potential SC providers, where  $j$  is employed as the index for an individual (sometimes representative) SC provider.  $\mathbf{N}$  denotes the set of SC providers; that is,  $\mathbf{N} = \{1, \dots, N\}$ .

Among  $N$  providers, some providers may not join the market. The strategic decision variable of SC provider  $j$  is its marketing efforts  $e_j$ . Those who do not join the market exercise 0 marketing efforts.

In our model, SC providers are assumed to be horizontally differentiated according to their marketing capabilities, which is the major factor characterizing the providers. We employ  $q_j$  to represent the overall marketing costs of provider  $j$  and assume that  $q_j$ 's are inversely proportional to the characteristic of marketing efficiency. Furthermore, the potential providers in  $N$  are given their index in an ascending order based on this attribute. Accordingly, the lower the index is, the more efficient it is in marketing; for example, the first provider in  $N$  (i.e.,  $j = 1$ ) bears the lowest marketing cost  $q_1$ .

In each time period, the entire value of the SC market,  $G$ , is determined by two factors. First, when all the providers in a subset  $P$  of  $N$  (i.e.,  $P \subseteq N$ ) are active in the market, the total marketing efforts  $E (= \sum_{j \in P} e_j)$  contribute to the market value  $G$  by stimulating consumers and boosting the market. However,  $E$  also exhibits a negative effect on  $G$  since too much or too little marketing efforts over- or underexploit the market. Thus, a deviation from the optimal level of marketing efforts in a certain situation may harm the market conditions in the following period (refer to (1) below).

Second, the entire value of the SC market is also affected by environmental factors such as consumer preference change and technological development. We abbreviate these environmental factors into  $M$  as in (1), which will be called "the market maturity factor." However,  $M$  will not be assumed to be given exogenously as in Kim's study [27]. Instead, we will develop a dynamic model where  $M$  is endogenously determined based on the providers' decisions (refer to Section 3).

As  $M$  and  $E$  change from one period to another,  $G$  also experiences a series of changes. We incorporate the following relationship between the market value and two major factors explained above:

$$G = G(E | M) = M \cdot E \cdot (2K - E), \tag{1}$$

where  $K$  in (1) represents the optimal level of the total marketing efforts  $E^*$  embedded (but probably hidden) in the SC industry. Accordingly, (1) implies that a total marketing effort lower than  $K$  leaves a room for further expansion of the market, while a total marketing efforts higher than  $K$  incurs an overheating and entails a contraction of the market in the following periods.

The market value  $G$  realized in the current period is distributed over the active SC providers in the corresponding period. We assume that the allocation of  $G$  is proportional to the marketing efforts  $e_j$ 's. Therefore, the share of the active provider  $j$ ,  $g_j$ , is determined by  $G(e_j/E) = M \cdot (2K - E) \cdot e_j$ . Then, the net benefit of the provider  $j$ ,  $r_j$ , is as follows:

$$r_j = g_j - q_j \cdot e_j = \{M(2K - E) - q_j\} \cdot e_j. \tag{2}$$

Those who decide not to join the market (i.e.,  $e_j = 0$ ) get 0 payoff. Others who participate in the market try to predict the total marketing efforts  $E$  and determine their marketing

efforts  $e_j$ 's, each of which maximizes the corresponding  $r_j$ . Unfortunately, however, possible miss predictions result in losses for some providers, that is, resulting  $r_j < 0$  for some providers. In the next period, the providers who experienced losses in the former period will leave the market or try to minimize its loss. In our model, once a provider decides to join the market at  $t$ , it cannot retreat at  $t$ . Therefore, when a provider experiences a negative payoff, the provider chooses the marketing level which actually minimizes its loss. Once the number of active providers  $P(t) = p$  is determined, one can show that providers' optimal marketing efforts are explicitly determined as in the following section.

**2.2. Static Analysis.** This section introduces Nash equilibria of the static model based on the previous study of Kim [27]. Before presenting some key results in Kim's study [27], let us define some notions and terms for ease of explanation and enhanced readability:

$$\Theta_n = \begin{bmatrix} 1 & \frac{1}{2} & \frac{1}{2} & \dots & \frac{1}{2} \\ \frac{1}{2} & 1 & \frac{1}{2} & \dots & \frac{1}{2} \\ \vdots & \vdots & \ddots & \ddots & \vdots \\ \frac{1}{2} & \frac{1}{2} & \frac{1}{2} & \dots & 1 \end{bmatrix}, \quad \mu_n = \begin{bmatrix} K - \frac{q_1}{2M} \\ K - \frac{q_2}{2M} \\ \vdots \\ K - \frac{q_n}{2M} \end{bmatrix}, \tag{3}$$

$$Q(n) = \sum_{j=1}^n q_j, \quad E(n) = \sum_{j=1}^n e_j,$$

where  $\Theta_n$  is  $(n \times n)$  square matrix and  $\mu_n$  is  $n$ -dimensional column vector whose elements start with  $j = 1$  in the increasing order. By the property of the symmetric matrix, the inverse matrix of  $\Theta_n$ ,  $\Theta_n^{-1}$ , is also symmetric and derived as follows:

$$\Theta_n^{-1} = \begin{bmatrix} \frac{2n}{n+1} & \frac{-2}{n+1} & \frac{-2}{n+1} & \dots & \frac{-2}{n+1} \\ \frac{-2}{n+1} & \frac{2n}{n+1} & \frac{-2}{n+1} & \dots & \frac{-2}{n+1} \\ \vdots & \vdots & \ddots & \ddots & \vdots \\ \frac{-2}{n+1} & \frac{-2}{n+1} & \frac{-2}{n+1} & \dots & \frac{2n}{n+1} \end{bmatrix}. \tag{4}$$

**Proposition 1** (see Kim's study [27]). *For readability, one omits  $t$  in  $M(t)$  and  $P(t)$ . Suppose that there are  $P(t) = p$  providers as in the increasing order of  $q_j$ 's. That is,  $p$  providers whose indices spread from 1 to  $p$  in  $N$  now enter the market at  $t$ . Let  $y (\leq p)$  denote the index of the provider with  $q_y \leq (2KM + Q(p))/(p + 1)$  and  $q_{y+1} > (2KM + Q(p))/(p + 1)$ . Then, the marketing effort profile  $(\bar{e}_1, \dots, \bar{e}_y, 0, \dots, 0)$ , where  $\bar{e}_j$ 's are determined as follows, constitute a Nash equilibrium:*

$$\bar{e}_j = \{\Theta_y^{-1} \cdot \mu_y\}_j = 2 \left( K - \frac{q_j}{2M} \right) - \frac{2pK}{p+1} + \frac{Q(p)}{M(p+1)}, \tag{5}$$

where  $\{x\}_j$  represents the  $j$ th element of the vector  $x$ .

*Proof.* Omitted (for proof, see Kim's study [27]). □

Proposition 1 presents a Nash equilibrium of the basic static model. Note that there is marginal provider represented by  $y$ . Then, those who have lower index than  $y$  earn positive profits (i.e.,  $r_j > 0$ , for all  $j \leq y$ ), while providers whose indices are larger than  $y$  do not join the industry, thereby earning nothing (i.e.,  $r_j = 0$ , for all  $j > y$ ). The size of active providers is a function of  $M(t)$  and  $Q(p)$ . Let us call  $y$  in Proposition 1 “the efficiency threshold” since  $y$  sets the upper bound on the number of active providers, each of which maintains a positive payoff. From Proposition 1 above, we also know that  $\bar{E} = \sum_{j=1}^p \bar{e}_j$  is described by the following equation:

$$\bar{E}(t) = \frac{2yK}{y+1} - \frac{Q(y)}{(y+1)M(t)} = \frac{2yKM(t) - Q(y)}{(y+1)M(t)}. \quad (6)$$

When all the potential providers are homogeneous (i.e.,  $q_j = q$ , for all  $j$ ), their strategies will be symmetric and result in a symmetric Nash equilibrium as follows.

**Corollary 2** (symmetric equilibrium with homogeneous players). *Let one considers the situation where all the providers are homogeneous in the sense of  $q_j = q$ , for all  $j \in \mathbf{N}$ . Suppose that the following inequality holds; that is,  $2M(t)K(t) > q$ . Then, at a symmetric equilibrium, all the potential providers join the market and exercise the same marketing effort  $\bar{e}$  determined as follows:*

$$\bar{e}_j = \bar{e} = \frac{2}{N+1} \left( K - \frac{q}{2M(t)} \right) \quad \forall j \in \mathbf{N}. \quad (7)$$

*Proof.* Omitted (for proof, see Kim’s study [27]).  $\square$

In the case of homogeneous players, we have much simpler expressions for the equilibrium strategies as above. First note that all the homogeneous players join the market or leave the market at the same time. Thus,  $y(t)$  in Proposition 1 will be either 0 or  $N$ , which establishes a key difference from the case of heterogeneous players. With the same  $K$  and  $M(t)$ , the marketing effort of a heterogeneous active player ( $\bar{e}_j$ ) will be higher than that of a homogeneous player ( $\bar{e}$ ) in general (Of course, the marketing effort of a heterogeneous player close to the marginal provider may be lower than  $\bar{e}$ ). The total marketing efforts in the homogeneous case amount to  $N\bar{e}$ . Subsequently, if  $Nq < Q(y)$ , then the total marketing efforts in the homogeneous case are larger than those in the heterogeneous case. If they are not, however, one cannot uniformly determine the size comparison; it depends on the distribution of  $q_j$ ’s.

### 3. Dynamic Model and Analysis

**3.1. Dynamic Model.** Now, we will extend the basic model together with its context from a new dynamic perspective. The analytical results above have been derived under the assumption that a certain number of providers ( $p$  providers) already exist in the industry and the market maturity factor  $M$  is given and fixed. However, these two parameters ( $p$  and  $M$ ) should also change in their turn after the agent behaviors (here, e.g., the best efforts  $\bar{e}_j$ ’s in the Nash equilibrium) are determined. Our dynamic model will reflect these

interactions between parameters and endogenous variables in the basic model. In particular, we incorporate the dynamics described below.

First note that it is natural as well as practical to set up the circumstances where the (potential) providers know only the parameter values in the last period. If this is the case, then the active providers try to predict the total marketing efforts  $E$  and adjust their marketing efforts  $e_j$ ’s, which optimizes their net benefits and results in nonnegative payoffs. However, their expectations and decisions do not always succeed, and some providers may receive negative payoffs at the end of the corresponding period. Those who experience a negative payoff in the current period will leave the industry in the next period. On the other hand, all the active providers enjoy positive payoffs at  $t$  and some potential providers inactive at  $t$  will try to join the market at  $t + 1$ .

According to Proposition 1 with given  $K$  and  $M(t)$  at  $t$ ,  $y$  sets the maximum number of the active providers, each of which earns nonnegative payoff from positive marketing efforts. Though the relationship between  $y$  and other parameters is implicitly determined, for a particular  $q_j$  distribution such as  $q_j = h \cdot j$  (i.e., marketing effort costs linearly increasing with a positive constant  $h$ ), we can explicitly determine  $y$  as a function of  $M(t)$  and  $P(t)$ ; for example, with the  $q_j$  specified above,  $Q(p) = (p(p+1)/2)h$  and  $y = \lfloor (2KM/h(p+1)) + (p/2) \rfloor = \lfloor (4KM + hp(p+1))/2h(p+1) \rfloor$ , where  $\lfloor x \rfloor$  rounds  $x$  down to the nearest integer. Furthermore, by pretending that  $y$  is continuous rather than discrete, one can approximate  $y(t)$  and, by plugging  $Q(p)$  into (6), one can approximate  $\bar{E}(t)$  as follows:

$$y(t) \cong \frac{2KM(t)}{hP(t)} + \frac{P(t)}{2}, \quad (8a)$$

$$\bar{E}(t) \cong 2K - \frac{h^2}{4K} \left\{ \frac{P(t)}{M(t)} \right\}^2. \quad (8b)$$

We establish a set of dynamics driven by both the market maturity factor  $M(t)$  and the number of active providers  $P(t)$ . That is, as a result of individual decisions of whether to join the market or not, both  $M(t)$  and  $P(t)$  are endogenously determined by the following systems of difference equations. We employ a set of adaptive dynamics where  $\alpha$  and  $\beta$  represent the weights associated with the current states of the active players and the market maturity, respectively. Consider

$$P(t+1) = \{ \alpha P(t) + (1-\alpha)(y(t) - P(t)) \wedge N \} \vee 0, \quad (9a)$$

$$M(t+1) = \{ \beta M(t) + (1-\beta)(K - \bar{E}(t)) \wedge M_{\max} \} \vee 0, \quad (9b)$$

where  $x \wedge y = \min\{x, y\}$ ,  $x \vee y = \max\{x, y\}$ , and  $M_{\max}$  represents the maximum level of  $M(t)$ .

Plugging ((8a) and (8b)) into ((9a) and (9b)) and rearranging the terms, we establish the systems of the following dynamic equations:

$$P(t+1) = \left\{ \alpha P(t) + (1-\alpha) \left[ \frac{2KM(t)}{hP(t)} - \frac{P(t)}{2} \right] \wedge N \right\} \vee 0, \quad (10a)$$

$$M(t+1) = \left\{ \beta M(t) + (1-\beta)K \left[ \left( \frac{hP(t)}{2KM(t)} \right)^2 - 1 \right] \wedge M_{\max} \right\} \vee 0. \tag{10b}$$

Equation (10a) explains the changes in the number of active providers. The size of active providers in the next period  $P(t+1)$  will increase if the current  $P(t)$  is smaller than  $y(t)$ , the efficiency threshold (i.e., the maximum number of efficient providers). On the other hand,  $P(t+1)$  will decrease if the current number of providers exceeds this threshold since some providers (most likely the ones with low marketing capabilities or high marketing costs) will experience a loss, thereby leaving the industry next time. Lastly, the adaptive dynamics are completed with  $\alpha$  as the associated weight. Equation (10b) also follows the similar reasoning as in (10a). It represents the adaptive adjustment process of  $M(t)$  (with  $\beta$  as its associated weight) when the current total marketing level  $\bar{E}(t)$  fails to hit the optimal level of marketing efforts  $K$ . If the total marketing efforts from the current active providers exceed (in the case of excessive marketing), the market is overexploited and  $M(t+1)$  decreases.

According to the system dynamics described in ((10a) and (10b)), a change in  $M(t)$  affects the market value  $G(t)$  (refer to (1)), which in turn influences the gains of the providers. As a result, some incumbent players exit or some new players enter the industry in the next period, and eventually the total marketing efforts are highly likely to vary. Thus, the possible difference in the speeds of the adjustments may result in a fluctuation in the number of providers, which may hinder the system from settling down to a steady state in the long-run. We will investigate this possibility together with the system performance such as the deviation of the total marketing efforts from the socially optimal level of the marketing.

**3.2. Dynamic Analysis.** Let us first define a positive constant  $\Phi \equiv \sqrt{K^2 + (4/3)h} - K$  to simplify the expressions hereafter. Proposition 3 shows an interior fixed point from the system dynamics. Proposition 4 provides the conditions that the interior fixed point (if exists) is stable or unstable.

**Proposition 3.** *Suppose that both  $\alpha$  and  $\beta$  belong to  $(0, 1)$ . The following state  $(\bar{P}, \bar{M})$  gives an interior fixed point of the system dynamics in ((10a) and (10b)):*

$$\bar{M} = \frac{\Phi}{2}, \quad \bar{P} = \sqrt{\frac{2K\Phi}{3h}}. \tag{11}$$

*Proof.* The interior equilibrium comes from the solution of the following simultaneous equation system:

$$\begin{aligned} P &= \alpha P + (1-\alpha) \left[ \frac{2KM}{hP} - \frac{P}{2} \right], \\ M &= \beta M + (1-\beta)K \left[ \left( \frac{hP}{2KM} \right)^2 - 1 \right]. \end{aligned} \tag{12}$$

By rearranging the two equations in terms of  $P$  and  $M$ , we get

$$\frac{3}{2}P^2 - \frac{2K}{h}M = 0, \quad M^3 + KM^2 - \frac{h^2}{4K}P^2 = 0. \tag{13}$$

Plugging the first equation into the second and rearranging the terms, we get

$$M \left( M^2 + KM - \frac{h}{3} \right) = 0. \tag{14}$$

Thus, either  $M = 0$  or  $M = \Phi/2$  provides the solution to the equation above. However, the first solution does not constitute an interior point (refer to Proposition 5). On the other hand, the second solution is indeed positive ( $\because \Phi > 0$ ) and constitutes the interior equilibrium above.  $\bar{P}$  in (11) comes from the relationship  $(3/2)P^2 = (2K/h)M$  above.  $\square$

**Proposition 4.** *Suppose that  $9\Phi^4 - 6\Phi^2 - 64h^2 > 0$  and  $(16/15)h < K^2$ . If  $\alpha < (5/3) - ((1 + \beta)\Phi^2/4h(1 - \beta))$  and  $\beta < (20h - 3\Phi^2)/(20h + 3\Phi^2)$ , then the fixed point in Proposition 3 is unstable.*

*Proof.* In this proof, we suppress the time index  $t$  for enhanced readability. We first consider linear approximation of the dynamics around the interior equilibrium. Applying the Taylor approximation to ((10a) and (10b)), we get the following matrix that governs the dynamics around an arbitrary point in the state space:

$$\begin{bmatrix} \frac{3\alpha - 1}{2} - \frac{2K(1-\alpha)}{h} \cdot \frac{M}{P^2} & \frac{2K(1-\alpha)}{h} \cdot \frac{1}{P} \\ \frac{h^2(1-\beta)}{2K} \cdot \frac{P}{M^2} & \beta - \frac{h^2(1-\beta)}{2K} \cdot \frac{P^2}{M^3} \end{bmatrix}. \tag{15}$$

In particular, the matrix reduces to the following one around the interior fixed point  $(\bar{P}, \bar{M})$ :

$$\begin{bmatrix} 1 & (1-\alpha) \sqrt{\frac{6K}{h\Phi}} \\ (1-\beta) \sqrt{\frac{1}{3K} \cdot \left( \frac{2h}{\Phi} \right)^3} & \beta + \frac{4h(1-\beta)}{3K\Phi - 2h} \end{bmatrix}. \tag{16}$$

Note that  $(3/2)\Phi^2 = 2h - 3K\Phi$ . Then, the characteristic equation of the matrix above comes as follows:

$$\begin{aligned} \lambda^2 + \left( \frac{8h(1-\beta)}{3\Phi^2} - 1 - \beta \right) \lambda + \beta \\ + \frac{4h(1-\beta)(3\alpha - 5)}{3\Phi^2} \\ = \lambda^2 + \Theta\lambda + \Omega = 0, \end{aligned} \tag{17}$$

where  $\Theta \equiv (8h(1 - \beta)/3\Phi^2) - 1 - \beta$  and  $\Omega \equiv \beta + (4h(1 - \beta)(3\alpha - 5)/3\Phi^2)$  denote two constants for simplification of the following expressions. The condition that the equation has two distinctive real roots  $\lambda_1$  and  $\lambda_2$  is  $\Theta^2 > 4\Omega$ , which is summarized as below by a chain of arithmetic operations:

$$\begin{aligned}
 &64h^2(1 - \beta)^2 + 9\Phi^4(1 + \beta)^2 \\
 &> 12\Phi^2 \{4h(1 - \beta)(1 + \beta) + \beta\} \quad (18) \\
 &+ 16h(1 - \beta)(3\alpha - 5).
 \end{aligned}$$

Since the second term (the last term) in the right-hand side is negative, it suffices that  $64h^2(1 - \beta)^2 + 9\Phi^4(1 + \beta)^2 > 12\Phi^2\{4h(1 - \beta)(1 + \beta) + \beta\}$  holds. Applying another arithmetic operation and collecting terms reorganize this relation as follows:

$$\begin{aligned}
 &(3\Phi^2 + 8h)^2\beta^2 - 2(64h^2 - 9\Phi^4 + 6\Phi^2)\beta + (3\Phi^2 - 8h)^2 \\
 &> 0. \quad (19)
 \end{aligned}$$

Therefore, if  $9\Phi^4 - 6\Phi^2 - 64h^2 > 0$ , then the inequality above holds and the characteristic equation has two distinctive real solutions.

Now, using the facts that  $\lambda_1 + \lambda_2 = -\Theta$  and  $\lambda_1\lambda_2 = \Omega$ , we can find sufficient conditions which establish stability or instability of the interior equilibrium. Indeed, if  $\lambda_1\lambda_2 < -1$ , then at least one eigenvalue is larger than 1 or less than -1, thereby making the system around the interior fixed point unstable. Since  $\lambda_1\lambda_2 = \Omega = \beta + 4h(1 - \beta)(3\alpha - 5)/3\Phi^2$ , the condition  $\lambda_1\lambda_2 < -1$  reduces into the following inequalities:

$$\begin{aligned}
 &3\beta\Phi^2 + 4h(1 - \beta)(3\alpha - 5) < -3\Phi^2 \\
 \text{or } \alpha < &\frac{5}{3} - \frac{(1 + \beta)\Phi^2}{4h(1 - \beta)}. \quad (20)
 \end{aligned}$$

The right-hand side of the inequality for  $\alpha$  is positive if  $\beta < (20h - 3\Phi^2)/(20h + 3\Phi^2)$ . The right-hand side of the inequality for  $\beta$  is also positive under the condition of  $(16/15)h < K^2$ . Thus, two conditions pertaining to  $\alpha$  and  $\beta$  are well established as a sufficient condition for the interior equilibrium to be unstable, which completes the proof.  $\square$

The proof needs to be complemented since Proposition 4 provides only a sufficient condition. We know that if  $|\lambda_1 + \lambda_2| < 1$  and  $\lambda_1\lambda_2 > 0$  then all the eigenvalues are less than 1, thereby making the system around the interior fixed point stable. However, one can show in a similar way that there is no  $\lambda_i$  that satisfies those conditions. Indeed, since  $\lambda_1 + \lambda_2 = -\Theta = 1 + \beta - (8h(1 - \beta)/3\Phi^2)$ , the condition  $|\lambda_1 + \lambda_2| < 1$  reduces to  $(6K\Phi/(6h - 3K\Phi)) < \beta < (4h/(6h - 3K\Phi))$ . On the other hand, the condition  $\lambda_1\lambda_2 = \Omega > 0$  reduces to  $\alpha > (5/3) - (\beta\Phi^2/4h(1 - \beta))$  and  $\beta > (4h/(6h - 3K\Phi))$ , which cannot be compatible with the previous condition. A similar type of incompatibility occurs in the case of  $\lambda_1\lambda_2 > 1$ . This possibility of instability is also frustrated since the

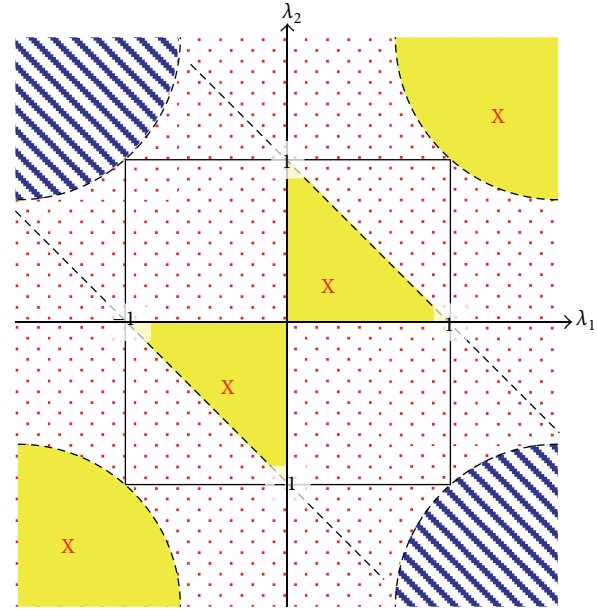


FIGURE 1: Regions of the  $\lambda_1$ - $\lambda_2$  space: explored and unexplored.

condition  $\lambda_1\lambda_2 > 1$  requires either  $\alpha > 1$  or  $\beta > 1$ , which is not acceptable. As a result, we have explored the following regions of the  $\lambda_1$ - $\lambda_2$  space in Figure 1. The shaded regions with “X” mark are the subsets whose  $(\lambda_1, \lambda_2)$ -tuples cannot be realized in our model. The two hatched regions depict the sufficient conditions in this proposition. Thus, Proposition 4 leaves some regions unexplored.

Proposition 3 reveals that there is a unique interior equilibrium if any one exists. Proposition 4, however, implies that the interior equilibrium is highly likely unstable. Though there remain some regions that should be explored in the  $\lambda_1$ - $\lambda_2$  space (see Figure 1), it may not be a good strategy to investigate the stability regions first, with a vague hope to discover such a case. In fact, it seems hard to find an instance in which the interior equilibrium is stable (refer to some experimental results in Section 5). And if this is true, one needs to analyze another possibility and different aspects of the dynamics.

Since the  $P(t)$ - $M(t)$  state space is bounded, the system dynamics may have a boundary equilibrium that needs to be investigated. Obviously, for example,  $(0, 0)$  cannot be a boundary fixed point which represents a complete collapse of both market and industry (Also note that the dynamic equations ((10a) and (10b)) are not defined at  $(0, 0)$ ). However, the system state may approach the origin very closely (refer to the proposition below and the discussions in the next section). Furthermore, neither  $(z, 0)$  with any positive  $z \in (0, N]$  nor  $(0, z)$  with  $z \in (0, M_{\max}]$  can be a Nash equilibrium since, at least for a (potential) player, a deviation from the corresponding state improves its gain. For example, an active player at  $(N, 0)$  will be better off if it leaves the market and avoids a negative payoff. The following proposition deals with the other types of possible boundary equilibria.

**Proposition 5.** *The following two states are (near) boundary fixed point equilibria (compatible with the static model as in*

*Proposition 1). However, both are unstable under the certain conditions (if any) specified below.*

- (i) For an arbitrary small  $\varepsilon$ ,  $(\varepsilon, \varepsilon)$  is a near boundary Nash equilibrium. However,  $(\varepsilon, \varepsilon)$  is unstable if  $h > 2K$ .
- (ii)  $(N, M_{\max})$  is a boundary Nash equilibrium if  $q_N \leq (2KM_{\max}/(N+1)) + (N/2)$ . However,  $(N, M_{\max})$  is unstable if  $4KM_{\max} < 3hN^2$  and  $h^2N^2 < 4KM_{\max}^2(K + M_{\max})$ .

*Proof.* It is easy to show that the two states asserted above become Nash equilibria in the sense compatible with Proposition 1. For  $\varepsilon$  is very close to 0, for example,  $(\varepsilon, \varepsilon) \approx (0, 0)$  implies that any potential provider (even the most efficient provider) outside of the industry cannot expect any positive gain from joining the industry. Thus, the best response of all the providers is to stay out of the industry. Similarly, in the other extreme cases of  $(N, M_{\max})$ , where all the providers join the industry, even the least efficient provider enjoys a positive gain from performing as much marketing effort as determined by Proposition 1 if  $q_N \leq (2KM_{\max}/(N+1)) + (N/2)$ . Therefore, no provider will leave the industry and  $M_{\max}$  is sustained.

In order to show the instability of  $(\varepsilon, \varepsilon)$ , we first apply the Taylor expansion to  $P(t+1) - P(t)$  and  $M(t+1) - M(t)$  at  $(\varepsilon, \varepsilon)$  and get

$$\begin{aligned} P(t+1) - P(t) &= (1 - \alpha) \left\{ \left( \frac{2K}{h\varepsilon} - \frac{3}{2} \right) P(t) + \frac{2K}{h\varepsilon} M(t) + \frac{2K}{h} \right\} - \frac{\alpha\varepsilon}{2} \end{aligned} \quad (21a)$$

$$\begin{aligned} M(t+1) - M(t) &= (1 - \beta) \\ &\times \left\{ \frac{h^2}{2K\varepsilon} P(t) - \left( 1 + \frac{h^2}{2K\varepsilon} \right) M(t) + \frac{h^2}{4K} - K \right\} + \varepsilon. \end{aligned} \quad (21b)$$

Now, we incorporate a small perturbation around  $(\varepsilon, \varepsilon)$  into ((21a) and (21b)). We will show that, for at least one type of perturbation, both  $P(t+1) - P(t)$  and  $M(t+1) - M(t)$  become positive, which means that the system state grows apart from the near boundary equilibrium  $(\varepsilon, \varepsilon)$ . For example, we take into account a small perturbation in a north-east direction such as  $(\varepsilon + \varepsilon_1, \varepsilon + \varepsilon_2)$  where both  $\varepsilon_1$  and  $\varepsilon_2$  are positive and sufficiently small. Then, after a series of arranging and collecting terms, ((21a) and (21b)) reduce as follows:

$$\begin{aligned} P(t+1) - P(t) &= \frac{2K(1-\alpha)}{h} \left( 3 + \frac{\varepsilon_1 + \varepsilon_2}{\varepsilon} \right) + \left( \alpha - \frac{3}{2} \right) \varepsilon + \frac{3}{2} (\alpha - 1) \varepsilon_1 \end{aligned} \quad (22a)$$

$$\begin{aligned} M(t+1) - M(t) &= (1 - \beta) \left\{ \frac{h^2}{2K} \left( \frac{\varepsilon_1 - \varepsilon_2}{\varepsilon} + \frac{1}{2} \right) - K \right\} + \beta(\varepsilon + \varepsilon_2) - \varepsilon_2. \end{aligned} \quad (22b)$$

The first term in the right-hand side of (22a) is always positive and the other two terms are arbitrary small enough for the overall magnitude of  $P(t+1) - P(t)$  to be positive. If  $\varepsilon_1 > \varepsilon_2$  and the condition in (i) holds, then the first two terms in the right-hand side of (22b) are positive. Thus, there are many directions in the north-east area of  $(\varepsilon, \varepsilon)$  along which both  $P(t+1) - P(t)$  and  $M(t+1) - M(t)$  become positive (One can also prove that both (21a) and (21b) lead to a divergence from  $(\varepsilon, \varepsilon)$  in the other areas, e.g., a south-east direction of  $(\varepsilon, \varepsilon)$ ).

One can apply a similar procedure to the case of the boundary equilibrium  $(N, M_{\max})$ . First, the dynamics around  $(N, M_{\max})$  can be written as follows:

$$\begin{aligned} P(t+1) - P(t) &= (\alpha - 1) \left\{ \left( \frac{3}{2} + \frac{2KM_{\max}}{hN^2} \right) P(t) \right. \\ &\quad \left. - \frac{2K}{hN} M(t) - \frac{2KM_{\max}}{hN} \right\} \end{aligned} \quad (23a)$$

$$\begin{aligned} M(t+1) - M(t) &= (1 - \beta) \left\{ \frac{h^2N}{2KM_{\max}^2} P(t) - \left( 1 + \frac{h^2N^2}{2KM_{\max}^3} \right) M(t) \right. \\ &\quad \left. + \frac{h^2N^2}{4KM_{\max}^2} - K \right\}. \end{aligned} \quad (23b)$$

To determine its stability, we again evaluate a small perturbation around  $(N, M_{\max})$ . In this case, however, one needs to examine only one direction of perturbation, that is,  $(N - \varepsilon, M_{\max} - \varepsilon)$ , where  $\varepsilon$  is positive and sufficiently small. After a series of operations, ((23a) and (23b)) reduce as follows:

$$\begin{aligned} P(t+1) - P(t) &= (1 - \alpha) \left\{ \frac{4KM_{\max} - 3hN^2}{2hN} \right. \\ &\quad \left. + \left( \frac{2K(M_{\max} - N)}{hN^2} + \frac{3}{2} \right) \varepsilon \right\} \end{aligned} \quad (24a)$$

$$\begin{aligned} M(t+1) - M(t) &= (1 - \beta) \left\{ \frac{h^2N^2}{4KM_{\max}^2} - M_{\max} - K \right. \\ &\quad \left. + \left( \frac{h^2N(N - M_{\max})}{2KM_{\max}^3} + 1 \right) \varepsilon \right\}. \end{aligned} \quad (24b)$$

Note that the last terms in the respective right-hand side of ((24a) and (24b)) are to be arbitrary small. Thus, the signs of

$P(t+1) - P(t)$  and  $M(t+1) - M(t)$  are determined by their first terms, each of which is negative if the conditions in (ii) hold. As a result, both  $P(t+1) - P(t)$  and  $M(t+1) - M(t)$  become negative, which establishes the instability of  $(N, M_{\max})$ .  $\square$

First note that the near boundary equilibrium  $(\varepsilon, \varepsilon)$  represents a virtual collapse of the market as well as the industry. On the other hand, the boundary equilibrium  $(N, M_{\max})$  represents a perfect prosperity of the business ecosystem. Thus, the stability analysis about those two boundary states suggests not only good news but also bad news. The good news is that as both the market force and the number of providers approach nil, at least a tiny fraction of providers still seize the opportunity to earn positive gains, which would in turn boost the market demand. This mechanism of escaping from almost complete destruction comes from the structural property of the dynamics that would not allow nil to be as a fixed point.

On the other hand, the instability of the complete prosperity presents a bad news. As shown in the proof, a small perturbation occurring around the boundary state may lead the system away from the ideal situation. This system behavior probably comes from the mechanism around the saturation state  $(N, M_{\max})$ . That is, with a shock making the system deviate from the saturation, some marginal providers on the limit of positive gain at the saturation now would experience a loss and leave the industry. This reduction of the number of providers is highly likely to cut back the market value, which would in turn disturb more providers on the verge of leaving the industry.

These results suggest that  $P(t)$  and  $M(t)$  which are sufficiently small [or close to their respect upper bounds] may approach the origin [or the saturation] over time but suddenly explodes near the origin [or shrink back near the saturation]. Thus, the stability analysis so far hints a possible cyclic solution to our dynamics. We will check out this possibility through numerical experiments in the next section.

Even though it is true that our system behavior has the property of natural resilience from deterioration, it may stay at the states near a collapse over a long period of time. Thus, we need to develop a policy measure that protects the system from moving toward the collapse and establishes a locally stable positive equilibrium that attracts system trajectories generated around it. If it is successful, the market and the industry will not only be sustained but also stabilized over time at some desirable states. We will also deal with this issue in the next section.

#### 4. Experiments and Discussions

We conduct some numerical simulations in order to examine more thoroughly the system behaviors in various scenarios. In our simulations, both  $P(t)$  and  $M(t)$  are endogenously determined according to the system dynamics presented in the previous section. Subsequently, the total marketing efforts are also changing as the system states vary, which provides a sharp contrast with the theoretical results in the static model

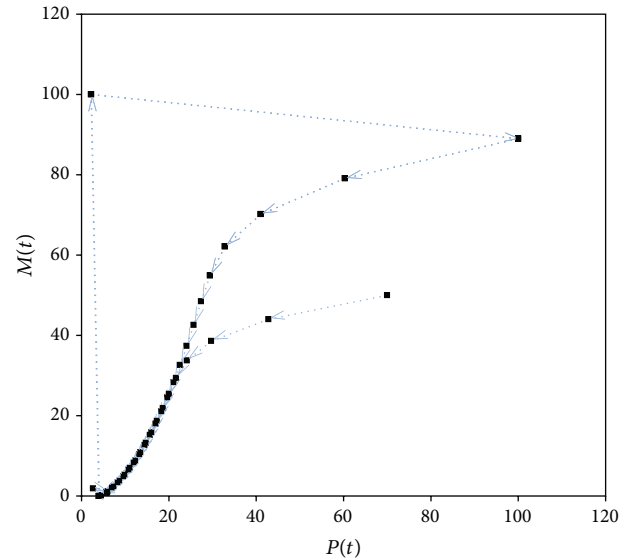


FIGURE 2: Experimental example. Here,  $\alpha = 0.7$ ,  $\beta = 0.9$ ,  $K = 10$ , and  $h = 1$ . The initial point is  $P_0 = 70$  and  $M_0 = 50$  with  $N = 100$  and  $M = 100$ . Arrows show the directions of the migration of the system state. The system state moves toward the origin after leaving the initial point. Interestingly, however, there is a loop starting from near the origin. The presence of the loops implies a cycle in the system behavior.

such as Kim's study [27] (This finding (and the followings) can be captured only in a dynamic setting).

As Propositions 3 to 5 reveal, the outcomes of the dynamic model are quite different from the ones of the static model described in Proposition 1. First of all, note that  $(\varepsilon, \varepsilon)$ , close to a complete collapse of the market and the industry, is not a stable equilibrium, but the system is highly likely to approach the origin. Thus, ToC (the tragedy of the commons) seems to be inevitable in some situations, particularly when the market is not mature (i.e., small  $M_0$ ) with many providers (i.e., large  $P_0$ ). Figure 2 depicts this possibility.

As raised in the previous section, a cycle or a sequence of periodic points seems to constitute a solution to our dynamic equations. In fact, the emergence of the ToC trap and the oscillation dynamics are neither a new phenomenon nor an unusual feature in dynamic models, particularly on the basis of structured interactions among agents (e.g., Perc and Szolnoki [21], Perc et al. [22], and Santos et al. [23]) (In particular, the emergence of cycles (or oscillations) has been observed in the context of adaptive networks (Szolnoki and Perc [24, 25]) and with three competing strategies (Szolnoki et al. [28]), as well as under a presence of punishment (Szolnoki et al. [29]) or a reward (Szolnoki and Perc [26])). However, our model does not assume a structured population; it is one of our future research topics to incorporate organized interactions among providers (see also our comment in the future works)). It is also well known that finding such a cycle is usually a very difficult task, and our model is no exception. However, our numerical experiments including the one above confirm (or at least indicate) that the cyclic solution commonly occurs for many initial states. For example, the experiment outcome

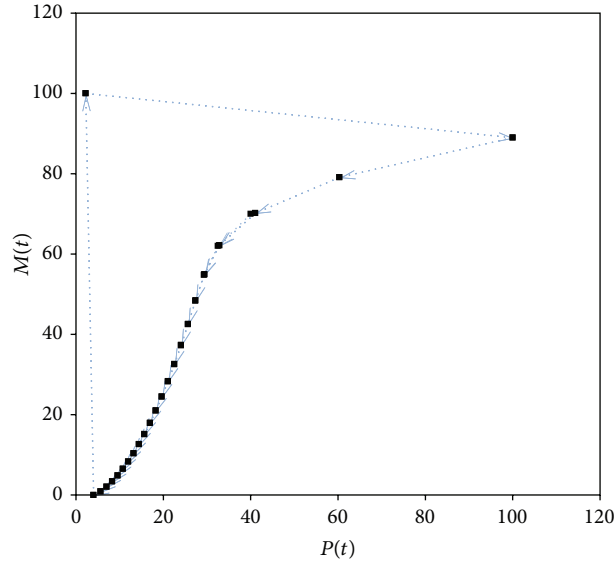


FIGURE 3: A cycle example. Here, all the parameters remain the same as the ones in Figure 2 except the initial states. As starting points,  $P_0 = 40$  and  $M_0 = 70$  are applied to this example.

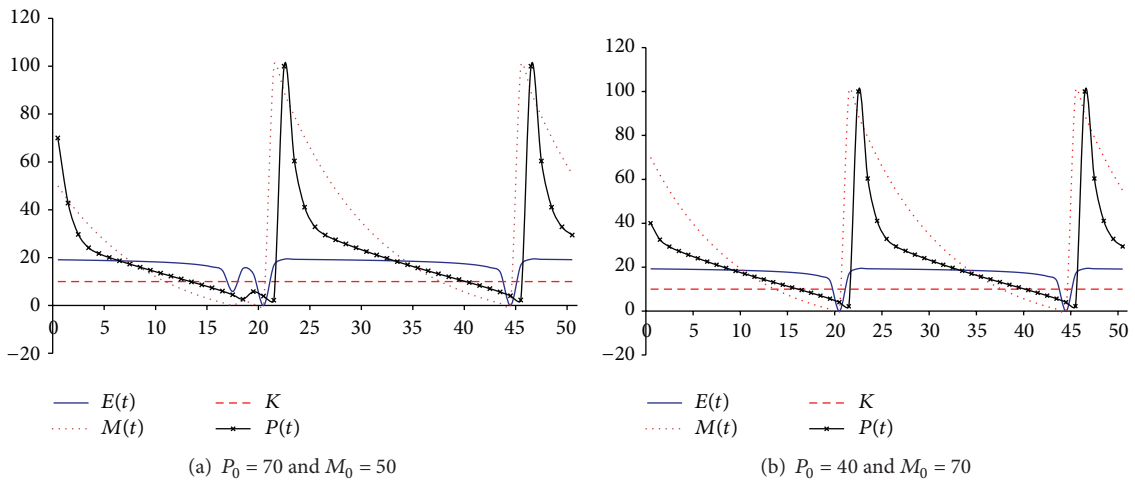


FIGURE 4: Behaviors of key attributes of system. Here, all the parameters and the initial states remain the same as the ones in Figure 2 for (a) and Figure 3 for (b). The time series graphs of  $P(t)$  and  $M(t)$  also clearly point out the cyclic pattern of the system behavior even though they look a little different in the first period due to different starting points. In both instances, the total marketing efforts  $E(t)$  are higher than their optimal level  $K$  most of the time.

depicted in Figure 3 shows a clear cycle of the particular dynamics specified in Figure 2 (except the initial point). In this instance, the initial state is deliberately set to  $(P_0, M_0) = (40, 70)$ , which closely lies on the cycle observed in Figure 2.

Moreover, Figure 4 represents the system behavior along the timeline. They show clear cycles repeating over time. In most of time, the total marketing efforts remain higher than the optimal level  $K$ . Thus, the market maturity eventually drops down to almost zero, which in turn results in deterioration of providers' gain, that is, the ToC trap. Whenever the market maturity approaches nil, most efficient few providers survive and are able to sweep all the gains from the market. Thanks to the monopolized benefits, they can boost the

market and the maturity rapidly increases. This explosion of the market opportunity attracts more providers, and the new cycle starts thereafter.

If this is the most common case then the remaining issue should be related to the ToC trap which seems inevitable in the cycle. In particular, we need to develop a remedy (a policy measure) to cope with ToC. One possible way to pursue is to introduce a regulation that makes providers keep the marketing efforts at their reasonable levels (probably coupled with their cost efficiencies). We may also implement a policy that puts some barriers to preserve a minimum level of the market maturity. Figure 5 shows the effect of the latter approach. One may consider a similar barrier set up for  $P(t)$

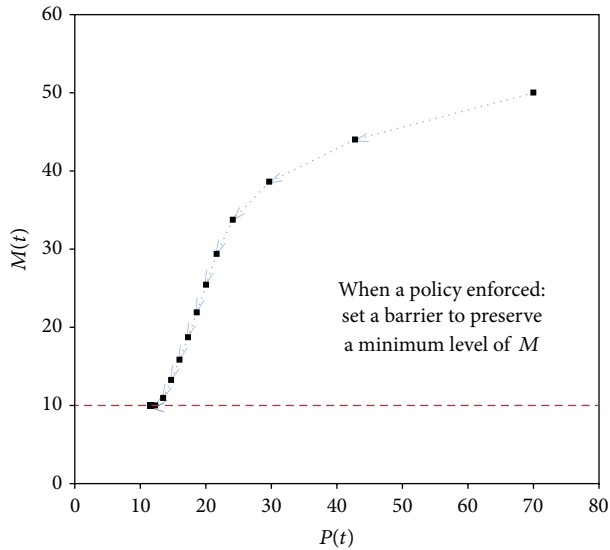


FIGURE 5: Experimental example, with a barrier to sustain the market. Here, all the parameters and the initial states remain the same as the ones in Figure 2 (but the axes have been scaled differently). In addition, however, there is a barrier set up for the market maturity. This barrier keeps the market maturity factor  $M(t)$  above 10. Arrows show the directions of the migration of the system state, which settles down to a fixed state, of which  $M(t)$  corresponds to the barrier. In this instance, there is no cycle.

and compare the outcomes of two approaches in terms of social welfare (As a matter of fact, we also tried this approach but omitted the results here since the outcomes of this policy do not seem to follow a rule; they produce nonstructured many small cycles. Thus, apparently (not rigorously), the policy to sustain at least a certain number of providers fails in providing better outcomes).

## 5. Conclusion and Future Works

This study examined the possibilities of a disruption of a business ecosystem, so-called the ToC trap, which describes the situation where the total marketing efforts  $\bar{E}$  exceed their socially optimal level  $K$ . Not only the interior but also the boundary equilibria were found and analyzed for their stability. We also conducted some numerical experiments and discovered cycles as solutions to some particular instances. Since those cycles contain the ToC traps, we simulated a policy measure to maintain a minimum level of market maturity and checked out the effectiveness of the policy. Even though we had in mind some ICT industries (e.g., the social commerce industry) with fierce marketing competition, our approach and results will not be confined to the ICT industries. And we hope this study helps to find a clue to avoid the ToC trap, thereby shedding new light on the sustainable growth of business ecosystems.

However, the analytical results and implications have been established on the basis of our modeling assumptions, and they may not be generalized into all the situations. In

particular, our assumption of perfectly mixed (or randomized) interactions among the players is not a fully realistic one. This remains as one of the limitations of our model and approach. Thus, it will be an obviously interesting direction of our next research step to extend the proposed game model with a structured population of providers (for benchmarking studies, refer to Szolnoki et al. [28], Szolnoki et al. [29], and Wang et al. [30]).

In our future works, we will also refine policy measures that were derived in the course of implementing our suggestions to alleviate the risk of the ToC trap. We will incorporate various regulatory schemes and other policy ideas (e.g., Greely [31]) and evaluate their effects on the long-run equilibrium. Lastly, we will compare the policy outcomes with one generated from a hypothetical social planner who determines the total marketing level that optimizes the entire market value. Case studies together with statistical analysis will be conducted in order to test these possibilities in practice and to investigate the effects of the parameters on expected results.

## Conflict of Interests

The author declares that there is no conflict of interests regarding the publication of this paper.

## References

- [1] D. MacMillan, "Groupon's stumbles may force it to pare back size of IPO," Bloomberg, 2011, <http://www.bloomberg.com>.
- [2] D. MacMillan, "LivingSocial aims to be different from Groupon," Business Week, 2011, <http://www.businessweek.com>.
- [3] D. MacMillan, "Groupon China venture said to fire workers for poor performance," Bloomberg, 2011, <http://www.bloomberg.com>.
- [4] D. Reibstein, "How sustainable is Groupon's business model?" Knowledge at Wharton, 2011, <http://knowledge.wharton.upenn.edu>.
- [5] K. Webster, "Groupon's business model: bubble or the real deal?" 2011, <http://pymnts.com>.
- [6] R. Wheeler, "Groupon gone wrong! Harvard business fellow's warning to investors and entrepreneurs," 2011, <http://pymnts.com>.
- [7] V. Kumar and B. Rajan, "Social coupons as a marketing strategy: a multifaceted perspective," *Journal of the Academy of Marketing Science*, vol. 40, no. 1, pp. 120–136, 2012.
- [8] K. Patel, "Groupon marketing spending works almost too well," Ad Age Digital, 2011, <http://adage.com>.
- [9] M. A. Cusumano, "Technology strategy and management platform wars come to social media," *Communications of the ACM*, vol. 54, no. 4, pp. 31–33, 2011.
- [10] N. Kruschwitz, "Size matters in social business adoption," MIT Sloan Management Review, 2012, <http://sloanreview.mit.edu>.
- [11] J. Leber, "The biggest cost of Facebook's Growth," Technology Review, 2012, <http://www.technologyreview.com>.
- [12] M. Anderson, J. Sims, J. Price, and J. Brusa, "Turning "like" to "buy": social media emerges as a commerce channel," White Paper, Booz & Company, 2012.
- [13] B. Urstadt, "Social networking is not a business," MIT Technology Review, 2008, <http://www.technologyreview.com>.

- [14] M. Lodefalk, "Servicification of manufacturing: evidence from Sweden," *International Journal of Economics and Business Research*, vol. 6, no. 1, pp. 87–113, 2013.
- [15] R. Schmitt and S. Hatfield, "Strategic servicification—a quality based approach beyond service-engineering," in *Manufacturing Systems and Technologies for the New Frontier*, M. Mitsuishi, K. Ueda, and F. Kimura, Eds., pp. 511–514, 2008.
- [16] A. T. Stephen and O. Toubia, "Deriving value from social commerce networks," *Journal of Marketing Research*, vol. 47, no. 2, pp. 215–228, 2010.
- [17] J. Alroy, "A multispecies overkill simulation of the end-Pleistocene megafaunal mass extinction," *Science*, vol. 292, no. 5523, pp. 1893–1896, 2001.
- [18] G. Hardin, "The tragedy of the commons," *Science*, vol. 162, no. 3859, pp. 1243–1248, 1968.
- [19] G. M. Greco and L. Floridi, "The tragedy of the digital commons," *Ethics and Information Technology*, vol. 6, no. 2, pp. 73–81, 2004.
- [20] Knowledge at Wharton, "Dot-com bubble, part II? Why it's so hard to value social networking sites?" Knowledge at Wharton, 2006, <http://knowledge.wharton.upenn.edu>.
- [21] M. Perc and A. Szolnoki, "Coevolutionary games—a mini review," *BioSystems*, vol. 99, no. 2, pp. 109–125, 2010.
- [22] M. Perc, J. Gómez-Gardeñes, A. Szolnoki, L. M. Floría, and Y. Moreno, "Evolutionary dynamics of group interactions on structured populations: a review," *Journal of the Royal Society Interface*, vol. 10, no. 80, Article ID 20120997, 2013.
- [23] F. C. Santos, J. M. Pacheco, and T. Lenaerts, "Evolutionary dynamics of social dilemmas in structured heterogeneous populations," *Proceedings of the National Academy of Sciences of the United States of America*, vol. 103, no. 9, pp. 3490–3494, 2006.
- [24] A. Szolnoki and M. Perc, "Resolving social dilemmas on evolving random networks," *Europhysics Letters*, vol. 86, no. 3, Article ID 30007, 2009.
- [25] A. Szolnoki and M. Perc, "Emergence of multilevel selection in the prisoner's dilemma game on coevolving random networks," *New Journal of Physics*, vol. 11, no. 9, Article ID 093033, 2009.
- [26] A. Szolnoki and M. Perc, "Evolutionary advantages of adaptive rewarding," *New Journal of Physics*, vol. 14, no. 9, Article ID 093016, 2012.
- [27] D. Kim, "A game theoretic analysis of social commerce ecosystem at the crossroads," *Asia Pacific Journal of Information Systems*, vol. 23, no. 2, pp. 67–86, 2013.
- [28] A. Szolnoki, M. Perc, and G. Szabó, "Phase diagrams for three-strategy evolutionary prisoner's dilemma games on regular graphs," *Physical Review E. Statistical, Nonlinear, and Soft Matter Physics*, vol. 80, no. 5, Article ID 056104, 2009.
- [29] A. Szolnoki, G. Szabó, and M. Perc, "Phase diagrams for the spatial public goods game with pool punishment," *Physical Review E. Statistical, Nonlinear, and Soft Matter Physics*, vol. 83, no. 3, Article ID 036101, 2011.
- [30] Z. Wang, A. Szolnoki, and M. Perc, "Interdependent network reciprocity in evolutionary games," *Scientific Reports*, vol. 3, 2013.
- [31] B. Greeley, "Should Google and the ad industry regulate themselves?" *Business Week*, 2012, <http://www.businessweek.com>.

## Research Article

# A Novel Classification Approach through Integration of Rough Sets and Back-Propagation Neural Network

Lei Si,<sup>1</sup> Xin-hua Liu,<sup>1,2</sup> Chao Tan,<sup>1</sup> and Zhong-bin Wang<sup>1</sup>

<sup>1</sup> School of Mechatronic Engineering, China University of Mining & Technology, Xuzhou 221116, China

<sup>2</sup> Xuyi Mine Equipment and Materials R&D Center, China University of Mining & Technology, Huai'an 211700, China

Correspondence should be addressed to Zhong-bin Wang; wangzbpaper@126.com

Received 13 September 2013; Revised 12 March 2014; Accepted 6 April 2014; Published 24 April 2014

Academic Editor: Olabisi Falowo

Copyright © 2014 Lei Si et al. This is an open access article distributed under the Creative Commons Attribution License, which permits unrestricted use, distribution, and reproduction in any medium, provided the original work is properly cited.

Classification is an important theme in data mining. Rough sets and neural networks are the most common techniques applied in data mining problems. In order to extract useful knowledge and classify ambiguous patterns effectively, this paper presented a hybrid algorithm based on the integration of rough sets and BP neural network to construct a novel classification system. The attribution values were discretized through PSO algorithm firstly to establish a decision table. The attribution reduction algorithm and rules extraction method based on rough sets were proposed, and the flowchart of proposed approach was designed. Finally, a prototype system was developed and some simulation examples were carried out. Simulation results indicated that the proposed approach was feasible and accurate and was outperforming others.

## 1. Introduction

Across a wide variety of fields, data are being accumulated at a dramatic pace, especially in the age of internet [1, 2]. There is much useful information hidden in the accumulated voluminous data, but it is very hard for us to obtain it. Thus, a new generation of computational tool is needed to assist humans in extracting knowledge and classifying the rapidly growing digital data; otherwise, these data are useless for us.

Neural networks are applied in several engineering fields such as classification problems and pattern recognition. Artificial neural network in its most general form attempts to produce systems that work in a similar way to biological nervous systems. It has the ability to simulate human thinking and owns powerful function and incomparable superiority in terms of establishing nonlinear and experiential knowledge simulation models [3–6]. Back-propagation neural network (BP neural network for short) is the core of feed-forward networks and embodies the essence of artificial neural network. However, conventional BP algorithm has slow convergence rate, weak fault tolerance, and nonunique results. Although many improved strategies have been proposed, such as additional momentum method, adaptive learning method,

elastic BP method, and conjugate gradient method [7–9], the problems above have still not been solved completely, especially when BP neural networks are applied in multidimensional and uncertain fields. Therefore, newer techniques must be coupled with neural networks to create more efficient and complex intelligent systems [10].

In an effort to model vagueness, rough sets theory was proposed by Pawlak in 1982 [11, 12]. Its outstanding feature is not to need the specific relation description about some characteristics or attributes, but to determine the approximate region of existing problems and find out the inherent rules through the indiscernibility relations and indiscernibility classes. This theory has been successfully applied in many fields such as machine learning, data mining, data analysis, and expert systems [13, 14]. In the paper, rough sets theory and BP neural network are presented as an integrated method because they can discover patterns in ambiguous and imperfect data and provide tools for data analysis. The decision table is established reasonably through discretizing attribution values. The features of decision table are analyzed using rough sets and subsequently a classification model based on these features is built through integration of rough sets and BP neural network. Actually, this model uses the

decision rules which are extracted by the algorithm based on value reduction for classification problems.

The paper is structured as follows. Some related works are outlined based on literature in Section 2. The basics of rough sets theory and BP neural network are presented in Section 3. The framework and key algorithms are proposed and the flowchart of the proposed approach is designed in Section 4. A simulation example and some comparisons are put forward to validate the proposed approach in Section 5. Our conclusions are summarized in Section 6.

## 2. Literature Review

In recent years, most of classifier architectures are mainly constructed based on artificial intelligence (AI) algorithms with the unceasing development and improvement of AI theory. In this section, we try to summarize some recent literatures which are relevant to the construction methods of classification system. Hassan et al. constructed a classifier based on neural networks and applied rough sets theory in attributes reduction to preprocess the training set of neural networks [15]. Berardi et al. proposed a principled approach to build and evaluate neural network classification models for the implementation of decision support system (DSS) and verified the optimization speed and classified samples accuracy [16]. In [17, 18], the architecture of neural network with fuzzy input was proposed to effectively improve the classification performance of neural network. Hu et al. presented a self-organized feature mapping neural network to reasonably determine the input parameters in pavement structure design [19]. In [20, 21], wavelet neural networks were applied in the construction of classification system and better prediction results were obtained. In [22, 23], a classifier in which improved particle swarm algorithm was used to optimize the parameters of wavelet neural network was established and the application in nonlinear identification problems demonstrated its strong generalization capability. Sengur et al. described the usage of wavelet packet neural networks for texture classification problem and provided a wavelet packet feature extractor and a multilayer perceptron classifier [24]. Hassan presented a novel classifier architecture based on rough sets and dynamic scaling in connection with wavelet neural networks and the effectiveness was verified by the experiments [25].

Although many approaches for the establishment of classification systems have been presented in above literatures, they have some common disadvantages summarized as follows. On one hand, the classification effect of signal neural network cannot be guaranteed when the networks are applied in multidimensional and uncertain fields. On the other hand, the combination method of rough sets and neural networks can only deal with classification and recognition problems that possess discretized dataset and cannot process the problems that contain continuous dataset.

In this paper, a novel classification system based on the integration of rough sets and BP neural network is proposed. The attribution values are discretized through PSO and the decision table is constructed. The proposed model

takes account of attributes reduction by discarding redundant attributes and a rule set is generated from the decision table. A simulation example and comparisons with other methods are carried out and the proposed approach is proved feasible and outperforming others.

## 3. Basic Theory

*3.1. Rough Sets Theory.* Fundamental to rough sets theory is the idea of an information system  $IS = (U, C)$ , which is essentially a finite data table consisting of different columns labeled by attributes and rows labeled by objects of interest, and entries of the table are attribute's values.  $U$  is nonempty finite set of objects called a universe and  $C$  is a nonempty finite, where each  $c \in C$  is called condition attribute. In  $IS = (U, C)$ , every  $B \subseteq C$  generates an indiscernibility relation  $Ind(B)$  on  $U$  which can be defined as follows:

$$Ind(B) = \{(x, y) \in U \times U : b(x) = b(y), \forall b \in B\}. \quad (1)$$

$U/Ind(B)$  is a partition of  $U$  by  $B$ . For all  $x \in U$ , the equivalence class of  $x$  in relation  $U/Ind(B)$  can be defined as follows:

$$[x]_{Ind(B)} = \{x \in U : b(y) = b(x), \forall b \in B\}. \quad (2)$$

According to  $I$ , two crisp sets  $\underline{B}X$  and  $\overline{B}X$  called the lower and the upper approximation of the set of objects  $X$  can be defined as follows:

$$\begin{aligned} \underline{B}X &= \{x \in U : [x]_{Ind(B)} \subseteq X\}, \\ \overline{B}X &= \{x \in U : [x]_{Ind(B)} \cap X \neq \Phi\}, \end{aligned} \quad (3)$$

where  $[x]_{Ind(B)}$  denotes the set of all equivalence classes of  $Ind(B)$ .  $\underline{B}X$  is the set of all objects from  $U$  which can be certainly classified as elements of  $X$  employing the set of attributes  $B$ .  $\overline{B}X$  is the set of objects of  $U$  which can be possibly classified as elements of  $X$  using the set of attributes  $B$  [25].

Decision table  $DT = (U, C \cup D)$  is a special form of an information system and the major feature is the distinguished attribute set  $D$ , where  $C \cap D = \Phi$  is called the decision attribute. Generally speaking, there is a certain degree of dependency between condition attribute and decision attribute, which can be defined as follows:

$$\gamma_C(D) = \frac{POS_C(D)}{|U|} = \frac{|\bigcup_{X \in U/D} \underline{C}X|}{|U|}, \quad (4)$$

where  $POS_C(D)$  is referred to the  $C$ -positive region of  $D$ .

Due to the relevance between condition attribute and decision attribute, not all condition attributes are necessary for decision attribute so as to introduce the attribute reduction which is a smaller set of attributes that can classify objects with the same discriminating capability as that of the original set. As well known, the reduct is not the only one [26, 27].

When we want to determine the reduct of decision table, the significance degree of attributes is commonly used and can be defined as follows:

$$\text{sig}(\alpha, B; D) = \gamma_{\{\alpha \cup B\}}(D) - \gamma_B(D), \quad (5)$$

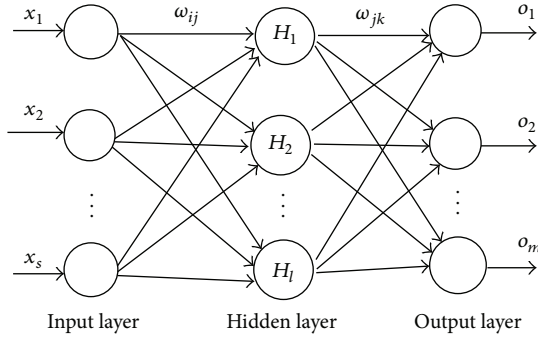


FIGURE 1: The topology structure of BP-NN.

where  $\text{sig}(\alpha, B; D)$  denotes the significance degree of attribute  $\alpha$  to attribute  $B$ , relative to decision attribute  $D$ .

For all  $R \in C$ , if  $\text{POS}_{\{C-R\}}(D) = \text{POS}_C(D)$ , then  $R$  in  $C$  is superfluous for  $D$ . Otherwise,  $R$  in  $C$  is indispensable for  $D$ . The set composed of all attributes that are indispensable for  $D$  is called the core of  $C$  relative to  $D$ , namely, relative core  $\text{CORE}_D(C)$ . This relative core cannot be removed from the system without a loss in the knowledge that can be derived from it.

When determined, the relative core of decision table must be firstly judged whether it is the reduct of  $C$  relative to  $D$ , namely, relative reduct. The judgment rules are shown as follows.

If the nonempty subset  $P$  of attribute set  $C$  satisfies the conditions: (1)  $\text{POS}_P(D) = \text{POS}_C(D)$ ; (2)  $\forall R \subseteq P$ ,  $\text{POS}_R(D) \neq \text{POS}_C(D)$ , then  $P$  is called a reduct of  $C$  relative to  $D$ , denoted as  $\text{RED}_D(C)$ .

In addition, decision rules can be perceived as data patterns which represent the relationship between the attributes values of a classification system [11, 12]. The form of the decision rules can be shown as IF  $\eta$  THEN  $\delta$ , where  $\eta$  is the conditional part of a rule set and it is a conjunction of selectors;  $\delta$  is the decision part of attribute  $d : (d \in D)$  and it usually describes the class of decision attribution.

**3.2. BP Neural Network.** BP neural network (BP-NN) which is surely a back-propagating neural network belongs to the class of networks whose learning is supervised and the learning rules are provided by the training set to describe the network behavior. The topology structure of BP-NN can be shown in Figure 1.

In Figure 1, input vector  $X = \{x_1, x_2, \dots, x_s\}$  is furnished by the condition attribution values of reduced decision table and output vector  $O = \{o_1, o_2, \dots, o_m\}$  is the prediction class of decision attribution. The output of hidden layer can be calculated as follows:

$$H_j = f\left(\sum_{i=1}^s \omega_{ij} x_i - a_j\right), \quad j = 1, 2, \dots, l, \quad (6)$$

where  $\omega_{ij}$  is the connection weight between input and hidden layers;  $l$  is the number of hidden layer nodes;  $a_j$  is the threshold of hidden layer node  $j$ ;  $f$  is the activation function

of hidden layer and can be chosen as linear function or sigmoid function  $f(x) = 1/(1 + e^{-x})$ .

The output of output layer can be calculated as follows:

$$o_k = \sum_{j=1}^l H_j \omega_{jk} - b_k, \quad k = 1, 2, \dots, m, \quad (7)$$

where  $\omega_{jk}$  is the connection weight between hidden and output layers;  $m$  is the number of output layer nodes;  $b_k$  is the threshold of output layer node  $k$ .

The training of network parameters  $\omega_{ij}$ ,  $\omega_{jk}$ ,  $a_j$ , and  $b_k$  would depend on the error value which can be calculated by the following equation:

$$e_k = Y_k - o_k, \quad k = 1, 2, \dots, m, \quad (8)$$

where  $o_k$  and  $Y_k$  are current and desired output values of the network, respectively. The weight values and thresholds of the network can be updated as follows:

$$\begin{aligned} \omega_{ij}(t+1) &= \omega_{ij}(t) + \zeta(t) H_j (1 - H_j) x_i \sum_{k=1}^m e_k \omega_{jk}, \\ \omega_{jk}(t+1) &= \omega_{jk}(t) + \zeta(t) H_j e_k, \end{aligned} \quad (9)$$

$$a_j(t+1) = a_j(t) + \zeta(t) H_j (1 - H_j) x_i \sum_{k=1}^m e_k \omega_{jk},$$

$$b_k(t+1) = b_k(t) + e_k,$$

where  $t$  is the current iteration times;  $\zeta(t)$  is the learning rate and the range is the interval of  $[0, 1]$ .

The learning rate has great influence on the generalization effect of neural network. Larger learning rate would significantly modify the parameters of weight values and thresholds and increase the learning speed. But overlarge learning rate would produce larger fluctuations in the learning process, and excessively small learning rate would generate slower network convergence and stabilize the weight values and thresholds difficultly. Therefore, this paper presents the variable learning rate algorithm to solve the above problems, which can be described as follows:

$$\zeta(t) = \zeta_{\max} - \frac{t(\zeta_{\max} - \zeta_{\min})}{t_{\max}}, \quad (10)$$

where  $\zeta_{\max}$  and  $\zeta_{\min}$  are the maximum and minimum of learning rate;  $t_{\max}$  is the number of maximum iterations.

## 4. The Proposed Approach

This section tries to present a new approach aiming at connecting rough sets with BP neural network to establish a classification system. The section has five main parts and can be elaborated through the following subsections.

**4.1. The System Construction Process.** The construction process of classification system can be shown as follows.

- (1) Preprocessing historical dataset to obtain the sample data is the application precondition of rough sets and BP neural network. In the process of preprocessing, the historical dataset would be discretized through PSO algorithm to construct the decision table.
- (2) Simplify the input of neural network including input dimension and training set number through the attribute reduction based on significance degree algorithm. Deleting the same row in the decision table can simplify the training samples and eliminating the superfluous column (condition attribute) can simplify the network input dimension number. Thus, reduce the decision table using some reduct or sum of several calculated reducts; that is, remove from the table attributes not belonging to the chosen reducts.
- (3) BP neural network integrated with rough sets is used to build the network over the reduced set of data. Decision rules are extracted from the reduced decision table as the basis of network structure through a value reduction algorithm of rough sets.
- (4) Perform network learning for parameters  $\omega_{ij}$ ,  $\omega_{jk}$ ,  $a_j$  and  $b_k$ . Do this step until there is no significant change in the output of network and the system construction process can be shown as Figure 2.

*4.2. The Discretization Algorithm for Decision Table.* Due to the fact that rough sets theory cannot directly process continuous values of attributes, the decision table composed of continuous values must be discretized firstly. Thus, the positions of breakpoints must be selected appropriately to discretize the attributes values, so as to obtain fewer breakpoints, larger dependency degree between attributes, and less redundant information.

In this paper, the basic particle swarm optimization algorithm (PSO) described in [28] is presented to optimize the positions of breakpoints. In PSO, a swarm of particles are initialized randomly in the solution space and each particle can be updated in a certain rule to explore the optimal solution  $P_{\text{best}}$  after several iterations. Particles are updated through tracking two "extremums" in each iteration. One is the optimal solution  $P_{\text{best}}$  found by the particle itself and another is the optimal solution  $G_{\text{best}}$  found by the particle swarm. The specific iteration formulas can be expressed as follows:

$$\begin{aligned} v_i^{n+1} &= \omega_n v_i^n + c_1 r (P_{\text{best}} - x_i^n) + c_2 r (G_{\text{best}} - x_i^n), \\ x_i^{n+1} &= x_i^n + v_i^{n+1}, \end{aligned} \quad (11)$$

where  $i = 1, 2, \dots, M$ ;  $M$  is the number of particles;  $n$  is the current iteration times;  $c_1$  and  $c_2$  are the acceleration factors;  $r$  is the random number between 0 and 1;  $x_i^n$  is the current position of particle  $i$ ;  $v_i^n$  is the current update speed of particle  $i$ ;  $\omega_n$  is the current inertia weight and can be updated by the following equation:

$$\omega_n = \frac{(\omega_{\max} - \omega_{\min})(N_{\max} - n)}{N_{\max}} + \omega_{\min}, \quad (12)$$

where  $\omega_{\max}$  and  $\omega_{\min}$  are the maximum and minimum of inertia weight;  $N_{\max}$  is the number of maximum iterations.

The main discretization steps for decision table through the PSO can be described as follows.

- (1) Normalize the attribute values and initialize the breakpoints number  $h$ , the maximum iterations  $N_{\max}$ , the minimum dependency degree between condition attribute and decision attribute  $\gamma_{\min}$ , the particles number  $M$ , the initial position  $x_i^0$ , and initial velocity  $v_i^0$  which are  $h \times \mu$  matrixes ( $\mu$  is the number of attributes).
- (2) Discretize the attribute values with the position of particle  $i$  and calculate the dependency degree  $\gamma_i$  as the fitness value of each particle to initialize  $P_{\text{best}}$  and  $G_{\text{best}}$ .
- (3) Update  $x_i$ ,  $v_i$  ( $v_i \leq v_{\max}$ ), and  $\omega_n$ . Discretize the attribute values and calculate the fitness value of each particle so as to update  $P_{\text{best}}$  and  $G_{\text{best}}$ .
- (4) If  $n > N_{\max}$  or  $\gamma_i \geq \gamma_{\min}$ , then the iteration is ended and  $G_{\text{best}}$  or  $x_i$  is output. Otherwise, go to step (3).
- (5) According to the needs, set different  $h$  and return to step (1) to search the optimal particles. Then, compare the optimal particles and select the better one as the basis of discretization for decision table. The more detailed discretization process is elaborated in Section 4.5.

*4.3. Rough Sets for the Attribution Reduction.* One of the fundamental steps in proposed method is reduction of pattern dimensionality through feature extraction and feature selection [10]. Rough sets theory provides tools for expressing inexact dependencies within data [29]. Features may be irrelevant (having no effect on the processing performance) and attribution reduction can neglect the redundant information to enable the classification of more objects with a high accuracy [30].

In this paper, the algorithm based on attribution significance degree is applied in the attribution reduction of decision table. The specific reduction steps can be described as follows.

- (1) Construct the decision table  $DT = (U, C \cup D)$  and calculate the relative core  $\text{CORE}_D(C)$  of original decision table. Initialize reduct =  $\text{CORE}_D(C)$  and the redundant attribute set  $\text{redundant} = C - \text{CORE}_D(C) = \{\alpha_1, \alpha_2, \dots, \alpha_\tau\}$  ( $\tau$  is the number of attributes in redundant).
- (2) If  $\text{POS}_{\text{reduct}}(D) = \text{POS}_C(D)$  and, for all  $R \subseteq \text{reduct}$ ,  $\text{POS}_R(D) \neq \text{POS}_C(D)$ , then the set reduct is a relative reduct of decision table.
- (3) Otherwise, calculate the significance degree of each attribute in redundant, respectively, through the following equation:

$$\text{sig}(\alpha_j, \text{reduct}; D) = \gamma_{\{\alpha_j \cup \text{reduct}\}}(D) - \gamma_{\text{reduct}}(D), \quad (13)$$

$j = 1, 2, \dots, \tau.$

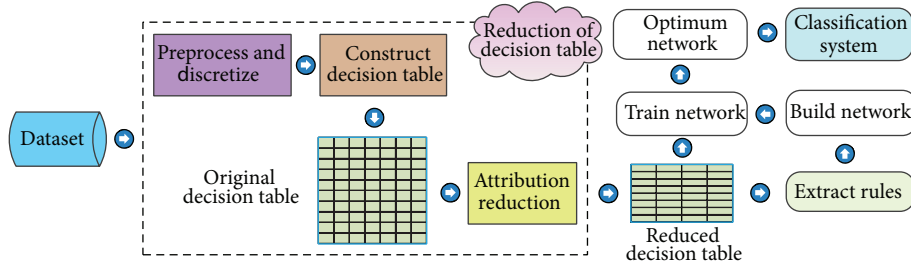


FIGURE 2: The system construction process.

The attribute in redundant with the maximum significance degree is marked as  $\alpha_{\max}$ . Update the reduct and redundant through the following equations:

$$\begin{aligned} \text{reduct} &= \text{reduct} \cup \{\alpha_{\max}\}, \\ \text{redundant} &= \text{redundant} - \{\alpha_{\max}\}. \end{aligned} \quad (14)$$

- (4) Go to step (2) until  $\text{POS}_{\text{reduct}}(D)$  satisfies the conditions; then output  $\text{RED}_D(C) = \text{reduct}$ .

Therefore, the irrelevant features are neglected and the DT is reduced. Thus, a reduced decision table will be constructed and can be regarded as the training set to optimize the structure of RS-BPNN classifier.

**4.4. Rough Sets for the Rules Extraction.** The knowledge in the trained network is encoded in its connection weights and it is distributed numerically throughout the whole structure of neural network. For the knowledge to be useful in the context of a classification system, it has to be articulated in a symbolic form usually in the form of IF-THEN rules. Since neural network is a “black box” for users, the rules which are implicit in the connection weights are difficult to understand, so extracting rules from neural network is extremely tough because of the nonlinear and complicated nature of data transformation conducted in the multiple hidden layers [31]. In this paper, the decision rules are indirectly extracted from the reduced decision table using the value reduction algorithm of rough sets [32]. This algorithm can be elaborated in the following steps.

*Step 1.* Checking the condition attributes of reduced decision table column by column. If bringing conflicting objects after deleting one column, then preserving the original attribute value of these conflicting objects; If not bringing conflicts, but containing duplicate objects, then marking this attribute value of duplicate objects as “\*”; marking this attribute value as “?” for the other objects.

*Step 2.* Deleting the possible duplicate objects and checking every object that contains the mark “?”. If the decisions can be determined only by the unmarked attribute values, then “?” should be modified as “\*”, or else as the original attribute value. If all condition attributes of a particular object are marked, then the attribute values marked with “?” should be modified as the original attribute value.

*Step 3.* Deleting the objects whose condition attributes are marked as “\*” and the possible duplicate objects.

*Step 4.* If only one condition attribute value is different between any two objects and this attribute value of one object is marked as “\*”, and for this object if the decision can be determined by the unmarked attribute values, then deleting another object, or else deleting this object.

Each object represents a classification rule in the decision table which is value-reduced through the above steps and the number of attributes which are not marked as “\*” of every object makes up the condition number of this rule. Moreover, this rule set can provide the rational basis for the structure of BP neural network.

**4.5. The Flowchart of the Proposed Approach.** According to the above description about the classifier based on integration algorithm of rough sets and BP neural network, the proposed approach is an iterative algorithm and can be coded easily on a computer, and the flowchart can be summarized as shown in Figure 3.

## 5. Simulation Example

A classifier named RS-BPNN (short for rough sets with BP neural network) has been set up and implemented by VC 6.0. In this section, an engineering application of shearer running status classification in a coal mine was put forward as a simulation example to verify the feasibility and effectiveness of the proposed approach. The classification capabilities of different types of neural network models were compared and the proposed approach was proved outperforming others.

**5.1. The Construction of Decision Table.** Due to the poor working conditions of coal mining, there are many parameters relating to the running status of shearer, mainly including cutting motor current, cutting motor temperature, traction motor current, traction motor temperature, traction speed, tilt angle of shearer body, tilt angle of rocker, and vibration frequency of rocker transmission gearbox, marked as  $C_1, C_2, C_3, C_4, C_5, C_6, C_7,$  and  $C_8,$  respectively. According to the information database acquired from the 11070 coal face in the number 13 Mine of Pingdingshan Coal Industry Group Co., 200 groups datasets of shearer running status were rearranged as shown in Table 1. This “running status” referred

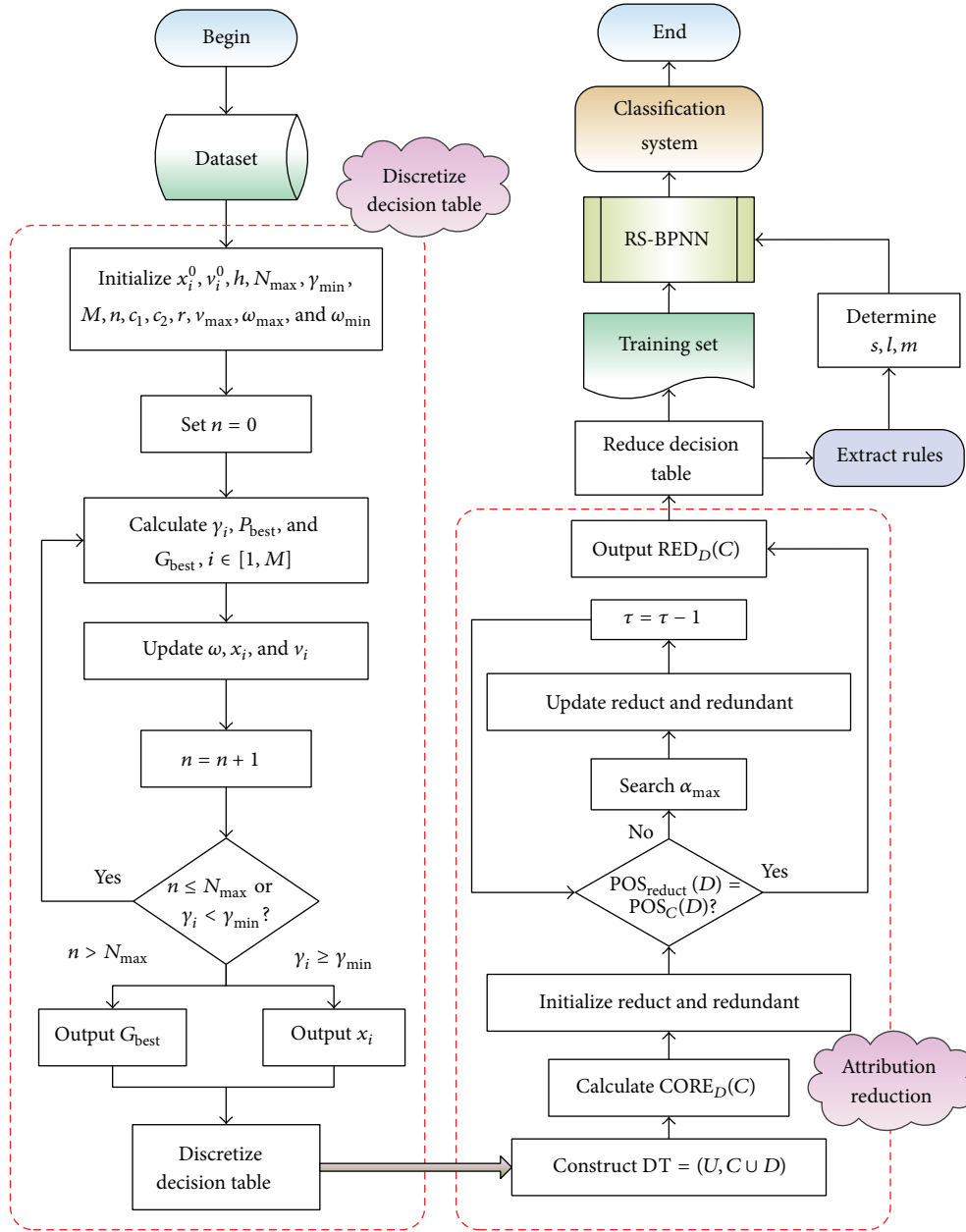


FIGURE 3: The flowchart of the proposed approach.

to the cutting status of shearer rocker and could be expressed by the ratio of actual cutting load to rated load.

Therefore, in decision table DT, the condition attribute set and decision attribute set could be expressed as  $C = \{C_1, C_2, C_3, C_4, C_5, C_6, C_7, C_8\}$  and  $D = \{d\}$  ( $d$  denoted the shearer running status). The values of decision attribution were discretized based on the following assumptions: for the ratio of actual cutting load to rated load of shearer being greater than 1.6,  $d = 4$ ; for the range of this ratio being in interval of (1.2, 1.6],  $d = 3$ ; for the range of this ratio being in interval of (0.8, 1.2],  $d = 2$ ; for this ratio being less than 0.8,  $d = 1$ . The discretized values of condition attributes could be determined through the algorithm described in Section 4.2.

The condition attributes to be discretized were  $C_1 \sim C_8$ , so  $\mu = 8$ . Other parameters of PSO were initialized as follows:  $M = 100$ ,  $N_{max} = 200$ ,  $\gamma_{min} = 0.9$ ,  $\gamma_{max} = 0.6$ ,  $c_1 = c_2 = 1.6$ ,  $r$  is a random number from  $[0, 1]$ ,  $\omega_{max} = 0.9$ , and  $\omega_{min} = 0.4$ . As the breakpoints number  $h$  had greater influence on the dependency degree  $\gamma_C(D)$  of discretized decision table, the comparison of two important parameters: dependency degree and simulation time, was analyzed when  $h$  was assigned various values. The comparison results were shown in Figure 4.

From Figure 4, it was observed that the dependency degree and simulation time both showed ascending tendency with the increase of breakpoints number  $h$ . The dependency

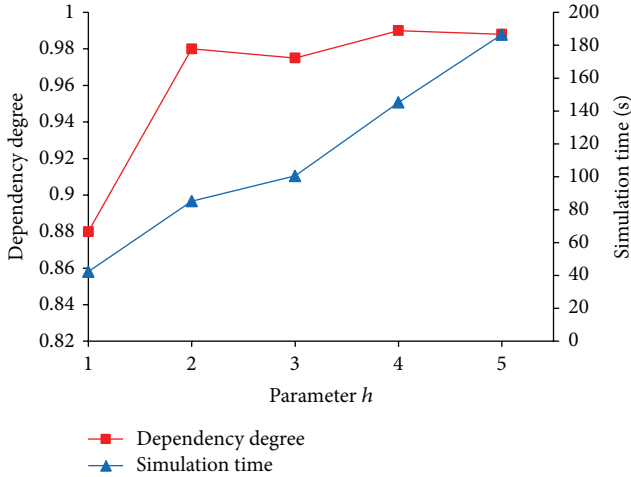


FIGURE 4: The change curves of dependency degree and simulation time.

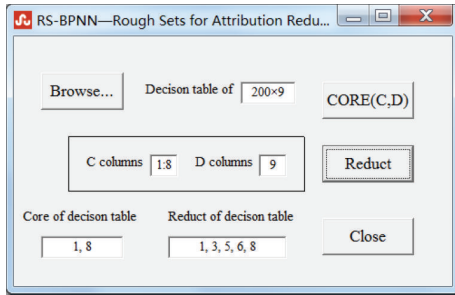


FIGURE 5: Attribution reduction.

degree was not significantly increased and the simulation time was obviously increased when  $h \geq 2$ . So,  $h$  was considered being equal to 2 and  $\gamma_C(D) = 0.98$ . The breakpoints of each attribute value were shown in Table 2. The breakpoints were applied to discretizing the parameter values in Table 1. If the value was in interval of  $(0, Br_1]$ , the discretized attribution value was labeled as 1; if the value was in interval of  $(Br_1, Br_2)$ , the discretized attribution value was labeled as 2; otherwise, it was labeled as 3. The discretized decision table was shown in Table 3.

**5.2. Relative Reduct and Rules Extraction.** Through the attribution reduction algorithm presented in Section 4.3, the function “CORE(C, D)” was invoked to obtain the relative core of decision table and  $CORE_D(C) = \{C_1, C_8\}$ , shown in Figure 5. As the minimum relative reduct of decision table,  $RED_D(C) = \{C_1, C_3, C_5, C_6, C_8\}$  was determined by invoking function “Reduct.”

In the module of “Rough Set for Attribution Reduction,” a new decision table of  $200 \times 6$  was established by the attributions  $\{C_1, C_3, C_5, C_6, C_8\}$  and decision attribution  $\{d\}$ . The function “Refresh (DT)” was called to reject the repeated objects in this new decision table and a reduced decision table was provided finally, containing 79 objects, as shown in Figure 6. Subsequently, the decision rules were extracted

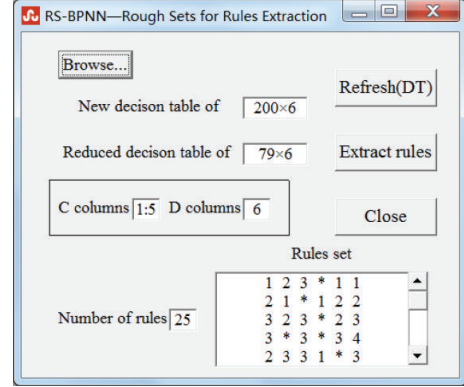


FIGURE 6: Rules extraction.

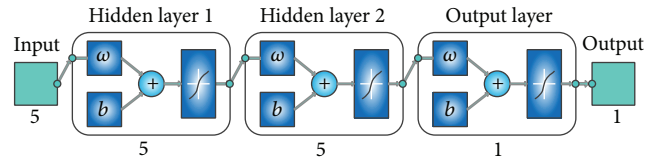


FIGURE 7: The structure of RS-BPNN classifier.

through function “Extract rules” which was based on the value reduction algorithm and 25 rules were obtained, as shown in Figure 6. The extracted rules could reveal the potential rules (knowledge) in dataset; for example, the first rule “123 \* 11” in Figure 6 illustrated that if cutting motor current  $C_1 \in (0, 48.56]$ , traction motor current  $C_3 \in (82.37, 95.42)$ , traction speed  $C_5 \in [3.24, +\infty)$ , tilt angle of shearer body  $C_6$  was arbitrary value, and vibration frequency of rocker transmission gearbox  $C_8 \in (0, 651.28]$ , then the running status class was 1, which was in accordance with engineering practice situation. Moreover, RS-BPNN classifier, in fact, was to diagnose the status of objects according to these potential rules (knowledge) and the structure of network could be constructed reasonably based on the number of rules so as to enhance the classification accuracy.

**5.3. The Structure and Testing of RS-BPNN Classifier.** Because the dataset obtained 25 rules (knowledge), the RS-BPNN should be constructed with double hidden layers and the number of neurons was  $5 \times 5$ , which must completely contain these rules (knowledge). The number of input layer nodes  $s = 5$ ; the number of output layer nodes  $m = 1$ . Other parameters of network were determined as follows:  $\zeta_{\max} = 0.9$ ;  $\zeta_{\min} = 0.4$ ;  $t_{\max} = 500$ ; the initial connection weights were assigned somewhat random values. The structure of RS-BPNN classifier was shown in Figure 7.

The reduced decision table, as the training set, was presented to the network several times. The testing set, composed of 40 samples extracted from the information database randomly, was not seen by the network during the training phase and it was only used for testing the generalization of neural network after it was trained, as shown in Table 4.

TABLE 1: The running status of shearer and its corresponding parameters.

Samples	$C_1$ (A)	$C_2$ ( $^{\circ}$ C)	$C_3$ (A)	$C_4$ ( $^{\circ}$ C)	$C_5$ (m/min)	$C_6$ ( $^{\circ}$ )	$C_7$ ( $^{\circ}$ )	$C_8$ (Hz)	Running status
1	45.12	78.74	65.46	88.16	3.51	2.52	45.12	628.85	0.78
2	48.19	75.22	70.78	84.28	3.42	3.62	53.22	683.46	0.79
3	50.25	80.19	85.14	91.25	2.88	5.36	40.22	705.76	0.82
4	45.26	82.43	62.45	84.15	3.12	2.85	49.36	642.14	0.76
5	64.28	77.16	90.45	91.41	2.56	2.26	58.55	823.29	1.22
6	46.22	85.24	68.55	80.46	3.26	2.86	58.46	711.24	0.83
7	72.56	85.12	102.42	102.36	2.76	10.26	38.41	881.25	1.17
8	62.33	74.24	92.46	84.46	3.56	8.26	60.27	821.46	1.12
9	44.23	89.19	63.15	85.78	3.82	3.22	46.25	578.26	0.75
10	89.23	81.24	120.36	86.14	2.01	1.05	50.36	1035.48	1.63
$\vdots$	$\vdots$	$\vdots$	$\vdots$	$\vdots$	$\vdots$	$\vdots$	$\vdots$	$\vdots$	$\vdots$
198	49.22	75.24	71.22	80.25	3.46	4.26	45.26	542.16	0.72
199	68.65	87.16	118.64	90.46	4.66	4.36	49.35	845.29	1.36
200	50.22	78.15	90.46	95.44	3.22	7.22	44.21	682.64	1.11

TABLE 2: The corresponding breakpoints of each attribute value at  $h = 2$ .

Breakpoints	$C_1$ (A)	$C_2$ ( $^{\circ}$ C)	$C_3$ (A)	$C_4$ ( $^{\circ}$ C)	$C_5$ (m/min)	$C_6$ ( $^{\circ}$ )	$C_7$ ( $^{\circ}$ )	$C_8$ (Hz)
$Br_1$	48.56	81.49	82.37	84.79	2.41	4.16	47.35	651.28
$Br_2$	65.25	85.78	95.42	90.25	3.24	7.38	54.25	847.46

TABLE 3: The discretized decision table.

$U$	$C$								$D$
	$C_1$	$C_2$	$C_3$	$C_4$	$C_5$	$C_6$	$C_7$	$C_8$	
1	1	1	1	2	3	1	1	1	1
2	1	1	1	1	3	1	2	2	1
3	2	1	2	3	2	2	1	2	2
4	1	2	1	1	2	1	2	1	1
5	3	1	2	3	2	1	3	2	3
6	1	2	1	1	3	1	3	2	2
7	3	2	3	3	2	3	1	3	2
8	2	1	2	1	3	3	3	2	2
9	1	3	1	2	3	1	1	1	2
10	3	1	3	2	1	1	2	3	4
$\vdots$									
198	2	1	1	1	3	2	1	1	1
199	3	3	3	3	3	2	2	2	2
200	2	1	2	3	2	2	1	2	2

After the training phase, the RS-BPNN classifier was obtained. In order to test the performance of this classifier expediently, a testing interface was designed as shown in Figure 8. The testing set was imported with the “Import samples” button and was processed with the functions of “Discretize” and “Reduce attribution.” The prediction results of RS-BPNN classifier were output through the function of “Classify” in Figure 8. The contrast of prediction class and actual class was shown brightly in Figure 9.

When the classification accuracy of RS-BPNN was computed in Figure 8, the output of classifier was impossibly equal

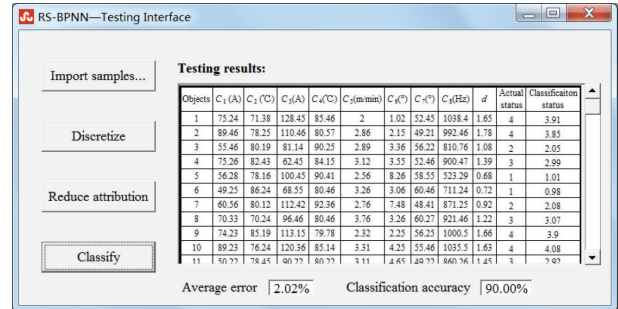


FIGURE 8: The testing interface of RS-BPNN classifier.

to desired output. Therefore, it allowed the output to differ from the desired value. If the difference between classifier output and required value of decision was less than some present value, it was regarded as a correct one. This tolerance margin was decided during simulation evaluation and finally it was 5% of the desired value. Seen from Figures 8 and 9, the classification accuracy was 90.00% and the average classification error was 2.02%. The present model showed higher accuracy and lower error for the classification of shearer running status. The testing results showed that the proposed classifier was proved to be satisfactory and could be used in engineering application in the future.

5.4. Discussion. To evaluate the classification capabilities of different types of neural network models (WNN short for wavelet neural network, RS-WNN short for rough sets coupling with wavelet neural network, BP-NN short for back-propagation neural network, and RS-BPNN short for rough

TABLE 4: The testing samples for the classifier.

Samples	$C_1$ (A)	$C_2$ (°C)	$C_3$ (A)	$C_4$ (°C)	$C_5$ (m/min)	$C_6$ (°)	$C_7$ (°)	$C_8$ (Hz)	$d$
1	75.24	71.38	128.45	85.46	2.00	1.02	52.45	1038.44	1.65
2	89.46	78.25	110.46	80.57	2.86	2.15	49.21	992.46	1.78
3	55.46	80.19	81.14	90.25	2.89	3.36	56.22	810.76	1.08
4	75.26	82.43	62.45	84.15	3.12	3.55	52.46	900.47	1.39
5	56.28	78.16	100.45	90.41	2.56	8.26	58.55	523.29	0.68
6	49.25	86.24	68.55	80.46	3.26	3.06	60.46	711.24	0.72
7	60.56	80.12	112.42	92.36	2.76	7.48	48.41	871.25	0.92
8	70.33	70.24	96.46	80.46	3.76	3.26	60.27	921.46	1.22
9	74.23	85.19	113.15	79.78	2.32	2.25	56.25	1000.46	1.66
10	89.23	76.24	120.36	85.14	3.31	4.25	55.46	1035.48	1.63
⋮	⋮	⋮	⋮	⋮	⋮	⋮	⋮	⋮	⋮
38	58.46	74.24	90.22	80.25	2.46	3.26	55.26	849.16	1.35
39	65.02	87.16	118.64	90.46	5.06	9.24	48.26	1025.29	1.75
40	50.22	85.15	81.25	89.44	3.34	3.46	44.25	672.64	0.72

TABLE 5: Classification performance of the four models of neural networks.

The models	Training accuracy (%)	Testing accuracy (%)	Classification error (%)	Classification time (s)
WNN	90.00	82.50	3.56	23.22
RS-WNN	92.50	87.50	2.66	18.48
BP-NN	90.00	85.00	2.86	22.26
RS-BPNN	95.00	90.00	2.02	18.33

TABLE 6: Classification results of the four methods.

The methods	Classification accuracy (%)		
	Class I	Class II	Class III
WNN	93.33	86.67	80.00
RS-WNN	100	93.33	86.67
BP-NN	93.33	80.00	86.67
RS-BPNN	100	93.33	100

sets coupling with back-propagation neural network), their best architecture and effective training parameters should be found. In order to obtain the best model, both inputs and outputs should be normalized. The number of nodes in the hidden layer of WNN and RS-WNN was equal to that of wavelet base. If the number was too small, WNN/RS-WNN may not reflect the complex function relationship between input data and output value. On the contrary, a large number may create such a complex network that might lead to a very large output error caused by overfitting of the training sample set.

Therefore, a search mechanism was needed to find the optimal number of nodes in the hidden layer for WNN and RS-WNN models. In this study, various numbers of nodes in the hidden layer had been checked to find the best one. WNN and RS-WNN yielded the best results when the number of hidden nodes was 8.

In this subsection, WNN, RS-WNN, BP-NN, and RS-BPNN were provided to solve the problem of above simulation example. The configurations of simulation environment for four algorithms were uniform and in common with

above simulation example. Initially, for each network, the connection weights were assigned somewhat random values. In order to avoid the random error, the training set of input was presented to the networks 100 times and the average values were calculated. The training accuracy, testing accuracy, classification error, and classification time of four algorithms were shown in Table 5.

From the table, it was observed that the proposed model had a better classification capability and better performance than other models of neural networks in predicting the nonlinear, dynamic, and chaotic behaviors in the dataset, and the proposed model was proved outperforming others. Furthermore, the comparison results were suggesting that the proposed model represents a new good method for classification and decision making, and the new method can be treated as a promising tool for extracting rules from the dataset in industrial fields.

In order to illustrate the superiority of proposed method, Iris data set [23], as a benchmark data set from UCI database, was used to verify the classifiers based on above four types of neural networks and the compared results were shown in Table 6. The sample data had been reduced firstly based on attribution reduction algorithm, and then they were used to train neural networks so the networks coupling with rough sets (RS-WNN and RS-RBNN) could acquire better classification accuracy than signal networks (WNN and BPNN). The rules were extracted through value reduction algorithm to construct RS-BPNN structure, so the classification accuracy of classifier based on RS-BPNN was higher than that of RS-WNN classifier.

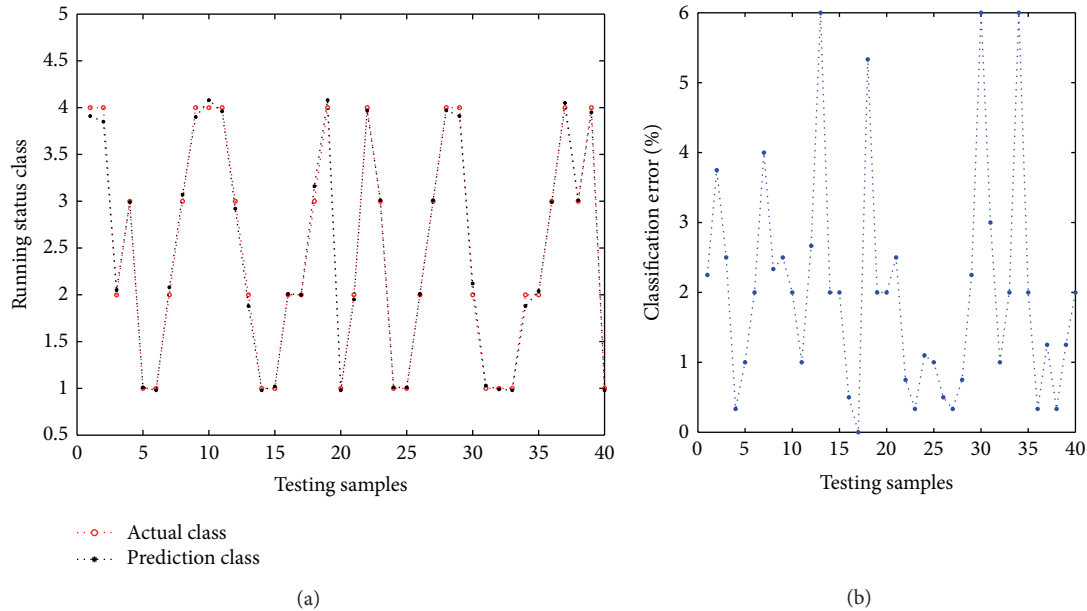


FIGURE 9: The contrast of prediction class and actual class.

## 6. Conclusions

This paper proposed a novel classifier model based on BP neural network and rough sets theory to be applied in nonlinear systems. The decision table was constructed and discretized reasonably through the PSO algorithm. The decision rules were extracted by the use of value reduction algorithm which provided the basis for the network structure. In order to verify the feasibility and superiority, the proposed approach was applied to a classification problem of an industrial example. The results of comparison simulations showed that the proposed approach could generate more accurate classification and cost less classification time than other neural network approaches and the rough sets based approach. The classification performance of proposed model demonstrated that this method could be extended to process other types of classification problems such as gear fault identification, lithology recognition, and coal-rock interface recognition.

## Conflict of Interests

The authors declare that there is no conflict of interests regarding the publication of this paper.

## Acknowledgments

The supports of National High Technology Research and Development Program of China (no. 2013AA06A411), National Natural Science Foundation of China (no. 51005231), Xuyi Mine Equipment and Materials R&D Center Innovation Fund Project (no. CXJJ201306), and Jiangsu Province National Engineering Research Center Cultivation Base for Coal Intelligent Mining Equipment in carrying out this research are gratefully acknowledged.

## References

- [1] W. Zhu and F. Wang, "On three types of covering-based rough sets," *IEEE Transactions on Knowledge and Data Engineering*, vol. 19, no. 8, pp. 1131–1143, 2007.
- [2] Z. Huang, Z. Yu, and Y. Zheng, "Simple method for predicting drag characteristics of the wells turbine," *China Ocean Engineering*, vol. 20, no. 3, pp. 473–482, 2006.
- [3] S. G. Sklavos and A. K. Moschovakis, "Neural network simulations of the primate oculomotor system: IV. A distributed bilateral stochastic model of the neural integrator of the vertical saccadic system," *Biological Cybernetics*, vol. 86, no. 2, pp. 97–109, 2002.
- [4] I. G. Belkov, I. N. Malyshev, and S. M. Nikulin, "Creating a model of passive electronic components using a neural network approach," *Automation and Remote Control*, vol. 74, no. 2, pp. 275–281, 2013.
- [5] J. S. Chen, "Neural network-based modelling and thermally-induced spindle errors," *International Journal of Advanced Manufacturing Technology*, vol. 12, no. 4, pp. 303–308, 1996.
- [6] A. D. Cartwright, I. S. Curthoys, and D. P. D. Gilchrist, "Testable predictions from realistic neural network simulations of vestibular compensation: integrating the behavioural and physiological data," *Biological Cybernetics*, vol. 81, no. 1, pp. 73–87, 1999.
- [7] B. Zou, X. Y. Liao, Y. N. Zeng, and L. X. Huang, "An improved BP neural network based on evaluating and forecasting model of water quality in Second Songhua River of China," *Chinese Journal of Geochemistry*, vol. 25, no. 1, pp. 167–170, 2006.
- [8] Y. X. Shao, Q. Chen, and D. M. Zhang, "The application of improved BP neural network algorithm in lithology recognition," in *Advances in Computation and Intelligence*, vol. 5370 of *Lecture Notes in Computer Science*, pp. 342–349, 2008.
- [9] W. H. Zhou and S. Q. Xiong, "Optimization of BP neural network classifier using genetic algorithm," in *Intelligence Computation and Evolutionary Computation*, vol. 180 of *Advances in Intelligent Systems and Computing*, pp. 599–605, 2013.

- [10] W. Duch, R. Setiono, and J. M. Zurada, "Computational intelligence methods for rule-based data understanding," *Proceedings of the IEEE*, vol. 92, no. 5, pp. 771–805, 2004.
- [11] Z. Pawlak, "Rough sets," *International Journal of Computer and Information Sciences*, vol. 11, no. 5, pp. 341–356, 1982.
- [12] Y. Wu and S. J. Wang, "Method for improving classification performance of neural network based on fuzzy input and network inversion," *Journal of Infrared and Millimeter Waves*, vol. 24, no. 1, pp. 15–18, 2005.
- [13] Z. Pawlak, "Some issues on rough sets," in *Transactions on Rough Sets I*, vol. 3100 of *Lecture Notes in Computer Science*, pp. 1–58, 2004.
- [14] Z. Pawlak and A. Skowron, "Rough sets: some extensions," *Information Sciences*, vol. 177, no. 1, pp. 28–40, 2007.
- [15] Y. Hassan, E. Tazaki, S. Egawa, and K. Suyama, "Decision making using hybrid rough sets and neural networks," *International Journal of Neural Systems*, vol. 12, no. 6, pp. 435–446, 2002.
- [16] V. L. Berardi, B. E. Patuwo, and M. Y. Hu, "A principled approach for building and evaluating neural network classification models," *Decision Support Systems*, vol. 38, no. 2, pp. 233–246, 2004.
- [17] H. Ishibuchi, K. Kwon, and H. Tanaka, "A learning algorithm of fuzzy neural networks with triangular fuzzy weights," *Fuzzy Sets and Systems*, vol. 71, no. 3, pp. 277–293, 1995.
- [18] Y. Hayashi, J. J. Buckley, and E. Czogala, "Fuzzy neural network with fuzzy signals and weights," *International Journal of Intelligent Systems*, vol. 8, no. 4, pp. 527–537, 1993.
- [19] C. C. Hu, D. Y. Wang, K. J. Wang, and J. Cable, "Seasonal roadway classification based on neural network," *Journal of South China University of Technology (Natural Science)*, vol. 37, no. 11, pp. 22–26, 2009.
- [20] A. Subasi, M. Yilmaz, and H. R. Ozcalik, "Classification of EMG signals using wavelet neural network," *Journal of Neuroscience Methods*, vol. 156, no. 1-2, pp. 360–367, 2006.
- [21] D. Sahoo and G. S. Dulikravich, "Evolutionary wavelet neural network for large scale function estimation in optimization," in *Proceedings of the 11th AIAA/ISSMO Multidisciplinary Analysis and Optimization Conference*, pp. 658–668, Portsmouth, Va, USA, September 2006.
- [22] J. R. Zhang, J. Zhang, T. M. Lok, and M. R. Lyu, "A hybrid particle swarm optimization-back-propagation algorithm for feedforward neural network training," *Applied Mathematics and Computation*, vol. 185, no. 2, pp. 1026–1037, 2007.
- [23] W. Zhang, Y. B. Shi, L. F. Zhou, and T. Lu, "Wavelet neural network classifier based on improved PSO algorithm," *Chinese Journal of Scientific Instrument*, vol. 31, no. 10, pp. 2203–2209, 2010.
- [24] A. Sengur, I. Turkoglu, and M. C. Ince, "Wavelet packet neural networks for texture classification," *Expert Systems with Applications*, vol. 32, no. 2, pp. 527–533, 2007.
- [25] Y. F. Hassan, "Rough sets for adapting wavelet neural networks as a new classifier system," *Applied Intelligence*, vol. 35, no. 2, pp. 260–268, 2011.
- [26] W. Ziarko, "The discovery, analysis and representation of data dependencies in databases," in *Knowledge Discovery in Databases*, pp. 213–228, 1993.
- [27] Y. Hassan and E. Tazaki, "Emergent rough set data analysis," in *Transactions on Rough Sets II: Rough Sets and Fuzzy Sets*, J. F. Peters, Ed., pp. 343–361, Springer, Berlin, Germany, 2005.
- [28] D. B. Chen and C. X. Zhao, "Particle swarm optimization with adaptive population size and its application," *Applied Soft Computing Journal*, vol. 9, no. 1, pp. 39–48, 2009.
- [29] K. Thangavel and A. Pethalakshmi, "Dimensionality reduction based on rough set theory: a review," *Applied Soft Computing Journal*, vol. 9, no. 1, pp. 1–12, 2009.
- [30] J. M. Wei, "Rough set based approach to selection of node," *International Journal of Computational Cognition*, vol. 1, no. 2, pp. 25–40, 2003.
- [31] E. Xu, L. S. Shao, Y. Z. Zhang, F. Yang, and H. Li, "Method of rule extraction based on rough set theory," *Chong Qing: Computer Science*, vol. 38, pp. 232–235, 2011.
- [32] L. Y. Chang, G. Y. Wang, and Y. Wu, "An approach for attribute reduction and rule generation based on rough set theory," *Bei Jing: Journal of Software*, vol. 10, pp. 1206–1211, 1999.

## Research Article

# Robot Calibration for Cooperative Process under Typical Installation

Yahui Gan,<sup>1,2</sup> Xianzhong Dai,<sup>1,2</sup> and Donghui Dong<sup>1,2</sup>

<sup>1</sup> School of Automation, Southeast University, Nanjing 210096, China

<sup>2</sup> Key Laboratory of Measurement and Control of Complex Systems of Engineering, Ministry of Education, Nanjing 210096, China

Correspondence should be addressed to Yahui Gan; ganyahui@yeah.net

Received 3 November 2013; Accepted 11 March 2014; Published 24 April 2014

Academic Editor: Olabisi Falowo

Copyright © 2014 Yahui Gan et al. This is an open access article distributed under the Creative Commons Attribution License, which permits unrestricted use, distribution, and reproduction in any medium, provided the original work is properly cited.

A method with easy operation procedure and simple calibration condition is presented in this paper to solve the base frame calibration problem for cooperative robots. It is carried out through constructing a series of handclasp configurations and recording coordinates of the contact points, respectively, in base frame of each robot. Then the rotation matrix and translation matrix between base frame of cooperative robots can be calculated which is just the calibration result for cooperative robots. Based on typical installation mode for industrial robot, the floor mounted, wall mounted and ceiling mounted, constraints between base frames of these robots are further explored. These constraints are used to improve the calibration results for base frame calibration problem. In order to validate the correctness and effectiveness of our method, experiments on two industrial robots (Motoman VA1400 and HP20) are carried out at the end of the paper. The calibration errors are less than 8 mm in most cases, which satisfies the requirement of positioning accuracy for most industrial process, such as arc welding, transporting, and cutting. These experiment results assert the correctness of our method which can be used effectively to solve the base frame calibration problem for cooperative robots in manufacturing process.

## 1. Introduction

Cooperative robot system is a hot topic in robotics and much literature has been reported in this field. A multiple robot system surpasses a single robot system greatly in terms of flexibility and versatility in task execution. Particularly, multiple robot cooperation is required if we are to assemble and manipulate parts without the aid of fixtures or jigs or if we to smoothly transfer heavy and voluminous objects from one place to another. In the case of cooperation control between two robots, one robot must be informed of the position and orientation of the other robots. Therefore, robot base frame between one and another must be calibrated out before the cooperation starts. This paper aims at presenting an effective solution to such a problem of base frame calibration between two cooperative robots.

“Base frame calibration, which is to determine the relative translation and rotation between

base frames of two cooperative robots, is a challenging and basic problem for multiple robot system. A direct measurement is unaccessible because origins of the robot base frames are out of reach. Calibrations for an individual robot have already been investigated extensively and many effective methods have been developed [1–3]. Nevertheless, few researches have been made on calibration problem between two robots. Reference [4] proposed a passive base frame calibration method for two cooperative industrial robots by using a series of “peg-into-hole” manipulations to set up the calibration equation as  $AX = XB$ . The calibration accuracy depends on how precisely the peg aligned with the hole, which is monitored and adjusted manually by human operator. Through a hand-mounted vision sensor, a more human-independent calibrating approach for dual robots system is

presented in [5]. It takes advantage of relative motion between the robot end-effectors which can be recorded by the vision sensor to calculate the transformation relation between the base frames of dual robots. However, vision sensor parameters and their mounted postures are required for calculation of the transformation. Therefore, calibration result would be poor if these prerequisites were unprecise. Reference [6] introduced another calibration method based on Direct Linear Transformation using two CCD (Charge Coupled Device) cameras for cooperative industrial robots. Without knowing the mounting information of the cameras, it just uses a set of motions commanded to each manipulator. By detecting the motion with the cameras, relative rotation and translation between base frames of the two robots can be obtained. A simpler but more effective calibration method is presented in [7]. It uses only two calibration plates which are inexpensive to manufacture and requires no other measuring instrument. Only by forming the cooperative manipulators into a closed chain, commanding them to move through a set of postures and recording the joint information, the calibration problem can be formulated as a nonlinear optimization problem.” (This paragraph is cited from our previously published paper in [8]. It has been included in this paper just for integrity reason.)

In one of our previous works [8], a new calibration method based on handclasp manipulation is proposed. This method uses only a series of handclasp manipulations and their corresponding joint information to calculate the transformation relation between base frames of the cooperative robots. No external calibration apparatus or elaborate setups are needed. Great advantages of this method are the easy operational procedure and simple calibrating condition, which makes it quite feasible for use in manufacturing field, whereas the calibration problem considered in [8] is a generic form. For industrial process, robot base installation has strong characteristics. These characteristics can be described by a concept of robot installation angle. Definite constraints exist between robot installation angle for typical installed robots. Considering these constraints, the calibration results in [8] can be greatly improved for typical installed robots. Therefore, further research has been conducted to improve the calibration accuracy of our previously proposed calibration method. Focus of the innovation in this paper lies in that constraints between robot installation angles for typical installed robots have been involved in the calibration process, which improves the calibration accuracy a lot. Remainder of this paper is organized as follows. Section 2 introduces theoretical analysis of the improved method for robot base calibration. Section 3 presents the calibration procedure of this method. In addition to the method introduction, calibration experiments for two cooperative industrial robots

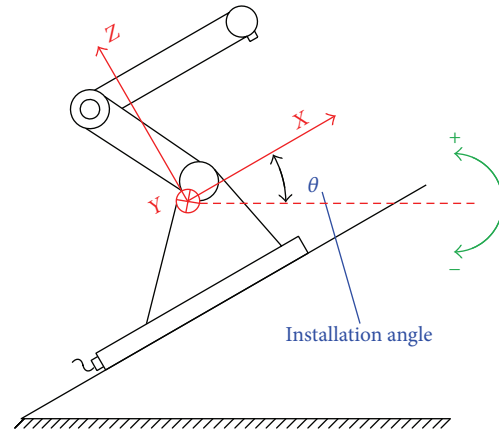


FIGURE 1: Robot base installation angle.

are presented in Section 4. Concluding remarks follow in Section 5.

## 2. Method of the Calibration

**2.1. Robot Installation Angle.** In applications with a single robot, the world system is usually chosen in the base of the robot. Yet, when several robots work together in a task, it is beneficial to use a world system independent of the individual robots. To enable this, the path controller has to manage the position of the individual robots in the world system by defining a separate robot base frame.

For most industrial applications, only three installation types exist for the robot base mounting, which is called floor mounted, wall mounted, and ceiling mounted. For quantitative descriptions of the aforementioned robot base installation types, concept of robot installation angle is defined as follows.

*Definition 1.* As shown in Figure 1, the installation angle is defined as the joint  $\theta$  between axis- $X$  of robot base frame and the ground level line.

Since the definition of robot base frame has a unique form in industry standard [9], the above definition of the robot installation angle is invariant with respect to the robot's front and rear. For further illustration, examples of typical installation angle are shown in Figure 2.

By the definition of robot installation angle, a floor mounted robot has an installation angle of  $0^\circ$ , a wall mounted robot has an installation angle of  $-90^\circ$  or  $90^\circ$ , and a ceiling mounted robot has an installation angle of  $180^\circ$ . Introducing these values to base frame calibration between typical installed robots, the calibration results will be improved greatly compared with the calibration results presented in [8].

**2.2. Calibration of Generally Installed Cooperative Robots.** In [8], we proposed a base frame calibration method for generally installed cooperative robots. Principle of the calibration method in [8] is used as the development basis for this paper.

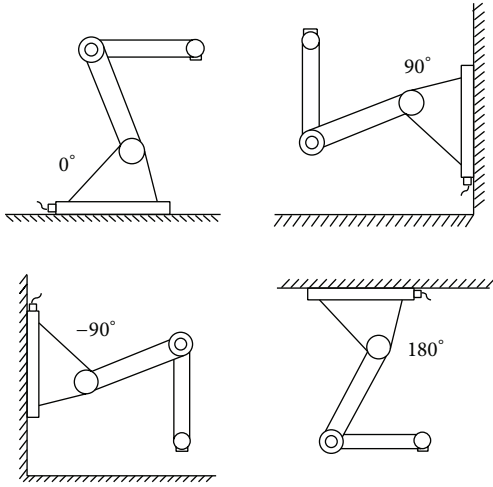


FIGURE 2: Examples of typical installation angle.

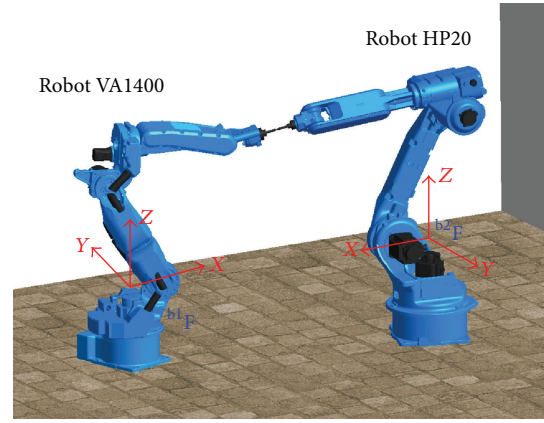


FIGURE 4: Handclasp manipulation between a floor mounted robot and a floor mounted robot.

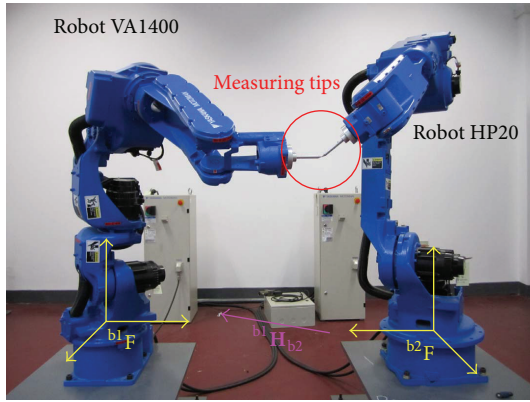


FIGURE 3: Handclasp manipulation for two cooperative industrial robots Motoman VA1400 and HP20.

For two cooperative robots as shown in Figure 3,  $b^1_F$  is the base frame system for robot Motoman VA1400 and  $b^2_F$  is the base frame system for robot Motoman HP20. These two robots form a handclasp configuration in Figure 3 with measuring tips mounted at the end of each robot. Let the homogenous matrix  $b^1_H_{b2} \in \mathbb{R}^{4 \times 4}$  be the relative position and orientation between these two robots.  $b^1_H_{b2}$  can be calibrated by 4 handclasp manipulations as shown in Figure 3.

Reference [8] presents basic forms of the base frame calibration equations for two cooperative robots. Those equations are generic forms. For typical installed robots, those equations can be refined to improve the calibration results as discussed in the next part of the paper.

**2.3. Calibration Equations for Typical Installed Robot.** In this paper, only three types of the robot base installation are considered, which are floor mounted, wall mounted, and ceiling mounted. Thereafter, only three types of the robot

base calibration problems are considered here, which are calibration of a floor mounted robot to a floor mounted robot, calibration of a floor mounted robot to a wall mounted robot, and calibration of a floor mounted robot to a ceiling mounted robot. Although the resulting classification is not exhaustive, it covers most cases of the industrial applications.

**2.3.1. Calibration of a Floor Mounted Robot Relative to a Floor Mounted Robot.**

As shown in Figure 4, a floor mounted robot is carrying out the handclasp manipulation with a floor mounted robot. By the above introduced method, relative position and orientation between base frames of the two robots can be calibrated. Theoretically speaking, the rotation matrix for orientation between the two base frames must be orthogonal and normalized, whereas the solution cannot ensure this characteristic, because resolution of transducer for robot joint positions is limited and error exists in system modeling. Therefore, an orthonormalization procedure is necessary to refine the calibrated result for frame rotation.

The criterion for rotation matrix orthonormalization is that modification made on frame rotation  $b^1_R_{b2}$  must be the least. The Frobenius norm of matrix  $\mathbf{A}$  is adopted to evaluate the difference between two matrices, which is

$$\|\mathbf{A}\|_F = \left( \sum_{i=1}^m \sum_{j=1}^n |a_{ij}|^2 \right)^{1/2}, \quad (1)$$

where  $\mathbf{A}$  is an  $m \times n$  matrix,  $\mathbf{A}_{m \times n} = (a_{ij})_{m \times n}$ . By the Frobenius norm, a cost function for the orthonormalization can be defined as

$$J = \|\mathbf{R} - b^1_R_{b2}\|_F^2 \quad (2)$$

s.t.  $\mathbf{R} \cdot \mathbf{R}^T = \mathbf{I}_{3 \times 3}, \quad \mathbf{R} \in \mathbb{R}^{3 \times 3}.$

The Frobenius distance between  $\mathbf{R}$  and  ${}^{b1}\mathbf{R}_{b2}$  is adopted as the cost function because each element difference will contribute to the increase of matrix distance. The Frobenius norm is much more sensitive to the element variation than other matrix norms. When  $J$  is minimized, it means that each element variation between  $\mathbf{R}$  and  ${}^{b1}\mathbf{R}_{b2}$  is averagely minimized. Let  ${}^{b1}\mathbf{R}_{b2}^*$  be the orthonormalized result; we have

$$J({}^{b1}\mathbf{R}_{b2}^*) = \min_{\mathbf{R} \cdot \mathbf{R}^T = \mathbf{I}_3} \|\mathbf{R} - {}^{b1}\mathbf{R}_{b2}\|_F^2. \quad (3)$$

Equation (3) means orthonormal matrix  ${}^{b1}\mathbf{R}_{b2}^*$  is the optimal Frobenius norm approximation for preliminary solution  ${}^{b1}\mathbf{R}_{b2}$ .

For the calibration case in Figure 4, relative orientation between the two cooperative robots exists in the form of a rotation around axis-Z of the robot base frame. Since the two robots have the same installation angle of  $0^\circ$ , rotation matrix between their base frames  ${}^{b1}\mathbf{F}$  and  ${}^{b2}\mathbf{F}$  will be

$$\text{Rot}(Z, \theta) = \begin{bmatrix} \cos \theta & -\sin \theta & 0 \\ \sin \theta & \cos \theta & 0 \\ 0 & 0 & 1 \end{bmatrix}, \quad (4)$$

where  $\theta$  is an arbitrary angle.

Let  $\alpha = \cos \theta$ ,  $\beta = \sin \theta$ ; then  $\alpha^2 + \beta^2 = 1$ . Substituting  $\alpha, \beta$  into (2) yields

$$J = \|\text{Rot}(Z, \theta(\alpha, \beta)) - {}^{b1}\mathbf{R}_{b2}\|_F^2 \quad (5)$$

s.t.  $\alpha^2 + \beta^2 = 1$ .

Equation (5) can be viewed as a mathematical optimization problem, which is to find the minimum of a multivariable function  $J$  subject to constraint  $\alpha^2 + \beta^2 = 1$ . The method of Lagrange multipliers [10] provides an effective strategy for solving these problems. Define the Lagrangian function as

$$J = \|\text{Rot}(\alpha, \beta) - {}^{b1}\mathbf{R}_{b2}\|_F^2 + \lambda(\alpha^2 + \beta^2 - 1). \quad (6)$$

Let the preliminary calibration result  ${}^{b1}\mathbf{R}_{b2}$  be

$${}^{b1}\mathbf{R}_{b2} = \begin{bmatrix} n_x & o_x & a_x \\ n_y & o_y & a_y \\ n_z & o_z & a_z \end{bmatrix}. \quad (7)$$

Substituting (7) into (6) and expanding the function  $J$  yields

$$\begin{aligned} J &= \|\text{Rot}(\alpha, \beta) - {}^{b1}\mathbf{R}_{b2}\|_F^2 + \lambda(\alpha^2 + \beta^2 - 1) \\ &= (\alpha - n_x)^2 + (-\beta - o_x)^2 + a_x^2 + (\beta - n_y)^2 \\ &\quad + (\alpha - o_y)^2 + a_y^2 + n_z^2 + o_z^2 + (1 - a_z)^2 \\ &\quad + \lambda(\alpha^2 + \beta^2 - 1). \end{aligned} \quad (8)$$

Minimizing the function  $J$  (8) with respect to  $\alpha, \beta$ , and  $\lambda$ , we obtain

$$\begin{aligned} \frac{\partial J}{\partial \alpha} &= 2(\alpha - n_x) + 2(\alpha - o_y) + 2\lambda\alpha = 0, \\ \frac{\partial J}{\partial \beta} &= 2(\beta + o_x) + 2(\beta - n_y) + 2\lambda\beta = 0, \end{aligned} \quad (9)$$

$$\frac{\partial J}{\partial \lambda} = \alpha^2 + \beta^2 - 1 = 0.$$

Unique solution exists for (9); that is,

$$\begin{aligned} \lambda &= \sqrt{(n_x + o_y)^2 + (n_y - o_x)^2} - 2, \\ \alpha &= \frac{n_x + o_y}{\sqrt{(n_x + o_y)^2 + (n_y - o_x)^2}}, \\ \beta &= \frac{n_y - o_x}{\sqrt{(n_x + o_y)^2 + (n_y - o_x)^2}}. \end{aligned} \quad (10)$$

After  $\alpha, \beta, \lambda$  are obtained, we have the refined calibration result for rotation as

$${}^{b1}\mathbf{R}_{b2}^* = \text{Rot}(\alpha, \beta) = \begin{bmatrix} \frac{n_x + o_y}{\sqrt{(n_x + o_y)^2 + (n_y - o_x)^2}} & -\frac{n_y - o_x}{\sqrt{(n_x + o_y)^2 + (n_y - o_x)^2}} & 0 \\ \frac{n_y - o_x}{\sqrt{(n_x + o_y)^2 + (n_y - o_x)^2}} & \frac{n_x + o_y}{\sqrt{(n_x + o_y)^2 + (n_y - o_x)^2}} & 0 \\ 0 & 0 & 1 \end{bmatrix} \quad (11)$$

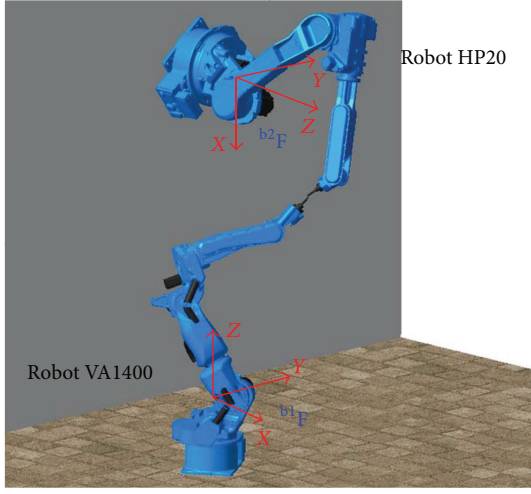


FIGURE 5: Handclasp manipulation between a floor mounted robot and a wall mounted robot.

in which  ${}^{b1}\mathbf{R}_{b2}^*$  is the orthonormalized and refined calibration result for rotation matrix. Thereafter, the translation vector also needs to be recalculated, which is

$${}^{b1}\mathbf{T}_{b2}^* = \frac{1}{4} \left[ ({}^{b1}P_1 - {}^{b1}\mathbf{R}_{b2}^* \cdot {}^{bj}P_1) + ({}^{b1}P_2 - {}^{b1}\mathbf{R}_{b2}^* \cdot {}^{b2}P_2) + ({}^{b1}P_3 - {}^{b1}\mathbf{R}_{b2}^* \cdot {}^{b2}P_3) + ({}^{b1}P_4 - {}^{b1}\mathbf{R}_{b2}^* \cdot {}^{b2}P_4) \right]. \quad (12)$$

Equations (11) and (12) are developed form of the calibration equations in [8], which will lead to more accurate calibration results compared with other methods as presented in [8].

**2.3.2. Calibration of a Floor Mounted Robot Relative to a Wall Mounted Robot.** As shown in Figure 5, a floor mounted robot is carrying out the handclasp manipulation with a wall mounted robot. For the calibration case in Figure 5, relative orientation between the two cooperative robots exists in the form of 3 successive rotations.

(I) A rotation of angle  $\alpha$  for Robot HP20 around axis-Z of the robot base frame  ${}^{b2}F$  to make axis-Y of  ${}^{b2}F$  horizontal, which is

$$\text{Rot}(Z, \alpha) = \begin{bmatrix} \cos \alpha & -\sin \alpha & 0 \\ \sin \alpha & \cos \alpha & 0 \\ 0 & 0 & 1 \end{bmatrix}. \quad (13)$$

(II) A rotation of  $-90^\circ$  for Robot HP20 around axis-Y of the robot base frame  ${}^{b2}F$  to make axis-Z of  ${}^{b2}F$  vertical to the ground, which is

$$\begin{aligned} \text{Rot}(Y, -90^\circ) &= \begin{bmatrix} \cos(-90^\circ) & 0 & \sin(-90^\circ) \\ 0 & 1 & 0 \\ -\sin(-90^\circ) & 0 & \cos(-90^\circ) \end{bmatrix} \\ &= \begin{bmatrix} 0 & 0 & -1 \\ 0 & 1 & 0 \\ 1 & 0 & 0 \end{bmatrix}. \end{aligned} \quad (14)$$

(III) A rotation of angle  $\beta$  for Robot HP20 around axis-Z of the robot base frame  ${}^{b2}F$  to make axis-X of  ${}^{b2}F$  stretch along the same direction as axis-X of  ${}^{b1}F$ , which is

$$\text{Rot}(Z, \beta) = \begin{bmatrix} \cos \beta & -\sin \beta & 0 \\ \sin \beta & \cos \beta & 0 \\ 0 & 0 & 1 \end{bmatrix}. \quad (15)$$

By (13), (14), and (15), we have the rotation matrix between robot base frame  ${}^{b1}F$  and  ${}^{b2}F$  as

$$\begin{aligned} \mathbf{R}(\alpha, \beta) &= \text{Rot}(Z, \beta) \cdot \text{Rot}(Y, -90^\circ) \cdot \text{Rot}(Z, \alpha) \\ &= \begin{bmatrix} \cos \beta & -\sin \beta & 0 \\ \sin \beta & \cos \beta & 0 \\ 0 & 0 & 1 \end{bmatrix} \cdot \begin{bmatrix} 0 & 0 & -1 \\ 0 & 1 & 0 \\ 1 & 0 & 0 \end{bmatrix} \\ &\quad \cdot \begin{bmatrix} \cos \alpha & -\sin \alpha & 0 \\ \sin \alpha & \cos \alpha & 0 \\ 0 & 0 & 1 \end{bmatrix} \\ &= \begin{bmatrix} 0 & -\sin \beta & -\cos \beta \\ 0 & \cos \beta & -\sin \beta \\ 1 & 0 & 0 \end{bmatrix} \begin{bmatrix} \cos \alpha & -\sin \alpha & 0 \\ \sin \alpha & \cos \alpha & 0 \\ 0 & 0 & 1 \end{bmatrix} \\ &= \begin{bmatrix} -\sin \beta \sin \alpha & -\sin \beta \cos \alpha & -\cos \beta \\ \cos \beta \sin \alpha & \cos \beta \cos \alpha & -\sin \beta \\ \cos \alpha & -\sin \alpha & 0 \end{bmatrix}. \end{aligned} \quad (16)$$

For simplicity, let  $\mu = \cos \alpha$ ,  $\nu = \sin \alpha$ ,  $\rho = \cos \beta$ ,  $\sigma = \sin \beta$ ; then  $\mu^2 + \nu^2 = 1$ ,  $\rho^2 + \sigma^2 = 1$ ,

$$\mathbf{R}(\alpha, \beta) = \begin{bmatrix} -\sigma\nu & -\sigma\mu & -\rho \\ \rho\nu & \rho\mu & -\sigma \\ \mu & -\nu & 0 \end{bmatrix} = \mathbf{R}(\mu, \nu, \rho, \sigma). \quad (17)$$

Substituting (17) into (2) yields

$$\begin{aligned} J &= \|\mathbf{R}(\mu, \nu, \rho, \sigma) - {}^{b1}\mathbf{R}_{b2}\|_F^2 \\ \text{s.t. } \mu^2 + \nu^2 &= 1, \quad \rho^2 + \sigma^2 = 1. \end{aligned} \quad (18)$$

Equation (18) also is a multivariable function optimization problem. By Lagrange multipliers method, define the Lagrangian function as

$$\begin{aligned} J &= \|\text{Rot}(\mu, \nu, \rho, \sigma) - {}^{b1}\mathbf{R}_{b2}\|_F^2 \\ &\quad + \lambda_1 (\mu^2 + \nu^2 - 1) + \lambda_2 (\rho^2 + \sigma^2 - 1). \end{aligned} \quad (19)$$

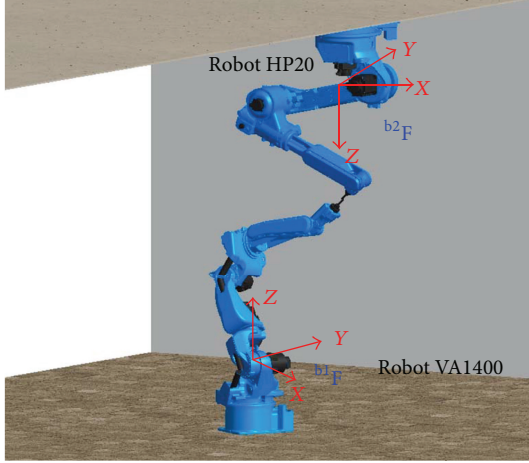


FIGURE 6: Handclasp manipulation between a floor mounted robot and a ceiling mounted robot.

Substituting (7) into (19) and expanding the function  $J$  yields

$$\begin{aligned}
 J = & (-\sigma v - n_x)^2 + (-\sigma \mu - o_x)^2 + (-\rho - a_x)^2 \\
 & + (\rho v - n_y)^2 + (\rho \mu - o_y)^2 + (-\sigma - a_y)^2 \\
 & + (\mu - n_z)^2 + (-v - o_z)^2 + (-a_z)^2 \\
 & + \lambda_1 (\mu^2 + v^2 - 1) + \lambda_2 (\rho^2 + \sigma^2 - 1).
 \end{aligned} \quad (20)$$

Minimizing the function  $J$  (20) with respect to  $\mu$ ,  $v$ ,  $\rho$ , and  $\sigma$ , we obtain

$$\begin{aligned}
 \frac{\partial J}{\partial \mu} &= 2\mu + o_x \sigma - o_y \rho + \mu \lambda_1 - n_z = 0 \\
 \frac{\partial J}{\partial v} &= 2v + n_x \sigma - n_y \rho + v \lambda_1 + o_z = 0 \\
 \frac{\partial J}{\partial \rho} &= 2\rho - n_y v - o_y \mu + \rho \lambda_2 + a_x = 0 \\
 \frac{\partial J}{\partial \sigma} &= 2\sigma + n_x v + o_x \mu + \sigma \lambda_2 + a_y = 0 \\
 \frac{\partial J}{\partial \lambda_1} &= \mu^2 + v^2 - 1 = 0 \\
 \frac{\partial J}{\partial \lambda_2} &= \rho^2 + \sigma^2 - 1 = 0.
 \end{aligned} \quad (21)$$

Collectively, there are 6 unique equations in (21) totaling the number of elements in function  $J$  (20). Therefore, unique solution exists for (21), which can be reached by Levenberg-Marquardt method with a numeric iterative procedure.

After  $\mu$ ,  $v$ ,  $\rho$ , and  $\sigma$  are obtained, an orthonormalized and refined calibration result  ${}^{b1}\mathbf{R}_{b2}^*$  for rotation matrix can be obtained by (17). Thereafter, the translation vector  ${}^{b1}\mathbf{T}_{b2}^*$  also needs to be recalculated as (12).

2.3.3. Calibration of a Floor Mounted Robot Relative to a Ceiling Mounted Robot. As shown in Figure 6, a floor mounted robot is carrying out the handclasp manipulation with a ceiling mounted robot. For the calibration case in Figure 6, relative orientation between the two cooperative robots exists in the form of 2 successive rotations.

(I) A rotation of  $180^\circ$  for Robot HP20 around axis- $X$  of the robot base frame  ${}^{b2}\mathbf{F}$  to make axis- $Z$  of  ${}^{b2}\mathbf{F}$  vertical to ground, which is

$$\begin{aligned}
 \text{Rot}(X, 180^\circ) &= \begin{bmatrix} 1 & 0 & 0 \\ 0 & \cos(180^\circ) & -\sin(180^\circ) \\ 0 & \sin(180^\circ) & \cos(180^\circ) \end{bmatrix} \\
 &= \begin{bmatrix} 1 & 0 & 0 \\ 0 & -1 & 0 \\ 0 & 0 & -1 \end{bmatrix}.
 \end{aligned} \quad (22)$$

(II) A rotation of angle  $\theta$  for Robot HP20 around axis- $Z$  of the robot base frame  ${}^{b2}\mathbf{F}$  to make axis- $X$  of  ${}^{b2}\mathbf{F}$  stretch along the same direction as axis- $X$  of frame  ${}^{b1}\mathbf{F}$ , which is

$$\text{Rot}(Z, \theta) = \begin{bmatrix} \cos \theta & -\sin \theta & 0 \\ \sin \theta & \cos \theta & 0 \\ 0 & 0 & 1 \end{bmatrix}. \quad (23)$$

By (22) and (23), we have the rotation matrix between robot base frame  ${}^{b1}\mathbf{F}$  and  ${}^{b2}\mathbf{F}$  as

$$\begin{aligned}
 \mathbf{R}(\theta) &= \text{Rot}(Z, \theta) \text{Rot}(X, 180^\circ) \\
 &= \begin{bmatrix} \cos \theta & -\sin \theta & 0 \\ \sin \theta & \cos \theta & 0 \\ 0 & 0 & 1 \end{bmatrix} \begin{bmatrix} 1 & 0 & 0 \\ 0 & -1 & 0 \\ 0 & 0 & -1 \end{bmatrix} \\
 &= \begin{bmatrix} \cos \theta & \sin \theta & 0 \\ \sin \theta & -\cos \theta & 0 \\ 0 & 0 & -1 \end{bmatrix}.
 \end{aligned} \quad (24)$$

Let  $\alpha = \cos \theta$ ,  $\beta = \sin \theta$ ; then  $\alpha^2 + \beta^2 = 1$ ,

$$\mathbf{R}(\theta) = \begin{bmatrix} \alpha & \beta & 0 \\ \beta & -\alpha & 0 \\ 0 & 0 & -1 \end{bmatrix} = \mathbf{R}(\alpha, \beta). \quad (25)$$

Substituting (25) into (2) yields

$$\begin{aligned}
 J &= \left\| \mathbf{R}(\alpha, \beta) {}^{b1}\mathbf{R}_{b2} \right\|_F^2 \\
 \text{s.t. } & \alpha^2 + \beta^2 = 1.
 \end{aligned} \quad (26)$$

Equation (26) also is a multivariable function optimization problem. By Lagrange multipliers method, define the Lagrangian function as

$$\begin{aligned}
 J &= \left\| \mathbf{R}(\alpha, \beta) {}^{b1}\mathbf{R}_{b2} \right\|_F^2 + \lambda (\alpha^2 + \beta^2 - 1) \\
 &= (-\alpha - n_x)^2 + (-\beta - o_x)^2 + (-a_x)^2
 \end{aligned}$$

$$\begin{aligned}
& + (\beta - n_y)^2 + (\alpha - o_y)^2 + (-a_y)^2 + (-n_z)^2 \\
& + (-o_z)^2 + (-1 - a_z)^2 + \lambda(\alpha^2 + \beta^2 - 1).
\end{aligned} \tag{27}$$

Minimizing the function  $J$  (27) with respect to  $\alpha, \beta$ , and  $\lambda$  yields

$$\begin{aligned}
\frac{\partial J}{\partial \alpha} &= 2(\alpha + n_x) + 2(\alpha - o_y) + 2\lambda\alpha = 0, \\
\frac{\partial J}{\partial \beta} &= 2(\beta + o_x) + 2(\beta - n_y) + 2\lambda\beta = 0, \\
\frac{\partial J}{\partial \lambda} &= \alpha^2 + \beta^2 - 1 = 0.
\end{aligned} \tag{28}$$

Unique solution exists for (28); that is,

$$\begin{aligned}
\lambda &= \sqrt{(n_x - o_y)^2 + (n_y + o_x)^2} - 2, \\
\alpha &= \frac{n_x - o_y}{\sqrt{(n_x - o_y)^2 + (n_y + o_x)^2}}, \\
\beta &= \frac{n_y + o_x}{\sqrt{(n_x - o_y)^2 + (n_y + o_x)^2}}.
\end{aligned} \tag{29}$$

After  $\alpha, \beta, \lambda$  are obtained, we have the refined calibration result for rotation as

$${}^{b1}\mathbf{R}_{b2}^* = \mathbf{R}(\alpha, \beta) = \begin{bmatrix} \frac{n_x - o_y}{\sqrt{(n_x - o_y)^2 + (n_y + o_x)^2}} & \frac{n_y + o_x}{\sqrt{(n_x - o_y)^2 + (n_y + o_x)^2}} & 0 \\ \frac{n_y + o_x}{\sqrt{(n_x - o_y)^2 + (n_y + o_x)^2}} & \frac{n_x - o_y}{\sqrt{(n_x - o_y)^2 + (n_y + o_x)^2}} & 0 \\ 0 & 0 & -1 \end{bmatrix} \tag{30}$$

in which  ${}^{b1}\mathbf{R}_{b2}^*$  is the orthonormalized and refined calibration result for rotation matrix. Thereafter, the translation vector  ${}^{b1}\mathbf{T}_{b2}^*$  also needs to be recalculated as (12).

Equations (30) and (12) are developed form of the calibration equations in [8], which will lead to more accurate calibration results compared with other methods as presented in [8].

### 3. Calibration Procedure

Base frame calibration between two cooperative robots is to identify elements of a rotation matrix  ${}^{b1}\mathbf{R}_{b2}$  and translation vector  ${}^{b1}\mathbf{T}_{b2}$ . Information that we need for our calibration method includes robot joint positions, robot link parameters, and measuring tip dimensions. Preparatory conditions for this calibration method are quite simple, which include only the installation of the measuring tips on both robots and dimensions input of the measuring tip for each robot.

After commencing of the calibration command, move one robot to an arbitrary position. Align the tool center point of the other robot to tool center point of the first robot by independent robot motion. The two robots form a handclasp configuration and the first measurement commences. Register the position as  $P_1$ . Repeat this handclasp manipulation process three more times and register  $P_2, P_3$ , and  $P_4$  in the same manner as  $P_1$ . Both robots are to be moved independently during the calibration procedure. After  $P_1, P_2, P_3$ , and  $P_4$  are registered, substitute

these points information into corresponding calibration equations. For calibration of floor mounted robot relative to floor mounted robot, the calibration equations are (11) and (12). For calibration of floor mounted robot relative to wall mounted robot, the calibration equations are (17) and (12). For calibration of floor mounted robot relative to ceiling mounted robot, the calibration equations are (30) and (12). Figure 7 shows the calibration procedure of our proposed method.

In order to optimize the calibration results, the handclasp points selected should be as far apart as possible. The standard distance between  $P_1$  and  $P_2, P_2$  and  $P_3$ , and  $P_3$  and  $P_4$  should be 1 m or more. Typical selection of these 4 points is shown in Figure 8. As shown in Figure 8, teach  $P_1, P_2$ , and  $P_3$  so that a triangle, not a straight line, is formed. Teach  $P_4$  far apart from planar  $P_1P_2P_3$  so that a triangular pyramid is formed. Otherwise, inaccurate calibration will result.

After the calibration procedure, a check should be made to see if the two robot base frames are correctly calibrated. Jog the two robots in a coupled synchronous motion [11] and move one of them to see if the other can follow the motion of the first robot. If yes, base frames of the two robots are correctly calibrated.

### 4. Experiment Result

In order to validate the above-proposed calibration method for typical installed robot, representative experiments have

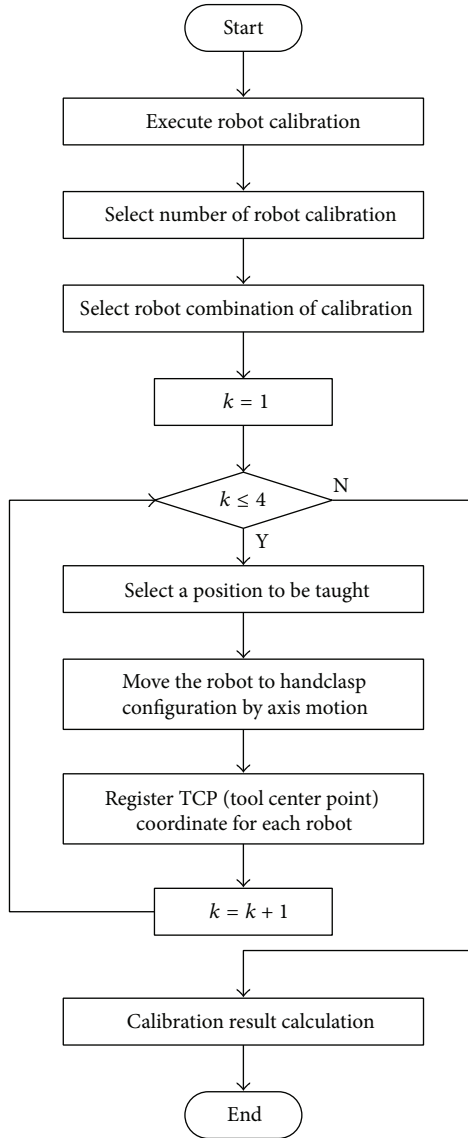


FIGURE 7: Calibration procedure of this method.

been carried out in our lab. The testbed is composed of two industrial robots, Motoman VA1400 and HP20, which are produced by YASKAWA Electronic Corporation, Japan. An external PC, DELL Optiplex 780, is used as a top layer controller to implement all the control logic and calculations. This external PC is connected to the robot controller DX100 by Ethernet cable. The communication software MotoCom SDK, which is also provided by YASKAWA Electronic Corporation, is installed on the PC to help transfer robot data and job files between the PC and DX100 robot controller. Figure 9 shows the experimental testbed we used here in our lab.

By the communication software MotoCom SDK, user applications can be developed and executed on a PC platform. MotoCom SDK provides users with the function to obtain coordinate of robot tool center point in its base frame, which forms the source data of calibration in the following analysis. Coordinate of robot tool center point in its base frame can be directly read out from the robot controller DX100 by function  $BscIsRobotPos()$ , which is one of the member functions provided by MotoCom SDK, whereas MotoCom SDK only provides a 6-dimensional vector  $(x, y, z, \phi, \theta, \psi) \in \mathbb{R}^6$  to represent position and orientation of the robot end-effector, 3-dimension  $(x, y, z)$  for tool center point position and 3-dimensional Euler angles  $(\phi, \theta, \psi)$  for tool orientation. The variables  $x, y,$  and  $z$  have a unit of millimetre (mm) while variables  $\phi, \theta,$  and  $\psi$  have a unit of degree ( $^\circ$ ). These coordinate values can also be found on the teaching pendant of the robot controller.

For consistency and coherence, transformations between Euler angle representation and a rotation matrix are presented here. In [12], successive rotations with angle  $\phi, \theta, \psi$  relative to axis  $Z, Y, Z$  will lead to a rotation matrix  $\mathbf{R}$  represented in (31) as follows:

$$\begin{aligned}
 & \text{Euler } (\phi, \theta, \psi) \\
 &= \text{Rot}(Z, \phi) \text{Rot}(Y, \theta) \text{Rot}(Z, \psi) \\
 &= \begin{bmatrix} \cos \phi \cos \theta \cos \psi - \sin \phi \sin \psi & -\cos \phi \cos \theta \sin \psi - \sin \phi \cos \psi & \cos \phi \sin \theta \\ \sin \phi \cos \theta \cos \psi + \cos \phi \sin \psi & -\sin \phi \cos \theta \sin \psi + \cos \phi \cos \psi & \sin \phi \sin \theta \\ -\sin \theta \cos \psi & \sin \theta \sin \psi & \cos \theta \end{bmatrix} = \mathbf{R}.
 \end{aligned} \tag{31}$$

Conversely, a rotation matrix  $\mathbf{R}$  can be decomposed into three successive rotations with  $\phi, \theta, \psi$  relative to axes  $Z, Y, Z$ ,

$$\begin{aligned}
 \text{Rot}(Z, \phi) \text{Rot}(Y, \theta) \text{Rot}(Z, \psi) &= \begin{bmatrix} n_x & o_x & a_x \\ n_y & o_y & a_y \\ n_z & o_z & a_z \end{bmatrix}, \\
 \phi &= \text{atan2}(a_y, a_x),
 \end{aligned}$$

$$\theta = \text{atan2}(\sin \phi a_y + \cos \phi a_x, a_z),$$

$$\psi = \text{atan2}(-\sin \phi n_x + \cos \phi n_y, -\sin \phi o_x + \cos \phi o_y). \tag{32}$$

Equation (32) will encounter degeneracy when  $\phi = 0^\circ$  or  $180^\circ$ . However, when  $\phi = 0^\circ$  or  $180^\circ$ , it means  $a_x = 0$  and  $a_y = 0$ . In such a case, we arbitrarily assume  $\phi = 0^\circ$ . When

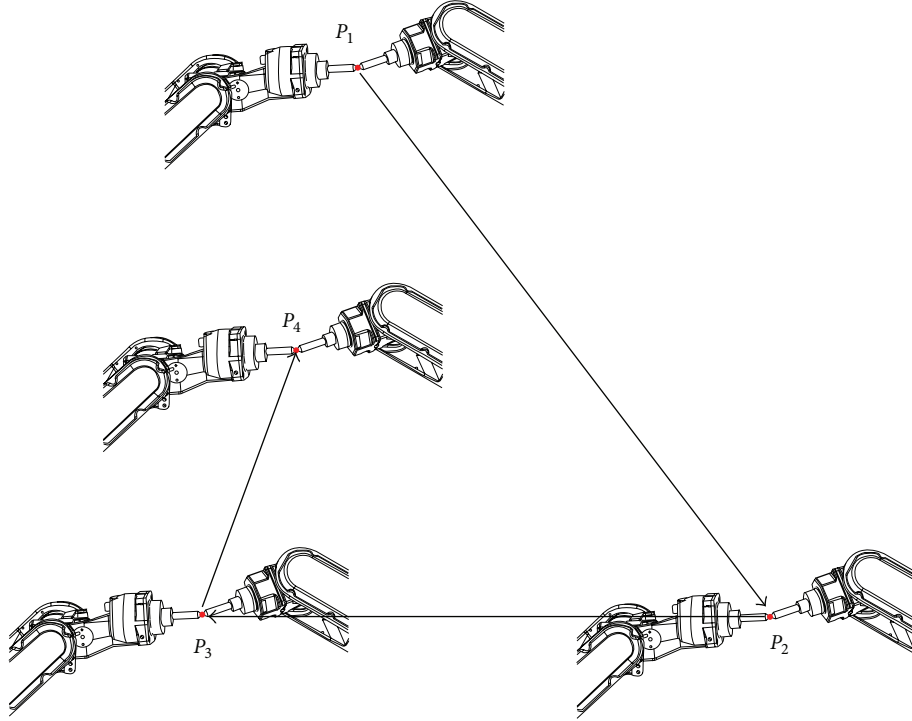


FIGURE 8: Example of 4 handclasp manipulations for two cooperative robots.

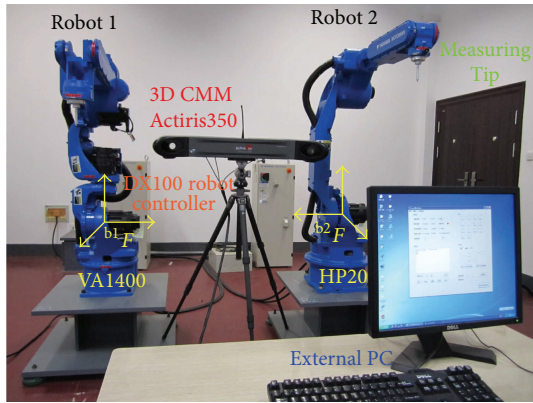


FIGURE 9: Testbed of calibration experiments in our lab.

$\theta = 0^\circ$  or  $180^\circ$ , we assume  $\theta = 0^\circ$ . Under this assumption, (32) is qualified for the rotation error assessment.

The 6-dimensional vector formation  $(x, y, z, \phi, \theta, \psi) \in \mathbb{R}^6$  is also adopted to represent the relative translation and rotation between based frames of the two robots. The aforementioned 3-dimension vector  $(x, y, z)$  indicates relative translation and 3-dimensional vector Euler angles  $(\phi, \theta, \psi)$  indicate relative rotation. The variables  $x, y,$  and  $z$  also have a unit of millimeter (mm) while variables  $\phi, \theta,$  and  $\psi$  have a unit of degree ( $^\circ$ ).

For accuracy assessment, the calibration error for relative rotation between the two robots can be defined as

$$e_{\text{rot}} = \left\| \text{Euler} \left( {}^{b1}\mathbf{R}_{b2}^{\text{tru}} \right) - \text{Euler} \left( {}^{b1}\mathbf{R}_{b2}^* \right) \right\|_{\infty} \quad (33)$$

in which  $\text{Euler}({}^{b1}\mathbf{R}_{b2}^{\text{tru}})$  is true values of the Euler form rotation between the two robots and  $e_{\text{rot}}$  is the error. The error  $e_{\text{rot}}$  with a unit of degree ( $^\circ$ ) has a definite meaning that represents the maximum error between Euler angle forms of the calibrated rotation matrix and its true value. The calibration error for the translation vector can be defined as

$$e_{\text{tran}} = \left\| {}^{b1}\mathbf{T}_{b2}^{\text{tru}} - {}^{b1}\mathbf{T}_{b2}^* \right\|_{\infty} \quad (34)$$

in which  ${}^{b1}\mathbf{T}_{b2}^{\text{tru}}$  is true values of translation vector between the two robots and  $e_{\text{tran}}$  is the error. The error  $e_{\text{tran}}$  has a unit of millimeter (mm), whose meaning represents the maximum error between calibrated translation vector and its true value.

True values for relative rotation  $\text{Euler}({}^{b1}\mathbf{R}_{b2}^{\text{tru}})$  and translation  ${}^{b1}\mathbf{T}_{b2}^{\text{tru}}$  between base frames of the two robots are calibrated by an external sensor Actiris350. The Actiris350 system is a 3D coordinate measuring machine manufactured by ActCM Corporation, France. Actiris350 system has a precision of  $\pm 15 \mu\text{m}$  for single point according to ISO 10360-2; repeatability is  $\pm 25 \mu\text{m}$ , acquisition speed is 15 measurements per second max, and measuring volume is  $3.5 \text{ m}^3$ . Figure 10 shows the 3D coordinate measuring machine Actiris350 we used.

Table 1 presents the robot base calibration results and comparisons with other methods. Data in column  $\mathbf{H}_{\text{tru}}$  are the true values of the relative rotation and translation between base frames of Motoman VA1400 and HP20, which are acquired by Actiris350,  $\mathbf{H}_{\text{tru}} = [{}^{b1}\mathbf{T}_{b2}^{\text{tru}}, \text{Euler}({}^{b1}\mathbf{R}_{b2}^{\text{tru}})]$ . Data in column  $\mathbf{H}_{\text{calib2}}$  are the calibrated results by our proposed method,  $\mathbf{H}_{\text{calib2}} = [{}^{b1}\mathbf{T}_{b2}^*, \text{Euler}({}^{b1}\mathbf{R}_{b2}^*)]$ .

TABLE I: Robot calibration results and comparisons.

$\mathbf{H}_{\text{tru}}$	$\mathbf{H}_{\text{calib1}}$	$e_{\text{tran1}}$ (mm)	$e_{\text{rot1}}$ ( $^{\circ}$ )	$\mathbf{H}_{\text{calib2}}$	$e_{\text{tran2}}$ (mm)	$e_{\text{rot2}}$ ( $^{\circ}$ )
(37.9, 1476.5, 54.5, -0.001, 0.001, -44.500)	(43.6, 1475.4, 58.8, 0, -0.167, -44.593)	5.7	0.167	(43.8, 1475.6, 58.2, 0, 0, -44.593)	5.9	0.093
(37.9, 1476.5, 54.5, -0.001, 0.001, -44.500)	(33.5, 1477.8, 51.4, 0, -0.352, -44.632)	4.5	0.352	(42.7, 1476.8, 57.7, 0, 0, -44.631)	4.8	0.131
(37.9, 1476.5, 54.5, -0.001, 0.001, -44.500)	(42.2, 1475.1, 55.5, 0, 0.070, -44.532)	4.3	0.070	(33.5, 1477.6, 52.8, 0, 0, -44.536)	4.4	0.036
(37.9, 1476.5, 54.5, -0.001, 0.001, -44.500)	(34.9, 1477.9, 47.5, 0, -0.178, -44.601)	7.2	0.178	(43.8, 1474.9, 56.3, 0, 0, -44.600)	5.9	0.100
(37.9, 1476.5, 54.5, -0.001, 0.001, -44.500)	(29.1, 1477.6, 47.8, 0, 0.144, -44.385)	8.8	0.147	(30.1, 1479.4, 51.8, 0, 0, -44.384)	7.8	0.116
(1500.1, 500.0, 1499.9, 0, 180.001, 0.001)	(1501.4, 508.6, 1496.2, 0, -179.941, -0.312)	8.6	0.312	(1500.4, 506.3, 1498.4, 0, 180, -0.312)	6.3	0.312
(1500.1, 500.0, 1499.9, 0, 180.001, 0.001)	(1499.1, 505.0, 1498.6, 0, 179.979, -0.163)	5.0	0.163	(1499.5, 503.3, 1499.2, 0, 180, -0.163)	3.3	0.163
(1500.1, 500.0, 1499.9, 0, 180.001, 0.001)	(1501.9, 492.0, 1501.8, 0, -179.946, 0.273)	8.0	0.273	(1501.0, 494.6, 1501.2, 0, 180, 0.273)	5.4	0.273
(1500.1, 500.0, 1499.9, 0, 180.001, 0.001)	(1498.5, 503.9, 1499.9, 0, 179.947, -0.157)	3.9	0.157	(1499.4, 503.0, 1499.5, 0, 180, -0.157)	3.0	0.157
(1500.1, 500.0, 1499.9, 0, 180.001, 0.001)	(1498.7, 511.9, 1496.1, 0, 179.982, -0.372)	11.9	0.372	(1499.0, 507.4, 1498.2, 0, 180, -0.372)	7.4	0.372
(1303.3, -102.3, 1386.3, 180, 89.874, -179.997)	(1307.8, -97.8, 1380.1, -179.695, 89.726, 179.686)	6.2	0.312	(1303.6, -97.8, 1383.3, -179.695, 90, 179.686)	4.5	0.311
(1303.3, -102.3, 1386.3, 180, 89.874, -179.997)	(1305.2, -101.2, 1384.0, -179.952, 89.753, 179.890)	2.3	0.121	(1301.5, -101.2, 1387.0, -179.952, 90, 179.890)	1.8	0.126
(1303.3, -102.3, 1386.3, 180, 89.874, -179.997)	(1308.6, -99.7, 1380.0, -179.650, 89.629, 179.547)	6.3	0.450	(1306.1, -99.7, 1386.7, -179.650, 90, 179.547)	2.8	0.449
(1303.3, -102.3, 1386.3, 180, 89.874, -179.997)	(1307.9, -100.4, 1381.8, -179.804, 89.694, 179.794)	4.6	0.203	(1305.8, -100.4, 1387.4, -179.804, 90, 179.794)	2.5	0.202
(1303.3, -102.3, 1386.3, 180, 89.874, -179.997)	(1307.6, -101.2, 1382.5, -179.782, 89.749, 179.604)	4.3	0.393	(1305.7, -101.2, 1387.1, -179.782, 90, 179.604)	2.4	0.393



FIGURE 10: 3D coordinate measuring machine Actiris350.

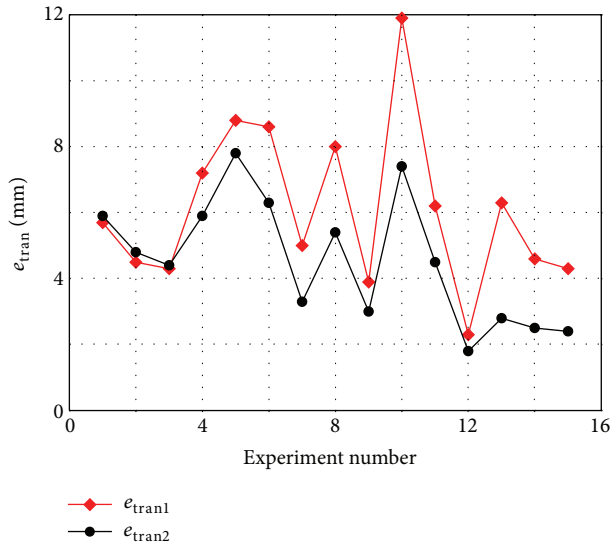


FIGURE 11: Translation error of calibration result.

The columns  $e_{tran2}$  obtained by (34) and  $e_{rot2}$  obtained by (33) are the calibration errors of robot base frame translation and rotation, respectively, for this method. Data in column  $\mathbf{H}_{calib1}$  are calibration results by the method proposed in [8]. The columns  $e_{tran1}$  obtained as  $e_{tran2}$  and  $e_{rot1}$  obtained as  $e_{rot2}$  are their calibration errors for robot base frame translation and rotation, respectively. Figure 11 shows the calibration error  $e_{tran1}$  and  $e_{tran2}$  for relative translation between the two robots. Figure 12 shows the calibration errors  $e_{rot1}$  and  $e_{rot2}$  for relative rotation between the two robots.

As shown in Figures 11 and 12, it is clear that the calibration accuracy by our proposed method is no more than 8 mm for relative translation and  $1^\circ$  for relative rotation,

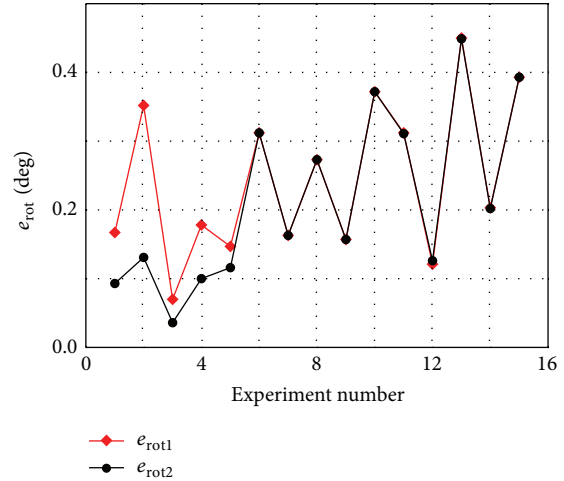


FIGURE 12: Rotation error of calibration result.

which indicates that calibration errors are relatively small. This precision level is quite satisfactory that can meet the requirement for most rough robot tasks, such as spraying, arc welding, or material transportation. So far, it can be concluded that the calibration method proposed in this paper is quite effective to solve the problem of base frame calibration for two cooperative robots.

## 5. Conclusion

A simple but effective method for calibrating the relative rotation and translation between base frames of two cooperative robots is presented in this paper. Greatest advantage of this method lies in its simple calibration setup and no other measuring apparatus required, which makes it quite feasible for applications in manufacturing works. The calibration procedure is based on a series of handclasp manipulations. Robot base installation angles are adopted to refine the preliminary calibration result.

Experimental testbed of base frame calibration with two cooperative industrial robots Motoman VA1400 and HP20 is presented here. Calibration results are quite satisfactory which asserts the validity and effectiveness of this method. The only defect of this calibration method may lie in that the handclasp manipulation for cooperative robots is driven by human operator. If the tool center point of each robot cannot be exactly driven to one same point, error will expand in the calibration result, whereas as long as the human operator drive the robot carefully and make the handclasp manipulation as accurate as possible, the calibration error can be reduced to relatively small.

## Conflict of Interests

The authors declare that there is no conflict of interests regarding the publication of this paper.

## Acknowledgments

This work was supported by the National Natural Science Foundation of China under Grant no. 61175113, National High Technology Research and Development Program of China under Grant nos. 2009AA043903-1-1 and 2007AA041703, Research Innovation Program for College Graduates of Jiangsu Province under Grant no. CX10B\_076Z, and Scientific Research Foundation of Graduate School of Southeast University under Grant nos. YBJJ1029 and YBPY1302.

## References

- [1] I.-C. Ha, "Kinematic parameter calibration method for industrial robot manipulator using the relative position," *Journal of Mechanical Science and Technology*, vol. 22, no. 6, pp. 1084–1090, 2008.
- [2] Y. Meng and H. Zhuang, "Autonomous robot calibration using vision technology," *Robotics and Computer-Integrated Manufacturing*, vol. 23, no. 4, pp. 436–446, 2007.
- [3] J. U. Dolinsky, I. D. Jenkinson, and G. J. Colquhoun, "Application of genetic programming to the calibration of industrial robots," *Computers in Industry*, vol. 58, no. 3, pp. 255–264, 2007.
- [4] X. X. Gu and C. B. Feng, "A calibration procedure for a system of two coordinated manipulators," *International Journal of Robotics and Automation*, vol. 10, no. 4, pp. 152–158, 1995.
- [5] J. Su, "Base calibration for dual robot system," *Control Theory and Applications*, vol. 15, no. 4, pp. 575–582, 1998.
- [6] T. Arai, Y. Maeda, H. Kikuchi, and M. Sugi, "Automated calibration of robot coordinates for reconfigurable assembly systems," *CIRP Annals: Manufacturing Technology*, vol. 51, no. 1, pp. 5–8, 2002.
- [7] R. G. Bonitz and T. C. Hsia, "Calibrating a multi-manipulator robotic system," *IEEE Robotics and Automation Magazine*, vol. 4, no. 1, pp. 18–22, 1997.
- [8] Y. Gan and X. Dai, "Base frame calibration for coordinated industrial robots," *Robotics and Autonomous Systems*, vol. 59, no. 7-8, pp. 563–570, 2011.
- [9] GB/T, 16977C1997, *National Standard of Peoples Republic of China: Naming Principles of Industrial Robot Frame and Motion*, National Standard Press, Beijing, China, 1997.
- [10] I. B. Vapnyarskii, "Lagrange multipliers," in *Encyclopedia of Mathematics*, M. Hazewinkel, Ed., Springer, New York, NY, USA, 2001.
- [11] Y. Gan and X. Dai, "Kinematic cooperation analysis and trajectory teaching in multiple robots system for welding," in *Proceedings of the 16th IEEE Conference on Emerging Technologies and Factory Automation (ETFA '11)*, pp. 1–8, Toulouse, France, September 2011.
- [12] Z. X. Cai, *Robotics*, Tsinghua University Press, Beijing, China, 2000.

## Research Article

# Modelling Laser Milling of Microcavities for the Manufacturing of DES with Ensembles

Pedro Santos,<sup>1</sup> Daniel Teixidor,<sup>2</sup> Jesus Maudes,<sup>1</sup> and Joaquim Ciurana<sup>2</sup>

<sup>1</sup> Department of Civil Engineering, Higher Polytechnic School, University of Burgos, Cantabria Avenue, 09006 Burgos, Spain

<sup>2</sup> Department of Mechanical Engineering and Industrial Construction, University of Girona, Maria Aurelia Capmany 61, 17003 Girona, Spain

Correspondence should be addressed to Jesus Maudes; [jmaudes@ubu.es](mailto:jmaudes@ubu.es)

Received 28 December 2013; Accepted 11 March 2014; Published 17 April 2014

Academic Editor: Aderemi Oluyinka Adewumi

Copyright © 2014 Pedro Santos et al. This is an open access article distributed under the Creative Commons Attribution License, which permits unrestricted use, distribution, and reproduction in any medium, provided the original work is properly cited.

A set of designed experiments, involving the use of a pulsed Nd:YAG laser system milling 316L Stainless Steel, serve to study the laser-milling process of microcavities in the manufacture of drug-eluting stents (DES). Diameter, depth, and volume error are considered to be optimized as functions of the process parameters, which include laser intensity, pulse frequency, and scanning speed. Two different DES shapes are studied that combine semispheres and cylinders. Process inputs and outputs are defined by considering the process parameters that can be changed under industrial conditions and the industrial requirements of this manufacturing process. In total, 162 different conditions are tested in a process that is modeled with the following state-of-the-art data-mining regression techniques: Support Vector Regression, Ensembles, Artificial Neural Networks, Linear Regression, and Nearest Neighbor Regression. Ensemble regression emerged as the most suitable technique for studying this industrial problem. Specifically, Iterated Bagging ensembles with unpruned model trees outperformed the other methods in the tests. This method can predict the geometrical dimensions of the machined microcavities with relative errors related to the main average value in the range of 3 to 23%, which are considered very accurate predictions, in view of the characteristics of this innovative industrial task.

## 1. Introduction

Laser-milling technology has become a viable alternative to conventional methods for producing complex microfeatures on difficult-to-process materials. It is increasingly employed in the industry, because of its established advantages [1]. As a noncontact material-removal process, laser machining removes smaller and more precise amounts of material, applies highly localized heat inputs to the workpiece, minimizes distortion, involves no tool wear, and is not subject to certain constraints such as maximum tool force, buildup edge formation, and tool chatter. Micromanufacturing processes in the field of electronics and medical and biological applications are a growing area of research. High-resolution components, high precision, and small feature size are needed in this field, as well as real 3D fabrication. Thus, the use of laser machining to produce medical applications has become a growing area of research, one example of which

is the fabrication of coronary stents. This research looks at the fabrication and performance of the DES. Some of these DES are metallic stents that include reservoirs that contain the polymer and the drug [2], such as the Janus TES stent [3] which incorporates microreservoirs cut into its abluminal side that are loaded with the drug. The selection of the laser system and the process parameters significantly affects the quality of the microfeature that is milled and the productivity of the process. Although there are several studies which deal with the effect of the process parameters on the quality of the final laser-milled parts, few of them study this effect on a microscale. The literature contains many examples of experimental research looking at the influence of scanning speed, pulse intensity, and pulse frequency on the quality and productivity of laser milling in different materials on a macroscale [4–7]. There are many works on microscale machining that have investigated laser-machining processes in laser microdrilling [8–10], laser microcutting

[11–13], and laser micromilling in 2D [14, 15]. However, there is little research on laser 3D micromilling. Pfeiffer et al. [16] studied the effects of laser-process parameters on the ablation behaviour of tungsten carbide hard metal and steel using a femtosecond laser for the generation of complex 3D microstructures. Karnakis et al. [17] demonstrated the laser-milling capacity of a picoseconds laser in different materials (stainless steel, alumina, and fused silica). Surface topology information was correlated with incident power density, in order to identify optimum processing. Qi and Lai [18] used a fiber laser to machine complex shapes. They developed a thermal ablation model to determine the ablated material volume and the dimensions and optimized the parameters to achieve maximum efficiency and minimum thermal effects. Finally, Teixidor et al. [19] studied the effects of scanning speed, pulse intensity, and pulse frequency on target width and depth dimensions and surface roughness for the laser milling of microchannels on tool steel. They presented a second-order model and a multiobjective process optimization to predict the responses and to find the optimum combinations of process parameters.

Although the manufacturing industry is interested in laser micromilling and some research has been done to understand the main physical and industrial parameters that define the performance of this process, the conclusions show that analytical approaches are necessary for all real cases due to their complexity. Data-mining approaches represent a suitable alternative to such tasks due to their capacity to deal with multivariate processes and experimental uncertainties. Data-mining is defined in [20] as “the process of discovering patterns in data” and “extracting’ or ‘mining’ knowledge from large amounts of data” [21]. “Useful patterns allow us to make nontrivial predictions on new data” [20] (e.g., predictions on laser-milling results based on experimental data). Many artificial intelligence techniques have been applied to macroscale milling [22–24], but there are few examples of the application of such techniques to laser micromilling [25]. Artificial neural networks (ANNs) have been proposed to predict the pulse energy for a desired depth and diameter in micromilling [26] and the material removal rate (MRR) for a fixed ablation depth depending on scanning velocity, pulse frequency [27], and cut kerf quality, in terms of dross adherence during nonvertical laser cutting of 1 mm thick mild-steel sheets [28]. Finally, regression trees have been proposed to optimize geometrical dimensions in the micromanufacturing of microchannels [29]. Neither of these studies used ensembles for process modeling, a learning paradigm in which multiple learners (or regressors) are combined to solve a problem. A regressor ensemble can significantly improve the generalization ability of a single regressor and can provide better results than an individual regressor in many applications [30–32]. Ensembles have demonstrated their suitability for modeling macroscale milling and drilling [33–36], especially because they can achieve highly accurate prediction with lower tuning time of the model parameters [35]. In view of the lack of published research on modeling the laser milling of 3D microgeometries with ensembles, the objective of this work is to study the modeling capability of these data-mining

TABLE 1: Sphere geometry dimensions.

Geometry	Depth ( $\mu\text{m}$ )	$\phi$ ( $\mu\text{m}$ )	Volume ( $\mu\text{m}^3$ )
Sphere 1 (e1)	50	166	721414
Sphere 2 (e2)	70	140	718377
Sphere 3 (e3)	90	124	724576

TABLE 2: Cylinder geometry dimensions.

Geometry	Depth ( $\mu\text{m}$ )	$\phi$ ( $\mu\text{m}$ )	Length ( $\mu\text{m}$ )	Volume ( $\mu\text{m}^3$ )
Cylinder 1 (c1)	50	130	55	723220
Cylinder 2 (c2)	70	110	46	721676
Cylinder 3 (c3)	90	100	36	725707

TABLE 3: Factors and factor levels.

Factors	Factor levels		
Scanning speed (SS) (mm/s)	200	400	600
Pulse intensity (PI) (%)	60	78	100
Pulse frequency (PF) (kHz)	30	45	60

techniques through the different inputs and outputs that may be considered priorities from an industrial point of view.

## 2. Experimental Procedure and Data Collection

The experimental apparatus described in this study gathered the data needed to create the models. The experimentation consisted of milling microcavities in a 316L Stainless Steel workpiece using a laser system. A Deckel Maho Nd:YAG Lasertec 40 machine with a 1,064 nm wavelength was used to perform the experiments. The system is a lamp-pumped solid-state laser that provides an ideal maximum (theoretically estimated) pulse intensity of 1.4 W/cm<sup>2</sup> [14], due to the 100 W average power and 30  $\mu\text{m}$  beam spot diameter. The SS316L workpiece material was selected because it is a biocompatible material commonly used in biomedical applications and specifically for the fabrication of coronary stents. Two different geometries were used for the experiments. The first geometry consisted of a half-spherical shape defined by depth and diameter dimensions. The second geometry was a half-cylindrical shape with a quarter sphere on both sides, defined by depth, diameter, and length dimensions. Both geometries and an example of a laser-milled cavity are presented in Figure 1. The geometries were fabricated with different combinations of dimensions, while maintaining the same volume. Tables 1 and 2 present the three combinations of dimensions for the spherical and the cylindrical geometries, respectively. These geometries and dimensions were selected, because they provide sufficient space to machine the cavities of these cardiovascular drug-eluting stent struts, which is an important part of their manufacturing process.

A full factorial design of experiments was developed, in order to analyze the effects of pulse frequency (PF), scanning speed (SS), and pulse intensity levels (PI, percentage of the

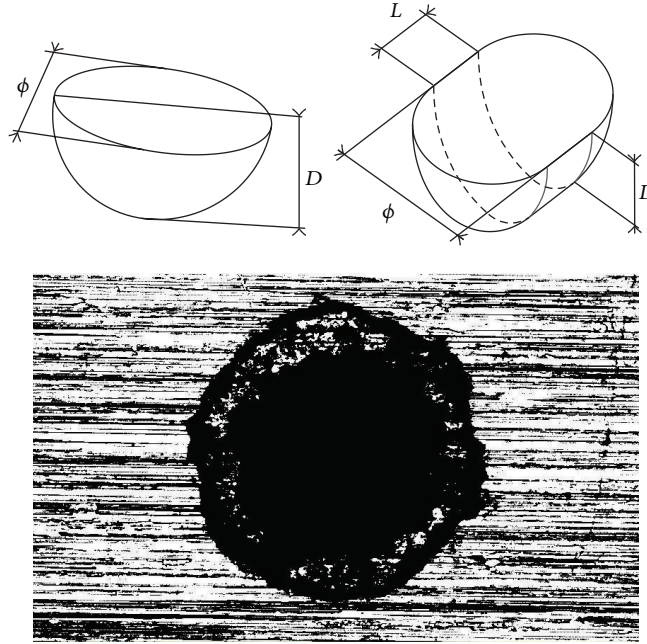


FIGURE 1: Cavity geometries used in the experiments.

ideal maximum pulse intensity) on the responses. Some screening experiments were performed to determine the proper parametric levels. Three different levels were selected from the results of each input factor, which are presented in Table 3. This design of experiments resulted in a total of 162 experiments: 27 combinations for each geometry under study. All the experiments were machined from the same 316L SS blank under the same ambient conditions. The response variables were the cavity dimensions (depth and radius) and the volume of removed material. A confocal Axio CSM 700 Carl Zeiss microscope was used for the dimensional measurements and for characterization of the cavities. Moreover, negatives of some of the samples were obtained with surface replicant silicone, in order to obtain 3D SEM images.

Having performed the experimental tests, the inputs and outputs for the datasets had to be defined, to generate the data sets for the data-mining modeling. On the whole, the selection of the inputs is easy, because they are set by the specifications of the equipment: the inputs are the parameters that the process engineer can change in the machine. They are the same as those considered to define the experimental tests explained above. Table 4 summarizes all the selected inputs, their units, ranges, and the relationship that they have with other inputs.

The definition of the data set outputs takes different interests into account that relate to the industrial manufacturing of DES. In some cases, a productivity orientation will encourage the process engineer to optimize productivity (in terms of the MRR) keeping geometrical accuracy under certain acceptable thresholds (by fixing a maximum relative error in geometrical parameters). In other cases, the geometrical accuracy will be the main requirement and productivity will be a secondary

objective. In yet other cases, only one geometrical parameter, for example, the depth of the DES, will be critical and the other geometrical parameters should be kept under certain thresholds, once again by fixing a maximum relative error for these geometrical parameters. Therefore, this work considers the geometrical dimensions and the MRR that is actually obtained as its output, their deviance from the programmed values, and the relative errors between the programmed and the real values. Table 5 summarizes all the calculated outputs, their units, ranges, and the relationship they have with other input or output variables. In summary, the 162 different laser conditions that were tested provided 14 data sets of 162 instances each with 9 attributes and one output variable to be predicted.

### 3. Data-Mining Techniques

In our study we consider the analysis of each output variable separately, by defining a one-dimensional regression problem for each case. A regressor is a data-mining model in which an output variable,  $y$ , is modelled as a function,  $f$ , of a set of independent variables,  $x$ , called *attributes* in the conventional notation of data-mining, where  $m$  is the number of *attributes*. The function is expressed as follows:

$$y_{\text{estimated}} = f(x), \quad x \in R^m, \quad y \in R. \quad (1)$$

The aim of this work is to determine the most suitable regressor for this industrial problem. The selection is performed by comparing the root mean squared error (RMSE) of several regressors over the data set. Having a data collection of  $n$  pairs of real values  $\{x_i, y_i\}_{i=1}^n$ , the RMSE is an estimation of the expected difference between the real and the forecasted

TABLE 4: Input variables.

	Variable	Units	Range	Relationship
$x_1$	Programmed depth	$\mu\text{m}$	50–90	Independent
$x_2$	Programmed radio	$\mu\text{m}$	50–83	Independent
$x_3$	Programmed length	$\mu\text{m}$	0–55	Independent
$x_4$	Programmed volume	$10^3 \times \mu\text{m}^3$	718–726	$4/3\pi x_2^3 + 1/2x_2^2 x_3$
$x_5$	Intensity	%	60–100	Independent
$x_6$	Frequency	KHz	30–60	Independent
$x_7$	Speed	mm/s	200–600	Independent
$x_8$	Time	s	9–24	Independent
$x_9$	Programmed MRR	$10^3 \times \mu\text{m}^3/\text{s}$	30–81	$x_4/x_8$

TABLE 5: Output variables.

	Variable	Units	Range	Relationship
$y_1$	Measured volume	$10^3 \times \mu\text{m}^3$	130–1701	Independent
$y_2$	Measured depth	$\mu\text{m}$	25–230.60	Independent
$y_3$	Measured diameter	$\mu\text{m}$	118.50–208.80	Independent
$y_4$	Measured length	$\mu\text{m}$	0–70.20	Independent
$y_5$	Measured MRR	$10^3 \times \mu\text{m}^3/\text{s}$	12–121	$y_1/x_8$
$y_6$	Volume error	$10^3 \times \mu\text{m}^3$	–980–596	$x_4 - y_1$
$y_7$	Depth error	$\mu\text{m}$	–180.60–56.90	$x_1 - x_2$
$y_8$	Width error	$\mu\text{m}$	–62.80––16.63	$2x_2 - y_3$
$y_9$	Length error	$\mu\text{m}$	–25.50–208.80	$x_3 - y_4$
$y_{10}$	MRR error	$10^3 \times \mu\text{m}^3/\text{s}$	–61–66	$x_9 - y_5$
$y_{11}$	Volume relative error	Dimensionless	–1.36–0.82	$y_6/x_4$
$y_{12}$	Depth relative error	Dimensionless	–3.61–0.63	$y_7/x_1$
$y_{13}$	Width relative error	Dimensionless	–0.55–0.10	$y_8/(2x_2)$
$y_{14}$	Length relative error	Dimensionless	–0.71–0.15	$y_9/x_3$

output by a regressor. It is expressed as the square root of the mean of the squares of the deviations, as shown in the following equation:

$$\text{RMSE} = \sqrt{\frac{\sum_{t=1}^n (y_t - f(x_t))^2}{n}}. \quad (2)$$

We tested a wide range of the main families of state-of-the-art regression techniques as follows.

- (i) Function-based regressors: we used two of the most popular algorithms, Support Vector Regression (SVR) [37] and ANNs [38], and also Linear Regression [39], which has an easier formulation that allows direct physical interpretation of the models. We should note the widespread use of SVR [40], while ANNs have been successfully applied to a great variety of industrial modeling problems [41–43].
- (ii) Instance-based methods, specifically their most representative regressor,  $k$ -nearest neighbors regressor [44]: in this type of algorithm, it is not necessary to express an analytic relationship between the input variables and the output that is modeled, an aspect that makes this approach totally different from the other. Instead of using an explicit formulation to

obtain a prediction, it is calculated from set values stored in the training phase.

- (iii) Decision-tree-based regressors: we have included these kinds of methods because they are used in the ensembles as regressors, as explained in Section 3.2.
- (iv) Ensemble techniques [45] are among the most popular in the literature. These methods have been successfully applied to a wide variety of industrial problems [34, 46–49].

**3.1. Linear Regression.** One of the most natural and simplest ways of expressing relations between a set of inputs and an output is by using a linear function. In this type of regressor the variable to forecast is given by a linear combination of the attributes, with predetermined weights [39], as detailed in the following equation:

$$y_{\text{estimated}}^{(i)} = \sum_{j=0}^k (w_j \times x_j^{(i)}), \quad (3)$$

where  $y_{\text{estimated}}^{(i)}$  denotes the output of the  $i$ th training instance and  $x_j^{(i)}$  the  $j$ th attribute of the  $i$ th instance. The sum of the squares of the differences between real and forecasted output

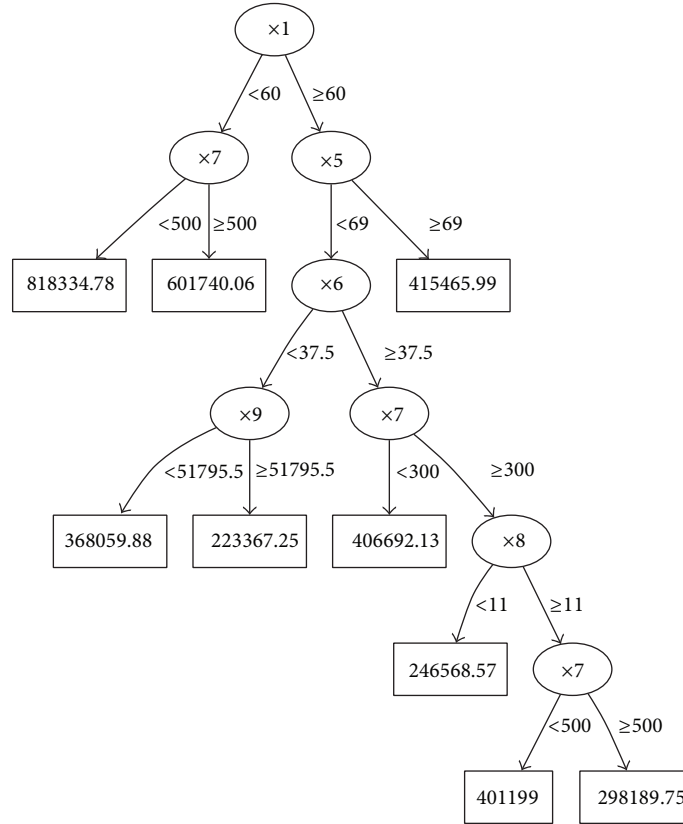


FIGURE 2: Model of the measured volume with a regression tree.

is minimized to calculate the most adequate weights,  $w_j$ , following the expression given in the following equation:

$$\sum_{i=0}^n \left[ y_{(i)} - \sum_{j=0}^k (w_j \times x_j^{(i)}) \right]. \quad (4)$$

We used an improvement to this original formulation, by selecting the attributes with the Akaike information criterion (AIC) [50]. In (5), we can see how the AIC is defined, where  $k$  is the number of free parameters of the model (i.e., the number of input variables considered) and  $P$  is the probability of the estimation fitting the training data. The aim is to obtain models that fit the training data but with as few parameters as possible:

$$AIC = -2 \ln(P) + 2k. \quad (5)$$

**3.2. Decision-Tree-Based Regressors.** The decision tree is a data-mining technique that builds hierarchical models that are easily interpretable, because they may be represented in graphical form, as shown in Figures 2 and 3, with an example of the output *measured length* as a function of the input attributes. In this type of model, all the decisions are organised around a single variable, resulting in the final hierarchical structure. This representation has three elements: the *nodes*, attributes taken for the decision (ellipses in the representation), the *leaves*, final forecasted values (squares),

and these two elements being connected by *arcs*, with the splitting values for each attribute.

As base regressors, we have two types of regressors, the structure of which is based on decision trees: *regression trees* and *model trees*. Both families of algorithms are hierarchical models represented by an abstract tree, but they differ with regard to what their leaves store [51]. In the case of *regression trees*, a value is stored that represents the average value of the instances enclosed by the leaf, while the *model trees* have a linear regression model that predicts the output value for these instances. The intrasubset variation in the class values down each branch is minimized to build the initial tree [52].

In our experimentation, we used one representative implementation of the two families, reduced-error pruning tree (REPTree) [20], a regression tree, and M5P [51], a model tree. In both cases we tested two configurations, pruned and unpruned trees. In the case of having one single tree as a regressor for some typologies of ensembles, it is more appropriate to prune the trees to avoid overfitting the training data, while some ensembles can take advantage of having unpruned trees [53].

**3.3. Ensemble Regressors.** An ensemble regressor combines the predictions of a set of so-called base regressors using a voting system [54], as we can see in Figure 4. Probably the three most popular ensemble techniques are Bagging [55], Boosting [56], and Random Subspaces [53]. For Bagging and

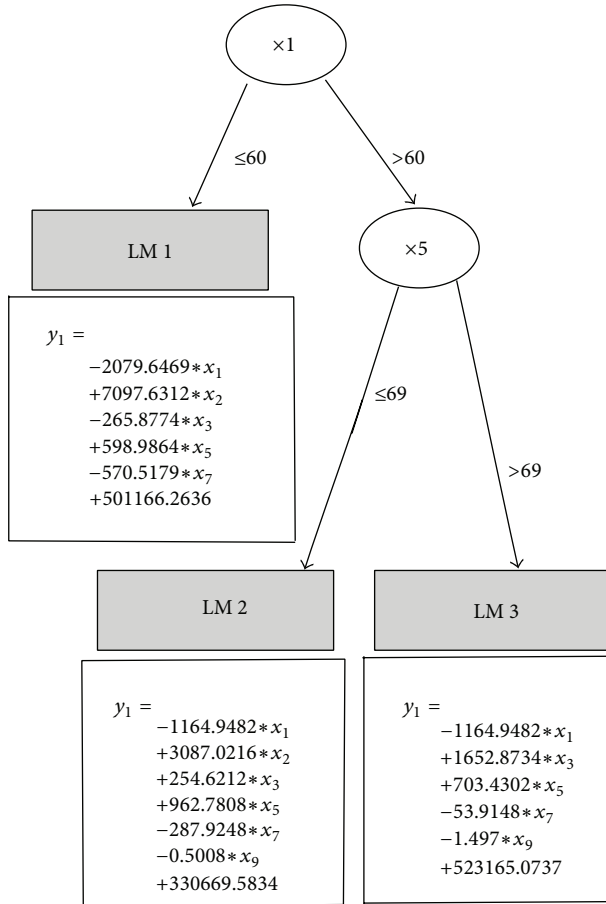


FIGURE 3: Model of the measured volume with a model tree.

Boosting, the ensemble regressor is formed from a set of weak base regressors, trained by applying the same learning algorithm to different sets obtained from the training set. In Bagging, each base regressor is trained with a dataset obtained from random sampling *with replacement* [55] (i.e., a particular instance may appear repeated several times or may not be considered in any base regressor). As a result, the base regressors are independent. However, Boosting uses all the instances and a set of weights to train each base regressor. Each instance has a weight pointing out how important it is to predict that instance correctly. Some base regressors can take weights into account (e.g., decision trees). Boosting trains base regressors sequentially, because errors for training instances in the previous base regressor are used for reweighting. The new base regressors are focused on instances that previous base regressors have wrongly predicted. The voting system for Boosting is also weighted by the accuracy of each base regressor [57].

Random Subspaces follow a different approach: each base regressor is trained in a subset of fewer dimensions than the original space. This subset of features is randomly chosen for all regressors. This procedure is followed with the intention of avoiding the well-known problem of the *curse of dimensionality* that occurs with many regressors when there are many features as well as improving accuracy by choosing

base regressors with low correlations between them. In total, we have used five ensemble regression techniques of the state of the art for regression, two variants of Bagging, one variant of Boosting, and Random Subspaces. The list of ensemble methods used in the experimentation is enumerated below.

- (i) Bagging is in its initial formulation for regression.
- (ii) Iterated Bagging combines several Bagging ensembles, the first one keeping to a typical construction and the others using residuals (differences between the real and the predicted values) for training purposes [58].
- (iii) Random Subspaces are in their formulation for regression.
- (iv) AdaBoost.R2 [59] is a boosting implementation for regression. Calculated from the absolute errors of each training example,  $l(i) = |f_R(x_i) - y_i|$ , the so-called *loss function*,  $L(i)$ , was used to estimate the error of each base regressor and to assign a suitable weight to each one. Let Den be the maximum value of  $l(i)$  in the training set; then three different loss functions are used: linear,  $L_L(i) = l(i)/\text{Den}$ , square,  $L_S(i) = [l(i)/\text{Den}]^2$ , and exponential,  $L_E(i) = 1 - \exp(-l(i)/\text{Den})$ .
- (v) Additive regression is this regressor that has a learning algorithm called Stochastic Gradient Boosting [60], which is a modification of Adaptive Bagging, a hybrid Bagging Boosting procedure intended for least squares fitting on additive expansions [60].

**3.4. *k*-Nearest Neighbor Regressor.** This regressor is the most representative algorithm among the instance-based learning. These kinds of methods forecast the output value using stored values of the most similar instances of the training data [61]. The estimation is the mean of the  $k$  most similar training instances. Two configuration decisions have to be taken:

- (i) how many nearest neighbors to use to forecast the value of a new instance?
- (ii) which distance function to use to measure the similarity between the instances?

In our experimentation we have used the most common definition of the distance function, the Euclidean distance, while the number of neighbors is optimized using cross-validation.

**3.5. Support Vector Regressor.** This kind of regressor is based on a parametric function, the parameters of which are optimized during the training process, in order to minimize the RMSE [62]. Mathematically, the goal is to find a function,  $f(x)$ , that has the most deviation,  $\epsilon$ , from the targets that are actually obtained,  $y_i$ , for all the training data, and at the same time is as flat as possible. The following equation is an example of SVR with the particular case of a linear function, called linear SVR, where  $\langle \cdot, \cdot \rangle$  denotes the inner product in the input space,  $X$ :

$$f(x) = \langle w, x \rangle + b \quad \text{with } w \in X, b \in \mathbb{R}. \quad (6)$$

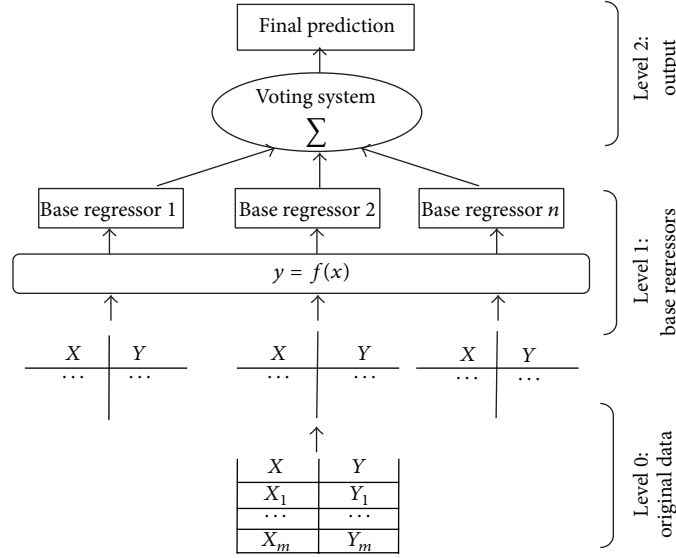


FIGURE 4: Ensemble regressor architecture.

The norms of  $w$  have to be minimized to find a flat function, but in real data solving this optimization problem can be unfeasible. In consequence, Boser et al. [37] introduced three terms into the formulation: the slack variables  $\xi, \xi^*$  and  $C$ , a trade-off parameter between the flatness and the deviations of the errors larger than  $\epsilon$ . In the following equation, the optimization problem is shown that is associated with a linear SVR:

$$\begin{aligned}
 &\text{minimize} && \frac{1}{2} \|w\|^2 + C \sum_{i=1}^l (\xi_i + \xi_i^*) \\
 &\text{s.t.} && y_i - \langle w, x_i \rangle - b \leq \epsilon + \xi_i \\
 &&& \langle w, x_i \rangle + b - y_i \leq \epsilon + \xi_i^* \\
 &&& \xi_i, \xi_i^* \geq 0.
 \end{aligned} \tag{7}$$

We have an optimization problem of the convex type that is solved in practice using the Lagrange method. The equations are rewritten using the *primal* objective function and the corresponding constraints, a process in which the so-called *dual* problem (see (8)) is obtained as follows:

$$\begin{aligned}
 &\text{maximize} && -\frac{1}{2} \sum_{i,j=1}^l (\alpha_i - \alpha_i^*) (\alpha_j - \alpha_j^*) \langle x_i, x_j \rangle \\
 &&& -\epsilon \sum_{i=1}^l (\alpha_i + \alpha_i^*) + \sum_{i=1}^l y_i (\alpha_i - \alpha_i^*) \\
 &\text{s.t} && \sum_{i=1}^l (\alpha_i - \alpha_i^*) = 0 \\
 &&& \alpha_i, \alpha_i^* \in [0, C].
 \end{aligned} \tag{8}$$

From the expression in (8), it is possible to generalize the formulation of the SVR in terms of a nonlinear function.

Instead of calculating the inner products in the original feature space, a kernel function,  $k(x, x')$ , that computes the inner product in a transformed space was defined. This kernel function has to satisfy the so-called Mercer's conditions [63]. In our experimentation, we have used the two most popular kernels in the literature [40]: linear and radial basis.

**3.6. Artificial Neural Networks.** We used the multilayer perceptron (MLP), the most popular ANN variant [64], in our experimental work. It has been demonstrated to be a universal approximator of functions [65]. ANNs are a particular case of neural networks, the mathematical formulation of which is inspired by biological functions, as they aim to emulate the behavior of a set of neurons [64]. This network has three layers [66], one with the network inputs (features of the data set), a hidden layer, and an output layer where the prediction is assigned to each input instance. Firstly the output of the hidden layer,  $y_{\text{hide}}$ , is calculated from the inputs, and then the output,  $y_{\text{hide}}$ , is obtained according to the expressions shown in the following equation [66]:

$$\begin{aligned}
 y_{\text{hide}} &= f_{\text{net}}(W_1 x + B_1) \\
 y_{\text{output}} &= f_{\text{output}}(W_2 y_{\text{hide}} + B_2),
 \end{aligned} \tag{9}$$

where  $W_1$  is the weight matrix of the hidden layer,  $B_1$  is the bias of the hidden layer,  $W_2$  is the weight matrix of the output layer (e.g., the identity matrix in the configurations tested),  $B_2$  is the bias of the output layer,  $f_{\text{net}}$  is the activation function of the hidden layer, and  $f_{\text{output}}$  is the activation function of the output layer. These two functions depend on the chosen structure but are typically the identity for the hidden layer and *tansig* for the output layer [66].

TABLE 6: Methods notation.

Bagging	BG
Iterated Bagging	IB
Random Subspaces	RS
Adaboost.R2	R2
Additive Regression	AR
REPTree	RP
M5P Model Tree	M5P
Support Vector Regressor	SVR
Multilayer Perceptron	MLP
$k$ -Nearest Neighbor Regressor	$k$ NN
Linear Regression	LR

#### 4. Results and Discussion

We compared the RMSE obtained for the regressors in a  $10 \times 10$  cross-validation, in order to choose the method that is most suited to model this industrial problem. The experiments were completed using the WEKA [20] implementation of the methods described above.

All the ensembles under consideration have 100 base regressors. The methods that depend on a set of parameters are optimized as follows:

- (i) SVR with linear kernel: the trade-off parameter,  $C$ , in the range 2–8;
- (ii) SVR with radial basis kernel:  $C$  from 1 to 16 and the parameter of the radial basis function,  $\gamma$ , from  $10^{-5}$  to  $10^{-2}$ ;
- (iii) multilayer perceptron: the training parameters *momentum*, *learning rate*, and *number of neurons* are optimized in the ranges 0.1–0.4, 0.1–0.6, and 5–15;
- (iv)  $k$ NN: the number of neighbours is optimized from 1 to 10.

The notation used to describe the methods is detailed in Table 6.

Regarding the notation, two abbreviations have been used besides those that are indicated in Table 6. On the one hand, we used the suffixes “L,” “S,” and “E” for the linear, square, and exponential loss functions of Adaboost.R2, and, on the other hand, the trees that are either pruned ( $P$ ) or unpruned ( $U$ ) appear between brackets. Tables 7, 8, and 9 set out the RMSE of each of the 14 outputs for each method.

Finally, a summary table with the best methods per output is shown. The indexes of the 39 methods that were tested are explained in Tables 10 and 11, and in Table 12 the method with minimal RMSE is indicated, according to the notation for these indexes. In the third column, we also indicate those methods that have larger RMSE, but, using a corrected resampled  $t$ -test [67], the differences are not statistically significant at a confidence level of 95%. Analyzing the second column of Table 12, among the 39 configurations tested, only 4 methods obtained the best RMSE for one of the 14 outputs: Adaboost.R2 with exponential loss and pruned M5P as base regressors—index 26—(5 times), SVR with radial

basis function kernel—index 6—(4 times), Iterated Bagging with unpruned M5P as base regressors—index 15—(4 times), and Bagging with unpruned RP as the base regressor - index 9—(1 time).

The performance of each method may be ranked. Table 13 presents the number of significative weaker performances of each method, considering the 14 outputs modeled. The most robust method is Iterated Bagging with unpruned M5P as base regressors - index 15 -, as in none of the 14 outputs was it outperformed by other methods. Besides selecting the best method, it is possible to obtain some additional conclusions from this ranking table.

- (i) Linear models like SVR linear—index 5— and LR—index 3—do not fit the datasets in the study very well. Both methods are ranked together at the middle of the table. The predicted variables therefore need methods that can operate with nonlinearities.
- (ii) SVR with Radial Basis Function Kernel—index 6—is the only nonensemble method with competitive results, but it needs to tune 2 parameters. MLP—index 7—is not a good choice. It needs to tune 3 parameters and is not a well-ranked method.
- (iii) For some ensemble configurations, there are differences in the number of statistically significative performances between the results from pruned and unpruned trees, while in other cases these differences do not exist; in general, though, the results of unpruned trees are more accurate, specially with the top-ranked methods. In fact, the only regressor which is not outperformed by other methods in any output has unpruned trees. Unpruned trees are more sensitive to changes in the training set. So, the predictions of unpruned trees, when their base regressors are trained in an ensemble, are more likely to output diverse predictions. If the predictions of all base regressors agreed there would be little benefit in using ensembles. Diversity balances faulty predictions by some base regressors with correct predictions by others.
- (iv) The top-ranked ensembles use the most accurate base regressor (i.e., M5P). All M5P configurations have fewer weaker performances than the corresponding RP configuration. In particular, the lowest rank was assigned to the AR - RP configurations, while AR M5P U came second best.
- (v) Ensembles that lose a lot of information, such as RS, are ranked at the bottom of the table. The table shows that the lower the percentage of features RS use, the worse they perform. In comparison to other ensemble methods, RS is a method that is very insensitive to noise, so it can point to data that are not noisy.
- (vi) In R2 M5P ensembles, the loss function does not appear to be an important configuration parameter.
- (vii) IB M5P U is the only configuration that never had significant losses when compared with the other methods.

TABLE 7: Root mean squared error 1/3.

	Volume	Depth	Width	Length	MRR
RP	216482.27	26.89	5.81	5.79	17166.73
M5P	210773.29	23.01	4.51	5.53	16076.33
LR	197521.89	23.84	7.04	14.73	15015.93
kNN	193756.62	23.57	5.42	6.84	15842.42
SVR linear	197894.5	24.19	7.07	16.23	14800.32
SVR radial basis	200774.24	18.85	4.38	5.35	14603.37
MLP	207646.99	22.98	4.7	5.39	16292.43
BG RP P	200212.92	21.49	4.97	5.08	15526.79
BG RP U	205290.8	19.98	4.66	4.9	15603.89
BG M5P P	200636.57	20.61	4.43	5.27	15293.92
BG M5P U	197546.75	19.5	4.31	5.38	15022.1
IB RP P	202767.85	22.05	4.87	5.14	15677.57
IB RP U	219388.93	21.7	5.01	5.11	15911.96
IB M5P P	197833.83	20.8	4.42	4.88	15318.01
IB M5P U	195154.16	19.65	4.3	4.78	14830.83
R2-L RP P	191765.23	22.27	4.94	5.07	15788.47
R2-L RP U	206369.82	21.71	5.25	5.29	17004.31
R2-L M5P P	186843.92	20.81	4.37	4.84	15031.37
R2-L M5P U	181587.4	20.51	4.34	4.84	15209.01
R2-S RP P	193908.39	23.03	5.1	5.18	16007.43
R2-S RP U	200453.21	21.21	5.11	5.31	16401.24
R2-S M5P P	173117.72	20.83	4.49	4.71	15070.05
R2-S M5P U	173914.36	20.87	4.52	4.72	15245.81
R2-E RP P	192529.31	22.59	5.02	5.07	15854.03
R2-E RP U	205920.86	21.44	5.22	5.21	17318.45
R2-E M5P P	171056.22	21.25	4.53	4.66	15078.01
R2-E M5P U	172948.95	21.32	4.55	4.67	15090.23
AR RP P	215750.39	25.51	5.42	5.56	17249.82
AR RP U	274467.43	24.71	5.83	6.15	18628.28
AR M5P P	208805.84	22.27	4.44	5.08	16076.5
AR M5P U	194572.79	19.58	4.51	4.94	15538.29
RS 50% RP P	200526.36	26.58	5.68	7.74	15854.27
RS 50% RP U	201946.24	25.33	5.35	7.54	15669.28
RS 50% M5P P	201013.27	26.6	5.38	15.42	15402.77
RS 50% M5P U	199166.84	25.65	5.39	15.45	15349.84
RS 75% RP P	199270.03	23.33	5.27	5.98	15861.58
RS 75% RP U	207845.67	21.61	5.04	6.25	16251.64
RS 75% M5P P	199648.96	23.55	4.65	8.29	15227.87
RS 75% M5P U	197420.35	22.11	4.6	8.39	15295.71

Once the best data-mining technique for this industrial task is identified, the industrial implementation of these results can follow the procedure outlined below.

- (1) The best model is run to predict one output, by changing two input variables of the process in small steps and maintaining a fixed value for the other inputs.
- (2) 3D plots of the output related to the two varied inputs should be generated. The process engineer can extract information from these 3D plots on the best milling conditions.

As an example of this methodology, the following case was built. Two Iterated Bagging ensembles with unpruned M5P as their base regressors are built for two outputs, the width and the depth errors, respectively. Then, the models were run by varying two inputs in small steps across the test range: pulse intensity (PI) and scanning speed (SS). This combination of inputs and outputs presents an immediate interest from the industrial point of view because, in a workshop, the DES geometry is fixed by the customer and the process engineer can only change three parameters of the laser milling process (pulse frequency (PF), scanning speed,

TABLE 8: Root mean squared error 2/3.

	Volume error	Depth error	Width error	Length error	MRR error
RP	216875.74	30.66	5.91	5.62	16355.57
M5P	214500.91	19.8	6.19	5.09	16009.84
LR	197521.93	23.92	6.76	14.67	14963.09
kNN	193696.36	23.69	4.98	6.6	14636.51
SVR linear	197817.88	24.17	7.1	16.23	14784.77
SVR radial basis	200785.96	18.98	4.42	5.37	14504.61
MLP	206753.61	21.96	4.93	5.37	17382.69
BG RP P	201037.57	23.18	4.62	4.98	15122.57
BG RP U	205341.53	21.6	4.4	4.87	15327.2
BG M5P P	200594.31	19.66	5.32	5.08	15162.5
BG M5P U	197575.49	19.19	5.22	5.15	14860.54
IB RP P	207848	23.05	4.78	5.18	15525.56
IB RP U	216631.14	23.79	4.79	5.2	16532.31
IB M5P P	201450.65	19.73	4.44	4.71	15177.67
IB M5P U	198261.22	19.44	4.33	4.58	14933.58
R2-L RP P	201365.5	24.08	4.64	5.03	15442.66
R2-L RP U	208500.97	23.95	4.87	5.38	16778.3
R2-L M5P P	184799.5	20.61	4.68	4.77	14732.4
R2-L M5P U	183740.85	20.71	4.7	4.81	14817.65
R2-S RP P	195592.43	24.75	4.65	5.24	16107.62
R2-S RP U	201017.69	22.87	4.71	5.39	15871.67
R2-S M5P P	172775.15	21.09	4.53	4.72	14459.98
R2-S M5P U	173892.35	20.88	4.52	4.74	14497.38
R2-E RP P	195657.69	24.26	4.62	5.12	15645.02
R2-E RP U	206275.71	24.38	4.82	5.35	16721.26
R2-E M5P P	172196.89	21.61	4.57	4.75	14324.48
R2-E M5P U	173356.89	21.61	4.58	4.79	14371.36
AR RP P	214978.3	27.77	5.49	5.43	16208.07
AR RP U	271926.55	27.43	5.29	6.1	20571.27
AR M5P P	211329.63	19.8	4.55	4.66	15995.84
AR M5P U	195497.5	19.55	4.78	4.82	15448.38
RS 50% RP P	200775.17	28.54	5.41	6.93	15217.65
RS 50% RP U	202354.2	26.84	5.24	6.94	15074.78
RS 50% M5P P	201054.45	25.91	5.98	11.81	15387.34
RS 50% M5P U	199246.1	25.61	5.79	11.75	14940.89
RS 75% RP P	199501.89	25.86	4.9	5.73	15165.01
RS 75% RP U	206467.56	24.5	4.75	6.06	15743.5
RS 75% M5P P	200160.47	22.05	5.76	6.66	15185.2
RS 75% M5P U	197431.78	21.79	5.53	6.75	14729.75

and pulse intensity). In view of these restrictions, the engineer will wish to know the expected errors for the DES geometry depending on the laser parameters that can be changed. The rest of the inputs for the models (DES geometry) are fixed at  $70 \mu\text{m}$  depth,  $65 \mu\text{m}$  width, and  $0 \mu\text{m}$  length, and

PF is fixed at 45 KHz. Figure 5 shows the 3D plots obtained from these calculations, allowing the process engineer to choose the following milling conditions: SS in the range of 325–470 mm/s and PI in the range of 74–91% for minimum errors in DES depth and width.

TABLE 9: Root mean squared error 3/3.

	Volume relative error	Depth relative error	Width relative error	Length relative error
RP	0.3	0.54	0.04	0.09
M5P	0.3	0.33	0.04	0.09
LR	0.27	0.43	0.05	0.13
kNN	0.27	0.38	0.04	0.1
SVR linear	0.27	0.44	0.05	0.15
SVR radial basis	0.28	0.29	0.04	0.1
MLP	0.29	0.34	0.04	0.1
BG RP P	0.28	0.4	0.04	0.08
BG RP U	0.29	0.36	0.04	0.08
BG M5P P	0.28	0.32	0.04	0.09
BG M5P U	0.27	0.31	0.04	0.09
IB RP P	0.29	0.38	0.04	0.09
IB RP U	0.3	0.38	0.04	0.09
IB M5P P	0.28	0.32	0.04	0.09
IB M5P U	0.28	0.3	0.04	0.09
R2-L RP P	0.27	0.39	0.04	0.08
R2-L RP U	0.29	0.38	0.04	0.1
R2-L M5P P	0.25	0.32	0.04	0.09
R2-L M5P U	0.26	0.32	0.04	0.09
R2-S RP P	0.27	0.39	0.04	0.09
R2-S RP U	0.28	0.38	0.04	0.1
R2-S M5P P	0.24	0.32	0.04	0.1
R2-S M5P U	0.24	0.33	0.04	0.1
R2-E RP P	0.27	0.4	0.04	0.09
R2-E RP U	0.29	0.38	0.04	0.11
R2-E M5P P	0.24	0.33	0.04	0.1
R2-E M5P U	0.24	0.33	0.04	0.1
AR RP P	0.3	0.47	0.04	0.09
AR RP U	0.38	0.44	0.05	0.11
AR M5P P	0.29	0.33	0.04	0.09
AR M5P U	0.27	0.29	0.04	0.09
RS 50% RP P	0.28	0.48	0.04	0.09
RS 50% RP U	0.28	0.44	0.04	0.09
RS 50% M5P P	0.28	0.43	0.04	0.09
RS 50% M5P U	0.28	0.42	0.04	0.09
RS 75% RP P	0.28	0.45	0.04	0.08
RS 75% RP U	0.29	0.41	0.04	0.08
RS 75% M5P P	0.28	0.36	0.04	0.09
RS 75% M5P U	0.27	0.35	0.04	0.09

TABLE 10: Index notation for the nonensemble methods.

1	2	3	4	5	6	7
RP	M5P	LR	kNN	SVR linear	SVR radial basis	MLP

## 5. Conclusions

In this study, extensive modeling has been presented with different data-mining techniques for the prediction of geometrical dimensions and productivity in the laser milling

of microcavities for the manufacture of drug-eluting stents. Experiments on 316L Stainless Steel have been performed to provide data for the models. The experiments vary most of the process parameters that can be changed under industrial conditions: scanning speed, laser pulse intensity, and laser pulse frequency; moreover 2 different geometries and 3 different sizes were manufactured within the experimental test to obtain informative data sets for this industrial task. Besides, a very extensive analysis and characterization of the results of the experimental test were performed to cover all the

TABLE 11: Index notation for the ensemble methods.

	BG	IB	R2-L	R2-S	R2-E	AR	RS 50%	RS 75%
RP P	8	12	16	20	24	28	32	36
RP U	9	13	17	21	25	29	33	37
M5P P	10	14	18	22	26	30	34	38
M5P U	11	15	19	23	27	31	35	39

TABLE 12: Summary table.

	Best method	Statistically equivalent
Volume	<b>26</b>	3, 4, 5, <b>6</b> , 7, 11, 14, <b>15</b> , 16, 18, 19 20, 22, 23, 27, 31, 35, 38, 39
Depth	<b>6</b>	9, 10, 11, 13, 14, <b>15</b> , 17, 18, 19, 21, 22 23, 25, 31
Width	<b>15</b>	2, <b>6</b> , 7, <b>9</b> , 10, 11, 12, 14, 18, 19, 22 23, <b>26</b> , 27, 30, 31, 39
Length	<b>26</b>	4, <b>6</b> , <b>9</b> , 12, 13, 14, <b>15</b> , 16, 17, 18, 19 22, 23, 24, 25, 27, 30, 31, 37
MRR	<b>6</b>	2, 3, 4, 5, 7, 8, <b>9</b> , 10, 11, 12, 13 14, <b>15</b> , 16, 17, 18, 19, 20, 21, 22, 23, 24 25, <b>26</b> , 27, 30, 31, 32, 33, 34, 35, 36, 38, 39
Volume error	<b>26</b>	3, 4, 5, <b>6</b> , 10, 11, <b>15</b> , 18, 19, 22, 23 27, 31, 34, 35, 36, 38, 39
Depth error	<b>6</b>	2, 10, 11, 14, <b>15</b> , 18, 19, 22, 23, <b>26</b> , 27 30, 31
Width error	<b>15</b>	6, 8, <b>9</b> , 12, 13, 14, 16, 17, 18, 19, 20 21, 22, 23, 24, 25, <b>26</b> , 27, 30, 37
Length	<b>15</b>	4, 8, <b>9</b> , 14, 16, 18, 19, 22, 23, <b>26</b> , 27 30, 31
MRR error	<b>26</b>	1, 2, 3, 4, 5, <b>6</b> , 8, <b>9</b> , 10, 11, 12 13, 14, <b>15</b> , 16, 17, 18, 19, 20, 21, 22, 23 24, 25, 27, 28, 30, 31, 32, 33, 34, 35, 36 37, 38, 39
Volume relative error	<b>26</b>	3, 4, 5, <b>6</b> , 10, 11, <b>15</b> , 18, 19, 22, 23 27, 31, 34, 35, 36, 38, 39
Depth relative error	<b>6</b>	2, 10, 11, 14, <b>15</b> , 18, 19, 22, 23, <b>26</b> , 27 30, 31
Width relative error	<b>15</b>	2, <b>6</b> , 7, <b>9</b> , 10, 11, 14, 24, 30, 31, 38, 39
Length relative error	<b>9</b>	1, 2, 8, 10, 11, 12, 13, 14, <b>15</b> , 16, 20 28, 30, 31, 32, 33, 34, 35, 36, 37, 38, 39

TABLE 13: Methods ranking.

Indexes	Methods	Number of defeats
15	IB M5P U	0
31	AR M5P U	1
6, 14, 18, 19, 22, 23	SVR radial basis, IB M5P P, R2-L M5P P, R2-L M5P U, R2-S M5P P, and R2-S M5P U	2
11, 26, 27	BG M5P U, R2-E M5P P, and R2-E M5P U	3
10, 30	BG M5P P and AR M5P P	4
9	BG RP U	5
39	RS 75% M5P U	6
2, 4, 16, 38	M5P, <i>k</i> NN, R2-L RP P, and RS 75% M5P P	7
12, 13, 35	IB RP P, IB RP U, and RS 50% M5P U	8
3, 5, 8, 17, 20, 24, 25, 34, 36	LR, SVR linear, BG RP P, R2-L RP U, R2-S RP P, R2-E RP P, R2-E RP U, RS 50% M5P P, and RS 75 % RP P	9
7, 21, 37	MLP, R2-S RP U, and RS 75% RP U	10
32, 33	RS 50% RP P and RS 50% RP U	11
1, 28	RP and AR RP P	12
29	AR RP U	14

possible optimization strategies that industry might require for DES manufacturing: from high-productivity objectives to high geometrical accuracy in just one geometrical axis. By doing so, 14 data sets were generated, each of 162 instances.

The experimental test clearly outlined that the geometry of the feature to be machined will affect the performance of the milling process. The test also shows that it is not easy to find the proper combination of process parameters to achieve the final part, which makes it clear that the laser micromilling of such geometries is a complex process to control. Therefore the use of data-mining techniques is proposed for the prediction and optimization of this process. Each variable to predict was modelled by regression methods to forecast a continuous variable.

The paper shows an exhaustive test covering 39 regression method configurations for the 14 output variables. A 10 × 10 cross-validation was used in the test to identify the methods with a relatively better RMSE. A corrected resampled *t*-test was used to estimate significant differences. The test showed that ensemble regression techniques using M5P unpruned trees gave a better performance than other well-established soft computing techniques such as ANNs and Linear Regression techniques. SVR with Radial Basis Function Kernel was also a very competitive method but required parameter tuning. We propose the use of an Iterated Bagging technique with an M5P unpruned tree as a base regressor, because its

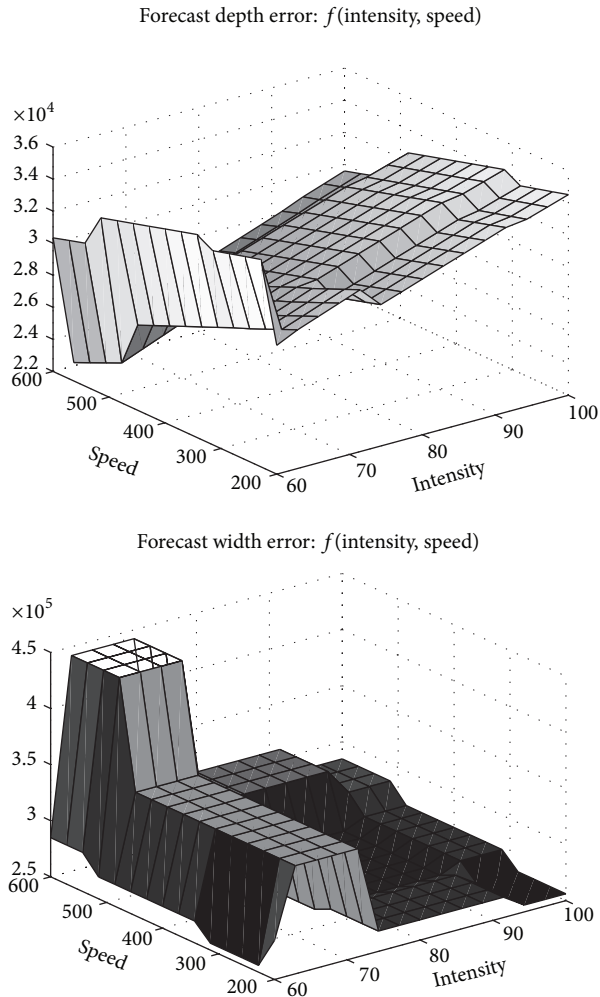


FIGURE 5: 3D plots of the predicted depth and width's errors from the Iterated Bagging ensembles.

RMSE was never significantly worse than the RMSE of any of the other methods for any of the 14 variables.

Future work will consider applying the experimental procedure to different polymers, magnesium, and other biodegradable and biocompatible elements, as well as to different geometries of industrial interest other than DES, such as microchannels. Moreover, as micromachining is a complex process where many variables play an important role in the geometrical dimensions of the machined workpiece, the application of visualization techniques, such as scatter plot matrices and start plots, to evaluate the relationships between inputs and outputs will help us towards a clearer understanding of this promising machining process at an industrial level.

### Conflict of Interests

The authors declare that there is no conflict of interests regarding the publication of this paper.

### Acknowledgments

The authors would like to express their gratitude to the GREP research group at the University of Girona and the Tecnológico de Monterrey for access to their facilities during the experiments. This work was partially funded through Grants from the IREBID Project (FP7-PEOPLE-2009-IRSES-247476) of the European Commission and Projects TIN2011-24046 and TECNIPLAD (DPI2009-09852) of the Spanish Ministry of Economy and Competitiveness.

### References

- [1] K. Sugioka, M. Meunier, and A. Piqué, *Laser Precision Microfabrication*, vol. 135, Springer, 2010.
- [2] S. Garg and P. W. Serruys, "Coronary stents: current status," *Journal of the American College of Cardiology*, vol. 56, no. 10, pp. S1-S42, 2010.
- [3] D. M. Martin and F. J. Boyle, "Drug-eluting stents for coronary artery disease: a review," *Medical Engineering and Physics*, vol. 33, no. 2, pp. 148-163, 2011.
- [4] S. Campanelli, G. Casalino, and N. Contuzzi, "Multi-objective optimization of laser milling of 5754 aluminum alloy," *Optics & Laser Technology*, vol. 52, pp. 48-56, 2013.
- [5] J. Ciurana, G. Arias, and T. Ozel, "Neural network modeling and particle swarm optimization (PSO) of process parameters in pulsed laser micromachining of hardened AISI H13 steel," *Materials and Manufacturing Processes*, vol. 24, no. 3, pp. 358-368, 2009.
- [6] J. Cheng, W. Perrie, S. P. Edwardson, E. Fearon, G. Dearden, and K. G. Watkins, "Effects of laser operating parameters on metals micromachining with ultrafast lasers," *Applied Surface Science*, vol. 256, no. 5, pp. 1514-1520, 2009.
- [7] I. E. Saklakoglu and S. Kasman, "Investigation of micro-milling process parameters for surface roughness and milling depth," *The International Journal of Advanced Manufacturing Technology*, vol. 54, no. 5-8, pp. 567-578, 2011.
- [8] D. Ashkenasi, T. Kaszemeikat, N. Mueller, R. Dietrich, H. J. Eichler, and G. Illing, "Laser trepanning for industrial applications," *Physics Procedia*, vol. 12, pp. 323-331, 2011.
- [9] B. S. Yilbas, S. S. Akhtar, and C. Karatas, "Laser trepanning of a small diameter hole in titanium alloy: temperature and stress fields," *Journal of Materials Processing Technology*, vol. 211, no. 7, pp. 1296-1304, 2011.
- [10] R. Biswas, A. S. Kuar, S. Sarkar, and S. Mitra, "A parametric study of pulsed Nd:YAG laser micro-drilling of gamma-titanium aluminide," *Optics & Laser Technology*, vol. 42, no. 1, pp. 23-31, 2010.
- [11] L. Tricarico, D. Sorgente, and L. D. Scintilla, "Experimental investigation on fiber laser cutting of Ti6Al4V thin sheet," *Advanced Materials Research*, vol. 264-265, pp. 1281-1286, 2011.
- [12] N. Muhammad, D. Whitehead, A. Boor, W. Oppenlander, Z. Liu, and L. Li, "Picosecond laser micromachining of nitinol and platinum-iridium alloy for coronary stent applications," *Applied Physics A: Materials Science and Processing*, vol. 106, no. 3, pp. 607-617, 2012.
- [13] H. Meng, J. Liao, Y. Zhou, and Q. Zhang, "Laser micro-processing of cardiovascular stent with fiber laser cutting system," *Optics & Laser Technology*, vol. 41, no. 3, pp. 300-302, 2009.

- [14] T.-C. Chen and R. B. Darling, "Laser micromachining of the materials using in microfluidics by high precision pulsed near and mid-ultraviolet Nd:YAG lasers," *Journal of Materials Processing Technology*, vol. 198, no. 1-3, pp. 248-253, 2008.
- [15] D. Bruneel, G. Matras, R. le Harzic, N. Huot, K. König, and E. Audouard, "Micromachining of metals with ultra-short Ti-Sapphire lasers: prediction and optimization of the processing time," *Optics and Lasers in Engineering*, vol. 48, no. 3, pp. 268-271, 2010.
- [16] M. Pfeiffer, A. Engel, S. Weißmantel, S. Scholze, and G. Reisse, "Microstructuring of steel and hard metal using femtosecond laser pulses," *Physics Procedia*, vol. 12, pp. 60-66, 2011.
- [17] D. Karnakis, M. Knowles, P. Petkov, T. Dobrev, and S. Dimov, "Surface integrity optimisation in ps-laser milling of advanced engineering materials," in *Proceedings of the 4th International WLT-Conference on Lasers in Manufacturing*, Munich, Germany, 2007.
- [18] H. Qi and H. Lai, "Micromachining of metals and thermal barrier coatings using a 532 nm nanosecond ber laser," *Physics Procedia*, vol. 39, pp. 603-612, 2012.
- [19] D. Teixidor, I. Ferrer, J. Ciurana, and T. Özel, "Optimization of process parameters for pulsed laser milling of micro-channels on AISI H13 tool steel," *Robotics and Computer-Integrated Manufacturing*, vol. 29, no. 1, pp. 209-219, 2013.
- [20] I. Witten and E. Frank, *Data Mining: Practical Machine Learning Tools and Techniques*, Morgan Kaufmann, 2nd edition, 2005.
- [21] J. Han, M. Kamber, and J. Pei, *Data Mining: Concepts and Techniques*, Morgan Kaufmann, 2006.
- [22] A. J. Torabi, M. J. Er, L. Xiang et al., "A survey on artificial intelligence technologies in modeling of high speed end-milling processes," in *Proceedings of the IEEE/ASME International Conference on Advanced Intelligent Mechatronics (AIM '09)*, pp. 320-325, Singapore, July 2009.
- [23] M. Chandrasekaran, M. Muralidhar, C. M. Krishna, and U. S. Dixit, "Application of soft computing techniques in machining performance prediction and optimization: a literature review," *The International Journal of Advanced Manufacturing Technology*, vol. 46, no. 5-8, pp. 445-464, 2010.
- [24] A. K. Choudhary, J. A. Harding, and M. K. Tiwari, "Data mining in manufacturing: a review based on the kind of knowledge," *Journal of Intelligent Manufacturing*, vol. 20, no. 5, pp. 501-521, 2009.
- [25] A. K. Dubey and V. Yadava, "Laser beam machining—a review," *International Journal of Machine Tools and Manufacture*, vol. 48, no. 6, pp. 609-628, 2008.
- [26] B. F. Yousef, G. K. Knopf, E. V. Bordatchev, and S. K. Nikumb, "Neural network modeling and analysis of the material removal process during laser machining," *The International Journal of Advanced Manufacturing Technology*, vol. 22, no. 1-2, pp. 41-53, 2003.
- [27] S. Campanelli, G. Casalino, A. Ludovico, and C. Bonserio, "An artificial neural network approach for the control of the laser milling process," *The International Journal of Advanced Manufacturing Technology*, vol. 66, no. 9-12, pp. 1777-1784, 2012.
- [28] C. Jimin, Y. Jianhua, Z. Shuai, Z. Tiechuan, and G. Dixin, "Parameter optimization of non-vertical laser cutting," *The International Journal of Advanced Manufacturing Technology*, vol. 33, no. 5-6, pp. 469-473, 2007.
- [29] D. Teixidor, M. Grzenda, A. Bustillo, and J. Ciurana, "Modeling pulsed laser micromachining of micro geometries using machine-learning techniques," *Journal of Intelligent Manufacturing*, 2013.
- [30] N. C. Oza and K. Tumer, "Classifier ensembles: select real-world applications," *Information Fusion*, vol. 9, no. 1, pp. 4-20, 2008.
- [31] P. Santos, L. Villa, A. Reñones, A. Bustillo, and J. Maudes, "Wind turbines fault diagnosis using ensemble classifiers," in *Advances in Data Mining. Applications and Theoretical Aspects*, vol. 7377, pp. 67-76, Springer, Berlin, Germany, 2012.
- [32] A. Bustillo and J. J. Rodríguez, "Online breakage detection of multitooth tools using classifier ensembles for imbalanced data," *International Journal of Systems Science*, pp. 1-13, 2013.
- [33] J.-F. Díez-Pastor, A. Bustillo, G. Quintana, and C. García-Osorio, "Boosting projections to improve surface roughness prediction in high-torque milling operations," *Soft Computing*, vol. 16, no. 8, pp. 1427-1437, 2012.
- [34] A. Bustillo, E. Ukar, J. J. Rodríguez, and A. Lamikiz, "Modelling of process parameters in laser polishing of steel components using ensembles of regression trees," *International Journal of Computer Integrated Manufacturing*, vol. 24, no. 8, pp. 735-747, 2011.
- [35] A. Bustillo, J.-F. Díez-Pastor, G. Quintana, and C. García-Osorio, "Avoiding neural network fine tuning by using ensemble learning: application to ball-end milling operations," *The International Journal of Advanced Manufacturing Technology*, vol. 57, no. 5-8, pp. 521-532, 2011.
- [36] S. Ferreira, B. Sierra, I. Irigoien, and E. Gorritxategi, "Data mining for quality control: burr detection in the drilling process," *Computers & Industrial Engineering*, vol. 60, no. 4, pp. 801-810, 2011.
- [37] B. E. Boser, I. M. Guyon, and V. N. Vapnik, "Training algorithm for optimal margin classifiers," in *Proceedings of the 5th Annual Workshop on Computational Learning Theory*, pp. 144-152, ACM, Pittsburgh, Pa, USA, July 1992.
- [38] R. Beale and T. Jackson, *Neural Computing: An Introduction*, IOP Publishing, Bristol, UK, 1990.
- [39] A. Sykes, *An Introduction to Regression Analysis*, Law School, University of Chicago, 1993.
- [40] X. Wu, V. Kumar, Q. J. Ross et al., "Top 10 algorithms in data mining," *Knowledge and Information Systems*, vol. 14, no. 1, pp. 1-37, 2008.
- [41] N. Tosun and L. Özler, "A study of tool life in hot machining using artificial neural networks and regression analysis method," *Journal of Materials Processing Technology*, vol. 124, no. 1-2, pp. 99-104, 2002.
- [42] A. Azadeh, S. F. Ghaderi, and S. Sohrabkhani, "Annual electricity consumption forecasting by neural network in high energy consuming industrial sectors," *Energy Conversion and Management*, vol. 49, no. 8, pp. 2272-2278, 2008.
- [43] P. Palanisamy, I. Rajendran, and S. Shanmugasundaram, "Prediction of tool wear using regression and ANN models in end-milling operation," *The International Journal of Advanced Manufacturing Technology*, vol. 37, no. 1-2, pp. 29-41, 2008.
- [44] S. Vijayakumar and S. Schaal, "Approximate nearest neighbor regression in very high dimensions," in *Nearest-Neighbor Methods in Learning and Vision: Theory and Practice*, pp. 103-142, MIT Press, Cambridge, Mass, USA, 2006.
- [45] L. Kuncheva, "Combining classifiers: soft computing solutions," in *Pattern Recognition: From Classical to Modern Approaches*, pp. 427-451, 2001.

- [46] J. Yu, L. Xi, and X. Zhou, "Identifying source (s) of out-of-control signals in multivariate manufacturing processes using selective neural network ensemble," *Engineering Applications of Artificial Intelligence*, vol. 22, no. 1, pp. 141–152, 2009.
- [47] T. W. Liao, F. Tang, J. Qu, and P. J. Blau, "Grinding wheel condition monitoring with boosted minimum distance classifiers," *Mechanical Systems and Signal Processing*, vol. 22, no. 1, pp. 217–232, 2008.
- [48] S. Cho, S. Binsaeid, and S. Asfour, "Design of multisensor fusion-based tool condition monitoring system in end milling," *The International Journal of Advanced Manufacturing Technology*, vol. 46, no. 5–8, pp. 681–694, 2010.
- [49] S. Binsaeid, S. Asfour, S. Cho, and A. Onar, "Machine ensemble approach for simultaneous detection of transient and gradual abnormalities in end milling using multisensor fusion," *Journal of Materials Processing Technology*, vol. 209, no. 10, pp. 4728–4738, 2009.
- [50] H. Akaike, "A new look at the statistical model identification," *IEEE Transactions on Automatic Control*, vol. 19, no. 6, pp. 716–723, 1974.
- [51] J. R. Quinlan, "Learning with continuous classes," in *Proceedings of the 5th Australian Joint Conference on Artificial Intelligence*, vol. 92, pp. 343–348, Singapore, 1992.
- [52] T. M. Khoshgoftaar, E. B. Allen, and J. Deng, "Using regression trees to classify fault-prone software modules," *IEEE Transactions on Reliability*, vol. 51, no. 4, pp. 455–462, 2002.
- [53] T. K. Ho, "The random subspace method for constructing decision forests," *IEEE Transactions on Pattern Analysis and Machine Intelligence*, vol. 20, no. 8, pp. 832–844, 1998.
- [54] T. G. Dietterich, "Ensemble learning," in *The Handbook of Brain Theory and Neural Networks*, pp. 405–408, 2002.
- [55] L. Breiman, "Bagging predictors," *Machine Learning*, vol. 24, no. 2, pp. 123–140, 1996.
- [56] Y. Freund and R. E. Schapire, "Experiments with a new boosting algorithm," in *Proceedings of the 13th International Conference on Machine Learning (ICML '96)*, vol. 96, pp. 148–156, Bari, Italy, 1996.
- [57] Y. Freund and R. E. Schapire, "A decision-theoretic generalization of on-line learning and an application to boosting," in *Computational Learning Theory*, pp. 23–37, Springer, Berlin, Germany, 1995.
- [58] L. Breiman, "Using iterated bagging to debias regressions," *Machine Learning*, vol. 45, no. 3, pp. 261–277, 2001.
- [59] H. Drucker, "Improving regressors using boosting techniques," in *Proceedings of the 14th International Conference on Machine Learning (ICML '97)*, vol. 97, pp. 107–115, Nashville, Tenn, USA, 1997.
- [60] J. H. Friedman, "Stochastic gradient boosting," *Computational Statistics & Data Analysis*, vol. 38, no. 4, pp. 367–378, 2002.
- [61] D. W. Aha, D. Kibler, and M. K. Albert, "Instance-based learning algorithms," *Machine Learning*, vol. 6, no. 1, pp. 37–66, 1991.
- [62] A. J. Smola and B. Schölkopf, "A tutorial on support vector regression," *Statistics and Computing*, vol. 14, no. 3, pp. 199–222, 2004.
- [63] C. Cortes and V. Vapnik, "Support-vector networks," *Machine Learning*, vol. 20, no. 3, pp. 273–297, 1995.
- [64] J. E. Dayhoff and J. M. DeLeo, "Artificial neural networks: opening the black box," *Cancer*, vol. 91, supplement 8, pp. 1615–1635, 2001.
- [65] K. Hornik, M. Stinchcombe, and H. White, "Multilayer feedforward networks are universal approximators," *Neural Networks*, vol. 2, no. 5, pp. 359–366, 1989.
- [66] W. H. Delashmit and M. T. Manry, "Recent developments in multilayer perceptron neural networks," in *Proceedings of the 7th Annual Memphis Area Engineering and Science Conference (MAESC '05)*, 2005.
- [67] C. Nadeau and Y. Bengio, "Inference for the generalization error," *Machine Learning*, vol. 52, no. 3, pp. 239–281, 2003.

## Research Article

# Lightweight Design of an Outer Tie Rod for an Electrical Vehicle

Young-Chul Park,<sup>1</sup> Seung-Kul Baek,<sup>1</sup> Bu-Kyo Seo,<sup>1</sup> Jong-Kyu Kim,<sup>2</sup> and Kwon-Hee Lee<sup>1</sup>

<sup>1</sup> Department of Mechanical Engineering, Dong-A University, Busan 604-714, Republic of Korea

<sup>2</sup> Central Corporation, Changwon 641-315, Republic of Korea

Correspondence should be addressed to Kwon-Hee Lee; [leekh@dau.ac.kr](mailto:leekh@dau.ac.kr)

Received 24 October 2013; Accepted 6 February 2014; Published 17 April 2014

Academic Editor: Olabisi Falowo

Copyright © 2014 Young-Chul Park et al. This is an open access article distributed under the Creative Commons Attribution License, which permits unrestricted use, distribution, and reproduction in any medium, provided the original work is properly cited.

The lightweight design of the outer tie rod installed on an electrical vehicle was achieved through material selection and optimization technique. The aluminum alloy Al6082M was selected as a steel-substitute, and its structural shape was optimized by applying metamodel-based optimization. In this process, finite element analysis was performed to predict the structural responses, such as buckling resistance and fatigue life. First, for an arbitrary base design made of steel, the structural responses were calculated. Then, the design variables were defined to find a lightweight design made of Al6082M. Secondly, metamodel-based optimization based on the kriging interpolation method was applied, leading to determination of an optimum design. The suggested optimum design has the minimum weight satisfying the critical design requirement. Finally, the numerical results of the buckling resistance and fatigue life were validated, through buckling and fatigue tests.

## 1. Introduction

The current trend of the structural design of automobile parts is towards lightweight design. Lightweight automobile parts can be developed by selecting steel substitutes, such as aluminum, magnesium, plastic, or composite material, applying manufacturing technology and/or adopting optimization techniques [1–3]. Lower weight requires lower energy consumption. In particular, the realization of lightweight design in electrical vehicles gives rise to an ecofriendly vehicle with high efficiency. The importance of lightweight design in the automotive industry has increased, due to the consistently tightening regulations for protecting the environment [3, 4].

There have been many cases of lightweight structural design in body and chassis parts during the past 20~30 years. Among the parts of suspension and steering systems, there have been many cases of lightweight design application for the control arm or knuckle, but there are very few cases for the outer tie rod [5]. This is because the OTR is relatively much lighter than the other parts. However, along with recent trends, car makers and parts manufacturers are interested in lightweight design of the OTR. That is why some parts are developed with their target weight predetermined in

units of gram-force during the proto-design stage [3, 5]. Furthermore, consistent lightweight design is an essential means of extending the driving range of electric vehicles [4].

In this study, a lightweight design of the OTR for an electrical vehicle is suggested, by substituting SM45C with Al6082M and applying optimization techniques, considering the buckling and durability performance. The structural responses of buckling and durability are considered in the structural design process of the outer tie rod. Usually, since the buckling is the critical performance, only the buckling is included in the optimization process. Then, after an optimum design is determined, the durability analysis is performed, to investigate whether the suggested design satisfies its criterion.

The most exact method to determine the optimum design is to utilize the sensitivity information of responses and a gradient-based algorithm, since it can provide one design satisfying the K-T necessary condition. In contrast, a metamodel-based optimization method is suitable for problems of structural design requiring much computation time, difficult computational sensitivity problems, or problems having a wavy response function, even though it cannot give the K-T point [3, 5]. The optimization problem of the OTR belongs to this category. Thus, this research

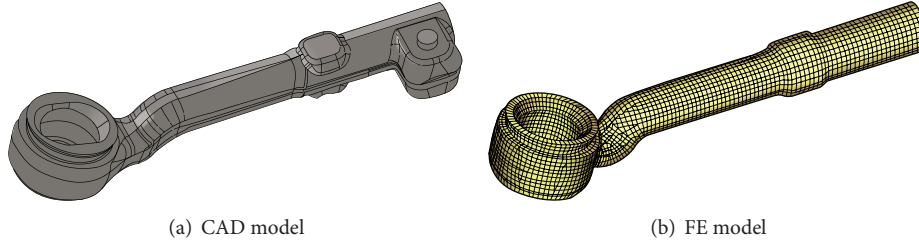


FIGURE 1: The base model of steel OTR.

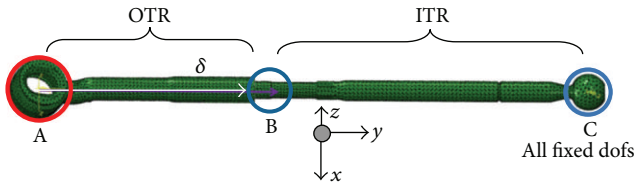


FIGURE 2: Loading condition for buckling analysis.

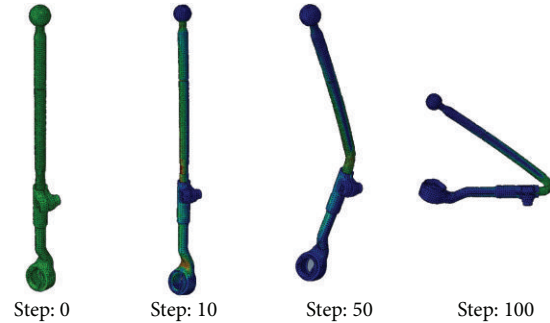


FIGURE 3: Buckling analysis result of steel OTR.

adopts metamodel-based optimization, to find an optimum design of the OTR. It is known that the kriging metamodel provides accurate predictions of highly nonlinear responses. The design process using the kriging metamodel is as follows [6, 7]. First, the DOE using Latin hypercube design is carried out, to define the design samples. Second, buckling analysis is performed for as many as the number of sample points. Third, surrogate models of the related responses are built. Thus, the responses of weight and buckling resistance force are replaced by kriging metamodels. It is easy to solve the approximated formulation, since all the responses are replaced by simple mathematical equations. Thus, it is not important to select an algorithm to solve the formulation in this step. As a final step, an optimum design is calculated, by considering formulation. Then, the fatigue life of the suggested optimum design is calculated.

For the validation of the suggested optimum design, buckling and fatigue tests were performed. The design of the OTR was done using CATIA [8], MSC. Nastran [9], and MSC. Fatigue [10] for the durability analysis and Abaqus [11] for the buckling analysis.

## 2. Base Design of the Steel OTR

The OTR is a part that belongs to the steering system changing directions, according to the motion of the steering wheel. Going from steering wheel to steering gear, pitman arm, relay rod, and ITR (inner tie rod), steering power is finally delivered to the wheel through the knuckle after passing through the OTR [5]. The ITR is attached to the OTR and is served as pivot point for the steering gear. The base design of the OTR and its structural analysis were executed for SM45C early on during this car program. However, its material was changed to Al6082M to reduce the weight more. Thus, the structural analysis of the steel OTR was investigated in the early proto-design stage.

The CAD model and FE model of the initial design are shown in Figure 1. The weight of the steel OTR without bolt and nut was about 378 g. Usually, buckling is the most critical performance in the structural design of an OTR. That is, if the constraint related to buckling is satisfied, the rest of the structural constraints lie in their allowable values. Thus, in this study, only the buckling is included in the optimization process.

The loading condition for buckling analysis is shown as Figure 2. The steel OTR is connected with the ITR at point B. Thus, the buckling analysis was performed in the combined state. The ITR was considered as a predetermined product, since the part manufacturer involved is just responsible for the design of the OTR. A load  $\delta$  is applied sequentially on point A in the  $y$  direction, by fixing all degree of freedoms of point C. At that time, the buckling resistance force can be determined. The buckling resistance force is the reaction force of point C, at the moment when the buckling is generated. The result of the buckling analysis is represented in Figure 3. The buckling resistance force of the steel OTR was obtained as 32.6 kN, which satisfies the design criterion specified by car maker A.

## 3. Structural Optimization of the Aluminum OTR

**3.1. Definition of Design Variable and Optimization Formulation.** In general, aluminum has been selected as a steel-substitute material to reduce the weight, since aluminum has almost one-third of the density of steel. In this research, aluminum called Al6082M [3, 5] developed by the part manufacturer was used to replace the steel. However,

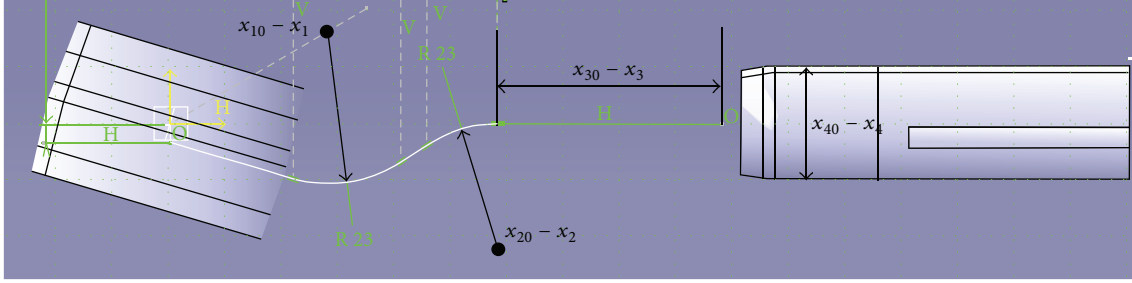


FIGURE 4: Shape design variables.

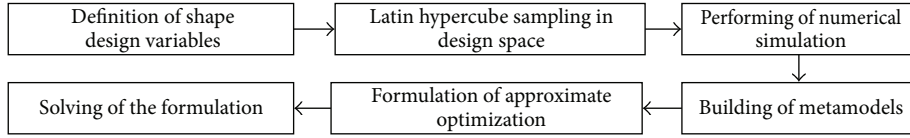


FIGURE 5: Flow chart for the structural design of Al6082M OTR.

TABLE 1: Material properties of SM45C and Al6082M.

Property	SM45C	Al6082M
Yield strength (MPa)	343	340
Tensile strength (MPa)	569	380
Young's modulus (GPa)	210	72
Density ( $\times 10^{-6}$ kg/mm <sup>3</sup> )	7.85	2.71

the strength and stiffness of aluminum have lower values than those of steel for the same structure. Thus, it is necessary to find an optimized shape of the OTR made of Al6082M. The material properties of SM45C and Al6082M are summarized in Table 1.

Based on the modified design of the steel OTR, the design variables defining its shape are represented in Figure 4. The design variables,  $x_1$  and  $x_2$ , are related to the shape of its neck, defining the radius curvatures, while the design variables,  $x_3$  and  $x_4$ , are related to the length and sectional size of the straight part. In Figure 4, the values of  $[x_{10} \ x_{20} \ x_{30} \ x_{40}]^T$  are  $[23^\circ \ 23^\circ \ 58 \text{ mm} \ 18.5 \text{ mm}]^T$ .

The optimization problem determining its optimum shape can be formulated as

$$\text{Minimize } W(\mathbf{x}) \quad (1)$$

$$\text{subject to } F_R(\mathbf{x}) \geq F_0 \quad (2)$$

$$\mathbf{x}_L \leq \mathbf{x} \leq \mathbf{x}_U, \quad (3)$$

where  $\mathbf{x} = [x_1 \ x_2 \ x_3 \ x_4]^T$ ,  $\mathbf{x}_L = [0^\circ \ 0^\circ \ 0 \text{ mm} \ 0 \text{ mm}]^T$ ,  $\mathbf{x}_U = [9.0^\circ \ 3.0^\circ \ 15.0 \text{ mm} \ 2.0 \text{ mm}]^T$ ,  $W$  is the weight of the aluminum OTR,  $F_R$  is its buckling load, and  $F_0$  is the allowable value.

Shape optimization based on the sensitivity information makes the setting of a shape variable difficult and distorts the finite elements in the optimization process [2, 3, 5, 6]. In addition, a number of nonlinear analyses are performed in an optimization process to solve (1)~(3), and the iterations

may not be terminated. Accordingly, it is more realistic that optimization is carried out by replacing the buckling load,  $F_R$  appearing in (2), with the metamodel. There are methods that generate a surrogate model, such as a response surface model, kriging, a neural network, and others. The present research utilizes the kriging metamodel, suitable for prediction of a highly nonlinear function [5, 6]. When an approximate model is used, the objective and constraint functions in (1)~(2) can be replaced as follows:

$$\text{Minimize } \hat{w}(\mathbf{x}) \quad (4)$$

$$\text{subject to } \hat{F}_R \geq F_0, \quad (5)$$

where  $\hat{\cdot}$  means the metamodel of a response.

The buckling load should be larger than the limit, 25.0 kN. However, the allowable value of  $F_0$  in (5) was set to 27.0 kN to compensate the discrepancy between numerical result and true response.

**3.2. Application of Kriging Method to the Aluminum OTR.** The flow chart for the structural design of the aluminum OTR is shown as in Figure 5 [7]. First, the DOE (design of experiments) is carried out to define the design samples. As a sampling method, the Latin hypercube design built into Matlab was utilized. In this step, the number of sample points was 50, which was determined by experience [2, 3, 5, 6]. Second, FE analysis using the Abaqus [6] was performed, with a number of sample points. The FE analysis on each row was carried out. The sample points and their responses are summarized in Table 2. Third, the kriging models of the weight and the buckling load were built. Thus, (4) and (5) could be solved by applying the GRG (generalized reduced gradient) algorithm.

In the kriging model, the global approximation model  $\hat{f}(\mathbf{x})$  for a response  $f(\mathbf{x})$  is represented as

$$\hat{f}(\mathbf{x}) = \hat{\beta} + \mathbf{r}^T(\mathbf{x}) \mathbf{R}^{-1}(\mathbf{f} - \hat{\beta}\mathbf{i}), \quad (6)$$

TABLE 2: Design of experiments using LHD.

Exp. number	$x_1$ (°)	$x_2$ (°)	$x_3$ (mm)	$x_4$ (mm)	$F_R$ (N)	$W$ (g)
1	0.2	1.8	11.1	1.5	26,083	135.1
2	5.4	2.0	1.9	0.1	26,821	143.5
3	71	1.0	5.8	0.2	28,825	143.1
4				0.8	26,380	139.0
⋮	⋮	⋮	⋮	⋮	⋮	⋮
49	3.5	2.3	14.0	0.2	26,429	136.2
50	1.4	1.8	5.3	0.9	26,961	140.0

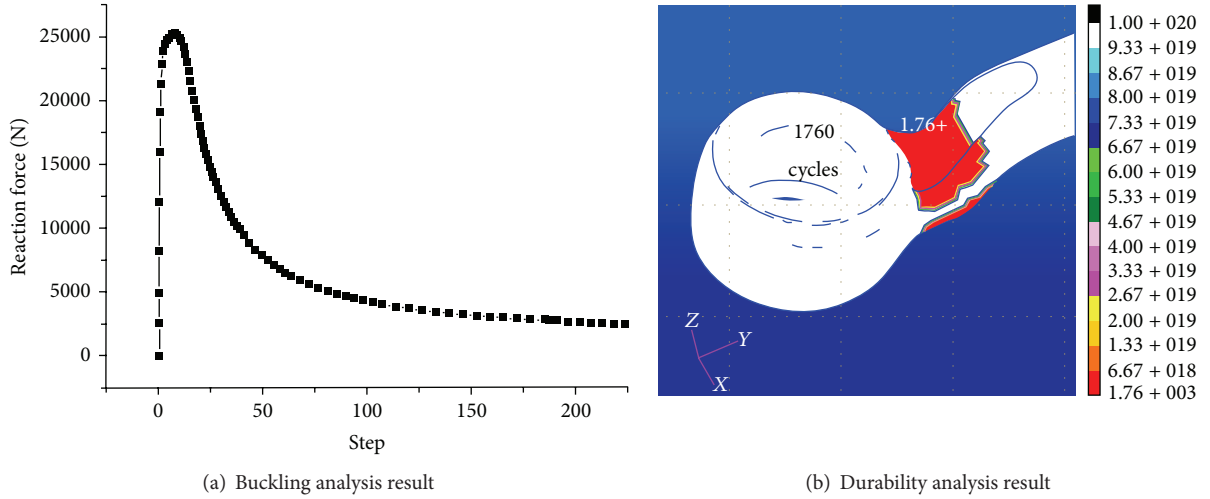


FIGURE 6: Buckling and durability analysis result of optimum Al6082M OTR.

where  $\mathbf{R}^{-1}$  is the inverse of the correlation matrix  $\mathbf{R}$ ,  $\mathbf{r}$  is the correlation vector,  $\mathbf{f}$  is the  $n_s$  observed data vector, and  $\mathbf{i}$  is the unit vector. The correlation matrix and correlation vector are defined as

$$R(\mathbf{x}^j, \mathbf{x}^k) = \text{Exp} \left[ - \sum_{i=1}^n \theta_i |x_i^j - x_i^k|^2 \right],$$

$$(j = 1, \dots, n_s, k = 1, \dots, n_s), \quad (7)$$

$$\mathbf{r}(\mathbf{x}) = [\mathbf{R}(\mathbf{x}, \mathbf{x}^{(1)}), \mathbf{R}(\mathbf{x}, \mathbf{x}^{(2)}), \dots, \mathbf{R}(\mathbf{x}, \mathbf{x}^{(n_s)})]^T,$$

where the number of observed data is 50, and the number of design variables is 4 in this study.

The unknown parameters  $\theta_1, \theta_2, \dots, \theta_n$  are obtained from the following equation:

$$\text{maximize} - \frac{[n_s \ln(\hat{\sigma}^2) + \ln |\mathbf{R}|]}{2}, \quad (8)$$

where  $\theta_i$  ( $i = 1, 2, \dots, n$ )  $> 0$ . To solve (8), the GRG algorithm built into EXCEL was utilized. The Kriging interpolation method is well explained in [2, 3, 12–14].

**3.3. Optimum Design Result and Durability Analysis.** This research utilized an in-house program [3] to solve the

optimization problem defined in (3)~(5). The optimizer of the in-house program is the GRG method, which is an optimization algorithm built into the EXCEL program. The optimum parameters were investigated by changing more than 10 initial values. Then, the metamodels were built, by setting the weight and reaction force as response values.

For the kriging models of weight and buckling load, their optimum parameters are summarized in Table 3. These optimal parameters were used to find the optimum design of (3)~(5), and as a result,  $[x_1^* x_2^* x_3^* x_4^*]^T = [4.24^\circ 2.39^\circ 11.29 \text{ mm } 1.86 \text{ mm}]^T$  was found, and the approximate weight and the approximate buckling load at the optimal solution were, respectively, 130.7 g and 27,205 N. The true weight of the optimum design was 131.0 g. The buckling analysis result represented as a force-displacement curve is shown in Figure 6(a). The true buckling load of the optimum design was calculated as 28,024 N.

For the suggested optimum design, durability analysis for the unit of OTR was performed, to investigate the design requirement imposed on the OTR. The loading condition applying an equivalent load is represented as a sine curve. The loading condition and design criterion were supplied by car maker A. The fatigue life calculated from MSC Fatigue is shown in Figure 6(b). The fatigue life of the suggested optimum design was determined as 1,760 cycles, which satisfies the design requirement specified by car maker A.

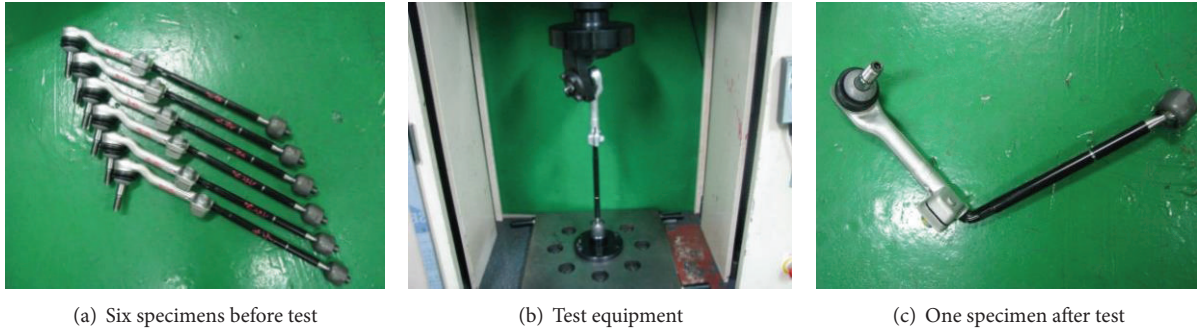


FIGURE 7: Buckling test result.

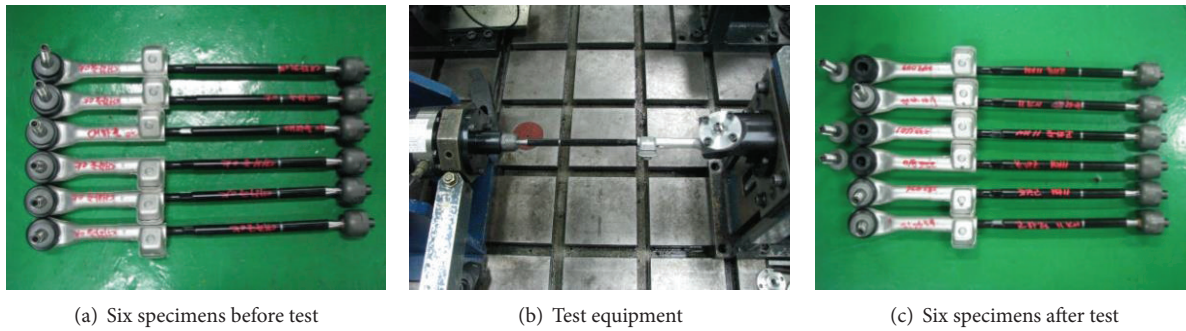


FIGURE 8: Fatigue test result.

TABLE 3: Optimal parameters of kriging models.

Response	$\beta$	$\theta_1$	$\theta_2$	$\theta_3$	$\theta_4$
$W$	138.6 kg <sub>r</sub>	0.004	20.54	4.74	10.33
$F_R$	27,690 N	0.001	5.07	18.90	50.00

**3.4. Buckling and Fatigue Tests.** Based on the suggested optimum design, twelve specimens were made to validate the buckling and durability performance. For the buckling test, six specimens of the OTR connected with the ITR are shown in Figure 7(a). The test equipment is shown in Figure 7(b), in which the loading and boundary conditions are the same as those of the buckling analysis. As a result, the buckling loads were between 25,900~27,550 N, and all of them satisfy the criterion. Comparing the average value obtained from six buckling loads, the simulation result has a relatively small error, of about 5%. One specimen after the buckling test is shown in Figure 7(c).

For the durability test, six other specimens were prepared, as shown in Figure 8(a). The test equipment for the durability was set up as shown in Figure 8(b). Through the test, their fatigue lives were between 249,049 cycles and 312,659 cycles. Those results satisfy the requirement set by car maker A. It is found that the test results of the buckling and durability are consistent with those of the simulations.

## 4. Conclusions

The present research suggested an optimum design of Al6082M OTR, which is one of the parts of the steering

system of an electrical vehicle. The following conclusions can be made from this study.

- (1) The present research has succeeded in the development of a lightweight OTR, by replacing the current OTR, whose initial model was made of steel, with an Al6082M OTR, and applying the optimization technique. The metamodel-based optimization technique provides a realistic optimum, even though it cannot be considered as an exact solution. The weight of the suggested optimum design is 131.0 g, which is 65.3% lighter weight than the initial steel model.
- (2) It is proven that the design requirements related to the buckling and durability performance were satisfied through the tests. For the buckling test, six specimens were used, and their buckling loads were between 25,900~27,550 N. In the case of the durability test, all the fatigue lives of the six specimens exceeded the allowable cycle.

## Conflict of Interests

The authors declare that there is no conflict of interests regarding the publication of this paper.

## Acknowledgments

This research was financially supported by the Ministry of Education Science and Technology (MEST) and the National Research Foundation of Korea (NRF), through

the Human Resource Training Project for Regional Innovation (2012H1B8A2026078).

## References

- [1] Porsche Engineering Services Inc., “The design, materials, manufacturing, structural performance and economic analysis of the ultra light steel auto closures program,” Engineering Report, 2000.
- [2] K. H. Lee and D. H. Kang, “Structural optimization of an automotive door using the kriging interpolation method,” *Proceedings of the Institution of Mechanical Engineers D: Journal of Automobile Engineering*, vol. 221, no. 12, pp. 1525–1534, 2007.
- [3] B. C. Song, Y. C. Park, S. W. Kang, and K. H. Lee, “Structural optimization of an upper control arm, considering the strength,” *Proceedings of the Institution of Mechanical Engineers D: Journal of Automobile Engineering*, vol. 223, no. 6, pp. 727–735, 2009.
- [4] T. Bein, “Advanced design for electric cars,” 2013, <http://www.emrs-strasbourg.com/files/FALL%202011/t.bein.pdf>.
- [5] J. K. Kim, Y. J. Kim, W. H. Yang, Y. C. Park, and K.-H. Lee, “Structural design of an outer tie rod for a passenger car,” *International Journal of Automotive Technology*, vol. 12, no. 3, pp. 375–381, 2011.
- [6] B. K. Seo, S. K. Baek, Y. C. Park, and K. H. Lee, “Structural optimization of outer tie rod for electrical vehicle,” in *Proceedings of the International Symposium on Green Manufacturing and Applications*, Honolulu, Hawaii, USA, June 2013.
- [7] K. H. Lee and J. I. Heo, “Metamodel-based optimum design examples of structures,” in *Handbook of Research on Novel Soft Computing Intelligent Algorithms: Theory and Practical Applications*, pp. 667–676, IGI Global.
- [8] 2013, <http://www.3ds.com/productsservices/catia>.
- [9] MSC Software, *Linear Static Analysis User's Guide: MSC Nastran*, 2012.
- [10] MSC Software, *MSC.fatigue version 2007 r2 user manual*, 2008.
- [11] Dassault Systèmes Simulia Software Corporation, *ABAQUS 6.8.1 Documentation*, Providence, RI, USA, 2008.
- [12] J. Sacks, W. J. Welch, T. J. Mitchell, and H. P. Wynn, “Design and analysis of computer experiments,” *Statistical Science*, vol. 4, no. 4, pp. 409–435, 1989.
- [13] A. Guinta and L. Watson, “A comparison of approximation modeling techniques: polynomial versus interpolating models,” in *Proceedings of the 7th AIAA/USAF/NASA/ISSMO Symposium on Multidisciplinary Analysis and Optimization*, vol. 2, pp. 392–440, AIAA, St. Louis, Mo, USA.
- [14] K. T. Fang, R. Li, and A. Sudjianto, *Design and Modeling for Computer Experiments*, Chapman & Hall/CRC, London, UK, 2006.

## Research Article

# Metaheuristic Algorithm for Solving Biobjective Possibility Planning Model of Location-Allocation in Disaster Relief Logistics

**Farnaz Barzinpour, Mohsen Saffarian, Ahmad Makoui, and Ebrahim Teimoury**

*Department of Industrial Engineering, Iran University of Science and Technology, Tehran 1684613114, Iran*

Correspondence should be addressed to Mohsen Saffarian; [mo.saffarian@iust.ac.ir](mailto:mo.saffarian@iust.ac.ir)

Received 20 October 2013; Revised 3 January 2014; Accepted 21 January 2014; Published 17 April 2014

Academic Editor: Adewumi Aderemi Oluyinka

Copyright © 2014 Farnaz Barzinpour et al. This is an open access article distributed under the Creative Commons Attribution License, which permits unrestricted use, distribution, and reproduction in any medium, provided the original work is properly cited.

Thousands of victims and millions of affected people are hurt by natural disasters every year. Therefore, it is essential to prepare proper response programs that consider early activities of disaster management. In this paper, a multiobjective model for distribution centers which are located and allocated periodically to the damaged areas in order to distribute relief commodities is offered. The main objectives of this model are minimizing the total costs and maximizing the least rate of the satisfaction in the sense of being fair while distributing the items. The model simultaneously determines the location of relief distribution centers and the allocation of affected areas to relief distribution centers. Furthermore, an efficient solution approach based on genetic algorithm has been developed in order to solve the proposed mathematical model. The results of genetic algorithm are compared with the results provided by simulated annealing algorithm and LINGO software. The computational results show that the proposed genetic algorithm provides relatively good solutions in a reasonable time.

## 1. Introduction

It is inevitable to have an integrated scientific system for crisis' logistics management with clearly defined functions and duties. Optimizing logistics and relief chain can affect issues such as relief logistics management [1]. Logistics can create greater coordination for delivering relief commodities while accelerating the delivery speed and reducing the response time [2, 3]. One of the logistics subproblems with strategic roles in a critical situation is to locate the depots and their supply savings [2]. In the depot locating, factors such as cost, response time, and justice in distribution have to be considered in preparedness phase [4]. Although researches in facilities location problems have been widely done both theoretically and practically, the problems have not been used in humanitarian logistics [2].

The application of operation research in disaster management programs has been one of the main issues in recent decades. Supply chain and logistics management are recently being used as analytical tools and techniques to provide

efficient and effective relief to people who need help in devastated areas with optimized functions and activities. Thus, emergency logistics management has been emerged as a worldwide noticeable theme as disasters may occur anytime around the world with enormous consequences. The aim of response to disasters in humanitarian relief chains is to provide a quick relief to the affected areas in order to minimize the death and pain of people. Proper design and operation of a relief chain are an essential element to achieve an effective and efficient response, but, only in recent years, humanitarian organizations have paid attention to its importance [5].

In urban areas, earthquakes can cause serious damage to inhabitation and force people to leave their homes. Therefore, at the preparation planning phase of disaster management, municipal authorities should consider emergency shelters, proper equipment, and supplies for the affected people in order to reduce the number of casualties and people's sufferings and bring relief to survivors [5].

The number and location of the facilities and distribution centers decrease the response time and the operation costs in relief chain. Therefore, Location-Allocation is an important issue in this process. Some of the applications of these locations in the relief logistics problem are listed as follows:

- (i) the location of critical management centers in the city or province and the allocation of emergency commodities such as water, food packages, and tents from these centers to damaged areas,
- (ii) Red Crescent depots' locating and these depots allocation to damaged cities and provinces in the situation of facing natural crisis or even war,
- (iii) locating ambulance centers inside and between the cities and provinces.

Actually in crisis management, we deal with locating process already in preparedness and response phase. Locating process and facility capacity determination are the two main topics in the disaster management, and a few researches have been focusing on this subject [6].

Barbarosoğlu and Arda [7] modeled the transportation planning in earthquake response by a scenario-based two stage stochastic programming over a multicommodity and multimodal network flow with uncertainty in demand, supply, and route capacities. The inclusion of uncertainties is an important advance in the analysis, but the focus is still postdisaster response. They did not consider the location of facilities or the inventory decisions in their model. Akkihal [8] has proposed a model for crisis management-center location in order to manage relief items. Tzeng et al. [9] have presented a certain multicriteria model in order to distribute relief commodities to damaged areas considering costs, response time, and damaged people satisfaction and solved it by fuzzy multiobjective programming. Jia et al. [10] presented an incapacitated facility location model to locate emergency service facilities in the event of a large-scale emergency.

Balcik and Beamon [2] considered the facility location problem for humanitarian relief chains in order to respond to quick onset disasters. Their proposed model aimed to locate and determine the situation and the number of distribution centers in relief network and the number of stored commodities in order to meet the demand of affected people.

Beraldi and Bruni [11] also offered a probable model to have a relief facility to optimize locating in an uncertain environment. Mete and Zabinsky [12] introduced a stochastic optimization model for disaster preparedness and response under demand/cost uncertainty in order to assist deciding on the location and allocation of medical supplies which are used during emergencies. They also offered a mixed-integer programming transportation model that is potentially useful in routing decisions during the response phase. Rawls and Turnquist [13] developed a two-stage, stochastic, mixed-integer program that determined the locations and quantities of various types of emergency commodities; their model also

contained the transportation network availability following a disaster under demand/cost uncertainty.

Moreover, Jabal-Ameli et al. [14] presented a location and distribution model and solved it by fuzzy methods. Duran et al. [15] studied inventory and location model and offered a mathematical model which investigates the effect of location on the average response time. Zeng and Wu [16] considered location and routing in relief situation in two steps. It means that they first solved the location problem and directly solved the routing problem in a way to minimize total costs and then they utilized a two-step heuristic algorithm to solve it.

Bozorgi-Amiri et al. [17] considered an uncertain model for relief logistics. They suggested that some prepositioned relief items might be destroyed after disasters based on this idea; they developed a robust multiobjective approach to their uncertain location problem and solved it for a real case study in Iran. Bozorgi-Amiri et al. [18] investigated uncertainty in many parameters of a relief operation like demand, supply, and operational costs associated with it. Location of relief centers and allocation of affected areas to these centers can be determined in situation described in their model. Yazdian and Shahanaghi [19] presented a multiobjective possibility programming approach for locating distribution centers and allocating customers' demands in supply chains.

In 2011, Barzinpour and Esmaeili [5] developed a multiobjective MILP model for a two-echelon relief chain in order to maximize coverage of urban populations and minimize logistics costs. Tancrez et al. [20] considered inventory-location problem for three-level supply chain in which distribution decisions of distribution centers, allocation, and number of the transported commodities were made altogether.

In 2012, Schmid [21] offered a probability model for relocation problem and dynamic distribution and solved it by dynamic programming. Chrétienne et al. [22] suggested location and dispatching problem which included minimizing setup and availability costs and then solved it through branch and cut algorithm. Toro-Diaz et al. [23] offered a mathematical model for location and distribution problem and solved it through genetic algorithm. In 2012, Guillermo Cabrera et al. [24] presented a hybrid approach using an artificial bee algorithm with mixed-integer programming applied to a large-scale capacitated facility location problem. Murali et al. [25] considered a facility location problem to determine the points in a city where medicine should be handed out to the population. They consider locating capacitated facilities in order to maximize the coverage, considering a distance-dependent coverage function.

In 2013, Xi et al. [26] developed a modified  $p$ -median problem model that accounts for rescue time limitations. A variable neighborhood search- (VNS-) based algorithm is developed for the model considered. Gharegozloo Hamedani et al. [27] studied a multiobjective location problem in a three-level supply chain network under uncertain environment, considering inventory decisions. The proposed model presents a robust optimization model, which specifies locations of distribution centers to be opened, inventory control parameters, and allocation of supply chain components, concurrently.

Abounacer et al. [28] proposed a three-objective location-transportation problem for disaster response. The location problem aims at determining the number, the position, and the mission of required humanitarian aid distribution centers (HADC) within the disaster region. Three conflicting objectives are considered. The first objective minimizes the total transportation duration of needed products from the distribution centers to the demand points. The second objective minimizes the number of agents (first-aiders) required to open and operate the selected distribution centers. The third objective minimizes the noncovered demand for all demand points within the affected area. They proposed an epsilon-constraint method for this problem. Esmaili and Barzinpour [29] based on a real world case study for a municipal district in Tehran developed a multiobjective mathematical model for the location-distribution problem.

Most of the researches in location and distribution of relief logistics are dependent on preparedness phase on the basis of predicting programming conditions. Now, the question is whether the same criterion in preparedness phase can be operation criterion or, based on the new conditions and available information, new programs should be suggested. Usually after any casualty, in the first 72 hours, based on the available commodities in the distribution centers, services are offered. Therefore, it would be possible to program for damaged areas during that time based on the received information. In this paper, the goal is to present a model to locate distribution centers periodically and to consider good distribution manner toward damaged areas.

This paper focuses on the logistics aspect of the response phase and more precisely on two important related problems: location and allocation. The location problem aims at designing a network for distributing humanitarian aids (e.g., water, food, medical commodities, and survival equipment). It mainly consists of determining the position and the mission of required humanitarian aid distribution centers (HADC) within the disaster region. The allocation problem deals with the distribution of humanitarian aid from HADCs to demand points. When both problems are solved simultaneously, we discuss a location-allocation problem. Based on this particular context, this paper has provided a biobjective location-allocation problem. The first objective is to minimize the total costs. The second objective is to maximize the covered demand for all demand points.

We propose a genetic algorithm and a simulated annealing algorithm to biobjective location-allocation problem addressed.

## 2. Problem Definition and Model Assumptions

A two-level system including distributors and damaged areas is considered. There are regions as candidate regions to establish distribution centers in this system. And also the number of commodities in distribution centers and demands of damaged areas in different periods are available. Our goal is to determine active distribution centers and their distribution manner in different periods. Location and allocation have to be done so that total costs become minimized and commodities have to be distributed in a fair manner.

### 2.1. Model Assumptions

- (i) The inventories of distribution centers in different periods are available in the form of triangular fuzzy numbers.
- (ii) The damaged area requests in different periods are available in the form of triangular fuzzy numbers.
- (iii) The maximum number of distribution centers that can be active in each period is determined.
- (iv) Some types of relief commodities are available.
- (v) It is possible to transfer inventories from one period to the next one.
- (vi) Unsatisfied request does not transfer from one period to the next one.

### 2.2. Model Indexes

- $I_t$ : set of distribution centers in period  $t$ ,
- $J_t$ : set of damaged areas in period  $t$ ,
- $C$ : set of relief commodities,
- $i$ : indexes related to distribution centers,
- $j$ : indexes related to damaged area,
- $c$ : indexes related to relief commodities.

### 2.3. Model Parameters

- $\tilde{q}_{it}$ : setup cost of distribution center  $i$  in period  $t$  that is a triangular fuzzy number,
- $p_t$ : the maximum number of distribution centers that can be active in period  $t$ ,
- $\tilde{c}_{cijt}$ : transporting cost of  $c$  commodity unit between distribution center  $i$  and damaged area  $j$  in period  $t$  that is a triangular fuzzy number,
- $\tilde{c}1_{cijt}$ : transporting cost of  $c$  commodity unit between distribution center  $i$  and distribution center  $j$  in period  $t$  that is a triangular fuzzy number,
- $\tilde{inv}_{cit}$ : the number of commodities  $c$  in distribution center  $i$  in period  $t$  that is a triangular fuzzy number,
- $\tilde{d}_{cjt}$ : the number demand commodities  $c$  in damaged area  $j$  in period  $t$  that is a triangular fuzzy number,
- $\beta_c$ : penalty costs for the shortage of good  $c$ ,
- $Mbig$ : a big number.

### 2.4. Decision Variables

- $x_{cijt}$ : number of commodities  $c$  that can be delivered in period  $t$  from distribution center  $i$  to damaged area  $j$ ,
- $x1_{cijt}$ : binary variable, it is 1 if commodity  $c$  transfers from distribution center  $i$  to distribution center  $j$  in period  $t$ ; otherwise, it is 0,

$y_{it}$ : binary variable, it is 1 if distribution center  $i$  becomes active in period  $t$ ; otherwise, it is 0,

$\text{inv}1_{cit}$ : amount of transferred supply of commodity  $c$  in period  $t$  to period  $t + 1$  in distribution center  $i$ .

2.5. *The Proposed Mathematical Model.* Consider

$$\min f_1 = \sum_{c \in C} \sum_{t \in T} \sum_{i \in I_t} \sum_{j \in J_t} \bar{c}c_{cijt} x_{cijt} + \sum_{t \in T} \sum_{i \in I_t} \max \left( 0, y_{it} - \sum_{k=1}^{t-1} y_{ik} \right) \bar{q}_{it} \quad (1)$$

$$+ \sum_{t \in T} \sum_{c \in C} \sum_{j \in J_t} \beta_c \left( \bar{d}_{cjt} - \sum_{i \in I_t} x_{cijt} \right) + \sum_{c \in C} \sum_{t \in T} \sum_{i \in I_t} \sum_{j \in J_t} \bar{c}c1_{cijt} \widetilde{\text{inv}}_{cit} x1_{cijt}, \quad (2)$$

$$\max f_2 = \sum_{t \in T} \sum_{c \in C} \sum_{j \in J_t} \min \frac{\sum_{i \in I_t} x_{cijt}}{\bar{d}_{cjt}}, \quad (2)$$

$$\sum_{i \in I_t} y_{it} \leq p_t, \quad \forall t \in T, \quad (3)$$

$$\sum_{c \in C} \sum_{j \in J_t} x_{cijt} + \sum_{c \in C} \sum_{j \in J_t} x1_{cijt} \leq M \text{big} y_{it}, \quad \forall t \in T, i \in I_t, \quad (4)$$

$$\text{inv}1_{cit} = \widetilde{\text{inv}}_{cit} + \text{inv}1_{ci(t-1)} y_{i(t-1)} + \sum_{j \in J_t} \widetilde{\text{inv}}_{cjt} x1_{cijt} - \sum_{j \in J_t} x_{cijt}, \quad \forall t \in T, c \in C, i \in I_t, \quad (5)$$

$$\sum_{i \in I_t} x_{cijt} \leq \bar{d}_{cjt}, \quad \forall t \in T, c \in C, j \in J_t, \quad (6)$$

$$\sum_{c \in C} \sum_{j \in J_t} x1_{cijt} = 1, \quad \forall t \in T, i \in I_t \quad (7)$$

$$x_{cijt} \in \text{Integer}, \quad \forall t \in T, c \in C, i \in I_t, j \in J_t, \quad (8)$$

$$x1_{cijt} \in \{0, 1\}, \quad \forall t \in T, c \in C, i \in I_t, j \in J_t, \quad (9)$$

$$y_{it} \in \{0, 1\}, \quad \forall t \in T, i \in I_t, \quad (10)$$

$$\text{inv}1_{cit} \in \text{Integer}, \quad \forall t \in T, c \in C, i \in I_t. \quad (11)$$

There are two objective functions in the above model.

*Objective 1.* It aims at minimizing total transportation costs between distribution centers and damaged areas and also minimizing setup costs and penalty costs for the shortage of goods.

*Objective 2.* It aims at maximizing damaged area satisfaction through maximizing satisfied requests of damaged areas.

Constraint (3) indicates the number of distribution centers that can be active. Constraint (4) shows that it will be

possible to send goods from one distribution center to a damaged area if that center becomes active in that period. Constraint (5) shows the way in which it will be possible to calculate transported inventories from one period to the next period. Constraint (6) indicates that the number of received commodities to one damaged area should not be more than its demand. Constraint (7) shows that it will be possible to send goods from one distribution center to another distribution center if that destination center becomes active in that period. Constraints (8)–(11) express the nature of decision variables used in the model.

2.6. *Linearization of the Proposed Model.* The second objective function is nonlinear term. To make it linear, we act as follows:

$$\max f_2 = \sum_{t \in T} \sum_{c \in C} k_{tc}, \quad (12)$$

$$k_{tc} \leq \frac{\sum_{i \in I_t} x_{cijt}}{\bar{d}_{cjt}}, \quad \forall t \in T, c \in C, j \in J_t.$$

In constraint (5),  $\text{inv}1_{ci(t-1)} y_{i(t-1)}$  is nonlinear. So, for linearization, it can be replaced with  $\text{inv}y_{ci(t-1)}$  and three constraints are added to models as follows:

$$\text{inv}y_{ci(t-1)} \leq \text{inv}1_{ci(t-1)}, \quad \forall t \in T, c \in C, i \in I_t,$$

$$\text{inv}y_{ci(t-1)} \leq M \text{big} y_{i(t-1)}, \quad \forall t \in T, c \in C, i \in I_t,$$

$$\text{inv}y_{ci(t-1)} \geq \text{inv}1_{ci(t-1)} - M \text{big} (1 - y_{i(t-1)}), \quad (13)$$

$$\forall t \in T, c \in C, i \in I_t,$$

$$\text{inv}y_{cit} \in \text{Integer}, \quad \forall t \in T, c \in C, i \in I_t.$$

2.7. *Multipurpose Linear Programming Approach.* Considering the following multiobjective model, using Zimmerman method, this problem can be changed into a single objective linear programming model using max-min operator [14, 30]:

$$\max Z = [c_1 x, c_2 x, \dots, c_l x]^T,$$

$$\min W = [d_1 x, d_2 x, \dots, d_r x]^T, \quad (14)$$

$$\text{s.t. } Ax \leq B; \quad x \geq 0.$$

Membership functions for objective functions are defined as follows:

$$\mu_k(z_k) = \frac{z_k(x) - z_k^{\text{pis}}}{z_k^{\text{pis}} - z_k^{\text{nis}}}, \quad k = \{1, 2, \dots, l\}, \quad (15)$$

$$\mu_s(w_s) = \frac{w_s^{\text{nis}} - w_s(x)}{w_s^{\text{nis}} - w_s^{\text{pis}}}, \quad s = \{1, 2, \dots, r\}.$$

In the above equations,  $w_s^{\text{pis}}, z_k^{\text{pis}}$  are positive ideal solutions and  $w_s^{\text{nis}}, z_k^{\text{nis}}$  are negative ideal solutions. Now, by max-min operator and satisfied degree, the multiobjective linear

programming problem has been written as a single-objective programming problem

$$\begin{aligned}
 & \max \quad \lambda \\
 \text{s.t.} \quad & \lambda \leq \frac{z_k(x) - z_k^{\text{nis}}}{z_k^{\text{pis}} - z_k^{\text{nis}}}, \quad k = 1 \dots l \\
 & \lambda \leq \frac{w_s^{\text{nis}} - w_s(x)}{w_s^{\text{nis}} - w_s^{\text{pis}}}, \quad s = 1 \dots r \\
 & Ax \leq B; \quad x \geq 0.
 \end{aligned} \tag{16}$$

2.8. Solving Proposed Model. The first objective function of the proposed model is a function with triangular fuzzy coefficient. Therefore, we can change it to 3 objective functions as follows:

$$\begin{aligned}
 \min f_{11} = & \sum_{c \in C} \sum_{t \in T} \sum_{i \in I_t} \sum_{j \in J_t} (cc_{cijt}^u - cc_{cijt}^m) x_{cijt} \\
 & + \sum_{t \in T} \sum_{i \in I_t} \max \left( 0, y_{it} - \sum_{k=1}^{t-1} y_{ik} \right) (q_{it}^u - q_{it}^m) \\
 & + \sum_{t \in T} \sum_{c \in C} \sum_{j \in J_t} \beta_c \left[ (d_{cjt}^u - d_{cjt}^m) - \sum_{i \in I_t} x_{cijt} \right] \\
 & + \sum_{c \in C} \sum_{t \in T} \sum_{i \in I_t} \sum_{j \in J_t} (cc1_{cijt}^u - cc1_{cijt}^m) \\
 & \quad \times (\text{inv}_{cit}^u - \text{inv}_{cit}^m) x1_{cijt}, \\
 \min f_{12} = & \sum_{c \in C} \sum_{t \in T} \sum_{i \in I_t} \sum_{j \in J_t} cc_{cijt}^m x_{cijt} \\
 & + \sum_{t \in T} \sum_{i \in I_t} \max \left( 0, y_{it} - \sum_{k=1}^{t-1} y_{ik} \right) q_{it}^m \\
 & + \sum_{t \in T} \sum_{c \in C} \sum_{j \in J_t} \beta_c \left( d_{cjt}^m - \sum_{i \in I_t} x_{cijt} \right) \\
 & + \sum_{c \in C} \sum_{t \in T} \sum_{i \in I_t} \sum_{j \in J_t} cc1_{cijt}^m \text{inv}_{cit}^m x1_{cijt}, \\
 \max f_{13} = & \sum_{c \in C} \sum_{t \in T} \sum_{i \in I_t} \sum_{j \in J_t} (cc_{cijt}^m - cc_{cijt}^l) x_{cijt} \\
 & + \sum_{t \in T} \sum_{i \in I_t} \max \left( 0, y_{it} - \sum_{k=1}^{t-1} y_{ik} \right) (q_{it}^m - q_{it}^l) \\
 & + \sum_{t \in T} \sum_{c \in C} \sum_{j \in J_t} \beta_c \left[ (d_{cjt}^m - d_{cjt}^l) - \sum_{i \in I_t} x_{cijt} \right] \\
 & + \sum_{c \in C} \sum_{t \in T} \sum_{i \in I_t} \sum_{j \in J_t} (cc1_{cijt}^m - cc1_{cijt}^l) \\
 & \quad \times (\text{inv}_{cit}^m - \text{inv}_{cit}^l) x1_{cijt}.
 \end{aligned} \tag{17}$$

There are three fuzzy constraints in the presented model. Therefore, we can change it to 3 certain constraints as follows [10]:

$$\begin{aligned}
 k_{tc} \leq & \frac{\sum_{i \in I_t} x_{cijt}}{\left( (d_{cjt}^u - d_{cjt}^l) + (d_{cjt}^m - d_{cjt}^l) \right) / 3 + d_{cjt}^l}, \\
 & \forall t \in T, \quad c \in C, \quad j \in J_t, \\
 \text{inv}1_{cit} = & \frac{(\text{inv}_{cit}^u - \text{inv}_{cit}^l) + (\text{inv}_{cit}^m - \text{inv}_{cit}^l)}{3} \\
 & + \text{inv}_{cit}^l + \text{inv}1_{ci(t-1)} y_{i(t-1)} \\
 & + \sum_{j \in J_t} \left[ \frac{(\text{inv}_{cjt}^u - \text{inv}_{cjt}^l) + (\text{inv}_{cjt}^m - \text{inv}_{cjt}^l)}{3} + \text{inv}_{cjt}^l \right] x1_{cijt} \\
 & - \sum_{j \in J_t} x_{cijt}, \quad \forall t \in T, \quad c \in C, \quad i \in I_t, \\
 \sum_{i \in I_t} x_{cijt} \leq & \frac{(d_{cjt}^u - d_{cjt}^l) + (d_{cjt}^m - d_{cjt}^l)}{3} + d_{cjt}^l, \\
 & \forall t \in T, \quad c \in C, \quad j \in J_t.
 \end{aligned} \tag{18}$$

Now, a certain linear multiobjective model can be achieved as follows:

MOLP:

$$\begin{aligned}
 \text{Min} \quad & Z = [f_{11}, f_{12}] \\
 \text{Max} \quad & W = [f_{13}, f_2] \\
 \text{S.t.} \quad & (3), (4), (7), (8), (9), (10), \\
 & (11), (13), (18).
 \end{aligned} \tag{19}$$

To solve this linear multiobjective model through Zimmermann fuzzy sets (15), membership functions are defined as follows for the objective functions of the problem [30]:

$$\begin{aligned}
 \mu_{f_{11}} = & \begin{cases} 1 & f_{11} \leq f_{11}^{\text{pis}} \\ \frac{f_{11}^{\text{nis}} - f_{11}}{f_{11}^{\text{nis}} - f_{11}^{\text{pis}}} & f_{11}^{\text{pis}} \leq f_{11} \leq f_{11}^{\text{nis}} \\ 0 & f_{11} \geq f_{11}^{\text{nis}} \end{cases} \\
 \mu_{f_2} = & \begin{cases} 1 & f_2 \geq f_2^{\text{pis}} \\ \frac{f_2 - f_2^{\text{nis}}}{f_2^{\text{pis}} - f_2^{\text{nis}}} & f_2^{\text{nis}} \leq f_2 \leq f_2^{\text{pis}} \\ 0 & f_2 \leq f_2^{\text{nis}} \end{cases}
 \end{aligned} \tag{20}$$

To calculate  $\mu_{f_{12}}$  and  $\mu_{f_{13}}$ , a procedure the same as that of  $\mu_{f_{11}}$  and  $\mu_{f_2}$  would be followed respectively. Now, we use

the following equations to obtain an ideal positive value (pis) and a negative value (nis):

$$\begin{aligned}
 f_{11}^{pis} &= \min f_{11}, & f_{11}^{nis} &= \max f_{11}, \\
 f_{12}^{pis} &= \min f_{12}, & f_{12}^{nis} &= \max f_{12}, \\
 f_{13}^{pis} &= \max f_{13}, & f_{13}^{nis} &= \min f_{13}, \\
 f_2^{pis} &= \max f_2, & f_2^{nis} &= \min f_2.
 \end{aligned}
 \tag{21}$$

Now, we change the multiobjective problem (19) to the single-objective problem (22) via (16). The model is defined as follows:

$$\begin{aligned}
 \max \quad & \lambda \\
 \text{s.t.} \quad & \lambda \leq \frac{f_{11}^{nis} - f_{11}}{f_{11}^{nis} - f_{11}^{pis}} \\
 & \lambda \leq \frac{f_{12}^{nis} - f_{12}}{f_{12}^{nis} - f_{12}^{pis}} \\
 & \lambda \leq \frac{f_{13}^{pis} - f_{13}}{f_{13}^{pis} - f_{13}^{nis}} \\
 & \lambda \leq \frac{f_2^{pis} - f_2}{f_2^{pis} - f_2^{nis}}
 \end{aligned}
 \tag{22}$$

(3), (4), (7), (8), (9),  
 (10), (11), (13), (18).

### 3. Genetic Algorithm

In the last decade, we have seen a growing interest in biologically motivated approaches such as evolutionary strategies and genetic algorithms (GAs) being applied to many complex optimization problems. The processes occurring in the natural systems have inspired the development of these algorithms. Evolutionary strategies and genetic algorithms are constructed based on the observation of evolutionary processes in biological systems. Evolutionary processes such as adaptation, selection, reproduction, mutation, and competition are closely studied and translated into the form of computer simulations. Although these algorithms are a crude simplification of the natural processes, they have been successfully applied to many complex problems that were once intractable [31, 32].

GA is a stochastic search technique that explores the problem domain by maintaining a population of individuals, which represents a set of potential solutions in the search space. GA attempts to combine the good features found in each individual using a structured yet randomized information exchange in order to construct individuals who are better suited to their environment than the individuals that were created through the evolution of better individuals; it is anticipated that the desired solution will be found. The following steps are defined to design this algorithm.

**3.1. Solution Representation.** To show the chromosome, we used three matrices; the first matrix amount is zero or one and the rest of them are positive integer numbers.

The first matrix is called location matrix that is related to distribution centers. Its lines are related to a time period and its columns are related to distribution centers. Its dimension is  $|T| \times \max_{t \in T} |I_t|$  in which lines are periods and columns are distribution centers. This matrix's elements are zero and one in a way that zero and one correspond to inactiveness and activeness of the distribution center, respectively,

$$\text{Location} = \begin{bmatrix} L_{11}L_{12} \cdots L_{1|I_1|} \\ L_{21}L_{22} \cdots L_{2|I_2|} \\ \vdots \\ L_{|T|1}L_{|T|2} \cdots L_{|T||I_{|T|}|} \end{bmatrix}. \tag{23}$$

The second matrix is called Commodity\_Allocated matrix. To each commodity, there is a combined matrix including  $|T|$  submatrix with  $|I_t| \times |J_t|$  dimension. Each element in these submatrices indicates the number of commodities which are sent to corresponding damaged areas from the distribution center

Commodity\_Allocated\_1

$$= \begin{bmatrix} \begin{bmatrix} i_{11}i_{12} \cdots i_{1|J_1|} \\ i_{21}i_{22} \cdots i_{2|J_1|} \\ \vdots \\ i_{|I_1|1}i_{|I_1|2} \cdots i_{|I_1||J_1|} \end{bmatrix}^1 \\ \dots \\ \begin{bmatrix} i_{11}i_{12} \cdots i_{1|J_{|T|}|} \\ i_{21}i_{22} \cdots i_{2|J_{|T|}|} \\ \vdots \\ i_{|I_{|T|}|1}i_{|I_{|T|}|2} \cdots i_{|I_{|T|}||J_{|T|}|} \end{bmatrix}^{|T|} \end{bmatrix}, \dots,$$

Commodity\_Allocated\_ |c|

$$= \begin{bmatrix} \begin{bmatrix} i_{11}i_{12} \cdots i_{1|J_1|} \\ i_{21}i_{22} \cdots i_{2|J_1|} \\ \vdots \\ i_{|I_1|1}i_{|I_1|2} \cdots i_{|I_1||J_1|} \end{bmatrix}^1 \dots \begin{bmatrix} i_{11}i_{12} \cdots i_{1|J_{|T|}|} \\ i_{21}i_{22} \cdots i_{2|J_{|T|}|} \\ \vdots \\ i_{|I_{|T|}|1}i_{|I_{|T|}|2} \cdots i_{|I_{|T|}||J_{|T|}|} \end{bmatrix}^{|T|} \end{bmatrix}. \tag{24}$$

The third matrix is called inventory matrix that indicates the amount of transported inventory from one period to the next one in each distribution center

$$\begin{aligned}
 \text{Inventory\_1} &= \begin{bmatrix} \text{inv}_{11} \text{inv}_{12} \cdots \text{inv}_{1|T|} \\ \text{inv}_{21} \text{inv}_{22} \cdots \text{inv}_{2|T|} \\ \vdots \\ \text{inv}_{|I_1|1} \text{inv}_{|I_2|2} \cdots \text{inv}_{|I_{|T|}||T|} \end{bmatrix}_{\max_{t \in T} |I_t| \times |T|}, \dots, \\
 \text{Inventory\_ |c|} &= \begin{bmatrix} \text{inv}_{11} \text{inv}_{12} \cdots \text{inv}_{1|T|} \\ \text{inv}_{21} \text{inv}_{22} \cdots \text{inv}_{2|T|} \\ \vdots \\ \text{inv}_{|I_1|1} \text{inv}_{|I_2|2} \cdots \text{inv}_{|I_{|T|}||T|} \end{bmatrix}_{\max_{t \in T} |I_t| \times |T|}.
 \end{aligned}
 \tag{25}$$

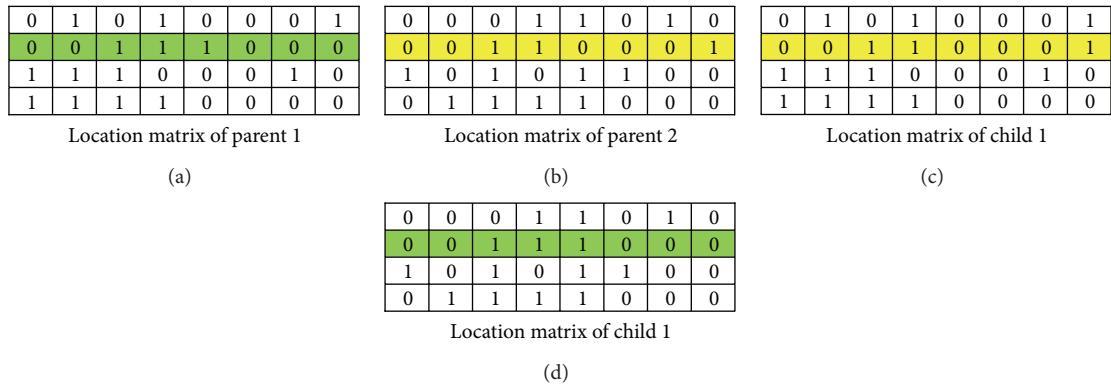


FIGURE 1: Crossover operator.

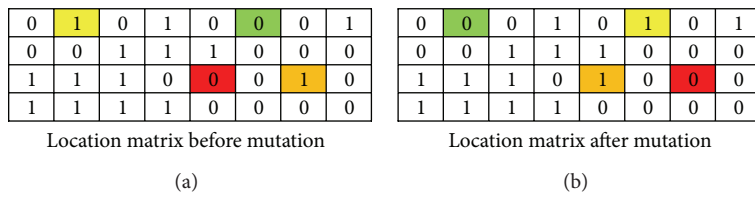


FIGURE 2: Mutation operator.

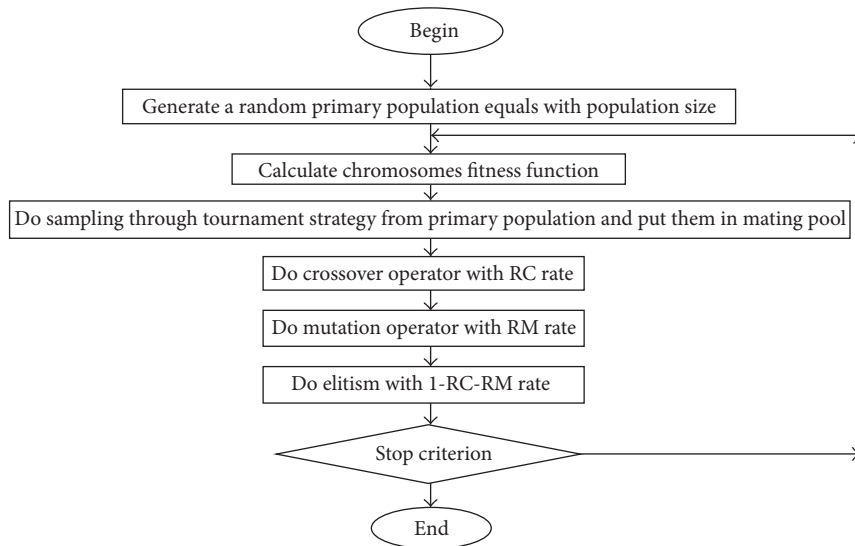


FIGURE 3: Genetic algorithm flowchart.

TABLE 1: Simulated annealing algorithm parameters and their levels.

Problem size	Levels	A		B		C		D	
		Cooling rate ( $\alpha$ )	Number of repetitions in each temperature ( $N$ )	Final temperature ( $T_f$ )	Initial temperature ( $T_0$ )				
Small	1	0.9	20	0.0000001	100				
	2	0.925	40	0.00001	10000				
	3	0.95	60	0.001	1000000				
Large	1	0.94	50	0.0000001	100				
	2	0.96	75	0.00001	10000				
	3	0.98	100	0.001	1000000				

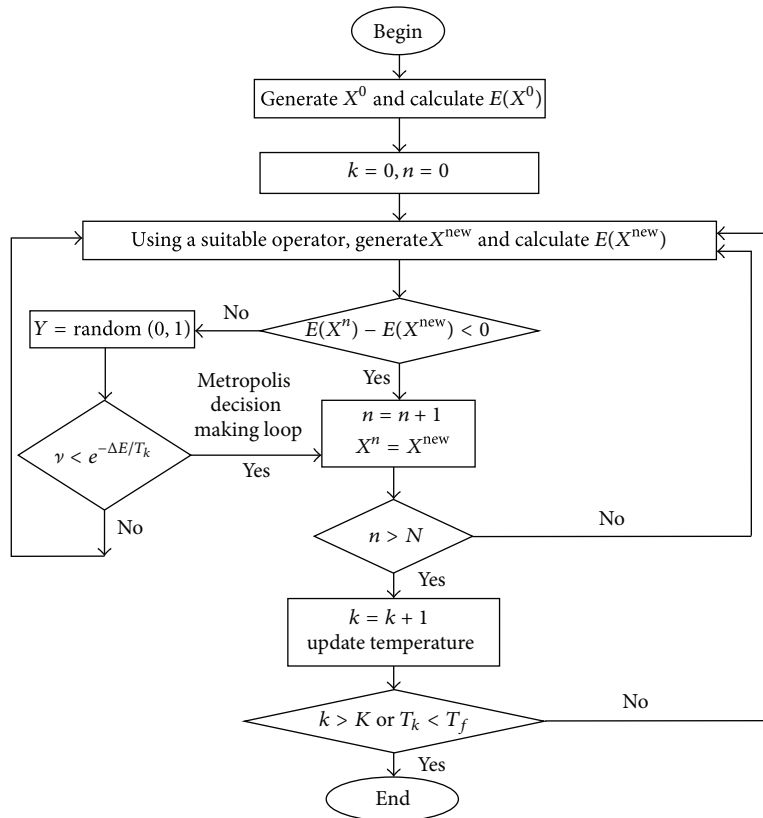


FIGURE 4: Simulated annealing flowchart.

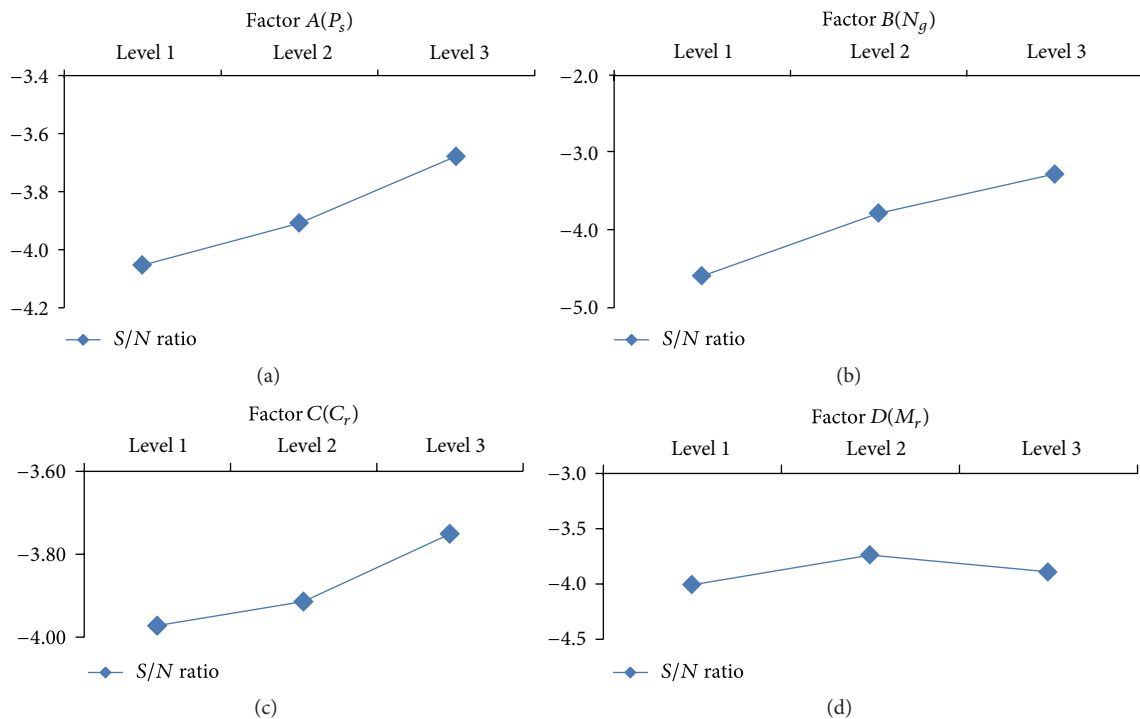


FIGURE 5: Diagram of mean effect of the S/N ratio for small problem in genetic algorithm.

TABLE 2: Genetic algorithm parameters and their levels.

Problem size	Levels	A	B	C	D
		Population size ( $P_g$ )	Number of generations ( $N_g$ )	Crossover rate ( $C_r$ )	Mutation rate ( $M_r$ )
Small	1	100	400	0.7	0.01
	2	120	500	0.75	0.02
	3	150	600	0.8	0.05
Large	1	180	600	0.8	0.01
	2	200	800	0.9	0.02
	3	220	1000	0.95	0.05

TABLE 3: Orthogonal array  $L9$ .

Experiments	A	B	C	D
1	A(1)	B(1)	C(1)	D(1)
2	A(1)	B(2)	C(2)	D(2)
3	A(1)	B(3)	C(3)	D(3)
4	A(2)	B(1)	C(2)	D(3)
5	A(2)	B(2)	C(3)	D(1)
6	A(2)	B(3)	C(1)	D(2)
7	A(3)	B(1)	C(3)	D(2)
8	A(3)	B(2)	C(1)	D(3)
9	A(3)	B(3)	C(2)	D(1)

TABLE 4: Characteristics of instances.

Problem size	Instance name	Number of periods	Number of damaged areas	Number of areas for distribution center	Maximum number of distribution centers in periods
Small	I1	5	(5, 5, 5, 6, 6)	(4, 4, 5, 5, 5)	(2, 2, 2, 2, 2)
	I2	5	(6, 6, 6, 6, 6)	(4, 4, 5, 5, 5)	(2, 2, 3, 3, 3)
	I3	5	(6, 6, 8, 8, 8)	(5, 5, 5, 6, 6)	(2, 2, 3, 3, 3)
	I4	3	(10, 10, 10)	(5, 6, 6)	(3, 4, 4)
	I5	3	(10, 12, 12)	(6, 6, 8)	(3, 4, 4)
	I6	3	(12, 12, 14)	(6, 8, 8)	(3, 5, 5)
	I7	3	(14, 14, 14)	(8, 10, 10)	(4, 5, 5)
	I8	3	(14, 14, 16)	(12, 14, 14)	(4, 5, 5)
Large	I9	5	(30, 30, 30, 35, 35)	(12, 12, 14, 14, 14)	(4, 4, 5, 5, 5)
	I10	5	(30, 30, 35, 35, 35)	(14, 14, 14, 15, 15)	(5, 5, 5, 5, 5)
	I11	5	(35, 35, 35, 40, 40)	(15, 15, 18, 18, 18)	(5, 5, 5, 5, 5)
	I12	5	(40, 40, 40, 45, 45)	(16, 16, 18, 20, 20)	(5, 5, 6, 6, 6)
	I13	5	(45, 45, 45, 48, 50)	(20, 20, 22, 22, 22)	(6, 6, 6, 6, 6)
	I14	5	(45, 48, 48, 48, 50)	(22, 24, 24, 25, 25)	(6, 6, 7, 7, 7)
	I15	5	(50, 55, 55, 50, 50)	(25, 28, 28, 28, 28)	(6, 6, 7, 7, 7)
	I16	5	(50, 55, 55, 55, 55)	(28, 30, 30, 30, 30)	(7, 7, 7, 7, 7)
	I17	3	(80, 100, 100)	(30, 30, 32)	(8, 8, 8)
	I18	3	(100, 100, 120)	(32, 35, 35)	(8, 10, 10)
	I19	3	(120, 120, 140)	(35, 35, 38)	(10, 10, 10)
	I20	3	(140, 140, 160)	(38, 40, 42)	(10, 10, 12)
	I21	3	(150, 160, 150)	(42, 45, 45)	(10, 12, 12)
	I22	3	(160, 160, 170)	(45, 50, 50)	(12, 12, 12)
	I23	3	(180, 180, 200)	(50, 50, 60)	(12, 12, 12)
	I24	3	(200, 220, 220)	(60, 60, 62)	(12, 14, 14)
	I25	3	(220, 250, 250)	(60, 65, 65)	(12, 14, 14)

TABLE 5: Characteristics of sample problems that have been used for Taguchi method.

Problem size	Number of periods	Number of damaged areas	Number of areas for distribution center	Maximum number of distribution centers in periods
Small	3	(10, 10, 10)	(5, 6, 6)	(3, 4, 4)
Large	5	(35, 35, 35, 40, 40)	(15, 15, 18, 18, 18)	(5, 5, 5, 5, 5)

TABLE 6: The optimum factor for genetic algorithm and simulated annealing.

	Problem size	Factors	Level 1	Level 2	Level 3	Optimum factor	
Genetic algorithm	Mean S/N ratio	Small	A	-4.0524	-3.9078	-3.6780	A(3)
			B	-4.5873	-3.7776	-3.2731	B(3)
			C	-3.9725	-3.9144	-3.7512	C(3)
		D	-4.0079	-3.7381	-3.8921	D(2)	
		Large	A	-5.5750	-5.4837	-5.4807	A(3)
			B	-6.0750	-5.4906	-4.9739	B(3)
	C		-5.6615	-5.4169	-5.4610	C(2)	
	Mean objective function	Small	D	-5.5713	-5.3525	-5.6156	D(2)
			A	0.6301	0.6395	0.6558	A(3)
			B	0.5914	0.6479	0.6861	B(3)
		Large	C	0.6360	0.6391	0.6502	C(3)
			D	0.6334	0.6514	0.6405	D(2)
A			0.5286	0.5339	0.5345	A(2), A(3)	
Simulated annealing	Mean S/N ratio	Small	B	0.4995	0.5323	0.5641	B(3)
			C	0.5235	0.5380	0.5345	C(2)
			D	0.5290	0.5412	0.5258	D(2)
		Large	A	-4.1877	-4.0033	-3.7003	A(3)
			B	-4.1164	-3.9694	-3.8055	B(3)
			C	-4.1038	-3.7080	-4.0795	C(2)
	Mean objective function	Small	D	-4.4123	-4.0730	-3.4060	D(3)
			A	-6.4144	-6.0149	-5.4369	A(3)
			B	-6.2095	-6.0824	-5.5743	B(3)
		Large	C	-5.9112	-5.8779	-6.0771	C(2)
			D	-6.3202	-5.8310	-5.7150	D(3)
			A	0.6209	0.6327	0.6544	A(3)
	Small	B	0.6262	0.6353	0.6464	B(3)	
		C	0.6272	0.6537	0.6270	C(2)	
		D	0.6048	0.6272	0.6760	D(3)	
	Large	A	0.4817	0.5032	0.5351	A(3)	
		B	0.4925	0.5006	0.5269	B(3)	
		C	0.5100	0.5108	0.4993	C(1), C(2)	
D	0.4880	0.5131	0.5189	D(3)			

TABLE 7: Tuned values of the simulated annealing parameters.

Problem size	$\alpha$	$N$	$T_f$	$T_0$
Small	0.95	60	0.00001	1000000
Large	0.98	100	0.00001	1000000

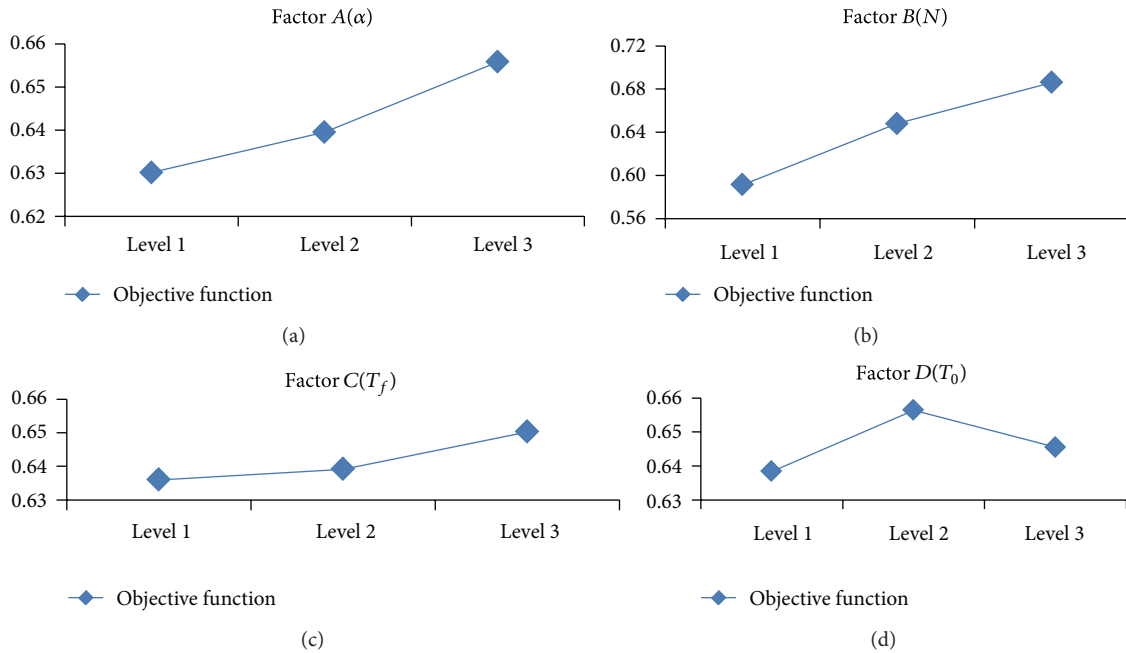


FIGURE 6: Diagram of mean effect of parameters based on the objective function for small problem in genetic algorithm.



FIGURE 7: Iran: South Khorasan.

3.2. *Generating Initial Population.* After determining a technique to assign a chromosome to each solution, one can create an initial population. In this process, the location matrix is generated randomly.

To initialize the Commodity Allocated matrices, we use a heuristic method so that first, for each commodity type, the total damaged area requests and total supply of active distribution centers have been evaluated, and, then, considering justice in distribution, commodities are distributed among damaged areas equally. Now, to allocate active centers to damaged areas, an area has been chosen randomly and it would be allocated to an active distribution center obtained by the roulette wheel, which is generated based on the allocation costs. If this distribution center cannot satisfy all predicted demands, the next center obtained by the roulette wheel will meet the remaining demands of this damaged area. Then, one area is chosen randomly from the other damaged areas. All the above-mentioned activities are executed until allocation manner of centers to damaged areas is determined for all the areas.

3.3. *Sampling Mechanisms.* This mechanism is related to selection chromosomes' method. Tournament selection has been used in this research. Based on this method, first, the value of each chromosome's fitness functions in a population has been calculated, and a tournament size is chosen (here, tournament size is 3). Then, chromosome from one population has been chosen randomly equal with tournament size and, at the end, the best chromosome based on suitability will be transferred to mating pool. This has been repeated up to the number of population. It is possible to create several copies from a chromosome with higher fitness function. This shows that better chromosomes have greater chance to be chosen.

3.4. *Genetic Operators.* To generate a new generation of the present chromosome, the following genetic operators could be used.

3.4.1. *Crossover Operator.* In this crossover operator, a row of location matrix of one chromosome is exchanged with the

TABLE 8: Tuned values of the genetic algorithm parameters.

Problem size	$P_s$	$N_g$	$C_r$	$M_r$
Small	150	600	0.8	0.02
Large	220	1000	0.9	0.02

same row of location matrix of another one and also corresponding elements are exchanged in Commodity\_Allocated matrices and inventory matrices. In other words, we choose a random number from  $\{1, \dots, T\}$  ( $T$  is the number of time periods), and we exchange corresponding row of location matrix of parent 1 with the same row of location matrix of parent 2 and also corresponding elements are exchanged in Commodity\_Allocated matrices and inventory matrices in two chromosomes. Figure 1 shows the crossover operator.

**3.4.2. Mutation Operators.** Mutation operator operates on location matrix in the developed algorithm. In the first mutation operator, elements corresponding to two distribution centers exchange in a row of location matrix. As distribution center locating conditions change, Commodity\_Allocated matrices are valued by the stated heuristic method in Section 3.2.

Figure 2 shows the mutation operator.

In the second mutation operator, one element corresponding to the distribution center in location matrix has been considered. It will be zero if it is one and it will be one if it is zero (provided that the number of active centers does not violate the number of authorized ones).

Now, as the location conditions of distribution center change, Commodity\_Allocated matrices are updated by explained heuristic method in Section 3.2.

**3.5. Elitism Selection.** When genetic operators (mutation and crossover) are used, it would be possible to lose the best chromosomes. Elitism is a method to keep a copy from the best chromosomes in the new generations. The above mechanism makes genetic algorithm keep some of the best solutions in each generation. Previous experiences have proved that this mechanism optimizes genetic algorithm operation and shortens coverage time.

**3.6. Algorithm Stop Criterion.** Since metaheuristic algorithms do not have any criteria for the global optima, a maximum number of iterations have been considered in order to stop the algorithm. Figure 3 shows the genetic algorithm flowchart.

## 4. Simulated Annealing Algorithm

Simulated annealing is a probabilistic metaheuristic algorithm which is a local search method. The simulated annealing begins its search from a random initial solution. The iteration loop that characterizes the main procedure randomly generates in each iteration only one neighbor  $s'$  of the current solution  $s$ . The variation  $\Delta$  for the value of the objective function  $f(x)$  is tested for each neighbor generation. To

test this variation,  $\Delta = f(s) - f(s')$  is computed. If the value of  $\Delta$  is less than 0 (zero), then the new solution  $s'$  is automatically accepted to replace  $s$ . Otherwise, accepting the new solution  $s'$  will depend on the probability established by the Metropolis criteria, which is given by  $e^{\Delta/T}$ , where  $T$  is a temperature parameter, a key variable for the method.

Figure 4 shows the simulated annealing flowchart. In Figure 4,  $n$  is the number of internal circles,  $k$  is the number of external circles, and  $E()$  is the objective function.

In the following, we discuss the proposed SA heuristic in detail, including the solution representation, the generation of the initial solution, and various types of neighborhood.

**Solution representation:** solution representation is similar to Section 3.1.

**Generation of the initial solution:** this is similar to Section 3.2.

**Neighborhood generation mechanism:** we produce neighborhood by mutation operators that is exhibited in Section 3.4.2.

## 5. Numerical Results

In this section, the developed algorithms have been used on the sample problems that have been generated randomly and the presented genetic algorithm efficacy has been studied. The characteristics of instances are shown in Table 3.

To solve the model used of LINGO 11 on a computer with the following characteristics: intel(R) core(TM) i3 cpuM330@2.13 Ghz, 4 G RAM. Considering the intense effect of parameter configuration on the performance of algorithms, the Taguchi method is used for the configuration of parameters. Before calibration of the employed algorithms, we run some preliminary tests to find appropriate parameter levels. To obtain more accurate, as well as better sustained, results for the offered algorithm, the following four parameters were configured:  $T_0$ ,  $T_f$ ,  $N$ , and  $\alpha$  for simulated annealing and  $C_r$ ,  $M_r$ ,  $N_g$ , and  $P_s$  for the genetic algorithm. These parameters and their levels are given in Tables 1 and 2. The square matrix with 4 parameters in 3 levels used in the Taguchi method is L9, which is given in Table 3. In Taguchi method, the variation of the output results is measured by means of signal-to-noise ( $S/N$ ) ratio. Here, the larger value of  $S/N$  ratio leads to the smaller variation of the response variable. Factor levels that maximize the appropriate  $S/N$  ratio are optimal [33]. The value of  $S/N$  ratio is computed by

$$\frac{S}{N} = -10 \log_{10} \left[ \frac{1}{n} \sum_{i=1}^n \frac{1}{y_i^2} \right], \quad (26)$$

where  $n$  is the number of repetitions under the same experimental conditions and  $y_i$  denotes the experimental result at each repetition.

TABLE 9: A summary of the computational results of the small and large instances.

Instance name	LINGO				SA in 10 iterations				GA in 10 iterations				PRAS%	PRBS%
	Exact solution	Time	Average solution	Average time (s)	Standard deviation	Best solution	The best solution's error %	Average solution	Average time (s)	Standard deviation	Best solution	The best solution's error %		
I1	0.5647	15657	0.56385	132.1	0.00056	<b>0.5647</b>	0.000	<b>0.5645</b>	125.0	<b>0.00028</b>	<b>0.5647</b>	0.000	0.115	0.000
I2	0.77818	38956	0.77551	157.2	0.00151	<b>0.7774</b>	0.100	<b>0.7757</b>	140.7	<b>0.00081</b>	0.7765	0.220	0.024	-0.116
I3	0.6429	74378	0.63241	158.1	0.00367	<b>0.6362</b>	1.042	<b>0.6304</b>	156.0	0.00703	<b>0.6362</b>	1.058	-0.319	0.000
I4	0.6938	57478	0.67563	142.7	0.00764	0.6837	1.456	<b>0.6798</b>	135.0	<b>0.00493</b>	<b>0.6874</b>	0.922	0.613	0.538
I5	0.78345	104563	<b>0.75765</b>	167.0	0.01028	0.7687	1.883	0.7554	150.6	<b>0.00838</b>	<b>0.7691</b>	1.835	-0.298	0.052
I6	0.5973	195468	0.57159	203.0	0.00605	0.5798	2.930	<b>0.5761</b>	192.0	0.00722	<b>0.5831</b>	2.377	0.783	0.566
I7	0.6832	246378	0.65593	241.2	0.01078	0.6684	2.166	<b>0.6594</b>	215.1	<b>0.00861</b>	<b>0.6701</b>	1.917	0.526	0.254
I8	0.8843	310234	0.84158	257.4	0.02066	0.8685	1.787	<b>0.8452</b>	222.3	<b>0.01939</b>	<b>0.8691</b>	1.719	0.428	0.069
Average	—	130389	—	182.34	0.00764	—	1.421	—	167.09	<b>0.00708</b>	—	1.256	0.234	0.168
I9	—	—	0.74823	1521	0.01755	0.7761	—	<b>0.7779</b>	1431	<b>0.00596</b>	<b>0.7834</b>	—	3.81782	0.93183
I10	—	—	0.63553	1560	0.01813	0.6598	—	<b>0.6633</b>	1492	<b>0.00632</b>	<b>0.6715</b>	—	4.18664	1.74236
I11	—	—	0.51612	1625	0.02334	0.5465	—	<b>0.5534</b>	1553	<b>0.00858</b>	<b>0.5698</b>	—	6.73990	4.08915
I12	—	—	0.71373	1758	0.02807	<b>0.7651</b>	—	<b>0.7353</b>	1661	<b>0.02576</b>	0.7601	—	2.92821	-0.6578
I13	—	—	0.73424	1821	0.04430	0.7924	—	<b>0.8055</b>	1749	<b>0.02185</b>	<b>0.8325</b>	—	8.84441	4.81681
I14	—	—	0.62172	1972	0.01734	0.6538	—	<b>0.6587</b>	1881	0.03170	<b>0.6947</b>	—	5.60835	5.88743
I15	—	—	0.55941	2084	0.04037	0.6089	—	<b>0.6099</b>	2007	<b>0.03593</b>	<b>0.6548</b>	—	8.27840	7.00977
I16	—	—	0.66088	2218	0.04091	<b>0.7191</b>	—	<b>0.6860</b>	2132	<b>0.03373</b>	0.7165	—	3.66461	-0.3628
I17	—	—	0.51391	1732	0.03563	0.5606	—	<b>0.5535</b>	1652	<b>0.03755</b>	<b>0.5963</b>	—	7.14931	5.98691
I18	—	—	0.6941	1829	0.05634	0.7723	—	<b>0.7729</b>	1784	<b>0.04592</b>	<b>0.8435</b>	—	10.1895	8.44102
I19	—	—	0.59042	1997	0.05718	0.6773	—	<b>0.6880</b>	1903	<b>0.03741</b>	<b>0.7326</b>	—	14.1843	7.54845
I20	—	—	0.73554	2132	0.05335	0.8231	—	<b>0.8227</b>	2012	<b>0.03815</b>	<b>0.8901</b>	—	10.5943	7.52724
I21	—	—	0.47935	2217	0.05890	0.5469	—	<b>0.5448</b>	2158	<b>0.03160</b>	<b>0.6035</b>	—	12.0103	9.37862
I22	—	—	0.57803	2349	0.05441	0.6642	—	<b>0.6463</b>	2263	<b>0.04003</b>	<b>0.7108</b>	—	10.5659	6.55599
I23	—	—	0.62408	2494	0.06076	0.6838	—	<b>0.6871</b>	2321	<b>0.04458</b>	<b>0.7593</b>	—	9.16923	9.94336
I24	—	—	0.570474	2683	0.05570	0.6419	—	<b>0.6260</b>	2532	<b>0.05311</b>	<b>0.6980</b>	—	8.87142	8.03724
I25	—	—	0.71449	2793	0.06001	0.7892	—	<b>0.7690</b>	2671	<b>0.054704</b>	<b>0.8326</b>	—	7.08601	5.21258
Average	—	—	—	2046.18	0.04249	—	—	—	<b>1953.06</b>	<b>0.03252</b>	—	—	7.786	5.417

TABLE 10: The amount of inventory has been estimated in the candidate areas for the establishment of distribution centers (\*1000).

		Sarayan	Qaen	Birjand
Period 1	Commodity 1	(19, 23, 30)	(54, 57, 59)	(128, 130, 134)
	Commodity 2	(96, 99, 107)	(144, 149, 162)	(274, 280, 291)
Period 2	Commodity 1	(47, 53, 55)	(67, 72, 79)	(175, 180, 182)
	Commodity 2	(102, 113, 124)	(192, 209, 223)	(389, 400, 419)
Period 3	Commodity 1	(41, 43, 48)	(69, 78, 85)	(192, 200, 212)
	Commodity 2	(89, 96, 109)	(117, 127, 139)	(270, 280, 296)

Characteristics of sample problems that have been used for Taguchi method are shown in Table 5. Calculating all test results using the Taguchi method, the mean rate of  $S/N$  for small-scale problem is presented in Figure 5 and the mean of the objective function for small-scale problem is shown in Figure 6.

Optimum factors for genetic algorithm and simulated annealing are given in Table 6. The final configurations of parameters for all algorithms are summarized in Tables 7 and 8.

Table 9 shows that the proposed genetic algorithm and simulated annealing algorithm operate faster than LINGO with little errors and the standard deviation is not considerable in ten iterations indicating that the solutions do not have deviation. Now, we generate a number of sample problems with small and large size that are exhibited in Table 4 and then operate the proposed genetic algorithm and simulated annealing algorithm on these problems. Table 9 shows more details on computational results for all test problems. The CPU times corresponding to the exact solution, as seen in Table 9, show that computational time grows exponentially by size of the problem. Unfortunately, for the large-scale calculations, LINGO cannot even find the feasible solution in the limited run time.

In Table 9, we present the following: average value, standard deviation, best solution, computational time, PRAS%, and PRBS% for each problem. As observed in Table 9, there are only 2 cases out of 25 for which the SA algorithm performs better than the GA. Also, in 2 cases out of 25, the SA algorithm and GA behave identically. Moreover, in the other cases than those mentioned, GA performs better than the SA. Finally, in an average sense, the genetic algorithm gives less standard deviation than the simulated annealing. These observations show that the GA gives more stable results than the SA. Solution average in genetic algorithm meets more suitable conditions especially in the case of large size problems. As can be seen, the percent reduction best solution (%PRBS) and the percent reduction average solution (%PRAS) are both positive values, so the GA performs better than the SA.

The percent reduction best solution (%PRBS) and the percent reduction average solution (%PRAS) are calculated using

$$\begin{aligned} \%PRBS &= \frac{Best_{GA} - Best_{SA}}{Best_{GA}} \times 100\%, \\ \%PRAS &= \frac{Average_{GA} - Average_{SA}}{Average_{GA}} \times 100\%. \end{aligned} \tag{27}$$

For the proposed algorithms, the average results of the ten simulations are also presented. The efficiency of the two algorithms is measured by the quality of the produced solutions. The quality is given in terms of the relative deviation from the optimum solution that the best solution's error = (LINGO solution – the best solution)/LINGO solution, where LINGO solution denotes the solution of the LINGO software and the best solution is considered to be the solution of the metaheuristic algorithms. As it can be seen from Table 9, the algorithms lead to very good and stable results for most cases. Also, the genetic algorithm performs better than the simulated annealing, in each and every instance.

The comparison of LINGO with the proposed genetic algorithm shows that the GA can find approximately an optimal solution in a shorter time compared to the LINGO as presented in Table 9. In Table 9, it is also shown that the average gap between the optimal and the GA solutions is 1.421%. The maximum gap is related to the test problem  $I_6$ .

As observed in Table 9, the standard deviation has increased as the problem's dimension increases. To obtain better solution in large dimensions, population size and the number of generations should both increase.

A small size example is considered to test the reliability of the model. Figure 7 shows the map of south-khorasan province of Iran that has been used at this example. Three cities (Birjand, Qaen, and Sarayan) are selected to set up relief commodities distribution centers for different periods. Furthermore, nine cities including Birjand, Qaen, Darmiyan, Nehbandan, Ferdows, Zirkoh, Sarayan, Sarbisheh, and Boshruyeh are considered as damaged areas. The fixed cost to open distribution centers for all the areas is \$25000, \$26000, and \$27500. The shortage penalty for each commodity is \$1.5 for commodity 1 and \$2.5 for commodity 2. These values are confirmed with experts' estimations. In this example, two types of relief commodities have been considered. In addition, there are two active centers for each period. The model has been solved for a situation that the number of planning periods is 3. The demand of damaged areas is available as triangular fuzzy numbers in Table 11. The amount of inventory in distribution centers is presented in Table 10. The proposed model tries to minimize the cost of commodities relocation and maximize the demand coverage ratio of damaged area for fair distribution. This is done by a multiobjective possibility linear programming model.

As shown in Tables 12 and 13, considering the inventories of distribution centers and damaged area demands in periods

TABLE II: Demand of damaged areas (\*1000).

	Ferdows	Boshruyeh	Darmiyan	Sarayan	Sarbisheh	Nehbandan	Zirkoh	Qaen	Birjand
Period 1	Commodity 1	(38, 40, 42)	(44, 50, 57)	(45, 50, 53)	(33, 36, 39)	(34, 38, 39)	(36, 40, 42)	(42, 45, 46)	(56, 60, 63)
	Commodity 2	(68, 70, 72)	(65, 69, 73)	(91, 95, 99)	(86, 89, 98)	(55, 60, 66)	(53, 55, 59)	(66, 70, 76)	(76, 80, 89)
Period 2	Commodity 1	(44, 45, 47)	(54, 55, 58)	(42, 45, 48)	(42, 46, 47)	(35, 39, 41)	(56, 60, 61)	(35, 38, 41)	(61, 65, 67)
	Commodity 2	(76, 80, 86)	(75, 79, 83)	(102, 110, 119)	76, 80, 88)	(72, 75, 79)	(66, 70, 78)	(71, 75, 79)	(74, 78, 84)
Period 3	Commodity 1	(48, 50, 52)	(47, 49, 51)	(56, 60, 63)	(36, 40, 42)	(27, 30, 32)	(43, 45, 47)	(41, 45, 49)	(64, 70, 74)
	Commodity 2	(91, 95, 99)	(85, 87, 94)	(76, 80, 84)	(77, 78, 83)	(62, 65, 69)	(71, 75, 79)	(80, 83, 88)	(87, 89, 99)

TABLE 12: Allocated commodity (type 1) (\*1000).

		Ferdows	Boshruyeh	Darmiyan	Sarayan	Sarbisheh	Nehbandan	Zirkoh	Qaen	Birjand
Period 1	Birjand			25	8	20	27	20		31
	Qaen	21	26		11				23	
Period 2	Birjand			32	32	27	42			46
	Qaen	32	40					25	27	
Period 3	Birjand			46	23	23	34	22		53
	Qaen	38	38		7			13	45	

TABLE 13: Allocated commodity (type 2) (\*1000).

		Ferdows	Boshruyeh	Darmiyan	Sarayan	Sarbisheh	Nehbandan	Zirkoh	Qaen	Birjand
Period 1	Birjand			57	47	46	43	13		76
	Qaen	54	53	17	23			42	63	
Period 2	Birjand			105	55	72	68			103
	Qaen	77	76		22			71	75	
Period 3	Birjand			52	29	42	49	30		80
	Qaen	61	58		22			24	59	

TABLE 14: The amount of inventory in established distribution centers (\*1000).

		Birjand	Qaen
Period 1	Commodity 1	(128, 130, 134)	(73, 80, 89)
	Commodity 2	(274, 280, 291)	(240, 248, 269)
Period 2	Commodity 1	(175, 180, 182)	(114, 125, 134)
	Commodity 2	(389, 400, 419)	(294, 322, 347)
Period 3	Commodity 1	(192, 200, 212)	(110, 121, 133)
	Commodity 2	(270, 280, 296)	(206, 223, 248)

1, 2, and 3, Birjand and Qaen are considered as active distribution centers. The amount of inventory in active distribution centers is presented in Table 14. Tables 12 and 13 show how to allocate goods from distribution centers to the affected areas. As demonstrated, it has been tried as much as possible to use one distribution center as a closest center to damaged area. However, if the inventory of a distribution center is not sufficient, several distribution centers will be used to fulfill all demands. Reviewing the tables shows that almost all damaged areas receive commodities equally to have fair distribution of commodities. For instance, almost 52% of the 1st commodity demands and 77% of the 2nd commodity demands are met in period 1. Therefore, accuracy and reliability of the model are both acceptable.

## 6. Conclusions

It is clear that logistic activities are very important in response phase of the disaster management. Also, precise programming can improve the efficacy of the system. According to the crucial role of location-allocation in reducing cost and time, a multiobjective possibility programming model has been developed for relief logistics. This model follows two main objectives. The first one is minimizing good distribution cost and the second one is justice in good distribution process,

while the efforts are to maximize the minimum number of satisfied requests. Considering estimated information from problem conditions, some of the model parameters such as the number of damaged area requests and distribution center supply in different periods and transportation cost have been seeded as triangular fuzzy numbers. As observed earlier, the quality of the genetic algorithm is relatively higher, especially in large-scale problems.

Finally, for future research, the relief chain can be reconfigured with three echelons: central disaster facilities of the city as main suppliers, local emergency facilities as distributors, and urban areas as customer. Also, location and routing can be considered simultaneously.

## Conflict of Interests

The authors declare that there is no conflict of interests regarding the publication of this paper.

## References

- [1] L. Douglas, "Logistics for disaster relief," *IIE Solutions*, vol. 29, no. 6, pp. 26–29, 1997.
- [2] B. Balcik and B. M. Beamon, "Facility location in humanitarian relief," *International Journal of Logistics Research and Applications*, vol. 11, no. 2, pp. 101–121, 2008.

- [3] A. Thomas, "Humanitarian logistics: enabling disaster response," The Fritz Institute, 2003, <http://www.fritzinstitute.org/>.
- [4] L. Brotcorne, G. Laporte, and F. Semet, "Ambulance location and relocation models," *European Journal of Operational Research*, vol. 147, no. 3, pp. 451–463, 2003.
- [5] F. Barzinpour and V. Esmaeili, "A multi-objective relief chain location distribution model for urban disaster management," *International Journal of Advanced Manufacturing Technology*, vol. 70, no. 5–8, pp. 1291–1302, 2014.
- [6] C. G. Rawls and M. A. Turnquist, "Pre-positioning of emergency supplies for disaster response," *Transportation Research B*, vol. 44, no. 4, pp. 521–534, 2010.
- [7] G. Barbarosoğlu and Y. Arda, "A two-stage stochastic programming framework for transportation planning in disaster response," *Journal of the Operational Research Society*, vol. 55, no. 1, pp. 43–53, 2004.
- [8] A. Akkihal, *Inventory pre-positioning for Humanitarian operations [M.S. thesis]*, MIT Center for Transportation & Logistics, 2006.
- [9] G. H. Tzeng, H. J. Cheng, and T. D. Huang, "Multi-objective optimal planning for designing relief delivery systems," *Transportation Research E*, vol. 43, no. 6, pp. 673–686, 2007.
- [10] H. Jia, F. Ordóñez, and M. Dessouky, "A modeling framework for facility location of medical services for large-scale emergencies," *IIE Transactions*, vol. 39, no. 1, pp. 41–55, 2007.
- [11] P. Beraldi and M. E. Bruni, "A probabilistic model applied to emergency service vehicle location," *European Journal of Operational Research*, vol. 196, no. 1, pp. 323–331, 2009.
- [12] H. O. Mete and Z. B. Zabinsky, "Stochastic optimization of medical supply location and distribution in disaster management," *International Journal of Production Economics*, vol. 126, no. 1, pp. 76–84, 2010.
- [13] C. G. Rawls and M. A. Turnquist, "Pre-positioning of emergency supplies for disaster response," *Transportation Research B*, vol. 44, no. 4, pp. 521–534, 2010.
- [14] M. S. Jabal-Ameli, A. Bozorgi-Amiri, and M. Heydari, "A multi-objective possibilistic programming model for relief logistics problem," *International Journal of Industrial Engineering & Production Management*, vol. 22, no. 1, pp. 65–75, 2011.
- [15] S. Duran, M. A. Gutierrez, and P. Keskinocak, "Pre-positioning of emergency items for CARE international," *Interfaces*, vol. 41, no. 3, pp. 223–237, 2011.
- [16] M. Zeng and X. Wu, "A location-routing problem model for emergency relief system of natural disaster," in *Logistics*, pp. 1643–1649, 2009.
- [17] A. Bozorgi-Amiri, M. S. Jabalameli, and S. M. J. Mirzapour Al-e-Hashem, "A multi-objective robust stochastic programming model for disaster relief logistics under uncertainty," *OR Spectrum*, vol. 35, no. 4, pp. 905–933, 2013.
- [18] A. Bozorgi-Amiri, M. S. Jabalameli, M. Alinaghian, and M. Heydari, "A modified particle swarm optimization for disaster relief logistics under uncertain environment," *International Journal of Advanced Manufacturing Technology*, vol. 60, no. 1–4, pp. 357–371, 2012.
- [19] S. A. Yazdian and K. Shahanaghi, "A multi-objective possibilistic programming approach for locating distribution centers and allocating customers demands in supply chains," *International Journal of Industrial Engineering Computations*, vol. 2, no. 1, pp. 193–202, 2011.
- [20] J. S. Tancrez, J. C. Lange, and P. Semal, "A location-inventory model for large three-level supply chains," *Transportation Research E*, vol. 48, no. 2, pp. 485–502, 2012.
- [21] V. Schmid, "Solving the dynamic ambulance relocation and dispatching problem using approximate dynamic programming," *European Journal of Operational Research*, vol. 219, no. 3, pp. 611–621, 2012.
- [22] P. Chrétienne, P. Fouilhoux, E. Gourdin, and J. M. Segura, "The location-dispatching problem: polyhedral results and content delivery network design," *Electronic Notes in Discrete Mathematics C*, vol. 36, pp. 867–874, 2010.
- [23] H. Toro-Diaz, M. E. Mayorga, S. Chanta, and A. M. Laura, "Joint location and dispatching decisions for Emergency Medical Services," *Computers & Industrial Engineering*, vol. 64, no. 4, pp. 917–928, 2013.
- [24] G. Guillermo Cabrera, E. Cabrera, R. Soto, L. Jose Miguel Rubio, B. Crawford, and F. Paredes, "A hybrid approach using an artificial bee algorithm with mixed integer programming applied to a large-scale capacitated facility location problem," *Mathematical Problems in Engineering*, vol. 2012, Article ID 954249, 14 pages, 2012.
- [25] P. Murali, F. Ordóñez, and M. M. Dessouky, "Facility location under demand uncertainty: response to a large-scale bio-terror attack," *Socio-Economic Planning Sciences*, vol. 46, no. 1, pp. 78–87, 2012.
- [26] M. Xi, F. Ye, Z. Yao, and Q. Zhao, "A modified  $p$ -median model for the emergency facilities location problem and its variable neighbourhood search-based algorithm," *Journal of Applied Mathematics*, vol. 2013, Article ID 375657, 10 pages, 2013.
- [27] S. Gharegozloo Hamedani, M. S. Jabalameli, and A. Bozorgi-Amiri, "A multi-objective model for locating distribution centers in a supply chain network considering risk and inventory decisions," *Management Science Letters*, vol. 3, pp. 1077–1088, 2013.
- [28] R. Abounacer, M. Rekik, and J. Renaud, "An exact solution approach for multi-objective location-transportation problem for disaster response," *Computers & Operations Research*, vol. 41, pp. 83–93, 2014.
- [29] V. Esmaeili and F. Barzinpour, "Integrated decision making model for urban disaster management: a multi-objective genetic algorithm approach," *International Journal of Industrial Engineering Computations*, vol. 5, no. 1, pp. 55–70, 2014.
- [30] H. J. Zimmermann, "Fuzzy programming and linear programming with several objective functions," *Fuzzy Sets and Systems*, vol. 1, no. 1, pp. 45–55, 1978.
- [31] D. E. Goldberg, *Genetic Algorithms in Search, Optimization and Machine Learning*, Addison-Wesley Publishing Company, 1986.
- [32] C. Cotta and V. Hemert, *Studies in Computational Intelligence: Recent Advances in Evolutionary Computation for Combinatorial Optimization*, Springer, 2008.
- [33] B. Naderi, M. Zandieh, and S. M. T. Fatemi Ghomi, "Scheduling job shop problems with sequence-dependent setup times," *International Journal of Production Research*, vol. 47, no. 21, pp. 5959–5976, 2009.

## Research Article

# Modeling and Optimization of Beam Pumping System Based on Intelligent Computing for Energy Saving

Xiaohua Gu,<sup>1</sup> Taifu Li,<sup>1</sup> Zhiqiang Liao,<sup>2</sup> Liping Yang,<sup>3</sup> and Ling Nie<sup>1</sup>

<sup>1</sup> Department of Electrical and Information Engineering, Chongqing University of Science and Technology, Chongqing 401331, China

<sup>2</sup> College of Electronic Engineering, Xi'an Shiyou University, Xi'an 710065, China

<sup>3</sup> College of Optoelectronic Engineering, Chongqing University, Chongqing 400044, China

Correspondence should be addressed to Xiaohua Gu; xhgu@cqu.edu.cn

Received 17 November 2013; Accepted 2 April 2014; Published 14 April 2014

Academic Editor: Olabisi Falowo

Copyright © 2014 Xiaohua Gu et al. This is an open access article distributed under the Creative Commons Attribution License, which permits unrestricted use, distribution, and reproduction in any medium, provided the original work is properly cited.

Beam pumping system which is widely used in petroleum enterprises of China is one of the most energy-consuming equipment. It is difficult to be modeled and optimized due to its complication and nonlinearity. To address this issue, a novel intelligent computing based method is proposed in this paper. It firstly employs the general regression neural network (GRNN) algorithm to obtain the best model of the beam pumping system, and secondly searches the optimal operation parameters with improved strength Pareto evolutionary algorithm (SPEA2). The inputs of GRNN include the number of punching, the maximum load, the minimum load, the effective stroke, and the computational pump efficiency, while the outputs are the electric power consumption and the oil yield. Experimental results show that there is good overlap between model estimations and unseen data. Then sixty-one sets of optimum parameters are found based on the obtained model. Also, the results show that, under the optimum parameters, more than 5.34% oil yield is obtained and more than 3.75% of electric power consumption is saved.

## 1. Introduction

Beam pumping system is one of the most important oil recovery equipment in China, the occupancy of which reaches to 70% [1]. However, its system efficiency is very low, due to the negative torque, long gear train, poor working conditions, and other reasons. Researching the energy saving of beam pumping system is very important and necessary [2].

Improving the structure of the beam pumping unit is a kind of effective methods for energy saving [3, 4]. Through optimizing of the four-bar linkage design and improving the balance system, the fluctuation of the net torque curve becomes flat and the loading coefficient of beam pumping unit is reduced, which leads to the increasing of motor's efficiency. Nonsynchronous crank balance beam pumping unit and secondary balanced beam pumping unit are the typical cases. It is reported that the nonsynchronous crank balance beam pumping unit can save 3~4% energy in some conditions and the secondary balanced beam pumping unit

can save 14% energy. However, they are not always energy-saving and their energy-saving levels are related to the working conditions. For instance, if the balance parameters are not adjusted properly, the efficiency of the secondary balanced beam pumping unit should not be increasing.

Changing the working characteristic of the motor is another solution of this issue [5–8]. This way is represented by high-slip motor and ultrahigh-slip motor. Under the same working condition of the well, the average of the power-current curve of ultrahigh-slip motor is much less than that of conventional-slip motor. The curve is flatter, and consequently the cyclic loading coefficient is greatly reduced and the efficiency of the beam pumping unit is increased. However, since the efficiency of the high-slip motor is lower than that of the conventional-slip motor, there is a small amount of space to cut down the energy consumption and the energy-saving effect is remarkable only in the light-load conditions.

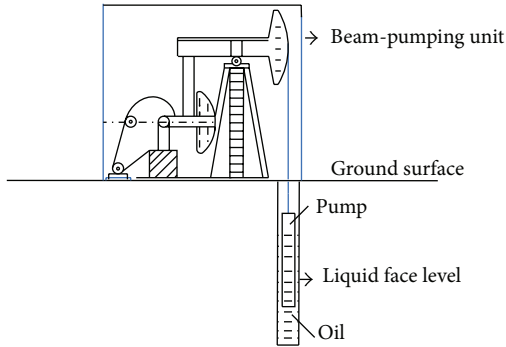


FIGURE 1: The schematic diagram of beam pumping system.

The aforementioned two ways, which try to improve the mechanical or electrical structures of the beam pumping system, need large investment and long time. It will be more economical to reduce the energy consumption based on the existing system by optimizing the operation parameters.

Only if we can build accurate and reliable process optimization model, the optimization of operation parameter is meaningful. Artificial neural network (ANN) modeling, because of its strong nonlinear approximation ability, is suitable for large-scale, parallel processing, and complex or unknown mechanism problems [9]. Since the beam pumping system is very complicated in nature, mainly due to unknown dynamic behaviors, nonlinear relations and numerous involved variables. In this paper, we proposed to build beam pumping system model by general regression neural network (GRNN). Then to identify the optimum operating parameters, multi-object optimization problem of minimizing the electric power consumption and maximizing the oil yield is solved by strength Pareto evolutionary algorithm (SPEA2).

The rest of this paper is organized as follows. Section 2 briefly introduces the beam pumping system. Section 3 presents the proposed modeling and optimization method for beam pumping system's energy saving. Experimental results and discussions are given in Section 4. The conclusions are finally drawn in Section 5.

## 2. A Sketch of Beam Pumping System

Beam pumping unit is the widely used traditional pumping equipment. A simple beam pumping system is sketched in Figure 1. The unit and motor at the surface supply the oscillating motion to the sucker and so to the pump. And the downhole oil is carried to the ground by the pump. In a rush time, the motor works in electrical state or generates electricity state, respectively, when the sucker is up or down.

The reservoirs are extremely complex, including rich oil, lean oil, thin oil, and thickened oil. The unit is impossible to work in constant speed. Additionally, there are many facts influencing the capacity and energy consumption of the oil pump, such as the leakage between the worn piston and the bush, and the polytropic stratum elements. It is hard or even impossible to develop an accurate mathematical model. This

TABLE 1: Parameters used for modeling.

	Inputs	Outputs parameters
Decision parameter	NP (time/min)	EPC (kw/h)
	MAXL (kN)	
Environment parameters	MINL (kN)	OY (t/d)
	ES (m)	
	CPE (%)	

paper tries to find the potential law of the beam pumping system by the history production data and then utilize the law to improve the yield and save the energy consumption.

## 3. Modeling and Optimization of Beam Pumping System

Different from the mechanical structure or electrical structure, modification method needs to replace the original equipment; the solution in this paper is to make the system work under the optimal operation parameters which are obtained by intelligent computing method based on the history production data of the original equipment.

As the analysis in Section 2, the beam pumping system is complicated and nonlinear. Its energy consumption is influenced by many factors. We first select the decision parameter and environment parameters, and then a GRNN model is built up to simulate the beam pumping system, and finally the optimization problem according to saving energy is constructed and solved by SPEA2 algorithm.

*3.1. Parameters Selection.* The monitored parameters of beam pumping system usually contain three-phase voltage, three-phase current, maximum load, the minimum load, theoretical pumpage, computational pump efficiency, effective stroke, number of punching, power factor, average power factor, average active power, average reactive power, electric power consumption, and oil yield, for the example of DaGang oilfield of China. Obviously, the first eight parameters are related to the system status, while the rest are related to the system efficiency.

In these parameters, the number of punching (NP) is adjustable and directly related to the status of the beam pumping unit. It is quite important to the energy consumption and the oil yield. Consequently, we selected it as the decision parameter. Moreover, it is not hard to find that some of these parameters show close relationship. In other word, there is redundancy in the parameters. Using all the parameters to model will increase the complexity of algorithm as well as reduce the reliability of the model. By analysis of their interrelation, we finally choose the maximum load (MAXL), the minimum load (MINL), the effective stroke (ES), and the computational pump efficiency (CPE) as the environment parameters and the electric power consumption (EPC) and the oil yield (OY) as the evaluation criterions. All the parameters used in modeling are shown in Table 1.

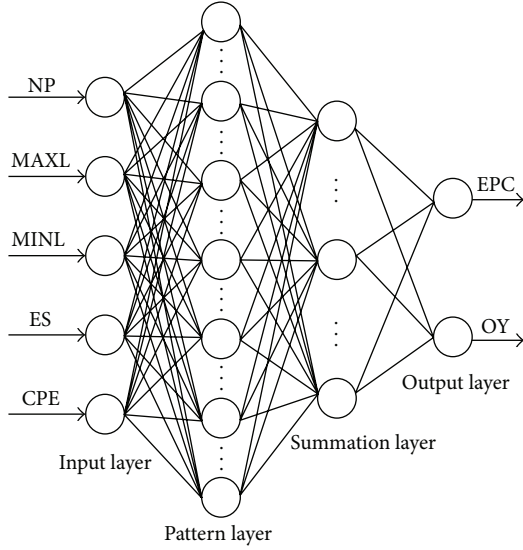


FIGURE 2: GRNN model of the beam pumping system.

**3.2. Modeling of Beam Pumping System.** GRNN [10], which evolved from probabilistic neural network (PNN) [11], belongs to the forward neural networks. It has many advantages: (1) strong nonlinear mapping ability and high error-tolerance, (2) strong approaching ability and high learning speed, (3) good performance for the small sample size problem, and (4) strong ability to deal with unstable data. So GRNN is quite suitable to model the complex nonlinear beam pumping system.

As Figure 2 shows, the GRNN model of beam pumping system comprises of four layers, namely, input layer, pattern layer, summation layer, and output layer. The input neurons in the first layer are distribution neurons which assigned all the measured values of  $\mathbf{X}$ , where  $\mathbf{X} = \{\mathbf{x}_1, \mathbf{x}_2, \dots, \mathbf{x}_n\}$ ,  $\mathbf{x}_i = (x_i^1, x_i^2, \dots, x_i^p)^T$ ,  $n$  is the number of samples, and  $p$  is the dimension of samples.

Most processing is done in the pattern layer and the summation layer. The number of neurons of pattern layer is equal to the number of training samples,  $n$ , and the transform function is shown as the following formula:

$$t_i = \exp \left[ -\frac{(\mathbf{X} - \phi_i^x)^T (\mathbf{X} - \phi_i^x)}{2\sigma^2} \right], \quad i = 1, 2, \dots, n, \quad (1)$$

where  $\mathbf{X}$  is the input vector of training sample,  $\phi_i^x$  is the input portion of the  $i$ th training vector represented by the  $i$ th neuron in the pattern layer, and  $\sigma$  is the smoothing parameter, which can be adjusted to provide different levels of function smoothing. Larger values for  $\sigma$  cause smoother estimated function.

In summation layer, arithmetic summations and weighted summations are performed in the neurons. The arithmetic summation of the output value of all pattern layer units is

$$s_D = \sum_{i=1}^n t_i. \quad (2)$$

And the weighted summation of the output value of all pattern layer units is

$$s_{Nj} = \sum_{i=1}^n y_{ij} t_i, \quad j = 1, 2, \dots, p, \quad (3)$$

where  $y_{ij}$  is the weight between the  $i$ th neuron of pattern layer and the  $j$ th neuron of summation layer; it is equal to the  $j$ th component of the output vector  $\mathbf{y}_i$  of the  $i$ th training sample.

The number of output layer neuron  $s$  equals the dimension of output vector of training sample, and every neuron divides the output values of summation layer; namely,

$$\hat{y}_j = \frac{s_{Nj}}{s_D}, \quad j = 1, 2, \dots, p, \quad (4)$$

where  $\hat{y}_j$  is the estimation value of  $j$ th component of output vector of forecasting sample.

**3.3. SPEA2 Optimization of Parameters.** Once the GRNN model of the beam pumping unit production system model is developed, it can be used to obtain the optimal values of the input variables. SPEA2 [12] is an improved version of the strength Pareto evolutionary algorithm (SPEA) also proposed by Zitzler and Thiele [13] in 1999. It is a multiobjective evolutionary algorithm characterized by the concepts of strength and density. Compared to SPEA, SPEA2 has an improved fitness assignment strategy and hence can search the global optimum of all objective functions. Consequently, SPEA2 becomes one of the most popular optimization techniques in nonlinear multiobjective combinatorial optimization problems. In this paper, the optimization problem for energy saving is solved using SPEA2 algorithm.

The objective functions are

$$\begin{aligned} y_{EPC} &= \min J_{EPC} = f(x_{NP}, x_{MAXL}, x_{MINL}, x_{ES}, x_{CPE}), \\ y_{OY} &= \max J_{OY} = f(x_{NP}, x_{MAXL}, x_{MINL}, x_{ES}, x_{CPE}). \end{aligned} \quad (5)$$

Considering that SPEA2 always searches the minimum fitness, the maximum objective is converted to minimum one by taking its negative. Finally, the multiobjective problem of the beam pumping system energy saving is described as follows:

$$\hat{y} = \min J(\hat{x}) = \min (J_1(\hat{x}), -J_2(\hat{x})). \quad (6)$$

In the above expression, it has

$$\begin{aligned} \hat{x} &= (x_{NP}, x_{MAXL}, x_{MINL}, x_{ES}, x_{CPE}) \in X \\ \hat{y} &= (y_{EPC}, -y_{OY}) \in Y \\ X &= \{(x_1, x_2, \dots, x_n) \mid l_i \leq x_i \leq u_i, i = 1, 2, \dots, 5\} \\ L &= (l_1, l_2, \dots, l_5) \\ U &= (u_1, u_2, \dots, u_5), \end{aligned} \quad (7)$$

where  $L$  and  $U$  are the lower and the upper boundaries of optimal parameters, respectively.

TABLE 2: Instances of experiment data from a certain oilfield.

Number	NP	MAXL	MINL	ES	CPE	EPC	OY
1	3.01	97.2	44.7	3.0746	69.2602	11.97	31.05
2	2.99	97.3	44.9	3.2502	73.1920	12.00	32.87
3	2.97	103.2	42.6	3.0683	70.7739	13.37	30.65
⋮	⋮	⋮	⋮	⋮	⋮	⋮	⋮

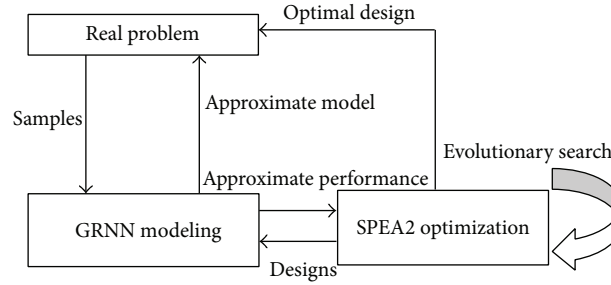


FIGURE 3: Framework of GRNN-SPEA2 strategy.

The main loop of the SPEA2 algorithm is as follows.

*Step 1.*  $i = 0$ : initialize population  $P_0$  and set archive population  $P'_0 = \emptyset$ .

*Step 2.* Function evaluation: calculate fitness values of all individuals in  $P_i \cup P'_i$ .

*Step 3.* Environmental selection: copy all nondominated individuals in  $P_i$  and  $P'_i$  to  $P'_{i+1}$ . If size of  $P'_{i+1}$  exceeds  $N$  (archive size), then reduce  $P'_{i+1}$  by means of the truncation operator; otherwise if size of  $P'_{i+1}$  is less than  $N$ , then fill  $P'_{i+1}$  with dominated individuals in  $P_i$  and  $P'_i$ .

*Step 4.* Termination: if stopping criterion (maximum generations) is satisfied, set  $P_{\text{final}} = P_{i+1}$  and terminate.

*Step 5.* Perform tournament selection with replacement on  $P'_{i+1}$  to fill the mating pool. Apply recombination and mutation operators to the mating pool and set  $P'_{i+1}$  to the resulting population.

*Step 6.*  $i = i + 1$ ; go to Step 2.

**3.4. GRNN-SPEA2 Strategy.** To obtain the optimal parameters, the modeling and the optimization procedure should be combined. The framework of GRNN-SPEA2 strategy is briefly illustrated in Figure 3.

The procedure can be briefly described as follows: as approximating the model of the real problem, GRNN is developed with certain calculated algorithm based on experiment data. The SPEA2 is applied to explore good solutions among solution spaces. Once the SPEA2 generates a new solution, the GRNN will be used to determine its fitness value for the SPEA2 to continue its searching process. Until the SPEA2 satisfies certain termination criterion, the strategy will export

TABLE 3: MSE and RE of GRNN model.

Performance index	EPC	OY
$E_{MS}$	0.0336	0.0951
$E_R$	0.0148	0.0071

the best solution and its performance determined by detail evaluation based on real problem.

## 4. Experimental Results and Analysis

**4.1. Experimental Data.** The proposed method is evaluated by real production data from a certain oilfield. Experiments employ 3234 samples which recorded the production status of 8 beam pumping wells from 6/1/2011 to 10/18/2011. Several instances of the dataset are listed in Table 2.

To void the influence caused by the difference between the absolute values of different parameters, the data were normalized to the range of  $[-1, 1]$  before used to model.

**4.2. GRNN Modeling.** In the GRNN modeling process, the data is divided randomly into two subsets, one is used to train the model called training set and the other one is used evaluate the model called test set. The training set and test set contain 3150 samples and 84 samples, respectively. Figure 4 shows the comparison of the predicted objectives and the real objectives.

It can be seen from Figure 4 that the predicted values and the real ones are very close. To show the diversity more clearly, the percentage errors of EPC and OY by GRNN model are shown in Figure 5. From Figure 5, we find that the absolute percentage error of EPC is less than 0.05%, while that of OY is less than 0.04%, which indicates that the obtained GRNN model gets nice description of the real model.

Also, the commonly used mean square error (MSE) and relative error (RE), whose formula is given in (8), are used to

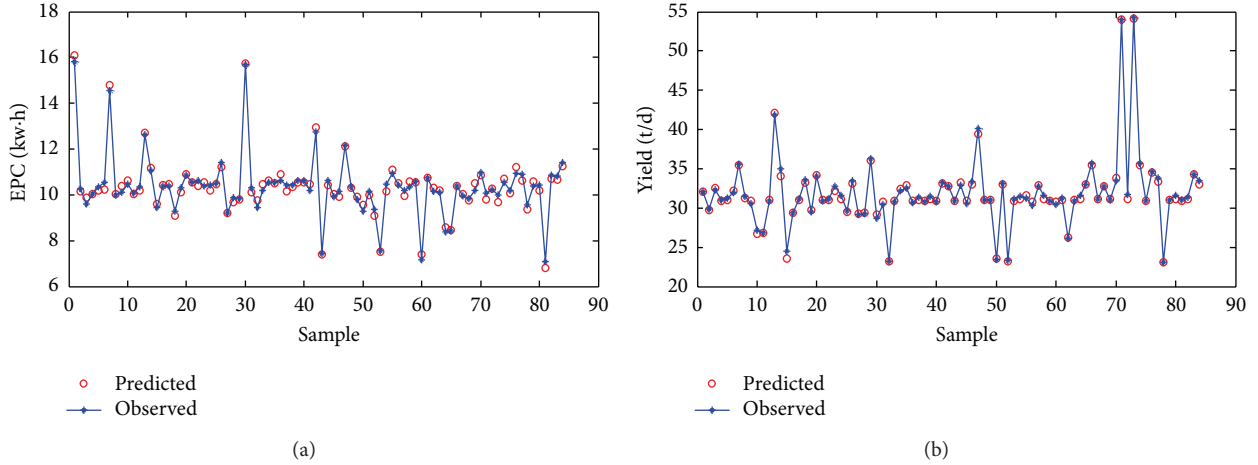


FIGURE 4: Comparison of the predicted and real objectives of GRNN model. (a) EPC and (b) OY.

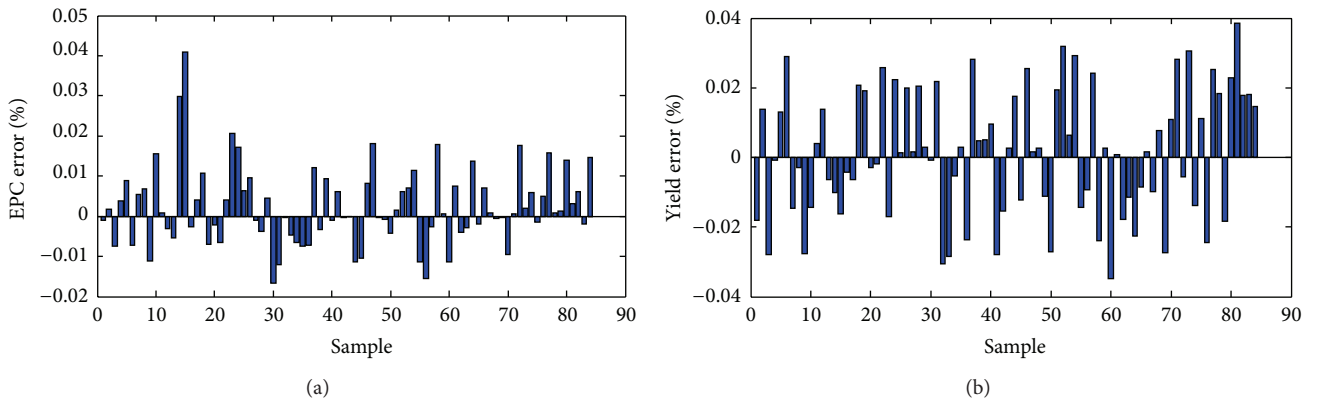


FIGURE 5: The percentage error of GRNN model.

further verify the performance of the model. The result is as shown in Table 3. Consider

$$E_{MS} = \sqrt{\frac{\sum (y - x)^2}{n - 1}} \tag{8}$$

$$E_R = \sum \left( \frac{|y - x|}{x} \right),$$

where  $x$  is the observed value and  $y$  is the prediction value;  $n$  is the dimensionality of  $x$  and  $y$ .

From the simulation results, it can be found that the simulated values match well with the measured values. This proves that the GRNN model of beam pumping system is stable and reliable and could be regarded as a knowledge source for follow-up parameters optimization.

**4.3. Optimal Parameters Searching by SPEA2.** As discussed in Section 3.3, the searching boundaries should be set at first. It is not difficult to understand that the parameters should not fluctuate too drastically, and then using the statistical range of each parameter as the boundary will be reasonable. The boundaries of the five inputs are shown in Table 4.

In experiments, the initial population is set to 50. Then the maximum generations are set to 20, 50, 100, and 200, respectively, to find the optimum generation. Figure 6 illustrates the result of Pareto frontiers when the maximum generation is 20, 50, 100 and 200, respectively. From Figure 6, it can be seen that when the maximum generation is 100, the Pareto front is basically stable. And hence, we set the generation to 100. In this case, there are 61 sets of optimum solutions. Some instances of the optimum solutions are shown in Table 5.

From Table 5, we find that the optimal number of punching is bigger than the original setting, which confirms with the fact that big number of punching will achieve high system efficiency. Comparing the optimized results and the original data, there are above 3.75% decreasing of the electric power consumption and above 5.34% increasing of the oil yield. It verifies the correctness of obtaining optimum decision parameters.

## 5. Conclusions

This paper presents a novel way to saving the energy consumption of beam pumping system by general regression neural network modeling and improved strength Pareto

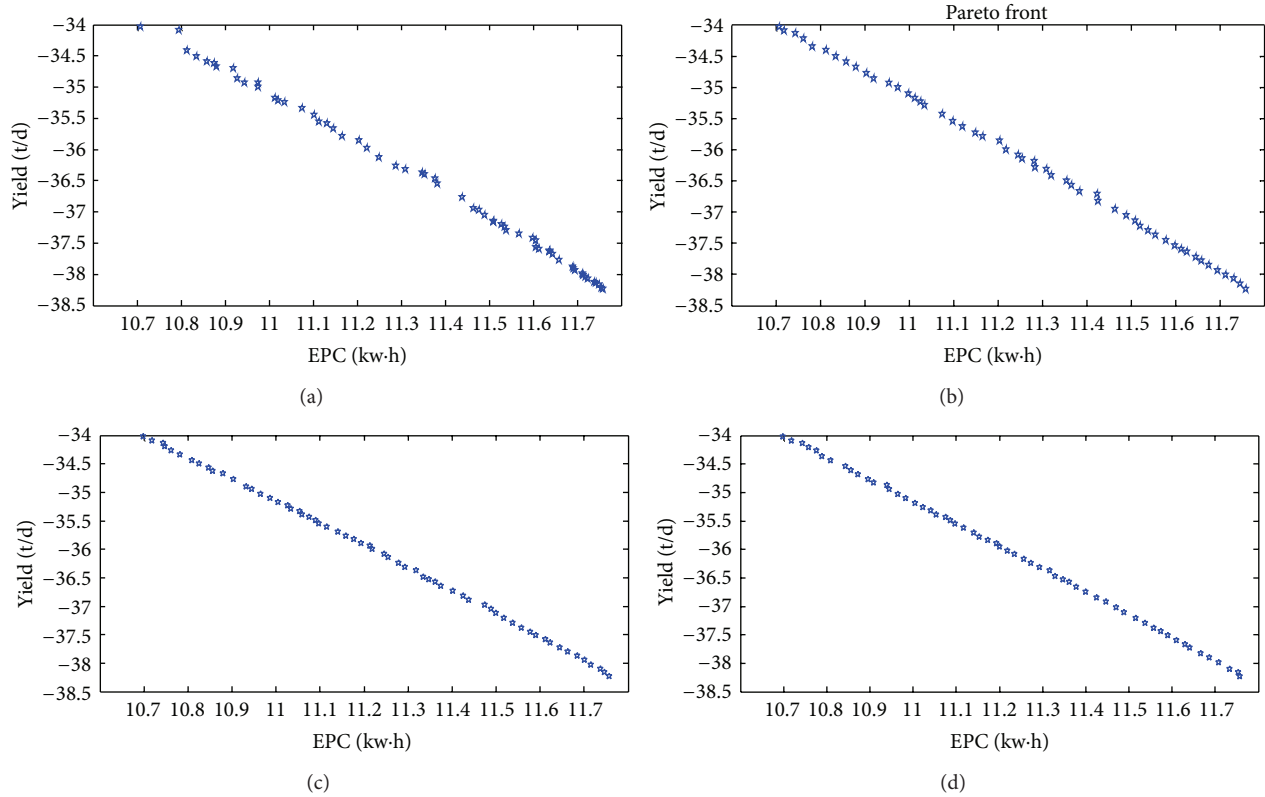


FIGURE 6: SPEA2 Pareto frontier when the maximum generations are 20, 50, 100, and 200. (a) Maximum generation is 20, (b) maximum generation is 50, (c) maximum generation is 100, and (d) maximum generation is 200.

TABLE 4: Searching boundaries of the parameters.

Boundary	NP	MAXL	MINL	ES	EPC
Upper	2.5	93.3	42.3	3.1	71
Lower	3.5	93.5	42.5	3.2	72

TABLE 5: Instances of solutions of Pareto optimal set.

Number	NP (time/min)	MAXL (kN)	MINL (kN)	ES (m)	CPE (%)	EPC (kw)	OY (t/d)
1	3.29	93.3	42.3	3.1034	71.2198	11.1938	35.89
2	3.29	93.4	42.3	3.1029	71.0810	11.5908	37.51
3	3.29	93.5	42.3	3.1030	71.3858	11.3190	36.37
4	3.31	93.5	42.5	3.1999	71.9633	11.3349	36.48
⋮	⋮	⋮	⋮	⋮	⋮	⋮	⋮
61	3.28	93.3	42.3	3.1000	71.3138	11.0982	35.54

evolutionary optimization. This method need not modify the original equipment but just tries to make the equipment work in energy-saving status. Experimental results on 3234 real samples from a certain oilfield show that the performance of the beam pumping system is significantly improved after using the optimum parameters. Specifically, the electric power consumption decreases more than 3.75% and the oil yield increases more than 5.34%. It verified that the proposed method is an alternative effective solution for energy saving of oilfield.

This paper puts forward a feasible solution for the intensive production of oilfield; however, the achieved result is not a determinate solution but a set of Pareto fronts. How to find the robust optimal solution to guide the production will be our future research direction.

### Conflict of Interests

The authors declare that there is no conflict of interests regarding the publication of this paper.

## Acknowledgments

Thanks are due to the support by Chongqing National Science Foundation (cstc2013jcyA40044), National Natural Science Foundation of China (51375520), and Research Foundation of Chongqing University of Science and Technology (CK2011B06 and CK2013Z11).

## References

- [1] L. P. Bai, W. Z. Ma, and Y. Yang, "The discussing of energy-saving of motor for beam balanced pump," *Oil Machinery*, vol. 27, no. 3, pp. 41–44, 1999.
- [2] D. S. Su, X. G. Liu, and W. X. Lu, "Overview of energy-saving mechanism of beam-balanced pump," *Oil Machinery*, vol. 19, no. 5, pp. 49–63, 2001.
- [3] J. Zhu, J. Q. Ruan, and H. F. Sun, "Comparative test study of energy-saving pumping and their effect," *Oil Field Equipment*, vol. 35, no. 3, pp. 60–62, 2006.
- [4] D.-M. Guo, F. Guan, Y.-M. Zhu, and Y.-Z. Liu, "Improved design of CYJY12-4. 8-73HB offset pumping unit support," *Journal of Jianghan Petroleum Institute*, vol. 27, no. 2, pp. 258–260, 2005.
- [5] Y. H. Gu, W. S. Xiao, X. X. Zhou, S. C. Zhang, and Y. H. Jin, "Full scale test of ZXCY-Series linear motor pumping units," *Petroleum Exploration and Development*, vol. 35, no. 3, pp. 366–372, 2008.
- [6] W. Li, Q. Yi, J. Cao, and L. Li, "The optimization calculation and analysis of energy-saving motor used in beam-pumping unit based on continuous quantum particle swarm optimization," in *Proceedings of the International Conference on Power System Technology (POWERCON '10)*, pp. 1–8, 2010.
- [7] M. V. O. Corpoven, "Real time expert system (R.T.E.S.) for rod pumping optimization," in *Proceedings of the Petroleum Computer Conference*, pp. 53–60, Society of Petroleum Engineers (SPE), Houston, Tex, USA, June 1995.
- [8] W.-G. Qi, X.-L. Zhu, and Y.-L. Zhang, "Study of fuzzy neural network control of energy-saving of oil pump," *Proceedings of the Chinese Society of Electrical Engineering*, vol. 24, no. 6, pp. 137–140, 2004.
- [9] G. Zahedi, F. Parvizian, and M. R. Rahimi, "An expert model for estimation of distillation sieve tray efficiency based on artificial neural network approach," *Journal of Applied Sciences*, vol. 10, no. 12, pp. 1076–1082, 2010.
- [10] D. F. Specht, "A general regression neural network," *IEEE Transactions on Neural Networks*, vol. 2, no. 6, pp. 568–576, 1991.
- [11] D. F. Specht, "Probabilistic neural networks," *Neural Networks*, vol. 3, no. 1, pp. 109–118, 1990.
- [12] E. Zitzler, M. Laumanns, and L. Thiele, "SPEA2: improving the strength pareto evolutionary algorithm for multi-objective optimization," in *Evolutionary Methods for Design, Optimisations and Control*, Swiss Federal Institute of Technology, Zürich, Switzerland, 2001.
- [13] E. Zitzler and L. Thiele, "Multiobjective evolutionary algorithms: a comparative case study and the strength Pareto approach," *IEEE Transactions on Evolutionary Computation*, vol. 3, no. 4, pp. 257–271, 1999.

## Research Article

# Hierarchical Agent-Based Integrated Modelling Approach for Microgrids with Adoption of EVs and HRES

**Peng Han, Jinkuan Wang, Yan Li, and Yinghua Han**

*School of Information Science and Engineering, Northeastern University, Shenyang 066004, China*

Correspondence should be addressed to Jinkuan Wang; [wjk@mail.neuq.edu.cn](mailto:wjk@mail.neuq.edu.cn)

Received 16 October 2013; Accepted 12 January 2014; Published 9 April 2014

Academic Editor: M. Montaz Ali

Copyright © 2014 Peng Han et al. This is an open access article distributed under the Creative Commons Attribution License, which permits unrestricted use, distribution, and reproduction in any medium, provided the original work is properly cited.

The large adoption of electric vehicles (EVs), hybrid renewable energy systems (HRESs), and the increasing of the loads shall bring significant challenges to the microgrid. The methodology to model microgrid with high EVs and HRESs penetrations is the key to EVs adoption assessment and optimized HRESs deployment. However, considering the complex interactions of the microgrid containing massive EVs and HRESs, any previous single modelling approaches are insufficient. Therefore in this paper, the methodology named Hierarchical Agent-based Integrated Modelling Approach (HAIMA) is proposed. With the effective integration of the agent-based modelling with other advanced modelling approaches, the proposed approach theoretically contributes to a new microgrid model hierarchically constituted by microgrid management layer, component layer, and event layer. Then the HAIMA further links the key parameters and interconnects them to achieve the interactions of the whole model. Furthermore, HAIMA practically contributes to a comprehensive microgrid operation system, through which the assessment of the proposed model and the impact of the EVs adoption are achieved. Simulations show that the proposed HAIMA methodology will be beneficial for the microgrid study and EV's operation assessment and shall be further utilized for the energy management, electricity consumption prediction, the EV scheduling control, and HRES deployment optimization.

## 1. Introduction

The worldwide constructions of the smart grid technology bring significant development to microgrids, HRES, and EV technology. The microgrid is an integrated energy system consisting of interconnected loads, energy resources, and storages that can operate in parallel with the grid or in the island mode. Due to the needs of distributed generation, such microgrids have been popular over the years of development of the smart grid. And with the integration of HRESs including photovoltaic, wind, and biomass generators, the microgrids can deliver many advantages including reduced cost, increased reliability and security, renewable power generation, and power system optimization, bringing significant benefits to the grid enterprises and the public [1, 2]. However, the variety of renewable energy does not precisely match the time distribution of the electricity demand of the microgrid load, and the considerable oversized deployment of the HRESs for power generation reliability in turn makes

the design costly. Moreover, the EVs' increasing adoption also brings potential challenges to the operations of the microgrid, and, considering the large adoption of EVs in residential areas in the near future, the massive and random recharging activities shall cause severe voltage fluctuations to the microgrid [3, 4]. Besides, the additional power generation for EVs might be idle for most of the time, which further degrades the microgrid efficiency and infrastructure utilization [5, 6].

Therefore, considering the complex operations and interactions of EVs and HRESs in the microgrid, the proper HRESs deployment assessment and EV-recharging prediction are the keys for minimizing the microgrid operation cost and maximizing the utilization of the HRES power volatility. And the modelling methodology for the microgrid with high penetrations of HRES and EVs is fundamental and critical to enable those abilities [7]. In recent years, various mathematical modelling techniques have been developed by many researchers, and the performance of the microgrid component is either modelled by deterministic or

probabilistic approaches. Bazan and German [8] proposed a hybrid simulation approach for the analysis of the domestic homes equipped with different microgenerations and storage devices, but the study lacks the analysis on the microgrid operations. Petermann et al. [9] and Weniun et al. [10] proposed a multiagent control model for microgrid and a two-layer control system of microgrid is built; however, the EVs' impact is not considered.

Considering the model of microgrid power system with HRES and loads from EVs and from original consumers, this paper develops the methodology named Hierarchical Agent-based Integrated Modelling Approach (HAIMA). HAIMA also constitutes a flexible simulation system to further investigate the operation and interactions of the microgrid and EVs.

## 2. Microgrid Analysis with EVs and HRES

The analysis of the microgrid architecture is critical for the development of its model. The microgrid consists of multiple components of HRESs and power load. The HRESs of the microgrid include photovoltaic, wind energy, biomass, and battery storage systems. Meanwhile the multiple load of the microgrid includes the original load, that is, the operation of industrial, commercial electric equipment and residents' home appliances, and the load of EV-recharging consumptions. All the components are connected together through a grid network and under the monitor of the microgrid management center.

Without loss of generality, the schematic figure of the proposed system under study is shown in Figure 1. Besides the mentioned HRES devices and load, the system consists of many power converters operating over a wide range of areas and interconnected with feeders and bus. The microgrid connects the distribution network through a single point of common coupling (PCC) and operates as a single unit. Two main types of EV energy supplement measures, that is, recharging and battery changing, are included in the system. Idle EVs can be recharged by the recharging electric vehicle supply equipment (EVSE) in the parking area or EV-recharging stations, and EVs with commute tasks and with depleted batteries can get a fast refuel service through battery-changing services, while the replaced depleted batteries shall be uniformly charged by the battery-recharging station through the logistics transportation by battery transport vehicles.

The structure in HAIMA is hierarchically divided into three layers: management layer, component layer, and event layer. The management layer consists of the control center and the sensors in the microgrid. It is responsible for communication with the smart grid control center and monitors and controls the flows on the microgrid bus with multiple energy inflows and outflows from the component layer. The component layer is formed by major power generation and consumption components of the microgrid including HRES devices, original electricity consumers, EVs, and service stations. And the event layer mainly focuses on equipment operation and processes in the EV service stations, that is, recharging and battery-changing stations.

## 3. Modelling Methodologies and Rationales

The proposed modelling methodologies of HAIMA are based on the ABM. As a computational approach to study multiagent systems (MASs), ABM has been a rapidly growing area for analyzing the electricity market in the past decade. The theoretical foundation of ABM mainly lies in complex system modelling (CSM), artificial life (AL), and swarm intelligence (SI). The fundamental approach of ABM is to simulate real-world systems with a group of interacting autonomous agents modelled as computer programs, and the agents shall interact with each other in the MAS [11]. As the objects with intelligence, the agents shall form the MAS with unique activity and interactions. And HAIMA adopts this character in modelling microgrid components including HRES devices, EV-recharging stations, and battery-changing stations. The other advantage of ABM is that it could efficiently model the complex behavior of massive system participants [12], which is particularly suitable for modelling massive consumption units such as EVs, enterprises, and residents with distinct characters and behaviors. Those electricity consumption units of the microgrid form up the electricity consumption in the microgrid and constitute an MAS which is well suited for agent-based modelling.

To further enhance the effectiveness of the proposed agents, in the modelling approach the statechart is adopted to specify their states and behaviors. The statechart is a state machine that consists of states containing corresponding actions and transitions that can be triggered by events. Statecharts in HAIMA usually graphically capture the operations and conditions of certain agents and enable fast and convenient structuring of the microgrid model.

The DEM and SDM are also adopted in HAIMA. As a modelling approach based on entities, resources, and block charts, DEM is capable of describing the entity flow and resource sharing. Such process-centric modelling is a medium-low abstraction level modelling approach and is well suited for exactly describing the EV refuel activities in both EV-recharging stations and battery-changing stations because refuel services in those stations can naturally be described as a sequence of operations. SDM is a rigorous modelling method that enables the building of complex systems simulations and the design of more effective policies and organizations [13]. SDM is typically used in long-term, strategic models and has been widely used in energy industries for demand forecasting [14] and energy flow modelling [8]. General system dynamics models consist of stocks and flows connected through auxiliaries depicting a system. And in HAIMA, the SDM is adopted for the management layer to generate energy consumptions and generations in the microgrid.

## 4. Hierarchical Agent-Based Model of Microgrid

*4.1. System Dynamic Modelling for the Management Layer.* In the management layer, SDM is adopted in the study of the energy supply in the microgrid. In this model, the stock

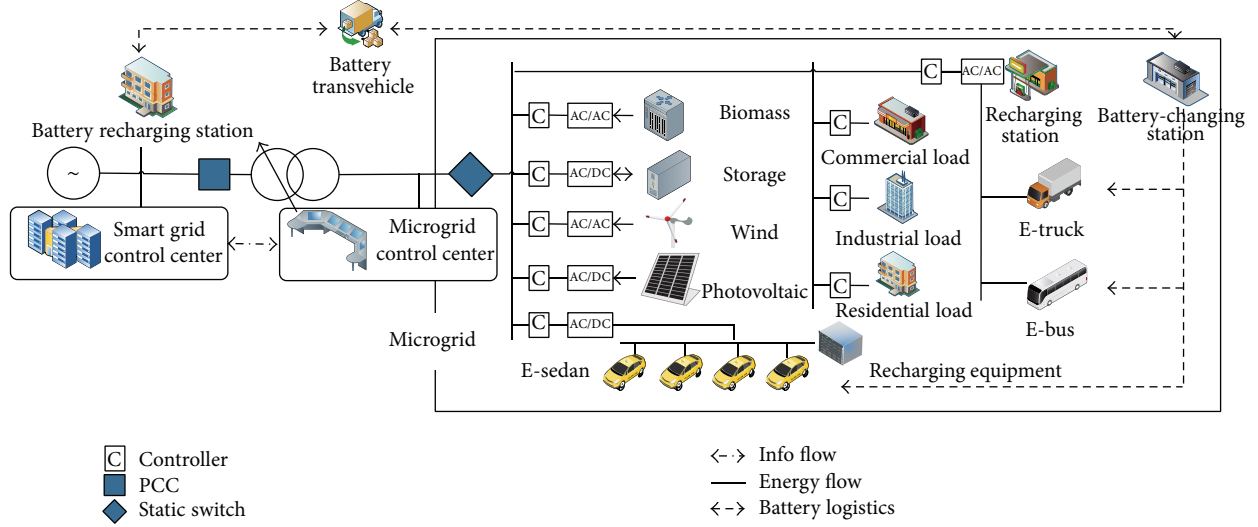


FIGURE 1: Typical HRES structure.

of the microgrid energy comprises inflows and outflows indicating energy generation and consumptions, and those flows are generated by the corresponding components in the component layer while being under the control of the microgrid management center. Figure 2 shows the logical setup of the proposed HAIMA management layer model, where the  $E_{WD}$ ,  $E_{PV}$ , and  $E_{BM}$  denote the energy generated by wind, photovoltaic, biomass generators in the HRES;  $E_{C\&D}$  is the energy flow in or out of the battery storage system depending on its charging or discharging operation;  $E_{RES}$ ,  $E_{IND}$ ,  $E_{COM}$ , and  $E_{EV}$  denote the residential, industrial, commercial, and EV energy consumptions; and  $E_{DSCD}$  is the discarded energy of the HRES. To guarantee the energy balance of the microgrid, the energy demand from the main grid can be calculated from the following equation:

$$E_{GRID} = E_{WD} + E_{PV} + E_{BM} + E_{C\&D} - E_{RES} - E_{IND} - E_{COM} - E_{EV} - E_{DSCD}, \quad (1)$$

and  $E_{GRID}$  is zero when the microgrid is working on islanding mode.

**4.2. Agent-Based Modelling for the Component Layer.** The agent modelling in HAIMA can be divided into two types, where HRES components are modelled as single, complete, static agents operating under the control of the management layer, and the load from residential, commercial, and industrial consumers as well as EVs is modelled as separated autonomous dynamic agents with unique statechart, electricity usage distribution, and so forth in order to utilize the advantages of ABM to generate a bottom-to-top electricity consumption phenomenon.

#### 4.2.1. Modelling of HRES Generation Components

**Wind Power System.** Wind power is one of the most popular renewable energy sources in the microgrid whose power

output at a specific site mainly depends on wind speed turbine characteristics. Typical hourly power output from a wind turbine can be calculated as

$$P_{WD}(t) = \begin{cases} 0, & V(t) \leq V_{\min} \\ AV(t)^3 - BP_r, & V_{\min} < V(t) \leq V_r \\ P_r, & V_r < V(t) \leq V_{\max} \\ 0, & V(t) > V_{\max} \end{cases} \quad (2)$$

where  $P_r$  is the rated power, while  $V_{\min}$ ,  $V_{\max}$ , and  $V_r$  are, respectively, the cut-in, cut-out, and rate speed of the wind turbine,  $V_t$  is the hourly average wind speed, and the factors  $A$  and  $B$  can be calculated as

$$A = \frac{P_r}{V_r^3 - V_{\max}^3}, \quad B = \frac{V_{\min}}{V_r^3 - V_{\min}^3}. \quad (3)$$

Therefore the actual total power output from a wind energy system can be calculated by

$$P_{WE}(t) = P_{WD}(t) A_{WD} \eta_{WD}, \quad (4)$$

where  $A_{WD}$  is the total turbine swept area of the wind energy system and the  $\eta_{WD}$  is the efficiency of the wind turbine generators and converters.

**Photovoltaic System.** The hourly power output from the photovoltaic system with an area  $A_{PV}$  can be calculated by

$$P_{PV}(t) = I_r(t) \eta_{PV} A_{PV}, \quad P_{PV}(t) \leq P_{PV \max}, \quad (5)$$

where  $I_r(t)$  is the total input solar radiation on unit area of the PV surface within an hour, and  $\eta_{PV}$  is the photovoltaic system efficiency.

**Biomass Power System.** Biopower or biomass power utilizes biomass to generate electricity. With the development of

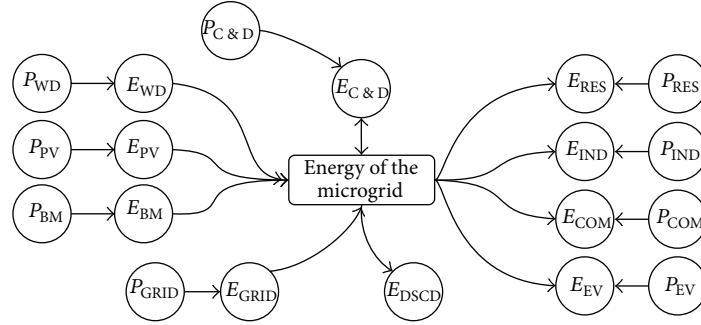


FIGURE 2: Logical setup of the management layer.

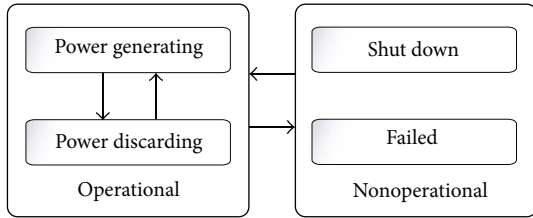


FIGURE 3: Statechart of the HRES generation devices.

biomass power technologies including direct-firing, cofiring, and gasification, biomass has provided a new option of renewable system for the microgrid. The power generated from direct-firing biomass power station can be calculated using

$$P_{BM}(t) = \eta_{BM} P_{BMr}(t), \quad P_{BM}(t) \leq P_{BM \max}, \quad (6)$$

where  $P_{BMr}(t)$  is the rate power at time  $t$  and  $\eta_{BM}$  the biomass power generation efficiency.

**HRES Generation Statechart.** The statechart of the proposed HRES generation devices can be illustrated in Figure 3. It contains four states that describes the main conditions of a renewable generator:

- (1) power generating: the generator is generating power to the microgrid;
- (2) power discarding: the generated power is discarded;
- (3) shut down: the generator is stopped for regular maintenance;
- (4) failed: the generator is temporarily out of work and needs repairs.

#### 4.2.2. Modelling of HRES Storage Components

**Battery Storage System.** In the HRES, battery storage is fundamental to alleviate the fluctuation of the renewable generations. And it is therefore sized to meet the load demand during the nonavailability period of the renewable energy source while absorbing the exceeded power generations in

HRES. The state of charge (SOC) of the battery storage system can be calculated by

$$\text{SOC}_{BS}(t) = \frac{E_{BS}(t)}{E_{BSr}} \times 100\%, \quad (7)$$

where  $E_{BSr}$  is the rated battery energy storage and the current stored energy  $E_{BS}(t)$  can be derived from the following equation:

$$E_{BS}(t) = E_{BS}(t - \Delta t)(1 - \sigma_{BS}) + E_{C\&D}(\Delta t), \quad (8)$$

where  $\sigma_{BS}$  is the hourly self-discharge rate and  $E_{C\&D}(\Delta t)$  is the charged or discharged energy in time period  $\Delta t$  and can be calculated by

$$E_{C\&D}(\Delta t) = \begin{cases} (E_{GE}(\Delta t) - E_L(\Delta t)) \eta_{Bc}, & E_{GE}(\Delta t) > E_L(\Delta t), \\ \frac{(E_{GE}(\Delta t) - E_L(\Delta t))}{\eta_{Bd}}, & E_{GE}(\Delta t) \leq E_L(\Delta t), \\ 0, & \text{else,} \end{cases} \quad (9)$$

where  $E_{GE}(\Delta t)$  and  $E_L(\Delta t)$  are the total generation and load of the microgrid system, while  $\eta_{Bc}$  and  $\eta_{Bd}$  are the recharging and discharging efficiency of the battery.  $E_{C\&D}(\Delta t)$  is subject to the battery maximum recharging and discharging constraints:

$$E_{C\&D \min} \leq E_{C\&D}(\Delta t) \leq E_{C\&D \max}. \quad (10)$$

The six states of the energy storage system are as follows, while the corresponding statecharts are illustrated in Figures 4 and 5:

- (1) recharging: the battery storage system is being recharged by the microgrid;
- (2) discharging: the battery storage system is discharging energy to the microgrid;
- (3) fully recharged: the maximum SOC of the battery storage system has been reached;

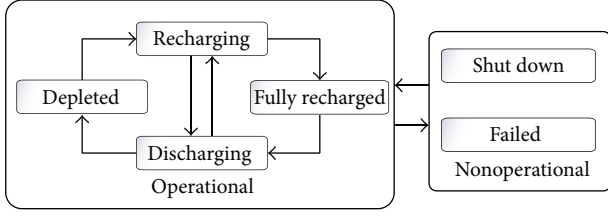


FIGURE 4: Statechart of the HRES energy storage system.

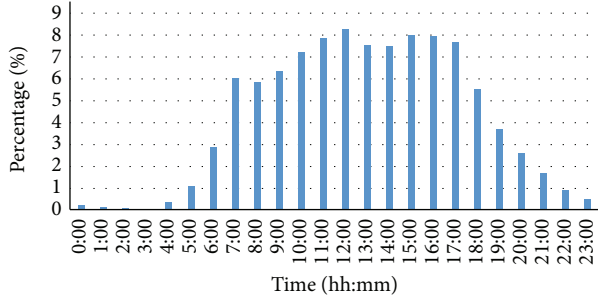


FIGURE 5: Distribution of the trip length.

- (4) depleted: the minimum SOC of the battery storage system has been reached;
- (5) shut down: the battery storage system is stopped for regular maintenance;
- (6) failed: the battery storage system is temporarily out of work and needs repairs.

**4.2.3. Modelling of EVs in the Microgrid.** As an active agent, the EV modelling in the microgrid should consider both the temporal and spatial aspects and the EVs' behaviors. The main parameters impacting the EV energy requirement can be classified into three aspects: environment characters, driver characters, and EV characters. Environment characters include time, weather, climate, distribution of the EV-recharging and battery-changing station, and transportation conditions; driver characters include distributions of driving time and trip length; and EV characters include EV types, rated battery storage, recharging/discharging power, and efficiency. Given those characters, the SOC of the EV agent can be derived in the following equation:

$$\begin{aligned}
 \text{SOC}_{\text{EV}}(t) &= \frac{E_{\text{EV}}(t)}{E_{\text{EVr}}} \times 100\% \\
 &= \frac{E_{\text{EV}}(t - \Delta t)(1 - \sigma_{\text{EV}}) + E_{\text{Charge}}(\Delta t) - E_{\text{Discharge}}(\Delta t)}{E_{\text{EVr}}} \\
 &\quad \times 100\%, \tag{11}
 \end{aligned}$$

where the recharged energy  $E_{\text{Charge}}(\Delta t)$  within time period  $\Delta t$  can be, respectively, calculated by the recharging power  $P_{\text{Charge}}(t)$  in the following equation:

$$E_{\text{Charge}}(\Delta t) = \int_0^{\Delta t} \kappa P_{\text{Charge}}(t) \eta_{\text{Charge}} dt, \tag{12}$$

$$P_{\text{Charge min}} \leq P_{\text{Charge}}(t) \leq P_{\text{Charge max}},$$

where variable  $\kappa$  is zero when EV is not plugged for recharging and is 1 when being recharged. And the total recharging load is

$$P_{\text{EV}}(t) = \sum_{i=1}^N \kappa P_{\text{Charge } i}(t), \tag{13}$$

$$P_{\text{Charge } i \text{ min}} \leq P_{\text{Charge } i}(t) \leq P_{\text{Charge } i \text{ max}}.$$

When EVs are driving on the trips, the discharged energy from the battery within time period  $\Delta t$   $E_{\text{Discharge}}(\Delta t)$  can be calculated with

$$E_{\text{Discharge}}(\Delta t) = \int_0^{\Delta t} \varepsilon P_{\text{Discharge}}(v(t)) dt, \tag{14}$$

$$0 \leq v(t) \leq v_{\text{max}},$$

where  $v(t)$  is the EV velocity and variable  $\varepsilon$  is zero when EV is parked and is 1 when being driven for a trip. Besides, assuming the transition from ordinary internal-combustion engine vehicle to the electric vehicle will not apparently change the resident driving behaviors, the distribution of the trip length  $l$  in this model is derived from the latest National Household Travel Survey report (NHTS 2009) in the United States, as is shown in Figure 5.

With the proposed key agent parameters, the EV agents' behavior can be derived through a series of functions. And the main behavior influencing the microgrid is the EV refuelling decision between EV recharging and battery changing. And with plenty of EVSEs available at parking lots of office buildings as well as a residential area, an ideal decision process for EV drivers is shown in Figure 6. The EVs finished tripping shall find whether there are available EVSEs to get a temporary refuelling, and when there are no available EVSEs while the EV battery is close to depleted, EVs shall go for the nearest ERS to get recharged and then wait for the next trip. Trip-unfinished EVs with nearly depleted batteries shall go to the nearest BCS and go on trips after the batteries have been changed.

Based on the proposed agent's behavior, the EV agents' states in the model can be described in the statechart as shown in Figure 7:

- (1) go tripping: the EV starts one trip of a day;
- (2) trip ending: the EV ends one trip of a day;
- (3) heading for BCS: the EV goes to the battery-changing station for refuelling;
- (4) heading for RS: the EV goes to the EV-recharging station for refuelling;

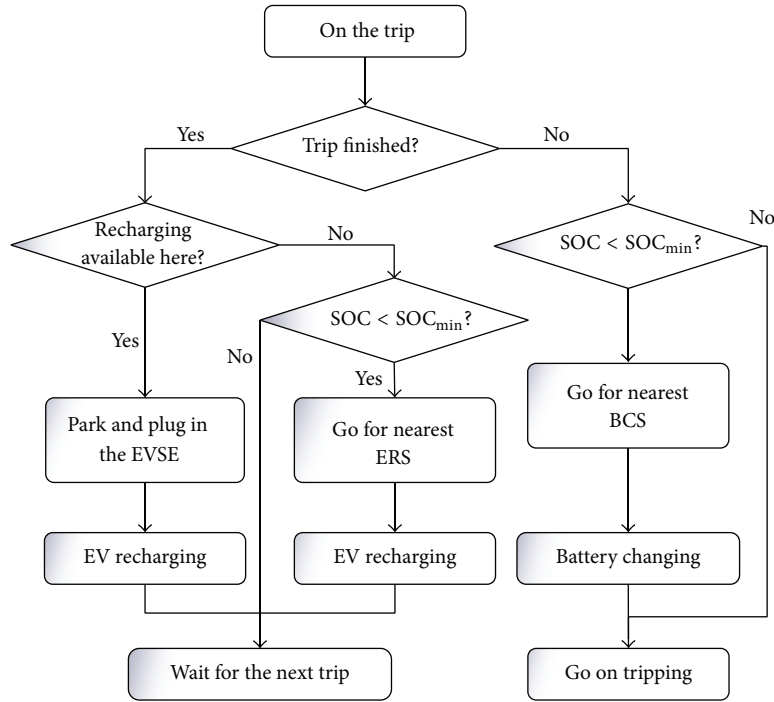


FIGURE 6: Decision process for EV driver.

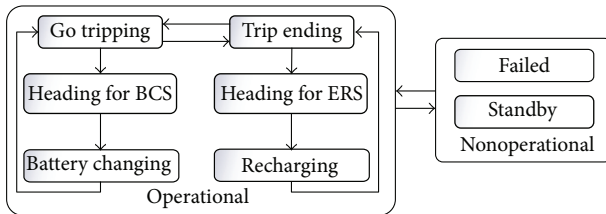


FIGURE 7: Statechart of the EV agent.

- (5) battery changing: the EV is under the service of battery changing;
- (6) recharging: the EV is under the recharging service;
- (7) standby: the EV ends all series of trips of a day;
- (8) failed: the EV encounters a breakdown and needs repairs.

**4.2.4. Modelling of the Original Microgrid Load.** The original load of the microgrid is mainly formed by residential, commercial, and industrial load and is mainly influenced by characters including population, electrical appliance types, and energy consumption per capita. In HAIMA, with the preset population and proportion of the microgrid, static agents have been adopted to represent the residential houses, commercial and industrial buildings, and other electrical appliances. Apart from the recharging load from EVs, the massive introduction of HRES and EVs does not apparently impact the load distribution and power consumption of a certain area, and the original load curves from residential,

commercial, and industrial load can be adopted to generate the original load agent.

**4.3. Discrete-Event Modelling for the Event Layer.** DEM is proposed to model the inner operation in EV-recharging stations as well as battery-changing stations to capture the detailed refuel event of EVs. The service ability, congestion situation, can therefore be observed and further improved to raise EV customer service satisfaction. In HAIMA, EVs and their batteries are all passive entities that travel in the stations through a series of blocks representing processes of the recharging/battery-changing service sequence, as illustrated in Figure 8, where the basic processes of the two sequences are waiting for service, applying for resources, being serviced, and departures. The service during time can be calculated, respectively, in

$$T_{ERS} = T_{Wait} + T_{Charge} + T_{ExERS}, \quad (15)$$

$$T_{BCS} = T_{Wait} + T_{Change} + T_{ExBCS}, \quad (16)$$

where the waiting time  $T_{Wait}$  is affected by the congestion conditions in the stations; the service time  $T_{Charge}$  is, respectively, affected by the EV SOC and recharging power;  $T_{Change}$  is due to battery-changing efficiency; and  $T_{ExERS}$ ,  $T_{ExBCS}$  are the extra auxiliary services provided by the stations.

**4.4. Interactions between Layers.** The interconnections and interactions are critical to the integrated operation of HAIMA. The communications between management layer and component layers are established in the model to transmit the data and control messages; therefore in component

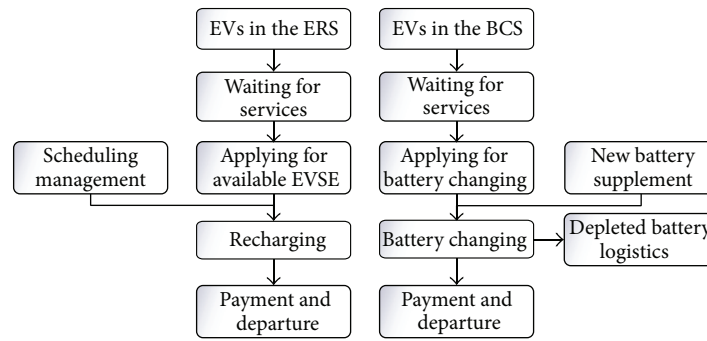


FIGURE 8: Process of the EV agent in ERS and BCS.

layer the component agents' behaviors can be controlled and their key parameters can then feedback to update the flow variables in the SDM of the management layers, which enables HAIMA to simulate the monitoring of the grid bus and the real-time control of the HRES. The EV agent in the component layer also serves as triggers to the event layers. With the EV agent states changing, relative blocks of the DEM will trigger the corresponding process in response, and the entities process of the DEM shall in turn trigger the transitions of the relevant EV agent statechart. The synchronization is also important for the model and should be guaranteed through time triggers.

## 5. Comprehensive Simulation System for the Microgrid

In order to support systematically in-depth exploration of the microgrid operation and energy consumers' behavior, the comprehensive simulation system is built which enables microgrid components to operate and interact with arbitrary virtual environments, enabling broader experimentation for the study of the HRESs and EVs in the microgrid.

The main interface of the simulation system in HAIMA is implemented by the AnyLogic software. As the only simulation tools that support DEM, ABM, and SDM, AnyLogic's object-oriented model design paradigm provides for modular, hierarchical, and incremental construction of large models [15]. In the simulation system of HAIMA, management layer is modelled with the SDM approach in AnyLogic, while agents of the component layer are implemented as JAVA objects, and the proposed agent behaviors, parameters, and statecharts can also be well constructed with AnyLogic provided functions, parameter widget, and the statechart pallet. Moreover, EVs agents in the simulation system are modelled dynamically on the microgrid traffic environment, which can help visualizing EV-caused emerging phenomenon such as traffic congestions in EV-recharging stations and battery-changing stations. To ensure the flexibility of the model, each component agent of the microgrid model is encapsulated to be independent active class object, and message ports as well as communication rules are also embedded on those objects to enable their interactions and communications among different agents and between different layers. The event layer

is implemented by the AnyLogic Enterprise Library. The main process of the battery-changing station is shown in Figure 9, where upper blocks marked in italic notes denote the sequence of the translation vehicle for the depleted batteries and recharged new batteries, while the roman notes marked blocks below are the sequence of the EVs with depleted batteries.

To make the system visual and interactive, many charts and graphics are adopted in the model. Animations including elementary graphical shapes as well as various types of indicators and graphs are developed to enable real-time illustration of the operation data in HAIMA. The user interaction is also considered in the simulation system. Interactive elements such as sliders, buttons, and text inputs are used to control the model's execution at run time, while the control panel and user interfaces of them are well designed. Moreover, the simulation system also prepares the open architecture and sockets for the database connection. This enables the real-time data exchange to the other software, databases, and microgrid utilities. With the advantages of AnyLogic to incorporate spatial data, GIS maps are used in HAIMA simulation system to generate the location of recharging stations and battery-changing stations.

With the reusable active objects, visual interactive elements, and function to import database and GIS data, the constructed simulation system is visual, flexible, and extensible, and besides HAIMA model, the component-based design of the system allows it for the efficient creation of new case studies including centralized/decentralized control design, microgrid islanding mode, and dynamic power flow computing.

## 6. Computer Simulation and Analysis

The Monte Carlo simulation is carried out to verify the effectiveness of the proposed microgrid model and simulation system. The electricity grid load consults are from the real load of the Electric Reliability Council of Texas (ERCOT) [16]. ERCOT is an isolated electrical system that manages the flow of electric power to 23 million customers in Texas [17], while the latest residential electricity consumption is 37.6% [18]. Considering the large-scale EV data is not presently available, the paper reasonably assumes a microgrid with one-thirty-thousandth Texas population, that is, 2300 residents in

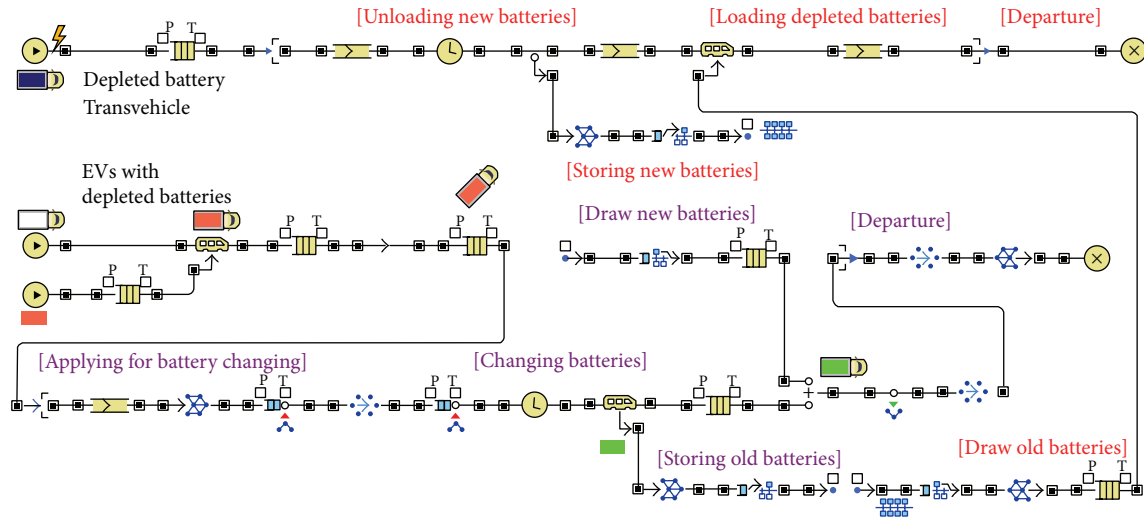


FIGURE 9: Main process of the battery-changing station.

Austin and TX, and with several industrial and commercial loads. The main information of HRES component and EV parameters used in the simulation is given in Table 1. The environment characters of Austin are acquired from the system advisor model (SAM) provided by the National Renewable Energy Laboratory (NREL), and the EV users' behavior is derived from the NHTS 2009.

Considering the reduction of the carbon emission, wind turbines and photovoltaic panels are firstly enabled to feed the energy consumptions, and extra generations can be absorbed by the unfulfilled battery storage system. The biomass generator is enabled only when the energy requirement of the load exceeds the outflow of the wind, photovoltaic, and battery storage systems. And the main grid shall supply insufficient energy when the total required energy goes beyond all the HRES generations in the microgrid.

Firstly, assume the EVSEs have been fully adopted in the proposed microgrid, and EVs shall immediately be recharged once parked. Therefore the simulation of microgrid energy supply and consumption is shown in Figures 10 and 11 based on the proposed parameters. Figure 10 indicates that wind and photovoltaic systems provide the most of the energy, the battery storage system, after recharged by the photovoltaic system at noon, and can supply the evening and night load with biomass systems, and the main grid only provides the exceeding energy at night peak. The energy consumption constitution in Figure 11 indicates that the recharging load conducts a severe grid fluctuation to the original load due to the convenient recharging facilities. The energy requirement caused by mass uncoordinated recharging activity significantly reshapes the original grid load power profile and enlarges the peak time as well as the peak value. And due to the battery storage system volume and power limitation, some generated energy by photovoltaic is discarded.

Then reduced the EVSE penetration ratio to be 60% and the corresponding simulation results are shown in Figures 12 and 13. It can be comparably concluded that electricity grid with fewer EVSEs enjoys a relatively stable recharging

load in peak hours, and fewer main grid energy supply is required. However the photovoltaic generated energy at noon is largely discarded, which indicates that the HRES battery storage system is insufficient and the photovoltaic generated energy exceeds the peak need of the microgrid. Further configuration optimization is in need with the simulation result of HAIMA.

Besides, the recharging and battery-changing times in continuous 48 hours are shown in Table 2. The large penetration of the EVSE shall reduce the need for battery-changing service but in turn significantly improves the recharging times and the energy consumption from the microgrid, causing enlarged PARs and reducing the independence of the microgrid. However, fewer EVSE penetration shall lead to the need of more battery-changing station, and a proper configuration of HRES is also in need.

## 7. Conclusion

Multiple modelling approaches have been developed in the research of the microgrid with EVs and HRESs, and by integrating them this paper proposes the hybrid agent-based integrated modelling methodology while developing a comprehensive simulation system. A hierarchical microgrid structure is proposed and with the integration of ABM, DEM, and SDM, the modelling methodology for each layer is proposed. Furthermore, based on the integrated modelling methodology, a visual, flexible, and extensible microgrid simulation system is designed to verify its effectiveness. The simulation examples indicate that the proposed model can well reflect the energy generation and consumptions in the microgrid, and HRES configuration defects, EV facility utilization, and the impact of EVs recharging load in a different time and penetrations can be reflected in detail. With the establishment of the proposed HAIMA and combining with the actual grid data and latest travel information, the impact of various parameters imported by the energy policy, scheduling management, weather and climate, population,

TABLE 1: HRES components and EV parameters in the microgrid.

HRES component	Type	Total number	Rate power
Wind turbine	Endurance E3120	10	50 kW
Photovoltaic panel	Sharp ND-62RU1	1000	1.1 kW
Battery storage	Hoppeche 600	1000	0.2 kW
Biomass generator	Grate stoker furnace	1	700 kW
Electric vehicle	Nissan LEAF	500	3.3 kW

TABLE 2: Statistics of PEV traveling in the microgrid.

EVSE penetration	Total EVs	Simulation time	Recharging times	Battery-changing times
100%	1700	48 h	4820	10
60%	1700	48 h	1950	110

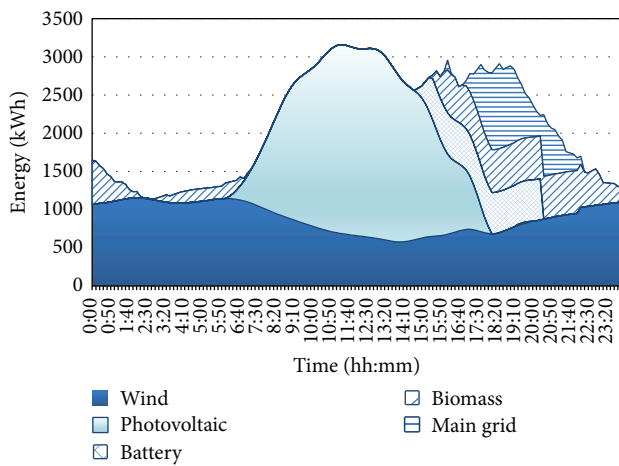


FIGURE 10: HRES energy supply with 100% EVSE penetration.

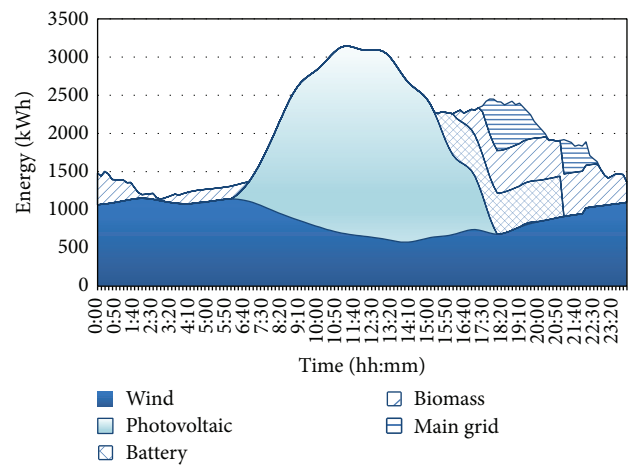


FIGURE 12: HRES energy supply with 60% EVSE penetration.

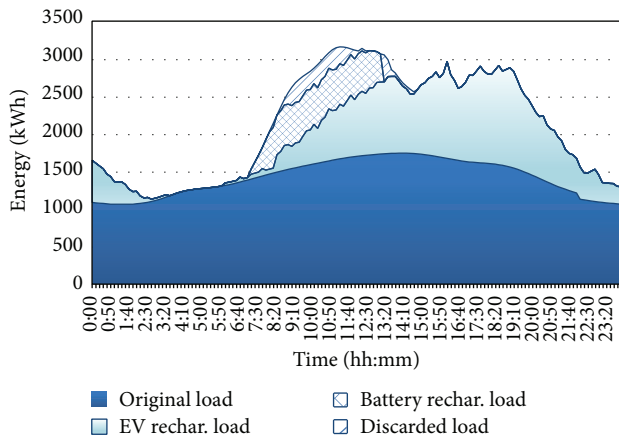


FIGURE 11: HRES energy consumption with 100% EVSE penetration.

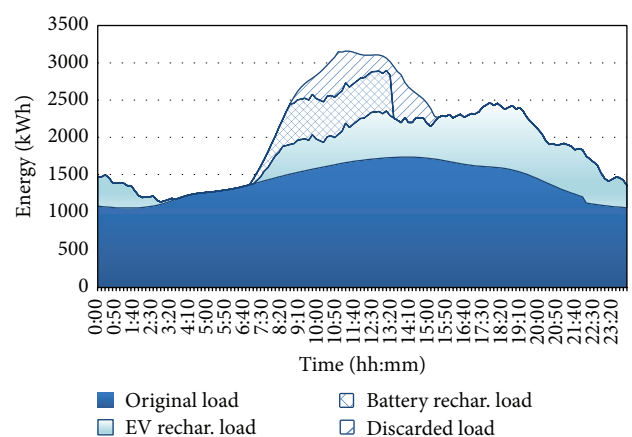


FIGURE 13: HRES energy supply with 60% EVSE penetration.

and personal behaviors can be tested in risk-free space at a very low cost, which will help to strategize the microgrid management, HRES optimized configuration, and EVs optimized scheduling as well as refuel facility construction.

### Conflict of Interests

The authors declare that there is no conflict of interests regarding the publication of this paper.

## Acknowledgments

This work is supported by the National Natural Science Foundation of China under Grants no. 61374097 and no. 201202073 and Science and Technology Research Project of Higher Education of Hebei Province under Grant no. QN20132010. The authors would also like to sincerely thank the AnyLogic Company (formerly XJ Technologies) and Beijing Greena Tech Ltd. for providing the necessary software in accomplishing the modelling and simulation work.

## References

- [1] Navigant Consulting, Microgrids Research Assessment-Phase 2, 2006.
- [2] EPRI/NRDC, Environmental Assessment of Plug-In Hybrid Electric Vehicles, 2007.
- [3] P. Han, J. Wang, Y. Han, and Y. Li, "Resident plug-in electric vehicle charging modeling and scheduling mechanism in the smart grid," *Mathematical Problems in Engineering*, pp. 1–8, 2014.
- [4] P. Han, J. Wang, and Y. Han, "Dynamic-priority-based real-time charging management for plug-in electric vehicles in smart grid," *Journal of University of Science and Technology of China*, vol. 42, no. 6, pp. 100–105, 2012.
- [5] J. T. Salihi, "Energy requirements for electric cars and their impact on electric power generation and distribution systems," *IEEE Transactions on Industry Applications*, vol. 9, no. 5, pp. 516–532, 1973.
- [6] A. Y. Saber and G. K. Venayagamoorthy, "Plug-in vehicles and renewable energy sources for cost and emission reductions," *IEEE Transactions on Industrial Electronics*, vol. 58, no. 4, pp. 1229–1238, 2011.
- [7] M. K. Deshmukh and S. S. Deshmukh, "Modeling of hybrid renewable energy systems," *Renewable and Sustainable Energy Reviews*, vol. 12, no. 1, pp. 235–249, 2008.
- [8] P. Bazan and R. German, "Hybrid simulation of renewable energy generation and storage grids," in *Proceedings of the Winter Simulation Conference*, 2012.
- [9] C. Petermann, S. Ben Amor, and A. Bui, "A complex system approach for a reliable smart grid modeling," *Advances in Knowledge-Based and Intelligent Information and Engineering Systems*, pp. 149–158, 2012.
- [10] W. Weniun, H. Wei, S. Yunling, and W. Guannan, "Study on control model of microgrid based on multi-agent method," *Modern Electric Power*, vol. 29, no. 5, pp. 6–11, 2012.
- [11] S. J. Russell and P. Norvig, *Artificial Intelligence: A Modern Approach*, Prentice Hall, Upper Saddle River, NJ, USA, 2nd edition, 2003.
- [12] Z. Zhou, W. K. Chan, and J. H. Chow, "Agent-based simulation of electricity markets: a survey of tools," *Artificial Intelligence Review*, vol. 28, no. 4, pp. 305–342, 2007.
- [13] J. Sterman and J. D. Sterman, *Business Dynamics: Systems Thinking and Modeling for a Complex World with CD-ROM*, McGraw-Hill, Irwin, Pa, USA, 2000.
- [14] S. A. Akhwanzada and R. M. Tahar, "Strategic forecasting of electricity demand using system dynamics approach," *International Journal of Environmental Science and Development*, vol. 3, no. 4, pp. 328–333, 2012.
- [15] AnyLogic-Multimethod Simulation Software and Solutions, <http://www.anylogic.com/>.
- [16] FERC Annual Electric Balancing Authority and Planning Area Report, <http://www.ferc.gov/docs-filing/forms.asp#714>.
- [17] A. Rachakonda, *Potentially Available Natural Gas Combined Cycle Capacity: Opportunities for Substantial CO<sub>2</sub> Emissions Reductions*, Massachusetts Institute of Technology, Cambridge, Mass, USA, 2010.
- [18] P. Han, J. Wang, Y. Han et al., "Assessment of smart grid pev charging management in grid safety and environmental impact," *Advances in Information Sciences and Service Sciences*, vol. 4, no. 13, pp. 144–152, 2012.

## Research Article

# Solving Dynamic Traveling Salesman Problem Using Dynamic Gaussian Process Regression

**Stephen M. Akandwanaho, Aderemi O. Adewumi, and Ayodele A. Adebisi**

*School of Mathematics, Statistics and Computer Science, University of KwaZulu-Natal, University Road, Westville, Private Bag X 54001, Durban, 4000, South Africa*

Correspondence should be addressed to Stephen M. Akandwanaho; [stephen.akandwanaho@gmail.com](mailto:stephen.akandwanaho@gmail.com)

Received 4 January 2014; Accepted 11 February 2014; Published 7 April 2014

Academic Editor: M. Montaz Ali

Copyright © 2014 Stephen M. Akandwanaho et al. This is an open access article distributed under the Creative Commons Attribution License, which permits unrestricted use, distribution, and reproduction in any medium, provided the original work is properly cited.

This paper solves the dynamic traveling salesman problem (DTSP) using dynamic Gaussian Process Regression (DGPR) method. The problem of varying correlation tour is alleviated by the nonstationary covariance function interleaved with DGPR to generate a predictive distribution for DTSP tour. This approach is conjoined with Nearest Neighbor (NN) method and the iterated local search to track dynamic optima. Experimental results were obtained on DTSP instances. The comparisons were performed with Genetic Algorithm and Simulated Annealing. The proposed approach demonstrates superiority in finding good traveling salesman problem (TSP) tour and less computational time in nonstationary conditions.

## 1. Introduction

A bulk of research in optimization has carved a niche in solving stationary optimization problems. As a corollary, a flagrant gap has hitherto been created in finding solutions to problems whose landscape is dynamic, to the core. In many real-world optimization problems a wide range of uncertainties have to be taken into account [1]. These uncertainties have engendered a recent avalanche of research in dynamic optimization. Optimization in stochastic dynamic environments continues to crave for trailblazing solutions to problems whose nature is intrinsically mutable. Several concepts and techniques have been proposed for addressing dynamic optimization problems in literature. Branke et al. [2] delineate them through different stratifications, for example, those that ensure heterogeneity, sustenance of heterogeneity in the course of iterations, techniques that store solutions for later retrieval and those that use different multiple populations. The ramp up in significance of DTSP in stochastic dynamic landscapes has, up to the hilt, in the past two decades attracted a raft of computational methods, congenial to address the floating optima (Figure 1). An in-depth exposition is available in [3, 4]. The traveling salesman

problem (TSP) [5], one of the most thoroughly studied NP-hard theory in combinatorial optimization, arguably remains a main research experiment that has hitherto been cast as an academic guinea pig, most notably in computer science. It is also a research factotum that intersects with a wide expanse of research areas; for example, it is widely studied and applied by mathematicians and operation researchers on a grand scale. TSP's prominence ascribe to its flexibility and amenability to a copious range of problems. Gaussian process regression is touted as a sterling model on account of its stellar capacity to interpolate the observations, its probabilistic nature, versatility, practical and theoretical simplicity. This research lays bare a dynamic Gaussian process regression (DGPR) with a nonstationary covariance function to give foreknowledge of the best tour in a landscape that is subject to change. The research is in concert with the argumentation that optima are innately fluid, cognizant that size, nature, and position are potentially volatile in the lifespan of the optima. This skittish landscape, most notably in optimization, is a cue for fine-grained research to track the moving and evolving optima and provide a framework for solving a cartload of pent-up problems that are intrinsically dynamic. We colligate DGPR with nearest neighbor (NN) algorithm and the iterated

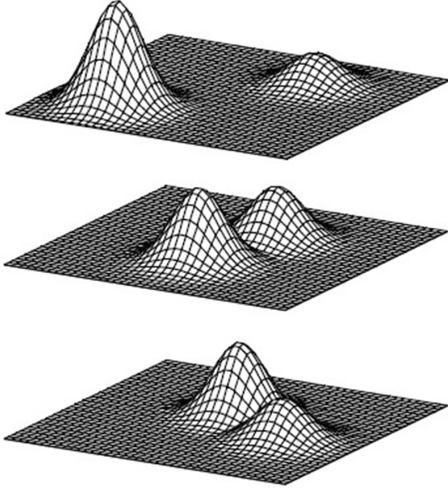


FIGURE 1: Nonstationary optima [6].

local search, a medley whose purpose is to refine the solution. We have arranged the paper in four sections. Section 1 is limited to introduction, Section 2's ambit includes review of all methods that form the mainspring of this work, which include Gaussian process, TSP, and DTSP. We elucidate DGPR for solving the TSP in Section 3. Section 4 discusses results obtained and draws conclusion.

## 2. The Traveling Salesman Problem (TSP)

The first researcher, in 1932, considered the traveling salesman problem [7]. Menger gives interesting ways of solving TSP. He lays bare the first approaches which were considered during the evolution of TSP solutions. An exposition on TSP history is available in [8–10].

*Basic Definitions and Notations.* It is imperative to note that in the gamut of TSP, both symmetric and asymmetric aspects are important threads in its fabric. We factor them into this work through the following expressions.

Basically, a salesman traverses across an expanse of cities culminating into a tour. The distance in terms of cost between cities is computed by minimizing the path length:

$$f(\pi) = \sum_{i=1}^{n-1} d_{\pi(i), \pi(i+1)} + d_{\pi(n), \pi(1)}. \quad (1)$$

We provide a momentary storage,  $D$  for cost distance. The distances between  $n$  cities are stored in a distance matrix  $D$ . For brevity, the problem can also be situated as an optimization problem. We minimize the tour length (Figure 5):

$$\sum_{i=1}^n d_{i, \pi(i)}. \quad (2)$$

The distance matrix of TSP has got certain features which come in handy in defining a set of classes for TSP [11]. If the city point,  $(x_i, y_i)$  in a tour is accentuated; then drawing from

Euclidean distance expression [11], we present the matrix  $C$  between separate distances as

$$c_{ij} = \sqrt{(x_i - x_j)^2 + (y_i - y_j)^2}. \quad (3)$$

Affixed to TSP are important aspects that we bring to the fore in this paper. We adumbrate a brief overview of symmetric traveling salesman problem (STSP) and asymmetric traveling salesman problem (ATSP) as follows.

STSP, akin to its name, ensures symmetry in length. The distances between points are equal for all directions while ATSP typifies different distance sizes of points in both directions. Dissecting ATSP gives us a handle to hash out solutions.

Let ATSP be expressed, subject to the distance matrix. In combinatorial optimization, an optimal value is sought, whereby in this case, we minimize using the following expression:

$$w_{\pi(n), \pi(1)} + \sum_{i=1}^{n-1} w_{\pi(i), \pi(i+1)}. \quad (4)$$

Reference [12] formulates ATSP in integer programming  $n^2 - n$  zero-one variables  $x_{ij}$  or else it is defined as

$$y = \sum_{i=1}^n \sum_{j=1}^n w_{ij} x_{ij} \quad (5)$$

such that

$$\begin{aligned} \sum_{i=1}^n x_{ij} &= 1, & j \in [n], \\ \sum_{j=1}^n x_{ij} &= 1, & i \in [n], \end{aligned} \quad (6)$$

$$\sum_{i \in S} \sum_{j \in S} x_{ij} \leq |S| - 1, \quad \forall |S| < n,$$

$$x_{ij} = 0 \text{ or } 1, \quad i \neq j \in [n].$$

There are different rules affixed to ATSP, inter alia, to ensure a tour does not overstay its one-off visit to each vertex. The rules also ensure that standards are defined for subtours.

In the symmetry paradigm, the problem is postulated. For brevity, we present subsequent work with tautness:

$$y = \sum_{1 \leq i \leq j \leq n} w_{ij} x_{ij} \quad (7)$$

such that

$$\begin{aligned} \sum_{i=1}^n x_{ij} &= 2, & j \in [n], \\ \sum_{i \in S} \sum_{j \in S} x_{ij} &\geq 2, & \forall 3 \leq |S| \geq \frac{n}{2}, \end{aligned} \quad (8)$$

$$0 \leq x_{ij} \leq 1, \quad i \neq j \in [n],$$

$$x_{ij} \quad \forall i \neq j \in [n].$$

TSP is equally amenable to the Hamiltonian cycle [11] and so we use graphs to ram home a different solution approach to the problem of traveling salesman. In this approach, we define  $G = (V, E)$  and  $(e_i \in E)w_i$ . This is indicative of the graph theory. The problem can be seen in the prism of a graph cycle challenge. Vertices and edges represent  $V$  and  $E$ , respectively.

It is also plausible to optimize TSP by adopting both an integer programming and linear programming approaches, pieced together in [13]:

$$\begin{aligned} & \sum_{i=1}^n \sum_{j=1}^n d_{ij} x_{ij}, \\ & \sum_{i=1}^n x_{ij} = 1, \\ & \sum_{j=1}^n x_{ij} = 1. \end{aligned} \tag{9}$$

We can also view it with linear programming, for example,

$$\sum_{i=1}^m w_i x_i = w^T x. \tag{10}$$

Astounding ideas have sprouted, providing profound approaches in solving TSP. In this case, few parallel edges are interchanged. We use the Hamilton graph cycle [11] equality matrix

$$\begin{aligned} & \forall i, j \ d_{ij} = d'_{ij}, \\ & \sum_{i,j \in H} d_{ij} = \alpha \sum_{i,j \in H} d'_{ij} + \beta \end{aligned} \tag{11}$$

subject to  $\alpha > 0, \beta \in \mathbb{R}$ . The common denominator of these methods is to solve city instances in a shortest time possible. A slew of approaches have been cobbled together extensively in optimization and other areas of scientific study. The last approach in this paper is to transpose asymmetric to symmetric. The early work of [14] explicates the concept. There is always a dummy city affixed to each city. The distances are the same between dummies and bona fide cities which makes distances symmetrical. The problem is then solved symmetrically thereby assuaging the complexities of NP-hard problems:

$$\begin{bmatrix} 0 & d_{12} & d_{13} \\ d_{21} & 0 & d_{23} \\ d_{31} & d_{32} & 0 \end{bmatrix} \longleftrightarrow \begin{bmatrix} 0 & \infty & \infty & -\infty & d_{21} & d_{31} \\ \infty & 0 & \infty & d_{12} & -\infty & d_{31} \\ \infty & \infty & 0 & d_{13} & d_{23} & -\infty \\ -\infty & d_{12} & d_{13} & 0 & \infty & \infty \\ d_{21} & -\infty & d_{23} & \infty & 0 & \infty \\ d_{31} & d_{32} & -\infty & \infty & \infty & 0 \end{bmatrix}. \tag{12}$$

**2.1. Dynamic TSP.** Different classifications of dynamic problems have been conscientiously expatiated in [15]. A wide array of dynamic stochastic optimization ontology ranges from a moving morphology to drifting landscapes. The dynamic optima exist owing to moving alleles in the natural

realm. Nature remains the fount of artificial intelligence. Optimization mimics the whole enchilada including the intrinsic floating nature of alleles, which provides fascinating insights into solving dynamic problems. Dynamic encoding problems were proposed by [16].

DTSP was initially introduced in 1988 by [17, 18]. In the DTSP, a salesman starts his trip from a city and after a complete trip, he comes back to his own city again and passes each city for once. The salesman is behooved to reach every city in the itinerary. In DTSP, cities can be deleted or added [19] on account of varied conditions. The main purpose for this trip is traveling the smallest distance. Our goal is finding the shortest route for the round trip problem.

Consider a city population,  $n$  and  $e$ , as the problem at hand where in this case we want to find the shortest path for  $n$  with a single visit on each. The problem has been modeled in a raft of prisms. A graph  $(N, E)$  with graph nodes and edges denoting routes between cities. For purpose of elucidation, the Euclidean distance between cities is  $i$  and  $j$  is calculated as follows [19]:

$$D_{i,j} = \sqrt{(x_i - x_j)^2 + (y_i - y_j)^2}. \tag{13}$$

**2.1.1. Objective Function.** The predictive function for solving the dynamic TSP is defined as follows.

Given a set of different costs  $(P_1, P_2, \dots, P_{n(t)})$ , the distance matrix is contingent upon time. Due to the changing routes in the dynamic setting, time is pivotal. So, it is expressed as a function of distance cost. The distance matrix has also been lucidly defined in the antecedent sections. Let us use the supposition that  $D = d_{ij}(t)$ , and  $i, j = 1, 2, \dots, n(t)$ . Our interest is bounded on finding the least distance from  $P_j$  and  $d_{ij}(t) = d_{ji}(t)$ . In this example, as aforementioned, time,  $t$  and of course, cost,  $d$ , play significant roles in the quality of the solution. DTSP is therefore minimized using the following expression:

$$d(T(t)) = \sum_{i=1}^{n(t)} d_{T_i, T_{i+1}}(t). \tag{14}$$

From Figures 2, 3, and 4, DTSP initial route is constructed upon visiting requests carried by the traveling salesman  $\{A, B, C, D, E\}$  [20]. As the traveling salesman sets forth, different requests  $(X, Y)$  come about which compels the traveling salesman to change the itinerary to factor in the new trip layover demands,  $\{A, B, C, D, X, E, Y\}$ .

**2.2. Gaussian Process Regression.** In machine learning, the primacy of Gaussian process regression cannot be overstated. The methods of linear and locally weighted regression have been outmoded by Gaussian process regression in solving regression problems. Gold mining was the major motivation for this method where Krige, whom Kriging is his brainchild [21], postulated that using posteriori, the cooccurrence of gold is encapsulated as a function of space. With Krige's interpolation mineral concentrations at different points can be predicted.

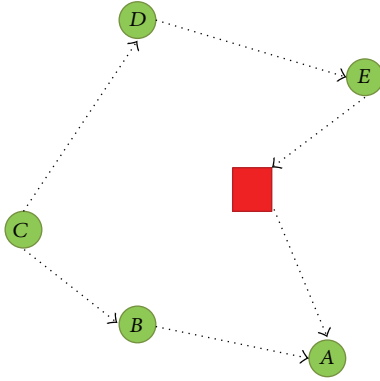


FIGURE 2: Initial request, A, B, C, D, E.

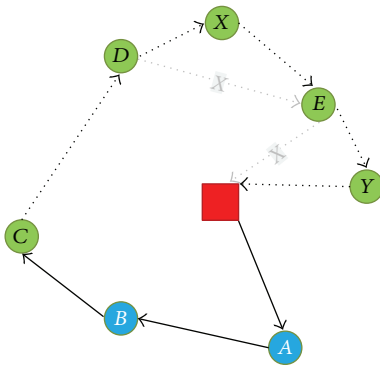


FIGURE 3: New requests for consideration.

In Gaussian process, we find a set of random variables. The specifications include covariance function  $n(x, x')$  and mean function  $p(x)$  that parameterize the Gaussian process. The covariance function determines the similarity of different variables. In this paper, we expand the ambit of study to nonstationary covariance:

$$p(f(x) \cdot f(x')) = N(\mu, \Sigma). \quad (15)$$

In the equation,  $\mu = \begin{pmatrix} \mu(x) \\ \mu(x') \end{pmatrix}$  and  $\Sigma = \begin{pmatrix} K(x,x) & K(x,x') \\ K(x',x) & K(x',x') \end{pmatrix}$ .

The matrices  $n \times 1$  for  $\mu$  and  $n \times n$  for  $\Sigma$  are presented in (15).

GPR (Figure 6) has been extensively studied across the expanse of prediction. This has resulted into different expressions to corroborate the method preference. In this study we have a constellation of training set  $P = (x^i, y^i)_{i=1}^m$ . The GPR model [22] then becomes

$$y^i = h(x^i) + \varepsilon^i \quad (16)$$

subject  $i = 1$  to  $m$ .

The probability density describes the likelihood for a certain value to be assumed by a variable. Given a set of observations bound by a number of parameters:

$$p(y | X, w) = \prod_{i=1}^n p(y_i | x_i, w) \sim N(X^T w, \sigma_n^2 I), \quad (17)$$

In this case, bias is denoted by  $w$ .

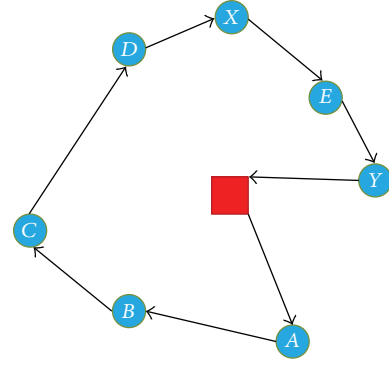


FIGURE 4: Previous route changed to meet new requests given to the traveling salesman.

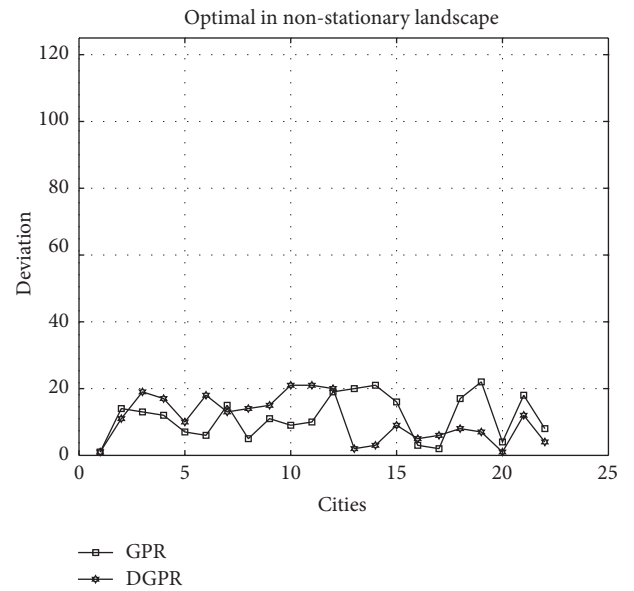


FIGURE 5: Minimum path generated by DGPR.

Gaussian process is analogous to Bayesian with a fractional difference [23]. In one of the computations by the Bayes' rule [23], is the Bayesian linear model parameterized by covariance matrix and mean denoted by  $A^{-1}$  and  $\bar{w}$ , respectively:

$$p(w | X, y) \sim N(\bar{w} = \sigma_n^{-2} A^{-1} X y, A^{-1}), \quad (18)$$

where

$$A = \sigma_n^{-2} X X^T + \sum_P^{-1}. \quad (19)$$

Using posterior probability, the Gaussian posterior is presented as

$$p(f_s | x_s, X, y) \sim N(\sigma_m^{-2} x_s^T A^{-1} X y, x_s^T A^{-1} x_s). \quad (20)$$

Also the predictive distribution, given the observed dataset,

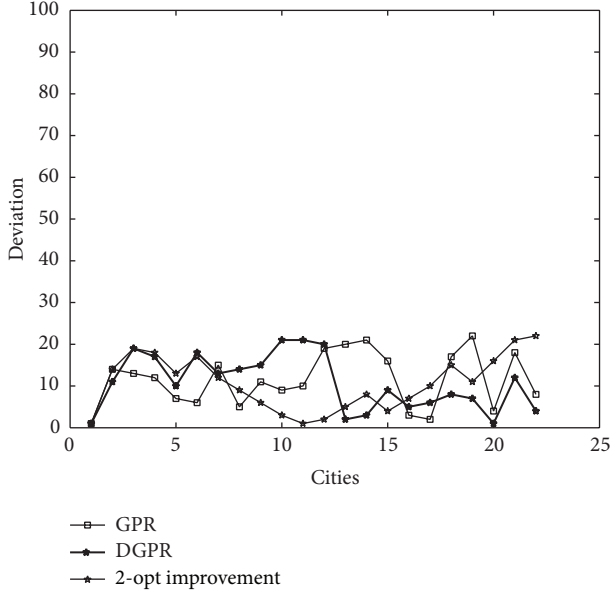


FIGURE 6: DGPR maintains superiority when juxtaposed with GPR and local search.

helps to model a probability distribution of an interval not estimating just a point:

$$p(f_s | x_s, X, y) \sim N(\sigma_m^{-2} \phi_s^T A^{-1} \Phi y, \phi_s^T A^{-1} \phi_s), \quad (21)$$

where by  $\Phi = \Phi(X)$ ,  $\phi_s = \phi(x_s)$ , and  $A = \sigma_n^{-2} \Phi \Phi^T + \sum_p^{-1}$ . If  $A^{-1}$  of size  $n \times n$  is needed when  $n$  is large. We rewrite as

$$N \phi_s^T \sum_p \Phi (K + \sigma_n^2 I)^{-1} y, \quad (22)$$

$$\phi_s^T \sum_p \phi_s - \phi_s^T \sum_p \Phi (K + \sigma_n^2 I)^{-1} \Phi^T \sum_p \phi_s.$$

The covariance matrix  $K$  is  $\Phi^T \sum_p \Phi$ .

**2.2.1. Covariance Function.** In simple terms, the covariance defines the correlation of function variables at a given time. A host of covariance functions for GPR have been studied [24]. In this example,

$$K(x_i, x_j) = v_0 \exp\left(-\left(\frac{x_i - x_j}{r}\right)^\sigma\right) + v_1 + v_2 \delta_{ij}, \quad (23)$$

the parameters are  $v_0$  (signal variance),  $v_1$  (variance of bias),  $v_2$  (noise variance),  $r$  (length scale), and  $\delta$  (roughness). However in finding solutions to dynamic problems, there is a mounting need for nonstationary covariance functions. The problem landscapes have increasingly become protean. The lodestar for this research is to use nonstationary covariance to provide an approach to dynamic problems.

A raft of functions have been studied. A simple form is described in [25]:

$$C^{NS}(x_i, x_j) = \sigma^2 |\Sigma_i|^{1/4} |\Sigma_j|^{1/4} \left| \frac{\Sigma_i + \Sigma_j}{2} \right|^{-1/2} \exp(-\mathbb{Q}_{ij}), \quad (24)$$

With quadratic form,

$$\mathbb{Q}_{ij} = (x_i - x_j)^T \left( \frac{\Sigma_i + \Sigma_j}{2} \right)^{-1} (x_i - x_j), \quad (25)$$

$\Sigma_i$  denotes the matrix of the covariance function.

### 3. Materials and Methods

Gaussian process regression method was chosen in this work, owing to its capacity to interpolate observations, its probabilistic nature, and versatility [26]. Gaussian process regression has considerably been applied in machine learning and other fields [27–29]. It has pushed back the frontiers of prediction and provided solutions to a mound of problems, for instance, making it possible to forecast in arbitrary paths and providing astounding results in a wide range of prediction problems. GPR has also provided a foundation for state of the art in advancing research in multivariate Gaussian distributions.

A host of different notations for different concepts are used throughout this paper:

- (i)  $T$  typically denotes the vector transpose,
- (ii)  $\hat{y}$  denotes the estimation,
- (iii) the roman letters typically denote what constitutes a matrix.

Our extrapolation is dependent on the training and testing datasets from the TSPLIB [30]. We adumbrate our approach as follows:

- (a) input distance matrix between cities,
- (b) invoke Nearest Neighbor method for tour construction,
- (c) tour encoding as binary for program interpretation,
- (d) as a drifting landscape, we set a threshold value  $\theta \in \mathbb{T}$ , where  $\mathbb{T}$  is the tour, and the error rate  $\varepsilon \in \mathbb{T}$  for the predicatability is

$$\forall_{1 \leq j \leq n} 0 < \text{severity } D_T(F_{ij}) \leq \theta, \quad (26)$$

$$\forall_{1 \leq j \leq n} 0 < \text{predict } D_{T,\varepsilon}(F_{ij}) \leq \theta,$$

- (e) get a cost sum,
- (f) determine the cost minimum and change to binary form,
- (g) present calculated total cost,
- (h) initialize the hyperparameters  $(\ell, \sigma_f^2, \sigma_n^2)$
- (i) we use the nonstationary covariance function  $K(X - X') = \sigma_o^2 + xx'$ . Constraints  $y_i = f(x_i + \varepsilon_i)$  realized in the TSP dataset,  $D = (x_i, y_i)_{i=1}^n$ ,  $y_i \in \mathbb{R}$  distances for different cities,  $x_i \in \mathbb{R}^d$ ,
- (j) calculate integrated likelihood in a dynamic regression,

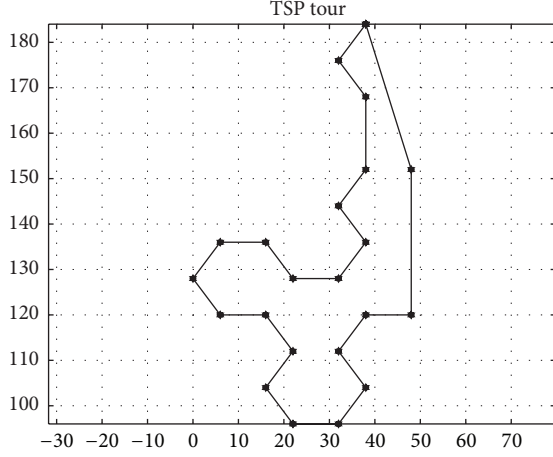


FIGURE 7: Generated tour in a drifting landscape for the best optimal route.

- (k) output the predicted optimal path  $\hat{x}^*$  and its length  $\hat{y}^*$ ,
- (l) implement the local search method  $x^*$ ,
- (m) estimate optimal tour  $\hat{x}^*$ ,
- (n) let the calculated route set the stage for iterations until no further need for refinement,
- (o) let the optimal value be stored and define the start for subsequent computations,
- (p) output optimal  $\hat{x}$  and cost ( $\hat{y}^*$ ).

3.1. *DTSP as a Nonlinear Regression Problem.* DTSP is formulated as a nonlinear regression problem. The nonlinear regression is part of the nonstationary covariance functions for floating landscapes [18]:

$$y_i = f(x_i + \varepsilon_i) \quad (27)$$

and  $D = \{(x_i, y_i)\}_{i=1}^n$  where  $y_i \in \mathbb{R}$ ,  $x_i \in \mathbb{R}^d$ . Our purpose is to define  $p(y^* | x^*, D)$ .

3.1.1. *Gaussian Approximation.* The Gaussian approximation is premised on the kernel, an important element of GPR.

The supposition for this research is that once  $x$  is known,  $y$  can be determined. By rule of thumb, the aspects of a priori (when the truth is patent, without need for ascertainment) and posteriori (when there is empirical justification for the truth or the fact is buttressed by certain experiences) play a critical role in shaping an accurate estimation. The kernel determines the proximate between estimated and nonestimated.

Nonstationarity, on the other hand, means that the mean value of a dataset is not necessarily constant and/or the covariance is anisotropic/varies with direction and spatially variant, as seen in [31]. We have seen a host of nonstationary

kernels in literature as discussed in previous chapters, for example in [32],

$$C^{\text{NS}}(x_i, x_j) = \int_{\mathcal{R}^2} K_{x_i}(u) K_{x_j}(u) du. \quad (28)$$

For  $(x_i, x_j, u) \in \mathcal{R}^2$ ,

$$f(x) = \int_{\mathcal{R}^2} K_x(u) \psi(u) du, \quad (29)$$

For  $\mathcal{R}^p$ ,  $p = 1, 2, \dots$ , we ensure a positive definite function between cities for dynamic landscapes:

$$\begin{aligned} & \sum_{i=1}^n \sum_{j=1}^n a_i a_j C^{\text{NS}}(x_i, x_j) \\ &= \sum_{i=1}^n \sum_{j=1}^n a_i a_j \int_{\mathcal{R}^p} K_{x_i}(u) K_{x_j}(u) du \\ &= \int_{\mathcal{R}^p} \sum_{i=1}^n a_i K_{x_i}(u) \sum_{j=1}^n a_j K_{x_j}(u) du \\ &= \int_{\mathcal{R}^p} \left( \sum_{i=1}^n a_i K_{x_i}(u) \right)^2 du \geq 0. \end{aligned} \quad (30)$$

In mathematics, convolution knits two functions to form another one. This cross relation approach has been successfully applied myriadly in probability, differential equations, and statistics. In floating landscapes, we see convolution at play which produces [31]

$$C^{\text{NS}}(x_i, x_j) = \sigma^2 \sigma^2 |\Sigma_i|^{1/4} |\Sigma_j|^{1/4} \left| \frac{\Sigma_i + \Sigma_j}{2} \right|^{-1/2} \exp(-\mathfrak{Q}_{ij}). \quad (31)$$

In mathematics, a quadratic form reflects the homogeneous polynomial expressed in

$$\mathfrak{Q}_{ij} = (x_i - x_j)^T \left( \frac{\Sigma_i + \Sigma_j}{2} \right)^{-1} (x_i - x_j). \quad (32)$$

A predictive distribution is then defined:

$$\begin{aligned} p(y^* | X^*, D, \theta) &= \int \int p(y^* | X^*, D, \exp(\ell^*), \exp(\ell), \theta_y) \\ &\quad \times p(\ell^*, \ell | X^*, \bar{X}, \bar{\Sigma}, \theta_\ell) d\ell d\ell^*. \end{aligned} \quad (33)$$

From the dataset, the most probable estimates are used, with the following equation:

$$p(y^* | X^*, D, \theta) \approx p(y^* | X^*, \exp(\ell^*), \exp(\ell), D, \theta_y). \quad (34)$$

3.2. *Hyperparameters in DGPR.* Hyperparameters define the parameters for the prior probability distribution [6]. We use  $\theta$  to denote the hyperparameters. From  $y$ , we get  $\theta$  that optimizes the probability to the highest point:

$$p(y | X, \theta) = \int p(y | X, \ell, \theta_y) \cdot p(\ell | X, \bar{\ell}, \bar{X}, \theta_\ell) d\ell. \quad (35)$$

From the hyperparameters  $p(y | X, \theta)$ , we optimally define the marginal likelihood and introduce an objective function for floating matrix:

$$\begin{aligned} \log p(y | X, \exp(\ell), \theta_y) \\ = -\frac{1}{2} y^T (K_{x,x} + \sigma_n^2 I)^{-1} y \\ - \frac{1}{2} \log \{K_{x,x} + \sigma_n^2 I\} - \frac{n}{2} \log(2\pi), \end{aligned} \quad (36)$$

and  $|M|$  is the factor of  $M$ .

In this equation the objective function is expressed as

$$\begin{aligned} L(\theta) = \log p(\ell | y, X, \theta) = c_1 + c_2 \\ \cdot [y^T A^{-1} y + \log |A| + \log |B|] \end{aligned} \quad (37)$$

and  $A$  is  $K_{x,x} + \sigma_n^2 I$ ,  $B$  is  $K_{\bar{x},\bar{x}} + \sigma_n^2 I$ .

The nonstationary covariance  $K_{x,x}$  is defined as follows.  $\ell$  represents the cost of  $X$  point:

$$K_{x,x} = \sigma_f^2 \cdot P_r^{1/4} \cdot P_c^{1/4} \cdot \left(\frac{1}{2}\right)^{-1/2} P_s^{-1/2} \cdot E \quad (38)$$

with

$$\begin{aligned} P_r &= p \cdot 1_n^T, \\ P_c &= 1_n^T \cdot p^T, \\ P &= \ell^T \ell, \\ P_s &= P_r + P_c, \\ E &= \exp \frac{[-s(X)]}{P_s}, \end{aligned} \quad (39)$$

$$\ell = \exp \left[ \bar{K}_{x,x}^T [\bar{K}_{\bar{x},\bar{x}} + \sigma_n^2 I]^{-1} \bar{\ell} \right].$$

After calculating the nonstationary covariance, we then make predictions [33]:

$$K_{x,\bar{x}} = \bar{\sigma} f^2 \cdot \exp \left[ -\frac{1}{2} s(\bar{\sigma}, \ell^{-2} X, \bar{\sigma}, \ell^{-2} \bar{X}) \right]. \quad (40)$$

## 4. Experimental Results

We use the Gaussian Processes for Machine Learning Matlab Toolbox. Its copious set of applicability dovetails with the purpose for this experiment. It was titivated to encompass all the functionalities associated with our study. We used

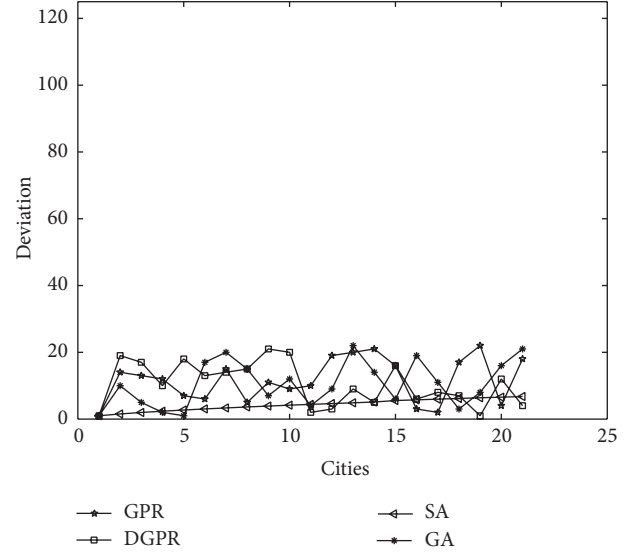


FIGURE 8: DGPR is juxtaposed with all other comparing methods in an instance of 22 cities for 200 iterations.

Matlab due to its robust platform for scientific experiments and sterling environment for prediction [26]. 22-city data instance were gleaned from the TSP library [34].

From the Dell computer, we set initial parameters:  $\ell = 2$ ,  $\sigma_f^2 = 1$ ,  $\sigma_n^2$ . The dynamic regression is lumped with the local search method to banish the early global and local convergence issues.

For global method (GA), the following parameters are defined. Sample = 22,  $(p_c) = 1$ ,  $(p_m) = 1.2$ , and 100 computations while SA parameters include  $T_{\text{int}} = 100$ ,  $T_{\text{end}} = 0.025$ , and 200 computations.

The efficacy level is always observed by collating the estimated tour with the nonestimated [35–37]:

$$\text{deviation (\%)} = \frac{\hat{y}^* - y^*}{y^*} \times 100. \quad (41)$$

The percentage of difference between estimated solution and optimal solution = 16.64%, which is indicative of a comparable reduction with the existing methods (Table 1). The computational time by GPR is 4.6402 and distance summation of 253.000. The varied landscape dramatically changes the length of travel for the traveling salesman. The length drops a notch suggestive of a better method and an open sesame for the traveling salesman to perform his duties.

The proposed DGPR (Figure 8) was fed with the sample TSP tours. The local search method constructs the initial route and 2-opt method used for interchanging edges. The local method defines starting point and all ports of call to painstakingly ensure that the loop goes to every vertex once and returns to the starting point. The 2-opt vertex interchange creates a new path through exchange of different vertices [38]. Our study is corroborated by less computation time and slumped distance when we subject TSP to predicting the optimal path. The Gaussian process runs on the shifting sands of landscape through dynamic instances. The nonstationary

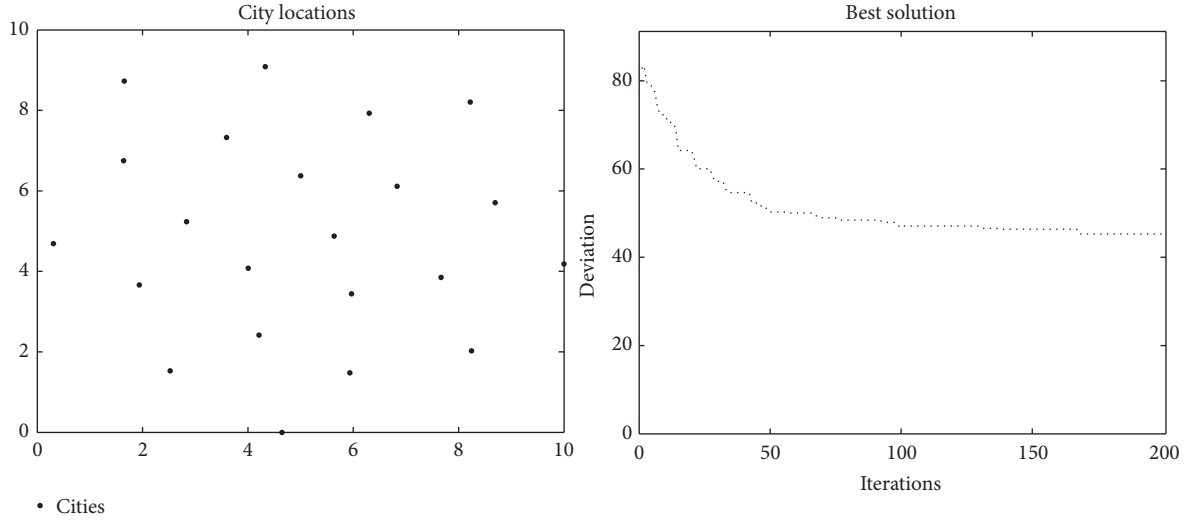


FIGURE 9: An example of best solution in stationarity. A sample of 22 cities generates a best route. As seen in the figure, there is a difference in optimality and time with nonstationarity.

TABLE 1: The extracted data is collated to show forth variations in different methods.

Method#	DTSP and DGPR collated data			
	Nodes#	Optimal#	T#	D#
GPR	22	253.00	4.64	0.42
DGPR	22	231.00	3.82	0.24
GA	22	288.817	5.20	0.40
SA	22	244.00	5.50	2.30
2-opt	22	240.00	4.20	0.30

functions described before brings to bare the residual, the similitude, between actual and estimate. In the computations, path is interpreted as  $\lceil \log_2 n \rceil$  and an ultimate route as  $n \lceil \log_2 n \rceil$ .

There are myriad methods over and above Simulated (Figure 10) Annealing and tabu search, set forth by the fecundity of researchers in optimization. The cost information determines the replacement of path in a floating turf. The lowest cost finds primacy over the highest cost. This process continues in pursuit of the best route (Figure 9) that reflects the lowest cost. In the dynamic setting, as the ports of call change, there is a new update on the cost of the path. The cost is always subject to change. The traveling salesman is desirous to travel the shortest distance which is the crux of this study (Figure 11). In the weave of this work, the dynamic facet of regression remains at the heartbeat of our contribution. The local methods are meshed together to ensure quality of the outcome. As a corollary our study has been improved with the integration of the Nearest Neighbor algorithm and the iterated 2-opt search method. We use the same number of cities; each tour is improved by 2-opt heuristics and the best result is selected.

In dynamic optimization, a complete solution of the problem at each time step is usually infeasible due to the floating optima. As a consequence, the search for exact global

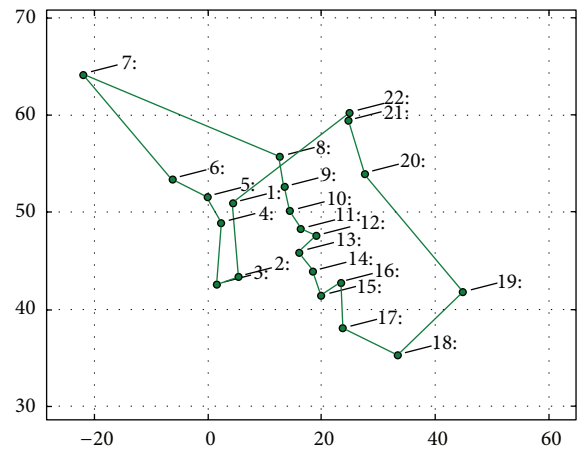


FIGURE 10: Optimal path is generated for Simulated Annealing in 22 cities.

optima must be replaced again by the search for acceptable approximations. We generate a tour for the nonstationary fitness landscape in Figure 7.

### 5. Conclusion

In this study, we use a nonstationary covariance function in GPR for the dynamic traveling salesman problem. We predict the optimal tour of 22 city dataset. In the dynamic traveling salesman problem where the optima shift due to environmental changes, a dynamic approach is implemented to alleviate the intrinsic maladies of perturbation. Dynamic traveling salesman problem (DTSP), as a case of dynamic combinatorial optimization problem, extends the classical traveling salesman problem and finds many practical importance in real-world applications, inter alia, traffic jams,

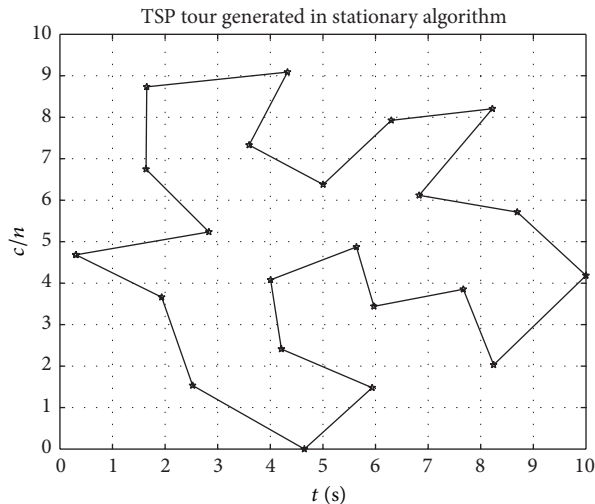


FIGURE 11: High amount of time and distance cost are needed to complete the tour vis-a-vis when prediction is factored.

network load-balance routing, transportation, telecommunications, and network designing. Our study produces a good optimal solution with less computational time in a dynamic environment. A slump in distance corroborates the argumentation that prediction brings forth a leap in efficacy in terms of overhead reduction, a robust solution born out of comparisons, that strengthen the quality of the outcome. This research foreshadows and gives interesting direction to solving problems whose optima are mutable. DTSP is calculated by the dynamic Gaussian process regression, cost predicted, local methods invoked, and comparisons made to refine and fossilize the optimal solution. MATLAB was chosen as the platform for the implementation, because development is straightforward with this language and MATLAB has many comfortable tools for data analysis. MATLAB also has an extensive cross-linking architecture and can interface directly with Java classes. The future of this research should be directed to design new nonstationary covariance functions to increase the ability to track dynamic optima. Also changes in size and evolution of optima should be factored in, over, and above changes in location.

### Conflict of Interests

The authors declare that there is no conflict of interests regarding the publication of this paper.

### Acknowledgments

The authors would like to acknowledge W. Kongkaew and J. Pichitlamken for making their code accessible which became a springboard for this work. Special thanks also go to the Government of Uganda for bankrolling this research through the PhD grant from Statehouse of the Republic of Uganda. The authors also express their appreciation to the incognito reviewers whose efforts were telling in reinforcing the quality of this work.

### References

- [1] A. Simões and E. Costa, "Prediction in evolutionary algorithms for dynamic environments," *Soft Computing*, pp. 306–315, 2013.
- [2] J. Branke, T. Kaussler, H. Schmeck, and C. Smidt, *A Multi-Population Approach to Dynamic Optimization Problems*, Department of Computer Engineering, Yeditepe University, Istanbul, Turkey, 2000.
- [3] K. S. Leung, H. D. Jin, and Z. B. Xu, "An expanding self-organizing neural network for the traveling salesman problem," *Neurocomputing*, vol. 62, no. 1–4, pp. 267–292, 2004.
- [4] M. Dorigo and L. M. Gambardella, "Ant colony system: a cooperative learning approach to the traveling salesman problem," *IEEE Transactions on Evolutionary Computation*, vol. 1, no. 1, pp. 53–66, 1997.
- [5] C. Jarumas and J. Pichitlamken, "Solving the traveling salesman problem with gaussian process regression," in *Proceedings of the International Conference on Computing and Information Technology*, 2011.
- [6] K. Weicker, *Evolutionary Algorithms and Dynamic Optimization Problems*, University of Stuttgart, Stuttgart, Germany, 2003.
- [7] K. Menger, *Das botenproblem. Ergebnisse Eines Mathematischen Kolloquiums*, 1932.
- [8] G. Gutin, A. Yeo, and A. Zverovich, "Traveling salesman should not be greedy: domination analysis of greedy-type heuristics for the TSP," *Discrete Applied Mathematics*, vol. 117, no. 1–3, pp. 81–86, 2002.
- [9] A. Hoffman and P. Wolfe, *The Traveling Salesman Problem: A Guided Tour of Combinatorial Optimization*, Wiley, Chichester, UK, 1985.
- [10] A. Punnen, "The traveling salesman problem: applications, formulations and variations," in *The Traveling Salesman Problem and Its Variations*, Combinatorial Optimization, 2002.
- [11] E. Ozcan and M. Erenturk, *A Brief Review of Memetic Algorithms for Solving Euclidean 2d Traveling Salesrep Problem*, Department of Computer Engineering, Yeditepe University, Istanbul, Turkey.
- [12] G. Clarke and J. Wright, "Scheduling of vehicles from a central depot to a number of delivery points," *Operations Research*, vol. 12, no. 4, pp. 568–581, 1964.
- [13] P. Miliotis, *Integer Programming Approaches To the Traveling Salesman Problem*, University of London, London, UK, 2012.
- [14] R. Jonker and T. Volgenant, "Transforming asymmetric into symmetric traveling salesman problems," *Operations Research Letters*, vol. 2, no. 4, pp. 161–163, 1983.
- [15] S. Gharan and A. Saberi, *The Asymmetric Traveling Salesman Problem on Graphs with Bounded Genus*, Springer, Berlin, Germany, 2012.
- [16] P. Collard, C. Esczut, and A. Gaspar, "Evolutionary approach for time dependent optimization," in *Proceedings of the IEEE 8th International Conference on Tools with Artificial Intelligence*, pp. 2–9, November 1996.
- [17] H. Psaraftis, "Dynamic vehicle routing problems," *Vehicle Routing: Methods and Studies*, 1988.
- [18] M. Yang, C. Li, and L. Kang, "A new approach to solving dynamic traveling salesman problems," in *Simulated Evolution and Learning*, vol. 4247 of *Lecture Notes in Computer Science*, pp. 236–243, Springer, Berlin, Germany, 2006.
- [19] S. S. Ray, S. Bandyopadhyay, and S. K. Pal, "Genetic operators for combinatorial optimization in TSP and microarray gene ordering," *Applied Intelligence*, vol. 26, no. 3, pp. 183–195, 2007.

- [20] E. Osaba, R. Carballedo, F. Diaz, and A. Perallos, "Simulation tool based on a memetic algorithm to solve a real instance of a dynamic tsp," in *Proceedings of the IASTED International Conference Applied Simulation and Modelling*, 2012.
- [21] R. Battiti and M. Brunato, *The Lion Way, Machine Learning Plus Intelligent Optimization. Applied Simulation and Modelling*, Lionsolver, 2013.
- [22] D. Chuong, *Gaussian Processes*, Stanford University, Palo Alto, Calif, USA, 2007.
- [23] W. Kongkaew and J. Pichitlamken, *A Gaussian Process Regression Model For the Traveling Salesman Problem*, Faculty of Engineering, Kasetsart University, Bangkok, Thailand, 2012.
- [24] C. Rasmussen and C. Williams MIT Press, Cambridge, UK, 2006.
- [25] C. J. Paciorek and M. J. Schervish, "Spatial modelling using a new class of nonstationary covariance functions," *Environmetrics*, vol. 17, no. 5, pp. 483–506, 2006.
- [26] C. E. Rasmussen and H. Nickisch, "Gaussian processes for machine learning (GPML) toolbox," *Journal of Machine Learning Research*, vol. 11, pp. 3011–3015, 2010.
- [27] F. Sinz, J. Candela, G. Bakir, C. Rasmussen, and K. Franz, "Learning depth from stereo," in *Pattern Recognition*, vol. 3175 of *Lecture Notes in Computer Science*, pp. 245–252, Springer, Berlin, Germany, 2004.
- [28] J. Ko, D. J. Klein, D. Fox, and D. Haehnel, "Gaussian processes and reinforcement learning for identification and control of an autonomous blimp," in *Proceedings of the IEEE International Conference on Robotics and Automation (ICRA '07)*, pp. 742–747, Roma , Italy, April 2007.
- [29] T. Idé and S. Kato, "Travel-time prediction using gaussian process regression: a trajectory-based approach," in *Proceedings of the 9th SIAM International Conference on Data Mining 2009 (SDM '09)*, pp. 1177–1188, May 2009.
- [30] G. Reinelt, "Tsp lib discrete and combinatorial optimization," 1995, <https://www.iwr.uni-heidelberg.de/groups/comopt/software/TSPLIB95/>.
- [31] C. Paciorek, *Nonstationary gaussian processes for regression and spatial modelling [Ph.D. thesis]*, Carnegie Mellon University, Pittsburgh, Pa, USA, 2003.
- [32] D. Higdon, J. Swall, and J. Kern, *Non-Stationary Spatial Modeling*, Oxford University Press, New York, NY, USA, 1999.
- [33] C. Plagemann, K. Kersting, and W. Burgard, "Nonstationary Gaussian process regression using point estimates of local smoothness," in *Machine Learning and Knowledge Discovery in Databases*, vol. 5212 of *Lecture Notes in Computer Science*, no. 2, pp. 204–219, Springer, Berlin, Germany, 2008.
- [34] G. Reinelt, "The tsp lib symmetric traveling salesman problem instances," 1995.
- [35] J. Kirk, *Matlab Central*.
- [36] X. Geng, Z. Chen, W. Yang, D. Shi, and K. Zhao, "Solving the traveling salesman problem based on an adaptive simulated annealing algorithm with greedy search," *Applied Soft Computing Journal*, vol. 11, no. 4, pp. 3680–3689, 2011.
- [37] A. Seshadri, *Traveling Salesman Problem (Tsp) Using Simulated Annealing*, IEEE, 2006.
- [38] M. Nuhoglu, Shortest path heuristics (nearest neighborhood, 2 opt, farthest and arbitrary insertion) for travelling salesman problem, 2007.

## Research Article

# Classification of Phishing Email Using Random Forest Machine Learning Technique

**Andronicus A. Akinyelu and Aderemi O. Adewumi**

*School of Mathematics, Statistics and Computer Science, University of KwaZulu-Natal, Private Bag Box X54001, Durban 4000, South Africa*

Correspondence should be addressed to Aderemi O. Adewumi; [laremtj@gmail.com](mailto:laremtj@gmail.com)

Received 23 January 2014; Accepted 11 March 2014; Published 3 April 2014

Academic Editor: Olabisi Falowo

Copyright © 2014 A. A. Akinyelu and A. O. Adewumi. This is an open access article distributed under the Creative Commons Attribution License, which permits unrestricted use, distribution, and reproduction in any medium, provided the original work is properly cited.

Phishing is one of the major challenges faced by the world of e-commerce today. Thanks to phishing attacks, billions of dollars have been lost by many companies and individuals. In 2012, an online report put the loss due to phishing attack at about \$1.5 billion. This global impact of phishing attacks will continue to be on the increase and thus requires more efficient phishing detection techniques to curb the menace. This paper investigates and reports the use of random forest machine learning algorithm in classification of phishing attacks, with the major objective of developing an improved phishing email classifier with better prediction accuracy and fewer numbers of features. From a dataset consisting of 2000 phishing and ham emails, a set of prominent phishing email features (identified from the literature) were extracted and used by the machine learning algorithm with a resulting classification accuracy of 99.7% and low false negative (FN) and false positive (FP) rates.

## 1. Introduction

Phishing is one of the different (and lucrative) types of fraud committed today. In criminal law, fraud is defined as a deliberate deception made for the sole aim of personal gains or for smearing an individual's image. In general terms, fraud can be defined as an act of deceiving people into revealing their personal information, basically for the purpose of financial or personal gains.

Phishing is an act that attempts to electronically obtain delicate or confidential information from users (usually for the purpose of theft) by creating a replica website of a legitimate organization. Phishing is usually perpetrated with the aid of an electronic device (such as ipads and computer) and a computer network; they target the weaknesses existing in various detection systems caused by end-users (who are considered to be the weakest element in the security chain) [1, 2]. Phishing attackers usually perpetrate their evil by communicating well composed messages (known as social engineered messages) to users in order to persuade them to reveal their personal information which will be used by the fraudster to gain unauthorized access to the user's account.

For example, a fraudulent email sent to a user might contain a malware (called man in the browser (MITB)), this malware could be in form of web browser ActiveX components, plugins, or email attachments; if this user ignorantly download this attachment to his pc, the malware will install itself on the user's pc and would in turn transfer money to the fraudster's bank account whenever the user (i.e., the legitimate owner of the bank account) tries to perform an online transaction [1].

Fraudulent activities is on the increase daily; individuals and companies who have been victims in the past now seek for ways to secure themselves from been attacked again. To achieve this, their defense mechanism has to be more secured to prevent them from falling prey again, which implies that the existing defense system (its designs and technology) needs to be greatly improved [3]. Behdad et al. [3] pointed out that improving the defense system is not enough to stop fraudsters as some of them could still penetrate; the system should also be able to identify fraudulent activities and prevent them from occurring.

Several traditional approaches used by various email filters today are static in nature; they are not robust enough to handle new and emerging phishing patterns; they only have

TABLE 1: Data used for testing.

Total Samples	2000
Total Phishing Emails	200
Total legitimate email	1800

the ability to handle existing phishing patterns, thus leaving email users prone to new phishing attacks. This is a loop hole because fraudsters are not static in their activities; they change their mode of operation as often as possible to stay undetected. This motivated many researchers into seeking for other effective techniques that can handle both known and emerging fraud, and this led to the discovery of machine learning algorithms.

Machine learning (ML) is a branch of artificial intelligence (AI) that employs the method of data mining to discover new or existing patterns (or features) from a dataset which is then used for the purpose of classification. In this work, we extracted a set of 15 prominent phishing features (identified from the literature) from a dataset consisting of 2000 emails; and after extraction, for each email, a vector representation of these features is formed, which is then used to train our classifier (see Table 1).

We present a detailed description of our machine learning method in this paper. In Section 2 we gave an overview of existing phishing detection techniques and also gave a brief description of our 15 features; in Section 3 we gave the details on our machine learning algorithm and also explained the result we obtained; finally we concluded the paper in Section 4.

## 2. Related Work

Prakash et al. [4] used a combination of blacklists and heuristics and they achieved a FP and FN rates of 5% and 3%, respectively. Cranor et al. [5] conducted an evaluation on some antiphishing toolbar and reported SpoofGuard (developed by Chou et al. [6]) to have a FP rate of 38% and a FN rate of 9%. Also, Yu et al. [7] developed a heuristics-based phishing detection system which achieved a FP and FN rates of 1% and 20%, respectively. Zhang et al. [8] also used heuristics and their method achieved a FP rate of 3% and FN rate of 11%. Fette et al. [9] used ML-based method and they achieved a FP rate of 0.0013% and a FN rate of 0.0036%. Bergholz et al. [10] combined the use of heuristics and ML-technique and their method achieved a FP rate of 0% and a FN rate of 1%.

All these proposed methods have relatively high FP rate and FN rate except for Fette et al. [9] and Bergholz et al. [10] whose methods achieved excellent results with very low FP and FN rates. However, Bergholz et al. [10] made use of model-based features involving the processing of images which in turn could lead to an increase in the run time and space. Fette et al. [9] also made use of a feature (the age of linked to domain names) that has to be obtained by sending of queries over the network, which could also lead to an increase in run time. In our method, all the features are extracted directly from each email itself; we do not need to send queries

over the network or store large data, thereby reducing the run time and space complexities.

## 3. Problem Description

*3.1. Email Filtering.* Phishing attacks are prominently perpetrated via sending of emails. These emails usually contain social engineering messages (with specific phrases) that demand users to perform specific actions (such as clicking a URL). Therefore, the content of these emails are useful features for phishing detection.

Very few phishing email filters have been developed as opposed to many existing email filters that have been developed for spam emails. Many of them used several phishing detection techniques ranging from blacklists [4], visual similarity [11], heuristic [12], and machine learning [10]. Of all these techniques, ML-based technique (such as our own) achieved the best result.

Many approaches have been proposed to build email filters but many of them are only suitable for handling spam emails. For example, a popular method (known as “bag-of-words”) extracts all the words present in an email, identifies the highest occurring words, and uses each of these words as the features for classification. This method (a.k.a. text classification method) works very well for filtering of spam emails but not for phishing emails, because phishing email contains some unique features that are only specific to phishing attacks, features such as presence of IP-based URLs and presence of nonmatching URLs. This indicates that spam filtering approaches cannot effectively handle phishing emails; therefore, a list of phishing-attack-specific features has to be defined and used to build an effective email filtering system. It is worth noting that some existing spam filtering approaches (such as SpamAssassin [13] and Spamato [14]) went beyond just “bag-of-word” methods; they designed a set of spam emails heuristics that could also successfully detect some existing phishing emails features (such as presence of IP-based URLs). These methods can be combined with our method to build a hybrid (phishing and spam) email filtering system with very low FPs and FNs.

*3.2. Features Used in the Email Classification.* The features we used for our email classification are described in this section. These features were identified from different literature; combination of these features together forms a feature set that effectively classified emails into phishing and nonphishing.

A group of 15 features frequently used by phishing attackers was identified from different literature and used in this paper. Although the features set are few (compared to some filters that used hundreds of features for detection), a high accuracy was still achieved. These features are described in the remaining part of this section.

*3.2.1. URLs Containing IP Address.* The URL for many legitimate websites usually contains the name of the website (e.g., <http://www.yahoo.com/>, which tells us that this URL can be used to connect to the website of yahoo). For the purpose of identity hiding, phishers usually mask their

website name by using URLs that contain IP address (e.g., “http://167.88.12.1/signin.ebay.com”); therefore the presence of IP-based URLs in an email is an indication that the email is a potential phishing email. This feature was used in [9].

**3.2.2. Disparities between “href” Attribute and LINK Text.** The HTML <a> tag defines an anchor that may be used to establish a link to another website. Linking to another website can be accomplished by defining a “href” attribute; this attribute describes the location of the website that is to be linked to. The links are usually rendered to the browser after the “Link text” has been clicked (e.g., <a href=“URL Address”>Link Text</a>). The link text could be a plain text (e.g., Click Here), a URL (yahoo.com), an image, or any other HTML element. If the link text is a URL (and it is a legitimate link), it should tally with the website location pointed to by the “href” attribute (e.g., <a href=“http://www.yahoo.com”> yahoo.com </a>); if there is a disparity between the href attribute and the link text (e.g., <a href=http://www.yahoo.com> boguus.com </a>), then the link is likely pointing to a phishing website. All the links (containing a URL-based link text) in an email are checked and if there is a disparity between the link text and the href attribute, then a positive Boolean feature is recorded. This feature was used in [9].

**3.2.3. Presence of “Link,” “Click,” and “Here” in Link Text of a Link.** The text of the links present in most phishing emails usually contain words like “Click,” “Here,” “Login,” and “Update.” For this feature, all the text of each link in an email is checked and a Boolean value is recorded based on the presence or absence of the words *Click*, *Here*, *Login*, *Update*, and *Link* in the Link text. Similar feature was used in [9, 10].

**3.2.4. Number of Dots in Domain Name.** The number of dots that should be contained in the domain name of a legitimate organization should not be more than three as proposed by Emigh [15]. A binary value of 1 is recorded if an email contains a URL whose number of dots is above three.

**3.2.5. HTML Email.** The email format for each email is defined by MIME standards. The MIME standard defines the type of content contained in each email. The content type (defined by the content-type attribute) could be plain text (indicated by “text/plain”), HTML (indicated by “text/html”). Fette et al. [9] proposed that an email is a potential phishing email if it contains a content-type with attribute “text/html”; they based their argument on the fact that it is almost impossible for phishing attacks to be launched without the use of HTML links.

**3.2.6. Presence of Javascript.** Javascript can either be embedded in the body of an email (using the script (<script>) tag) or in a link (using the anchor (<a>) tag). Some phishers use Javascript to hide information from users. Fette et al. [9] suggested that an email is a potential phishing email if the “javascript” string is contained in either the body of the email or in a link.

**3.2.7. Number of Links.** The total number of links embedded in an email is recorded and used as a feature for classification. Zhang and Yuan [16] explained that phishing emails usually contain multiple numbers of links to illegitimate websites.

**3.2.8. Number of Linked To Domain.** This feature (used in [9]) refers to all the URLs present in an email that are extracted, and a count is recorded for the number of distinct domain names present in each of the extracted URLs. The recorded value is used as a feature.

Take note that each domain name in an email is only counted once; subsequent occurrence (of an already counted domain name) is discarded not counted.

**3.2.9. From\_Body\_MatchDomain Check.** To extract this feature, all the domain names in an email are extracted and each of these domain names is matched with the sender’s domain (i.e., the domain name referred to by the “From” field of the same email); If there is disparity between any of the comparisons, then Almomani et al. [17] suggest that the email is likely a phishing email.

**3.2.10. Word List Features.** Some group of words that frequently appear in phishing emails were used as features. We grouped these words into six different groups and each of these groups is used as a single feature (making a total of six different features). For each group, presence of each word is counted and normalized. The groups of words include the following.

- (1) Update; Confirm;
- (2) User; Customer; Client;
- (3) Suspend; Restrict; Hold;
- (4) Verify; Account; Notif;
- (5) Login; Username; Password; Click; Log;
- (6) SSN; Social Security; Secur; Inconvinien.

This feature is similar to the one proposed by Basnet et al. [18]. Take note that some stemmed words (like secur and inconvinien were used).

## 4. Simulation Experiment

**4.1. Data Used.** For the implementation and testing of our machine learning algorithm, we used two publicly available datasets. We got our ham mails from the ham corpora provided by spam assassin project [13], and our phishing emails were gotten from the publicly available phishing corpus [19] provided by Nazario. We programmatically extracted the features described in Section 3.2 above using C#. All the emails coming from the ham corpora were labeled as ham emails and the emails coming from the phishing corpora was labeled as phishing email.

**4.2. Machine Learning Implementation.** When constructing our classifier, we first transformed each email into a format that will be suitable for our machine learning algorithm. Each

**Begin RF Algorithm**

Input:  $N$ : number of nodes  
 $M$ : number of features  
 $D$ : number of trees to be constructed

Output:  $V$ : the class with the highest vote

**While** stopping criteria is false **do**

Randomly draw a bootstrap sample  $A$  from the training data  $D$

Use the steps below to construct tree  $T_i$  from the drawn bootstrapped sample  $A$ :

- (I) Randomly select  $m$  features from  $M$ ; where  $m \ll M$
- (II) For node  $d$ , calculate the best split point among the  $m$  features
- (III) Split the node into two daughter nodes using the best split
- (IV) Repeat I, II and III until  $n$  number of nodes has been reached

Build your forest by repeating steps I–IV for  $D$  number of times

**End While**

Output all the constructed trees  $\{T_i\}_1^D$

Apply a new sample to each of the constructed trees starting from the root node

Assign the sample to the class corresponding to the leaf node.

Combine the decisions (or votes) of all the trees

Output  $V$ , that is, the class with the highest vote.

**End RF Algorithm**

ALGORITHM 1

of the emails is represented by a vector that contains a value (binary or continuous) for all the extracted features. For the purpose of testing our algorithm, we used random forest (RF) classifier [20]. More details on RF algorithm are provided below.

**4.3. Random Forest: Overview.** Random forest (RF) is an ensemble learning classification and regression method suitable for handling problems involving grouping of data into classes. The algorithm was developed by Breiman and Cutler [21]. In RF, prediction is achieved using decision trees. During the training phase, a number of decision trees are constructed (as defined by the programmer) which are then used for the class prediction; this is achieved by considering the voted classes of all the individual trees and the class with the highest vote is considered to be the output.

RF method has also been used to solve similar problem in the literature, such as in [9, 22, 23]. A summary of how a forest (i.e., collection of trees) is constructed is explained in Algorithm 1.

For more details about random forest, kindly refer to [20, 24].

In this work, we trained and tested our classifier using 10-fold cross validation. In 10-fold cross validation, the dataset is divided into 10 different parts; 9 of the 10 parts are used to train the classifier and the information gained from the training phase would be used to validate (or test) the 10th part; this is done 10 times, such that, at the end of the training and testing phase, each of the parts would have been used as both training and testing data. This method (i.e., cross validation method) ensures that the training data is different from the test data. In machine learning, this method is known to provide a very good estimate of the generalization error of a classifier.

**4.4. Result and Discussion.** Machine learning involves two major phases: the training phase and the testing phase. The predictive accuracy of the classifier solely depends on the information gained during the training process; if the information gained (IG) is low, the predictive accuracy is going to be low, but if the IG is high, then the classifier's accuracy will also be high.

As stated above, we used 10-fold cross validation. In our random forest classification, before the decision trees are constructed, the information gained for all the 15 features is calculated (using the IG method explained by Mitchell [24]) and the features with the best eight IG are selected and used for constructing the decision trees; the mode vote (from all the trees) is then calculated and used for the email prediction. Information gain is one of the feature ranking metric highly used in many text classification problems today. More details about our algorithm are described in the next section below.

We tested our method using varied dataset sizes (as shown in Table 2); this was done to know the performance of the algorithm on both small and large datasets. The full result is reported in Table 2. As shown in the table, the algorithm performed best when tested on the dataset that has the largest size (having an overall accuracy of 99.7%, FN rate of 2.50%, and FP rate of 0.06%); this implies that our method will work effectively if applied to real world dataset, which is usually large in size. Our method also achieved a higher prediction accuracy (99.7%) compared to an accuracy of 97% achieved by Fette et al. [9].

The computer used in running this test is a 32-bit desktop, having a processor speed of 2.20 GHz and a RAM size of 2.00 GB.

Table 3 and Figure 1, respectively, show a comparison between our method and another similar work in literature that also had a good result.

TABLE 2: 10-Fold cross validation Result.

S/N	Dataset Information			Performance Evaluation							
	Email Per Folder	Total Email	P : H Ratio (%)	PA (%)	SR	FP (%)	FN (%)	R (%)	Pr (%)	F-M (%)	T (s)
1	15	150	48 : 52	98.00	0.98	0.00	4.11	95.80	100	97.79	11.82
2	30	300	33 : 67	98.33	0.99	0.00	4.00	96.00	100	97.75	21.03
3	50	500	20 : 80	99.20	0.99	0.00	4.00	96.00	100	97.78	33.47
4	100	1000	10 : 90	99.60	0.99	0.00	4.00	96.00	100	97.78	65.46
5	200	2000	10 : 90	99.70	0.99	0.06	2.50	97.50	99.47	98.45	141.25

Key: PA: Prediction Accuracy, SR: Success Rate, FP: False Positive, FN: False Negative, R: Recall, Pr: Precision, T: Time, F-M: F-Measure, P : H: Phish : Ham.

TABLE 3: Classification Result for Random Forest ML on the best eight features.

Technique	FP-Rate	FN-Rate	Precision	Recall	F-Measure
Fette et al. [9]	0.13%	3.62%	98.92%	96.38%	97.64%
RF Result	0.06%	2.50%	99.47%	97.50%	98.45%

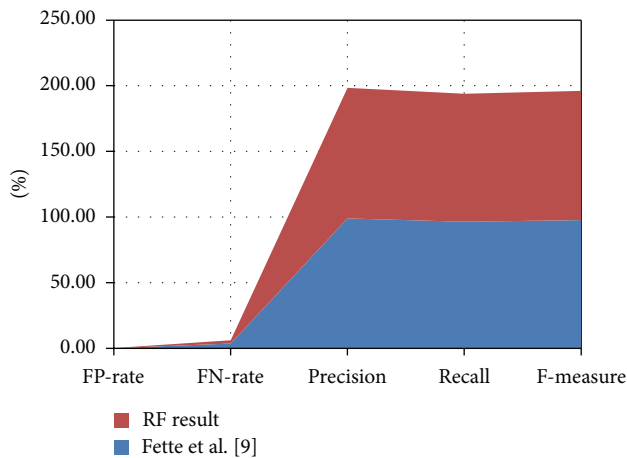


FIGURE 1: ROC curve showing the comparison between our work and Fette et al.'s [9].

## 5. Conclusion

Phishing has become a serious threat to global security and economy. The fast rate of emergence of new phishing websites and distributed phishing attacks has made it difficult to keep blacklists up to date. Therefore, in this paper, we have presented a content-based phishing detection approach which has bridged the current gap identified in the literature. This approach yielded high classification accuracy of 99.7% with negligible false positive rate of about 0.06%.

In the future, we plan on improving this work by combining this approach with a nature inspired (NI) technique. NI techniques (such as PSO or ACO) can be used to automatically and dynamically identify the best phishing features (from a feature space) that can be used to build a robust phishing email filter with very high classification accuracy. Using this technique will with no doubt enhance the predictive accuracy of a classifier since effective classification of emails depends on the phishing features identified during the learning stage of the classification.

Due to the rapid change in phishing attack patterns, current phishing detection techniques need to be greatly enhanced to effectively combat emerging phishing attacks. An online report noted that, in the future, phishers will shift their attention from syntactic attacks (i.e., attacks exploiting technical vulnerabilities) to semantic attacks (i.e., attacks exploiting social vulnerabilities). To handle some of these emerging phishing attacks, an online report recommended that companies should move from session-based security (based on a secure log-in), to message-based security (based on explicit authentication of individual transactions). Also, Fette et al. [9] suggested that using knowledge-based models built on federated identities and semantic based technologies will also help to combat carefully planned phishing attacks in the future.

## Conflict of Interests

The authors declare that there is no conflict of interests regarding the publication of this paper.

## References

- [1] M. Khonji, Y. Iraqi, and A. Jones, "Phishing detection: a literature survey," *IEEE Communications & Surveys Tutorials*, vol. 15, no. 4, pp. 2091–2121, 2013.
- [2] S. Sheng, M. Holbrook, P. Kumaraguru, L. F. Cranor, and J. Downs, "Who falls for phish?: a demographic analysis of phishing susceptibility and effectiveness of interventions," in *Proceedings of the 28th Annual SIGCHI Conference on Human Factors in Computing Systems (CHI '10)*, pp. 373–382, Atlanta, Ga, USA, April 2010.
- [3] M. Behdad, L. Barone, M. Bennamoun, and T. French, "Nature-inspired techniques in the context of fraud detection," *IEEE Transactions on Systems, Man, and Cybernetics C: Applications and Reviews*, vol. 42, no. 6, pp. 1273–1290, 2012.
- [4] P. Prakash, M. Kumar, R. R. Kompella, and M. Gupta, "Phish-Net: predictive blacklisting to detect phishing attacks," in *Proceedings of the IEEE Conference on Computer Communications (IEEE INFOCOM '10)*, pp. 1–5, IEEE, San Diego, Calif, USA, March 2010.

- [5] L. F. Cranor, S. Egelman, J. I. Hong, and Y. Zhang, "Phishing phish: an evaluation of anti-phishing toolbars," in *Proceedings of the 14th Annual Network & Distributed System Security Symposium (NDSS '07)*, San Diego, Calif, USA, 2007.
- [6] N. Chou, R. Ledesma, Y. Teraguchi, and J. C. Mitchell, "Client-side defense against web-based identity theft," in *Proceedings of the 11th Annual Network & Distributed System Security Symposium (NDSS '04)*, San Diego, Calif, USA, February 2004.
- [7] W. D. Yu, S. Nargundkar, and N. Tiruthani, "PhishCatch—a phishing detection tool," in *Proceedings of the 33rd Annual IEEE International Computer Software and Applications Conference (COMPSAC '09)*, vol. 2, pp. 451–456, Seattle, Wash, USA, July 2009.
- [8] Y. Zhang, J. I. Hong, and L. F. Cranor, "Cantina: a content-based approach to detecting phishing web sites," in *Proceedings of the 16th International World Wide Web Conference (WWW '07)*, pp. 639–648, ACM, Alberta, Canada, May 2007.
- [9] I. Fette, N. Sadeh, and A. Tomasic, "Learning to detect phishing emails," in *Proceedings of the 16th International World Wide Web Conference (WWW '07)*, pp. 649–656, Alberta, Canada, May 2007.
- [10] A. Bergholz, J. de Beer, S. Glahn, M. F. Moens, G. Paaß, and S. Strobel, "New filtering approaches for phishing email," *Journal of Computer Security*, vol. 18, no. 1, pp. 7–35, 2010.
- [11] Y. Cao, W. Han, and Y. Le, "Anti-phishing based on automated individual white-list," in *Proceedings of the 4th ACM Workshop on Digital Identity Management (DIM '08)*, pp. 51–59, ACM, Alexandria, Va, USA, October 2008.
- [12] L. Ma, B. Ofoghi, P. Watters, and S. Brown, "Detecting phishing emails using hybrid features," in *Proceedings of the Symposia and Workshops on Ubiquitous, Autonomic and Trusted Computing (UIC-ATC '09)*, pp. 493–497, IEEE, Brisbane, Australia, July 2009.
- [13] Apache Software Foundation, "Spam assassin homepage," 2006, <http://spamassassin.apache.org/>.
- [14] K. Albrecht, N. Burri, and R. Wattenhofer, "Spamato—an extendable spam filter system," in *Proceedings of the 2nd Conference on Email and Anti-Spam (CEAS '05)*, Stanford, Calif, USA, 2005.
- [15] A. Emigh, "Phishing attacks: information flow and chokepoints," in *Phishing and Countermeasures: Understanding the Increasing Problem of Electronic Identity Theft*, M. Jakobsson and S. Myers, Eds., pp. 31–64, John Wiley & Sons, New York, NY, USA, 2007.
- [16] N. Zhang and Y. Yuan, "Phishing detection using neural network," <http://cs229.stanford.edu/proj2012/ZhangYuan-PhishingDetectionUsingNeuralNetwork.pdf>.
- [17] A. Almomani, T.-C. Wan, A. Altaher et al., "Evolving fuzzy neural network for phishing emails detection," *Journal of Computer Science*, vol. 8, no. 7, pp. 1099–1107, 2012.
- [18] R. Basnet, S. Mukkamala, and A. H. Sung, "Detection of phishing attacks: a machine learning approach," in *Soft Computing Applications in Industry*, pp. 373–383, Springer, Berlin, Germany, 2008.
- [19] J. Nazario, "Phishingcorpus homepage," 2006, <http://monkey.org/%7Ejose/wiki/doku.php?id=PhishingCorpus>.
- [20] L. Breiman, "Random forests," *Machine Learning*, vol. 45, no. 1, pp. 5–32, 2001.
- [21] L. Breiman and A. Cutler, "Random forests-classification description," Department of Statistics Homepage, 2007, [http://www.stat.berkeley.edu/~breiman/RandomForests/cc\\_home.htm](http://www.stat.berkeley.edu/~breiman/RandomForests/cc_home.htm).
- [22] I. Koprinska, J. Poon, J. Clark, and J. Chan, "Learning to classify e-mail," *Information Sciences*, vol. 177, no. 10, pp. 2167–2187, 2007.
- [23] C. Whittaker, B. Ryner, and M. Nazif, "Large-scale automatic classification of phishing pages," in *Proceedings of the 17th Annual Network & Distributed System Security Symposium (NDSS '10)*, The Internet Society, San Diego, Calif, USA, 2010.
- [24] T. M. Mitchell, *Machine Learning*, McGraw-Hill, New York, NY, USA, 1997.

## Research Article

# Numerical Investigation of Gas Mixture Length of Nitrogen Replacement in Large-Diameter Natural Gas Pipeline without Isolator

Hongjun Zhu<sup>1</sup> and Qinghua Han<sup>2</sup>

<sup>1</sup> State Key Laboratory of Oil and Gas Reservoir Geology and Exploitation, Southwest Petroleum University, Chengdu, Sichuan 610500, China

<sup>2</sup> Petroleum Engineering Institute, Southwest Petroleum University, Chengdu, Sichuan 610500, China

Correspondence should be addressed to Hongjun Zhu; ticky863@126.com

Received 6 December 2013; Accepted 15 February 2014; Published 25 March 2014

Academic Editor: M. Montaz Ali

Copyright © 2014 H. Zhu and Q. Han. This is an open access article distributed under the Creative Commons Attribution License, which permits unrestricted use, distribution, and reproduction in any medium, provided the original work is properly cited.

Nitrogen replacement is a key process for natural gas pipeline before it is put into operation. A computational fluid dynamic model coupled to a species-transportation model has been used to investigate the gas mixture length of nitrogen replacement in large-diameter pipeline without isolator. A series of numerical simulations are performed over a range of conditions, including pipe length and diameter, inlet rate, and inclination angle of pipe. These affecting factors are analyzed in detail in terms of volume fraction of nitrogen, the maximum gas mixture length, and gas mixture length varied with time. Gas mixture length increases over time, and the maximum gas mixture length is present at outlet of pipe. Long and large-diameter pipe and fast speed of nitrogen lead to long length of mixed gas, while large inclination angle of pipe brings about short length. Several fitting formulas have been obtained, which can predict the maximum gas mixture length in gas pipelines. The used method of fitting formula is shown in the paper by examples. The results provide effective guidance for practical operation of nitrogen replacement.

## 1. Introduction

Facing the increasing gas consumption, natural gas pipeline is progressing towards large diameter and long distance, resulting in high investment. It is very important to ensure the safety of gas pipeline operation. However, explosion is easily caused when the content of natural gas in air reaches 5~15% [1, 2]. Therefore, before the natural gas pipeline is put into operation, the air in pipe must be replaced by an inert gas. In practice, nitrogen, as the most readily available and least expensive inert gas, is usually used to replace air in pipe. And qualified replacement is performed when the content of air in pipe is less than 2% [3].

To ensure safety, isolator is commonly employed to separate the nitrogen and air. As shown in Figure 1(a), before pumping the nitrogen into pipe, isolator is firstly placed at the entrance of pipe. Then nitrogen flow pushes the

isolator moving forward together [4]. However, a number of natural gas pipelines are laid in mountains and plateaus. The undulating terrain makes the passing through of isolator more difficult. And in larger diameter, the cost of isolator is doubled up. In addition, the isolator seal failure usually occurs due to wear. Therefore, nitrogen replacement without isolator is popular in today's natural gas pipeline engineering as shown in Figure 1(b). After all, the receiving and transmitting cost of isolator can be saved. In this process, the gas mixture length becomes a key parameter to determine the displacement effect. According to the gas mixture length, appropriate operating parameters such as pumping volume and forward speed of nitrogen can be defined. However, in China, the amount of nitrogen is mainly determined by experience with great blindness [5–7]. And the mixture rule of nitrogen and air and affecting factors on mixture length are still unclear.

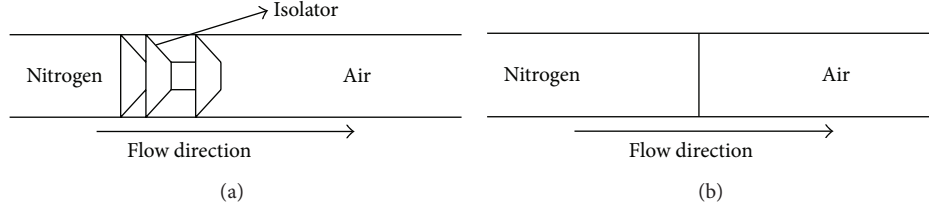


FIGURE 1: Schematic diagram of nitrogen replacement: (a) with isolator; (b) without isolator.

Several works in the literature focus on nitrogen injection to develop gas and gas condensate fields [8–10]. However, the mixture rule in formation pore is different with it in large-diameter pipeline, due to the great difference in scales. Therefore, an in-depth research for gas mixture length of nitrogen replacement in large-diameter pipeline without isolator is urgently needed in natural gas pipeline engineering.

Since numerical simulation can provide detailed information of flow field which is not easily obtained by physical experiments and has advantages of low cost and short research time, in present work, CFD model coupling with a species-transportation model has been employed to investigate the gas mixture length of nitrogen replacement in large-diameter pipeline without isolator. The gas mixture length has been examined in terms of volume fraction of nitrogen. By conducting a series of numerical simulations, effects of pipe length, pipe diameter, inlet rate, and inclination angle of pipe are examined. Then, the maximum gas mixture length is analyzed and the fitting formulas are obtained. Using these formulas, we can predict the maximum gas mixture length in gas pipelines. The used method of fitting formula is shown in the paper by examples. The results provide useful guidance for practical operation of nitrogen replacement.

The remaining part of this paper is organized as follows. In Section 2, the description of simulation problem is provided; Section 3 presents the governing equations and numerical method; Section 4 presents the numerical results and discussion; Section 5 is the concluding remarks.

## 2. Problem Description

Straight pipe and undulating pipe with an inclined upward section are adopted in this study. Figure 2 shows a sketch of the geometry and numerical grid for computational domain. The straight pipe is placed horizontally. And the length of it ( $L_1$ ) ranges from 50 m to 1000 m in comparing cases, in order to examine the effect of pipe length on gas mixture length, while the diameter of straight pipe is set to 346.0 mm, 647.2 mm, 851.2 mm, and 1000.2 mm to explore the effect of pipe diameter.

The undulating pipe consists of three sections: straight pipe section, bend section, and inclined upward section. The bend curvature ( $R/D$ ) is defined as 3, the common one used in practice. The length of inclined upward section is fixed at 600 m, while the inclination angle changes from  $10^\circ$  to  $40^\circ$

in comparing cases conducted to observe the effect of pipe inclination.

Gas flow in pipeline is a symmetric problem, so two-dimensional flow simulation is accurate enough to capture the gas mixture length. In addition, three-dimensional simulation needs a higher CPU cost. Due to time limitations, 2D simulation is applied in this work. All geometry generation and meshing are performed using GAMBIT 2.3 mesh-generator. As shown in Figure 2, quadrilateral grids are used in the whole computational domain of both straight pipe and undulating pipe. And progressive mesh is used near the pipe wall. The computational domain of undulating pipe is divided into three blocks. Denser mesh is employed in the bend section. A suitable grid density is reached by repeating computations until a satisfactory independent grid is found. For example, the number of quadrilateral cells for straight pipe with diameter of 647.2 mm and length of 600 m is 480000 at last.

The velocity of gas flow is slow in pipe (2~5 m/s), so both nitrogen and air can be seen as incompressible fluids. In simulations, density and viscosity of nitrogen are defined as  $1.138 \text{ kg/m}^3$  and  $1.663 \times 10^{-5} \text{ Pa}\cdot\text{s}$ , respectively. And the density and viscosity of air are set to  $1.225 \text{ kg/m}^3$  and  $1.8 \times 10^{-5} \text{ Pa}\cdot\text{s}$ , respectively.

## 3. Governing Equations and Numerical Method

**3.1. Governing Equations.** The gas flows of nitrogen and air are governed by the Reynolds-Averaged-Navier-Stokes (RANS) equations, including continuity and momentum equations written as follows [11]:

$$\frac{\partial \bar{u}_i}{\partial x_i} = 0, \quad (1)$$

$$\frac{\partial \bar{u}_i}{\partial t} + \frac{\partial \bar{u}_i \bar{u}_j}{\partial x_j} = -\frac{1}{\rho} \frac{\partial \bar{p}}{\partial x_i} + \nu \nabla^2 \bar{u}_i - \frac{\partial \overline{u'_i u'_j}}{\partial x_j} + g_i,$$

where

$$\rho = \alpha \rho_n + (1 - \alpha) \rho_a, \quad (2)$$

$$v = \alpha v_n + (1 - \alpha) v_a,$$

where  $u_i$  represents instantaneous velocity component in  $i$  direction, for example,  $u$  and  $v$  are velocity in  $x$  and

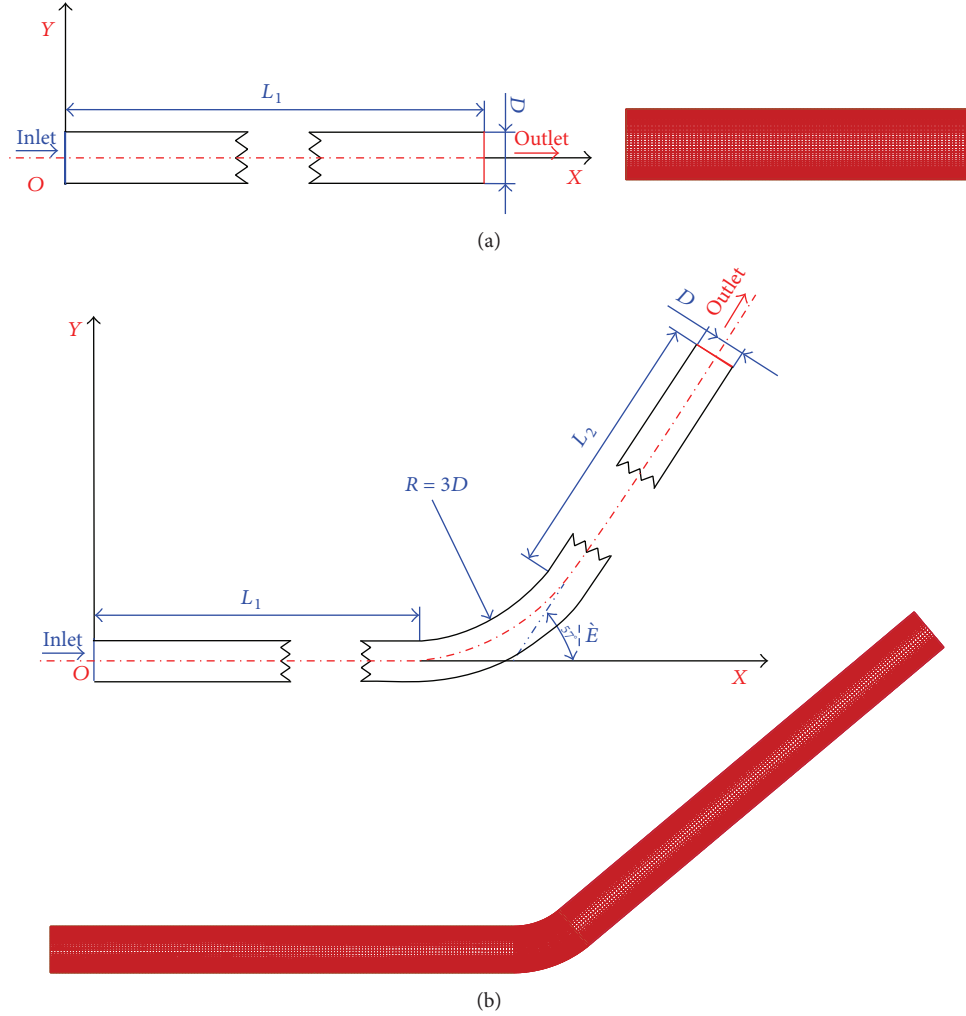


FIGURE 2: Sketch of the geometry and numerical grid for computational domain: (a) straight pipe; (b) undulating pipe with an inclined upward section.

$y$  direction, respectively, while  $u'_i$  is fluctuation velocity component in  $i$  direction,  $x_i$  is space coordinate in  $i$  direction,  $g_i$  is gravitational acceleration in  $i$  direction,  $t$  is time,  $p$  is pressure,  $\rho$  is density of mixed gas,  $\rho_n$  and  $\rho_a$  are density of nitrogen and air, respectively,  $\nu$  is kinematic viscosity of mixed gas, and  $\nu_n$  and  $\nu_a$  are viscosity of nitrogen and air, respectively.

Reynolds number ranges from  $7.06 \times 10^4$  to  $2.21 \times 10^5$  in calculations. Thus, a realizable  $k-\varepsilon$  turbulence model [12–14] is employed to close the flow governing equations and describe the turbulent properties:

$$\begin{aligned} \frac{\partial(\rho k)}{\partial t} + \frac{\partial(\rho k u_i)}{\partial x_i} &= \frac{\partial}{\partial x_j} \left[ \left( \mu + \frac{\mu_t}{\sigma_k} \right) \frac{\partial k}{\partial x_j} \right] + G_k + G_b - \rho \varepsilon, \\ \frac{\partial(\rho \varepsilon)}{\partial t} + \frac{\partial(\rho \varepsilon u_i)}{\partial x_i} &= \frac{\partial}{\partial x_j} \left[ \left( \mu + \frac{\mu_t}{\sigma_\varepsilon} \right) \frac{\partial \varepsilon}{\partial x_j} \right] + \rho C_{1\varepsilon} S \varepsilon \\ &\quad - \rho C_{2\varepsilon} \frac{\varepsilon^2}{k + \sqrt{\nu \varepsilon}} + C_{1\varepsilon} (1 - C_{3\varepsilon}) \frac{\varepsilon}{k} G_b, \end{aligned} \quad (3)$$

where

$$\begin{aligned} C_1 &= \max \left( 0.43, \frac{\eta}{\eta + 5} \right), \\ \eta &= S \frac{k}{\varepsilon}, \\ S &= (2S_{ij} \cdot S_{ij})^{1/2}, \\ S_{ij} &= \frac{1}{2} \left( \frac{\partial u_i}{\partial x_j} + \frac{\partial u_j}{\partial x_i} \right), \\ G_k &= -\rho u'_i u'_j \frac{\partial u_j}{\partial x_i}, \\ G_b &= -g_i \frac{\mu_t}{Pr_t} \frac{\partial \rho}{\rho \partial x_i}, \\ \mu_t &= \rho C_\mu \frac{k^2}{\varepsilon}, \end{aligned} \quad (4)$$

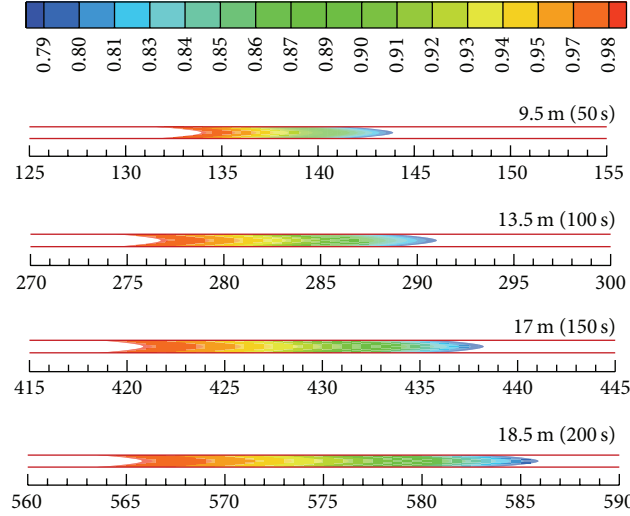


FIGURE 3: Gas mixture length at different times.

where  $k$  and  $\varepsilon$  represent turbulent kinetic energy and turbulent kinetic energy dissipation rate per unit mass, respectively,  $\eta$  is the relative strain parameter,  $S$  is the strain rate,  $G_k$  and  $G_b$  represent production term of turbulent kinetic energy due to the average velocity gradient and production term of turbulent kinetic energy due to lift, respectively,  $\mu_t$  is turbulent viscosity,  $pr_t$  is Prandtl number taken as 0.85,  $C_\mu$ ,  $C_{1\varepsilon}$ ,  $C_2$ , and  $C_{3\varepsilon}$  are empirical model constants taken as 0.09, 1.44, 1.9, and 0.9, respectively, and  $\sigma_t$  and  $\sigma_\varepsilon$  are turbulent Prandtl numbers taken as 1.0 and 1.2, respectively.

There is no reaction between nitrogen and air in the replacement process, so a simplified species-transportation model is employed to capture the mixture of nitrogen and air written as [15] follows:

$$\begin{aligned} & \frac{\partial(\alpha\rho_n)}{\partial t} + \frac{\partial(\alpha\rho_n u)}{\partial x} + \frac{\partial(\alpha\rho_n v)}{\partial y} \\ & = \frac{\partial}{\partial x} \left[ D_n \frac{\partial(\alpha\rho_n)}{\partial x} \right] + \frac{\partial}{\partial y} \left[ D_n \frac{\partial(\alpha\rho_n)}{\partial y} \right], \end{aligned} \quad (5)$$

where  $\alpha$  is nitrogen volume fraction and  $D_n$  and  $D_a$  are diffusion coefficient of nitrogen and air, respectively.

**3.2. Numerical Method.** Finite volume method (FVM) is employed to discretize above equations. All the calculations are performed using a commercial software package FLU-ENT 14.5. Patankar's well-known SIMPLE algorithm [16] is adopted to solve the pressure-velocity coupling. In order to ensure the accuracy of calculation, second-order upwind scheme and second-order central-differencing scheme are used for convective terms and diffusion terms, respectively. The convergent criteria for all calculations are set as that the residual in the control volume for each equation is smaller than  $10^{-5}$ .

**3.3. Boundary and Initial Conditions.** Velocity inlet boundary condition is used for the inlet, and the inlet rates of nitrogen

are taken as 2 m/s, 3 m/s, 4 m/s, and 5 m/s in comparing cases. In the outlet of computational domain, pressure outlet boundary condition is employed, and the value is defined as 0 Pa in order to facilitate comparative analysis. No slip boundary condition is imposed on the pipe wall.

Since it is an unsteady problem, the whole computational domain of pipe is defined as being filled with air at the initial time. And the time step in simulations is set to 0.001 s. The information of simulation cases is listed in Table 1, in which pipe length, pipe diameter, and inlet rate and inclination angle are the four variables.

## 4. Numerical Results and Discussion

**4.1. Standard Case Analysis.** Case 6 is adopted as the standard case. Figure 3 shows the gas mixture length at different times, which is reflected by the volume fraction of nitrogen. The volume fraction of nitrogen more than 98% can be considered to meet the safe replacement requirement. And the content of nitrogen in air is 79%. Therefore, volume fraction of nitrogen ranging from 0.79 to 0.98 corresponds to the mixed gas. And the length of this mixed gas is called gas mixture length.

It is seen that the head of the mixed gas shows a bullet-shaped distribution. Frictional resistance at pipe wall is the major cause for this phenomenon. It is well known that there is a viscous sublayer near pipe wall. The closer the gas is to the wall, the greater the viscosity resistance gas gets. So the gas in the axis of pipe moves ahead. It is worth noting that the gas mixture length increases over time. At the time of 50 s, the gas mixture length is 9.5 m, while it increases to 18.5 m at the time of 200 s. In the mixed gas, the volume fraction of nitrogen gradually decreases along the pipe axis direction. And the decreasing rate is gradually reduced with time. This is because nitrogen is mixed with air more fully as time passes. However, the growth rate of mixture length is reducing over time. In the period from 50 s to 100 s, the mixture length is increased by 4 m, while it is increased by 3.5 m in the same

TABLE 1: Simulation cases.

Case	The length of straight pipe, $L_1$ (m)	Pipe diameter, $D$ (mm)	Inlet rate, $v$ (m/s)	Inclination angle, $\theta$ ( $^\circ$ )	The length of inclined pipe, $L_2$ (m)
1	50	647.2	3	0	0
2	150	647.2	3	0	0
3	300	647.2	3	0	0
4	400	647.2	3	0	0
5	500	647.2	3	0	0
6	600	647.2	3	0	0
7	700	647.2	3	0	0
8	800	647.2	3	0	0
9	900	647.2	3	0	0
10	1000	647.2	3	0	0
11	600	346.0	3	0	0
12	600	851.2	3	0	0
13	600	1000.2	3	0	0
14	600	647.2	2	0	0
15	600	647.2	4	0	0
16	600	647.2	5	0	0
17	600	647.2	3	10	600
18	600	647.2	3	20	600
19	600	647.2	3	30	600
20	600	647.2	3	40	600

interval of time (from 100 s to 150 s). And the increment is just 1.8 m for time increased from 150 s to 200 s. It can be explained that kinetic energy of nitrogen flow is consumed continuously as time goes. Therefore, the driving force and forward speed decrease gradually.

**4.2. Effect of Pipe Length.** Since gas mixture length increases over time, the maximum mixture length will appear at the outlet of pipe. Figure 4 illustrates the maximum gas mixture length for different pipe lengths. It is observed that the maximum gas mixture length increases with the increase in pipe length. The maximum gas mixture length reaches 24 m in 1000 m long pipe, which is about six times longer than that in 50 m long pipe. The main reason is that the longer the pipe is, the more the time is required for gas flow passing through, resulting in more gas mixed. However, the increment of the maximum gas mixture length reduces for pipe with length ranging from 400 m to 1000 m. And the increment is not decreased linearly.

The gas mixture length curves, as shown in Figure 5, also show nonlinear relationship. Gas mixture length increases rapidly at the beginning, while the growth rate decreases after a period of time. This main reason is that, at the beginning of replacement, the volume fraction gradient and velocity gradient in pipe are both large, but the two gradients decrease gradually over time.

The longest pipeline used in simulation is just 1000 m. However, actual piping often has hundreds or thousands of kilometers. In order to predict the maximum gas mixture length in longer pipelines, the maximum gas mixture length

( $l_m$ ) versus the pipe length ( $L$ ) is analyzed, and we have obtained the fitting formula, as shown in Figure 6. The adjusted  $R$ -squares reach 0.98722. Namely, the error in mixing length prediction is of the order of 1~2%. The fitting formula is written as

$$l_m = 2.03004 + 0.03149L - 8.67344 \times 10^{-6}L^2. \quad (6)$$

If the actual parameters are the same as that used in this paper such as  $D = 647.2$  mm and  $v = 3$  m/s, we can calculate the maximum gas mixture length in an arbitrary long pipe using this formula. For example, if the length of pipe is  $1 \times 10^5$  m,  $l_m$  would be calculated as 1998.13 m. In order to detect the accuracy of this prediction equation, 1D simulation for pipe length  $1 \times 10^5$  m has been conducted. One order central difference method is employed to discrete one-dimensional governing equations. For  $1 \times 10^5$  m long pipe with diameter 647.2 mm and inlet rate 3 m/s, the calculated maximum mixing length by 1D simulation is 1959.62 m. So the error in mixing length prediction is less than 2%.

Therefore, the actual replacement time is not simply equal to pipe length divided by the flow speed. Qualified replacement is achieved until the mixed gas flows out thoroughly. So the replacement time should be more than the sum of pipe length divided by flow velocity and the maximum gas mixture length divided by flow rate.

**4.3. Effect of Pipe Diameter.** Figure 7 presents the maximum gas mixture length for different pipe diameters. It can be seen that the maximum gas mixture length increases with the increase in pipe diameter. The main cause of this result is

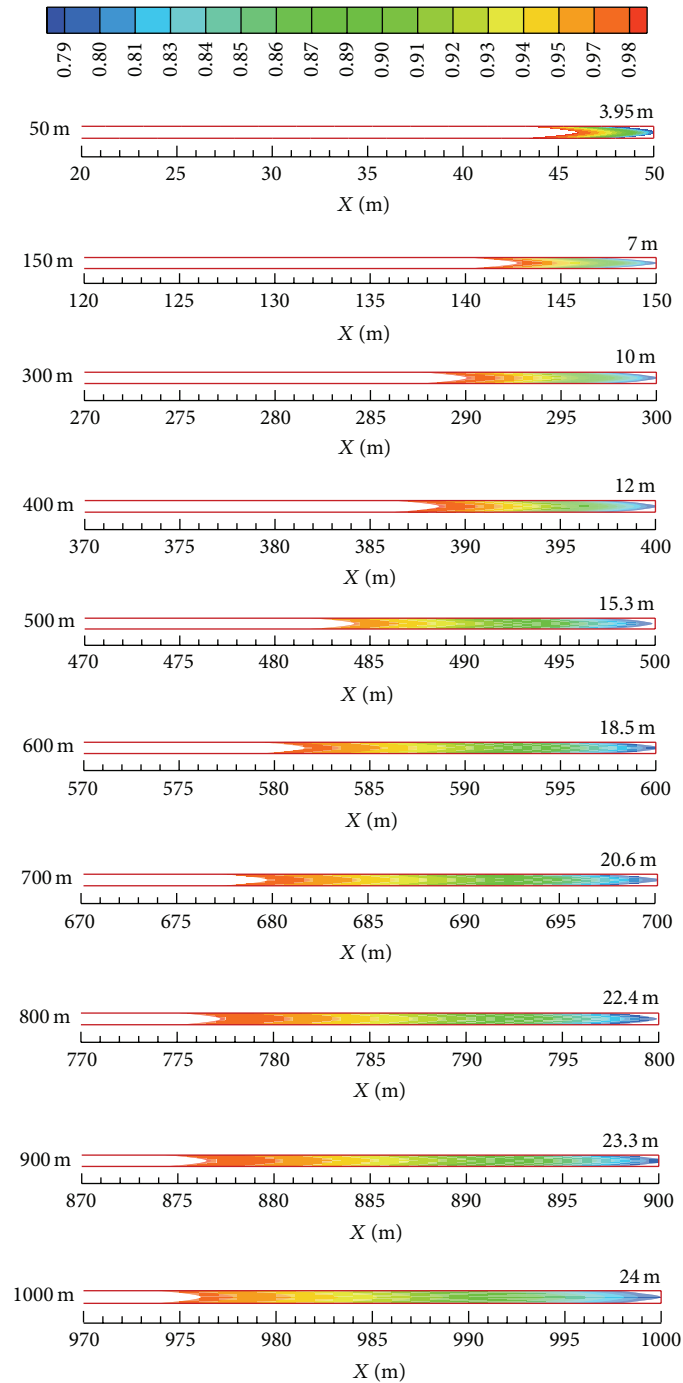


FIGURE 4: The maximum gas mixture length for different pipe lengths.

that the total kinetic energy of nitrogen flow is more in large-diameter pipe as the same inlet rate. Affected by the impact of friction, the smaller the pipe diameter is, the sharper the bullet-shaped head is.

The gas mixture length varied with time in pipes of different diameters is shown in Figure 8. The growth trend of mixture length is similar for different diameters. However, in small-diameter pipe, the growth rate of mixture length is relatively small. It is attributed to the joint action of kinetic energy and frictional resistance.

The actual pipe diameter is not only the four we have studied. So we also get the fitting formula of  $l_m$  versus  $D$ , as shown in Figure 9. The fitting line meets the linear distribution well, and the adjusted  $R$ -squares are 0.99295. The fitting formula is written as

$$l_m = 16.30719 + 0.00561D. \quad (7)$$

If the pipe diameter is 800.2 mm,  $l_m$  would be calculated as 20.8 m.

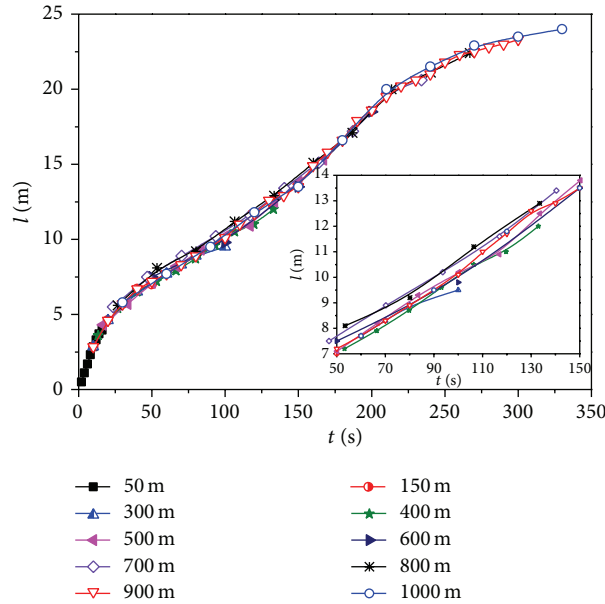


FIGURE 5: The gas mixture length varied with time in pipes of different lengths.

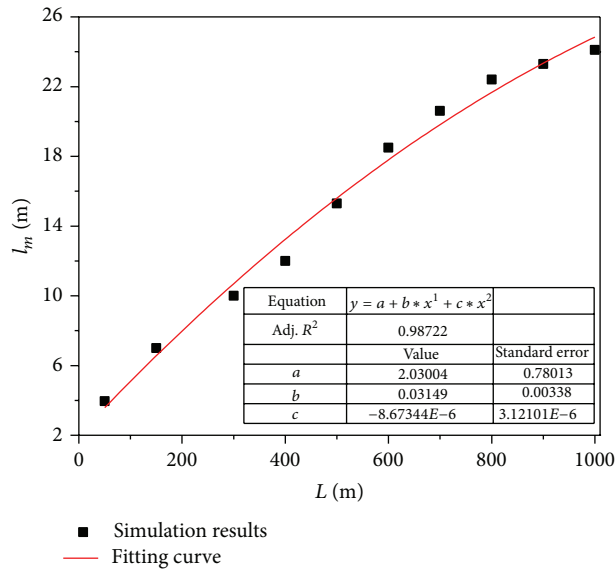


FIGURE 6: The maximum gas mixture length ( $l_m$ ) versus the pipe length ( $L$ ).

4.4. *Effect of Inlet Rate.* Figure 10 depicts the maximum gas mixture length at different inlet rates. The faster the nitrogen forward, the longer the maximum gas mixture length. It is attributed to that high speed of nitrogen flow has more kinetic energy. Gas mixed more fuller at large inlet rate, resulting in the longer mixture length. As inlet rate increases 1 m/s, the increments of the maximum gas mixture length are basically the same, about 1.9 m.

The gas mixture length varied with time at different inlet rates is shown in Figure 11. The growth rate of mixture length presents the maximum value (0.2 m/s) at  $v = 5$  m/s, which is about 3.33 times than that at  $v = 2$  m/s. Less time required for high-speed flow to pass through the pipe is the main cause.

Though faster replacement is reached by high inlet rate, the rate cannot be set to too large. Residue particles will be carried by high-speed flow and strike pipe wall, leading to electric spark. Therefore, inlet rate should be controlled in a certain range. In practice, 4 m/s is an appropriate choice.

As shown in Figure 12, the fitting formula of  $l_m$  versus  $v$  is obtained. This fitting line also meets the linear distribution, and the adjusted  $R$ -squares are 0.99483. The fitting formula is as follow:

$$l_m = 13.86 + 2.04v. \tag{8}$$

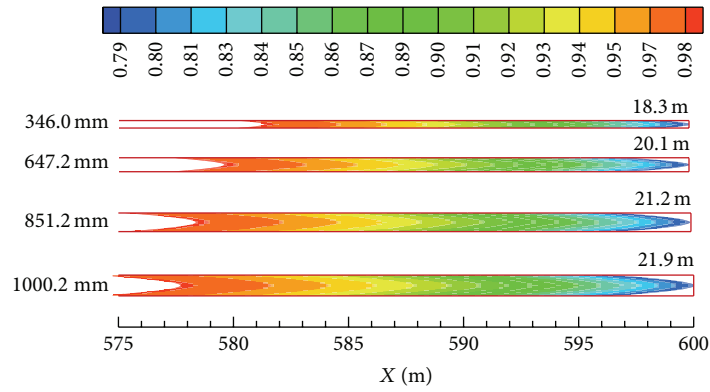


FIGURE 7: The maximum gas mixture length for different pipe diameters.

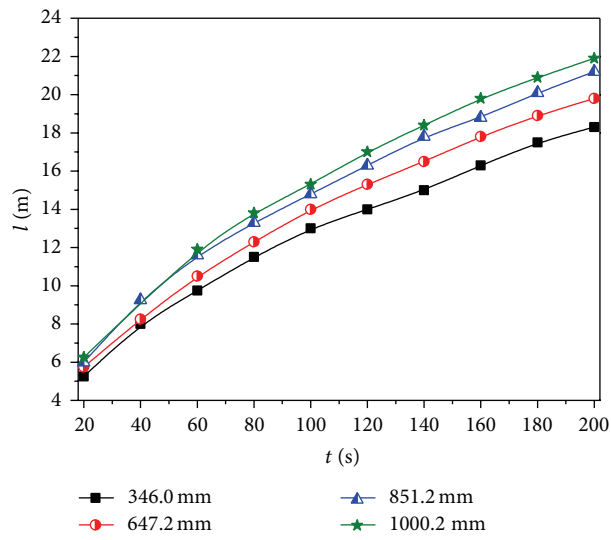


FIGURE 8: The gas mixture length varied with time in pipes of different diameters.

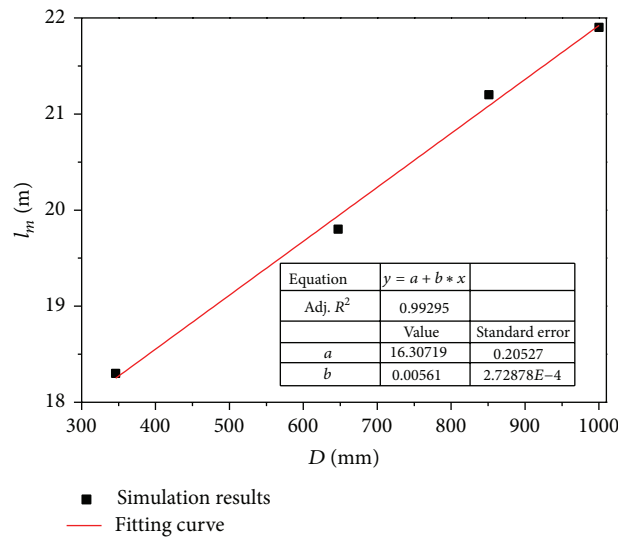


FIGURE 9: The maximum gas mixture length ( $l_m$ ) versus the pipe diameter ( $D$ ).

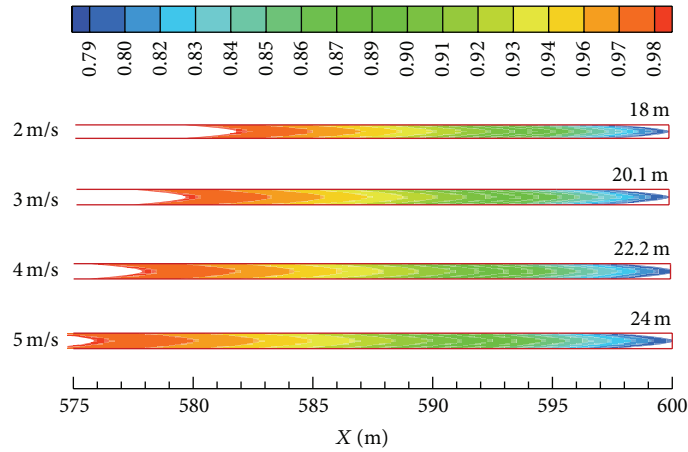


FIGURE 10: The maximum gas mixture length at different inlet rates.

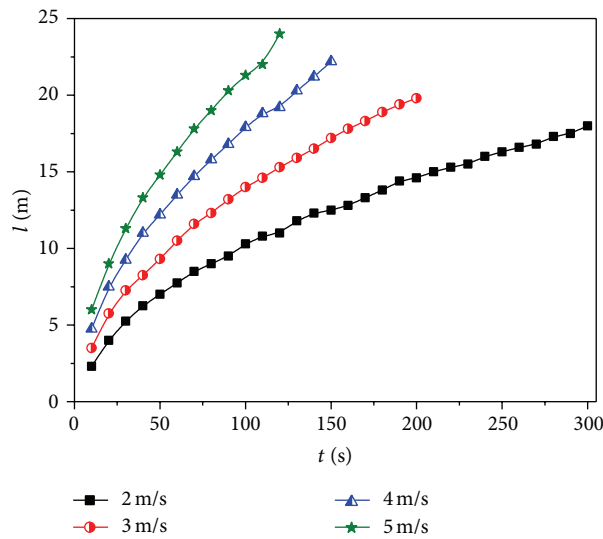


FIGURE 11: The gas mixture length varied with time at different inlet rates.

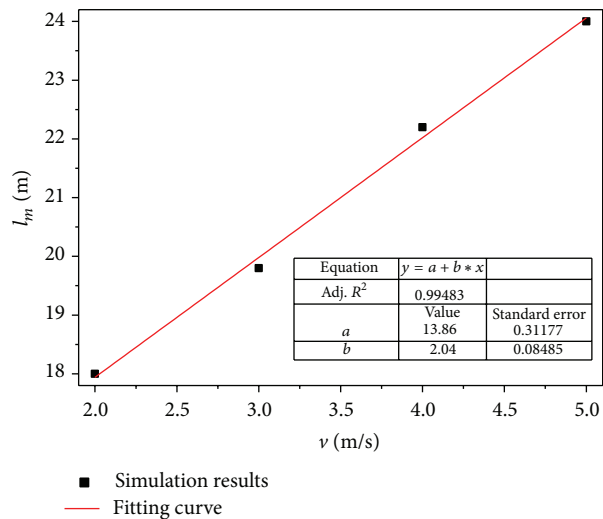


FIGURE 12: The maximum gas mixture length ( $l_m$ ) versus the inlet rate ( $v$ ).

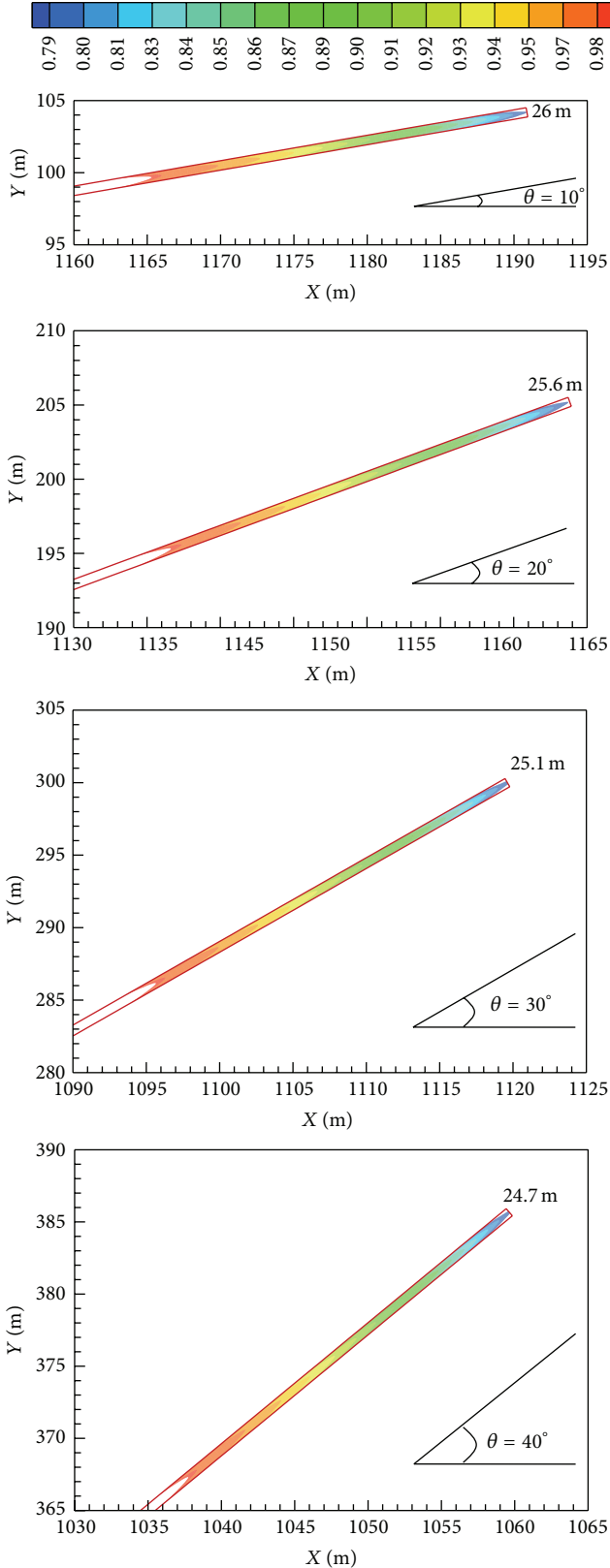


FIGURE 13: The maximum gas mixture length at different inclination angles.

Using this formula,  $l_m$  would be calculated as 21 m if the inlet rate is 3.5 m/s.

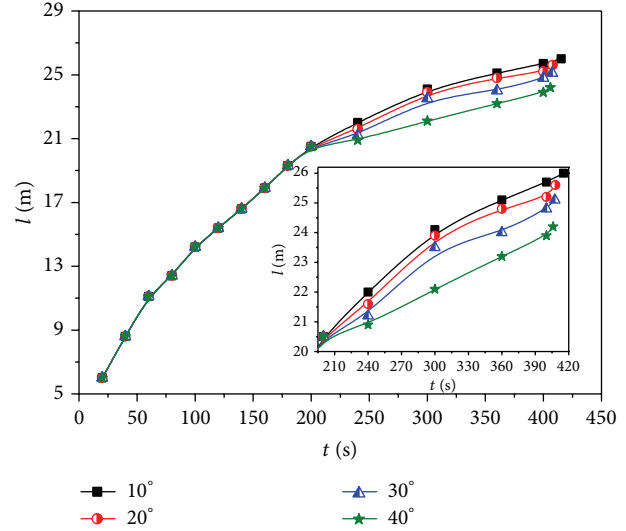


FIGURE 14: The gas mixture length varied with time at different inclination angles.

4.5. *Effect of Inclination Angle of Pipe.* Taking the terrain into account, four undulating pipes with different inclination angles are analyzed. Figure 13 provides the maximum gas mixture length at different inclination angles. We find an obvious reduction in mixture length as inclination angle increases. For  $\theta = 10^\circ$ , the maximum gas mixture length is 26 m, while it decreases to 24.7 m for  $\theta = 40^\circ$ . The main cause is that partial energy of gas flow is used to overcome gravity acting, and more energy is consumed for steep pipe.

Figure 14 shows the gas mixture length varied with time at different inclination angles. There is no difference in straight pipe section. The significant difference appears in inclined upward section. The larger the inclination angle, the smaller the growth rate of mixture length.

The fitting formula of  $l_m$  versus  $\theta$  is shown in Figure 15. This fitting line is a negative slope straight line, and the adjusted  $R$ -squares reach 0.99691. The fitting formula is

$$l_m = 26.45 - 0.044\theta. \tag{9}$$

If the inclination angle is  $50^\circ$ ,  $l_m$  would be calculated by the formula as 24.25 m.

### 5. Conclusions

A computational fluid dynamic model coupled to a species-transportation model has been used to investigate the gas mixture length of nitrogen replacement in large-diameter pipeline without isolator. Effects of pipe length and diameter, inlet rate, and inclination angle of pipe are examined by conducting a series of simulations. Based on the numerical results, the following conclusions can be drawn.

- (1) Gas mixture length increases over time, and the maximum gas mixture length is present at outlet of pipe. Long and large-diameter pipe and fast speed of nitrogen lead to long length of mixed gas, while large inclination angle of pipe brings about short length.

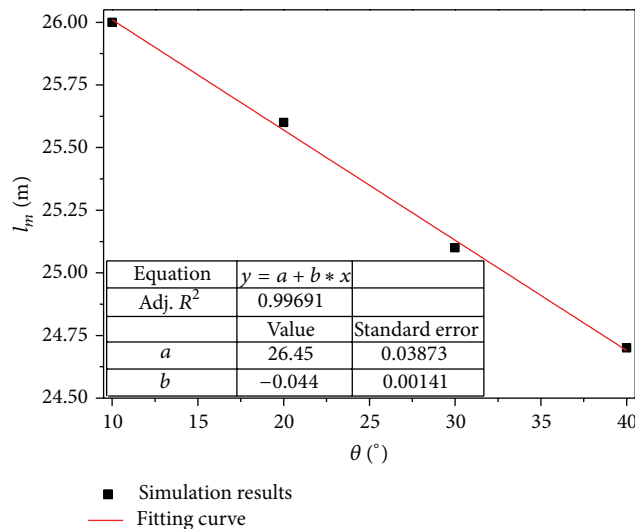


FIGURE 15: The maximum gas mixture length ( $l_m$ ) versus the inclination angle ( $\theta$ ).

- (2) Four fitting formulas have been obtained, which can predict the maximum gas mixture length in gas pipelines. Besides that the formula for pipe length is a quadratic polynomial, the other formulas meet linear relationship. The calculation results provide effective guidance for practical operation of nitrogen replacement.

## Conflict of Interests

The authors declare that there is no conflict of interests regarding the publication of this paper.

## Acknowledgments

Research work was supported by Open Fund (no. PLN1210) of State Key Laboratory of Oil and Gas Reservoir Geology and Exploitation (Southwest Petroleum University) and Key Project of Sichuan Provincial Education Department (No. 12ZA189). Without the support, this work would not have been possible.

## References

- [1] G. Liu and G. W. Wang, "Method to control gas displacement velocity in gas pipeline commissioning," *Oil & Gas Storage and Transportation*, vol. 26, no. 22, pp. 53–56, 2007.
- [2] W. Duan, J. Zhang, S. Zhang, and H. P. Liu, "Study on length of gas mixture segment for commissioning replacement of long-distance gas pipeline," *Oil & Gas Storage and Transportation*, vol. 30, no. 3, pp. 5–7, 2012.
- [3] L. W. Tan, J. Q. Jing, Z. X. Dai, Z. Lv, and H. M. Shao, "Study of natural gas pipeline replacement technology by nitrogen gas," *Pipeline Technique and Equipment*, vol. 15, no. 3, pp. 25–28, 2007.
- [4] K. F. Fan, W. Q. Wang, Y. Ma, H. Jiang, and Z. X. Pang, "The numerical simulation on mixture gas of nitrogen replacement in natural gas pipeline," *Journal of Petrochemical Universities*, vol. 26, no. 1, pp. 63–67, 2013.
- [5] L. W. Tan, J. Q. Jing, Z. X. Dai, Z. Lv, and H. Zhang, "Determination of process parameters of nitrogen replacement in gas pipeline," *Petroleum Planning & Engineering*, vol. 18, no. 5, pp. 43–45, 2007.
- [6] Y. M. Guo and J. J. Xue, "Numerical simulation on gas mixing rule in course of nitrogen isolation gas displacement technology for commissioning of gas transmission pipeline," *Oil Field Equipment*, vol. 35, no. 5, pp. 31–34, 2006.
- [7] J. Z. Huang and L. Fang, "Analysis of nitrogen replacement in gas pipeline," *Petroleum and Chemical Construction*, vol. 32, no. 3, pp. 73–75, 2010.
- [8] J. E. Hanssen, "Nitrogen as a low-cost replacement of natural gas reinjection offshore," in *Proceedings of the SPE Gas Technology Symposium*, SPE 17709, Dallas, Tex, USA, June 1988.
- [9] L. C. Berger and J. P. Arnoult, "Production of inert gas for partial replacement of natural gas trapped in an underground aquifer storage reservoir," in *Proceedings of the SPE Gas Technology Symposium*, SPE 19089, Dallas, Tex, USA, June 1989.
- [10] X. R. Wu, K. G. Liang, and D. X. Liu, "Nitrogen injection experience to development gas and gas condensate fields in rocky mountains," in *Proceedings of the International Petroleum Technology Conference*, IPTC 16830, Beijing, China, March 2013.
- [11] G. Alfonsi, "Reynolds-averaged Navier-Stokes equations for turbulence modeling," *Applied Mechanics Reviews*, vol. 62, no. 4, Article ID 040802, pp. 1–20, 2009.
- [12] K. van Maele and B. Merci, "Application of two buoyancy-modified k- $\epsilon$  turbulence models to different types of buoyant plumes," *Fire Safety Journal*, vol. 41, no. 2, pp. 122–138, 2006.
- [13] P. Rohdin and B. Moshfegh, "Numerical predictions of indoor climate in large industrial premises. A comparison between different k- $\epsilon$  models supported by field measurements," *Building and Environment*, vol. 42, no. 11, pp. 3872–3882, 2007.
- [14] M. Ji, T. Utomo, J. Woo, Y. Lee, H. Jeong, and H. Chung, "CFD investigation on the flow structure inside thermo vapor compressor," *Energy*, vol. 35, no. 6, pp. 2694–2702, 2010.
- [15] Y. Sun, J. N. Petersen, and T. P. Clement, "Analytical solutions for multiple species reactive transport in multiple dimensions," *Journal of Contaminant Hydrology*, vol. 35, no. 4, pp. 429–440, 1999.
- [16] S. V. Patankar, *Numerical Heat Transfer and Fluid Flow*, McGraw-Hill Press, New York, NY, USA, 1980.

## Research Article

# Track-to-Track Association Based on Structural Similarity in the Presence of Sensor Biases

**Hongyan Zhu and Suying Han**

*School of Electronic and Information Engineering, Xi'an Jiaotong University, Xi'an 710049, China*

Correspondence should be addressed to Hongyan Zhu; [hyzhu2011@gmail.com](mailto:hyzhu2011@gmail.com)

Received 23 October 2013; Accepted 26 February 2014; Published 25 March 2014

Academic Editor: Nachamada Blamah

Copyright © 2014 H. Zhu and S. Han. This is an open access article distributed under the Creative Commons Attribution License, which permits unrestricted use, distribution, and reproduction in any medium, provided the original work is properly cited.

The paper addresses the problem of track-to-track association in the presence of sensor biases. In some challenging scenarios, it may be infeasible to implement bias estimation and compensation in time due to the computational intractability or weak observability about sensor biases. In this paper, we introduce the structural feature for each local track, which describes the spatial relationship with its neighboring targets. Although the absolute coordinates of local tracks from the same target are severely different in the presence of sensor biases, their structural features may be similar. As a result, instead of using the absolute kinematic states only, we employ the structural similarity to define the association cost. When there are missed detections, the structural similarity between local tracks is evaluated by solving another 2D assignment subproblem. Simulation results demonstrated the power of the proposed approach.

## 1. Introduction

The potential advantages of fusing information from disparate sensor systems to achieve better surveillance have been recognized. Track-to-track association [1, 2] is a crucial step in the distributed estimation fusion system, which seeks to determine the correspondence between local tracks from different sensors. Unfortunately, sensor reports may be influenced by systematic errors (sensor biases) besides random errors. In this case, sensor registration [3, 4] is required to remove the sensor biases from the biased reports. When track association and sensor registration meet each other, there are more challenges. On the one hand, sensor registration is based on the common sensor reports from the same target. On the other hand, the removal of the sensor biases contributes greatly to making correct association assignments. In this sense, sensor registration and track association are tightly coupled together.

An alternative way to tackle this problem is to implement bias estimates and track-to-track association jointly. Several heuristic algorithms, including centroid matching and singleton matching algorithms, for estimating the relative sensor biases in track-to-track association were explored in [5]. Considering the effects of biases, Stone et al. estimated the relative

biases based on the fast Fourier transform (FFT) and multiple dimensional spatial cross-correlation function in [6]. In [7], Levedahl modeled this problem as a global nearest pattern (GNP) problem. It produced the bias estimates for each association hypothesis firstly, and the association probability was computed based on the given bias estimates. The final association hypothesis was determined with the maximum probability. In [8], Papageorgiou and Sergi optimized the computation complexity of the GNP algorithm to get the trading-off between the optimality and computation time. In [9, 10], Papageorgiou et al. computed the pure association probability by assuming a prior distribution of sensor biases. However, it is hard to get the prior distribution of sensor biases. A joint track association and relative bias estimation problem was formulated and a solution based on the Dijkstra search was developed in [11]. A solution based on the branch-and-bound framework for the same problem was described in [12]. In [13], the performance comparisons of several algorithms for estimating relative sensor bias were given. In [14], a feature called “reference topology” based on the relative coordinates is presented. However, its association performance depends on the granularity of cell partitions greatly. Moreover, no systematic method is given to handle the case of missed detections. In [15, 16], the joint approaches

to data association, sensor registration, and track fusion were given by means of the expectation-maximization (EM) algorithm.

In some challenging scenarios, it is impossible in practice to implement bias estimation and compensation in time due to the computational intractability or weak observability about sensor biases. In this paper, we turned to implement track-to-track association without bias estimation. As we know, it is extremely essential to establish a reasonable metric to measure the similarity of local tracks in track-to-track association problem. In general, the similarity of local tracks is based on the absolute kinematic parameters. However, the absolute kinematic parameters are corrupted greatly in the presence of sensor biases. For example, when given the azimuth bias of 3 degrees, the position deviation could reach up to 10 kilometers for a target located 200 km from the sensor. In this case, the similarity measure based on absolute coordinates is unbelievable anymore. In this paper, we introduce the structural feature for each local track describing the spatial relationship with its neighboring targets. Although the absolute coordinates of local tracks from the same target are severely different in the presence of sensor biases, their structural features may be similar. So, instead of using the absolute kinematic states only, we employ the structural similarity to measure the distance of two local tracks from different sensors.

In this paper, we develop a structural similarity-based approach to deal with the problem of track association in the presence of sensor biases. Main contributions are given as follows. Firstly, under appropriate assumptions, the distance invariance between two targets detected by different sensors is verified in the presence of sensor biases. Secondly, the structural feature is introduced for each local track, which is represented by the distance set from the track to all the other tracks from the same sensor. Thirdly, a two-dimensional (2D) assignment model is established to implement track-to-track association in the presence of sensor biases. Instead of using the absolute kinematic states only, the structural similarity between local tracks is adopted to measure the association cost and is evaluated by solving another 2D assignment sub-problem. Moreover, the dummy track is introduced for each sensor to cope with possibly missed detections. Simulation results demonstrated the power of the proposed approaches.

The rest of the paper is organized as follows. In Section 2 we describe the measurement model and formulate the problem of track-to-track association. Section 3 shows how to implement the track association based on structural similarity. Simulation results are given in Section 4 to demonstrate the effectiveness of the proposed approaches. Finally, concluding remarks and further research directions are in Section 5.

## 2. Problem Formulation

Consider a multitarget tracking scenario with two sensors and  $N_t$  targets in the surveillance region. In this paper, false alarms are not considered since they can also be viewed as the targets. In references with the radar sensor which measures the range and azimuth to the target, the measurement process

is implemented in the local polar coordinate system (LPCS). Let  $z^{m,i} \triangleq \{r^{m,i}, \theta^{m,i}\}$  be the  $i$ th measurement ( $i = 1, 2, \dots, n_m$ ) from sensor  $m$  ( $m = 1, 2$ ) at the time instant  $k$ , in which  $r^{m,i}$  and  $\theta^{m,i}$  mean the range and angle measurement, respectively.

Two kinds of sensor biases are considered in general: range bias and azimuth bias. Since there are systematic biases and random errors, the original measurement  $\{r^{m,i}, \theta^{m,i}\}$  from sensor  $m$  can be modeled as

$$\begin{aligned} r^{m,i} &= \bar{r}^{m,i} + \Delta r^m + v_r^m, \\ \theta^{m,i} &= \bar{\theta}^{m,i} + \Delta \theta^m + v_\theta^m, \end{aligned} \quad (1)$$

where  $\bar{r}^{m,i}$  and  $\bar{\theta}^{m,i}$  denote the real range and azimuth of target  $i$  from sensor  $m$ , respectively.  $\Delta r^m$  and  $\Delta \theta^m$  are systematic biases and  $v_r^m$  and  $v_\theta^m$  are random noises. The random noises  $\bar{V}^m = [v_r^m \ v_\theta^m]^T$  are white Gaussian with zero mean and variances of  $(\sigma_r^m)^2$  and  $(\sigma_\theta^m)^2$ , respectively.

Figure 1 depicts a scenario with two sensors and two targets.  $\mathbf{T}_a(\bar{x}^a, \bar{y}^a)$  and  $\mathbf{T}_b(\bar{x}^b, \bar{y}^b)$  are the real positions of targets.  $\mathbf{T}_{m,a}(x^{m,a}, y^{m,a})$  and  $\mathbf{T}_{m,b}(x^{m,b}, y^{m,b})$  are the position measurements given by sensor  $m$  ( $m = 1, 2$ ).

Based on the biased measurements  $\{r^{m,i}, \theta^{m,i}\}$ , each sensor  $m$  produces its own local tracks represented by two tuples  $\{\hat{\mathbf{x}}^{m,i}, \mathbf{P}^{m,i}\}$  ( $m = 1, 2; i = 1, 2, \dots, n_m$ ).  $\hat{\mathbf{x}}^{m,i}$  and  $\mathbf{P}^{m,i}$  mean the state estimate and error covariance, respectively. For simplicity, we omit the time index here. Track-to-track association seeks to determine the correspondence between local tracks from different sensors. The key point is to measure the similarity of local tracks. Traditionally, it is defined by the weighted statistical distance under the independence assumption:

$$\begin{aligned} \alpha_{i_1 i_2} &= (\hat{\mathbf{x}}^{1,i_1} - \hat{\mathbf{x}}^{2,i_2})^T (\mathbf{P}^{1,i_1} + \mathbf{P}^{2,i_2})^{-1} (\hat{\mathbf{x}}^{1,i_1} - \hat{\mathbf{x}}^{2,i_2}) \\ & \quad (i_1 = 1, 2, \dots, n_1, \ i_2 = 1, 2, \dots, n_2). \end{aligned} \quad (2)$$

However, local tracks are biased estimates in the presence of sensor biases. The direct association of biased estimates will not produce a satisfactory result.

## 3. Track Association Based on Structural Similarity

In traditional approaches to track-to-track association, only the absolute kinematic states of targets are considered. In the presence of sensor biases, it does not work well especially for the large azimuth bias, since it may result in severe deviations of absolute coordinates. In this section, the basic principle of the structural similarity is firstly verified, and then the structural similarity is used to measure the distance of local tracks instead of using the absolute kinematic states only. A complete 2D assignment model to deal with possible missed detections is also addressed.

*3.1. Basic Principle of Structural Similarity.* In what follows, by assuming small range biases, the distance invariance

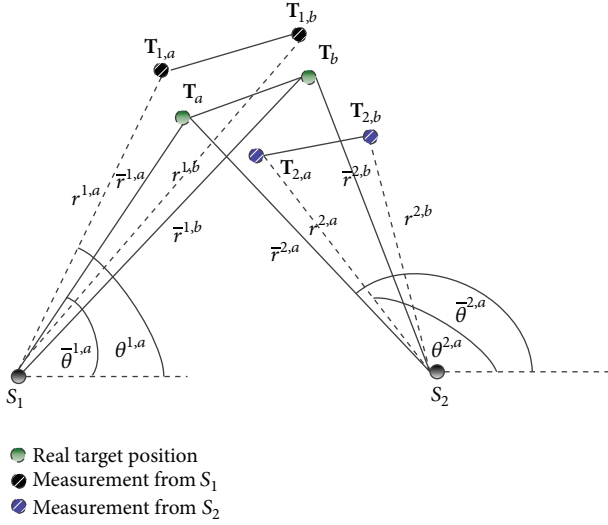


FIGURE 1: Sensor configuration geometry.

between two targets detected by different sensors is verified in the presence of sensor biases. We introduce a structural feature for each local track, which describes the spatial relationship with its neighboring targets. According to the distance invariance, the structural feature of local tracks from the same target is similar. As a result, the structural similarity is employed to define the association cost between local tracks.

The random error  $\tilde{V}^m$  ( $m = 1, 2$ ) is ignored in the following derivation for the simplicity; thus we have

$$\begin{aligned} r^{m,i} &= \bar{r}^{m,i} + \Delta r^m, \\ \theta^{m,i} &= \bar{\theta}^{m,i} + \Delta \theta^m. \end{aligned} \quad (3)$$

In the absence of sensor biases, the real position measurement of the target state is

$$\begin{bmatrix} \bar{x}^{m,i} \\ \bar{y}^{m,i} \end{bmatrix} = \begin{bmatrix} \bar{r}^{m,i} \cos(\bar{\theta}^{m,i}) \\ \bar{r}^{m,i} \sin(\bar{\theta}^{m,i}) \end{bmatrix}. \quad (4)$$

In the presence of sensor biases, it becomes

$$\begin{bmatrix} x^{m,i} \\ y^{m,i} \end{bmatrix} = \begin{bmatrix} (\bar{r}^{m,i} + \Delta r^m) \cos(\bar{\theta}^{m,i} + \Delta \theta^m) \\ (\bar{r}^{m,i} + \Delta r^m) \sin(\bar{\theta}^{m,i} + \Delta \theta^m) \end{bmatrix}. \quad (5)$$

Manipulating the items in the above equations, we have

$$\begin{aligned} \begin{bmatrix} x^{m,i} \\ y^{m,i} \end{bmatrix} &= \begin{pmatrix} \cos \Delta \theta^m & -\sin \Delta \theta^m \\ \sin \Delta \theta^m & \cos \Delta \theta^m \end{pmatrix} \begin{bmatrix} \bar{x}^{m,i} \\ \bar{y}^{m,i} \end{bmatrix} \\ &+ \begin{pmatrix} \Delta r^m \cos(\bar{\theta}^{m,i} + \Delta \theta^m) \\ \Delta r^m \sin(\bar{\theta}^{m,i} + \Delta \theta^m) \end{pmatrix}. \end{aligned} \quad (6)$$

From (6), it can be observed that the range bias  $\Delta r^m$  brings about the translation for targets, and the azimuth

bias  $\Delta \theta^m$  produces the rotation and also contributes to the translation of targets when the range bias is nonzero. Moreover, the azimuth bias is the critical factor compared with the range bias, which produces more severe influence on the target's abstract coordinate and will be enlarged as the distance from the sensor to the target increases.

The real squared distance between two targets  $\mathbf{T}_a$  and  $\mathbf{T}_b$  is

$$d^2(\mathbf{T}_a, \mathbf{T}_b) = (\bar{x}^a - \bar{x}^b)^2 + (\bar{y}^a - \bar{y}^b)^2. \quad (7)$$

For sensor  $m$  ( $m = 1, 2$ ), the squared distance  $d_m^2(\mathbf{T}_a, \mathbf{T}_b)$  between two position measurements  $\mathbf{T}_{m,a}$  and  $\mathbf{T}_{m,b}$  is

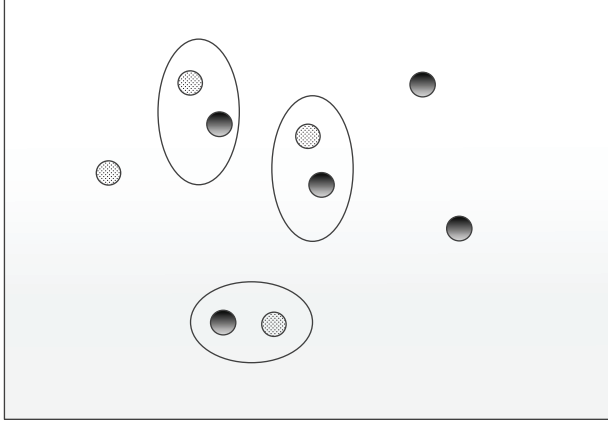
$$\begin{aligned} d_m^2(\mathbf{T}_a, \mathbf{T}_b) &\triangleq d^2(\mathbf{T}_{m,a}, \mathbf{T}_{m,b}) \\ &= (x^{m,a} - x^{m,b})^2 + (y^{m,a} - y^{m,b})^2 \\ &= (\bar{r}^{m,a} + \Delta r^m)^2 + (\bar{r}^{m,b} + \Delta r^m)^2 \\ &\quad - 2(\bar{r}^{m,a} + \Delta r^m)(\bar{r}^{m,b} + \Delta r^m) \\ &\quad \times \cos(\theta^{m,a} - \theta^{m,b}). \end{aligned} \quad (8)$$

In this way, the difference between  $d_m^2(\mathbf{T}_a, \mathbf{T}_b)$  and  $d^2(\mathbf{T}_a, \mathbf{T}_b)$  can be expressed by

$$\begin{aligned} D &\triangleq d_m^2(\mathbf{T}_a, \mathbf{T}_b) - d^2(\mathbf{T}_a, \mathbf{T}_b) \\ &= 2(\Delta r^m)^2 + 2\Delta r^m \bar{r}^{m,a} + 2\Delta r^m \bar{r}^{m,b} \\ &\quad - 2((\Delta r^m)^2 + \Delta r^m \bar{r}^{m,a} + \Delta r^m \bar{r}^{m,b}) \\ &\quad \times \cos(\bar{\theta}^{m,a} - \bar{\theta}^{m,b}) \\ &= 2((\Delta r^m)^2 + \Delta r^m \bar{r}^{m,a} + \Delta r^m \bar{r}^{m,b}) \\ &\quad \times [1 - \cos(\bar{\theta}^{m,a} - \bar{\theta}^{m,b})]. \end{aligned} \quad (9)$$

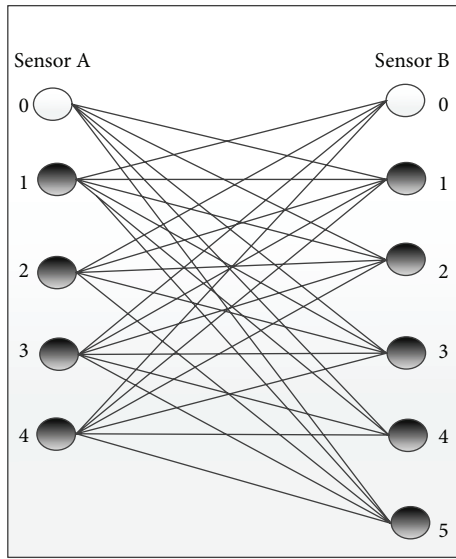
From (9), it is seen that the difference  $D$  is only influenced by the range bias  $\Delta r^m$  and the real position of the target but is independent of azimuth bias  $\Delta \theta^m$ . This reveals that although the azimuth bias may cause a severe impact on the absolute coordinate, it causes less impact on the relative coordinate. When the range bias is too large, the difference  $D$  may be severe. Fortunately, the range bias in practical applications is generally at a low level. That means that the distance between two targets detected by different sensors differs slightly, which is less sensitive to sensor biases. In what follows, we employ the structural similarity to measure the distance between two local tracks from different sensors.

**3.2. 2D Assignment Model for Track Association.** As we know, it is very important to establish a reasonable metric to measure the similarity of local tracks from different sensors. This problem becomes extremely complicated in the presence of sensor bias, random errors, and missed tracks. Figure 2



- Measurement from sensor 1
- Measurement from sensor 2
- In which measurements from the same target

FIGURE 2: Distribution of measurements from different sensors.



- Dummy node
- Local tracks
- Connecting cost

FIGURE 3: Graphical representation of track association problem.

illustrates a scenario with two sensors and six targets. Here, sensor 1 detects 4 targets, and sensor 2 detects 5 targets. That means that  $n_1 = 4$ ,  $n_2 = 5$ , and there are 3 common targets.

For the scenario in Figure 2, a graphical representation of track association is shown in Figure 3. We introduce a node for each local track. To deal with possible missed detections, a dummy node is introduced for each local sensor which provides the access to link an isolated track with the dummy track. The edges mean possible links between different local tracks.

In the following, a 2D assignment model with given constraints is established by minimizing the sum of all pairwise costs:

$$\begin{aligned}
 \min \quad & \sum_{i_1=0}^{n_1} \sum_{i_2=0}^{n_2} c_{i_1 i_2} \rho_{i_1 i_2} \\
 \text{s.t.} \quad & \sum_{i_2=0}^{n_2} \rho_{i_1 i_2} = 1, \quad \forall i_1 = 1, 2, \dots, n_1 \\
 & \sum_{i_1=0}^{n_1} \rho_{i_1 i_2} = 1, \quad \forall i_2 = 1, 2, \dots, n_2 \\
 & \rho_{i_1 i_2} \in \{0, 1\}, \quad \forall i_1 = 0, 1, 2, \dots, n_1, \\
 & \quad \quad \quad \forall i_2 = 0, 1, 2, \dots, n_2.
 \end{aligned} \tag{10}$$

**3.3. Association Cost of Local Nodes Based on the Structural Similarity.** The model (10) can be solved efficiently and optimally by the general 2D assignment algorithms, such as auction algorithm and Hungarian algorithm. Now, the remaining problem in solving (10) is how to define the connecting cost  $c_{i_1 i_2}$ . Instead of using the absolute kinematic states only, the structural similarity of local tracks is employed here. Three kinds of costs need to be specified: between local tracks, between dummy tracks, and between local track and the dummy track.

Firstly, we define a structural feature for each node  $N_{i_m}$  ( $m = 1, 2; i_m = 1, \dots, n_m$ ), which is represented by the set  $I_{i_m}$  including all the distances from local track  $i_m$  to  $j$  ( $j = 1, 2, \dots, n_m, j \neq i_m$ ); that is,

$$I_{i_m} = \{d(j, i_m)\}_{j=1, 2, \dots, n_m, j \neq i_m}. \tag{11}$$

We discuss the definition of  $c_{i_1 i_2}$  in terms of the following three cases.

(1) *With Unity Detection Probability*  $P_{D_m}$  ( $P_{D_m} = 1, m = 1, 2$ ). If  $P_{D_m} = 1$  ( $m = 1, 2$ ), then  $n_1 = n_2 = n$ . We order the elements of set  $I_{i_m}$  from the smallest to largest:  $\tilde{d}_{i_m, 1} \leq \tilde{d}_{i_m, 2} \leq \dots \leq \tilde{d}_{i_m, n-1}$ . In this way, the cost  $c_{i_1 i_2}$  (for all  $i_1 = 1, 2, \dots, n_1$ , for all  $i_2 = 1, 2, \dots, n_2$ ) can be defined by

$$c_{i_1 i_2} = D(I_{i_1}, I_{i_2}) = \sum_{j=1}^{n-1} |\tilde{d}_{i_1, j} - \tilde{d}_{i_2, j}|. \tag{12}$$

(2) *Without Unity Detection Probability*  $P_{D_m}$  ( $P_{D_1} \cdot P_{D_2} \neq 1$ ). If  $P_{D_m} < 1$  ( $m = 1, 2$ ), the computation of  $c_{i_1 i_2}$  (for all  $i_1 = 1, 2, \dots, n_1$ , for all  $i_2 = 1, 2, \dots, n_2$ ) becomes complicated due to possible missed detections. To define the connection cost  $c_{i_1 i_2}$ , a 2D assignment subproblem (13) is constructed. As shown in Figure 4, a graphical representation is established to compute the cost  $c_{23}$ . As done in the optimization model

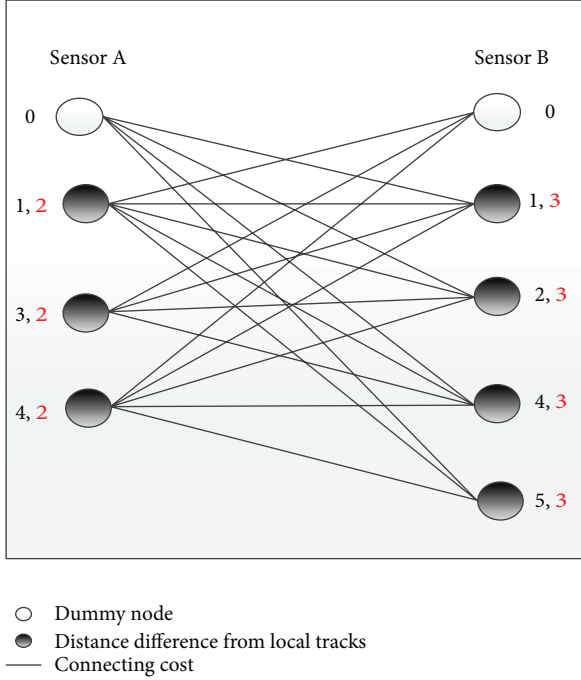


FIGURE 4: Graphical representation of 2D assignment subproblem to compute the cost  $c_{23}$ .

(10), two dummy nodes are introduced to cope with the case of missed detections:

$$\begin{aligned}
 J_{i_1 i_2} &= \min \sum_{j_1=0, j_1 \neq i_1}^{n_1} \sum_{j_2=0, j_2 \neq i_2}^{n_2} \tilde{c}_{j_1 j_2} \tilde{\rho}_{j_1 j_2} \\
 \text{s.t.} \quad &\sum_{j_2=0, j_2 \neq i_2}^{n_2} \tilde{\rho}_{j_1 j_2} = 1, \quad \forall j_1 = 1, 2, \dots, n_1, \quad j_1 \neq i_1 \\
 &\sum_{j_1=0, j_1 \neq i_1}^{n_1} \tilde{\rho}_{j_1 j_2} = 1, \quad \forall j_2 = 1, 2, \dots, n_2, \quad j_2 \neq i_2 \\
 &\tilde{\rho}_{j_1 j_2} \in \{0, 1\}, \quad \forall j_1 = 0, 1, 2, \dots, n_1, \\
 &\forall j_2 = 0, 1, 2, \dots, n_2, \quad j_1 \neq i_1, \quad j_2 \neq i_2.
 \end{aligned} \tag{13}$$

In this optimization model (13), the critical part is to define the cost  $\tilde{c}_{j_1 j_2}$ . For all  $j_1 = 1, 2, \dots, n_1$ ,  $j_1 \neq i_1$ , and for all  $j_2 = 1, 2, \dots, n_2$ ,  $j_2 \neq i_2$ , the cost  $\tilde{c}_{j_1 j_2}$  is defined by the absolute value of distance difference:

$$\tilde{c}_{j_1 j_2} = |d(j_1, i_1) - d(j_2, i_2)|. \tag{14}$$

If track-pair  $\{i_1, j_1\}$  from sensor 1 and  $\{i_2, j_2\}$  from sensor 2 share the same two targets, then  $\tilde{c}_{j_1 j_2}$  would be a small quantity due to the structural similarity. When given a threshold  $\lambda$ , we compare  $\tilde{c}_{j_1 j_2}$  and the gate value  $\lambda$ . If  $\tilde{c}_{j_1 j_2} > \lambda$ , then it means that track-pair  $\{i_1, j_1\}$  from sensor 1 and  $\{i_2, j_2\}$  from sensor 2 do not share the same targets. To prevent them from associating, we set  $\tilde{c}_{j_1 j_2} = +\infty$ . In practical operations,

we set  $\tilde{c}_{j_1 j_2} = \Gamma$ , where  $\Gamma$  is a large positive integer. In addition, we set  $\tilde{c}_{0 j_2} = \tilde{c}_{j_1 0} = 10^{-2}\Gamma$  to encourage the isolated node to link with the dummy node. In addition, we set  $\tilde{c}_{00} = \Gamma$ .

As far, a complete 2D assignment subproblem (13) is well defined. By solving it, the optimal fitness  $J_{i_1 i_2}^*$  can be obtained. It is noted that  $c_{i_1 i_2}$  cannot be defined directly by  $J_{i_1 i_2}^*$ ; further processing is required considering possible isolated tracks. We denote the number of valid associations by  $\beta$ , which is defined as the number of association assignments between local tracks (not with dummy nodes). If  $\beta$  is close enough to the expected number  $\alpha$  of common targets ( $|\beta - \alpha| \leq \varepsilon$ ,  $\varepsilon$  is a small positive integer), then  $c_{i_1 i_2} = J_{i_1 i_2}^*$ . Otherwise, set  $c_{i_1 i_2} = \Gamma$ , where the expected number  $\alpha$  of common targets is computed by

$$\alpha = \frac{P_{D_1} P_{D_2} (n_1 + n_2)}{(1 + P_{D_1} P_{D_2})}. \tag{15}$$

It is proportional to the detection probability  $P_{D_m}$  ( $m = 1, 2$ ) of sensors. If  $P_{D_m} = 1$  ( $m = 1, 2$ ), then  $\alpha = n_1 = n_2$ .

(3) *Connection Cost with Dummy Node.* When a local node ( $i_1$  or  $i_2$ ) is declared isolated, we set  $c_{0 i_2} = c_{i_1 0} = 10^{-2}\Gamma$  to encourage it to link with the dummy node. In addition, we set  $c_{00} = \Gamma$  to discourage the association between dummy tracks.

### 3.4. Discussions

(1) *Approximation Solution Based on the Nearest Neighborhood Method.* A new approach to track-to-track association in the presence of sensor biases is given in Sections 3.2 and 3.3, which requires solving two 2D optimal assignment models. One serves to compute the connecting cost between two local tracks, and the other one is to determine the final association assignment between two sets of local tracks. To simplify, we call this method “structural similarity-based 2D assignment” (SS-based 2D assignment). Considering the complexity of the proposed model, an approximation solution can be obtained by using the nearest neighborhood (NN) method when determining the final association assignment, instead of using the optimal assignment. Such a scheme is denoted by structural similarity-based nearest neighborhood (SS-based NN). Simulation results provided before indicate that such an approximate method can also provide a better association result, because the structural property is considered when constructing the connection cost between local tracks.

(2) *Possible Extensions.* In practical fusion applications, heterogeneous sensors are commonly found. The proposed approach can also work well in this case, since what we handle here are local tracks after local processing. Although the measuring process is implemented in the local measurement coordinate system, local tracks from heterogeneous sensors may be in the common Cartesian coordinate system.

In addition, in short-range applications or for maritime surveillance, different scattering centres of the objects under consideration may give rise to several distinct detections. At this time, what one is concerned with includes the state

for both the target kinematics and the target extension. The proposed approach fails to deal with the case that the targets have more than one scattering centers. Readers may refer to literatures concerning extended target tracking [17, 18]. It is still a problem which few people get into to implement track-to-track association between extended targets.

#### 4. Simulation Results

**4.1. Scenario Setup and Results.** In this section, we provide some simulation results to illustrate the efficiencies of the proposed approaches (“SS-based 2D assignment” and “SS-based NN”). Here, we consider a multiple target tracking scenario with two sensors. At the beginning of the tracking process, 30 targets are distributed uniformly in the region  $[20 \text{ km}, 40 \text{ km}] \times [20 \text{ km}, 40 \text{ km}]$ . The motion of all the targets follows the constant acceleration (CA) model with acceleration  $1 \text{ m/s}^2$ . The process noise is assumed white Gaussian with zero mean and covariance matrix  $Q = (0.1 \text{ m/s}^3)\mathbf{I}_2$ , where  $\mathbf{I}_2$  is an  $2 \times 2$  identity matrix. The initial direction of velocity occurs randomly in  $[0, 2\pi]$  with the amplitude  $100 \text{ m/s}$ . The sample interval  $T$  is set to  $1 \text{ s}$ , and the tracking time is  $30 \text{ s}$ . Two sensors are located at  $(40000 \text{ m}, 5000 \text{ m})$  and  $(15000 \text{ m}, 10000 \text{ m})$  in the global Cartesian coordinate system (GCCS), respectively. Each sensor measures the range and angle to the target. The random range error for both sensors is modelled as white Gaussian noises with the standard deviations  $\sigma_r^1 = 30 \text{ m}$  and  $\sigma_r^2 = 40 \text{ m}$ , respectively. The random angle error is also modelled as white Gaussian noises with standard deviations  $\sigma_\theta^1 = 0.2^\circ$  and  $\sigma_\theta^2 = 0.1^\circ$ . Both of the sensors employ EKF to obtain the local tracks based on their own measurement information. The measurements are supported by 50 Monte-Carlo runs performed on the same target trajectories but with independently generated measurements for each trial. Except for the special declaration in the following simulations, the detection probabilities of the two sensors are  $P_{d_1} = 0.8$  and  $P_{d_2} = 0.7$ ; the systematic biases are set to  $\Delta r_1 = 400 \text{ m}$ ,  $\Delta r_2 = 500 \text{ m}$ ,  $\Delta \theta_1 = 6^\circ$ ,  $\Delta \theta_2 = -5^\circ$ .

Performance comparisons are made between the proposed approaches and the competing algorithms. In competing algorithms, the square Mahalanobis distance is chosen as the similarity measure of two local tracks. The final association assignment is determined based on the 2D assignment algorithm and the nearest neighborhood (NN) algorithm, respectively. To simplify, they are called “bias-ignorant 2D assignment” and “bias-ignorant NN.”

We adopt the probability of correct association  $P_c(t)$  at the time  $t$  to evaluate the association performance:

$$P_c(t) = \frac{\sum_{i=1}^L C^i(t)}{L \times N}, \quad (16)$$

where  $C^i(t)$  denotes the number of tracks with correct association at time  $t$  at the  $i$ th Monte-Carlo run,  $L$  is the total number of Monte-Carlo runs, and  $N$  is the number of targets.

The average probability of correct association  $AP_c$  is computed by

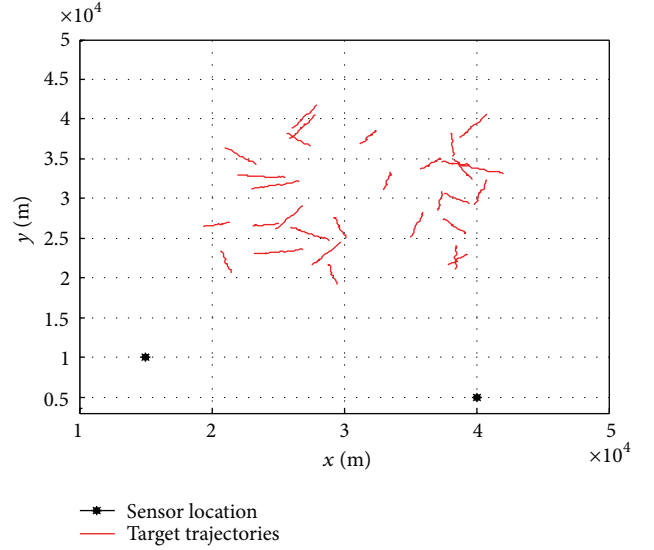


FIGURE 5: Sensors and target trajectories.

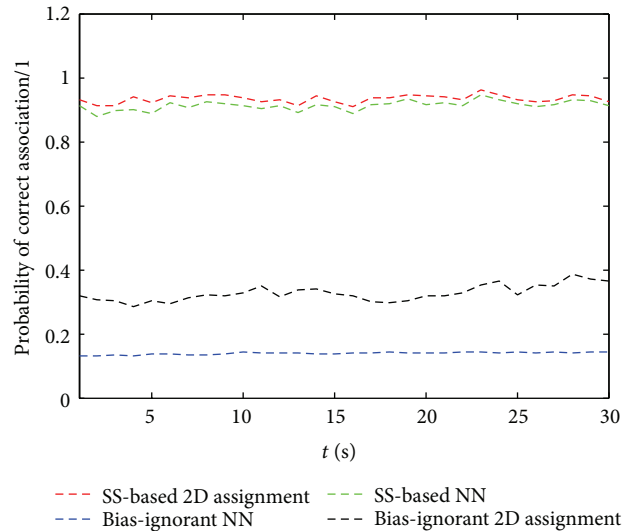


FIGURE 6: Probability of correct association via the whole tracking time.

$$AP_c = \frac{\sum_{i=1}^K P_c(t)}{K}, \quad (17)$$

where  $K$  is the overall tracking time.

Figure 5 shows sensor locations and target trajectories during the whole tracking time in one run. The probability comparison of the correct association via the tracking time is shown in Figure 6.

Figures 7–10 illustrate the average probabilities of correct association via different detection probability, angle bias, range bias, and the total number of targets, respectively. In Figure 7, the detection probability  $P_{D_1}$  of sensor 1 is set to 0.8, and the detection probability  $P_{D_2}$  of sensor 2 varies from 0.5 to 1. In Figure 8, the angle bias  $\Delta \theta_1$  of sensor 1 is  $1^\circ$ , and the angle bias  $\Delta \theta_2$  of sensor 2 varies from  $0^\circ$  to  $7^\circ$ . In Figure 9,

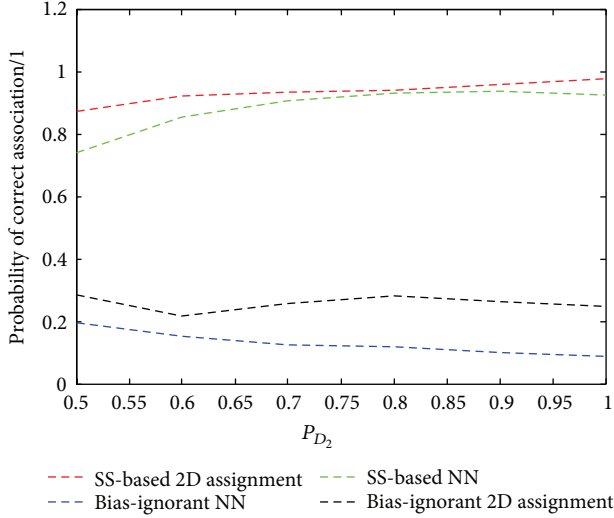


FIGURE 7: Average probability of correct association via different detection probabilities.

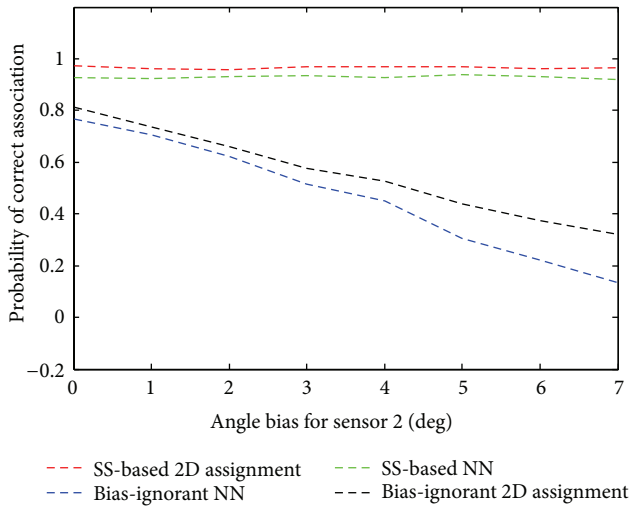


FIGURE 8: Average probability of correct association via different angle biases.

the range bias of sensor 1  $\Delta r_1$  varies from 0 m to 1000 m, and the one of sensor 2  $\Delta r_2$  is 500 m. In Figure 10, the total number of targets varies from 10 to 70.

**4.2. Result Analysis.** From Figures 6–10, it is shown that the proposed “SS-based 2D assignment” and “SS-based NN” outperform the competing algorithms. Moreover, “SS-based NN” is inferior to “SS-based 2D assignment” just a little bit due to the fact that the structural property is considered when constructing the association cost. From Figure 8, it is seen that, as the angle bias increases, the association performances of the “bias-ignorant 2D assignment” and “bias-ignorant NN” experience severe degradations. However, the proposed approaches still perform well, which are insensitive to the angle bias. In addition, it is observed from Figure 10 that the probabilities of correct association given by all methods

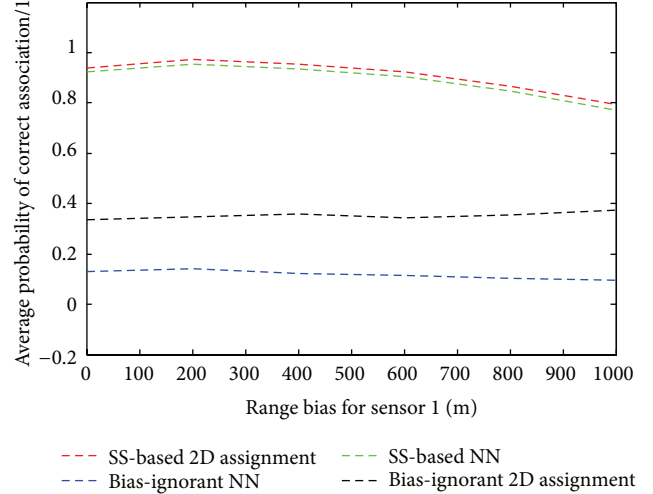


FIGURE 9: Average probability of correct association via different range biases.

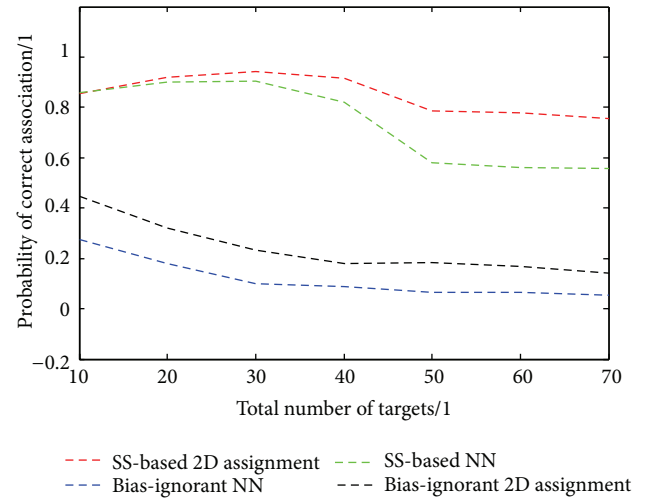


FIGURE 10: Average probability of correct association via the total number of targets.

decrease to some extent as the total number of targets becomes large.

Although the proposed approach performs well in the simulation experiments, it has some flaws. Firstly, the range bias is assumed to be a small one when using the proposed approach; otherwise, the distance invariance between two targets detected by different sensors cannot hold. Secondly, it is required to solve a 2D assignment model when computing the association cost. Doing so may result in a high computational burden, especially for a large number of targets.

### 5. Conclusions

The sensor reports are disturbed by not only random errors, but also sensor biases. When track-to-track association and sensor registration meet each other, some challenging problems arise since they are tightly coupled together. In this

paper, instead of using the absolute kinematic states only, the structural features of local tracks are employed for track-to-track association in the presence of sensor biases. A complete 2D assignment model for track-to-track association is given to deal with possibly missed detections. Lots of simulation results demonstrated the power of the proposed approaches. Further work includes the utilization of multiscan information and the extension of the proposed approach to the multisensor case.

### Conflict of Interests

The authors declare that there is no conflict of interests regarding the publication of this paper.

### Acknowledgments

This research is sponsored by the National Natural Science Foundation of China (61203220/F030307) and State Key Program for Basic Research of China (2013CB329405).

### References

- [1] L. M. Kaplan, Y. Bar-Shalom, and W. D. Blair, "Assignment costs for multiple sensor track-to-track association," *IEEE Transactions on Aerospace and Electronic Systems*, vol. 44, no. 2, pp. 655–677, 2008.
- [2] Y. Bar-Shalom and H. Chen, "Multisensor track-to-track association for tracks with dependent errors," *Journal of Advances in Information Fusion*, vol. 1, no. 1, pp. 3–14, 2006.
- [3] N. Okello and B. Ristic, "Maximum likelihood registration for multiple dissimilar sensors," *IEEE Transactions on Aerospace and Electronic Systems*, vol. 39, no. 3, pp. 1074–1083, 2003.
- [4] X. Lin, Y. Bar-Shalom, and T. Kirubarajan, "Exact multisensor dynamic bias estimation with local tracks," *IEEE Transactions on Aerospace and Electronic Systems*, vol. 40, no. 2, pp. 576–590, 2004.
- [5] S. Mori and Y. Chong, "Effects of unpaired objects and sensor biases on track-to-track association: problems and solutions," in *Proceedings of MSS National Symposium on Sensor and Data Fusion*, vol. 1, pp. 137–151, San Antonio, Tex, USA, June 2000.
- [6] L. D. Stone, M. L. Williams, and T. M. Tran, "Track-to-track association and bias removal," in *Signal and data Processing of Small Targets*, Proceedings of SPIE, pp. 315–329, Orlando, Fla, USA, April 2002.
- [7] M. Levedahl, "An explicit pattern matching assignment algorithm," in *Signal and data Processing of Small Targets*, Proceedings of SPIE, pp. 461–469, Orlando, Fla, USA, April 2002.
- [8] D. J. Papageorgiou and J.-D. Sergi, "Simultaneous track-to-track association and bias removal using multistart local search," in *Proceedings of the IEEE Aerospace Conference (AC '08)*, March 2008.
- [9] D. J. Papageorgiou and M. Holender, "Track-to-track association and ambiguity management in the presence of sensor bias," in *Proceedings of the 12th International Conference on Information Fusion (FUSION '09)*, pp. 2012–2019, Seattle, Wash, USA, July 2009.
- [10] J. P. Ferry, "Exact bias removal for the track-to-track association problem," in *Proceedings of the 12th International Conference on Information Fusion (FUSION '09)*, pp. 1642–1649, Seattle, Wash, USA, July 2009.
- [11] M. Levedahl, "Method and System for Assigning Observations," United States Patent US, 7092924 B1, 2006.
- [12] S. Danford, S. Herman, B. Kragel, and A. Poore, "A branch and bound framework for joint MAP bias estimation and data association," in *Proceedings of the Workshop on Radar Resolution, Nonlinear Estimation, and the Gratuitous Remarks on the Back of Envelope: A Tribute to Fred Daum*, Monterey, Calif, USA, May 2007.
- [13] S. Mori and C. Chong, "Comparison of bias removal algorithms in track-to-track association," in *Signal and Data Processing of Small Targets*, vol. 6699 of *Proceedings of SPIE*, pp. 1–9, San Diego, Calif, USA, August 2007.
- [14] X. Du, Y. Wang, and X. Shan, "Track-to-track association using reference topology in the presence of sensor bias," in *Proceedings of the 10th International Conference on Signal Processing (ICSP '10)*, pp. 2196–2201, Beijing, China, October 2010.
- [15] Z. Li, S. Chen, H. Leung, and É. Bossé, "Joint data association, registration, and fusion using EM-KF," *IEEE Transactions on Aerospace and Electronic Systems*, vol. 46, no. 2, pp. 496–507, 2010.
- [16] D. L. Huang, H. Leung, and E. Bosse, "A pseudo-measurement approach to simultaneous registration and track fusion," *IEEE Transactions on Aerospace and Electronic Systems*, vol. 48, no. 3, pp. 2315–2331, 2012.
- [17] J. W. Koch, "Bayesian approach to extended object and cluster tracking using random matrices," *IEEE Transactions on Aerospace and Electronic Systems*, vol. 44, no. 3, pp. 1042–1059, 2008.
- [18] K. Granström and U. Orguner, "A PHD filter for tracking multiple extended targets using random matrices," *IEEE Transactions on Signal Processing*, vol. 60, no. 11, pp. 5657–5671, 2012.

## Research Article

# Partitioned Quasi-Newton Approximation for Direct Collocation Methods and Its Application to the Fuel-Optimal Control of a Diesel Engine

Jonas Asprión,<sup>1</sup> Oscar Chinellato,<sup>2</sup> and Lino Guzzella<sup>1</sup>

<sup>1</sup> Institute for Dynamic Systems and Control, ETH Zurich, Sonneggstrasse 3, 8092 Zurich, Switzerland

<sup>2</sup> FPT Motorenforschung AG, Schlossgasse 2, 9320 Arbon, Switzerland

Correspondence should be addressed to Jonas Asprión; [jonas.asprien@alumni.ethz.ch](mailto:jonas.asprien@alumni.ethz.ch)

Received 26 November 2013; Revised 17 February 2014; Accepted 18 February 2014; Published 25 March 2014

Academic Editor: M. Montaz Ali

Copyright © 2014 Jonas Asprión et al. This is an open access article distributed under the Creative Commons Attribution License, which permits unrestricted use, distribution, and reproduction in any medium, provided the original work is properly cited.

The numerical solution of optimal control problems by direct collocation is a widely used approach. Quasi-Newton approximations of the Hessian of the Lagrangian of the resulting nonlinear program are also common practice. We illustrate that the transcribed problem is separable with respect to the primal variables and propose the application of dense quasi-Newton updates to the small diagonal blocks of the Hessian. This approach resolves memory limitations, preserves the correct sparsity pattern, and generates more accurate curvature information. The effectiveness of this improvement when applied to engineering problems is demonstrated. As an example, the fuel-optimal and emission-constrained control of a turbocharged diesel engine is considered. First results indicate a significantly faster convergence of the nonlinear program solver when the method proposed is used instead of the standard quasi-Newton approximation.

## 1. Introduction

Quasi-Newton (QN) methods have become very popular in the context of nonlinear optimisation. Above all, in nonlinear programs (NLPs) arising from direct transcription of optimal control problems (OCPs), the Hessian of the Lagrangian often cannot be derived analytically in a convenient way. Algorithmic differentiation may fail due to unsupported operations or black-box parts in the model functions. Furthermore, both approaches are computationally expensive if the model functions are complex and yield long expressions for the second derivatives. On the other hand, numerical approximation by finite differences is inaccurate and hardly improves the computational performance.

A common approach in these cases is to approximate the Hessian by QN updates using gradient information collected during the NLP iterations. However, if applied to real-world OCPs, several limitations arise. These problems often exhibit large dimensions; thus limited-memory versions of the approximations are applicable only. Since many updates

may be necessary until a good approximation of the full Hessian is obtained, the approximation remains poor when using the most recent steps only. Furthermore, the favourable sparsity structure of the underlying discretisation scheme is generally not preserved. This fill-in drastically reduces the performance of solvers for the linear system of equations defining the step direction during each NLP iteration.

Partial separability, a concept introduced by [1], describes a structural property of a nonlinear optimisation problem. When present, this property allows for partitioned QN updates of the Hessian of the Lagrangian (or of the objective, in the unconstrained case). For unconstrained optimisation, this approach was proposed and its convergence properties were analysed in [2]. Although only superlinear local convergence can be proven, a performance close to that obtained with exact Newton methods, which exhibit quadratic local convergence, was observed in practical experiments [3, 4].

This brief paper presents how partitioned QN updates can be applied to the NLPs resulting from direct collocation of OCPs. The concept of direct collocation to solve OCPs

has been widely used and analysed [5–9]. We will show that the Lagrangian of the resulting NLPs is separable in the primal variables at each discretisation point. Due to this separability, its Hessian can be approximated by full-memory QN updates of the small diagonal blocks. This procedure increases the accuracy of the approximation, preserves the sparsity structure, and resolves memory limitations. The results are first derived for Radau collocation schemes, which include the right interval boundary as a collocation point. The adaptations to Gauss schemes, which have internal collocation points only, and to Lobatto schemes, which include both boundaries, are provided thereafter in condensed form. A consistent description of all three families of collocation is provided in [10].

The partitioned update is applied to a real-world engineering problem. The fuel consumption of a turbocharged diesel engine is minimised while the limits on the cumulative pollutant emissions need to be satisfied. This problem is cast in the form of an OCP and is transcribed by Radau collocation. The resulting NLP is solved by an exact and a quasi-Newton method. For the latter, the partitioned update achieves an increased convergence rate and a higher robustness with respect to a poor initialisation of the approximation as compared to the full QN update. Therefore, the findings for the unconstrained case seem to transfer to the NLPs resulting from direct collocation of OCPs.

## 2. Material and Methods

Consider the system of nonautonomous ordinary differential equations (ODEs)  $\dot{\mathbf{x}} = \mathbf{f}(\mathbf{x}, \mathbf{u})$  on the interval  $[t_0, t_f]$ , with  $\mathbf{x}, \mathbf{f} \in \mathbb{R}^{1 \times n_x}$ ,  $\mathbf{u} \in \mathbb{R}^{1 \times n_u}$ . Radau collocation represents each element of the state vector  $\mathbf{x}(t)$  as a polynomial, say of degree  $N$ . The time derivative of this polynomial is then equated to the values of  $\mathbf{f}$  at  $N$  collocation points  $t_0 < \tau_1 < \tau_2 < \dots < \tau_N = t_f$ ,

$$\begin{pmatrix} \dot{\mathbf{x}}_1 \\ \dot{\mathbf{x}}_2 \\ \vdots \\ \dot{\mathbf{x}}_N \end{pmatrix} \approx \underbrace{[\mathbf{d}_0, \tilde{\mathbf{D}}]}_{=: \mathbf{D}} \cdot \begin{pmatrix} \mathbf{x}_0 \\ \mathbf{x}_1 \\ \mathbf{x}_2 \\ \vdots \\ \mathbf{x}_N \end{pmatrix} \stackrel{!}{=} \begin{pmatrix} \mathbf{f}(\mathbf{x}_1, \mathbf{u}_1) \\ \mathbf{f}(\mathbf{x}_2, \mathbf{u}_2) \\ \vdots \\ \mathbf{f}(\mathbf{x}_N, \mathbf{u}_N) \end{pmatrix}. \quad (1)$$

The notation  $\mathbf{x}_j := \mathbf{x}(\tau_j)$  is adopted. The left boundary  $\tau_0 = t_0$  is a noncollocated point in Radau collocation schemes. By introducing the appropriate matrices, this matrix equation in  $\mathbb{R}^{N \times n_x}$  can be written in short as

$$\mathbf{D} \begin{bmatrix} \mathbf{x}_0 \\ \mathbf{X} \end{bmatrix} = \mathbf{F}(\mathbf{X}, \mathbf{U}). \quad (2)$$

The rows of  $\mathbf{X}$  and  $\mathbf{F}$  correspond to one collocation point each. In turn, the columns of  $\mathbf{X}$  and  $\mathbf{F}$  represent one state variable and its corresponding ODE right-hand side at all collocation points. In the following, consider the notation in (2) as shorthand for stacking the transpose of the rows in one large column vector.

The step length  $h = t_f - t_0$  of the interval is assumed to be accounted for in the differentiation matrix  $\mathbf{D}$ . Lagrange

interpolation by barycentric weights is used to calculate  $\mathbf{D}$  along with the vector of the quadrature weights  $\mathbf{w}$  [11]. The latter may be used to approximate the definite integral of a function  $g(t)$  as  $\int_{t_0}^{t_f} g(t) dt \approx \sum_{j=1}^N w_j g(\tau_j)$ .

*2.1. Direct Collocation of Optimal Control Problems.* We consider an OCP of the form

$$\min_{\mathbf{x}(\cdot), \mathbf{u}(\cdot)} \int_0^T L(\mathbf{x}(t), \mathbf{u}(t)) dt \quad (3a)$$

$$\text{s.t.} \quad \dot{\mathbf{x}}(t) - \mathbf{f}(\mathbf{x}(t), \mathbf{u}(t)) = 0, \quad \forall t \in [0, T], \quad (3b)$$

$$\int_0^T \mathbf{g}(\mathbf{x}(t), \mathbf{u}(t)) dt \leq 0, \quad (3c)$$

$$\mathbf{c}(\mathbf{x}(t), \mathbf{u}(t), t) \leq 0, \quad \forall t \in [0, T], \quad (3d)$$

where  $L \in \mathbb{R}$ ,  $\mathbf{g} \in \mathbb{R}^{n_g}$ , and  $\mathbf{c} \in \mathbb{R}^{n_c}$ . Simple bounds on  $\mathbf{x}$  and  $\mathbf{u}$ , equality constraints, and a fixed initial or end state can be included in the path constraints (3d). An objective term in Lagrange form is used, which is preferable over an equivalent Mayer term [12, Section 4.9].

Direct transcription discretises all functions and integrals by consistently applying an integration scheme. Here,  $k = 1, \dots, m$  integration intervals  $[t_{k-1}, t_k]$  are used with  $0 = t_0 < t_1 < \dots < t_m = T$ . The number of collocation points  $N_k$  can be different for each interval. Summing up the collocation points throughout all integration intervals results in a total of  $M = l(m, N_m)$  discretisation points. The “linear index”  $l$  thereby corresponds to collocation node  $i$  in interval  $k$ ,

$$l := l(k, i) = i + \sum_{\alpha=1}^{k-1} N_\alpha. \quad (4)$$

The transcribed OCP reads

$$\min_{\mathbf{x}, \mathbf{u}} \sum_{l=1}^M W_l \cdot L(\mathbf{x}_l, \mathbf{u}_l) \quad (5a)$$

$$\text{s.t.} \quad \mathbf{D}^{(k)} \begin{bmatrix} \mathbf{X}_{N_{k-1}, \bullet}^{(k-1)} \\ \mathbf{X}_{N_k, \bullet}^{(k)} \end{bmatrix} - \mathbf{F}(\mathbf{X}^{(k)}, \mathbf{U}^{(k)}) = 0, \quad k = 1, \dots, m, \quad (5b)$$

$$\sum_{l=1}^M W_l \cdot \mathbf{g}(\mathbf{x}_l, \mathbf{u}_l) \leq 0, \quad (5c)$$

$$\mathbf{c}_l(\mathbf{x}_l, \mathbf{u}_l) \leq 0, \quad l = 1, \dots, M. \quad (5d)$$

The notation  $x_l$  denotes all instances of variable  $x_i$  at any applicable index  $l$ . The vector of the “global” quadrature weights  $\mathbf{W}$  results from stacking the vectors of the quadrature weights  $\mathbf{w}^{(k)}$  of each interval  $k$  after removing the first element, which is zero. For the first interval,  $\mathbf{X}_{N_{k-1}, \bullet}^{(k-1)}$  is the initial state  $\mathbf{x}(0)$ .

The Lagrangian of the NLP (5a)–(5d) is the sum of the objective (5a) and all constraints (5b), (5c), and (5d), which are weighted by the Lagrange multipliers  $\lambda$ . To clarify the

notation, the Lagrange multipliers are grouped according to the problem structure. The  $n_x \cdot N_k$  multipliers for the discretised dynamic constraints on each integration interval  $k$  are denoted by  $\lambda_d^{(k)}$ , the  $n_g$  multipliers for the integral inequalities are stacked in  $\lambda_g$ , and the  $n_c$  multipliers for the path constraints at each discretisation point  $l$  are gathered in the vector  $\lambda_{c,l}$ .

**2.2. Separability in the Primal Variables.** The objective (5a), the integral inequalities (5c), and the path constraints (5d) are inherently separated with respect to time; that is, the individual terms are pairwise disjoint in  $\mathbf{x}_i$  and  $\mathbf{u}_i$ . We thus focus on the separability of the dynamic constraints (5b). For the derivation, we assume that  $f$ ,  $x$ , and  $u$  are scalar. The extension to the vector-valued case is straightforward and will be provided subsequently.

Consider the term of the Lagrangian representing the discretised dynamic constraints (5b) for interval  $k$ ,

$$\widetilde{\mathcal{L}}_d^{(k)} := \sum_{i=1}^{N_k} \lambda_{d,i}^{(k)} \left( d_{0,i}^{(k)} x_{N_{k-1}}^{(k-1)} + \sum_{j=1}^{N_k} \widetilde{D}_{ij}^{(k)} x_j^{(k)} - f(x_i^{(k)}, u_i^{(k)}) \right). \quad (6)$$

This formulation constitutes a separation in the dual variables (the Lagrange multipliers). By collecting terms at each collocation point and accounting for the  $d_0$  terms in the previous interval, we obtain a separation in the primal variables,

$$\mathcal{L}_d^{(k)} = \sum_{i=1}^{N_k} \left( \left[ \sum_{j=1}^{N_k} \widetilde{D}_{ji}^{(k)} \lambda_{d,j}^{(k)} + \delta_i^{(k)} \sum_{j=1}^{N_{k+1}} d_{0,j}^{(k+1)} \lambda_{d,j}^{(k+1)} \right] x_i^{(k)} - \lambda_{d,i}^{(k)} f(x_i^{(k)}, u_i^{(k)}) \right), \quad (7)$$

with

$$\delta_i^{(k)} = \begin{cases} 1, & \text{if } i = N_k, k \neq m, \\ 0, & \text{otherwise.} \end{cases} \quad (8)$$

Each term inside the round brackets in (7) is a collocation-point separated part of the Lagrangian which stems from the dynamic constraints. We denote these terms by  $\mathcal{L}_{d,i}^{(k)}$  and introduce the notation

$$\omega := (x, u), \quad \omega_i^{(k)} := (x_i^{(k)}, u_i^{(k)}). \quad (9)$$

The gradient with respect to the primal variables is

$$\nabla_{\omega} \mathcal{L}_{d,i}^{(k)} = \left( \lambda_d^{(k)T} \widetilde{D}_{\cdot i}^{(k)} + \delta_i^{(k)} \lambda_d^{(k+1)T} \mathbf{d}_0^{(k+1)}, 0 \right) - \lambda_{d,i}^{(k)} \frac{\partial f(\omega_i^{(k)})}{\partial \omega}. \quad (10)$$

The Hessian is simply

$$\nabla_{\omega}^2 \mathcal{L}_{d,i}^{(k)} = -\lambda_{d,i}^{(k)} \frac{\partial^2 f(\omega_i^{(k)})}{\partial \omega^2}. \quad (11)$$

### 2.2.1. Vector-Valued Case and Complete Element Lagrangian.

For multiple control inputs and state variables, the primal variables  $\omega_l$  at each collocation point become a vector in  $\mathbb{R}^{1 \times (n_u + n_x)}$ . Consistently, we define the gradient of a scalar function with respect to  $\omega$  as a row vector. Thus, the model Jacobian  $\partial \mathbf{f} / \partial \omega$  is a matrix in  $\mathbb{R}^{n_x \times (n_u + n_x)}$ , and the Hessian of each model-function element  $s$ ,  $\partial^2 f_s / \partial \omega^2$ , is a square matrix of size  $(n_u + n_x)$ . The multiplier  $\lambda_{d,i}^{(k)}$  itself also becomes a vector in  $\mathbb{R}^{n_x}$ . All terms involving  $\mathbf{f}$ , its Jacobian, or its Hessian therefore turn into sums.

The full element Lagrangian  $\mathcal{L}_i^{(k)}$  consists of the terms of the dynamic constraints  $\mathcal{L}_{d,i}^{(k)}$  as derived above, plus the contributions of the objective, the integral inequalities, and the path constraints,

$$\begin{aligned} \mathcal{L}_i^{(k)} &= W_l \cdot L(\omega_l) \\ &+ \mathbf{x}_i^{(k)} \cdot \left( \sum_{j=1}^{N_k} \widetilde{D}_{ji}^{(k)} \lambda_{d,j}^{(k)} + \delta_i^{(k)} \sum_{j=1}^{N_{k+1}} d_{0,j}^{(k+1)} \lambda_{d,j}^{(k+1)} \right) \\ &- \mathbf{f}(\omega_i^{(k)}) \lambda_{d,i}^{(k)} + W_l \cdot \lambda_g^T \mathbf{g}(\omega_l) + \lambda_{c,l}^T \mathbf{c}_l(\omega_l). \end{aligned} \quad (12)$$

The Lagrangian of the full NLP is obtained by summing these element Lagrangians, which are separated in the primal variables. Its Hessian thus is a perfect block-diagonal matrix with uniformly sized square blocks of size  $(n_u + n_x)$ .

**2.2.2. Extension to Gauss and Lobatto Collocation.** Gauss collocation does not include the right interval boundary. Thus, the terms involving  $\mathbf{d}_0$  can be included locally in each interval, which simplifies the separation in the primal variables. However, the continuity constraint

$$\mathbf{x}_0^{(k+1)} = \mathbf{x}_0^{(k)} + \mathbf{w}^{(k)T} \mathbf{F}(\mathbf{X}^{(k)}, \mathbf{U}^{(k)}) \quad (13)$$

has to be introduced for each interval. Similarly to the procedure above, this constraint can be separated. The quadrature weights  $\mathbf{w}^{(k)}$  are stacked in  $\mathbf{W}$  without any modification.

Lobatto collocation includes both boundaries as collocation points. Thus, the matrix  $\mathbf{D}$  in (1) and (2) has an additional ‘‘zeroth’’ row, and the argument of  $\mathbf{F}$  becomes  $[\mathbf{x}_0^T, \mathbf{X}^T]^T$  in (2). The additional term

$$-\delta_i^{(k)} \lambda_{d,0}^{(k+1)} f(\omega_i^{(k)}) \quad (14)$$

arises in  $\mathcal{L}_{d,i}^{(k)}$ . Each element of  $\mathbf{W}$  corresponding to the interval boundary between any two neighbouring intervals  $k$  and  $k+1$  is a sum of the two weights  $w_{N_k}^{(k)}$  and  $w_0^{(k+1)}$ .

**2.3. Block-Diagonal Approximation of the Hessian.** The separability of the problem with respect to the primal variables allows a perfect exploitation of the problem sparsity. In fact, the Jacobian of the objective and the constraints, as well as the Hessian of the Lagrangian, can be constructed from the first and second partial derivatives of the nonlinear model functions  $L$ ,  $\mathbf{f}$ ,  $\mathbf{g}$ , and  $\mathbf{c}$  at each discretisation point [13].

We propose to also exploit the separability when calculating QN approximations of the Hessian. These iterative updates collect information about the curvature of the Lagrangian by observing the change of its gradient along the NLP iterations. Although they perform well in practice, they exhibit several drawbacks for large problems.

- (I) *Loss of sparsity.* QN approximations generally do not preserve the sparsity pattern of the exact Hessian, which leads to low computational performance [12, Section 4.13]. Enforcing the correct sparsity pattern results in QN schemes with poor performance [14, Section 7.3].
- (II) *Storage versus accuracy.* Due to the loss of sparsity, the approximated Hessian needs to be stored in dense format. To resolve possible memory limitations, “limited-memory” updates can be applied, which rely on a few recent gradient samples only. However, these methods provide less accuracy than their full-memory equivalents [14, Section 7.2].
- (III) *Dimensionality versus sampling.* When sampling the gradient of a function that lives in a high-dimensional space, many samples are required to construct an accurate approximation. In fact, to obtain an approximation that is valid along any direction, an entire spanning set needs to be sampled. Although QN methods require accurate second-order information only along the direction of the steps [15], the step direction may change fast in highly nonlinear problems such as the one considered here. In these cases, an exhaustive set of gradient samples would ensure a fast convergence, which conflicts with (II).

Using approximations of the small diagonal blocks, that is, exploiting the separability illustrated in Section 2.2, resolves these problems.

- (I) The exact sparsity pattern of the Hessian is preserved.
- (II) Only  $M(n_x + n_u)^2$  numbers have to be stored, compared to  $M^2(n_x + n_u)^2$  for the full Hessian.
- (III) Since the dimension of each diagonal block is small, a good approximation is already obtained after few iterations of the Hessian update [3, 4].

The partitioned QN update can be combined with the exploitation of the problem sparsity to reduce the number of the model evaluations required. In fact, when these two concepts are combined, the gradients of the model functions at each collocation point are sufficient to construct an accurate and sparsity-preserving approximation of the Hessian of the Lagrangian.

**2.4. Implementation.** Any QN approximation operates with the differences between two consecutive iterates and the corresponding gradients of the Lagrangian. For constrained problems,

$$\mathbf{s}^T := \widehat{\boldsymbol{\omega}} - \boldsymbol{\omega}, \quad (15)$$

$$\mathbf{y}^T := \nabla_{\boldsymbol{\omega}} \mathcal{L}(\widehat{\boldsymbol{\omega}}, \widehat{\boldsymbol{\lambda}}) - \nabla_{\boldsymbol{\omega}} \mathcal{L}(\boldsymbol{\omega}, \boldsymbol{\lambda}). \quad (16)$$

The hat indicates the values at the current iteration, that is, the new data. In the following formulas,  $\mathbf{B}$  denotes the QN approximation. Here, the damped BFGS update is used [14, Section 18.3], which reads

$$\theta = \begin{cases} 1, & \text{if } \mathbf{s}^T \mathbf{y} \geq 0.2 \mathbf{s}^T \mathbf{B} \mathbf{s} \\ \frac{0.8 \mathbf{s}^T \mathbf{B} \mathbf{s}}{\mathbf{s}^T \mathbf{B} \mathbf{s} - \mathbf{s}^T \mathbf{y}}, & \text{otherwise,} \end{cases} \quad (17a)$$

$$\mathbf{r} = \theta \mathbf{y} + (1 - \theta) \mathbf{B} \mathbf{s}, \quad (17b)$$

$$\widehat{\mathbf{B}} = \mathbf{B} - \frac{\mathbf{B} \mathbf{s} \mathbf{s}^T \mathbf{B}}{\mathbf{s}^T \mathbf{B} \mathbf{s}} + \frac{\mathbf{r} \mathbf{r}^T}{\mathbf{s}^T \mathbf{r}}. \quad (17c)$$

This update scheme preserves positive definiteness, which is mandatory if a line-search globalisation is used. In a trust-region framework, indefinite approaches such as the safeguarded SR1 update [14, Section 6.2] could be advantageous since they can approximate the generally indefinite Hessian of the full or element Lagrangian more accurately.

The Hessian block  $\mathbf{B}_l$  corresponding to the element Lagrangian (12) at collocation point  $l$  is approximated as follows. In the difference of the gradients, all linear terms cancel. Thus, (16) becomes

$$\begin{aligned} \mathbf{y}_l^T &= \nabla_{\boldsymbol{\omega}} \mathcal{L}_l(\widehat{\boldsymbol{\omega}}, \widehat{\boldsymbol{\lambda}}) - \nabla_{\boldsymbol{\omega}} \mathcal{L}_l(\boldsymbol{\omega}, \boldsymbol{\lambda}) \\ &= W_l \cdot \left( \frac{\partial L(\widehat{\boldsymbol{\omega}}_l)}{\partial \boldsymbol{\omega}} - \frac{\partial L(\boldsymbol{\omega}_l)}{\partial \boldsymbol{\omega}} \right) \\ &\quad + \boldsymbol{\lambda}_{d,l}^T \cdot \left( \frac{\partial \mathbf{f}(\boldsymbol{\omega}_l)}{\partial \boldsymbol{\omega}} - \frac{\partial \mathbf{f}(\widehat{\boldsymbol{\omega}}_l)}{\partial \boldsymbol{\omega}} \right) \\ &\quad + W_l \cdot \boldsymbol{\lambda}_g^T \cdot \left( \frac{\partial \mathbf{g}(\widehat{\boldsymbol{\omega}}_l)}{\partial \boldsymbol{\omega}} - \frac{\partial \mathbf{g}(\boldsymbol{\omega}_l)}{\partial \boldsymbol{\omega}} \right) \\ &\quad + \boldsymbol{\lambda}_{c,l}^T \cdot \left( \frac{\partial \mathbf{c}_l(\widehat{\boldsymbol{\omega}}_l)}{\partial \boldsymbol{\omega}} - \frac{\partial \mathbf{c}_l(\boldsymbol{\omega}_l)}{\partial \boldsymbol{\omega}} \right). \end{aligned} \quad (18)$$

Recall that the linear index  $l$  is defined such that  $\boldsymbol{\lambda}_{d,l} = \boldsymbol{\lambda}_{d,i}^{(k)}$ . The QN update (17a)–(17c) is applied to each diagonal block  $\mathbf{B}_l$  individually, with  $\mathbf{s}_l^T = \widehat{\boldsymbol{\omega}}_l - \boldsymbol{\omega}_l$  and  $\mathbf{y}_l$  given by (18). As initialisation, one of the approaches described in [14, Chapter 6] can be used.

**2.5. Engineering Test Problem.** As a real-world engineering problem, we consider the minimisation of the fuel consumption of a turbocharged diesel engine. The statutory limits for the cumulative  $\text{NO}_x$  and soot emissions are imposed as  $n_g = 2$  integral inequality constraints. The  $n_u = 4$  control inputs are the position of the variable-geometry turbine, the start of the main injection, the common-rail pressure, and the fuel mass injected per cylinder and combustion cycle. The model is described and its experimental validation is provided in [16]. It features a dynamic mean-value model for the air path with  $n_x = 5$  state variables, and physics-based models for the combustion and for the pollutant emissions. The resulting OCP is stated in [17, 18]. The desired load torque, the bounds

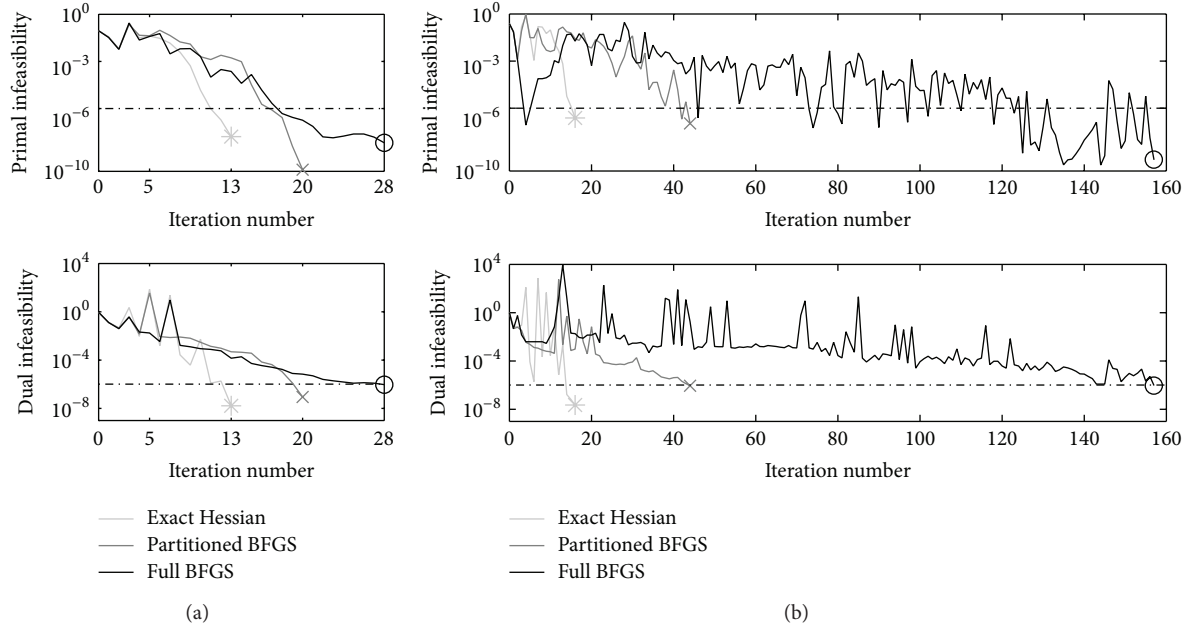


FIGURE 1: Convergence behaviour of IPOPT on the two test cases.

on the actuator ranges, and mechanical and thermal limits are imposed as nonlinear and linear path constraints (3d).

The model evaluations are expensive. Therefore, QN updates are preferable over exact Newton methods to achieve a fast solution process. The main drawback is the slow local convergence rate of QN methods when applied to the large NLPs resulting from the consideration of long time horizons in the OCP [18].

### 3. Results and Discussion

The results presented here are generated using the NLP solver IPOPT [19, 20] with the linear solver MUMPS [21] and the fill-reducing preordering implemented in METIS [22]. Either the exact Hessian, calculated using central finite differences on the model functions, or a full or the partitioned QN update just described is supplied to the solver as user-defined Hessian. In all cases, the first derivatives are calculated by forward finite differences.

Radau collocation at flipped Legendre nodes is applied. These collocation points are the roots of the orthogonal Legendre polynomials and have to be computed numerically [23, Section 2.3]. The resulting scheme, sometimes termed Radau IIA, exhibits a combination of advantageous properties [24, [25, Section 3.5].

Two test cases for the engineering problem outlined in Section 2.5 are considered. Case (a) is a mild driving pattern of 6 s duration which is discretised by first-order collocation with a uniform step length of 0.5 s. This discretisation results in  $M = 13$  total collocation points and 117 NLP variables. Test case (b) considers a more demanding driving pattern of 58 s duration and uses third-order collocation with a step size of 0.8 s, resulting in  $M = 217$  collocation points and 1,953 NLP variables.

The performance is assessed in terms of the number of iterations required to achieve the requested tolerance. Figure 1 shows the convergence behaviour of the exact-Newton method and of the two QN methods. Starting with iteration 5, the full Newton step is always accepted. Thus, the difference between the local quadratic convergence of the exact Newton method and the local superlinear convergence of the full BFGS update becomes obvious. The partitioned update performs substantially better than the full update. Moreover, the advantage becomes more pronounced when the size (longer time horizon) and the complexity (more transient driving profile, higher-order collocation) of the problem are increased from the simple test case (a) to the more meaningful case (b).

The Hessian approximation is initialised by a multiple of the identity matrix;  $\mathbf{B}_0 = \beta \mathbf{I}$ . A factor of  $\beta = 0.05$  is found to be a good choice for the problem at hand. Table 1 shows the number of iterations required as  $\beta$  is changed. The partitioned update is robust against a poor initialisation, whereas the full update requires a significant number of iterations to recover. This finding confirms that an accurate approximation is obtained in fewer iterations when the partitioned QN update is applied.

### 4. Conclusion

We illustrated the separability of the nonlinear program resulting from the application of direct collocation to an optimal control problem. Subsequently, we presented how this structure can be exploited to apply a partitioned quasi-Newton update to the Hessian of the Lagrangian. This sparsity-preserving update yields a more accurate approximation of the Hessian in fewer iterations and thus increases the convergence rate of the NLP solver.

TABLE 1: Effect of the initialisation of the Hessian approximation on the number of NLP iterations until convergence, test case (a).

Method	$\beta = 0.01$	$\beta = 0.05$	$\beta = 0.1$
Full BFGS	36	28	38
Partitioned BFGS	22	20	21

A more accurate approximation of the second derivatives from first order information is especially beneficial for highly nonlinear problems for which the exact second derivatives are expensive to evaluate. In fact, for the real-world engineering problem used as a test case here, symbolic or algorithmic differentiation is not an expedient option due to the complexity and the structure of the model. In this situation, using a quasi-Newton approximation based on first derivatives calculated by finite differences is a valuable alternative. The numerical tests presented in this paper indicate that a convergence rate close to that of an exact Newton method can be reclaimed by the application of a partitioned BFGS update.

A self-contained implementation of the partitioned update in the framework of an NLP solver itself could fully exploit the advantages of the method proposed. Furthermore, it should be assessed whether a trust-region globalisation is able to take advantage of an indefinite but possibly more accurate quasi-Newton approximation of the diagonal blocks of the Hessian of the Lagrangian.

## Conflict of Interests

The authors declare that there is no conflict of interests regarding the publication of this paper.

## Acknowledgment

This work was partially funded by the Swiss Innovation Promotion Agency CTI under Grant no. 10808.1 PFIW-IW.

## References

- [1] A. Griewank and A. Toint, "On the unconstrained optimization of partially separable functions," in *Nonlinear Optimization*, M. Powell, Ed., Academic Press, New York, NY, USA, 1981.
- [2] A. Griewank and P. L. Toint, "Local convergence analysis for partitioned quasi-Newton updates," *Numerische Mathematik*, vol. 39, no. 3, pp. 429–448, 1982.
- [3] D. C. Liu and J. Nocedal, "On the limited memory BFGS method for large scale optimization," *Mathematical Programming*, vol. 45, no. 1–3, pp. 503–528, 1989.
- [4] J. Nocedal, "Large scale unconstrained optimization," in *The State of the Art in Numerical Analysis*, pp. 311–338, Oxford University Press, New York, NY, USA, 1996.
- [5] L. T. Biegler, "Solution of dynamic optimization problems by successive quadratic programming and orthogonal collocation," *Computers and Chemical Engineering*, vol. 8, no. 3–4, pp. 243–247, 1984.
- [6] D. Tieu, W. R. Cluett, and A. Penlidis, "A comparison of collocation methods for solving dynamic optimization problems," *Computers and Chemical Engineering*, vol. 19, no. 4, pp. 375–381, 1995.
- [7] A. L. Herman and B. A. Conway, "Direct optimization using collocation based on high-order Gauss-Lobatto quadrature rules," *Journal of Guidance, Control, and Dynamics*, vol. 19, no. 3, pp. 592–599, 1996.
- [8] D. A. Benson, G. T. Huntington, T. P. Thorvaldsen, and A. V. Rao, "Direct trajectory optimization and costate estimation via an orthogonal collocation method," *Journal of Guidance, Control, and Dynamics*, vol. 29, no. 6, pp. 1435–1440, 2006.
- [9] S. Kameswaran and L. T. Biegler, "Convergence rates for direct transcription of optimal control problems using collocation at Radau points," *Computational Optimization and Applications*, vol. 41, no. 1, pp. 81–126, 2008.
- [10] D. Garg, M. Patterson, W. W. Hager, A. V. Rao, D. A. Benson, and G. T. Huntington, "A unified framework for the numerical solution of optimal control problems using pseudospectral methods," *Automatica*, vol. 46, no. 11, pp. 1843–1851, 2010.
- [11] J.-P. Berrut and L. N. Trefethen, "Barycentric Lagrange interpolation," *SIAM Review*, vol. 46, no. 3, pp. 501–517, 2004.
- [12] J. T. Betts, *Practical Methods for Optimal Control and Estimation Using Nonlinear Programming*, Advances in Design and Control, Society for Industrial and Applied Mathematics, Philadelphia, Pa, USA, 2nd edition, 2010.
- [13] M. A. Patterson and A. V. Rao, "Exploiting sparsity in direct collocation pseudospectral methods for solving optimal control problems," *Journal of Spacecraft and Rockets*, vol. 49, no. 2, pp. 364–337, 2012.
- [14] J. Nocedal and S. J. Wright, *Numerical Optimization*, Springer Series in Operations Research and Financial Engineering, Springer, New York, NY, USA, 2nd edition, 2006.
- [15] P. E. Gill and E. Wong, "Sequential quadratic programming methods," in *Mixed Integer Nonlinear Programming*, J. Lee and S. Leyffer, Eds., vol. 154 of *The IMA Volumes in Mathematics and its Applications*, pp. 301–312, Springer, New York, NY, USA, 2012.
- [16] J. Asprion, O. Chinellato, and L. Guzzella, "Optimisation-oriented modelling of the NO<sub>x</sub> emissions of a diesel engine," *Energy Conversion and Management*, vol. 75, pp. 61–73, 2013.
- [17] J. Asprion, C. H. Onder, and L. Guzzella, "Including drag phases in numerical optimal control of diesel engines," in *Proceedings of the 7th IFAC Symposium on Advances in Automotive Control*, pp. 489–494, Tokyo, Japan, 2013.
- [18] J. Asprion, O. Chinellato, and L. Guzzella, "Optimal control of diesel engines: numerical methods, applications, and experimental validation," *Mathematical Problems in Engineering*, vol. 2014, Article ID 286538, 21 pages, 2014.
- [19] A. Wächter and L. T. Biegler, "On the implementation of an interior-point filter line-search algorithm for large-scale nonlinear programming," *Mathematical Programming*, vol. 106, no. 1, pp. 25–57, 2006.
- [20] "IPOPT homepage," 2013, <http://www.coin-or.org/Ipopt>.
- [21] "MUMPS homepage," 2013, <http://mumps.enseiht.fr>.
- [22] "METIS—serial graph partitioning and fill-reducing matrix ordering," 2013, <http://glaros.dtc.umn.edu/gkhome/metis/metis/overview>.
- [23] C. Canuto, M. Y. Hussaini, A. Quarteroni, and T. A. Zang, *Spectral Methods: Fundamentals in Single Domains*, Scientific Computation, Springer, Berlin, Germany, 2006.
- [24] E. Hairer and G. Wanner, "Stiff differential equations solved by Radau methods," *Journal of Computational and Applied Mathematics*, vol. 111, no. 1–2, pp. 93–111, 1999.
- [25] J. C. Butcher, *Numerical Methods for Ordinary Differential Equations*, John Wiley & Sons, Winchester, UK, 2003.

## Research Article

# Finite Queueing Modeling and Optimization: A Selected Review

F. R. B. Cruz<sup>1</sup> and T. van Woensel<sup>2</sup>

<sup>1</sup> Departamento de Estatística, Universidade Federal de Minas Gerais, 31270-901 Belo Horizonte, MG, Brazil

<sup>2</sup> Department of Industrial Engineering & Innovation Sciences, Eindhoven University of Technology,  
P.O. Box 513, 5600 MB, Eindhoven, The Netherlands

Correspondence should be addressed to F. R. B. Cruz; [fcruz@est.ufmg.br](mailto:fcruz@est.ufmg.br)

Received 6 December 2013; Accepted 30 January 2014; Published 23 March 2014

Academic Editor: Nachamada Blamah

Copyright © 2014 F. R. B. Cruz and T. van Woensel. This is an open access article distributed under the Creative Commons Attribution License, which permits unrestricted use, distribution, and reproduction in any medium, provided the original work is properly cited.

This review provides an overview of the queueing modeling issues and the related performance evaluation and optimization approaches framed in a joined manufacturing and product engineering. Such networks are represented as queueing networks. The performance of the queueing networks is evaluated using an advanced queueing network analyzer: the generalized expansion method. Secondly, different model approaches are described and optimized with regard to the key parameters in the network (e.g., buffer and server sizes, service rates, and so on).

## 1. Introduction

Queueing theory is the mathematical study of waiting lines and it enables the mathematical analysis of several related processes, including arrivals at the queue, waiting in the queue, and being served by the server. The theory enables the derivation and calculation of several performance measures which can be used to evaluate the performance of the queueing system under study. More specifically, the focus in this paper is on finite buffer queueing networks which are characterized by the blocking effect, which eventually degrades the performance, commonly measured via, for example, the throughput of the network.

Queueing modeling and optimization of large scale manufacturing systems and complex production lines have been and continue to be the focus of numerous studies for decades (e.g., see Smith [1–3]). Queueing networks are commonly used to model such complex systems (see Suri [4]). The main reason to use queueing modeling is because of their ability to accurately model the resource allocation problems we are interested in (i.e., the buffer, server, and buffer-server combination problems), under approximate Poisson arrivals and general service rates. Of course, there are other methodologies tailored for different settings as, for instance, simulation methods (see Law and Kelton [5]) and advanced methods that explore the spectral characteristics of the

associated matrices in Markovian models (e.g., see the works of Yeralan and Tan [6] and Fadiloglu and Yeralan [7], among others).

This review aims at providing an overview of modeling, performance evaluation, and optimization approaches from a queueing theory point of view. Additionally, the algorithms selected were implemented and tested in some basic queueing network topologies, namely, series, merges, and splits. The numerical results provide new insight into this important class of manufacturing network design problems.

The paper is structured as follows. In Section 2, we present the performance evaluation method considered for the queueing networks analyzed. Also in Section 2, we elaborate on the different optimization models that exist and discuss some of the optimization tools that are used to optimize these models. Section 3 gives computational results for some selected optimization models for a complex network. Finally, Section 4 concludes the paper and gives some pointers for future research in the area.

## 2. Material and Methods

**2.1. Finite Queueing Networks.** Queueing networks are defined as either open, closed, or mixed. In open queueing networks, customers enter the system from outside, receive some service at one or more nodes, and then leave the system.

In closed queueing networks, customers never leave or enter the system but a fixed number of customers circulate within the network (see Whitt [9] and Smith [10]). Mixed queueing networks are systems that are open with respect to some customers and are closed with respect to other customers (see Balsamo et al. [11]). Research in the area of queueing networks is very active as we shall see and resulted in a vast amount of journal papers, books, and reports. For a more general discussion on queueing networks, the reader is referred to Walrand [12] among others. In this paper, we will focus on *finite* queueing networks.

The assumption is that the capacity of the buffer space between two consecutive connected service stations is finite. As a consequence, each node in the network might be affected by events at other nodes, leading to the phenomena of blocking or starvation. In the literature, two general blocking mechanisms are presented: blocking after service (BAS) and blocking before service (BBS). BAS occurs when after service a customer sees that the buffer in front of her/him is full and as a consequence s/he cannot continue her/his way in the network. BBS implied that a server can start processing a next customer only if there is a space available in the downstream buffer. If not, the customer has to wait until a space becomes available. Most production lines operate under BAS system. Moreover, in the literature it is the most commonly made assumption regarding the buffer behavior (see Dallery and Gershwin [13]).

**2.2. Network Performance Evaluation.** Performance evaluation tools for queues include *product form methods*, *numerical methods*, *approximate methods*, and *simulation*. Let us discuss each of them a bit more in detail. More in-depth information can be found in the references mentioned as follows.

Initially, the *product form methods* decompose the system into single pairs or triplets of nodes instead of analyzing the entire system at once. Details may be found in Perros [14]. Each decomposed node can then be treated as an independent service provider, for which all results and insights of the single node queueing models can be used (see, e.g., Gross et al. [15]). Jackson [16, 17] firstly showed that the joint distribution of the entire network is made up of the product of the marginal distributions at each of the nodes under some strict conditions (e.g., exponential arrivals and services, under no blocking). A decomposition technique yields exact results for queueing networks with product form solutions. For networks without a product form solution, the technique gives a good approximation (see Balsamo et al. [11]).

The *numerical methods* are also useful, as in theory these methods can be used to solve every Markovian model. The problem, however, with numerical solutions is that the state space of queueing networks grows exponentially with the number of nodes, the number of customers, and the number of buffers. As a consequence, numerical methods consume extensive computer time to get to the solution. Numerical methods are applied to smaller networks though (e.g., see Balsamo et al. [11]).

Among the *approximate methods*, the decomposition methods are very popular. These methods are approximate because the subnetworks are only a part of the whole line

and, as such, do not have exactly the same behavior (see Dallery and Gershwin [13]). However, if obtaining an exact solution is too expensive in terms of computational effort, approximate methods are justified. The main challenge with approximate methods is to be as close as possible to the exact values. The accuracy of an approximate method can be tested with numerical solutions (for smaller networks) or by using simulation. The main idea of the decomposition methods is to try to generalize the ideas of independence and product form solutions from the Jackson networks to more general systems. Reiser and Kobayashi [18] and Kuehn [19] were the first to develop this approach. After them, several researchers came up with a similar approach (e.g., Buzacott and Shanthikumar [20] and Alves et al. [21]).

Finally, *simulation* is another way to obtain all relevant performance measures for a queueing network (see Law and Kelton [5]). Successful results on simulation based methods were reported by Cruz et al. [22, 23], Pereira et al. [24], Dorda and Teichmann [25], and Cardoso et al. [26], among many others.

**2.3. The Generalized Expansion Method.** In this paper, the Generalized Expansion Method (GEM) is used as the prime performance evaluation tool. Consequently, this paper provides a selected review based on the GEM and does not explicitly consider other methodologies to obtain the performance measures. Note that the models described fit any performance evaluation tool.

In general, we evaluate the performance of the network via its throughput  $\theta$ . This throughput (and all other measures, e.g., blocking probability, sojourn time, work-in-process, etc.) can be obtained via a queueing network representation. This queueing network representation then needs to be “solved” to obtain the performance of the given network. Notice that we will focus here on  $M/G/c/K$  queueing models, which in Kendall notation means a queueing system with Markovian arrival rates, generally distributed service times,  $c$  servers in parallel in the queue, and a *total* capacity of  $K$  users in the queue (*including* those under service).

As it will be detailed soon, the GEM transforms the queueing network into an equivalent Jackson network, which can be decomposed so that each node can be solved independently of each other (similar to a product form solution approach). The GEM is an effective and robust approximation technique to measure the performance of open finite queueing networks. The effectiveness of GEM as a performance evaluation tool has been presented in many papers, including Kerbache and Smith [27–29], Jain and Smith [30], Smith [31], and Andriansyah et al. [32].

The GEM uses BAS, which is prevalent in most systems including production and manufacturing (see Dallery and Gershwin [13]), transportation (see van Woensel and Vandaele [33, 34]), and other similar systems. Developed by Kerbache and Smith [27], the GEM has become an appealing approximation technique for performance evaluation of queueing networks due to its accuracy and relative simplicity. Moreover, exact solutions to performance measurement are restricted only to very simple networks and simulation requires a considerable amount of computational effort.

The GEM is basically a combination of two approximation methods, namely, the repeated trials and the node-by-node decomposition. In order to evaluate the performance of a queueing network, the method first divides the network into single nodes with revised service and arrival parameters. Blocked customers are registered into an artificial “holding node” and are repeatedly sent to this node until they are serviced. The addition of the holding node *expands* the network and transforms the network into an equivalent Jackson network in which each node can be solved independently.

In the remaining part of this section, we will present a high-level overview of the method. For more detailed information and applications of the GEM, the reader is referred to, for example, Kerbache and Smith [28]. The GEM described below assumes that one wants to solve  $M/G/c/K$  queueing networks. Note that the methodology is generic such that  $M/M/1/K$ ,  $M/M/c/K$ ,  $M/G/1/K$ ,  $GI/G/1/K$ , and  $GI/G/c/K$  queueing networks could also be analyzed. Only the relevant equations (e.g., the blocking probabilities) need to be adapted for these other cases.

There are three main steps in the GEM, namely, *network reconfiguration*, *parameter estimation*, and *feedback elimination*. The notation for the GEM, presented in Basic Network Notation section will be used throughout the paper. The steps are described as follows.

*Stage I: Network Reconfiguration.* For each finite node in the queueing network, an artificial node is created to register the blocked jobs. By introducing such artificial nodes, we also create new routing probabilities in the network. The result of network reconfiguration can be seen from Figure 1.

There are two possible states of the finite node, namely, the *saturated* and the *unsaturated* states. Arriving jobs will try to access the finite node  $j$ . With a probability of  $(1 - p_{K_j})$ , the job will find the the finite node unsaturated, when it will enter the queue and eventually be serviced. However, if the finite node  $j$  is saturated (with a probability of  $p_{K_j}$ ), then the job will be directed to the artificial holding node  $h_j$ , where it will be delayed. The delay at the artificial node is modeled using a  $M/G/\infty$  queue, representing a delay time without queueing. Afterward, the blocked job will try to reenter the finite queue with a success probability of  $(1 - p'_{K_j})$ . There is a probability of  $p'_{K_j}$  that the blocked job still finds the finite node saturated and thus it will be directed again to the artificial holding node  $h_j$ . This process repeats until the blocked job is able to enter the finite node.

*Stage II: Parameter Estimation.* At this stage, the values for parameters  $p_K$ ,  $p'_{K_j}$ , and  $\mu_h$  are determined. Notice that the node index  $j$  is omitted for the sake of simplicity.

$p_K$ : In order to determine  $p_K$ , exact analytical formulas should be used whenever possible (see Kerbache and Smith [29]). For cases where exact  $p_K$  formula is unavailable, approximations for  $p_K$  in  $M/G/c/K$  setting provided by Smith [31] can be used. These approximations are based on a closed-form expression derivable from the finite capacity exponential queue ( $M/M/c/K$ ) using Kimura’s [35]

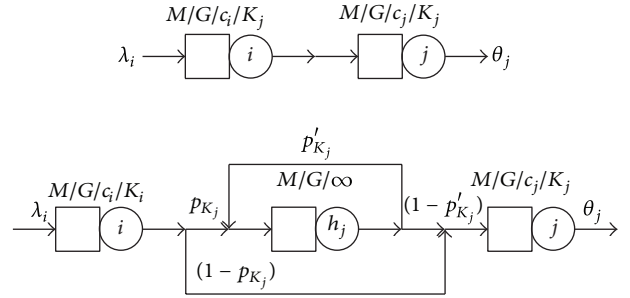


FIGURE 1: The generalized expansion method.

two-moment approximation. The following  $p_K$  formula for  $M/G/2/K$  is presented as an example (see Smith [31]):

$$p_K = \frac{2\rho^{2((\sqrt{\rho/e}s^2 - \sqrt{\rho/e+K})/(2+\sqrt{\rho/e}s^2 - \sqrt{\rho/e}))} (2\mu - \lambda)}{-2\rho^{2((\sqrt{\rho/e}s^2 - \sqrt{\rho/e+K})/(2+\sqrt{\rho/e}s^2 - \sqrt{\rho/e}))} \lambda + 2\mu + \lambda} \quad (1)$$

The  $p_K$  for the  $M/G/c/K$ , for  $c = 3, 4, \dots$ , will not be shown for brevity but are available in Smith [31].

$p'_{K_j}$ , since no exact method is available to calculate  $p'_{K_j}$ , an approximation from Labetoulle and Pujolle [36], based on diffusion techniques, is used:

$$p'_{K_j} = \left[ \frac{\mu_j + \mu_h}{\mu_h} - \frac{\lambda [(r_2^K - r_1^K) - (r_2^{K-1} - r_1^{K-1})]}{\mu_h [(r_2^{K+1} - r_1^{K+1}) - (r_2^K - r_1^K)]} \right]^{-1} \quad (2)$$

in which  $r_1$  and  $r_2$  are the roots of the polynomial.

Consider

$$\lambda - (\lambda + \mu_h + \mu_j)x + \mu_h x^2 = 0, \quad (3)$$

in which  $\lambda = \lambda_j - \lambda_h(1 - p'_{K_j})$ , and  $\lambda_j$  and  $\lambda_h$  are the actual arrival rates to the finite and artificial holding nodes, respectively. Furthermore, it can be argued that

$$\lambda_j = \tilde{\lambda}_i (1 - p_K) = \tilde{\lambda}_i - \lambda_h. \quad (4)$$

$\mu_h$ , the delay distribution at the holding node  $h$ , is actually nothing but the remaining service time of the finite node  $j$ . Based on the renewal theory, one can formulate the remaining service time distribution as the following rate  $\mu_h$ :

$$\mu_h = \frac{2\mu_j}{1 + \sigma_j^2 \mu_j^2}, \quad (5)$$

in which  $\sigma_j^2$  is the service time variance of the finite node  $j$ . At this point, one should notice that if the service time of the finite node is exponentially distributed with rate  $\mu_j$ , then the memoryless property of exponential distribution will hold, such that

$$\mu_h = \mu_j. \quad (6)$$

*Stage III: Feedback Elimination.* As a result of the feedback loop at the holding node, a strong dependency on the arrival

process is created. In order to eliminate such dependency, the service rate at the holding node must be adjusted as follows:

$$\mu'_h = (1 - p'_K) \mu_h. \quad (7)$$

As a consequence, the service rate at node  $i$  preceding the finite node  $j$  is affected as well. One can see that the mean service time at node  $i$  is  $\mu_i^{-1}$  when the finite node is unsaturated, and  $\mu_i^{-1} + \mu'_h{}^{-1}$  when the finite node is saturated. Thus, on average, the mean service time of node  $i$  preceding the finite node  $j$  is

$$\mu_i^{-1} = \mu_i^{-1} + p_K \mu'_h{}^{-1}. \quad (8)$$

The above equations apply to all finite nodes in the queueing network.

*Summary.* To sum up, all performance measures of the network can be obtained by solving the following equations simultaneously:

$$\begin{aligned} \lambda &= \lambda_j - \lambda_h (1 - p'_K), \\ \lambda_j &= \tilde{\lambda}_i (1 - p_K), \\ \lambda_j &= \tilde{\lambda}_i - \lambda_h, \\ \lambda_j &= \tilde{\lambda}_i - \lambda_h, \\ p'_K &= \left[ \frac{\mu_j + \mu_h}{\mu_h} - \frac{\lambda \left[ (r_2^K - r_1^K) - (r_2^{K-1} - r_1^{K-1}) \right]}{\mu_h \left[ (r_2^{K+1} - r_1^{K+1}) - (r_2^K - r_1^K) \right]} \right]^{-1}, \quad (9) \\ z &= (\lambda + 2\mu_h)^2 - 4\lambda\mu_h, \\ r_1 &= \frac{[(\lambda + 2\mu_h) - z^{1/2}]}{2\mu_h}, \\ r_2 &= \frac{[(\lambda + 2\mu_h) + z^{1/2}]}{2\mu_h}, \\ p_K &\equiv \text{Equation (1)}. \quad (10) \end{aligned}$$

Note that (1), for  $p_K$ , only applies to an  $M/G/2/K$  setting. Other expressions for  $p_K$  for  $M/G/c/K$  queues, with  $c = 3$  to  $c = 10$ , have been developed by Smith [31] and can be used in the set of (9) and (1).

**2.4. Optimization Models.** In this section, we review some of the optimization models found in the literature. Given a directed graph  $G(V, A)$  to represent the queueing network, characterized by Poisson arrivals, in which  $V$  is the set of node (queues), with nonnegative buffers, multiple servers, and a general service time distribution, and in which  $A$  is the set of directed arcs (pairs of queues) interconnecting the nodes, we can optimize (i) on the number of buffers, (ii) on the number of servers used in each vertex  $V_i$ , (iii) on the characteristics of the service distribution (e.g., the service rates and/or the service variability), (iv) on the routing probabilities related

to the arcs  $A$ , or (v) on any combination of these possible decision variables.

In general, we can write the generic optimization model as follows:

$$Z = \min f(\mathbf{x}), \quad (11)$$

subject to

$$\begin{aligned} \Theta(\mathbf{x}) &\geq \Theta^\tau, \\ \mathbf{x} &\geq 0, \end{aligned} \quad (12)$$

which minimizes the total allocation  $f(\mathbf{x}) = \sum_{i \in V} x_i$  (i.e., over all vertices  $i \in V$ ), constrained to provide a minimum throughput of  $\Theta^\tau$ .

A number of specific models can be specified based on the above generic model.

- (i) When we set  $\mathbf{x} \equiv \mathbf{B}$ , the buffer allocation problem (BAP) appears. One extra constraint needs to be added to reflect the integrality condition,  $B_i \in \mathcal{N}$ , for all  $i \in V$ . The objective function is then  $Z_{\text{BAP}} = \min \sum_{i \in V} B_i$ . This is a model formulation presented and discussed in detail in Smith [37], Smith and Cruz [8], and Smith et al. [38] in which series, merge, and split topologies were examined using the GEM to estimate the performance of these queueing networks and an iterative search methodology based on Powell's [39] algorithm to find the optimal buffer allocation within the network. The papers of Gershwin and Schor [40] and Shi and Gershwin [41] also deal with buffer allocation.
- (ii) The server allocation problem (CAP) appears if we have  $\mathbf{x} \equiv \mathbf{c}$ . Again, an extra integrality constraint is needed,  $c_i \in \mathcal{N}$ , for all  $i \in V$ . The objective function is then  $Z_{\text{CAP}} = \min \sum_{i \in V} c_i$ . The CAP was considered by Smith et al. [42] in which a methodology was developed built upon two-moment approximations to the service time distribution embedded in the GEM for computing the performance measures in complex finite queueing networks and Powell's [39] algorithm for optimally allocating servers to the network topology.

- (iii) Combining the server and buffer allocation problems by setting  $\mathbf{x} \equiv (\mathbf{B}, \mathbf{c})$  results in the joint buffer and server allocation problem (BCAP). In this case, the integrality constraints are  $B_i, c_i \in \mathcal{N}$ , for all  $i \in V$ . Next to this integrality constraint, one more constraint is needed. It is necessary to ensure that the traffic intensity is such that  $\rho_i \equiv \lambda_i / (c_i \mu_i) < 1$  to ensure a finite optimal solution. Note that buffers can be equal to zero, hence, having a zero-buffer system (more on bufferless systems in Andriansyah et al. [32] in which such networks were evaluate in terms of the throughput using the GEM that was compared to simulations and a multiobjective optimization approach was adopted to derive the Pareto efficient curves showing the trade-off between the total number of servers used and the throughput). Secondly, note that

the objective function needs to be adapted slightly to take into account the two objectives (i.e., buffers and servers).

We consider two options to rewrite the objective function depending on how to deal with the multiobjective issue.

- (a) First, the objective function can be written as a weighted sum of the two objectives; that is,

$$Z_{\text{BCAP1}} = \min \left\{ \omega \sum_{i \in V} c_i + (1 - \omega) \sum_{i \in V} B_i \right\}. \quad (13)$$

We assign a cost of  $\omega$  to servers and  $(1 - \omega)$  to buffers. We can then modify the value of  $\omega$ , such that  $0 < \omega < 1$ , to reflect the relative cost of servers versus buffers. As  $\omega$  is decreased, the cost of servers will become relatively lower than that of buffers. That is, buffers are then more expensive than servers. Alternatively, when the value of  $\omega$  is increased, the servers become more costly relative to the buffers. In this way, we evaluate whether different pricing of servers and buffers results in a significantly different buffer and server allocation. It is worthwhile to mention that if  $\omega = 0$ , the above problem reduces to the pure BAP and if  $\omega = 1$ , the pure CAP is obtained. The BCAP1 problem was treated in details by Woensel et al. [43], when the joint optimization of the number of buffers and servers was firstly solved by means of Powell's [39] method, a classical nonlinear derivative-free optimization algorithm, while a two-moment approximation and the GEM compute the performance measure of interest (the throughput). The proposed methodology was capable of handling the trade-off between the number of servers and buffers, yielding better throughput than previously published studies. Also, the importance of the squared coefficient of variation of the service time was stressed, since it strongly influenced the approximate optimal allocation.

- (b) Secondly, the objective function can be formulated in a multicriteria way; that is,

$$Z_{\text{BCAP2}} = \min \{f_1(\mathbf{c}), f_2(\mathbf{B})\}, \quad (14)$$

in which each one of the two objectives are considered explicitly, with  $f_1(\mathbf{c}) \equiv \sum_{i \in V} c_i$ , and  $f_2(\mathbf{B}) \equiv \sum_{i \in V} B_i$ .

Consequently, one obtains an approximation of the Pareto set of solutions for the two objectives. As such, this perspective is more general than the BCAP1 formulation. For further details on multiobjective optimization in general, see Chankong and Haimes [44]. The BCAP2 formulation was treated by Cruz et al. [45, 46] which

developed a multiobjective genetic algorithm to satisfy these conflicting objectives and to produce an approximation of the complete set of all best solutions, known as the Pareto optimal or noninferior set.

- (iv) A slightly different formulation is the optimal routing problem (OROP). Here, the routing probabilities  $\alpha_{i,j}$  are determined such that the throughput is maximized. Of course, the sum of all routing probabilities  $\alpha_{i,j}$  in the arcs leaving each vertex  $i \in V$  and reaching its successors  $j$ , such that  $(i, j) \in A$  should sum up to one

$$Z_{\text{ORAP}} = \max \Theta(\boldsymbol{\alpha}), \quad (15)$$

subject to

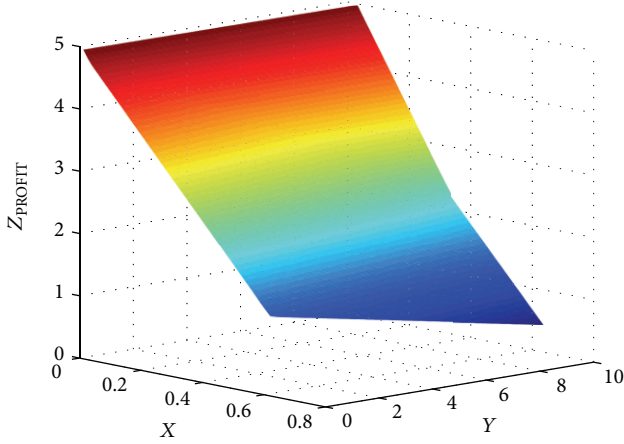
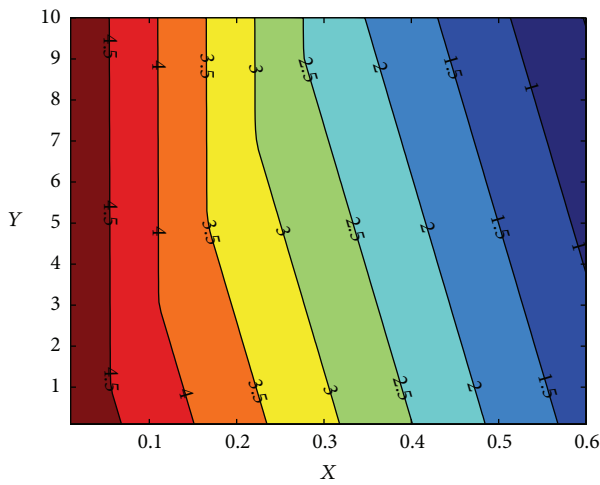
$$\begin{aligned} 0 \leq \alpha_{i,j} \leq 1, \quad \forall (i, j) \in A, \\ \sum_{j \in \delta(i)} \alpha_{i,j} = 1, \quad \forall i \in V, \end{aligned} \quad (16)$$

in which  $\Theta(\boldsymbol{\alpha})$  is the throughput, which is the objective that must be maximized,  $\boldsymbol{\alpha}$  the optimal routing probability matrix,  $\boldsymbol{\alpha} \equiv [\alpha_{i,j}]$ , that is, the matrix that maximizes the objective function of this predefined network, and  $\delta(i)$  is the set of succeeding vertexes of vertex  $i$ ; that is,  $\delta(i) \equiv \{j \mid (i, j) \in A\}$ .

The throughput will thus be affected by the effective routing of jobs through the network, the variability of the service distribution, the number of servers, and the number of buffers. Among the papers that dealt with the ORAP, we could mention Gosavi and Smith [47] and Daskalaki and Smith [48]. Additionally, Cruz and van Woensel [49] solved the ORAP by using the GEM as the performance evaluation tool of the finite queueing network and optimizing by means of a heuristics based on Powell's [39] algorithm.

- (v) A last variation considered is the profit maximization model. The models are thus expanded with financial indicators in order to maximize the profit generated. This profit will be a function of the quantity one can set in the market (i.e., the throughput) and the costs to realize this throughput, which could be the buffer and/or server allocation. The decision variable is thus the investment in buffers or servers ( $(\mathbf{B}, \mathbf{c})$ ). Assume the cost of the buffers or servers is  $\gamma$  and the gain of a unit of throughput is equal to  $\phi$ . Then we can formulate the objective function as follows:

$$Z_{\text{PROFIT}} = \max \left\{ \phi \Theta(\mathbf{B}, \mathbf{c}) - \gamma \sum_{i \in V} (B_i + c_i) - \beta [\Theta^{\tau} - \Theta(\mathbf{B}, \mathbf{c})] \right\}, \quad (17)$$

(a)  $Z_{\text{PROFIT}}$  versus  $X \equiv \gamma/\phi$  and  $Y \equiv \beta/\phi$ 

(b) contour plot

FIGURE 2: Achieved profit at the optimal buffer allocation for  $\Theta^\tau = 5$ .

in which  $[\Theta^\tau - \Theta(\mathbf{B}, \mathbf{c})]$  is either positive or zero (i.e.,  $\Theta(\mathbf{B}, \mathbf{c}) \leq \Theta^\tau$ ). Penalty costs of size  $\beta$  are charged when the system throughput does not meet the market demand (i.e.,  $\Theta(\mathbf{B}, \mathbf{c}) < \Theta^\tau$ ). Penalty costs can include the cost of outsourcing production to another factory. Figure 2 displays the behavior of this optimization function for a network of three  $M/G/c/K$  queues in tandem, with  $\mu_i = 10$ ,  $s_i^2 = 1.5$ , for all  $i$ , an external arrival rate  $\Lambda_1 = 5$  and  $\Theta^\tau = 5$ . It shows the achieved profit,  $Z_{\text{PROFIT}}$ , at the optimal buffer allocation, for  $\phi = 1$  and different cost settings  $\gamma$  and  $\beta$ . When the operational expense increases ( $X \equiv \gamma/\phi$ ), it is more attractive to underachieve market demand (i.e.,  $\Theta(\mathbf{B}, \mathbf{c}) \ll \Theta^\tau$ ); optimal throughput decreases. When the penalty costs increase ( $Y \equiv \beta/\phi$ ), it becomes less attractive to underachieve market demand; optimal throughput increases.

It is worthwhile to state that the models described above are difficult nonlinear integer programming problems.

Considering the BCAP model, it can be shown that for a network with  $N$  nodes, the complexity involved is

$$\left[ \frac{K(K+1)}{2} \right]^N. \quad (18)$$

Clearly, the solution space grows exponentially in the number of nodes, but not (exponentially) in the capacity of each node. The complexity of the BCAP model can thus be written as  $O(K^N)$ .

**2.5. Optimization Methodologies.** While the GEM computes the performance measures for the queueing network, many of the above discussed models need to be optimized on the decision variables defined in  $\mathbf{x}$ . Note that there, of course, exist many optimization methods. An exhaustive discussion is left out of this paper, but the interested reader is referred to Aarts and Lenstra [50] and the references therein. We describe two methodologies which have proven to be successful for the above described models, namely, the Powell's [39] algorithm and a genetic algorithm approach. Of course, small problems can always be enumerated.

Powell's [39] algorithm can be described as an unconstrained optimization procedure that does not require the calculation of first derivatives of the function. Numerical examples from Himmelblau [51] have shown that the method is capable of minimizing a function with up to twenty variables. Powell's method locates the minimum of  $f(\mathbf{x})$  of a nonlinear function by successive unidimensional searches from an initial starting point  $\mathbf{x}^{(0)}$  along a set of conjugate directions. These conjugate directions are generated within the procedure itself. Powell's method is based on the idea that if a minimum of a nonlinear function  $f(\mathbf{x})$  is found along  $p$  conjugate directions in a stage of the search, and an appropriate step is made in each direction, the overall step from the beginning to the  $p$ -th step is conjugate to all of the  $p$  subdirections of the search.

Genetic algorithms (GA) are optimization algorithms to perform an approximate global search relying on the information obtained from the evaluation of several points in the search space and obtaining a population of these points that converges to the optimum through the application of the genetic operators *mutation*, *crossover*, *selection*, and *elitism*. Each of these operators may be implemented in several different ways, each one of them characterizing a specific instance of GA. Additionally, convergence of GA is guaranteed by assigning fitness to each population member and preserving diversity at the same front. For instance, recent successful applications of GA were reported by Lin [52] and Calvete et al. [53], for single-objective applications, and by Carrano et al. [54] and Cruz et al. [45, 46], for multiple-objective applications. A wealth of references is given by these authors. For an application of GA to manufacturing problems, see Andriansyah et al. [32].

### 3. Results and Insights

In this section, we will focus on one example network and describe the results for some of the different optimization

TABLE 1: Results for the buffer allocation problem (see Smith and Cruz [8]).

$s^2$	$\mathbf{c}$	$\mathbf{B}$	$\sum_i c_i$	$\sum_i B_i$	$\theta(\mathbf{c}, \mathbf{B})$
0.5	(1111111111111111)	(8 4 4 4 4 4 4 4 4 4 4 4 4 4 4 5)	16	69	4.9899
1.0	(1111111111111111)	(10 5 5 5 5 4 4 4 4 4 4 4 4 4 5 5 5)	16	77	4.9879
1.5	(1111111111111111)	(11 5 5 5 5 5 5 5 5 5 5 5 5 5 5 6)	16	87	4.9877

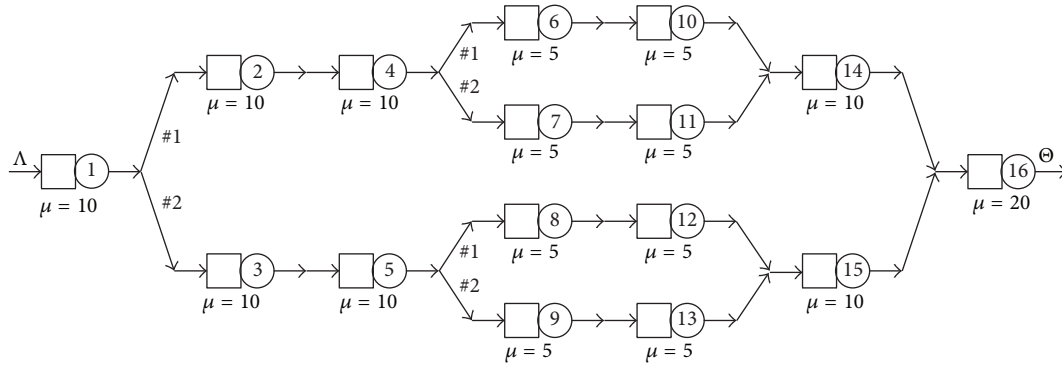


FIGURE 3: Combined topology.

models discussed above. We consider a combination of the three basic topologies (series, split, and merge), as shown in Figure 3. This network consists of 16 nodes with the processing rate of servers in each node given in the figure. The network is adopted from Smith and Cruz [8]. We use exactly the same values for  $\Lambda$ ,  $\mu$ ,  $s^2$ , and the routing probabilities for the splitting node (#1 and #2). Note that the routing probability #1 refers to the up tier of the node, while #2 refers to the low tier. Refer to Figure 3 for the position of each node in the network.

**3.1. The Buffer Allocation Problem (BAP).** We reproduce in Table 1 the results from Smith and Cruz [8] for this network structure with  $\Lambda = 5$  and the routing probabilities equal to 0.5 (Table 29 in their paper). The optimization method used was Powell with multiple restarts to avoid local optima. Note that Smith and Cruz [8] considered an  $M/G/1/K$  setting and therefore the number of servers in all nodes is set to 1 while optimizing on the buffer allocation. Based on Table 1, we see that the first node (most congested) is receiving more buffers to cope with the relatively high arrival rate.

**3.2. The Server Allocation Problem (CAP).** Let us now fix the number of buffers beforehand and then optimize on the number of servers used. More specifically, we set all buffers equal to 1 and look at the resulting server allocation. The results are given in Table 2, also obtained from Powell algorithm with multiple restarts to avoid local optima. Interestingly, we observe the same behavior as for the buffer allocation; that is, the first node is receiving more resources than the remaining nodes. On the other hand, the number of servers added is relatively low compared to the buffers added (e.g., 5 versus 8, for  $s^2 = 0.5$ ). This is because a server is also acting as a buffer, but a server adds more value, measured in throughput, as servers actually provide service.

**3.3. The Joint Buffer-Server Allocation Problem (BCAP).**

Before going to the results for the example network, we analyze the difference between buffers and servers. We saw that the BAP and CAP give different results in terms of number of servers versus number of buffers used. Let us assume that we have a *single* zero-buffer node with one server (i.e.,  $K = 1$ ,  $B = 0$ , and  $c = 1$ ), submitted to an external arrival rate  $\Lambda = 5.0$ , service rate  $\mu = 10$  and a squared coefficient of variation of the service time distribution  $s^2 = \{0.5, 1.0, 1.5\}$ . Figure 4 gives the percentage increase of adding either a server (adding one to nine servers compared to the base case) or a buffer (adding one to eleven buffers compared to the base case) to the zero buffer base situation.

It is clear that in this case, the first added buffer or first added server gives the largest contribution to the throughput value, which is limited by the external arrival rate  $\Lambda$ . Note that the addition of the first extra server gives an increase in throughput of about 58% to 78%, depending upon the squared coefficient of variation of the service time distribution  $s^2$ , while the first added buffer only gives a 36% to 39% increase. Important to mention is that, in order to achieve the same increase in throughput by only using buffers, we need four to six extra buffer spaces, depending on the  $s^2$ , rather than only one server space.

The results for the joint buffer-server allocation problem are presented in Table 3, in which the  $c/B$  price ratio gives an indication of the relative costs of servers compared to buffers, obtained from Powell. A price ratio of 8:1, for example, means that servers are 8 times more expensive than buffers. The results from Table 3 show a higher throughput than for the pure BAP, Table 1, for every setting. As expected, we found that the optimal server allocation in the BCAP is different from the server settings in the pure BAP. This, however, depends strongly upon the price ratio of buffers versus servers. We found that  $M/G/1/K$  is not an optimal

TABLE 2: Results for the server allocation problem.

$s^2$	$\mathbf{c}$	$\mathbf{B}$	$\sum_i c_i$	$\sum_i B_i$	$\theta(\mathbf{c}, \mathbf{B})$	$Z_\alpha$
0.5	(5 2 2 2 2 2 2 2 2 2 2 2 2 2 2 2)	(1 1 1 1 1 1 1 1 1 1 1 1 1 1 1 1)	34	16	4.9997	35.29
1.0	(5 2 2 2 2 2 2 2 2 2 2 2 2 2 2 2)	(1 1 1 1 1 1 1 1 1 1 1 1 1 1 1 1)	36	16	4.9996	35.33
1.5	(5 2 2 2 2 2 2 2 2 2 2 2 2 2 2 2)	(1 1 1 1 1 1 1 1 1 1 1 1 1 1 1 1)	34	16	4.9996	35.37

TABLE 3: Results for the joint buffer-server allocation problem.

$\Lambda$	$s^2$	$c/B$	$\mathbf{c}$	$\mathbf{K}$	$\sum_i c_i$	$\sum_i K_i$	$\sum_i B_i$	$\theta(\mathbf{c}, \mathbf{B})$	$Z_\alpha$
5.0	0.5	1:8	(3 3 3 3 3 3 3 3 3 3 3 3 3 3 3 3)	(3 3 3 3 3 3 3 3 3 3 3 3 3 3 3 3)	48	48	0	4.9996	5.76
		1:4	(3 3 3 3 3 3 3 3 3 3 3 3 3 3 3 3)	(3 3 3 3 3 3 3 3 3 3 3 3 3 3 3 3)	48	48	0	4.9996	10.0
		1:2	(3 3 3 3 3 3 3 3 3 3 3 3 3 3 3 3)	(3 3 3 3 3 3 3 3 3 3 3 3 3 3 3 3)	48	48	0	4.9996	16.4
		1:1	(5 3 3 3 3 2 2 2 2 2 2 2 2 3 3 5)	(5 3 3 3 3 2 2 2 2 2 2 2 2 3 3 5)	44	44	0	4.9998	22.2
		2:1	(2 2 2 2 2 2 2 2 2 2 2 2 2 2 2 2)	(5 3 3 3 3 2 2 2 2 2 2 2 2 3 3 5)	32	44	12	4.9989	26.5
		4:1	(3 1 1 1 1 1 1 1 1 1 1 1 1 1 1 3)	(3 5 5 5 5 3 3 3 3 3 3 3 3 5 5 3)	20	60	40	4.9974	26.6
		8:1	(1 1 1 1 1 1 1 1 1 1 1 1 1 1 1 1)	(11 6 6 6 6 4 4 4 4 4 4 4 4 6 6 11)	16	90	74	4.9994	23.0
		1.0	1:8	(3 3 3 3 3 3 3 3 3 3 3 3 3 3 3 3)	(3 3 3 3 3 3 3 3 3 3 3 3 3 3 3 3)	48	48	0	4.9994
	1:4		(5 3 3 3 3 2 2 2 2 2 2 2 2 3 3 5)	(5 3 3 3 3 2 2 2 2 2 2 2 2 3 3 5)	44	44	0	4.9997	9.09
	1:2		(5 3 3 3 3 2 2 2 2 2 2 2 2 3 3 5)	(5 3 3 3 3 2 2 2 2 2 2 2 2 3 3 5)	44	44	0	4.9997	15.0
	1:1		(5 3 3 3 3 2 2 2 2 2 2 2 2 3 3 5)	(5 3 3 3 3 2 2 2 2 2 2 2 2 3 3 5)	44	44	0	4.9997	22.3
	2:1		(3 2 2 2 2 2 2 2 2 2 2 2 2 2 2 3)	(3 3 3 3 3 2 2 2 2 2 2 2 2 3 3 3)	34	40	6	4.9984	26.2
	4:1		(2 2 2 2 2 1 1 1 1 1 1 1 1 1 2 2 3)	(6 3 3 3 3 4 4 4 4 4 4 4 4 4 3 3 4)	25	60	35	4.9989	28.1
	8:1		(1 1 1 1 1 1 1 1 1 1 1 1 1 1 1 1)	(13 6 6 6 6 4 4 4 4 4 4 4 4 6 6 13)	16	94	78	4.9987	24.1
	1.5		1:8	(5 3 3 3 3 2 2 2 2 2 2 2 2 3 3 5)	(5 3 3 3 3 2 2 2 2 2 2 2 2 3 3 5)	44	44	0	4.9996
		1:4	(5 3 3 3 3 2 2 2 2 2 2 2 2 3 3 5)	(5 3 3 3 3 2 2 2 2 2 2 2 2 3 3 5)	44	44	0	4.9996	9.15
		1:2	(5 3 3 3 3 2 2 2 2 2 2 2 2 3 3 5)	(5 3 3 3 3 2 2 2 2 2 2 2 2 3 3 5)	44	44	0	4.9996	15.0
		1:1	(5 3 3 3 3 2 2 2 2 2 2 2 2 3 3 5)	(5 3 3 3 3 2 2 2 2 2 2 2 2 3 3 5)	44	44	0	4.9996	22.4
		2:1	(3 2 2 2 2 2 2 2 2 2 2 2 2 2 2 3)	(3 3 3 3 3 2 2 2 2 2 2 2 2 3 3 3)	34	40	6	4.9979	26.8
		4:1	(2 2 2 2 2 1 1 1 1 1 1 1 1 1 2 2 3)	(6 3 3 3 3 4 4 4 4 4 4 4 4 4 3 3 4)	25	60	35	4.9983	28.7
		8:1	(1 1 1 1 1 1 1 1 1 1 1 1 1 1 1 1)	(15 7 7 7 7 4 4 4 4 4 4 4 4 7 7 15)	16	104	88	4.9986	25.4

configuration for this particular queueing network structure, except when buffers are becoming relatively too expensive. For these cases, we found that single-servers are optimal indeed (see rows where  $c/B$  ratio is 8 : 1).

We observe that (near) zero-buffer configurations are identified where appropriate; that is, where the servers are relatively cheaper compared to buffers. Varying the squared coefficient of variation of the service time distribution  $s^2$  does result in some changes in the optimal server and buffer allocation, which shows the importance of models dealing with general service times. The results show that the number of buffers seems to be large under high variability, which could be expected since the increase in  $s^2$  means an increase in the variability. The extra buffers are there to handle this high variability.

3.4. *Final Remarks and Insights.* The above numerical results for the buffer allocation problem, the server allocation problem, and the joint buffer-server allocation problem show that significant gains can be achieved in manufacturing systems. Specifically, setting the buffers and servers in an appropriate way greatly affects the throughput for these manufacturing systems. This is important as these systems need to be as

highly utilized as possible, given the high investments. Our models and optimizations show that the optimal configurations are not always straightforward and thus advanced models and solution methods are needed. We have followed a queueing network approach with finite buffers, as this resembles reality the closest. This modeling approach is of course much harder than, for example, infinite queueing networks. We see based on the various experiments that our solution methodology is powerful and suitable for the different types of models handled in this paper. This offers managers and manufacturing systems designers a powerful tool to work with.

We saw that the BAP and CAP obviously give different results. We also note that while the addition of the first extra server gives a certain amount of increase in the throughput, the addition of the first buffer space generally will give a lower increase. In other words, in order to achieve the same increase in throughput by only using buffers, we need more extra buffer spaces rather than only a few server space.

**4. Conclusions**

This review provided an overview of the different modeling issues, the performance evaluation, and optimization

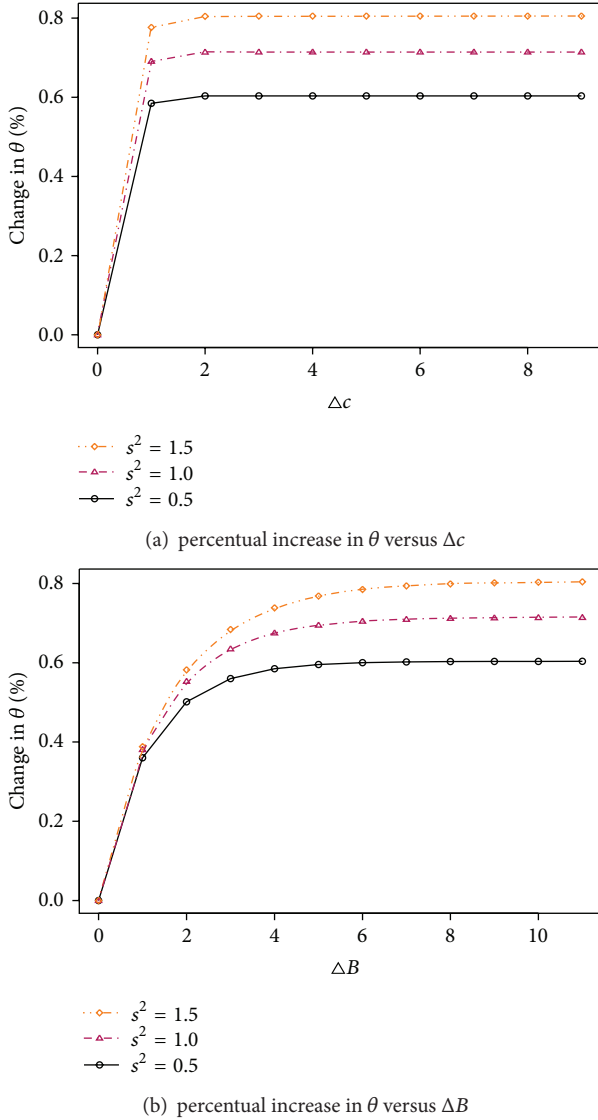


FIGURE 4: Throughput increase versus added number of servers ( $\Delta c$ ) and buffers ( $\Delta B$ ).

approaches of the manufacturing systems assuming a queueing theory approach. We discussed the merits of the Generalized Expansion Method as a performance evaluation tool of the finite queueing networks. This methodology has proved in the literature to be a valuable approach. Secondly, different optimization models are discussed, namely the buffer allocation problem, the server allocation problem, the joint buffer, server allocation problem, and some other models. The different optimization models are shown to be hard nonlinear integer programming problems which are able to be approximately solved with a Powell heuristic. The paper ended with an overview of some results for the different models considered on a complex queueing network.

**4.1. Future Research Suggestions.** In this paper, we considered the throughput as the main performance measure. Instead of the throughput, it would be interesting to evaluate the

behavior of the models based on cycle time, work-in-process (WIP), or other performance measures.

In a number of industrial improvement projects carried out, we observed that the critical issue to be able to use the above models is related to data availability. More specifically, processing rates, arrival rates, uncertainty in the service process, and so on need to be extracted from the available databases. An interesting approach to obtaining the relevant data is the effective process time (EPT) point of view (see Hopp and Spearman [55]). The advantage of the effective process time (EPT) approach is that various types of disturbances on the shop-floor are aggregated into EPT distributions, this enables effective modeling. However, it is important to note that, disturbances which are aggregated into the EPT distribution cannot be analyzed afterwards. Hence, shop-floor realities or disturbances which are modeled explicitly and excluded from aggregation in the EPT are defined beforehand.

Topics for future research on the queueing part include the analysis and optimization of networks with cycles, for example, to model many important industrial systems that have loops, such as systems with captive pallets and fixtures or reverse streams of products due to rework, or even the extension to  $GI/G/c/K$  queueing networks with generally distributed and independent arrivals.

### Basic Network Notation

$\Lambda$ :	External Poisson arrival rate to the network
$\lambda_j$ :	Poisson arrival rate to node $j$
$\tilde{\lambda}_j$ :	Effective arrival rate to node $j$
$\mu_j$ :	Exponential mean service rate at finite node $j$
$\tilde{\mu}_j$ :	Effective service rate at finite node $j$ due to blocking
$p_{K_j}$ :	Blocking probability of finite queue $j$ of size $K_j$
$p'_{K_j}$ :	Feedback blocking probability in the expansion method
$h_j$ :	The artificial holding node (queue) preceding node $j$ created in the GEM
$c_j$ :	Number of servers at node $j$
$K_j$ :	Total capacity at node $j$ including the items in service
$B_j \equiv K_j - c_j$ :	Buffer capacity at node $j$ excluding the items in service
$N$ :	Set of nodes (queues) in the queueing network
$V$ :	Set of arcs (pairs of nodes) in the queueing network
$\rho_j \equiv \lambda_j / (c_j \mu_j)$ :	Traffic intensity at node $j$
$\theta_j$ :	Mean throughput rate at node $j$
$s_j^2$ :	Squared coefficient of variation of the service time distribution at node $j$ .

### Conflict of Interests

The authors declare that there is no conflict of interests regarding the publication of this paper.

## Acknowledgments

The research of professor Frederico Cruz has been partially funded by the Brazilian agencies, CNPq (*Conselho Nacional de Desenvolvimento Científico e Tecnológico*) of the Ministry for Science and Technology of Brazil, CAPES (*Coordenação de Aperfeiçoamento de Pessoal de Nível Superior*), and FAPEMIG (*Fundação de Amparo à Pesquisa do Estado de Minas Gerais*).

## References

- [1] J. M. Smith, "M/G/c/K performance models in manufacturing and service systems," *Asia-Pacific Journal of Operational Research*, vol. 25, no. 4, pp. 531–561, 2008.
- [2] J. M. Smith, "Properties and performance modelling of finite buffer M/G/1/K networks," *Computers & Operations Research*, vol. 38, no. 4, pp. 740–754, 2011.
- [3] J. M. Smith, "M/G/c/K performance models in manufacturing and service systems," *International Journal of Production Research*, 2013.
- [4] R. Suri, "An overview of evaluative models for flexible manufacturing systems," *Annals of Operations Research*, vol. 3, no. 1, pp. 13–21, 1985.
- [5] A. M. Law and W. D. Kelton, *Simulation Modeling and Analysis*, McGraw-Hill, New York, NY, USA, 3rd edition, 1982.
- [6] S. Yeralan and B. Tan, "Analysis of multistation production systems with limited buffer capacity—I. The subsystem model," *Mathematical and Computer Modelling*, vol. 25, no. 7, pp. 109–122, 1997.
- [7] M. M. Fadiloglu and S. Yeralan, "General theory on spectral properties of state-homogeneous finite-state quasi-birth-death processes," *European Journal of Operational Research*, vol. 128, no. 2, pp. 402–417, 2001.
- [8] J. M. Smith and F. R. B. Cruz, "The buffer allocation problem for general finite buffer queueing networks," *IIE Transactions*, vol. 37, no. 4, pp. 343–365, 2005.
- [9] W. Whitt, "Open and closed models for networks of queues," *AT&T Bell Laboratories Technical Journal*, vol. 63, no. 9, pp. 1911–1979, 1984.
- [10] J. M. Smith, "Optimal workload allocation in closed queueing networks with state dependent queues," *Annals of Operations Research*, 2013.
- [11] S. Balsamo, V. de Nitto Personé, and R. Onvural, *Analysis of Queueing Networks with Blocking*, Kluwer Academic Publishers, Dordrecht, The Netherlands, 2001.
- [12] J. Walrand, *An Introduction to Queueing Networks*, Prentice-Hall, Englewood Cliffs, NJ, USA, 1988.
- [13] Y. Dallery and S. B. Gershwin, "Manufacturing flow line systems: a review of models and analytical results," *Queueing Systems*, vol. 12, no. 1-2, pp. 3–94, 1992.
- [14] H. G. Perros, "Queueing networks with blocking: a bibliography," *ACM Sigmetrics*, vol. 12, pp. 8–12, 1984.
- [15] D. Gross, J. F. Shortle, J. M. Thompson, and C. M. Harris, *Fundamentals of Queueing Theory*, Wiley-Interscience, Hoboken, NJ, USA, 4th edition, 2008.
- [16] J. R. Jackson, "Networks of waiting lines," *Operations Research*, vol. 5, pp. 518–521, 1957.
- [17] J. R. Jackson, "Jobshop-like queueing systems," *Management Science*, vol. 10, no. 1, pp. 131–142, 1963.
- [18] M. Reiser and H. Kobayashi, "Accuracy of the diffusion approximation for some queueing systems," *Journal of Research and Development*, vol. 18, pp. 110–124, 1974.
- [19] P. J. Kuehn, "Approximate analysis of general queueing networks by decomposition," *IEEE Transactions on Communications*, vol. 27, no. 1, pp. 113–126, 1979.
- [20] J. A. Buzacott and J. G. Shanthikumar, *Stochastic Models of Manufacturing Systems*, Prentice-Hall, Englewood Cliffs, NJ, USA, 1993.
- [21] F. S. Q. Alves, H. C. Yehia, L. A. C. Pedrosa, F. R. B. Cruz, and L. Kerbache, "Upper bounds on performance measures of heterogeneous M/M/c queues," *Mathematical Problems in Engineering*, vol. 2011, Article ID 702834, 18 pages, 2011.
- [22] F. R. B. Cruz, J. M. Smith, and R. O. Medeiros, "An M/G/c/C state-dependent network simulation model," *Computers and Operations Research*, vol. 32, no. 4, pp. 919–941, 2005.
- [23] F. R. B. Cruz, P. C. Oliveira, and L. Duczmal, "State-dependent stochastic mobility model in mobile communication networks," *Simulation Modelling Practice and Theory*, vol. 18, no. 3, pp. 348–365, 2010.
- [24] L. A. Pereira, L. H. Duczmal, and F. R. B. Cruz, "Congested emergency evacuation of a population using a finite automata approach," *Safety Science*, vol. 51, no. 1, pp. 267–272, 2013.
- [25] M. Dorda and D. Teichmann, "Modelling of freight trains classification using queueing system subject to breakdowns," *Mathematical Problems in Engineering*, vol. 2013, Article ID 307652, 11 pages, 2013.
- [26] R. T. N. Cardoso, R. H. C. Takahashi, and F. R. B. Cruz, "Pareto optimal solutions for stochastic dynamic programming problems via Monte Carlo simulation," *Journal of Applied Mathematics*, vol. 2013, Article ID 801734, 9 pages, 2013.
- [27] L. Kerbache and J. M. Smith, "The generalized expansion method for open finite queueing networks," *European Journal of Operational Research*, vol. 32, no. 3, pp. 448–461, 1987.
- [28] L. Kerbache and J. M. Smith, "Asymptotic behavior of the expansion method for open finite queueing networks," *Computers and Operations Research*, vol. 15, no. 2, pp. 157–169, 1988.
- [29] L. Kerbache and J. M. Smith, "Multi-objective routing within large scale facilities using open finite queueing networks," *European Journal of Operational Research*, vol. 121, no. 1, pp. 105–123, 2000.
- [30] S. Jain and J. M. Smith, "Open finite queueing networks with M/M/C/K parallel servers," *Computers and Operations Research*, vol. 21, no. 3, pp. 297–317, 1994.
- [31] J. M. Smith, "M/G/c/K blocking probability models and system performance," *Performance Evaluation*, vol. 52, no. 4, pp. 237–267, 2003.
- [32] R. Andriansyah, T. van Woensel, F. R. B. Cruz, and L. Duczmal, "Performance optimization of open zero-buffer multi-server queueing networks," *Computers & Operations Research*, vol. 37, no. 8, pp. 1472–1487, 2010.
- [33] T. van Woensel and N. Vandaele, "Empirical validation of a queueing approach to uninterrupted traffic flows," *4OR*, vol. 4, no. 1, pp. 59–72, 2006.
- [34] T. van Woensel and N. Vandaele, "Modeling traffic flows with queueing models: a review," *Asia-Pacific Journal of Operational Research*, vol. 24, no. 4, pp. 435–461, 2007.
- [35] T. Kimura, "A transform-free approximation for the finite capacity M/G/s queue," *Operations Research*, vol. 44, no. 6, pp. 984–988, 1996.

- [36] J. Labetoulle and G. Pujolle, "Isolation method in a network of queues," *IEEE Transactions on Software Engineering*, vol. 6, no. 4, pp. 373–381, 1980.
- [37] J. M. Smith, "Optimal design and performance modelling of  $M/G/1/K$  queueing systems," *Mathematical and Computer Modelling*, vol. 39, no. 9–10, pp. 1049–1081, 2004.
- [38] J. M. Smith, F. R. B. Cruz, and T. van Woensel, "Topological network design of general, finite, multi-server queueing networks," *European Journal of Operational Research*, vol. 201, no. 2, pp. 427–441, 2010.
- [39] M. J. D. Powell, "An efficient method for finding the minimum of a function of several variables without calculating derivatives," *The Computer Journal*, vol. 7, pp. 155–162, 1964.
- [40] S. B. Gershwin and J. E. Schor, "Efficient algorithms for buffer space allocation," *Annals of Operations Research*, vol. 93, pp. 117–144, 2000.
- [41] C. Shi and S. B. Gershwin, "An efficient buffer design algorithm for production line profit maximization," *International Journal of Production Economics*, vol. 122, no. 2, pp. 725–740, 2009.
- [42] J. M. Smith, F. R. B. Cruz, and T. van Woensel, "Optimal server allocation in general, finite, multi-server queueing networks," *Applied Stochastic Models in Business and Industry*, vol. 26, no. 6, pp. 705–736, 2010.
- [43] T. van Woensel, R. Andriansyah, F. R. B. Cruz, J. M. Smith, and L. Kerbache, "Buffer and server allocation in general multi-server queueing networks," *International Transactions in Operational Research*, vol. 17, no. 2, pp. 257–286, 2010.
- [44] V. Chankong and Y. Y. Haimes, *Multiobjective Decision Making: Theory and Methodology*, vol. 8, North-Holland, New York, NY, USA, 1983.
- [45] F. R. B. Cruz, T. Van Woensel, and J. M. Smith, "Buffer and throughput trade-offs in  $M/G/1/K$  queueing networks: a bi-criteria approach," *International Journal of Production Economics*, vol. 125, no. 2, pp. 224–234, 2010.
- [46] F. R. B. Cruz, G. Kendall, L. While, A. R. Duarte, and N. L. C. Brito, "Throughput maximization of queueing networks with simultaneous minimization of service rates and buffers," *Mathematical Problems in Engineering*, vol. 2012, Article ID 692593, 19 pages, 2012.
- [47] H. D. Gosavi and J. M. Smith, "An algorithm for sub-optimal routing in series-parallel queueing networks," *International Journal of Production Research*, vol. 35, no. 5, pp. 1413–1430, 1997.
- [48] S. Daskalaki and J. M. Smith, "Combining routing and buffer allocation problems in series-parallel queueing networks," *Annals of Operations Research*, vol. 125, pp. 47–68, 2004.
- [49] F. R. B. Cruz and T. van Woensel, "Optimal routing in general finite multi-server queueing networks," under review, 2014.
- [50] E. Aarts and J. K. Lenstra, *Local Search in Combinatorial Optimization*, Princeton University Press, Princeton, NJ, USA, 2nd edition, 2003.
- [51] D. M. Himmelblau, *Applied Nonlinear Programming*, McGraw-Hill, New York, NY, USA, 1972.
- [52] F.-T. Lin, "Solving the knapsack problem with imprecise weight coefficients using genetic algorithms," *European Journal of Operational Research*, vol. 185, no. 1, pp. 133–145, 2008.
- [53] H. I. Calvete, C. Galé, and P. M. Mateo, "A new approach for solving linear bilevel problems using genetic algorithms," *European Journal of Operational Research*, vol. 188, no. 1, pp. 14–28, 2008.
- [54] E. G. Carrano, L. A. E. Soares, R. H. C. Takahashi, R. R. Saldanha, and O. M. Neto, "Electric distribution network multiobjective design using a problem-specific genetic algorithm," *IEEE Transactions on Power Delivery*, vol. 21, no. 2, pp. 995–1005, 2006.
- [55] W. J. Hopp and M. L. Spearman, *Factory Physics*, Waveland Press, Long Grove, Ill, USA, 3 edition, 2011.

## Research Article

# Quality Prediction and Control of Reducing Pipe Based on EOS-ELM-RPLS Mathematics Modeling Method

Dong Xiao,<sup>1</sup> Jichun Wang,<sup>1</sup> and Huixin Tian<sup>2</sup>

<sup>1</sup> State Key Laboratory of Synthetical Automation for Process Industries, Northeastern University, Shenyang 110004, China

<sup>2</sup> Electrical Engineering and Automation Department, Tianjin Polytechnic University, Tianjin 300387, China

Correspondence should be addressed to Dong Xiao; xiaodong@ise.neu.edu.cn

Received 27 December 2013; Accepted 12 February 2014; Published 20 March 2014

Academic Editor: Nachamada Blamah

Copyright © 2014 Dong Xiao et al. This is an open access article distributed under the Creative Commons Attribution License, which permits unrestricted use, distribution, and reproduction in any medium, provided the original work is properly cited.

The inspection of inhomogeneous transverse and longitudinal wall thicknesses, which determines the quality of reducing pipe during the production of seamless steel reducing pipe, is lags and difficult to establish its mechanism model. Aiming at the problems, we proposed the quality prediction model of reducing pipe based on EOS-ELM-RPLS algorithm, which taking into account the production characteristics of its time-varying, nonlinearity, rapid intermission, and data echelon distribution. Key contents such as analysis of data time interval, solving of mean value, establishment of regression model, and model online prediction were introduced and the established prediction model was used in the quality prediction and iteration control of reducing pipe. It is shown through experiment and simulation that the prediction and iteration control method based on EOS-ELM-RPLS model can effectively improve the quality of steel reducing pipe, and, moreover, its maintenance cost was low and it has good characteristics of real time, reliability, and high accuracy.

## 1. Introduction

As seamless tubes are widely used in various fields such as automobile, aviation, petroleum, chemical industry, architecture, boiler, and military industry and are playing a very important role in national economy, the seamless tubes are called industrial blood vessels. With the rapid development of economy, the service fields of seamless tube expand ceaselessly and the requirements for product quality also become more and more urgent and higher. The working procedure of seamless steel pipe consists of piercing, tube rolling, and tube reducing. Due to the restriction of mandril rigidity during piercing and tube rolling, it is difficult to obtain the seamless steel pipe whose diameter is below 70 mm on tube rolling train. Also, even a small-sized seamless steel pipe hot rolled whose diameter is greater than 70 mm is not expected to be produced by rolling a small tubular billet because this will decrease the train productivity by leaps and bounds. Therefore, it is reasonable to produce steel pipe with a small diameter using reducing mode. Owing to the use of reducing process, people can use tubular billet with a large diameter for piercing and rolling, larger reducing can be achieved in

reducing mill train, and hence long pipe with a small diameter is obtained, which is an effective technical measure in increasing the output, expanding product variety, and reducing consumption. Various countries throughout the world tend to adopt continuous rolling process with high efficiency in steel pipe extending working procedure to produce shell with single specification and alter technical process in reducing working procedure to obtain finished pipes in different specifications.

Since tension reducing mill is the last forming equipment in steel pipe hot rolling production and has big influence on the steel pipe quality, the deviation of wall thickness is an important index in deciding the steel pipe quality. However, as the mechanism model for pipe reducing process is limited and the quality monitoring of the pipe is accomplished by the periodical spot-check of technical personnel, the inspection results lag severely. Thus, it is significant in theory and economy to establish the wall thickness prediction model of steel pipe reducing with a sufficient accuracy. Macrea and Cepisca [1], Bayoumi [2], and Zhang et al. [3] established a mechanism model of reducing mill and analyzed the indexes such as tension, velocity, and wall thickness during reducing

process but there are too many restraints in his model, and his model is appropriate for individual production train and is bad in versatility. Yu et al. [4, 5], Yi et al. [6], Xu and Du [7], Du et al. [8], Yuan et al. [9], and Shi et al. [10] utilized finite element software to simulate the reducing process of seamless steel pipe, performed prediction for the key indexes such as dimensions and wall thickness of reduced steel pipe. Their works were used for setting the technical parameters in reducing production and achieved a certain practical effect. However, due to the restriction of finite element software, its precision of prediction is not high and is more appropriate for the development of products with new specifications instead of the online real time control of steel pipe. Shuang et al. [11] analyzed different processes of incoming material and the pipe thicknesses and lengths during tension-reduction process in an iron and steel company using neural network BP algorithm but they only considered the influence of incoming shell dimension and entrance temperature, and did not consider the effect of reducing production process on product quality.

It takes dozen of seconds to produce a piece of steel pipe using reduction. Thus it can be seen that the seamless steel pipe reducing production process is a typical rapid intermittent one. Plentiful production data on site provide convenience for our use of soft measurement method during intermittent production process. Data from reducing production process take on echelon distribution. In the meantime, as the product specifications often change, it is very difficult to guarantee the same adjustment of stand this time as that of last time for products with the same specification. This will lead to the occurrence of a certain time-varying in model. These problems result in low precision of modeling established by traditional intermittent process modeling method such as multiway PLS. The modeling is difficult to be used in prediction and control of field products. Aiming at the production process characteristics such as time-varying, nonlinearity, rapid intermission, and data echelon distribution, we proposed to use EOS-ELM-RPLS (ensemble of online sequential-extreme learning machine-recursive partial least square) algorithm to establish the quality prediction model for reducing production. Under the circumstance of ensuring high precision, the model has high flexibility and adaptability and can be well used in the prediction and control of product quality on production site.

## 2. Time Interval Division of Reducing Production Process and Analysis of Quality Influential Factors of Reducing Pipe

**2.1. Time Interval Division of Reducing Production Process.** In order to establish accurately the quality prediction model of reducing pipe, one should firstly analyze the factors influencing the quality of reducing pipe to prevent incomplete information and existed redundancy during modeling from decreasing the precision of model. It is known through the analysis of process characteristic that the effect of various independent variables on the quality of reducing pipe during different time intervals is different. Part of variables only

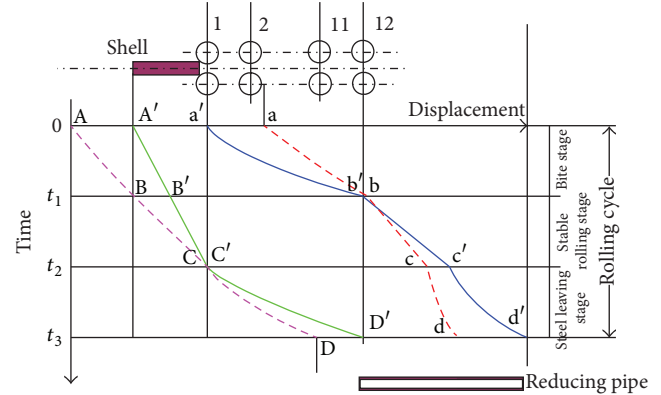


FIGURE 1: The relation between time and displacement of reducing tube.

exist in some time intervals and can be treated as factors observing quality of reducing pipe, whereas another part of variables run through entire production process and has large influence on the quality of reducing pipe.

Steel pipe reducing process is substantially a hollow body sinking continuous rolling process. As shown in Figure 1, three stages can be divided from the head of steel pipe to entrance of the first stand until away from the last stand in the tail.

- (1) Bite stage: bite stage means the stage from pipe head to enter the first stand till the pipe head to enter the last stand. As shown in Figure 1, begin when the steel pipe head enters the first rolling mill and end when the steel pipe head encounters the 12th rolling mill. Steel pipe head moves from point  $a'$  to point  $b'$ , and steel pipe tail moves from point  $A'$  to point  $B'$  when the pipe head gradually passes various stands and its speed increases with increasing coefficient of extension. At this stage, the influence variables of various rolling mills increase according to advance stepping of steel pipe.
- (2) Stable rolling stage: from pipe head to enter the last stand till the pipe tail still not to be away from the first stand, when whole mill train rolls the same piece of steel pipe, and rolling load and speed are all stable, called stable rolling stage. As shown in Figure 1, begin when the steel pipe head meets the 12th rolling mill, and end when the steel pipe tail encounters the 1st rolling mill. Steel pipe head moves from point  $b'$  to point  $c'$ , and steel pipe tail moves from point  $B'$  to point  $C'$ . At this stage, the variables of various rolling mills have influence on steel pipe.
- (3) Steel leaving stage: from pipe tail away from the 1st stand till away from the last stand. As shown in Figure 1, begin when the steel pipe tail meets the 1st rolling mill, and end when the steel pipe tail encounters the 12th rolling mill. Steel pipe head moves from point  $c'$  to point  $d'$ , and steel pipe tail moves from point  $C'$  to point  $D'$ . At this stage, the number of stands taking part in rolling this piece of steel pipe at

the same time decreases gradually until single stand rolling in the last stand, and whole piece of steel pipe finishes rolling. Then the steel pipe is expelled out of the stand. At this stage, the influence variables of various rolling mills decrease according to advance stepping of steel pipe.

## 2.2. Analysis of Quality Influential Factors of Reducing Pipe

**2.2.1. Influence of Shell Heating Temperature.** The heating temperature of shell will bring about the variation of metallic resistance to deformation and result in the variation in rolling force and average tension coefficient. The higher the heating temperature of shell is, the lower the metallic resistance to deformation is, the smaller the rolling force is, and the smaller the external diameter undulation of steel pipe is. In addition, the heating temperature of shell is a function of steel pipe diameter and obvious positive correlation exists between the heating temperature and the diameter. The higher the heating temperature of shell is, the bigger the thermal external diameter of steel pipe is after metal is subjected to thermal expansion.

**2.2.2. Influence of Rolling Speed.** It is generally recognized that friction factor plays a role concerning the effect of rolling speed on metallic transverse inhomogeneous deformation during reduction of shell. The lower the rolling speed is, the larger the friction force is, and hence the more favorable it reduces the in-homogeneity of steel pipe wall thickness.

**2.2.3. Influence of Shell Quality.** When the shell reduces, it is difficult to control its wall thickness because its inner surface is not supported by mandril and the pipe wall of the shell will be in a free varying state with changing rolling process condition. Moreover, the in-homogeneity wall thickness of the shell will be inherited to the finished steel pipe after reduction. Therefore, it is an important condition to improve the wall thickness homogeneity of shell in order to guarantee the wall thickness precision of finished steel pipe.

**2.2.4. Influence of Tension.** When tension reducing mill is used for the reducing of shell, due to the existence of tension, the diameter of shell decreases while the wall thickness thins. Under stable tension condition, metallic transverse deformation is small, which is favorable for the improvement of the precision of steel pipe wall thickness. However, tension cannot be established or tension undulation occurs among stands when the head of pierced pipe enters in turn various reducing roll stands and the tail end of shell leaves in turn various reducing roll stands. Thus the in-homogeneity of longitudinal wall thickness in the steel pipe certainly will occur.

**2.3. Determination of Input and Output Variables.** The output of quality prediction model is the quality of reducing pipe. The quantification index of judging the quality of reducing pipe is the transverse and longitudinal wall thickness. Transverse wall thickness in-homogeneity is the ratio of maximum

wall thickness deviation to nominal wall thickness. Its calculation formula is shown as follows:

$$\Delta S \% = \frac{\delta_{\max} - \delta_{\min}}{\delta_{\text{HOM}}} \times 100, \quad (1)$$

where  $\Delta S\%$ : relative in-homogeneity of transverse wall thickness;  $\delta_{\max}$ : maximum wall thickness of steel pipe;  $\delta_{\min}$ : minimum wall thickness of steel pipe;  $\delta_{\text{HOM}}$ : nominal wall thickness of steel pipe.

The size of in-homogeneity of longitudinal wall thickness in steel pipe is determined by the difference between the mean value of rough pipe front-end wall thickness and the mean value of rear-end wall thickness. Its calculation formula is shown as follows:

$$\Delta S_{\text{np}} = \frac{\sum_{i=1}^n \delta_{\text{nep}}}{n} - \frac{\sum_{i=1}^n \delta_{\text{3an}}}{n}, \quad (2)$$

where  $\sum_{i=1}^n \delta_{\text{nep}}$  and  $\sum_{i=1}^n \delta_{\text{3an}}$  are the sum of measured front-end wall thickness and rear-end wall thickness of steel pipe, respectively;  $n$  is the number of measured points at each end [12].

## 3. EOS-ELM-RPLS Algorithm

**3.1. Nonlinear PLS.** Since linear PLS model cannot describe correctly the nonlinear relation between independent variable  $X$  and dependent variable  $Y$ , nonlinear PLS method is required to solve this issue. Wold et al. extended at the PLS method to nonlinear field [13, 14]. There are two feasible methods in nonlinear PLS methods: one is to perform array extension for input matrix, introduce some nonlinear terms of original variable, for example, the square term, and then regress the extended input and output matrix using PLS method. If prior knowledge on the relation of original input variable does not exist, this method cannot guide the selection of combined mode and may lead to oversized dimension of input matrix and the difficulties of processing; the other is to reserve the linear external model of PLS method. Internal model is nonlinear.

(1) External relation model:

$$\begin{aligned} X &= TP^T + E = \sum_{a=1}^A t_a p_a^T + E, \\ Y &= UQ^T + F = \sum_{a=1}^A u_a q_a^T + F, \end{aligned} \quad (3)$$

where  $A$  is the number of reserved eigenvector,  $t_a$  ( $n \times 1$ ) and  $u_a$  ( $n \times 1$ ) are the score vector of  $X$  and  $Y$ , respectively,  $p_a$  ( $m \times 1$ ) and  $q_a$  ( $p \times 1$ ) are the load vector of  $X$  and  $Y$ , respectively,  $T$  ( $n \times A$ ) and  $U$  ( $n \times A$ ) are the score matrix of  $X$  and  $Y$ , respectively,  $P$  ( $m \times A$ ) and  $Q$  ( $p \times A$ ) are the load matrix of  $X$  and  $Y$ , respectively, and  $E$  and  $F$  are the fit residual matrix of  $X$  and  $Y$ , respectively.

(2) Internal relation model:

$$\hat{u}_a = f(t_a) + \varepsilon, \quad (4)$$

where  $f(\cdot)$  is the nonlinear function and  $\varepsilon$  is the residual.

Since neural network has the capability of fitting nonlinearity, during the modeling of batch process, nonlinear multiway PLS method that internal model adopts neural network gains extensive application. As traditional feedforward neural network adopts gradient learning algorithm during training, parameters in network needs iteration and update. Not only does the training time last long but also it easily results in the issues of local minimum and excessive training [15].

**3.2. ELM Algorithm.** In supervised batch learning, the learning algorithms use a finite number of input-output samples for training [16, 17]. For  $N$  arbitrary distinct samples  $(x_i, t_i) \in R^n \times R^m$ , where  $x_i$  is a  $n \times 1$  input vector and  $t_i$  is a  $m \times 1$  target vector, if an SLFN (single-hidden layer feedforward neural network [18, 19]) with  $\tilde{N}$  hidden nodes can approximate these  $N$  samples with zero error, it then implies that there exists  $\beta_i$ ,  $a_i$ , and  $b_i$  such that

$$f_{\tilde{N}}(x_j) = \sum_{i=1}^{\tilde{N}} \beta_i G(a_i, b_i, x_j) + \varepsilon_j = t_j, \quad (5)$$

where  $j = 1, \dots, N$ ,  $a_i$  and  $b_i$  are the learning parameters of hidden nodes (weight vector connecting the input node to the hidden node and threshold of the hidden node) which are randomly selected according to the proof given by Huang et al. and  $\beta_i$  is the weight connecting the  $i$ th hidden node to the output node. To avoid overfitting the noise in the data, an error term  $\varepsilon_j$  is added.  $G(a_i, b_i, x)$  is the output of the  $i$ th hidden node with respect to the input  $x$  and  $\tilde{N}$  is the number of hidden nodes which can be determined by trial and error or prior expertise. Then, the equation can be written compactly as

$$H\beta = T, \quad (6)$$

where

$$H(a_1, \dots, a_{\tilde{N}}, b_1, \dots, b_{\tilde{N}}, x_1, \dots, x_N) = \begin{bmatrix} G(a_1, b_1, x_1) & \cdots & G(a_{\tilde{N}}, b_{\tilde{N}}, x_1) \\ \vdots & \cdots & \vdots \\ G(a_1, b_1, x_N) & \cdots & G(a_{\tilde{N}}, b_{\tilde{N}}, x_N) \end{bmatrix}_{N \times \tilde{N}}, \quad (7)$$

$$\beta = \begin{bmatrix} \beta_1^T \\ \vdots \\ \beta_{\tilde{N}}^T \end{bmatrix}_{\tilde{N} \times m}, \quad T = \begin{bmatrix} t_1^T \\ \vdots \\ t_N^T \end{bmatrix}_{N \times m}, \quad (8)$$

where  $H$  is called the hidden layer output matrix of the network; the  $i$ th column of  $H$  is the  $i$ th hidden node's output vector with respect to inputs  $x_1, x_2, \dots, x_N$  and the  $j$ th row of  $H$  is the output vector of the hidden layer with respect to input  $x_j$ . The hidden node parameters  $a_i$  and  $b_i$  need not be tuned during training and may simply be assigned with random values. Equation (6) then becomes a linear system and the output weights  $\beta$  are estimated as

$$\tilde{\beta} = H^+ T, \quad (9)$$

where  $H^+$  is the Moore-Penrose generalized inverse of the hidden layer output matrix  $H$  [20].

**3.3. OS-ELM Algorithm.** In real applications, the training data may arrive chunk-by-chunk or one-by-one; hence, the batch ELM algorithm has to be modified for this case so as to make it online sequential [21, 22].

The output weight matrix  $\tilde{\beta}(\tilde{\beta} = H^+ T)$  given in (9) is a least-squares solution of (7). Here we consider the case where  $\text{rank}(H) = \tilde{N}$  is the number of hidden nodes. Under this condition,  $H^+$  of (9) is given by

$$H^+ = (H^T H)^{-1} H^T. \quad (10)$$

If  $H^T H$  tend to become singular, one can make it nonsingular by choosing smaller network size  $\tilde{N}$  or increasing data number  $N$  in the initialization phase of OS-ELM. Substituting (10) to (9),  $\tilde{\beta}$  becomes

$$\tilde{\beta} = (H^T H)^{-1} H^T T. \quad (11)$$

Equation (11) is called the least-squares solution to  $H\beta = T$ . Sequential implementation of least-squares solution of (11) results in the OS-ELM.

Given a chunk of initial training set  $\aleph_0 = \{(x_i, t_i)\}_{i=1}^{N_0}$  and  $N_0 \geq \tilde{N}$ , if one considers using the batch ELM algorithm, one need to consider the solution of minimizing  $\|H_0 \beta - T\|$ , which is given by  $\beta_0 = K_0^{-1} H_0^T T_0$ , where  $K_0 = H_0^T H_0$ .

Suppose that we have another chunk of data  $\aleph_1 = \{(x_i, t_i)\}_{i=N_0+1}^{N_0+N_1}$ , where  $N_1$  is the number of samples in this chunk. The problem becomes minimizing

$$\left\| \begin{bmatrix} H_0 \\ H_1 \end{bmatrix} \beta - \begin{bmatrix} T_0 \\ T_1 \end{bmatrix} \right\|. \quad (12)$$

Considering both  $\aleph_0$  and  $\aleph_1$ , the output weight  $\beta$  becomes

$$\beta_1 = K_1^{-1} \begin{bmatrix} H_0 \\ H_1 \end{bmatrix}^T \begin{bmatrix} T_0 \\ T_1 \end{bmatrix}, \quad \text{where } K_1 = \begin{bmatrix} H_0 \\ H_1 \end{bmatrix}^T \begin{bmatrix} H_0 \\ H_1 \end{bmatrix}. \quad (13)$$

For sequential learning, we have to express  $\beta_1$  as a function of  $\beta_0$ ,  $K_1$ ,  $H_1$ , and  $T_1$  and not a function of the data set  $\aleph_0$ . Now  $K_1$  can be written as

$$K_1 = \begin{bmatrix} H_0^T & H_1^T \end{bmatrix} \begin{bmatrix} H_0 \\ H_1 \end{bmatrix} = K_0 + H_1^T H_1, \quad (14)$$

$$\begin{aligned} \begin{bmatrix} H_0 \\ H_1 \end{bmatrix}^T \begin{bmatrix} T_0 \\ T_1 \end{bmatrix} &= H_0^T T_0 + H_1^T T_1 = K_0 K_0^{-1} H_0^T T_0 + H_1^T T_1 \\ &= K_0 \beta_0 + H_1^T T_1 = (K_1 - H_1^T H_1) \beta_0 + H_1^T T_1 \\ &= K_1 \beta_0 - H_1^T H_1 \beta_0 + H_1^T T_1. \end{aligned} \quad (15)$$

Combining (13) and (15),  $\beta_1$  is given by

$$\begin{aligned}\beta_1 &= K_1^{-1} \begin{bmatrix} H_0 \\ H_1 \end{bmatrix}^T \begin{bmatrix} T_0 \\ T_1 \end{bmatrix} = K_1^{-1} (K_1 \beta_0 - H_1^T H_1 \beta_0 + H_1^T T_1) \\ &= \beta_0 + K_1^{-1} H_1^T (T_1 - H_1 \beta_0),\end{aligned}\quad (16)$$

where  $K_1 = K_0 + H_1^T H_1$ .

When  $(k+1)$ th chunk of data set

$$\mathfrak{N}_{k+1} = \{(x_i, t_i)\}_{i=(\sum_{j=0}^k N_j)+1}^{\sum_{j=0}^{k+1} N_j} \quad (17)$$

is received, where  $k \geq 0$  and  $N_{k+1}$  denotes the number of samples in  $(k+1)$ th chunk, we have

$$\begin{aligned}K_{k+1} &= K_k + H_{k+1}^T H_{k+1}, \\ \beta_{k+1} &= \beta_k + K_{k+1}^{-1} H_{k+1}^T (T_{k+1} - H_{k+1} \beta_k).\end{aligned}\quad (18)$$

$K_{k+1}^{-1}$  rather than  $K_{k+1}$  is used to compute  $\beta_{k+1}$  from  $\beta_k$  in (18). The update formula for  $K_{k+1}^{-1}$  is derived using the Woodbury formula:

$$\begin{aligned}K_{k+1}^{-1} &= (K_k + H_{k+1}^T H_{k+1})^{-1} \\ &= K_k^{-1} - K_k^{-1} H_{k+1}^T (I + H_{k+1} K_k^{-1} H_{k+1}^T)^{-1} \times H_{k+1} K_k^{-1}.\end{aligned}\quad (19)$$

Let  $P_{k+1} = K_{k+1}^{-1}$ , then the equation for updating  $\beta_{k+1}$  can be written as

$$\begin{aligned}P_{k+1} &= P_k - P_k H_{k+1}^T (I + H_{k+1} P_k H_{k+1}^T)^{-1} H_{k+1} P_k, \\ \beta_{k+1} &= \beta_k + P_{k+1} H_{k+1}^T (T_{k+1} - H_{k+1} \beta_k).\end{aligned}\quad (20)$$

Equation (20) gives the recursive formula for  $\beta_{k+1}$ .

**3.4. Ensemble of OS-ELM Algorithm.** EOS-ELM consists of many OS-ELM networks with the same number of hidden nodes and the same activation function for each hidden node [23]. It has constructed  $P$  OS-ELM networks to form our EOS-ELM. All  $P$  OS-ELMs are trained with new data in each incremental step. The input parameters for each OS-ELM network are randomly generated and the output weights are obtained analytically based on the sequential arrived input data. Then we compute the average of the outputs of each OS-ELM network, which is the final output of the EOS-ELM.

Assume the output of each OS-ELM network is  $g^j(x_i)$ ,  $j = 1, 2, \dots, P$ . Hence, we have

$$g(x_i) = \frac{1}{P} \sum_{j=1}^P g^j(x_i). \quad (21)$$

**3.5. EOS-ELM-RPLS Modeling Steps.** The difference of nonlinear RPLS modeling method based on OS-ELM from linear PLS method is that it uses ELM to establish internal nonlinear model and in the meantime and achieve the update of internal and external models. This method reserves linear external model, extracts through PLS the attributive information of process, eliminates the colinearity of data, reduces the dimension of input variable, then adopts ELM to establish nonlinear internal model between input score vector matrix and output score vector, and raises the nonlinear processing capability of internal model. Thus, EOS-ELM-RPLS method has the advantages of PLS and ELM, that is, the characteristics of robustness and feature extraction of PLS method and quick nonlinear processing capability of ELM as well as the precision accuracy through model real-time update.

The modeling and testing steps of nonlinear RPLS method based on EOS-ELM are as follows.

- (1) Assign two standardized data matrices,  $X \in R^{n \times m}$  and  $Y \in R^{n \times p}$ ; dynamic nonlinear PLS regression model can be expressed as follows:

$$\mathbf{X} = [\mathbf{x}_1, \mathbf{x}_2, \dots, \mathbf{x}_p]. \quad (22)$$

- (2) Deploy the batch data of batch process, use cross-validation method to determine the number of latent variable, adopt linear PLS method to calculate the score vector matrices  $T$  and  $U$ , and load vector matrices  $P$  and  $Q$  for modeling sample  $X$  and  $Y$ :

$$X = TP^T + E = \sum_{a=1}^A t_a P_a^T + E, \quad (23)$$

$$Y = UQ^T + F = \sum_{a=1}^A u_a Q_a^T + F.$$

- (3) Assign the node number of ELM hidden layer and activation function (e.g., sigmoid function), use ELM to establish nonlinear model between internal model  $T$  and  $U$ , and gain  $U = f_{\text{ELM}}(T)$ , where  $f_{\text{ELM}}(\cdot)$  is the nonlinear function indicated by EOS-ELM.
- (4) When new batch data  $X_1, Y_1$  are obtained, we perform PLS decompose firstly, and obtain score vector and load vector  $T_1, U_1, P_1, Q_1$ :

$$\begin{aligned}X_1 &= T_1 P_1^T + E, \\ Y_1 &= U_1 Q_1^T + F.\end{aligned}\quad (24)$$

According to formula (19), EOS-ELM algorithm is adopted to update output layer weight value and achieve the update of internal model; in the meantime, conduct weighted mean on load matrix of external model and achieve external RPLS update, where  $w$  is the weight value factor. Repeat above steps; conduct model update on every batch:

$$\begin{aligned}P^T &= w P^T + (1-w) P_1^T, \\ Q^T &= w Q^T + (1-w) Q_1^T.\end{aligned}\quad (25)$$

TABLE 1: Size table of reducing tube.

Ser. number	External diameter of shell	Wall thickness of shell	External diameter of finished pipe	Wall thickness of finished pipe	Number of variable stands	Number of total stands
1	152.5	4.25	42.2	3.56	18	24
2	152.5	10.25	70	10.25	12	18
3	152.5	7.75	139.7	7.72	12	16
4	152.5	6	73.03	5.51	12	12
5	152.5	9.75	114.3	10	10	16
6	152.5	25	121	25	10	12
7	152.5	6	139.7	6.2	10	10

TABLE 2: Variable table for modeling of reducing tube quality.

Ser. number	Variable name	Variable meaning
1	$x_1, x_2, x_3$	Motor speed, current, and torque of Number 1 reducing mill
2	$x_4, x_5, x_6$	Motor speed, current, and torque of Number 2 reducing mill
3	$x_7, x_8, x_9$	Motor speed, current, and torque of Number 3 reducing mill
4	$x_{10}, x_{11}, x_{12}$	Motor speed, current, and torque of Number 4 reducing mill
5	$x_{13}, x_{14}, x_{15}$	Motor speed, current, and torque of Number 5 reducing mill
6	$x_{16}, x_{17}, x_{18}$	Motor speed, current, and torque of Number 6 reducing mill
7	$x_{19}, x_{20}, x_{21}$	Motor speed, current, and torque of Number 7 reducing mill
8	$x_{22}, x_{23}, x_{24}$	Motor speed, current, and torque of Number 8 reducing mill
9	$x_{25}, x_{26}, x_{27}$	Motor speed, current, and torque of Number 9 reducing mill
10	$x_{28}, x_{29}, x_{30}$	Motor speed, current, and torque of Number 10 reducing mill
11	$x_{31}, x_{32}, x_{33}$	Motor speed, current, and torque of Number 11 reducing mill
12	$x_{34}, x_{35}, x_{36}$	Motor speed, current, and torque of Number 12 reducing mill
13	$x_{37}$	The temperature of shell
14	$x_{38}$	The transverse wall thickness of shell
15	$x_{39}$	The longitudinal wall thickness of shell

- (5) Use testing data to check model precision. Conduct PLS decomposition on the testing data  $X_2$ , gain score vector  $T_2$ ,

$$X_2 = T_2 P^T + E. \quad (26)$$

Introduce  $T_2$  into EOS-ELM model, gain  $U_2 = f_{\text{EOS-ELM}}(T_2)$ , find out model prediction value through  $\hat{Y} = UQ^T$ .

#### 4. Modeling and Control of Reducing Pipe Quality

*4.1. Establishment of Quality Prediction Model of Reducing Pipe.* As there are many specifications of reducing pipe products, one cannot predict accurately the quality of steel pipe using single model. One must classify data in accordance with the specifications of products. As shown in Table 1, production data were classified into seven categories and seven quality prediction models of reducing pipe were established.

Taking the specification of steel pipe in series Number 4 with the maximum output as an example, detailed information of various input variables using this model is shown in Table 2.

Prior to establishing quality prediction model of reducing pipe, one must preprocess modeling data and conduct batch treatment, time interval division, mean value treatment, and two-dimensional spread on the modeling data. On the basis of obtaining three-dimensional data, one must process the process data into subsections according to different time intervals of production operation. In this work, according to the variation of roll current, one firstly classified the production process of reducing pipe into bite subtime interval, stable rolling subtime interval, and steel leaving subtime interval. Then according to the sequence of roll addition, bite and steel leaving stages were divided in detail. Bite stage was divided into eleven subtime intervals and in the same way, steel leaving stage was divided into eleven subtime intervals. After process variables in various time intervals required by modeling were determined, one took the mean value of each process variable in this time interval. Practical data treatment is shown in Figure 2.

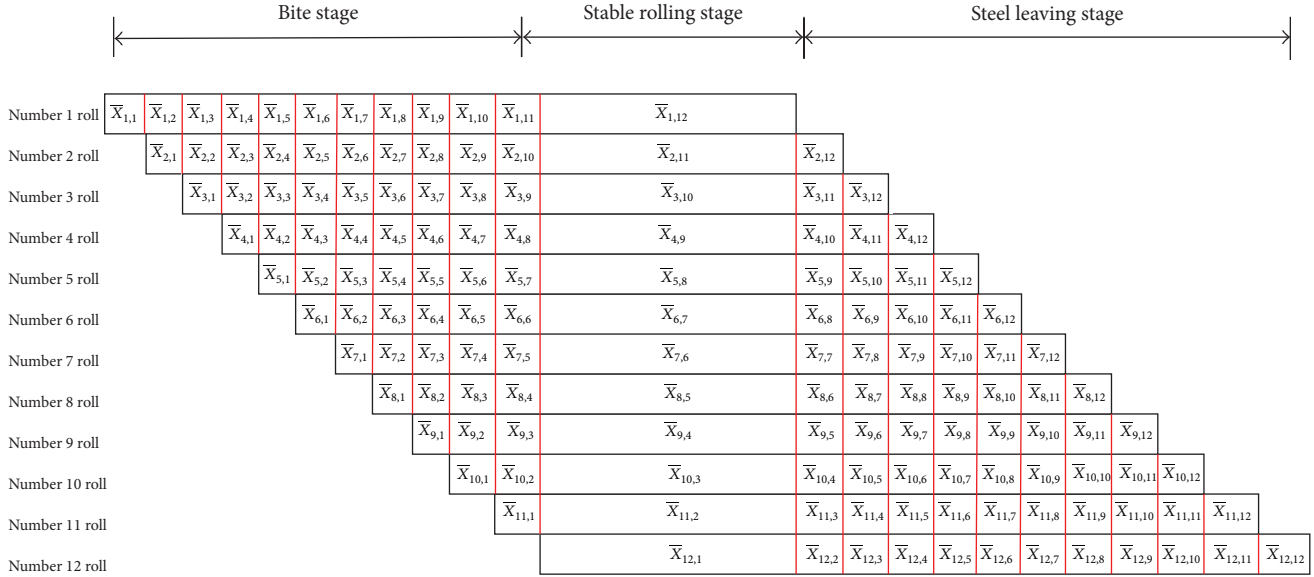


FIGURE 2: The relation between time and variables of reducing tube.

Adding shell heating temperature  $X_T$ , quality precision variable  $X_{\text{transverse}}$  and  $X_{\text{longitudinal}}$ , one got final input matrix

$$\begin{bmatrix} \bar{X}_{10,11}, \bar{X}_{11,10}, \bar{X}_{12,9}, \bar{X}_{10,12}, \bar{X}_{11,11}, \bar{X}_{12,10}, \bar{X}_{11,12}, \\ \bar{X}_{12,11}, \bar{X}_{12,12} \end{bmatrix}.$$

(27)

$$X = [X_T, X_{\text{transverse}}, X_{\text{longitudinal}}, \bar{X}_{1,1}, \bar{X}_{1,2}, \bar{X}_{2,1}, \bar{X}_{1,3}, \bar{X}_{2,2}, \bar{X}_{3,1}, \bar{X}_{1,4}, \bar{X}_{2,3}, \bar{X}_{3,2}, \bar{X}_{4,1}, \bar{X}_{1,5}, \bar{X}_{2,4}, \bar{X}_{3,3}, \bar{X}_{4,2}, \bar{X}_{5,1}, \bar{X}_{1,6}, \bar{X}_{2,5}, \bar{X}_{3,4}, \bar{X}_{4,3}, \bar{X}_{5,2}, \bar{X}_{6,1}, \bar{X}_{1,7}, \bar{X}_{2,6}, \bar{X}_{3,5}, \bar{X}_{4,4}, \bar{X}_{5,3}, \bar{X}_{6,2}, \bar{X}_{7,1}, \bar{X}_{1,8}, \bar{X}_{2,7}, \bar{X}_{3,6}, \bar{X}_{4,5}, \bar{X}_{5,4}, \bar{X}_{6,3}, \bar{X}_{7,2}, \bar{X}_{8,1}, \bar{X}_{1,9}, \bar{X}_{2,8}, \bar{X}_{3,7}, \bar{X}_{4,6}, \bar{X}_{5,5}, \bar{X}_{6,4}, \bar{X}_{7,3}, \bar{X}_{8,2}, \bar{X}_{9,1}, \bar{X}_{1,10}, \bar{X}_{2,9}, \bar{X}_{3,8}, \bar{X}_{4,7}, \bar{X}_{5,6}, \bar{X}_{6,5}, \bar{X}_{7,4}, \bar{X}_{8,3}, \bar{X}_{9,2}, \bar{X}_{10,1}, \bar{X}_{1,11}, \bar{X}_{2,10}, \bar{X}_{3,9}, \bar{X}_{4,8}, \bar{X}_{5,7}, \bar{X}_{6,6}, \bar{X}_{7,5}, \bar{X}_{8,4}, \bar{X}_{9,3}, \bar{X}_{10,2}, \bar{X}_{11,1}, \bar{X}_{2,12}, \bar{X}_{3,11}, \bar{X}_{4,10}, \bar{X}_{5,9}, \bar{X}_{6,8}, \bar{X}_{7,7}, \bar{X}_{8,6}, \bar{X}_{9,5}, \bar{X}_{10,4}, \bar{X}_{11,3}, \bar{X}_{12,2}, \bar{X}_{3,12}, \bar{X}_{4,11}, \bar{X}_{5,10}, \bar{X}_{6,9}, \bar{X}_{7,8}, \bar{X}_{8,7}, \bar{X}_{9,6}, \bar{X}_{10,5}, \bar{X}_{11,4}, \bar{X}_{12,3}, \bar{X}_{4,12}, \bar{X}_{5,11}, \bar{X}_{6,10}, \bar{X}_{7,9}, \bar{X}_{8,8}, \bar{X}_{9,7}, \bar{X}_{10,6}, \bar{X}_{11,5}, \bar{X}_{12,4}, \bar{X}_{5,12}, \bar{X}_{6,11}, \bar{X}_{7,10}, \bar{X}_{8,9}, \bar{X}_{9,8}, \bar{X}_{10,7}, \bar{X}_{11,6}, \bar{X}_{12,5}, \bar{X}_{6,12}, \bar{X}_{7,11}, \bar{X}_{8,10}, \bar{X}_{9,9}, \bar{X}_{10,8}, \bar{X}_{11,7}, \bar{X}_{12,6}, \bar{X}_{7,12}, \bar{X}_{8,11}, \bar{X}_{9,10}, \bar{X}_{10,9}, \bar{X}_{11,8}, \bar{X}_{12,7}, \bar{X}_{8,12}, \bar{X}_{9,11}, \bar{X}_{10,10}, \bar{X}_{11,9}, \bar{X}_{12,8}, \bar{X}_{9,12},$$

Mean values of aforementioned three stage data were arranged from left to right and a data vector  $\mathbf{X}(I \times 147)$  consisting of 147 mean values was obtained. The production data of 70 pieces of reducing pipes produced by reducing mill train in Baogang Iron and Steel Group in October 2012 were obtained. Shell diameter was 152.5 mm and its wall thickness was 6 mm. The reduced diameter was 73.03 mm and the wall thickness was 5.51 mm. There are total 12 stands. The data were classified into two groups: former 45 pieces were used for establishing quality prediction model, and latter 25 pieces were used for testing the model and checking the estimation precision of reducing pipe quality. The production data of 45 pieces of reducing pipes were spread and a two-dimensional data matrix  $X(45, 30062)$  was obtained where data gathering cycle was 20 ms, gathering time at bite stage was 2.5 s, gathering time at stable rolling stage was 13 s, and gathering time at steel leaving stage was 1.2 s. Aiming at above data and treating them as shown in Figure 2, one got data matrix  $X(45, 147)$ . Quality prediction model was established using EOS-ELM-RPLS algorithm as Figure 3. In the same way, the production data  $X_{\text{new}}(25, 147)$  of 25 pieces of reducing pipes were gathered and quality prediction inspection was performed. In order to compare with the quality prediction model during conventional intermittent process, for the production data of 45 pieces of reducing pipes modeled previously, 39 variables such as motor rotary speeds, currents and torques, heating temperature of shell, and quality precision error of shell for 1st to 12th reducing mills were chosen to act as input variables. Data gathering cycle was 20 ms and gathering time was 16.7 s. The quality prediction model was established for data matrix

$X(45, 30062)$  using conventional multiway PLS algorithm during simulation modeling.

Similarly, one reorganized the production data of 25 pieces of reducing pipes to form test data matrix  $Xn(25, 30062)$  and perform quality prediction inspection. Figures 4 and 5 show the results of test data prediction for two prediction models.

It is seen in Figures 4 and 5 that within the prediction results of transverse and longitudinal wall thickness in various stages, the prediction precisions of transverse and longitudinal wall thickness based on EOS-ELM-RPLS algorithm were 94.2% and 93.7%, and the prediction precisions based on conventional multiway PLS algorithm were 90.8% and 90.3%. This shows that EOS-ELM-RPLS algorithm model possesses higher prediction precision than multiway PLS algorithm model. Based on the quality model using EOS-ELM-RPLS algorithm, using iteration learning control method to modify continuously the variable traces, counteract the influence of model error and unknown undulation; one make the quality of reducing pipe continuously tend to attain ideal indexes.

**4.2. Quality Iteration Control of Reducing Pipe Based on Model.** After quality model was obtained by calculation, iteration learning control method based on mathematical model was applied to improve the product quality of reducing pipe. Due to the model-plant mismatch and unknown disturbances from batch to batch, the final quality does not always meet the desired product quality in real industry. Batch-to-batch iterative learning control can be used to solve this problem by using the information of previous batch and current batch to revise the next batch input trajectory. The following model is used to express the input-output relationship:

$$Y = f(R), \quad (28)$$

where  $Y$  represents the product quality variables and  $R = [r_1, r_2, \dots, r_N]^T$  is a vector of input variables. The nonlinear function  $f(\cdot)$  is expressed by the online sequential EOS-ELM-RPLS. The first order Taylor series expansion of (28) can be given by

$$\hat{y} = f_0 + \frac{\partial f}{\partial r_1} \Delta r_1 + \frac{\partial f}{\partial r_2} \Delta r_2 + \dots + \frac{\partial f}{\partial r_n} \Delta r_n. \quad (29)$$

For the  $k$ th batch, the actual product quality can be written as the sum of the model prediction and its error

$$y_k = \hat{y}_k + \varepsilon_k. \quad (30)$$

The prediction of the  $(k+1)$ th batch can be approximated and expressed as follows:

$$\begin{aligned} \hat{y}_{k+1} &= \hat{y}_k + \frac{\partial f}{\partial r_1} (r_1^{k+1} - r_1^k) + \dots + \frac{\partial f}{\partial r_N} (r_N^{k+1} - r_N^k) \\ &= \hat{y}_k + \left[ \frac{\partial f}{\partial r_1}, \frac{\partial f}{\partial r_2}, \dots, \frac{\partial f}{\partial r_N} \right] \end{aligned}$$

$$\begin{aligned} &\times [(r_1^{k+1} - r_1^k), (r_2^{k+1} - r_2^k), \dots, (r_N^{k+1} - r_N^k)]^T \\ &= \hat{y}_k + G \Delta R_{k+1}, \end{aligned} \quad (31)$$

$$\begin{aligned} \Delta R_{k+1} &= [(r_1^{k+1} - r_1^k), (r_2^{k+1} - r_2^k), \dots, (r_N^{k+1} - r_N^k)]^T \\ &= [\Delta r_1^{k+1}, \Delta r_2^{k+1}, \dots, \Delta r_N^{k+1}]^T G \\ &= \frac{\partial y_i}{\partial r_j} = \left[ \frac{\partial f}{\partial r_1}, \frac{\partial f}{\partial r_2}, \dots, \frac{\partial f}{\partial r_N} \right] = Q \sum_{l=1}^{\tilde{N}} \frac{\partial y_i}{\partial H_l} \frac{\partial H_l}{\partial r_j} P^T \\ &= Q \sum_{k=1}^{\tilde{N}} \beta_k^{l,i} H_k (1 - H_k) \alpha^{j,l} P^T, \end{aligned} \quad (32)$$

where  $G$  is the gradient of model output with respect to the input of the EOS-ELM-RPLS.  $\alpha_k^{j,k}$  is input layer weight from the  $j$ th input to the  $l$ th hidden node,  $\beta^{k,i}$  is the output layer weight from the  $l$ th hidden node to the  $i$ th output layer node,  $H_k$  is output of the  $l$ th hidden node, and  $\tilde{N}$  is the number of the hidden nodes. The subscript  $k$  represents the  $k$ th batch.

Let  $e$  and  $\hat{e}$ , respectively, express the actual error and the predicting error corresponding to the desired target. Thus, for the  $k$ th batch, the following can be obtained:

$$\hat{e}_k = y_d - \hat{y}_k, \quad (33)$$

$$e_k = y_d - y_k = y_d - \hat{y}_k - \varepsilon_k.$$

The same as above, the errors for the  $(k+1)$ th batch are given by

$$\hat{e}_{k+1} = y_d - \hat{y}_{k+1}, \quad (34)$$

$$e_{k+1} = y_d - y_{k+1} = y_d - \hat{y}_{k+1} - \varepsilon_{k+1}.$$

Assume that the model prediction errors for the  $k$ th batch and the  $(k+1)$ th batch are the same. Combining (33) and (34), it gives

$$e_{k+1} = e_k - G^T \Delta R_{k+1}. \quad (35)$$

The objective of the ILC is to control the input trajectory in order to make the final product quality achieve the desired target. By solving the following optimal quadratic objective function (36), one can get the revised input trajectory for the  $(k+1)$ th batch:

$$\begin{aligned} \min_{\Delta U_{k+1}} J &= \|e_{k+1}\|_{Z_1}^2 + \|\Delta R_{k+1}\|_{Z_2}^2 \\ &= e_{k+1}^T Z_1 e_{k+1} + \Delta R_{k+1}^T Z_2 \Delta R_{k+1}, \end{aligned} \quad (36)$$

where  $Z_1$  and  $Z_2$  are positive definite weight matrices. Set  $(\partial J / \partial \Delta R_{k+1}) = 0$ ; the partial derivative of the quadratic objective function with respect to the input change  $\Delta R_{k+1}$  can be obtained:

$$\begin{aligned} \Delta R_{k+1} &= (G Z_1 G^T + Z_2)^{-1} G Z_1 e_k, \\ R_{k+1} &= R_k + \Delta R_{k+1}. \end{aligned} \quad (37)$$

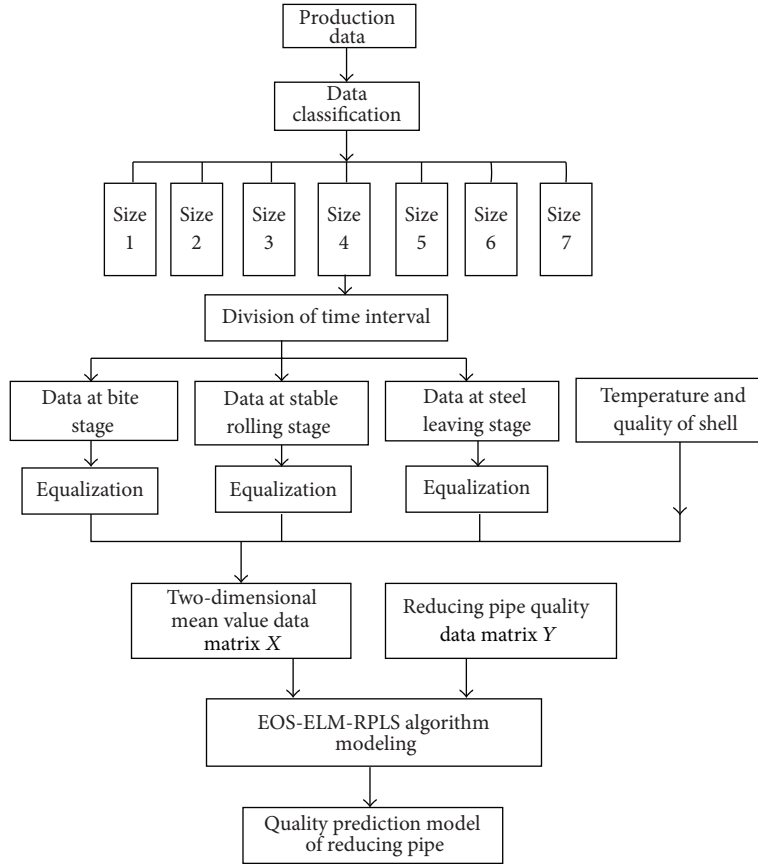


FIGURE 3: Frame chart of reducing tube quality prediction model.

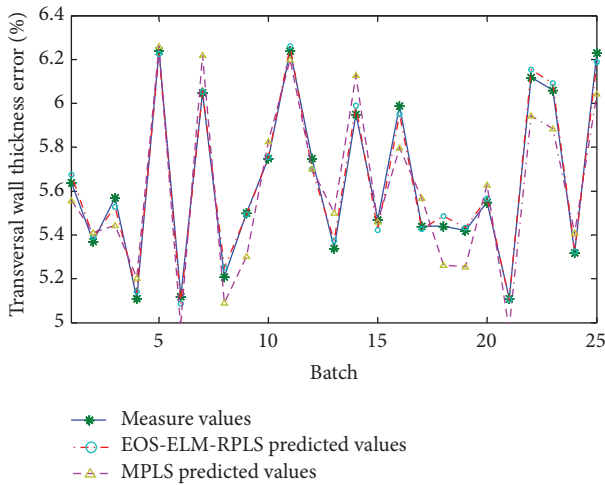


FIGURE 4: Prediction result of transverse wall thickness.

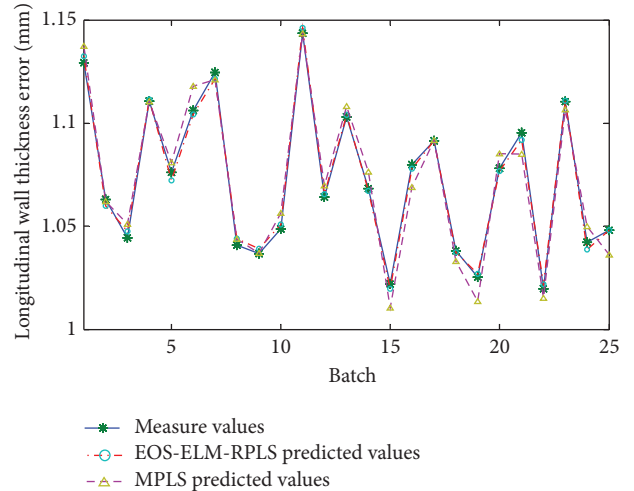


FIGURE 5: Prediction result of longitudinal wall thickness.

It is to be noted that the change of control trajectory  $\Delta R_{k+1}$  is directly updated by the actual tracking error of the process. In many chemical batch processes, however, the actual final quality is impossible to obtain immediately. Thus, the model prediction value could be an alternative. Thus, the tracking performance will depend on the accuracy of the model. The

convergence of the ILC can directly be derived from the convergence theorems in the literature [24]. It is shown that  $e_k$  will converge as  $k \rightarrow \infty$  if

$$\|I - GK\| < 1, \quad (38)$$

where  $K = (GZ_1G^T + Z_2)^{-1}GZ_1$ .

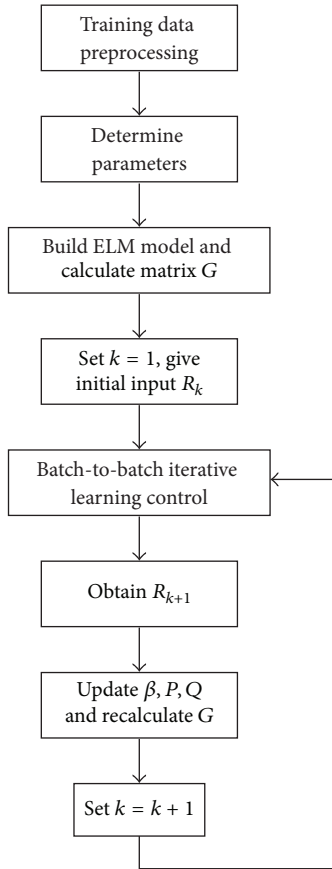


FIGURE 6: Scheme of ILC based on OSELM-RPLS.

The batch-to-batch iterative learning control scheme of the EOS-ELM-RPLS based method is illustrated in Figure 6.  $Q$  and  $P$  are the load matrix of PLS decomposition.

Table 3 shows the calculation results of quality iteration learning of reducing pipe. Figures 7 and 8 show the effect of iteration control. The results showed that the quality error of reducing pipe decreased by about 12% compared with initial error after rolling proceeded to 5 pieces of reducing pipes.

## 5. Conclusions

The production process of reducing pipe continuous rolling has the characteristics of typical multi-time-intervals and dynamic multi-variables. In the meantime, there are many specifications of products, and minor variation of model will occur due to the adjustment of stand for same specification of product; in the meantime, the production of wall reduction and diameter reduction possesses the characteristics of typical multi-time-intervals and dynamic multivariables. The production process was classified into three big time intervals such as bite stage, stable rolling stage, and steel leaving stage influenced by different variables, and according to the sequence that roll touches steel, the production process was further classified into 23 sub-time-intervals; we proposed the reducing production process model based on EOS-ELM-RPLS algorithm. This algorithm overcame the shortcomings

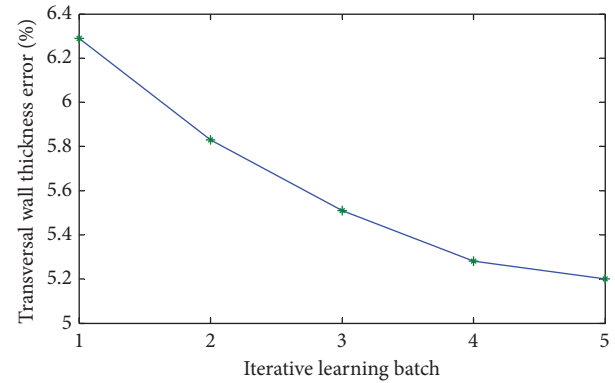


FIGURE 7: Iterative learning control effect of transverse wall thickness.

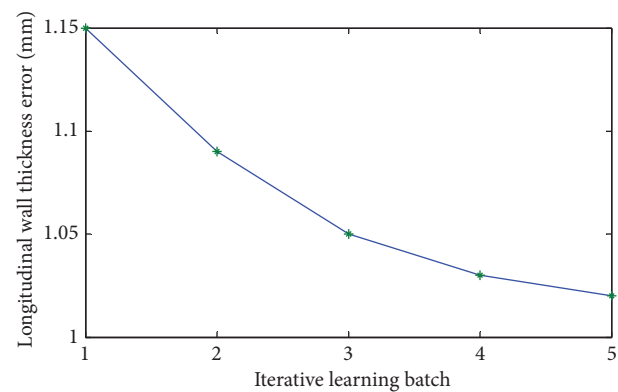


FIGURE 8: Iterative learning control effect of longitudinal wall thickness.

that quality modeling algorithm has complex structure, big calculation load, and bad capability in processing nonlinear problem during conventional intermittent process. Based on the quality prediction model of reducing pipe, we applied iteration learning control technique to the control system of wall thickness deviation and improved the production quality of reducing pipe. Field data simulation and the test results of reducing production in Baogang Iron and Steel Group Steel Pipe Subcompany revealed the validity of this method.

## Conflict of Interests

The authors declare that there is no conflict of interests regarding the publication of this paper.

## Acknowledgment

This research is supported by National Natural Science Foundation of China (Grant no. 61203214), Provincial Science and Technology Department of Education Projects, the General Project (L2013101), National Natural Science Foundation of China (Grant nos. 61203103, 61374146, and 61374147). The study is sponsored by National Natural Science Foundation of China (61203214).

TABLE 3: Iterative learning calculating result of wall thickness of reducing tube.

Ser. number	Variable name	Initial value	First learning value	Second learning value	Third learning value	Fourth learning value
1	Rotary speed of Number 1 reducing mill	1137.52	1136.51	1134.25	1133.15	1132.53
2	Rotary speed of Number 2 reducing mill	1133.82	1132.65	1131.58	1130.52	1130.22
3	Rotary speed of Number 3 reducing mill	1288.24	1288.93	1289.36	1290.05	1290.22
4	Rotary speed of Number 4 reducing mill	1409.32	1408.31	1407.15	1406.53	1406.17
5	Rotary speed of Number 5 reducing mill	1485.26	1483.84	1482.37	1480.98	1480.68
6	Rotary speed of Number 6 reducing mill	1458.81	1459.84	1460.37	1460.64	1460.87
7	Rotary speed of Number 7 reducing mill	1179.95	1178.68	1177.55	1177.09	1176.95
8	Rotary speed of Number 8 reducing mill	1110.95	1109.72	1108.66	1107.85	1107.62
9	Rotary speed of Number 9 reducing mill	1290.43	1291.42	1292.37	1293.21	1293.38
10	Rotary speed of Number 10 reducing mill	1220.67	1219.55	1218.76	1217.84	1217.52
11	Rotary speed of Number 11 reducing mill	1143.38	1141.75	1140.53	1139.61	1138.92
12	Rotary speed of Number 12 reducing mill	1103.21	1102.33	1101.36	1100.52	1100.22
13	Current of Number 1 reducing mill	35.46	34.75	34.24	33.97	33.91
14	Current of Number 2 reducing mill	52.48	51.62	51.28	51.07	50.98
15	Current of Number 3 reducing mill	41.54	42.37	42.97	43.31	43.42
16	Current of Number 4 reducing mill	134.52	133.75	133.24	133.94	133.87
17	Current of Number 5 reducing mill	218.21	217.47	216.84	216.37	216.28
18	Current of Number 6 reducing mill	332.46	333.23	333.86	334.32	334.44
19	Current of Number 7 reducing mill	324.46	323.71	323.14	322.71	322.62
20	Current of Number 8 reducing mill	302.35	301.43	300.85	300.18	300.02
21	Current of Number 9 reducing mill	326.87	327.95	328.56	328.83	328.92
22	Current of Number 10 reducing mill	324.37	323.65	323.15	322.97	322.88
23	Current of Number 11 reducing mill	325.84	324.77	324.24	323.95	323.86
24	Current of Number 12 reducing mill	274.94	274.04	273.65	273.13	273.04
25	Torque of Number 1 reducing mill	251.64	252.31	252.88	253.23	253.32
26	Torque of Number 2 reducing mill	320.48	321.25	321.93	322.35	322.52
27	Torque of Number 3 reducing mill	62.44	63.12	63.34	63.52	63.57

TABLE 3: Continued.

Ser. number	Variable name	Initial value	First learning value	Second learning value	Third learning value	Fourth learning value
28	Torque of Number 4 reducing mill	445.85	446.87	447.66	448.02	448.21
29	Torque of Number 5 reducing mill	652.48	650.36	648.82	647.74	647.48
30	Torque of Number 6 reducing mill	1042.68	1040.24	1039.07	1038.21	1037.98
31	Torque of Number 7 reducing mill	1204.15	1203.26	1202.77	1202.35	1202.12
32	Torque of Number 8 reducing mill	1251.42	1250.15	1249.14	1248.48	1248.22
33	Torque of Number 9 reducing mill	1175.25	1176.37	1177.06	1177.84	1178.12
34	Torque of Number 10 reducing mill	1214.85	1213.45	1212.84	1212.25	1212.07
35	Torque of Number 11 reducing mill	1316.47	1317.57	1318.16	1318.54	1318.75
36	Torque of Number 12 reducing mill	1224.46	1223.24	1222.63	1222.22	1221.97
37	The temperature of shell	886	892	896	898	901

## References

- [1] D. Macrea and C. Cepisca, "Algorithms for speed and stretch control of the main drives of a stretch-reducing tube mill," *Revue Roumaine des Sciences Techniques, Serie Electrotechnique et Energetique*, vol. 53, no. 1, pp. 99–107, 2008.
- [2] L. S. Bayoumi, "Analysis of flow and stresses in a tube stretch-reducing hot rolling schedule," *International Journal of Mechanical Sciences*, vol. 45, no. 3, pp. 553–565, 2003.
- [3] F.-P. Zhang, B.-Y. Sun, and J.-M. Wang, "Energy method in stretch reducing process of steel tube," *Journal of Iron and Steel Research International*, vol. 15, no. 6, pp. 39–43, 2008.
- [4] H. Yu, F. Du, and F. Wang, "Finite element model development and application on stretch reducing process of seamless tube," *Journal of Mechanical Engineering*, vol. 47, no. 22, pp. 74–79, 2011.
- [5] H. Yu, F. S. Du, and F. X. Wang, "FE analysis of tube thickness variation in process of 14-stand slight stretch sizing (reducing) mill," *Steel Pipe*, vol. 35, no. 5, pp. 17–20, 2006 (Chinese).
- [6] W. S. Yi, R. Y. Hao, and H. Yu, "Finite-element analysis and experimental research of in-process gage variation of steel tube being slight-stretch reduced," *Steel Pipe*, vol. 30, no. 1, pp. 15–20, 2001 (Chinese).
- [7] Z. Q. Xu and F. S. Du, "A integrated simulation system of stretch reducing of tube and verification," *Journal of Yanshan University*, vol. 28, no. 1, pp. 36–39, 2004 (Chinese).
- [8] F. S. Du, Q. X. Huang, and C. Liu, "The computer predicting in the process of 3-roll reducing of seamless tube," *Iron and Steel*, vol. 30, no. 7, pp. 28–31, 1995 (Chinese).
- [9] Q. Yuan, L. H. Lv, and P. Liu, "Study of the math model of WT variation in 12-stand mini-stretch reducing mill," *Steel Pipe*, vol. 32, no. 6, pp. 5–8, 2003 (Chinese).
- [10] J. H. Shi, C. J. Zhao, and L. P. Bian, "FEA of oval pass of 21-stand stretch reducing mill," *Steel Pipe*, vol. 41, no. 4, pp. 18–22, 2012 (Chinese).
- [11] Y. Shuang, J. Fan, and M. Lai, "Prediction of accuracy of stretch reduction by artificial neural networks," *Iron and Steel*, vol. 35, no. 2, pp. 28–31, 2000 (Chinese).
- [12] B. M. Wang, *Hot Rolled Steel Tubes Quality*, Metallurgical Industry Press of China, Beijing, China, 1987 (Chinese).
- [13] S. Wold, N. Kettaneh-Wold, and B. Skagerberg, "Nonlinear PLS modeling," *Chemometrics and Intelligent Laboratory Systems*, vol. 7, no. 1-2, pp. 53–65, 1989.
- [14] S. J. Qin, "Recursive PLS algorithms for adaptive data modeling," *Computers & Chemical Engineering*, vol. 22, no. 4-5, pp. 503–514, 1998.
- [15] B. Hu, Z. Zhao, and J. Liang, "Multi-loop nonlinear internal model controller design under nonlinear dynamic PLS framework using ARX-neural network model," *Journal of Process Control*, vol. 22, no. 1, pp. 207–217, 2012.
- [16] G. Feng, Z. Qian, and N. Dai, "Reversible watermarking via extreme learning machine prediction," *Neurocomputing*, vol. 82, pp. 62–68, 2012.
- [17] Y. Yu, T.-M. Choi, and C.-L. Hui, "An intelligent quick prediction algorithm with applications in industrial control and loading problems," *IEEE Transactions on Automation Science and Engineering*, vol. 9, no. 2, pp. 276–287, 2012.
- [18] Y. M. Yang, Y. N. Wang, and X. F. Yuan, "Bidirectional extreme learning machine for regression problem and its learning effectiveness," *IEEE Transaction on Neural Network*, vol. 23, no. 9, pp. 1498–1505, 2012.
- [19] G.-B. Huang, H. Zhou, X. Ding, and R. Zhang, "Extreme learning machine for regression and multiclass classification," *IEEE Transactions on Systems, Man, and Cybernetics B: Cybernetics*, vol. 42, no. 2, pp. 513–529, 2012.
- [20] H.-X. Tian and Z.-Z. Mao, "An ensemble ELM based on modified AdaBoost.RT algorithm for predicting the temperature of molten steel in ladle furnace," *IEEE Transactions on Automation Science and Engineering*, vol. 7, no. 1, pp. 73–80, 2010.

- [21] S. J. Xie, J. Yang, H. Gong, S. Yoon, and D. S. Park, "Intelligent fingerprint quality analysis using online sequential extreme learning machine," *Soft Computing*, vol. 16, no. 9, pp. 1555–1568, 2012.
- [22] J. Zhao, Z. Wang, and D. S. Park, "Online sequential extreme learning machine with forgetting mechanism," *Neurocomputing*, vol. 87, pp. 79–89, 2012.
- [23] Y. Lan, Y. C. Soh, and G.-B. Huang, "Ensemble of online sequential extreme learning machine," *Neurocomputing*, vol. 72, no. 13–15, pp. 3391–3395, 2009.
- [24] J. H. Lee, K. S. Lee, and W. C. Kim, "Model-based iterative learning control with a quadratic criterion for time-varying linear systems," *Automatica*, vol. 36, no. 5, pp. 641–657, 2000.

## Research Article

# Airline Overbooking Problem with Uncertain No-Shows

Chunxiao Zhang,<sup>1,2</sup> Congrong Guo,<sup>2</sup> and Shenghui Yi<sup>2</sup>

<sup>1</sup> Tianjin Key Laboratory for Civil Aircraft Airworthiness and Maintenance, Civil Aviation University of China, Tianjin 300300, China

<sup>2</sup> College of Science, Civil Aviation University of China, Tianjin 300300, China

Correspondence should be addressed to Chunxiao Zhang; [cxzhang@cauc.edu.cn](mailto:cxzhang@cauc.edu.cn)

Received 5 December 2013; Accepted 14 February 2014; Published 16 March 2014

Academic Editor: Aderemi Oluyinka Adewumi

Copyright © 2014 Chunxiao Zhang et al. This is an open access article distributed under the Creative Commons Attribution License, which permits unrestricted use, distribution, and reproduction in any medium, provided the original work is properly cited.

This paper considers an airline overbooking problem of a new single-leg flight with discount fare. Due to the absence of historical data of no-shows for a new flight, and various uncertain human behaviors or unexpected events which causes that a few passengers cannot board their aircraft on time, we fail to obtain the probability distribution of no-shows. In this case, the airlines have to invite some domain experts to provide belief degree of no-shows to estimate its distribution. However, human beings often overestimate unlikely events, which makes the variance of belief degree much greater than that of the frequency. If we still regard the belief degree as a subjective probability, the derived results will exceed our expectations. In order to deal with this uncertainty, the number of no-shows of new flight is assumed to be an uncertain variable in this paper. Given the chance constraint of social reputation, an overbooking model with discount fares is developed to maximize the profit rate based on uncertain programming theory. Finally, the analytic expression of the optimal booking limit is obtained through a numerical example, and the results of sensitivity analysis indicate that the optimal booking limit is affected by flight capacity, discount, confidence level, and parameters of the uncertainty distribution significantly.

## 1. Introduction

Overbooking is a strategy that airlines accept the booking reservations of customers more than flight capacity in order to make up for the vacancy loss caused by no-shows who do not show up for check-in without canceling their booking requests before the flight takes off or are late for their scheduled flights. A lot of examples can reflect that overbooking strategy contributes to huge profits for airlines. Smith et al. [1] estimated that 15 percent of seats on sold-out flights would be lost if overbooking were not practiced and that the benefit of overbooking at America in 1990 exceeded \$225 million. Overbooking can reduce the waste of seats and maximize airlines' profits, but it also brings potential risk. When the number of arrival passengers exceeds flight capacity, it might cause that some arrival passengers cannot board flight (denied boarding); thus, airlines need to compensate this part of passengers (denied-boarding compensation), which lead to losses on both social reputation and profits of airlines.

Overbooking is one of the oldest problems and most effective revenue management practices and was officially sanctioned and published by the American Civil Aeronautics Board in 1965 [2]. In 1958, Beckmann [3] established a single period static model on overbooking, and a booking-limit policy, which instructed the manager to set a certain limit to accept reservations up to the limit, was proved to be optimal. Rothstein [4] formulated the problem as a nonhomogenous Markovian decision process and solved it by a dynamic programming method in 1971. Alstrup et al. [5] in 1986 as well proposed a dynamic programming formulation of a problem with two cabins, in which the terminal conditions allowed for upgrading and downgrading. Chatwin [6] in 1993 considered a multiperiod overbooking problem relating to a single-leg flight and a single fare class, gave conditions that ensure a booking-limit policy to be optimal, and described the continuous model with stationary fares and refunds as a birth and death process. Robert [7] in 2005, on the assumption that passengers' arriving obeyed the binomial distribution,

established a single-fare-class overbooking model and then extended to the conditions of multiple-fare classes and dynamic.

In the previous researches on overbooking problem, the arrival rate of customers is an important element and is usually assumed to be a random variable, and probability theory plays a great important character in the optimization of the overbooking strategy. We will consider an airline overbooking problem of a new single-leg flight with discount fare in this paper. Due to the absence of demand data for a new flight and various uncertain human behaviors or unexpected events which causes that a few passengers cannot board their aircraft on time, we have to invite some domain experts to provide belief degree to estimate the distribution of no-shows. However, human beings often overestimate unlikely events, which makes the variance of belief degree much greater than that of the frequency (Kahneman and Tversky [8]). In this case, if we regard the belief degree as a subjective probability, the derived results will exceed our expectations. In order to deal with the involved human uncertainty, uncertainty theory was founded by Liu [9] in 2007 and was refined by Liu [10] in 2010 based on normality, duality, subadditivity, and product axioms.

Nowadays, uncertainty theory has become a branch of axiomatic mathematics for modelling human uncertainty, and a lot of applications can be found in various fields such as uncertain programming [11], uncertain statistics [10], uncertain risk analysis [12], uncertain reliability analysis [12], uncertain logic [13], uncertain inference [14], uncertain process [15], uncertain calculus [15], and uncertain finance [16]. Based on the theory of uncertain renewal process, Yao and Ralescu [17] investigated the uncertain age replacement policy and obtained the long-run average replacement cost. Zhang and Guo [18] applied the uncertain renewal process to the ordering problem of spare parts for aircrafts assuming the interarrival times to be uncertainty variables. With uncertainty theory, Liu and Yao [19] presented an uncertain expected value model for multilevel programming with equivalent crisp form.

In this paper, we consider the airline overbooking problem of new flight in uncertain environment and assume the number of no-shows as an uncertain variable. The rest of this paper is organized as follows. Section 2 recalls some basic concepts and properties about uncertainty theory which will be used throughout the paper. In Section 3, we build the model of airline overbooking in uncertain environment and get some theorems. We apply our model to practical overbooking system, and sensitivity analysis is given in Section 4. Finally, conclusions are drawn in Section 5.

## 2. Preliminaries

Let  $\Gamma$  be a nonempty set. A collection  $\mathcal{L}$  of  $\Gamma$  is called a  $\sigma$ -algebra if (a)  $\Gamma \in \mathcal{L}$ ; (b) if  $\Lambda \in \mathcal{L}$ , then  $\Lambda_c \in \mathcal{L}$ ; and (c) if  $\Lambda_1, \Lambda_2, \dots \in \mathcal{L}$ , then  $\Lambda_1 \cup \Lambda_2 \cup \dots \in \mathcal{L}$ . Each element  $\Lambda$  in the  $\sigma$ -algebra  $\mathcal{L}$  is called an event. Uncertain measure is a function from  $\mathcal{L}$  to  $[0, 1]$ . In order to present an axiomatic definition of uncertain measure, it is necessary to

assign to each event  $\Lambda$  a number  $\mathcal{M}\{\Lambda\}$  which indicates the belief degree that the event  $\Lambda$  will occur. In order to ensure that the number  $\mathcal{M}\{\Lambda\}$  has certain mathematical properties, Liu [9] proposed the following axioms.

*Axiom 1* (normality axiom).  $\mathcal{M}\{\Gamma\} = 1$  for the universal set  $\Gamma$ .

*Axiom 2* (duality axiom).  $\mathcal{M}\{\Lambda\} + \mathcal{M}\{\Lambda^c\} = 1$  for any event  $\Lambda$ .

*Axiom 3* (subadditivity axiom). For every countable sequence of events  $\Lambda_1, \Lambda_2, \dots$ , we have

$$\mathcal{M}\left\{\bigcup_{i=1}^{\infty} \Lambda_i\right\} \leq \sum_{i=1}^{\infty} \mathcal{M}\{\Lambda_i\}. \quad (1)$$

*Definition 1* (Liu [9]). The set function  $\mathcal{M}$  is called an uncertain measure if it satisfies the normality, duality, and subadditivity axioms.

The triplet  $(\Gamma, \mathcal{L}, \mathcal{M})$  is called an *uncertainty space*. Besides, in order to provide the operational law, Liu [20] defined the product uncertain measure on the product  $\sigma$ -algebra  $\mathcal{L}$  as follows.

*Axiom 4* (product axiom). Let  $(\Gamma_k, \mathcal{L}_k, \mathcal{M}_k)$  be uncertainty spaces for  $k = 1, 2, \dots$ . Then the product uncertain measure  $\mathcal{M}$  is an uncertain measure satisfying

$$\mathcal{M}\left\{\prod_{i=1}^{\infty} \Lambda_k\right\} = \prod_{k=1}^{\infty} \mathcal{M}_k\{\Lambda_k\}, \quad (2)$$

where  $\Lambda_k$  are arbitrarily chosen events from  $\mathcal{L}_k$  for  $k = 1, 2, \dots$ , respectively.

*Definition 2* (Liu [9]). An uncertain variable is a measurable function  $\xi$  from an uncertainty space  $(\Gamma, \mathcal{L}, \mathcal{M})$  to the set of real numbers; that is, for any Borel set  $B$  of real numbers, the set

$$\{\xi \in B\} = \{\gamma \in \Gamma \mid \xi(\gamma) \in B\} \quad (3)$$

is an event.

*Definition 3* (Liu [9]). The uncertainty distribution  $\Phi$  of an uncertain variable  $\xi$  is defined by

$$\Phi(x) = \mathcal{M}\{\xi \leq x\}, \quad (4)$$

for any real number  $x$ .

*Definition 4* (Liu [10]). Let  $\xi$  be an uncertain variable with regular uncertainty distribution  $\Phi(x)$ . Then the inverse function  $\Phi^{-1}(\alpha)$  is called the inverse uncertainty distribution of  $\xi$ .

**Theorem 5** (Liu [9]). Let  $\xi$  be an uncertain variable with uncertainty distribution  $\Phi$ . If the expected value exists, then

$$E[\xi] = \int_0^{+\infty} (1 - \Phi(x)) dx - \int_{-\infty}^0 \Phi(x) dx. \quad (5)$$

Uncertain programming is a type of mathematical programming involving uncertain variables [9]. Assume that  $x$  is a decision vector,  $\xi$  is an uncertain vector, and  $f(x, \xi)$  is an uncertain objective function. Liu [11] proposed the following uncertain programming model:

$$\begin{aligned} \min_x \quad & E[f(x, \xi)] \\ \text{subject to: } \quad & \mathcal{M}\{g_j(x, \xi) \leq 0\} \geq \alpha_j, \quad j = 1, 2, \dots, p, \end{aligned} \tag{6}$$

where  $\mathcal{M}\{g_j(x, \xi) \leq 0\} \geq \alpha_j$  ( $j = 1, 2, \dots, p$ ) are a set of chance constraints. It is naturally desired that the uncertain constraints  $g_i(x, \xi) \leq 0$  ( $j = 1, 2, \dots, p$ ) hold with confidence levels  $\alpha_1, \alpha_2, \dots, \alpha_p$ .

**Theorem 6** (Liu [11]). *Assume that the constraint function  $g(x, \xi_1, \xi_2, \dots, \xi_n)$  is strictly increasing with respect to  $\xi_1, \xi_2, \dots, \xi_k$  and strictly decreasing with respect to  $\xi_{k+1}, \xi_{k+2}, \dots, \xi_n$ . If  $\xi_1, \xi_2, \dots, \xi_n$  are independent uncertain variables with uncertainty distributions  $\Phi_1, \Phi_2, \dots, \Phi_n$  respectively, then the chance constraint*

$$\mathcal{M}\{g(x, \xi_1, \xi_2, \dots, \xi_n) \leq 0\} \geq \alpha \tag{7}$$

holds if and only if

$$\begin{aligned} g(x, \Phi_1^{-1}(\alpha), \dots, \Phi_k^{-1}(\alpha), \Phi_{k+1}^{-1}(1-\alpha), \dots, \Phi_n^{-1}(1-\alpha)) \\ \leq 0. \end{aligned} \tag{8}$$

### 3. Mathematical Formulation

First of all, some notations are made as follows for the mathematical formulation:

- $m$ : Booking limit of a new flight
- $n$ : Capacity of an aircraft
- $\xi$ : The number of no-shows with uncertainty distribution  $\Phi$
- $g$ : Price of a new flight ticket
- $r$ : Total cost of a flight
- $p$ : Penalty cost which is paid to each crowded-out customer who is denied boarding because the number of arrival passengers exceeds flight capacity
- $\beta$ : A discount of fare,  $0 \leq \beta \leq 1$
- $s(m, \xi)$ : Profit rate function of the new flight when booking limit is  $m$  and the number of no-shows is  $\xi$
- $j$ : The maximum permissible number of crowded-out customers.

We suppose that an airline is planning to open up a new single-leg flight with discount fares and a booking limit should be decided to match the new flight. Due to the absence of historical data, the airline cannot obtain the probability distribution of no-shows. In this case, the number  $\xi$  of no-shows is assumed to be a positive uncertain variable,

and its uncertainty distribution  $\Phi$  can be obtained by the belief degree of the invited experts. We suppose that the airline provides no refunds for the no-shows, and compensates those crowded-out customers. Our objective function is the profit rate that is the profit divided by the total cost of a new flight; then it is expressed as

$$s(m, \xi) = \begin{cases} \frac{mg\beta}{r} - 1, & \text{if } m - \xi \leq n \\ \frac{mg\beta}{r} - \frac{(m - \xi - n)p}{r} - 1, & \text{if } m - \xi \geq n. \end{cases} \tag{9}$$

Since the number  $\xi$  of no-shows is an uncertain variable, the profit rate function  $s(m, \xi)$  is an uncertain variable as well. As  $s(m, \xi)$  cannot be directly maximized, we may maximize its expected value; that is,

$$\max_m E[s(m, \xi)]. \tag{10}$$

The purpose of decision-maker of airline is to find the optimal booking limit that maximizes the profit. However, if the number of arrival passengers exceeds flight capacity when the flight takes off, it will cause that some arrival passengers could not board flight, which lead to not only profit losses but also bad social reputation. For reducing the negative impact on the airline, a chance constraint is given that the uncertain measure of the event that the number of crowded-out customers is less than  $j$  is greater than a given confidence level of  $\alpha$ ; that is,

$$\mathcal{M}\{m - n - \xi \leq j\} \geq \alpha. \tag{11}$$

In order to find the optimal booking limit  $m^*$ , we present the following theorems.

**Theorem 7.** *Let  $\xi$  be a positive uncertain variable with an uncertainty distribution  $\Phi$ . Given that*

$$s(m, \xi) = \begin{cases} \frac{mg\beta}{r} - 1, & \text{if } m - \xi \leq n \\ \frac{mg\beta}{r} - \frac{(m - \xi - n)p}{r} - 1, & \text{if } m - \xi \geq n, \end{cases} \tag{12}$$

the uncertain variable  $s(m, \xi)$  has an uncertainty distribution

$$\begin{aligned} \Psi(x) &= \begin{cases} 0, & \text{if } x < \frac{mg\beta}{r} - \frac{(m-n)p}{r} - 1 \\ \Phi\left(\frac{rx + r - mg\beta}{p} + m - n\right), & \text{if } \frac{mg\beta}{r} - \frac{(m-n)p}{r} - 1 \leq x < \frac{mg\beta}{r} - 1 \\ 1, & \text{if } x \geq \frac{mg\beta}{r} - 1. \end{cases} \end{aligned} \tag{13}$$

*Proof.* It is easy to know that  $s(m, \xi) \geq mg\beta/r - (m-n)p/r - 1$ ; therefore,

$$\Psi(x) = \mathcal{M}\{s(m, \xi) \leq x\} = 0, \tag{14}$$

for any  $x \in (-\infty, mg\beta/r - (m - n)p/r - 1)$ . If  $x \in [mg\beta/r - (m - n)p/r - 1, mg\beta/r - 1)$ , then

$$\begin{aligned} \Psi(x) &= \mathcal{M}\{s(m, \xi) \leq x\} \\ &= \mathcal{M}\left\{\frac{mg\beta}{r} - \frac{(m - \xi - n)p}{r} - 1 \leq x\right\} \\ &= \mathcal{M}\left\{\xi \leq \frac{rx + r - mg\beta}{p} + m - n\right\} \\ &= \Phi\left(\frac{rx + r - mg\beta}{p} + m - n\right). \end{aligned} \tag{15}$$

Since  $s(m, \xi) \leq mg\beta/r - 1$ , we have

$$\Psi(x) = \mathcal{M}\{s(m, \xi) \leq x\} = 1, \tag{16}$$

for any  $x \in [mg\beta/r - 1, +\infty)$ . The theorem is verified.  $\square$

**Theorem 8.** Let  $\xi$  be a positive uncertain variable with an uncertainty distribution  $\Phi$ . Given that

$$s(m, \xi) = \begin{cases} \frac{mg\beta}{r} - 1, & \text{if } m - \xi \leq n \\ \frac{mg\beta}{r} - \frac{(m - \xi - n)p}{r} - 1, & \text{if } m - \xi \geq n, \end{cases} \tag{17}$$

then

$$E[s(m, \xi)] = \frac{mg\beta}{r} - \frac{p}{r} \int_0^{m-n} \Phi(x) dx - 1. \tag{18}$$

*Proof.* The expected value of the uncertain variable  $s(m, \xi)$  is

$$\begin{aligned} E[s(m, \xi)] &= \int_0^{+\infty} [1 - \Psi(x)] dx - \int_{-\infty}^0 \Psi(x) dx \\ &= \int_0^{mg\beta/r - (m-n)p/r - 1} 1 dx \\ &\quad + \int_{mg\beta/r - (m-n)p/r - 1}^{mg\beta/r - 1} \left[1 - \Phi\left(\frac{rx + r - mg\beta}{p} + m - n\right)\right] dx \\ &\quad + \int_{mg\beta/r - 1}^{+\infty} 0 dx - \int_{-\infty}^0 0 dx = \int_0^{mg\beta/r - 1} 1 dx \\ &\quad - \int_{mg\beta/r - (m-n)p/r - 1}^{mg\beta/r - 1} \Phi\left(\frac{rx + r - mg\beta}{p} + m - n\right) dx \\ &= \frac{mg\beta}{r} - \frac{p}{r} \int_0^{m-n} \Phi(x) dx - 1. \end{aligned} \tag{19}$$

The theorem is verified.  $\square$

Since the constraint function  $(m - n - \xi \leq j)$  is strictly decreasing with respect to the uncertain variable  $\xi$ , the chance constraint (11) can be converted to crisp formula according to Theorem 6; then

$$m \leq n + j + \Phi^{-1}(1 - \alpha). \tag{20}$$

Therefore, the uncertain programming model is developed as follows:

$$\begin{aligned} \max_m \quad & \left[ \frac{mg\beta}{r} - \frac{p}{r} \int_0^{m-n} \Phi(x) dx - 1 \right] \\ \text{subject to:} \quad & m \leq n + j + \Phi^{-1}(1 - \alpha). \end{aligned} \tag{21}$$

### 4. Application

In this section, we will present a numerical case to illustrate the aforementioned model. Suppose that the overbooking problem is considered for a new single-leg flight of an airline. Assume that the number  $\xi$  of no-shows is a positive uncertain variable with linear uncertainty distribution  $\mathcal{L}(a, b)$  ( $a \geq 0$ ) (Liu [21]); that is,

$$\Phi(x) = \begin{cases} 0, & \text{if } x \leq a \\ \frac{(x - a)}{(b - a)}, & \text{if } a \leq x \leq b \\ 1, & \text{if } x \geq b. \end{cases} \tag{22}$$

Then, the inverse uncertainty distribution of linear uncertain variable  $\mathcal{L}(a, b)$  (Liu [21]) is

$$\Phi^{-1}(\alpha) = (1 - \alpha)a - \alpha b. \tag{23}$$

From the uncertain programming model (21), we can obtain that the optimal booking limit with discount fare is

$$m^* = \begin{cases} \left(\frac{g\beta(b - a)}{p} + a + n\right) \wedge (n + j + \alpha a + (1 - \alpha)b), & \text{if } g\beta \leq p \\ n + j + \alpha a + (1 - \alpha)b, & \text{if } g\beta > p. \end{cases} \tag{24}$$

We consider two familiar types of aircraft A320-200 and B747-300 with capacity of 150 and 416, respectively. We give that  $a = 0$  and the price of the flight ticket  $g = \text{RMB } 960$  yuan. According to the general provision set by the airline, we suppose that the penalty cost  $p$  is 30% of the face value of the ticket and  $p$  will be counted by RMB 200 yuan if it is less than RMB 200 yuan; that is,

$$p = \max\{1.3g\beta, g\beta + 200\}. \tag{25}$$

For instance, if the upper limit of no-shows  $b = 8$ , the permissible maximum of crowded-out passages  $j = 5$ , aircraft capacity  $n = 150$ , the chance constraint  $\alpha = 0.95$ , the discount  $\beta = 0.4$ , then the optimal booking limit  $m^*$  is 155.

Figure 1 shows the optimal booking limit  $m^*$  changing with discount  $\beta$  for  $b = 8, j = 5$ . On the whole,

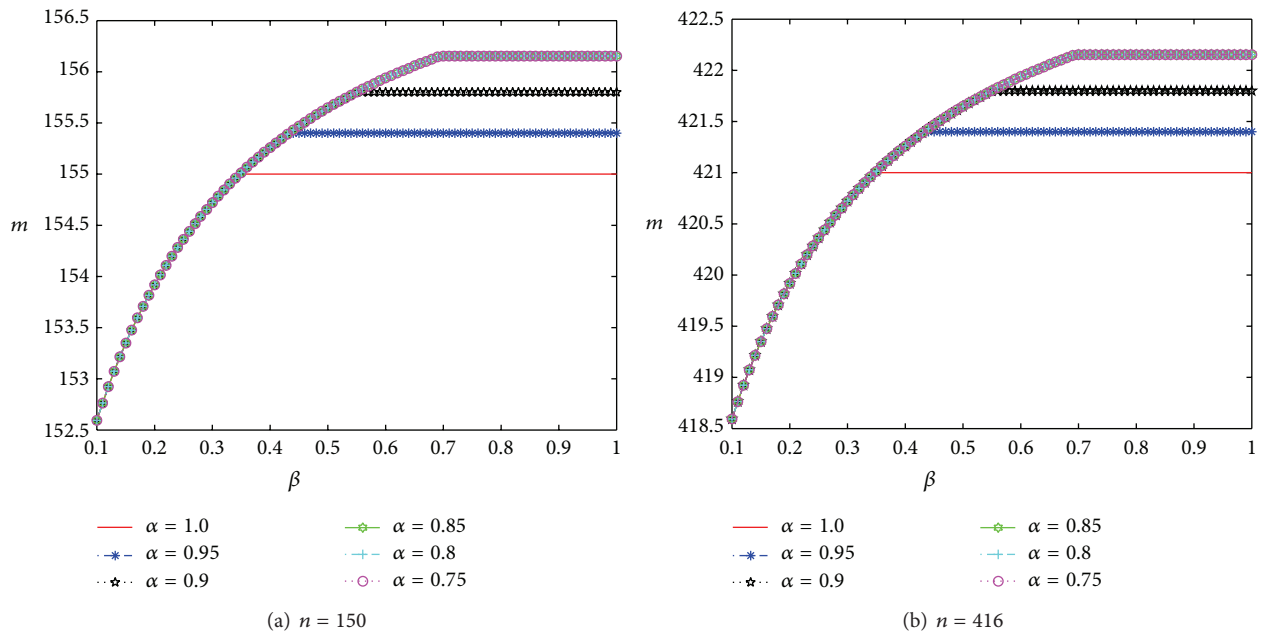


FIGURE 1: Optimal booking limit  $m^*$  under the changes of  $\alpha$  and  $\beta$  when  $b = 8, j = 5$ .

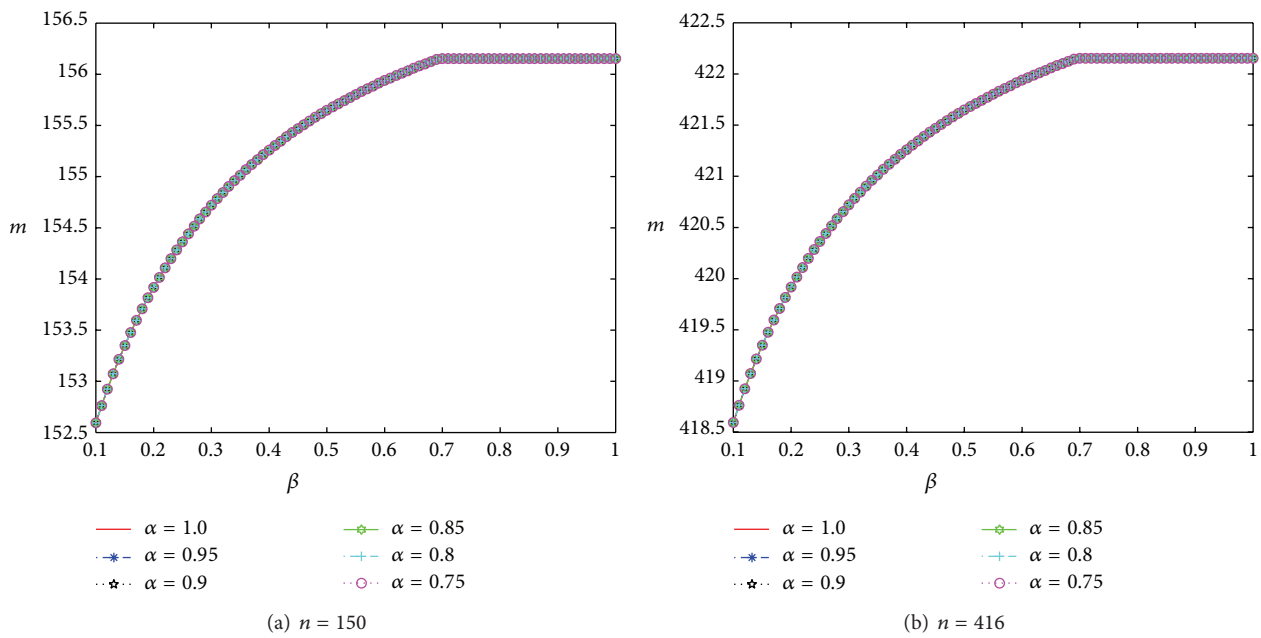


FIGURE 2: Optimal booking limit  $m^*$  under the changes of  $\alpha$  and  $\beta$  when  $b = 8, j = 8$ .

with a gradually reduced slope, the optimal booking limit  $m^*$  increases in discount  $\beta$  till  $\beta$  reaches a certain value. The optimal booking limit  $m^*$  does not increase in the confidence level  $\alpha$ , and, when  $\beta \leq 0.4$ ,  $\alpha$  has no effect on  $m^*$ . By the comparison of Figures 1(a) and 1(b), we can see that the increase of  $m^*$  caused by the increase of flight capacity  $n$  is distinct.

Figure 2 shows the optimal booking limit  $m^*$  changing with discount  $\beta$  for  $b = 8, j = 8$ . Compared with Figure 1, due to a little increase of  $j$ ,  $m^*$  increases still in  $\beta$  and  $n$ , while the variation trend of  $m^*$  with  $\beta$  has nearly nothing to do with  $\alpha$ . As can be seen from the comparison between Figures 1 and 2, the turning point of the slope of the optimal booking limit curve increases in  $j$ .

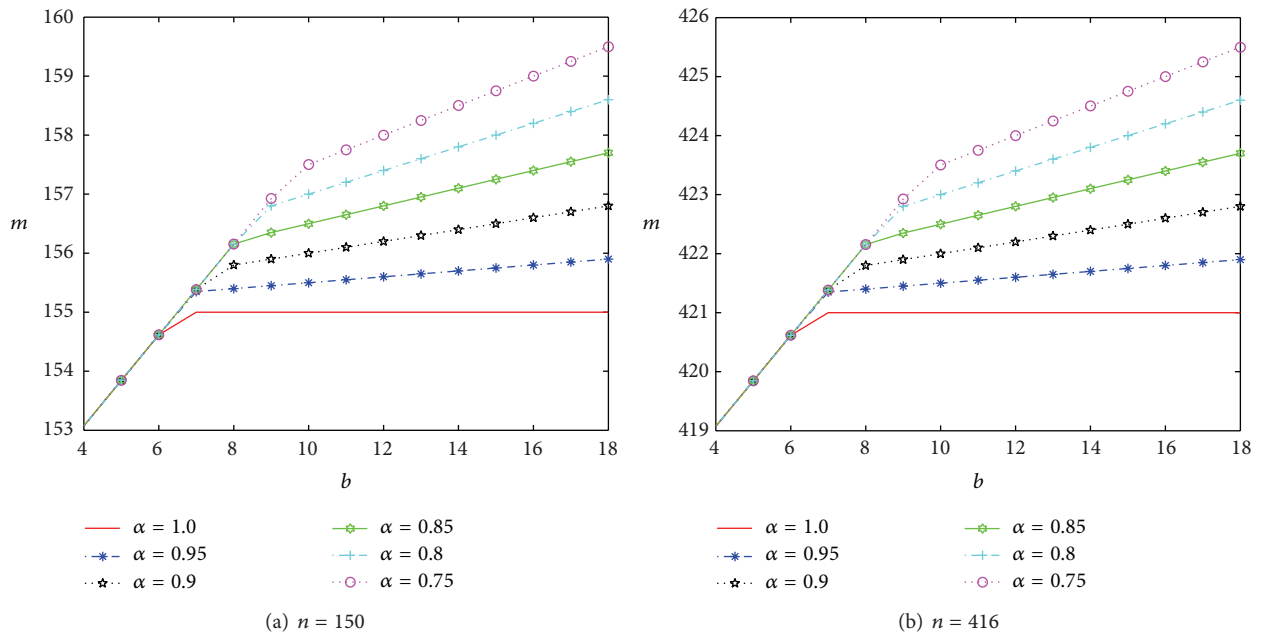


FIGURE 3: Optimal booking limit  $m^*$  under the changes of  $\alpha$  and  $b$  when  $\beta = 0.8, j = 5$ .

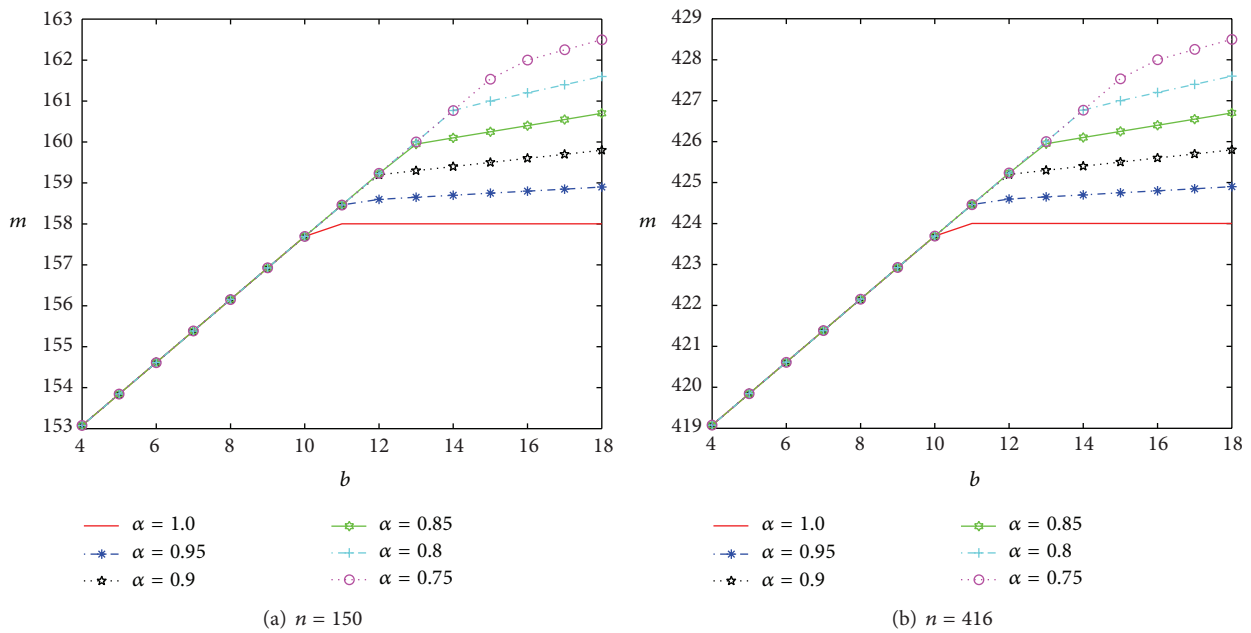


FIGURE 4: Optimal booking limit  $m^*$  under the changes of  $\alpha$  and  $b$  when  $\beta = 0.8, j = 8$ .

Figures 3 and 4 show the optimal booking limit  $m^*$  changing with the parameter  $b$  for  $j = 5$  and  $j = 8$ , respectively. The optimal booking limit  $m^*$  increases in  $b$ , and, when  $b$  reaches a certain value, the slope becomes smaller. In the case of  $\alpha = 1.0$ , when  $b$  is bigger than a certain value,  $m^*$  remains the same. We also observe that  $m^*$  still does

not increase in the confidence level  $\alpha$ , and the closer  $\alpha$  gets to 1, the less sensitive  $m^*$  is to  $b$ . The flight capacity  $n$  still has a great influence on  $m^*$ .

As can be seen from the comparison between Figures 3 and 4, the turning point of the slope of the optimal booking limit curve increases in  $j$ .

## 5. Conclusions

Overbooking problem is an important strategy for airline revenue management. For a new flight, there is no historical data to obtain the probability distribution of the number of no-shows; therefore, stochastic method is not suitable. This paper introduced an uncertain variable to describe the number of no-shows. An airline overbooking model with discount fare was developed with chance constraint, and it was converted to a crisp programming based on uncertain programming theory. Through a numerical case, we obtained the analytic expression of the optimal booking limit to maximize the profit rate function of the new flight. The results of sensitivity analysis indicated that flight capacity, discount, confidence level, and parameters of the uncertainty distribution significantly affected the optimal booking limit.

However, there is still a lot of work to be done in the future research. The dynamic nature of the booking process can be taken into account. Furthermore, randomness and uncertainty may coexist in practical situation; thus an uncertain random overbooking model might be our future research.

## Conflict of Interests

The authors declare that there is no conflict of interests regarding the publication of this paper.

## Acknowledgments

This work is supported by the Fundamental Research Funds for the Central Universities under Grant no. ZXH2012K005 and the Undergraduate Training Programs for Innovation and Entrepreneurship no. IECAUC13037.

## References

- [1] B. C. Smith, J. F. Leimkuhler, and R. M. Darrow, "Yield management at American Airlines," *Interfaces*, vol. 22, no. 1, pp. 8–31, 1992.
- [2] K. T. Talluri and G. van Ryzin, *The Theory and Practice of Revenue Management*, Kluwer, Boston, Mass, USA, 2004.
- [3] M. J. Beckmann, "Decision and team problem in airline reservations," *Econometrica*, vol. 26, no. 1, pp. 134–145, 1958.
- [4] M. Rothstein, "An airline overbooking model," *Transportation Science*, vol. 5, pp. 180–192, 1971.
- [5] J. Alstrup, S. Boas, O. B. G. Madsen, and R. V. V. Vidal, "Booking policy for flights with two types of passengers," *European Journal of Operational Research*, vol. 27, no. 3, pp. 274–288, 1986.
- [6] R. E. Chatwin, *Optimal airline overbooking [Ph.D. dissertation]*, Department of Operations Research, Stanford University, Palo Alto, Calif, USA, 1993.
- [7] L. P. Robert, *Pricing and Revenue Optimization*, Stanford University Press, Palo Alto, Calif, USA, 2005.
- [8] D. Kahneman, A. Tversky, and Prospect theory, "An analysis of decision under risk," *Econometrica*, vol. 47, no. 2, pp. 263–292, 1979.
- [9] B. Liu and Uncertainty Theory Springer, Berlin, Germany, 2nd edition, 2007.
- [10] B. Liu, *Uncertainty Theory: A Branch of Mathematics for Modeling Human Uncertainty*, Springer, Berlin, Germany, 2010.
- [11] B. Liu, *Theory and Practice of Uncertain Programming*, Springer, Berlin, Germany, 2nd edition, 2009.
- [12] B. Liu, "Uncertain risk analysis and uncertain reliability analysis," *Journal of Uncertain Systems*, vol. 4, no. 3, pp. 163–170, 2010.
- [13] B. Liu, "Uncertain logic for modeling human language," *Journal of Uncertain Systems*, vol. 5, no. 1, pp. 3–20, 2011.
- [14] B. Liu, "Uncertain set theory and uncertain inference rule with application to uncertain control," *Journal of Uncertain Systems*, vol. 4, no. 2, pp. 83–98, 2010.
- [15] B. Liu, "Fuzzy process, hybrid process and uncertain process," *Journal of Uncertain Systems*, vol. 2, no. 1, pp. 3–16, 2008.
- [16] B. Liu, "Toward uncertain finance theory," *Journal of Uncertainty Analysis and Application*, vol. 1, article 1, 2013.
- [17] K. Yao and D. A. Ralescu, "Age replacement policy in uncertain environment," *Iranian Journal of Fuzzy Systems*, vol. 10, no. 2, pp. 29–39, 2013.
- [18] C. Zhang and C. Guo, "An ordering policy based on uncertain renewal theory with application to aircraft spare parts," <http://orsc.edu.cn/online/130116.pdf>.
- [19] B. Liu and K. Yao, "Uncertain multilevel programming: algorithm and applications," <http://orsc.edu.cn/online/120114.pdf>.
- [20] B. Liu, "Some research problems in uncertainty theory," *Journal of Uncertain Systems*, vol. 3, no. 1, pp. 3–10, 2009.
- [21] B. Liu, *Uncertainty Theory*, Uncertainty Theory Laboratory, 4th edition, 2013.

## Research Article

# An Inventory Model under Trapezoidal Type Demand, Weibull-Distributed Deterioration, and Partial Backlogging

**Lianxia Zhao**

*School of Management, Shanghai University, Shanghai 200444, China*

Correspondence should be addressed to Lianxia Zhao; [zhaolianxia@staff.shu.edu.cn](mailto:zhaolianxia@staff.shu.edu.cn)

Received 7 November 2013; Revised 19 January 2014; Accepted 21 January 2014; Published 6 March 2014

Academic Editor: Nachamada Blamah

Copyright © 2014 Lianxia Zhao. This is an open access article distributed under the Creative Commons Attribution License, which permits unrestricted use, distribution, and reproduction in any medium, provided the original work is properly cited.

This paper studies an inventory model for Weibull-distributed deterioration items with trapezoidal type demand rate, in which shortages are allowed and partially backlogging depends on the waiting time for the next replenishment. The inventory models starting with no shortage are to be discussed, and an optimal inventory replenishment policy of the model is proposed. Finally, numerical examples are provided to illustrate the theoretical results, and a sensitivity analysis of the major parameters with respect to the optimal solution is also carried out.

## 1. Introduction

The effect of deteriorating for items cannot be disregarded in many inventory systems and it is a general phenomenon in real life. Deterioration is defined as any process that decreases the usefulness or the value of the original item, such as decay or physical depletion. For example, fruits, vegetables, or foodstuffs are subject to spoilage directly while being kept in store, and electronic products, radioactive substances, and photographic film deteriorate through a gradual loss of potential or utility with the passage of time.

Due to the variability in economic circumstances, the basic assumptions of the EOQ model should be constantly modified according to the studied inventory model. In recent years, many researchers have studied kinds of EOQ models for deteriorating items. Ghare and Schrader [1] established the classical no-shortage inventory model with a constant rate of decay. Wu et al. [2] studied an inventory model with a Weibull-distributed deteriorating rate for items and assumed the demand rate with a continuous function of time. Wee [3] developed an inventory model with quantity discount, pricing, and partial backordering when the product in stock deteriorates with time. Related literature also includes Skouri and Papachristos [4], Wee [5], and Dye et al. [6].

practically, the demand rate of deterioration items is impossible to increase continuously all the time. Hill [7]

proposed an inventory model with ramp type demand rate. Mandal and Pal [8] extended the inventory model with ramp type demand for deterioration items and allowed shortage. Wu [9] considered an inventory model with Weibull distribution deterioration and ramp type demand rate in which shortages are allowed and the backlogging rate is dependent on waiting time. Giri et al. [10] extended the ramp type demand inventory model with a more generalized Weibull deterioration distribution. Manna and Chaudhuri [11] developed an inventory model for time-dependent deteriorating items with ramp type demand rate. Skouri et al. [12] considered an inventory model with general ramp type demand rate, partial backlogging, and Weibull deterioration rate. Hung [13] extended their inventory model from ramp type demand rate and Weibull deterioration rate to arbitrary demand rate and arbitrary deterioration rate. Kumar et al. [14] studied fuzzy EOQ models with ramp type demand rate, partial backlogging, and time-dependent deterioration rate. Cheng et al. [15] considered an inventory model for time-dependent deteriorating items with trapezoidal type demand rate and partial backlogging. Uthayakumar and Rameswari [16] studied an inventory model for defective items with trapezoidal type demand rate to determine the optimal product reliability. Tan and Weng [17] considered a discrete-in-time inventory model for deteriorating items with partially backlogged. Ahmed et al. [18] proposed a method for

finding the economic order quantity for an inventory model with ramp type demand rate, partial backlogging, and general deterioration rate. Lin [19] explored the inventory model with a general demand rate in which both the Weibull-distributed deterioration and partial backlogging are considered.

In the above mentioned research, one of assumptions was considered: the ramp type demand rate, partial backlogging, and Weibull-distributed deterioration rate. However, for fashionable commodities, high-tech products, and other short life cycle products, the demand rate should increase with the time up to certain point at first stage then reach a stabilized period and finally the demand rate decrease to zero and the products retreat from market in their product life cycle, that is, the demand rate with continuous trapezoidal function of time. On the other hand, in many real situations, customers encountering shortages will respond differently. Some customers are willing to wait until the next replenishment, while others may be impatient and go elsewhere as waiting time increases; that is, the willingness for a customer to wait for backlogging is diminishing with the length of the waiting time. In this paper, we consider an inventory model with Weibull-distributed deterioration items, trapezoidal type demand rate, and time-dependent partial backlogging. By analyzing the inventory model, a useful inventory replenishment policy is proposed. Finally, numerical examples are provided to illustrate the theoretical results, and a sensitivity analysis of the optimal solution with respect to major parameters is also carried out.

The rest of the paper is organized as follows. Section 2 describes the notation and assumptions used throughout this paper. Section 3 analyzes the inventory model, and some numerical examples to illustrate the solution procedure are provided. Sensitivity analysis of the major parameters is also carried out in Section 4, and the final Section concludes this paper.

## 2. Notations and Assumptions

The fundamental notations and assumptions used in inventory model and considered in this paper are given as below.

- (i)  $I(t)$  the level of inventory at time  $t$ ,  $0 \leq t \leq T$ .
- (ii)  $T$  the fixed length of each ordering cycle.
- (iii)  $t_1$  the time when the inventory level reaches zero for the inventory model.
- (iv)  $t_1^*$  the optimal point.
- (v)  $S$  the maximum inventory level for each ordering cycle.
- (vi)  $Q^*$  the optimal ordering quantity.
- (vii)  $A_0$  the fixed cost per order.
- (viii)  $c_1$  the cost of each deteriorated item.
- (ix)  $c_2$  the inventory holding cost per unit per unit of time.
- (x)  $c_3$  the shortage cost per unit per unit of time.
- (xi)  $c_4$  the lost sales cost per unit.
- (xii)  $C_i(t_1)$   $i = 1, 2, 3$ , the average total cost per unit time under different conditions, respectively.

(xiii)  $TC(t_1)$  the average total cost per unit time.

(xiv) The demand rate,  $D(t)$ , which is positive and consecutive, is assumed to be a trapezoidal type function of time; that is,

$$D(t) = \begin{cases} f(t), & t \leq \mu_1; \\ D_0, & \mu_1 < t < \mu_2; \\ g(t), & \mu_2 \leq t < T, \end{cases} \quad (1)$$

where  $\mu_1$  is time point changing from the increasing demand function  $f(t)$  to constant demand  $D_0$ , and  $\mu_2$  is time point changing from the constant demand  $D_0$  to the decreasing demand function  $g(t)$ .

(xv) The replenishment rate is infinite; that is, replenishment is instantaneous.

(xvi) The deterioration rate of the item is defined as Weibull  $(\alpha, \beta)$ ; that is the deterioration rate is  $\theta(t) = \alpha\beta t^{\beta-1}$  ( $\alpha > 0, \beta > 0, t > 0$ ).

(xvii) Shortages are allowed and they adopt the notation used in Abad [20], where the unsatisfied demand is backlogged and the fraction of shortages backordered is  $e^{-\delta t}$ , where  $t$  is the waiting time up to the next replenishment. We also assume that  $te^{-\delta t}$  is an increasing function, which had appeared in Skouri et al. [12].

(xviii) The time horizon of the inventory model is finite.

## 3. Model Formulation

In this section, we consider an inventory model starting with no shortage. The behavior of the model during a given cycle is depicted in Figure 1. Replenishment occurs at time  $t = 0$  and the inventory level attains its maximum. From  $t = 0$  to  $t_1$ , the inventory level reduces due to demand and deterioration. At  $t_1$ , the inventory level achieves zero, then shortage is allowed to occur during the time interval  $(t_1, T)$ , and all of the demand during the shortage period  $(t_1, T)$  is partially backlogged. According to the notations and assumptions mentioned above, the behavior of the model at any time can be described by the following differential equations:

$$\frac{dI(t)}{dt} = \begin{cases} -\theta(t)I(t) - D(t), & 0 < t < t_1; \\ -e^{-\delta(T-t)}D(t), & t_1 < t < T, \end{cases} \quad (2)$$

with boundary conditions  $I(0) = S, I(t_1) = 0$ .

In the following, we consider three possible cases based on the values of  $t_1, \mu_1$ , and  $\mu_2$ . These three cases are shown.

*Case 1* ( $0 < t_1 \leq \mu_1$ ). Due to the deteriorating and trapezoidal type demand rate, the inventory level gradually diminishes during the time interval  $[0, t_1]$  and ultimately falls to zero at time  $t_1$ . Thus, from (2), we have

$$\frac{dI(t)}{dt} = \begin{cases} -\alpha\beta t^{\beta-1}I(t) - f(t), & 0 < t < t_1; \\ -e^{-\delta(T-t)}f(t), & t_1 < t < \mu_1; \\ -e^{-\delta(T-t)}D_0, & \mu_1 < t < \mu_2; \\ -e^{-\delta(T-t)}g(t), & \mu_2 < t < T. \end{cases} \quad (3)$$

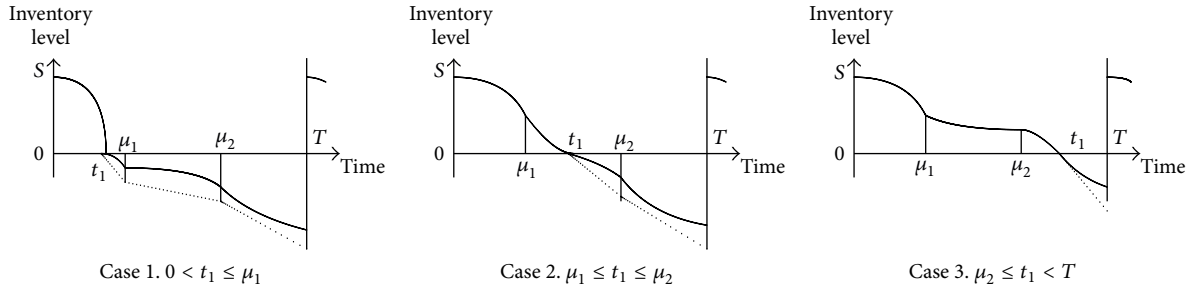


FIGURE 1: Graphical representation of inventory level over the cycle.

By using the boundary condition  $I(t_1) = 0$ , the solutions of (3) are given by

The total shortage quantity  $B_T$  during the interval  $[t_1, T]$  is

$$I(t) = \begin{cases} \int_t^{t_1} f(x) e^{\alpha(x^\beta - t^\beta)} dx, & 0 < t < t_1; \\ -\int_{t_1}^t e^{\delta(x-T)} f(x) dx, & t_1 < t < \mu_1; \\ \frac{D_0}{\delta} (e^{\delta(\mu_1-T)} - e^{\delta(t-T)}) - \int_{t_1}^{\mu_1} e^{\delta(x-T)} f(x) dx, & \mu_1 < t < \mu_2; \\ -\int_{\mu_2}^t g(x) e^{\delta(x-T)} dx + \frac{D_0}{\delta} (e^{\delta(\mu_1-T)} - e^{\delta(\mu_2-T)}) - \int_{t_1}^{\mu_1} e^{\delta(x-T)} f(x) dx, & \mu_2 < t < T. \end{cases} \quad (4)$$

$$B_T = - \int_{t_1}^T I(t) dt = \int_{t_1}^{\mu_1} \left[ \int_{t_1}^t e^{\delta(x-T)} f(x) dx \right] dt - \int_{\mu_1}^{\mu_2} \left[ \frac{D_0}{\delta} (e^{\delta(\mu_1-T)} - e^{\delta(t-T)}) - \int_{t_1}^{\mu_1} e^{\delta(x-T)} f(x) dx \right] dt + \int_{\mu_2}^T \left[ \int_{\mu_2}^t e^{\delta(x-T)} g(x) dx - \frac{D_0}{\delta} (e^{\delta(\mu_1-T)} - e^{\delta(\mu_2-T)}) + \int_{t_1}^{\mu_1} e^{\delta(x-T)} f(x) dx \right] dt \quad (8)$$

The maximum inventory level per cycle is

$$S = I(0) = \int_0^{t_1} f(x) e^{\alpha x^\beta} dx. \quad (5)$$

Then, the total number of deteriorated items  $D_T$  in the interval  $[0, t_1]$  is

$$D_T = S - \int_0^{t_1} D(t) dt = \int_0^{t_1} f(x) (e^{\alpha x^\beta} - 1) dx. \quad (6)$$

The total number of inventory  $H_T$  carried during the interval  $[0, t_1]$  is

$$H_T = \int_0^{t_1} I(t) dt = \int_0^{t_1} \int_t^{t_1} f(x) e^{\alpha(x^\beta - t^\beta)} dx dt. \quad (7)$$

$$= \int_{t_1}^{\mu_1} (T-t) e^{\delta(t-T)} f(t) dt + \int_{\mu_2}^T (T-t) e^{\delta(t-T)} g(t) dt + \frac{D_0}{\delta^2} (e^{\delta(\mu_2-T)} - e^{\delta(\mu_1-T)}) + \frac{D_0}{\delta} [(T-\mu_2) e^{\delta(\mu_2-T)} - (T-\mu_1) e^{\delta(\mu_1-T)}].$$

The total of lost sales  $L_T$  during the interval  $[t_1, T]$  is

$$L_T = \int_{t_1}^{\mu_1} (1 - e^{\delta(t-T)}) f(t) dt + \int_{\mu_1}^{\mu_2} (1 - e^{\delta(t-T)}) D_0 dt + \int_{\mu_2}^T (1 - e^{\delta(t-T)}) g(t) dt. \quad (9)$$

Therefore, the average total cost per unit time under the condition  $t_1 \leq \mu_1$  can be given by

$$\begin{aligned}
 C_1(t_1) &= \frac{1}{T} [A_0 + c_1 D_T + c_2 H_T + c_3 B_T + c_4 L_T] \\
 &= \frac{1}{T} \left\{ A_0 + c_1 \int_0^{t_1} f(x) (e^{\alpha x^\beta} - 1) dx \right. \\
 &\quad + c_2 \int_0^{t_1} \int_t^{t_1} f(x) e^{\alpha(x^\beta - t^\beta)} dx dt \\
 &\quad + c_4 \left[ \int_{t_1}^{\mu_1} (1 - e^{\delta(t-T)}) f(t) dt \right. \\
 &\quad + \int_{\mu_1}^{\mu_2} (1 - e^{\delta(t-T)}) D_0 dt \\
 &\quad + \left. \int_{\mu_2}^T (1 - e^{\delta(t-T)}) g(t) dt \right] \\
 &\quad + c_3 \left[ \int_{t_1}^{\mu_1} e^{\delta(t-T)} (T-t) f(t) dt \right. \\
 &\quad + \int_{\mu_2}^T e^{\delta(t-T)} (T-t) g(t) dt \\
 &\quad + \frac{D_0}{\delta^2} (e^{\delta(\mu_2-T)} - e^{\delta(\mu_1-T)}) \\
 &\quad + \frac{D_0}{\delta} ((T-\mu_2) e^{\delta(\mu_2-T)} \\
 &\quad \left. \left. - (T-\mu_1) e^{\delta(\mu_1-T)}) \right] \right\}. \tag{10}
 \end{aligned}$$

Case 2 ( $\mu_1 \leq t_1 \leq \mu_2$ ). The differential equations governing the inventory model can be expressed as follows:

$$\frac{dI(t)}{dt} = \begin{cases} -\alpha\beta t^{\beta-1} I(t) - f(t), & 0 < t < \mu_1; \\ -\alpha\beta t^{\beta-1} I(t) - D_0, & \mu_1 < t < t_1; \\ -e^{-\delta(T-t)} D_0, & t_1 < t < \mu_2; \\ -e^{-\delta(T-t)} g(t), & \mu_2 < t < T. \end{cases} \tag{11}$$

Solving the differential equation (11) with  $I(t_1) = 0$ , we have

$$I(t) = \begin{cases} \int_t^{\mu_1} f(x) e^{\alpha(x^\beta - t^\beta)} dx \\ \quad + D_0 \int_t^{t_1} e^{\alpha(x^\beta - t^\beta)} dx, & 0 < t < \mu_1; \\ D_0 \int_t^{t_1} e^{\alpha(x^\beta - t^\beta)} dx, & \mu_1 < t < t_1; \\ \frac{D_0}{\delta} (e^{\delta(t_1-T)} - e^{\delta(t-T)}), & t_1 < t < \mu_2; \\ -\int_{\mu_2}^t e^{\delta(x-T)} g(x) dx \\ \quad + \frac{D_0}{\delta} (e^{\delta(t_1-T)} - e^{\delta(\mu_2-T)}), & \mu_2 < t < T. \end{cases} \tag{12}$$

The beginning inventory level can be computed as

$$S = I(0) = \int_0^{\mu_1} f(x) e^{\alpha x^\beta} dx + D_0 \int_{\mu_1}^{t_1} e^{\alpha x^\beta} dx. \tag{13}$$

The total number of items which perish in the interval  $[0, t_1]$  is

$$D_T = \int_0^{\mu_1} f(x) (e^{\alpha x^\beta} - 1) dx + D_0 \int_{\mu_1}^{t_1} (e^{\alpha x^\beta} - 1) dx. \tag{14}$$

The total number of inventory carried during the interval  $[0, t_1]$  is

$$H_T = \int_0^{\mu_1} \int_t^{\mu_1} e^{\alpha(x^\beta - t^\beta)} f(x) dx dt + D_0 \int_{\mu_1}^{t_1} \int_t^{t_1} e^{\alpha(x^\beta - t^\beta)} dx dt. \tag{15}$$

The total shortage quantity during the interval  $[t_1, T]$  is

$$\begin{aligned}
 B_T &= \int_{\mu_2}^T (T-t) e^{\delta(t-T)} g(t) dt \\
 &\quad + \frac{D_0}{\delta} \left[ e^{\delta(t_1-T)} \left( T - t_1 + \frac{1}{\delta} \right) \right. \\
 &\quad \left. - e^{-\delta(\mu_2-T)} \left( T - \mu_2 + \frac{1}{\delta} \right) \right]. \tag{16}
 \end{aligned}$$

The total of lost sales during the interval  $[t_1, T]$  is

$$L_T = D_0 \int_{t_1}^{\mu_2} (1 - e^{\delta(t-T)}) dt + \int_{\mu_2}^T (1 - e^{\delta(t-T)}) g(t) dt. \tag{17}$$

Therefore, the average total cost per unit time under the condition  $\mu_1 \leq t_1 \leq \mu_2$  can be given by

$$\begin{aligned}
 C_2(t_1) &= \frac{1}{T} [A_0 + c_1 D_T + c_2 H_T + c_3 B_T + c_4 L_T] \\
 &= \frac{1}{T} \left\{ A_0 + c_1 \left[ \int_0^{\mu_1} f(x) (e^{\alpha x^\beta} - 1) dx \right. \right. \\
 &\quad \left. \left. + D_0 \int_{\mu_1}^{t_1} (e^{\alpha x^\beta} - 1) dx \right] \right. \\
 &\quad + c_2 \left[ \int_0^{\mu_1} \int_t^{\mu_1} e^{\alpha(x^\beta - t^\beta)} f(x) dx dt \right. \\
 &\quad \left. + D_0 \int_0^{t_1} \int_t^{t_1} e^{\alpha(x^\beta - t^\beta)} dx dt \right] \tag{18}
 \end{aligned}$$

$$\begin{aligned}
 &+ c_3 \left[ \int_{\mu_2}^T (T-t) e^{\delta(t-T)} g(t) dt \right. \\
 &\quad + \frac{D_0}{\delta} \left( e^{\delta(t_1-T)} \left( T-t_1 + \frac{1}{\delta} \right) \right. \\
 &\quad \quad \left. \left. - e^{\delta(\mu_2-T)} \left( T-\mu_2 + \frac{1}{\delta} \right) \right) \right] \\
 &+ c_4 \left[ D_0 \int_{t_1}^{\mu_2} (1 - e^{\delta(t-T)}) dt \right. \\
 &\quad \left. + \int_{\mu_2}^T (1 - e^{\delta(t-T)}) g(t) dt \right] \}. \tag{18}
 \end{aligned}$$

Case 3 ( $\mu_2 \leq t_1 < T$ ). The differential equations governing the inventory model can be expressed as follows:

$$\frac{dI(t)}{dt} = \begin{cases} -\alpha\beta t^{\beta-1} I(t) - f(t), & 0 < t < \mu_1; \\ -\alpha\beta t^{\beta-1} I(t) - D_0, & \mu_1 < t < \mu_2; \\ -\alpha\beta t^{\beta-1} I(t) - g(t), & \mu_2 < t < t_1; \\ -e^{-\delta(T-t)} g(t), & t_1 < t < T. \end{cases} \tag{19}$$

Solving the differential equation (19) with  $I(t_1) = 0$ , we have

$$I(t) = \begin{cases} \int_t^{\mu_1} e^{\alpha(x^\beta - t^\beta)} f(x) dx + D_0 \int_{\mu_2}^{\mu_1} e^{\alpha(x^\beta - t^\beta)} dx + \int_{\mu_2}^{t_1} e^{\alpha(x^\beta - t^\beta)} g(x) dx, & 0 < t < \mu_1; \\ D_0 \int_t^{\mu_2} e^{\alpha(x^\beta - t^\beta)} dx + \int_{\mu_2}^{t_1} e^{\alpha(x^\beta - t^\beta)} g(x) dx, & \mu_1 < t < \mu_2; \\ \int_t^{t_1} e^{\alpha(x^\beta - t^\beta)} g(x) dx, & \mu_2 < t < t_1; \\ -\int_{t_1}^t e^{\delta(x-T)} g(x) dx, & t_1 < t < T. \end{cases} \tag{20}$$

The beginning inventory level can be computed as

$$\begin{aligned}
 S &= I(0) \\
 &= \int_0^{\mu_1} e^{\alpha x^\beta} f(x) dx \\
 &\quad + D_0 \int_{\mu_2}^{\mu_1} e^{\alpha x^\beta} dx + \int_{\mu_2}^{t_1} e^{\alpha x^\beta} g(x) dx. \tag{21}
 \end{aligned}$$

The total number of items which perish in the interval  $[0, t_1]$  is

$$\begin{aligned}
 D_T &= \int_0^{\mu_1} (e^{\alpha x^\beta} - 1) f(x) dx + D_0 \int_{\mu_2}^{\mu_1} (e^{\alpha x^\beta} - 1) dx \\
 &\quad + \int_{\mu_2}^{t_1} (e^{\alpha x^\beta} - 1) g(x) dx. \tag{22}
 \end{aligned}$$

The total number of inventory carried during the interval  $[0, t_1]$  is

$$\begin{aligned}
 H_T &= \int_0^{\mu_1} \int_t^{\mu_1} e^{\alpha(x^\beta - t^\beta)} f(x) dx dt \\
 &\quad + D_0 \int_0^{\mu_1} \int_{\mu_2}^{\mu_1} e^{\alpha(x^\beta - t^\beta)} dx dt \\
 &\quad + D_0 \int_{\mu_2}^{\mu_1} \int_t^{\mu_2} e^{\alpha(x^\beta - t^\beta)} dx dt
 \end{aligned}$$

$$\begin{aligned}
 &+ \int_0^{\mu_2} \int_{\mu_2}^{t_1} e^{\alpha(x^\beta - t^\beta)} g(x) dx dt \\
 &+ \int_{\mu_2}^{t_1} \int_t^{t_1} e^{\alpha(x^\beta - t^\beta)} g(x) dx dt. \tag{23}
 \end{aligned}$$

The total shortage quantity during the interval  $[t_1, T]$  is

$$B_T = \int_{t_1}^T (T-t) e^{-\delta(T-t)} g(t) dt. \tag{24}$$

The total of lost sales during the interval  $[t_1, T]$  is

$$L_T = \int_{t_1}^T (1 - e^{-\delta(T-t)}) g(t) dt. \tag{25}$$

Therefore, the average total cost per unit time under the condition  $\mu_2 \leq t_1 \leq T$  can be given by

$$\begin{aligned}
 C_3(t_1) &= \frac{1}{T} [A_0 + c_1 D_T + c_2 H_T + c_3 B_T + c_4 L_T] \\
 &= \frac{1}{T} \left\{ A_0 + c_1 \left[ \int_0^{\mu_1} (e^{\alpha x^\beta} - 1) f(x) dx \right. \right. \\
 &\quad \left. \left. + D_0 \int_{\mu_2}^{\mu_1} (e^{\alpha x^\beta} - 1) dx \right. \right. \\
 &\quad \left. \left. + \int_{\mu_2}^{t_1} (e^{\alpha x^\beta} - 1) g(x) dx \right] \right\}
 \end{aligned}$$

$$\begin{aligned}
 &+ c_2 \left[ \int_0^{\mu_1} \int_t^{\mu_1} e^{\alpha(x^\beta - t^\beta)} f(x) dx dt \right. \\
 &\quad + D_0 \int_0^{\mu_1} \int_{\mu_1}^{\mu_2} e^{\alpha(x^\beta - t^\beta)} dx dt \\
 &\quad + D_0 \int_{\mu_1}^{\mu_2} \int_t^{\mu_2} e^{\alpha(x^\beta - t^\beta)} dx dt \\
 &\quad + \int_0^{\mu_2} \int_{\mu_2}^{t_1} e^{\alpha(x^\beta - t^\beta)} g(x) dx dt \\
 &\quad \left. + \int_{\mu_2}^{t_1} \int_t^{t_1} e^{\alpha(x^\beta - t^\beta)} g(x) dx dt \right] \\
 &+ c_3 \left[ \int_{t_1}^T (T - t) e^{\delta(t-T)} g(t) dt \right] \\
 &+ c_4 \left[ \int_{t_1}^T (1 - e^{\delta(t-T)}) g(t) dt \right] \Big\}. \tag{26}
 \end{aligned}$$

From the above analysis, we obtain that the total average cost of the model over the time interval  $[0, T]$  is

$$TC(t_1) = \begin{cases} C_1(t_1), & 0 < t_1 \leq \mu_1; \\ C_2(t_1), & \mu_1 < t_1 \leq \mu_2; \\ C_3(t_1), & \mu_2 < t_1 < T, \end{cases} \tag{27}$$

where  $C_1(t_1)$ ,  $C_2(t_1)$ , and  $C_3(t_1)$  are obtained from (10), (18), and (26), respectively.

In the following, we will provide the results which ensure the existence of a unique  $t_1$ , say  $t_1^*$ , so as to minimize the total average cost for the model system starting with no shortages.

If  $0 < t_1 \leq \mu_1$ , taking the first-order derivative of  $C_1(t_1)$  with respect to  $t_1$ , we obtain

$$\frac{dC_1(t_1)}{dt_1} = \frac{f(t_1)}{T} h(t_1), \tag{28}$$

where

$$\begin{aligned}
 h(t_1) &= c_1 \left( e^{\alpha t_1^\beta} - 1 \right) \\
 &+ c_2 \int_0^{t_1} e^{\alpha(t_1^\beta - t^\beta)} dt + c_3 (t_1 - T) e^{\delta(t_1 - T)} \\
 &+ c_4 \left( e^{\delta(t_1 - T)} - 1 \right), \tag{29}
 \end{aligned}$$

then we can obtain  $h(0) < 0$  and  $h(T) > 0$ . By using the assumption ( $te^{-\delta t}$  is an increasing function, where  $t$  is the waiting time up to the next replenishment), we have

$$\begin{aligned}
 \frac{dh(t_1)}{dt_1} &= \alpha \beta t_1^{\beta-1} \left( c_1 e^{\alpha t_1^\beta} + c_2 \int_0^{t_1} e^{\alpha(t_1^\beta - t^\beta)} dt \right) \\
 &+ [c_3 (\delta(t_1 - T) + 1) + c_4 \delta] e^{\delta(t_1 - T)} + c_2 > 0, \tag{30}
 \end{aligned}$$

which implies that  $h(t_1)$  is a strictly monotone increasing function. Therefore, the equation

$$\begin{aligned}
 h(t_1) &= c_1 \left( e^{\alpha t_1^\beta} - 1 \right) + c_2 \int_0^{t_1} e^{\alpha(t_1^\beta - t^\beta)} dt \\
 &+ c_3 (t_1 - T) e^{\delta(t_1 - T)} + c_4 \left( e^{\delta(t_1 - T)} - 1 \right) \\
 &= 0 \tag{31}
 \end{aligned}$$

has a unique root  $t_1^* \in (0, T)$  obtained by using Mathematica 9.0. Further,  $t_1^*$  is the only zero-point of  $dC_1(t_1)/dt_1 = 0$  since  $f(t_1) > 0$ .

If  $0 < t_1^* \leq \mu_1$ , for this  $t_1^*$ , we have

$$\left. \frac{d^2 C_1(t_1)}{dt_1^2} \right|_{t_1=t_1^*} = f(t_1^*) \frac{dh(t_1^*)}{T dt_1^*} > 0, \tag{32}$$

which means that the total average cost  $C_1(t_1)$  can obtain its minimum value at  $t_1^*$ .

The optimal value of the order level,  $S = I(0)$ , is

$$S^* = \int_0^{t_1^*} f(x) e^{\alpha x^\beta} dx, \tag{33}$$

and the optimal order quantity  $Q^*$  is

$$\begin{aligned}
 Q^* &= S^* + \int_{t_1^*}^{\mu_1} e^{\delta(t-T)} f(t) dt \\
 &+ D_0 \int_{\mu_1}^{\mu_2} e^{\delta(t-T)} dt + \int_{\mu_2}^T e^{\delta(t-T)} g(t) dt. \tag{34}
 \end{aligned}$$

If  $t_1^* \geq \mu_1$ , then the optimal value of  $C_1(t_1)$  is obtained at  $t_1 = \mu_1$ .

If  $\mu_1 < t_1 \leq \mu_2$ , taking the first-order and second-order derivative of  $C_2(t_1)$  with respect to  $t_1$ , respectively, we obtain

$$\frac{dC_2(t_1)}{dt_1} = \frac{D_0}{T} h(t_1). \tag{35}$$

If  $\mu_1 < t_1^* \leq \mu_2$ , for this  $t_1^*$ , we have

$$\left. \frac{d^2 C_2(t_1)}{dt_1^2} \right|_{t_1=t_1^*} = D_0 \frac{dh(t_1^*)}{T dt_1^*} > 0, \tag{36}$$

where the function  $h(t_1)$  is given by (31), and (36) implies that  $C_2(t_1)$  is a strictly convex function in  $t_1$  and obtained its minimum value at  $t_1^*$ . Therefore, the equation  $h(t_1) = 0$  has a unique root  $t_1^*$  in  $(0, T)$ .

The optimal value of the order level,  $S = I(0)$ , is

$$S^* = \int_0^{\mu_1} f(x) e^{\alpha x^\beta} dx + D_0 \int_{\mu_1}^{t_1^*} e^{\alpha x^\beta} dx, \tag{37}$$

and the optimal order quantity  $Q^*$  is

$$Q^* = S^* + \int_{t_1^*}^{\mu_2} e^{\delta(t-T)} D_0 dt + \int_{\mu_2}^T e^{\delta(t-T)} g(t) dt. \tag{38}$$

If  $t_1^* \leq \mu_1$ , then the optimal value of  $C_2(t_1)$  is obtained at  $t_1^* = \mu_1$ , and if  $t_1^* \geq \mu_2$ , then the optimal value of  $C_2(t_1)$  is obtained at  $t_1^* = \mu_2$ .

If  $\mu_2 < t_1 \leq T$ , taking the first-order and second-order derivative of  $C_3(t_1)$  with respect to  $t_1$ , respectively, we obtain

$$\frac{dC_3(t_1)}{dt_1} = \frac{g(t_1)}{T}h(t_1). \tag{39}$$

If  $\mu_2 < t_1^* \leq T$ , for this  $t_1^*$ , we have

$$\left. \frac{d^2C_3(t_1)}{dt_1^2} \right|_{t_1=t_1^*} = g(t_1^*) \frac{dh(t_1^*)}{Tdt_1^*} > 0. \tag{40}$$

The function  $h(t_1)$  is given by (31), and (40) implies that  $C_3(t_1)$  can obtain its minimum value at  $t_1^*$ .

The optimal value of the order level,  $S = I(0)$ , is

$$S^* = \int_0^{\mu_1} e^{\alpha x^\beta} f(x) dx + D_0 \int_{\mu_1}^{\mu_2} e^{\alpha x^\beta} dx + \int_{\mu_2}^{t_1^*} e^{\alpha x^\beta} g(x) dx, \tag{41}$$

and the optimal order quantity  $Q^*$  is

$$Q^* = S^* + \int_{t_1^*}^T e^{\delta(t-T)} g(t) dt. \tag{42}$$

If  $t_1^* \leq \mu_2$ , then the optimal value of  $C_3(t_1)$  is obtained at  $t_1^* = \mu_2$ .

The above analysis shows that the three average cost functions  $C_1(t_1)$ ,  $C_2(t_2)$ , and  $C_3(t_1)$  can obtain their minimum value at  $t_1^* \in (0, T)$  which is determined by (31). Therefore, based on the results analyzed above, this paper derives a procedure to locate the optimal replenishment policy starting with no shortage for the three cases. The procedure is as follows.

*Step 1.* Solve  $t_1^*$  from (31).

*Step 2.* Compare  $t_1^*$  to  $\mu_1$  and  $\mu_2$ , respectively.

*Step 2.1.* If  $t_1^* \in (0, \mu_1]$ , then the optimal total average cost and the optimal order quantity can be obtained by (10) and (34), respectively.

*Step 2.2.* If  $t_1^* \in (\mu_1, \mu_2]$ , then the optimal total average cost and the optimal order quantity can be obtained by (18) and (38), respectively.

*Step 2.3.* If  $t_1^* \in (\mu_2, T]$ , then the optimal total average cost and the optimal order quantity can be obtained by (26) and (42), respectively.

*Remark 1.* In such considered inventory model starting with no shortage, if  $t_1$  satisfies  $\mu_1 < t_1 \leq T < \mu_2$ , the considered inventory model reduces to that of Skouri et al. [12].

### 4. Numerical Example

In order to demonstrate the above procedure which can be applied to obtain the optimal solution of the model, this

paper presents several examples for the model, respectively. Examples are based on piecewise demand rate, such as  $f(t) = a_1 + b_1t$  and  $g(t) = a_2e^{-b_2t}$ .

*Example 1.* The parameter values are given as follows:  $T = 12$  weeks,  $\mu_1 = 4$  weeks,  $\mu_2 = 8$  weeks,  $\alpha = 0.005$ ,  $\beta = 2$ ,  $\delta = 0.04$ ,  $a_1 = 30$  unit,  $b_1 = 5$  unit,  $a_2 = 100$  unit,  $A_0 = \$500$ ,  $c_1 = \$2$ ,  $c_2 = \$3$ ,  $c_3 = \$12$ , and  $c_4 = \$8$ .

The model starting with no shortage; by solving the equation  $h(t_1) = 0$ , we have  $t_1^* = 8.7622$ . From (42) and (26), we obtain  $Q^* = 582.5217$  and  $TC(t_1^*) = 793.9986$ , respectively.

*Example 2.* The parameter values are given as follows:  $T = 12$  weeks,  $\mu_1 = 4$  weeks,  $\mu_2 = 8$  weeks,  $\alpha = 0.005$ ,  $\beta = 2$ ,  $\delta = 0.02$ ,  $a_1 = 30$  unit,  $b_1 = 5$  unit,  $a_2 = 100$  unit,  $A_0 = \$500$ ,  $c_1 = \$5$ ,  $c_2 = \$10$ ,  $c_3 = \$12$ , and  $c_4 = \$8$ .

The model starting with no shortage, by solving the equation  $h(t_1) = 0$ , we have  $t_1^* = 5.8330$ . From (38) and (18), we obtain  $Q^* = 528.4725$  and  $TC(t_1^*) = 1601.4013$ , respectively.

*Example 3.* The parameter values are given as follows:  $T = 12$  weeks,  $\mu_1 = 4$  weeks,  $\mu_2 = 6$  weeks,  $\alpha = 0.005$ ,  $\beta = 1.6$ ,  $\delta = 0.2$ ,  $a_1 = 30$  unit,  $b_1 = 5$  unit,  $a_2 = 100$  unit,  $A_0 = \$500$ ,  $c_1 = \$5$ ,  $c_2 = \$10$ ,  $c_3 = \$12$ , and  $c_4 = \$8$ .

The model starting with no shortage, solving the equation  $h(t_1) = 0$ , the optimal value of  $t_1$  is  $t_1^* = 2.3235$ . The optimal ordering quantity is  $Q^* = 272.6678$ , and the minimum cost  $TC(t_1^*) = 1258.82$ .

In order to clearly indicate the effects of parameters such as  $\delta$ ,  $\alpha$ ,  $\beta$ ,  $c_1$ ,  $c_2$ ,  $c_3$ , and  $c_4$  on the optimal on-hand inventory  $S^*$ , the optimal ordering quantity  $Q^*$ , and the optimal total cost  $TC(t_1^*)$ , respectively, the paper will study the sensitivity of the optimal solution to changes in the value of different parameter associated with the studied inventory model. The sensitivity analysis is performed on the base of Example 1, and the results are shown in Table 1–7.

By studying the results of Table 1, it is found that the shortage time  $t_1^*$ , inventory level  $S^*$ , order quantity  $Q^*$ , and the total average cost  $TC(t_1^*)$  gradually decrease as the shortage parameter  $\delta$  increases for the model, respectively. We also find that the percentage increase of  $\delta$  from 14.3% to 100% causes  $TC(t_1^*)$  to decrease from 0.45% to 0.34%,  $Q^*$  decrease from 0.75% to 0.52%,  $t_1^*$  decrease from 0.78% to 0.53%, and  $S^*$  decrease from 1.02% to 0.69%. It is also observed that the value of  $t_1^*$ ,  $S^*$ ,  $Q^*$ , and  $TC(t_1^*)$  all are lowly sensitive to the changes of  $\delta$  for the considered inventory model.

By studying the results of Table 2, it is found that  $S^*$ ,  $Q^*$ , and  $TC(t_1^*)$  coordinates to the deterioration parameter  $\alpha$ ; the shortage time  $t_1^*$  decreases as  $\alpha$  increases for the model. It is also found that the percentage increase of  $\alpha$  from 16.7% to 100% causes  $TC(t_1^*)$  to decrease by 2.066%–2.595%,  $Q^*$  to increase by 1.597%–2.44%, the shortage time  $t_1^*$  to decrease by 1.513%–1.455%, and  $S^*$  to increase by 0.917%–1.651%. It also observes that the value of  $t_1^*$ ,  $S^*$ ,  $Q^*$ , and  $TC(t_1^*)$  all are moderately sensitive to the changes of  $\alpha$  for the considered inventory model.

TABLE 1: The sensitivity of  $\delta$  for the models in Example 1.

$\delta$	0	0.01	0.02	0.03	0.04	0.05	0.06	0.07	0.08
$t_1^*$	8.9664	8.9187	8.8689	8.8167	8.7622	8.7049	8.6449	8.5817	8.5152
$S^*$	472.9889	469.7083	466.2823	462.7001	458.9498	455.0167	450.8910	446.5519	441.9829
$Q^*$	595.6569	592.5872	589.3822	586.0308	582.5217	578.8412	574.9771	570.9112	566.6265
$TC(t_1^*)$	805.6323	802.8699	800.0139	797.0588	793.9986	790.8268	787.5365	784.1200	780.5690

TABLE 2: The sensitivity of  $\alpha$  for the models in Example 1.

$\alpha$	0	0.001	0.002	0.003	0.004	0.005	0.006	0.007
$t_1^*$	9.4545	9.3115	9.1702	9.0312	8.8950	8.7622	8.6328	8.5072
$S^*$	428.3286	435.4002	442.0048	448.1317	453.7785	458.9498	463.6555	467.9088
$Q^*$	523.8866	536.6685	548.9558	560.7091	571.9025	582.5217	592.5618	602.0259
$TC(t_1^*)$	704.6045	722.8867	741.0107	758.9297	776.6035	793.9986	811.0872	827.8474

TABLE 3: The sensitivity of  $\beta$  for the models in Example 1.

$\beta$	1.4	1.6	1.8	2.0	2.2	2.4	2.6	2.8
$t_1^*$	9.2876	9.1810	9.0142	8.7622	8.4047	7.9422	7.4073	6.8496
$S^*$	442.9058	447.5894	453.1802	458.9076	462.8345	461.6422	453.4686	438.8904
$Q^*$	545.1340	554.1055	566.4485	582.4772	601.2274	774.6099	766.4364	751.8582
$TC(t_1^*)$	745.7703	764.3043	791.7624	790.7114	829.3653	588.7417	473.1282	391.1266

TABLE 4: The sensitivity of  $c_1$  for the models in Example 1.

$c_1$	0	0.4	1	1.6	2	2.4	2.6	3	3.6
$t_1^*$	8.8225	8.8103	8.7921	8.7741	8.7622	8.7503	8.7443	8.7326	8.7150
$S^*$	463.0980	462.2595	461.0101	459.7707	458.9498	458.1333	457.7266	456.9164	455.7090
$Q^*$	584.1909	583.8529	583.3499	582.8514	582.5217	582.1940	582.5217	581.7061	581.2226
$TC(t_1^*)$	783.5429	785.6518	788.7984	791.9251	793.9986	796.0633	797.0925	799.1443	802.2061

TABLE 5: The sensitivity of  $c_2$  for the model in Example 1.

$c_2$	0	0.4	0.8	1.2	1.8	2.4	3	3.4	3.8
$t_1^*$	11.8343	11.267	10.7698	10.326	9.7377	9.2216	8.7622	8.4819	8.2196
$S^*$	673.7217	633.0852	597.9589	566.9228	526.1187	490.5382	458.9498	439.6922	421.6606
$Q^*$	679.6039	659.4483	642.7261	628.4787	610.4744	595.4175	582.5217	574.8648	567.8284
$TC(t_1^*)$	67.2679	193.9216	308.8975	413.9636	555.8150	681.6692	793.9986	862.3253	925.9516

TABLE 6: The sensitivity of  $c_3$  for the models in Example 1.

$c_3$	10.4	10.6	10.8	11	11.2	11.6	12	12.4	12.8
$t_1^*$	8.4424	8.4859	8.5284	8.5698	8.6102	8.6879	8.7622	8.8329	8.9005
$S^*$	436.9771	439.9713	442.889	445.7332	448.5071	453.854	458.9498	463.8114	468.4587
$Q^*$	573.7973	574.9747	576.1255	577.2506	578.3509	580.4809	582.5217	584.4787	586.3587
$TC(t_1^*)$	763.8057	767.9203	771.9299	775.8387	779.6505	786.9976	793.9986	800.6779	807.0579

TABLE 7: The sensitivity of  $c_4$  for the models in Example 1.

$c_4$	0	2	4	6	8	10	12	14	16
$t_1^*$	8.6989	8.7150	8.7309	8.7466	8.7622	8.7775	8.7928	8.8078	8.82272
$S^*$	454.6069	455.7103	456.8017	457.8815	458.9498	460.0048	461.0527	462.0877	463.1120
$Q^*$	580.7818	581.2231	581.6601	582.0929	582.5217	582.9455	583.367	583.7837	584.1966
$TC(t_1^*)$	788.1626	789.6445	791.1109	792.5621	793.9986	795.4203	796.8276	798.2207	799.5999

By studying the results of Table 3, it is found that  $S^*$ ,  $Q^*$ , and  $TC(t_1^*)$  coordinate to the deterioration parameter  $\beta$ , while the shortage time  $t_1^*$  decreases as  $\beta$  increases for the model. It is also found that the increase of  $\beta$  from 1.4 to 2.2 causes  $S^*$  to increase, while the increase of  $\beta$  from 2.4 to 2.8 causes  $S^*$  to decrease,  $Q^*$  to increase by 2.44%–1.597%,  $TC(t_1^*)$  to increase by 2.595%–2.066%, and the shortage time  $t_1^*$  to decrease by 1.513%–1.455%. It is also observed that the value of  $t_1^*$ ,  $S^*$ ,  $Q^*$ , and  $TC(t_1^*)$  all are moderately sensitive to the changes of  $\beta$  for the considered inventory model.

By studying the results of Table 4, it is found that  $TC(t_1^*)$  coordinate to  $c_1$ , while the shortage time  $t_1^*$ ,  $S^*$ , and  $Q^*$  decrease as  $c_1$  increases for the model. It is also found that  $c_1$  increases from 8.3% to 150%,  $TC(t_1^*)$  decreases by 0.269%–0.383%,  $Q^*$  decreases by 0.083%–0.058%,  $t_1^*$  decreases by 0.264%–0.181%, and  $S^*$  decreases by 0.203%–0.138%, respectively. It is also observed that the values of  $t_1^*$ ,  $S^*$ ,  $Q^*$ , and  $TC(t_1^*)$  all are lowly sensitive to the changes of  $c_1$  for the considered inventory model.

By studying the results of Table 5, it is found that  $TC(t_1^*)$  coordinates to  $c_2$ , while  $S^*$ ,  $Q^*$ , and  $t_1^*$  decrease as  $c_2$  increases for the model. It is also found that  $c_2$  increases by 100%,  $TC(t_1^*)$  decreases by 0.269%–0.383%,  $Q^*$  decreases by 0.083%–0.058%,  $t_1^*$  decreases by 0.264%–0.181%, and  $S^*$  decreases by 0.203%–0.138%.

By studying the results of Table 6, it is found that  $t_1^*$ ,  $S^*$ ,  $Q^*$ , and  $TC(t_1^*)$  coordinate to  $c_3$ . It is also observed that the value of  $t_1^*$ ,  $S^*$ ,  $Q^*$ , and  $TC(t_1^*)$  all are lowly sensitive to the changes of  $c_3$  for the inventory models; that is,  $c_3$  increases from 1.9% to 3.2%, the change of all the parameters is no more than 1%.

By studying the results of Table 7, it is found that  $t_1^*$ ,  $S^*$ ,  $Q^*$ , and  $TC(t_1^*)$  coordinate to  $c_4$ . It is also observed that the value of  $t_1^*$ ,  $S^*$ ,  $Q^*$ , and  $TC(t_1^*)$  all are lowly sensitive to the changes of  $c_4$  for the inventory models; that is,  $c_4$  increases from 14.3% to 100%, the change of all the parameters is no more than 1%.

## 5. Conclusion

An inventory model starting without shortage for Weibull-distributed deterioration with trapezoidal type demand rate and partial backlogging is considered in this paper. The optimal replenishment policy for the inventory model is proposed, and numerical examples are provided to illustrate the theoretical results. A sensitivity analysis of the optimal solution with respect to major parameters is also carried out. From Table 1–7, it can be found that the shortage time point  $t_1^*$ , order quantity  $Q^*$ , and the total average cost  $TC(t_1^*)$  are moderately sensitive to the changes of  $\alpha$  and  $\beta$  and lowly sensitive to the changes of  $\delta$ ,  $c_i$  ( $i = 1, 2, 3, 4$ ), respectively. The paper provides an interesting topic for further study, such that the joint influence from some of these parameters may be investigated to show the effects; the model starting with shortage will be studied and other types of models for deteriorating items in supply chain situation are also to be studied in the future.

## Conflict of Interests

The author declares that there is no conflict of interests regarding the publication of this paper.

## Acknowledgments

The author is grateful to the anonymous referees who provided valuable comments and suggestions to significantly improve the quality of the paper. This work was supported partly by Humanities and Social Science Fund of the Ministry of Education of China (no. 11YJCZH019).

## References

- [1] P. M. Ghare and G. F. Schrader, "A model for exponentially decaying inventories," *Journal of Industrial Engineering*, vol. 14, pp. 238–243, 1963.
- [2] J.-W. Wu, C. Lin, B. Tan, and W.-C. Lee, "An EOQ inventory model with time-varying demand and Weibull deterioration with shortages," *International Journal of Systems Science*, vol. 31, no. 6, pp. 677–683, 2000.
- [3] H.-M. Wee, "Deteriorating inventory model with quantity discount, pricing and partial backordering," *International Journal of Production Economics*, vol. 59, no. 1, pp. 511–518, 1999.
- [4] K. Skouri and S. Papachristos, "A continuous review inventory model, with deteriorating items, time-varying demand, linear replenishment cost, partially time-varying backlogging," *Applied Mathematical Modelling*, vol. 26, no. 5, pp. 603–617, 2002.
- [5] H.-M. Wee, J. C. P. Yu, and S. T. Law, "Two-warehouse inventory model with partial backordering and Weibull distribution deterioration under inflation," *Journal of the Chinese Institute of Industrial Engineers*, vol. 22, no. 6, pp. 451–462, 2005.
- [6] C.-Y. Dye, T.-P. Hsieh, and L.-Y. Ouyang, "Determining optimal selling price and lot size with a varying rate of deterioration and exponential partial backlogging," *European Journal of Operational Research*, vol. 181, no. 2, pp. 668–678, 2007.
- [7] R. M. Hill, "Inventory models for increasing demand followed by level demand," *Journal of the Operational Research Society*, vol. 46, no. 10, pp. 1250–1259, 1995.
- [8] B. Mandal and A. K. Pal, "Order level inventory system with ramp type demand rate for deteriorating items," *Journal of Interdisciplinary Mathematics*, vol. 1, no. 1, pp. 49–66, 1998.
- [9] K.-S. Wu, "An EOQ inventory model for items with Weibull distribution deterioration, ramp type demand rate and partial backlogging," *Production Planning & Control*, vol. 12, no. 8, pp. 787–793, 2001.
- [10] B. C. Giri, A. K. Jalan, and K. S. Chaudhuri, "Economic order quantity model with Weibull deterioration distribution, shortage and ramp-type demand," *International Journal of Systems Science*, vol. 34, no. 4, pp. 237–243, 2003.
- [11] S. K. Manna and K. S. Chaudhuri, "An EOQ model with ramp type demand rate, time dependent deterioration rate, unit production cost and shortages," *European Journal of Operational Research*, vol. 171, no. 2, pp. 557–566, 2006.
- [12] K. Skouri, I. Konstantaras, S. Papachristos, and I. Ganas, "Inventory models with ramp type demand rate, partial backlogging and Weibull deterioration rate," *European Journal of Operational Research*, vol. 192, no. 1, pp. 79–92, 2009.

- [13] K.-C. Hung, "An inventory model with generalized type demand, deterioration and backorder rates," *European Journal of Operational Research*, vol. 208, no. 3, pp. 239–242, 2011.
- [14] R. S. Kumar, S. K. De, and A. Goswami, "Fuzzy EOQ models with ramp type demand rate, partial backlogging and time dependent deterioration rate," *International Journal of Mathematics in Operational Research*, vol. 4, no. 5, pp. 473–502, 2012.
- [15] M. B. Cheng, B. X. Zhang, and G. Q. Wang, "Optimal policy for deteriorating items with trapezoidal type demand and partial backlogging," *Applied Mathematical Modelling*, vol. 35, no. 7, pp. 3552–3560, 2011.
- [16] R. Uthayakumar and M. Rameswari, "An economic production quantity model for defective items with trapezoidal type demand rate," *Journal of Optimization Theory and Applications*, vol. 154, no. 3, pp. 1055–1079, 2012.
- [17] Y. Tan and M. X. Weng, "A discrete-in-time deteriorating inventory model with time-varying demand, variable deterioration rate and waiting-time-dependent partial backlogging," *International Journal of Systems Science*, vol. 44, no. 8, pp. 1483–1493, 2013.
- [18] M. A. Ahmed, T. A. Al-Khamis, and L. Benkherouf, "Inventory models with ramp type demand rate, partial backlogging and general deterioration rate," *Applied Mathematics and Computation*, vol. 219, no. 9, pp. 4288–4307, 2013.
- [19] K.-P. Lin, "An extended inventory models with trapezoidal type demands," *Applied Mathematics and Computation*, vol. 219, no. 24, pp. 11414–11419, 2013.
- [20] P. L. Abad, "Optimal pricing and lot-sizing under conditions of perishability and partial backordering," *Management Science*, vol. 42, no. 8, pp. 1093–1104, 1996.

## Research Article

# Predictive Models of Current, Voltage, and Power Losses on Electric Transmission Lines

O. M. Bamigbola,<sup>1</sup> M. M. Ali,<sup>2</sup> and K. O. Awodele<sup>3</sup>

<sup>1</sup> Department of Mathematics, University of Ilorin, Ilorin 240003, Nigeria

<sup>2</sup> School of Computational and Applied Mathematics, Faculty of Science, and TCSE, Faculty of Engineering and the Built Environment, University of the Witwatersrand (Wits), Private Bag 3, Johannesburg 2050, South Africa

<sup>3</sup> Department of Electrical Engineering, University of Cape Town, Private Bag X3, Rondebosch, Cape Town 7701, South Africa

Correspondence should be addressed to M. M. Ali; [montaz.ali@wits.ac.za](mailto:montaz.ali@wits.ac.za)

Received 2 January 2014; Accepted 1 February 2014; Published 5 March 2014

Academic Editor: Aderemi Oluyinka Adewumi

Copyright © 2014 O. M. Bamigbola et al. This is an open access article distributed under the Creative Commons Attribution License, which permits unrestricted use, distribution, and reproduction in any medium, provided the original work is properly cited.

A modern and civilized society is so much dependent on the use of electrical energy because it has been the most powerful vehicle for facilitating economic, industrial, and social developments. Electrical energy produced at power stations is transmitted to load centres from where it is distributed to its consumers through the use of transmission lines run from one place to another. As a result of the physical properties of the transmission medium, some of the transmitted power is lost to the surroundings. The overall effect of power losses on the system is a reduction in the quantity of power available to the consumers. An accurate knowledge of transmission losses is hinged on the ability to correctly predict the available current and voltage along transmission lines. Therefore, mathematical physics expressions depicting the evolution of current and voltage on a typical transmission line were formulated, and derived therefrom were models to predict available current and voltage, respectively, at any point on the transmission line. The predictive models evolved as explicit expressions of the space variable and they are in close agreement with empirical data and reality.

## 1. Introduction

The importance of electric power in today's world cannot be overemphasized for it is the key energy source for industrial, commercial, and domestic activities [1]. Its availability in the right quantity is essential to the advancement of civilization.

Electrical energy is generated at power stations which are usually situated far away from load centers. As such, an extensive network of conductors between the power stations and the consumers is required. This network of conductors may be divided into two main components, called the transmission system and the distribution system. The transmission system is to deliver bulk power from power stations to load centers and large industrial consumers while the distribution system is to deliver power from substations to various consumers.

The efficiency of the transmission component of the electric power system is known to be hampered by a number

of problems, especially in third-world countries. The major problems identified in [2] include application of inappropriate technology, inadequacy of materials, equipment, and man power.

From the physics of electric power transmission, when a conductor is subjected to electric power (or voltage), electric current flows in the medium. Resistance to the flow produces heat (thermal energy) which is dissipated to the surroundings. This power loss is referred to as ohmic loss [3]. Furthermore, if the applied voltage exceeds a critical level, another type of power loss, called the corona effect [4], occurs. The power losses accumulate as the induced current flows and the corona effect propagate along the transmission lines. The power losses could take off a sizeable portion of the transmitted power since transmission lines usually span a long distance, sometimes several hundred kilometers [5]. The overall effect of power losses on the system is a reduction in the quantity of power available to the consumers. Therefore,

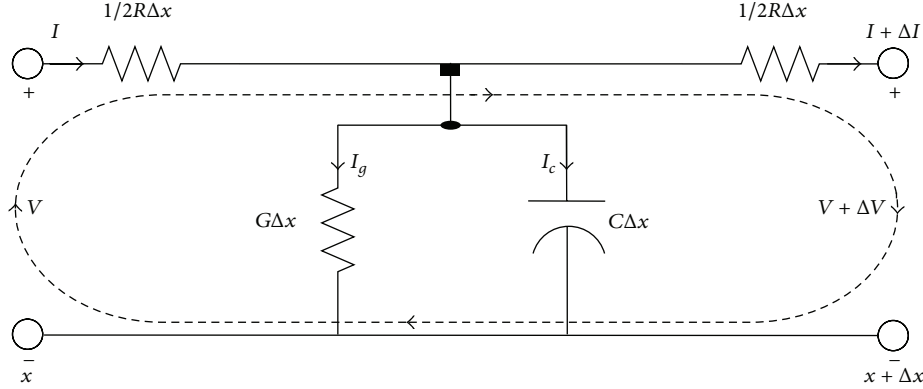


FIGURE 1: Equivalent circuit of a transmission line.

an accurate knowledge of power losses on transmission lines will be useful in planning for the supply of sufficient quantity of power needed in an electrical network.

One way of mitigating losses in the process of transmitting electric power is to apply some strategies to reduce the losses. Ramesh et al. [6] looked at minimization of power loss in distribution networks by using feeder restructuring, implementation of distributed generation, and capacitor placement method. Rugthaicharoencheep and Sirisumranukul [7] employed the use of feeder reconfiguration for loss reduction in distribution system with distributed generators by Tabu Search. Sinsuphun et al. [8] worked on loss minimization using optimal power flow based on swarm intelligences. Recently, the classical optimization technique was applied to formulate the optimal strategy that reduces the transmission power losses to the barest minimum [9]. The strategy is to transmit electric power at very low current with high operating voltage close to the critical disruptive voltage and the spacing between the transmission lines not less than the value of  $r \cdot e^{U_p/18r}$  where  $r$  and  $U_p$  are radiuses of the transmission medium and the phase voltage, respectively.

In this paper, we propose mathematical models for predicting available current and voltage as well as the power losses along a typical transmission line so as to be able to reckon the net electric power available to be used to meet customers' demands. In the process, the evolution of current and voltage on the transmission line is studied and models to predict both current and voltage were constructed. In the end, the desired model for predicting power losses along transmission lines were formulated by reframing the power loss function as a mathematical physics problem. This strategy led to the exclusion of all the transmission parameters from the model.

In the next section, we derive the equations that characterise the evolution of electric current and voltage on a typical transmission line. In Section 3, a predictive model of the power losses incurred at different locations on the transmission line is obtained. An analysis of the models is conducted and discussed in Section 4, while the paper is concluded in Section 5.

## 2. Power Flow on Transmission Lines

In this section, we derive the expressions which voltage and current must satisfy on uniform transmission lines. A real transmission line will have some series resistance associated with power losses in the conductor [10]. There may also be some shunt conductance if the insulating material holding two conductors has some leakage current. Therefore, resistance and conductance are responsible for power losses on transmission lines [11]. To this end, we formulate a model for a lossy transmission line where the effect of the series resistance ( $R$ ) and shunt conductance ( $G$ ) is taken care of on the transmission lines.

*2.1. Model Formulation.* Herein, we are interested in determining the extent to which voltage and current outputs differ from their input values over an elemental portion of the transmission line. As such, we consider an equivalent circuit of a transmission line of length  $\Delta x$  containing resistance  $R\Delta x$  and conductance  $G\Delta x$  as shown in Figure 1. The circuit illustrates how power (both voltage and current) flow through the transmission medium is considered positioned along the space variable  $x$  ([12], pp. 255–260). Applying the Kirchoff voltage law [13] on the equivalent circuit of the transmission line, we have

$$V = \frac{1}{2}RI\Delta x + \frac{1}{2}R[I + \Delta I]\Delta x + V + \Delta V, \quad (1)$$

which on simplification, dividing through by  $\Delta x$  and taking limits as  $\Delta x$  tends to zero, is simplified to

$$\frac{dV}{dx} = -RI, \quad (2)$$

and from which we have

$$\frac{d^2V}{dx^2} = -R\frac{dI}{dx}. \quad (3)$$

Using the Kirchoff current law [13],

$$I = \frac{1}{2}G\left(V + \frac{\Delta V}{2}\right)\Delta x + C\frac{d}{dt}\left(V + \frac{\Delta V}{2}\right)\Delta x + I + \Delta I, \quad (4)$$

which also on simplification, dividing through by  $\Delta x$  and taking limits as  $\Delta x$  tends to zero, is simplified to

$$\frac{dI}{dx} = - \left[ GV + C \frac{dV}{dt} \right], \quad (5)$$

which is further simplified to

$$\frac{dI}{dx} = -GV, \quad (6)$$

since  $V$  is independent of  $t$ . Differentiating (6) with respect to  $x$  again results in

$$\frac{d^2 I}{dx^2} = -G \frac{dV}{dx}. \quad (7)$$

Substituting (6) into (3) and (2) into (7) yields

$$\frac{d^2 V}{dx^2} = RGV, \quad (8)$$

$$\frac{d^2 I}{dx^2} = RGI. \quad (9)$$

Equations (8) and (9) are mathematical physics expressions that characterise the power flow along the transmission lines.

Solving power (voltage) flow equation (8) which is subject to the boundary conditions,

$$\begin{aligned} V(0) &= V_0 \\ V(l) &= 0, \quad l \rightarrow \infty, \end{aligned} \quad (10)$$

where  $V_0$  is the initial voltage, results in

$$V(x) = V_0 e^{-x\sqrt{RG}}. \quad (11)$$

The equivalent solution to (9) for current flow along the transmission line is

$$I(x) = I_0 e^{-x\sqrt{RG}}, \quad (12)$$

where  $I_0$  denotes the initial current in the circuit.

With the aid of the last two equations, the quantity of current and voltage at any point on the transmission line can be discerned. Table 1 presents the predicted current and voltage at some points on a typical 330 kV single circuit of the Nigerian transmission network. Presently, the maximum length of the transmission network is about 300 km.

In the next section, we seek to predict the total power losses over a typical transmission line.

### 3. Power Losses on Transmission Lines

The main reason for losses on transmission lines is the resistance of the conductor against the flow of current [14]. As a result, heat is produced in the conductor and this increases the temperature of the conductor. The rise in the conductor's temperature further increases the resistance of the conductor

TABLE 1: Current and voltage along a 330 kV single circuit of a typical transmission network with  $RG = 7.15 \times 10^{-5}$ .

Length of line (km)	Current (A)	Voltage (kV)
10	19.14	329.5
20	19.09	329.1
50	19.00	327.6
100	18.87	325.3
200	18.60	320.7
300	18.33	316.1

and this consequently increases the power losses. The value of the ohmic power loss [15] is given as

$$L_O = I^2 R, \text{ (kW)}, \quad (13)$$

where  $I$  denotes current along the conductor and  $R$  represents resistance of the conductor.

The formation of corona on transmission lines is associated with loss of power too, which will have some effect on the efficiency of the transmission line [16]. Corona discharge has to do with emission of ions from the surface of the transmission medium [17]. The corona power loss for a fair weather condition [18, 19] has the value

$$L_C = 242 \frac{(f + 25)}{\delta} \cdot \sqrt[4]{\frac{r}{d}} (V - V_c)^2 \cdot (10)^{-5} \text{ kW}, \quad (14)$$

where  $f$  represents the frequency of transmission,  $\delta$  denotes the air density factor,  $r$  is radius of the conductor,  $d$  represents the space between the transmission lines,  $V$  is the operating voltage, and  $V_c$  denotes the disruptive voltage. High voltage gradients of above 18 kV/cm surrounding conductors is known to cause corona discharge ([20], pg. 645).

The total losses on a transmission line is then given as

$$T_L = L_O + L_C. \quad (15)$$

That is,

$$T_L = I^2 R + 242 \frac{(f + 25)}{\delta} \cdot \sqrt[4]{\frac{r}{d}} (V - V_c)^2 \cdot (10)^{-5}. \quad (16)$$

The power losses are therefore given by

$$T_L = RI^2 + 242 \frac{(f + 25)}{\delta} \cdot \sqrt[4]{\frac{r}{d}} (V - V_c)^2 \cdot (10)^{-5} \text{ kW}. \quad (17)$$

*3.1. Predictive Model.* It would have sufficed to substitute  $V$  and  $I$  from (11) and (12) into (17) so as to obtain an expression for the transmission losses but the transmission parameters  $f$ ,  $\delta$ ,  $r$ , and  $d$  would have remained as undetermined factors. As such, it is more desirable to rewrite (17) implicitly in terms of the space variable  $x$ . Thus from (17),

$$\frac{d^2 T_L}{dx^2} = R \frac{d^2}{dx^2} I^2 + 242 \frac{(f + 25)}{\delta} \cdot \sqrt[4]{\frac{r}{d}} \frac{d^2}{dx^2} (V - V_c)^2 \cdot (10)^{-5}. \quad (18)$$

TABLE 2: Predicted power losses for a 330 kV single circuit of the typical transmission network.

Length of line in km	Power losses (in MW) for a load of 100 MW $\alpha = 0.00005$	Power losses (in MW) for a load of 200 MW $\alpha = 0.00009$	Power losses (in MW) for a load of 300 MW $\alpha = 0.00014$
10	0.0500	0.1800	0.4300
20	0.1000	0.3598	0.8594
50	0.2500	0.8983	2.1438
100	0.5000	1.7927	4.2724
200	0.9953	3.5694	8.4839
300	1.4892	5.3301	12.6354

TABLE 3: Simulated results of power losses on 330 kV single circuit of the Nigerian transmission network.

Length of line in km	Power losses (in MW) for a load of 100 MW	Power losses (in MW) for a load of 200 MW	Power losses (in MW) for a load of 300 MW
10	0.05	0.18	0.43
20	0.09	0.37	0.87
40	0.18	0.73	1.75
60	0.26	1.10	2.84
100	0.41	1.85	4.66
200	0.76	3.77	10.86
300	1.10	5.85	24.40

On integrating and utilising (2)–(9), (18) is simplified to

$$\frac{d^2 T_L}{dx^2} - 2RG(1 + RG)T_L = 0. \quad (19)$$

Solving (19) together with the requisite boundary conditions

$$\begin{aligned} T_L(0) &= 0, \\ T_L(l) &= P_0, \quad l \rightarrow \infty, \end{aligned} \quad (20)$$

where  $P_0$  denotes the transmitted power. The solution to the transmission power losses model is obtained as

$$T_L = P_0(1 - e^{-\alpha x}), \quad (21)$$

where  $\alpha = \sqrt{2RG(1 + RG)}$ .

Table 2 presents the predicted power losses for a 330 kV single circuit of the Nigerian transmission network.

Table 3 presents the results obtained by Onohaebi and Odiase [21] using the power world simulator for loads of 100 MW, 200 MW, and 300 MW with the associated impedances for various lengths.

#### 4. Analysis and Discussion of Results

Perusal of the results presented in Tables 1 and 2 confirms consistency in reduction of the numerical solutions returned,

and so the results are in line with reality. On the other hand the results in Table 3 show close agreement with those in Table 2. Hence, the predictions are in line with reality and empirical data.

The evolution of current and voltage on high tension transmission lines as well as the power losses when modelled evolved as second order ordinary differential equations. With appropriate boundary conditions, the solutions obtained are prescribed in closed forms. Allotting values to the input factors, numerical values were obtained for the requisite factors—current, voltage, and power losses.

An advantage of the analytic expressions obtained in this study is that numerical values can be computed with a hand-held calculator unlike in the method of Král et al. [22] that requires the use of a software package.

Based on the above observations, the models can be used to predict requisite electrical measures along typical transmission lines. With these measures, electric transmission-related activities can be planned with a view to enhancing efficiency of the electric power system.

#### 5. Conclusion

The equations describing the evolution of current and voltage along transmission lines have been utilised to fashion tools to predict requisite electrical measures such as current, voltage, and power losses.

The evolution of current and voltage on transmission lines is a process that can aid the determination of current and voltage as a function of the space variable  $x$  on transmission lines. Fashioning the power loss function as a mathematical physics expression led to the formulation of a predictive model for power losses explicitly in terms of the space variable only.

#### Conflict of Interests

The authors declare that there is no conflict of interests regarding the publication of this paper.

#### References

- [1] O. I. Okoro and E. Chikuni, “Power sector reforms in Nigeria: opportunities and challenges,” *Journal of Energy in Southern Africa*, vol. 18, no. 3, pp. 52–57, 2007.
- [2] A. P. Kenneth and A. T. John, “The benefit of distribution generation to the Nigerian electric utility system,” *Journal of Basic and Applied Scientific Research*, vol. 3, no. 2, pp. 381–385, 2013.
- [3] T. Smed, G. Andersson, G. B. Sheble, and L. L. Grigsby, “A new approach to AC/DC power flow,” *IEEE Transactions on Power Systems*, vol. 6, no. 3, pp. 1238–1244, 1991.
- [4] A. Sakhavati, M. Yaltagiani, S. S. Ahari, and S. S. Mahaei, “765 kV transmission line design (Electrical section),” *International Journal of Electrical and Computer Engineering*, vol. 2, no. 5, pp. 698–707, 2012.
- [5] M. W. Gustafson and J. S. Baylor, “Transmission loss evaluation for electric systems,” *IEEE Transactions on Power Systems*, vol. 3, no. 3, pp. 1026–1032, 1988.

- [6] L. Ramesh, S. P. Chowdhury, S. Chowdhury, A. A. Natarajan, and C. T. Gaunt, "Minimization of power loss in distribution networks by different techniques," *International Journal of Electrical Power and Energy Systems Engineering*, vol. 2, no. 1, pp. 1–6, 2009.
- [7] N. Rugthaicharoencheep and S. Sirisumrannukul, "Feeder reconfiguration for lossreduction in distribution system with distributed generators by Tabu Search," *GMSARN International Journal*, vol. 3, pp. 47–54, 2009.
- [8] N. Sinsuphun, U. Leeton, U. Kwannetr, D. Uthitsunthorn, and T. Kulworawanichpong, "Loss minimization using optimal power flow based on swarm intelligences," *Transactions on Electrical Engineering, Electronics, and Communications*, vol. 9, no. 1, pp. 212–222, 2011.
- [9] O. M. Bamigbola, M. M. Ali, and M. O. Oke, "Mathematical modeling of electric power flow and the minimization of power losses on power transmission lines," submitted.
- [10] H. Ambriz-Pérez, E. Acha, and C. R. Fuerte-Esquivel, "High voltage direct current modelling in optimal power flows," *International Journal of Electrical Power and Energy Systems*, vol. 30, no. 3, pp. 157–168, 2008.
- [11] T. Dhaene and D. De Zutter, "Selection of lumped element models for coupled lossy transmission lines," *IEEE Transactions on Computer-Aided Design of Integrated Circuits and Systems*, vol. 11, no. 7, pp. 805–815, 1992.
- [12] J. D. Glover, M. S. Sarma, and T. J. Overby, *Power System and Design*, Cengage Learning, Stamford, Conn, USA, 5th edition, 2008.
- [13] C. R. Paul, *Fundamentals of Electric Circuit Analysis*, John Wiley, 2001.
- [14] V. Král, S. Rusek, and L. Rudolf, "Calculation and estimation of technical losses in transmission networks," *Electrical Review*, vol. 88, no. 8, pp. 88–91, 2012.
- [15] I. Sarajcev, M. Majstrovic, and I. Medic, "Calculation of losses in electric power cables as the base for cable temperature analysis," *Journal of Advanced Computational Methods in Heat Transfer*, vol. 4, pp. 529–537, 2003.
- [16] M. H. Hesse, "Electromagnetic and electrostatic transmission line parameters by digital computer," *IEEE Transactions on Power Apparatus and Systems*, vol. 82, pp. 282–291, 1963.
- [17] M. Abdel-Salam, *Electrical Breakdown of Gases in High-Voltage Engineering: Theory and Practice*, Marcel Dekker, New York, NY, USA, 2000, edited by, M.E. Khalifa.
- [18] A. M. James, *Electric Power System Applications of Optimization*, McGraw-Hill, 2005.
- [19] M. P. Bahrman and B. K. Johnson, "The ABCs of HVDC transmission technologies," *IEEE Power and Energy Magazine*, vol. 5, no. 2, pp. 32–44, 2007.
- [20] C. R. Bayliss and B. J. Hardy, *Transmission and Distribution Electrical Engineering*, Elsevier, Amsterdam, The Netherlands, 2007.
- [21] O. S. Onohaebi and O. F. Odiase, "Empirical modelling of power losses as a function of line loadings and lengths in the Nigeria 330 kV transmission lines," *International Journal of Academic Research*, vol. 2, no. 3, pp. 47–53, 2010.
- [22] V. Král, S. Rusek, and L. Rudolf, "Software for calculation of technical losses in transmission network," *Przegląd Elektrotechniczny*, vol. 87, no. 2, pp. 91–93, 2011.

## Research Article

# Centralized Resource Allocation for Connecting Radial and Nonradial Models

A. Mirsalehy,<sup>1</sup> M. R. Abu Bakar,<sup>1,2</sup> G. R. Jahanshahloo,<sup>3</sup>  
F. Hosseinzadeh Lotfi,<sup>3</sup> and L. S. Lee<sup>1,2</sup>

<sup>1</sup> Department of Mathematics, Faculty of Science, Universiti Putra Malaysia (UPM), 43400 Serdang, Selangor, Malaysia

<sup>2</sup> Institute for Mathematical Research, Universiti Putra Malaysia (UPM), 43400 Serdang, Selangor, Malaysia

<sup>3</sup> Department of Mathematics, Science and Research Branch, Islamic Azad University, Tehran, Iran

Correspondence should be addressed to A. Mirsalehy; [mirsalehi.ali@yahoo.com](mailto:mirsalehi.ali@yahoo.com)

Received 21 October 2013; Revised 8 January 2014; Accepted 8 January 2014; Published 4 March 2014

Academic Editor: Aderemi Oluyinka Adewumi

Copyright © 2014 A. Mirsalehy et al. This is an open access article distributed under the Creative Commons Attribution License, which permits unrestricted use, distribution, and reproduction in any medium, provided the original work is properly cited.

This paper examines an alternative approach to the centralized resource allocation model that indicates that all the units are under the control of an entity of the centralized decision maker. The proposed approach is a technique for connecting the two basic Radial CRA-BCC and Nonradial CRA-SBM models in an integrated structure called connected CRA-SBM. In the proposed model, exchanging the two parameter amounts can change the location of the analysis between the CRA-BCC and the CRA-SBM models and deal with the weaknesses inherent in such models. By remedying all the weaknesses in one model, the entire units are simply projected on the frontier line and one can obtain suitable benchmarks for each of them. In the offered model, all of the inputs and outputs, respectively, decrease and increase simultaneously. Lastly, numerical examples emphasize the significance of the offered method.

## 1. Introduction

The Data Envelopment Analysis (DEA) was first presented by Charnes et al. [1] and further developed by Banker et al. [2]. The DEA is a nonparametric LP-based method for evaluating the efficiency score of a number of homogeneous decision-making units (DMUs). There has been literature over the years concerned with the new corrections and developments in both the DEA notion and procedure (see Liu et al. [3], Emrouznejad et al. [4], and Gattoufi et al. [5]).

As a matter of fact, the DEA models are commonly categorized into two types with distinguishing qualities, namely, the radial and nonradial models. In effect, the preliminary works on the radial models were undertaken by Debreu [6] and Farrell [7]. By now, numerous desirable features have been identified in radial measures; for instance, they can generally obtain the relative development in inputs and outputs; moreover, they are potential of estimating the efficiency based on the attainable data or they can provide an obvious economic explanation without considering the

prices. Notwithstanding their strengths, these models suffer from the subsequent drawbacks.

- (a) They assess the efficiency based on the existing data without considering the decision maker's (DM's) precedence knowledge.
- (b) Due to the proportional improvement in these models, they cannot be employed for the cases with inputs such as labors, materials, and capital.
- (c) The DM does not have the flexibility to select a reference unit for an inefficient unit.
- (d) Finally, they are unable to essentially achieve an efficient goal in the DEA.

At first, analyzing the nonradial models was carried out by Koopmans [8] and Robert Russell [9]. Yet, numerous studies have attempted to explain the nonradial measures for the technical efficiency based on the performance estimation (see Cooper et al. [10], Charnes et al. [11], Cooper et al. [12], Pastor et al. [13], and Cooper et al. [14]). In one major study,

Tone [15] employed a new and suitable synthetic procedure to obtain a nonradial measure which was termed the slacks-based measure (SBM) in which both the input and output slacks could be maximized. A number of methods have been also used to describe the nonradial measure, each of which has its own advantages and disadvantages. These models have a number of attractive features; for example, they put aside the supposition of proportional reduction in the inputs and target at earning maximum amounts of contraction in inputs which might abandon the changing rates of the original input resources. Nevertheless, the nonradial models suffer from several major downsides listed below in spite of their safety and efficacy.

- (a) When we evaluate changes in the efficiency during the time, the nonzero pattern of the slacks at time period  $t$  can meaningfully differ from that of the time period  $t + 1$ . Therefore, we cannot ascertain whether the pattern is rational or not.
- (b) When we miss the primary proportionality, it would be then unsuitable for the investigation.
- (c) At last, in models like the SBM model, the optimum slacks would exhibit an acute conflict in catching the positive and zero amounts.

Avkiran et al. [16] proposed the “connected-SBM” model using two scalar parameters which could deal with the above-mentioned weaknesses of the radial and nonradial models. In their approach, they relocated the analysis anywhere between the radial and nonradial models by exchanging the parameter amounts and making an appropriate selection.

In a large longitudinal study by Lozano and Villa [17], there were various conditions in which all the DMUs could be in the possession of the central entity (public or private) so that it prepared the DMUs with the resources essential for earning their inputs. In particular, various applications related to the DEA (e.g., public transportation, police stations, university departments, bank branches, and hospitals) have been taken into account as centralized decision makers that manage and supervise such DMUs. Prior to this, Lozano and Villa [17], attempted to handle the DMUs in a common manner (see Thanassoulis and Dyson [18], Golany [19], Färe et al. [20], Kumar and Sinha [21], Beasley [22], and Athanassopoulos [23, 24]). To this end, it can be said that numerous studies have attempted so far to explain the allocating resources as well as the evaluating goals. Lozano and Villa [17] and Lozano et al. [25] presented the CRA-BCC models wherein the resolving one model in two phases causes the entire DMUs to be reflected on the frontier line. Their study can be majorly mentioned as an unusual item based on the radial model. The assertion behind this model is to consider a situation in which the centralized decision maker decides to minimize the total input consumption or maximize the total output production, simultaneously. Lozano and Villa [26] also proposed the models which deliberated the CRA models when some of the inputs reductions and the outputs remained unchanged. Moreover, a DEA approximation for the emission permits along with a discussion on the desired and undesired levels has been proposed by Lozano et al. [27]. Several studies

have produced estimates of the CRA models as well (see Pachkova [28], Liu and Tsai [29], and Fang and Zhang [30]). In another main study, Asmild et al. [31] reported a CRA model for the BCC model in which all the inefficient DMUs had been only reflected on the frontier line. In a randomized controlled study on the CRA, Hosseinzadeh Lotfi et al. [32] described a centralized model for the enhanced Russell model (CRA-ERM) and the SBM model (CRA-SBM) so that all the DMUs could be easily projected onto the frontier line by solving only one model.

Although there have been many suppositions about the idea of the centralized resource allocation, it has not been recognized as a perfect viewpoint yet. When bearing in mind the organizations which function under a multilevel supervision hierarchy, definite resources utilized or the outputs created which cannot be controlled must be recognized using the local DMUs. Consequently, it is pertinent to mention the potential of improving these centrally allocated resources in a central manner for manufacturing purposes.

This study seeks to alleviate these problems by introducing alternative new CRA-DEA models while consequently creating new tools ready for use in central management. In fact, the purpose of this paper is to minimize the total input consumption and maximize the total output production of the DMUs at the same time. Moreover, we will demonstrate that the CRA-BCCI and CRA-SBMI models can be joined by retouching the two parameters and selecting them. The objectives of this research are to determine whether we can oversee the appropriateness of slacks (inefficiencies) with the resources essential for the user, and whether we can solve the issue of the mixed slacks amounts in conditions existing at the same time for the DEA with parametric methods.

The remainder of this paper has been divided into five parts. In Section 2, the CRA-BCCI, the CRA-SBMI and the connected-SBM models are presented while Section 3 presents our proposed model and explains it with numerical examples. In Section 4, by considering our procedure in organizations, we extend it into a weighted nonoriented model and following that, the results are also checked out using the numerical examples as well as comparing them with the previous models (Lozano and Villa [17] and Hosseinzadeh Lotfi et al. [32]). In Section 5, we apply our model on gas companies during 2008 [33] for better exploring the models and representing their capabilities. Finally, the discussion and conclusion are provided in Section 6.

## 2. Preparations

In this section, we discuss two of the renowned CRA-DEA models, namely, the CRA-BCCI and CRA-SBMI proposed by Lozano and Villa [17] and Hosseinzadeh Lotfi et al. [32], respectively. Afterward, we elaborate on some of their attributes for obtaining our targets. Lastly, the connected-SBM model is also deliberated briefly.

Having considered no existing production function for determining the operational performances, a production possibility set (PPS) is mentioned and its frontier is designated for approximating the production function. The PPS is

defined as follows:

$$\bar{T}_v = \left\{ (X, Y) : X \geq \sum_{r=1}^n \sum_{j=1}^n \lambda_{jr} X_j, Y \leq \sum_{r=1}^n \sum_{j=1}^n \lambda_{jr} Y_j, \right. \\ \left. \sum_{j=1}^n \lambda_{jr} = 1, \lambda_{jr} \geq 0, r = 1, \dots, n, j = 1, \dots, n \right\} \quad (1)$$

The following symbolizations are also utilized in this part:

- $n$ : the number of DMUs;
- $m$ : the number of inputs;
- $s$ : the number of outputs;
- $j, r$ : the indices for DMUs;
- $i$ : the index for inputs;
- $k$ : the index for outputs;
- $x_{ij}$ : the observed value of input  $i$  of DMU $r$ ;
- $y_{kj}$ : the observed value of output  $k$  of DMU $r$ ;
- $\lambda_r$ : the vector for projecting DMU $r$ ;
- $\theta$ : the radial constriction of the aggregate input vector;
- $s_i^-$ : the nonnegative radial slack along the input dimension  $i$  of DMU $r$ ;
- $z_i^-, t_i^-$ : the nonnegative nonradial slack along the input dimension  $i$  of DMU $r$ ;
- $s_i^{-*}$ : the optimal radial slack to recognize an excess use of input  $i$  of DMU $r$ ;
- $z_i^{-*}, t_i^{-*}$ : the optimal nonradial slack to recognize an excess use of input  $i$  of DMU $r$ ;
- $\theta^*$ : the optimal group efficiency by the CRA-BCCI model;
- $\delta^*$ : the optimal group efficiency by the CRA-SBMI model;
- $\lambda_r^*$ : the optimal vector for projecting DMU $r$ ;
- $x_{ir}^*$ : the operating point target with the CRA models for input  $i$  of DMU $r$ ;
- $y_{kr}^*$ : the operating point target with the CRA models for output  $k$  of DMU $r$ .

2.1. The CRA-BCCI and CRA-SBMI Models. What follows is a succinct description of the CRA-BCCI and CRA-SBMI models in addition to mentioning their properties.

2.1.1. The Input-Oriented CRA-BCCI Model. The input-oriented CRA-BCCI model reported by Lozano and Villa [17] estimates the group efficiency  $\theta^*$  of DMUs by solving the following linear program:

$$\theta^* = \text{Min } \theta \quad (2)$$

$$\text{s.t. } \sum_{r=1}^n \sum_{j=1}^n \lambda_{jr} x_{ij} + t_i^- = \theta \sum_{j=1}^n x_{ij}, \quad i = 1, \dots, m, \quad (3)$$

$$\sum_{r=1}^n \sum_{j=1}^n \lambda_{jr} y_{kj} \geq \sum_{j=1}^n y_{kj}, \quad k = 1, \dots, s, \quad (4)$$

$$\sum_{j=1}^n \lambda_{jr} = 1, \quad r = 1, \dots, n, \quad (5)$$

$$\lambda_{jr} \geq 0, \quad r, j = 1, \dots, n, \quad (6)$$

$$t_i^- \geq 0, \quad i = 1, \dots, m. \quad (7)$$

Note that  $\lambda_r = (\lambda_{1r}, \lambda_{2r}, \dots, \lambda_{nr})$  is the vector for projecting DMU $r$  and denotes the intensity vector, while  $t_i^-$  also designates the nonradial slacks. Generally, to solve CRA-BCCI, there are two phases. In the first phase, we seek an equiproportional reduction along the entire input measurements and find  $\theta^*$ . Subsequently, we determine the radial input slacks  $s_i^{-*}$  as follows:

$$s_i^{-*} = (1 - \theta^*) \sum_{j=1}^n x_{ij}, \quad i = 1, \dots, m. \quad (8)$$

Thus, we have

$$\theta^* = \frac{\sum_{j=1}^n x_{ij} - s_i^{-*}}{\sum_{j=1}^n x_{ij}}, \quad i = 1, \dots, m. \quad (9)$$

Then, we will maximize  $\sum_{i=1}^m (t_i^- / \sum_{j=1}^n x_{ij})$  according to  $\lambda_r$  and  $t_i^-$ , subject to (3) to (7) and  $\theta = \theta^*$  in the second phase. Now, if  $(\lambda_r^*, t_i^{-*})$  is an optimal solution of the second phase, then  $t_i^{-*}$  remains as the nonradial slacks after elimination of the radial slacks  $s_i^{-*}$ . Hence, the total slacks  $u_i^{-*}$  of the CRA-BCCI model will be determined as  $u_i^{-*} = t_i^{-*} + s_i^{-*}$ . Despite the fact that ever nonradial projections can be presented in association with radial projections, nonradial slacks cannot be projected in the scalar  $\theta^*$ .

2.1.2. The Input-Oriented CRA-SBMI Model. At this time, we demonstrate the input-oriented CRA-SBMI model with the variable returning to the scale supposition of technology proposed by Hosseinzadeh Lotfi et al. [32] which assesses the group efficiency  $\delta^*$  by solving the following linear program:

$$\delta^* = \text{Min} \left( 1 - \frac{1}{m} \sum_{i=1}^m \frac{z_i^-}{\sum_{j=1}^n x_{ij}} \right)$$

$$\text{s.t. } \sum_{r=1}^n \sum_{j=1}^n \lambda_{jr} x_{ij} + z_i^- = \sum_{j=1}^n x_{ij}, \quad i = 1, \dots, m,$$

$$\sum_{r=1}^n \sum_{j=1}^n \lambda_{jr} y_{kj} \geq \sum_{j=1}^n y_{kj}, \quad k = 1, \dots, s, \quad (10)$$

$$\sum_{j=1}^n \lambda_{jr} = 1, \quad r = 1, \dots, n,$$

$$\lambda_{jr} \geq 0, \quad r, j = 1, \dots, n,$$

$$z_i^- \geq 0, \quad i = 1, \dots, m,$$

where  $\lambda_r = (\lambda_{1r}, \lambda_{2r}, \dots, \lambda_{nr})$  is the vector for projecting DMU $r$  and denotes the intensity vector, and  $z_i^-$  also defines the nonradial slacks. At this point, if we consider the case of input-orientated model in accordance with our explanation of the CRA-BCCI model in the previous section and if also  $(\lambda_r^*, z_i^{-*})$  is one of its optimal solutions, then the CRA-SBMI score  $\delta^*$  can be rewritten as follows:

$$\delta^* = \frac{1}{m} \sum_{i=1}^m \frac{\sum_{j=1}^n x_{ij} - z_i^{-*}}{\sum_{j=1}^n x_{ij}}. \quad (11)$$

The CRA-SBMI model is nonradial model and  $\delta^*$  identifies the mean of the decreased rates.

2.1.3. *Properties of the Radial and Nonradial Models.* The above two models have some properties as follows.

- (a) All of the inefficient DMUs are reflected on the efficient frontier to solve only one model rather than solving a model for each DMU independently.
- (b) The existent technically efficient DMUs can be reflected onto a certain point on the efficient frontier but they must be reflected onto themselves in the original DEA models.
- (c) The CRA-BCCI evaluates just the radial inefficiency in the scalar  $\theta^*$  while the CRA-SBM model measures just the nonradial inefficiency.
- (d) When the CRA-SBMI and the CRA-BCCI models are resolved, by bearing in mind vector  $\lambda_r^* = (\lambda_{1r}^*, \lambda_{2r}^*, \dots, \lambda_{nr}^*)$ , for each DMU $r$  as the value of optimal, we can obtain the operating point so that the CRA-SBMI and the CRA-BCCI targets for the inputs and outputs of any such point can be as follows:

$$\begin{aligned} x_{ir}^* &= \sum_{j=1}^n \lambda_{jr}^* x_{ij}, \quad r = 1, \dots, n, \quad i = 1, \dots, m, \\ y_{kr}^* &= \sum_{j=1}^n \lambda_{jr}^* y_{kj}, \quad r = 1, \dots, n, \quad k = 1, \dots, s. \end{aligned} \quad (12)$$

2.2. *The Connected-SBM Model.* In a large longitudinal study to deal with the weaknesses associated with the radial and nonradial models in the first one, Avkiran et al. [16] presented the connected-SBM model in which there were two nonnegative scalar parameters as  $L$  ( $0 \leq L \leq 1$ ) and  $U$  ( $\geq 1$ ). By taking into consideration the DMUs, the connected-SBM model with the introduced PPS for the variable returns to

the scale supposition of the technology [2] estimates the efficiency  $\rho^*$  of DMU $o$  ( $o = 1, 2, \dots, n$ ) as follows:

$$\rho^* = \text{Min}(1 - f) \quad (13)$$

$$\text{s.t.} \quad f = \frac{1}{m} \sum_{i=1}^m \frac{z_i^-}{x_{io}} \quad (14)$$

$$Lf \leq \frac{z_i^-}{x_{io}} \leq Uf, \quad i = 1, \dots, m, \quad (15)$$

$$\sum_{j=1}^n \lambda_j x_{ij} + z_i^- + v_i^- = x_{io}, \quad i = 1, \dots, m, \quad (16)$$

$$\sum_{j=1}^n \lambda_j y_{kj} \geq y_{ko}, \quad k = 1, \dots, s, \quad (17)$$

$$\sum_{j=1}^n \lambda_j = 1, \quad (18)$$

$$\lambda_j \geq 0, \quad j = 1, \dots, n, \quad (19)$$

$$z_i^- \geq 0, \quad i = 1, \dots, m, \quad (20)$$

$$v_i^- \geq 0, \quad i = 1, \dots, m. \quad (21)$$

In this model,  $v_i^-$  designates the nonradial input slacks persuaded to keep with the constraint (15). In addition,  $f$  is the mean of the normalized slacks  $\{z_i^-/x_{io}\}$  and each normalized slack  $z_i^-/x_{io}$  to the range  $[Lf, Uf]$  is restricted by the constraint (15). Reciprocally, the average nonradial input inefficiency for the existing DMU explains  $f$ . Therefore, the perversion from the mean value  $f$  can be restricted according to the lower bound  $L$  and upper bound  $U$ . The above- considered model has attributes as follows.

- (a) If  $L = 1$  or  $U = 1$ , then SBM-I-C( $L, U$ ) converts BCC-I.
- (b) If  $L = 0$  and  $U \geq m$ , then SBM-I-C( $0, U$ ) transforms SBM-I.
- (c) Give some freedom to the perversion of the normalized slacks which contain the assumed range around the average.
- (d)  $Lf^*$  and  $Uf^*$  for all the inputs restrict the relative perversion of the reflected input from the original amount.
- (e) The parameters  $L$  and  $U$  can be detracted to a single parameter as  $U = m - (m - 1)L$ .

### 3. Centralized Resource Allocation Connected Models

In this section, we propose a new model for the abovementioned weaknesses and change the connected-SBM model to deal with computing one instead of  $n$  mathematical programming problems and decreasing the aggregate input at the same time. In fact, we intend to present that the DEA

model can handle the target setting process by presenting the data envelopment scenario analysis. We call our models as the centralized resource allocation connected models. By bearing in mind the DMUs in the above models, their conforming input and output vectors, and the defined PPS for CRA models, the centralized resource allocation connected-SBMI model (CRA-CSBMI) can be described as follows:

$$\text{Model (1): } \gamma^* = \text{Min}(1 - h) \tag{22}$$

$$\text{s.t. } h = \frac{1}{m} \sum_{i=1}^m \frac{z_i^-}{\sum_{j=1}^n x_{ij}} \tag{23}$$

$$Lh \leq \frac{z_i^-}{\sum_{j=1}^n x_{ij}} \leq Uh, \quad i = 1, \dots, m, \tag{24}$$

$$\sum_{r=1}^n \sum_{j=1}^n \lambda_{jr} x_{ij} + z_i^- + v_i^- = \sum_{j=1}^n x_{ij}, \quad i = 1, \dots, m, \tag{25}$$

$$\sum_{r=1}^n \sum_{j=1}^n \lambda_{jr} y_{kj} \geq \sum_{j=1}^n y_{kj}, \quad k = 1, \dots, s, \tag{26}$$

$$\sum_{j=1}^n \lambda_{jr} = 1, \quad r = 1, \dots, n, \tag{27}$$

$$\lambda_{jr} \geq 0, \quad r, j = 1, \dots, n, \tag{28}$$

$$z_i^- \geq 0, \quad i = 1, \dots, m, \tag{29}$$

$$v_i^- \geq 0, \quad i = 1, \dots, m. \tag{30}$$

In this case study,  $v_i^-$  designates the nonradial input slacks inferred with regard to the constraint (24). Additionally,  $h$  is termed as the average nonradial input inefficiency. Indeed,  $h$  can be defined as the mean of the return to normal slacks  $\{z_i^- / \sum_{j=1}^n x_{ij}\}$  and each normalized slack  $z_i^- / \sum_{j=1}^n x_{ij}$  to the range  $[Lh, Uh]$  is delimited by the constraint (24). Mutually, the average nonradial input inefficiency for the existing DMU gives details  $h$ . Hence, perversion from the mean value  $h$  can be limited to be consistent with the lower bound  $L$  and upper bound  $U$ , accordingly.

Once this model is solved, the conforming vector  $\lambda_r^* = (\lambda_{1r}^*, \lambda_{2r}^*, \dots, \lambda_{nr}^*)$  can be determined for each DMU  $r$  to achieve the projected point which should be gained. The targets of the inputs and outputs of each of the mentioned points can be computed in a similar manner as follows:

$$x_{ir}^* = \sum_{j=1}^n \lambda_{jr}^* x_{ij}, \quad r = 1, \dots, n, \quad i = 1, \dots, m, \tag{31}$$

$$y_{kr}^* = \sum_{j=1}^n \lambda_{jr}^* y_{kj}, \quad r = 1, \dots, n, \quad k = 1, \dots, s.$$

According to Avkiran et al. [16], it is motivating to discuss the following propositions.

**Proposition 1.** *If  $L = 1$  or  $U = 1$ , then  $\theta^* = \gamma^*$ .*

*Proof.* By considering  $L = 1$ , we will have  $z_i^- / \sum_{j=1}^n x_{ij} \geq h = (1/m) \sum_{i=1}^m (z_i^- / \sum_{j=1}^n x_{ij})$  ( $\forall i$ ) and then  $z_i^- = h \sum_{j=1}^n x_{ij}$  because  $h$  is the mean of  $z_i^- / \sum_{j=1}^n x_{ij}$ . Now, we can remove the constraint (24) since the right constraint (24) is spontaneously contented. Thus, we can obtain CRA-BCCI by substituting  $1 - h$  to  $\theta$  and we have  $\theta^* = \gamma^*$ . By the same token, if  $U = 1$ , then  $\theta^* = \gamma^*$ .  $\square$

**Proposition 2.** *If  $L = 0$  and  $U \geq m$ , then  $\rho^* = \gamma^*$ .*

*Proof.* By taking into account  $U \geq m$ , since  $h$  is the mean of  $z_i^- / \sum_{j=1}^n x_{ij}$  the right constraint (24) is contented and by considering  $L = 0$ , the left constraint (24) is also spontaneously contented. Moreover, because the objective function is to reduce in  $z_i^-$ , the term  $v_i^-$  disappears in the constraint (25). Obviously, we can obtain CRA-SBMI and we will have then  $\rho^* = \gamma^*$ .  $\square$

It can be realized by the above two propositions that the CRA-CSBMI model consists of CRA-BCCI and CRA-SBMI as particular states in terms of the values intended for  $L$  and  $U$  and as if the logical sort of  $L$  is  $[0, 1]$  and  $U$  is  $[1, m]$ , too.

It is worth mentioning that with these methods not only all of the inefficient DMUs will be projected onto the frontier line but also the efficient DMUs are projected onto a certain point on the frontier line. This model differs from the previous model in a number of noteworthy ways.

- (a) The decrease in the  $r$ th input is wasted while there is a rise in the  $k$ th output generated with no restrictions to select the preference quantities.
- (b) This model gives some freedom to the perversion of the normalized slacks but it contains the assumed range around the average. While all of the inputs decrease equally in the radial models, they supply the highest value of reduction in all the inputs and also input ingredients are not all reduced in an equal manner for nonradial models.
- (c) This model does not require solving the phase-II model in CRA-BCCI because all of the input constraints are binding in every optimal solution.
- (d) The feasible region will be narrowed down, if  $L$  increases ( $U$  decreases) and hence the  $\gamma^*$  will increase.

The aggregate input or output can be minimized or maximized in the CRA models. With regard to the proposed model in this paper, which follows the idea of the CRA models, the benchmark for each DMU can be obtained so that the benchmark can have a lesser value of the total inputs but a bigger value of the total outputs compared to the DMU itself. Therefore, this study can yield results in order to supply an explanation for the suggested model. By this illustration, we demonstrate that the CRA-CSBM is a particular state which differs from the previous work in this field.

As exhibited in Table 1, we assume three DMUs, namely A, B, and C, containing two inputs along with one single constant output wherein DMUs A and B remain efficient while being placed on the frontier line, whereas DMU C

TABLE 1: The data related to the three DMUs.

DMU	Existing		$y$
	$x_1$	$x_2$	
A	3	10	1
B	4	1	1
C	4	25	1
Total	11	36	3

remains inefficient in the entire conventional DEA model. It should be asserted that although we extracted the original data from Avkiran et al. [16], the idea slightly modified in this study to become more suitable for our method. Hereby, our assumption was that there existed a centralized decision maker (DM) that was potential of overseeing the entire DMUs while it is simultaneously interested to reduce the global input consumption. Besides, we made use of the formula  $U = m - (m - 1)L$  which could be suitably determined in this case as  $U = 2 - L$ . Subsequently, by dialing a quantity among 0-1, we modified the appropriateness parameter  $L$  from the nonradial to the radial model.

For illustrating the mentioned projected points, we were able to distinguish them after solving the CRA-CSBMI model for  $L = 0, 0.2, 0.588, 0.8$  and 1, while utilizing the variable  $\lambda_{jr}^*$ 's (solved by GAMS which is known as a potent software package). Table 2 demonstrates the results which were acquired by analyzing the proposed model in line with the lower  $L$  and the upper  $U$  amounts.

The feasible region (which is shaped by the dashed lines) is demarcated by  $L$  and  $U$  values as illustrated in Figure 1. Provided that  $0 \leq L \leq 1$  and  $U \geq m$  hold, the CRA-BCCI and CRA-SBMI solutions have been contained within the feasible region in any choice of  $L$  and  $U$ . Moreover, Figure 2 shows the difference existing in projection onto the efficient frontier by the radial CRA-BCCI and the nonradial CRA-SBMI models while setting the proportionality parameter  $L = 0$  and  $L = 1$  corresponding to [CRA-SBMI] and [CRA-BCCI], in that order. Consistent with the magnitude of  $L$ , the normalized slacks  $z_i^- / \sum_{j=1}^n x_{ij}$  revealed a tendency to be uniform. To be precise, a slight  $L$  allows fairly great variations of the normalized slacks; contrariwise, a huge  $L$  limits them to a restricted range.

At  $L = 0$ , both DMU A and DMU C were, respectively, reflected onto DMU B and DMU A while DMU B was reflected onto itself which were CRA-SBMI solution's points. Figure 2 exhibits the results relevant to this case. The normalized deviations  $z_1^- / \sum_{j=1}^n x_{1j}$  and  $z_2^- / \sum_{j=1}^n x_{2j}$  are considered as the quantities 0 and 0.66. It is maintained that the proposed model at  $L = 0.2$  would indicate that DMU A could be reflected onto itself while DMU B is done so onto a portion of the frontier line; in addition, DMU C could be reflected onto DMU B. Then,  $z_1^- / \sum_{j=1}^n x_{1j}$  is augmented to 0.05, whereas  $z_2^- / \sum_{j=1}^n x_{2j}$  is reduced to 0.51. Moreover, DMU C was reflected onto DMU A at  $L = 0.588$ , whereas DMU A was projected onto itself and DMU B was done so onto a nonextreme point related to the frontier line. Similarly, DMU B and DMU C were projected at  $L = 0.8$  onto DMU A,

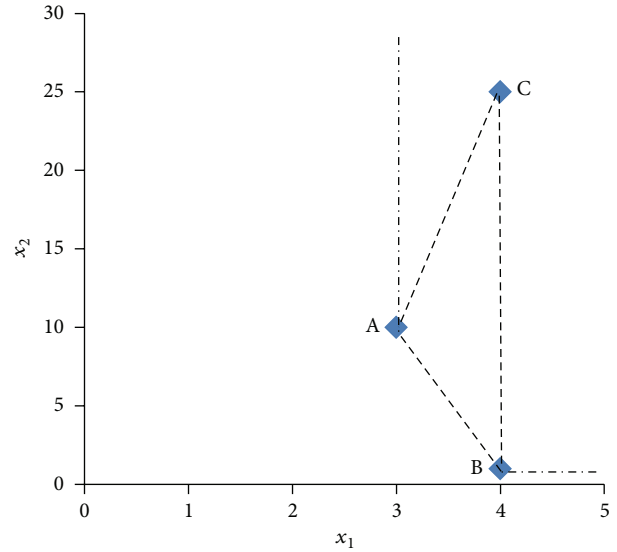


FIGURE 1: Feasible region bounded by  $L$  and  $U$ .

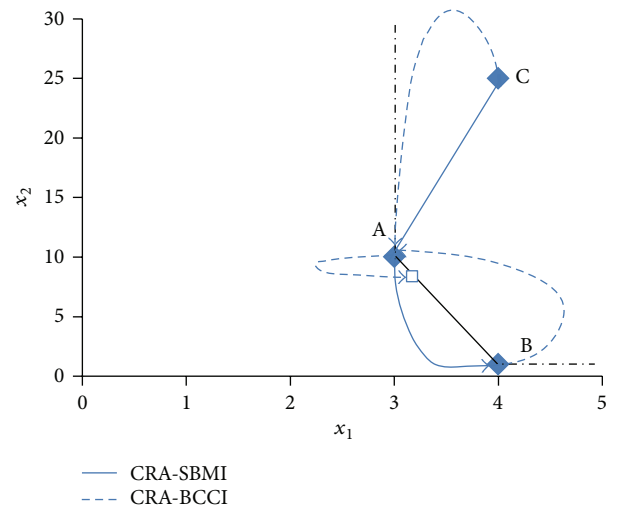


FIGURE 2: CRA-BCCI and CRA-SBMI projections onto the frontier line.

whereas DMU A was done so onto a nonextreme point related to the frontier line. Lastly, DMUs B and C were reflected onto the DMU A at  $L = 1$ , whereas DMU A was reflected onto  $x_1^* = 3.04$  and  $x_2^* = 9.60$ ; as shown in Figure 2, these latter are considered as the points related to the CRA-BCCI solution. Because the normalized deviations  $z_1^- / \sum_{j=1}^n x_{1j}$  and  $z_2^- / \sum_{j=1}^n x_{2j}$  are the equal value of 0.17, the two DMUs are correspondingly decreased by 17%. The point of interest is that the group efficiency score ( $\gamma^*$ ) upsurges from 0.66 (CRA-SBMI) to 0.82 (CRA-BCCI); in other words, the quantity  $\gamma^*$  upsurges in  $L$  while it diminishes in  $U$ .

We need to notice that by assuming the model proposed by Avkiran et al. [16], for this example, only DMU C projects onto the frontier line while it is potential of acquiring diverse projections for DMU C. Conversely, in our proposed model,

TABLE 2: The results related to the three DMUs.

$L$	0	0.2	0.588	0.8	1										
$\gamma^*$	0.66	0.71	0.77	0.80	0.82										
$h^*(1 - \gamma^*)$	0.34	0.29	0.23	0.20	0.18										
$z_1^*$	0	0.62	1.42	1.72	1.95										
$z_2^*$	24	18.36	11.18	8.47	6.40										
$z_1^- / \sum_{j=1}^n x_{1j}$	0	0.05	0.12	0.15	0.17										
$z_2^- / \sum_{j=1}^n x_{2j}$	0.66	0.51	0.31	0.23	0.17										
Projections	$x_1^*$	$x_2^*$	$y^*$												
DMU A	4	1	1	3	10	1	3	10	1	3.2	7.5	1	3.04	9.60	1
DMU B	4	1	1	3.3	6.6	1	3	10	1	3	10	1	3	10	1
DMU C	3	10	1	4	1	1	3.5	4.8	1	3	10	1	3	10	1
Total	11	12	3	10.3	17.6	3	9.5	24.8	3	9.2	27.5	3	9.04	29.6	3

the inefficient DMUs were able to project onto the frontier line; in addition, the efficient DMUs could project onto the other part of the frontier line.

### 4. Extension

The proposed approach can be developed into numerous statuses such as being output-oriented, having different settings of the lower bounds or the upper bounds, and being nonoriented. The next step is to improve our procedure to a weighted nonoriented model.

Having considered the DMUs and their matching input and output vectors, the extended centralized resource allocation connected-SBM model (ECRA-CSBM) is reported as follows:

$$\text{Model (2): } \varphi^* = \text{Min } \frac{1-h}{1+g} \tag{32}$$

$$\text{s.t. } h = \frac{1}{m} \sum_{i=1}^m \frac{w_i z_i^-}{\sum_{j=1}^n x_{ij}} \tag{33}$$

$$g = \frac{1}{s} \sum_{k=1}^s \frac{w_k z_k^+}{\sum_{j=1}^n y_{kj}} \tag{34}$$

$$L^- h \leq \frac{w_i z_i^-}{\sum_{j=1}^n x_{ij}} \leq U^- h, \quad i = 1, \dots, m, \tag{35}$$

$$L^+ g \leq \frac{w_k z_k^+}{\sum_{j=1}^n y_{kj}} \leq U^+ g, \quad k = 1, \dots, s, \tag{36}$$

$$\sum_{r=1}^n \sum_{j=1}^n \lambda_{jr} x_{ij} + z_i^- + v_i^- = \sum_{j=1}^n x_{ij}, \quad i = 1, \dots, m, \tag{37}$$

$$\sum_{r=1}^n \sum_{j=1}^n \lambda_{jr} y_{kj} - z_k^+ - v_k^+ = \sum_{j=1}^n y_{kj}, \quad k = 1, \dots, s, \tag{38}$$

$$\sum_{j=1}^n \lambda_{jr} = 1, \quad j = 1, \dots, n, \tag{39}$$

$$\sum_{i=1}^m w_i = m, \tag{40}$$

$$\sum_{k=1}^s w_k = k, \tag{41}$$

$$z_i^- \geq 0, \quad v_i^- \geq 0, \quad w_i^- \geq 0, \quad i = 1, \dots, m, \tag{42}$$

$$z_k^+ \geq 0, \quad v_k^+ \geq 0, \quad w_k^+ \geq 0, \quad k = 1, \dots, s, \tag{43}$$

$$\lambda_{jr} \geq 0, \quad r, j = 1, \dots, n, \tag{44}$$

where  $v_k^+$  denotes the nonradial output slacks concluded in connection with the constraint (36). The constraint (36) has the same properties as the constraint (24), which was observed in the input-oriented model. Moreover, the input and output take different amounts of  $L$  and  $U$ ; the perversion from the mean value  $h$  can be restricted according to the lower bound  $L^-$  and the upper bound  $U^-$ . Moreover, the perversion from the mean value  $g$  can be restricted according to the lower bound  $L^+$  and upper bound  $U^+$ . Additionally, the weights ( $w_i^-$  and  $w_k^+$ ) are provided in an exogenous manner and the average, the lower, and the upper bounds will be affected by an input or an output item with a great weight. In fact,  $w_i^-$  and  $w_k^+$  are the preference coefficients for the decreases and increases of the total consumption and the production of input  $i$  and output  $k$ , respectively.

It is significant to mention the following properties of the above model.

- (a) Unlike the previous model, this model is not a linear programming problem but can be simply converted into a linear programming problem by using Charnes and Cooper [34] conversions (see Hosseinzadeh Lotfi et al. [32] for particularity) in the first step and then choosing two appropriate independent  $w_i^-$  and  $w_k^+$  as the preference coefficients for the decreases and increases of the total consumption and the production of input  $i$  and output  $k$ , respectively.
- (b) All input and output constraints are binding in each optimal solution.

- (c) For any DMU $r$ , the points  $x_{ir}^* = \sum_{j=1}^n \lambda_{jr}^* x_{ij}$ ,  $\forall i = 1, \dots, m$  and  $y_{kr}^* = \sum_{j=1}^n \lambda_{jr}^* y_{kj}$ ,  $\forall k = 1, \dots, s$  are the Pareto efficient.
- (d) The  $\varphi^*$  obtained from the objective function is  $0 < \varphi^* \leq 1$ .

A numerical model of this has been provided by Lozano and Villa's study [17] wherein seven DMUs with an input could engender an output. We need to bear in mind the proposed model as in the cases of  $L^- = 0$ ,  $U^- = 2$ ,  $L^+ = 0$ , and  $U^+ = 1$ . Further, we were able to acquire the projecting point, in order to illustrate it afterward solving our developed model as well as utilizing the variable  $\lambda_{jr}^*$ 's (which was solved using the GAMS known as a potent software package). Figures 3, 4, and 5 present the graphical interpretation related to the CRA-BCCI, CRA-SBMI, and our proposed model while Table 3 exhibits the original DMUs along with the ones to which they are reflected by making use of the CRA-BCCI, CRA-SBMI, and the proposed model. As it can be discerned, our developed method finds alternative projection points in comparison with developed procedure which finds alternative projection points compared with previous procedures.

As it is apparent in Lozano and Villa's model [17], the entire DMUs are reflected onto DMU 2; the exception goes with the inefficient DMU 3. Moreover, DMU 3 is reflected onto a nonextreme point related to the frontier line. However, DMUs 1, 4, 5, 6, and 7 in the approach proposed by Hosseinzadeh Lotfi et al. [32] are projected onto the identical projections point (4.13, 8.26) of the frontier line. Likewise, DMUs 4, 5, and 6 are reflected onto the equivalent nonextreme point (5.16, 10.32) of the frontier line.

Stimulatingly, the findings obtained from the proposed model reveal that the entire DMUs were reflected onto the DMU 3; in other words, they were reflected onto the identical hyperplan of the frontier line. When establishing a comparison between these results, it is observed that the quantity of the global output production to the global input decrease of illustration DMUs are respectively, 1.95 and 2 for the Lozano and Villa's approach [17] and the Hosseinzadeh Lotfi et al.'s approach [32]. Yet, this proportion equals 2 in the proposed approach which resembles that of the Hosseinzadeh Lotfi et al.'s approach [32]. By this, we can conclude that the propounded method is precisely suitable.

### 5. An Application

We need to assume an empirical example on gas companies during 2008 [33] for better investigating the models and demonstrating their competences. The National Gas Company (NGC) of Iran encompasses 14 large branches which are situated in 13 provinces of Iran. While every branch functions independently in its province, the companies are entirely categorized under the NGC. Distributing the gas to domestic and industrial customers is reported as the branches' foremost task that is these 14 companies are responsible for distributing the service to end users (domestic and industrial). These companies have utilized seven variables

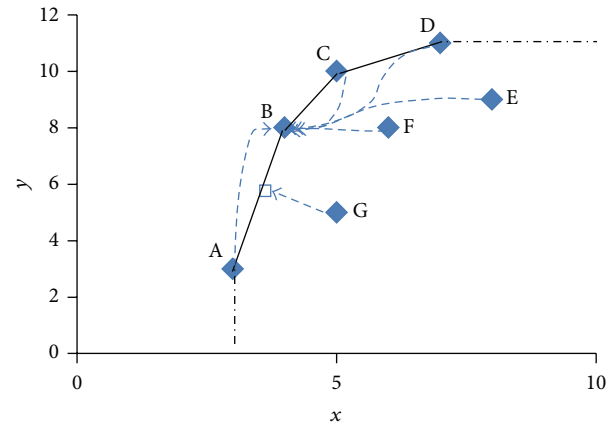


FIGURE 3: The CRA-BCCI projections onto the frontier line.

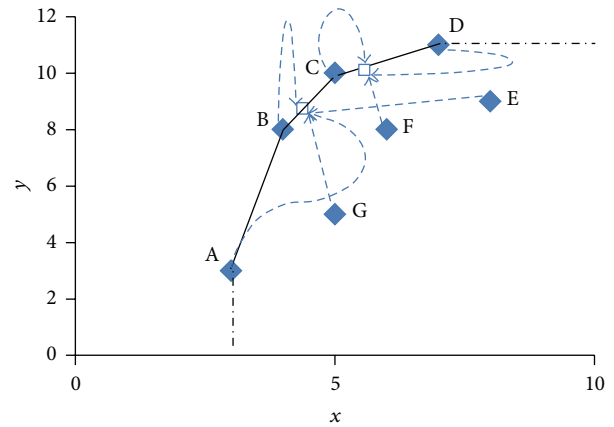


FIGURE 4: The CRA-SBMI projections onto the frontier line.

from the dataset with three inputs (budget, number of staff, comprehensive cost (operational cost and labour cost)), and four outputs (number of customers, length of gas network (km), delivered volumes (m<sup>3</sup>), and sold-out gas (Rials)), which are labeled as  $x_1, x_2$  and  $x_3$  for inputs and  $y_1, y_2, y_3$  and  $y_4$  for outputs in Table 4.

It is distinguished in DEA that those DMUs are more efficient which consume less input to yield more output; therefore, they are typically taken into account as benchmarks [19, 35]. Traditional DEA models can be employed for acquiring an appropriate benchmark for each DMU. The point to highlight is that the DMU benchmark consumes a lesser sum of inputs while yielding a bigger quantity of outputs in comparison with the DMU itself. Indeed the mentioned models separately decline (elevate) the inputs (outputs) of each DMU. Nevertheless, the results differ if centralized models are used. The reason is that such models are unable to decline (elevate) the inputs (outputs) of the individual DMUs.

It should be highlighted that the centralized models reduce (elevate) the aggregate inputs (outputs). Then the benchmark gained by our proposed method for each DMU

TABLE 3: Data and results of the seven DMUs with one-input and one-output.

DMU	Existing		Lozano and Villa's approach		Hosseinzadeh Lotfi et al.'s approach		Proposed approach	
	$x$	$y$	$x^*$	$y^*$	$x^*$	$y^*$	$x^*$	$y^*$
1	3	3	4	8	4.13	8.26	5	10
2	4	8	4	8	4.13	8.26	5	10
3	5	5	3.6	6	4.13	8.26	5	10
4	5	10	4	8	5.16	10.32	5	10
5	6	8	4	8	5.16	10.32	5	10
6	7	11	4	8	5.16	10.32	5	10
7	8	9	4	8	4.13	8.26	5	10
Total	38	54	27.6	54	32	64	35	70

TABLE 4: Data related to 14 gas companies.

DMU	$x_1$	$x_2$	$x_3$	$y_1$	$y_2$	$y_3$	$y_4$
1	177,430	401	528,325	801	41,675	77,564	201,529
2	221,338	1,094	1,186,905	803	34,960	44,136	840,446
3	267,806	1,079	1,323,325	251	24,461	27,690	832,616
4	160,912	444	648,685	816	23,744	45,882	251,770
5	177,214	801	909,539	654	36,409	72,676	443,507
6	146,325	686	545,115	177	18,000	19,839	341,585
7	195,138	687	790,348	695	31,221	40,154	233,822
8	108,146	152	236,722	606	23,889	37,770	118,943
9	165,663	494	523,899	652	25,163	28,402	179,315
10	195,728	503	428,566	959	43,440	63,701	195,303
11	87,050	343	298,696	221	9,689	17,334	106,037
12	124,313	129	198,598	565	21,032	30,242	61,836
13	67,545	117	131,649	152	10,398	14,139	46,233
14	47,208	165	228,730	211	9,391	13,505	42,094
Total	2,141,816	7,095	7,979,102	7,563	353,472	533,034	3,895,036

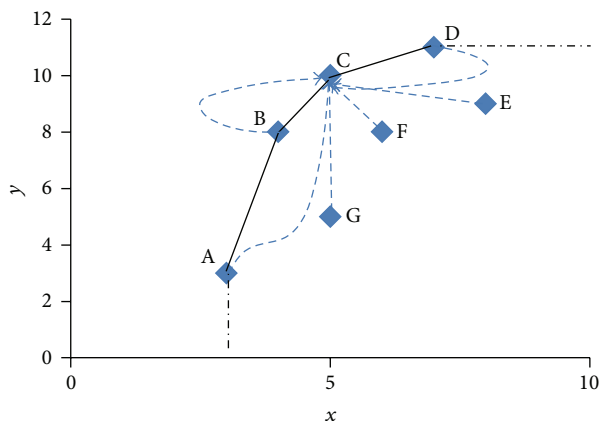


FIGURE 5: The CRA-CSBM projections onto the frontier line.

reveals a slighter amount of aggregate inputs and a corresponding larger amount of aggregate outputs than the DMU itself because of the fact that the proposed approach lends its basis to the centralized models. We need to take into

consideration each of the mentioned branches as a DMU with the purpose of attaining proper benchmarks for the branches and then solve the proposed model (1) for the DMUs in the case of  $L = 0.588$ . In details, the relevant results are provided in Table 5.

If we take into account branch 5 as an example, the first, second, and third inputs related to this branch are a smaller amount than the relevant inputs of the benchmark shown for this DMU, according to Table 5. Considering the related outputs, it should be also mentioned that only the benchmark's first output is a smaller amount than the output of the DMU itself; this is not in effect a desirable quantity from the DEA viewpoint. At this point, let us consider branch 14 while its relevant results are unlike: the entire outputs related to the mentioned branch are smaller than the outputs of the benchmark given for the branch, with the approximation used, which is theoretically more desired. Still, the branch's first and third inputs are smaller than the inputs related to the benchmark; in fact, since the objective in DEA is to detect a benchmark for a DMU having a slighter input and a larger output than the DMU itself, this amount is not desired from the DEA perspective. As for branch 9, it is observed that its

TABLE 5: Benchmarks for each branch by using the proposed model.

DMU	$x_1^*$	$x_2^*$	$x_3^*$	$y_1^*$	$y_2^*$	$y_3^*$	$y_4^*$
1	108,146.06	152.00	236,722.47	606.00	23,889.00	37,770.00	118,943.22
2	108,146.06	152.00	236,722.47	606.00	23,889.00	37,770.00	118,943.22
3	177,213.97	801.00	909,538.52	654.00	36,408.98	72,675.95	443,506.77
4	84,935.82	245.52	322,248.05	402.22	17,844.93	29,515.80	121,358.87
5	108,146.06	152.00	236,722.47	606.00	23,889.00	37,770.00	118,943.22
6	69,319.49	160.28	231,630.37	354.33	14,651.62	22,309.59	69,978.98
7	108,146.06	152.00	236,722.47	606.00	23,889.00	37,770.00	118,943.22
8	187,249.86	810.31	900,754.21	743.67	31,625.93	42,218.86	623,162.83
9	187,249.86	810.31	900,754.21	743.67	31,625.93	42,218.86	623,162.83
10	182,913.27	787.18	876,891.51	728.93	30,989.15	41,456.01	603,280.41
11	108,146.06	152.00	236,722.47	606.00	23,889.00	37,770.00	118,943.22
12	108,146.06	152.00	236,722.47	606.00	23,889.00	37,770.00	118,943.22
13	187,249.86	810.31	900,754.21	743.67	31,625.93	42,218.86	623,162.83
14	72,320.18	159.64	232,023.91	373.78	15,365.53	23,504.44	73,763.150
Total	1,797,328.68	5,496.57	6,694,929.80	8,380.27	353,473	542,738.35	3,895,037

entire inputs are smaller than the benchmark's inputs which are given for the branch and again this is not desired from the DEA perspective; however, the entire outputs related to this branch are smaller than the ones for the benchmark presented for the branch, with the approximation utilized, which is theoretically desired.

It can be discerned that our proposed approach lends its basis to the centralized models wherein not all the inputs (outputs) are probably reduced (elevated). Indeed, it is possible to reduce/elevate a DMU's inputs/outputs only in case the traditional DEA models are exploited.

In practice, the centralized models aim at reducing the aggregate inputs while elevating the aggregate outputs. It is observed that the benchmarks' aggregate inputs/outputs are reduced/elevated in comparison with the corresponding branches and this in turn is said to be desirable. The quantities of the reduction in the provided benchmarks' aggregate inputs, compared to the respective branches, are 1,797,328.68, 5,496.57 and 6,694,929.80 for the first, second, and third inputs, respectively. As for the aggregate outputs, the ones related to the benchmarks show a rise of 8,380.27, 353,473, 542,738.35, and 3,895,037 for the first, second, third, and fourth outputs, respectively; in effect, this can be desirable while taking into account the properties associated with the centralized models.

It should be noticed that branches 8, 9, and 13 entail identical projection points on the efficient frontier; therefore, they entail the similar benchmark, too. Moreover, the projection points related to branches 1, 2, 5, 7, 11, and 12 coincide with the ones related to branch 8, implying the fact that they entail the similar benchmark. Besides, the remainder of the branches is reflected onto the other part of the frontier line.

At this instant, with the purpose of comparing the approach introduced in this paper with the ones presented in the previous models, we would be able to attain the benchmarks consistent with the branches by the approach utilized

by the CRA-BCCI model [17] and CRA-SBMI model [32] which stand as two extreme cases of the CRA-CSBM model.

Furthermore, in case of employing the connected-SBM [16] for attaining the benchmark for every branch, the acquired results will indicate that the benchmark presented for every branch contains a slighter quantity of inputs as well as a larger quantity of outputs than the branch itself. Nonetheless, neither the CRA-BCCI and CRA-SBMI nor the model proposed in this paper has such characteristic; it is impossible to declare that the entire input/output components corresponding to each branch are slighter/larger than the ones for each single branch. We can merely affirm that the aggregate input/output related to the benchmark for every branch is slighter/larger than that of the branch itself.

## 6. Discussions and Conclusions

There is a need for a different approach which can project the entire units simultaneously because of the fact that by now the conventional DEA models set the targets independently for each DMU. In brief, an intraorganizational scenario was addressed in this paper wherein the entire units could be categorized under the supervision of a centralized decision maker. This decision maker required them to be efficient and considered the total input consumption and total output production. A new DEA model is introduced in this paper for centralized resource allocation.

The foremost finding here is illustrating a scheme for integrating the radial and nonradial CRA-DEA models with the intention of controlling the proportionality of slacks. Such a control will supply the decision maker with a superior chance of taking the appropriate benchmarks which stand as superior reflections of the expected patterns of the potential improvements. Two parameters are used by the CRA-CSBM model to limit the variations related to the normalized slacks in a certain range. The renowned CRA-BCC and

CAR-SBM models are considered as the two extreme cases of the mentioned model. Likewise, the sensitivity analysis by altering the CRA-CSBM model's parameters can allow incapacitating the latent problem of the mixed value slacks that would then confuse other analyses which rely on slacks.

We are able to project the entire DMUs in our method onto the efficient frontier. This can be achieved through solving only one model. Furthermore, in comparison with the preceding methods we can attain unlike benchmarks for all the DMUs by exploiting the given approximation. We also indicated by presenting an applied example that more appropriate benchmarks can be commonly acquired by the suggested approximation than by the preceding ones. Besides, the appropriate benchmarks can be suitably presented for the entire DMUs through solving one model for the case wherein the amount of DMUs is big. Moreover, for obtaining an insight into the way this approach functions, a graphical interpretation of two-dimensional cases are also provided.

To put it briefly, researchers and practitioners in the DEA field can currently match the estimated contraction of the resources and expansion of the outputs in a certain production system for establishing more realistic benchmarks. The proposed approach here is fairly simple which is also able to be simply extended in different directions. In effect, we are able to project only the inefficient DMUs by splitting the efficient and inefficient DMUs. The proposed models can also be employed for discretionary and nondiscretionary data.

## Conflict of Interests

The authors declare that there is no conflict of interests regarding the publication of this paper.

## References

- [1] A. Charnes, W. W. Cooper, and E. Rhodes, "Measuring the efficiency of decision making units," *European Journal of Operational Research*, vol. 2, no. 6, pp. 429–444, 1978.
- [2] R. D. Banker, A. Charnes, and W. W. Cooper, "Some models for estimating technical and scale inefficiencies in data envelopment analysis," *Management Science*, vol. 30, no. 9, pp. 1078–1092, 1984.
- [3] J. S. Liu, L. Y. Y. Lu, W.-M. Lu, and B. J. Y. Lin, "Data envelopment analysis 1978–2010: a citation-based literature survey," *Omega*, vol. 41, no. 3, pp. 3–15, 2013.
- [4] A. Emrouznejad, B. R. Parker, and G. Tavares, "Evaluation of research in efficiency and productivity: a survey and analysis of the first 30 years of scholarly literature in DEA," *Socio-Economic Planning Sciences*, vol. 42, no. 3, pp. 151–157, 2008.
- [5] S. Gattoufi, M. Oral, and A. Reisman, "Data envelopment analysis literature: a bibliography update (1951–2001)," *Socio-Economic Planning Sciences*, vol. 38, no. 2-3, pp. 159–229, 2004.
- [6] G. Debreu, "The coefficient of resource utilization," *Econometrica*, pp. 273–292, 1951.
- [7] M. J. Farrell, "The measurement of productive efficiency," *Journal of the Royal Statistical Society A*, vol. 120, no. 3, pp. 253–290, 1957.
- [8] T. C. Koopmans, "Analysis of production as an efficient combination of activities," in *Activity Analysis of Production and Allocation*, vol. 13, pp. 33–37, 1951.
- [9] R. Robert Russell, "Measures of technical efficiency," *Journal of Economic Theory*, vol. 35, no. 1, pp. 109–126, 1985.
- [10] W. W. Cooper, K. S. Park, and G. Yu, "Idea and AR-IDEA: models for dealing with imprecise data in DEA," *Management Science*, vol. 45, no. 4, pp. 597–607, 1999.
- [11] A. Charnes, W. W. Cooper, B. Golany, L. Seiford, and J. Stutz, "Foundations of data envelopment analysis for Pareto-Koopmans efficient empirical production functions," *Journal of Econometrics*, vol. 30, no. 1-2, pp. 91–107, 1985.
- [12] W. W. Cooper, K. S. Park, and J. T. Pastor Ciurana, "Marginal rates and elasticities of substitution with additive models in DEA," *Journal of Productivity Analysis*, vol. 13, no. 2, pp. 105–123, 2000.
- [13] J. T. Pastor, J. L. Ruiz, and I. Sirvent, "Enhanced DEA Russell graph efficiency measure," *European Journal of Operational Research*, vol. 115, no. 3, pp. 596–607, 1999.
- [14] W. W. Cooper, K. S. Park, and J. T. Pastor, "The range adjusted measure (RAM) in DEA: a response to the comment by Steinmann and Zweifel," *Journal of Productivity Analysis*, vol. 15, no. 2, pp. 145–152, 2001.
- [15] K. Tone, "Slacks-based measure of efficiency in data envelopment analysis," *European Journal of Operational Research*, vol. 130, no. 3, pp. 498–509, 2001.
- [16] N. K. Avkiran, K. Tone, and M. Tsutsui, "Bridging radial and non-radial measures of efficiency in DEA," *Annals of Operations Research*, vol. 164, no. 1, pp. 127–138, 2008.
- [17] S. Lozano and G. Villa, "Centralized resource allocation using data envelopment analysis," *Journal of Productivity Analysis*, vol. 22, no. 1-2, pp. 143–161, 2004.
- [18] E. Thanassoulis and R. G. Dyson, "Estimating preferred target input-output levels using data envelopment analysis," *European Journal of Operational Research*, vol. 56, no. 1, pp. 80–97, 1992.
- [19] B. Golany, "An interactive MOLP procedure for the extension of DEA to effectiveness analysis," *Journal of the Operational Research Society*, vol. 39, no. 8, pp. 725–734, 1988.
- [20] R. Färe, R. Grabowski, S. Grosskopf, and S. Kraft, "Efficiency of a fixed but allocatable input: a non-parametric approach," *Economics Letters*, vol. 56, no. 2, pp. 187–193, 1997.
- [21] C. K. Kumar and B. K. Sinha, "Efficiency based production planning and control models," *European Journal of Operational Research*, vol. 117, no. 3, pp. 450–469, 1999.
- [22] J. E. Beasley, "Allocating fixed costs and resources via data envelopment analysis," *European Journal of Operational Research*, vol. 147, no. 1, pp. 198–216, 2003.
- [23] A. D. Athanassopoulos, "Goal programming & data envelopment analysis (GoDEA) for target-based multi-level planning: allocating central grants to the Greek local authorities," *European Journal of Operational Research*, vol. 87, no. 3, pp. 535–550, 1995.
- [24] A. D. Athanassopoulos, "Decision support for target-based resource allocation of public services in multiunit and multi-level systems," *Management Science*, vol. 44, no. 2, pp. 173–187, 1998.
- [25] S. Lozano, G. Villa, and B. Adenso-Díaz, "Centralised target setting for regional recycling operations using DEA," *Omega*, vol. 32, no. 2, pp. 101–110, 2004.
- [26] S. Lozano and G. Villa, "Centralized DEA models with the possibility of downsizing," *Journal of the Operational Research Society*, vol. 56, no. 4, pp. 357–364, 2005.
- [27] S. Lozano, G. Villa, and R. Brännlund, "Centralised reallocation of emission permits using DEA," *European Journal of Operational Research*, vol. 193, no. 3, pp. 752–760, 2009.

- [28] E. V. Pachkova, "Restricted reallocation of resources," *European Journal of Operational Research*, vol. 196, no. 3, pp. 1049–1057, 2009.
- [29] F. H. F. Liu and L. C. Tsai, "Reallocating multiple inputs and outputs of units to improve overall performance," *Applied Mathematics and Computation*, vol. 219, no. 1, pp. 237–247, 2012.
- [30] L. Fang and C.-Q. Zhang, "Resource allocation based on the DEA model," *Journal of the Operational Research Society*, vol. 59, no. 8, pp. 1136–1141, 2008.
- [31] M. Asmild, J. C. Paradi, and J. T. Pastor, "Centralized resource allocation BCC models," *Omega*, vol. 37, no. 1, pp. 40–49, 2009.
- [32] F. Hosseinzadeh Lotfi, A. A. Noora, G. R. Jahanshahloo, J. Gerami, and M. R. Mozaffari, "Centralized resource allocation for enhanced Russell models," *Journal of Computational and Applied Mathematics*, vol. 235, no. 1, pp. 1–10, 2010.
- [33] A. Amirteimoori, D. K. Despotis, and S. Kordrostami, "Variables reduction in data envelopment analysis," *Optimization*, vol. 62, no. 2, pp. 1–11, 2013.
- [34] A. Charnes and W. W. Cooper, "Programming with linear fractional functionals," *Naval Research Logistics*, vol. 9, no. 3-4, pp. 181–186, 1973.
- [35] J. Zhu, "Data envelopment analysis with preference structure," *Journal of the Operational Research Society*, vol. 47, no. 1, pp. 136–150, 1996.

## Research Article

# Flow Merging and Hub Route Optimization in Collaborative Transportation

**Kerui Weng and Zi-hao Xu**

*School of Economics & Management, China University of Geosciences, Wuhan 430074, China*

Correspondence should be addressed to Kerui Weng; [wengkerui@gmail.com](mailto:wengkerui@gmail.com)

Received 18 November 2013; Accepted 18 January 2014; Published 4 March 2014

Academic Editor: Aderemi Oluyinka Adewumi

Copyright © 2014 K. Weng and Z.-h. Xu. This is an open access article distributed under the Creative Commons Attribution License, which permits unrestricted use, distribution, and reproduction in any medium, provided the original work is properly cited.

This paper studies the optimal hub routing problem of merged tasks in collaborative transportation. This problem allows all carriers' transportation tasks to reach the destinations optionally passing through 0, 1, or 2 hubs within limited distance, while a cost discount on arcs in the hub route could be acquired after paying fixed charges. The problem arises in the application of logistics, postal services, airline transportation, and so forth. We formulate the problem as a mixed-integer programming model, and provide two heuristic approaches, respectively, based on Lagrangian relaxation and Benders decomposition. Computational experiments show that the algorithms work well.

## 1. Introduction

With the rapid growth of manufacturing industry and E-commerce in recent years, logistics industry is constantly expanding. However, many carriers still show small scale and low load ratio in developing countries such as China. At the same time, a number of consignors choose multibatch *less-than-truck-loads* instead of single-batch *full-truck-loads* in order to adapt to flexible production plans, which increases logistics costs. One promising way of improvement is a new transportation model called collaborative transportation (CT), which integrates all transportation demands and transportation resources to achieve economies of scale. For example, if transport tasks shown in Figure 1 dealt with a CT program as shown in Figure 2, then routing costs could be reduced by combing several transportation flows on a few arcs. A transportation task from node  $i$  to  $j$  is called O-D flow  $i \rightarrow j$ . The route passing through no more than 2 hubs, such as  $i \rightarrow k \rightarrow m \rightarrow j$ , is called hub route. An arc  $(k, m)$  is called hub arc if it carries enough O-D flows and produces a freight cost discount on the arc due to economies of scale, which is the most favourable feature of CT. However, two unfavourable characteristics exist in CT. First, O-D flows may increase touring distance. For instance, the distance of route A-B-E-D is obviously longer than the direct distance

of route A-D. Second, to achieve discount, we have to pay a fixed charge to build hub arc, such as building railroad instead of highroad or buying heavy trucks to replace light-vans. Therefore, hub route with merging flows obtains discount on hub arc at the expense of additional transportation range and fixed charge. This encourages us to seek the optimal hub route of merging flows to maximize the profit of CT.

Flow merging and hub routing problem of collaborative transportation exists in many practices. For example, flight courses between small cities can be integrated into hub arcs of big cities, such as hub route *small city—big city—big city—small city*. In road line between two Chinese cities *Guangzhou and Hong Kong*, a logistics company may quote 2700 yuan, 3000 yuan, 3400 yuan, and 3600 yuan for full-truck-loads of 3 tons, 5 tons, 10 tons, and 12 tons, respectively, and the expenses per ton are 900 yuan, 600 yuan, 340 yuan, and 300 yuan. Petroleum exploitation companies in north China considered whether and where to build a railway to convey merging materials and reduce costs. The above applications indicate that larger vehicles loading larger flows generate cheaper transport costs. In other applications of CT where high response speed is required, we need to consider the distance constraints. For example, in express delivery business, customers require that the total transportation time of O-D flow is less than the promised hour such as 24-hour delivery

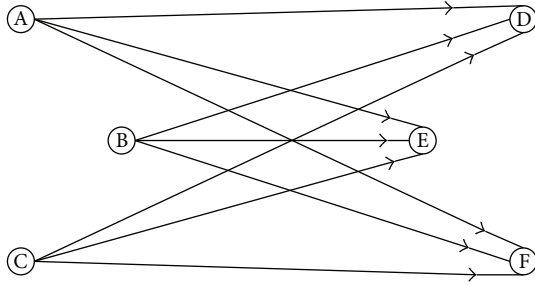


FIGURE 1: Transportation task I.

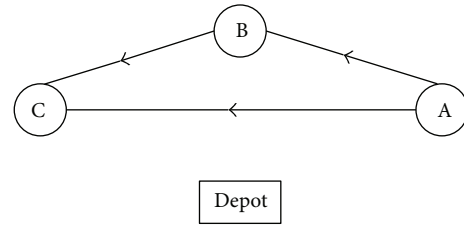


FIGURE 3: Transportation task II.

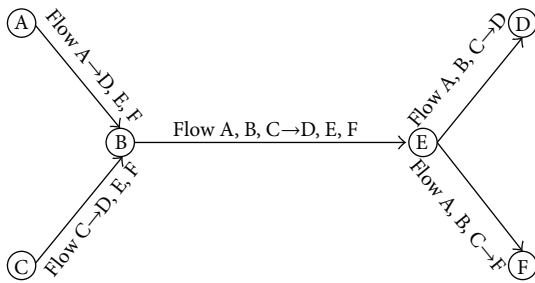


FIGURE 2: Collaborative transportation.

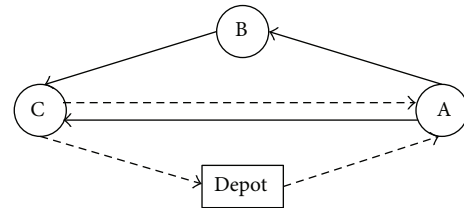


FIGURE 4: MDARP.

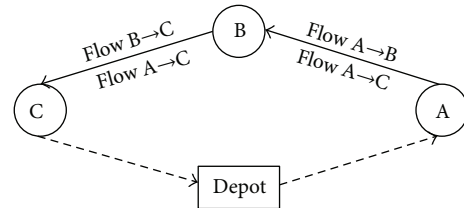


FIGURE 5: MDPDP.

or 48-hour delivery. But in order to save transportation costs, most O-D flows have to give up the direct paths and select longer hub routes. How to generate the *saving-and-fast* transportation plan with distance constraints? To reach this, we research flow merging and hub route problem in collaborative transportation (FMRICT) which finds the optimal hub route of merged flows within limited detouring distance, while hub arc can cut cost from discount if paid a fixed charge.

At present study of CT, the optimized route can be categorized into fleet's route and flow's hub route. Literatures about multidepot arc routing problem (MDARP) and multidepot pickup and delivery problem (MDPDP) are researches on fleet's route. A fleet finished a task  $i \rightarrow j$  in MDARP if its tour starting and ending a depot directly passed arc  $(i, j)$ . But to finish a task  $i \rightarrow j$  in MDPDP, fleet needs to find a minimal cost tour while node  $i$  is before but not necessary last to node  $j$ , which means picking up freight at  $i$  and delivering it at  $j$ . Obviously, MDPDP can achieve a lower cost than MDARP as shown in Figures 3, 4, and 5. However, MDPDP is more complex and extremely harder to solve large scale instances than MDARP. Most researches on MDPDP are tested on instances with single depot. Reference [1] tries to solve MDARP with 200 tasks by particle swarm optimization but does not provide the benchmark of computational time and solution quality. To the best of our knowledge there are no other efficient approaches with benchmark to large scale MDPDP, while MDARP with more than 1000 tasks can be solved with good benchmark in [2–4]. As shown in Figure 6, a promising innovation is the two-stage CT program which takes full advantage of scale effect and decreases the complexity. The first stage merges the flows, and the second stage obtains the fleet's tour by solving a

MDARP which already has good heuristics. Accordingly, it is an important step to find the optimal hub route of merging flow.

Current studies on O-D flow's hub route of CT focus on the hub-and-spoke network design problem (HASNDP). Assuming that all arcs between hubs have transportation discount and requiring that all the O-D flows have to pass one or two hubs, HASNDP seeks the best selecting of hub and arranges the right hub routes of O-D flows to minimize the total cost. HASNDP was initially proposed by O'Kelly (1988) who built a quadratic programming model and provided two types of heuristic algorithms. In recent years, many studies are devoted to improve the model and the solution [5–8], while some scholars concentrate on the extension problem of HASNDP [9–16]. HASNDP and hub location problem have gained much attention. However, there still exist two defects. Firstly, requiring all the O-D flows passing hubs may cause lots of detouring. For instance, in the conclusion of Weng [7], Xi'an was chosen as hub in Chinese airline Lhasa  $\rightarrow$  Xi'ning according to the result of HASNDP, which is obviously not right due to over detouring. Secondly, current researches of HASNDP emphasize on nodes' cost while neglect arcs' cost and the demand of incremental flows. HASNDP assumes that all arcs between hubs can automatically obtain economies of scale as long as hub costs are paid and O-D flows pass one or

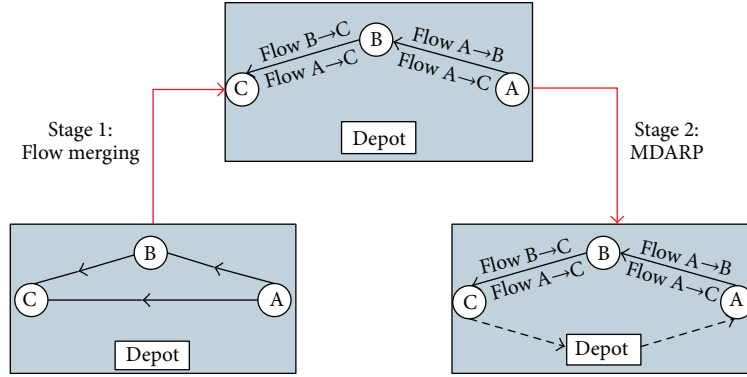


FIGURE 6: Two-stage CT program.

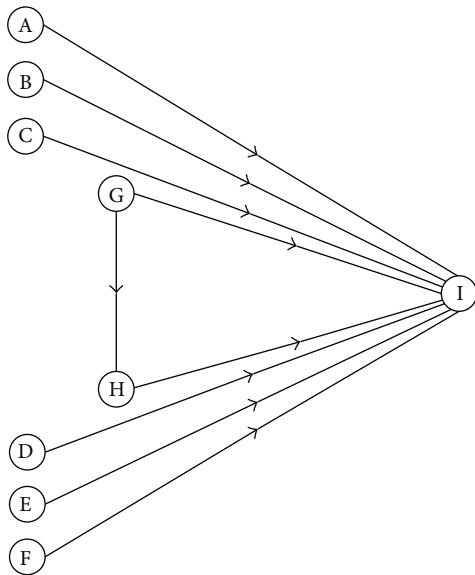


FIGURE 7: Transportation task III.

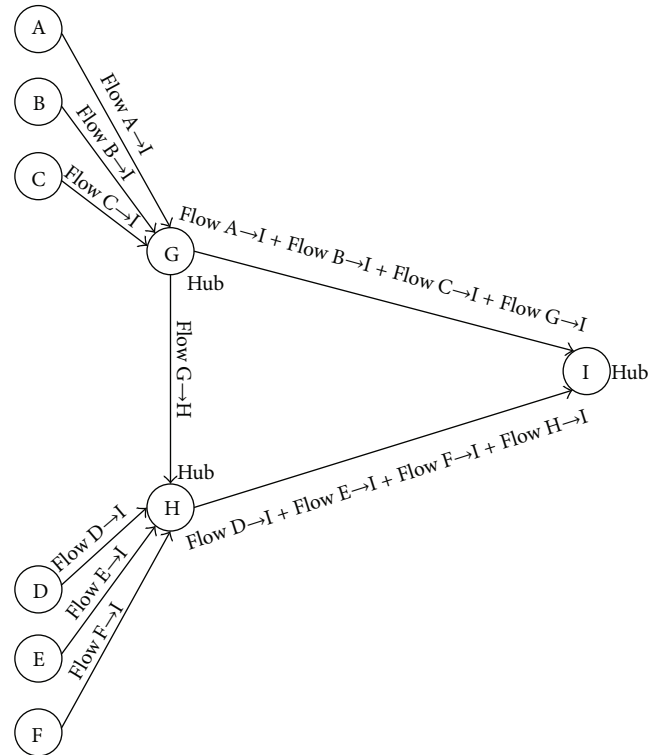


FIGURE 8: HASNDP.

two hubs, which conflicts some practice. For example, tasks shown in Figure 7 will be designed as hub-and-spoke network shown in Figure 8. Nodes  $H$ ,  $I$ , and  $J$  are chosen as hubs and all arcs between them enjoy discount of transportation costs. However, as we can see from Figure 8, no incremental flows pass through arc  $(H, I)$  and it should not be given the transportation discount. In fact, the economies of scale for hub arcs need other two conditions including the incremental flows and the fixed charge to build more economic transport facilities. Researches [17–20] also find that some hub arcs do not have quantity strength after paying the hub costs while they still require tasks passing hubs and neglect the detouring distance limitation, which are distinguished from our work.

This paper is organized as follows. In Section 2, we formulate the mixed-integer programming model for FMRICT. Sections 3 and 4 provide two heuristic approaches, respectively, based on Lagrangian relaxation and Benders decomposition. Section 5 shows test performance of the algorithms.

## 2. Formulation

Consider a connected network  $G(N, A)$ , where  $A$  is the set of edges and  $N = \{1, 2, \dots, n\}$  is the set of nodes. For all  $i \neq j$ , let  $h_{ij}$  denote the O-D flow from  $i$  to  $j$ .  $D_{ij}$  is the limited detouring distance of flow  $i \rightarrow j$ .  $c_{km}$  is the unit flow cost of arc  $(k, m)$ , and  $f_{km}$  is the fixed cost when arc  $(k, m)$  is selected as a hub arc.  $a$  ( $0 < a < 1$ ) denotes the transportation cost discount of hub arcs. Binary decision variable  $Y_{km} = 1$  if arc  $(k, m)$  is selected as a hub arc and 0 otherwise.  $X_{ij}^{km}$  is the quantity of flow  $i \rightarrow j$  on non-hub-arc  $(k, m)$ .  $W_{ij}^{km}$  is the quantity of flow  $i \rightarrow j$  on hub arc  $(k, m)$ . Binary variable

$Z_{ij}^{km} = 1$  if flow  $i \rightarrow j$  chooses route  $i \rightarrow k \rightarrow m \rightarrow j$  and 0 otherwise. FMRICT model could be formulated as (P1),

$$(P1) \quad \min \quad \sum_i \sum_j \sum_k \sum_m (X_{ij}^{km} c_{km} + aW_{ij}^{km} c_{km}) \\ + \sum_k \sum_m f_{km} Y_{km}, \quad (1)$$

$$\text{S.T.} \quad \sum_{k \notin \{i,j\}} \sum_{m \notin \{i,j\}} (X_{ij}^{km} + W_{ij}^{km}) + X_{ij}^{ij} + W_{ij}^{ij} = h_{ij} \quad (2)$$

$$\forall i, j \in N; \quad i \neq j,$$

$$\sum_{m \notin \{i,j\}} (X_{ij}^{km} + W_{ij}^{km}) = X_{ij}^{ik} + W_{ij}^{ik} \quad (3)$$

$$\forall i, j, k \in N; \quad i \neq j; \quad k \notin \{i, j\},$$

$$\sum_{m \notin \{i,j\}} (X_{ij}^{km} + W_{ij}^{km} = X_{ij}^{mj} + W_{ij}^{mj}) \quad (4)$$

$$\forall i, j, m \in N; \quad i \neq j; \quad m \notin \{i, j\},$$

$$W_{ij}^{km} \leq Y_{km} h_{ij} \quad (5)$$

$$\forall i, j, k, m \in N; \quad i \neq j; \quad k \neq j; \quad m \neq i,$$

$$Z_{ij}^{ik} c_{ik} + Z_{ij}^{km} c_{km} + Z_{ij}^{mj} c_{mj} - D_{ij} \leq 0 \quad (6)$$

$$\forall i \neq j; \quad k \neq j; \quad m \neq i,$$

$$X_{ij}^{km} + W_{ij}^{km} = Z_{ij}^{km} h_{ij} \quad (7)$$

$$\forall i, j, k, m \in N; \quad i \leq j; \quad k \leq j; \quad m \leq i,$$

$$W_{ij}^{km}, X_{ij}^{km} \geq 0; \quad Z_{ij}^{km}, Y_{ij} = 0, 1 \quad (8)$$

$$\forall i, j, k, m \in N, \quad k \leq j; \quad m \leq i.$$

In (P1), objective function (1) accounts for the minimization of total routing costs plus fixed costs. Constraint (2) requires all tasks be finished. Constraint (3) and constraint (4) ensure the flow balance. If flow  $i \rightarrow j$  goes through the hub  $k$  ( $k \notin \{i, j\}$ ), then the flow going in  $k$  must equal the flow going out of  $k$ . Constraint (5) restricts  $W_{ij}^{km}$  to be 0 if arc  $(k, m)$  is not selected as hub arc.  $k \neq j$  and  $m \neq i$  in constraints (5) and (6) are to avoid roundabout transportation. For instance, route  $i \rightarrow j \rightarrow i \rightarrow j$  and route  $i \rightarrow j \rightarrow k \rightarrow j$  are not acceptable. Constraint (6) controls the route distance, and constraint (7) is to define  $Z_{ij}^{km}$ .

Compared to HASNDP which neglects detouring distance, (P1) makes tasks choose detour routes instead of direct routes if only they are more saving and control the distance by constraint (6). (P1) also helps the incremental flows of hub arcs by importing fixed charge as shown in Lemma 1. Define  $Z_{km} = \sum_i \sum_j (X_{ij}^{km} + W_{ij}^{km})$  as the total flow on arc  $(k, m)$ .

**Lemma 1.** *In optimal solution of FMRICT, if  $(k, m)$  is selected as a hub arc, then  $Z_{km} \geq f_{km}/(1-a)c_{km}$ .*

*Proof.* When  $Y_{km} = 1$ , we can decrease the transportation costs of  $(1-a)Z_{km}c_{km}$  but increase fixed charge of  $f_{km}$ . For every selected hub arc  $(k, m)$ , it is optimal only if  $(1-a)Z_{km}c_{km} \geq f_{km}$ ; otherwise we can decrease costs by set  $Y_{km} = 0$  and it is a contradiction to optimal solution. Therefore, the optimal flow on hub arc must satisfy  $Z_{km} \geq f_{km}/(1-a)c_{km}$ .  $\square$

### 3. Heuristic Algorithm Based on Lagrange Relaxation

(P1) is a complicated mixed-integer programming model that possesses about  $3n^4 + n^2$  variables and  $5n^4 + 2n^3 + n^2$  constraints. The decision variables and constraints would be more than 50 thousands only if 10 nodes are included. FMRICT can be proven NP hard since it is an extension of fixed charge multicommodity network flow problem. Therefore, heuristic is needed for large scaled FMRICT. This section proposes a heuristic procedure based on Lagrange relaxation. The procedure uses the idea of relaxing parts of constraints by bringing them into the objective function with associated vector  $\lambda$  called the Lagrange multiplier and builds relaxed problem called Lagrangian dual problem which is relatively easily solved. A lower bound can be obtained from the solution of the Lagrangian dual problem, and an upper bound was found by refining the solution to a feasible solution of the original problem. The heuristic iteratively reduces the gap between upper bound and lower bound by updating the Lagrange multiplier. The main algorithm elements include the way of building relaxed problem called Lagrange dual problem, the way of constructing feasible solution, and the way of updating Lagrangian multipliers.

If we relax constraint (5) in (P1) and define  $\lambda_{ij}^{km}$  as the Lagrangian multiplier of corresponding constraint, then the Lagrange dual problem (P2) can be obtained as follows:

$$(P2) \quad \min \quad \sum_i \sum_j \sum_k \sum_m X_{ij}^{km} c_{km} \\ + \sum_i \sum_j \sum_k \sum_m W_{ij}^{km} (\alpha c_{km} + \lambda_{ij}^{km}) \\ + \sum_k \sum_m Y_{km} \left( f_{km} - \sum_i \sum_j \lambda_{ij}^{km} h_{ij} \right) \\ \text{S.T.} \quad \text{Constraints (2) - (4), (6) - (8).} \quad (9)$$

Given  $\lambda_{ij}^{km}$ , we can easily minimize the objective of (P2). For fixed costs, if  $f_{km} - \sum_i \sum_j \lambda_{ij}^{km} h_{ij} < 0$ , then  $Y_{km} = 1$ , and 0 otherwise. For transportation costs, O-D flow will select the shortest hub route. Let  $\text{isarc}_{ij}^{km} = 1$  if flow  $i \rightarrow j$  going through hub arc  $(k, m)$ , and  $\text{isarc}_{ij}^{km} = 0$  otherwise. Let  $lk$  be the objective of (P2). The approaching procedure can be constructed as Algorithm 2.

The first step is to calculate the cost of arc  $(k, m)$  for flow  $i \rightarrow j$ . The second step is to find the optimal hub route  $i \rightarrow k^* \rightarrow m^* \rightarrow j$  that satisfies distance constraints and to determine  $W_{km}^{ij}$ . The last step is to find hub arcs.  $lk$

is the optimal solution of (P2) and also becomes the lower bound of (P1). In this heuristic, we will augment lower bound to approach optimal value by subgradient optimization.

*Algorithm 2* (solving the relaxed problem). (1) For  $\forall i, j, k, m$  that satisfy  $i \neq j, k \neq j$  and  $m \neq i$ , let  $C_{ij}^{km} = \min(c_{km}, \alpha c_{km} + \lambda_{ij}^{km})$ , and

$$\text{isarc}_{ij}^{km} = \begin{cases} 1 & \text{if } C_{ij}^{km} = \alpha c_{km} + \lambda_{ij}^{km} \\ 0 & \text{else;} \end{cases} \quad (10)$$

$lk = 0, W_{ij}^{km} = 0$ .

(2) For  $\forall i \neq j$ : find  $(k^*, m^*) = \arg \min\{C_{ij}^{ik} + C_{ij}^{km} + C_{ij}^{mj} \mid c_{ik} + c_{km} + c_{mj} \leq D_{ij}, k \neq j, m \neq i\}$ ; let  $lk = lk + C_{ij}^{ik^*} + C_{ij}^{k^*m^*} + C_{ij}^{m^*j}$ ; if  $\text{isarc}_{ij}^{ik^*} = 1$ , then  $W_{ij}^{ik^*} = h_{ij}$ ; if  $\text{isarc}_{ij}^{k^*m^*} = 1$ , then  $W_{ij}^{k^*m^*} = h_{ij}$ ; if  $\text{isarc}_{ij}^{m^*j} = 1$ , then  $W_{ij}^{m^*j} = h_{ij}$ .

(3) For  $\forall k \neq m$ , if  $f_{km} - \sum_i \sum_j \lambda_{ij}^{km} h_{ij} < 0$ , then  $Y_{km} = 1, lk = lk + f_{km} - \sum_i \sum_j \lambda_{ij}^{km} h_{ij}$ ; else  $Y_{km} = 0$ .

*Algorithm 3* (construct feasible solution). (1)  $uk = 0, \widehat{W}_{ij}^{km} = 0, \widehat{X}_{ij}^{km} = 0, \widehat{F}_{ij}^{km} = 0$ .

(2) For  $\forall k \neq m$ , let  $\widehat{Y}_{km} = Y_{km}$  while  $Y_{km}$  is the result of step (3) of Algorithm 2. If  $\widehat{Y}_{km} = 1$ , then  $uk = uk + f_{km}$ .

(3) For  $\forall i, j, k, m$  having  $k \neq j, m \neq i$ , let

$$C_{ij}^{km} = \begin{cases} \alpha c_{km} & \text{if } \widehat{Y}_{km} = 1 \\ c_{km} & \text{else.} \end{cases} \quad (11)$$

(4) For  $\forall i \neq j$ , find  $(k^*, m^*) = \arg \min\{C_{ij}^{ik} + C_{ij}^{km} + C_{ij}^{mj} \mid c_{ik} + c_{km} + c_{mj} \leq D_{ij}, k \neq j, m \neq i\}$ ; let  $F_{ij}^{ik^*} = h_{ij}, F_{ij}^{k^*m^*} = h_{ij}, F_{ij}^{m^*j} = h_{ij}, uk = uk + C_{ij}^{ik^*} + C_{ij}^{k^*m^*} + C_{ij}^{m^*j}$ .

However, the optimal solution of (P2) may not be feasible to FMRICT by violating constraint (5) such as  $W_{ij}^{km} > Y_{km} h_{ij}$ . Consequently, solution of (P2) will be adapted to feasible solution of the original problem. Let  $\widehat{X}_{ij}^{km}, \widehat{W}_{ij}^{km}$ , and  $\widehat{Y}_{km}$  be the feasible solution of  $X_{ij}^{km}, W_{ij}^{km}$ , and  $Y_{km}$ , respectively. Let  $F_{ij}^{km}$  denote the quantity of flow  $i \rightarrow j$  going through arc  $(k, m)$ . The definition means that  $\widehat{W}_{ij}^{km} = F_{ij}^{km}$  and  $\widehat{X}_{ij}^{km} = 0$  if  $(k, m)$  is hub arc; else  $\widehat{W}_{ij}^{km} = 0$  and  $\widehat{X}_{ij}^{km} = F_{ij}^{km}$ . Let  $uk$  be the objective value of feasible solution. Algorithm 3 is the procedure of obtaining feasible solution. After initialization in the first step, the second step is to determine the hub arc and to count fixed costs. The third step is to calculate the transportation costs of tasks in all arcs, and the last step is to make O-D flow select the shortest hub route.

For given Lagrangian multiplier  $\lambda_{ij}^{km}$ , both upper bound  $uk$  and lower bound  $lk$  could be obtained from Algorithms 2 and 3. Updating Lagrangian multiplier is to adjust the value of  $\lambda_{ij}^{km}$  so that the upper bound and the lower bound would be more and more closer to the optimal value. Subgradient algorithm is such a method to update  $\lambda_{ij}^{km}$ .

Let  $l^t$  be the step length of iteration  $t$  and be computed as

$$l^t = \frac{\alpha^t (\text{UB} - lk)}{\sum_i \sum_j \sum_k \sum_m (Y_{km} h_{ij} - W_{ij}^{km})^2}. \quad (12)$$

In (12),  $\alpha^t$  is the step length parameter at iteration  $t$ , and  $\alpha^1$  is usually initialized by 2. Let UB be the current best upper bound and let  $Y_{km}$  and  $W_{ij}^{km}$  be solutions of the relaxed problem at current iteration. Lagrangian multiplier is updated as formula (13) to heighten the lower bound,

$$\lambda_{ij}^{km} = \max\{0, \lambda_{ij}^{km} - l^t (Y_{km} h_{ij} - W_{ij}^{km})\}. \quad (13)$$

The main program of Lagrangian relaxation algorithm for solving FMRICT is as follows.

*Algorithm 4* (Lagrangian relaxation algorithm for solving FMRICT). (1) Initialize the parameters. Let  $t = 1, \lambda_{ij}^{km} = c_{km}, \alpha^t = 2$ , and  $\text{UB} = \infty$ . Set the current optimal lower bound  $\text{LB} = -\infty$ .

(2) Solve Lagrangian relaxation problem with Algorithm 2 to get  $W_{ij}^{km}, Y_{ij}^k$ , and  $lk$ . Update  $\text{LB} = \max(\text{LB}, lk)$ .

(3) According to Algorithm 3, acquire the feasible solution  $\widehat{Y}_{ij}^k$  and  $F_{ij}^{km}$  and compute objective function (1) to get  $uk$ . Update  $\text{UB} = \max(\text{UB}, uk)$ .

(4) Update step length parameter  $\alpha^k$ . If LB is not improved within 65 steps, then let  $\alpha^{k+1} = \alpha^k / 2$ .

(5) Update Lagrangian multiplier according to (12) and (13).

(6) Determine if it has reached the termination criterion. End algorithm if any one of the following three criterions is established to be true: (1)  $\text{UB} - \text{LB} \leq 0.1$ , (2)  $l^t \leq 0.0001$ , and (3)  $t = 1000$ .

(7) Update iteration numbers  $t = t + 1$  and return to step (2).

#### 4. Heuristic Algorithm Based on Benders Decomposition

This section approaches FMRICT with another method based on Benders decomposition to compare performance with Algorithm 4. By fixing some variables of the original problem, Benders decomposition partitions the original problem into master problem and subproblem which are easy to solve. Solve the subproblem to produce the upper bound and increase Benders' cut to the master problem based on the solution of dual variable of the subproblem, and then solve the master problem to acquire the lower bound. The algorithm will iteratively reduce the gap between upper bound and lower bound.

For model (P1), fix all  $Y_{km}$  to  $\bar{Y}_{km}$  at the iteration  $t$ ; then the subproblem is shown as in (P3),

$$(P3) \quad \min \sum_{i,j,k,m} X_{ij}^{km} c_{km} + \sum_{i,j,k,m} a W_{ij}^{km} c_{km} + \sum_{k,m} f_{km} \bar{Y}_{km} \quad (14)$$

$$\text{S.T. } -w_{ij}^{km} \geq -\bar{Y}_{km} h_{ij} \quad \forall i \neq j; k \neq j; m \neq i, \quad (15)$$

Constraints (2) – (4), (6) – (8)

$$W_{ij}^{km}, X_{ij}^{km}, Z_{ij}^{km} \geq 0 \quad \forall k \neq j; m \neq i. \quad (16)$$

(P3) is easy to solve, and we only need to make all O-D flows select the minimum cost hub route within distance limitations. Let  $U_{ijkm}^t$  and  $v_{ij}^t$  be the dual variables of constraints (15) and (2) of (P3) at the iteration  $t$ .

Feasible solution of  $U_{ijkm}^t$  and  $v_{ij}^t$  could be obtained according to duality theory, as shown in (17),

$$U_{ijkm}^t = \min_{\forall k \neq j, m \neq i} \left( R_{ik} + R_{km} + R_{mj} d_{ij}^{km} \leq D_{ij} \right),$$

$$= \begin{cases} \max \left[ 0, V_{ij} - \min_m \left( ad_{ik} + R_{km} + R_{mj} \mid d_{ij}^{km} \leq D_{ij} \right) \right] & \text{if } k = i \\ \max \left[ 0, V_{ij} - \min_k \left( R_{ik} + R_{km} + ad_{mj} \mid d_{ij}^{km} \leq D_{ij} \right) \right] & \text{if } m = j \\ \max \left[ 0, V_{ij} - R_{ik} - R_{mj} - ad_{mk} \mid d_{ij}^{km} \leq D_{ij} \right] & \text{if } k \neq i, \quad m \neq j \\ 0 & \text{otherwise.} \end{cases} \quad (17)$$

In (17),

$$R_{km} = \begin{cases} ad_{km} & \text{if } \hat{Y}_{km} = 1 \\ d_{km} & \text{if } \hat{Y}_{km} = 0, \end{cases} \quad (18)$$

$d_{ij}^{km} = d_{ik} + d_{km} + d_{mj}$ . The economic meaning of  $V_{ij}^t$  is the incremental costs for adding one unit flow  $i \rightarrow j$ . And  $U_{ijkm}^t$  denotes the cutting route costs for unit flow  $i \rightarrow j$  when  $(k, m)$  is selected as hub arc.

Benders' cut at iteration  $t$  is  $\beta_t(Y) = \sum_{i,j} V_{ij}^t + \sum_{i,j,k,m} (f_{km} - U_{ijkm}^t) Y_{km}$ . And the master problem at iteration  $k$  can be designed as model (P4),

$$(P4) \quad \min \quad z \quad (19)$$

$$\text{s.t. } z \geq \sum_{i,j} V_{ij}^t + \sum_{i,j,k,m} (f_{km} - U_{ijkm}^t) Y_{km} \quad (20)$$

$$\forall t \in 1, 2, \dots, T,$$

$$Y_{km} = 0, 1; \quad z > 0. \quad (21)$$

In the iterative process, Benders decomposition gradually increases Benders' cut by constraints (20), rather than considering all constraints at once, so that the algorithm efficiency is improved. Solving the master problem (P4) gives us the updated variables  $\{\bar{Y}_{km}\}$  to try out for the next iteration, while solving the subproblem of (P3) provides us new trying schemes. Let  $lk, uk$  be the objective value of (P4) and (P3)

at iteration  $t$ . And let LB, UB be the current best lower bound and upper bound. The procedure is designed as in Algorithm 5.

*Algorithm 5* (Benders decomposition method for solving FMRICT). (1) Initialize parameters,  $UB = \infty$ ,  $LB = -\infty$ , and  $t = 1$ . Initialize hub arcs, and let  $\bar{Y}_{km} = 0$  for  $\forall(k, m)$ , which means that no hub arcs are selected at iteration 1. Initialize constraints in model (P4) by setting constraint (20) to be empty at first.

(2) Calculate the dual variables of model (P3) according to (17). Compute  $uk = \sum_{i,j} V_{ij}^t + \sum_k \sum_m \sum_i \sum_j (f_{km} - U_{ijkm}^t) \bar{Y}_{km}$ . If  $uk < UB$ , then  $UB = uk$ .

(3) Add Benders cut constraint  $z \geq \sum_{i,j} V_{ij}^t + \sum_k \sum_m \sum_i \sum_j (f_{km} - U_{ijkm}^t) Y_{km}$  to model (P4) and solve (P4) to get the lower bound  $lk$ . If  $lk > LB$ , then  $LB = lk$ . If there is no solution to (P4), then the original problem is unsolvable and the algorithm is terminated.

(4) Determine if it has reached the termination criterions. End algorithm if any one of the following two criterions is true: (1)  $UB - lb \leq 0.01$ , (2)  $t = 20$ .

(5) Update  $\{\bar{Y}_{km}\}$  according to the solution of model (P4). Update  $t = t + 1$  and return to step two.

## 5. Computational Experiments

We code the algorithms in c# based on the VS2008 and run them on ThinkPad x60 notebook computer which is equipped with 2.1GHZ Core2 CPU. In the procedure of Algorithm 5, we call Gurobi to solve model (P3). The test instances are from AP data package that can be downloaded from <http://people.brunel.ac.uk/mastjib> and includes postal flow data and distances data of 200 cities in Australia. With data about  $h_{ij}$ ,  $c_{ij}$ , and so forth, AP data package has become a very famous algorithm testing platform for hub-and-spoke network design, while still lacking data about  $f_{km}$  and  $D_{ij}$ . In our experiments, we let  $f_{km} = 2h_{km}c_{km}(1 - a)$  so that flow quantity of hub arcs is at least twice as much as directed flow quantity according to Lemma 1. Let  $D_{ij} = 1.2d_{ij}$ , which means that the length of hub route is no more than 20 percent of the directed route. Moreover, the first 10, 15, 20, 25, and 30 nodes were taken as instances in the AP data package, and the discount number  $a$  is set by 0.6, 0.7, or 0.8. At first, we apply Gurobi's *Branch & Cut* algorithm to obtain the exact solution of test cases, as shown in Table 1. We find that decision variables and constraints in the mixed-integer programming model (P1) would exceed 1510 thousands when  $n \geq 25$ , which is too large to solve by *Branch & Cut* algorithm on Gurobi. Then all the cases are tested with Algorithms 4 and 5. The result is shown in Table 2, in which the gap between upper bound and lower bound is defined by  $\text{gap} = 100(UB - LB)/LB$ .

The experiment indicates that Algorithms 4 and 5, compared to *Branch & Cut* algorithm on Gurobi, are much more time-saving and capable of solving large scaled instances with more than 25 nodes. Upper bounds obtained from Algorithm 5 have already reached the optimal solution in most instances. For all tested instances, maximum gaps

TABLE 1: Problem parameters of AP data package and computational result of *Branch & Cut* algorithm.

Problem	Problem parameters			<i>Branch &amp; Cut</i> algorithm	
	$a$	$n$	Number of transportation tasks	Optimal solution	Time (s)
AP10-6	0.6	10	90	251524	2.55
AP15-6	0.6	15	210	337655	62.59
AP20-6	0.6	20	380	1214739	255.85
AP25-6	0.6	25	600	—	—
AP30-6	0.6	30	870	—	—
AP10-7	0.7	10	90	281348	2.43
AP15-7	0.7	15	210	379664	24.82
AP20-7	0.7	20	380	1384638	86.78
AP25-7	0.7	25	600	—	—
AP30-7	0.7	30	870	—	—
AP10-8	0.8	10	90	311134	1.05
AP15-8	0.8	15	210	421537	5.27
AP20-8	0.8	20	380	1553251	21.62
AP25-8	0.8	25	600	—	—
AP30-8	0.8	30	870	—	—

TABLE 2: Computational result of Algorithms 4 and 5 for AP data package.

Instance	Algorithm 4				Algorithm 5			
	UB	LB	Gap	Time (s)	UB	LB	Gap	Time (s)
AP10-6	254741	251370	1.34	2.45	251524	250711	0.32	3.26
AP15-6	343625	334800	2.63	12.50	338031	334540	1.03	16.19
AP20-6	1243835	1197288	3.88	51.21	1221368	1204513	1.38	53.80
AP25-6	1588608	1487350	6.80	40.17	1557496	1522760	2.23	185.26
AP30-6	2607031	2457319	6.09	15.49	2581828	2477115	4.05	283.75
AP10-7	281812	278790	1.08	2.18	281348	280792	0.20	3.51
AP15-7	384132	377457	1.76	15.21	380079	377841	0.58	15.78
AP20-7	1412754	1370593	3.07	50.01	1390699	1375812	1.07	53.28
AP25-7	1795345	1720306	4.36	20.91	1767833	1745691	1.25	128.3
AP30-7	2950418	2830074	4.25	15.1	2926752	2847984	2.69	292.95
AP10-8	311723	311068	0.21	2.30	311128	310799	0.11	3.32
AP15-8	425198	420009	1.23	13.4	422749	420408	0.55	17.28
AP20-8	1574894	1548196	1.72	17.08	1556208	1545625	0.68	52.4
AP25-8	1998599	1959522	1.99	7.3	1980503	1965095	0.77	132.11
AP30-8	3274275	3219604	1.69	14.01	3267612	3213814	1.64	283.20

obtained from Algorithms 4 and 5 are 6.8% and 4.05%, averagely 2.86% and 1.24%, respectively. It is clear that both Benders decomposition method and Lagrangian relaxation algorithm possess pretty good performances on solving FMRICT problems.

As shown in Table 2, for small scaled instances with less than 15 nodes, Benders decomposition method could give the gap between upper bound and lower bound that is no more than 2.7% within 16 seconds, while Lagrangian relaxation algorithm no more than 1.03% within 63 seconds. For larger scaled problems with more than 20 nodes, Benders decomposition method gives the gap that is no more than 6.9% within 52 seconds, while Lagrangian relaxation algorithm no more

than 4.05% within 293 seconds. It implies that Algorithm 4 solves FMRICT problem faster, while Algorithm 5 gives better solutions.

## 6. Conclusion

The current collaborative transportation researches mainly consider the nodes cost of hubs, while ignore detouring cost, hub arcs cost, or incremental flows. FMRICT seeks a way of cutting down detouring route and building infrastructure or conveyances for hub arc and at the same time satisfies the demand of incremental flows by charge costs of building hub arc according to Lemma 1. All of them are very important

in practice and are foundations of achieving economies of scale in collaborative transportation. We build a mixed-integer programming model of FMRICT and then construct Lagrangian relaxation algorithm and Benders decomposition method to solve FMRICT. The experiments indicate that both algorithms have pretty good computational performance. However, FMRICT considers only one discount rate. In many cases, flow quantity and transportation cost show a piecewise linear relationship, so that different scales of flow quantity and transportation tools produce different discount rates. Therefore, collaborative transportation routing problem with piecewise linear relationship between flow quantity and transportation costs is prospective for the next research.

### Conflict of Interests

The authors declare that there is no conflict of interests regarding the publication of this paper.

### Acknowledgments

The research was supported by the National Natural Science Foundation of China (NSFC no. 71102151) and the Fundamental Research Funds for the Central Universities, China University of Geosciences (Wuhan), with nos. CUGL140424 and CUG120111. Thanks are also due to the anonymous referees who provided very valuable comments and pieces of advice.

### References

- [1] P. Sombuntham and V. Kachitvichayanukul, "A particle swarm optimization algorithm for multi-depot vehicle routing problem with pickup and delivery requests," in *Proceedings of the International MultiConference of Engineers and Computer Scientists (IMECS '10)*, pp. 1998–2003, March 2010.
- [2] R. Liu, Z. Jiang, R. Y. K. Fung, F. Chen, and X. Liu, "Two-phase heuristic algorithms for full truckloads multi-depot capacitated vehicle routing problem in carrier collaboration," *Computers & Operations Research*, vol. 37, no. 5, pp. 950–959, 2010.
- [3] L. Xing, P. Rohlfshagen, Y. Chen, and X. Yao, "An evolutionary approach to the multidepot capacitated arc routing problem," *IEEE Transactions on Evolutionary Computation*, vol. 14, no. 3, pp. 356–374, 2010.
- [4] A. Kansou and A. Yassine, "New upper bounds for the multi-depot capacitated arc routing problem," *International Journal of Metaheuristics*, vol. 1, no. 1, pp. 81–95, 2010.
- [5] V. Filipovic, J. Kratica, D. Tosic et al., "GA inspired heuristic for uncapacitated single allocation hub location problem," *Applications of Soft Computing*, vol. 58, pp. 149–158, 2009.
- [6] M. Köksalan and B. Soyly, "Bicriteria  $p$ -hub location problems and evolutionary algorithms," *INFORMS Journal on Computing*, vol. 22, no. 4, pp. 528–542, 2010.
- [7] K. R. Weng, *Research on Location and Routing Optimization for Hub-and-Spoke Logistics Network Design*, University of Electronic Science and Technology Press, 2009, (Chinese).
- [8] M. R. Silva and C. B. Cunha, "New simple and efficient heuristics for the uncapacitated single allocation hub location problem," *Computers & Operations Research*, vol. 36, no. 12, pp. 3152–3165, 2009.
- [9] M. Randall, "Solution approaches for the capacitated single allocation hub location problem using ant colony optimisation," *Computational Optimization and Applications*, vol. 39, no. 2, pp. 239–261, 2008.
- [10] I. Contreras, J. A. Díaz, and E. Fernández, "Lagrangian relaxation for the capacitated hub location problem with single assignment," *OR Spectrum. Quantitative Approaches in Management*, vol. 31, no. 3, pp. 483–505, 2009.
- [11] I. Rodríguez-Martín and J. J. Salazar-González, "A local branching heuristic for the capacitated fixed-charge network design problem," *Computers & Operations Research*, vol. 37, no. 3, pp. 575–581, 2010.
- [12] I. Correia, S. Nickel, and F. Saldanha-da-Gama, "The capacitated single-allocation hub location problem revisited: a note on a classical formulation," *European Journal of Operational Research*, vol. 207, no. 1, pp. 92–96, 2010.
- [13] I. Correia, S. Nickel, and F. Saldanha-da-Gama, "Single-assignment hub location problems with multiple capacity levels," *Transportation Research B*, vol. 44, no. 8-9, pp. 1047–1066, 2010.
- [14] J. Puerto, A. B. Ramos, and A. M. Rodríguez-Chía, "Single-allocation ordered median hub location problems," *Computers & Operations Research*, vol. 38, no. 2, pp. 559–570, 2011.
- [15] J. F. Chen, "The uncapacitated hub location problem with allocation constraints," in *Proceedings of the 8th International Conference on Information and Management Sciences*, vol. 8 of *Information and Management Sciences*, pp. 30–35, 2009.
- [16] H. A. Eiselt and V. Marianov, "A conditional  $p$ -hub location problem with attraction functions," *Computers & Operations Research*, vol. 36, no. 12, pp. 3128–3135, 2009.
- [17] J. F. Campbell, A. T. Ernst, and M. Krishnamoorthy, "Hub arc location problems: part I—introduction and results," *Management Science*, vol. 51, no. 10, pp. 1540–1555, 2005.
- [18] J. F. Campbell, A. T. Ernst, and M. Krishnamoorthy, "Hub arc location problems: part II—formulations and optimal algorithms," *Management Science*, vol. 51, no. 10, pp. 1556–1571, 2005.
- [19] J. F. Campbell, "Hub location for time definite transportation," *Computers & Operations Research*, vol. 36, no. 12, pp. 3107–3116, 2009.
- [20] R. S. De Camargo, G. De Miranda Jr., and H. P. L. Luna, "Benders decomposition for hub location problems with economies of scale," *Transportation Science*, vol. 43, no. 1, pp. 86–97, 2009.

## Research Article

# Weighted Multimodel Predictive Function Control for Automatic Train Operation System

Shuhuan Wen,<sup>1,2</sup> Jingwei Yang,<sup>1</sup> Ahmad B. Rad,<sup>3</sup> Shengyong Chen,<sup>4</sup> and Pengcheng Hao<sup>1</sup>

<sup>1</sup> Key Laboratory of Industrial Computer Control Engineering of Hebei Province, Yanshan University, Qinhuangdao 066004, China

<sup>2</sup> State Key Laboratory of Rail Traffic Control and Safety, Beijing Jiaotong University, Beijing 100044, China

<sup>3</sup> School of Engineering Science, Simon Fraser University, 250-13450, 102 Avenue, Surrey, BC, Canada V3T 0A3

<sup>4</sup> College of Computer Science and Technology, Zhejiang University of Technology, Hangzhou 310023, China

Correspondence should be addressed to Shengyong Chen; [csy@zjut.edu.cn](mailto:csy@zjut.edu.cn)

Received 23 September 2013; Accepted 28 November 2013; Published 3 February 2014

Academic Editor: M. Montaz Ali

Copyright © 2014 Shuhuan Wen et al. This is an open access article distributed under the Creative Commons Attribution License, which permits unrestricted use, distribution, and reproduction in any medium, provided the original work is properly cited.

Train operation is a complex nonlinear process; it is difficult to establish accurate mathematical model. In this paper, we design ATO speed controller based on the input and output data of the train operation. The method combines multimodeling with predictive functional control according to complicated nonlinear characteristics of the train operation. Firstly, we cluster the data sample by using fuzzy-c means algorithm. Secondly, we identify parameter of cluster model by using recursive least square algorithm with forgetting factor and then establish the local set of models of the process of train operation. Then at each sample time, we can obtain the global predictive model about the system based on the weighted indicators by designing a kind of weighting algorithm with error compensation. Thus, the predictive functional controller is designed to control the speed of the train. Finally, the simulation results demonstrate the effectiveness of the proposed algorithm.

## 1. Introduction

With rapid expansion of the nationwide metropolitan population, people put forward higher requirement for the speed and quality of the urban railway traffic train. The Automatic Train Control (ATC) system, as an important subsystem of the automatic train control system, can replace the drivers to realize automatic train operation. On the basis of ensuring safety and punctuality, it can furthest implement the demand of energy conservation and improve passengers comfort. It is the prospective development direction of the railway train.

Train operation is a complex nonlinear process; it is difficult to establish accurate mathematical model because of nonlinearities and complex operating environments such as ramps, curves, and tunnels. So it increases difficulties to realize the ATO system. Based on the input and output data, people will apply some normal nonlinear system identification methods, like Hammerstein model structure [1], Wiener model structure [2], and so forth. But the model structure cannot reveal global performance of the complicated system.

Multimodel method based on decomposition combination rule can provide an effective way for the modeling and control problem of complicated nonlinear system. Multiple linear local models are used to replace the complicated controlled object to simplify the nonlinear system structure. And the control algorithm based on linear model can be applied conveniently to nonlinear control system.

For multimodel control system, firstly we should build local linear model set of the nonlinear system. The common method is to linearize the nonlinear system near the equilibrium point to get local model set [3]. However, it is difficult to confirm the equilibrium point and model because of the complication of train operation. Based on the input and output data of nonlinear systems, cluster analysis divides the data according to some kind of similarity criterion. The method that combines cluster analysis with traditional identification provides an effective way to establish the local model set of nonlinear system.

Predictive functional control is the third generation of model-predictive control algorithm. It not only has the main

features of model-predictive control, but also owns its unique advantages. The introduction of base function can make the control input structure more clear, and obviously reduces online computation. This paper proposes a method based on the actual train operation. It combines cluster multi-model weighted modeling with predictive functional control algorithm to design ATO speed controller. Firstly, we use fuzzy c-means (FCM) clustering algorithm with recursive least square algorithm of forgetting factor to establish the local model set of nonlinear operation process. In order to improve the performance of control system, we design a kind of weighted algorithm with error compensation. The global model will be achieved through weighted combination of local models, and then we can design predictive functional controller.

## 2. Problem Information

According to the train dynamics, the dynamic equations can be described as follows [4]:

$$\begin{aligned} \frac{ds(t)}{dt} &= v(t), \\ \frac{dv(t)}{dt} &= u(t) - w(v(t)) - g(s(t)), \\ w(v(t)) &= av(t)^2 + bv(t) + c, \\ g(s(t)) &= l \sin(\alpha(s)), \end{aligned} \quad (1)$$

where  $s$  is the train position coordinate,  $v$  is the velocity of train,  $u$  is the traction force or breaking force,  $w(v)$  is motion resistance related to velocity,  $g(s)$  is external resistance caused by the slope, curve, and wind,  $l$  is a constant, and  $\alpha(s)$  is slope degree of  $s$  point.

In (1), we can see that train operation is a nonlinear process. As the speed increases, the nonlinearity will get stronger, and the operation speed will be easily affected by external resistance. The purpose of this paper is to design reasonable ATO speed control algorithm to make train operation as objective speed curve and distance curve. The objective speed curve and distance curve are obtained by computing optimal operation figure.

## 3. The Establishment of Multimodels Set

Cluster analysis is a kind of data mining technology, which is widely researched and applied. It can divide physical or abstract data into groups in accordance to similarity degree. This feature provides an effective way to divide models into the groups of multimodel modeling. In the field of process modeling, cluster multimodel modeling adequately excavates relationships between the data based on the input and output data. It divides the data into different features groups reasonably. In recent years, multimodel modeling method based on clustering is widely used and a large number of cluster algorithms emerge. The fuzzy c-means clustering algorithm is a simple and effective clustering method.

The FCM is an unsupervised clustering algorithm. A clustering problem can be expressed as follows.

Let  $X = \{x_1, \dots, x_n\}$  be a set of given data, where each data point  $x_k$  ( $k = 1, \dots, n$ ) is a vector in  $\mathfrak{R}^p$  and  $n$  is the number of sample data. Its aim is to find the membership matrix  $R = [r_{ij}]_{c \times n}$  and the cluster centers of sample data set  $O = [o_1, o_2, \dots, o_c]$  that minimize a dissimilarity function. When the clustering number is given, FCM can be described as a mathematical programming problem [5]:

$$\begin{aligned} \min \quad & J_m(R, o) = \sum_{j=1}^n \sum_{i=1}^c r_{ij}^m \|x_j - o_i\|^2 \\ \text{s.t.} \quad & \sum_{i=1}^c r_{ij} = 1, \quad 1 \leq j \leq n \\ & r_{ij} \in [0, 1], \quad 1 \leq j \leq n, \quad 1 \leq i \leq c \\ & 0 < \sum_{j=1}^n r_{ij} < n, \end{aligned} \quad (2)$$

where  $r_{ij}$  represents the membership of  $x_j$  in the cluster  $i$ ,  $x_j \in \mathfrak{R}^p$  is the  $j$ th measured data,  $o_i \in \mathfrak{R}^p$  is the  $i$ th center of the cluster,  $\| * \|$  denotes the distance of the measured data from the cluster center which can be measured by means of Euclidean norm,  $m$  is any real number larger than 1, and  $m = 2$  is used in this contribution.  $r_{ij}$  and  $o_i$  can be obtained from the paper [5].

In multimodel control, it is important to establish the multiple models set. Xie and Beni introduced a valid measure. The separation measure  $V_{xb}$  is defined as in [6].

The optical cluster number is

$$c_{\text{opt}} = \arg \min_c (V_{xb}). \quad (3)$$

In summary, the procedure for the fuzzy c-means algorithm is as follows.

*Step 1.* Collect the input and output data of training operation, and assume the maximum cluster number is 10. We apply Xie-Beni cluster validity index to assure the optical cluster number  $c$ . Initialize  $R = R_0$ , preset the index weight  $m$ , and  $\varepsilon > 0$ .

*Step 2.* At  $k$ th iteration, compute the cluster centers  $o_i^k$  where  $r_{ij} \in R^k$  ( $o_i^k$  and  $R^k$ , are resp., the cluster centers of sample data set and the membership matrix of the  $k$ th iteration).

*Step 3.* Update  $R^{k+1}$  using  $r_{ij}$  ( $R^{k+1}$  is the membership matrix of the  $(k+1)$ th iteration).

*Step 4.* If  $\|R^{k+1} - R^k\| > \varepsilon$ , then  $k = k + 1$ ; go to Step 2, otherwise stop.

For each cluster set, the parameters of sublinear model are identified by using the forgetting factor recursive least squares (RLS) algorithm. To design GPC controller conveniently, we

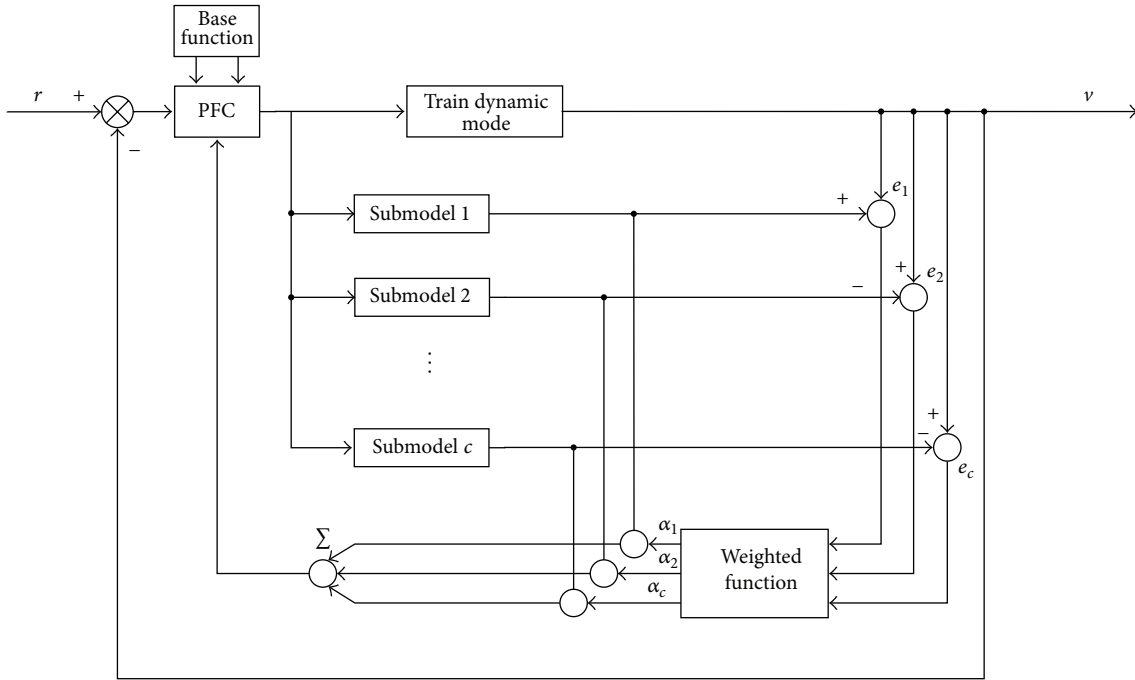


FIGURE 1: The structure of multimodel weighted predictive function control for train.

choose SISO (single-input single-output) Controlled Auto-Regressive Integrated Moving Average (CARIMA) model. So the sublinear model is described as follows [7]:

$$A(z^{-1})y(t) = B(z^{-1})u(t-1) + \frac{\zeta(t)}{\Delta}, \quad (4)$$

$$\begin{aligned} A(z^{-1}) &= 1 + a_1z^{-1} + \dots + a_{n_a}z^{-n_a}, \\ \deg A(z^{-1}) &= n_a, \\ B(z^{-1}) &= b_0 + b_1z^{-1} + \dots + b_{n_b}z^{-n_b}, \\ \deg B(z^{-1}) &= n_b, \end{aligned} \quad (5)$$

where  $u(t)$  is the control input and  $y(t)$  is the measured variable or output; in this paper  $y(t) = v(t)$ , and  $\zeta(t)$  is the white noise in which the mean value is zero;  $n_a$  and  $n_b$  are the orders of output and input, respectively.  $\Delta = 1 - z^{-1}$  is the differencing operator;  $A(z^{-1})$ ,  $B(z^{-1})$ , and  $C(z^{-1})$  are polynomials with the backward shift operator  $z^{-1}$ . Among them, the first several elements of the polynomial  $B(z^{-1})$  can be zero to express the corresponding delay numbers. The sublinear model can be identified by using the form of regression equation.

#### 4. Multimodel Predictive Function Controller

##### 4.1. The Structure of Multimodel Weighted Predictive Function.

The structure of multimodel weighted predictive function is shown in Figure 1. In Figure 1, the submodels are obtained by clustering and identification algorithm. At each control time, we compare the error of real output and the output

of submodel  $i$ . According to the matching degree, the corresponding weights are assigned to each submodel by weighted function. The bigger weight value represents the smaller mismatch of submodel.

**4.2. Multimodel Weighted Strategy.** Multimodel control algorithm based on weighted method can make full advantage of system information of each local model and describe the dynamics of nonlinear system more accurately at the overlap of multiple subspace. The key question is to find the appropriate weighted strategy to enable local model to approach nonlinear dynamics effectively. Based on the multimodel integration strategy proposed in the literature [8], this paper proposes an improved multimodel weighted strategy with error compensation.

Define  $e_i(t) = y(t) - \hat{y}_i(t)$ . The expression denotes the error between real output and the output of the submodel  $i$  at time  $t$ . The average matching error between submodel  $i$  and system at time  $t$  is shown as follows:

$$me_i(t) = \frac{e_i(t) + \sum_{j=1}^L \eta^L e(t-j)}{L+1}, \quad (6)$$

where  $L$  denotes the error length in the past time at the average error computation and  $\eta$  denotes the forgetting degree of the past error.

The performance index based on model matching degree is defined as follows:

$$\tilde{J}_i(t) = \frac{|e_i(t) - me_i(t)| + \sum_{j=1}^L \eta^L |e_i(t-j) - me_i(t)|}{L+1}. \quad (7)$$

As (7) shows, the weight of submodel  $i$  is

$$\alpha_i(t) = \frac{\tilde{J}_i(t)^{-1}}{\sum_{i=1}^c \tilde{J}_i(t)^{-1}}, \quad (8)$$

where  $c$  is the number of local models.

After adding weighted value, the global predictive model is

$$\begin{aligned} \hat{y}(t) = & \sum_{i=1}^c \alpha_i a_1^i y(t-1) + \sum_{i=1}^c \alpha_i a_2^i y(t-2) \\ & + \cdots + \sum_{i=1}^c \alpha_i a_{n_a}^i y(t-n_a) \\ & + \sum_{i=1}^c \alpha_i b_0^i u(t-1) + \sum_{i=1}^c \alpha_i b_1^i u(t-2) \\ & + \cdots + \sum_{i=1}^c \alpha_i b_{n_b}^i u(t-n_b-1). \end{aligned} \quad (9)$$

**4.3. Predictive Function Controller Design.** Because of its convenient derivation and strong robustness, predictive function control absorbs many scholars. At the present stage, the research of PFC mostly aims at first-order system or first-order plus pure delay system. Because the first-order system, first-order plus pure delay system, and second-order system can be described by CARIMA model, it is more general to study the PFC algorithm based on CARIMA model. In this paper, we study the predictive function control based on CARIMA model; the structure of predictive model is shown as (4).

Designing ATO system needs to guarantee the travelling comfort, and it is closely related to operation velocity. So the control input should decrease large fluctuation in designing ATO system. For this purpose, we add summation form of control increment to optimized performance indicator; optimized performance is shown as follows [9]:

$$\min J = \min \left[ (Y_b - Y_r)^T (Y_b - Y_r) + \rho \Delta U^T \Delta U \right], \quad (10)$$

where

$$\begin{aligned} Y_b &= [y_b(t+1), y_b(t+2), \dots, y_b(t+N_1)]^T; \\ Y_r &= [y_r(t+1), y_r(t+2), \dots, y_r(t+N_1)]^T; \\ \Delta U &= [\Delta u(t), \Delta u(t+1), \dots, \Delta u(t+N_u-1)]^T. \end{aligned} \quad (11)$$

In predictive function control, control input is regarded as a linear combination of base function which is given advance [9]; generally ramp function and step functions can satisfy most of the control requirements. So in this paper, control input is regarded as weight combination of two base function proposed before; the form is shown as follows:

$$u(t+i) = \mu_1 + \mu_2 i, \quad (i = 0, 1, \dots, N_u - 1). \quad (12)$$

Equation (12) can be rewritten as

$$U = \begin{bmatrix} u(t) \\ u(t+1) \\ \vdots \\ u(t+N_u-1) \end{bmatrix} = \begin{bmatrix} 1 & 0 \\ 1 & 1 \\ \vdots & \vdots \\ 1 & N_u-1 \end{bmatrix} \begin{bmatrix} \mu_1 \\ \mu_2 \end{bmatrix} = C_1 \bar{\mu}, \quad (13)$$

where

$$C_1 = \begin{bmatrix} 1 & 0 \\ 1 & 1 \\ \vdots & \vdots \\ 1 & N_u-1 \end{bmatrix}_{N_u \times 2}, \quad \bar{\mu} = \begin{bmatrix} \mu_1 \\ \mu_2 \end{bmatrix}. \quad (14)$$

In PFC, the output  $y(t)$  of predictive model is composed of free response  $y_f(t)$  and forced response  $y_p(t)$ ; the form is shown as follows [9]:

$$y(t) = y_p(t) + y_f(t). \quad (15)$$

So the predictive output of PFC is

$$y(t+i) = y_p(t+i) + y_f(t+i), \quad (i = 1, 2, \dots, N_1). \quad (16)$$

As for the model free response output  $Y_f = [y_f(t+1), y_f(t+2), \dots, y_f(t+N_1)]^T$ , Zhang and Wangquanling, and so forth proposed a kind of recursive deprivation [10]:

$$\begin{aligned} y_f(t+1|t) &= \sum_{j=1}^{n_a} (-a_j) y'(t+i-j) \\ &+ \sum_{j=1}^{n_b} b_j u'(t+i-j), \quad i = 1, 2, \dots, N_1, \end{aligned} \quad (17)$$

where

$$y'(t+i-j) = \begin{cases} y(t+i-j), & i < j+1, \\ y_f(t+i-j|t), & i \geq j+1, \end{cases} \quad (18)$$

$$u'(t+i-j) = \begin{cases} u(t+i-j), & i < j, \\ 0, & i \geq j. \end{cases}$$

As for the model forced response output  $Y_p = [y_p(t+1), y_p(t+2), \dots, y_p(t+N_1)]^T$  can be derived as follows:

$$y_p(t+i|t) = \sum_{j=1}^i r_j u(t+i-j), \quad (i = 1, 2, \dots, N_1), \quad (19)$$

where

$$\begin{aligned} r_1 &= b_1, \\ r_j &= \sum_{k=1}^{\min(j-1, n_a)} (-a_k) r_{j-k} + b_j, \quad 2 \leq j \leq n_b, \\ r_j &= \sum_{k=1}^{\min(j-1, n_a)} (-a_k) r_{j-k}, \quad n_b < j \leq N_1. \end{aligned} \quad (20)$$

From (13) and (19), it can derived that

$$\begin{aligned}
 Y_p &= \begin{bmatrix} y_p(t+1) \\ y_p(t+2) \\ \vdots \\ y_p(t+N_1) \end{bmatrix} \\
 &= \begin{bmatrix} r_1 & 0 & \cdots & 0 \\ r_2 & r_1 & \cdots & 0 \\ \vdots & \vdots & \ddots & \vdots \\ r_{N_1} & r_{N_1-1} & \cdots & r_1 \end{bmatrix} \begin{bmatrix} 1 & 0 \\ 1 & 1 \\ \vdots & \vdots \\ 1 & N_1 - 1 \end{bmatrix} \begin{bmatrix} \mu_1 \\ \mu_2 \end{bmatrix} \\
 &= C_2 C_3 \bar{\mu},
 \end{aligned} \tag{21}$$

where

$$C_2 = \begin{bmatrix} r_1 & 0 & \cdots & 0 \\ r_2 & r_1 & \cdots & 0 \\ \vdots & \vdots & \ddots & \vdots \\ r_{N_1} & r_{N_1-1} & \cdots & r_1 \end{bmatrix}; \quad C_3 = \begin{bmatrix} 1 & 0 \\ 1 & 1 \\ \vdots & \vdots \\ 1 & N_1 - 1 \end{bmatrix}. \tag{22}$$

To reduce the effect caused by model mismatch, error correction is used to compensate the predictive output.

Consider

$$y_b(t+i) = y(t+i) + e(t+i). \tag{23}$$

Predictive error is described as the following form:

$$e(t+i) = y(t) - y_m(t), \quad i = 0, 1, \dots, N_1, \tag{24}$$

where  $y(t)$  is the output of the predictive model and  $y_m(t)$  is the actual output of the system.

So

$$Y_b = Y_p + Y_f + C_4 e(t) = C_2 C_3 \bar{\mu} + Y_f + C_4 e(t), \tag{25}$$

where  $C_4 = [1; 1; \dots; 1]_{N_1 \times 1}$ .

Because  $\Delta u(t) = u(t) - u(t-1)$ , from (13), we can get that

$$\begin{aligned}
 \Delta U &= \begin{bmatrix} \Delta u(t) \\ \Delta u(t+1) \\ \vdots \\ \Delta u(t+N_u-1) \end{bmatrix} \\
 &= \begin{bmatrix} u(t) - u(t-1) \\ u(t+1) - u(t) \\ \vdots \\ u(t+N_u-1) - u(t+N_u-2) \end{bmatrix} \\
 &= \begin{bmatrix} 1 & 0 & \cdots & 0 \\ -1 & 1 & \cdots & 0 \\ \vdots & \vdots & \cdots & 0 \\ 0 & 0 & \cdots & 1 \end{bmatrix} \begin{bmatrix} u(t) \\ u(t+1) \\ \vdots \\ u(t+N_u-1) \end{bmatrix} - \begin{bmatrix} u(t-1) \\ 0 \\ \vdots \\ 0 \end{bmatrix} \\
 &= C_5 U - U_0 = C_5 C_1 \bar{\mu} - U_0,
 \end{aligned} \tag{26}$$

where

$$C_5 = \begin{bmatrix} 1 & 0 & \cdots & 0 \\ -1 & 1 & \cdots & 0 \\ \vdots & \vdots & \cdots & 0 \\ 0 & 0 & \cdots & 1 \end{bmatrix}_{N_u \times N_u}, \quad U_0 = \begin{bmatrix} u(t-1) \\ 0 \\ \vdots \\ 0 \end{bmatrix}_{N_u \times 1}. \tag{27}$$

Substituting (23) and (26) into (10) and letting  $\partial J / \partial \bar{\mu} = 0$ , we can get that

$$\begin{aligned}
 \bar{\mu} &= \left[ (C_2 C_3)^T (C_2 C_3) + \rho (C_5 C_1)^T (C_5 C_1) \right]^{-1} \\
 &\quad \times \left[ (C_2 C_3)^T (Y_r - Y_f - C_4 e(t)) + \rho (C_5 C_1)^T U_0 \right].
 \end{aligned} \tag{28}$$

Let  $C_2 C_3 = C_6$ ,  $C_5 C_1 = C_7$ ; we can get that

$$\bar{\mu} = (C_6^T C_6 + \rho C_7^T C_7)^{-1} \left[ C_6^T (Y_r - Y_f - C_4 e(t)) + \rho C_7^T U_0 \right]. \tag{29}$$

From (12) and (29), we can get control subsequence of the future time. Predictive function control retains the rolling optimization strategy and just applies the current control input to system. So the current control input of predictive function control is

$$u(t) = \mu_1 + \mu_2 \times 0 = \mu_1 = [1, 0] \bar{\mu}. \tag{30}$$

### 5. Simulation Results and Discussions

A concrete train operation system [11] is used to test the performance of the proposed algorithm. We consider a 17285.5 meters long trail line. Because curves and tunnel external force will convert to ramp force under a certain condition, we just consider a length of ramp force in simulation. It is defined as follows:

$$g(s(t)) = \begin{cases} \left( \frac{0.2}{1000} \right) \times s(t) - 1.0, & 5000 < s(t) \leq 6000, \\ 0.2, & 6000 < s(t) \leq 7000, \\ - \left( \frac{0.2}{800} \right) \times s(t) + 1.95, & 7000 < s(t) \leq 7800. \end{cases} \tag{31}$$

The unit basic resistance model is determined empirically from empirical formula which is derived by experiments. In this paper we choose unit basic resistance model of Shenzhen metro line 3. It is defined as follows:

$$w_0(v(t)) = 0.00675v^2(t) + 0.394v(t) + 20.89. \tag{32}$$

In the operation process of the train, one of energy-saving control scheme is to keep a constant speed in the cruise stage, reducing unnecessary braking and acceleration. This simulation imitates the constant-speed cruise motion of

TABLE 1: The result of cluster.

$C$	$V_{xb}$	$C$	$V_{xb}$
2	0.1344	7	0.0431
3	0.0798	8	0.0410
4	0.0451	9	0.1505
5	0.0221	10	0.1602
6	0.0816	—	—

the rail train. We can obtain the ATO speed by composite computation:

$$v_d(t) = \begin{cases} 0.75t, & 0 \leq t \leq 40, \\ 30, & 40 < t \leq 560, \\ -0.35t + 226, & 560 < t \leq 600, \\ -0.7t + 436, & 600 < t \leq 610, \\ -t + 619, & 610 < t \leq 619. \end{cases} \quad (33)$$

The distance profile in the simulation is as follows:

$$s_d(t) = \begin{cases} 0.375t^2, & 0 \leq t \leq 40, \\ 600 + 30(t - 40), & 40 < t \leq 560, \\ -0.175t^2 + 226t - 55480, & 560 < t \leq 600, \\ -0.35t^2 + 436t - 118480, & 600 < t \leq 610, \\ -0.5t^2 + 619t - 174295, & 610 < t \leq 619. \end{cases} \quad (34)$$

First of all, we obtain the input and output data of train operation based on dynamic model. According to the fuzzy  $c$ -means cluster algorithm and Xie-Beni cluster valid measure, we can obtain the optimal number of submodels. The result of clustering is shown in Table 1.

In Table 1,  $C$  denotes the number of cluster;  $V_{xb}$  denotes the value of cluster valid measure. When the cluster number is 5, the value of  $V_{xb}$  is the minimum. So the optimal number of cluster is 5. According to the clustering set and forgetting factor recursive least squares identification algorithm, the submodels set can be defined as follows.

Submodel 1:

$$y(t) - 0.9515y(t-1) = 0.0375u(t-1) + \zeta(t); \quad (35)$$

Submodel 2:

$$y(t) - 0.9790y(t-1) = 0.0150u(t-1) + \zeta(t); \quad (36)$$

Submodel 3:

$$y(t) - 0.9891y(t-1) = 0.0020u(t-1) + \zeta(t); \quad (37)$$

Submodel 4:

$$y(t) - 0.9748y(t-1) = 0.0161u(t-1) + \zeta(t); \quad (38)$$

Submodel 5:

$$y(t) - 0.9902y(t-1) = 0.0051u(t-1) + \zeta(t). \quad (39)$$

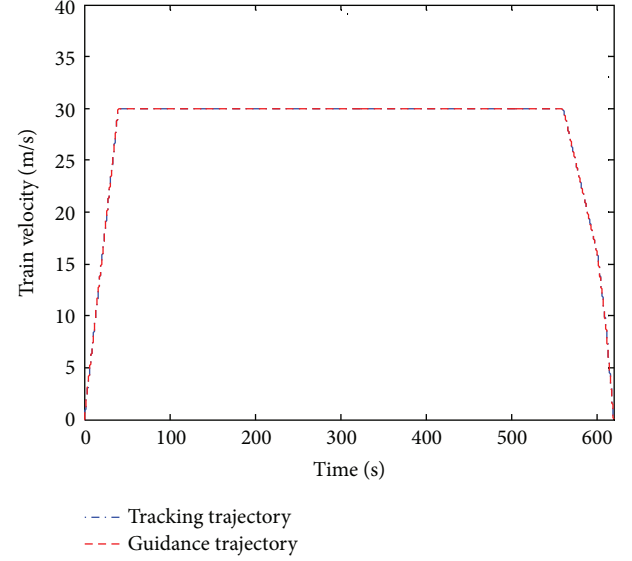


FIGURE 2: Train velocity tracking curve (this paper).

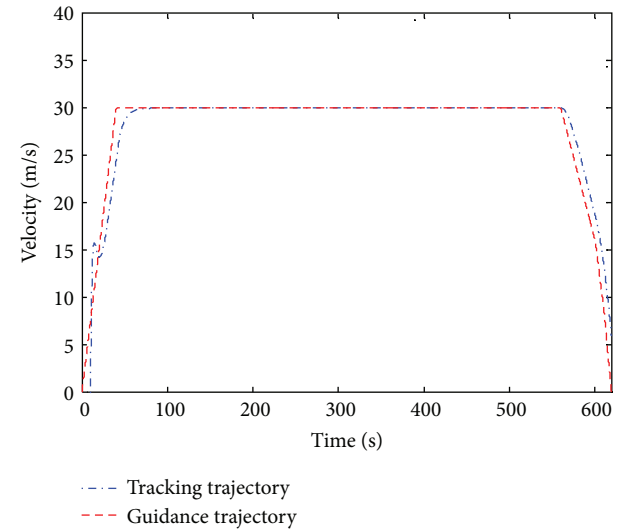


FIGURE 3: Train velocity tracking curve (single model PFC).

In controller designing, we define  $L = 2$ ,  $\eta = 0.9$  according to the weighted scheme; the parameters of predictive function controller are  $N_1 = 5$  and  $N_u = 2$ . The algorithm proposed in this paper is compared with single-model PFC algorithm and the result is shown in Figures 2 and 3.

From Figures 2 and 3, we can see that the proposed scheme can track the ATO speed profile precisely and achieve the tracking task. But at some local working points, the single-model predictive function control algorithm cannot track the objective curve precisely. The reason is that single-model predictive function control algorithm cannot describe the global performance of nonlinear train operation. The multimodel control algorithm has better control performance, and can describe global state of nonlinear system.

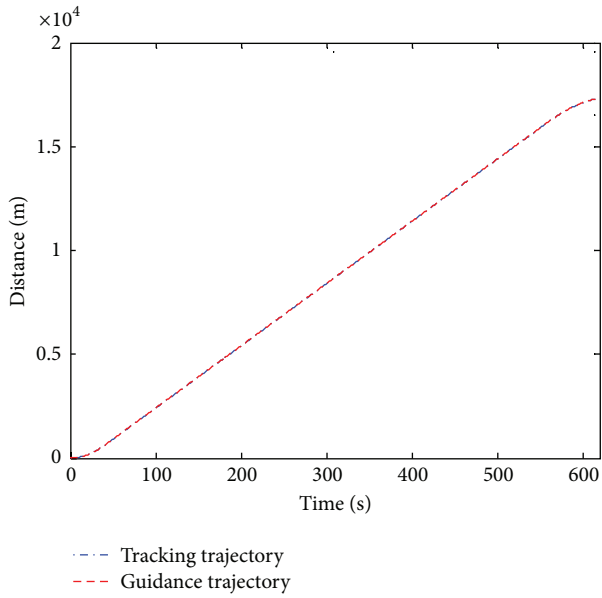


FIGURE 4: Train distance tracking curve (this paper).

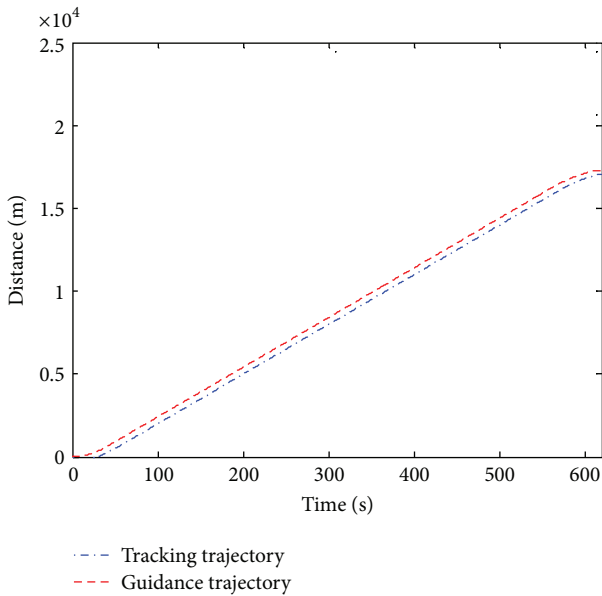


FIGURE 5: Train distance tracking curve (single model PFC).

In Figures 4 and 5, we can see that the algorithm of the ATO speed controller proposed in this paper can make the curve almost match together. And the results meet the accurate requirement of the stopping. Because at some local working points the single-model PFC algorithm cannot describe the operation character precisely, the distance trajectory cannot track the given trajectory.

Figure 6 shows the tracking situation of train acceleration and the given acceleration under the control of multimodel predictive function control. Figure 7 shows the part weighted changing curves of local model in multimodel control. The results show that more placidly the stable weights changing

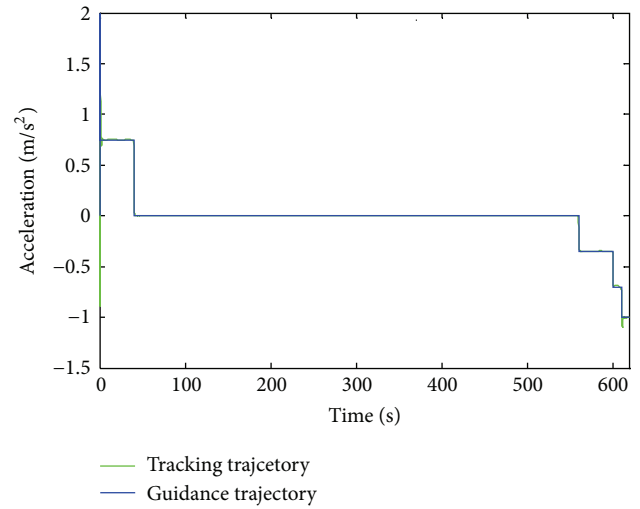


FIGURE 6: Train acceleration tracking curve (this paper).

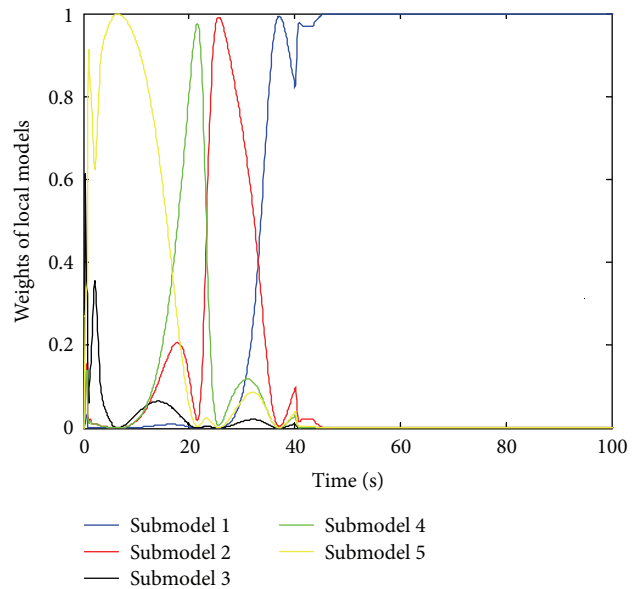


FIGURE 7: The figure of weight change of local model.

can assure the transformation of global model. Then the acceleration will not vibrate largely when the models transform.

## 6. Conclusions

In this paper, we studied the speed controller of ATO system by combining clustering multimodel weighted modeling method with predictive function control algorithm. The proposed algorithm solved the modeling and control problem of nonlinear train operation system. Firstly, we used clustering and identification algorithm to build local model set of train operation process. At each sample time, weighted scheme with error compensation is combined with every local model according to the respective weight to obtain global model.

After meeting linear requirement, we can design predictive function controller. Finally, the simulation results are provided to show the effectiveness of the proposed algorithm.

### Conflict of Interests

The authors declare that there is no conflict of interests regarding the publication of this paper.

### Acknowledgments

This work is supported by the State Key Laboratory of Rail Traffic Control and Safety (Contract no. RCS2011K007), Beijing Jiaotong University and the Hebei Province Natural Science Foundation under project Grant no. F2014203095, the Young Teacher of Yanshan University under the project no. 13LGA007, National Natural Science Foundation of China (61325019, 61173096, and R1110679), and International Science & Technology Cooperation Program of China (S2014GAT030).

### References

- [1] F. Ding and T. Chen, "Identification of Hammerstein nonlinear ARMAX systems," *Automatica*, vol. 41, no. 9, pp. 1479–1489, 2005.
- [2] G. Shafiee, M. M. Arefi, M. R. Jahed-Motlagh, and A. A. Jalali, "Nonlinear predictive control of a polymerization reactor based on piecewise linear Wiener model," *Chemical Engineering Journal*, vol. 143, no. 1–3, pp. 282–292, 2008.
- [3] X. Yugeng and W. Fan, "Nonlinear multi-model predictive control," *Acta Automatica Sinica*, vol. 22, no. 4, pp. 456–460, 1996.
- [4] Y. Wang and Z. S. Hou, "Terminal iterative learning control for station stop control of a train," in *Proceedings of the Symposium on Learning Control at IEEE CDC*, vol. 6, pp. 3119–3124, Shanghai, China, December 2009.
- [5] T. Velmurugan and T. Santhanam, "Performance evaluation of K-means and fuzzy C-means clustering algorithms for statistical distributions of input data points," *European Journal of Scientific Research*, vol. 46, no. 3, pp. 320–330, 2010.
- [6] C.-H. Chou, M.-C. Su, and E. Lai, "A new cluster validity measure and its application to image compression," *Pattern Analysis and Applications*, vol. 7, no. 2, pp. 205–220, 2004.
- [7] D. W. Clarke, C. Mohtadi, and P. S. Tuffs, "Generalized predictive control—part I. The basic algorithm," *Automatica*, vol. 23, no. 2, pp. 137–148, 1987.
- [8] P. P. Bonissone, F. Xue, and R. Subbu, "Fast meta-models for local fusion of multiple predictive models," *Applied Soft Computing Journal*, vol. 11, no. 2, pp. 1529–1539, 2011.
- [9] S. Wen, "A fast algorithm for adaptive predictive function of Hénon chaotic system," *Acta Physica Sinica*, vol. 58, no. 8, pp. 5209–5213, 2009.
- [10] Q. L. Zhang and S. Q. Wang, "Adaptive predictive function control using ARMAX models," *Information and Control*, vol. 29, no. 5, pp. 431–436, 2000.
- [11] X. Dexin, "Choice of maximum running speed of vehicles for urban mass transit," *Journal of Railway Engineering*, vol. 2, no. 113, pp. 97–99, 2008.

## Research Article

# Mathematical Model of Pipeline Abandonment and Recovery in Deepwater

Xia-Guang Zeng,<sup>1,2</sup> Meng-Lan Duan,<sup>1,2</sup> and Chen An<sup>1,2</sup>

<sup>1</sup> College of Mechanical and Transportation Engineering, China University of Petroleum, Beijing 102249, China

<sup>2</sup> Offshore Oil and Gas Research Center, China University of Petroleum, Beijing 102249, China

Correspondence should be addressed to Xia-Guang Zeng; xiaguangzeng@126.com

Received 28 September 2013; Accepted 10 December 2013; Published 29 January 2014

Academic Editor: M. Montaz Ali

Copyright © 2014 Xia-Guang Zeng et al. This is an open access article distributed under the Creative Commons Attribution License, which permits unrestricted use, distribution, and reproduction in any medium, provided the original work is properly cited.

In offshore oil and gas engineering the pipeline abandonment and recovery is unavoidable and its mechanical analysis is necessary and important. For this problem a third-order differential equation is used as the governing equation in this paper, rather than the traditional second-order one. The mathematical model of pipeline abandonment and recovery is a moving boundary value problem, which means that it is hard to determine the length of the suspended pipeline segment. A novel technique for the handling of the moving boundary condition is proposed, which can tackle the moving boundary condition without contact analysis. Based on a traditional numerical method, the problem is solved directly by the proposed technique. The results of the presented method are in good agreement with the results of the traditional finite element method coupled with contact analysis. Finally, an approximate formula for quick calculation of the suspended pipeline length is proposed based on Buckingham's Pi-theorem and mathematical fitting.

## 1. Introduction

Bad weather is frequent during laying offshore pipelines, so the pipeline abandonment and recovery operation is unavoidable. In offshore oil and gas engineering the pipeline laying engineers need to do detailed mechanical analysis to determine the operation parameters and then make sure that the pipeline will not overstress during the operation. To do the mechanical analysis the mathematical model is a very important problem. In the abandonment operation the A&R cable lowers a pipeline down to the seabed by a pull head and in the recovery operation lifts it up to the sea level. During the process the pipeline's axial forces, bending moments must be controlled in a reasonable scope to prevent its strength damage. The calculation of these quantities is very useful to guide the operation. So the mathematical model of pipeline abandonment and recovery should be established.

The sketch of the pipeline abandonment and recovery operation is shown in Figure 1. In the processes a pipeline is lifted up from the seabed to the sea surface or put down to the seabed from the sea surface by joint A. The two physical

processes are generally called one point lifting and lowering. The processes are mutually inversed and can be described by the same mathematical model. A lot of papers have reported the pipeline installation of mathematical models which are closely related to this operation. Palmer et al. [1] investigated the stresses and configurations of the pipelines being laid from a lay barge over a stinger. They derived equations governing the configuration and solved them by different techniques. Meanwhile they suggested a nondimensionalized governing equation. Mattheij and Rienstra [2] studied the pipeline S-laying model based on a second-order nonlinear differential equation. In the work they explained some difficulties in approximating the numerical solutions. Zhu and Cheung [3] presented an analytical method for finding the elastic deflection of submerged pipelines laid with an adjustable stinger. They claimed that the method costs less computational time than the finite element method (FEM). Guarracino and Mallardo [4] showed a refined analytical analysis of the pipeline S-lay problem. They used a singular perturbation technique and found out a useful analytical solution which took into account the overall effects of

the pipe cross-section ovalization. Timoshenko et al. [5] provided some analytical and numerical solutions for the pipeline deepwater S-lay which quantified the loading history effects. The analytical solution was fully developed for an arbitrary pipe material model and it was agreed well with the numerical results. Lenci and Callegari [6] developed three simple analytical models for the J-lay problem. By the models the boundary layer phenomenon was correctly detected and the influence of the soil stiffness was studied. By the means of extensive numerical studies, Kashani and Young [7] found that in ultradeepwater pipeline laying problem the installation parameters were sensitive to pipe wall thickness. Gong et al. [8, 9] made a parameter sensitivity analysis of S-lay technique for deepwater pipelines. The stiffened catenary theory was applied to establish the governing differential equations. They also presented a numerical iteration method for solving the pipeline configurations, and its validity was further verified by means of a comparison with results obtained from OFFPIPE. Wang et al. [10–12] did some analyses on both S-lay and J-lay problems. They proposed a novel numerical model which could take into account the influence of ocean currents and seabed stiffness. In the model the pipeline was divided into two parts and the continuity of the two parts was guaranteed at the touch down point (TDP). They also presented an analytical model for the pipeline J-lay behavior with plastic seabed. Duan et al. [13] proposed an installation system for deepwater riser S-laying and carried some laboratory scale pipeline lifting experiments by this system. Szczotka [14] studied the pipeline J-lay problem by a modified rigid finite element method (RFEM). A modification of the stiffness coefficients and the corresponding model was proposed. They claimed the model could take into account wave and sea current loads, hydrodynamic forces and material nonlinearity. Yuan et al. [15] presented a novel numerical model for the pipeline S-lay problem. They claimed that the model could be used to investigate the overall configuration, internal forces, and strain of the pipelines. On the pipeline abandonment and recovery problem which is very similar to the pipeline laying problem, Andreuzzi and Maier [16] and Datta [17] did the pioneering works. They presented an analytical and a graphical approach for the problem and adopted the finite difference method to analyze the pipeline configurations. Dai et al. [18] studied the configuration of pipelines by the spline collocation method and presented a graphical approach showing the relationship between the configuration and axial forces of the pipeline. Xing et al. [19] continued the research. They built a nonlinear equation system and modeled the pipeline lifting process as a moving boundary problem. By numerical methods the limit moments of some pipelines were obtained. In the researches of pipeline abandonment and recovery, most previous researchers seemed to investigate the problem by a second-order beam equation. However, in our previous research [20] we found that the boundary value problems with the second-order equation cannot tackle the beginning stage of pipeline lifting and the ending stage of pipeline lowering accurately. They produced very different configurations, bending moments at the two stages than the third-order equation boundary value problem

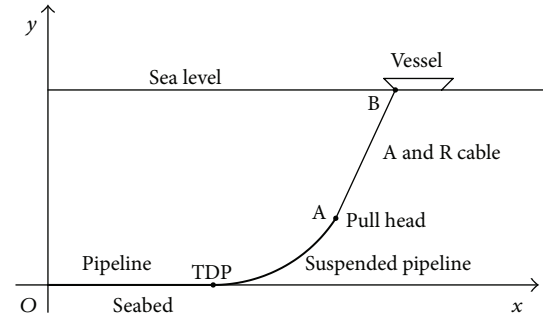


FIGURE 1: Pipeline abandonment and recovery operation.

or Orcaflex. The pipeline in abandonment and recovery operation undergoes a process from a large-angle deflection to a small-angle deflection or from a small-angle deflection to a large-angle deflection. In the problem the boundary condition is moving, which means that it is hard to determine the length of the suspended pipeline segment. The finite element method coupled with contact elements can be used to analyze this problem. However, sometimes it is hard to converge and costs time. Obviously the simple catenary model [21] or stiffened catenary model [22] can never be used to simulate the whole process, so a new mathematical model should be established.

In this paper a mathematical model and a new strategy to tackle the moving boundary without contact analysis are presented. On the other hand the length of the suspended pipeline segment is very important because it can quicken the calculation. So finally a length approximate formula is presented based on Buckingham's Pi-theorem and mathematical fitting.

## 2. Mathematical Model

On the problem the following simplifications are made based on offshore engineering experience [4, 6, 17, 19]: the marine environment is stable, the seabed can be regarded as rigid plane, the lifting and lowering processes are slow, and the material of pipelines is isotropic and always in the elastic state. As shown in Figure 2, the touch down point (TDP, the point where the suspended pipeline contacts with the seabed) is located at the origin  $O$  of the Cartesian coordinate system, where  $T_0$  is the resultant force at joint A,  $H_0$  and  $V_0$  are the horizontal force and the vertical force at the origin,  $w$  is the pipeline submerged weight per unit length,  $\theta$  is the angle between the pipeline axis and the horizon, and  $\theta_0$  is the angle between the direction of  $T_0$  and the horizon. The natural coordinate system is established along the pipeline. It is clear that the physical quantities of the pipeline are the functions of the arc length  $s$ .

**2.1. Governing Differential Equations.** The pipeline is regarded as a tensioned beam. There are usually two kinds of differential equations which are used to analyze this problem, a second-order one and a third-order one, and the third-order one is more suitable for the beginning stage of

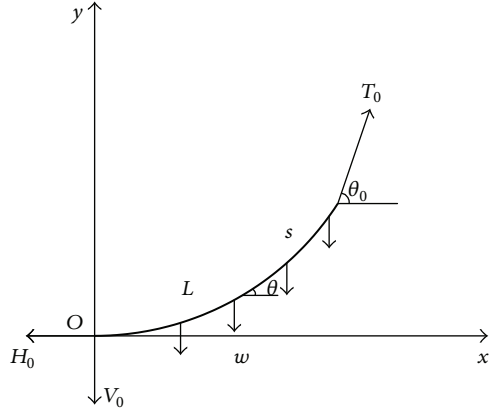


FIGURE 2: Mechanical parameters of the pipeline single point lifting and lowering model.

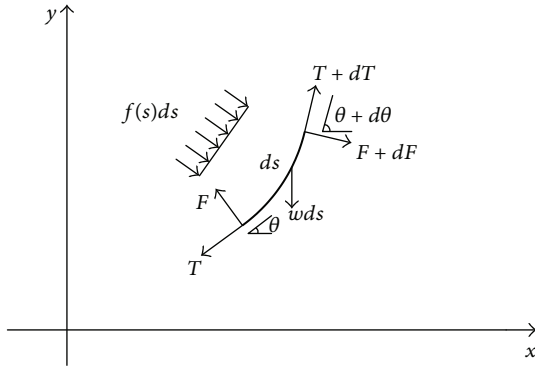


FIGURE 3: Force analysis of a short pipeline segment.

pipeline lifting and the ending stage of pipeline lowering [20]. So in this paper the third-order one has been used. Taking a short segment of the pipeline, as shown in Figure 3, it is easy to deduce the basic governing differential equations [23].

Resolving forces normal to the segment axis leads to

$$dF - Td\theta + wds \cos \theta + f(s) ds = 0. \quad (1)$$

According to  $F = dM/ds$ , (1) leads to

$$\frac{d^2M}{ds^2} - T \frac{d\theta}{ds} + w \cos \theta + f(s) = 0. \quad (2)$$

According to beam theory, there is the following equation, where  $E$  is elastic modulus and  $I$  is second moment of area of the pipe cross section:

$$\frac{M}{EI} = \frac{d\theta}{ds}. \quad (3)$$

Substituting (3) into (2), then (2) becomes

$$EI \frac{d^3\theta}{ds^3} - T \frac{d\theta}{ds} + w \cos \theta + f(s) = 0. \quad (4)$$

Resolving forces in the segment axis leads to

$$\frac{dT}{ds} = w \sin \theta. \quad (5)$$

In the pipeline abandonment and recovery problem,  $f(s)$  is assumed to be zero, so the governing differential equations for the pipeline lifting and lowering by one point are shown as follows:

$$\begin{aligned} EI \frac{d^3\theta}{ds^3} - T \frac{d\theta}{ds} + w \cos \theta &= 0, \\ \frac{dT}{ds} - w \sin \theta &= 0. \end{aligned} \quad (6)$$

2.2. *Boundary Conditions.* According to the similar problems [10, 24], the following boundary conditions are chosen for this problem:

$$\text{at the origin: } \theta(0) = 0, T(0) = H_0 = T_0 \cos \theta_0, M(0) = 0,$$

$$\text{at the joint: } M(L) = 0, T(L) = T_0,$$

where  $M$  is the bending moment of the suspended pipeline segment and  $L$  is its length. According to (3),  $M(0) = 0$  and  $M(L) = 0$  are equivalent to  $(d\theta/ds)(0) = 0$  and  $(d\theta/ds)(L) = 0$ .

To sum up, the whole mathematical model for the pipeline abandonment and recovery is the following boundary value problem:

$$\begin{aligned} EI \frac{d^3\theta}{ds^3} - T \frac{d\theta}{ds} + w \cos \theta &= 0, \\ \frac{dT}{ds} - w \sin \theta &= 0, \end{aligned} \quad (7)$$

$$\theta(0) = 0, \quad \frac{d\theta}{ds}(0) = 0,$$

$$T(0) = H_0 = T_0 \cos \theta_0, \quad \frac{d\theta}{ds}(L) = 0.$$

### 3. Numerical Solutions

3.1. *Numerical Solution Method.* It is hard to get the analytical solutions of the mathematical model presented above. So in this research the traditional numerical method, fourth-order accurate finite difference has been used to get the numerical solutions.

3.2. *Tackling the Moving Boundary.* Notice that the boundary conditions of the model are moving; in another word, the parameter  $L$  is usually an unknown before numerical solving. Solving this problem with moving boundary is challenging. The parameter  $L$  must be given first then the problem can be solved in numerical methods. The method of variable substitution,  $s = \varepsilon L$ , has been taken, so the boundary becomes 0 and 1, and (7) becomes

$$\begin{aligned} \frac{EI}{L^3} \frac{d^3\theta}{d\varepsilon^3} - \frac{T}{L} \frac{d\theta}{d\varepsilon} + w \cos \theta &= 0, \\ \frac{dT}{d\varepsilon} - wL \sin \theta &= 0, \end{aligned}$$

$$\begin{aligned} \theta(0) = 0, \quad \frac{d\theta}{d\varepsilon}(0) = 0, \\ T(0) = H_0 = T_0 \cos \theta_0, \quad \frac{d\theta}{d\varepsilon}(1) = 0. \end{aligned} \quad (8)$$

However, the unknown parameter  $L$  just goes into the differential equations and still cannot be determined. According to the balance of axial forces at the lifting joint, the equation  $T(L) = T_0 \cos(\theta_0 - \theta(L))$  has been added as a supplementary boundary condition herein. Using this condition  $L$  can be calculated in the following steps:

- (1) suppose  $L = T_0(\sin \theta_0/w)$ ;
- (2) solve the boundary value problem (8) by the fourth-order accurate finite difference method or other numerical methods;
- (3) get axial force  $T_n$  at the joint of the pipeline from the results (provided the pipeline divided into  $n$  pieces); then compare the value  $T_n$  and  $T_0 \cos(\theta_0 - \theta_n)$ . If the absolute value of their difference is very small, the  $L$  decided in the last step is approximately equal to the length of suspended pipelines and the work is finished. Otherwise, take the following step;
- (4) decrease the value of  $L$  with a suitable increment if  $T_n > T_0 \cos(\theta_0 - \theta_n)$  and repeat from the second step to the third step until  $T_n < T_0 \cos(\theta_0 - \theta_n)$ , or increase the value of  $L$  with a suitable increment if  $T_n < T_0 \cos(\theta_0 - \theta_n)$  and repeat from the second step to the third step until  $T_n > T_0 \cos(\theta_0 - \theta_n)$ .

*Note.* the value of the increment controls the precision of the calculation of  $L$ . To improve the precision, one can repeat the fourth step with a smaller increment. Finally if the increment is smaller than the allowable error, the length parameter  $L$  is determined.

## 4. Engineering Application

**4.1. Calculation of Pipeline's Physical Quantities.** For engineering application, the pipeline's physical quantities during abandonment or recovery, such as pipeline's configuration, bending moments, must be calculated. After numerical calculation of (8), the angle  $\theta_i$ , the tension force  $T_i$ , and the suspended pipeline length  $L$  are all known, and then the coordinates of the suspended pipeline can be calculated by the following formulas:

$$\begin{aligned} x_i &= x_{i-1} + L(\varepsilon_i - \varepsilon_{i-1}) \cos \theta_{i-1}, \\ y_i &= y_{i-1} + L(\varepsilon_i - \varepsilon_{i-1}) \sin \theta_{i-1}. \end{aligned} \quad (9)$$

And the bending moment of the pipeline can be calculated by the following formula:

$$M_i = \frac{EI}{L} \frac{\theta_i - \theta_{i-1}}{\varepsilon_i - \varepsilon_{i-1}}. \quad (10)$$

TABLE 1: Basic values of the pipeline in the example.

Size (inch)	$EI$ (Pa·m <sup>2</sup> )	$w$ (N/m)
12	31399320	350

TABLE 2: Different loads on the pipeline in the first case.

$T_0$ (KN)	100	300	500	700	900	1100	1300	1500

TABLE 3: Different angles of the loads in the second case.

$\theta_0$ (°)	70	72	74	76	78	80	82	84	86	88	90

**4.2. A Numerical Calculation Example.** Using MATLAB, (8) with the basic values shown in Table 1 is calculated as an example. More details for the numerical solving method of this problem can refer to solving ODEs with MATLAB [25].

Consider the first case. Suppose that the angle  $\theta_0$  keeps as a constant of 80°, and the loads are varying in the pipeline abandonment or recovery operation, as shown in Table 2. The results corresponding to these loads are obtained. The configurations of the pipeline and the corresponding bending moments are shown in Figures 4 and 5, respectively. From Figure 4 we know that the mathematical model proposed above can be used in a large scope of water depth (deeper than 3500 m) and can simulate the whole lowering and lifting process. And from Figure 5 we know that the bending moment becomes bigger and bigger when the pipeline is lifting. So the most dangerous situation usually happens at the beginning of abandonment or at the end of recovery.

Consider the second case. Keeping the tension  $T_0$  as a constant of 800 KN, varying the angle  $\theta_0$ , as shown in Table 3, the pipeline configurations and bending moments are also obtained by calculations, as shown in Figures 6 and 7 separately.

From Figures 6 and 7 we know that the angle has a great effect on the pipeline configuration and bending moments. It can be seen that while the angle  $\theta_0$  increases from 70 degree to 90 degree the bending moment of the pipeline increases greatly, especially when  $\theta_0 > 84$ . And it is clear that the bending moment is more sensitive to the parameter angle  $\theta_0$  than to the parameter load  $T_0$ .

**4.3. Results Comparison.** It is necessary to compare the results calculated by the presented model and method with the traditional finite element analysis results. The software called DRICAS is developed by the model and method presented above. Meanwhile Orcaflex is also used, which is a world's leading package for pipeline finite element analysis and it tackles the moving boundary condition by the contact analysis formula [26]. The comparisons of one of their configuration results and bending moments are shown in Figures 8 and 9, respectively. It can be seen that these results are in good agreement. That indicates that the model and the method established for tackling the moving boundary condition in this paper are correct and effective.

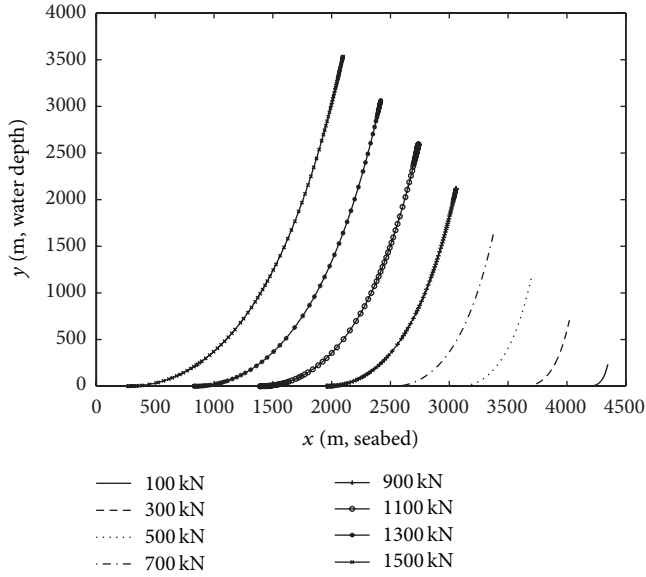


FIGURE 4: Configurations of the suspended pipeline in the first case.

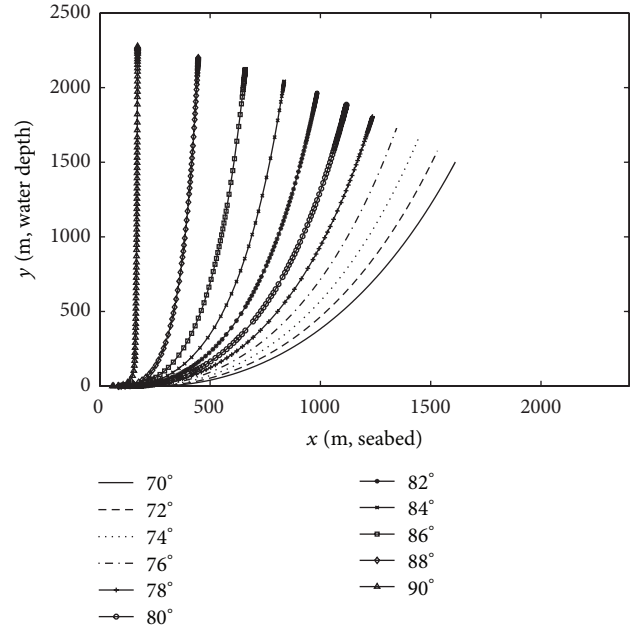


FIGURE 6: Configurations of the suspended pipeline in the second case.

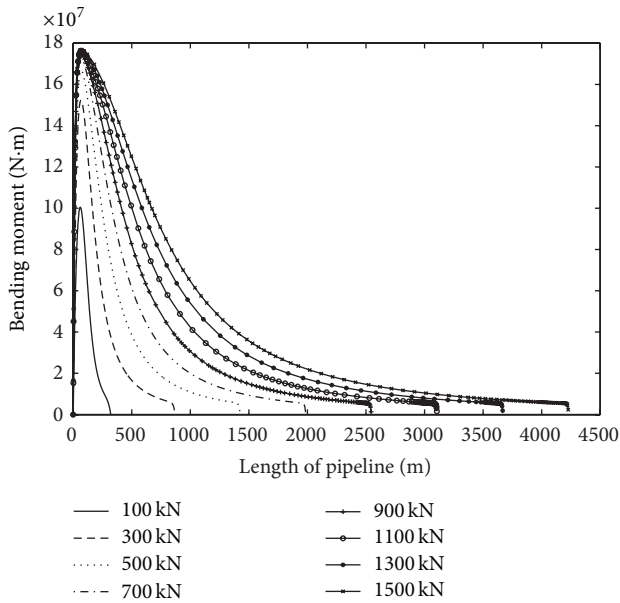


FIGURE 5: Bending moments of the suspended pipeline in the first case.

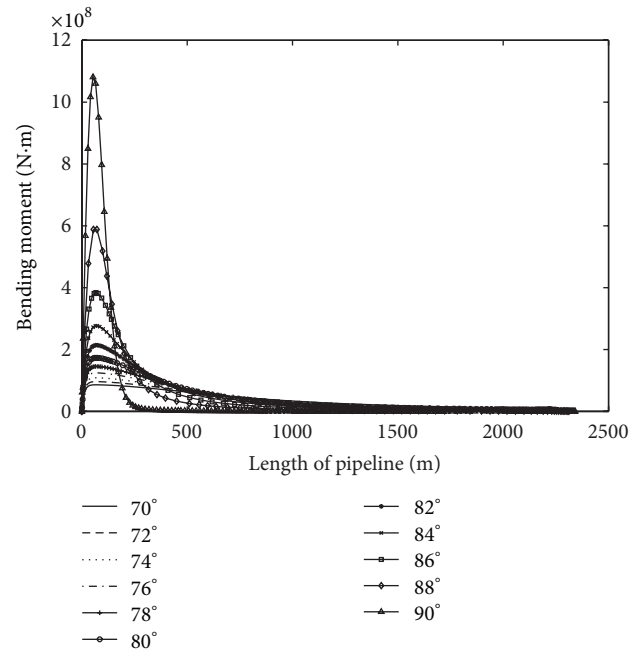


FIGURE 7: Bending moments of the suspended pipelines in the second case.

### 5. Simple Calculation Methods

5.1. *Similarity Criteria of Model Experiment.* Sometimes it is necessary to simulate the pipeline recovery and abandonment by model experiments. According to dimensional analysis theory [27], by equation  $(dT/d\varepsilon) - \omega L \sin \theta = 0$  and equation  $(EI/L^3)(d^3\theta/d\varepsilon^3) - (T/L)(d\theta/d\varepsilon) + \omega \cos \theta = 0$ , the similarity criteria of such kind of model experiments are obtained; that is,  $EI/\omega L^3$  and  $T/\omega L$ , respectively. That means if we want to simulate the pipeline abandonment and recovery processes in the laboratory, we should make sure that the values of  $EI/\omega L^3$  and  $T/\omega L$  of the model are equal

to the corresponding values of the actual offshore pipeline operation project.

5.2. *Approximate Formula of Suspended Pipeline Length.* From the numerical calculation procedures it is known that the length of the suspended pipeline is a key parameter of this problem. A simple approximate formula will be very useful to quicken the solving of this boundary value problem. It is

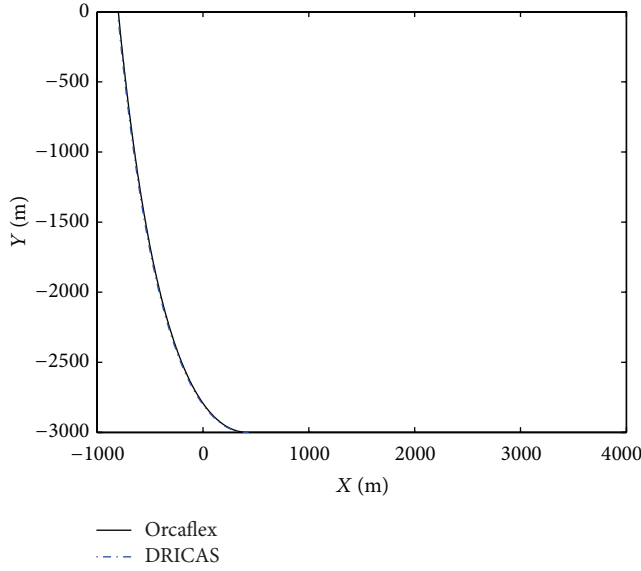


FIGURE 8: Configuration result comparison between DRICAS and Orcaflex.

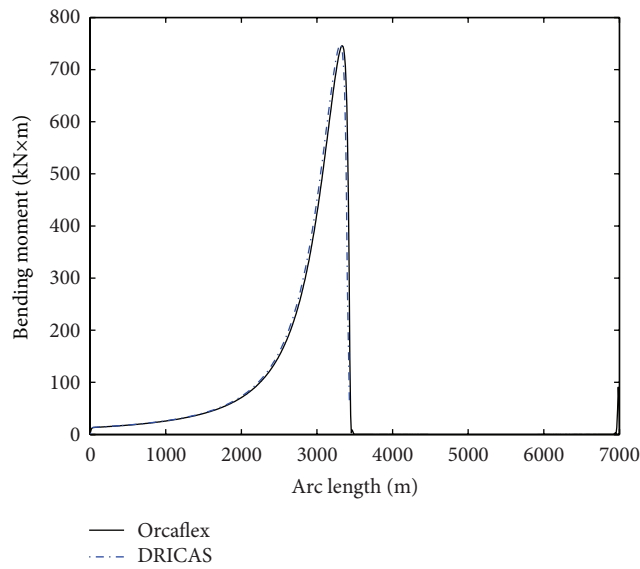


FIGURE 9: Bending moment result comparison between DRICAS and Orcaflex.

known that the length of suspended pipeline is related to  $T_0$ ,  $EI$ ,  $w$ , and  $\theta_0$ . According to Buckingham's Pi-Theorem [27], a dimensionless function is derived as shown in (11)

$$\frac{wL}{T_0} = f\left(\frac{EIw^2}{T_0^3}, \theta_0\right). \quad (11)$$

To determine (11) completely, the boundary value problem (8) has been solved extensively within the range  $0 < \pi_1 \leq 500$ ,  $(76/180\pi) < \pi_2 \leq (90/180\pi)$ , where supposing  $\pi_1 = EIw^2/T_0^3$ ,  $\pi_2 = \theta_0$ , and  $\pi_L = T/wL$ . Using these results the approximate formula for  $\pi_L$  has been obtained by mathematical fitting as shown in (12). Once  $\pi_L$  is known, the

suspended pipeline length  $L$  can be calculated by equation  $L = \pi_L T_0/w$ . And if the suspended pipeline length  $L$  is known, the steps presented in Section 3.2 can be reduced and hence the computational time for solving the problem:

$$\begin{aligned} \pi_L &= -0.4085\pi_1^{0.4} + 5.162\pi_1^{0.5} - 3.895\pi_1^{0.6} \\ &\quad - 0.773\pi_2^{-0.9793} + 1.5435, \\ &\quad \left(0 < \pi_1 \leq 1, \frac{76}{180\pi} < \pi_2 \leq \frac{90}{180\pi}\right), \quad (12) \\ &= -0.124\pi_1^{-1.011} - 0.773\pi_2^{0.9793} + 2.526, \\ &\quad \left(1 < \pi_1 \leq 500, \frac{76}{180\pi} < \pi_2 \leq \frac{90}{180\pi}\right). \end{aligned}$$

## 6. Conclusions

In offshore engineering the pipeline S-laying, J-laying, abandonment and recovery operations can be all governed by (6) which is suitable for the deepwater situation. The differences between these processes are mainly in the boundary conditions.

Reasonable boundary conditions for the problem of pipeline abandonment and recovery are that at the TDP the angle and the bending moment are equal to zero and the tension loading is equal to the loading force horizontal component, and at the joint the bending moment is equal to zero. The whole mathematical model for this problem is (7) or (8), a moving boundary value problem.

The new direct tackling method for the moving boundary of this problem is effective and can get as accurate results as the traditional finite element method coupled with contact analysis.

The similarity criterions for model experiments of pipeline abandonment and recovery are  $EI/wL^3$  and  $T/wL$ .

The suspended pipeline length can be calculated first by approximate formula (12) which can quicken the solving of the pipeline abandonment and recovery problem.

## Conflict of Interests

The authors declare that there is no conflict of interests regarding the publication of this paper.

## Acknowledgments

The authors have been supported by the National Basic Research Program of China (no. 2011CB013702) and the National Natural Science Foundation of China (no. 51379214).

## References

- [1] A. C. Palmer, G. Hutchinson, and J. W. Ells, "Configuration of submarine pipelines during laying operations," *ASME Journal of Engineering for Industry*, vol. 96, no. 4, pp. 1112–1118, 1974.
- [2] R. M. M. Mattheij and S. W. Rienstra, "On an off-shore pipe laying problem," in *Proceedings of the 2nd European Symposium*

- on *Mathematics in Industry* (ESMI '88), H. Neunzert, Ed., pp. 37–55, Springer, 1988.
- [3] D. S. Zhu and Y. K. Cheung, "Optimization of buoyancy of an articulated stinger on submerged pipelines laid with a barge," *The Ocean Engineering*, vol. 24, no. 4, pp. 301–311, 1997.
- [4] F. Guarracino and V. Mallardo, "A refined analytical analysis of submerged pipelines in seabed laying," *Applied Ocean Research*, vol. 21, no. 6, pp. 281–293, 1999.
- [5] S. Timoshenko, S. Woinowsky-Krieger, and S. Woinowsky, *Theory of Plates and Shells*, McGraw-Hill, New York, NY, USA, 1959.
- [6] S. Lenci and M. Callegari, "Simple analytical models for the J-lay problem," *Acta Mechanica*, vol. 178, no. 1-2, pp. 23–39, 2005.
- [7] M. Kashani and R. Young, "Installation load consideration in ultra-deepwater pipeline sizing," *Journal of Transportation Engineering*, vol. 131, no. 8, pp. 632–639, 2005.
- [8] S. F. Gong, Y. He, J. Zhou et al., "Parameter sensitivity analysis of S-lay technique for deepwater submarine pipeline," *The Ocean Engineering*, vol. 4, p. 014, 2009.
- [9] S.-F. Gong, K. Chen, Y. Chen, W.-L. Jin, Z.-G. Li, and D.-Y. Zhao, "Configuration analysis of deepwater S-lay pipeline," *China Ocean Engineering*, vol. 25, no. 3, pp. 519–530, 2011.
- [10] L.-Z. Wang, F. Yuan, and Z. Guo, "Numerical analysis for pipeline installation by S-lay method," in *Proceedings of the 29th ASME International Conference on Ocean, Offshore and Arctic Engineering (OMAE '10)*, pp. 591–599, ASME, Shanghai, China, June 2010.
- [11] L.-Z. Wang, F. Yuan, Z. Guo, and L.-L. Li, "Numerical analysis of pipeline in J-lay problem," *Journal of Zhejiang University A*, vol. 11, no. 11, pp. 908–920, 2010.
- [12] L.-Z. Wang, F. Yuan, Z. Guo, and L.-L. Li, "Analytical prediction of pipeline behaviors in J-lay on plastic seabed," *Journal of Waterway, Port, Coastal and Ocean Engineering*, vol. 138, no. 2, pp. 77–85, 2012.
- [13] M.-L. Duan, Y. Wang, S. Estefen, N. He, L.-N. Li, and B.-M. Chen, "An installation system of deepwater risers by an S-lay vessel," *China Ocean Engineering*, vol. 25, no. 1, pp. 139–148, 2011.
- [14] M. Szczotka, "A modification of the rigid finite element method and its application to the J-lay problem," *Acta Mechanica*, vol. 220, no. 1–4, pp. 183–198, 2011.
- [15] F. Yuan, Z. Guo, L. Li, and L. Wang, "Numerical model for pipeline laying during S-lay," *Journal of Offshore Mechanics and Arctic Engineering*, vol. 134, no. 2, Article ID 021703, 2011.
- [16] F. Andreuzzi and G. Maier, "Simplified analysis and design of abandonment and recovery of offshore pipelines," *Ocean Management*, vol. 7, no. 1–4, pp. 211–230, 1981.
- [17] T. K. Datta, "Abandonment and recovery solution of submarine pipelines," *Applied Ocean Research*, vol. 4, no. 4, pp. 247–252, 1982.
- [18] Y. J. Dai, J. Z. Song, and G. Feng, "A study on abandonment and recovery operation of submarine pipelines," *The Ocean Engineering*, vol. 18, pp. 75–78, 2000 (Chinese).
- [19] J. Z. Xing, C. T. Liu, and X. H. Zeng, "Nonlinear analysis of submarine pipelines during single point lifting," *The Ocean Engineering*, vol. 20, pp. 29–33, 2002 (Chinese).
- [20] X. G. Zeng, M. L. Duan, and J. H. Chen, "Research on several mathematical models of offshore pipe lifting or lowering by one point," *The Ocean Engineering*, vol. 31, pp. 32–37, 2013 (Chinese).
- [21] H. M. Irvine, *Cable Structures*, MIT Press, Cambridge, Mass, USA, 1981.
- [22] D. Dixon and D. Rutledge, "Stiffened catenary calculations in pipeline laying problem," *ASME Journal of Engineering for Industry*, vol. 90, no. 1, pp. 153–160, 1968.
- [23] C. P. Sparks, *Fundamentals of Marine Riser Mechanics—Basic Principles and Simplified Analysis*, PennWell, 2007.
- [24] G. A. Jensen, N. Säfström, T. D. Nguyen, and T. I. Fossen, "A nonlinear PDE formulation for offshore vessel pipeline installation," *The Ocean Engineering*, vol. 37, no. 4, pp. 365–377, 2010.
- [25] L. F. Shampine, I. Gladwell, and S. Thompson, *Solving ODEs with MATLAB*, 2003.
- [26] O. Manual, 2009, <http://www.orcina.com/SoftwareProducts/OrcaFlex/Documentation>.
- [27] A. A. Sonin, *The Physical Basis of Dimensional Analysis*, Department of Mechanical Engineering, MIT, Cambridge, Mass, USA, 2001.

## Research Article

# A New Decision Model for Reducing Trim Loss and Inventory in the Paper Industry

**Fu-Kwun Wang and Feng-Tai Liu**

*Department of Industrial Management, National Taiwan University of Science and Technology, Taipei 106, Taiwan*

Correspondence should be addressed to Fu-Kwun Wang; [fukwun@mail.ntust.edu.tw](mailto:fukwun@mail.ntust.edu.tw)

Received 1 October 2013; Revised 27 November 2013; Accepted 7 December 2013; Published 21 January 2014

Academic Editor: Aderemi O. Adewumi

Copyright © 2014 F.-K. Wang and F.-T. Liu. This is an open access article distributed under the Creative Commons Attribution License, which permits unrestricted use, distribution, and reproduction in any medium, provided the original work is properly cited.

In the paper industry, numerous studies have explored means of optimizing order allocation and cutting trim loss. However, enterprises may not adopt the resulting solutions because some widths of the inventory exceed or are less than those required for acceptable scheduling. To ensure that the results better suit the actual requirements, we present a new decision model based on the adjustment of scheduling and limitation of inventory quantity to differentiate trim loss and inventory distribution data. Differential analysis is used to reduce data filtering and the information is valuable for decision making. A numerical example is presented to illustrate the applicability of the proposed method. The results show that our proposed method outperforms the manual method regarding scheduling quantity and trim loss.

## 1. Introduction

Numerous industries with bulk production modes, such as the industrial-use paper industry, have gradually changed their production environments to high-mix low-volume production. Customer requirements for high-mix low-volume production and instant supply also increase the difficulty of optimizing production scheduling. An issue with even greater significance is how to properly employ production scheduling flexibility and coordinated supplementary measures. In this paper, we consider two main issues in relation to the production planning of industrial paper. (1) If production scheduling is fixed, how may the trim loss ratio and production inventory be reduced, whether evenly distributed in different widths of inventory or not. (2) Does increasing or decreasing the production of scheduling produce better results for inventory distribution and trim loss ratio better than the original scheduling? Since the 1960s [1], numerous studies have examined how to configure orders most effectively to optimize production scheduling. However, these optimized results have not been able to satisfy the requirements of numerous managers because, in situations of raw order production, if the structure remains poor after the permutation and combination of orders, significant trim loss can occur. Thus,

managers must abandon optimized scheduling and use their experience to identify the best solution.

Most cutting stock problems (CSPs) are classified as NP-complete, meaning that it is difficult to obtain optimal solutions. Gilmore and Gomory [1] presented a delayed pattern generation technique for solving a one-dimensional cutting problem using linear programming. Other methods can also be found in the literature [2–13]. Morabito and Arenales [14] considered different objectives (e.g., cutting time and trim loss) in the preparation of the cutting plan. Menon and Schrage [15] proposed a bound-based approach to solve the problem of allocating orders to machines in the paper industry. Wäscher et al. [16] provided a good review of several efficient heuristic methods utilizing either pattern-oriented or item-oriented approaches. Matsumoto et al. [17] proposed a generalization of the cutting pattern called the cutting group in a paper tube factory. Mobasher and Ekici [18] developed two local search algorithms and a column generation based heuristic algorithm to solve the cutting stock problem with setup cost.

In the overall order optimization process, not every cutting configuration meets the needs of the manager because some cutting configurations produce greater trim losses. Generally, managers assign the inventory quantity according

to the size of the trim loss and then search for another optimized solution. Therefore, appropriate replanning of inventory and orders is undertaken to ensure that it is closer to the producer's requirements. Gramani and França [19] proposed a mathematical model for coupling lot sizing and two-dimensional cutting stock problems. Ritvirol [20] presented an integer linear programming (ILP) model to minimize trim loss in a produce-handling vehicle production plant. Chauhan et al. [21] presented a model to decide the parent roll assortment and assignments to finished products based on these products demand processes, desired service levels, trim loss, and inventory holding costs in a paper mill. Poltroniere et al. [22] presented a mixed linear integer optimization model to couple the production planning and the cutting process in the paper industry.

To prevent the trim loss generated after optimization, Kos and Duhovnik [23] included reusable inventory, which is an extension of the usable leftover solution. The usable leftover material is used in the next cutting plan. Related studies [24–28] all propose similar optimal solutions. Erjavec et al. [29] considered trim loss, inventory costs, and shortage costs and developed a model for the solution of the inventory level with the lowest overall cost. Regarding the delivery period, some industries add 1 to 3 days after the paper type is produced as the product delivery period. These additional days are used to increase production flexibility and prevent late deliveries because of transportation factors. This supply chain mode is similar to the process improvements proposed by Erjavec et al. [30].

This study proposes a model based on the adjustment of scheduling and the limitation of inventory quantity to differentiate trim loss ratio and inventory distribution data. We also use the integer programming method to determine the optimal adjustment of order allocation, inventory filtering, and production scheduling. Finally, we use differential analysis to reduce data filtering. This valuable information should enable companies to solve the problems of inventory distribution and the depletion ratio more effectively. The remainder of this paper is organized as follows. In Section 2, the definition of the problem in the paper industry is presented. A decision model is developed in Section 3. In Section 4, an empirical case is employed to calculate and illustrate the proposed model. Finally, conclusions are drawn in Section 5.

## 2. Problem Definition

The production of industrial-use paper begins from raw material to reels and then from reels to rolls as finished goods. The entire operation mode is cyclical production, which is the only method for achieving efficient production. Therefore, the leftover material is not used in a follow-up production cycle. For this scheduling, the customer's paper requirements are obtained and the market demand is predicted. In the combined production-marketing meeting, the number of production days and the production quantity of paper types are determined.  $N$  number of reels is considered as the production quantity and  $st$  number of rolls can be produced from

each reel. Thus, the problem encountered is the optimization of  $N$  number of reels for  $st$  number of rolls to fulfill customers' orders (see Figure 1).

Regarding production planning, actual supply and demand figures are obtained for scheduling. In order to meet the overall order specifications and reduce trim loss during the production process, the decision-making model proposed by Keskinocak et al. [31] is used to optimize overall production scheduling. However, actual production cannot achieve the optimal result of zero depletion. Indeed, the overall production capacity is typically greater than the order to ensure that the customer's and production requirements are met (see Figure 2). Therefore, decision makers often encounter difficulties in determining the scheduling quantity and production inventory so that they are evenly distributed in different widths. To solve these two issues, decision makers use their experience to adjust the scheduling quantity to meet production requirements. Unfortunately, these solutions are not optimized or efficient. In order to improve the overall production efficiency and reduce the time required for manual calculation, a new decision model is needed to react more flexibly to the market and increase the comprehensiveness of the production structure.

## 3. Decision Model for Scheduling

In order to formulate a decision-making model or a mathematical model, we consider the following notation:

$OW_i$  = an order width, with  $i = 1, \dots, m$ , and  $m$  is the number of order width;

$D_i$  = demand for  $OW_i$ , with  $i = 1, \dots, m$ , and  $m$  is the number of order width;

$IW_j$  = an inventory width, with  $j = 1, \dots, n$ , and  $n$  is the number of inventory width;

$PW_k$  = a production width, with  $k = 1, \dots, o$ , and  $o$  is the number of production width;

$DPW_k$  = demand for  $PW_k$ , with  $k = 1, \dots, o$ , and  $o$  is the number of production width;

$PPW_{ks}$  = the pattern for  $PW_k$ , with  $s = 1, \dots, c$ , and  $c$  is the number of pattern;

$QIL_{ks}$  = the quantity of inventory limit for  $PW_k$ , with  $s = 1, \dots, c$ , and  $c$  is the number of pattern;

$PSQ$  = production scheduling quantity;

$T$  = flexible adjustment multiple;

$PSR = PSQ * T$  = reels set in production scheduling;

$UB$  = upper bound for trim loss;

$PSQ_f$  = a production scheduling quantity, with  $f = 1, \dots, v$ , and  $v$  is the number of production scheduling quantity;

$TL_{fs}$  = postoptimization trim loss ratio;

$NPW_{fsk}$  = the number of  $PW_k$ ; for nonfulfilled order, with  $f = 1, \dots, v$ , and  $s = 1, \dots, c$ ;

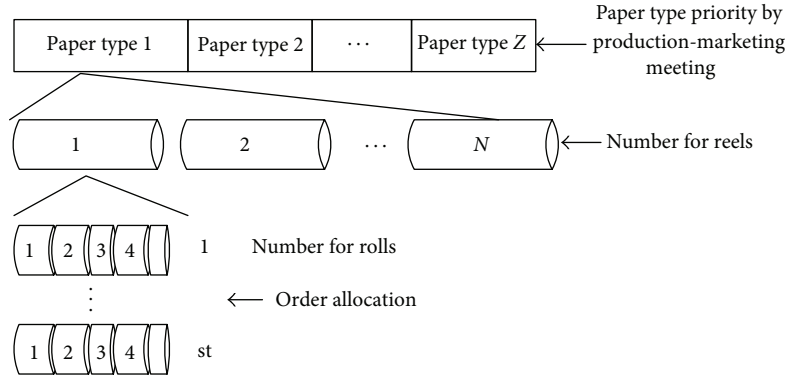


FIGURE 1: Production planning in the paper industry.

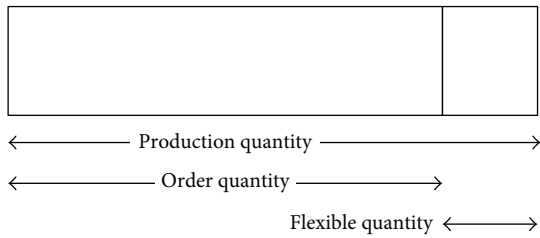


FIGURE 2: Information of order and production.

$SI_{fs} = TL_{(f+1)s} - TL_{fs}$  = difference of trim loss ratio of the scheduled quantities for each item of inventory limit, with  $f = 1, \dots, v$ , and  $s = 1, \dots, c$ ;

$IS_{fs} = TL_{f(s-1)} - TLP_{fs}$  = difference of trim loss ratio of inventory limit for each item of scheduled quantities, with  $f = 1, \dots, v$ , and  $s = 1, \dots, c$ .

**3.1. Decision Model.** To meet customer needs and optimize scheduling quantity, when decision makers analyze production planning, they must consider the trim loss, production volume, and the inventory required to satisfy the practical production requirements. Controlling trim loss, production volume, and inventory is the only strategy to improve production decision making. The decision-making model consists primarily of configuring the production inventory paper width according to the paper width and volume in the order. The minimum production capacity and overall trim loss can be obtained after aggregating the paper width and minimum requirements. If the production capacity, trim loss, and inventory are within a tolerable range for the decision maker, the production scheduling is completed. If the trim loss is excessive or the inventory must be retained, the production capacity must be adjusted and the maximum production capacity must be obtained using the minimum depletion level. The maximum production capacity is used to confirm the quantity of production capacity required to meet the ideal scheduling quantity. This enables the decision makers to obtain the optimized production capacity, trim loss, and inventory configuration between the minimum production volume and the maximum production volume.

In addition, this enables the overall trim loss to be controlled within the decision maker’s ideal range, without limitations from a preset allowable trim loss value that would prevent an optimized solution from being identified.

The steps in the overall decision-making model in Figure 3 are as follows.

*Step 1.* Define the order and inventory paper width and volume. The inventory paper width is the high turnover of inventory paper.

*Step 2.* Define the limits of inventory paper width and volume for each item. Aggregate the order and inventory paper width and volume to the production paper width and volume and limit the inventory paper quantity to ensure that it correlates with the actual production paper width and volume.

*Step 3.* Define the maximum tolerable scheduling quantity as a multiple of the production scheduling quantity to maintain a flexible future scheduling quantity and optimize trim loss.

*Step 4.* Limit the trim loss quantity and obtain the minimum trim loss using the integer programming method. The production quantity for each paper width must be equal to or greater than the quantity required by the customer.

*Step 5.* Store the optimized scheduling quantity, trim loss ratio, and nonorder (inventory) paper width and volume.

*Step 6.* Determine whether an optimal solution exists. If so, go to Step 8. If not, go to Step 7.

*Step 7.* Adjust the scheduling quantity. To reduce this, return to Step 4.

*Step 8.* Determine whether the number of items in the inventory limit derived from the solution is greater than the total number of items. If yes, go to Step 10. If not, go to Step 9.

*Step 9.* Aggregate the production paper width and quantity and adjust the inventory paper width and quantity to the actual production paper width and quantity. Return to Step 3.

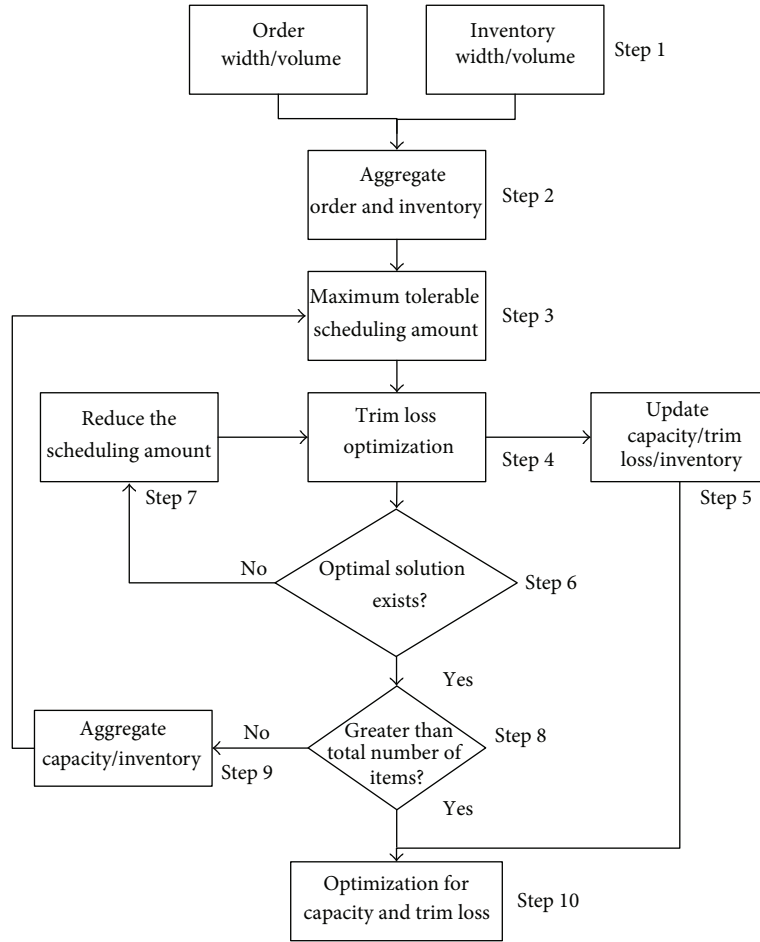


FIGURE 3: Decision model.

*Step 10.* Obtain the differential analysis of the trim loss ratio and then optimize the storage-scheduling quantity and trim loss information. Following optimization, the decision makers finally confirm the production scheduling quantity.

In production planning for industrial paper, each reel produces  $st$  number of sets, and an  $st$  multiple of products is produced by cutting the reels. To allow the production trim loss to be controlled within a certain range and to provide a flexible scheduling quantity, the overall production paper width is aggregated as  $IW_j$  and  $OW_i$ , and the producible paper width  $PW_k$  is obtained. Regarding the control of paper width and volume, the produced paper width and volume must meet  $D_i$ . The level of inventory controls the quantity of  $QIL_{ks}$ . Here,  $D_i$  and  $QIL_{ks}$  are aggregated and the producible paper width and quantity  $DPW_{ks}$  are obtained.

The scheduling quantity is adjusted according to how the production decision makers view the trim loss level and the urgency of the order. Therefore, although the PSQ can be optimized, they do not represent the production capacity that is acceptable to the decision makers. Instead, the trim loss and production capacity data are provided to the decision makers who make the final decision. After obtaining the  $DPW_{ks}$  and PSR, the integer programming method is used to

optimize trim loss. The postoptimization scheduling quantity and trim loss are then stored in the data table. After the related data are stored, the scheduling quantity is reduced to obtain the next scheduling quantity. Next, optimization is again conducted, and the PSR and trim loss data are again stored. Thus, the scheduling quantity is reduced and optimized repeatedly until optimal or lower than the PSQ. Subsequently, the inventory quantities  $QIL_{ks}$  and  $PPW_{ks}$  are changed and optimization is conducted again until  $s$  is greater than  $c$ , which completes the entire operation. The optimization process is shown in Algorithm 1, where  $a_{kj}$  = the number of width  $k$  in pattern  $j$  and is integer;  $x_j$  = the number of pattern  $j$  and is integer;  $L$  = the width of reel;  $st$  = the number of set in reel; Solve = whether optimization is possible; TTL = postoptimization trim loss;  $f$  = optimized solution number.

*3.2. Decision Making for Scheduling Quantity and Trim Loss.* Typically, a larger scheduling quantity produces greater trim loss. Therefore, the scheduling quantity is multiplied to prevent situations in which the scheduling quantity and trim loss cannot be optimized because of a limited scheduling quantity.

```

s = 1
While (s ≤ c)
Begin
  PSR = PSQ * T
  f = 1
  While (Solve or PSR ≥ PSQ)
  Begin
    TTL = min ∑j=1n (L - ∑k=1o akj wk) × xj (minimize trim loss)
    Subject to ∑k=1o akj wk ≤ L (width of reel constraint)
              UB ≤ L - ∑k=1o akj wk (trim loss constraint)
              PSR = (∑j=1n xj) / st (reel set constraint)
              Dk ≤ ∑j=1n akj xj (order constraint)
              ∑j=1n akj xj ≤ PPWks (capacity constraint)
    If (Solve) then
      TLfs = (TTL / (∑j=1n L × xj)) * 100
    End
    PSQf = PSR
    PSR = PSR - 1
    f = f + 1
  End
  s = s + 1
End

```

ALGORITHM 1

Therefore,  $PSQ_f$  and  $TL_{f_s}$  are entered during the optimization process to increase decision makers' understanding of the influence that increases or decreases in production capacity have on the trim loss level. In this study, a differential analysis of the trim loss was conducted to ensure that the scheduling quantity and trim loss met the decision makers' requirements.

In the  $PSQ_f$  and  $TL_{f_s}$  table,  $s$  was selected as the set value and  $f$  was the variable value employed to conduct differential analysis of the trim loss. First, the difference between  $TL_{f_s}$  and  $TL_{(f+1)_s}$  is entered into  $SI_{f_s}$ , and the result of  $SI_{f_s}$  is used to obtain the mean. When  $SI_{f_s}$  is greater than the mean, the maximum value of  $f$  is reduced. If  $SI_{(f+1)_s}$  cannot be optimized and  $SI_{f_s}$  is greater than the mean, plan A of the decision suggestion can be obtained.

Similarly, the difference between  $TL_{f_s}$  and  $TL_{(f+1)_s}$  is entered into  $IS_{f(s+1)}$ , and the result of  $IS_{f_s}$  is used to obtain the mean. When  $IS_{f_s}$  is greater than the mean, the minimum value of  $s$  is summed. If  $IS_{f_s}$  cannot be optimized and  $IS_{f(s+1)}$  exceeds the mean, plan B of the decision suggestion can be obtained.

Intersection analysis is conducted on plans A and B to obtain the scheduling solution C. The values of C are organized in sequence from large to small, and the smaller

number is subtracted from the larger number. The result of this subtraction is used to obtain the mean, and the items that exceed the mean are filtered out to obtain the optimal decision suggestion. The decision makers can select the desired inventory results according to their requirements and perform a final confirmation of the scheduling and inventory quantity.

#### 4. Illustrative Example

In an actual case of industrial paper production, we set the current scheduling quantity as PSQ reels, and each reel can produce  $st$  number of roll sets. The cutting machine's maximum width limit is  $L$  and the maximum trim loss is UB. These parameters are defined as  $st = 3$ ,  $L = 4600$  mm,  $PSQ = 46$ , and  $UB = 999$ .

The application program was implemented to provide the described optimization functionality. As optimization is numerically intensive, the application program was divided into the engine and the user interface. The engine interface was written in Lingo Software [32]. The user interface in Visual Basic 5 enables the navigation of data flow from various input sources from/to a common company database.

TABLE 1: Product order information and adjusted data for  $PW_k$ ,  $QIL_{ks}$ , and  $PPW_{ks}$ .

$k$	$OW_k$ (mm)	$IW_k$ (mm)	$PW_k$ (mm)	$D_k$	$QIL_{ks}$	$PPW_{ks}$
1	X	1000	1000	0	5/10/15/20/100	5/10/15/20/100
2	X	1100	1100	0	5/10/15/20/100	5/10/15/20/100
3	1200	1200	1200	7	5/10/15/20/100	12/17/22/27/107
4	1300	1300	1300	22	5/10/15/20/100	27/32/37/42/122
5	X	1400	1400	0	5/10/15/20/100	5/10/15/20/100
6	1500	1500	1500	28	5/10/15/20/100	33/38/43/48/128
7	1600	1600	1600	58	5/10/15/20/100	63/68/73/78/158
8	1700	1700	1700	47	5/10/15/20/100	52/57/62/67/147
9	1800	1800	1800	43	5/10/15/20/100	48/53/58/63/143
10	1900	1900	1900	7	5/10/15/20/100	12/17/22/27/107
11	2000	2000	2000	20	5/10/15/20/100	25/30/35/40/120
12	2100	2100	2100	9	5/10/15/20/100	14/19/24/29/109
13	2200	2200	2200	30	5/10/15/20/100	35/40/45/50/130
14	2300	2300	2300	7	5/10/15/20/100	12/17/22/27/107
15	2400	2400	2400	12	5/10/15/20/100	17/22/27/32/112
16	2500	2500	2500	20	5/10/15/20/100	25/30/35/40/120

Note: X = not available.

TABLE 2: The results of  $TL_{fs}$  under different optimized solution numbers.

$f$	$PSQ_f$	$s$				
		1	2	3	4	5
1	52	X	X	0.08	0	0
2	51	X	X	0.10	0	0
3	50	X	0.43	0.13	0.04	0
4	49	X	0.50	0.16	0.09	0.03
5	48	X	0.60	0.21	0.15	0.12
6	47	X	0.74	0.31	0.23	0.22
7	46	3.0	0.95	0.41	0.33	0.32
8	45	3.3	1.20	0.61	0.43	0.42
9	44	X	X	X	X	X

Note: X = not available.

TABLE 3: The results of differential analysis between  $TL_{fs}$  and  $TL_{(f+1)s}$ .

$f$	$PSQ_f$	$s$				
		1	2	3	4	5
1	52			0.02	0	0
2	51			0.03	0.04	0
3	50		0.07	0.03	0.05	0.03
4	49		0.10	0.05	0.06	0.09
5	48		0.14	0.10	0.08	0.10
6	47		0.21	0.10	0.10	0.10
7	46	0.3	0.25	0.20	0.10	0.10
8	45					
9	44					
Average value		0.3	0.15	0.08	0.06	0.06

According to the decision model and the optimization process described in Section 3, the details are as follows.

*Step 1.* Collect  $OW_i$ ,  $IW_j$ , and  $Di$ , where  $i = 1, 2, \dots, 12$  and  $j = 1, 2, \dots, 15$ .

*Step 2.* Aggregate  $OW_i$  and  $IW_j$  to  $PW_k$ , define the limitation quantity  $QIL_{ks}$ , and aggregate  $Di$  and  $QIL_{ks}$  to  $PPW_{ks}$ , where  $k = 1, 2, \dots, 16$  and  $s = 1, 2, \dots, 5$  (see Table 1).

*Step 3.* Define the parameter  $T = 1.15$  and  $PSR = PSQ * T$  to obtain  $PSR = 52$ .

*Step 4.* Obtain the minimum trim loss using the integer programming method.

*Step 5.* Store the optimized scheduling quantity  $PSQ_f$ , depletion ratio  $TL_{fs}$ , and nonorder (inventory) paper width and quantity  $NPW_{fsk}$ .

*Step 6.* Determine whether an optimal solution exists or not. If yes, go to Step 8. If no, go to Step 7.

*Step 7.* Adjust the scheduling quantity  $PSR$ .

*Step 8.* Determine whether the number of items in the inventory limit derived from the solution is greater than the total number of items. If yes, go to Step 10. If not, go to Step 9.

*Step 9.* Obtain the next  $QIL_{ks}$  and aggregate  $Di$  to  $PPW_{ks}$ ; then go to Step 3.

*Step 10.* Obtain  $PSQ_f$  and  $TL_{fs}$  (see Table 2).

Conducting differential analysis of the trim loss, the difference between  $TL_s$  and  $TL_{(f+1)s}$  is entered into  $SI_{fs}$ , and

TABLE 4: The results of differential analysis between  $TL_{f_s}$  and  $TL_{f(s+1)}$ .

$f$	PSQ $_f$	$s$					Average value
		1	2	3	4	5	
1	52				0.08	0	0.04
2	51				0.10	0	0.05
3	50			0.30	0.09	0.04	0.14
4	49			0.34	0.07	0.06	0.16
5	48			0.39	0.06	0.03	0.16
6	47			0.43	0.08	0.01	0.17
7	46	2.05		0.54	0.08	0.01	0.67
8	45	2.10	0.59		0.18	0.01	0.72
9	44						

TABLE 5: The comparison results of  $TL_{f_s}$  (%) for different scenarios.

$s$	1	1	2	2	2	3	3	Differential mean
PSQ	45	46	45	46	47	47	48	
Trim loss (%)	3.3	3.0	1.2	0.95	0.74	0.31	0.21	
Deviation		0.3	1.8	0.25	0.21	0.43	0.10	0.52

the mean is obtained from the result of  $SI_{f_s}$ . When  $SI_{f_s}$  is greater than the mean,  $\{SI_{44}, SI_{45}, SI_{53}, SI_{54}, SI_{55}, SI_{62}, SI_{63}, SI_{64}, SI_{65}, Sdec_{71}, SI_{72}, SI_{73}, SI_{74}, SI_{75}\}$  is obtained. If  $SI_{(f+1)s}$  cannot be optimized and  $SI_{f_s}$  is greater than the mean, the decision suggestion plan can be obtained (see Table 3). That is, we have  $\{SI_{81}, SI_{82}, SI_{83}, SI_{84}, SI_{85}\}$ .

With  $s = 2$  as the paradigm,  $SI_{82} = TL_{92} - TL_{82}$  and is consistently calculated as  $SI_{12} = TL_{22} - TL_{12}$ . If  $TL_{f_s}$  cannot be optimized, such as in  $TL_{22}$ , the calculation is ignored. In this case, the differential mean of 0.15 is obtained and  $SI_{72}$  and  $SI_{62}$  are greater than the mean. However,  $SI_{82}$  cannot be optimized and  $SI_{72}$ , is greater than the mean; thus,  $SI_{82}$  must be included for consideration.

Similarly, the difference between  $TL_{f_s}$  and  $TL_{f(s+1)}$  is entered into  $IS_{f(s+1)}$ , and the mean is obtained from the result of  $IS_{f_s}$ . When  $IS_{f_s}$  is greater than the mean,  $\{IS_{33}, IS_{43}, IS_{53}, IS_{63}, IS_{72}, IS_{82}\}$  is obtained. If  $IS_{f_s}$  cannot be optimized and  $IS_{f(s+1)}$  exceeds the mean, the decision suggestion plan can be obtained in Table 4. That is, we have  $\{IS_{32}, IS_{42}, IS_{52}, IS_{62}, IS_{71}, IS_{81}\}$ .

With  $f = 2$  as the paradigm,  $IS_{62} = TL_{61} - TL_{62}$  and is consistently calculated as  $IS_{65} = TL_{64} - TL_{65}$ . If  $TL_{f_s}$  cannot be optimized, such as in  $TL_{61}$ , the calculation is ignored. In this case, a differential mean of 0.17 was obtained and  $IS_{63}$  was greater than the mean. However,  $IS_{62}$  cannot be optimized and  $IS_{63}$  is greater than the mean; thus,  $IS_{62}$  must also be considered.

We conduct intersection analysis from Tables 3 and 4 to obtain the scheduling solution. That is, we have  $\{TL_{17}, TL_{18}, TL_{26}, TL_{27}, TL_{28}, TL_{35}, TL_{36}\}$ , where the values are organized from large to small, and the smaller number is subtracted from the larger number. The result of the subtraction is used to obtain the mean of 0.52. The items larger than the mean are filtered out to obtain the results

shown in Table 5, and the optimal decision suggestion is obtained as  $\{TL_{18}, TL_{28}\}$ .

The optimal solution displayed in Table 6 shows that, when the scheduling quantity is 45 reels, the trim loss ratio could be 3.3% or 1.2%. Although the quantity of increased inventory differs, decision makers can select the desired inventory results according to their actual needs. The original scheduling quantity was 46 reels, and an optimal solution was not obtained. This means that, for  $s = 1$  or 2 cases with 45 or 46 reels, trim loss rate differences do not change significantly, and these two reels may be randomly selected. Thus, the scheduling quantity can be reduced to meet the actual requirements.

Concerning the unrestricted inventory quantity, such as  $s = 5$ , this is a commonly obtained CSP result. Although the trim loss rate is 0.42%, this optimal solution is occasionally unacceptable to the decision makers because it concentrates on the inventory production of 32 rolls of a specific paper width, such as 1000 mm (see Table 6). This poses significant challenges when considering how to reduce the paper width and quantity; this issue has consistently frustrated decision makers.

In the method ordinarily used in the paper industry, the first solution is typically aimed at implementing the order. The  $\{1000, 1100, 1400\}$  inventory paper widths are not included. After optimization, the added paper widths with an inventory quantity of  $\{1200, 1900\}$  with  $\{17, 1\}$  are obtained. The total number of rolls is 134, and the trim loss ratio is 5.2% (see Table 7). The postoptimization problems that occurred were as follows: (1) the rolls were not in multiples of 3; (2) the trim loss of 5.2% was excessive.

Therefore, manually disassembling the trim loss and the rolls with excessively varying patterns can be considered the optimal solution. The total numbers of rolls are confirmed as 135, 138, 141, and so forth. In this case, the entire trim loss can only be reduced using 138 rolls or more. The rolls are adjusted manually to combine patterns  $\{1, 4\}$  with patterns  $\{1, 4\}$ . To reduce the trim loss, the pattern  $\{10\}$  configuration can be included in the inventory paper width, providing combinations of  $\{1300, 1400, 1900\}$  or  $\{1200, 1500, 1900\}$  or  $\{1900, 2500\}$  to obtain the combination  $\{1000, 1700, 1900\}$ . Finally, the order paper width  $\{1800\}$  with pattern  $\{1\}$  that cannot be allocated is combined with pattern  $\{9\}$ . A manual fine-tuning procedure is conducted to produce the scheduling quantity of 138 rolls and a trim loss ratio of 4.6% (see Table 8).

In Tables 6–8, we found that two solutions using the proposed method are obtained as follows: (1) the scheduling quantity is 45 reels with a trim loss ratio of 3.3%; (2) the scheduling quantity is 45 reels with a trim loss ratio of 1.2%. The solution using a traditional CSP is obtained as the scheduling quantity is 45 reels with a trim loss ratio of 0.42%. The paper width with an inventory quantity of  $\{1000, 1100, 1400\}$  with  $\{32, 4, 3\}$  is obtained. However, this solution is unacceptable because these paper widths are not met for customers' requirements. We delete the  $\{1000, 1100, 1400\}$  inventory paper width. After optimization, we obtain the added paper widths with an inventory quantity of  $\{1200, 1900\}$  with  $\{17, 1\}$ , and the total number

TABLE 6: Optimal solutions using our proposed method and the traditional method.

PW <sub>k</sub> (mm)	S							
	1*	1	2*	2	2	3	3	5 <sup>#</sup>
	PSQ							
	45	46	45	46	47	47	48	45
NPW <sub>fsk</sub>								
1000	5	5	10	10	10	15	15	32
1100	5	5	10	10	10	15	15	4
1200	5	5	10	10	10	15	15	13
1300	5	5	10	10	10	9	11	0
1400	5	5	4	9	9	0	1	3
1500	4	4	0	2	2	0	0	0
1600	0	0	0	0	0	1	0	0
1700	0	0	0	0	0	0	0	0
1800	0	0	0	0	0	0	0	0
1900	0	0	0	0	0	0	0	0
2000	0	0	0	0	0	0	0	0
2100	0	0	0	0	0	0	0	0
2200	0	0	0	0	0	0	0	0
2300	0	0	0	0	0	0	0	0
2400	0	2	0	0	0	9	14	0
2500	1	5	0	2	8	0	0	0
Trim loss (%)	3.3	3.0	1.2	0.95	0.74	0.31	0.21	0.42
Trim loss (mm)	20300	19300	7200	6000	4800	2000	1400	2600

Note: <sup>#</sup>a traditional CSP solution; \* optimal CSP solution.

TABLE 7: The results of a traditional CSP method.

PW <sub>k</sub> (mm)	Order	Optimal solution	Inventory	Pattern													
				1	2	3	4	5	6	7	8	9	10	11	12	13	
1000*	0	0	0														
1100*	0	0	0														
1200	7	24	17	1	1												
1300	22	22	0			1	1										
1400*	0	0	0														
1500	28	28	0					2									
1600	58	58	0	1		2	1	1									
1700	47	47	0		2		1										
1800	43	43	0	1					1	1	1	1					
1900	7	8	1										2				
2000	20	20	0												2		
2100	9	9	0						1								
2200	30	30	0													2	
2300	7	7	0							1							2
2400	12	12	0								1						
2500	20	20	0										1				
Usage				1	23	21	1	14	9	1	12	20	4	10	15	3	
Pattern trim loss				0	0	100	0	0	700	500	400	300	800	600	200	0	

Note: total rolls used = 134; percent waste = 5.2%; \* nonorder product.

TABLE 8: The results of a manual fine-tuning procedure.

PW <sub>k</sub> (mm)	Order	Adjusted quantity	Inventory	Pattern															
				1	2	3	4	5	6	7	8	9	10	11	12	13			
1000*	0	7	7												1				
1100*	0	0	0																
1200	7	23	16	1	1														
1300	22	23	1			1	1												
1400*	0	0	0																
1500	28	28	0					2											
1600	58	58	0	1		2	1	1											
1700	47	55	8		2		1								1				
1800	43	43	0	1					1	1	1	1							
1900	7	7	0												1				
2000	20	20	0													2			
2100	9	9	0						1										
2200	30	30	0															2	
2300	7	7	0							1									2
2400	12	12	0								1								
2500	20	21	1									1							
Usage				0	23	21	2	14	9	1	12	21	7	10	15	3			
Pattern trim loss				0	0	100	0	0	700	500	400	300	0	600	200	0			

Note: total rolls used = 138; percent waste = 4.6%; \* nonorder product.

of rolls is 134 with a trim loss ratio of 5.2%. Unfortunately, the number of rolls (=134) is not in multiples of 3. Thus, this solution is still unacceptable. The solution of the scheduling quantity using the manual method is obtained as 46 reels with a trim loss ratio of 4.6%. We found that the scheduling quantity of our method is 45 reels that it is less than 46 reels obtained using the manual method. In addition, the trim loss using our method is lower than that of the manual method. Thus, we conclude that our method outperforms the other two methods.

## 5. Conclusions

In this study, we propose a new decision model for the CSP to improve the overall production efficiency in the paper industry. Not only using the mutual collocation of scheduling volume adjustment, orders, and inventory reduces the ratio of depletion to total production amount, but also the model for adjusting the scheduling amount proposed in this study obtains the data differentiation of the depletion ratio. This information can enable decision makers to solve the inventory and depletion problems related to CSP issues efficiently. In illustrative example, we found that the scheduling quantity of our method is 45 reels that it is less than 46 reels obtained using the manual method. That is, the cost effect of the number of reels can be reduced by 1. Furthermore, it allows decision makers to determine the optimal configurations and controls for scheduling, orders, inventory, and trim loss.

In this study, we do not include the due date for the order. Future research should address this issue. In addition, we will conduct the flexible inventory allocation and trim loss control

to determine the production scheduling quantity in the paper industry.

## Conflict of Interests

The authors declare that there is no conflict of interests regarding the publication of this paper.

## Acknowledgments

The authors gratefully acknowledge three reviewers of this paper who helped clarify and improve this presentation.

## References

- [1] P. C. Gilmore and R. E. Gomory, "A linear programming approach to the cutting-stock problem," *Operations Research*, vol. 9, no. 6, pp. 849–859, 1961.
- [2] W. Gochet and M. Vandebroek, "A dynamic programming based heuristic for industrial buying of cardboard," *European Journal of Operational Research*, vol. 38, no. 1, pp. 104–112, 1989.
- [3] C. H. Dağlı, "Knowledge-based systems for cutting stock problems," *European Journal of Operational Research*, vol. 44, no. 2, pp. 160–166, 1990.
- [4] H. Foerster and G. Wäscher, "Simulated annealing for order spread minimization in sequencing cutting patterns," *European Journal of Operational Research*, vol. 110, no. 2, pp. 272–281, 1998.
- [5] P. H. Vance, "Branch-and-price algorithms for the one-dimensional cutting stock problem," *Computational Optimization and Applications*, vol. 9, no. 3, pp. 211–228, 1998.
- [6] M. Gradišar, G. Resinovič, J. Jesenko, and M. Kljajić, "A sequential heuristic procedure for one-dimensional cutting," *European Journal of Operational Research*, vol. 114, no. 3, pp. 557–568, 1999.

- [7] M. Sakawa, "Interactive fuzzy programming for multi-level 0-1 programming problems through genetic algorithms," *European Journal of Operational Research*, vol. 114, no. 3, pp. 580–588, 1999.
- [8] S. M. A. Suliman, "Pattern generating procedure for the cutting stock problem," *International Journal of Production Economics*, vol. 74, no. 1–3, pp. 293–301, 2001.
- [9] W. Weng and T. Sung, "Optimization of a line-cutting procedure for ship hull construction by an effective tabu search," *International Journal of Production Research*, vol. 46, no. 21, pp. 5935–5949, 2007.
- [10] J. A. Abbasi and M. H. Sahir, "Development of optimal cutting plan using linear programming tools and MATLAB algorithm," *International Journal of Innovation, Management and Technology*, vol. 1, pp. 483–492, 2010.
- [11] G. C. Wang, C. P. Li, J. Lv, X. X. Zhao, and H. Y. Cuo, "An effect algorithm design for the one-dimensional cutting-stock problem," *Advanced Materials Research*, vol. 602–604, pp. 1753–1756, 2013.
- [12] M. Ali, C. W. Ahn, and M. Pant, "Trim loss optimization by an improved differential evolution," *Mathematical Problems in Engineering*, vol. 2013, Article ID 706350, 8 pages, 2013.
- [13] W. Tharmmaphornphilas, S. Puemsin, and P. Siripongwutikorn, "A MILP model to select cutting machines and cutting patterns to minimize paper loss," in *Proceedings of the International MultiConference of Engineers and Computer Scientists*, pp. 1155–1160, Hong Kong, March 2013.
- [14] R. Morabito and M. Arenales, "Optimizing the cutting of stock plates in a furniture company," *International Journal of Production Research*, vol. 38, no. 12, pp. 2725–2742, 2000.
- [15] S. Menon and L. Schrage, "Order allocation for stock cutting in the paper industry," *Operations Research*, vol. 50, no. 2, pp. 324–332, 2002.
- [16] G. Wäscher, H. Haußner, and H. Schumann, "An improved typology of cutting and packing problems," *European Journal of Operational Research*, vol. 183, no. 3, pp. 1109–1130, 2007.
- [17] K. Matsumoto, S. Umetani, and H. Nagamochi, "On the one-dimensional stock cutting problem in the paper tube industry," *Journal of Scheduling*, vol. 14, no. 3, pp. 281–290, 2011.
- [18] A. Mobasher and A. Ekici, "Solution approaches for the cutting stock problem with setup cost," *Computers & Operations Research*, vol. 40, no. 1, pp. 225–235, 2013.
- [19] M. C. Gramani and P. M. França, "The combined cutting stock and lot-sizing problem in industrial processes," *European Journal of Operational Research*, vol. 174, no. 1, pp. 509–521, 2006.
- [20] A. Ritvirool, "A trim-loss minimization in a produce-handling vehicle production plant," *Journal of Science and Technology*, vol. 29, no. 1, pp. 157–164, 2007.
- [21] S. S. Chauhan, A. Martel, and S. D'Amour, "Roll assortment optimization in a paper mill: an integer programming approach," *Computers and Operations Research*, vol. 35, no. 2, pp. 614–627, 2008.
- [22] S. C. Poltroniere, K. C. Poldi, F. M. B. Toledo, and M. N. Arenales, "A coupling cutting stock-lot sizing problem in the paper industry," *Annals of Operations Research*, vol. 157, no. 1, pp. 91–104, 2008.
- [23] L. Kos and J. Duhovnik, "Cutting optimization with variable-sized stock and inventory status data," *International Journal of Production Research*, vol. 40, no. 10, pp. 2289–2301, 2002.
- [24] M. Gradišar, G. Resinovič, and M. Kljajić, "Evaluation of algorithms for one-dimensional cutting," *Computers & Operations Research*, vol. 29, no. 9, pp. 1207–1220, 2002.
- [25] P. Trkman and M. Gradišar, "One-dimensional cutting stock optimization in consecutive time periods," *European Journal of Operational Research*, vol. 179, no. 2, pp. 291–301, 2007.
- [26] A. C. Cherri, M. N. Arenales, and H. H. Yanasse, "The one-dimensional cutting stock problem with usable leftover—a heuristic approach," *European Journal of Operational Research*, vol. 196, no. 3, pp. 897–908, 2009.
- [27] Y. Cui and Y. Yang, "A heuristic for the one-dimensional cutting stock problem with usable leftover," *European Journal of Operational Research*, vol. 204, no. 2, pp. 245–250, 2010.
- [28] S. A. Araujo, A. A. Constantino, and K. C. Poldi, "An evolutionary algorithm for the one-dimensional cutting stock problem," *International Transactions in Operational Research*, vol. 18, no. 1, pp. 115–127, 2011.
- [29] J. Erjavec, M. Gradišar, and P. Trkman, "Assessment of stock size to minimize cutting stock production costs," *International Journal of Production Economics*, vol. 135, no. 1, pp. 170–176, 2012.
- [30] J. Erjavec, M. Gradišar, and P. Trkman, "Renovation of the cutting stock process," *International Journal of Production Research*, vol. 47, no. 14, pp. 3979–3996, 2009.
- [31] P. Keskinocak, F. Wu, R. Goodwin et al., "Scheduling solutions for the paper industry," *Operations Research*, vol. 50, no. 2, pp. 249–259, 2002.
- [32] "Lingo Software," Version 11, Lindo Systems, Chicago, Ill, USA, 2009.

## Research Article

# New Product Development in an Emerging Economy: Analysing the Role of Supplier Involvement Practices by Using Bayesian Markov Chain Monte Carlo Technique

Kanagi Kanapathy,<sup>1</sup> Kok Wei Khong,<sup>2</sup> and Rob Dekkers<sup>3</sup>

<sup>1</sup> Faculty of Business and Accountancy, University of Malaya, 50603 Kuala Lumpur, Malaysia

<sup>2</sup> Taylor's Business School, Taylor's University, No. 1 Jalan Taylor's, 47500 Subang Jaya, Selangor, Malaysia

<sup>3</sup> UWS Business School, University of the West of Scotland, Paisley PA1 2BE, UK

Correspondence should be addressed to Kanagi Kanapathy; [kanagik@um.edu.my](mailto:kanagik@um.edu.my)

Received 20 September 2013; Accepted 2 December 2013; Published 8 January 2014

Academic Editor: Nachamada Blamah

Copyright © 2014 Kanagi Kanapathy et al. This is an open access article distributed under the Creative Commons Attribution License, which permits unrestricted use, distribution, and reproduction in any medium, provided the original work is properly cited.

The research question is whether the positive relationship found between supplier involvement practices and new product development performances in developed economies also holds in emerging economies. The role of supplier involvement practices in new product development performance is yet to be substantially investigated in the emerging economies (other than China). This premise was examined by distributing a survey instrument (Jayaram's (2008) published survey instrument that has been utilised in developed economies) to Malaysian manufacturing companies. To gauge the relationship between the supplier involvement practices and new product development (NPD) project performance of 146 companies, structural equation modelling was adopted. Our findings prove that supplier involvement practices have a significant positive impact on NPD project performance in an emerging economy with respect to quality objectives, design objectives, cost objectives, and "time-to-market" objectives. Further analysis using the Bayesian Markov Chain Monte Carlo algorithm, yielding a more credible and feasible differentiation, confirmed these results (even in the case of an emerging economy) and indicated that these practices have a 28% impact on variance of NPD project performance. This considerable effect implies that supplier involvement is a must have, although further research is needed to identify the contingencies for its practices.

## 1. Introduction

The drive to improve product development efficiency and effectiveness, as well as to utilise suppliers' technological capabilities, is the main motive for early supplier involvement [1]. The importance of early supplier involvement, or supplier integration into new product development (NPD), has been emphasised in various research works [1–13]. Previous studies have revealed that supplier integration leads to significant improvements in NPD processes in terms of development time, cost, and quality [2, 6–8, 14–16]. For example, Cousineau et al. [17] reported that implementation of supplier integration in product development led to positive results such as enabling the supplier to meet the required

timeline, providing the supplier better knowledge of the customer's needs, and enhancing customer-supplier relationships. Hence, there is little doubt that supplier involvement during NPD is beneficial for time-to-market, quality, and cost.

Although the empirical evidence found by previous studies indicates that supplier involvement leads to positive outcomes in terms of new product development performance, that finding is not necessarily valid for firms in emerging economies. It is presumed that these economies lack manufacturing and innovative capabilities [18, 19]. Looking back at the studies mentioned so far, those have often taken place in mature economies or developed nations, such as the USA [2, 3, 12], the UK [10], Denmark [1], and Germany [20].

An exception would be the case of China, which has drawn attention from academics looking into innovation practices [21–25]. However, this might mean that China is a specific case from which findings might have restricted generalisation towards other emerging economies. Nevertheless, this implies that the role of supplier involvement practices in new product development is yet to be substantially investigated in the emerging economies other than China, which is the aim of our study.

The aim of the study fits with the growing trend amongst researchers to explore the relevance of existing theoretical perspectives in emerging economies [26–30]. With that same intention, we seek to explore the impact of supplier involvement practices on new product development performance in a developing economy, Malaysia. As a country that is moving “towards becoming more innovation driven” [31], its firms need to improve their new product development performance. Thus, there is a need to ascertain the level of supplier integration into new product development amongst Malaysian manufacturers and its impact on new product development performance, particularly because the manufacturing sector is still growing, while already contributing 27.5% to GDP in 2011 [32]. The objective of this research is to determine whether the positive relationship found between supplier involvement practices and new product development performance in developed economies is also valid in an emerging economy, using Malaysia as a case in point. To that purpose, this empirical study presents data and findings from a survey conducted in the manufacturing sector in Malaysia.

While studies of supplier involvement in new product development (NPD) have already taken place in generic terms related to innovation processes, fewer have taken the individual project as a starting point. Taking individual NPD projects as a starting point [2, 33, 34] could lead to more meaningful answers on performance than can be found by discussing this in more generic terms of relationships with suppliers, as is more commonly done [3, 6, 8, 35, 36]; ultimately, that should lead to less bias in the responses, allowing us to draw more definite conclusions. An instrument utilised in the developed economies (developed by Jayaram) [2] was used here to ascertain the validity of the findings in an emerging economy. In addition, a more robust research method has been used to analyse the data; the Bayesian approach allowed a more credible and feasible differentiation during the analysis. Hence, this paper not only investigates the specific practices of supplier involvement in Malaysian firms but also introduces a research method for this and future research on this topic.

The paper is organised as follows. Section 2 presents a review of the literature providing current insights into supplier involvement in the form of a narrative literature review, conforming to the guidelines of Green et al. [37]. Section 3 discusses the rationale for the methodology used, including the specific data analysis techniques, structural equation modelling in combination with a Bayesian Markov Chain Monte Carlo algorithm. This is followed by a discussion of results and a conclusion in the final section.

## 2. Literature Review

The beneficiary role of suppliers and purchasing as the linchpin for new product development has been recognised, as stated above, and links to theoretical perspectives. For example, the resource-based view focuses on the strategic importance of a firm’s resources and capabilities [3, 38, 39], although its propositions have been questioned [40, 41]. Referring to this theoretical perspective, Hart [42] turned to Porter’s model of competitive advantage and proposed a framework that placed the purchasing function as an essential capability of an organisation. In his framework, Hart linked the activities of purchasing to the organisation’s unique capabilities that are imperative in sustaining a competitive advantage. In other words, an effective purchasing function can help a firm to sustain its competitive advantage by selecting and appropriately working together with suppliers. As clearly highlighted by Ansari and Modarress [35], “an important area for purchasing and suppliers to be integrated is in the firm’s product development process.” Hence, the literature review focuses on the practices related to involving suppliers in new product development.

Collaboration between customer and supplier during new product development (NPD), better known as supplier integration or early supplier involvement (ESI), has been in existence for more than half a century [43]. However, it is only over the past twenty years that early supplier integration in NPD has gained much interest in academic literature [44], particularly, because supplier integration is highly influential in determining NPD performance in terms of productivity, quality, and cost [45]. As a case in point, Zirpoli and Caputo [46] studied an Italian car maker (Fiat) to explore codesign practices between Fiat and its suppliers and confirmed that supplier integration in the NPD process had benefited Fiat in achieving its NPD objectives. Furthermore, Fliess and Becker [47] studied twelve companies based in Germany and concluded that proficient coordination leads to successful supplier involvement in new product development. In addition, some other studies have confirmed the benefits of supplier involvement. Liker et al. [33] found that early supplier involvement in automobile suppliers led to cost saving and improved product quality and design. Carr and Pearson’s study [3] showed that early supplier involvement had a positive influence on firms’ financial performance. Handfield and Lawson [6] conducted a survey of 134 companies that revealed that supplier involvement practices improved the financial performance of the firm and product design. Therefore, the advantages of (early) supplier involvement during new product development have been broadly identified.

Recognising the need to identify the critical supplier involvement practices that lead to successful new product development (NPD), recent studies on supplier integration have focused on timing (at what stage of NPD suppliers are involved) and level of supplier integration (the depth of supplier involvement) [2]. In that regard, Mikkola and Skjoett-Larsen [1] conducted case studies in three Danish firms and pointed out that supplier integration can take place in different stages of new product development, based

on the technical complexity of the product. Prencipe [48] also links the involvement of suppliers with the complexity of the product and the relevance of components for the total product performance. Hence, the complexity of the product, the role of supplied components in the product configuration, and stages of development have a potential impact on modes of supplier integration. In that sense, Jayaram [2] found during a survey of 338 companies in high-tech industries in the USA that communication and information sharing, design participation, and infrastructure development through supplier integration could lead to positive NPD performance in the areas of product cost, conformance quality, design quality, and time-to-market. Parker et al. [44] also found these factors to have significant impact on NPD performance. Likewise, Wasti and Liker [43, 49] found that there was a positive relationship between product design improvement and frequency of design-related communication with supplier. In addition, Handfield and Lawson [6] and Peterson et al. [34] found that careful selection of suppliers prior to NPD commencement and involving suppliers in setting technical goals will determine NPD performance. McGinnis and Vallopora [36] also identified similar factors for new product success. Later, van Echtelt et al. [50] conducted an in-depth four-year case study of a Dutch company and pointed out that the success of supplier integration depends on a firm's ability to manage supplier involvement effectively, to capture both short- and long-term benefits. Therefore, the complexity of the product, the role of supplied components in the product configuration, and the stages of development are ubiquitously related to the interaction with suppliers, even though they have been separately treated in academic literature so far, despite all being related to beneficial outcomes for the NPD.

Even though a wide range of studies support the notion that supplier integration brings improvements in new product development (NPD), some have raised doubts about the effectiveness of supplier involvement. For example, an early study by Ittner and Larcker [51] highlighted that supplier integration had a negative impact on NPD by increasing product development lead times. However, the researchers did acknowledge that the result could be due to insufficiencies in their measures and suggested that research on the impact of supplier involvement practices on new product performance should be conducted in different settings, noting that this would make a substantial contribution to the study of best practices in new product development. McIvor and Humphreys' [10] study of an electronic firm and its suppliers in the UK found the presence of barriers in supplier integration in the NPD process and concluded that, for early supplier involvement to be successful, there is a need for supplier and buyer firms to increase joint problem-solving and decision-making, which actually points to communication and information sharing and strategic infrastructure, as proposed by Jayaram [2] and Parker et al. [44]. The word of caution is then that supplier involvement does not necessarily lead to beneficial outcomes for NPD, even though the majority of studies point in the other direction; the contingencies and conditions under which supplier integration and involvement are successful will need separate studies.

Another significant observation from the literature reviewed is that all studies on supplier involvement practices were conducted in countries from mature economies. None were conducted in countries from the emerging economies (excluding China). This validates the starting point of our study. Henceforth, there is a need for studies looking into supplier involvement in the setting of an emerging economy to ascertain whether supplier involvement practices lead to improved new product performance, just as has been proven in previous studies conducted in the mature economies.

In summary, the literature reviewed leads us to conclude that previous research focused on identifying interfirm collaborative practices (between suppliers and customers) that can positively influence NPD performance, mostly in matured economies. Few studies identified barriers and problems in supplier integration in NPD [10, 51], but these studies stressed the need to improve joint problem-solving and decision-making and suggested more studies in different settings to ascertain best practices in NPD. Amongst the supplier involvement practices identified as influencing NPD performance, the main emphasis has been on two interfirm collaborative practices, that is, communication and information sharing and strategic infrastructure [2, 16, 44]. Hence, to address this gap in the literature, this research attempts to determine whether these supplier involvement practices (communication and information sharing and strategic infrastructure) affect new product development project performance in terms of conformance with performance objectives in the setting of a developing economy. The following depicts the proposed conceptual framework of this study. The parameters derived in the framework are discussed in the following section.

### 3. Research Method

This is a confirmatory study regarding beneficial supplier involvement practices during new product development conducted in an emerging economy, specifically in the Malaysian manufacturing sector. The Malaysian manufacturing sector contributed 27.5% to GDP in 2011 [32]. Small, emerging economies such as Malaysia need to increase their competitive advantage through advances in innovation, technology, and value addition. This can transform a "low value assembly line to one that is driven by innovation" [52]. Innovation relates to new product development performance. As previous studies in developed countries have shown that supplier involvement leads to positive outcomes in terms of new product development performance, this study intends to ascertain the impact of supplier involvement practices on new product development performance in a developing economy: Malaysia.

Jayaram [2] provides a survey instrument for this objective. The constructs used in our study were taken from his study to measure supplier involvement practices: communication and information sharing and strategic infrastructure (Table 1). In addition, the constructs used to measure individual NPD project performances (Table 2) are quality, design, cost, and time-to-market objectives; these are commensurate

TABLE 1: The variables manifesting supplier involvement practices.

Variable label	Variable description
C1	Participation of key suppliers in NPD team
C2	Direct communication with key suppliers
C3	Shared design knowledge with key suppliers
C4	Common linked information systems (EDI, CAD/CAM)
C5	Shared education and training programs with key suppliers
C6	Colocation of project personnel and key suppliers

TABLE 2: The variables manifesting project performance.

Variable label	Variable description
E1	Conformance to quality objectives set
E2	Conformance to design objectives set
E3	Conformance to cost objectives set
E4	Conformance to “time-to-market” targets set

with other studies like those of Ragatz et al. [53] and Johnsen [54]. These constructs in the survey instrument replicate the ones used by Jayaram [2] in his study of 338 companies in high-tech industries in the USA; this will allow a direct comparison of findings.

**3.1. Survey Instrument.** Relevant sections of Jayaram’s published survey form [2] were slightly modified for use in this survey. A pilot study was conducted to fine-tune the survey form before distributing it to manufacturing firms throughout Malaysia. In the first section of the survey, the respondents were asked to denote the extent of supplier involvement practices used in new product development (where 0 means not used and 10 means used to a great extent). The supplier involvement practices are listed in Table 1. The first three items represented communication and information sharing while the next three items represented strategic infrastructure. In the second section of the survey, the respondents were requested to rate the level of NPD project performance in four different aspects (where 0 means significantly worse than expectations and 10 means significantly better than expectations). These measures of NPD project performance are listed in Table 2.

Since the unit of analysis was a new product development project, the questionnaire specified the desired respondent as a person (at executive level and above) from design/ engineering/quality/production/purchasing, who had been engaged in all stages of the project. The respondents were requested to answer the survey based on a new product development project concluded in the past three years for which they were either project leaders or project members.

**3.2. Data Collection.** The survey instrument was distributed using two channels. Questionnaires were distributed to managers from the manufacturing sector who attended training sessions at the Federation of Malaysian Manufacturers (FMM) Institute. This was augmented by questionnaires

that were distributed to the researchers’ contacts in the manufacturing sector. The administering of questionnaires was carefully done in order to ensure that only relevant respondents filled in the survey forms. After 12 weeks, the researchers had obtained a total of 168 responses. Of these 168, 22 were discarded due to noncompletion or 50% or above missing values. As a result, 146 responses were available for further analysis. Based on the sample size of 146, further analysis is viable.

**3.3. Data Analysis.** Because this is a confirmatory study conducted in an emerging economy, there is a need to apply a strong, robust methodology. The path diagram in Figure 1 depicts the conceptual framework developed to address the research objective of this paper. The path diagram indicates a causal relationship between supplier involvement practices and NPD project performance. To empirically gauge the extent of the relationship between supplier involvement practices and project performance, a series of techniques was introduced. These techniques are the reliability test, exploratory factor analysis (EFA), confirmatory factor analysis (CFA) and structural equation modelling (SEM). The reliability test is a measure of internal consistency of a summated scale of the variables manifesting the hypothetical concepts, the supplier involvement practices, and the NPD project performance (see Tables 1 and 2). These techniques have been supplemented by a Bayesian Markov Chain Monte Carlo algorithm to ensure that a robust method is utilised in the statistical analysis. It is noteworthy that, for reasons of robustness with respect to analysis, this approach has gained popularity in evolutionary biology [55–57] and to a lesser extent in econometrics [58, 59] and engineering [60]. Commensurate with the research objectives, the solid approach of combining a Bayesian method with more traditional SEM will allow us to draw more definite conclusions about the relationship between supplier involvement practices and new product development project performance.

This deviates from the research designs used for investigating supplier involvement practices so far, which include qualitative analysis [35, 46, 47], variance and means analysis [8, 36, 61], regression analysis [2, 6, 14, 33, 34], and sole SEM [3, 12, 44]. Hence, this confirms the unique and robust approach taken in our study as new to the domain.

## 4. Analysis of Results

The first step in the analysis is determining the reliability and consistency of the collected data. For that purpose, a recommended threshold of 0.7 for the reliability test depicts a meaningful manifestation of variables on their respective concepts [62, 63]. The reliability test was carried out using SPSS, a statistical software package by IBM. Results show, in Table 3, that “supplier involvement practices” have a Cronbach’s alpha of 0.882 while “NPD project performance” has 0.928. Both concepts are well above the 0.7 threshold and therefore have internal consistency amongst the variables in a summated scale. In short, it can be seen that the questionnaire

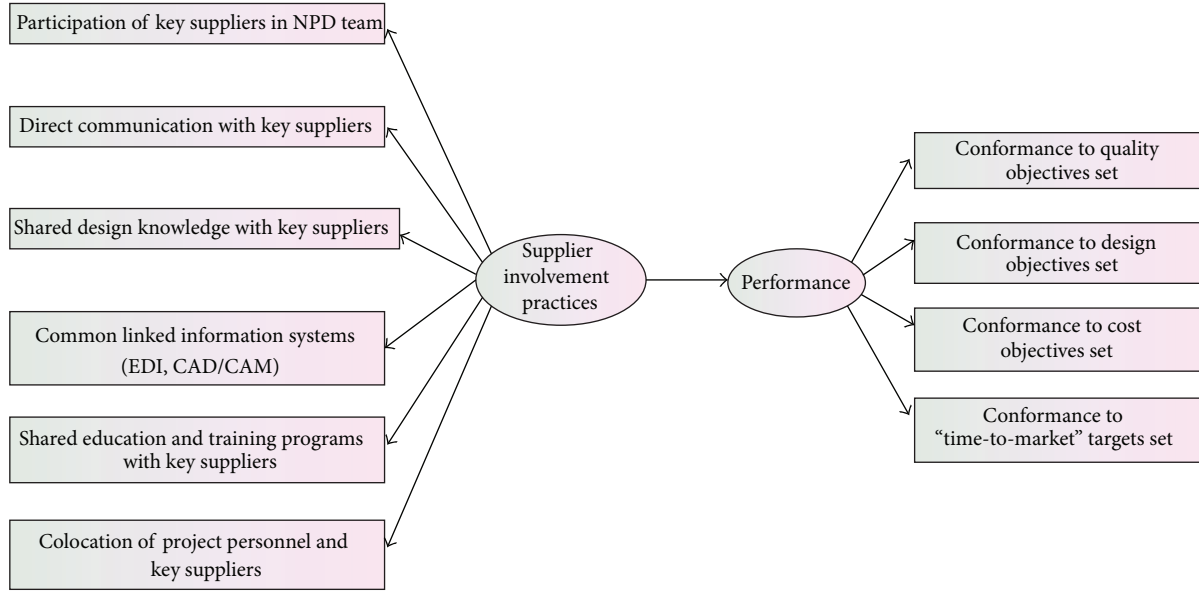


FIGURE 1: Shows the conceptual framework of supplier involvement practices.

is measuring the antecedents of the concept in a consistent and reliable way.

A next step in the analysis is the extraction of relevant factors. In that respect, exploratory factor analysis (EFA) is conducted to examine “possible relationships in only the most general form and then allows the multivariate technique to estimate relationships” [66, page 580]. Ultimately, the objective of EFA is to reduce the number of variables manifesting the hypothetical concepts into a manageable set of factors (see Table 4). It is recommended that factors are extracted using the principal component matrix (PCM) and rotated via Varimax. Two factors were extracted as they were clear factor structures, in the form of factor 1 (manifested by variables  $E1$ ,  $E2$ ,  $E3$ , and  $E4$ ) and factor 2 (manifested by variables  $C1$ ,  $C2$ , ...,  $C6$ ). Results from the Kaiser-Meyer-Olkin measure (0.842) and Bartlett’s Test ( $P$  value  $< 0.01$ ) show that the factors extracted have high correlation amongst manifesting variables. These highly correlated manifesting variables will enable clear factor structure detection.

**4.1. Factor Analysis.** This brings the analysis to the step of excavation of constructs. When conducting confirmatory factor analysis (CFA), also known as the measurement model, variables are assigned to manifest a specific factor, now called a *construct*. Variables with high factor loadings are chosen to manifest the construct. Factor loadings above 0.6 within the complex factor structures are the recommended threshold [64]. Based on Table 4, the confirmed variables manifesting the respective constructs are as follows: participation of key suppliers ( $C1$ ), direct communication with key suppliers ( $C2$ ), shared design knowledge with key suppliers ( $C3$ ), common linked information systems ( $C4$ ), shared education and training programmes with key suppliers ( $C5$ ) and co-location of project personnel and key suppliers ( $C6$ ) manifest supplier involvement practices, while conforming to quality objectives

( $E1$ ), design objectives ( $E2$ ), cost objectives ( $E3$ ), and “time-to-market” targets ( $E4$ ) manifest project performance.

From the results of CFA, a series of equations can be notated on the two constructs. In order to do so, let the measurement models of supplier involvement practices and project performance be defined by the vectors of observed variables, where  $C = (x_1, x_2, \dots, x_6)$  and  $E = (y_1, y_2, y_3, y_4)$ . Then let the general equation of the measurement models be given as

$$C = \Lambda_x \xi + \delta, \tag{1}$$

$$E = \Lambda_y \eta + \varepsilon, \tag{2}$$

where  $X$  and  $Y$  are the vectors of observed variables of the constructs  $C$  and  $E$ , respectively.  $\xi$  is the exogenous construct and  $\delta$  is the measurement error for the constructs (note  $E(\delta) = 0$ ) [65].  $\Lambda$  represents the regression weights between the observed variables and constructs. Equations (1) and (2) are general equations of the measurement model in SEM [66, 67]. Further corresponding equations for (1) could be written as follows:

Exogenous constructs

$$\begin{pmatrix} x_1 \\ x_2 \\ x_3 \\ x_4 \\ x_5 \\ x_6 \end{pmatrix} = \begin{pmatrix} \lambda_1^x \\ \lambda_2^x \\ \lambda_3^x \\ \lambda_4^x \\ \lambda_5^x \\ \lambda_6^x \end{pmatrix} \xi + \begin{pmatrix} \delta_1 \\ \delta_2 \\ \delta_3 \\ \delta_4 \\ \delta_5 \\ \delta_6 \end{pmatrix}. \tag{3}$$

TABLE 3: The reliability of supplier involvement practices and NPD project performance.

Concepts		Variables	Corrected item-total correlation	Cronbach's alpha
Supplier involvement practices	C1	Participation of key suppliers	0.638	0.882
	C2	Direct communication with key suppliers	0.769	
	C3	Shared design knowledge with key suppliers	0.826	
	C4	Common linked information systems (EDI, CAD/CAM)	0.585	
	C5	Shared education and training programs with key suppliers	0.679	
	C6	Co-location of project personnel and key suppliers	0.666	
NPD project performance	E1	Conformance to quality objectives set	0.874	0.928
	E2	Conformance to design objectives set	0.849	
	E3	Conformance to cost objectives set	0.807	
	E4	Conformance to "time-to-market" targets set	0.807	

TABLE 4: The factors extracted via principal component analysis and rotated via Varimax.

	Component	
	1	2
C1		0.642
C2		0.745
C3		0.851
C4		0.766
C5		0.714
C6		0.831
E1	0.918	
E2	0.877	
E3	0.856	
E4	0.868	

Endogenous construct

$$\begin{pmatrix} y_1 \\ y_2 \\ y_3 \\ y_4 \end{pmatrix} = \begin{pmatrix} \lambda_1^y \\ \lambda_2^y \\ \lambda_3^y \\ \lambda_4^y \end{pmatrix} \eta + \begin{pmatrix} \varepsilon_1 \\ \varepsilon_2 \\ \varepsilon_3 \\ \varepsilon_4 \end{pmatrix}. \quad (4)$$

Structural equation modelling (SEM) is a technique encompassing structure analysis, latent variable analysis, confirmatory factor analysis, path analysis, and linear structural relation analysis [66, page 584]. SEM consists of the structural model and measurement model (CFA). The former is made up of a "set of one or more dependence relationships linking the hypothesized model's constructs" [66, page 583]. Subsequent to CFA, SEM is conducted to analyse a series of interdependent regression equations simultaneously. Its ability in simultaneous estimation of regression equations makes it the most suitable analysis for this research. In order

to mathematically correspond to the structural model, let the general equation of the structural model be given as

$$\eta = \gamma\xi + \zeta, \quad (5)$$

where  $\gamma$  is the associations between the exogenous constructs ( $\xi$ ) and endogenous construct ( $\eta$ ).  $\zeta$  is the measurement error for the concept ( $\eta$ ) as shown in Figure 2 (note  $E(\zeta) = 0, \beta\eta = 0$ ) [65]. The figure shows the causal relationships between the structural and measurement models given in (1) and (5). Based on the equations, the structural model is therefore notated as

$$\eta = \lambda_{1,1}\xi + \zeta. \quad (6)$$

Based on the results in Figure 2, (6) can be simplified to:

$$\eta = 0.53\xi. \quad (7)$$

Referring to Figure 2, the results show that the model is estimated with a chi-square of 38.024 and degrees of freedom of 34. These results represent an overidentified model. The chi-square  $P$ -value of the model is reported at 0.291, indicating that the model has a good fit. The absolute fit measure is good, as RMSEA is 0.067 (below the 0.08 threshold). The results imply that the model fits the variance-covariance matrix. Incremental fit measures are also good, with both Incremental Fit Index (IFI) and Tucker-Lewis Index (TLI) reported at 0.977 and 0.968 (above the 0.90 threshold). These results indicate that the model is robust and met the requirements of a good model. There is good model parsimony, since the chi-square/degrees of freedom ( $\chi^2/df = 1.118$ ) is between 1 and 2. This result suggests that the model is estimated without overfitting it with too many parameters. The model also depicts that supplier involvement practices explain 28% of total variance of NPD project performance; this constitutes a major finding of the analysis.

4.2. Bayesian Estimation. While in general the model has achieved overall goodness of fit measures, to further substantiate the results of fit indices a Bayesian estimation is

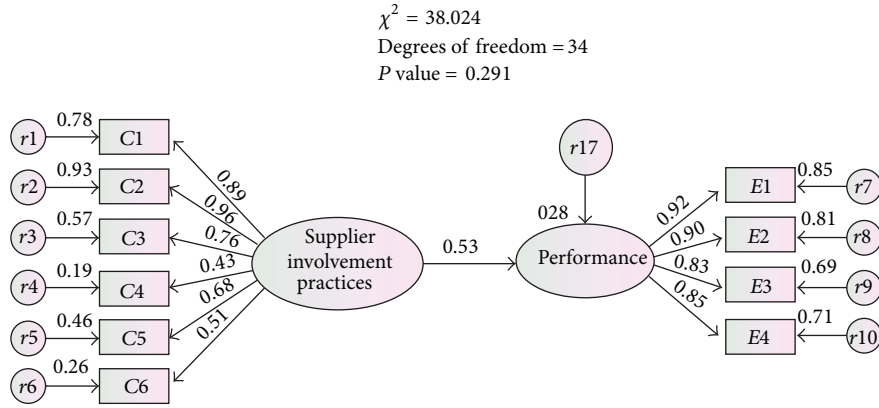


FIGURE 2: Shows the results of SEM. Note: results are depicted in standardized estimates.

conducted to investigate the robustness of the findings (both the association and the 28% of total variance of NPD project performance). The Bayesian estimation approach is useful when applied to models estimated using maximum likelihood estimation (MLE) in SEM, where the measurement models in the structural model are latent in nature. Furthermore, this approach is very useful when the sample size is small, which is the case for the 146 responses to the survey. In this paper the Bayesian estimation approach is used to substantiate the SEM model validation of substantive theory (via hypotheses shown earlier) that uses stringent MLE and  $\chi^2$  estimation procedures [68]. The Bayesian approach, unlike MLE, looks at the parameter estimates as variables that then diffuse the posterior distribution from mean, median, and mode. For that purpose, the Bayesian approach on the SEM model is computed via the Markov Chain Monte Carlo (MCMC) algorithm. It is hoped that the Bayesian SEM (BSEM) can estimate results that are more reflective of the substantive theories.

The computational efforts in this paper are done using SPSS AMOS, a statistical software package from IBM. The BSEM MCMC algorithm computed by AMOS diffuses the posterior distribution through the drawing of random values of parameters that are viewed as variables [59]. The posterior mean values are estimated based on the averages of drawn analysis samples generated by MCMC. Based on the SEM model, AMOS drew 74,500 analysis samples from the dataset and discarded 500 burn-in samples from the 74,500 analysis samples to allow a clearer estimation of the posterior distribution of the *supplier involvement practices*  $\rightarrow$  *NPD project performance*. The MCMC BSEM estimation via AMOS uses a random number seed where the model is simulated on a range of random numbers invoked by the respective seed.

From the analysis samples drawn, the posterior distribution is present in Figure 3; this figure depicts the similarity between the first and last thirds of the analysis samples in the posterior distribution. This invariably suggests that the features of the posterior distribution of *supplier involvement practices*  $\rightarrow$  *NPD project performance* are clearly identified. The posterior mean of *supplier involvement practices*  $\rightarrow$  *NPD project performance* appears to be approximately 0.38, which

is rather similar to the nonstandardised regression weights (0.37) of the path diagram. In short, the generated posterior mean could be generated into (5), where we contrast both models as follows:

$$\eta = 0.37\xi + \zeta, \tag{8}$$

$$\eta = 0.38\xi + \zeta, \tag{9}$$

where (8) is the structural model based on unstandardised  $\gamma$  while (9) is the BSEM MCMC model based on posterior mean.

The min-max threshold of the posterior distribution is between 0.150 and 0.689. This suggests that the *supplier involvement practices*  $\rightarrow$  *NPD project performance* association is always positive, also implying evidential support that the true value of the parameter is larger than zero and hence supporting the literature; this is also consistent with the SEM results.

The trace plot shown in Figure 4 suggests that the resonating patterns of *supplier involvement practices*  $\rightarrow$  *NPD project performance* converged between the threshold of 0.150 and 0.689. The plot also depicts the consistency of the resonating pattern. There are some spikes, approximately at iterations 15,000 and 57,000. However these spikes were not regular and did not affect the convergence of the distribution.

The autocorrelation plot in Figure 5 depicts the convergence that took place when the MCMC method was deployed. The correlation between the drawn samples started to decay to 0.50 at around lag-17 and the autocorrelation coefficient is close to 0 in lag-90 henceforth. At this point, convergence to the posterior distribution is achieved, indicating that the 500-burn-in drawn samples previously mentioned were more than adequate [59]. More specifically, the convergence of posterior distribution for the BSEM is 1.005 and the posterior predictive *P*-value is 0.001. In short, when convergence happened at lag-90, the posterior summaries of the distribution stabilised, implying that the initial samples drawn no longer correlate with the samples drawn last. Based on these results the posterior mean converged, which is approximately similar to the nonstandardised regression weights, portraying an excellent predictive value to the association between supplier involvement practices and NPD project performance.

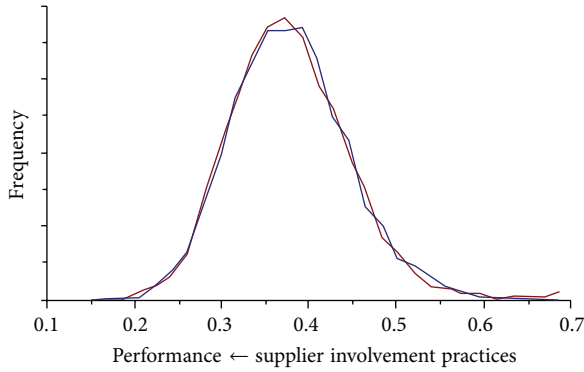


FIGURE 3: The posterior distribution of the first and last thirds of the drawn analysis samples of *supplier involvement practices* → *NPD project performance*. Note: Blue depicts post-convergence posterior distribution and red pre-convergence posterior distribution.

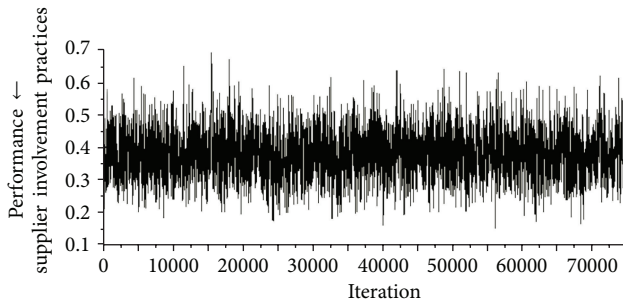


FIGURE 4: Shows the trace plot of *supplier involvement practices* → *NPD project performance*.

We define the total variance ( $R^2$ ) of *NPD project performance* as the square of the association between *supplier involvement practices* and *NPD project performance* ( $\lambda$ ). Since the nonstandardised  $\lambda$  of the SEM model is similar to the posterior mean of *supplier involvement practices* → *NPD project performance*, we can deduce that the BSEM results confirm the extent of the impact of *supplier involvement practices* on *NPD project performance*. Furthermore, the BSEM simulation results also showed that there were no multicollinearity problems as the correlation between the two constructs was between 0.4 and 0.5 [69]. This finding was substantiated by the discriminant validity proposed by Fornell and Larcker [70], where both constructs were distinct. Based on this measure, the average variance extracted (AVE) of *supplier involvement practices* (0.5328) and *NPD project performance* (0.7674) were greater than the square of correlation between the two constructs (0.2767). Additionally, the AVE of these constructs showed convergent validity as they met the threshold of 0.5 and above [71].

## 5. Discussion of Findings

This study investigated the association between supplier integration practices and new NPD project performance within a sample of 146 companies in an emerging economy, Malaysia. We examined the association between key factors

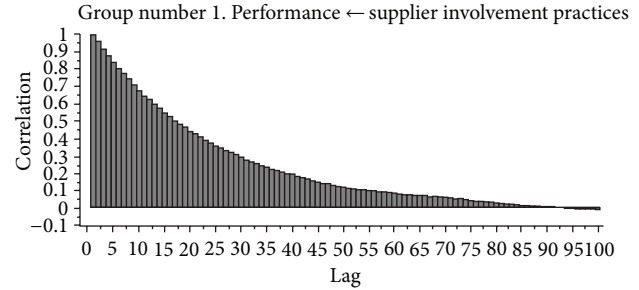


FIGURE 5: Shows the autocorrelation plot of *supplier involvement practices* → *NPD project performance*.

of *supplier involvement practices* (communication and information sharing, and development of strategic infrastructure) and *NPD project performance*. The project performance measures include conformance to quality objectives, design objectives, cost objectives, and “time-to-market” objectives set. We proposed that there is a positive association between *supplier involvement practices* and *NPD project performance*. Our results using SEM show that there is a positive association between *supplier involvement practices* and *NPD project performance*. Further analysis using a Bayesian MCMC algorithm confirmed that the *supplier involvement practices* → *NPD project performance* association is always positive, also implying evidential support that the true value of the parameter is larger than zero and hence supporting the literature.

The findings of this study are comparable with the study conducted by Jayaram [2] in the USA, a mature, developed economy. Jayaram’s large-scale study focused on 338 firms manufacturing high-tech products and was the first study to use *NPD project performance* measures, instead of firm performance or manufacturing performance measures, to assess the impact of *supplier involvement practices*. Jayaram found that communication and information sharing and developing strategic infrastructure were the two main *supplier integration* factors that positively influenced *NPD project performance*, measured in terms of product cost, conformance quality, design quality, and “time-to-market.” Our study confirmed the importance of communication and information sharing and developing strategic infrastructure in *NPD project performance*. In addition, our study did not specifically focus on firms producing high-tech products, as Jayaram’s study did, but considered all subsectors of the Malaysian manufacturing sector. Thus, the findings of this study can be generalised to the entire manufacturing sector in Malaysia and potentially to all emerging economies.

Despite our strong findings, research on *supplier involvement* is marred by contradictions. This study provides support for initial findings by Swink et al. [13] that *supplier involvement* reduced development time (in our study, this is part of time-to-market) in new product development projects. However, this contradicts findings by Trygg [72] and Ittner and Larcker [51] that showed that *supplier involvement* in *NPD* did not have substantial positive impact on development time. In our study, *supplier involvement practices*

had the least impact on time-to-market ( $E4$ ) but still had a significant positive impact.

More interestingly, our study has provided a figure for the impact of supplier involvement practices on the performance of new product development projects. Because of the reliability of the structural equation modelling (SEM) outcomes, the analysis shows that 28% of total variance of NPD project performance can be related to supplier involvement practices. The use of the Bayesian MCMC algorithm confirmed that the relationship between the two constructs is constantly positive. This indicates a relatively high impact of supplier involvement practices despite its controversies.

## 6. Concluding Remarks

Our findings proved that supplier involvement practices have a significant positive impact on NPD project performance in an emerging economy in the areas of quality objectives, design objectives, cost objectives, and “time-to-market” objectives; consistency with Jayaram’s study [2] confirms that supplier involvement practices have a positive impact on NPD performance in an emerging economy just as they do in mature, developed economies. Our research findings are also comparable and consistent with the findings of Clark [14], Gadde and Snehota [73], and Rubenstein and Ettlé [74].

*6.1. Practical Implications.* Stiff competition throughout the world has pushed firms to strive harder to produce high-quality, innovative products. This has been quite a challenge for firms in developing economies. Competition is no longer between firms—it is often suggested that competition is now between supply chains [75]. This study provides strong encouragement for firms in emerging economies to start early collaboration with suppliers in terms of communication and information sharing and strategic infrastructure development, to realise worthy improvements in terms of new product quality, design, cost, and “time-to-market.”

Indirectly, this research has also highlighted the potential role of the purchasing function in firms’ competitive position. During the analysis using structural equation modelling it emerged that supplier involvement practices account for 28% of total variance of NPD project performance; this is a significant number, even though it might depend on the complexity of products, the role of supplied components in the product configuration, and the stages of NPD. It is the purchasing function—not to be confused with a department per se—that needs to facilitate communication, information sharing, and development of a strategic infrastructure. Conversely, in reality, the indirect contributions of purchasing, in terms of product quality, innovation, and lead time, can be significant compared to direct contributions in terms of cost savings [45]. In that sense, the purchasing function has a noteworthy influence on manufacturing quality and new product development in addition to delivery and cost [76]. Our study confirms that the purchasing function has evolved to be a major contributor to organisational competitiveness, as Cavinato [77] notes.

*6.2. Further Research.* The model also indicates that supplier involvement practices explain 28% of total variance of NPD project performance. It was possible to extract this figure using the performance of individual projects as a differentiator for determining the impact of individual supplier involvement practices. Not only does this mean that manufacturing might benefit from this insight, but we also suggest that this research should be extended to the services sector, to investigate the impact of early supplier involvement on new service development. However, it also means that further research is needed to confirm this figure for both developed and emerging economies and for the services sector.

Furthermore, the literature review identified that separate studies are required to look into the contingencies and conditions under which supplier integration and involvement are successful. This should be positioned within Tidd’s [78] call for more integrated approaches to innovation management and Damanpour’s [79] plea for considering contingencies. Specifically, in the literature review, we have identified the complexity of the product, the role of supplied components in the product configuration, and stages of development as contingencies. Exploration of the factors influencing supplier integration into NPD will provide useful insights for practitioners in order to focus on the factors that have positive influence on supplier involvement practices. Hence, this study needs augmentation by research that explores the specific contingencies for supplier involvement practices to be most effective.

In any case, the survey instrument used in this research has proven to be a reliable tool for gauging the impact of supplier involvement practices on NPD project performance. The SEM algorithm proposed is also a feasible and practical approach to empirical measurement of the association of both constructs mentioned above. We believe that SEM MCMC provides a credible approach with which to substantiate associations in the structural model of SEM, especially as SEM incorporates stringent model testing and is very sensitive to large sample sizes. This study could be further improved should the sample size increase, as possible multigroup SEM analyses could then be conducted.

The limitation of this research is that the data relied on a single NPD’s project performance per firm. The respondents’ selection of NPD projects could have caused bias in the results, especially in terms of NPD project performance. Assessing NPD performance in general terms, as is commonly done [3, 6, 36, 61], leads to less specific outcomes. A possible extension of the research approach to cover more NPD projects per firm could overcome this but might be more challenging; again, multigroup SEM analyses might be useful in this matter.

*6.3. Conclusion.* Despite the need to search for contingencies and the limitations noted above, our study leaves little doubt regarding the positive impact of supplier involvement practices on NPD project performance. The role of facilitating communication, information sharing, and development of a strategic infrastructure as constituent components of supplier

involvement practices has also been confirmed. Hence, both researchers and practitioners could take this as a starting point for successful new product development projects.

### Conflict of Interests

The authors declare that there is no conflict of interests regarding the publication of the article.

### Acknowledgments

The authors acknowledge the financial support provided by the University of Malaya, Research Grant no. RG068-10SBS. The authors also thank Abdul Razak Ibrahim, Chua Hock Joo, and the Federation of Malaysian Manufacturers Institute for their assistance in data collection.

### References

- [1] J. H. Mikkola and T. Skjoett-Larsen, "Early supplier involvement: implications for new product development outsourcing and supplier-buyer interdependence," *Global Journal of Flexible Systems Management*, vol. 4, pp. 31–41, 2003.
- [2] J. Jayaram, "Supplier involvement in new product development projects: dimensionality and contingency effects," *International Journal of Production Research*, vol. 46, no. 13, pp. 3717–3735, 2008.
- [3] A. S. Carr and J. N. Pearson, "The impact of purchasing and supplier involvement on strategic purchasing and its impact on firm's performance," *International Journal of Operations and Production Management*, vol. 22, no. 9–10, pp. 1032–1053, 2002.
- [4] J. Dyer and W. Ouchi, "Japanese-style partnerships: giving companies a competitive edge," *Sloan Management Review*, vol. 35, pp. 51–63, 1993.
- [5] A. K. Gupta and W. E. Souder, "Key drivers of reduced cycle time," *Research Technology Management*, vol. 41, no. 4, pp. 38–43, 1998.
- [6] R. B. Handfield and B. Lawson, "Integrating suppliers into new product development," *Research Technology Management*, vol. 50, no. 5, pp. 44–51, 2007.
- [7] R. B. Handfield and C. Bechtel, "The role of trust and relationship structure in improving supply chain responsiveness," *Industrial Marketing Management*, vol. 31, no. 4, pp. 367–382, 2002.
- [8] R. B. Handfield, G. L. Ragatz, K. J. Petersen, and R. M. Monczka, "Involving suppliers in new product development?" *California Management Review*, vol. 42, no. 1, pp. 59–82, 1999.
- [9] C. Luo, D. N. Mallick, and R. G. Schroeder, "Collaborative product development: exploring the role of internal coordination capability in supplier involvement," *European Journal of Innovation Management*, vol. 13, no. 2, pp. 244–266, 2010.
- [10] R. McIvor and P. Humphreys, "Early supplier involvement in the design process: lessons from the electronics industry," *Omega*, vol. 32, no. 3, pp. 179–199, 2004.
- [11] M. A. M. Primo and S. D. Amundson, "An exploratory study of the effects of supplier relationships on new product development outcomes," *Journal of Operations Management*, vol. 20, no. 1, pp. 33–52, 2002.
- [12] G. L. Ragatz, R. B. Handfield, and K. J. Petersen, "Benefits associated with supplier integration into new product development under conditions of technology uncertainty," *Journal of Business Research*, vol. 55, no. 5, pp. 389–400, 2002.
- [13] M. L. Swink, J. C. Sandvig, and V. A. Mabert, "Customizing concurrent engineering processes: five case studies," *Journal of Product Innovation Management*, vol. 13, no. 3, pp. 229–244, 1996.
- [14] K. B. Clark, "Project scope and project performance: the effect of parts strategy and supplier involvement on product development," *Management Science*, vol. 35, pp. 1247–1263, 1989.
- [15] K. Imai, I. Nonaka, and H. Takeuchi, "Managing the new product development process: how Japanese companies learn and unlearn," in *The Uneasy Alliance: Managing the Productivity-Technology Dilemma*, R. H. Hayes, K. Clark, and Lorenz, Eds., pp. 337–375, 1985.
- [16] X. A. Koufteros, T. C. Edwin Cheng, and K.-H. Lai, "'Black-box' and 'gray-box' supplier integration in product development: antecedents, consequences and the moderating role of firm size," *Journal of Operations Management*, vol. 25, no. 4, pp. 847–870, 2007.
- [17] M. Cousineau, T. W. Lauer, and E. Peacock, "Supplier source integration in a large manufacturing company," *Supply Chain Management*, vol. 9, no. 1, pp. 110–117, 2004.
- [18] G. D. Bruton and Y. Rubanik, "Resources of the firm, Russian high-technology startups, and firm growth," *Journal of Business Venturing*, vol. 17, no. 6, pp. 553–576, 2002.
- [19] J. Li, D. Chen, and D. M. Shapiro, "Product innovations in emerging economies: the role of foreign knowledge access channels and internal efforts in Chinese firms," *Management and Organization Review*, vol. 6, no. 2, pp. 243–266, 2010.
- [20] K. E. Gruner and C. Homburg, "Does customer interaction enhance new product success?" *Journal of Business Research*, vol. 49, no. 1, pp. 1–14, 2000.
- [21] T. Feng, L. Sun, and Y. Zhang, "The effects of customer and supplier involvement on competitive advantage: an empirical study in China," *Industrial Marketing Management*, vol. 39, no. 8, pp. 1384–1394, 2010.
- [22] G. Q. Huang, J. Huang, and K. L. Mak, "Early supplier involvement in new product development on the internet: implementation perspectives," *Concurrent Engineering Research and Applications*, vol. 8, no. 1, pp. 40–49, 2000.
- [23] Y.-Y. Jiao, J. Du, R. J. Jiao, and D. L. Butler, "Operational implications of early supplier involvement in semiconductor manufacturing firms: a case study," *Journal of Manufacturing Technology Management*, vol. 19, no. 8, pp. 913–932, 2008.
- [24] A. K. W. Lau, "Supplier and customer involvement on new product performance: contextual factors and an empirical test from manufacturer perspective," *Industrial Management and Data Systems*, vol. 111, no. 6, pp. 910–942, 2011.
- [25] M. Lockstrom, J. Schadel, R. Moser, and N. Harrison, "Domestic supplier integration in the chinese automotive industry: the buyer's perspective," *Journal of Supply Chain Management*, vol. 47, no. 4, pp. 44–63, 2011.
- [26] G. D. Bruton, G. G. Dess, and J. J. Janney, "Knowledge management in technology-focused firms in emerging economies: caveats on capabilities, networks, and real options," *Asia Pacific Journal of Management*, vol. 24, no. 2, pp. 115–130, 2007.
- [27] X. Fu, C. Pietrobelli, and L. Soete, "The role of foreign technology and indigenous innovation in the emerging economies: technological change and catching-up," *World Development*, vol. 39, no. 7, pp. 1204–1212, 2011.

- [28] R. E. Hoskisson, R. A. Johnson, L. Tihanyi, and R. E. White, "Diversified business groups and corporate refocusing in emerging economies," *Journal of Management*, vol. 31, no. 6, pp. 941–965, 2005.
- [29] K. E. Meyer, "Asian contexts and the search for general theory in management research: a rejoinder," *Asia Pacific Journal of Management*, vol. 24, no. 4, pp. 527–534, 2007.
- [30] A. S. Tsui, "Contextualization in Chinese management research," *Management and Organization Review*, vol. 2, pp. 1–13, 2006.
- [31] X. Sala-i-Martin, "Global competitiveness report 2011–2012, 2011, Geneva," *World Economic Forum*, p. 29, 2011.
- [32] B. N. Malaysia, Quarterly bulletin, Bank Negara Malaysia, 2012.
- [33] J. K. Liker, R. R. Kamath, and S. N. Wasti, "Supplier involvement in design: a comparative survey of automotive suppliers in the USA, UK and Japan," *International Journal of Quality Science*, vol. 3, pp. 214–238, 1998.
- [34] K. J. Petersen, R. B. Handfield, and G. L. Ragatz, "Supplier integration into new product development: coordinating product, process and supply chain design," *Journal of Operations Management*, vol. 23, no. 3–4, pp. 371–388, 2005.
- [35] A. Ansari and B. Modarress, "Quality function deployment: the role of suppliers," *Journal of Supply Chain Management*, vol. 30, pp. 27–35, 1994.
- [36] M. A. McGinnis and R. M. Vallopra, "Purchasing and supplier involvement: issues and insights regarding new product success," *Journal of Supply Chain Management*, vol. 35, pp. 4–15, 1999.
- [37] B. N. Green, C. D. Johnson, and A. Adams, "Writing narrative literature reviews for peer-reviewed journals: secrets of the trade," *Journal of Chiropractic Medicine*, vol. 5, no. 3, pp. 101–117, 2006.
- [38] J. Barney, "Firm resources and sustained competitive advantage," *Journal of Management*, vol. 17, pp. 99–120, 1991.
- [39] B. Wernerfelt, "A resource-based view of the firm," *Strategic Management Journal*, vol. 5, pp. 171–180, 1984.
- [40] V. Mahnke, "The process of vertical dis-integration: an evolutionary perspective on outsourcing," *Journal of Management and Governance*, vol. 5, no. 3–4, pp. 353–379, 2001.
- [41] R. L. Priem and J. E. Butler, "Is the resource-based 'view' a useful perspective for strategic management research?" *Academy of Management Review*, vol. 26, no. 1, pp. 22–40, 2001.
- [42] S. L. Hart, "A natural-resource-based view of the firm," *Academy of Management Review*, pp. 986–1014, 1995.
- [43] S. N. Wasti and J. K. Liker, "Risky business or competitive power? supplier involvement in Japanese product design," *Journal of Product Innovation Management*, vol. 14, no. 5, pp. 337–355, 1997.
- [44] D. B. Parker, G. A. Zsidisin, and G. L. Ragatz, "Timing and extent of supplier integration in new product development: a contingency approach," *Journal of Supply Chain Management*, vol. 44, no. 1, pp. 71–83, 2008.
- [45] A. J. van Weele, "Purchasing and supply chain management: analysis," in *Planning and Practice*, Thomson Learning, London, UK, 3rd edition, 2002.
- [46] F. Zirpoli and M. Caputo, "The nature of buyer-supplier relationships in co-design activities: the Italian auto industry case," *International Journal of Operations and Production Management*, vol. 22, no. 12, pp. 1389–1410, 2002.
- [47] S. Fliess and U. Becker, "Supplier integration-controlling of co-development processes," *Industrial Marketing Management*, vol. 35, pp. 28–44, 2006.
- [48] A. Prencipe, "Technological competencies and product's evolutionary dynamics a case study from the aero-engine industry," *Research Policy*, vol. 25, no. 8, pp. 1261–1276, 1997.
- [49] S. Nazli Wasti and J. K. Liker, "Collaborating with suppliers in product development: A U.S. and Japan comparative study," *IEEE Transactions on Engineering Management*, vol. 46, no. 4, pp. 444–461, 1999.
- [50] F. E. A. van Echtelt, F. Wynstra, A. J. van Weele, and G. Duysters, "Managing supplier involvement in new product development: a multiple-case study," *Journal of Product Innovation Management*, vol. 25, no. 2, pp. 180–201, 2008.
- [51] C. D. Ittner and D. F. Larcker, "Product development cycle time and organizational performance," *Journal of Marketing Research*, vol. 34, no. 1, pp. 13–23, 1997.
- [52] D. Tanggapan, C. Geetha, R. Mohidin, and V. Vincent, "The relationship between economic growth and foreign direct investment in Malaysia: analysis based on location advantage theory," *Management*, vol. 1, pp. 24–31, 2011.
- [53] G. L. Ragatz, R. B. Handfield, and T. V. Scannell, "Success factors for integrating suppliers into new product development," *Journal of Product Innovation Management*, vol. 14, no. 3, pp. 190–202, 1997.
- [54] T. E. Johnsen, "Supplier involvement in new product development and innovation: taking stock and looking to the future," *Journal of Purchasing and Supply Management*, vol. 15, no. 3, pp. 187–197, 2009.
- [55] S. Cheon and F. Liang, "Bayesian phylogeny analysis via stochastic approximation Monte Carlo," *Molecular Phylogenetics and Evolution*, vol. 53, no. 2, pp. 394–403, 2009.
- [56] B. Mau, M. A. Newton, and B. Larget, "Bayesian phylogenetic inference via Markov chain Monte Carlo methods," *Biometrics*, vol. 55, no. 1, pp. 1–12, 1999.
- [57] B. Rannala, "Identifiability of parameters in MCMC Bayesian inference of phylogeny," *Systematic Biology*, vol. 51, no. 5, pp. 754–760, 2002.
- [58] A. Ansari, K. Jedidi, and S. Jagpal, "A hierarchical Bayesian methodology for treating heterogeneity in structural equation models," *Marketing Science*, vol. 19, no. 4, pp. 328–347, 2000.
- [59] J. Arbuckle, *Amos 18*, Amos Development Corporation, Crawfordville, Fla, USA, 2009.
- [60] X. Jiang and S. Mahadevan, "Bayesian structural equation modeling method for hierarchical model validation," *Reliability Engineering and System Safety*, vol. 94, no. 4, pp. 796–809, 2009.
- [61] L. M. Birou and S. E. Fawcett, "Supplier involvement in integrated product development: a comparison of US and European practices," *International Journal of Physical Distribution & Logistics Management*, vol. 24, pp. 4–14, 1994.
- [62] J. C. Nunnally, *Psychometric Theory*, McGraw-Hill, 1978.
- [63] B. W. Yap and K. W. Khong, "Examining the effects of customer service management (CSM) on perceived business performance via structural equation modelling," *Applied Stochastic Models in Business and Industry*, vol. 22, no. 5–6, pp. 587–605, 2006.
- [64] E. G. Carmines and R. A. Zeller, *Reliability and Validity Assessment*, vol. 17, SAGE Publications, 1979.
- [65] E. W. Anderson and C. Fornell, "Foundations of the American customer satisfaction index," *Total Quality Management*, vol. 11, no. 7, pp. S869–S882, 2000.
- [66] J. F. Hair, R. E. Anderson, R. L. Tatham, and W. C. Black, *Multivariate Data Analysis*, Prentice Hall International, New York, NY, USA, 5th edition, 1998.

- [67] K. W. Khong, "Service quality index: a study on Malaysian banks," *Contemporary Management Research*, vol. 5, pp. 109–124, 2009.
- [68] B. Muthén and T. Asparouhov, "Bayesian SEM: a more flexible representation of substantive theory," *Psychological Methods*, vol. 17, no. 3, pp. 313–335, 2012.
- [69] R. Grewal, J. A. Cote, and H. Baumgartner, "Multicollinearity and measurement error in structural equation models: implications for theory testing," *Marketing Science*, vol. 23, no. 4, pp. 519–629, 2004.
- [70] C. Fornell and D. F. Larcker, "Evaluating structural equation models with unobservable variables and measurement error," *Journal of Marketing Research*, pp. 39–50, 1981.
- [71] Y. S. Chen and C. H. Chang, "Greenwash and green trust: the mediation effects of green consumer confusion and green perceived risk," *Journal of Business Ethics*, pp. 1–12, 2012.
- [72] L. Trygg, "Concurrent engineering practices in selected Swedish companies: a movement or an activity of the few?" *The Journal of Product Innovation Management*, vol. 10, no. 5, pp. 403–415, 1993.
- [73] L.-E. Gadde and I. Snehota, "Making the most of supplier relationships," *Industrial Marketing Management*, vol. 29, no. 4, pp. 305–316, 2000.
- [74] A. H. Rubenstein and J. E. Ettlé, "Innovation among suppliers to automobile manufacturers: an exploratory study of barriers and facilitators," *R&D Management*, vol. 9, pp. 65–76, 1979.
- [75] J. H. Heizer and B. Render, *Operations Management*, Pearson, England, UK, 10th edition, 2011.
- [76] A. Das and R. Narasimhan, "Purchasing competence and its relationship with manufacturing performance," *Journal of Supply Chain Management*, vol. 36, pp. 17–28, 2000.
- [77] J. L. Cavinato, "Fitting purchasing to the five stages of strategic management," *European Journal of Purchasing and Supply Management*, vol. 5, no. 2, pp. 75–83, 1999.
- [78] J. Tidd, "Innovation management in context: environment, organization and performance," *International Journal of Management Reviews*, vol. 3, no. 3, pp. 169–183, 2001.
- [79] F. Damanpour, "Organizational complexity and innovation: developing and testing multiple contingency models," *Management Science*, vol. 42, no. 5, pp. 693–716, 1996.

## Research Article

# Three-Dimensional Temperature Distribution Produced by a Moving Laser Beam

R. Uyhan

Mathematics Department, University of Suleyman Demirel, 32260 Isparta, Turkey

Correspondence should be addressed to R. Uyhan; ramazanuyhan@sdu.edu.tr

Received 6 September 2013; Accepted 5 November 2013

Academic Editor: M. Montaz Ali

Copyright © 2013 R. Uyhan. This is an open access article distributed under the Creative Commons Attribution License, which permits unrestricted use, distribution, and reproduction in any medium, provided the original work is properly cited.

An axisymmetric laser beam, moving with constant speed, heats a thin infrared absorbing layer sandwiched between two plastic sheets. We use a simplified theoretical model to study the three-dimensional unsteady temperature field produced by the moving laser beam.

## 1. Introduction

High quality hard copy of electronically stored images can be produced by thermal dye diffusion printing [1]. Such copies are of near photographic quality and have been used in such diverse areas as medical imaging and credit card personalisation. A theoretical model of the laser induced thermal dye-diffusion process for a stationary axisymmetric laser was given by [2], based upon the ICI Imagedata L2T2 system as described by [3].

In the L2T2 system a thin  $2\ \mu\text{m}$  dye layer is sandwiched between a  $6\ \mu\text{m}$  layer of PET (polyethylene-tetrathalate) and a relatively thick receiver sheet of thickness  $40\ \mu\text{m}$ . Heat is supplied directly to the dye-coat layer by a laser (see Figure 1). A suitable infrared absorbing material such as substituted copper phthalocyanine is incorporated into the dye coat layer which absorbs radiation strongly at about  $800\ \text{nm}$  [3]. The dye therefore diffuses rapidly into the receiver sheet producing a small dye dot. The total amount of dye transferred depends on the temperature because the diffusion coefficient is known experimentally to be a sensitive function of temperature [4]. In the L2T2 system there is a thin barrier layer at the PET/dye layer interface which prevents dye diffusing into the PET film.

The required image is formed by a large number of small dye dots produced in the receiver sheet as the pulsed laser beam moves relative to the layered system. In [2] a simplified model of the thermal dye diffusion process was studied in

which the laser beam was fixed relative to the receiver sheet over the heating period typically  $100\ \mu\text{s}$ . The laser beam was then moved to the next pixel and the process was repeated and so on, producing a series of dots. It was assumed that there was no thermal interaction between adjacent pixels, so that we could consider the thermal dye diffusion process for a single typical pixel. In this case the time-dependent temperature and dye diffusion fields produced by the laser beam are axi-symmetric. A review of previous theoretical studies is given in [2, 5].

In practice the axisymmetric laser beam is moved continuously relative to the receiver sheet and is switched on and off in a periodic fashion, so that a series of dots is produced. In this situation both the temperature and the dye diffusion fields will depend on three space coordinates and time, so the task of finding the temperature and dye fields is more difficult. In this paper we will use a simple mathematical model to study the temperature field.

The temperature field produced by a Gaussian laser beam is of interest in other practical applications. Thus, for example, [6] studied the temperature field when the beam moves over the surface of a metal sheet of finite thickness, a study relevant to metal forming, while [7] studied the temperature field in a thin metal sheet, so that it could be assumed that the temperature was constant across it. In both these studies the beam had constant wattage and moved with constant speed, so that the temperature distribution took the form of a travelling wave.

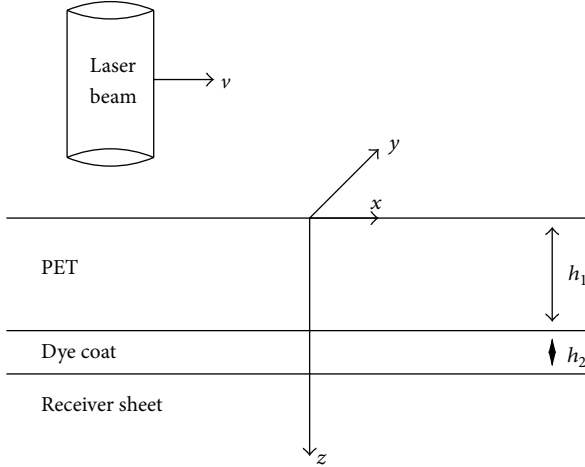


FIGURE 1: Illustration of the geometrical situation (not to scale).

In the present case the polymer layers have relatively low conductivity. As a consequence the receiver sheet of thickness  $40 \mu\text{m}$  can be regarded as infinitely thick for all practical purposes over the time scales of interest, but the finite thickness of the top  $6 \mu\text{m}$  PET layer, above the dye layer, has to be taken into account.

## 2. The Mathematical Model

Consider the layered system illustrated in Figure 1. The  $z$ -coordinate is measured into the layered system from the air interface which is situated at  $z = 0$ . The top (PET) carrier layer has thickness  $h_1$  and the dye-coat layer has thickness  $h_2$ . The receiver sheet is relatively thick (about  $40 \mu\text{m}$ ) and can be regarded as infinitely thick in practice. We take a frame of reference in which the polymer sheet is stationary and the laser beam is moved with constant speed  $v$  in the positive  $x$ -direction over the surface  $z = 0$ . We will assume that the axis of the laser is at  $x = 0, y = 0$  at time  $t = 0$ , so that at time  $\tau$ , its axis will be at  $x = v\tau, y = 0$ . It is assumed in this paper that the thermal properties of the three layers shown in Figure 1 have the same constant values.

Consider first the absorption of laser radiation by the infrared absorber in the dye-coat layer. Assuming that the distribution of the absorber is uniform, then the laser radiation flux per unit area,  $I(r, z, \tau)$  at time  $\tau$ , satisfies the differential equation:

$$\frac{\partial I}{\partial z} = -\frac{\lambda}{h_2} I, \quad (1)$$

for  $h_1 \leq z \leq h_1 + h_2$  where  $\lambda$  is a constant. The quantity which is measured experimentally is the optical density which equals  $\lambda/\ln 10$ . Assuming that the radial dependence of the radiation flux on  $z = h_1$  is Gaussian, it follows that, at time  $\tau$ ,

$$I(r, z, \tau) = I_0 \exp\left(-\frac{\lambda(z-h_1)}{h_2} - \frac{r^2}{r_0^2}\right), \quad (2)$$

where  $I_0$  depends on  $\tau$ ,  $r_0$  is a characteristic radius for the moving beam, and  $r^2 = (x - v\tau)^2 + y^2$ . The wattage of the beam  $W(\tau)$  is found by integrating  $2\pi r I(r, z, \tau)$  radially over the beam at  $z = h_1$ , and we find that  $W = \pi r_0^2 I_0$ . It follows that the laser energy absorbed per unit volume per unit time in the dye layer is

$$-\frac{\partial I}{\partial z} = \frac{W(\tau)\lambda}{\pi r_0^2 h_2} \exp\left(-\frac{\lambda(z-h_1)}{h_2} - \frac{r^2}{r_0^2}\right). \quad (3)$$

This is of course the largest at the top of the dye layer,  $z = h_1$ . We note that the total energy absorbed per unit area per unit time is

$$\frac{W}{\pi r_0^2} (1 - e^{-\lambda}) \exp\left(-\frac{r^2}{r_0^2}\right). \quad (4)$$

This is the largest when  $\lambda = \infty$ , in which case all the heat is generated in an infinitely thin layer at  $z = h_1$ .

Since, by assumption, the thermal properties have the same constant values in the three layers, we can construct the temperature field produced by the moving laser by combining instantaneous source solutions.

At time  $\tau$  and at  $z = z'$ , the laser beam generates a heat source distribution in the dye layer  $q(\tau, z') \exp(-r^2/r_0^2) dz' d\tau$  over a short time  $d\tau$  in a thin layer of thickness  $dz'$ .

Then from (3),

$$q(\tau, z') = \frac{W(\tau)\lambda}{\pi r_0^2 h_2} \exp\left[-\frac{\lambda(z'-h_1)}{h_2}\right]. \quad (5)$$

If the medium is infinite, has uniform properties, and has zero initial temperature, the temperature field for  $t > \tau$  is given by

$$G(x, y, z, t, z', \tau) = \frac{q(\tau, z') \gamma(u)}{2\rho c_p \sqrt{\pi\alpha u}} \exp\left[-\frac{(z-z')^2}{4\alpha u} - \frac{\gamma(u)r^2}{r_0^2}\right], \quad (6)$$

where  $u = t - \tau$ ,  $\gamma = r_0^2/(r_0^2 + 4\alpha u)$ ,  $\alpha$  is the thermal diffusivity,  $\rho$  is the density, and  $c_p$  is the specific heat.

The solution (6) satisfies the heat conduction equation

$$\frac{\partial G}{\partial t} = \alpha \left\{ \frac{\partial^2 G}{\partial z^2} + \frac{1}{r} \frac{\partial}{\partial r} \left( r \frac{\partial G}{\partial r} \right) \right\}. \quad (7)$$

As  $t \rightarrow \tau$ , we can see that  $G \rightarrow 0$ , except near  $z = z'$ , where it is large, and then (6) takes the approximate form

$$G \approx \frac{q(\tau, z')}{2\rho c_p \sqrt{\pi\alpha u}} \exp\left[-\frac{(z-z')^2}{4\alpha u} - \frac{r^2}{r_0^2}\right], \quad (8)$$

which is the corresponding "one-dimensional" heat source solution of

$$\frac{\partial G}{\partial t} = \alpha \frac{\partial^2 G}{\partial z^2} \quad (9)$$

(see, e.g., [8, 9]). If instead heat is produced throughout the dye-coat layer  $h_1 < z < h_1 + h_2$ , the corresponding temperature field  $T$  can be found by integrating the instantaneous heat source solution  $G$  with respect to  $z'$  from  $h_1$  to  $h_1 + h_2$  and with respect to  $\tau$  from  $-\infty$  to the current time  $t$ .

Thus we find that

$$T(x, y, z, t) = \int_{-\infty}^t \int_{h_1}^{h_1+h_2} \frac{q(\tau, z') \gamma(u)}{2\rho c_p \sqrt{\pi\alpha u}} \times \exp\left[-\frac{(z-z')^2}{4\alpha u} - \frac{\gamma(u)r^2}{r_0^2}\right] dz' d\tau, \quad (10)$$

where  $q(\tau, z')$  is defined in (5). This is the temperature field produced by a moving laser in an infinite medium initially at zero temperature.

In the real problem, the initial temperature is  $T_A$  and there is no heat flux at  $z = 0$ , the air-polymer interface. To incorporate this boundary condition into the model, we introduce an appropriate image heat source distribution in  $z < 0$ . Then by symmetry, there will be no heat flux across  $z = 0$ . The effect of this is to give, after some manipulation,

$$T - T_A = \int_{-\infty}^t \int_{h_1}^{h_1+h_2} \frac{q(\tau, z') \gamma(u)}{2\rho c_p \sqrt{\pi\alpha u}} \times f(z, z', u) \exp\left[-\frac{\gamma(u)r^2}{r_0^2}\right] dz' d\tau, \quad (11)$$

where

$$f(z, z', u) = \exp\left(\frac{-(z-z')^2}{4\alpha u}\right) + \exp\left(\frac{-(z+z')^2}{4\alpha u}\right). \quad (12)$$

In normal operation the laser beam is switched on and off in a periodic fashion. Assuming that the period is  $\tau_p$  and the laser is switched on for a time  $\tau_{on}$  and that when it is operating  $W = W_0$ , a constant, then we can take

$$W(\tau) = \begin{cases} W_0, & a(n) \leq \tau < b(n), \\ 0, & \text{otherwise,} \end{cases} \quad (13)$$

where  $a(n) = n\tau_p$ ,  $b(n) = \min(a(n) + \tau_{on}, t)$ , and  $n$  takes all integer values from  $-\infty$  to  $n = n^*$ , where  $a(n^*) \leq \tau < a(n^* + 1)$ . Thus

$$T - T_A = Q_0 \sum_{n=-\infty}^{n^*} \int_{a(n)}^{b(n)} \int_{h_1}^{h_1+h_2} \frac{\gamma(u)}{\sqrt{\pi\alpha\tau}} f(z, z', u) \times \exp\left[-\frac{\lambda(z' - h_1)}{h_2} - \frac{\gamma(u)r^2}{r_0^2}\right] dz' d\tau, \quad (14)$$

where  $u = t - \tau$ ,  $r^2 = (x - v\tau)^2 + y^2$ , and  $Q_0 = W_0\lambda/2\pi r_0^2 h_2 \rho c_p$ .

For the L2T2 system, typical values of physical parameters are  $v = 0.15$  m/s,  $\tau_p = 150 \mu\text{s}$ ,  $\tau_{on} = 100 \mu\text{s}$ ,  $\rho = 1.3 \times 10^3$  kg/m<sup>3</sup>,  $c_p = 1.9 \times 10^3$  J/kg·K,  $\alpha = 3.2 \times 10^{-8}$  m<sup>2</sup> s<sup>-1</sup>,  $h_1 = 6 \mu\text{m}$ ,  $h_2 = 2 \mu\text{m}$ ,  $W_0 = 75$  mW,  $r_0 = 15 \mu\text{m}$ ,  $\mu = 0.7$ ,  $\lambda = 1$ , and  $T_A = 20^\circ\text{C}$ .

### 3. Results and Discussion

The double integral (14) was evaluated using a standard NAG library routine. For the values of the parameters chosen, we found that the number of terms in the infinite series is small. This is because the axis of the beam passes over any given point in a time of order  $2r_0/v = 200 \mu\text{s}$ , which is comparable to the heating time  $\tau_{on} = 100 \mu\text{s}$ . Thus only a few laser pulses can affect the temperature at a given point.

Consider the temperature field at  $y = 0$  near  $x = 0$ . The axis of the laser passes over  $x = 0$  at time  $\tau = 0$ . However, the temperature field near  $x = 0$  will depend on the precise times when the laser was switched on and off. In our calculations we have assumed that the laser is switched on at  $\tau = 0, \pm\tau_p, 2 \pm \tau_p, \dots$ . In particular this means that the laser was turned off for  $-50 \mu\text{s} < \tau < 0$  if  $\tau_{on} = 100 \mu\text{s}$ , and consequently the maximum temperature in the dye coat layer cannot be at  $x = 0$ . Numerical calculation shows that the maximum temperature in the dye coat layer is near  $x = 2.5 \mu\text{m}$ , and hence our numerical results are shown for this value of  $x$ . The position of maximum temperature will depend on the parameter values chosen.

The  $z$ -temperature profile at various times for  $x = 2.5 \mu\text{m}$ ,  $y = 0$  is shown in Figure 2. It can be seen that the temperature rises between  $-100 \mu\text{s}$  and  $-50 \mu\text{s}$  but then falls until  $t = 0$  because the laser is turned off. The temperature then rises rapidly to about  $900^\circ\text{C}$  over the next  $100 \mu\text{s}$  because the laser is switched on at  $\tau = 0$ , and its axis is close to  $x = 2.5 \mu\text{m}$ . The laser is then turned off again and the temperature falls slowly to  $700^\circ\text{C}$  at  $t = 200 \mu\text{s}$ , as heat conducts upwards and downwards from the dye coat layer, with negligible heat input from the laser. This is shown in Figure 3.

The  $z$ -temperature profiles shown in Figures 2 and 3 are complicated mainly because they show that at least two laser pulses contribute significantly. These profiles are much more complicated than these for a stationary laser (see Figures 4 and 5) reproduced from our paper [2] for the same heating time. Note that the maximum temperature is about  $1000^\circ\text{C}$  in this case. This suggests that for these standard values, the process of dye diffusion is not well described by our stationary laser model. In general the maximum temperatures will be reduced as  $v$  increases from zero and so will be dye diffusion, which is a sensitive function of temperature.

The effect of an increase in the speed of the laser to  $0.5$  m/s is illustrated in Figures 6 and 7. As before, the laser is turned off at  $\tau = -50 \mu\text{s}$ , but now the laser beam axis is at  $v\tau = -25 \mu\text{m}$ . The heating before this time is therefore unimportant since  $x = 2.5 \mu\text{m}$  is well outside the laser beam. Note that we have chosen to show the  $z$ -temperature profiles at  $x = 2.5 \mu\text{m}$ , as in the standard case. The maximum temperatures will be at a slightly larger value of  $x$ .

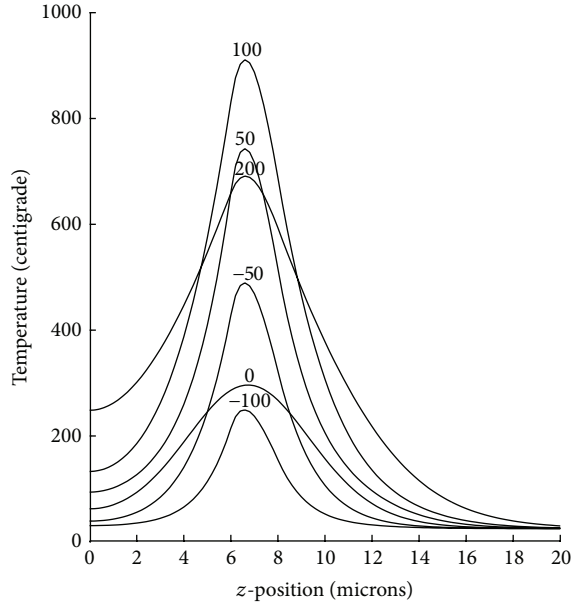


FIGURE 2: Temperature profiles on  $x = 2.5 \mu\text{m}$ ,  $y = 0$  as a function of  $z$  at times  $-100, -50, 0, 50, 100,$  and  $200 \mu\text{s}$ .

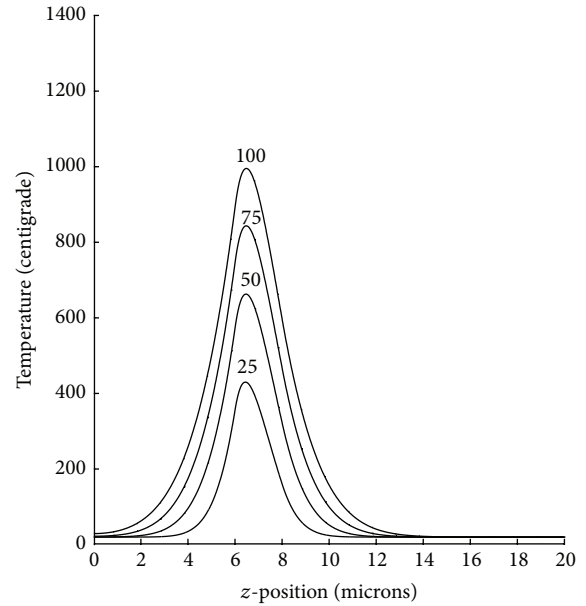


FIGURE 4: Temperature profiles on  $r = 0$  at times  $t = 25, 50, 75,$  and  $100 \mu\text{s}$  for a uniformly distributed absorber in the dye layer (heating phase). The laser is stationary.

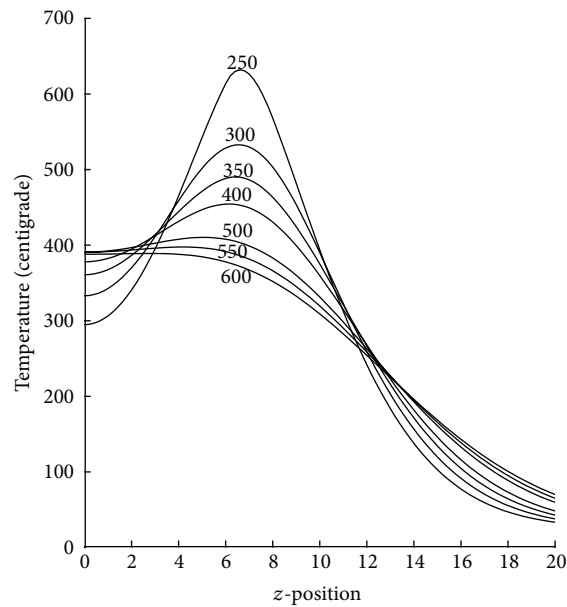


FIGURE 3: Temperature profiles on  $x = 2.5 \mu\text{m}$ ,  $y = 0$  as a function of  $z$  at times  $250, 300, 350, 400, 500, 550,$  and  $600 \mu\text{s}$ .

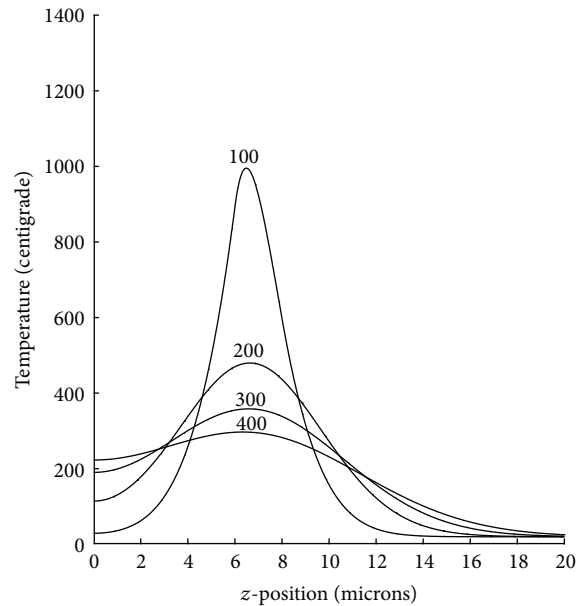


FIGURE 5: Temperature profiles on  $r = 0$  at times  $t = 100, 200, 300,$  and  $400 \mu\text{s}$  for a uniformly distributed absorber in the dye layer (cooling phase). The laser is stationary.

The laser is turned on at  $\tau = 0$  for  $100 \mu\text{s}$ , but for much of that time, little heating occurs at  $x = 2.5 \mu\text{m}$  since the laser beam has moved further to the right. Thus much lower temperatures of order  $400^\circ\text{C}$  are achieved at  $t = 50 \mu\text{s}$ . Figure 5 shows the typical cooling curves as heat conducts upwards and downwards from the dye coat layer. In Figure 8 the temperature profiles on  $y = 0, z = 7$  micro meter and  $v = 0.1 \text{ m/s}$  as a function of  $x$  for the different of time.

The diffusion coefficient will be much smaller at these lower temperatures, but there will be negligible interaction

with other pulses. Higher temperatures could of course be achieved by increasing the laser wattage.

#### 4. Conclusions

We have developed a simple theoretical model which allows us to calculate the  $z$ -temperature field in the dye coat layer produced by a moving laser beam. Our main conclusion is

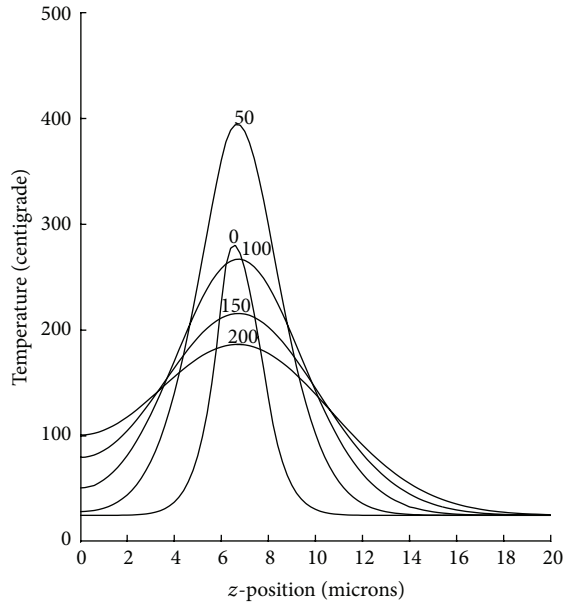


FIGURE 6: Temperature profiles on  $x = 2.5 \mu\text{m}$ ,  $y = 0$ , and  $v = 0.5$  as a function of  $z$  at times 0, 50, 100, 150, and 200  $\mu\text{s}$ .

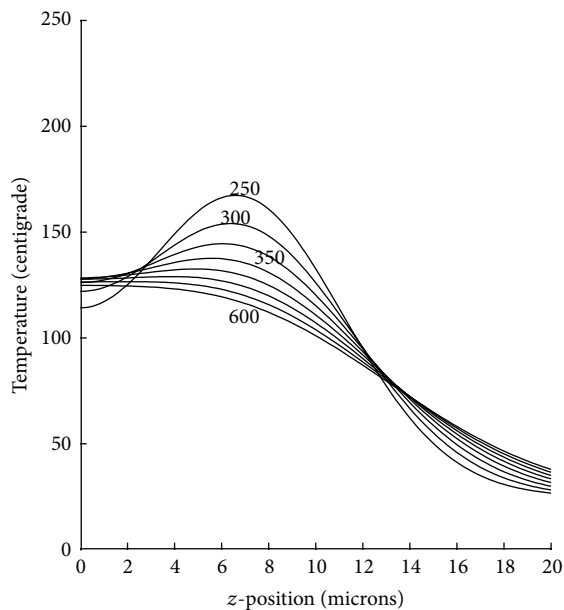


FIGURE 7: Temperature profiles on  $x = 2.5 \mu\text{m}$ ,  $y = 0$ , and  $v = 0.5$  as a function of  $z$  at times 250, 300, 350, 400, 450, 500, 550, and 600  $\mu\text{s}$ .

that, for the standard data, the temperature at a given point is significantly influenced by at least two pulses leading to a complicated  $z$ -temperature profile in the dye coat layer as time changes. This implies that the dye-diffusion process is much more complicated than that predicted by a stationary laser model.

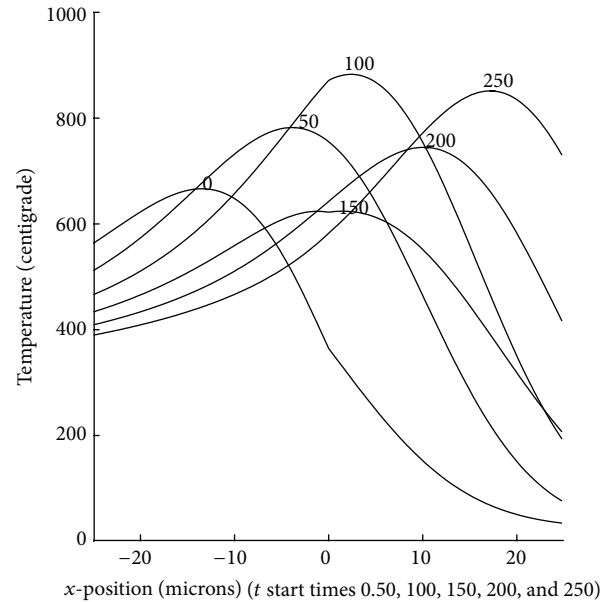


FIGURE 8: Temperature profiles on  $z = 7$ ,  $y = 0$ , and  $v = 0.1$  as a function of  $x$  at times 0, 50, 100, 150, 200, and 250  $\mu\text{s}$ .

## Nomenclature

- $C_p$  : Specific heat
- $h_1$  : Thickness of top melinex layer
- $h_2$  : Thickness of dye-coat layer
- $r_0$  : Radial length scale of laser beam
- $\alpha$  : A typical thermal diffusivity
- $t$  : Time
- $t'$  : Time at which heat source generated
- $G$  : Instantaneous heat source solution
- $T$  : Temperature
- $\rho$  : Density
- $T_A$  : Initial temperature
- $\tau$  : Time ( $t - t'$ )
- $v$  : Speed of laser beam
- $W_0$  : Wattage of laser
- $\mu$  : Optical density
- $\lambda$  :  $\mu \ln 10$ .

## Acknowledgments

The author wishes to thank Dr. Richard Hann and Dr. Ken Hutt of ICI Imagedata for introducing them to this problem and for providing representative data.

## References

- [1] R. A. Hann and N. C. Beck, "Dye diffusion thermal transfer (D2T2) color printing," *Journal of Imaging Technology*, vol. 16, pp. 238–241, 1990.
- [2] R. Uyhan and J. A. King-Hele, "Dye diffusion by laser heating," *Mathematical Engineering in Industry*, vol. 8, no. 4, pp. 275–292, 2002.

- [3] W. Hutt, I. R. Stephenson, H. C. V. Tran, A. Kaneko, and R. A. Hann, "Laser dye transfer," in *Proceedings of the IS & T 8th International Congress on Advances in Non-Impact Printing Technologies*, pp. 367–369, 1992.
- [4] N. C. Beck and R. A. Hann, "Thermal transfer printing project: measurement of the diffusion coefficients of dyes in a range of polyesters," ICI Imagedata report, 1986.
- [5] G. Araya and G. Gutierrez, "Analytical solution for a transient, three-dimensional temperature distribution due to a moving laser beam," *International Journal of Heat and Mass Transfer*, vol. 49, no. 21-22, pp. 4124–4131, 2006.
- [6] P. J. Cheng and S. C. Lin, "Analytical model for the temperature field in the laser forming of sheet metal," *Journal of Materials Processing Technology*, vol. 101, no. 1, pp. 260–267, 2000.
- [7] R. Brockmann, K. Dickmann, P. Geshev, and K.-J. Matthes, "Calculation of temperature field in a thin moving sheet heated with laser beam," *International Journal of Heat and Mass Transfer*, vol. 46, no. 4, pp. 717–723, 2003.
- [8] H. S. Carslaw and J. C. Jaeger, *Conduction of Heat in Solids*, Clarendon Press, Oxford, UK, 1946.
- [9] R. Uyhan and J. A. King-Hele, "Modelling of thermal printers," *Applied Mathematical Modelling*, vol. 32, no. 4, pp. 405–416, 2008.